Wireless Communications and Mobile Computing

Intelligent Sensing and Cognition of Electromagnetic Signals

Lead Guest Editor: Mingqian Liu
Guest Editors: Yunfei Chen and Ning Zhang

Intelligent Sensing and Cognition of Electromagnetic Signals

Wireless Communications and Mobile Computing

Intelligent Sensing and Cognition of Electromagnetic Signals

Lead Guest Editor: Mingqian Liu
Guest Editors: Yunfei Chen and Ning Zhang

Contents

Contents

Hindawi
Wireless Communications and Mobile Computing
Volume 2023, Article ID 2328249, 14 pages
https://doi.org/10.1155/2023/2328249

Research Article

Joint Optimization of Spectrum Resource Management and Position Placement for UAV Base Station Networks

Tianyao Zhong, Ducheng Wu, Guoxin Li, Haichao Wang, Runfeng Chen, and Jihao Cai

College of Communications Engineering, PLA Army Engineering University, Nanjing, China

Correspondence should be addressed to Ducheng Wu; wuducheng@foxmail.com

Received 7 August 2022; Accepted 6 October 2022; Published 27 April 2023

Academic Editor: Mingqian Liu

The unmanned aerial vehicle (UAV) base station plays a significant role in enhancing the terrestrial network, when the ground base station (GBS) is destroyed in emergent cases or its load exceeds the capacity of the terrestrial network. Presently, many papers focus on optimizing the UAV position deployment and user access, while ignoring the optimization about the spectrum resource management. To solve this problem, we formulate a joint optimization problem of the spectrum resource management and the position placement for UAVs with the constraint of the limited backhaul capacity. Later, the joint optimization problem is modeled as a hierarchical game decision architecture comprised of a UAV position placement game and a spectrum resource management game. Further, we analyze the equilibrium property of the two games and propose two best response- (BR) based optimization algorithms to reach the Nash Equilibriums (NEs) of the two games, respectively. Specifically, the proposed algorithm about the UAV deployment considers the variable granularity local exploration and global random exploration. Simulation results show that the proposed UAV deployment algorithm can improve the total throughput by 7% and 20% at least in comparison with the K-means deployment algorithm and the fixed granularity exploration algorithm, respectively.

1. Introduction

When the ground base station (GBS) is destroyed in emergent cases or when the data demand of users increases sharply, the excessive load will cause network congestion and reduce the quality of service for users. Due to the advantages such as high flexibility, reliable communication, and low cost, unmanned aerial vehicles (UAVs) are popularly used to help the terrestrial base station and are expected to be deployed in the next generation Wireless Communications Networks (WCNs) to enhance the communication and expand the coverage [1].

Presently, many papers investigate the UAV-assisted network, and the problem of UAV deployment and user access receives much attention [2–6]. The farther the UAV is from the base station, the lower the backhaul link capacity is, and the farther the UAV is from the user, the lower the UAV-user link capacity. The network throughput is the minimum value of the backhaul link capacity and the UAV-user link capacity, so the reasonable position placement helps the network achieve higher throughput. Because UAVs have different backhaul link capacities, reasonable user association can make the UAV with higher backhaul link capacity serve more users so as to make full use of UAV resources.

However, the management of spectrum resources is equally important [7] but has been neglected in related researches. Due to the limited spectrum resources and the increasing communication users, spectrum resources become scarce, and it becomes unavoidable for different communication users to use the same segment of spectrum resources at the same time. Although different communication users will interfere with each other when using the same spectrum resources, the intensity of interference depends on the transmission power and the distance between communication users. Therefore, the reasonable management of spectrum resources, that is to say allow users far from each other to use the same spectrum resource, can reduce the

interference among users in the network and improve the total throughput of the network. If the communication is maliciously interfered, the identification technology about interference signal is also essential [8, 9].

We investigate the joint optimization problem of the spectrum resource management and the position placement for UAV base stations. To simplify the optimization problem, the part about the UAV-user association is solved by a matching-based mechanism. While there are some challenges needing to overcome. Firstly, considering the decision optimization of multiple UAVs and multiple users, it is difficult to describe and analyze the influence between UAVs and users. Then, there is a coupling relationship between the optimization variable of the spectrum resource allocation and the UAV position. UAVs that use the same spectrum tend to be spaced far from each other, and UAVs that spaced far from each other tend to use the same spectrum. At last, the strategy space of the optimization problem is huge. If M UAVs and N users exist in the network, K channels can be used and the space size of discrete location of UAVs is I , then the space size of the joint strategy is $I^M K^N$. So the optimal solution is hardly to obtain by a search method.

To solve the challenge of multiuser optimization, we model the joint optimization problem as a game model. Because the game theory is a theoretical tool often used in the multiagent decision making, and through a clever design, all agents can reach a Nash Equilibrium through the distributed optimization of agents, and the best solution to the optimization problem is often a Nash Equilibrium (NE) [10–17]. To solve the challenge of the coupling relationship between optimization variables, we adopt a hierarchical optimization framework. We use the inner and outer layer structure instead of the upper and lower layer structure to improve the network performance. To solve the challenge of huge strategy space, we propose two best response- (BR- [18]) based optimization algorithms to optimize the spectrum resource management and the UAV position, respectively.

Our paper's main contributions are the following:

(i) In the network assisted by the UAV base station, the problem of spectrum resource management in non-orthogonal channel is considered, and the spectrum resource management and UAV position placement are jointly optimized

(ii) The above joint optimization problem is modeled as a hierarchical game decision architecture comprised of a UAV position placement game and a spectrum resource management game, and both the two games are proved to be exact potential games (EPGs) [19]

(iii) Two BR-based optimization algorithms are proposed to optimize the spectrum resource management and the UAV position, respectively. Simulation are conducted to show that the proposed UAV deployment algorithm can improve the total throughput by 7% and 20% at least in comparison with the K-means [20] deployment algorithm and the fixed granularity exploration algorithm, respectively

2. Related Work

The UAV deployment has been extensively investigated because UAVs have faster deployment speed, lower cost, and larger coverage in comparison with terrestrial base station UAVs [21–23]. In [21], the authors proposed a multi-UAV coverage model and investigated the multi-UAV deployment considering energy efficiency. The authors in [22] considered the minimum average UAV-user distance as the quality of coverage, and the UAVs were deployed in a distributed way without global information. A new framework to predict the traffic in hot spots for the UAV deployment in wireless networks was proposed in [23]. The problem of UAV-user association in UAV-assisted networks is addressed in [24–26]. In [24], the authors maximized users' QoE jointly optimizing the UAV position placement, caching deployment, and user access. In [25], the authors considered a UAV communicating with the sensors along the way in wireless sensor networks (WSNs) and considered that ground sensors converged data on several head nodes and got the head nodes to communicate with the UAV to improve the data transmission efficiency. The authors in [26] jointly optimized the UAV 3D deployment and user access to improve users' satisfaction.

However, the papers mentioned did not consider the impact of UAV backhaul links in the study of UAV deployment. Therefore, some authors made a further study considering the constraint of backhaul links [27–33]. [27] investigated the 3D deployment of a single UAV in two different networks to serve as many users as possible and maximize the sum-rates of the network. [28] investigated the UAV deployment in a post-disaster scenario and proposed an algorithm based on artificial bee colony to deploy the UAV. The authors in [29] proposed an efficient heuristic algorithm with lower computational complexity to address the resource management problem and used a search algorithm to determine the UAV location. The authors in [30] investigated a scenario using a UAV-network to replace the terrestrial backhaul network and proposed a heuristic approach to address the access problem and a genetic algorithm to deploy the UAVs. The authors in [31] considered the in-band wireless backhaul and proposed an novel method to optimize the user access and UAV deployment. Then the authors made a further study proposing a novel framework to optimize the network throughput with consideration of fairness among the users in [32]. In [33], the authors proposed a decentralized deployment algorithm to decrease the average distance between the UAVs and users, and this algorithm could be applicable to large-scale. While none of the above papers [27–33] investigated the spectrum resource management about users' channel selection and almost all papers fail to consider users sharing the same channel. Thus, the above researches cannot meet the increasingly access requirement of users.

3. System Model and Problem Formulation

3.1. Network Model. As shown in Figure 1, there is a GBS, multiple UAVs, and multiple ground users (GUs) in the

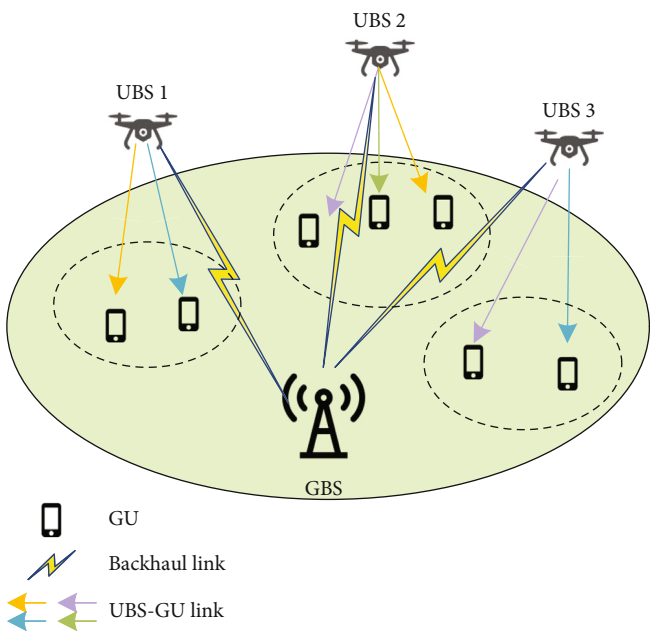

Figure 1: System model.

network. It is assumed that GUs cannot be served by the GBS directly due to a large path loss caused by the blockage. The UAVs are deployed to provide wireless communication service for GUs and have a backhaul link with the GBS. The sets of the UAVs and GUs are denoted as $\mathscr{M} = \{1, 2, 3, \cdots, M\}$ and $\mathscr{N} = \{1, 2, 3, \cdots, N\}$, respectively. The ground locations of the GBS, UAVs, and GUs are denoted by $\mathrm{w}_0 = (x_0, y_0)^T$, $\mathrm{s}_i = (x_i, y_i)^T, \forall i \in \mathscr{M}$, and $\mathrm{w}_j = (x_j, y_j)^T, \forall j \in \mathscr{N}$, respectively. The UAVs are assumed to be deployed at a fixed altitude h. The altitude of the GBS and GUs is negligible. The mobility of the GUs is assumed to be low and the GUs' locations are seemed as unchanged during the placement update process of the UAVs.

3.2. Channel Model. According to [34], UAVs communicate with ground users in a line-of-sight (LoS) transmission link and a non-line-of-sight (NLoS) transmission link. For convenience, we denote the GBS and UAVs set as $\mathscr{N}^0 = \mathscr{N} \cup \{0\}$, and 0 is used to denote the GBS. Then, the probability of LoS between the UAVs and the GBS or between the UAVs and the GUs is denoted by

$$P_{ij}^{\mathrm{LOS}} = \frac{1}{1 + a \exp\left(-b\left[\theta_{ij} - a\right]\right)}, i \in \mathscr{M}, j \in \mathscr{N}^0, \tag{1}$$

where a and b are environment impact factors which are related to the density, height of buildings, and street width, etc., $\theta_{ij} = \tan^{-1}(\|\mathbf{s}_i - \mathbf{w}_j\|_2 / h)$ and $\|\cdot\|_2$ denotes the 2-norm. Furthermore, the probability of NLoS is denoted by $P_{ij}^{\mathrm{NLOS}} = 1 - P_{ij}^{\mathrm{LOS}}$.

Hence, the average pathloss [32] is expressed as

$$PL_{ij} = \left(\frac{4\pi f_c d_{ij}}{c_0}\right)^2 \left(P_{ij}^{\mathrm{LOS}} \eta_{LOS} + P_{ij}^{\mathrm{NLOS}} \eta_{NLOS}\right), \tag{2}$$

where $d_{ij} = \sqrt{\|\mathbf{s}_i - \mathbf{w}_j\|_2^2 + h^2}$, f_c, c_0, η_{LOS}, and η_{NLOS} are the carrier frequency, speed of light, and average additional losses for LoS and NLoS links, respectively.

The UAVs use different channels to communicate with the GBS, and the channel bandwidth is B_0. Therefore, the backhaul rate of UAV i is expressed as

$$R_{i0} = B_0 \log_2\left(1 + \frac{P_{BS}/PL_{i0}}{\sigma^2}\right), i \in \mathscr{M}, \tag{3}$$

where P_{BS} is the transmission power of the GBS and σ^2 is the variance of the additive white Gaussian noise.

The channel set used by the UAVs to communicate with the GUs is denoted as $\mathscr{K} = \{1, 2, 3, \cdots, K\}$. The channel bandwidth is B_1. Every GU can access a UAV at most, and should be assigned only one channel after access. Each channel should only be assigned once at most by every UAV. Limited by hardware conditions, each UAV can serve up to L GUs at the same time. The GUs served by different UAVs can use the same channel, but there will be interference. Hence, the rate of GU j received from UAV i on channel k is written as

$$R_{ijk} = z_{ijk} B_1 \log_2\left(1 + \frac{P_{UAV}/PL_{ij}}{\sum_{i' \in \mathscr{M} \setminus \{i\}} \sum_{j' \in \mathscr{N}} P_{UAV}/PL_{i'j'} z_{i'j'k} + \sigma^2}\right), \tag{4}$$

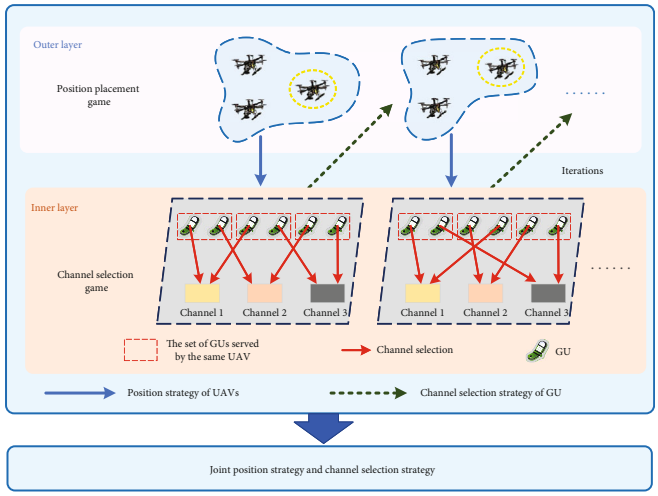

Figure 2: Hierarchical game decision architecture.

where P_{UAV} is the transmission power of the UAV, and $z_{ijk} \in \{0, 1\}$ is a binary association indicator variable for UAV i, GU j, and channel k and 1 indicates that UAV i communicates with GU j in channel k.

3.3. Problem Formulation. The backhaul rate of the UAVs is closely related to the UAVs' locations, and choosing which UAV and channel to access also affects the GUs' communication rate. Hence, to improve the throughput of the entire network, we optimize the locations of the UAVs and the channel selections of the GUs. The problem is modeled in the following:

$$\mathrm{P}: \max_{\mathbf{s}_i, Z_{ijk}} \sum_{i \in \mathscr{M}} \sum_{j \in \mathscr{N}} \sum_{k \in \mathscr{K}} R_{ijk}, \tag{5a}$$

$$\text{subject to} \sum_{i \in \mathscr{M}} \sum_{k \in \mathscr{K}} z_{ijk} \leq 1, \forall j \in \mathscr{N}, \tag{5b}$$

$$\sum_{j \in \mathscr{N}} z_{ijk} \leq 1, \forall i \in \mathscr{M}, \forall k \in \mathscr{K}, \tag{5c}$$

$$\sum_{j \in \mathscr{N}} \sum_{k \in \mathscr{K}} z_{ijk} \leq L, \forall i \in \mathscr{M}, \tag{5d}$$

$$\sum_{j \in \mathscr{N}} \sum_{k \in \mathscr{K}} R_{ijk} \leq R_{i0}, \forall i \in M, \tag{5e}$$

$$z_{ijk} \in \{0, 1\}, \forall i \in \mathscr{M}, \forall j \in \mathscr{N}, \forall k \in \mathscr{K}. \tag{5f}$$

In this optimization problem, constraint (5b) indicates that each GU should access one UAV and one channel at most. Constraint (5c) represents that each channel should only be assigned once at most by every UAV. Constraint (5d) indicates that each UAV can serve up to L GUs at the same time. At last, constraint (5e) requires that each UAV's backhaul rate is greater than the total communication rate of the users they served, respectively.

4. Hierarchical Game Decision Architecture

Game theory has been widely used in multiagent decision making, and when there are multiple optimization variables, the problem is usually modeled as a hierarchical game decision architecture [10, 12, 26]. Similarly, a hierarchical game decision architecture is proposed to optimize the spectrum resource management and UAV position placement jointly. The schematic diagram of the hierarchical game decision architecture is shown in Figure 2. The UAV position placement game is in the outer layer, while the spectrum management game is in the inner layer.

When the UAVs choose a new position strategy in the outer game, the UAV-user association strategy corresponding to the new position strategy will be obtained through a mechanism based on matching theory. Then according to the position strategy and the UAV-user association strategy, UAVs constantly update their channel selection strategy for users they serve until they reach an NE of the inner game. Further, the channel selection strategy is outputted to the outer game, and the UAVs calculate their payoffs in the outer game. At last, the UAVs decide whether to update the position strategy based on the payoffs and start the next new position update process until they reach an NE of the outer game.

The mechanism used to decide the UAV-user association is described as follows:

(1) Users prefer to be served by the nearest UAV. So each user applies to access to its nearest UAV

(2) Adhering to the principle of first application, first service, UAVs also tend to serve the closer user. Each UAV agrees to the user's application under the limit of the number of access and rejects unwanted applications

(3) The remaining rejected users continue to apply to access to the nearest UAVs that have not rejected them until all the users have accessed UAVs, or all UAVs have accessed the maximum number of UAVs

4.1. Inner Game: Spectrum Resource Management Game. The inner game is expressed as $\mathscr{G}_1 = \{\mathscr{N}_1, \mathscr{K}, \{c_j\}_{j\in\mathscr{N}_1}, \{v_j\}_{j\in\mathscr{N}_1}\}$. $\mathscr{N}_1$ is the set of GUs served by the UAVs. $\mathscr{K} = \{1, 2, 3, \cdots, K\}$ is the channel set. $\{c_j\}_{j\in\mathscr{N}_1}$ and $\{v_j\}_{j\in\mathscr{N}_1}$ are the channel selection strategy and payoff of GU j, respectively. Because users who use the same channel will interfere with each other, and if the interference decreases, the throughput of the network will increase. The inner game is modeled as a bilateral symmetric interaction game [35], and the payoff of GU j is defined as the negative sum of the interference it received from other UAVs and the interference it caused to other users [36].

Therefore, the payoff of GU j is expressed as

$$v_j(c_j, c_{-j}) = -\sum_{j'\in\mathscr{N}_1\setminus\{j\}} \left(I_{j,j'}(c_j, c_{j'}) + I_{j',j}(c_{j'}, c_j)\right), \tag{6}$$

where c_{-j} is the channel access selection of the GUs in set $\mathscr{N}_1$ except GU j, and $I_{j,j'}(c_j, c_{j'})$ denotes the interference received by GU j from GU j'. $I_{j,j'}(c_j, c_{j'})$ is defined as

$$I_{j,j'}(c_j, c_{j'}) = \delta_{j,j'}(c_j, c_{j'}) \frac{P_{UAV}}{PL_{\mu(j')j}}, \tag{7}$$

where $\mu(j')$ is the UAV access selection of GU j', and $\delta_{j,j'}(c_j, c_{j'})$ is boolean variable which denotes the interference situation between GU j and j'. $\delta_{j,j'}(c_j, c_{j'})$ is defined as

$$\delta_{j,j'}(c_j, c_{j'}) = \begin{cases} 1, & c_j = c_{j'}, \\ 0, & c_j \neq c_{j'}. \end{cases} \tag{8}$$

Then, the game $\mathscr{G}_1$ is expressed as

$$(\mathscr{G}_1)\text{: maximize } v_j(c_j, c_{-j}), \forall j \in \mathscr{N}_1. \tag{9}$$

The important concept about Nash equilibrium is defined as follows:

Definition 1 (Nash Equilibrium [37]). A strategy profile $c^* = (c_1^*, \cdots, c_{N_2}^*)$ is a pure strategy NE if and only if no player can improve its payoff by changing its strategy unilaterally:

$$\begin{aligned} &v_j\left(c_j^*, c_{-j}^*\right) \geq v_j\left(c_j, c_{-j}^*\right), \\ &\forall j \in \mathscr{N}_1, \forall c_j \in \mathscr{K}, c_j \neq c_j^*, \end{aligned} \tag{10}$$

where $\{c_j\}_{j\in\mathscr{N}_1}$ and $\{v_j\}_{j\in\mathscr{N}_1}$ are the strategy and payoff of player j, respectively, and N_2 is the number of players in set $\mathscr{N}_1$.

Further, we define Exact Potential Game (EPG) in the following, which has several nice properties.

Definition 2 (Exact Potential Game [19]). A game is EPG if there is a potential function satisfying

$$\Phi\left(c_j^*, c_{-j}\right) - \Phi(c_j, c_{-j}) = v_j\left(c_j^*, c_{-j}\right) - v_j(c_j, c_{-j}), \forall j \in \mathscr{N}. \tag{11}$$

For an EPG, the most important properties are as follows:

(i) Every potential game has at least one pure strategy NE

(ii) Any global or local maxima of the potential function constitutes a pure strategy NE

Theorem 3. *The game $\mathscr{G}_1$ is an EPG and has at least one NE.*

Proof. The potential function of the outer game is constructed as

$$\Phi_1(c_j, c_{-j}) = -\frac{1}{2}\sum_{j_1\in\mathscr{N}_1}\sum_{j_2\in\mathscr{N}_1\setminus\{j_1\}} \left(I_{j_1,j_2}\left(c_{j_1}, c_{j_2}\right) + I_{j_2,j_1}\left(c_{j_2}, c_{j_1}\right)\right). \tag{12}$$

Firstly, we define a set as follows:

$$\mathscr{A}_{k,j} = \left\{j' \middle| z_{ij'k} = 1, i \in \mathscr{M}, j' \in \mathscr{N}_1 \setminus \{j\}, k \in \mathscr{K}\right\}, \tag{13}$$

which means the set of the GUs who use channel k except GU j. If an arbitrary GU j, $\forall j \in \mathscr{N}$, changes its channel from c_j to $\bar{c}_j$, only the interference between GU j and the GU in set $\mathscr{B}$ will change, where $\mathscr{B} = \mathscr{A}_{c_j,j} \cup \mathscr{A}_{\bar{c}_j,j}$.

Then, if GU j changes its channel selection from c_j to $\bar{c}_j$, the change of its payoff function is expressed as

$$\begin{aligned} v_j(\bar{c}_j, c_{-j}) - v_j(c_j, c_{-j}) = &-\sum_{j'\in\mathscr{B}} \left(I_{j,j'}(\bar{c}_j, c_{j'}) + I_{j',j}(c_{j'}, \bar{c}_j)\right) \\ &+ \sum_{j'\in\mathscr{B}} \left(I_{j,j'}(c_j, c_{j'}) + I_{j',j}(c_{j'}, c_j)\right). \end{aligned} \tag{14}$$

The change of potential function is expressed as

$$\begin{aligned} &\Phi_1(\bar{c}_j, c_{-j}) - \Phi_1(c_j, c_{-j}) \\ &= -\frac{1}{2}\sum_{j_1=j}\sum_{j_2\in\mathscr{B}} \left(I_{j_1,j_2}\left(c_{j_1}, c_{j_2}\right) + I_{j_2,j_1}\left(c_{j_2}, c_{j_1}\right)\right)\Big|_{z_{\mu(j)\bar{c}_j}=1} \\ &\quad - \frac{1}{2}\sum_{j_1\in\mathscr{B}}\sum_{j_2=j} \left(I_{j_1,j_2}\left(c_{j_1}, c_{j_2}\right) + I_{j_2,j_1}\left(c_{j_2}, c_{j_1}\right)\right)\Big|_{z_{\mu(j)\bar{c}_j}=1} \\ &\quad + \frac{1}{2}\sum_{j_1=j}\sum_{j_2\in\mathscr{B}} \left(I_{j_1,j_2}\left(c_{j_1}, c_{j_2}\right) + I_{j_2,j_1}\left(c_{j_2}, c_{j_1}\right)\right)\Big|_{z_{\mu(j)jc_j}=1} \\ &\quad + \frac{1}{2}\sum_{j_1\in\mathscr{B}}\sum_{j_2=j} \left(I_{j_1,j_2}\left(c_{j_1}, c_{j_2}\right) + I_{j_2,j_1}\left(c_{j_2}, c_{j_1}\right)\right)\Big|_{z_{\mu(j)jc_j}=1}. \end{aligned} \tag{15}$$

Because

$$\begin{aligned}
&\sum_{j'\in\mathscr{B}}\left(I_{j,j'}\left(\bar{c}_j,c_{j'}\right)+I_{j,j'}\left(\bar{c}_j,c_{j'}\right)\right)\\
&\quad=\frac{1}{2}\sum_{j_1=j}\sum_{j_2\in\mathscr{B}}\left(I_{j_1,j_2}\left(c_{j_1},c_{j_2}\right)+I_{j_2,j_1}\left(c_{j_2},c_{j_1}\right)\right)\Big|_{z_{\mu(j)\bar{c}_j}=1}\\
&\qquad+\frac{1}{2}\sum_{j_1\in\mathscr{B}}\sum_{j_2=j}\left(I_{j_1,j_2}\left(c_{j_1},c_{j_2}\right)+I_{j_2,j_1}\left(c_{j_2},c_{j_1}\right)\right)\Big|_{z_{\mu(j)\bar{c}_j}=1},\\
&\sum_{j'\in\mathscr{B}}\left(I_{j,j'}\left(c_j,c_{j'}\right)+I_{j,j'}\left(c_j,c_{j'}\right)\right)\\
&\quad=\frac{1}{2}\sum_{j_1=j}\sum_{j_2\in\mathscr{B}}\left(I_{j_1,j_2}\left(c_{j_1},c_{j_2}\right)+I_{j_2,j_1}\left(c_{j_2},c_{j_1}\right)\right)\Big|_{z_{\mu(j)c_j}=1}\\
&\qquad+\frac{1}{2}\sum_{j_1\in\mathscr{B}}\sum_{j_2=j}\left(I_{j_1,j_2}\left(c_{j_1},c_{j_2}\right)+I_{j_2,j_1}\left(c_{j_2},c_{j_1}\right)\right)\Big|_{z_{\mu(j)c_j}=1},
\end{aligned}\tag{16}$$

then the formula (15) is transformed as

$$\begin{aligned}
\Phi_1\left(\bar{c}_j,c_{-j}\right)-\Phi_1\left(c_j,c_{-j}\right)=&-\sum_{j'\in\mathscr{B}}\left(I_{j,j'}\left(\bar{c}_j,c_{j'}\right)+I_{j',j}\left(c_{j'},\bar{c}_j\right)\right)\\
&+\sum_{j'\in\mathscr{B}}\left(I_{j,j'}\left(c_j,c_{j'}\right)+I_{j',j}\left(c_{j'},c_j\right)\right).
\end{aligned}\tag{17}$$

Therefore,

$$\Phi_1\left(\bar{c}_j,c_{-j}\right)-\Phi_1\left(c_j,c_{-j}\right)=v_j\left(\bar{c}_j,c_{-j}\right)-v_j\left(c_j,c_{-j}\right).\tag{18}$$

Then, according to the definition 2, the inner game $\mathscr{G}_1$ is an EPG and has at least one NE [38]. This completes the proof. □

4.2. Outer Game: Position Deploy Game. The outer game is expressed as $\mathscr{G}_2=\{\mathscr{M},\{\mathrm{s}_i\}_{i\in\mathscr{M}},\{u_i\}_{i\in\mathscr{M}}\}$. $\mathscr{M}=\{1,2,3,\cdots,M\}$ is the UAV set. s_i is the position of the UAV i. u_i is the payoff of the UAV i.

Because the marginal contribution [21] can well reflect the influence of the UAV's position strategy on the global optimization objective, u_i is defined as UAV i's marginal contribution to the overall network throughput and is given as

$$u_i(\mathrm{s}_i,\mathrm{s}_{-i})=\sum_{i\in\mathscr{M}}\sum_{j\in\mathscr{N}}\sum_{k\in\mathscr{K}}R_{ijk}(\mathrm{s}_i,\mathrm{s}_{-i})-\sum_{i\in\mathscr{M}}\sum_{j\in\mathscr{N}}\sum_{k\in\mathscr{K}}R_{ijk}(\mathrm{s}_i,\mathrm{s}_{-i})\big|_{\mathrm{s}_i=\varnothing},\tag{19}$$

where $R_{ijk}(\mathrm{s}_i,\mathrm{s}_{-i})|_{\mathrm{s}_i=\varnothing}$ is the communication rate without deploying the UAV i and $\mathrm{s}_{-i}=(\mathrm{s}_1,\cdots,\mathrm{s}_{i-1},\mathrm{s}_{i+1},\cdots,\mathrm{s}_M)$.

Then, game $\mathscr{G}_2$ is expressed as follows:

$$(\mathscr{G}_1):\ \text{maximize}\ u_i(\mathbf{s}_i,\mathbf{s}_{-i}),\forall i\in\mathscr{M}.\tag{20}$$

Theorem 4. *The game $\mathscr{G}_2$ is an EPG and has at least one NE.*

Proof. The potential function of the outer game is constructed as

$$\Phi_2(\mathrm{s}_i,\mathrm{s}_{-i})=\sum_{i\in\mathscr{M}}\sum_{j\in\mathscr{N}}\sum_{k\in\mathscr{K}}R_{ijk}(\mathrm{s}_i,\mathrm{s}_{-i}).\tag{21}$$

If UAV i, $\forall i\in\mathscr{M}$, changes its position from s_i to $\bar{\mathrm{s}}_i$, then the change of its payoff function is expressed as

$$\begin{aligned}
&u_i(\bar{s}_i,s_{-i})-u_i(s_i,s_{-i})\\
&\quad=\sum_{i\in\mathscr{M}}\sum_{j\in\mathscr{N}}\sum_{k\in\mathscr{K}}R_{ijk}(\bar{s}_i,s_{-i})-\sum_{i\in\mathscr{M}}\sum_{j\in\mathscr{N}}\sum_{k\in\mathscr{K}}R_{ijk}(\bar{s}_i,s_{-i})\big|_{s_i=\varnothing}\\
&\qquad-\sum_{i\in\mathscr{M}}\sum_{j\in\mathscr{N}}\sum_{k\in\mathscr{K}}R_{ijk}(s_i,s_{-i})+\sum_{i\in\mathscr{M}}\sum_{j\in\mathscr{N}}\sum_{k\in\mathscr{K}}R_{ijk}(s_i,s_{-i})\big|_{s_i=\varnothing}\\
&\quad=\sum_{i\in\mathscr{M}}\sum_{j\in\mathscr{N}}\sum_{k\in\mathscr{K}}R_{ijk}(\bar{s}_i,s_{-i})-\sum_{i\in\mathscr{M}}\sum_{j\in\mathscr{N}}\sum_{k\in\mathscr{K}}R_{ijk}(s_i,s_{-i}),
\end{aligned}\tag{22}$$

where $R_{ijk}(\bar{s}_i,s_{-i})|_{s_i=\varnothing}$ is equal to $R_{ijk}(s_i,s_{-i})|_{s_i=\varnothing}$.

The change of potential function is expressed as

$$\Phi_2(\bar{\mathrm{s}}_i,\mathrm{s}_{-i})-\Phi_2(\mathrm{s}_i,\mathrm{s}_{-i})=\sum_{i\in\mathscr{M}}\sum_{j\in\mathscr{N}}\sum_{k\in\mathscr{K}}R_{ijk}(\bar{s}_i,s_{-i})-\sum_{i\in\mathscr{M}}\sum_{j\in\mathscr{N}}\sum_{k\in\mathscr{K}}R_{ijk}(s_i,s_{-i}).\tag{23}$$

Therefore,

$$\Phi_2(\bar{\mathrm{s}}_i,\mathrm{s}_{-i})-\Phi_2(\mathrm{s}_i,\mathrm{s}_{-i})=u_i(\bar{s}_i,s_{-i})-u_i(s_i,s_{-i}).\tag{24}$$

Then, according to the definition 2, the inner game $\mathscr{G}_2$ is an EPG and has at least one NE [38]. This completes the proof. □

Remark 5. Both game $\mathscr{G}_1$ and game $\mathscr{G}_2$ are potential games with at least one NE. The physics significance of potential function Φ_1 is the negative sum of the total interference in network and the physics significance of potential function Φ_2 is the throughput of the entire network. Due to the important properties of an EPG, the best NE of $\mathscr{G}_1$ is the channel strategy with the minimum interference of the entire network and the best NE of $\mathscr{G}_2$ is the position strategy of the UAVs with maximum throughput of the entire network based on the game theory.

Remark 6. When the UAV position strategy is inputted to game $\mathscr{G}_1$ from game $\mathscr{G}_2$, UAVs start to update their channel selection strategies until they reach the corresponding NE of game $\mathscr{G}_1$. Then, the channel selection strategy is outputted to game $\mathscr{G}_2$ and UAVs update their positions. After multiple iterations, UAVs reach an NE of game $\mathscr{G}_2$.

4.3. Solution Approach. We propose two BR-based algorithms to optimize the spectrum resource management and the UAV position placement, respectively. If the finial channel selection strategy and the finial UAV position strategy do not satisfy constraint (5e), there are many heuristic methods to reduce the UAV transmission power to solve the problem, such as dichotomy.

4.3.1. BR-Based Channel Selection Algorithm. The details of channel selection algorithm are shown in Algorithm 1. Every time the UAVs choose a new position strategy in game $\mathscr{G}_2$, Algorithm 1 will be executed to produce the corresponding

Initialization:

(1) Input the UAV position strategy from Algorithm 2 and decide the UAV-user association by the mechanism based on matching theory

(2) All UAVs randomly assign channels to the GUs. The initial channel allocated to GU j is denoted as $c_j(0), \forall j \in \mathcal{N}_1$

(3) Set the iteration time $n_1 = 1$ and the max iteration time N_1

While$n_1 \leq N_1$:

(4) Update $c_j(n_1) = c_j(n_1 - 1), \forall j \in \mathcal{N}_1$

(5) Randomly select a UAV i. The set of channels used by UAV i is denoted as $\mathcal{C}_i$. The maximum number of GUs which UAV i allows to update the channel selection during the same time is denoted as $m \coloneqq \mathrm{Card}(\mathcal{K}) - \mathrm{Card}(\mathcal{C}_i)$, where $\mathrm{Card}(\mathcal{K})$ means the number of elements in the set $\mathcal{K}$. Randomly select no more than m GUs from the GUs served by GU i to update the channel selection

(6) UAV i randomly assigns different channels from set $\mathcal{K} \setminus \mathcal{C}_i$ to the above selected GUs

(a) Assume that GU j updates its channel selection and its probable new channel selection is $\bar{c}_j$

(b) Calculate payoff $v_j(c_j(n_1), c_{-j})$ and $v_j(\bar{c}_j, c_{-j}(n_1))$ according to formula (6)

(c) If $v_j(\bar{c}_j, c_{-j}) > v_j(c_j(n_1 - 1), c_{-j})$, update $c_j(n_1) = \bar{c}_j$.

(7) Update $n_1 = n_1 + 1$

End loop.

Output: The UAV-user association and channel selection strategy Z.

Algorithm 1: BR-based channel selection algorithm.

Initialization:

(1) Initialize the UAV position as $\mathrm{s}_i(0), \forall i \in \mathcal{M}$

(2) Set iteration times $n_2 = 1$ and max iteration times N_2

While$n_2 \leq N_2$:

(3) Update $\mathrm{s}_i(n_2) = \mathrm{s}_i(n_2 - 1), \forall i \in \mathcal{M}$

(4) Execute Algorithm 1 within position strategy $\mathrm{s}(n_2) = (\mathrm{s}_1(n_2), \cdots, \mathrm{s}_M(n_2))$, then receive the corresponding the UAV-user association and channel selection strategy Z, where $Z \in \{0, 1\}^{M \times N \times K}$, $z_{ijk} = [Z]_{i,j,k}$

(5) Randomly select a UAV i. Calculate UAV i's payoff $u_i(\mathrm{s}_i(n_2), \mathrm{s}_{-i}(n_2))$ according to formula (19)

(6) UAV i explores 8 positions near the position $s_i(n_2)$

(a) The current position explored is denoted as $\bar{s}_i \coloneqq (\bar{x}_i, \bar{y}_i)$ where $\bar{x}_i \in \{x_i + \Delta, x_i, x_i - \Delta\}$, $\bar{y}_i \in \{y_i + \Delta, y_i, y_i - \Delta\}$, and $\bar{s}_i \neq s_i$

(b) Execute Algorithm 1 within position strategy $\bar{s} = (\bar{s}_i, s_{-i}(n_2))$, then receive the corresponding the UAV-user association and channel selection strategy Z

(c) Calculate UAV i's payoff $\bar{u}_i(\bar{s}_i, s_{-i}(n_2))$ according to formula (19)

(d) If $\bar{u}_i(\bar{s}_i, s_{-i}(n_2)) > u_i(s_i(n_2), s_{-i}(n_2))$, update $s_i(n_2) = \bar{s}_i$ and jump to step (9), else keep exploring other locations

(7) Randomly select a position $\bar{s}_i$ throughout the mission area, do the same process as step (4) and (5), then calculate the payoff $\bar{u}_i(\bar{s}_i, s_{-i}(n_2))$

(8) If $\bar{u}_i(\bar{s}_i, s_{-i}(n_2)) > u_i(s_i(n_2), s_{-i}(n_2))$, update $s_i(n_2) = \bar{s}_i$

(9) Update $n_2 = n_2 + 1$

End loop.

Δ is the exploration step size of the UAV and becomes shorter as the iteration increases.

Algorithm 2: BR-based position placement algorithm.

UAV-user association and channel selection strategy. Assume that there are M UAVs, K channels and every UAV serves up to L GUs. Because Algorithm 1 randomly picks between 1 and $K - L$ users to update their channel selections in each iteration, then the computational complexity of Algorithm 1 is expressed as $N_1(K - L/2)\mathcal{O}(C_1)$, where $\mathcal{O}(C_1)$ is the computational complexity required for a user to update its channel selection in each iteration and C_1 is a constant.

4.3.2. BR-Based Position Placement Algorithm. The details of position placement algorithm are shown in Algorithm 2. In each iteration of Algorithm 2, the UAV firstly explores the surrounding position of the current position. If there is no better position around, the UAV explores a random position in the whole space. Assume that the max iteration times of Algorithm 2 is N_2, then the computational complexity of Algorithm 2 is at least N_2.

$[\mathcal{O}(C_2) + N_1(K - L/2)\mathcal{O}(C_1)]$ where $\mathcal{O}(C_2)$ is the computational complexity required for a UAV to update its position and C_2 is a constant.

Remark 7. In each iteration of the proposed algorithm, the optimization of the strategy will improve the potential

Table 1: Parameter settings in simulations.

Parameter	Value
Area	2 km × 2 km
${w_0}^T$	(0, 0)
h	200 m
P_{GBS}	24 dBW
P_{UAV}	14 dBW
M	4
N	20
L	5
K	10
f_c	2 GHz
B_0	20 MHz
B_1	1 MHz
a, b	12.081, 0.11395
n_0	-174 dBm/Hz
η_{LOS}, η_{NLOS}	1.44544, 199.526

function. Because the strategy space of the problem is limited, the potential function has a maximum value, and the potential function will not increase all the time in the proposed algorithm, and the strategy will converge to the Nash Equilibrium at last. In the proposed algorithm, the strategy selected by the player always moves towards a Nash Equilibrium in the strategy space and players do not search the whole strategy space. Therefore, the proposed algorithm greatly saves the computation and solves the challenge of the huge strategy space to a certain extent.

5. Simulation Results and Analysis

In this section, simulations are made to verify the convergence performance and effectiveness of the proposed algorithm. The corresponding simulation parameters and analysis of results are also presented.

5.1. Simulation Parameter Setting. The mission area of the UAVs deployment is a square area of 2 km. The GBS is deployed in the lower left corner of the mission area and its coordinate is denoted as (0, 0). The GUs are evenly distributed within a circle whose center is (1000, 1000) and radius is 750 m. The specific simulation parameters are shown in Table 1, where the UAV height $h = 200$ m, GBS transmission power $P_{GBS} = 24$ dBW, UAV transmission power $P_{UAV} = 14$ dBW, number of UAVs $M = 4$, number of GUs $N = 20$, maximum number of GUs which the UAV can serve $L = 5$, number of channels $K = 10$, maximum carrier frequency $f_c = 2$ GHz, channel bandwidth between the UAV and the GBS B_0 =20 MHz, channel bandwidth between the UAV and the GU $B_1 = 1$ MHz, propagation environment parameters $(a, b) = (12.081, 0.11395)$ and attenuation factors $(\eta_{LOS}, \eta_{NLOS}) = (1.44544, 199.526)$. Specifically, we referred to a, b, η_{LOS}, η_{NLOS}, and σ^2 in reference [32].

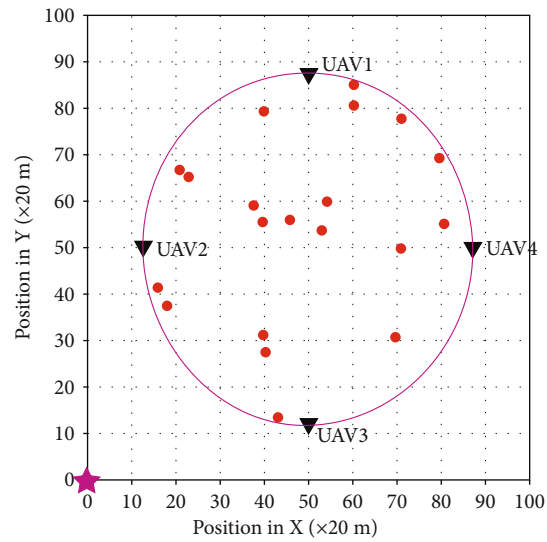

Figure 3: Initial deployment of the UAVs ($M = 4$, $N = 20$, $L = 5$, $K = 10$, and $B_0 = 20$ MHz).

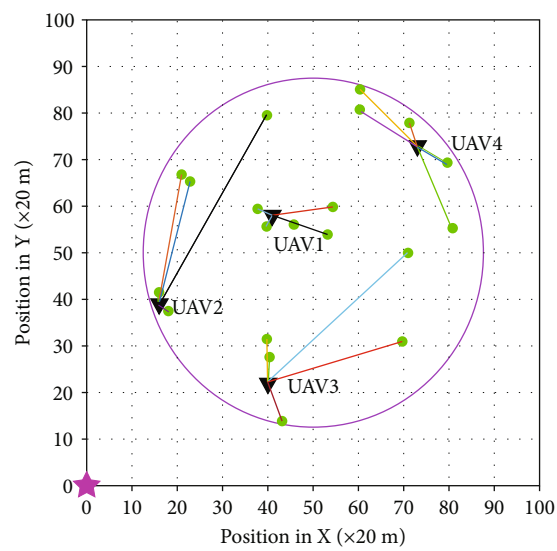

Figure 4: Result of the UAVs deployment and the UAV-user association ($M = 4$, $N = 20$, $L = 5$, $K = 10$, and $B_0 = 20$ MHz).

5.2. Deployment Effect Description. The deployment effect is shown in Figures 3 and 4. The GBS is indicated by the pink pentacle, the UAV is indicated by the black triangles, and the GU is indicated by the dot. The red dots represent the unserved GUs and the green dots represent the GUs served by the UAVs. As shown in Figure 3, in the initial state, the UAVs are evenly deployed along the boundary of the GU's distribution. Figure 4 shows the result of deployment solution. According to the matching theory, the UAV tends to serve GUs who are closer to it. Affected by the constraint (5e), the UAV tends to be closer to the GBS.

5.3. Result of Convergence Performance Simulation. To avoid the contingency, the convergence performances of

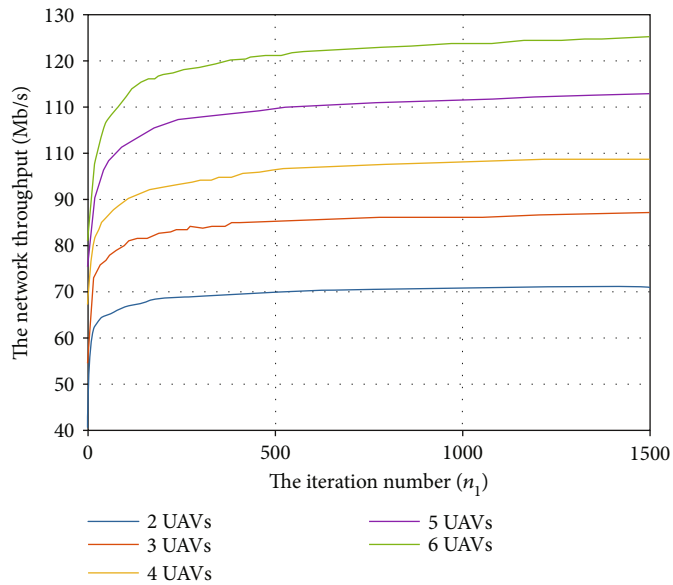

Figure 5: The convergence performance of Algorithm 2 ($N = 20$, $L = 5$, $K = 10$, and $B_0 = 20$ MHz).

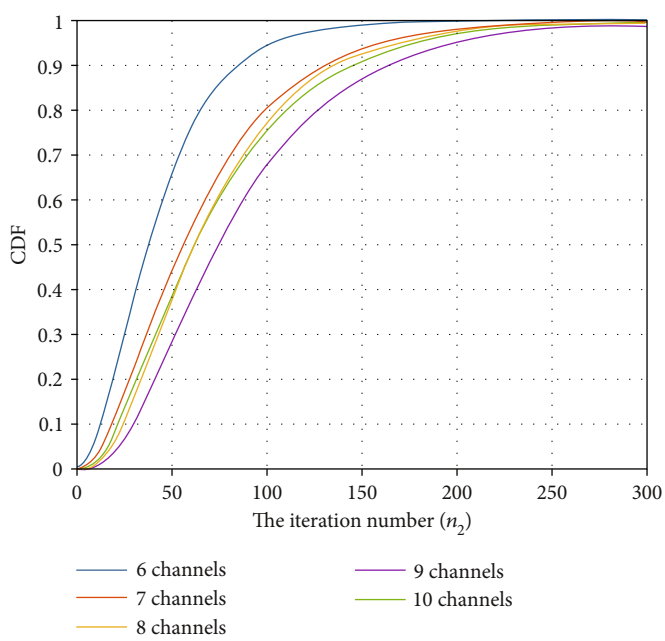

Figure 6: The convergence performance of Algorithm 1 ($M = 4$, $N = 20$, $L = 5$, and $B_0 = 20$ MHz).

Algorithm 1 and Algorithm 2 are obtained by running each algorithm 1500 times and 100 times, respectively.

Figure 5 shows the convergence time of Algorithm 2 in networks with different numbers of UAVs. The network which has more UAVs needs more time to converge. It is seen that 1500 iterations are enough for the network who has no more than 5 UAVs and 20 GUs. Figure 6 shows the cumulative distribution function (CDF) of the convergence time of Algorithm 1. It is seen that no more than 300 iterations are needed by the network with 4 UAVs, 20 GUs, and 10 channels to converge, and there is an 80% chance that Algorithm 1 will converge within 150 times.

5.4. Results of Different Deployment Methods' Performance. In this subsection, we analyze the impact of different factors on the throughput of the network: B_0 (the bandwidth of the backhaul link), K (the number of channels), L (the maximum number of GUs which the UAV can serve), M (the number of UAVs), and N (the number of GUs). In addition, the proposed UAV deployment algorithm is compared with three other deployment methods, which are listed as follows:

(i) *K-Means Deployment.* Use K-means algorithm [20] to deploy the UAVs, and then use Algorithm 1 to decide the channel selection of the GUs

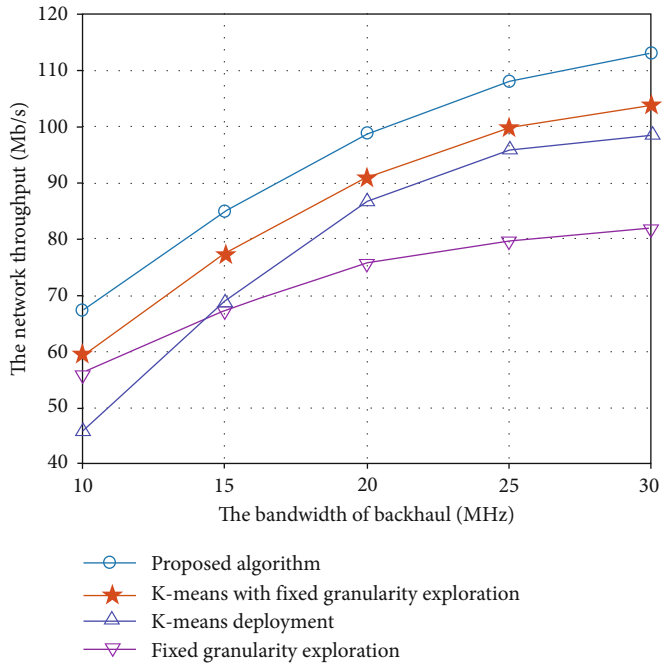

Figure 7: Network throughput versus the bandwidth of backhaul by different methods ($M = 4$, $N = 20$, $L = 5$, and $K = 10$).

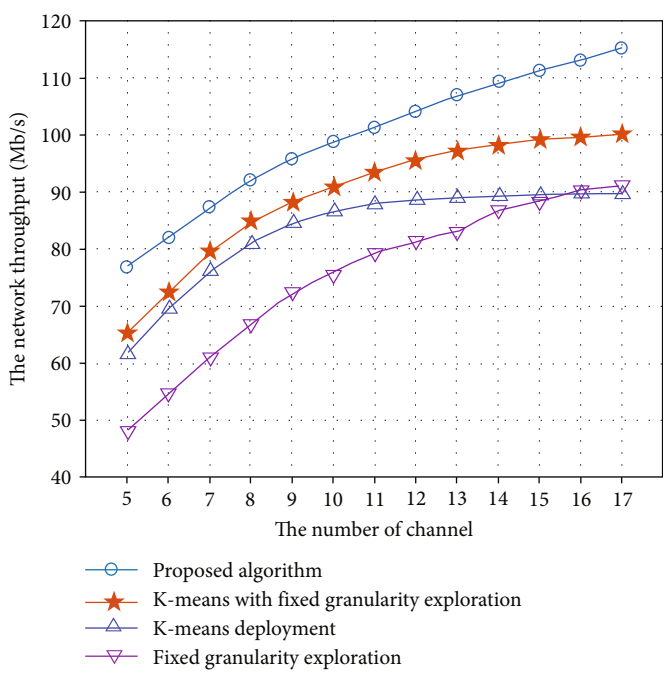

Figure 8: Network throughput versus the number of channel by different methods ($M = 4$, $N = 20$, $L = 5$, and $B_0 = 20$ MHz).

(ii) *Fixed Granularity Exploration*. Different from Algorithm 2, the exploration step size Δ of the UAV is fixed and the UAV only explores positions near the current position

(iii) *K-Means with Fixed Granularity Exploration*. Use K-means algorithm [20] to decide the UAVs' initial positions, then use fixed granularity exploration approach to further optimize the UAVs' positions

5.4.1. Impact of the Backhaul Bandwidth. Figure 7 compares the network throughput of different deployment methods when varying the backhaul bandwidth. As shown in Figure 7, the higher backhaul bandwidth improves the

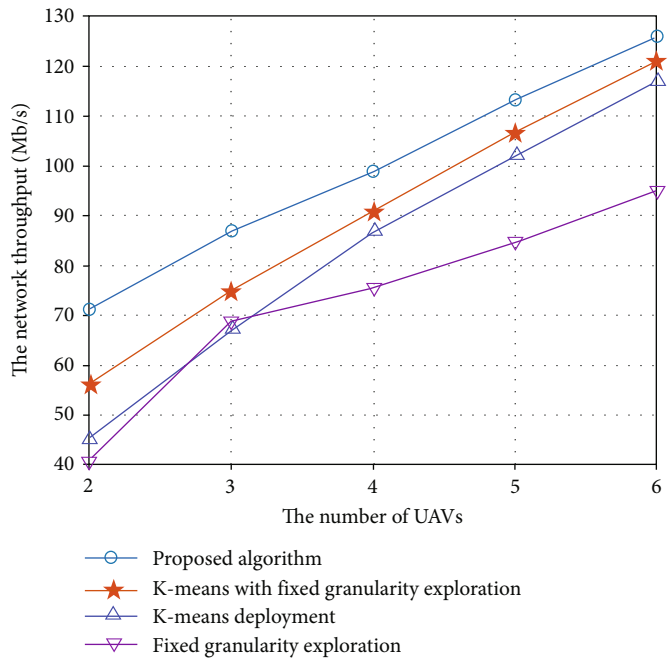

Figure 9: Network throughput versus the number of UAVs by different methods ($N = 20$, $L = 5$, $K = 10$, $B_0 = 20$ MHz).

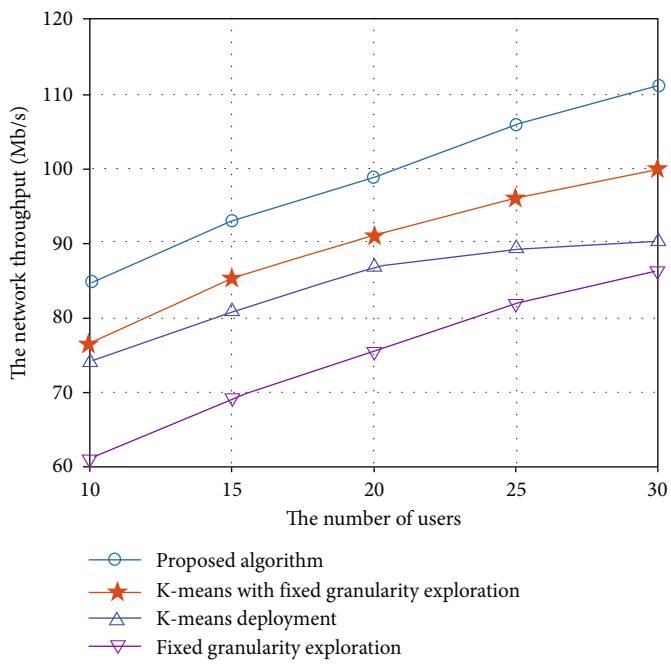

Figure 10: Network throughput versus the number of users by different methods ($M = 4$, $L = 5$, $K = 10$, and $B_0 = 20$ MHz).

network throughput, while the improvement is limited. The performance of the proposed algorithm outperforms the other methods, the main reason is that the proposed algorithm considers the global random exploration, it makes the result less trapped in local optimality. Compared the performance of K-means and K-means with fixed granularity exploration, the fixed granularity exploration method can further improve the performance of K-means method. Compared the performance of fixed granularity exploration and K-means with fixed granularity exploration, the initial position of UAVs is closely related to the performance of fixed granularity exploration method.

5.4.2. Impact of the Number of Channels. The network throughputs of different deployment methods with different numbers of channels are shown in Figure 8. The performance of the proposed deployment solution outperforms the other methods in networks with different numbers of

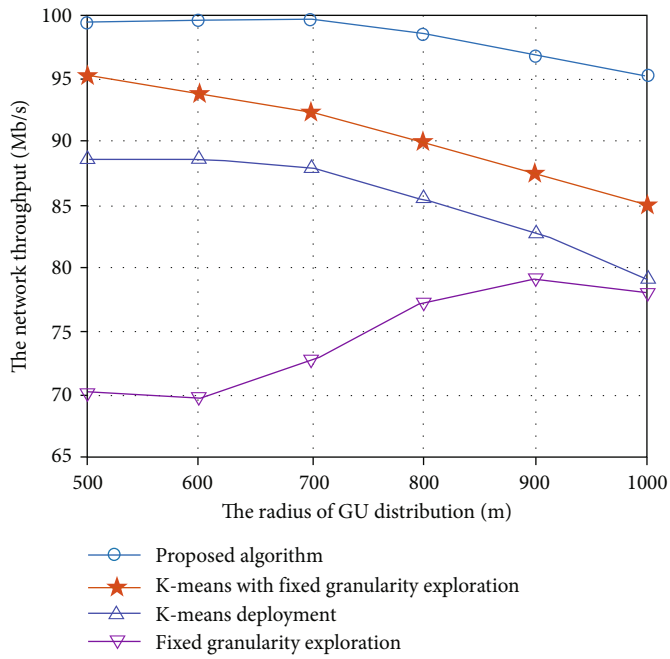

Figure 11: Network throughput versus the radius of GU distribution by different methods ($M = 4$, $N = 20$, $L = 5$, $K = 10$, and $B_0 = 20$ MHz).

channels. When the number of channels exceeds 13, the performance of the proposed algorithm keeps increasing, while the performance of K-means deployment algorithm no longer increases because the deployment result is independent of the number of channels, and 13 channels are enough for the GUs to communicate without interference.

5.4.3. Impact of the Number of UAVs. Figure 9 compares the network throughput of different deployment methods when varying the number of UAVs. Similarly, the performance of the proposed algorithm is the best and the network throughput increases with the increase of the number of the UAVs. With the increase of the number of the UAVs, the performance difference between the proposed algorithm and other deployment methods decreases.

5.4.4. Impact of the Number of GUs. Figure 10 compares the network throughput of different deployment methods when varying the number of GUs. With the increase of the number of the GUs, the performance of the proposed algorithm increases and is always better than the other deployment methods. The reason is that the GUs are evenly distributed, the greater the number of GUs, the more GUs are close to the GBS, then the UAVs are deployed closer to the GBS, and the throughput of the network is improved at last.

5.4.5. Impact of the Radius of GU Distribution. The influence of the radius of GU distribution on the network throughput in different deployment algorithms is shown in Figure 11. The distribution radius varies from 500 to 1000 meters and the performance of the proposed algorithm always outperforms other algorithms. Furthermore, with the increase of the distribution radius, the performance of the proposed algorithm decreases. The reason may be that the GUs are assumed to obey uniform distribution, and when the distance between GUs is farther, the average distance between UAV and served GUs is farther, causing the throughput of GUs decreased. In addition, the network throughput trend of the purple line is different from the other three. The difference between the algorithm of the purple line and the algorithm of the orange line is that the initial position of UAVs is different. We can see that the network throughput trend of the orange line is the same as the proposed algorithm and the deployment method based on K-means algorithm. So the initial position of UAVs is the key factor that needs to be considered.

6. Conclusion

Different from the previous researches that ignored spectrum resource management, we investigated the joint optimization of the position placement and the spectrum resource management for UAV base station networks with the constraint of the limited backhaul capacity in this study. To resolve the challenge of multiuser optimization and the challenge of the coupling relationship between optimization variables, we modeled the joint optimization problem as a hierarchical game decision architecture. The UAV placement was modeled as an outer game while the spectrum resource management was modeled as an inner game, and both of the two games were proved to be EPGs. Furthermore, we proposed two BR-based algorithms to optimize the spectrum resource management and the UAV position, respectively. Compared with the K-means deployment algorithm and the fixed granularity exploration algorithm, the proposed UAV deployment algorithm can improve the total throughput by 7% and 20% at least, respectively.

Data Availability

The simulation data used to support the findings of this study are included within the article.

Conflicts of Interest

The authors declare that they have no conflicts of interest.

Acknowledgments

This work was supported in part by the National Natural Science Foundation of China under Grant No. 61901517, No. 62101595, No. 62001514, and No. 61931011, in part by the Jiangsu Province Natural Science Foundation under Grant BK20200580, and in part by the National Postdoctoral Program for Innovative Talents under Grant BX2021371.

References

[1] J. G. Andrews, S. Buzzi, W. Choi et al., "What will 5G be?," *IEEE Journal on Selected Areas in Communications*, vol. 32, no. 6, pp. 1065–1082, 2014.

[2] M. Mozaffari, W. Saad, M. Bennis, Y.-H. Nam, and M. Debbah, "A tutorial on UAVs for wireless networks: applications, challenges, and open problems," *IEEE Communications Surveys & Tutorials*, vol. 21, no. 3, pp. 2334–2360, 2019.

[3] D. Liu, J. Wang, K. Xu et al., "Task-driven relay assignment in distributed UAV communication networks," *IEEE Transactions on Vehicular Technology*, vol. 68, no. 11, pp. 11003–11017, 2019.

[4] Y. Huang, M. Cui, G. Zhang, and W. Chen, "Bandwidth, power and trajectory optimization for UAV base station networks with backhaul and user QoS constraints," *IEEE Access*, vol. 8, 2020.

[5] M. Hua, L. Yang, Q. Wu, C. Pan, C. Li, and A. L. Swindlehurst, "UAV-assisted intelligent reflecting surface symbiotic radio system," *IEEE Transactions on Wireless Communications*, vol. 20, no. 9, pp. 5769–5785, 2021.

[6] M. Hua, Y. Wang, Q. Wu, H. Dai, Y. Huang, and L. Yang, "Energy-efficient cooperative secure transmission in multi-UAV-enabled wireless networks," *IEEE Transactions on Vehicular Technology*, vol. 68, no. 8, pp. 7761–7775, 2019.

[7] Z. Feng, L. Ji, Q. Zhang, and W. Li, "Spectrum management for mmWave enabled UAV swarm networks: challenges and opportunities," *IEEE Communications Magazine*, vol. 57, no. 1, pp. 146–153, 2019.

[8] M. Liu, Z. Liu, W. Lu, Y. Chen, X. Gao, and N. Zhao, "Distributed fewshot learning for intelligent recognition of communication jamming," *IEEE Journal of Selected Topics in Signal Processing*, vol. 16, no. 3, pp. 395–405, 2022.

[9] M. Liu, J. Wang, N. Zhao, Y. Chen, H. Song, and R. Yu, "Radio frequency fingerprint collaborative intelligent identification using incremental learning," *IEEE Transactions on Network Science and Engineering*, vol. 9, no. 5, 2021.

[10] X. Yu, X. Dong, X. Yang et al., "Air–ground integrated deployment for UAV-enabled mobile edge computing: a hierarchical game approach," *IET Communications*, vol. 14, no. 15, pp. 2491–2499, 2020.

[11] L. Ruan, J. Wang, J. Chen et al., "Energy-efficient multi-UAV coverage deployment in UAV networks: a game-theoretic framework," *China Communications*, vol. 15, no. 10, pp. 194–209, 2018.

[12] D. Liu, Y. Xu, J. Wang et al., "Opportunistic utilization of dynamic multi-UAV in device-to-device communication networks," *IEEE Transactions on Cognitive Communications and Networking*, vol. 6, no. 3, pp. 1069–1083, 2020.

[13] H. El Hammouti, D. Hamza, B. Shihada, M.-S. Alouini, and J. S. Shamma, "The optimal and the greedy: drone association and positioning schemes for internet of UAVs," *IEEE Internet of Things Journal*, vol. 8, no. 18, pp. 14066–14079, 2021.

[14] O. Thakoor, J. Garg, and R. Nagi, "Multiagent UAV routing: a game theory analysis with tight price of anarchy bounds," *IEEE Transactions on Automation Science and Engineering*, vol. 17, no. 1, pp. 100–116, 2020.

[15] S. Yan, M. Peng, and X. Cao, "A game theory approach for joint access selection and resource allocation in UAV assisted IoT communication networks," *IEEE Internet of Things Journal*, vol. 6, no. 2, pp. 1663–1674, 2018.

[16] R. Chen, L. Cui, M. Wang et al., "Joint computation offloading, channel access and scheduling optimization in UAV swarms: a game-theoretic learning approach," *IEEE Open Journal of the Computer Society*, vol. 2, pp. 308–320, 2021.

[17] M. E. Mkiramweni, C. Yang, J. Li, and W. Zhang, "A survey of game theory in unmanned aerial vehicles communications," *IEEE Communications Surveys & Tutorials*, vol. 21, no. 4, pp. 3386–3416, 2019.

[18] F. Tang, Z. M. Fadlullah, N. Kato, F. Ono, and R. Miura, "AC-POCA: anticoordination game based partially overlapping channels assignment in combined UAV and D2D-based networks," *IEEE Transactions on Vehicular Technology*, vol. 67, no. 2, pp. 1672–1683, 2018.

[19] Y. Xu, J. Wang, Q. Wu, A. Anpalagan, and Y.-D. Yao, "Opportunistic spectrum access in cognitive radio networks: global optimization using local interaction games," *IEEE Journal of Selected Topics in Signal Processing*, vol. 6, no. 2, pp. 180–194, 2011.

[20] H. Qu, W. Zhang, J. Zhao, Z. Luan, and C. Chang, "Rapid deployment of UAVs based on bandwidth resources in emergency scenarios," in *2020 Information communication technologies conference (ICTC)*, pp. 86–90, Nanjing, China, 2020.

[21] L. Ruan, J. Chen, Q. Guo, H. Jiang, Y. Zhang, and D. Liu, "A coalition formation game approach for efficient cooperative multi-UAV deployment," *Applied Sciences*, vol. 8, no. 12, p. 2427, 2018.

[22] A. V. Savkin and H. Huang, "Deployment of unmanned aerial vehicle base stations for optimal quality of coverage," *IEEE Wireless Communications Letters*, vol. 8, no. 1, pp. 321–324, 2019.

[23] Q. Zhang, W. Saad, M. Bennis, X. Lu, M. Debbah, and W. Zuo, "Predictive deployment of UAV base stations in wireless networks: machine learning meets contract theory," *IEEE Transactions on Wireless Communications*, vol. 20, no. 1, pp. 637–652, 2021.

[24] T. Zhang, Y. Wang, Y. Liu, W. Xu, and A. Nallanathan, "Cache-enabling UAV communications: network deployment and resource allocation," *IEEE Transactions on Wireless Communications*, vol. 19, no. 11, pp. 7470–7483, 2020.

[25] D. Liu, Y. Xu, Y. Xu et al., "Opportunistic data collection in cognitive wireless sensor networks: air–ground collaborative online planning," *IEEE Internet of Things Journal*, vol. 7, no. 9, pp. 8837–8851, 2020.

[26] X. Yu, D. Wu, D. Liu, H. Wang, and Z. Qin, "The heterogeneous demands satisfaction in IoT network: air-ground collaborative deployment," *IEEE Transactions on Vehicular Technology*, vol. 70, no. 12, pp. 12713–12724, 2021.

[27] E. Kalantari, M. Z. Shakir, H. Yanikomeroglu, and A. Yongacoglu, "Backhaul-aware robust 3D drone placement in 5G+ wireless networks," in *2017 IEEE International Conference on Communications Workshops (ICC Workshops)*, pp. 109–114, Paris, France, 2017.

[28] J. Li, D. Lu, G. Zhang, J. Tian, and Y. Pang, "Post-disaster unmanned aerial vehicle base station deployment method based on artificial bee colony algorithm," *IEEE Access*, vol. 7, pp. 168327–168336, 2019.

[29] C. T. Cicek, H. Gultekin, B. Tavli, and H. Yanikomeroglu, "Backhaul-aware optimization of UAV base station location and bandwidth allocation for profit maximization," *IEEE Access*, vol. 8, pp. 154573–154588, 2020.

[30] M. K. Shehzad, A. Ahmad, S. A. Hassan, and H. Jung, "Backhaul-aware intelligent positioning of UAVs and association of terrestrial base stations for fronthaul connectivity," *IEEE Transactions on Network Science and Engineering*, vol. 8, no. 4, pp. 2742–2755, 2021.

[31] C. Qiu, Z. Wei, Z. Feng, and P. Zhang, "Joint resource allocation, placement and user association of multiple UAV-mounted base stations with in-band wireless backhaul," *IEEE Wireless Communications Letters*, vol. 8, no. 6, pp. 1575–1578, 2019.

[32] C. Qiu, Z. Wei, X. Yuan, Z. Feng, and P. Zhang, "Multiple UAV-mounted base station placement and user association with joint fronthaul and backhaul optimization," *IEEE Transactions on Communications*, vol. 68, no. 9, pp. 5864–5877, 2020.

[33] H. Huang and A. V. Savkin, "Deployment of heterogeneous UAV base stations for optimal quality of coverage," *IEEE Internet of Things Journal*, vol. 9, no. 17, 2022.

[34] M. Mozaffari, W. Saad, M. Bennis, and M. Debbah, "Unmanned aerial vehicle with underlaid device-to-device communications: performance and tradeoffs," *IEEE Transactions on Wireless Communications*, vol. 15, no. 6, pp. 3949–3963, 2016.

[35] K. Yamamoto, "A comprehensive survey of potential game approaches to wireless networks," *IEICE Transactions on Communications*, vol. 98, no. 9, pp. 1804–1823, 2015.

[36] N. Nie and C. Comaniciu, "Adaptive channel allocation spectrum etiquette for cognitive radio networks," *Mobile Networks and Applications*, vol. 11, no. 6, pp. 779–797, 2006.

[37] R. B. Myerson, *Game Theory: Analysis of Conflict*, Harvard university press, 1997.

[38] D. Monderer and L. S. Shapley, "Potential Games," *Games and Economic Behavior*, vol. 14, no. 1, pp. 124–143, 1996.

Hindawi
Wireless Communications and Mobile Computing
Volume 2023, Article ID 1033371, 9 pages
https://doi.org/10.1155/2023/1033371

Research Article

Learning to Track Multiple Radar Targets with Long Short-Term Memory Networks

Fei Song,[1,2] **Yong Li**,[1] **Wei Cheng**,[1] **and Limeng Dong**[1]

[1]*School of Electronic Information, Northwestern Polytechnical University, Xi'an 710072, China*
[2]*School of Electronic Engineering, Xi'an Aeronautical Institute, Xi'an 710077, China*

Correspondence should be addressed to Yong Li; ruikel@nwpu.edu.cn

Received 12 August 2022; Revised 30 September 2022; Accepted 14 October 2022; Published 15 February 2023

Academic Editor: Mingqian Liu

Radar multitarget tracking in a dense clutter environment remains a complex problem to be solved. Most existing solutions still rely on complex motion models and prior distribution knowledge. In this paper, a new online tracking method based on a long short-term memory (LSTM) network is proposed. It combines state prediction, measurement association, and trajectory management functions in an end-to-end manner. We employ LSTM networks to model target motion and trajectory associations, relying on their strong learning ability to learn target motion properties and long-term dependence of trajectory associations from noisy data. Moreover, to address the problem of missing appearance information of radar targets, we propose an architecture based on the LSTM network to calculate similarity function by extracting long-term motion features. And the similarity is applied to trajectory associations to improve their robustness. Our proposed method is validated in simulation scenarios and achieves good results.

1. Introduction

In an environment with much clutter, multitarget tracking based on radar detection results is a challenging task. An important branch of its solution is the multitarget tracking algorithm based on data association, which can be generally decomposed into the following three aspects: modeling the motion of the tracked target to estimate trajectory parameters and filter measurements, associating the measurements with the motion trajectory to distinguish the measurements from different targets or background noise and clutter interference, and effectively managing different motion trajectories to determine the birth, retention identity, and termination of different target trajectories.

For modeling the motion of the tracked target, the traditional method is based on the Bayesian filtering theory [1, 2]. Earlier, the Kalman filter is used to obtain unbiased optimal estimation of Gaussian linear targets. For nonlinear motion targets, the following developed methods consist of extended Kalman filter (EKF) [3], unsensitive Kalman filter (UKF) [4], interactive multiple model (IMM) [5] algorithm, and so on. All of these methods require limited motion models in advance. Particle filtering (PF) [6], which does not need the aforementioned assumptions, however, has low computational efficiency and sample poverty problem.

For tracking trajectory association and trajectory management, it can theoretically be regarded as a maximum matching problem of a bipartite graph. For this problem, the Hungarian algorithm (HA) [7] and Kuhn and Munkres algorithm (KM) are first used. Later, many more complex algorithms have appeared, including multiple hypothesis tracker (MHT) [8], which establishes a potential tracking hypothesis tree for each candidate target and calculates the tracking probability to select the most likely tracking combination. Another popular technique is joint probabilistic data association (JPDA) [9]. By building a validation matrix, it can calculate all feasible joint association event probabilities and associate targets based on the obtained scores. However, these traditional methods not only require knowing the number of targets, starting positions, and clutter distribution

but also result in "combination explosions" increase of calculation when the number of targets or clutter is enlarged. This will not only reduce the tracking accuracy but also may lead to trace association errors.

Recently, deep learning has made great progress in classification and detection applications in many fields. For example, it is widely used in identifying interference in wireless communication systems [10] and lightweight radio frequency fingerprint identification (RFFID) systems [11]. Especially in computer vision, the target tracking methods in video based on deep learning have also improved, such as pedestrian monitoring [12, 13], car driving monitoring [14, 15], and biological sequence tracking [16]. However, deep learning-based multitarget tracking algorithms that are applied to radar targets are relatively rare. This may be caused by several reasons. First, deep learning requires a large amount of annotated training data, but real data is difficult to obtain in radar multitarget scenarios. Secondly, the measurement of radar targets nearly has no apparent information, which prevents the appearance detection information commonly used in video target tracking. Thirdly, radar target tracking and detection have real-time requirements, and the tracking algorithm generally needs to be used online.

The main contributions of this paper are as follows:

(1) To overcome these problems in traditional radar multitarget tracking based on data association, inspired by deep learning ideas, we propose an end-to-end multitarget tracking structure based on recurrent neural networks. We use LSTM networks to model the state prediction and measurement association parts of the multitarget tracking algorithm, respectively. Relying on the powerful learning ability of LSTM networks, it is able to obtain the long-term dependence of multiple tracking target motion states and measurement association by learning from a large amount of training data. Then, it combines status update and tracking management into a unified network structure and finally realizes multitarget tracking. The advantages of this method are that the target motion models and clutter distribution are not required to be known in advance, and the combination explosion problem in the traditional data association method is alleviated. Meanwhile, the tracking process runs online without caching any future frame information

(2) To solve the problem of missing appearance information when the neural network is applied to the radar multitarget tracking algorithm, we creatively design a motion feature extraction LSTM to extract motion features from the speed of the targets and calculate the similarity scores, which are used to learn long-dependent measurement associations

(3) To address the problem of insufficient training data, we propose a method to obtain extensive training data from simulation models. Our multitarget tracking architecture is also confirmed by a simulation analysis of the simulated data

2. Related Work

Lately, target tracking in the video application field has been extended from a single target to multitarget tracking [17]. And the specific methods have also been extended from constructing complex appearance models to focusing on the motion model and interaction of the targets simultaneously [18]. In these applications, deep learning methods play an important role, mainly reflected in the following three aspects:

(1) Using the deep neural network to extract high-order features of the tracking targets, especially for the appearance model, this can effectively improve the target tracking performance. Earlier, Reid [8] use AlexNet for extracting deep features from targets for the use of the MHT framework. Leal-Taixe et al. [19] use the Siamese network structure to extract deep features. By combining the depth features and motion information with a gradient enhancement algorithm, the tracking problem is expressed as linear programming and solved effectively. However, there is no apparent information in the radar signal, so these methods are not suitable for extracting the depth features of the radar signal

(2) Deep neural networks are used to directly learn key components of a multitarget tracking framework. Chen et al. [20] construct two CNN-based classifiers using the features of fasterRCNN [21] from the VGG-16 model [22] as input and combining the confidence degree of the classifier as particle weights to obtain tracking results by particle filtering. Xiang et al. [23] propose a CNN based on triplet state loss to learn the distance measure between tracker and detection and thus constitute the cost of the bipartite graph, which can be effectively solved by the Hungarian algorithm. However, radar targets are different from video targets. It often has a poor performance to extract radar target features and classify them using the CNN network

(3) Deep neural networks are designed directly in an end-to-end manner to obtain multitarget tracking results. The multitarget tracking task involves many interwoven components and is difficult to be modeled as a whole for learning. There have been some preliminary researches recently. Milan et al. [24] unify target state prediction, state update, and existence probability calculation under a whole RNN. Also, they design a set of LSTM networks for data matching matrix calculation and act on the state update process. These architectures achieved good results. Sadeghian et al. [25] design a more complex RNN structure, which is divided into three subnetworks to extract multiframe appearance features, motion features, and interaction features, respectively, and integrate them into a top-

level RNN for time-dependent comprehensive inferring, so as to obtain the final matching probability. Experimental results show that this method is more robust

Our architecture is similar to that of [24] but different in three key aspects: First, RNN is used in [24] to deal with motion state prediction. If the time interval is too long, the time dependence will be weakened. Instead, we use the LSTM network for motion state prediction, which enhances the long-term dependence learning ability of target states. Secondly, in the measurement association part, we use the motion feature extraction network based on LSTM to calculate the similarities for data associations, which has stronger anti-interference ability than the method in [24] only using the Euclidean distance between the target and each measurement to carry out data associations. Thirdly, we use different loss functions due to different network architectures.

3. Our Approach

For addressing the aforementioned radar target tracking problem, we propose an online end-to-end radar multitarget tracking network architecture based on LSTM (see Figure 1). Our architecture implements target state prediction, measurement association, state update, and tracking path management under a unified LSTM network architecture, and all model learning is completed in an online end-to-end manner.

3.1. Notations. In our application scenario, the target state vector we care about is $x_t \in R^{N \cdot D}$, including x coordinate, y coordinate, x axis velocity v_x, and y axis velocity v_y, as represented (x, y, v_x, v_y), $D = 4$, N represents the maximum number of targets tracked simultaneously in a frame. The measurement value vector is $z_t \in R^{M \cdot D}$, whose dimension D is the same as the target state vector, and M represents the maximum number of detected values in a frame, including the targets and clutter. The association probability matrix of the measurement association part is expressed as $A_t \in [0, 1]^{N \cdot (M+1)}$, each row of which represents the probability that each measurement value belongs to a certain target. That is, A_t^{ij} presents the probability of the jth measurement value belonging to the ith target. The added column indicates the probability that the target lacks measurement, so that each row is satisfied $\forall_i : \sum_j A_t^{ij} = 1$. The path management section uses a probability vector $\eta_t \in [0, 1]^N$ to express the probability of each target's existence, which can accurately describe the target generation and termination processes.

3.2. Motion-Association Multitarget Tracking with LSTMs (MA-LSTM). In our architectural design (see Figure 1), we partition the state prediction, state update, and path management into a target motion module and measurement association into another target association module. This primarily deals with the diversity of measurement association algorithms and facilitates the replacement of this part for tracking effectiveness comparison. At the same time, the two modules are trained separately for easy convergence.

3.2.1. State Prediction in Motion Module. State prediction is the first submodule of the motion module. The task of this module is to learn a complex motion pattern, which can be noisy and nonlinear, and predict the future motion states based on the trend of the past motion states. This is actually a time series prediction problem, which we designed to achieve by using a LSTM network structure, as shown in Figure 2. We train the network on noisy motion trajectories so that the network can completely learn the long-term dependent motion pattern from the training data without prior knowledge.

More specifically, at the current moment t, both the hidden state h_t and the cell state c_t of the prediction LSTM come from the learning of the previous target motion state, and the input x_t is the target motion state at the current moment. Through the internal processing of the LSTM network, as described below, the predicted motion state $\hat{x}_{t+1}$ at the next moment as well as the hidden state h_{t+1} and cell state c_{t+1} can be obtained to continue the transmission.

The formula is expressed as follows:

$$\begin{aligned} h' &= W_{hh'} h_t + W_{xh'} x_t, \\ c_{t+1} &= \sigma\left(h'\right) c_t + \sigma\left(h'\right) \tanh\left(h'\right), \\ h_{t+1} &= \sigma\left(h'\right) \tanh\left(c_{t+1}\right), \\ \hat{x}_{t+1} &= W_{ho} h_{t+1}, \end{aligned} \tag{1}$$

where $\sigma()$ is the sigmoid and tanh () is the hyperbolic tangent activation functions, and the learnable parameters are expressed as $W_{hh'} W_{xh'} W_{ho}$.

3.2.2. State Update and Track Management in Motion Module. Status update and track management is the second submodule of the motion module. The task of this module is to update the motion state of the target and identify and judge the start and end of the target trajectory on the basis of the obtained target prediction, measured values, and association matrix. This is an important step in the multitarget tracking architecture, for taking into account the clutter interference in the multitarget measurements and the association of the measured data. The network structure we designed is shown in Figure 3.

In detail, the measured values z_{t+1} at $t + 1$ moment are combined with the predicted values $\hat{x}_{t+1}$ output by the state prediction submodule, as $[\hat{x}_{t+1}; z_{t+1}]$. Then, using the dot product with the association matrix A_{t+1} output by the target association module, the possible state of the target is $[\hat{x}_{t+1}; z_{t+1}] \cdot A_{t+1}$. Then, it is multiplied by the target existence probability η_t. With the multiplied result and the hidden state of the prediction module h_{t+1}, the updated motion state x_{t+1}^* is obtained after a nonlinear transformation, and the target existence probability η_{t+1}^* is also calculated.

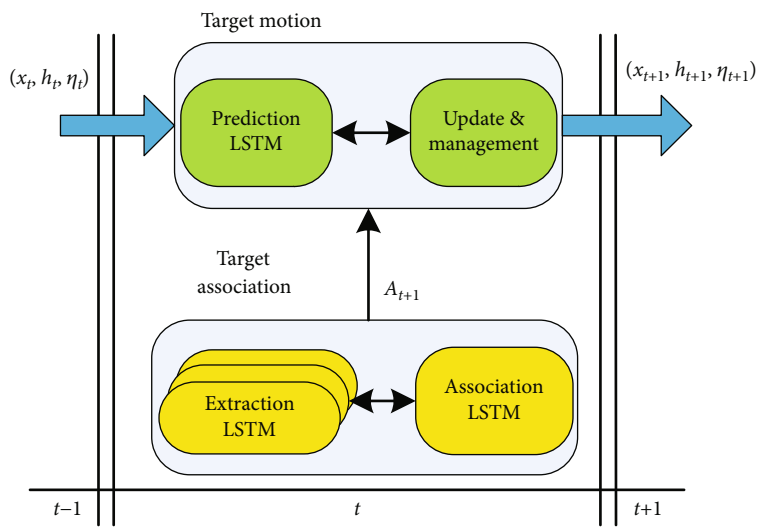

Figure 1: Overview of our architecture. In a time step t, the architecture is composed of two parts as target motion module and target association module (see Section 3.2 for details). The input can be expressed as the following: at the current moment t, the target motion state x_t, the hidden state h_t, and the probability vector η_t (see below) come from the learning of the previous moment $t-1$. After the processing of our architecture, the output is the estimated target motion state x_{t+1}, the hidden state h_{t+1}, and the probability vector η_{t+1} of the next moment $t+1$.

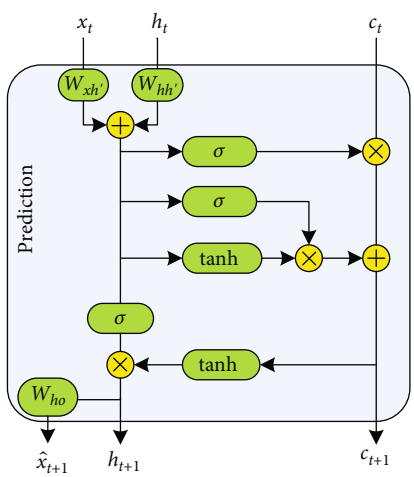

Figure 2: Prediction submodule of motion module on the basis of LSTM is used to estimate target state without the help of measurement.

The formula is expressed as follows:

$$\begin{aligned}\tilde{x}_{t+1} &= [\hat{x}_{t+1}; z_{t+1}] \cdot A_{t+1},\\ \tilde{h}_{t+1} &= h_{t+1} + W_{x\tilde{h}}(\tilde{x}_{t+1}\eta_t),\\ x^*_{t+1} &= W_{x^*o} \tanh\left(\tilde{h}_{t+1}\right),\\ \eta^*_{t+1} &= \sigma\left(W_{\eta^*o} \tanh\left(\tilde{h}_{t+1}\right)\right),\end{aligned} \tag{2}$$

where $\sigma()$ is the sigmoid and tanh () is the hyperbolic tangent activation functions, and the learnable parameters are expressed as $W_{x\tilde{h}} W_{x^*o} W_{\eta^*o}$.

3.2.3. Loss of Motion Module. In our architecture, we are interested in tracking performance-related losses and propose the following loss functions that meet our needs:

$$\begin{aligned}L(\hat{x}_{t+1}, x^*_{t+1}, \eta^*_{t+1}, x_{t+1}, \eta_{t+1}) &= \alpha \sum \|\hat{x}_{t+1} - x_{t+1}\|^2\\ &+ \beta \sum \|x^*_{t+1} - x_{t+1}\|^2 + \mu L_\eta + \psi \bar{\eta}_{t+1},\end{aligned} \tag{3}$$

$$L_\eta(\eta^*_{t+1}, \eta_{t+1}) = \eta_{t+1} \log \eta^*_{t+1} + (1 - \eta_{t+1}) \log (1 - \eta^*_{t+1}), \tag{4}$$

$$\bar{\eta}_{t+1} = abs(\eta^*_{t+1} - \eta_t), \tag{5}$$

where $\hat{x}_{t+1}$ is the predicted value of the prediction module, x^*_{t+1} is the predicted value of the update module, and η^*_{t+1} is the predicted value of the existence probability. x_{t+1}, η_{t+1} are true values.

This loss function in formula (3) we designed consists of four parts. The first part is to predict the motion state $\hat{x}_{t+1}$ of the targets without measured values, and we take the mean square error (MSE) of the predicted values and the real values. The second part is the state prediction x^*_{t+1} after the measurement update. We take the mean square error of the updated values and the real values. The third part is to predict the probability of the target's existence η^*_{t+1} at each moment, and we use binary cross entropy loss function, as shown in formula (4). The fourth part is the additional smoothing variable $\bar{\eta}_{t+1}$, in order to smooth the absolute difference between two consecutive η values, so as to prevent the loss of the target in the tracking process.

3.2.4. Target Association Module. The target association module is the most challenging and creative part of the multitarget tracking architecture. We design it as an independent association module and further subdivide it into two parts: motion extraction LSTM and association LSTM.

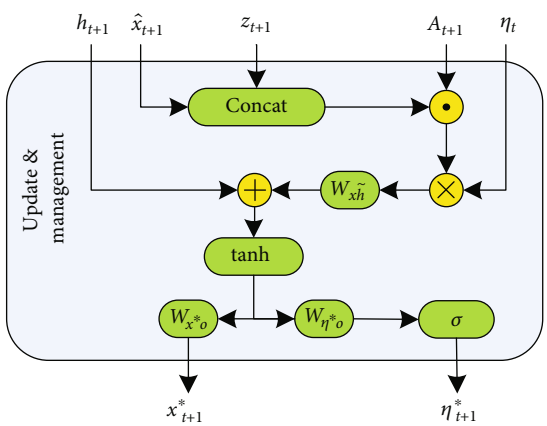

Figure 3: Update and management submodule of motion module is used to update target state and identify and manage the target trajectory with the help of the known target state prediction, measured values, and association matrix.

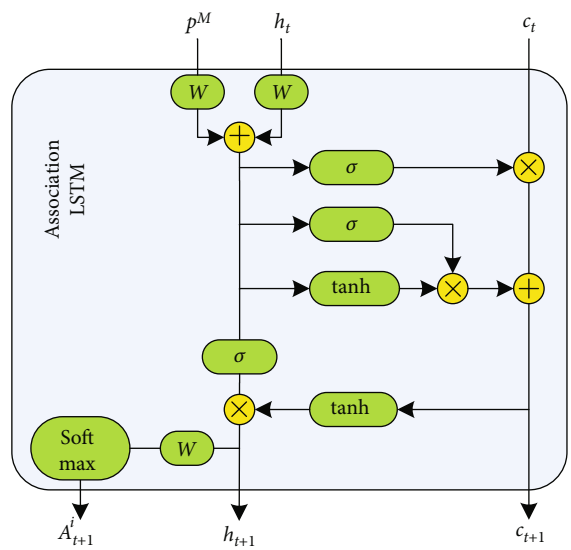

Figure 4: The association LSTM submodule of association module is used to learn the long-term dependence of targets and measurement association. The input p^M are motion eigenvectors from the extraction LSTM.

The fundamental task of target association is to uniquely partition the corresponding measurement values for each tracking target in a clutter interference environment, which is essentially a maximum matching problem of a binary graph. Different from the traditional solution mentioned above, we construct the association LSTM in an end-to-end manner. Relying on the powerful memory learning ability of LSTM, by learning and remembering the long-term dependence of target and measurement associations from abundant data, the association probability of each target to all measurement values is predicted, and finally, the association matrix of all targets is obtained. Our association method satisfies the one-to-one association constraint and is online without viewing future frames. This network structure is shown in Figure 4.

To be more specific, at time t, its input is feature vector p^M from the extraction LSTM (see below), and the hidden state h_t and cell state c_t both come from the learning of the previous target assignment. Through the LSTM network, we can get a target distribution probability vector A^i_{t+1} for all available measurements at the last softmax layer, and multiple targets constitute the association matrix A_{t+1}.

The input of the association LSTM requires eigenvectors representing similarity measures. The traditional similarity measure function solutions are handmade, and as aforementioned, radar target appearance feature information is absent. In order to solve these problems, we put forward the motion extraction LSTM, an architecture of computing similarity function based on the LSTM network (see Figure 5). Through the long-term time-dependent learning of the target motion velocity features, the similarity score of the target and the measurement can be calculated end-to-end without manually specifying parameters or weights, so as to determine whether the new measurement value is similar to the target motion features in the previous period of time.

As shown in Figure 5, we designed the motion extraction LSTM. The input $v^i_1 \cdots v^i_t$ are the motion velocity features of the ith tracked target at the specified time step $1 \cdots t$, producing the H-dimensional output p^i after processing through LSTM networks. The other input v^j_{t+1} is the jth measured velocity vector at the $t+1$ time step, which we map to an H-dimensional vector p^j via an FC layer. The two vectors are then connected and passed to another FC layer, which transforms the $2H$-dimensional vector into a K-dimensional eigenvector p^M. In the pretraining process, we use the softmax classifier at the end to train our model parameters to judge whether the measured velocity feature v^j_{t+1} corresponds to the real trajectory's velocity feature $v^i_1 \cdots v^i_t$.

3.2.5. Loss of Association Module. For motion extraction LSTM, we use the classifier and cross-entropy loss function for pretraining.

For association LSTM, in order to measure the cost of inappropriate associations, we adopt the common negative log likelihood loss, as below:

$$L\left(A^i_{t+1}, m^i_{t+1}\right) = -\log\left(A^{im}_{t+1}\right), \tag{6}$$

where m^i_{t+1} is the correct assignment of target i and A^{ij}_{t+1} is the probability of measurement j assigned to target i at time $t+1$.

3.3. Implementation Details. We use the TensorFlow architecture to implement our design. We designed the state prediction LSTM with a single layer of 256 hidden cells. The measurement of association task requires more representation ability. The association LSTM uses 256 hidden units in two layers, and the motion extraction LSTM uses 128 hidden units in one layer. The output feature vector is 100 dimensions, and the length of the specific extracted sequence is 10. We use grid search to select the optimal network hyperparameters [26]. We use Adam to update and optimize

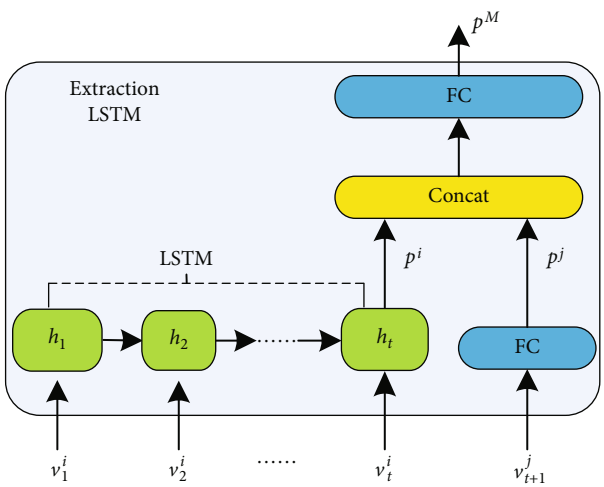

Figure 5: The extraction LSTM submodule of association module is used to extract the velocity features of the target's long-term motion and calculate the similarity between the new measurement and the existing trajectory.

our framework. The learning rate is initially set at 0.001 decreasing by 10% for every 10 periods. We set the maximum number of iterations to 10,000, which is enough to achieve convergence. Training for these network architectures takes about 10 hours on a GPU.

3.3.1. Training Data. As mentioned above, deep learning network learning requires a large amount of training data. However, there are very few open marker datasets for multitarget tracking of radar signals. Therefore, we generate training data from radar motion simulation models. The training trajectories we generated are set with multiple targets, whose birth time and lifetime are random, and incorporate a large number of random uniformly distributed clutter. The initial position and velocity of each target are randomly distributed within a certain range, and the conventional constant-velocity motion model and constant acceleration motion model of the radar target are adopted. The radar measurements are sampled every 2 seconds, and a Gaussian measurement noise is added, while the annotations for multitarget associations are manually added.

4. Experiments

We have proposed a radar multitarget tracking network architecture. To demonstrate its functionality, we first present experiments on simulated data and then give more insights and analysis of our performance.

In the simulation experiment scene, we choose 2D radar to track multiple moving targets, assuming that the target movements are independent of each other, and trajectory crossing may occur. The equation of motion for each target is

$$X_k = F_{k-1}X_{k-1} + G_{k-1}w_{k-1}, \tag{7}$$

where $X_k = (x, y, v_x, v_y, a_x, a_y)$ is the target state. W_{k-1} is process noise representing random acceleration in the x and y axis direction, $w_k \sim N(0, \sigma_w^2 I_2), \sigma_w = 10\,\mathrm{m/s}^2$.

We assume that the target follows the constant acceleration (CA) model and the constant velocity (CV) model [27]. Their process equation F and process noise G are

$$\begin{aligned}
F_{\mathrm{CA}} &= \begin{bmatrix} 1 & 0 & T & 0 & \frac{T^2}{2} & 0 \\ 0 & 1 & 0 & T & 0 & \frac{T^2}{2} \\ 0 & 0 & 1 & 0 & T & 0 \\ 0 & 0 & 0 & 1 & 0 & T \\ 0 & 0 & 0 & 0 & 1 & 0 \\ 0 & 0 & 0 & 0 & 0 & 1 \end{bmatrix}, \\
G_{\mathrm{CA}} &= \begin{bmatrix} \frac{T^2}{2} & 0 & T & 0 & 1 & 0 \\ 0 & \frac{T^2}{2} & 0 & T & 0 & 1 \end{bmatrix}, \\
F_{\mathrm{CT}} &= \begin{bmatrix} 1 & 0 & T & 0 & 0 & 0 \\ 0 & 1 & 0 & 0 & 0 & 0 \\ 0 & 0 & 1 & 0 & T & 0 \\ 0 & 0 & 0 & 1 & 0 & 0 \\ 0 & 0 & 0 & 0 & 1 & 0 \\ 0 & 0 & 0 & 0 & 0 & 1 \end{bmatrix}, \\
G_{\mathrm{CT}} &= \begin{bmatrix} \frac{T^2}{2} & 0 & T & 0 & 1 & 0 \\ 0 & \frac{T^2}{2} & 0 & T & 0 & 1 \end{bmatrix},
\end{aligned} \tag{8}$$

where T is the sampling period.

The target observation equation is

$$Z_k = H_k X_k + v_k, \tag{9}$$

where H_k is the observation matrix; the measurement noise v_k is the Gaussian white noise with zero mean and covariance matrix R_k.

The observation vector of radar is $Z_k = (\theta_k, r_k)$, where θ_k is the azimuth of the sensor observation target and r_k is the distance of the sensor observation target. The target observation model is

$$\begin{bmatrix} \theta_k \\ r_k \end{bmatrix} = \begin{bmatrix} \arctan \dfrac{y_k - y}{x_k - x} \\ \sqrt{(x_k - x)^2 + (y_k - y)^2} \end{bmatrix} + \begin{bmatrix} v_\theta \\ v_r \end{bmatrix}, \tag{10}$$

where $v_\theta \sim N(0, \sigma_\theta^2), \sigma_\theta = 1 \times (\pi/180)\mathrm{rad/s}$ and $v_r \sim N(0, \sigma_r^2), \sigma_r = 10\,\mathrm{m}$.

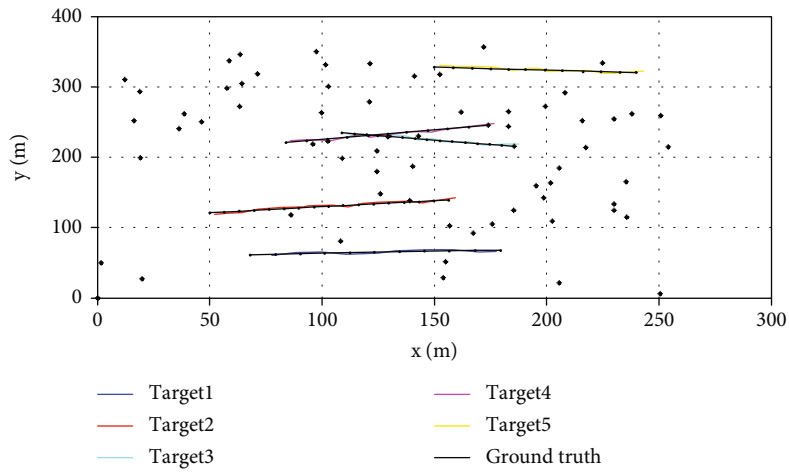

Figure 6: The tracking results of our method on 5 targets. The different color curves represent the different predicted target trajectories. The black curve is the ground truth.

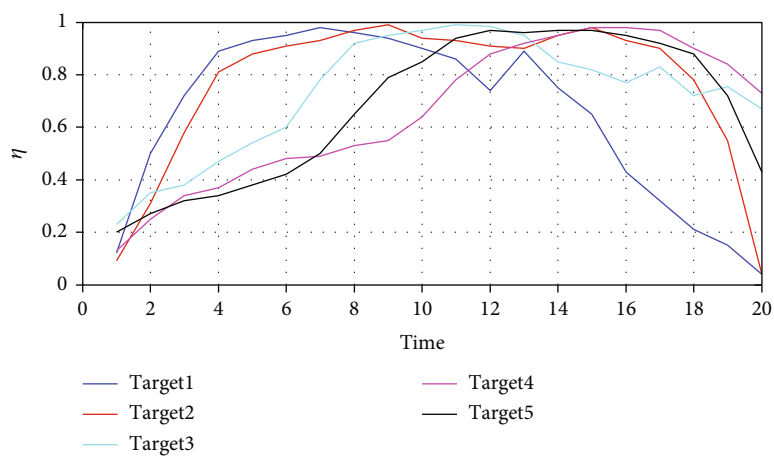

Figure 7: The predicted value of the existence probability η of the 5 targets in the time frame. The threshold is set as 0.6.

Table 1: OSPA distance of the four methods.

Method	OSPA ↓	OSPA Loc ↓	OSPA card ↓
KF-HA	83.79	77.48	8.09
JPDA	79.86	75.39	8.22
M-HA	79.12	73.15	12.44
MA-LSTM	70.08	65.78	7.86

On this basis, we set an observation area of 1 km × 1 km, 5 radar tracking targets with random birth and death time. Each target has detected probability $P_D = 0.99$. In the observed region, the clutter follows a uniform Poisson distribution, and the clutter intensity is set as$\lambda_k = 30$.

To generate large amounts of training data, the initial position of the target is randomly distributed within the observation area, the initial linear velocity is randomly distributed from 100 m/s to 300 m/s, and the acceleration is randomly distributed from 0 m/s^2 to 8 m/s^2. The times of birth and death for each target are randomly distributed between 3 and 18 s. At the same time, the number of targets at each sampling time is manually annotated. From this, we produce 10,000 random paths and their observation data, respectively. These are sufficient to train our network architecture.

The results of the tracking are shown in Figures 6 and 7. From this, we can qualitatively conclude that our method can track multiple moving radar targets in a large number of clutter environments, although the trajectories of these targets may be crossed. Furthermore, we also see that the predicted trajectories always start and end one or two points later than the real trajectories, which is difficult to avoid with the online method.

For quantitative analysis, we compare our proposed method (MA-LSTM) with three baseline methods. The first baseline method is the traditional KF-HA, which employs a combination of Kalman filter and data association via the Hungarian algorithm. The second baseline approach is JPDA mentioned above. The third comparison is comprised of our motion module and the data association using the Hungarian algorithm (M-HA). The optimal submode allocation (OSPA) [28] distance for each method is calculated.

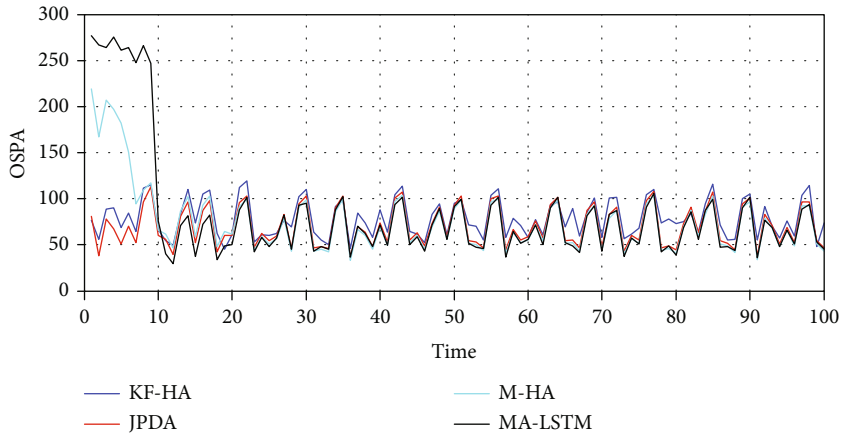

Figure 8: The OSPA values for different methods.

OSPA is a consistency measurement method for the overall performance evaluation of the target tracking system, which can be used to measure the error between real track and estimated track and can separate the total error into distance errors and correlation errors. For the tunable parameter distance sensitivity parameter p and associated sensitivity parameter c, we set $p = 20$ and $c = 350$, respectively.

The calculation results are shown in Table 1. MA-LSTM outperforms the other methods in all three aspects. It has great advantages in overall OSPA and associated OSPA and is slightly better than JPDA in terms of distance OSPA. It is worth noting that compared with the HA method for data association, the proposed method of using LSTM for data association and using motion velocity features to calculate similarity has a positive impact on the overall tracking effect, especially on the reduction of association error.

As shown in Figure 8, this intuitively shows the trend of different method OSPA values over time under a long period of test data. It can be seen that in the early stage of the test, the OSPA value of the learning method is high and then decreases rapidly after that, because of the learning of motion properties in the early stages of tracking. The OSPA value of our method is significantly reduced from the 10th frame, because the speed feature extraction sequence length in the data association module is set to 10. That is, the role of data association can be fully played after 10 frames; after that, the performance of our method is better than other methods.

5. Conclusion

This paper presents an LSTM-based network architecture for radar multitarget tracking. This architecture can effectively solve the problems of state prediction, measurement association, and trajectory management for radar multitarget tracking under much clutter. In addition, we propose to use the motion extraction LSTM to extract motion features to calculate similarity scores and use it to learn long-dependent target associations, which achieves good results. Our architecture is able to accomplish tracking tasks online and has been verified in simulation scenarios. In future work, we plan to expand it into the video tracking field and make association strategies more robust by combining more clues to achieve better performance.

Data Availability

The experimental data used to support the findings of this study are available from the corresponding authors upon request.

Conflicts of Interest

The authors declare that there are no conflicts of interest regarding the publication of this article.

Acknowledgments

This research was supported by the Fundamental Research Funds for the Central Universities under Grant 3102019ZX015 and in part by the Fundamental Research Funds for the Central Universities under Grant D5000220131.

References

[1] R. E. Kalman, "A new approach to linear filtering and prediction problems," *Journal of Basic Engineering*, vol. 82, no. 1, pp. 35–45, 1960.

[2] S. J. Julier and J. K. Uhlmann, "A new extension of the Kalman filter to nonlinear systems," *Proceedings of SPIE-The International Society for Optical Engineering*, vol. 3068, pp. 182–193, 1999.

[3] H. Kushner, "Approximations to optimal nonlinear filters," *IEEE Transactions on Automatic Control*, vol. 12, no. 5, pp. 546–556, 1967.

[4] S. J. Julier, J. K. Uhlmann, and H. F. Durrant-Whyte, "A new approach for filtering nonlinear systems," in *IEEE Proceedings of 1995 American Control Conference-ACC'95*, pp. 1628–1632, Seattle, WA, USA, 1995.

[5] X. R. Li, X. Zhi, and Y. Zhang, "Multiple-model estimation with variable structure. V. Likely-model set algorithm," *IEEE*

Transactions on Aerospace and Electronic Systems, vol. 36, no. 2, pp. 448–466, 2000.

[6] A. Doucet, S. Godsill, and C. Andrieu, "On sequential Monte Carlo methods for Bayesian filtering," *Statistics and Computing*, vol. 10, no. 3, pp. 197–208, 2000.

[7] H. W. Kuhn, "The Hungarian method for the assignment problem," *Naval Research Logistics Quarterly*, vol. 2, no. 1-2, pp. 83–97, 1955.

[8] D. B. Reid, "An algorithm for tracking multiple targets," *IEEE Transactions on Automatic Control*, vol. 24, no. 6, pp. 843–854, 1979.

[9] T. Fortmann, Y. B. Shalom, and M. Scheffe, "Sonar tracking of multiple targets using joint probabilistic data association," *IEEE Oceanic Engineering*, vol. 8, no. 3, pp. 173–184, 1983.

[10] M. Liu, Z. Liu, W. Lu, Y. Chen, X. Gao, and N. Zhao, "Distributed few-shot learning for intelligent recognition of communication jamming," *IEEE Journal of Selected Topics in Signal Processing*, vol. 16, no. 3, pp. 395–405, 2022.

[11] M. Liu, J. Wang, N. Zhao, Y. Chen, H. Song, and F. R. Yu, "Radio frequency fingerprint collaborative intelligent identification using incremental learning," *IEEE Transactions on Network Science and Engineering*, vol. 9, no. 5, pp. 3222–3233, 2021.

[12] J. Berclaz, F. Fleuret, E. Turetken, and P. Fua, "Multiple object tracking using k-shortest paths optimization," *IEEE Transactions on Pattern Analysis and Machine Intelligence*, vol. 33, no. 9, pp. 1806–1819, 2011.

[13] Y. Li, C. Huang, and R. Nevatia, "Learning to associate: hybrid boosted multi-target tracker for crowded scene," in *IEEE Conference on Computer Vision and Pattern Recognition*, pp. 2953–2960, Miami, FL, USA, 2009.

[14] A. A. K. Runyoro, V. A. Ndume, Z. Mganilwa, and I. Kambira, "A smart approach for vehicle speed monitoring and accidents trend at black spot areas in Tanzania," *Open Access Library Journal*, vol. 9, no. 3, pp. 1–14, 2022.

[15] J. R. Perello-March, C. G. Burns, R. Woodman, M. T. Elliott, and S. A. Birrell, "Driver state monitoring: manipulating reliability expectations in simulated automated driving scenarios," *IEEE Transactions on Intelligent Transportation Systems*, vol. 99, pp. 1–11, 2021.

[16] N. Chenouard, I. Bloch, and J. C. Olivo-Marin, "Multiple hypothesis tracking for cluttered biological image sequences," *IEEE Transactions on Software Engineering*, vol. 35, no. 11, pp. 2736–2750, 2013.

[17] Y. Xiang, A. Alahi, and S. Savarese, "Learning to track: online multi-object tracking by decision making," in *IEEE International Conference on Computer Vision*, pp. 4705–4713, Santiago, Chile, 2015.

[18] A. Alahi, K. Goel, V. Ramanathan, A. Robicquet, L. Fei-Fei, and S. Savarese, "Social lstm: human trajectory prediction in crowded spaces," in *IEEE Conference on Computer Vision and Pattern Recognition (CVPR)*, pp. 961–971, Las Vegas, NV, USA, 2016.

[19] L. Leal-Taixé, C. Canton-Ferrer, and K. Schindler, "Learning by tracking: Siamese CNN for robust target association," in *IEEE Conference on Computer Vision and Pattern Recognition Workshops(CVPRW)*, pp. 418–425, Las Vegas, NV, USA, 2016.

[20] L. Chen, H. Ai, C. Shang, Z. Zhuang, and B. Bai, "Online multi-object tracking with convolutional neural networks," in *IEEE International Conference on Image Processing (ICIP)*, pp. 645–649, Beijing, China, 2017.

[21] S. Ren, K. He, R. Girshick, and J. Sun, "Faster R-CNN: towards real-time object detection with region proposal networks," *IEEE Transactions on Pattern Analysis and Machine Intelligence*, vol. 39, no. 6, pp. 1137–1149, 2017.

[22] K. Simonyan and A. Zisserman, "Very deep convolutional networks for large scale image recognition," 2015, http://arxiv.org/abs/1409.1556.

[23] J. Xiang, G. Zhang, J. Hou, N. Sang, and R. Huang, "Multiple target tracking by learning feature representation and distance metric jointly," 2018, http://arxiv.org/abs/1802.03252.

[24] A. Milan, S. H. Rezatofighi, A. Dick, I. Reid, and K. Schindler, "Online multi-target tracking using recurrent neural networks," in *31st AAAI Conference on Artificial Intelligence (AAAI 2017)*, pp. 4225–4232, San Francisco, USA, 2017.

[25] A. Sadeghian, A. Alahi, and S. Savarese, "Tracking the untrackable: learning to track multiple cues with long-term dependencies," in *IEEE International Conference on Computer Vision (ICCV)*, pp. 300–311, Venice, Italy, 2017.

[26] A. Karpathy, J. Johnson, and F. F. Li, "Visualizing and understanding recurrent networks," 2015, http://arxiv.org/abs/1506.02078.

[27] C. Wang, P. Wu, S. He, and P. Yun, "Robust CPHD algorithm for maneuvering targets tracking via airborne pulsed Doppler radar," *Optik-International Journal for Light and Electron Optics*, vol. 178, pp. 285–296, 2019.

[28] B. Ristic, B. N. Vo, D. Clark, and B. T. Vo, "A metric for performance evaluation of multi-target tracking algorithms," *IEEE Transactions on Signal Processing*, vol. 59, no. 7, pp. 3452–3457, 2011.

Hindawi
Wireless Communications and Mobile Computing
Volume 2023, Article ID 3625917, 15 pages
https://doi.org/10.1155/2023/3625917

Research Article

A DRL-Based Intelligent Jamming Approach for Joint Channel and Power Optimization

Luguang Wang, Guoxin Li, Fei Song, Yunyi Qin, Yangyang Li, Songyi Liu, Yuping Gong, and Yifan Xu

College of Communications Engineering, Army Engineering University of PLA, Nanjing 210000, China

Correspondence should be addressed to Fei Song; songfei2021123@163.com

Received 19 September 2022; Revised 18 October 2022; Accepted 24 November 2022; Published 6 February 2023

Academic Editor: Mingqian Liu

The traditional jamming methods mainly focus on the optimization of a single domain, such as frequency domain. However, in the practical wireless communication, the jamming methods in single dimension domain are limited and difficult to cope with multidomain scenarios. To overcome these issues, this paper investigates the problem of joint decision-making for jamming channel and power in a dynamic spectrum environment. Firstly, the Markov decision process (MDP) is used to formulate the jamming channel and power joint selection problem. Then, a deep reinforcement learning- (DRL-) based jamming algorithm is proposed with the function of parallel learning and joint decision-making. Specially, to accelerate the learning speed of the algorithm, the prioritized experience reply (PER) technology is introduced. Finally, a practical jamming testbed is built to evaluate the proposed algorithm. The simulation results and the testbed results demonstrate the effectiveness of the proposed algorithm, which can guarantee the jamming effect and maximize the utilization of jamming resources.

1. Introduction

Spectrum competition has become a research hotspot in recent years [1, 2]. On one hand, as the main attack way of the attacker, communication jamming technology still stays on the traditional jamming method. These jamming methods excessively rely on the prior information, which makes it difficult to adjust its own jamming strategy adaptively according to the spectrum environment. On the other hand, the increasing level of intelligence in the field of antijamming and the increasing diversity of antijamming methods have brought huge challenges to jamming [3–12]. Therefore, to cope with the increasing powerful antijamming technology and overcome the disadvantages of the traditional jamming patterns being single and inflexible, many scholars have carried out researches on communication jamming technology [13–19]. However, these jamming theories mainly focus on the jamming methods of a single dimensional domain, which can not be extended to other domains. As a result, there is a need to continuously strengthen the intelligent jamming capability in multidomain confrontation scenarios. In this paper, we investigate the problem of joint decision-making for jamming channel and power in the dynamic spectrum environment.

The several problems have not been solved in the existing researches on intelligent jamming: first of all, in practical communication environment, the total power of a jammer is not infinite but limited, and pursuing only jamming effect tend to result in a waste of jamming resources. Then, the jamming methods for single domain are difficult to overcome the challenge caused by the change of other domains in the opponent's communication behavior. Finally, some researches propose the jamming theory methods but did not complete the practical system verification. Obviously, it is necessary to investigate a jamming method that can save the jamming power while ensuring the jamming performance and can be applied in a practical communication environment.

To tackle the abovementioned problems, the following challenges need to be considered: (1) the system model

should be reasonable and effective. A reasonable system model is the key factor to analyze the jamming decision problem. (2) The jamming method must be real-time and efficient. Multidimensional decision-making inevitably brings with it the problem of a large decision space, and it is essential to accelerate the learning and updating process of the algorithm. (3) The proposed jamming method can be deployed in the practical communication system. The practical application of jamming method is necessary to test the jamming performance, so as to promote the deployment of theoretical algorithms to realistic communication confrontation environments.

In response to the above challenges, we model the multidomain joint jamming decision problem based on the Markov decision process (MDP) in the communication confrontation scenario. Also to maximize the utilization of jamming resources, the jamming power is taken into account, and a joint channel and power decision jamming algorithm is proposed. The specific contributions of this paper are summarized as follows:

(i) To make full use of the spectrum features, the Markov decision process is used to model the interaction process between the jammer and the communication user. In particular, the spectrum waterfall (SW) is defined as a state and is used to describe the detailed characteristics of the communication user's frequency usage

(ii) To address the problem of large decision space caused by joint decision, we propose a joint channel and power decision algorithm based on deep reinforcement learning (DRL) with the function of "parallel learning and joint decision-making". By improving the learning network structure, we divide the policy network into two parallel subnetworks for channel decision and power decision, respectively, thus reducing the difficulty of exploration

(iii) To evaluate the performance of the proposed algorithm in the practical communication environment, a software-defined radio- (SDR-) based testbed is designed and built, which contains two subsystems: a wireless communication subsystem and an intelligent jamming subsystem. The proposed jamming algorithm is verified in the testbed and the test results are consistent with the simulations

It should be noted that we have carried out relevant studies on intelligent jamming [20, 21]. The main difference between this paper and [20, 21] is that both [20, 21] investigated only channel-based jamming decision problem without considering power optimization, and secondly, this paper gives solutions to the decision problem in large state space.

The rest of this paper is organized as follows. In Section 2, the related work is presented. The system model and problem formulation are given in Section 3. The details of the proposed joint jamming decision algorithm are introduced in Section 4. In Section 5, simulation results and discussions are given. In Section 6, the jamming testbed platform and practical test results are introduced. Finally, the conclusion is conducted in Section 7.

2. Related Work

With the development of software-defined radio, artificial intelligence, and communication countermeasure technology, wireless communication confrontation has become a major research topic [2]. In recent years, the intelligent antijamming methods have been widely studied, which are represented by game theory [3–7] and machine learning [8–12]. The authors in [3–5] modeled and solved the interaction between the jammers and users using the Stackelberg game to find the optimal antijamming strategies. The authors in [6, 7] used the Markov game to solve the "coordination" and "competition" problem in the multiuser scenarios. In [8], the authors proposed a radio frequency fingerprint identification (RF-FI) framework based on incremental learning to solve the problem of blind signal individual identification of the distributed system, which can overcome the shortcoming of low accuracy of RF-FI identification and poor adaptability to the environment in complex electromagnetic environment. Liu et al. [9] used the SW graph to represent the time-frequency information and proposed the antijamming algorithm based on the DRL. On the basis of [9], Wang et al. [10] proposed a new antijamming scheme called dynamic spectrum antijamming (DSA), which can obtain the optimal strategy with the help of cognitive radio and machine learning. Liu et al. [11] used the spectrum waterfall to recognize the characteristics of different jamming modes and achieved antijamming communication under different jamming modes. The author in [12] introduced a novel jamming recognition method based on distributed few-shot learning to achieve the global optimization of multiple subnetworks by federated learning with the help of the time-frequency diagram of the communication jamming signal. Therefore, to cope with the increasingly powerful antijamming technologies, it is important to investigate the intelligent jamming method.

Based on the abovementioned studies, various types of methods have made a breakthrough in the field of intelligent jamming [13–19]. In [13], the authors proposed an intelligent jamming algorithm based on the Q-learning and evaluated the jamming performance of the algorithm in different antijamming strategies. On this basis, Zhang et al. [14] proposed a jamming framework of "offline learning and virtual decision-making" based on the Q-learning and verified the effectiveness of the algorithm in practical communication environment. Furthermore, Rao et al. [15] utilized the value variance of effective jamming action to set the confidence interval and eliminate the jamming action with low confidence from the action space, which accelerated the optimal strategy learning process. In terms of power domain jamming, the authors in [16, 17] modeled the interaction between the user and jammer as the Stackelberg game, analysed optimal strategies of user and jammer, respectively, and obtained the Stackelberg equilibrium of the game. A power domain jamming algorithm was proposed in [18],

where the jammer could adaptively adjust its own power strategy to jam according to the working state of the user, and the algorithm could guarantee converge to the optimal jamming strategy. RaoHua et al. [19] proposed a jamming resource allocation method based on the maximum policy entropy DRL to enhance the exploration of the strategy to determine the optimal jamming power allocation scheme.

However, all the above jamming methods focused on a single domain, such as the frequency or power domain, making it difficult to address other domains in which the communication user can make adjustments or changes. For example, once the user adjusts its strategy in the power domain, the jamming effect cannot be guaranteed by the simple channel jamming, and vice versa. The jamming effect is poor if the power is low, and the jamming resources will be wasted if the jamming power is too high. Therefore, it is necessary to consider the multidomain jamming method which can adjust both power and channel to improve the jamming effect.

It is significant to study the joint decision of channel and power, and several literatures in antijamming communication have focused on joint channel and power decision-making [22–24]. The literature [22, 23] investigated the problem of joint channel and power decision-making based on reinforcement learning (RL) and DRL, respectively, and the proposed algorithms achieved high throughput while reducing the power of signal transmission. Zhang et al. [24] proposed a novel communication/deception dual mode mechanism and an antijamming communication method based on joint channel and power optimization, which can ensure the normal communication of communication user by attracting jamming with deception user, so as to obtain the maximum communication rate, while little research has been done on joint channel and power jamming decision to ensure the jamming effect and reduce the consumption of jamming power. For the jammer, the jamming power is limited, and it is necessary to study a jamming method that can save jamming resources and guarantee the jamming performance.

The above research on methods of joint channel and power decision-making has led to a series of results and developments; however, the proposed algorithms have not been tested and verified in the practical system. Therefore, it is impossible to evaluate the gap between theoretical simulation and practical application of the algorithm. In this paper, we investigate the jamming problem of joint channel and power decision-making based on DRL and evaluate the algorithm performance in the built testbed platform.

3. System Model and Problem Formulation

3.1. System Model. In this paper, a spectrum confrontation scenario is considered, where there exist a jamming system and a communication system. As shown in Figure 1, the communication system consists of a transmitter-transceiver pair for the transmission and reception of information. The transmission signal is sent at a constant power during the information transmission. The jamming system comprises a spectrum sensing device, a jammer, and an intelligent terminal (agent). The spectrum sensing device and the jammer are connected via the agent. The sensing device can sense the current spectrum state and send the sensed data to the agent, which has the ability of intelligent decision-making and online learning according to analysing the current spectrum information. The jammer can receive the decision information from the agent and emit jamming signal to disturb the user's communication link. The jamming system has multiple power emission levels, which can be denoted as $\mathscr{P} = \{p_1, \cdots, p_S\}$, and is able to select jamming power level in the dynamical spectrum confrontation environment.

Both the jamming system and communication system have the same frequency range, and the frequency range is uniformly divided into K available channels. The set of channel can be denoted as $\mathscr{K} = \{f_1, \cdots, f_K\}$, where $f_k \in \mathscr{K}$ indicates the kth channel's centre frequency, the jamming system and the communication system work according to a time slot division structure. In each time slot, the communication system and the jamming system selects a channel to complete a data transmission process and to emit jamming signal, respectively. The $f_u(t)$ and $f_j(t)$ represent the channel selected by communication system and jamming system, respectively. Furthermore, the jamming system can also select a jamming power level in each time slot to complete the purpose of optimizing the jamming resources.

3.1.1. Time Slot Structure. Figure 2 shows the time slot structure of the user and the jammer. T_u represents the length of a single communication time slot and T_{JW} represents the length of a single jamming time slot, which contains three subslots: spectrum sensing subslot T_{wbss}, jamming emitting sub-slot T_j, and online learning subslot T_l. The specific description is as follows:

(i) *Spectrum sensing subslot* T_{wbss}: the sensing device senses the spectrum environment of the whole frequency range to get the spectrum data; i.e., it continuously senses the spectrum energy intensity and sends it to the agent

(ii) *Jamming emitting subslot* T_j: the agent receives the sensed information from the sensing device and decides on the jamming channel $f_j(t) \in \mathscr{K}$ and jamming power level $p_j(t) \in \mathscr{P}$ according to the state of the spectrum environment. Then, the agent sends the decision information to the jammer, which releases the jamming signal

(iii) *Online learning subslot* T_l: The jamming system learns the frequency usage patterns of communication systems based on spectrum information from sensing device and continuously updates the joint strategy

3.1.2. Communication-Jamming Model. We assume that the bandwidth of each available channel $f_k\{f_k \in (f_1, \cdots, f_K)\}$ is b, and the frequency range of f_k can be represented as $[f_k - b/2, f_k + b/2]$. The power spectral density (PSD) of the

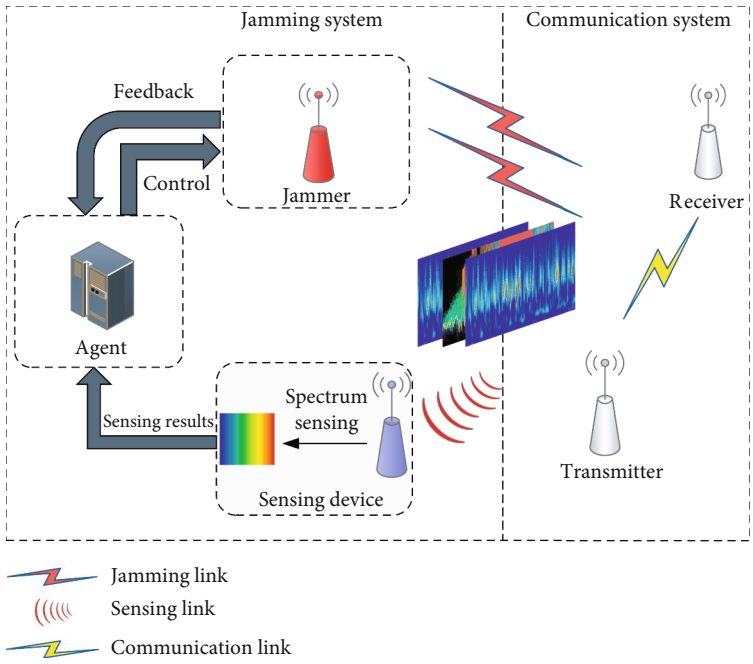

Figure 1: System model.

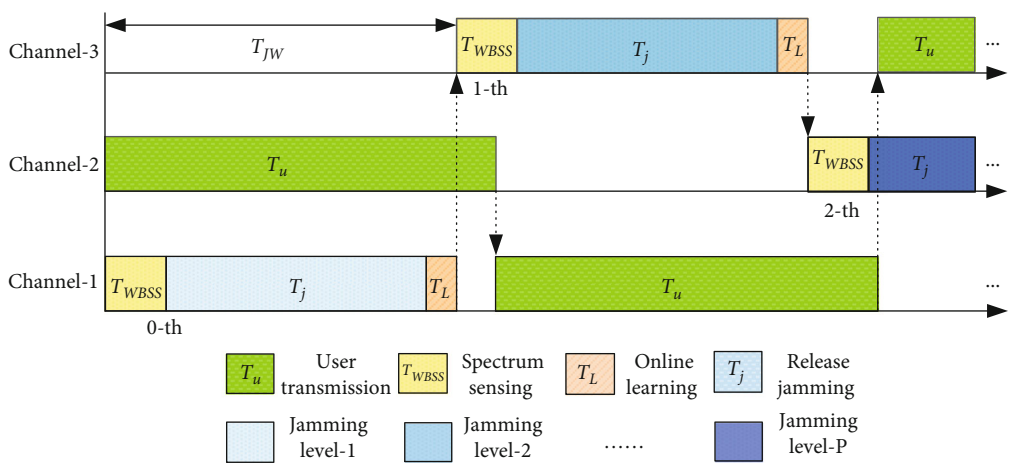

Figure 2: The diagram of jamming communication time slot structure. (T_u indicates the length of a communication time slot and T_{JW} indicates the length of a jamming time slot, where $T_{\mathrm{JW}} = T_j + T_{\mathrm{wbss}} + T_l$.)

user's signal is assumed as $U(f)$, so the user's signal transmitting power can be expressed as $p_u = \int_{f_u-b/2}^{f_u+b/2} U(f - f_u)df$. The PSD function of jamming signal is denoted as $J_s(f)$, where s denotes the jammer's jamming power level. The $N(f)$ represents the PSD function of environment noise. According to the literature [8], the signal-to-interference-plus-noise ratio (SINR) can be represented as

$$\beta_t = \frac{g_u \int_{f_u-b/2}^{f_u+b/2} U(f - f_u(t))}{\int_{f_u-b/2}^{f_u+b/2} \left[g_j J_s\left(f - f_j(t)\right) + N(f) \right]}, \tag{1}$$

where g_u and g_j denote the channel gain from the transmitter to the receiver and the channel gain from the jammer to the receiver, respectively. Referring to [25], we assume that the gain g_l of each channel in the same frequancy range is the same at any time and the value can be obtained in a discrete set of values, i.e., $g_l^t \in \{g_1, \cdots, g_n\}$. And the channel quality is often modeled as a finite-state Markov chain (FSMC) [26]; therefore, we model the channel gain in licensed bandwidth an FSMC chain in this paper. According to literature [27, 28], the user adopts the pattern of fast frequency hopping, with channel switching based on a specific frequency-hopping sequence.

We assume that β_{th} is the threshold for determining whether a user can successfully transmit; therefore, the communication rate of the user can be expressed as

$$C = \begin{cases} b \cdot \log_2(1+\beta_t), & \beta_t \geq \beta_{\text{th}}, \\ 0, & \beta_t < \beta_{\text{th}}. \end{cases} \tag{2}$$

According to [9], we assume that all of the above signals are present at moment t, so the result of the spectrum sensed by the sensing device at moment t can be expressed as

$$S_t(f) = g_j U_t(f - f_u(t)) + J_s\left(f - f_j(t)\right) + N_t(f), \tag{3}$$

the sampled values are expressed as

$$o_i = 10 \log \left[\int_{i\Delta f}^{(i+1)\Delta f} S_t(f) df\right], \tag{4}$$

where Δf is the sample rate of the spectrum. Thus, the sensed spectrum characteristics can be expressed as

$$\mathbf{o}_t = [o_{t,1}, \cdots, o_{t,L}], \tag{5}$$

where $o_{t,L}$ represent the energy intensity at time t when the frequency is f_L.

3.2. Problem Formulation. The MDP is used for modelling the sequential decision problems in a dynamic environment [29], where the jamming system and the communication system interact to make decisions. The MDP can be expressed as $<\mathcal{S}, \mathcal{A}, \mathcal{P}, \mathcal{R}>$, where $\mathcal{S}$ is the environment state space, $\mathcal{A}$ is the action space that the jammer can take, $\mathcal{P}$ is the transition probability of the environment state, and $\mathcal{R}$ is the reward function obtained by the jammer after emitting jamming. The specific meaning of each element in the MDP is as follows:

State. Referring to [9, 21], to avoid loss of spectrum features and to make better use of historical spectrum information, the spectrum waterfall, a two-dimensional time-frequency matrix, is used as state:

$$s_t = \begin{bmatrix} \mathbf{o}_{t-1} \\ \mathbf{o}_{t-2} \\ \vdots \\ \mathbf{o}_{t-M} \end{bmatrix} = \begin{bmatrix} o_{t-1,1} & o_{t-1,2} & \cdots & o_{t-1,K} \\ o_{t-2,1} & o_{t-2,2} & \cdots & o_{t-2,K} \\ \vdots & \vdots & \ddots & \vdots \\ o_{t-M,1} & o_{t-M,2} & \cdots & o_{t-M,K} \end{bmatrix}, \tag{6}$$

where M indicates the size of the recorded spectrum capacity, and the specific value of M can be determined according to the characteristics of the environment.

Action. The action space of the jammer can be expressed as

$$\mathcal{A} \triangleq \left\{a = \left(f_j, p_j\right) : f_j \in \mathcal{K}, p_j \in \mathcal{P}\right\}, \tag{7}$$

where $f_j \in \mathcal{K}$ and $p_j \in \mathcal{P}$ denote the jamming channel and the jamming power level selected by the jammer, respectively.

Reward. In the practical spectrum confrontation scenario, the jammer aims to suppress the normal communication of the user, and therefore, we take the throughput of the communication system into account. Meanwhile, the jamming power is taken into account in order to maximize the avoidance of wasted jamming power. The reward function is designed as follows:

$$r(s_t, a_t) = \delta(C_t) - \lambda p_j(t), a_t = \left(f_j, p_j\right), \tag{8}$$

where C_t denotes the user throughput and can be obtained in Equation (2). $\delta(\cdot)$ denotes the indicator function and the specific expression of which is

$$\delta(x) = \begin{cases} 1, & x = 0, \\ -1, & x \neq 0. \end{cases} \tag{9}$$

The value of the user throughput C_t is zero indicating that the jammer successfully performs jamming and non-zero indicating the jammer unsuccessfully disturbs the communication. So the value of $\delta(\cdot)$ is 1 and -1 in the two cases.

The goal of the intelligent jamming system is to find the best jamming strategy to maximize the cumulative reward value through continuous learning and training; hence, the optimization objective of this paper is as follows:

$$G : \max_a \mathbf{E}_a \left[\sum_{\tau=0}^{\infty} \gamma^\tau r(s_{t+\tau}, a_{t+\tau})\right], a \in \mathcal{A}, \tag{10}$$

where $s_{t+\tau}$ and $a_{t+\tau}$ denote the state and action in the time slot $t+\tau$, $\mathbf{E}_a[\cdot]$ is the mathematical expectation, and $0 < \gamma < 1$ is the long-term discount factor.

4. Joint Power and Channel Jamming Algorithm Based on Deep Reinforcement Learning

A traditional RL algorithm is Q-learning, which sets up a look-up table to record the state-action value $Q(s, a)$. However, for the above proposed MDP process, there are multiple signals existing at the same time, and therefore, the number of available SWs is huge, and the Q-learning algorithm faces difficulty in convergence or even will be out of work. This function can be fitted using deep neural network (DNN), and the deep Q-network (DQN) is proposed to solve high-dimensional state [30]. The DQN method uses a deep convolutional neural network (CNN) to fit the optimal action value, and the action value can be denoted as $Q(s_t, a_t; \theta)$, where θ is the network parameter. Furthermore, the corresponding action can be decided based on the estimated Q function. In our paper, the essential reason in using DQN network is that CNN network has a better performance in image recognition [31, 32], which can be used to identify

the communication behavior of the user using the spectrum waterfall.

4.1. Algorithm Description. As shown in Figure 3, a "parallel learning and joint decision-making" mechanism is designed to accelerate the process of policy learning and updating. The single policy network in the DQN network is divided into two parallel decision subnetworks for channel decision (channel policy subnetwork) and power decision (power policy subnetwork). Each policy subnetwork learns independently and updates the network parameters according to the common reward function. The main benefit of this is to reduce the network decision space. We assume that there are M decisions to select for channel and N decisions for power. A single policy network, where the channel and power are jointly decided by the same policy network, requires a number of $M \times N$ output neurons. In parallel learning network, the number of output neurons required is only $M + N$, which reduces the space for exploratory learning.

A target network update mechanism is also introduced. The two deep Q-networks are defined as the evaluation Q-network and the target Q-network, respectively. To reduce the correlation between the target Q-network and the evaluation Q-network, a separate network is used to fit the target Q-network table during the neural network training, and the network parameters of the evaluation Q-network are periodically copied to the target Q-network.

For the jamming system, the sensed SW is used as the input to the joint channel-power decision network. Based on this, the jamming system makes a joint channel-power decision and receives reward from the spectrum environment. For the Q value of the channel network $Q_f(s_t, a_t)$ or the power network $Q_p(s_t, a_t)$, both are updated by the following Bellman formula:

$$Q(s_t, a_t) = Q(s_t, a_t) + \alpha\left[r(s_t, a_t) + \gamma \max_{a^*} Q(s_{t+1}, a^*) - Q(s_t, a_t)\right], \tag{11}$$

where α and γ indicate the learning rate and discount factor. Small batches of data are selected from the replay memory as debug samples for data replay. Based on this, the loss function is calculated as follows:

$$L(\theta_t) = [y_t - Q(s_t, a_t\,; \theta_t)]^2, \tag{12}$$

where θ_t denotes the network parameters of the evaluation network of the jammer and y_t denotes the target Q value, which is calculated by the following equation:

$$y_t = r_t + \gamma \max_a Q(s_{t+1}, a\,; \theta_t^-), \tag{13}$$

in which the θ_t^- is the network parameters of the target network model. The network uses stochastic gradient descent (SGD) for updating the network parameters with the following specific update formula:

$$\theta_{i+1} = \theta_i + \beta \nabla_{\theta_i} L(\theta_i), \tag{14}$$

where β denotes the learning rate and θ_i denotes the channel network parameter θ_f or the power decision network parameter θ_p in the evaluation network.

Thus, the channel policy subnetwork and the power policy subnetwork are updated by the above equations, completing the policy learning and updating.

4.2. Prioritized Experience Replay. A critical component of algorithm-based DQN networks is the experience replay. The agent collects the transition (s_t, a_t, r_t, s_{t+1}) during the training process and stores them in the replay memory, which is a fixed size buffer that holds the most recent transitions collected. It can reuse data multiple times for training, rather than discarding it immediately after it is collected. In [33], the author adopts the way of random sampling for replay to reduce the correlation of training samples, but to some certain extent, random sample limits the efficiency of replay. For communication confrontation scenario in particular, the reward of jamming is obtained relatively sparsely, and a large number of useless samples may be sampled during empirical playback, thus reducing the learning efficiency. The authors in [34–35] proposed a framework for prioritizing experience, which can replay important transitions more frequently and learn more efficiently. Motivated by them, the PER technology is introduced to improve the efficiency of the algorithm.

The core of prioritized replay is a measure of the importance of each transition, and temporal difference-error (TD-error) is used as a metric to judge the priority of sampling. For each transition, we calculate its TD-error value as follows:

$$\delta_t^j = r_t^j + \gamma \max_a Q(s_t, a^*\,; \theta_t^-) - Q(s_t, a_t\,; \theta_t), \tag{15}$$

where δ_t^j and r_t^j denote the TD-error value and the reward for the jth sample generated by the jammer in the tth iteration. A larger δ_t^j value means that the transition has greater replay significance. Replaying these samples can improve the efficiency of network training and promote the convergence of the algorithm. The probability value of jth sample can be defined as

$$P(j) = \frac{p_j^\alpha}{\sum_j p_j^\alpha}, \tag{16}$$

where $p_j > 0$ is the priority of transition. α is used to control the coefficient applied to the priority, and it can be seen that when the $\alpha = 0$, it indicates uniform sampling. We give the form of p_j in the following:

$$p_j = |\delta_j| + \sigma, \tag{17}$$

and σ is a small positive constant to prevent the edge-case of

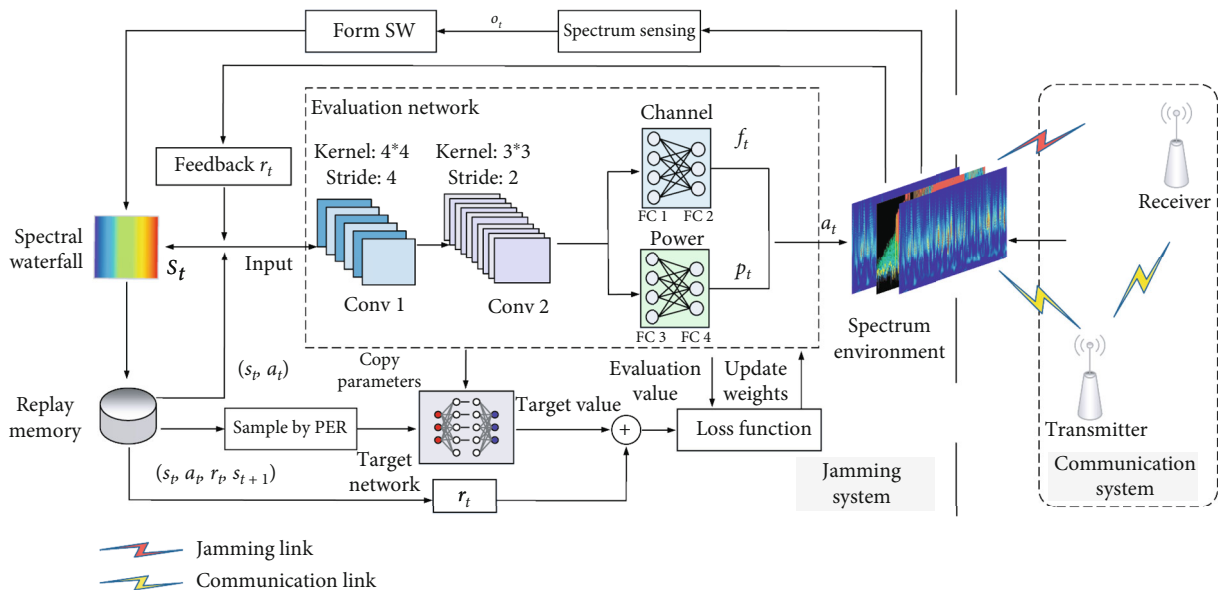

Figure 3: Schematic showing of the proposed jamming framework.

transitions not being revisited once the TD-error is almost zero. However, the PER technology introduces a new bias due to overfitting of the network as a result of reduced training sample diversity. We can correct this bias by using importance-sampling (IS) weights:

$$w_j = \left(\frac{1}{M_e} \cdot \frac{1}{P(j)}\right)^u, \tag{18}$$

where M_e indicates the capacity of the replay memory and u indicates the degree of correction. These weights can be used to update the network parameters using $w_j\delta_j$ instead of δ_j. So the corrected loss function can be obtained from the following equation:

$$L(\theta_t) = \sum_j w_j \left[y_j^t - Q(s_t, a_t; \theta_t)\right]^2, \tag{19}$$

where the y_j is the target value of jth sample and can be obtained by

$$y_j^t = r_j^t + \gamma \max_a Q(s_{t+1}, a; \theta_t^-). \tag{20}$$

ε – greedy is widely used in previous works that mainly tends to solve the dilemma of "exploration" and "exploitation." To enhance the "exploration" ability, the dynamic ε – greedy is introduced, and ε is updated in each time slot according to the following rules:

$$\varepsilon = \begin{cases} \varepsilon_0 e^{-\lambda t}, & \varepsilon \geq \varepsilon_f, \\ \varepsilon_f, & \varepsilon < \varepsilon_f, \end{cases} \tag{21}$$

where ε_0 is the initial exploration value, ε_f is the final exploration value, and λ is the decay rate. Therefore, the selection of the jammer action is carried out according to the following rules:

$$a(f_t) = \begin{cases} \text{random}, & \varepsilon, \\ \underset{\text{ft}}{\operatorname{argmax}} Q_f(s_{t+1}, f_t; \theta_f), & 1-\varepsilon, \end{cases} \tag{22}$$

$$a(p_t) = \begin{cases} \text{random}, & \varepsilon, \\ \underset{p_t}{\operatorname{argmax}} Q_p(s_{t+1}, p_t; \theta_p), & 1-\varepsilon, \end{cases} \tag{23}$$

where f_t and p_t denote the channel decision and power decision of the jammer, respectively, and $Q_f(s_{t+1}, f_t; \theta_f)$ and $Q_p(s_{t+1}, p_t; \theta_p)$ denote the channel Q value and power Q value.

Therefore, a channel-power joint decision jamming algorithm based on parallel DQN (CPJ-PDQN) is proposed, whose details are shown in Algorithm 1.

4.3. Network Structure. Deep reinforcement learning is a method that combines the strong feature extraction ability of deep learning in complex environments with the decision-making advantage of reinforcement learning. The network structure proposed in this paper comprises convolution layers (CL) and full connection layers (FCL), which are used for feature extraction and policy decision, respectively.

The neural network structure is shown in Figure 4. The first CL uses 32 filters with size 4×4 and stride 4, and the second CL uses 64 filters with size 3×3 and stride 2. The FCL1 and FCL2 of channel network have 256 neurons and $|\mathscr{K}|$ neurons, respectively, and the FCL3 and FCL4 of power network have 256 neurons and $|\mathscr{P}|$ neurons, respectively. Each neuron in FCL2 and FCL4 represents one available channel action f_t and one available power channel action p_t. The final jamming action a_t is combined by the f_t and

Initialization:
The parameters of channel network θ_f and power network θ_p are initialized to random value.
Initialize the replay memory $D_f = \emptyset$, $D_p = \emptyset$ and the iteration time $t = 0$.
For $\boldsymbol{t} = \mathbf{1}, \mathbf{2}, \mathbf{3} \cdots \infty$ do
Sense to construct state $s_t = [\mathbf{o}_t, \mathbf{o}_{t-1}, \cdots, \mathbf{o}_{t-M+1}]^T$.
Calculate Q value Q_f and Q_p, select jamming channel f_t and jamming power f_p according to the ε – greedy strategy.
Execute joint action $a_t = (f_t, p_t)$ and emit jamming signals.
Calculate its reward $r(s_t, a_t)$ in Equation (8).
Obtain $\mathbf{o}_{t+1}$ by spectrum sensing. Update the next state $s_{t+1} = [\mathbf{o}_{t+1}, \mathbf{o}_t, \cdots, \mathbf{o}_{t-M+2}]^T$, add the experience (s_t, f_t, r_t, s_{t+1}) in replay memory D_f and add the experience (s_t, p_t, r_t, s_{t+1}) in replay memory D_p.
If $|\boldsymbol{D_f}| \geq \boldsymbol{M_e}$ and $|\boldsymbol{D_p}| \geq \boldsymbol{M_e}$ do
Sample minibatch of (s_t, f_t, r_t, s_{t+1}) from D_f and
(s_t, p_t, r_t, s_{t+1}) from D_p according to the PER method
by Equations (15)–(18). Calculate loss value according to Equation (19).
Update network parameters θ_f and θ_p by SGD.
Update target network $\theta^- = \theta$ every N_t iteration.
End If
End For

Algorithm 1: Channel and power joint decision jamming algorithm based on parallel DQN (CPJ-PDQN).

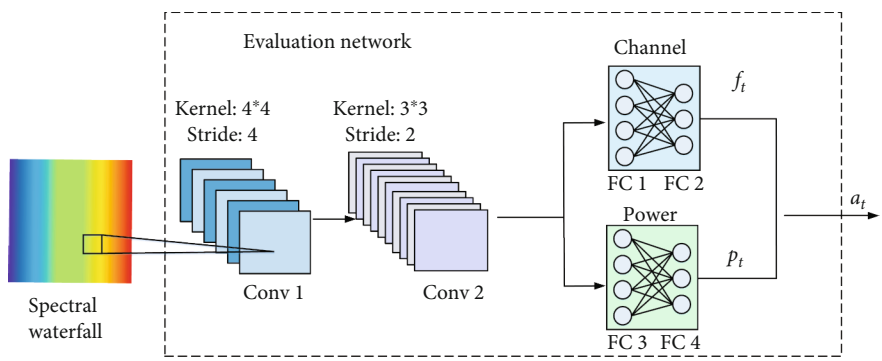

Figure 4: Deep neural network structure.

p_t, i.e., $a_t = (f_t, p_t)$. The specific network parameters are shown in Table 1.

4.4. Algorithm Complexity Analysis. Inspired by the literature [36], we use the index of floating-point operations (FLOPs) to measure the algorithm complexity, which is calculated as

$$\text{Time} \sim \mathrm{O}_c\left(\sum_{l_c} H_{l_c} \cdot B_{l_c} \cdot F_{l_c}{}^2 \cdot C_{l_c-1} \cdot C_{l_c}\right) + \mathrm{O}_f\left(\sum_{l_f}\left(2I_{l_f}E_{l_f} - 1\right)\right) + \mathrm{O}_p\left(\sum_{l_p}\left(2I_{l_p}E_{l_p} - 1\right)\right), \tag{24}$$

where O_c, O_f, and O_p denote the complexity of convolution layer, channel subnetwork (FCL1, FCL2), and power subnetwork (FCL3, FCL4), respectively. l_c, l_f, and l_p denote the number of CL layers, FCL layers in channel subnetwork, and FCL layers in power subnetwork, respectively. In CL layers, H and B denote the length and width of the output feature, F is the size of filter, and C_{l_c} is the number of filters in l_c layer. In FCL layer, I and E denote the number of input neurons and output neurons, respectively. According to the network parameters in Table 1, the algorithm proposed in this paper requires 5×10^7 FLOPs every second, and the computation requirements can be satisfied by the common multicore central processing unit (CPU).

5. Simulation Results and Analysis

In this section, simulations are performed to evaluate the effectiveness of the proposed algorithm. We assume that the bandwidth of the available frequency band for the user and jammer is 20 MHz, which can be divided into 10 channels with a bandwidth of 2 MHz. Spectrum sensing is performed with spectrum resolution $\Delta f = 100$ kHz per millisecond, resulting to 200 spectrum samples. The constructed SW saves a historical length $\Phi = 200$ ms, so the size of SW is 200×200. The transmission power of transmitter is constant at 20 dBm, and the power of the background noise is -90 dBm. The jamming power is divided into high, medium, and low levels with power values of 30 dBm, 20 dBm, and 10 dBm, respectively, which can be denoted as $\mathscr{P} = \{30,20,10\}$. According to [26, 37], the channel gain

Table 1: Structural parameters of the policy network.

Network layer	Input	Output	Parameter
Conv 1	$200 * 200$	$50 * 50 * 32$	Kernel: 4×4; stride: 4; filter: 32
Conv 2	$50 * 50 * 32$	$25 * 25 * 64$	Kernel: 3×3; stride: 2; filter: 64
FCL 1	$25 * 25 * 64$	256	$\lvert\mathscr{K}\rvert$ represents the number of available channel action.
FCL 2	256	$\lvert\mathscr{K}\rvert$	
FCL 3	$25 * 25 * 64$	256	$\lvert\mathscr{P}\rvert$ represents the number of available power action.
FCL 4	256	$\lvert\mathscr{P}\rvert$	

can be modeled as FSMC and can be denoted as $g = g_p|h_r|^2$, where g_p and $|h_r|^2$ represent the path loss and the Rayleigh fading. The threshold of correcting demodulation for user is 10 dB. And the user adopts the fast frequency-hopping communication pattern (FFH) to communicate according to [27, 28]. Other simulation parameters are shown in Table 2.

ADAM optimizer is used to train the deep Q-network, and the minibatch size is 64. In simulation, the user's throughput rate (UTR) and the jammer's jamming success efficiency (JSE) are introduced to evaluate the performance of proposed algorithm. The UTR can be defined as

$$\mathrm{UTR} = \frac{S_{\mathrm{cur}}}{S_{\mathrm{all}}}, \tag{25}$$

where S_{cur} indicates the number of packets correctly demodulated by the receiver and S_{all} indicates the number of all packets sent by the transmitter. The JSE can be defined as

$$\mathrm{JSE} = \frac{\delta(C_t)}{p_j}, \tag{26}$$

where $\delta(C_t)$ can be obtained from Equations (2) and (9), indicating that whether the jamming is successful. The p_j indicates the power policy adopted for jamming. The JSE reflects the value of the jammer's utility per unit power, and a higher value of JSE indicates higher jamming efficiency and higher resource utilization.

In the simulation, the several jamming algorithms are introduced as comparison to evaluate the proposed jamming algorithm:

(i) Collaborative power and channel jamming algorithm (CPCJA): the algorithm in [23] is introduced as the benchmark, and the channel and power decision are determined by a single policy network

(ii) DQN-based channel decision algorithm with high power level (DQNCD-HP): in this algorithm, the jammer only makes channel decision-based DQN network, and the jammer remains the constant highest jamming power level to jam

(iii) DQN-based channel decision algorithm with medium power level (DQNCD-MP): in this algorithm, the jammer only makes channel decision-based DQN network, and the jammer remains the constant medium jamming power level to jam

(iv) DQN-based channel decision algorithm with low power level (DQNCD-LP): in this algorithm, the jammer only makes channel decision-based DQN network, and the jammer remains the constant lowest jamming power level to jam

In Figure 5, we compare the performance of different jamming algorithms in UTR. From the graph, it can be seen that the performance of DQNCD-LP algorithm is the worst, followed by the DQNCD-MP. A low jamming power level is bound to cause a decrease in jamming effectiveness, which can not jam all the transmitted packets. Conversely, when the jammer works on the highest jamming power level, i.e., DQNCD-HP, almost all the packets are successfully jammed, and the value of UTR is close to 10%. The proposed CPJ-PDQN algorithm and the CPCJA algorithm are basically consistent with the highest power effect, which is maintained at about 14% and 16%, respectively. And the convergence speed of the proposed algorithm is faster than that of CPCJA, which also indicates the advantages of parallel network structure and prioritized experience replay technique in algorithm performance. Therefore, we can conclude that there is little difference in the actual jamming effect between the proposed CPJ-PDQN algorithm, CPCJA, and the DQNCD-HP algorithm, and all of them can eventually reduce the user's throughput rate to less than 20%.

Figure 6 shows the JSE comparison curves of the CPJ-PDQN algorithm and the comparison algorithms. It is obvious that the CPJ-PDQN algorithm has the highest JSE value, followed by the CPCJA algorithm, and finally the three constant power level jamming algorithms (DQNCD-HP/MP/LP). Combined with the UTR performance in Figure 5, we focus on the analysis of the JSE value of the DQNCD-HP algorithm, CPCJA algorithm, and the proposed algorithm. Although the DQNCD-HP algorithm has the lowest UTR value, the overall JSE is low because the whole jamming process is continuously performed at the highest power level, which may cause a waste of jamming resources. The JSE value in the CPCJA algorithm is higher than that of the DQNCD-HP algorithm. This is because during the learning process, the jammer can learn the appropriate power level according to the transmission power, and can achieve the same performance with the DONCD-HP with a smaller

Table 2: Parameter values used in the simulation.

Meaning	Parameter	Value
Discount factor	γ	0.5
Initial exploration probability	ε_0	0.95
Final exploration probability	ε_f	0.05
Decay rate	λ	0.0002
Learning rate	α	0.001
Communication time slot	T_u	100 ms
Spectrum sensing subslot	T_{wbss}	3 ms
Jamming emitting subslot	T_j	90 ms
Online learning subslot	T_l	2 ms
Jamming time slot	T_{JW}	95 ms
Number of iterations	Ite	2900

power. The proposed CPJ-PDQN algorithm has the highest JSE value due to the parallel network structure and the introduction of PER sample. The PER technique plays back continuously for samples with higher priority and therefore plays back more often for samples with higher priority, which leads the highest JSE value. Therefore, we conclude that the JSE of the proposed algorithm is much greater than that of the comparison algorithms under the condition that the UTR values are basically the same. Therefore, the proposed algorithm has a greater advantage in terms of resource utilization.

From the simulation results and analysis, it can be seen that the proposed algorithm exhibits superior performance compared to other algorithms. The proposed algorithm combines the advantage of parallel networks and PER technique, which makes the algorithm more suitable for practical communication environment by reducing user throughput while saving jamming resources. To evaluate the performance of the proposed jamming algorithm, we build a practical jamming system to verify it, and the details will be presented in the next section.

6. Intelligent Jamming System Implementation and Testing

In this section, an intelligent communication confrontation system based on SDR is designed and built to evaluate the performance of the proposed algorithm in practical wireless communication. The SDR system has many advantages over conventional radio systems, such as the function to be implemented can be designed by software, the system structure is universal, and the operation performance is fine, which can be used to quickly design and build powerful and independent wireless communication system. In addition, the SDR equipment are flexibility in function, and its hardware can be updated or extended with the development of devices and technology. Therefore, the SDR technology is introduced to verify the proposed algorithm. In terms of hardware selection, the USRP B210 devices are chosen as the RF-front and the industrial personal computer (IPC) X-86 as the signal processor. The B210 is used to complete sending and receiving signals, and the IPC is used to analyze and process data.

6.1. System Scheme Design. Figure 7 shows the hardware composition of the practical communication confrontation system. Functionally, the system can be divided into two separate subsystem: a jamming subsystem and a wireless communication subsystem. The whole process of the two subsystems working is demonstrated through a public visual platform. The visual platform is designed to evaluate the jamming effect, which can display the real-time spectrum environment, spectrum waterfall, and user's throughput.

The jamming subsystem is divided into two submodules: a spectrum sensing submodule and an intelligent decision submodule. The spectrum sensing submodule sends the sensed spectrum information to the intelligent decision submodule and drives the intelligent decision submodule to make a joint channel and power decision to emit the jamming signal.

The communication system consists of a transmitting submodule and a receiving submodule, and the two modules coordinate to complete the data transmission and reception. The modulation and demodulation of the signals are performed in the IPC device. The relevant parameters and strategies can be set in the PC terminal.

6.2. System Implementation. For the communication confrontation system built in this paper, we focused on the design and implementation of the spectrum sensing submodule and the intelligent decision submodule. The wide-band spectrum sensing technology is used in the spectrum sensing submodule to achieve the acquisition and processing of spectrum information [38].

The intelligent decision submodule is completed in the IPC, and its main function is to determine the jamming channel and jamming power by implementing the channel power joint decision algorithm proposed in this paper. Figure 8 shows the working process of the decision submodule. Firstly, the sensing device transmits the sensed the spectrum information to the intelligent jammer. Secondly, the intelligent decision submodule makes decision according to the decision-making algorithm in the IPC and updates network parameters according to the reward value obtained. Finally, the USRP device parameters (jamming signal bandwidth, jamming duration, and jamming gain) are configured and jamming signals are emitted, and all the above process is looped to drive the continuous operation of the intelligent jamming system.

6.3. System Test and Result Analysis. Based on the above system scheme design and system implementation, the practical platform diagram of the confrontation system is shown in Figure 9. In the practical system test, the range of communication frequency is 840-860 MHz, which is divided into 10 communication channels with a bandwidth of 2 MHz. The jamming time slot T_{JW} of the jammer is set to 550 ms, and the length of a user's communication time slot T_u is set to

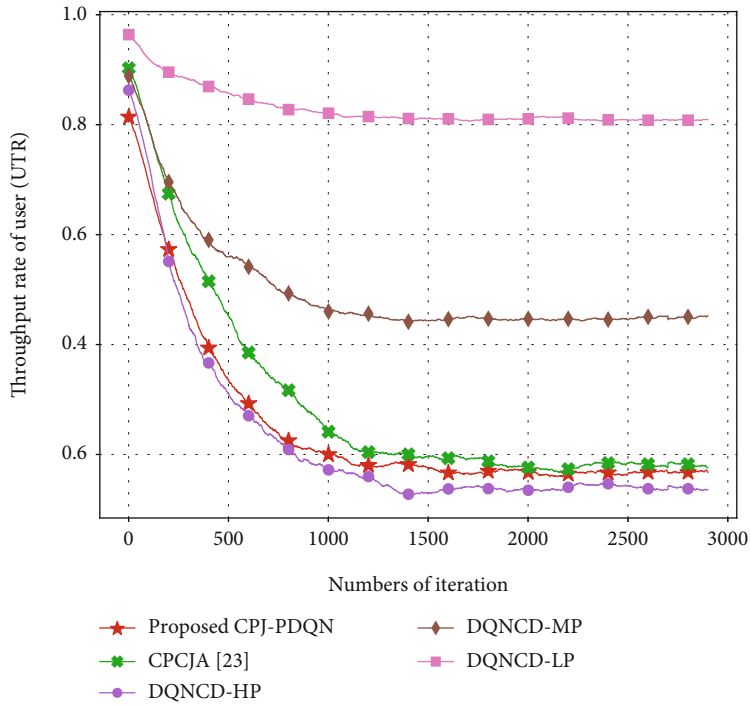

Figure 5: User's throughput rate comparison.

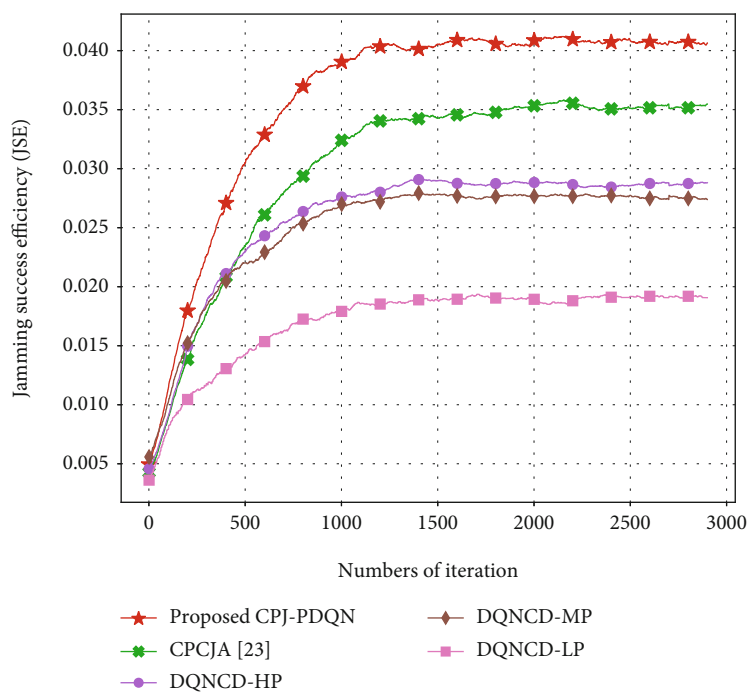

Figure 6: Jamming success efficiency comparison.

650 ms. The UTR in Equation (25) and JSE in Equation (26) are also introduced as the evaluation indicators.

It should be pointed out that the value of C_t in Equation (26) can be obtained in Equation (2) in the simulations. However, in the practical system test, the SINR value at the receiver is difficult to obtain during the system testing. Therefore, when verifying the proposed algorithm in the SDR platform, we equate the user's throughput by counting the number of ACKs and NCKs on the communication user.

In the system test verification, the transmitter sends K packets per second to the receiver, and for each packet, the receiver sends an ACK frame or NCK frame to the transmitter, which indicates whether the packet was transmitted properly. The user throughput rate per unit time can

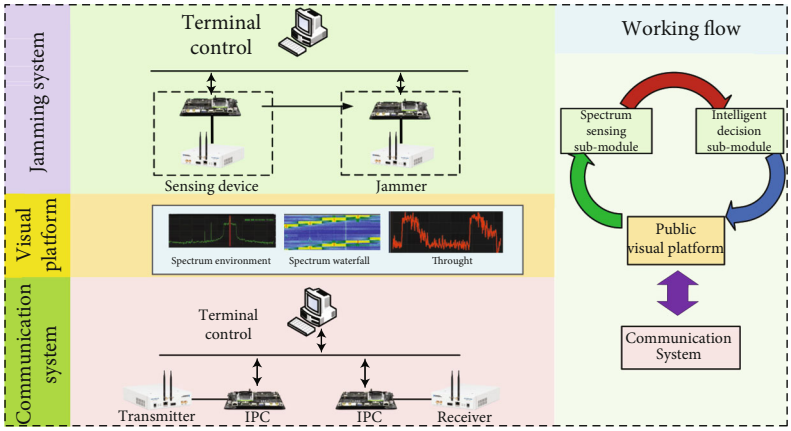

Figure 7: Hardware composition of intelligent jamming system. (The jamming system is composed of a spectrum sensing submodule for obtaining spectrum state and intelligent decision submodule for intelligent decision-making. The communication system serves as the companion system.)

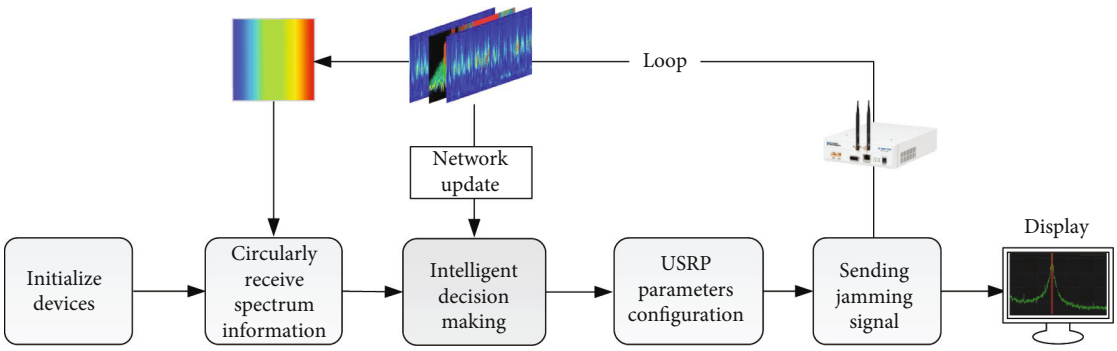

Figure 8: The working process of the intelligent decision-making submodule.

Figure 9: Diagram of the practical SDR testbed.

therefore be defined as

$$\text{thr} == N_{\text{ack}} + N_{\text{nck}}, \tag{27}$$

where N_{ack} and N_{nck} indicate the number of ACK frames and NCK frames received per second, respectively. Therefore the practical test value C_t can be defined as

$$C = \begin{cases} 1, & \text{thr} > \beta, \\ 0, & \text{thr} \leq \beta. \end{cases} \tag{28}$$

where β indicates the threshold value used to determine whether the user's transmission is successful. The value β in our system verification is set to 0.7.

To clearly compare the jamming performance of the proposed algorithm and comparison algorithms, we make statistics of the test data in the whole online process and redraw them in the same graph. To accurately display the trend of the proposed algorithm, we count data every 20 user time slots. The practical test results are shown in Figures 10 and 11.

Figure 10 shows the real-time curve of UTR in the practical system test. The green curve indicates the DQNCD-LP

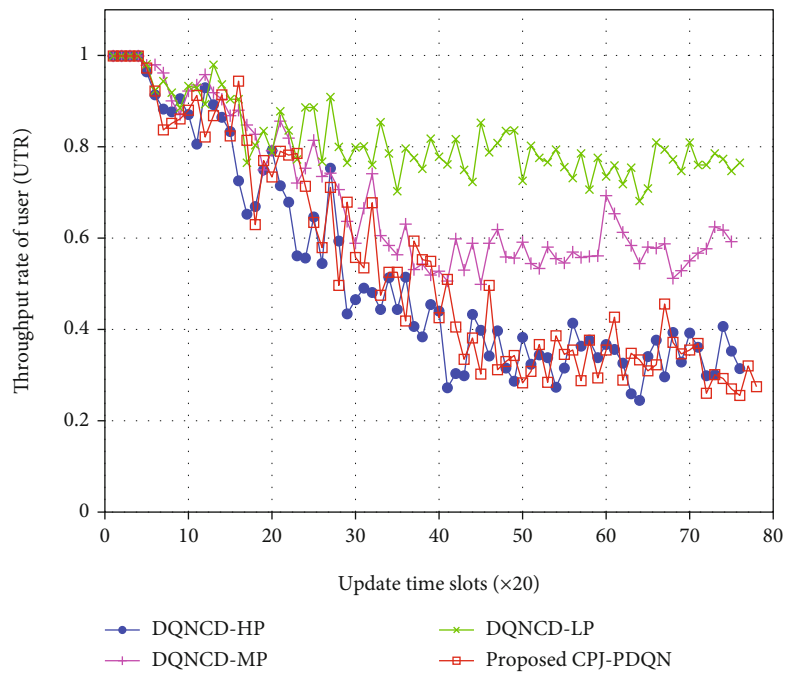

Figure 10: User's throughput rate comparison in testbed test.

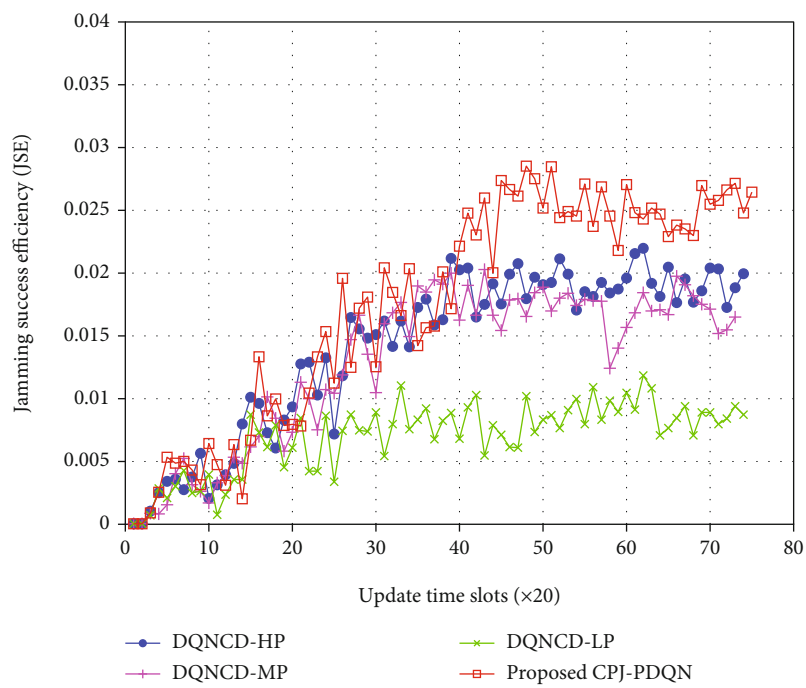

Figure 11: Jamming success efficiency comparison in testbed test.

algorithm with low power. Consistent with the simulation results, the performance of this algorithm is poor because the jamming power is low and the jamming signal cannot completely suppress the communication signal. Therefore, the UTR is maintained at 78%. The pink curve indicates the DQNCD-MP algorithm with medium power level, and the performance of it is better than the DQNCD-LP method with a UTR value about 60%. The blue curve represents the DQNCD-HP algorithm using the highest jamming power, and the performance is the best. The UTR value when using the DQNCD-HP is around 34.1%. The red curve indicates the performance of the proposed CPJ-PDQN algorithm and the UTR value is about 36.7%. Obviously, it can be seen that the jamming effect of the proposed algorithm is basically the same as the suppression effect of the user throughput when using the highest power level (DQNCD-HP).

However, the practical test results shown in Figure 10 are inferior to the simulation results in Figure 5. The reason

causing this phenomenon is that there is a certain delay in signal processing and channel switching in practical system. The influence of the external environment also causes uncertainty, which leads to the poor test result compared with the theoretical simulations.

Figure 11 shows the comparison curve of the JSE in system test. The DQNCD-LP algorithm has the lowest JSE value. The main reason is that the low-power algorithm has a poor jamming performance, and the number of successful jamming is few. The difference between DQNCD-MP and DQNCD-HP in JSE value is not significant. For the DQNCD-MP algorithm, although the performance is poor in the UTR value, the power level used is not high. For the DQNCD-HP algorithm, although the performance is the best in UTR value, the power level used is also the highest. Therefore, there is little difference between the two algorithms in JSE values, which are about 0.017 and 0.019, respectively. Obviously, the JSE value of the proposed CPJ-PDQN algorithm is the highest, because the UTR performance of the proposed algorithm is equivalent to that of DQNCD-HP, but the power level in the convergence stage is lower than that of DQNCD-HP, so the JSE value is the highest, about 0.025. It can be seen that the proposed CPJ-PDQN algorithm not only successfully jams on the transmission signal but also significantly saves the jamming resources. Although the practical test results are not as intuitive as the simulation results, the overall trend shown is consistent with the simulation results, which also shows the effectiveness of the algorithm.

6.4. Application Scenarios. From the analysis above, it can be seen that the proposed CPJ-PDQN algorithm can optimize both the jamming channel and the jamming power at the same time and is suitable for the confrontation scenario where the jammer's energy is limited. In addition, the SDR technology is currently developing in the direction of miniaturisation and intelligence and has great prospects in the field of spectrum confrontation [39, 40]. Therefore, the proposed scheme can be deployed in the UAV electronic jamming system because the UAV electronic jamming system require multiple jammers to work together in a coordinated manner to complete the jamming task. The proposed algorithm can guarantee the jamming effect and save the jamming power at the same time, so as to ensure the endurance of the jammer and its continuous operation.

7. Conclusion

In this paper, we investigated the problem of jamming channel and power joint selection in the dynamic spectrum environment. Firstly, we introduced the MDP framework to model and analyze the problem of joint jamming channel and power selection. Secondly, a joint channel and power jamming algorithm was proposed, which works on the parallel learning and joint decision mechanism. In particular, the PER technology replaced the random sampling to accelerate the convergence of algorithm. Furthermore, verification of the proposed algorithm was performed on the SDR testbed. The performance of the simulation results and testbed results indicated that the proposed algorithm can be applied to practical system, which could guarantee the jamming performance and save jamming resources simultaneously.

Data Availability

The data in this article are generated by simulation, and the simulation process is described in the article.

Conflicts of Interest

The authors declare that they have no conflicts of interest.

Acknowledgments

This work was supported in part by the National Natural Science Foundation of China under Grants 62071488, 62101594, 62101595, 62061013, and 62001514 and in part by the Jiangsu Province Natural Science Foundation under Grant BK20200580.

References

[1] Q. Wu and R. Jing, "New paradigm of electromagnetic spectrum space: spectrum situation (in Chinese)," *Journal of Nanjing University of Aeronautics and Aeronautics*, vol. 48, no. 5, pp. 625–632, 2016.

[2] K. Grover, A. Lim, and Q. Yang, "Jamming and anti-jamming techniques in wireless networks: a survey," *International Journal of Ad Hoc and Ubiquitous Computing*, vol. 17, no. 4, pp. 197–215, 2014.

[3] Z. Su, N. Qi, Y. Yan et al., "Guarding legal communication with smart jammer: Stackelberg game based power control analysis," *China Communications*, vol. 18, no. 4, pp. 126–136, 2021.

[4] N. Qi, W. Wang, M. Xiao et al., "A learning-based spectrum access Stackelberg game: friendly jammer-assisted communication confrontation," *IEEE Transactions on Vehicular Technology*, vol. 70, no. 1, pp. 700–713, 2021.

[5] L. Xiao, T. Chen, J. Liu, and H. Dai, "Anti-Jamming transmission Stackelberg game with observation errors," *IEEE Communications Letters*, vol. 19, no. 6, pp. 949–952, 2015.

[6] F. Yao and L. Jia, "A collaborative multi-agent reinforcement learning anti-jamming algorithm in wireless networks," *IEEE Wireless Communications Letters*, vol. 8, no. 4, pp. 1024–1027, 2019.

[7] Q. Zhou, Y. Li, and Y. Niu, "Intelligent anti-jamming communication for wireless sensor networks: a multi-agent reinforcement learning approach," *IEEE Open Journal of the Communications Society*, vol. 2, pp. 775–784, 2021.

[8] M. Liu, J. Wang, N. Zhao, Y. Chen, H. Song, and R. Yu, "Radio frequency fingerprint collaborative intelligent identification using incremental learning," *IEEE Transactions on Network Science and Engineering*, vol. 9, no. 5, pp. 3222–3233, 2021.

[9] X. Liu, Y. Xu, L. Jia, Q. Wu, and A. Anpalagan, "Anti-jamming communications using spectrum waterfall: a deep reinforcement learning approach," *IEEE Communications Letters*, vol. 22, no. 5, pp. 998–1001, 2018.

[10] X. Wang, J. Wang, Y. Xu et al., "Dynamic spectrum anti-jamming communications: challenges and opportunities,"

IEEE Communications Magazine, vol. 58, no. 2, pp. 79–85, 2020.

[11] S. Liu, Y. Xu, X. Chen et al., "Pattern-aware intelligent anti-jamming communication: a sequential deep reinforcement learning approach," *IEEE Access*, vol. 7, pp. 169204–169216, 2019.

[12] M. Liu, Z. Liu, W. Lu, Y. Chen, X. Gao, and N. Zhao, "Distributed few-shot learning for intelligent recognition of communication jamming," *IEEE Journal of Selected Topics in Signal Processing*, vol. 16, no. 3, pp. 395–405, 2022.

[13] H. Yang and J. Zhang, "Research on intelligent jamming algorithms based on reinforcement learning (in Chinese)," *Electronic Measurement Technology*, vol. 41, no. 20, pp. 49–54, 2018.

[14] S. Zhang, H. Tian, X. Chen et al., "Design and implementation of reinforcement learning-based intelligent jamming system," *IET Communications*, vol. 14, no. 18, pp. 3231–3238, 2020.

[15] N. Rao, H. Xu, and B. Song, "Q-learning intelligent jamming decision algorithm based on efficient upper confidence bound variance (in Chinese)," *Journal of Harbin Institute of Technology*, vol. 54, no. 5, pp. 162–170, 2022.

[16] Y. Li, S. Bai, and Z. Gao, "A multi-domain anti-jamming strategy using Stackelberg game in wireless relay networks," *IEEE Access*, vol. 8, pp. 173609–173617, 2020.

[17] Y. Li, L. Xiao, J. Liu, and Y. Tang, "Power control Stackelberg game in cooperative anti-jamming communications," in *International Conference on Game Theory for Networks*, pp. 1–6, Beijing, China, 2014.

[18] S. Amuru, C. Tekin, M. . der Schaar, and R. M. Buehrer, "Jamming bandits—a novel learning method for optimal jamming," *IEEE Transactions on Wireless Communications*, vol. 15, no. 4, pp. 2792–2808, 2016.

[19] N. Rao, X. U. Hua, Q. I. Zisen, S. O. N. G. Bailin, and S. H. I. Yunhao, "Allocation method of communication interference resource based on deep reinforcement learning of maximum policy entropy," *Journal of Northwestern Polytechnical University*, vol. 39, no. 5, pp. 1077–1086, 2021.

[20] L. Wang, F. Song, G. Fang et al., "A multi-agent reinforcement learning-based collaborative jamming system: algorithm design and software-defined radio implementation," *China Communications*, vol. 19, no. 10, pp. 38–54, 2022.

[21] L. Wang, F. Song, Z. Feng et al., "Intelligent jamming against dynamic spectrum access user: algorithm design and verification system implementation," *IEEE Communications Letters*, vol. 11, no. 11, pp. 2405–2409, 2022.

[22] X. Pei, X. Wang, L. Ruan, L. Huang, X. Yu, and H. Luan, "Joint power and channel selection for anti-jamming communications: a reinforcement learning approach," in *International Conference on Machine Learning and Intelligent Communications*, pp. 551–652, Springer, Cham, 2019.

[23] Y. Li, Y. Xu, X. Wang, W. Li, and W. Bai, "Power and frequency selection optimization in anti-jamming communication: a deep reinforcement learning approach," *IEEE 5th International Conference on Computer and Communications (ICCC)*, 2019, pp. 815–820, Chengdu, China, 2019.

[24] X. Zhang, H. Wang, L. Ruan, Y. Xu, and Z. Feng, "Joint channel and power optimisation for multi-user anti-jamming communications: a dual mode Q-learning approach," *IET Communications*, vol. 16, no. 6, pp. 619–633, 2022.

[25] B. Wang, Yongle Wu, K. J. R. Liu, and T. C. Clancy, "An anti-jamming stochastic game for cognitive radio networks," *IEEE Journal on Selected Areas in Communications*, vol. 29, no. 4, pp. 877–889, 2011.

[26] Q. Zhang and S. A. Kassam, "Finite-state Markov model for Rayleigh fading channels," *IEEE Transactions on Communications*, vol. 47, no. 11, pp. 1688–1692, 1999.

[27] W. Ye, P. Fan, and L. Hao, "Two-stage FFH/MFSK system based on frequency hopping sequence with no-hitzone (in Chinese)," *Journal of Southwest Jiantong University*, vol. 45, no. 2, pp. 268–289, 2011.

[28] G. Li, W. Wang, G. Ding, Q. Wu, and Z. Liu, "Frequency-hopping frequency reconnaissance and prediction for non-cooperative communication network," *China Communications*, vol. 18, no. 12, pp. 51–64, 2021.

[29] R. S. Sutton and A. G. Barto, *Reinforcement Learning: An Introduction*, MIT press, 2018.

[30] V. Mnih, K. Kavukcuoglu, D. Silver et al., "Human-level control through deep reinforcement learning," *Nature*, vol. 518, no. 7540, pp. 529–533, 2015.

[31] S. Lawrence, C. L. Giles, A. C. Tsoi, and A. D. Back, "Face recognition: a convolutional neural-network approach," *IEEE Transactions on Neural Networks*, vol. 8, no. 1, pp. 98–113, 1997.

[32] C. Nebauer, "Evaluation of convolutional neural networks for visual recognition," *IEEE Transactions on Neural Networks*, vol. 9, no. 4, pp. 685–696, 1998.

[33] L.-J. Lin, "Self-improving reactive agents based on reinforcement learning, planning and teaching," *Machine Learning*, vol. 8, no. 3-4, pp. 293–321, 1992.

[34] T. Schaul, J. Quan, I. Antonoglou, and D. Silver, "Prioritized experience replay," 2015, arXiv preprint arXiv:1511.05952.

[35] W. Fedus, P. Ramachandran, R. Agarwal et al., *Revisiting Fundamentals of Experience Replay*, International Conference on Machine Learning, 2020.

[36] K. He and J. Sun, "Convolutional neural networks at constrained time cost," in *2015 IEEE Conference on Computer Vision and Pattern Recognition (CVPR)*, pp. 5353–5360, Boston, MA, USA, 2015.

[37] L. Zhang, J. Tan, Y. C. Liang, G. Feng, and D. Niyato, "Deep reinforcement learning-based modulation and coding scheme selection in cognitive heterogeneous networks," *IEEE Transactions on Wireless Communications*, vol. 18, no. 6, pp. 3281–3294, 2019.

[38] J. Ge, X. Chen, and L. Ge, "Fast wideband spectrum sensing method based on USRP (in Chinese)," *Communication Technology*, vol. 50, no. 12, 2017.

[39] S. Sawant, R. Kumar, M. K. Hanawal, and S. J. Darak, "Learning to coordinate in a decentralized cognitive radio network in presence of jammers," *IEEE Transactions on Mobile Computing*, vol. 19, no. 11, pp. 2640–2655, 2019.

[40] S. Bhunia, E. Miles, S. Sengupta, and F. Vázquez-Abad, "CR-Honeynet: a cognitive radio learning and decoy-based sustenance mechanism to avoid intelligent jammer," *IEEE Transactions on Cognitive Communications and Networking*, vol. 4, no. 3, pp. 567–581, 2018.

Hindawi
Wireless Communications and Mobile Computing
Volume 2022, Article ID 1690667, 14 pages
https://doi.org/10.1155/2022/1690667

Research Article

Optimization of LoRa SF Allocation Based on Deep Reinforcement Learning

Han Zhong,[1,2] **Lei Ning**,[1] **Junsong Wang**,[1] **Siliang Suo**,[3] **and Liming Chen**[3]

[1]*College of Big Data and Internet, Shenzhen Technology University, Shenzhen, China*
[2]*College of Applied Technology, Shenzhen University, Shenzhen, China*
[3]*Electric Power Research Institute Co., Ltd, Guangzhou, China*

Correspondence should be addressed to Lei Ning; ninglei@sztu.edu.cn

Received 9 July 2022; Revised 4 September 2022; Accepted 23 September 2022; Published 12 October 2022

Academic Editor: Mingqian Liu

LoRa is an IoT communication technology that realizes ultra-long-distance transmission through spread spectrum modulation. However, its ultra-long-distance transmission also sacrifices the corresponding rate, and data conflicts are prone to occur when the number of nodes is large. In this article, we investigate various types of data collisions in LoRa wireless work, most of which are affected by Spreading Factor (SF) assignment. At present, the distribution of the SF for LoRa in the industry is mostly based on Min-airtime and Min-distance. In the case of a large number of nodes, the data collision between nodes will increase sharply. This paper proposes a SF redistribution scheme under limited network resources, in order to improve the terminal capacity of the LoRa gateway. First, the problem of minimizing the data collision rate without expanding gateway or network resources is presented. Specifically, the reallocation of SF with increasing number of terminals is studied. Finally, considering the randomness of the data sent by the terminal, SF redistribution schemes based on deep reinforcement learning (DRL) are developed. The simulation results show that the collision rate of the proposed SF redistribution scheme is nearly 30% lower than Min-airtime and Min-distance, and its total energy consumption is close to Min-distance. Therefore, the proposed SF redistribution scheme can effectively improve the gateway capacity of LoRa wireless network.

1. Introduction

In recent years, the Internet of Things industry has developed rapidly, existing mobile cellular communication technology cannot meet the communication requirements of long-distance, low power consumption, and large connection of IoT node equipment [1, 2]. In this context, low power wide area network (LPWAN) [3] came into being, which is a general term for a communication technology suitable for long distance, low power consumption, low bandwidth, and multiconnection IoT connections [4]. LPWAN includes LoRa, NB-IoT [4], RPMA [5, 6], Sigfox [7, 8], LTE-M [9, 10], and other wireless communication technologies [11, 12]. Among them, it can be divided into two categories according to whether authorization is required. In the unlicensed frequency band, LoRa has been widely used in the field of IoT since its invented due to its long transmission distance and low power consumption. Compared with NB-IoT, which requires operator authorization, its on-demand deployment and low deployment cost also make it favored by many organizations and companies with ad hoc [13] network needs. Especially in scenarios with weak signal, long transmission distance and low power consumption requirements, LoRa has more advantages than other communication technologies [14].

LoRa [15, 16] achieves super anti-interference and long-distance transmission through spread spectrum modulation technology. This technology trades bandwidth for sensitivity [17] and is used in communication technologies such as WiFi [18, 19] and Zigbee [20]. LoRa modulation is characterized by maximizing sensitivity, even approaching the limit of Shannon's theorem [21]. While LoRa achieves such long-distance transmission, it also sacrifices some speed. When the anti-interference ability

is stronger and the transmission distance is longer, the amount of data that can be transmitted per unit time is less. In this process, the main parameter of the SF plays an important role [22].

At present, the mainstream method for setting the SF is based on Min-distance and Min-airtime [23]. The two methods determine the optimal SF selection based on the optimal selection of distance and transmission time, respectively. Therefore, neither of the two methods considers the correlation between nodes when the node data is large or the data sending time is close, so the data conflict will increase as the number of nodes increases. How to reduce the data collision rate between LoRa nodes has become a major concern in this paper.

In this paper, we develop a DRL-based LoRa SF allocation optimization method to dynamically optimize the SF allocation of LoRa nodes, thereby reducing the occurrence of collisions between nodes. To showcase the efficiency, we compare the proposed DRL-based method with traditional node feature-based SF assignment methods. Contributions can be summarized as follows:

(i) We first study the performance characteristics of nodes under different SFs for the LoRa collision problem. For different SFs, virtual simulation scenarios are built to simulate the characteristics of transmission under different SFs. Through comparative analysis, it is shown that the optimal rate does not necessarily have the lowest collision rate in the selection of the SF

(ii) Aiming at the existing algorithm for selecting SF based on feature, this paper proposes to consider the influence of channel environment on SF. An optimization algorithm based on DRL framework is proposed. The algorithm considers selecting the optimal SF by combining the node's own characteristics and channel environment information. Considering that the gateway cannot know whether there is a collision between nodes, we consider whether the node is retransmitted to determine whether the node collides or loses packets. Finally, we redesign the state and action parameters of the algorithm

(iii) On the simulation platform, we compare the performance of the DRL-based SF optimization algorithm with the feature-based Min-distance and Min-airtime algorithms. When the number of nodes reaches 1000, the optimization algorithm we propose collides with each other. The rate is reduced by nearly 30%, and the total energy consumption is close to the Min-distance

The rest of the paper is organized as follows. Section 2 presents related works. Section 3 provides the problem formulation and system model. Section 4 proposes DQN based SF allocation. Section 5 elaborates the numerical results, and finally, Section 6 summarizes the conclusion and future work.

2. Related Work

At the beginning of the invention of LoRa, the node uses the pure ALOHA [24] protocol to send data, and the node does not perform channel detection but sends it directly. In this way, as the number of terminals increases or the number of sent packets increases, the probability of packets from multiple terminals colliding on the channel is greatly increase. Since the LoRa mechanism is too simple, on the basis of LoRa, the LoRa Alliance has launched the LoRaWAN protocol [25, 26]. In LoRaWAN, a duty cycle is proposed to constrain the node to occupy the channel all the time, thus avoiding data conflict to a certain extent, but in the case of a large amount of data, due to the duty cycle, the data delay will be increased. In the case of a large amount of data concurrency, its advantages are not obvious. In addition, LoRaWAN also introduces a CAD [27] mechanism to reduce the probability of LoRa conflict, but this undoubtedly increases the power consumption of LoRa. The most important thing is that this does not improve the situation of LoRa nodes crowding the channel and increase the capacity of the gateway. At present, the Class A mode in LoRaWAN still uses pure ALOHA. According to calculations, the channel utilization of the pure ALOHA protocol is only 18.4%, and most nodes send collisions in the channel. Therefore, how to improve LoRa to increase its gateway capacity and reduce the collision rate has become a major research point in the industry.

To this end, the industry has also done a lot of work and research on LoRa collision optimization. Edward et al. [28] expect to increase the capacity of the gateway by introducing Interleaved Chirp Spreading LoRa- (ICS-LoRa-) based modulation. In [29], The authors optimize the transmission parameters of a LoRaWAN system in high density smart city traffic environment using golden section search and parabolic interpolation. Floris et al. [30] used ns-3 to simulate and analyze the LoRa network. The analysis shows that increasing gateway density can ameliorate but not eliminate this effect, as stringent duty cycle requirements for gateways continue to limit downstream opportunities. Reynders et al. [31] present a scheme to efficiently optimize the packet error rate fairness inside a LoRaWAN cell. This is achieved by optimizing the power and SF for each node while avoiding near-far problems by allocating distant users to different channels. In [32], Abdelfadeel et al. present results of a study of the data rate fairness among nodes within a LoRaWAN cell. In order to make the rate of each node more relatively fair, they secondly develop a transmission power control algorithm to balance the received signal powers from all nodes regardless of their distances from the gateway for a fair data extraction. But this algorithm only considers the case where the set of nodes is close to the network.

As a new intelligent decision-making algorithm, AI has been widely used in many fields. In network resource scheduling, many scholars have also introduced AI for scheduling and decision optimization. Jiang et al. [33] used reinforcement learning to optimize the throughput and transmission time interval of NB-IoT. Yang et al. [34] utilize deep neural network (DNN) to configure optimized NOMA for network

resource management. The DNN not only greatly improves the computational efficiency but also improves the summation rate of the system. In [35], a DQN method is used to control the Handover (HO) procedure of the User Equipments (UEs) by well capturing the characteristics of wireless signals interference and network load. Experimental results show that the proposed scheme can reduce HO rate and guarantee the system throughput, which is better than the traditional HO scheme.

In this article, we consider using the reinforcement learning algorithm to further improve and optimize the distance-based optimization algorithm and redistribute the SF of the nodes to reduce the collision rate of the channel with the growth of nodes or data explosion. Finally, increase the capacity of channel nodes under a single gateway. In Section 3, we will first introduce LoRa's communication collision model and the problem formulation will be presented as follows.

3. System Model and Problem Analysis

3.1. LoRa Communication Model. On the basis of the LoRa physical layer, the LoRa Alliance released the LoRaWAN protocol to adapt to the LoRa physical layer. In LoRaWAN [36], Class A mode must be implemented by default, and it mainly uses the ALOHA protocol for data transmission [37]. The basic idea is that each node can send data frames at any time, and then monitor the channel to see if there is a conflict. If a conflict occurs, then the node will wait for a random period of time to retransmit until the retransmission is successful. The collision process is shown in Figure 1.

In LoRa, there are four main parameters that generally affect the conflict between data, namely center frequency, SF, Bandwidth(BW), and Coding Rate(CR). Through reasonable configuration, there can be a variety of mutually orthogonal combinations to avoid conflicts [38]. The four parameters are described as follows

(1) *CR*. The coding rate is the ratio of the useful part of the data stream. LoRa uses cyclic error correction coding for forward error detection and error correction. However, using this method will generate transmission overhead. The specific overhead is shown in Table 1

(2) *Center Frequency*. The frequency in the middle of the filter passband, in LoRa, the corresponding frequency needs to be set according to laws and regulations. There is a random frequency hopping mechanism in LoRaWAN. This mechanism is mainly to deal with the regulations of LoRa duty cycle, so as to solve the problem of transmitting large data packets. This mechanism can also be effective in reducing collisions at certain times

(3) *BW*. The signal bandwidth is to limit the lower frequency and upper frequency of the signal allowed to pass through the channel. In LoRa, increasing the BW can improve the transmission rate of the payload, but it will also reduce the receiver sensitivity while reducing the transmission time

(4) *SF*. LoRa spread spectrum modulation is realized by representing each bit of data in the payload information with multibit chip information. Since different SFs are orthogonal to each other, the SFs must be known in advance in a group of transceiver links

The modulation modes of LoRa signals are orthogonal to each other under different SF and BW combinations, and data transmission can be performed using Code Division Multiple Access (CDMA). In the same channel, if the BW is unchanged, the multichannel orthogonal data can be transmitted without interfering with each other by changing the SF. The SF ranges from 5 to 12, and a total of 8 addresses are used. In LoRaWAN, a total of six addresses are used from 7 to 12, and the rate corresponding to each multiple access is also different. The speed will affect its air flight time, and the air flight time can be calculated by the following formula.

$$ToA = N_{\text{sym}} * \frac{2^{\text{SF}}}{\text{BW}}. \tag{1}$$

ToA is the air time, and N_{sym} is the number of symbols. Due to the different modulation parameters, the calculation of the number of symbols is also different, and the specific calculation is given in the following formula.

For $SF = 5$, and $SF = 6$,

$$\begin{aligned} N_{\text{sym}} &= N_{\text{sympream}} + 6.25 + 8 + \text{ceil}\left(\frac{\max\left(N_{bit}, 0\right)}{4 * \text{SF}}\right), \\ N_{\text{bit}} &= 8 * N_{\text{bp}} + N_{\text{bitCRC}} - 4 * \text{SF} + N_{\text{symheader}}. \end{aligned} \tag{2}$$

For other SF,

$$\begin{aligned} N_{\text{sym}} &= N_{sympream} + 4.25 + 8 + ceil\left(\frac{\max\left(N_{bit}, 0\right)}{4 * SF}\right), \\ N_{bit} &= 8 * N_{bp} + N_{bitCRC} - 4 * \text{SF} + 8 + N_{symhead}, \end{aligned} \tag{3}$$

When CRC is turned on, $N_{\text{bitCRC}} = 16$, otherwise it is 0. $N_{\text{symhead}} = 20$ in explicit header mode, 0 in recessive header mode. N_{bp} represents the byte payload. The air interface time required for different SFs and different packet lengths can be calculated through the above calculation formula. The air time is shown in Figure 2.

If the air time of transmission is longer, it means that the time of occupying the channel is longer. At this time, if other nodes in LoRa transmit with the same SF, the data of the two nodes will interfere with each other, which will cause the gateway to fail to receive. At this time, the node will retransmit when no response is received. The larger the SF, the smaller the capacity of the channel and the greater the probability of collision. How to make a reasonable distribution of the SF becomes a problem we are concerned about. In the

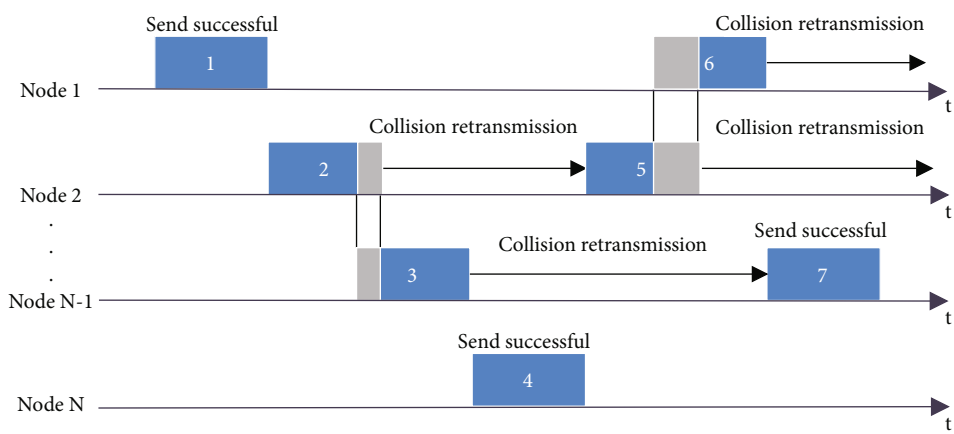

Figure 1: The collision process of the pure ALOHA protocol.

Table 1: CR Parameters.

CR	Cyclic coding rate	Overhead ratio
1	4/5	1.25
2	4/6	1.5
3	4/7	1.75
4	4/8	2

next subsection, we will further analysis of the success rate of data reception by LoRa's SF.

3.2. Problem Analysis and Description. In LoRa, there are four main factors that affect the collision of node data, namely, Frequency Collision, SF Collision, Power Collision, and Timing Collision. SF is an important parameter of LoRa communication transmission. The effect of setting different SFs on collision is particularly obvious. In order to verify the impact of LoRa nodes using different SFs on the success rate of network data transmission, this paper uses the Python simulation simulator LoRaSim to simulate the collision of LoRa nodes and verify the impact of different SFs on the success rate of LoRa gateway data reception. Nodes are randomly distributed within a radius of 2 kilometers with the gateway as the center. The spreading factor $SF \in [7, 8, 9,10,11,12]$, which ensures that each node can communicate with the LoRa gateway normally. The packet sending interval of each node is 5 minutes; the packet load length is 20 bytes; the bandwidth is 125 kHz, and the number of gateway channels is 1. The total simulation time is 2 hours. Finally, under different SFs, as the number of nodes increases, the graph of the successful data reception rate is obtained, as shown in Figure 3.

In Figure 3, there are differences in the data transmission success rates corresponding to different SFs under the same number of nodes, which shows that the low SF has a higher data transmission success rate, while the high SF has a lower data transmission success rate. As the number of nodes increases, the success rate of data transmission is also affected by the SF. When $SF = 12$, the number of nodes exceeds 300; the success rate of data transmission is already lower than 30%, which seriously affects the reliability of the network.

Since a higher SF has a stronger anti-interference ability, the transmission of the same size of data needs to occupy the channel for a longer time, and the energy consumption is also higher. Additional energy consumption is also required for data retransmission due to packet loss or data collision. Figure 4 shows the energy consumption of data transmission with different SFs. Therefore, when the data is reachable, a lower SF is generally preferred for transmission.

The optimal SF transmission has its advantages, but in the case of a large number of nodes, if many nodes select the optimal SF, the collision rate of the optimal SF will increase. Due to the orthogonal relationship between the SFs, the LoRa gateway can receive a variety of node data with different SFs or bandwidths at the same time. The communication multiple access that LoRa can be expressed is as follows:

$$N_{\text{channel}} = N_{\text{SF}} * \sum N_{\text{BW}} \qquad \text{BW} \in [62.5,125,250,500] \tag{4}$$

In the actual deployment situation, letting all nodes select the optimal SF may increase the collision rate instead. With the help of LoRa's feature that different SFs can be demodulated at the same time, how to allocate SFs more reasonably, so as to maximize the utilization of network resources and reduce the collision rate of nodes can be described as follows:

$$\text{Node}_i^{\text{SF}} = argmin \sum \left(\beta * N_i^{\text{collision}} + \gamma * N_i^{\text{lost}} \right) \tag{5}$$

The formula describes that the optimal SF allocated should be the smallest collision rate and no packet loss. In Formula (5), $i \in M$, M is the number of nodes; β and γ are reduction coefficients. In order to prevent packet loss as much as possible, gamma weights should be larger.

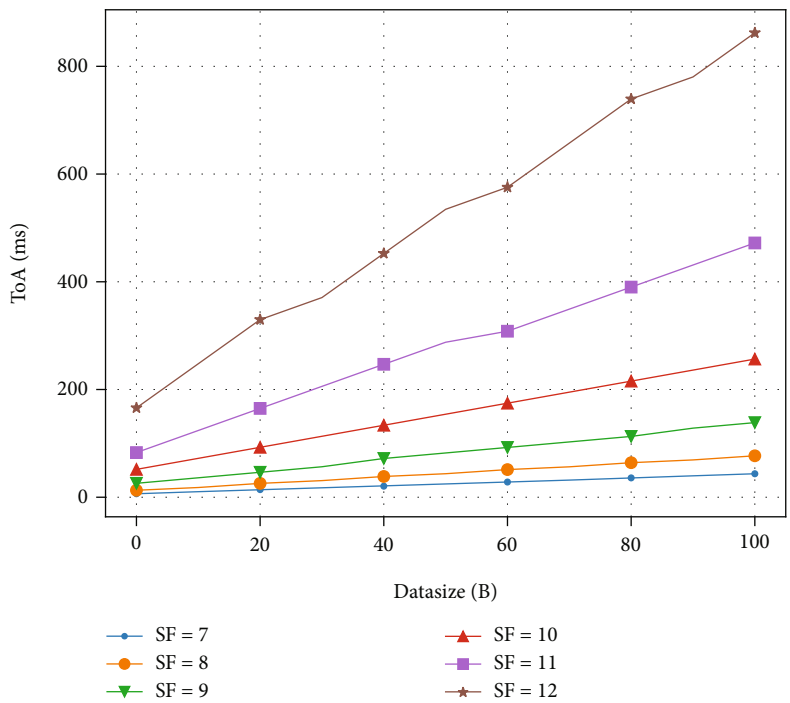

Figure 2: Time required to send data with different SF.

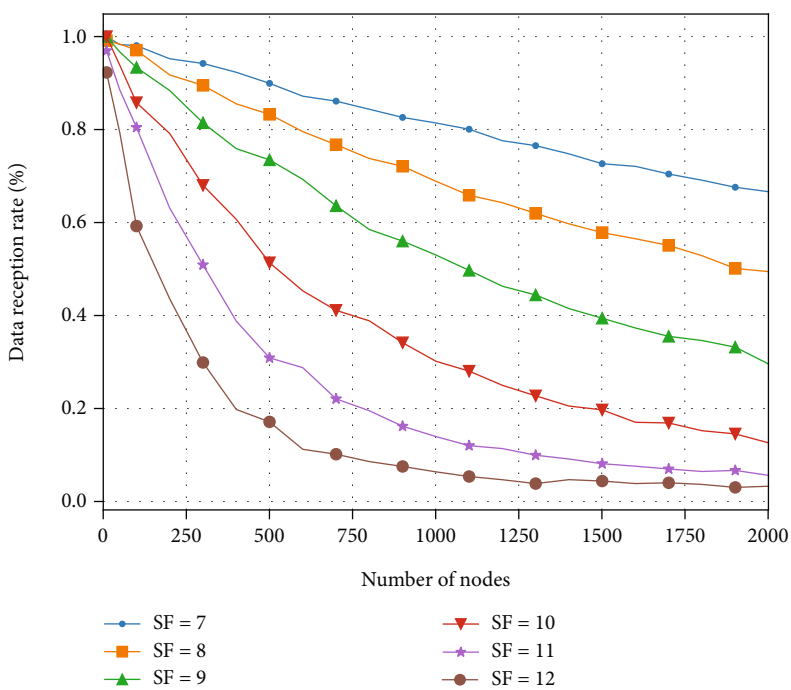

Figure 3: Successful reception rates for different SF.

4. SF Allocation Based on DRL

A reinforcement learning algorithm is an AI algorithm that optimizes itself according to changes in the environment. It is mainly composed of agents and environments. The agent observes some state parameters required by itself from the environment, and gives corresponding action parameters according to the state parameters. At present, reinforcement learning algorithms have shined in many fields, such as game AI, autonomous driving, etc.

In order to optimize the distribution of the SF, in this section, the reinforcement learning algorithm combined with the distance optimization algorithm of LoRa is proposed to be embedded in the LoRa network server. Figure 5 shows a schematic diagram of the Deep Reinforcement Learning (DRL) algorithm embedded in the network server.

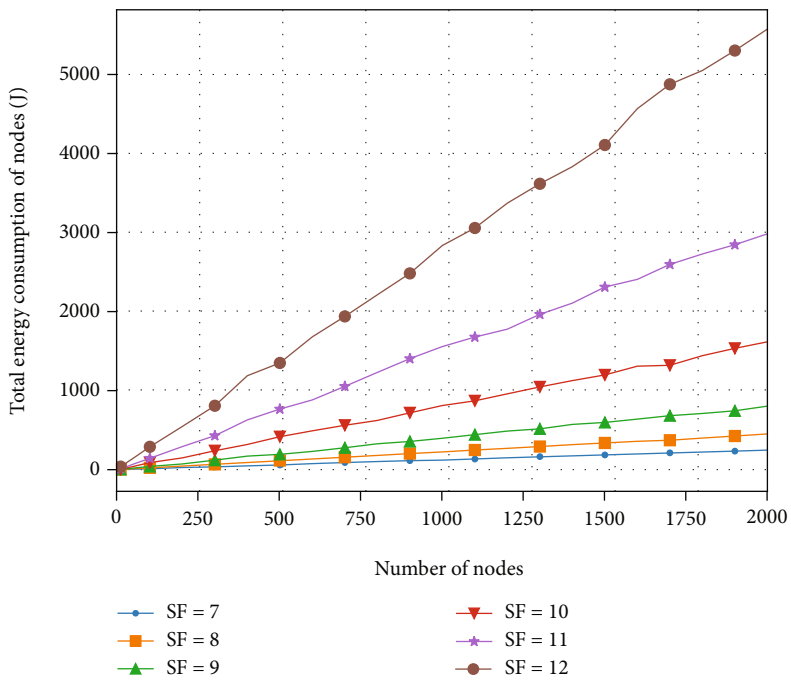

Figure 4: Energy consumption under different SF.

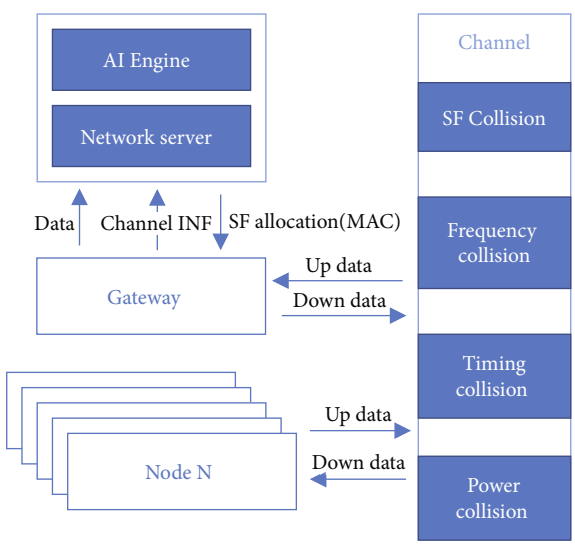

Figure 5: AI embed in the network server.

In Figure 5, the AI algorithm is designed to be embedded in the network server, and the LoRa gateway performs the forwarding function of the node. The LoRa node sends uplink data based on the ALOHA mechanism. Only when the data does not collide in the channel can the LoRa gateway successfully receive the data sent by the node (Data) and forward it to the network server, which also includes the channel environment information (Channel INF); after the network server receives the data, it will parse it; through the environment information recorded by each node (whether retransmission occurs, sending time, etc.), it determines if there is a collision between nodes. The AI algorithm will give the corresponding adjustment strategy according to the node information and channel information. The strategy will be forwarded through the gateway, and the gateway will send the MAC command when the node's receiving window is opened, so as to adjust the channel parameter settings of each node to maximize the use of each channel resources and reduce the collision rate of data.

4.1. Deep Reinforcement Learning Algorithm Model. The deep reinforcement learning algorithm plans to use the Deep Q Network (DQN) algorithm [39]. The DQN algorithm is a method of approximating the value function of Q-learning through a neural network [40]. Q-learning is a model-free reinforcement learning technique proposed by Watkins in 1989. For a given environmental state, it can have relatively good operational expectations without the need for an environmental model. At the same time, it can handle random transitions and reward issues without adjustment. It has been shown that, for any finite MDP, Q-learning will eventually find an optimal policy, i.e., starting from the current state, the expected value of the total return over all successive steps is the maximum achievable [41]. Before learning begins, Q is initialized to a possibly arbitrary fixed value. Then, at each time t, the agent chooses an action a_t, gets a reward R_t and enters a new state S_{t+1}, and the Q value is updated. Its core is the value function iteration process, namely,

$$\begin{aligned} Q(s_t, a_t) &\longleftarrow Q(s_t, a_t) + \alpha \cdot U_{t+1} U_{t+1} \\ &= r_t + \gamma \max_{\pi} Q(s_{t+1}, a_t) - Q(s_t, a_t). \end{aligned} \tag{6}$$

However, when encountering a large number of state spaces or a continuous state, Q-learning will face the disaster of dimensionality or the difficulty of storing rough retrieval, so a neural network is introduced to approximate the value

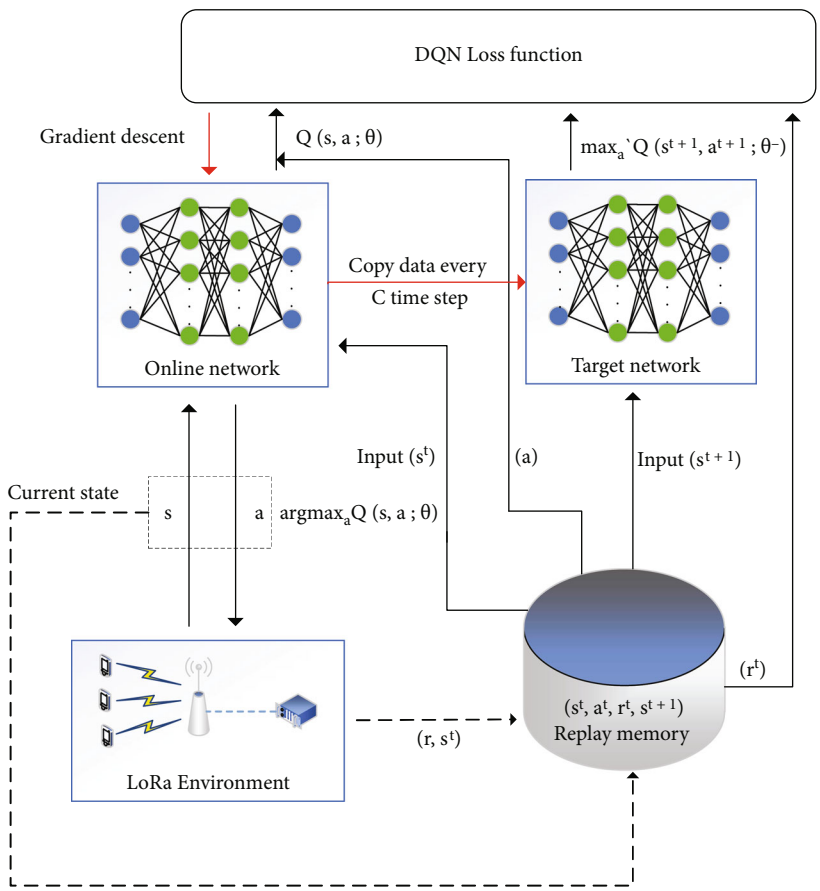

Figure 6: DQN algorithm framework.

function [42, 43]. After the introduction of the neural network, the whole process becomes how to determine θ to approximate the value function. In this paper, gradient descent is used to minimize the loss function to debug the network weight θ. At this time, the Loss Function is defined as follows:

$$L_i(\theta_i) = E_{(s,a,r,s^i)\sim U(D)}\left[\left(r + \gamma \max_{a'} Q\left(s', a^i; \theta_i^-\right) - Q(s, a; \theta_i)\right)^2\right]. \tag{7}$$

In the given formula, we use two neural networks; one is called the Q neural network, and the other is called the target neural network. The purpose of introducing the target neural network is to reduce the correlation between the current Q value and the target Q value, thereby improving the stability of the algorithm. Specifically, θ_i^- is the target network parameter of the i iteration, and θ_i is the current Q neural network parameter.

In addition, experience playback is also introduced to store the past state, and the method of random sampling from the experience pool is adopted to update the neural network parameters, thereby breaking the correlation between data and improving the utilization of data. The learning process of DQN is shown in Figure 6.

4.2. DQN Parameters Design. In this section, we will introduce how DQN integrates and interacts with LoRa's network server, including some specific parameters of the environment state as well as the action parameters generated by DQN.

4.2.1. State. The LoRa network server receives the packet data in the LoRaWAN format from the gateway. The data packet includes the node ID, packet length, transmission interval, SF, encoding rate, and bandwidth. Each node has a unique ID number. From the node number information, the network server can know the location of each node and the distance dis from the forwarding gateway. At the same time, it is also possible to know whether retransmission has occurred from the information of the data packet. If the data packet is retransmitted, it means that the data packet has a data collision or is lost. Then, the state of the environment can be represented as a 7-dimensional vector.

$$s_t^{node} = \left\{s_{id}, s_{dis}, s_{sf}, s_{bw}, s_{len}, s_{interval}, s_{col}\right\}. \tag{8}$$

s_{dis} represents the distance between the gateway and the node device. This data is added to the network server when the node is initialized to join the network for the first time. The SF is an integer of 7-12, and the BW optional frequency bands are 125, 250, and 500.

```
Initialize LoRa node based on LoRaWAN
Initialize replay memory D to capacity N
Initialize action-value function Q with random weights θ
Initialize target action-value function Q⁻ with weights θ⁻ = θ
For episode =1,M do do
    Initialize and choose state
    S_{sf,bw} from LoRa network server(MAC)
    For t = 1, T do
        With probability ε select a random action a_t otherwise select a_t = argmax_a Q(s_t, a ; θ) execute action a_t in emulator
        Observe reward r_t and next state s_{t+1}
        Store experience (s_t, a_t, r_t, s_{t+1}) ⟶ D
        D ⟶ (s_i, a_i, r_i, s_{i+1})_{(i∈B)}
        If episode terminates at step j +1 then
            y_j = r_j
        Else
            y_j = r_j + γ_{a'} Q⁻(s_{j+1}, a' ; θ⁻)
        End if
        Perform a gradient descent step on (y_j − Q(s_j, a_j ; θ))² with respect to the network parameters θ
        If batch size > = memory capacity then
            Update Q⁻ ⟵ Q
        End if
    End for
End for
```

Algorithm 1: Procedure of deep Q network.

4.2.2. Action. The action parameter consists of two parts, namely, the selection of the SF and the selection of the bandwidth. There are a total of 18 combinations of the two to choose from. So the output of the neural network is an 18-dimensional vector, and the one with the largest value is selected from the 18-dimensional vector.

$$a_t = \text{argmax}\left\{a_{sf1,bw1}, a_{sf1,bw2}, a_{sf1,bw3}, \cdots a_{sf12,bw3}\right\}. \tag{9}$$

4.2.3. Reward. In reinforcement learning, the agent's goal is formally represented as a special signal, called a reward, which is passed to the agent through the environment. At each instant, the reward is a single scalar value. In this paper, the expected maximum goals are the collision rate between nodes and the packet loss rate of nodes. The reward function in this paper is set as follows:

$$r_i^t = -\frac{N_{\text{col}} + N_{\text{lost}}}{1 + N_{\text{rec}}} - \frac{f_{\text{lost}} + f_{\text{col}}}{(1 + N_{rec})/(1 + N_{\text{col}} + N_{\text{lost}})}, \tag{10}$$

where

$$f_{\text{lost/col}} = \begin{cases} 1, & \text{either collision or packet lost,} \\ 0, & \text{neither collision nor packet lost.} \end{cases} \tag{11}$$

The goal of RL is to maximize the cumulative discounted reward functions by finding an optimal policy. We then define long-term reward V_i as the accumulated and discounted reward.

$$V_i = \sum_{t=0}^{T-1} \gamma^t r_i^t. \tag{12}$$

Table 2: Environmental parameters.

Parameter	Value
Working channel (MHz)	471.5
Max BS receive	8
γ	2.08
d_0	40
L_{pl}	127.41
Bandwidth(kHz)	125, 250, 500
SF	7, 8, 9, 10, 11, 12
C/R	4/5

Table 3: DQN algorithm parameters.

Parameter	Value
Greedy policy ε	0.9
Batch size	256
Reward discount γ	0.9
Target update frequency	100
Memory capacity	5000
Actions	18
States	7

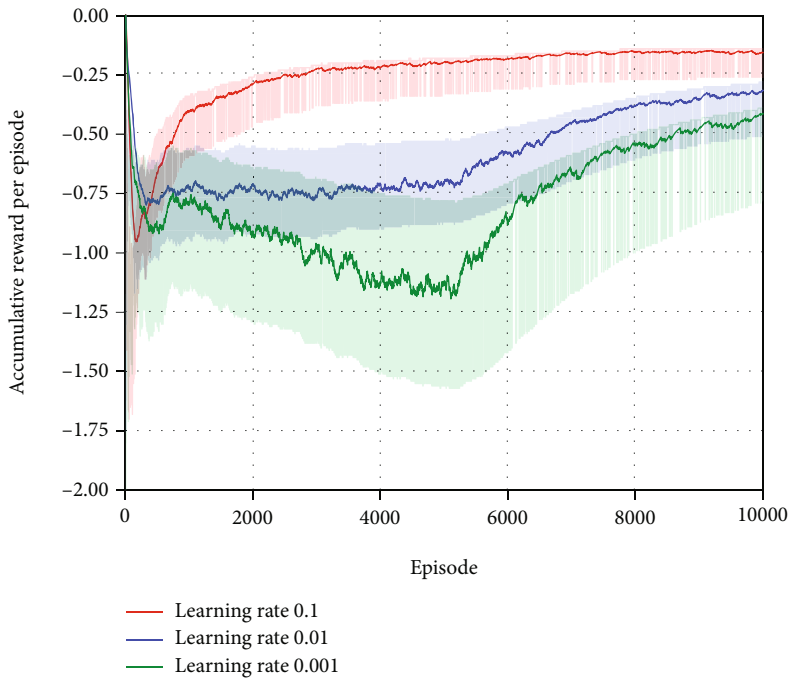

Figure 7: Different learning rate of training DQN.

γ is the reduction coefficient, which belongs to $[0, 1]$. When the reduction coefficient is 0, it means that only current interests are considered. When the reduction coefficient is larger, it means that longer-term interests are considered.

At the end of this section, we present the procedure of the DQN-based SF allocation optimization algorithm. The algorithm will be shown in Algorithm 1.

5. Performance Evaluation

In this section, we will first introduce the LoRa network environment and the settings of related parameters, and secondly, we will optimize the algorithm model for training based on the LoRaSim simulator. Finally, we will give a performance comparison of LoRa based on different algorithms.

5.1. Parameter Settings. We will use the Python-based LoRa simulator LoRaSim to simulate the LoRa network communication environment. In LoRaSim, the process of communication between multiple nodes and gateways is simulated through the SimPy-based discrete event library, and each node and gateway is maintained by a thread. When each thread is simulating sending packets, a collision function will be used to simulate whether a collision occurs. The settings of the collision function include SF collision, frequency collision, and time collision. In order to be as close to the real communication environment as possible, the parameters of the network environment will be set according to the LoRaWAN protocol. The specific environment parameter settings are shown in Table 2.

For the neural network model, considering that the number of states and actions are not large, the two neural network models in DQN adopt a three-layer network model with 50 neurons in each layer. Other algorithm parameters are shown in Table 3.

In the training simulation environment of the algorithm model, we set 1500 nodes and initialize the default allocation of SF = 7; the data volume of each node is 50 bytes; the sending interval is 5 minutes, and the total simulation time is 2 hours. In order to prevent overfitting, the number of rounds is taken as the first 10000. Three different learning rates are set, and the training curve of the algorithm is presented in Figure 7.

As shown in Figure 7, when the learning rate is 0.001 and 0.01, the training requires a large number of rounds to achieve a good effect, and after the algorithm convergence, its collision rate is still higher than that of the algorithm with a learning rate of 0.1. Therefore, we choose a learning rate of 0.1.

5.2. Algorithm Performance and Comparison. In the LoRa simulation experiment in this article, we will select two widely used algorithms for comparison, namely, Min-distance and Min-airtime. The Min-distance allocation strategy allocates the SF according to the range of the RSSI value received by the gateway. A low RSSI value corresponds to a high SF, and a high RSSI value corresponds to a low SF. This method uses a low SF to improve the success rate of data transmission but does not fully consider the orthogonality between SFs. It assigns almost all nodes to SF = 7 and SF = 8. The Min-airtime allocation strategy is to adaptively select the minimum combination of air transmission time corresponding to bandwidth, SF and coding rate according to the situation of the node itself. Compared with Min-distance, this deployment has better flexibility.

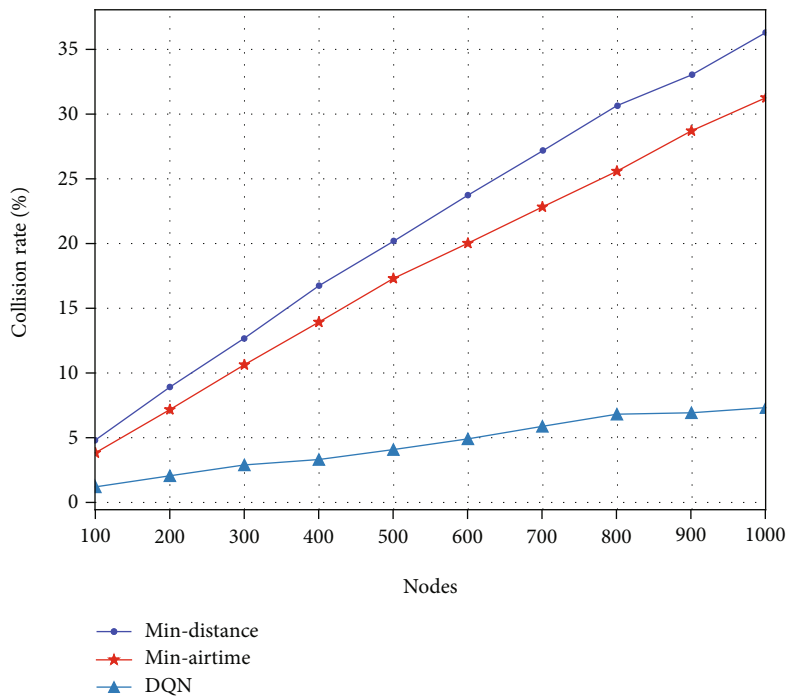

Figure 8: LoRa collision rate comparison.

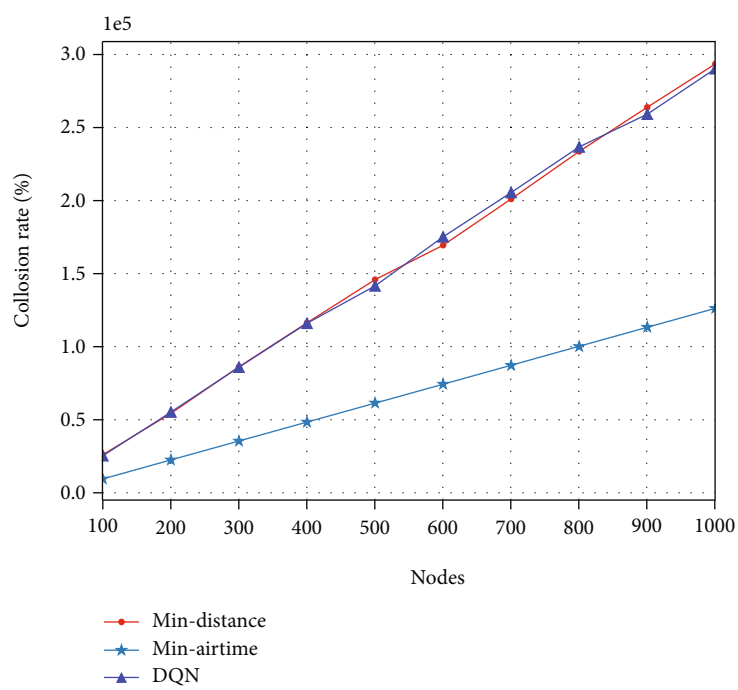

Figure 9: Total energy consumption.

In this experiment, the number of nodes in the range from 100 to 1000 will be selected, and the value will be taken every 100 nodes. The node location information is initialized and fixed when entering the network. The transmission time interval is set to 5 minutes, and the packet length is set to 50 bytes. The total simulation time is 12 hours. The DQN algorithm proposed in this paper and the comparison of the two algorithms are shown in Figure 8.

In Figure 8, the DQN algorithm redistributes the SF, and as the number of nodes increases, the data collision rate is significantly reduced compared with the other two algorithms. At 1000 nodes, its collision rate is reduced by 24%. During the same period, node collisions tend to be clustered. If a large number of collisions occur in the short-term SF = 7 , due to the need for retransmission, the collision of data cannot be alleviated in the short-term. And DQN considers

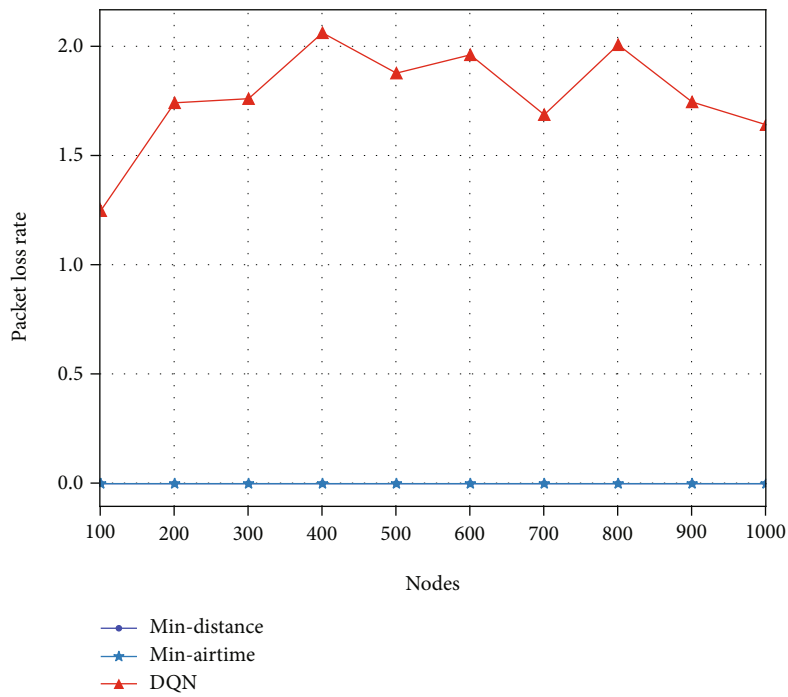

Figure 10: LoRa packet loss rate comparison.

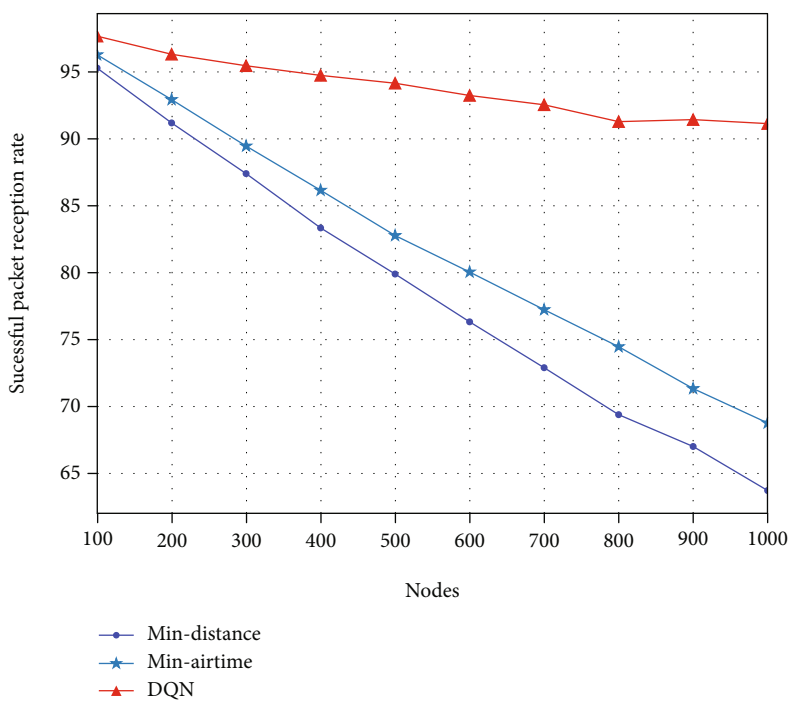

Figure 11: Successful data reception rate.

using more spreading factors, including some SF options with poor rate, in order to reduce the collision explosion for a period of time. Therefore, compared with the Min-distance and Min-airtime methods, when there are more nodes, DQN can play a more significant role in reducing collisions.

In Figure 9, the energy consumption comparison chart under the three methods is shown. Due to the assignment of a higher SF, a larger energy consumption is required to complete the data transmission. Therefore, its energy consumption is slightly higher than that of Min-airtime, but it is basically the same as that of Min-distance. SF is

proportional to energy consumption. Although DQN reduces the collision of nodes, from the perspective of energy consumption, energy consumption increases due to the allocation of higher SF.

DQN also brings a certain degree of packet loss after adjusting the SF. The packet loss problem is due to the assignment of unreasonable SFs to nodes that suffer from strong interference. Min-airtime and Min-distance allocate the SF by calculating in advance to ensure that the node will not lose packets when sending data, and then select the optimal SF. It can also be found in the simulation experiment that the packet loss rate of the two methods is 0. DQN will search for better SF when assigning SF. If an unreasonable SF is selected, packet loss will occur. In the DQN algorithm, the packet loss rate of a node has nothing to do with the number of nodes but is related to the DQN learning exploration rate. The packet loss phenomenon generally occurs in the stage of DQN learning the environment. As the algorithm observes and learns from the environment, the total packet loss rate is not more than 3%. The packet loss rate comparison chart is shown in Figure 10.

In Figure 11, we give the success rate of the gateway receiving data under different methods. The main factor that affects the success rate of Min-airtime and Min-distance data receiving is the conflict between data. In DQN, the algorithm uses the SF. The adjustment has resulted in a certain degree of packet loss but greatly reduced the conflict between data. With the increasing number of nodes, DQN data reception success rate is better than Min-airtime and Min-distance. In the case of 1000 nodes, the data reception success rate of the DQN algorithm is 27% higher than that of Min-airtime and 28% higher than that of Min-distance.

6. Conclusion

Aiming at the problem that LoRa is prone to data collision in large-scale node scenarios, this paper proposes an optimization algorithm for LoRa SF allocation based on deep reinforcement learning. By analyzing the performance of different LoRa SF and the impact on the collision rate, it is found that the collision between nodes can be effectively reduced by reasonably configuring the SF of LoRa nodes. We developed a LoRa SF allocation optimization algorithm based on the DQN algorithm. According to the analysis of the LoRa SF, the environmental state information that has a major impact on the collision rate was selected, and the action information was combined and configured. The simulation results show that as the number of nodes increases, the algorithm we developed can effectively reduce the data collision rate between LoRa nodes, and the energy consumption is close to Min-distance.

Due to exploration characteristics of the DRL algorithm, a small part of the packet loss phenomenon will occur in LoRa nodes. In the future, we will expect to further optimize the LoRa packet loss situation. And with the maturity of satellite-based cooperative communication, the optimization for joining multimode communication will also become a research direction. This kind of multiobjective optimization is very challenging and should be solved in the future.

Data Availability

The data used to support the findings of this study are available from the corresponding author upon request.

Conflicts of Interest

The authors declare that they have no conflicts of interest.

Acknowledgments

This work was sponsored by SZTU-Winoble Cooperation Research Project (No. 2021010802015 and No. 20213108010030); Scientific Research Capacity Improvement Project from Guangdong Province (No.2021ZDJS109); SZTU Experimental Equipment Development Foundation (No. JSZZ202102007).

References

[1] A. S. Shaker, "A survey of smart buildings and homes using low-powerwide-area network (LoRa WAN)," in *2020 4th International Symposium on Multidisciplinary Studies and Innovative Technologies (ISMSIT)*, pp. 1–7, Istanbul, Turkey, 2020.

[2] L. Da Xu, W. He, and S. Li, "Internet of things in industries: a survey," *IEEE Transactions on Industrial Informatics*, vol. 10, no. 4, pp. 2233–2243, 2014.

[3] U. Raza, P. Kulkarni, and M. Sooriyabandara, "Low power wide area networks: an overview," *IEEE Communications Surveys & Tutorials*, vol. 19, no. 2, pp. 855–873, 2017.

[4] S. Popli, R. K. Jha, and S. Jain, "A survey on energy efficient narrowband internet of things (NBIoT): architecture, application and challenges," *IEEE Access*, vol. 7, pp. 16739–16776, 2019.

[5] M. I. Nashiruddin, M. T. B. Sihotang, and M. A. Nugraha, "Random phase multiple access network planning for smart city deployment in urban area," in *2021 International Conference on Radar, Antenna, Microwave, Electronics, and Telecommunications (ICRAMET)*, pp. 232–237, Bandung, Indonesia, 2021.

[6] M. I. Nashiruddin, S. Winalisa, and M. A. Nugraha, "Random phase multiple access network for public internet of things in Batam island," in *2021 8th International Conference on Electrical Engineering, Computer Science and Informatics (EECSI)*, pp. 311–316, Semarang, Indonesia, 2021.

[7] K. Mekki, E. Bajic, F. Chaxel, and F. Meyer, "Overview of cellular LPWAN technologies for IoT deployment: Sigfox, LoRaWAN, and NB-IoT," in *2018 IEEE International Conference on Pervasive Computing and Communications Workshops (PerCom Workshops)*, pp. 197–202, Athens, Greece, March 2018.

[8] A. Lavric, A. I. Petrariu, and V. Popa, "Long range SigFox communication protocol scalability analysis under large-scale, high-density conditions," *IEEE Access*, vol. 7, pp. 35816–35825, 2019.

[9] "LTE-advanced in 3GPP Rel -13/14: an evolution toward 5G | IEEE Journals & Magazine | IEEE Xplore," http://ieee.org/abstract/document/7432169.

[10] M. Mezzavilla, M. Zhang, M. Polese et al., "End-to-end simulation of 5G mmWave networks," *IEEE Communications Surveys & Tutorials*, vol. 20, no. 3, pp. 2237–2263, 2018.

[11] W. Ayoub, A. E. Samhat, F. Nouvel, M. Mroue, and J.-C. Prévotet, "Internet of mobile things: overview of LoRaWAN, DASH7, and NB-IoT in LPWANs standards and supported mobility," *IEEE Communications Surveys & Tutorials*, vol. 21, no. 2, pp. 1561–1581, 2019.

[12] S.-H. Hwang and S.-Z. Liu, "Survey on 3GPP low power wide area technologies and its application," in *2019 IEEE VTS Asia Pacific Wireless Communications Symposium (APWCS)*, pp. 1–5, Singapore, 2019.

[13] V. Geetha, S. Aithal, and K. Chandra Sekaran, "Effect of mobility over performance of the ad hoc networks," in *2006 International Symposium on Ad Hoc and Ubiquitous Computing*, pp. 138–141, Mangalore, India, 2006.

[14] O. Georgiou and U. Raza, "Low power wide area network analysis: can LoRa scale?," *IEEE Wireless Communications Letters*, vol. 6, no. 2, pp. 162–165, 2017.

[15] A. J. Wixted, P. Kinnaird, H. Larijani et al., "Evaluation of LoRa and LoRaWAN for wireless sensor networks," in *2016 IEEE SENSORS*, pp. 1–3, Orlando, FL, USA, 2016.

[16] P. Edward, S. Elzeiny, M. Ashour, and T. Elshabrawy, "On the coexistence of LoRa- and interleaved chirp spreading LoRa-based modulations," in *2019 International Conference on Wireless and Mobile Computing, Networking and Communications (WiMob)*, pp. 1–6, Barcelona, Spain, 2019.

[17] P. Gkotsiopoulos, D. Zorbas, and C. Douligeris, "Performance determinants in LoRa networks: a literature review," *IEEE Communications Surveys & Tutorials*, vol. 23, no. 3, pp. 1721–1758, 2021.

[18] D. Suh, H. Ko, and S. Pack, "Efficiency analysis of WiFi offloading techniques," *IEEE Transactions on Vehicular Technology*, vol. 65, no. 5, pp. 3813–3817, 2016.

[19] "WiFi and bluetooth security | IEEE Courses | IEEE Xplore," https://ieeexplore.ieee.org/courses/details/EDP457.

[20] G. Pan, J. He, W. Qin, R. Fang, J. Cao, and D. Liao, "Automatic stabilization of Zigbee network," in *2018 International Conference on Artificial Intelligence and Big Data (ICAIBD)*, pp. 224–227, Chengdu, China, 2018.

[21] G. Zhu, C.-H. Liao, T. Sakdejayont, I. W. Lai, Y. Narusue, and H. Morikawa, "Improving the capacity of a mesh LoRa network by spreading-factor-based network clustering," *IEEE Access*, vol. 7, pp. 21584–21596, 2019.

[22] J. P. S. Sundaram, D. Wan, and Z. Zhao, "A survey on LoRa networking: research problems, current solutions, and open issues," *IEEE Communications Surveys & Tutorials*, vol. 22, no. 1, pp. 371–388, 2020.

[23] T. Voigt, M. Bor, U. Roedig, and J. Alonso, "Mitigating internetwork interference in lora networks," in *In EWSN '17 Proceedings of the 2017 International Conference on Embedded Wireless Systems and Networks*, pp. 323–328, ACM Press, New York, 2017.

[24] F. Baccelli, B. Blaszczyszyn, and P. Muhlethaler, "An Aloha protocol for multihop mobile wireless networks," *IEEE Transactions on Information Theory*, vol. 52, no. 2, pp. 421–436, 2006.

[25] A. Lavric, A. I. Petrariu, and L. Anchidin, "Internet of things software defined radio technology for LoRaWAN wireless communication: a survey," in *2021 12th International Symposium on Advanced Topics in Electrical Engineering (ATEE)*, pp. 1–4, Bucharest, Romania, March 2021.

[26] N. P. Manchev, K. K. Angelov, P. G. Kogias, and S. M. Sadinov, "Development of multichannel LoRaWAN gateway for educational applications in low-power wireless communications," in *2019 IEEE XXVIII International Scientific Conference Electronics (ET)*, pp. 1–4, Sozopol, Bulgaria, September 2019.

[27] F. Lehmann, "Joint user activity detection, channel estimation, and decoding for multiuser/multiantenna OFDM systems," *IEEE Transactions on Vehicular Technology*, vol. 67, no. 9, pp. 8263–8275, 2018.

[28] P. Edward, M. El-Aasser, M. Ashour, and T. Elshabrawy, "Interleaved chirp spreading LoRa as a parallel network to enhance LoRa capacity," *IEEE Internet of Things Journal*, vol. 8, no. 5, pp. 3864–3874, 2021.

[29] A. L. Emmanuel, X. Fernando, F. Hussain, and W. Farjow, "Optimization of spreading factor distribution in high density LoRa networks," in *2020 IEEE 91st Vehicular Technology Conference (VTC2020-Spring)*, pp. 1–5, Antwerp, Belgium, 2020.

[30] F. Van den Abeele, J. Haxhibeqiri, I. Moerman, and J. Hoebeke, "Scalability analysis of large-scale LoRaWAN networks in ns-3," *IEEE Internet of Things Journal*, vol. 4, no. 6, pp. 2186–2198, 2017.

[31] B. Reynders, W. Meert, and S. Pollin, "Power and spreading factor control in low power wide area networks," in *2017 IEEE International Conference on Communications (ICC)*, pp. 1–6, Paris, France, 2017.

[32] Q. Khaled, V. C. Abdelfadeel, and D. Pesch, "Fair adaptive data rate allocation and power control in LoRaWAN," in *2018 IEEE 19th International Symposium on "A World of Wireless, Mobile and Multimedia Networks" (WoWMoM)*, pp. 14-15, Chania, Greece, June 2018.

[33] N. Jiang, Y. Deng, A. Nallanathan, and J. A. Chambers, "Reinforcement learning for real-time optimization in NB-IoT networks," *IEEE Journal on Selected Areas in Communications*, vol. 37, no. 6, pp. 1424–1440, 2019.

[34] N. Yang, H. Zhang, K. Long, H. Hsieh, and J. Liu, "Deep neural network for resource management in NOMA networks," *IEEE Transactions on Vehicular Technology*, vol. 69, no. 1, pp. 876–886, 2020.

[35] M. Wu, W. Huang, K. Sun, and H. Zhang, "A DQNbased handover management for SDN-enabled ultra-dense networks," in *2020 IEEE 92nd Vehicular Technology Conference (VTC2020-Fall)*,, Victoria, BC, Canada, 2020.

[36] F. Adelantado, X. Vilajosana, P. Tuset-Peiro, B. Martinez, J. Melia-Segui, and T. Watteyne, "Understanding the limits of Lo-RaWAN," *IEEE Communications Magazine*, vol. 55, no. 9, pp. 34–40, 2017.

[37] L. Beltramelli, A. Mahmood, P. Österberg, and M. Gidlund, "LoRa beyond ALOHA: an investigation of alternative random access protocols," *IEEE Transactions on Industrial Informatics*, vol. 17, no. 5, pp. 3544–3554, 2021.

[38] M. Bor and U. Roedig, "LoRa transmission parameter selection," in *2017 13th International Conference on Distributed Computing in Sensor Systems (DCOSS)*, pp. 27–34, Ottawa, ON, Canada, June 2017.

[39] R. S. Sutton and A. G. Barto, "Reinforcement Learning: An Introduction," *IEEE Transactions on Neural Networks*, vol. 9, no. 5, p. 1054, 1998.

[40] V. Mnih, K. Kavukcuoglu, D. Silver et al., "Human-level control through deep reinforcement learning," *Nature*, vol. 518, no. 7540, pp. 529–533, 2015.

[41] Q. Lan, Y. Pan, A. Fyshe, and M. White, "Maxmin Q-learning: controlling the estimation bias of Q-learning," 2020, https://arxiv.org/abs/2002.06487.

[42] F. Skomorokhov and G. Ovchinnikov, "Reinforcement learning for assignment problem," 2020, http://arxiv.org/abs/2011.03909.

[43] K. Arulkumaran, M. P. Deisenroth, M. Brundage, and A. A. Bharath, "Deep reinforcement learning: a brief survey," *IEEE Signal Processing Magazine*, vol. 34, no. 6, pp. 26–38, 2017.

Hindawi
Wireless Communications and Mobile Computing
Volume 2022, Article ID 3183699, 12 pages
https://doi.org/10.1155/2022/3183699

Research Article

Dynamic Resource Allocation in an Adversarial Urban IoBT Environment

Weiwei Wu and Di Lin

University of Electronic Science and Technology of China, China

Correspondence should be addressed to Di Lin; lindi@uestc.edu.cn

Received 8 August 2022; Revised 19 September 2022; Accepted 23 September 2022; Published 11 October 2022

Academic Editor: Mingqian Liu

The advances of the Internet of Battlefield Things (IoBT) would improve the flexibility and efficiency of military operations. Without an effective dynamic adversarial mechanism, soldier devices might malfunction, and machine intelligence technologies could hardly support military operations on a battlefield. In this paper, we propose a game theoretical model considering the adversarial and dynamic nature of the urban IoBT environment. Our algorithm is designed to optimize the whole network's efficiency with the premise that both the attacking and defending parties can maximize their benefit. Meanwhile, we also attempt to consider the interactive effects of channel fading by using a Nakagami distribution based Markov process. The experimental results show that considering the impact of the adversarial and dynamic nature of urban IoBT, our proposed algorithm can improve network performance by 30%-50%.

1. Introduction

In the Internet of Things (IoT) applications, a remarkable amount of data has been produced by intelligent mobile devices such as sensors, mobile computers, and drones [1–7]. As a potential technology, IoT has been applied and promoted in various industrial domains. For example, in an application of Internet of Medical Things (IoMT), an intelligent hospital collects information through sensors and uploads it to a doctor's device for real-time monitoring. In case of emergency, the patient's medical examination reports can timely be transferred to remote experts, thereby reducing the risk of accidental death [8–10].

Unlike the consistent network environment in a regular IoT, e.g., IoMT, the Internet of Battlefield Things (IoBT) has highly changeable and adversarial characteristics in nature [11, 12]. The overall vision of an IoBT is to minimize soldier mortality by collecting battlefield information through intelligent devices and by enabling human decision-making with intelligent means [13]. However, in an extreme battlefield scenario, physical devices and channels are vulnerable to various adversarial attacks [11]. For example, high-power electromagnetic weapon attacks might lead to the physical destruction of base stations or end devices for network communication [14]. Thus, the dynamic adaptability for a highly adversarial environment is the most dominant feature in IoBT, so it is crucial to establish a dynamic mechanism to optimize the entire network's utility [11, 13, 15].

In the special interest of mitigating the adversarial problems in urban IoBT environments, we propose a dynamic adversarial mechanism under a Stackelberg game theoretic framework in consideration of channel fading effects. Despite a bunch of literature on the optimization of IoBT networks [16–18], most existing algorithms may not work well in urban adversarial scenarios, which face the challenges of adversarial battlefield environment and changeable fading channels. The main contributions of our work are summarized as follows:

(1) We address the architecture of communication networks in adversarial urban scenarios, and propose a network utility optimization problem in consideration of each player's benefit on a battlefield. To

Table 1: Description table for key notations.

Key notations	Descriptions
$F(\alpha)$	Nakagami distribution of channel fading
$\Gamma(.)$	Gamma function
ϕ, m	Parameters of a Nakagami distribution
h_{t_i}	Channel fading characteristics at time slot t_i
$I_m(.)$	The m-order Bessel function;
ρ	Correlation between channels
I_0	Zero-order Bessel function
f_d	Doppler frequency
μ	Angle of arrival
λ	A parameter of bandwidth
p_{ij}	Transition probability
U_k^a	Overall utility of attacker k
L_i^d	Decrease of channel capacity of defender i
L_k^a	Cost of attacker k to degrade the network performance
P_i^d	Transmission power defender i
h_{mi}^k	Interferences of defender i at kth stage
δ	Power of noise
M	Number of attackers
N	Number of defenders
P_k^a	Transmission power of attacker k
α	Cost per unit power consumption by an attacker
C_i^d	Channel capacity of defender i after being attacked
$\widehat{L_i^d}$	Cost of defender i to maintain the capacity of channel
η	Cost per unit power consumption by a defender

our knowledge, there are very few studies on network optimization in a secure IoU network in an adversarial scenario

(2) We establish a Stackelberg game theoretic model to characterize the dynamic adversarial process between both parties of a battlefield in an IoBT. The existence of Nash equilibrium is proofed in such a game, and a closed-form mathematical expression of equilibrium is presented when an inequality constraint holds

(3) We also show the existence of Nash equilibrium in the proposed Stackelberg game when an inequality constraint does not hold, and present a numerical algorithm to compute the equilibrium

In Section 2, we review the literature on adversarial cases in IoBT. Following this, Section 3 demonstrates a system model of an adversarial game with both defenders and attackers. Based on the system model, we describe the optimal solutions in Section 4. Section 5 shows the simulation results. The conclusion is finally discussed in Section 6.

2. Related Work

Military missions depend on real-time information processing and data analysis for making accurate decisions in IoBT networks. However, any connectivity problems might result in inaccurate decisions on military operations, so the connectivity problem has triggered much academic debate. For example, in [15], a mechanism on connectivity reestablishment at the presence of dumb nodes that cannot transmit the data to the neighborhood nodes is proposed, and it can enable reestablishment of connectivity between dumb nodes and the centralized node. In [17], a fusion-based defense scheme is employed for defending the attacks at the network level. By characterizing the attack and defense as a zero-sum game, the proposed method can effectively improve network stability even with a fragile network structure. The above-mentioned studies merely consider all sensors/devices with the same type and capabilities. To remedy this issue, in consideration of heterogeneous characteristics of the devices in a network, Abuzainab and Saad use a multistage Stackelberg game to mitigate the IoBT connectivity problem by either activating sleeping nodes or by changing the roles of current nodes [13].

For adversarial IoBT networks, security attacks can be categorized into two types including disruption ones and manipulation ones. While disruption attacks try to paralyze IoT networks by launching physical destructions or jamming the entire system, i.e., denial of service attacks (DDoS) and manipulation attacks seek to control a few nodes in network to inject false information. The attacks mentioned in the previous paragraph are mostly relevant to disruption ones. However, other literature also considers the impact of the action that injects misinformation or imposes human interventions on IoBT nodes. In [18], the misinformation attack has been countered by determining the optimal probability of accepting the information. Similarly, building on a psychological game theory, the authors focus on how the misinformation from human psychological interventions influences game-theoretic decision making on the battlefield [19].

Most previous studies on IoBT have paid particular attention to connectivity problems in which the researchers focus on optimizing the network by measuring the number of connected nodes from the network layer. However, few studies have attempted to use a specific indicator such as bit error rate (BER) or power to optimize network resources from the physical layer. Building on the work [20], a power control based connectivity reconstruction game can reduce energy consumption while maintaining the performance of localization. That is, the number of connected nodes is a fairly broad indicator that can hardly reflect the quality of services (QoS) in an IoBT network. Even if all nodes in the network are successfully connected, the quality of communication might still be unsatisfactory. Thus, it is necessary to use a specific indicator such as power to measure the QoS of IoBT. Furthermore, the current relevant studies primarily

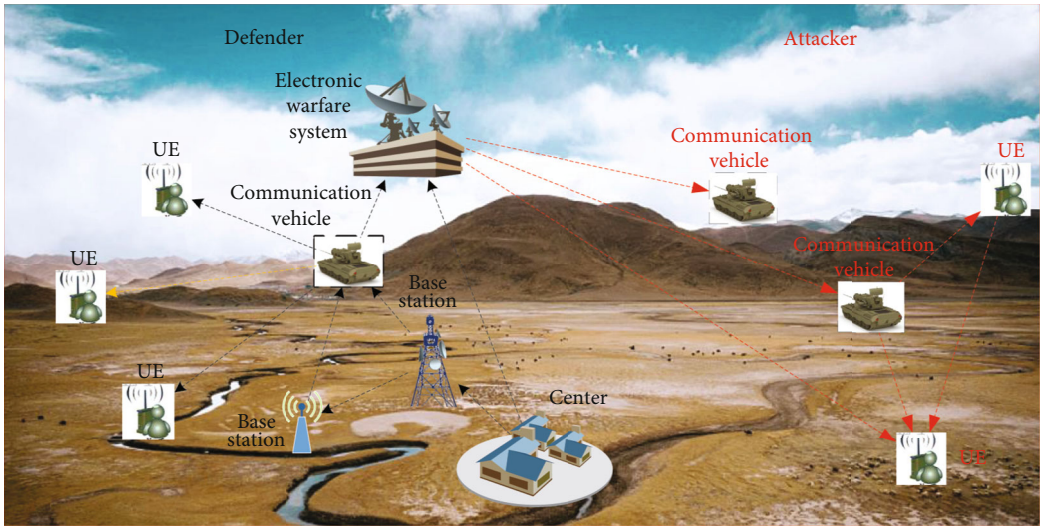

Figure 1: System architecture in an urban IoBT.

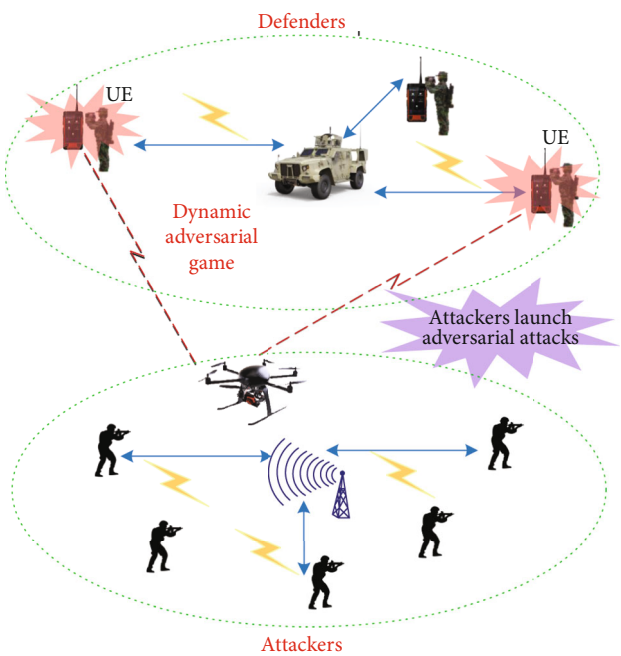

Figure 2: An adversarial game model in the IoBT.

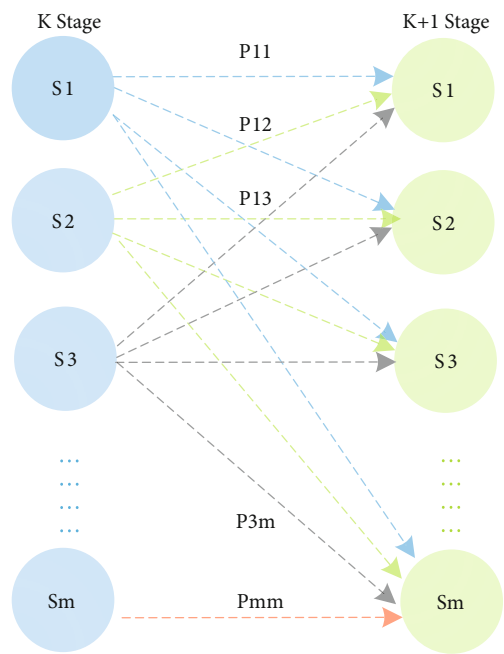

Figure 3: Dynamic channel fading in the IoBT.

focus on building a dynamic scheme to adjust the focal network's topology, but they have not taken into account the dynamic adjustment to channel changes.

3. System Model

As discussed in the previous section, the two factors that dynamic adjustment to the fading channels and reasonable allocation for network resources are fairly important in the urban IoBT environment. To familiarize readers, in the following, we firstly discuss a model that reflects the effects of channel fading in the urban IoBT environment. By using Stackelberg game theory, we then propose a dynamic channel-based adversarial game model that reflects the adversarial process between both parties of a battlefield. The strategies of the network players depend on those of their competitors. To be specific, the attackers in the network actively deploy strategies, while the defenders make passive adjustments based on the attackers™ strategies. This framework can match the adversarial situation in an IoBT well. The key notations in Table 1 will be used in the following sections.

3.1. Channel Fading Models. By facilitating an effective decision making process, intelligent tools used in the urban IoBT scenarios may include on-board servers, sensors, mobile computers, and drones. In cities, vehicle speed is limited to less than 60 meters per minute, and intervehicle distance is from a few meters to approximately 100 meters. As shown

Step 1: Initialize the relevant parameters: B that represents bandwidth, h_{mi} that represents a set for interferences at the first round (h_{mi} would dynamically change according to the Markov transition probability matrix), δ that represents the power of noise, and P_m that represents a reasonable maximum power that the attackers can accept. Additionally, set $U_a = U_d = P_a = 0$.
Step 2: By using a searching algorithm, the maximum value of U_a can be found. The maximum U_a corresponds to the optimal solution of the attacker's power P_a^*.
Let $X = 0$: ΔP: P_m, $\Delta P = \lceil P_m/N \rceil$
For $i = 1$: ΔP
Set $P_a = X(i)$
Compute U_a based on the function (18)
If $U_a(P_a) > U_a$
Update $U_a^* = U_a(P_a)$
Set $P_a^* = P_a$
Step 3: Building on the above steps, the algorithm searches the optimal solution within the closed interval range$[0, P_m]$ to determine the game equilibrium P_a^* and the corresponding utilities of the attackers and defenders U_a^*, U_d^*.

Algorithm 1: Computing algorithm for achieving Stackelberg game equilibrium.

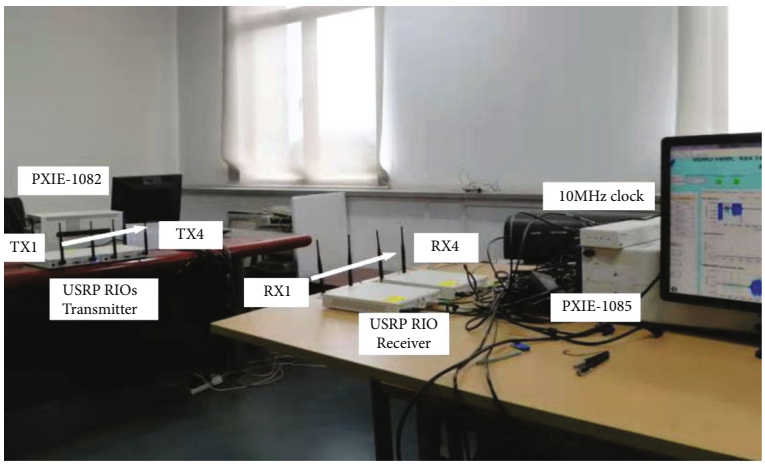

Figure 4: Experimental settings for data collection in the simulation.

in Figure 1, two sides including defenders and attackers are involved in an IoBT network. The center on the defending side plays an essential role in monitoring and decision making. An electronic defending system could facilitate communication tasks between user ends (UEs) and the centralized node, as well as monitoring tasks. The collected information and data would be forwarded to the center for further analysis and actions.

By considering both the urban IoBT environment and widely used channel models, in [21–23], the researchers conclude that the channel fading in all line of sight and nonline of sight cases can be modeled as Nakagami distributions with particular parameters. The Nakagami distribution can be used to capture the changes of signal amplitude after channel fading in an urban IoT scenario. The channel characteristics of Nakagami are determined by parameters ϕ and m, and thus the generalized Nakagami distribution of channel fading α can be shown as

$$F(\alpha) = \frac{2m^m \alpha^{2m-1}}{\phi^m \Gamma(m)}, \tag{1}$$

where $\Gamma(.)$ is a gamma function and ϕ, m are two determinant parameters of a Nakagami distribution.

Represent h_{t_1} and h_{t_2} as the channel fading characteristics at the time slots of t_1 and t_2, respectively. Building on the generalized Nakagami channel model Formula (1), we can denote the joint probability density function as [24]:

$$F(h_{t_1}, h_{t_2}) = \frac{4(h_{t_1} h_{t_2})^m}{(1-\rho)\Gamma(m)\rho^{m-1/2}} \left(\frac{m}{\phi}\right)^{m+1} \times I_{m-1}\left\{\frac{2m\sqrt{\rho} h_{t_1} h_{t_2}}{(1-\rho)\phi}\right\} \times \exp\left\{-\frac{m\left(h_{t_1}^2 + h_{t_2}^2\right)}{1-\rho}\right\}, \tag{2}$$

where $I_m(.)$ denotes the m-order Bessel function, ϕ and m denote the parameters of a Nakagami fading channel (1), and ρ denotes the correlation between channels [24]:

$$\rho(\tau) = \frac{I_0\left(\sqrt{\lambda^2 - 2\pi f_d(\tau)^2 + j4\pi\lambda f_d(\tau)\cos\mu}\right)}{I_0(\lambda)}, \tag{3}$$

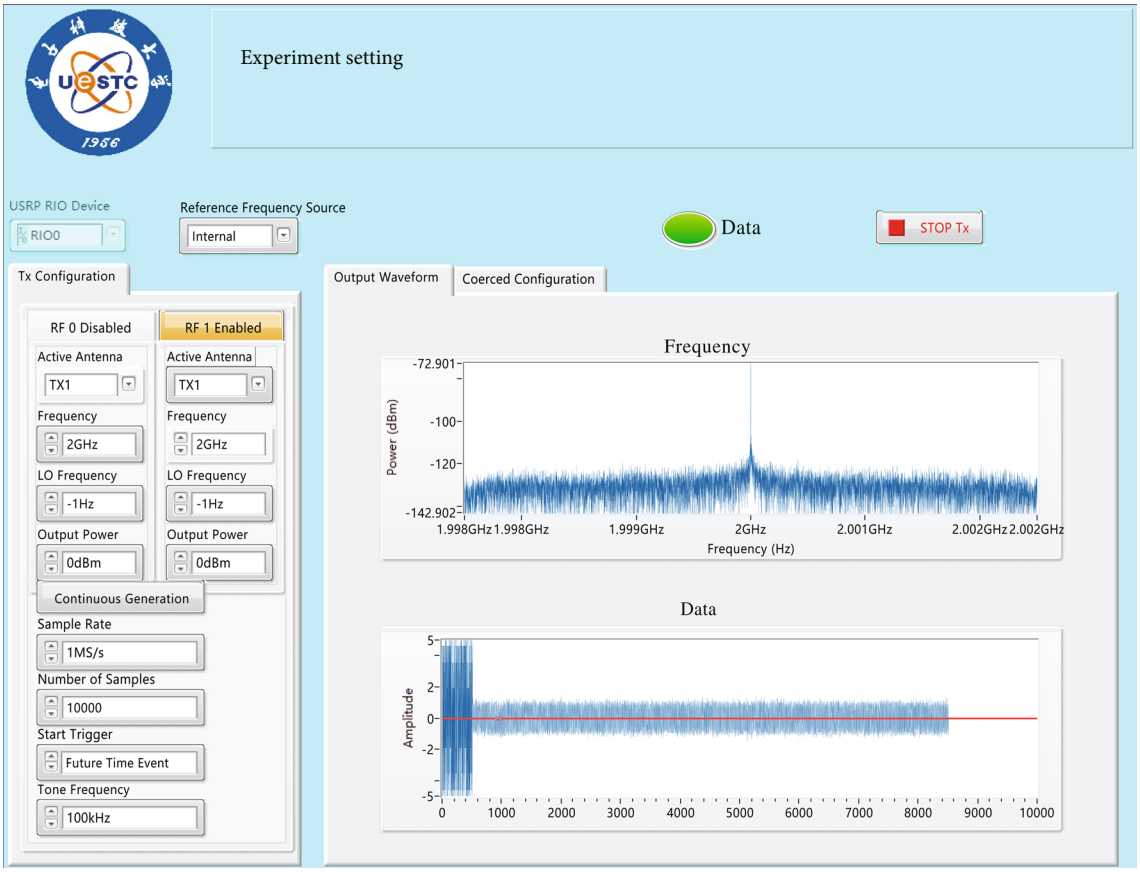

Figure 5: User interface of experimental setting.

where I_0 denotes zero-order Bessel function, f_d denotes the Doppler frequency, μ denotes the angle of arrival, and λ denotes a parameter of bandwidth.

In the following, we consider M channel states, i.e., $S_i (i = 1, 2 \cdots M)$. S_i is dependent on the values of channel fading h_k at time slot k. Let $h_k \in (S_{i-1}^t, S_i^t)$, and let h_k and h_{k+1} denote the channel fading at the kth and $(k+1)$th time slots, respectively. Thus, the transition probability p_{ij} can be characterized as

$$\begin{aligned} p_{ij} &= \Pr\left\{h_{k+1} \in \left(S_{i-1}^k, S_i^k\right) \middle| h_k \in \left(S_{j-1}^t, S_j^t\right)\right\} \\ &= \frac{\Pr\left\{h_{k+1} \in \left(S_{i-1}^k, S_i^k\right), h_k \in \left(S_{j-1}^k, S_j^k\right)\right\}}{\Pr\left\{h_k \in \left(S_{j-1}^k, S_j^k\right)\right\}} \\ &= \frac{\int_{S_{i-1}^k}^{S_i^k} \int_{S_{j-1}^k}^{S_j^k} F\left(h_{t_1}, h_{t_2}\right) \mathrm{d}h_{t_1} \mathrm{d}h_{t_2}}{\int_0^{\infty} \int_{S_{j-1}^t}^{S_j^t} F\left(h_{t_1}, h_{t_2}\right) \mathrm{d}h_{t_1} \mathrm{d}h_{t_2}}. \end{aligned} \tag{4}$$

By submitting (2) into (4), we can achieve the probability of a transition between channel states and simulate the future channel states based on previous information. We denote Equation (4) as the probability of one-step transition between channel states, and build up the matrix of probabilities as one-step transition matrix. Mathematically, we can denote the one-step transition matrix as

$$\begin{bmatrix} \mathrm{p}_{11} & \mathrm{p}_{12} & \cdots & \mathrm{p}_{1m} \\ \mathrm{p}_{21} & \mathrm{p}_{22} & \cdots & \mathrm{p}_{2m} \\ \vdots & \vdots & \cdots & \vdots \\ \vdots & \vdots & \cdots & \vdots \\ \mathrm{p}_{m1} & \mathrm{p}_{22} & \cdots & \mathrm{p}_{\mathrm{mm}} \end{bmatrix}. \tag{5}$$

Based on the Markov properties of Nakagami fading channels [25], we can compute the N-step transition matrix as P^N. Actually, we can estimate one-step transition probability by statistically averaging the data of observations in a long period.

3.2. Adversarial Game Model. As shown in Figure 2, attackers might launch adversarial attacks on defenders by using high power electromagnetic weapons. The performance of base station or edge server would degrade or even corrupt in the presence of attackers, so computing tasks need to be processed from the cloud server to heterogeneous edge servers or end devices. Thus, it is essential to build a dynamic algorithm to optimize insufficient network resources in such a dynamic, adversarial, and unpredictable scenario. The adversarial process between defenders and

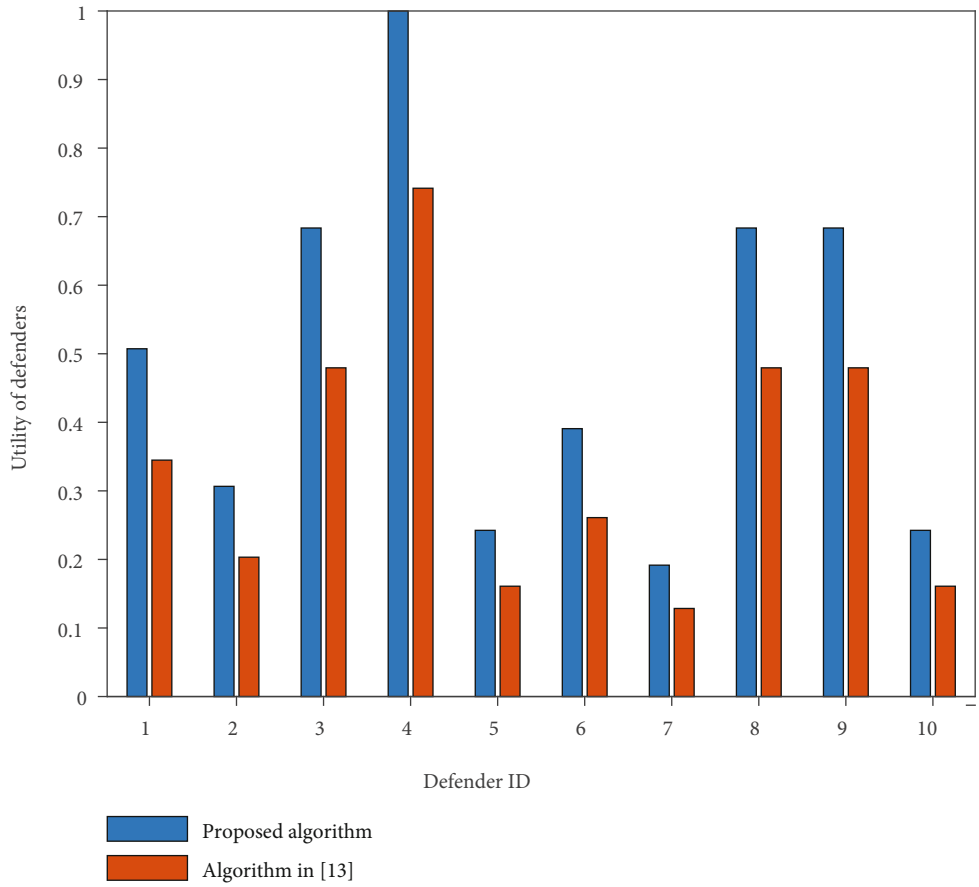

Figure 6: Individual utility of defenders (proposed vs. traditional algorithm [12]).

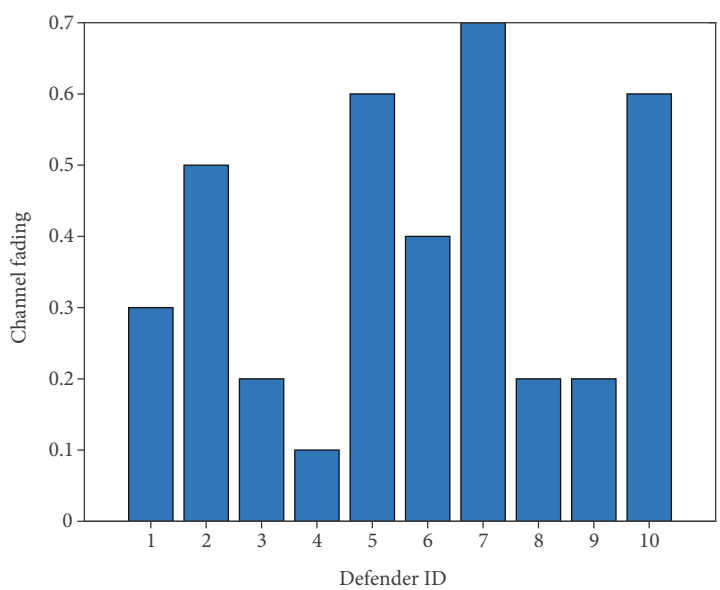

Figure 7: Individual channel fading of defenders.

attackers can be regarded as a classic game theory problem. By ensuring the optimization of the overall network resources, the Stackelberg game theory is proposed. An attacker actively deploys military strategy, while a defender makes passive adjustments based on the attacker's strategy, assuming that both parties are aware of the other's strategy.

At each stage of a game, attackers and defenders have their respective strategy sets. In the following, we will

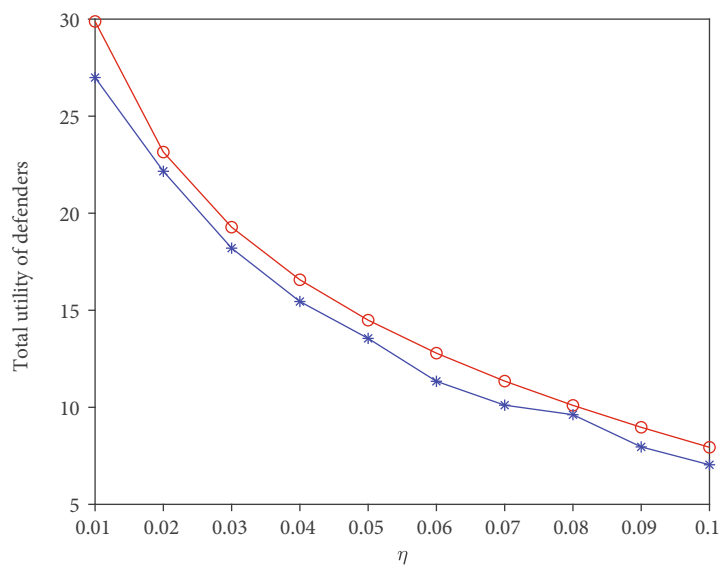

Figure 8: Total utility of defenders with different η (proposed vs. traditional algorithm [12]).

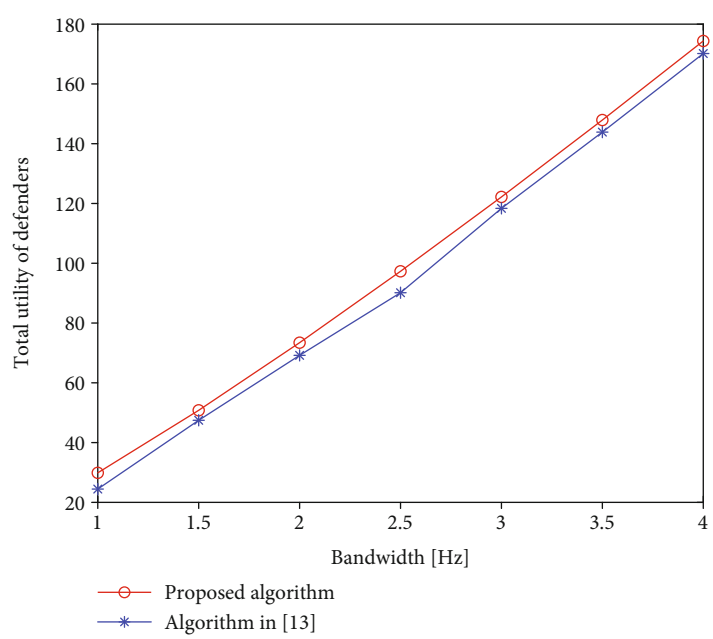

Figure 9: Total utility of defenders with different bandwidth (proposed vs. traditional algorithm [12].

consider the utility function from the attacker or the defender perspective. Firstly, the attackers' strategies primarily depend on two factors, including the decrease of network performance and the cost of interference to defenders. Therefore, the overall utility of attacker k, i.e., U_k^a can be expressed as

$$U_k^a = \sum_{i=1}^{N} L_i^d - L_k^a, \tag{6}$$

where L_i^d represents the decrease of channel capacity of defender i. L_k^a represents the cost of attacker k to degrade the network performance. N represents the number of defenders in a network.

Building on the channel fading model in the previous section, the transfer of channel fading h_{mi}^k between stage k and stage $k+1$ follows a transfer matrix, shown in Equation (5). The dynamic channel fading h_{mi}^k is illustrated in Figure 3. S_1, $S_2 \ldots S_M$ refer to M states of channel fading.

Thus, L_i^d can be denoted as

$$L_i^d = B\log_2\left(1 + \frac{P_i^d}{\delta}\right) - B\log_2\left(1 + \frac{P_i^d}{\sum_{k=1}^{M} P_k^a h_{\mathrm{mi}}^k + \delta}\right), \tag{7}$$

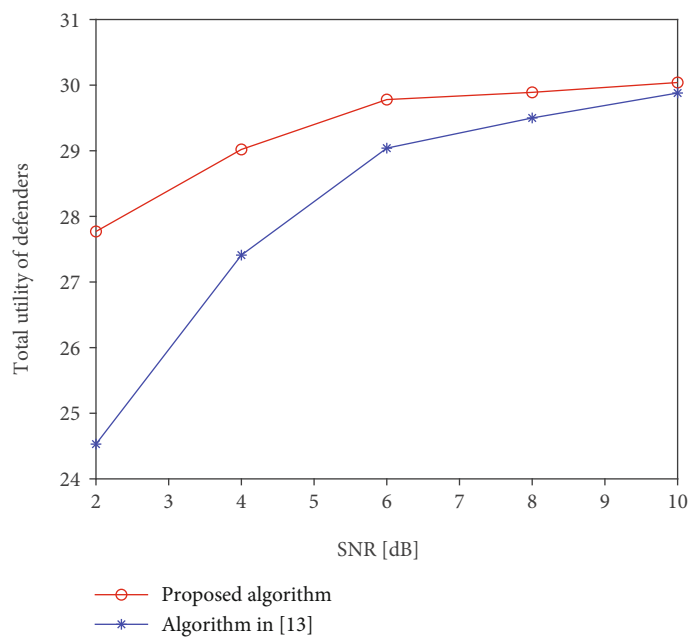

Figure 10: Total utility of defenders with different SNRs (proposed vs. traditional algorithm [12].

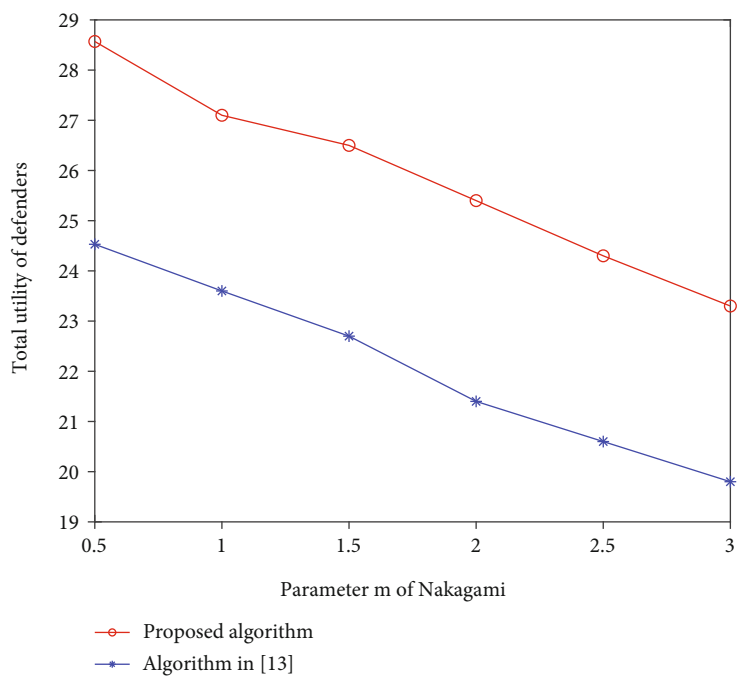

Figure 11: Total utility of defenders with different values of m in Nakagami (proposed vs. traditional algorithm [12]).

where P_i^d represents the transmission power defender i, h_{mi}^k represents the dynamic interferences of defender i at kth stage, and δ represents the power of noise. In equation (7), $B\log_2(1+P_i^d/\delta)$ represents the channel capacity of defender i before a network is attacked, and $B\log_2(1+P_i^d/\sum_{k=1}^{M}P_k^a h_{\mathrm{mi}}^k+\delta)$ represents the channel capacity of defender i after the network is attacked. M represents the number of attackers in a network.

Similarly, by Shannon formula, the cost of the kth attacker L_k^a can be denoted as

$$L_k^a = \alpha P_k^a, \tag{8}$$

where P_k^a represents the transmission power of attacker k and α represents the cost per unit power consumption by an attacker.

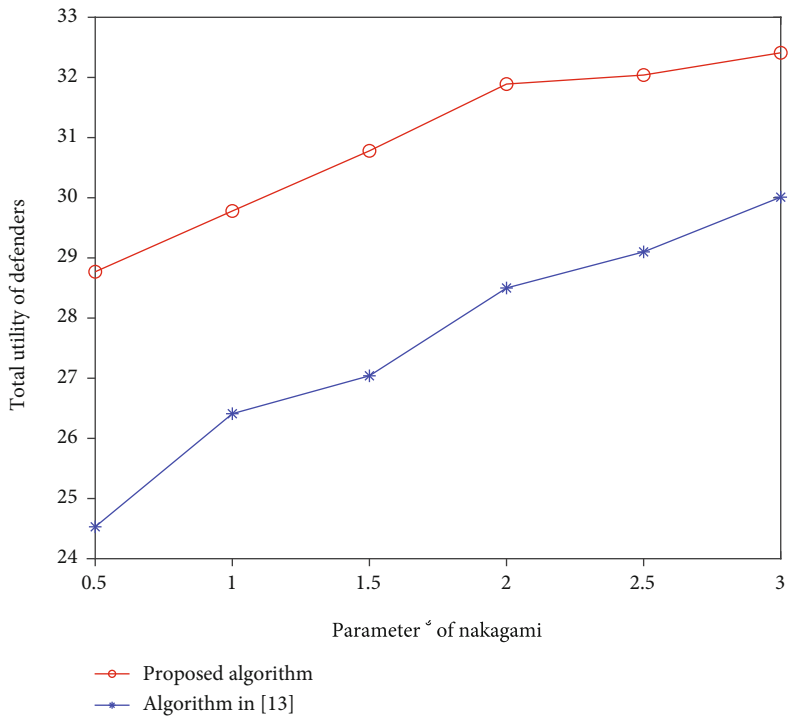

Figure 12: Total utility of defenders with different values of ϕ in Nakagami (proposed vs. traditional algorithm [12]).

Replacing Equation (6) with both Equation (7) and Equation (8), we can mathematically denote U_k^a as

$$U_k^a = \sum_{i=1}^{N}\left(B\log_2\left(1+\frac{P_i^d}{\delta}\right) - B\log_2\left(1+\frac{P_i^d}{\sum_{k=1}^{M}P_k^a+\delta}\right)\right) - \alpha P_k^a. \tag{9}$$

On the other hand, a defender's strategy is primarily dependent on two factors, including the defender's channel capacity after being attacked and the defender's transmission power. Therefore, the overall utility of defender i, i.e., U_i^d can be expressed as

$$U_i^d = C_i^d - \widehat{L_i^d}, \tag{10}$$

where C_i^d is defined as the channel capacity of defender i after being attacked and $\widehat{L_i^d}$ is defined as the cost of defender i to maintain the capacity of his/her channel.

By Shannon formula, C_i^d can be denoted as

$$C_i^d = B\log_2\left(1+\frac{P_i^d}{\sum_{k=1}^{M}P_k^a h_{\mathrm{mi}}^k+\delta}\right). \tag{11}$$

Also, by Shannon formula, L_i^d can be denoted as

$$\widehat{L_i^d} = \eta P_i^d, \tag{12}$$

where η represents the cost per unit power consumption by a defender.

Similarly, U_i^d can be formulated as

$$U_i^d = B\log_2\left(1+\frac{P_i^d}{\sum_{k=1}^{M}P_k^a h_{\mathrm{mi}}^k+\delta}\right) - \eta P_i^d. \tag{13}$$

4. Optimal Solution

Each party in a battlefield expects to adjust power to maximize its user capacity. This utility optimization problem can be defined as a Stackelberg game. In this section, a Nash equilibrium for the game would eventually be achieved on both sides. The defender always adjusts its strategy based on the attacker's, so the defender is defined as a leader while the attacker as a follower. Building on the above-mentioned mechanism, we would explore and prove the existence and exact solution of the best responses of both parties on a battlefield.

4.1. Optimal Strategy of the Defender. In the following, we discuss the optimal solution to maximize the utility of (13), and it can be characterized as Theorem 1.

Theorem 1. *The optimal solution of U_i^d to function (13) for the defender exists and can be denoted as*

$$\widehat{P}_i^d = \frac{B}{\eta} - \sum_{k=1}^{M}P_k^a h_{mi}^k - \delta. \tag{14}$$

Proof. We first prove the existence of the optimal solution of U_i^d. The existence can be proved by computing the second

derivative of the utility function.

$$\frac{\partial^2 U_i^d}{\partial^2 P_i^d} = \frac{-B}{\left(\sum_{k=1}^{M} P_k^a h_{\mathrm{mi}}^k + \delta + P_i^d\right)^2} < 0. \tag{15}$$

In the equation, bandwidth is positive, so the second-order derivative $-B/(\sum_{k=1}^{M} P_k^a h_{mi}^k + \delta + P_i^d)^2 < 0$, which proves that the utility function U_i^d is concave. The optimal solution of the function that would maximize the utility of the defender can be computed by setting the first-order derivative to 0.

$$\frac{\partial U_i^d}{\partial P_i^d} = \frac{B}{\sum_{k=1}^{M} P_k^a + \delta + P_i^d} - \eta = 0. \tag{16}$$

By employing the equation, we can attain the optimal utility of the defender as $\widehat{P}_i^d = B/\eta - \sum_{k=1}^{M} P_k^a h_{\mathrm{mi}}^k - \delta$. □

4.2. Optimal Strategy of the Attacker. In the following, we discuss the optimal solution to maximize the utility of (9), and it can be characterized as Theorem 2.

Theorem 2. *In consideration of the optimal strategy of the defender, the optimal solution of U_k^a to function (9) for the attacker can be achieved when the following equation holds:*

$$\sum_{i=1}^{N} \frac{\delta h_{mi}^k}{\left(\sum_{k=1}^{M} P_k^a h_{mi}^k - B/\eta\right)} + \sum_{i=1}^{N} \frac{h_{mi}^k}{\left(\sum_{k=1}^{M} P_k^a h_{mi}^k + \delta\right)} = \frac{\alpha}{B}. \tag{17}$$

Proof. By substituting the optimal solution of the defender into the function (9), and the function can be transformed into

$$\begin{aligned} U_k^a = &\sum_{i=1}^{N} \left\{ B \log_2 \left[1 + \frac{1}{\delta} \left(\frac{B}{\eta} - \sum_{k=1}^{M} P_k^a h_{\mathrm{mi}}^k - \delta \right) \right] \right\} \\ &- \sum_{i=1}^{N} \left\{ B \log_2 \left[1 + \frac{B/\eta - \sum_{k=1}^{M} P_k^a h_{\mathrm{mi}}^k - \delta}{\sum_{k=1}^{M} P_k^a h_{\mathrm{mi}}^k + \delta} \right] \right\} - \alpha P_k^a. \end{aligned} \tag{18}$$

Based on the function (18), we first prove the existence of the optimal solution of U_k^a. The existence can be proved by computing the second derivative of the utility function.

$$\frac{\partial^2 U_k^a}{\partial^2 P_k^a} = \sum_{i=1}^{N} \left[-B\delta \left(h_{\mathrm{mi}}^k \right)^2 \right] \left(\frac{B}{\eta} - \sum_{k=1}^{M} P_k^a h_{\mathrm{mi}}^k \right)^{-2} + \sum_{i=1}^{N} \left(-\mathrm{Bh}_{\mathrm{ki}}^2 \right) \left(\delta + \sum_{k=1}^{M} P_k^a h_{\mathrm{mi}}^k \right)^{-2} < 0. \tag{19}$$

It is not hard to reach the conclusion that the second-order derivative of U_k^a is less than 0, so the utility function U_k^a is concave. The optimal solution of the function that would maximize the utility of the attacker can be computed by setting the first-order derivative to 0.

$$\frac{\partial U_k^a}{\partial P_k^a} = \sum_{i=1}^{N} \frac{B\delta h_{\mathrm{mi}}^k}{\sum_{k=1}^{M} P_k^a h_{\mathrm{mi}}^k - B/\eta} + \sum_{i=1}^{N} \frac{\mathrm{Bh}_{\mathrm{mi}}^k \left(\delta + \sum_{k=1}^{M} P_k^a h_{\mathrm{mi}}^k \right)}{\left(\sum_{k=1}^{M} P_k^a h_{\mathrm{mi}}^k + \delta \right)^2} - \alpha. \tag{20}$$

Let $\partial U_k^a / \partial P_k^a = 0$, we have

$$\frac{\alpha}{B} = \sum_{i=1}^{N} \frac{\delta h_{\mathrm{mi}}^k}{\sum_{k=1}^{M} P_k^a h_{\mathrm{mi}}^k - B/\eta} + \sum_{i=1}^{N} \frac{h_{\mathrm{mi}}^k \left(\delta + \sum_{k=1}^{M} P_k^a h_{\mathrm{mi}}^k \right)}{\left(\sum_{k=1}^{M} P_k^a h_{\mathrm{mi}}^k + \delta \right)^2}. \tag{21}$$

□

4.3. Stackelburg Equilibrium Algorithm. The mutual best response is the Nash equilibrium of the Stackelberg game that maximizes the utility for both attackers and defenders. Building on the above-mentioned description on the Stackelberg game, we present an algorithm to determine the Nash equilibrium using a searching algorithm within a reasonable range of power that the attackers can accept. As shown in the Pseudo codes of Algorithm 1, we firstly initialize the relevant parameters, including B that represents bandwidth, h_{mi} that represents a set for interferences at the first round (h_{mi} would dynamically change according to the Markov transition probability matrix), δ that represents the power of noise, and P_m that represents a reasonable maximum power that the attackers can accept. Following this, we use a search algorithm with a reasonable range of power $[0, P_m]$ for the attackers to determine the game equilibrium P_a^* and the corresponding utilities of the attackers and defenders U_a^*, U_d^*.

5. Simulation Results

We experiment through a hardware platform that includes a NI-PXIe 1085 and three USRP-RIO-1082 devices. As shown in Figure 4, the NI-PXIe 1085 device is designed to display graphic results, while three USRP RIO-1082 devices are designed to simulate transmitters, receivers, and interference generators. Two USRP devices are equipped with four antennas, and we use them to simulate two transmitters and two receivers. The third USRP device is equipped with two antennas to simulate two interference generators. Additionally, we use a NI-PXIe 1085 platform to monitor the graphic results of interference, shown in Figure 5. We also load the data generated by USRP-RIO-1082 devices to MATLAB for subsequent numerical analysis. We compare the analytic results using the proposed algorithm and the algorithm in [19], respectively.

The simulation parameters are set as follows: the parameters of Nakagami channel models are $m = 1$ and $\eta = 0.5$; the signal to noise ratio ranges from 0 dB to 20 dB; the level of signal to interference ratio ranges from 0 dB to 20 dB; the cost parameter of transmission power by defenders ranges from 0.1 to 1.

5.1. Individual Utility of Defenders. In this section, we compare the individual utility of defenders using our proposed algorithm with the algorithm in [19], which is viewed as a benchmark. As shown in Figure 6, for each of defenders, our proposed algorithm can achieve a higher individual utility in comparison with the benchmark algorithm. The comparison result illustrates that our proposed algorithm outperforms the benchmark algorithm. Specifically, an extra 30%-50% of individual utility can be achieved using the proposed algorithm than the benchmark algorithm. The reason is that the proposed algorithm considers the dynamic variation of the system environment, and defenders can adjust their own strategies in view of both attackers' strategies and channel fading.

Across the defenders, the individual utility of each defender primarily depends on the strategies of attackers and the channel fading. Given the same attacker's strategies in each round of game, the difference of individual utility among defenders is dependent on their own channel fading. In the following, we investigate the channel fading of each defender. As shown in Figure 7, the individual utility decreases with the channel fading. For example, while defender 4 has the lowest channel fading and has the highest individual utility, defender 7 has the highest channel fading and has the lowest individual utility.

5.2. Total Utility of Defenders. In section, we investigate the total utility of defenders using both our proposed algorithm and the benchmark algorithm in [19]. Specifically, we consider the total utility with different values of cost parameter η, bandwidth, signal to noise ratio (SNRs), Nakagami channel model parameters m and ϕ, respectively.

As shown in Figure 8, the total utility of defenders decreases with the values of η, and the proposed algorithm can achieve a higher utility than the benchmark algorithm across various η. The reason is that a higher η indicates the defenders need to achieve a certain level of utility with a higher level of cost, and thus the total utility of defenders decreases with the values of η.

As shown in Figure 9, the total utility of defenders increases with the values of bandwidths, and the proposed algorithm can achieve a higher utility than the benchmark algorithm across various bandwidth. The reason is that a higher bandwidth indicates the defenders can achieve a higher utility with the same cost of transmission power, and thus the total utility of defenders increases with the values of bandwidth.

As shown in Figure 10, the total utility of defenders increases with the values of SNRs, and the proposed algorithm can achieve a higher utility than the benchmark algorithm across various SNRs. The reason is that a higher level of SNR indicates the defenders can achieve a higher utility when occupying the same amount of bandwidth, and thus the total utility of defenders increases with the values of SNRs.

As shown in Figure 11, the total utility of defenders decreases with the values of m in Nakagami, and the proposed algorithm can achieve a higher utility than the benchmark algorithm across various values of m. The reason is that a larger value of m in Nakagami leads to a higher channel fading, and thus the utility achieved by defenders is lower when occupying the same amount of bandwidth and paying the same cost of transmission power. Thus, the total utility of defenders decreases with the values of m in Nakagami.

As shown in Figure 12, the total utility of defenders increases with the values of ϕ in Nakagami, and the proposed algorithm can achieve a higher utility than the benchmark algorithm across various values of ϕ. The reason is that a smaller value of ϕ in Nakagami leads to a higher channel fading, and thus the utility achieved by defenders is lower when occupying the same amount of bandwidth and paying the same cost of transmission power. Thus, the total utility of defenders increases with the values of ϕ in Nakagami.

6. Conclusion

This paper has proposed a game theoretic model in consideration of the adversarial and dynamic nature of the urban IoBT environment. By employing a Stackelberg game theoretic method, our proposed framework can effectively leverage network resources and improve network performance in an adversarial scenario. We also consider the interactive effects of dynamic channel fading by using a Nakagami distribution based Markov process. The detailed analysis illustrates that with considering the impact of the adversarial and dynamic nature of urban IoBT, our proposed algorithm can improve the entire network performance. It is known that the security issues are the most significant perspective in the IoBT environment. So in our future work, in combination of network optimization, we will explore an authentication model to fit in the characteristics of IoBT scenario.

Data Availability

We have no data used in this work.

Conflicts of Interest

The authors declare that they have no conflicts of interest.

Acknowledgments

This work is partially funded by Science and Technology Program of Sichuan Province (2021YFG0330), partially funded by Intelligent Terminal Key Laboratory of Sichuan Province (SCITLAB-0001), and partially funded by Fundamental Research Funds for the Central Universities (ZYGX2019J076).

References

[1] W. D. Lu, Y. Ding, Y. Gao et al., "Resource and trajectory optimization for secure communications in dual unmanned aerial vehicle mobile edge computing systems," *IEEE Transactions on Industrial Informatics*, vol. 18, no. 4, pp. 2704–2713, 2022.

[2] Y. Xu, J. Tang, B. Li, N. Zhao, D. Niyato, and K. K. Wong, "Adaptive aggregate transmission for device-to-multi-device aided cooperative NOMA networks," *IEEE Journal on Selected Areas in Communications*, vol. 40, no. 4, pp. 1355–1370, 2022.

[3] W. D. Lu, P. Y. Si, Y. Gao et al., "Trajectory and resource optimization in OFDM-based UAV-powered IoT network," *IEEE Transactions on Green Communications and Networking*, vol. 5, no. 3, pp. 1259–1270, 2021.

[4] W. D. Lu, P. Y. Si, G. X. Huang et al., "SWIPT cooperative spectrum sharing for 6G-enabled cognitive IoT network," *IEEE Internet of Things Journal*, vol. 8, no. 20, pp. 15070–15080, 2021.

[5] C. Kai, H. Li, L. Xu, Y. Li, and T. Jiang, "Energy-efficient device-to-device communications for green smart cities," *IEEE Transactions on Industrial Informatics*, vol. 14, no. 4, pp. 1542–1551, 2018.

[6] X. Li, R. Fan, H. Hu, N. Zhang, X. Chen, and A. Meng, "Energy-efficient resource allocation for mobile edge computing with multiple relays," *IEEE Internet of Things Journal*, vol. 9, no. 13, pp. 10732–10750, 2022.

[7] X. An, R. Fan, H. Hu, N. Zhang, S. Atapattu, and T. A. Tsiftsis, "Joint task offloading and resource allocation for IoT edge computing eith sequential task dependency," *IEEE Internet of Things Journal*, vol. 9, no. 17, pp. 16546–16561, 2022.

[8] H. N. Dai, Z. Zheng, and Y. Zhang, "Blockchain for Internet of Things: a survey," *IEEE Internet of Things Journal*, vol. 6, no. 5, pp. 8076–8094, 2019.

[9] J. Huang, L. Kong, G. Chen, M.-Y. Wu, X. Liu, and P. Zeng, "Towards secure industrial IoT: blockchain system with credit-based consensus mechanism," *IEEE Transactions on Industrial Informatics*, vol. 15, no. 6, pp. 3680–3689, 2019.

[10] K. L. Ang and J. K. P. Seng, "Application specific internet of things (ASIoTs): taxonomy, applications, use case and future directions," *IEEE Access*, vol. 7, pp. 56577–56590, 2019.

[11] A. Kott, A. Swami, and B. J. West, "The Internet of Battle Things," *Computer*, vol. 49, no. 12, pp. 70–75, 2016.

[12] R. Yang, F. Yu, P. Si, Z. Yang, and Y. Zhang, "Integrated blockchain and edge computing systems: a survey, some research issues and challenges," *IEEE Communications Surveys & Tutorials*, vol. 21, no. 2, pp. 1508–1532, 2019.

[13] N. Abuzainab and W. Saad, "Dynamic connectivity game for adversarial internet of battlefield things systems," *IEEE Internet of Things Journal*, vol. 5, no. 1, pp. 378–390, 2018.

[14] J. F. Harvey, M. B. Steer, and T. S. Rappaport, "Exploiting high millimeter wave bands for military communications, applications, and design," *IEEE Access*, vol. 7, pp. 52350–52359, 2019.

[15] P. Kar, A. Roy, and S. Misra, "Connectivity reestablishment in self-organizing sensor networks with dumb nodes," *ACM Transactions on Autonomous and Adaptive Systems (TAAS)*, vol. 10, no. 4, 2016.

[16] A. R. Elsherif, W.-P. Chen, A. Ito, and Z. Ding, "Adaptive resource allocation for interference management in small cell networks," *IEEE Transactions on Communications*, vol. 63, no. 6, pp. 2107–2125, 2015.

[17] P. Chen, S. Cheng, and K. Chen, "Information fusion to defend intentional attack in internet of things," *IEEE Internet of Things Journal*, vol. 1, no. 4, pp. 337–348, 2014.

[18] N. Abuzainab and W. Saad, "Misinformation control in the internet of battlefield things: a multiclass mean-field game," in *2018 IEEE Global Communications Conference (GLOBECOM)*, Abu Dhabi, United Arab Emirates, 2018.

[19] Y. Hu, A. Sanjab, and W. Saad, "Dynamic psychological game theory for secure internet of battlefield things (IoBT) systems," *IEEE Internet of Things Journal*, vol. 6, no. 2, pp. 3712–3726, 2019.

[20] W. Lee, J. Choi, J. Lee, Y. Kim, and S. Kim, "Distributed power control-based connectivity reconstruction game in wireless localization," *IEEE Communications Letters*, vol. 21, no. 2, pp. 334–337, 2017.

[21] D. Lin and L. Fabrice, "An algorithm that predicts CSI to allocate bandwidth for healthcare monitoring in hospital's waiting rooms," *International Journal of Telemedicine and Applications*, vol. 2012, Article ID 843527, 13 pages, 2012.

[22] D. W. Matolak, I. Sen, W. H. Xiong, and N. T. Yaskoff, "5 GHZ wireless channel characterization for vehicle to vehicle communications," in *MILCOM 2005 - 2005 IEEE Military Communications Conference*, pp. 3016–3022, Atlantic City, NJ, USA, 2005.

[23] Y. Xu, B. Li, N. Zhao et al., "Coordinated direct and relay transmission with NOMA and network coding in Nakagami-m fading channels," *IEEE Transactions on Communications*, vol. 69, no. 1, pp. 207–222, 2021.

[24] L. C. Wang, W. C. Liu, A. Chen, and K. N. Yen, "Joint rate and power adaptation for wireless local area networks in generalized Nakagami fading channels," *IEEE Transactions on Vehicular Technology*, vol. 58, no. 3, pp. 1375–1386, 2009.

[25] C. D. Iskander and P. T. Mathiopoulos, "Fast simulation of diversity Nakagami fading channels using finite-state Markov models," *IEEE Transactions on Broadcasting*, vol. 49, no. 3, pp. 26–277, 2003.

Hindawi
Wireless Communications and Mobile Computing
Volume 2022, Article ID 5249449, 14 pages
https://doi.org/10.1155/2022/5249449

Research Article

A Lightweight Stereo Visual Odometry System for Navigation of Autonomous Vehicles in Low-Light Conditions

Jie Li,[1] **Zhenfei Kuang**,[1] **Guangman Lu**,[1] **Yuyang Peng**,[2] **Wenli Shang**,[1] **Jun Li**,[1] **and Wei Wei**[1]

[1]*Research Center of Intelligent Communication Engineering, School of Electronics and Communication Engineering, Guangzhou University, Guangzhou 510006, China*
[2]*School of Computer Science and Engineering, Macau University of Science and Technology, Taipa, 999078 Macau SAR, China*

Correspondence should be addressed to Wenli Shang; shangwl@gzhu.edu.cn, Jun Li; lijun52018@gzhu.edu.cn, and Wei Wei; wei@gzhu.edu.cn

Received 19 July 2022; Revised 30 August 2022; Accepted 23 September 2022; Published 6 October 2022

Academic Editor: Mingqian Liu

Localization of vehicles in a 3D environment is a basic task in autonomous driving. In the low-light environments, it is difficult to navigate independently using a visual odometry for autonomous driving. The main reason for this challenge is the blurred images in the scenes with insufficient illumination. Although numerous works focused on this issue, it still has a number of inherent drawbacks. In this paper, we propose a lightweight stereo visual odometry system for navigation of autonomous vehicles in low-light situations. Contrary to the existing recovery methods, we aim to divide the captured image into the illumination image as well as the reflectance image and only estimate the illumination one, where the enhanced map of the low-light image is acquired by using the retinex theory. In addition, we further utilize a simplified and rapid feature detection scheme, which reduces the computation time by about 85% but maintaining the matching accuracy similar to that of ORB features. Finally, the experiments show that our average memory consumption of our proposed method is much less than the conventional algorithm.

1. Introduction

Localization is one of the tasks for autonomous driving, and it is also a necessity to achieve automatic navigation, whereas visual odometry (VO) and visual simultaneous localization and mapping (VSLAM) are considered to be the primary technologies to achieve this goal [1]. Visual odometry is the process of estimating the relative camera poses by observing two cameras sharing a common field-of-view [2]. A core part of it is to be able to track a sufficient number of points during the continuous camera movements. These points will be used to calculate the body pose (translation and rotation). Visual odometry can be broadly divided into two categories according to the method of processing the input images. On the one hand, it is an indirect method based on features; on the other hand, it is a direct method based on pixels [3]. The heart of the indirect method is to extract representative points from an image, which are often called features. Then, these points are tracked in the successive frames. The body pose is recovered by minimizing the reprojection error. In contrast, direct methods do not require features. The pixels are usually tracked directly. The body pose is achieved by minimizing the photometric error between pixels. However, one downside of the direct method is that it is highly sensitive to the light of environment. When the illumination changes dramatically, it is often impossible to track the correct points. Further, it might lead to a failure of body pose calculation, that is still a challenge for poor lighting conditions, although the indirect method overcomes this limitation. The intensity of image texture will be diminished in dimly lit scenes. In other words, the indirect methods need to select features based upon the difference of intensity between pixels. Therefore, the darker the image brightness, the smaller the overall

difference in intensity, which is not conducive to feature extraction. This may result in the collapse of tracking eventually. Consequently, this paper has made a number of improvements to a visual odometry system for low-light environments to solve the described problems. Our target is to recover as much content as possible from a dark image. Then, robust features are extracted from the images. Ultimately, accurate pose is available.

There are two key components in our work: firstly, recovering detailed information of objects in low-light scenes; and secondly, improving the robustness of features as much as possible. To solve these two challenges, we first make use of the retinex theory [4] in the field of image. We add more realistic content to the recovered reflectance image. This enables us to obtain an enhanced image under low illumination situation. Then, a simple but effective detection scheme is used to extract features from the enhanced image. The feature computation time is cut down as far as possible while maintaining the matching accuracy. Furthermore, we chose the novel 4Seasons dataset [5] to evaluate our method, which contains a wide range of real-world conditions (see Figure 1). It is sufficient to verify the practicality of our approach. In addition, we have compared our method with ORB-SLAM2 [6] which has comparatively good performance at present. The results validate the effectiveness of our method.

The rest of this paper is organized as follows. We introduce the related work on visual odometry in Section 2. The main part of the article is given in Section 3, containing the low-light image enhancement scheme as well as the boosted feature detection method. Experiments and evaluation are illustrated in Section 4, comparing our proposed system in detail from various aspects. Finally, a summary of our work is given in Section 5.

2. Related Work

On the one hand, for feature-based VO/VSLAM systems, the abundant texture is a prerequisite for both accurate and robust tracking. However, the image may be blurred in low illumination scenes. We are unable to extract high-quality features in such cases, which will cause the failure of tracking. Thus, obtaining rich and realistic content from low-light conditions is an urgent challenge. Fortunately, there is a lot of research that addresses this problem. Histogram equalization (HE) and gamma correction (GC) are two widely used approaches at present. Through changing the histogram of an image to alter the distribution of pixel intensity, HE can enhance the low-light images to a certain extent. However, overenhancement is a potential risk in some parts of the image [7] as HE is a global process. In addition, for GC, the local area is not naturalized due to the uniform gamma coefficient used for the global image. A sea of work has patched the weakness of HE and GC, such as [8–12]. But there are still a few remaining problems. In recent years, image enhancement schemes based on retinex theory have been attracting the focus. Its core idea is to decompose the captured image into an illumination image and a reflectance image. An advanced low-light image enhancement algorithm (LIME) was proposed [13] based on this theory. Different from the previous method [14], LIME only estimates the illumination image. The complexity of the computation process is significantly reduced by using the Augmented Lagrangian Multiplier (ALM).

At present, most of VO/VSLAM utilize HE or GC when dealing with low-light scenes, like [15–18]. As mentioned before, they are not up to our requirements. Thanks to the retinex theory, which provides a new perspective for image enhancement, our demands are satisfied. We use the LIME image enhancement method to get the result.

On the other hand, one of the keys to achieving accurate localization for VO and VSLAM lies in selecting a series of features. They are tracked in the continuous frames. Then, the body pose is computed [19]. Although the Scale Invariant Feature Transform (SIFT) [20] has been proposed for almost twenty years, it remains of substantial interest due to its excellent performance in a variety of domains. However, an important drawback of SIFT features is that it imposes a large computational burden. This makes it difficult to employ for VO/VSLAM, which need to be processed in real-time. For this reason, a series of outstanding improvements have followed. In 2006, the notable Speeded Up Robust Features (SURF) was presented [21]. Compared to a previous work, SURF significantly cuts down on the time for feature extraction. Unfortunately, this comes at the cost of retaining the support of GPU devices [22].

Instead of focusing attention on features exclusively, some concentrate on key points or descriptors separately. For key points, the popular one is the Features from Accelerated Segment Test (FAST) detector [23]. This determines whether a pixel is a key point by comparing its intensity with the surrounding pixels. Contrast with other key points such as [24], the FAST key points only need to compare the difference in intensity. Therefore, it is quite fast to compute and holds promise for applications in scenarios in which real-time performance is required. Despite the fast computation speed of FAST, it also has shortcomings. Unlike [20, 21], there is no orientation information for FAST key points. And in a few cases, we want the change of the orientation not to affect the expression of the same key point when the observation angle undergoes a shift. So, FAST may encounter certain difficulties in this situation. For descriptors, the Binary Robust Independent Elementary Feature (BRIEF) [25] has received a lot of attention since it was proposed. The authors use a specific procedure to select multipaired image blocks (usually $9 * 9$ and Gaussian smoothed) centered on a key point. A string of binary is generated according to the discrepancy of the intensity between the image blocks. This is the main thought behind the BRIEF descriptor, which has the strength of being a binary descriptor. We can calculate the hamming distance between descriptors when matching features. It is a simple task for a computer. Unfortunately, as with FAST, BRIEF is also sensitive to rotation.

Considering the strength and weakness of FAST key points as well as BRIEF descriptors, the Oriented FAST and Rotated BRIEF (ORB) features was presented [26]. It keeps the speed merit of them. For their downsides, the

Figure 1: The 4Seasons dataset. We have selected several sequences, containing different environments and weather. The common trait of these sequences is that all of them are low-light scenes.

intensity centroid method [27] was applied. Orientation information is added to the FAST key points so that when the camera rotates, it still corresponds to the same place. Additionally, the descriptors depend on the key points. Therefore, when the key points are rotation invariant, the descriptors will naturally have orientation information as well. It is far less prone to features tracking loss when the image is spun.

Our feature detection scheme is similar to ORB. The difference is that we have chosen the Boosted Efficient Binary Local Image Descriptor (BEBLID) [28] as an alternative instead of BRIEF. The representative intensity pairwise tests were selected within local image regions via a Boosting scheme. Experimentally, our feature detection scheme has proven to reduce the computation time by more than 80% while guaranteeing matching accuracy.

3. Methodology

In this section, we will introduce the theoretical part of our proposed visual odometry system. The experimental part will be given in the next section. The framework of our proposed system is shown in Figure 2. Four main blocks are included: (1) an input data processing component focusing on low-light image enhancement, (2) a tracking component for features reprojection and matching (this is the core body of the system), (3) the initialization stage of the system (the principal function is to initialize the visual odometry system and generate map points), and (4) a map segment containing local map. Here, the map points for the body pose calculation and the candidates of unknown tracking quality are maintained primarily.

In the rest of this section, we will discuss the details of each individual part in more depth.

3.1. Low-Light Image Enhancement. In this paper, images are preprocessed using the LIME algorithm and the Fast Global Image Smoothing algorithm (FGS) [29]. Firstly, FGS is employed to process the low-light image in order to obtain the temporary one. Then, we used LIME to get the enhanced result. The method has been experimentally proven to be able to recover the information of low-light images successfully. It is beneficial to the feature extraction and matching.

The core idea of retinex theory is to decompose the captured image ($\mathbf{L}$) into an illumination image ($\mathbf{T}$) and a reflectance image ($\mathbf{R}$), as shown in Figure 3. According to this, the relationship between these three is as follows:

$$\mathbf{L} = \mathbf{R} * \mathbf{T}, \tag{1}$$

where $*$ stands for element-by-element multiplication.

Let us do a simple transformation of Equation (1) to get

$$\mathbf{R} = \frac{\mathbf{L}}{\mathbf{T}}. \tag{2}$$

The notation '-' in Equation (2) stands for the element-by-element division. By a simple transformation, we change the objective of the solution from $\mathbf{R}$ to $\mathbf{T}$. Thus, estimating $\mathbf{T}$ is the key to solving for $\mathbf{R}$.

We define the problem of solving the illumination image as an optimization problem by minimizing the following

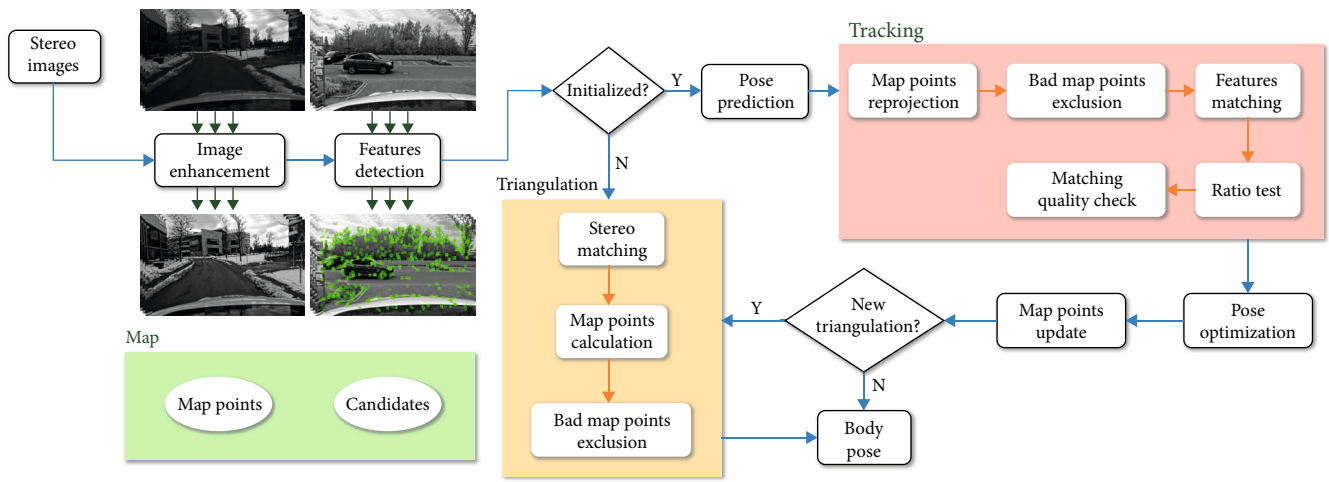

Figure 2: The framework of our proposed system. Our method consists of four parts: preprocessing, tracking, triangulation, and maps. We mainly did some work in the first part so as to improve the quality of the input data. For the other three parts, we implemented simple but useful strategies to realize decent performance.

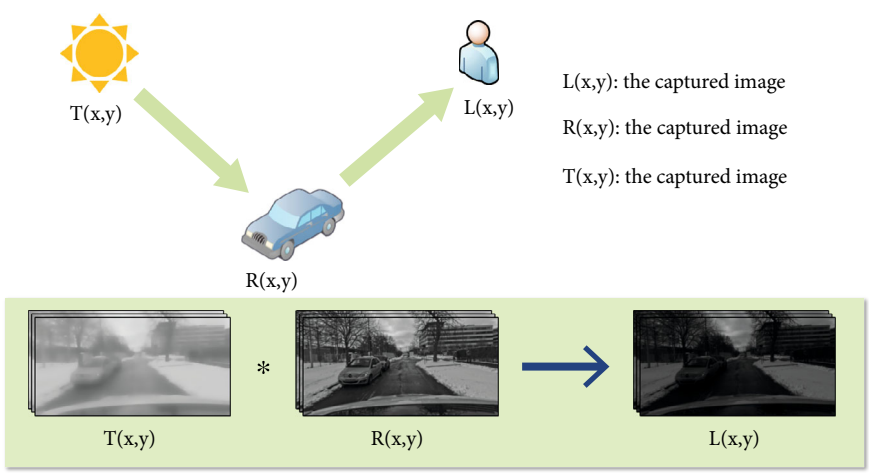

Figure 3: The retinex theory. This theory divides the pictures we observed into illuminated and reflected pictures. It gives us a fresh perspective to understand the recovery of low-light images.

weighted least squares (WLS) function [29].

$$J(T) = \sum_{p} \left(\left(T_p - Q_p\right)^2 + \lambda \sum_{q \in N(p)} \omega_{p,q}(L) \left(T_p - T_q\right)^2 \right), \quad (3)$$

where $Q = \|L\|$; T_p represents the intensity of pixel p, $p = (x, y), 0 \le x < W, 0 \le y < H$; W, H are the width and height of the image, respectively; λ is a control parameter to balance the terms on both sides of the plus sign; $N(p)$ represents the neighbourhood pixels of p; and $\omega_{p,q}(L)$ is a weighting function defined on $\mathbf{L}$.

$$\omega_{p,q}(L) = \exp\left(\frac{-\left(L_p - L_q\right)^2}{\sigma}\right), \quad (4)$$

where σ is a range parameter. The effect of Equation (4) is to smooth the image texture at the rest of the location while preserving the object edge features.

To minimize the problem (1), let the derivative of $J(T)$ be zero. The following system of linear equations is derived:

$$(\mathbf{I} + \lambda \mathbf{A})\mathbf{T} = \mathbf{Q}, \quad (5)$$

where $\mathbf{I}$ represents the identity matrix; $\mathbf{T}$ and $\mathbf{Q}$ are $S \times 1$-dimensional column vectors containing elements T and Q, $S = W \times H$; and $\mathbf{A}$ is a spatially varying Laplacian matrix of size $S \times S$ similar to the one defined in [30].

However, for a two-dimensional image, Equation (3) is a weighted L_2 norm objective function that is very difficult to solve directly. In order to satisfy the requirement of visual odometry, problem (3) can be decomposed into two subproblems (the vertical direction and the horizontal direction). As each subproblem is a one-dimensional linear system, the solution method is mature. Therefore, a fast and accurate calculation can be achieved.

(a) (b)

Figure 4: The low-light scene enhancement method. (a) The original image. (b) The enhanced image.

Figure 4 shows the results of the low-light image processing, from which it can be indicated that our method can recover the image detail information. More comparative experiments can be found in Section 4.1.

3.2. Key Point Extraction and Descriptor Calculation. After the low-light image is enhanced, the next important step is to extract features from the enhanced one. We use a fusion of ORB key points and BEBLID descriptors. ORB key points are built on the famous FAST corners, and it performs the following detection procedure.

As shown in Figure 5, the central pixel is set to be p in a small adjacent area and its intensity is noted as I_p. Firstly, a circle with a radius of three is constructed by taking the pixel p as the center. Secondly, the sixteen pixels located on the circumference of the circle are selected, and their serial numbers $i\,(i = 1, \cdots, 16)$ are recorded in clockwise direction. Thirdly, a threshold T is set for comparing the discrepancy between the intensity of the central pixel and the individual circumference points. Fourthly, the absolute value of the difference in intensity between p and the sixteen points is calculated in turn $S_i = |I_p - I_i|$, and compare S_i with T. Finally, if there are N consecutive pixels with S_i greater than T, the central one is considered to be the key point.

For the descriptors, we use the BEBLID descriptor which was published recently. By choosing a series of specific weak learners (WLs) and using the integral image, it can outperform the fastest ORB descriptor in terms of speed. It is also comparable to SIFT in accuracy. The BEBLID descriptor is based on the work of the Boosted Efficient Local Image Descriptor (BELID) [31]. The major change between these is that the former converts the real-type descriptor into a binary one. Apart from this, it also uses the AdaBoost algorithm for WL selection and then combines all WLs to form a stronger message.

$$\mathscr{L}_{\text{BEBLID}} = \sum_{i=1}^{N} \exp\left(-\gamma l_i \sum_{k=1}^{K} h_k(\mathbf{x}) h_k(\mathbf{y})\right). \tag{6}$$

Equation (6) is the loss function for BEBLID, where γ is the weight of WLs, l_i is the training sample label, $\{\mathbf{x}, \mathbf{y}\}$ is a training set consisting of image block pairs, and $h_k(\mathbf{z}) \equiv h_k(\mathbf{z}; f, T)$ represents the kth WLs, which depends on the feature extraction function $f : \mathscr{X} \longrightarrow \mathbb{R}$ and the threshold T. By giving these two parameters, we derive

$$h(\mathbf{x}; f, T) = \begin{cases} 1, & \text{if } f(\mathbf{x}) \le T, \\ 0, & \text{if } f(\mathbf{x}) > T. \end{cases} \tag{7}$$

In particular, the key for the BEBLID descriptor is the choice of $f(\mathbf{x})$ in Equation (7). The authors define it as the difference in the average intensity of the pixels between the two image blocks.

$$f(\mathbf{x}; p_1, p_2, s) = \frac{1}{s^2}\left(\sum_{q \in R(p_1, s)} I(q) - \sum_{r \in R(p_2, s)} I(r)\right), \tag{8}$$

where $I(t)$ denotes the intensity of pixel t and $R(p, s)$ represents a square adjacent area with pixel p as the center and side length s.

In summary, we are able to access the BEBLID descriptor. It is worth mentioning that, unlike the previous work, the weights of all WLs are set to the same value.

3.3. Feature Matching and Map Point Tracking. In this part, we will illustrate the step of features matching and map points tracking. The performance of features matching is closely related to the accuracy of the camera pose. Therefore, we adopt a coarse-to-fine approach. Firstly, the features in two images are matched roughly. Then, a ratio test is used to select the best descriptor among them. A typical feature matching result is shown in Figure 6, where it is clear that most of the initial matches are correct. This proves the effectiveness of our method. Also note that there are two parts of this system that use the features matching algorithm. One is that the system is not initialized. Stereo matching is employed for the first frame to initialize the entire visual odometry system. It is at this stage that the map points are generated. The second is after initialization. In the tracking phase, the map points are tracked between the two frames. These two parts will be described in detail below.

When the visual odometry is started, the first frame is used for initialization. First of all, we follow the method in the previous two parts (see Sections 3.1 and 3.2) to enhance the low-light image and extract the features. Subsequently,

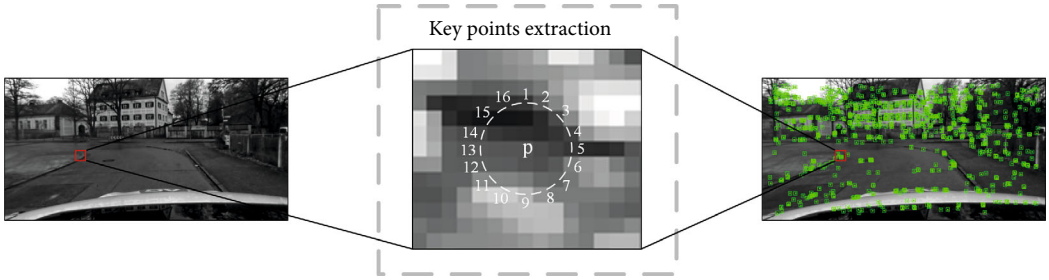

Figure 5: The FAST corner. We determine whether a central pixel p is a key point based on the difference between the intensity of that it and the sixteen circumference points in the adjacent domain.

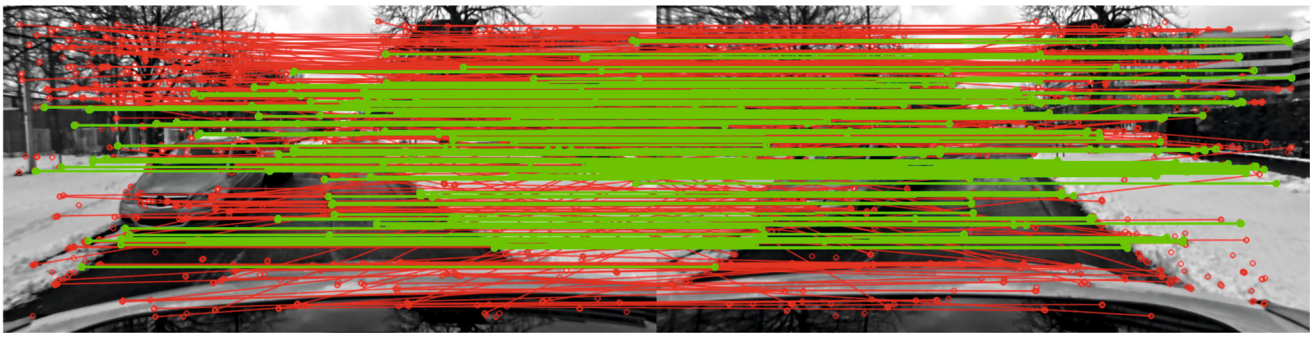

Figure 6: The result of image features matching. Green lines indicate correctly matched features. Conversely, wrong match relationships are represented using red lines.

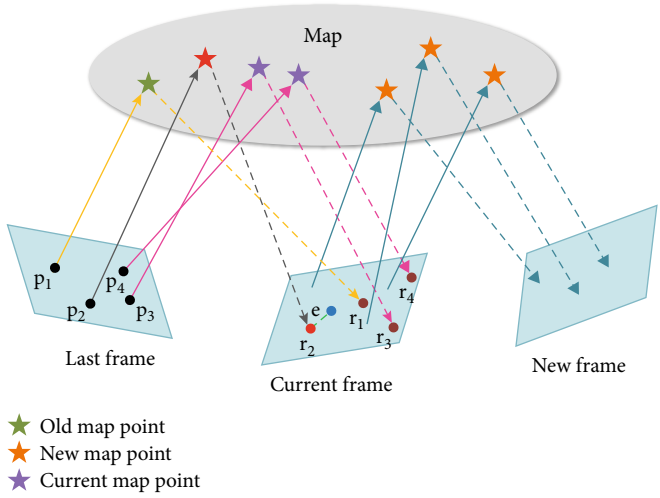

Figure 7: The reprojection model and local map. The spatial point, which is represented as a red pentagram, is reprojected into the current frame. The letter e denotes the reprojection error, which is also the variable to be optimized (see Section 3.4).

we find the initial matching points in the left and right images with the function from the OpenCV library. Next, we use the ratio test to pick out the best match. In particular, we used the local domain search method to reduce the load during searching. Once the features have been matched in the first frame, we should compute the corresponding map points according to the matched features and track them in the subsequent frames.

As soon as the second frame is available, there are already map points at this stage. Therefore, we employ a reprojection model $\pi(\cdot)$ to reproject the map points from the previous frame into the left image of the current frame, as shown in Figure 7. The red solid point indicates reprojection point, which is converted from a map point (red pentagon) using the reprojection model. Afterwards, the reprojection points are matched with features. Similar to the previous paragraph, we continue to reduce the search load as well as improve the matching accuracy by using local domain search and ratio test. If the amount of map points tracked successfully for the first time is inadequate, we also

extend the search radius to twice the original size. The reprojection and matching of map points is performed again in the enlarged area. This is done in the hope that a sufficient number of correct matches can be found. Ultimately, the possibility of successful tracking is boosted.

3.4. Pose Estimation and Optimization. The prediction and optimization of camera pose is another central part of visual odometry. It receives matching information from the features and recovers the pose based on these matches. We set the camera pose to $\mathbf{T}^k$ for the kth frame with consist of a quaternion $\mathbf{q}_k \in SO(3)$ as rotation and a position $\mathbf{t}_k \in \mathbb{R}^3$ as translation. We rely on the algorithm in [32] to predict the pose of the current frame.

Once the pose is estimated, the map points from the previous frame are reprojected into the current frame using the reprojection method (see Section 3.3). Then, we track between the reprojected points and the features in the current frame. Finally, the predicted poses are jointly optimized using the updated map points and the matched points. The cost function of the poses is defined as follows:

$$\{\mathbf{R}, \mathbf{t}\} = \underset{\mathbf{R},\mathbf{t}}{\operatorname{argmin}} \sum_{i \in S} \rho\left(\left\|p^i - \pi\left(\mathbf{R}P^i + \mathbf{t}\right)\right\|^2\right). \tag{9}$$

In Equation (9), $\mathbf{R}, \mathbf{t}$ refers to the camera pose, which we split into a rotation matrix and a translation vector. S denotes the set of all matched points. ρ is the Cauchy cost function. p^i indicates the ith features. $\pi(\cdot)$ stands for the reprojection model. As mentioned earlier, we use this model to compute the reprojection points of the previous map points. P^i represents the ith spatial map point.

Lastly, we use the g2o optimization library [33] to solve problem (9). The objective is to obtain the rotation matrix and translation vector corresponding to minimize the cost function and use them as the optimized camera pose.

3.5. Local Map. To improve the performance of the proposed system, we also maintain a local map. In the local map, the map points for pose optimization are included. In other words, not all map points are in this space. We refer to map points that are not in the local map as "candidates". They are always ready to be added to local map. All map points calculated by features matching are considered candidates initially. None of them belong to the local map. The map points are only added to the local map when they can be successfully tracked in a certain number of consecutive frames. We believe that the tracking quality of these map points is better. The new map point is a transformation from the candidates, which is represented by the orange pentagram in Figure 7. However, there is a special case. That is to say, if the number of map points in the local map falls below a threshold, we consider that there is a risk of tracking failure. Therefore, candidates should be joined to the local map immediately regardless of the quality of tracking to prevent failure. In particular, we directly add the map points generated in the first frame to the local map during the initialization phase. There are no map points in the local map at this time. In the subsequent step, the new map points are treated as candidates using the method described above. Tracking quality is used to judge whether or not it should be inserted into the local map.

4. Experiments

To evaluate our proposed method, the 4Seasons dataset is used and compared with the current superior performance of ORB-SLAM2. As a novel dataset, it has a wide range of abundant scenarios, from urban to rural and from parking to motorway. Unlike some previous datasets [34], the 4Seasons dataset also includes a variety of weather and lighting conditions. Meanwhile, the 4Seasons dataset utilizes a simple data acquisition system consisting of a stereo camera vision system (Basler acA2040-35gm), an inertial measurement unit system (Analog Devices ADIS16465), and an RTK-GNSS system (mosaic-X5). Finally, the fusion of the visual system with the RTK-GNSS data provides centimetre-level positioning accuracy, which will greatly contribute to the performance evaluation of the algorithm. More details on the 4Seasons dataset can be found in [5]. In addition, ORB-SLAM2, one of the more outstanding SLAM algorithms, has received considerable attention from a broad mass of researchers since it was proposed. Different from our proposed algorithm, ORB-SLAM2 is a complete SLAM system that supports multiple functions, including loop closing, place recognition, and so on. However, it is the power of its features that brings a heavy computation burden. In the experimental section, qualitative and quantitative results will be given in order to demonstrate the merits of our proposed system.

4.1. Dark Image Recovery. We investigate the capabilities of our low-light image enhancement algorithm. To demonstrate the superiority, we compare other low-light image restoration schemes commonly used today, including histogram equalization and adaptive gamma correction. We selected a number of representative raw images from the 4Seasons dataset, containing various scenes, weather, etc., as shown in Figure 8. The strengths of ours can be clearly observed by doing different processing methods on the same image. We are able to maintain both the detail information and the global quality of the image in comparison to the other two methods. In particular, there is hardly any illumination in the first row of images. Although our result is not as bright as the other two, we succeed in recovering the full content of the image. For the other two methods it fails, as shown at the top of the image. There are a few completely dark areas that indicate the recovery was not successful. For the rest of low-light environments, our method takes into account the local details while keeping the whole content consistent. This will be analysed in the following.

With histogram equalization, the inherent drawbacks lead to a situation where the image appears exposed unnaturally. This is shown by the snow in the bottom right corner of the third row of images and the edge of the road on the left in the fourth row of images. The details are also not handled well enough. Examples include the tree branches in the

(a) (b)

Figure 8: Continued.

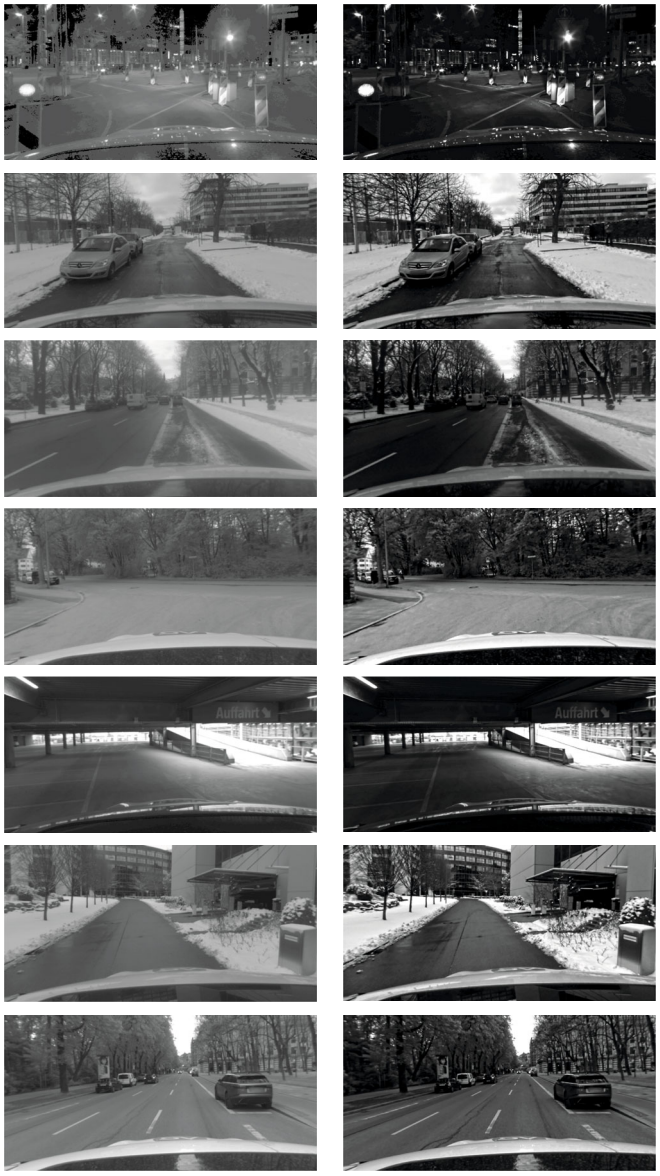

(c) (d)

Figure 8: Results of the histogram equalization, adaptive gamma correction, and low-light image enhancement schemes. (a) The original image. (b) The results of histogram equalization. (c) The outcome of adaptive gamma correction. (d) The results of low-light image enhancement we used.

second row and the road in front of the vehicle in the seventh row. The histogram equalization comes closest to the performance of our method in the sixth row of images, but the image contrast is still inadequate for minor information such as roads and bushes.

For adaptive gamma correction, it can automatically adjust the gamma parameter according to the image content, avoiding the shortcomings of fixed parameter. However, there are still challenges. The most noticeable of these can be identified in all images. The results are not sharp sufficiently and look like a haze image. This causes a deterioration in the general quality and is not conducive to the feature extraction and matching.

In our method, it is possible to restore local details while taking into account the global content of the image. Especially for almost dark scenes (as in the first line of Figure 8), we recovered all parts of the image successfully, whereas the other two methods failed. In the fifth row, our method does not seem to work as well as histogram equalization, for example, in the upper part of the image. Nevertheless, our aim is to make the enhanced image more realistic. It avoids the local distortion of content. Yet histogram equalization has led to a partial overexposure of information, as in the case of the garage exit.

Besides, in order to quantify the superiority of ours, we make use of PSNR and SSIM [35] as evaluation metrics.

Table 1: Comparison of PSNR&SSIM for adaptive gamma correction, histogram equalization and our method.

Images	Ada-gamma correction		Histogram equalization		Ours	
	PSNR (dB)	SSIM	PSNR (dB)	SSIM	PSNR (dB)	SSIM
1st row	7.8633	0.0837	4.3233	0.0229	16.1813	0.1802
2nd row	10.8508	0.5457	8.7224	0.4692	10.6581	0.5003
3rd row	10.5836	0.5674	8.4229	0.4509	17.4225	0.7377
4th row	9.9263	0.4876	7.8555	0.3623	11.6864	0.5310
5th row	11.6111	0.3531	7.5862	0.2236	17.4387	0.5689
6th row	9.9133	0.4696	7.8530	0.4106	10.0635	0.4492
7th row	11.1430	0.5586	8.5902	0.4063	16.5346	0.6859
Average	10.2702	0.4380	7.6219	0.3351	14.2836	0.5219

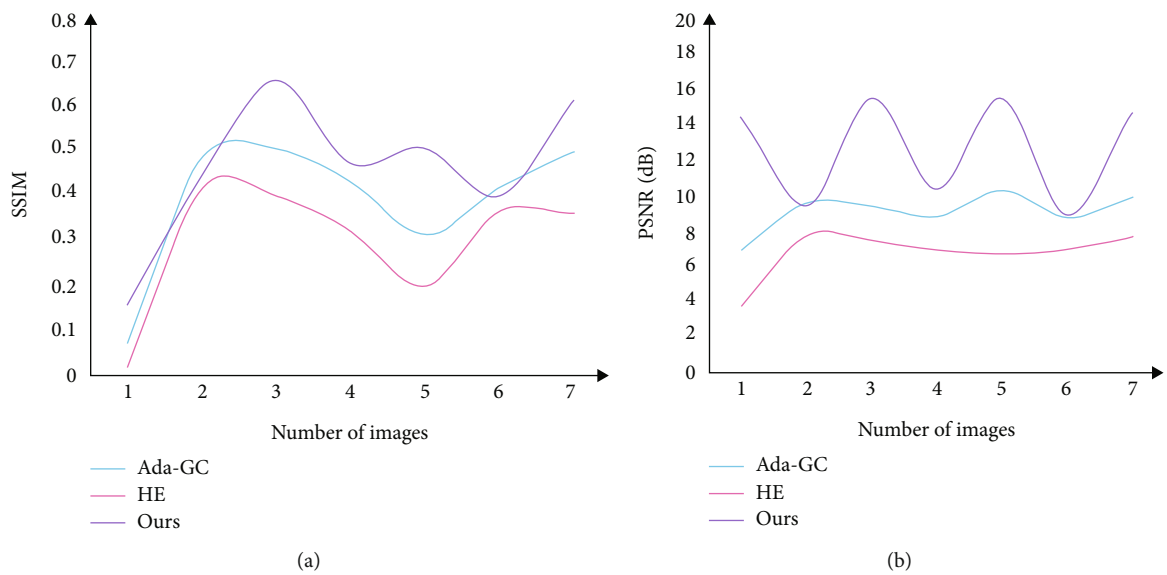

Figure 9: Comparing PSNR and SSIM for adaptive gamma correction, histogram equalization, and our method. Ada-GC: adaptive gamma correction; HE: histogram equalization; Ours: for low-light image recovery method we used. (a) Comparison of SSIM. (b) Comparison of PSNR.

SSIM means structural similarity. It compares the similarity between the processed result and the original image in three different aspects. A larger value of SSIM means a higher similarity between the two images. PSNR, on the other hand, represents the peak signal-to-noise ratio. Similar to SSIM, the higher the value, the better the result.

Table 1 shows the outcome of our PSNR and SSIM compared to the others. From the table, it can be concluded that our low-light image enhancement algorithm achieves decent performance on both PSNR and SSIM. Although for the second image the adaptive gamma correction is processed optimally, our results are similar to it. Not to mention that we have pretty good results in all the other images. In Figure 9, we visualize the performance of three algorithms. As reflected in the table, neither the adaptive gamma correction nor the histogram equalization performs as well as ours.

4.2. Stereo Matching. This part compares the benefits of the fusion methods we used for key points and descriptors. We still selected images in the dark image recovery part as test data. Figure 10 depicts the correct matching rate and the time loss of descriptor computation between our method and the ORB features with the better performance at present. We do feature extraction on the low illumination enhanced images. Then, the right match was found between the stereo images. In the figure on the right, it can be noticed that our approach is up to par with the ORB features with respect to the correct matching rate. In the test data, the average right match percentage for the ORB features is about 63.27%, while ours is about 61.25%. The graph on the left represents the time loss of descriptor computation for both methods. We can identify the upper hand of our method clearly. In terms of speed, our method improves by about 84.52%. Thus, our time loss is substantially reduced at a similar correct matching rate to the ORB features. It is sufficient to demonstrate the strengths of our method.

4.3. Accuracy. We have examined the performance of our system in the recently released 4Seasons dataset. Eleven sequences were selected to suit our requirements. We have

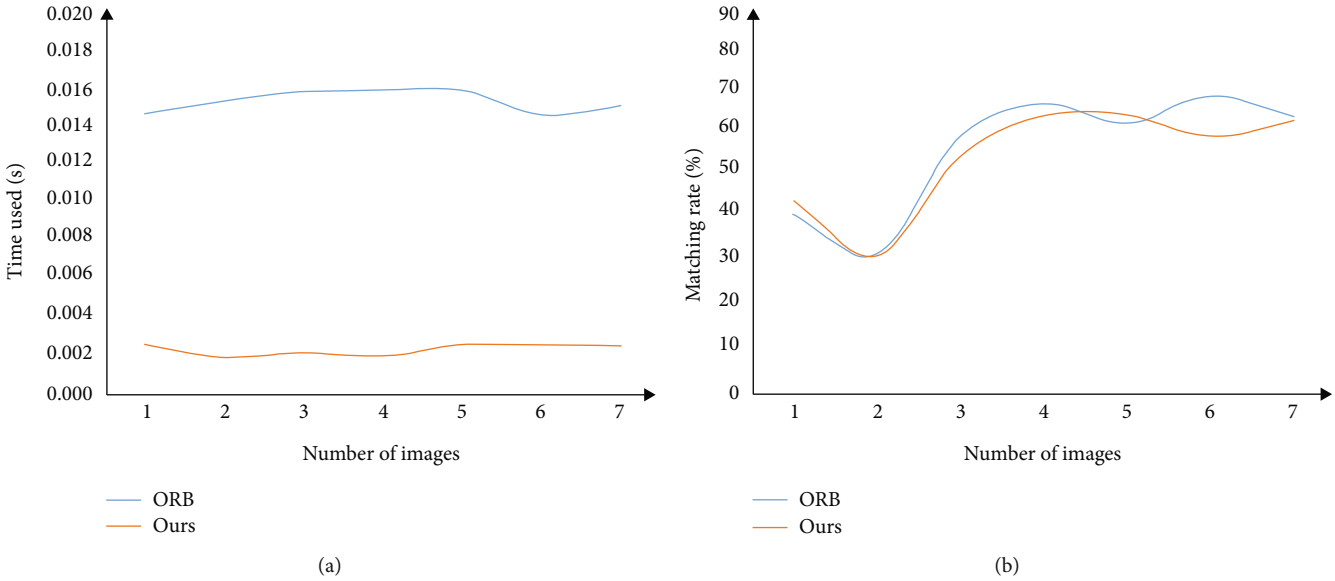

Figure 10: Comparison of ORB features with the method we used. (a) Comparison of descriptor computation time. (b) Comparison of correct matching rate.

Table 2: Comparison of accuracy and memory in the 4Seasons dataset.

Scenes	Sequences	Number of images	ORB-SLAM2		Ours	
			RMSE (m)	MEMORY (GiB)	RMSE (m)	MEMORY (MiB)
OLD TOWN	2021-01-07-10-49-45	24629	0.084	4.9	0.079	66.2
	2021-05-10-21-32-00	24658	*	*	0.605	71.8
	2020-10-08-11-53-41	28999	0.053	3.5	0.044	79.1
COUNTRYSIDE	2021-01-07-13-30-07	14729	0.111	3.8	0.115	48.3
OFFICE LOOP	2021-01-07-12-04-03	13746	0.034	2.2	0.034	51.2
BUSINESS CAMPUS	2021-01-07-13-12-23	12023	0.064	1.3	0.064	24.3
NEIGHBORHOOD	2021-05-10-18-02-12	11674	0.036	1.6	0.034	43.4
	2021-05-10-18-32-32	10760	0.037	1.6	0.034	44.0
	2020-12-22-11-54-24	9775	0.057	2.8	0.056	40.1
PARKING GARAGE	2021-05-10-19-15-19	5257	0.069	1.0	0.063	35.9
	2020-12-22-12-04-35	7793	0.050	1.5	0.029	31.1
AVERAGE [1]			0.059	2.4	0.055	46.4

*This symbol means the algorithm failed to work. [1]The AVERAGE represents a sequence without trace failure.

run our method in an Intel(R) Core (TM) i7-10700 desktop computer with 16.0GB RAM. For accuracy evaluation, we have chosen the relative pose error (RPE) proposed in [36] as the indicator. Table 2 shows the results of our method compared with ORB-SLAM2. From the experiments, our results are pretty similar to those of ORB-SLAM2. For some sequences, our method is even better than it which is a complete visual SLAM system. In particular, ORB-SLAM2 does not work for the second sequence in OLD-TOWN, because the system is unable to track a sufficient number of features. In contrary, our method achieves stable tracking. This indicates that our system is robust.

Furthermore, we have also compared the memory consumption to highlight the lightness of our method. In Table 2, MEMORY indicates the memory usage during the algorithm running. We can observe that the minimum memory requirement for our method is approximately 24.0 MiB, while the minimum for ORB-SLAM2 is 1.0 GiB. For all sequences (excluding the untraceable one), our average memory usage is 46.4 MiB, which is an accuracy of 0.055 m at this point. Correspondingly, the comparison algorithm is 2.4 GiB, with an average accuracy of 0.059 m. We can claim that we achieved the approximate localization accuracy with a comparatively minor memory consumption.

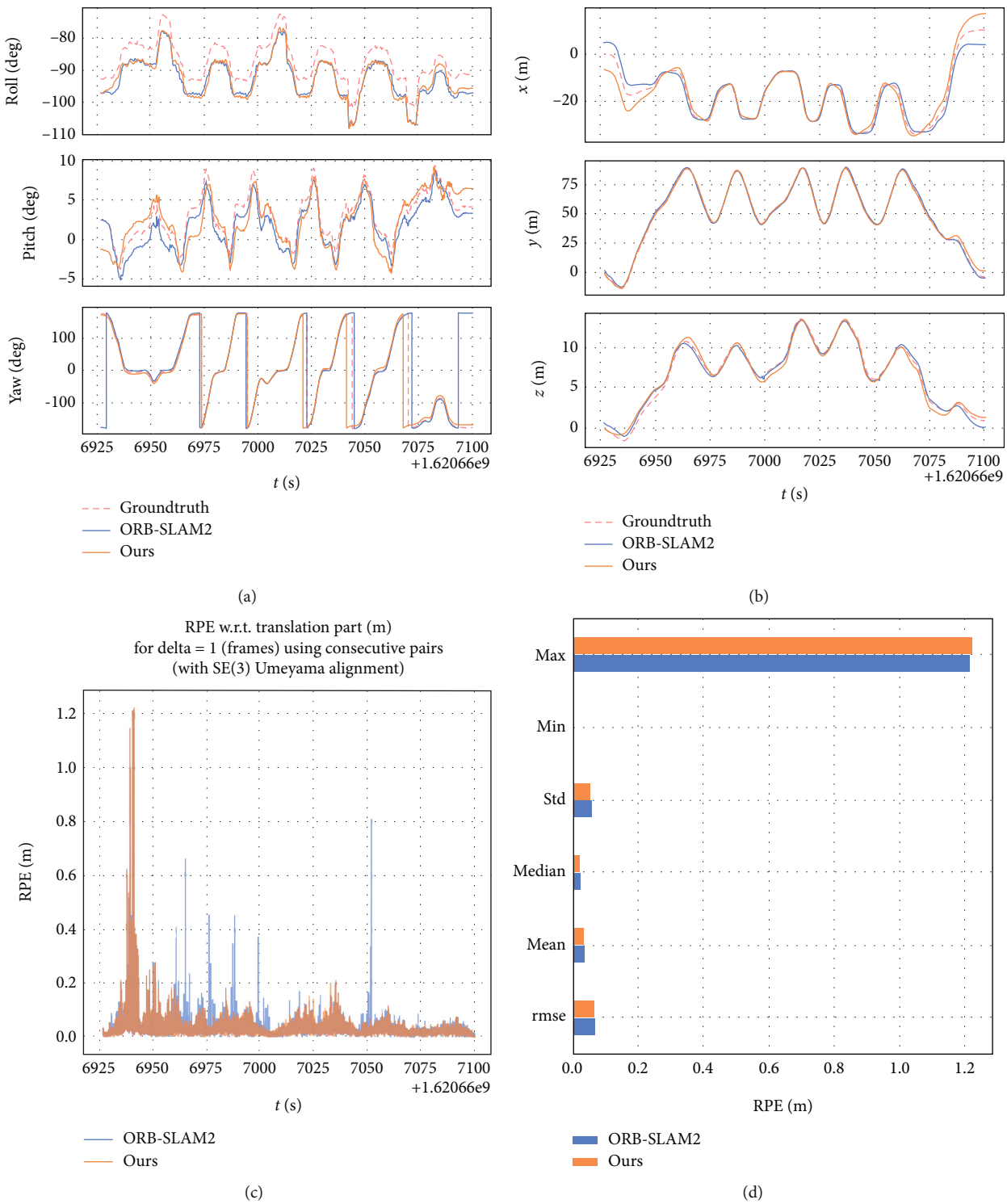

Figure 11: The accuracy comparison of ORB-SLAM2 and ours. (a, b) The accuracy comparison in the roll, pitch, yaw, and x, y, z aspects. (c, d) The relative pose error and other metrics comparison.

In order to demonstrate the contrast qualitatively, we chose the packet 2021-05-10-19-15-19 from the PARKING GARAGE scenario to compare their trajectories and other various metrics separately. We present a summary of how our method compares to ORB-SLAM2 and real trajectories as shown in Figure 11. The top row indicates the comparison of our method with ORB-SLAM2 in the roll, pitch, and yaw dimensions and the x-, y-, and z-axes. The strengths of our method can be observed by comparing each of the six different perspectives. In terms of rotation error, the mistake of ORB-SLAM2 is larger than ours. The advantage of our approach is particularly evident in the yaw dimension. The

comparison of the RPE is shown in the bottom row, where the left panel illustrates the absolute translation root-mean-square error (RMSE) of our method against ORB-SLAM2. The graph reveals that our error is smaller than that of the comparison method. In the right picture, a contrast of other metrics such as the mean is included. It can be noted that our results are approximately the same as ORB-SLAM2. As stated earlier, it is a complete SLAM system. In other words, we have achieved a comparable result to the full system for a lower cost, which shows the excellence of our method.

5. Conclusion

In this paper, we proposed a lightweight stereo visual odometry system based on the indirect methods for low-light scenes. The image decomposition is applied to our proposed system according to retinex theory. Specifically, we first utilized the thought of LIME to obtain the enhanced image of a low-light scene and only estimate the illumination image. This reduces the computational burden of the proposed system to a large extent. Then, we applied an efficient detection scheme to acquire the high-quality features, which significantly reduces the calculation time. Meanwhile, a coarse-to-fine process was employed to find out the best match in the points matching phase by sorting the descriptors according to their Hamming distance. In addition, an efficient local map for pose optimization was maintained to keep the tracking accuracy. Moreover, we defined an optimization function to minimize the reprojection error for pose estimation. Finally, the experiments using the 4Seasons datasets showed that our proposed approach is superior to the existing methods. It should be noted that we will apply the proposed method to intelligent vehicular networks in our future work [37–39].

Data Availability

The data used to support the findings of this study are available from the corresponding authors upon request.

Conflicts of Interest

The authors declare that they have no conflicts of interest.

Acknowledgments

This work was supported in part by the National Natural Science Foundation of China under Grants 62173101 and 61905045, in part by the Open Research Project of Zheijiang Laboratory under Grant 2021KF0AB06, in part by the Guangzhou Science and Technology Project under Grants 202102010501 and 202102010416, in part by the International Collaborative Research Program of Guangdong Science and Technology Department under Grant 2020A0505100061, and in part by GZU-HKUST Joint Research Program under Grant YH202110.

References

[1] G. Bresson, Z. Alsayed, L. Yu, and S. Glaser, "Simultaneous localization and mapping: a survey of current trends in autonomous driving," *IEEE Transactions on Intelligent Vehicles*, vol. 2, no. 3, pp. 194–220, 2017.

[2] H. Alismail, M. Kaess, B. Browning, and S. Lucey, "Direct visual odometry in low light using binary descriptors," *IEEE Robotics and Automation Letters*, vol. 2, no. 2, pp. 444–451, 2017.

[3] J. Engel, V. Koltun, and D. Cremers, "Direct sparse odometry," *IEEE Transactions on Pattern Analysis and Machine Intelligence*, vol. 40, no. 3, pp. 611–625, 2018.

[4] E. H. Land, "The retinex theory of color vision," *Scientific American*, vol. 237, no. 6, pp. 108–128, 1977.

[5] P. Wenzel, R. Wang, N. Yang et al., "4Seasons: a cross-season dataset for multi-weather SLAM in autonomous driving," in *Proceedings of the DAGM German Conference on Pattern Recognition*, pp. 404–417, Tübingen, 2020.

[6] R. Mur-Artal and J. D. Tardós, "ORB-SLAM2: an open-source SLAM system for monocular, stereo, and RGB-D cameras," *IEEE Transactions on Robotics*, vol. 33, no. 5, pp. 1255–1262, 2017.

[7] M. Kim and M. G. Chung, "Recursively separated and weighted histogram equalization for brightness preservation and contrast enhancement," *IEEE Transactions on Consumer Electronics*, vol. 54, no. 3, pp. 1389–1397, 2008.

[8] D. J. Ketcham, R. W. Lowe, and J. W. Weber, *Image Enhancement Techniques for Cockpit Displays*, Defense Technical Information Center, Fort Belvoir, VA, USA, 1974.

[9] S. M. Pizer, E. P. Amburn, J. D. Austin et al., "Adaptive histogram equalization and its variations," *Computer Vision, Graphics, and Image Processing*, vol. 39, no. 3, pp. 355–368, 1987.

[10] S. Srinivasan and N. Balram, "Adaptive contrast enhancement using local region stretching," in *Proceedings of the 9th Asian Symposium on Information Display*, pp. 152–155, New Delhi, 2006.

[11] S. Rahman, M. M. Rahman, M. Abdullah-Al-Wadud, G. D. Al-Quaderi, and M. Shoyaib, "An adaptive gamma correction for image enhancement," *EURASIP Journal on Image and Video Processing*, vol. 2016, no. 1, p. 13, 2016.

[12] S.-C. Huang, F.-C. Cheng, and Y.-S. Chiu, "Efficient contrast enhancement using adaptive gamma correction with weighting distribution," *IEEE Transactions on Image Processing*, vol. 22, no. 3, pp. 1032–1041, 2013.

[13] X. Guo, Y. Li, and H. Ling, "LIME: low-light image enhancement via illumination map estimation," *IEEE Transactions on Image Processing*, vol. 26, no. 2, pp. 982–993, 2017.

[14] X. Fu, D. Zeng, Y. Huang, X.-P. Zhang, and X. Ding, "A weighted variational model for simultaneous reflectance and illumination estimation," in *Proceedings of the IEEE Conference on Computer Vision and Pattern Recognition*, pp. 2782–2790, Las Vegas, 2016.

[15] C. Won, H. Seok, Z. Cui, M. Pollefeys, and J. Lim, "OmniSLAM: Omnidirectional localization and dense mapping for wide-baseline multi-camera systems," in *Proceedings of the 2020 IEEE International Conference on Robotics Automation*, pp. 559–566, Paris, 2020.

[16] Q. Fu, H. Yu, X. Wang et al., "Fast ORB-SLAM without keypoint descriptors," *IEEE Transactions on Image Processing*, vol. 31, pp. 1433–1446, 2022.

[17] S. Ji, Z. Qin, J. Shan, and M. Lu, "Panoramic SLAM from a multiple fisheye camera rig," *ISPRS Journal of Photogrammetry and Remote Sensing*, vol. 159, pp. 169–183, 2020.

[18] S. Rahman, A. Q. Li, and I. Rekleitis, "Svin2: An underwater slam system using sonar, visual, inertial, and depth sensor," in *Proceedings of the 2019 IEEE/RSJ International Conference on Intelligent Robots Systems*, pp. 1861–1868, Macau, 2019.

[19] R. Wang, M. Schworer, and D. Cremers, "Stereo DSO: Large-scale direct sparse visual odometry with stereo cameras," in *Proceedings of the IEEE International Conference on Computer Vision*, pp. 3903–3911, Venice, 2017.

[20] D. G. Lowe, "Distinctive image features from scale-invariant keypoints," *International Journal of Computer Vision*, vol. 60, no. 2, pp. 91–110, 2004.

[21] H. Bay, T. Tuytelaars, and L. Van Gool, "SURF: speeded up robust features," in *Proceedings of the European Conference on Computer Vision*, pp. 404–417, Graz, 2006.

[22] S. N. Sinha, J.-M. Frahm, M. Pollefeys, and Y. Genc, "GPU-based video feature tracking and matching," in *Proceedings of the Workshop on Edge Computing Using New Commodity Architectures*, p. 4321, Chapel Hill, 2006.

[23] E. Rosten and T. Drummond, "Machine learning for high-speed corner detection," in *Proceedings of the European Conference on Computer Vision*, pp. 430–443, Graz, 2006.

[24] C. Harris and M. Stephens, "A combined corner and edge detector," in *Proceedings of the 4th Alvey Vision Conference*, pp. 147–151, Manchester, 1988.

[25] M. Calonder, V. Lepetit, C. Strecha, and P. Fua, "Brief: binary robust independent elementary features," in *Proceedings of the European Conference on Computer Vision*, pp. 778–792, Heraklion, 2010.

[26] E. Rublee, V. Rabaud, K. Konolige, and G. Bradski, "ORB: an efficient alternative to SIFT or SURF," in *Proceedings of the 2011 International Conference on Computer Vision*, pp. 2564–2571, Barcelona, 2011.

[27] P. L. Rosin, "Measuring corner properties," *Computer Vision and Image Understanding*, vol. 73, no. 2, pp. 291–307, 1999.

[28] I. Suárez, G. Sfeir, J. M. Buenaposada, and L. Baumela, "BEBLID: boosted efficient binary local image descriptor," *Pattern Recognition Letters*, vol. 133, pp. 366–372, 2020.

[29] D. Min, S. Choi, J. Lu, B. Ham, K. Sohn, and M. N. Do, "Fast global image smoothing based on weighted least squares," *IEEE Transactions on Image Processing*, vol. 23, no. 12, pp. 5638–5653, 2014.

[30] L. Grady, "Random walks for image segmentation," *IEEE Transactions on Pattern Analysis and Machine Intelligence*, vol. 28, no. 11, pp. 1768–1783, 2006.

[31] I. Suárez, G. Sfeir, J. M. Buenaposada, and L. Baumela, "BELID: boosted efficient local image descriptor," in *Proceedings of the Iberian Conference on Pattern Recognition and Image Analysis*, pp. 449–460, Madrid, 2019.

[32] M. Aladem and S. A. Rawashdeh, "Lightweight visual odometry for autonomous mobile robots," *Sensors*, vol. 18, no. 9, 2018.

[33] R. Kümmerle, G. Grisetti, H. Strasdat, K. Konolige, and W. Burgard, "G2o: a general framework for graph optimization," in *Proceedings of the 2011 IEEE International Conference on Robotics and Automation*, pp. 3607–3613, Shanghai, 2011.

[34] A. Geiger, P. Lenz, C. Stiller, and R. Urtasun, "Vision meets robotics: the Kitti dataset," *The International Journal of Robotics Research*, vol. 32, no. 11, pp. 1231–1237, 2013.

[35] Z. Wang, A. C. Bovik, H. R. Sheikh, and E. P. Simoncelli, "Image quality assessment: from error visibility to structural similarity," *IEEE Transactions on Image Processing*, vol. 13, no. 4, pp. 600–612, 2004.

[36] J. Sturm, N. Engelhard, F. Endres, W. Burgard, and D. Cremers, "A benchmark for the evaluation of RGB-D SLAM systems," in *Proceedings of the 2012 IEEE/RSJ International Conference on Intelligent Robots and Systems*, pp. 573–580, Vilamoura-Algarve, 2012.

[37] L. Zhang, W. Zhou, J. Xia et al., "DQN-based mobile edge computing for smart Internet of vehicle," *EURASIP Journal on Advances in Signal Processing*, vol. 2022, no. 1, p. 10, 2022.

[38] J. Lu, L. Chen, J. Xia et al., "Analytical offloading design for mobile edge computing-based smart internet of vehicle," *EURASIP Journal on Advances in Signal Processing*, vol. 2022, no. 1, p. 10, 2022.

[39] L. Chen, R. Zhao, K. He, Z. Zhao, and L. Fan, "Intelligent ubiquitous computing for future UAV-enabled MEC network systems," *Cluster Computing*, vol. 25, no. 4, pp. 2417–2427, 2022.

Hindawi
Wireless Communications and Mobile Computing
Volume 2022, Article ID 8614952, 14 pages
https://doi.org/10.1155/2022/8614952

Research Article

Identification of Shortwave Radio Communication Behavior Based on Autocorrelation Spectrogram Features

Haitao Li,[1] **Xiang Chen**,[1] **Yingke Lei**,[1] **Pengcheng Li**,[1] **and Caiyi Lou**[2]

[1]*College of Electronic Countermeasures, National University of Defense Technology, Hefei 230037, China*
[2]*36th Research Institute of China Electronics Technology Group Corporation, Jiaxing 314033, China*

Correspondence should be addressed to Caiyi Lou; loucaiyi@126.com

Received 13 May 2022; Revised 25 August 2022; Accepted 29 August 2022; Published 22 September 2022

Academic Editor: Mingqian Liu

Cognitive communication behavior is becoming a research hotspot in the field of communication confrontation. In theory, the behavioral intention of noncooperating parties can be obtained by analyzing communication signals. Considering the complexity of the actual electromagnetic environment, even when the signal-to-noise ratio (SNR) is low, a certain accuracy still needs to be guaranteed. In this paper, according to five types of physical burst waveforms defined by the shortwave radio interoperability standard, a signal feature extraction method based on autocorrelation spectrogram features is proposed, and a two-input convolutional neural network (CNN) for classification is designed to improve the identification ability of shortwave communication behavior. The experimental results illustrate that the five kinds of shortwave radio communication behaviors can be accurately identified even when the noise is large. The research in this paper can directly analyze the communication behavior through physical layer signal without demodulation, which has the ability to grasp the communication behavior of the shortwave radio station in real time.

1. Introduction

Behavior is the active response of an organism such as a person or an animal to the internal and external environment under the control of thought. Research on behavior recognition based on machine learning (ML) [1–3] and probabilistic methods [4–7] has been developing rapidly. In recent years, the proposal of cognitive electronic warfare (CEW) requires that communication countermeasures be intelligent, and the concept of cognition has begun to receive attention in the field of communication. Research on cognitive radio [8], cognitive radar [9], cognitive Internet of Things (IoT) [10], and cognitive electronic jamming [11] has developed rapidly. Cognitive communication behavior is a potentially hot area. In electronic warfare, if enemy behaviors can be analyzed in real time, we can take actions in a timely manner, which is conducive to gaining advantages.

In 2010, a project called Behavioral Learning for Adaptive Electronic Warfare (BLADE) [12] was proposed to meet the needs of intelligent electromagnetic spectrum operations. The importance of behavioral learning was emphasized in the field of electronic warfare for the first time. It is meaningful to carry out behavioral recognition research based on wireless signals from communication radiation sources (CRSs). CRS itself is a concept without biological characteristics, but because of human operation, it has observable behavioral information that reflects the behavior of the operator. Taking a radio station as an example, its operator will perform operations such as calling, data transmission, image transmission, and switching on and off. The radio station will change its working mode and send different signals according to what the operator does; therefore, it has observable behavioral information. By analyzing the wireless signals obtained by reconnaissance, a series of behavioral information can be unscrambled, and the operator's task, situation, status, and other key information can be understood.

In recent years, machine learning (ML) has been applied in the field of signal processing, including signal modulation pattern recognition [13–16], CRS individual recognition [17–19], communication specific signal type recognition [20, 21], and other fields, and a series of achievements have

been achieved. However, research on CRS behavior recognition is still in the beginning stage. There have been very few relevant studies in the published literature thus far.

Research on communication behavior can be divided into communication group behavior [22, 23] and communication individual behavior [24–36]. The former mainly refers to a series of combat tasks coordinated by groups equipped with CRS, while the latter mainly refers to the working modes, tasks of a certain CRS, and the actions of the person or unit operating the CRS. Individual communication behavior is the focus of our research. At present, relevant research is mainly based on the following three methods. The first method is data mining for spectrum monitoring data to gain communication relationships [24–29]. The second method is to obtain the communication behavior by parsing the communication protocol. [30, 31]. The third method transforms the problem of communication behavior recognition into the problem of radio signal classification recognition by analyzing the behavior connotation of intercepted radio signals [32–36]. Liu et al. proposed a method to discover the communication relationship of ultrashort-wave radio stations [24]. In the literature [25], DBSCAN is improved and used to mine the hidden communication behavior of spectrum data. By mining the physical characteristics of the spectrum monitoring signal and analyzing their statistical laws, individual communication behavior can be known [26]. Mining of communication relations in the case of missing and disordered data is realized in the literature [27]. Pan et al. proposed a communication behavior structure mining algorithm, which can be used without analyzing the signal content to obtain the communication relation and the communication node of the target field communication [28]. Cheng et al. proposed a method called DECBR, which DCGAN was used for data enhancement and realized the identification of communication behaviors under small sample conditions [29]. Zhang et al. obtained the behavioral intention of the frequency hopping transmitter by analyzing the TDMA protocol [30]. You and Ge proposed a regular expression-based Fetion communication message identification method through the analysis of specific fields in the Fetion protocol, so as to achieve the purpose of inferring the Fetion communication behavior [31]. Zhou et al. observed the differences in the deep-level features of shortwave burst waveforms and demonstrated the feasibility of directly identifying shortwave communication behaviors based on physical layer signals [32]. Wu et al. used the improved LeNet to identify five communication behaviors [33]. Wu et al. [34] used the improved one-dimensional DenseNet to identify seven automatic link establishment (ALE) behaviors under the same types of burst waveform BW0. Furthermore, literature [35] conducted visualization research of the seven ALE behaviors mentioned in literature [34] and observed the deep-level feature differences of the seven ALE signals. Based on this, ACGAN was used to recognize seven types of ALE behavior under small sample conditions [36].

In this paper, the relationship between burst waveforms and communication behaviors is first introduced according to the five types of burst waveforms specified by the MIL-STD-188-141B standard, and then a feature extraction method is proposed for extracting the features of the autocorrelation spectrogram of the signal. The features extracted by this method are not easily polluted by noise, especially under the condition of low SNR, and more original features of the signal can be presented on the spectrogram. The main contributions of this paper are as follows:

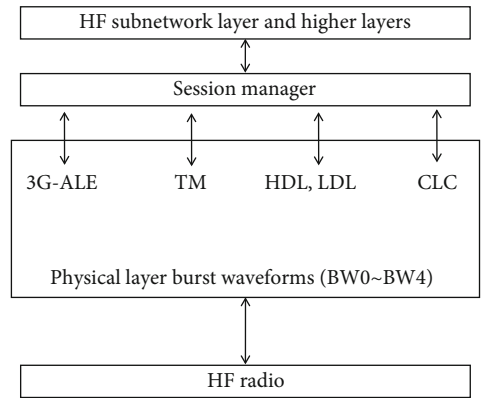

Figure 1: 3G HF protocol suite.

(i) we use the autocorrelation method to preprocess the signal and convert the noise-containing signal into an autocorrelation time series. This method is simple to calculate, can effectively reduce the interference of Gaussian white noise, and can facilitate subsequent feature extraction

(ii) we perform bispectral transformation on the autocorrelation time series and extract bispectral features. The higher-order spectral domain can present some feature differences that cannot be presented in the time domain. It is convenient to save the extracted features in a format similar to a picture, which is beneficial to the processing of the CNN. Compared with traditional method, this method can significantly improve the recognition accuracy under low SNR conditions

(iii) we design a two-input CNN for classification recognition. The extracted autocorrelation spectral features are input into the two branches of the neural network, and then the outputs of the two branches are processed. This two-input CNN can further extract features and reduce the possibility of incorrect decisions, meanwhile, it does not require much additional computing time

2. Background

The third-generation shortwave communication protocol standard MIL-STD-188-141B is proposed to develop adaptive short-wave communication, realize shortwave link establishment, link maintenance, shortwave network construction, and improve communication quality. Corresponding burst waveforms are defined in this standard for the various kinds of signaling required in the short-wave

Wave form	Used for	Burst duration	Payload	Preamble	FEC coding	Inter-leaving	Data format	Effective code rate
BW0	3G-ALE PDUs	613.33ms 1472 PSK symbols	26 bits	160.00 ms 384 PSK symbols	Rate = 1/2, K = 7 convolutional (No flush bits)	4 × 13 block	16-ary orthogonal walsh function	1/96
BW1	Traffic management PDUs, HDL acknowledgement PDUs	1.30667 seconds 3136 PSK symbols	48 bits	240.00 ms 576 PSK symbols	Rate = 1/3, K = 9 convolutional (No flush bits)	16 × 9 block	16-ary orthogonal walsh function	1/144
BW2	HDL traffic data PDUs	640 + (n*400) ms 1536 + (n*960) PSK symbols n = 3, 6, 12, or 24	n*1881 bits	26.67 ms 64 PSK symbols (for equalizer training)	Rate = 1/4, K = 8 convolutional' (7 flush bits)	None	32 unknown/ 16 known	Variable 1/1 to 1/4
BW3	LDL traffic data PDUs	373.33 + (n*13.33) ms 32n + 896 PSK symbols, n = 64, 128, 256 or 512	8n + 25 bits	266.67 ms 640 PSK symbols	Rate = 1/2, K = 7 convolutional' (7 flush bits)	24 × 24, 32 × 3444 × 48, or 64 × 65 convolutional block	16-ary orthogonal walsh function	Variable 1/12 to 1/24
BW4	LDL acknowledgement PDUs	640.00 ms 1536 PSK symbols	2 bits	None	None	None	4-ary orthogonal walsh function	1/1920

Figure 2: Details of different burst waveforms.

communication system, to meet distinctive requirements for payload, duration, time synchronization, acquisition, and demodulation performance in the presence of noise, fading, and multipath. Figure 1 shows its basic architecture.

Among them, the physical layer defines five burst waveforms to perform different tasks, including BW0, BW1, BW2, BW3, and BW4. In Figure 2, the details of the five types of burst waveforms are summarized, which contain signal parameters, application scenarios, and other information.

Further, the generation process of the five burst waveforms is shown in Figure 3.

Each type of burst waveform can achieve its own function in short-wave communication. BW0 is used for third-generation automatic link establishment (3G ALE), BW1 is used for traffic management (TM), BW2 and BW3 are used for data transmission, respectively, high-rate data link (HDL) and low-rate data link (LDL) transmission, and BW4 is used for LDL acknowledgment. To clarify what these behaviors are, we will explain them one by one.

ALE encompasses establishing a communication link for shortwave communication. TM represents coordinating traffic exchanges on connections established based on the 3G-ALE protocol, and establishing a traffic link on which traffic can be delivered. HDL consists of providing reliable high-rate point-to-point data transfer service over the established links, while LDL means providing reliable low-rate point-to-point data transfer service.

This also illustrates that different burst waveforms correspond to different communication behaviors, which is summarized in Table 1.

3. Methods

Figure 4 shows the simple technical route of our research. On the basis of the burst waveforms of the physical layer, we carry out research on the identification of the communication behavior of the shortwave radio. Since behavior is a concept that describes biology, it is necessary to explain its meaning in the field of communication. Then, the mapping relationship between communication behaviors and burst waveforms needs to be found; both steps are mentioned in the second section. After the previous steps, the problem is transformed into the problem of signal processing and classification. In this section, the method of signal preprocessing is given, while the structure of the network model is designed.

3.1. Signal Denoising by the Autocorrelation Method. Suppose $x(t)$ is a random signal, R_{xx} is the autocorrelation function of $x(t)$, which is defined as the degree of correlation of $x(t)$ at different times. Then the definition formula of R_{xx} is as follows:

$$R_{xx}(\tau) = E\{x(t+\tau)x(t)\} \tag{1}$$

Therefore, assume $n(t)$ is the additive white Gaussian noise (AWGN), its mean is 0 and its variance is δ_n^2, $x(t)$ is the transmitter signal, $n(t)$ and $x(t)$ are uncorrelated, and $s(t)$ is the receiver signal, that is,

$$s(t) = x(t) + n(t). \tag{2}$$

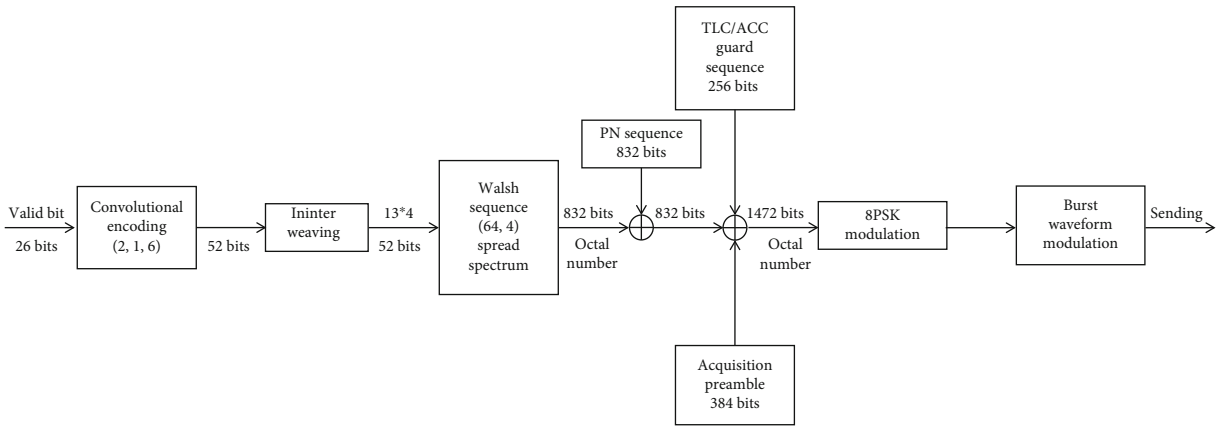

(a) The generation process of BW0

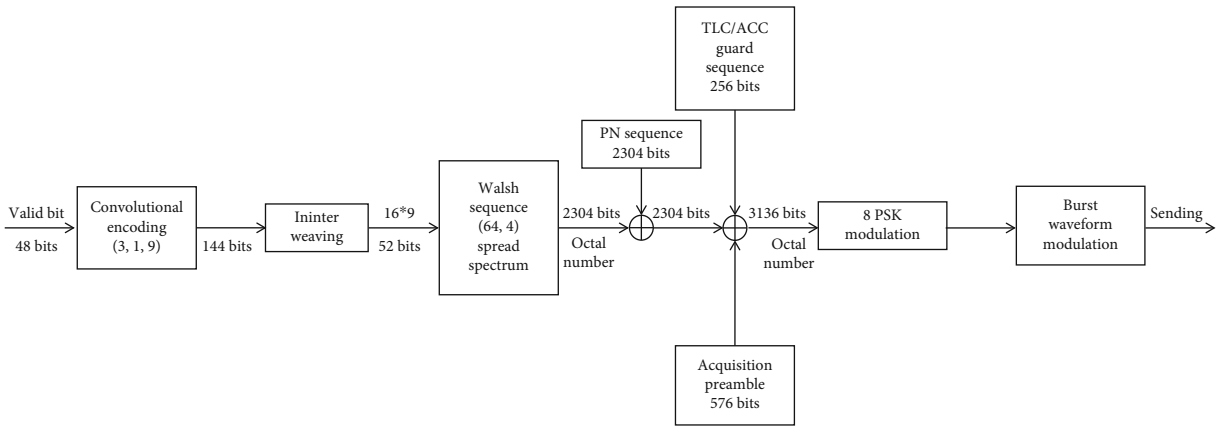

(b) The generation process of BW1

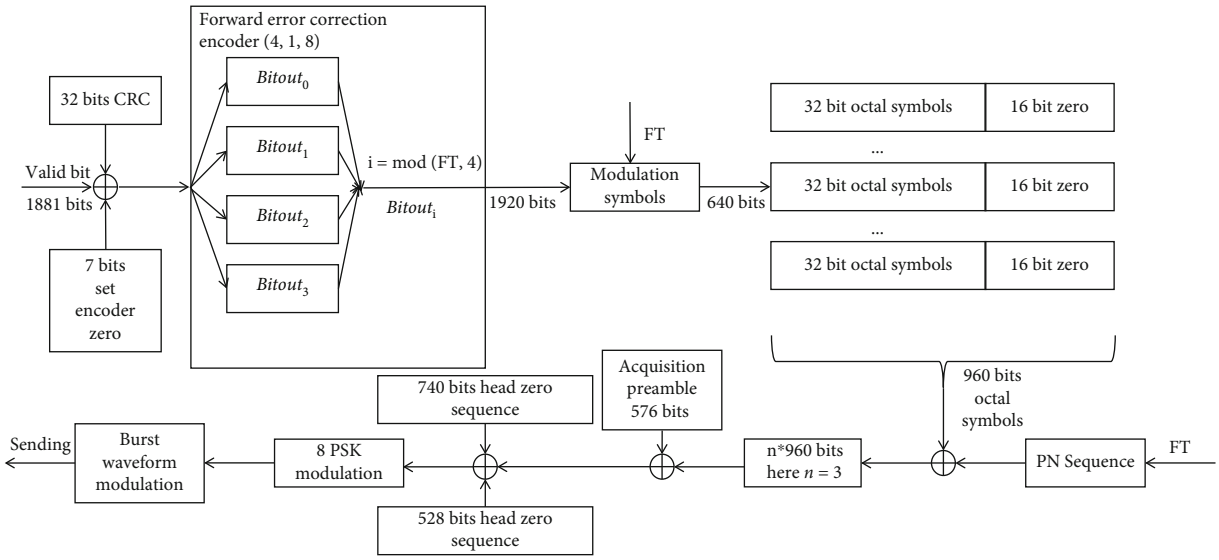

(c) The generation process of BW2

Figure 3: Continued.

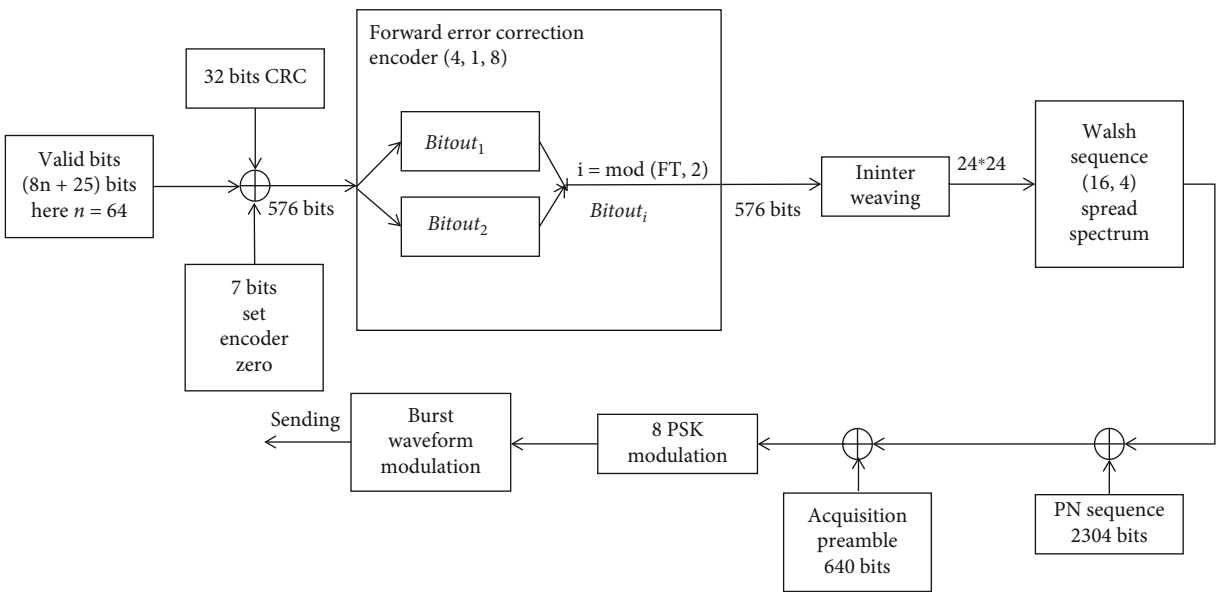

(d) The generation process of BW3

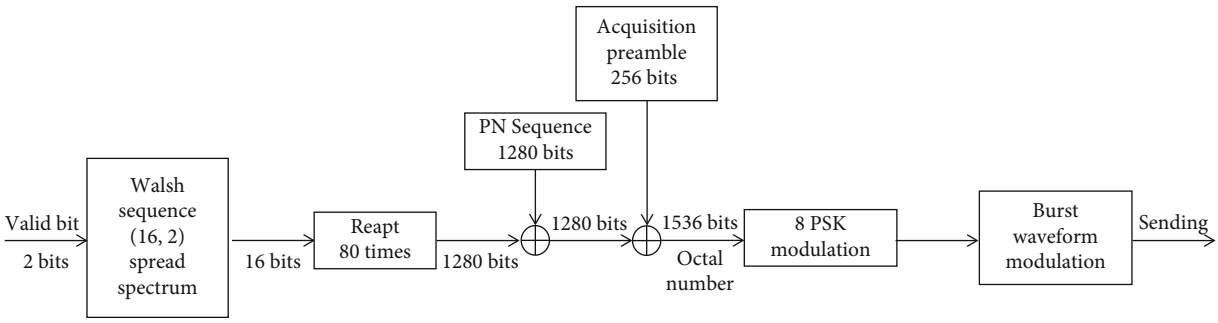

(e) The generation process of BW4

Figure 3: Signal generation process of burst waveforms.

Table 1: The connection between burst waveforms and behaviors.

Physical layer signal	Behavioral meaning
BW0 burst waveform	Automatic link establishment
BW1 burst waveform	Traffic management and HDL acknowledgment
BW2 burst waveform	Transfers of traffic data by the HDL protocol
BW3 burst waveform	Transfers of traffic data by the LDL protocol
BW4 burst waveform	LDL acknowledgment

Then, according to Equation (1), the autocorrelation function of $s(t)$ can be expressed as

$$\begin{aligned} R_{ss}(\tau) &= E\{s(t+\tau)(s(t)\} = E\{(x(t+\tau)+n(t+\tau))(x(t)+n(t))\} \\ &= R_{xx}(\tau)+R_{xn}(\tau)+R_{nx}(\tau)+R_{nn}(\tau) = R_{xx}(\tau)+R_{nn}(\tau). \end{aligned} \tag{3}$$

Since $n(t)$ has the following nature

$$R_{nn}(\tau) = E\{n(t+\tau)(n(t)\} = \begin{cases} 0, & \tau \neq 0, \\ \delta_n^2, & \tau = 0. \end{cases} \tag{4}$$

Then, (Equation (3)) can be converted to (Equation (5))

$$R_{ss}(\tau) = \begin{cases} R_{xx}(\tau), & \tau \neq 0, \\ R_{xx}(\tau)+\delta_n^2, & \tau = 0. \end{cases} \tag{5}$$

where τ is the time difference, which can take positive or negative numbers.

Therefore, it is proven that the autocorrelation function of $s(t)$ is not easily affected by AWGN. When the SNR is 0 dB, the time domain waveform of BW0 is shown in Figure 5. The abscissa represents the duration of the signal, and the ordinate represents the amplitude of the signal.

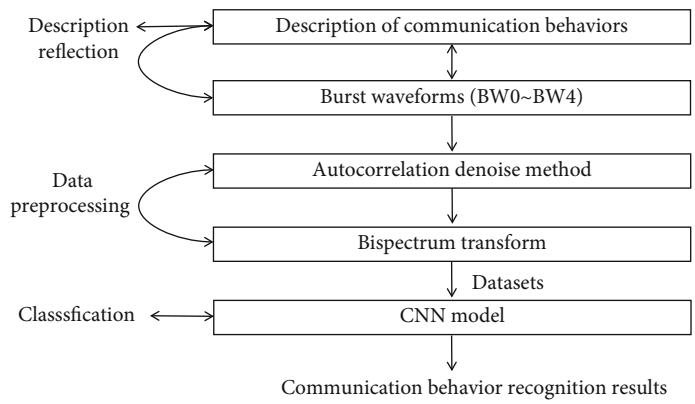

Figure 4: Simple technical route.

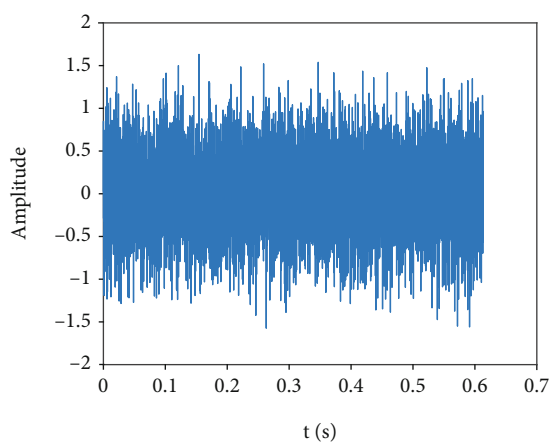

Figure 5: BW0 time domain signal (SNR = 0 dB).

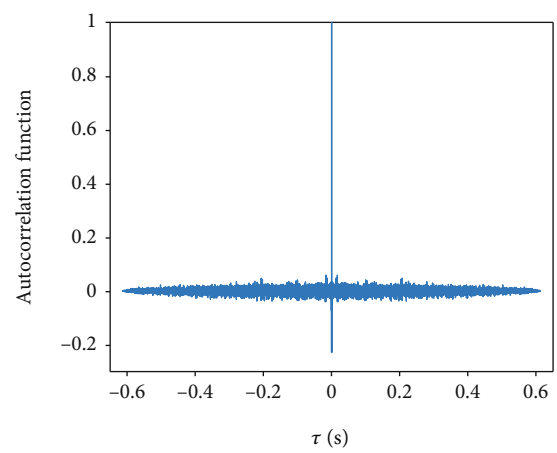

Figure 6: Autocorrelation function of BW0 (SNR = 0 dB).

According to Equation (5), the autocorrelation denoising curve of BW0 is shown in Figure 6. The abscissa is the time difference, and the ordinate is the autocorrelation function.

3.2. High-Order Spectral Analysis of Signals. Compared with the power spectrum, the higher-order spectrum contains more useful information, therefore, it can be considered as the development of the power spectrum. The bispectrum of the signal, also called the third-order spectrum, is the most basic higher-order spectrum. It has the advantages of requiring a small amount of calculation, suppressing AWGN to a certain extent [37], and retaining the original information of the signal as much as possible, so it is widely used in the field of signal processing.

The bispectrum S_{3x} and third-order cumulant c_{3x} of $x(t)$ are defined as follows:

$$S_{3x}(\omega_1, \omega_2) = \sum_{\tau_1=-\infty}^{\infty} \sum_{\tau_2=-\infty}^{\infty} c_{3x}(\tau_1, \tau_2) e^{-j(\omega_1\tau_1+\omega_2\tau_2)}, \tag{6}$$

$$\begin{aligned} c_{3x}(\tau_1, \tau_2) &= E[x(t)x(t+\tau_1)x(t+\tau_2)] - E[x(t)]E[x(t+\tau_1)x(t+\tau_2)] \\ &\quad - E[x(t+\tau_1)]E[x(t)x(t+\tau_2)] - E[x(t+\tau_2)]E[x(t)x(t+\tau_1)] \\ &\quad + 2E[x(t)]E[x(t+\tau_1)]E[x(t+\tau_2)] = cum[x(t)x(t+\tau_1)x(t+\tau_2)]. \end{aligned} \tag{7}$$

Among them, the necessary and sufficient condition for the existence of S_{3x} is that the third-order cumulant c_{3x} is absolutely summable, that is,

$$\sum_{\tau_1=-\infty}^{\infty} \sum_{\tau_2=-\infty}^{\infty} |c_{3x}(\tau_1, \tau_2)| < \infty, \tag{8}$$

where $\tau_1$and τ_2 are independent variables of c_{3x}, representing two time differences, ω_1 and ω_2 are the axes of the bispectral two-dimensional plane [38]. Through bispectrum transformation, the signal is transformed from the time domain to the spatial domain, which can retain more useful information.

3.3. Feature Extraction Process. The autocorrelation spectrum of the signal $s(t)$ can be calculated according to Equations (5), (6), and (7), and the specific process is as follows:

(a) According to Equation (5), calculate the autocorrelation function R_{ss} of $s(t)$.

(b) Calculate the third-order cumulant c_{3s} of R_{ss}, and then calculate the bispectrum S_{3x} of R_{ss} according to Equation (7). Here, we denote S_{3x} as the autocorrelation spectrum of $s(t)$.

When the SNR is 0 dB, we plot the autocorrelation spectrogram pictures of five kinds of burst waveforms, as shown in Figure 7, where f_1 and f_2 are normalized frequencies.

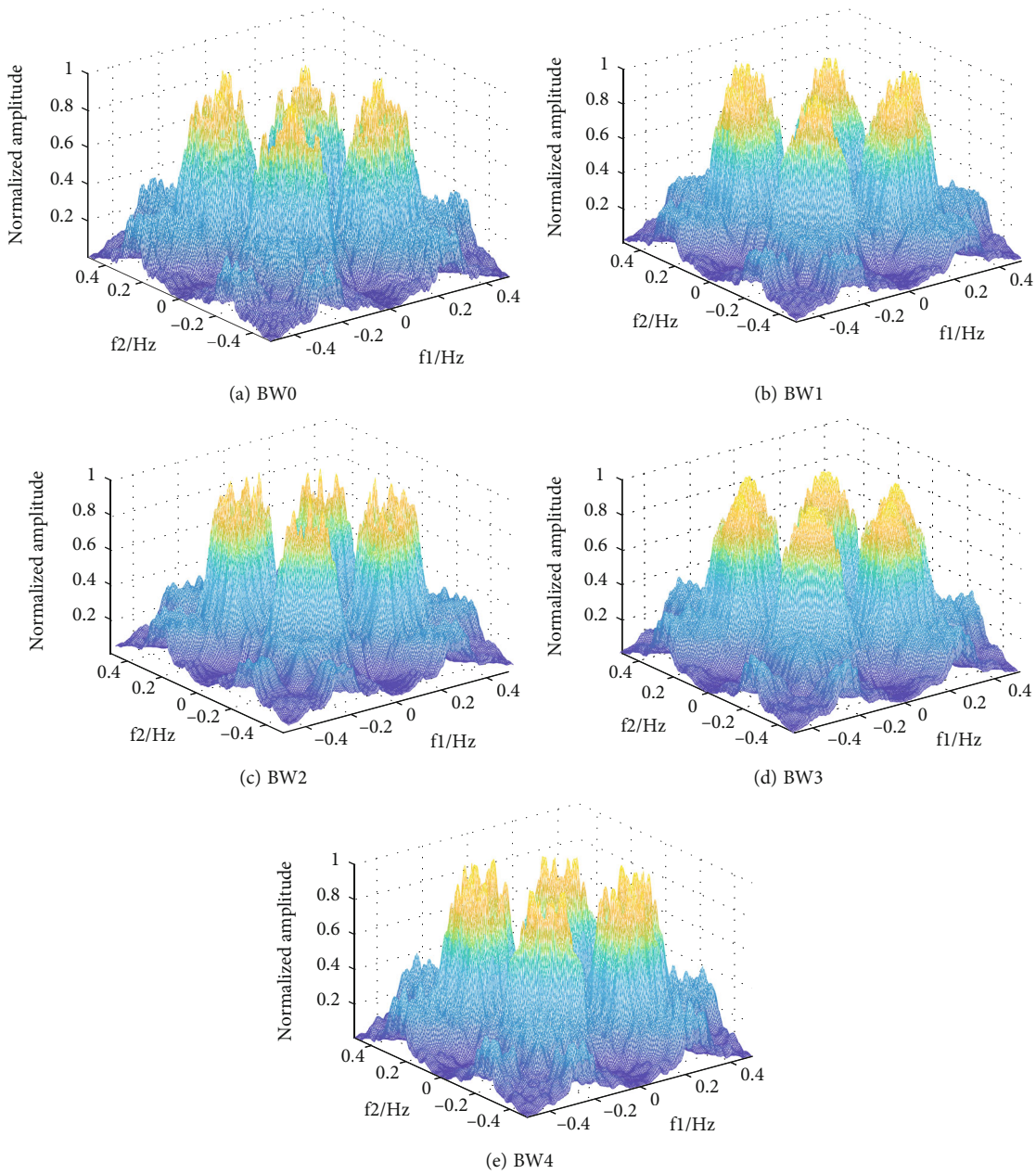

Figure 7: Autocorrelation spectrogram (SNR = 0 dB).

For the convenience of observation, in Figure 8(a), we draw the contour map of Figure 7(a). The contour map can be considered as a two-dimensional representation of the three-dimensional autocorrelation spectrogram image. As a comparison, we also draw the autocorrelation spectrogram contour map of BW0 when the SNR is 5 dB, as shown in Figure 8(b).

According to Figure 8, we know that when the SNR is 0 dB, the autocorrelation spectrogram contour map is cluttered due to the influence of noise. When the SNR increases to 5 dB, the noise part is basically invisible, which proves the effectiveness of the autocorrelation method we select in denoising. It is feasible to extract the autocorrelation spectrogram features of the signal.

The process of extracting features is shown in Table 2.

3.4. Neural Network Model. In this section, we design a two-input CNN. Compared with the traditional CNN, two independent inputs represent two different network models, which can further learn the extracted features, which further reduces the probability of misclassification. The network model we designed can be considered to have two independent model structures because of its two branches. These two independent models only have convolutional layers, pooling layers, and fully connected layers, which are simple in structure, easy to implement, and fast to compute. Figure 9 is the framework of the two-input CNN we designed, which shows the basic structure of the network in this paper.

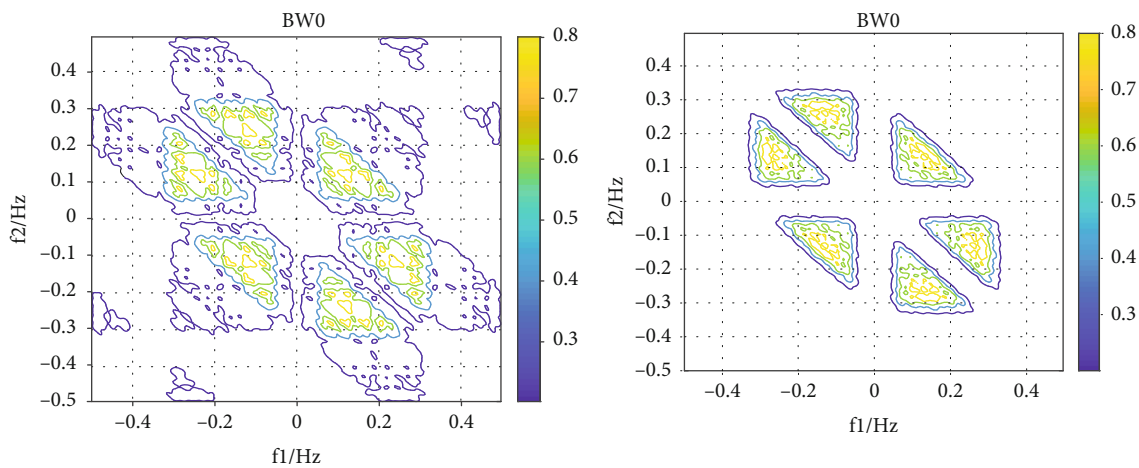

(a) BW0, SNR = 0 dB

(b) BW0, SNR = 5 dB

Figure 8: Contour maps of autocorrelation spectrogram.

Table 2: The process of extracting autocorrelation spectrogram features.

Step	Detailed process
Step 1	signal generation: According to the MIL-STD-188-141B standard, generate five types of burst waveforms with noise
Step 2	calculate the autocorrelation function: Based on Equation (5), calculate the autocorrelation function R_{ss}, to achieve the purpose of noise reduction
Step 3	bispectrum transformation: According to Equation (6) and (7), calculate the bispectrum transformation matrix S_{3s} of R_{ss}. The dimension of S_{3s} is 256×256
Step 4	down sampling: For matrix S_{3s}, sample one sample point for every two points, so that the matrix dimension becomes 256×128, to realize the dimension reduction of the matrix
Step 5	constructing a three-dimensional matrix: Extract the odd and even rows of the matrix, respectively, and construct matrices S_{3s1} and S_{3s2} with a dimension of 128×128. S_{3s1} and S_{3s2} are the first and second channels of the three-dimensional matrix M, and the dimension of M becomes $128 \times 128 \times 2$
	M is the extracted feature matrix

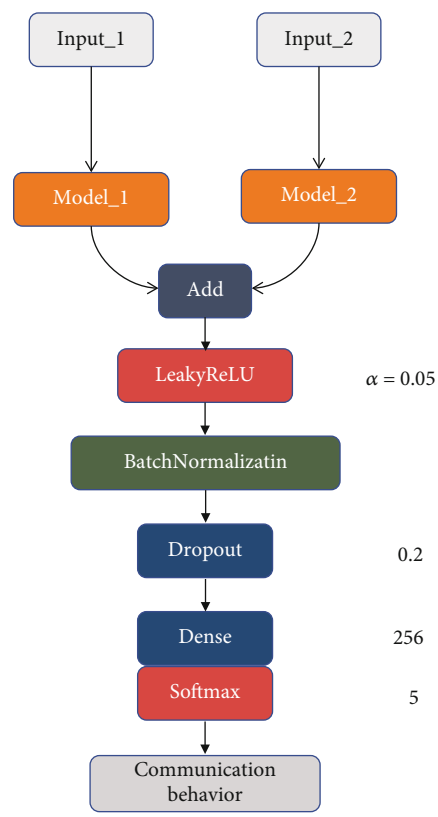

Figure 9: Network framework.

The extracted features are subjected to convolution operations in the two models, and then two outputs are obtained. The two outputs are merged through the add layer, and then through the subsequent layers, the classification task can be completed.

Figure 10 shows the specific structure of the two branches Model 1 and Model 2. Among them, the first branch has a small number of layers, only two convolution layers and two fully connected layers. After convolution calculation, features can be learned quickly and effectively. The second branch has more convolutional and fully connected layers than the first branch. The operation time of this branch is longer, but further features can be learned. Compared with traditional CNN, the model has stronger learning ability by using two branches to learn features separately. At the same time, because the number of layers in the first branch is relatively small, the extra calculation time consumption brought by the design of the two inputs is not much.

In this paper, the inputs of both two branches are autocorrelation spectrogram feature matrix M extracted in Table 2.

The training process of our neural networks is summarized in Table 3.

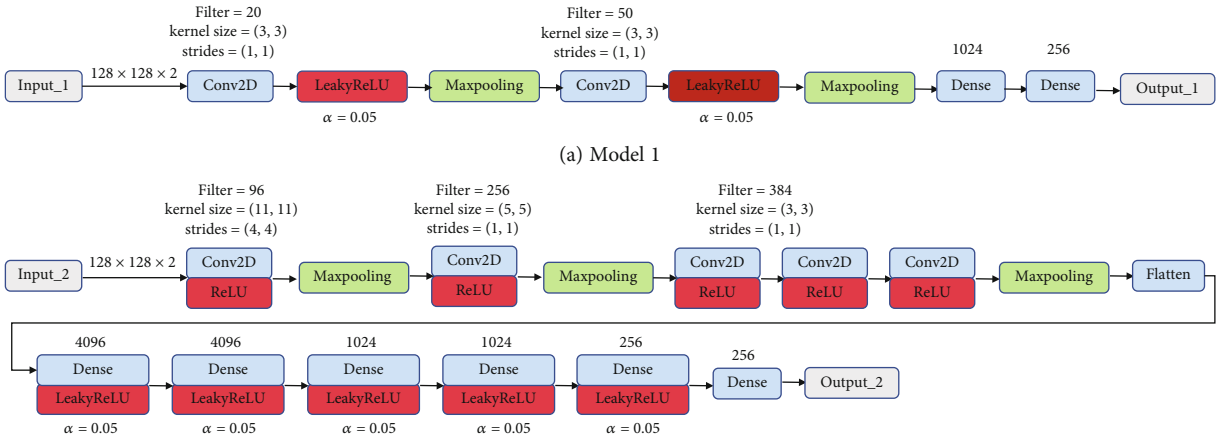

Figure 10: Network model.

Table 3: Training process.

Step	Training process
Step1	send the feature matrix M obtained by Table 2 to the two inputs of the network
Step2	convolutional calculations, obtain two outputs X_1 and X_2, both of them have 256 dimensions
Step3	consider X_1 and X_2 as two new inputs, and through the add layer, X is obtained, $X = X_1 + X_2$
Step4	let X pass through the last few layers, the communication behavior identification is completed

4. Experiments

The experiments consist of the following parts. First, the recognition accuracy of the proposed algorithm for five communication behaviors is compared under different SNR conditions, meanwhile, the effects of different parameters on the experimental results are compared. Then, the improvement in the results of our proposed algorithm is verified by comparison with the previous algorithm. Finally, the recognition results of different network models are compared.

The experimental parameters are set as follows: 5000 samples are selected. The number of training sets and test sets is divided into 4 to 1, and 25% of the training sets are randomly selected as validation sets. We use the momentum optimizer, which dynamically adjusts the learning rate. The initial learning rate of the network is 0.01; the attenuation factor of the learning rate is 1e-6; the batch size is 64, and the epoch is 500.

Experimental Environment: Windows 10 Operating System, 11th Gen Intel (R) Core (TM) I5-11260H CPU, NVIDIA GeForce RTX3050, Python 3.7, TensorFlow 2.5.0, and Keras 2.8.0.

4.1. Verify the Validity of the Algorithm. According to the experimental parameters, the algorithm should first be verified. When the SNR is 0 dB, 5 dB, 8 dB, 10 dB, and 15 dB, respectively; the recognition results on the test set are shown in Figure 11. The results illustrate that BW1 and BW2 are most easily classified into wrong classes. When the SNR is not lower than 5 dB, the recognition accuracy of each communication behavior can reach more than 80%, and with the reduction of noise, the recognition accuracy can reach close to 100%.

Figures 12–14 show the comparison of different initial learning rates, different attenuation factors, and different batch sizes, respectively.

The experimental results show that when the initial learning rate is 0.01, and the attenuation factor is 1e-6; the learning ability of our designed network is the best. When the batch size is 64, 32 and 16, the learning ability of the network is not much different. However, according to Table 4, when the batch size is 64, the learning time per epoch is the shortest. As a result, it is reasonable to set the batch size to 64.

4.2. Experimental Comparison of Different Algorithms. Currently, the research on radio behavior recognition based on signals from the physical layer is in its infancy, and only the study in [33] carries out communication behavior recognition based on five types of burst waveforms. When the SNR is 15 dB, the recognition accuracy can reach 99.3%, but with the increase in noise, the recognition accuracy obviously decreases. When the SNR is lower than 8 dB, the overall recognition accuracy is lower than 80%. When the SNR is 0 dB, it is even lower than 50%. In this experiment, we compare the algorithm proposed in this paper with the algorithm in the literature [33] as well as the network model in this paper plus, the features in the literature [33], and the network model in this paper plus the features in the literature [33]. The experimental results are illustrated in Figure 15.

It can be observed that the algorithm proposed in this letter offers the best results, especially on the lower SNR

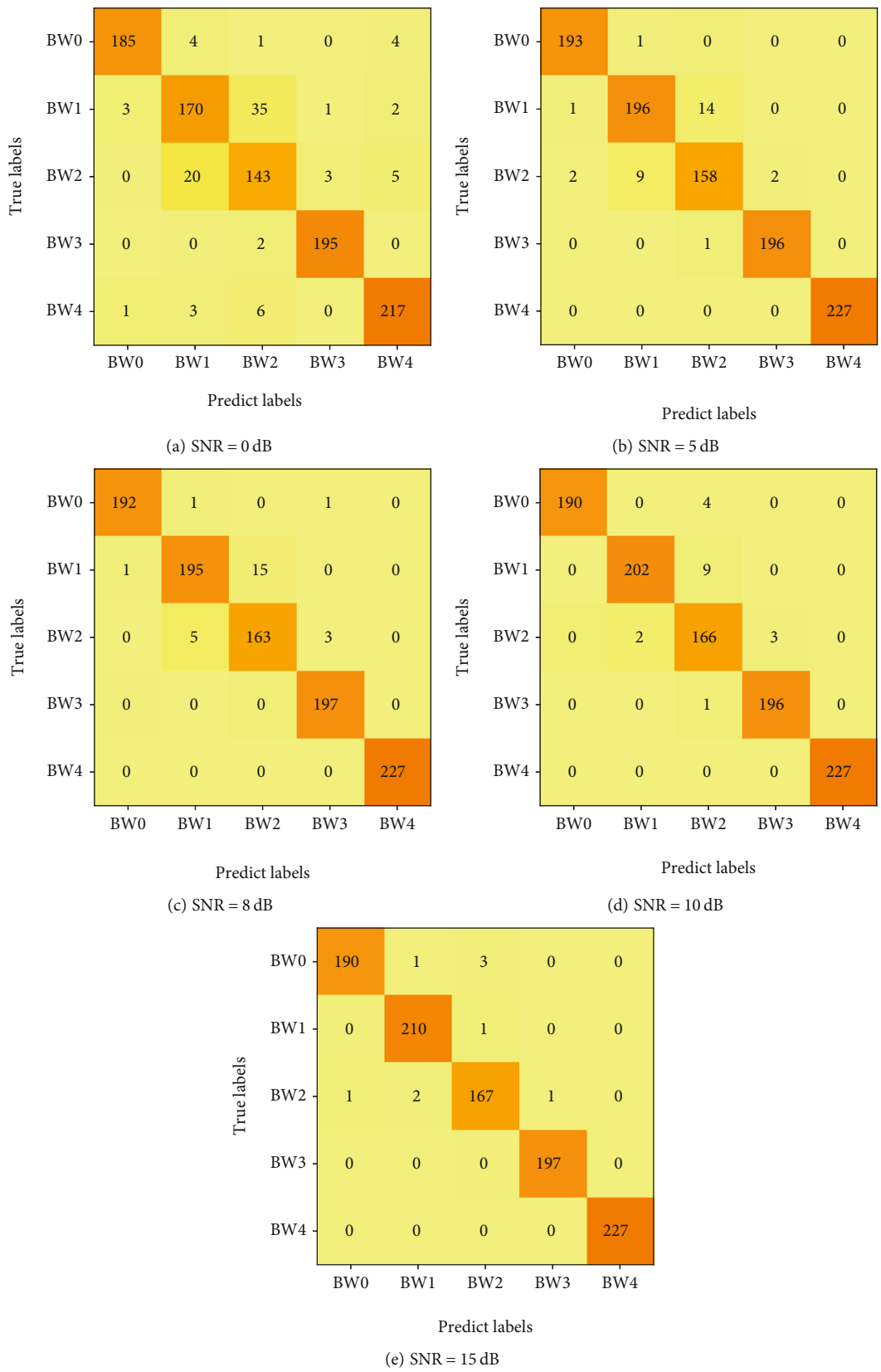

Figure 11: Confusion matrices for five communication behaviors.

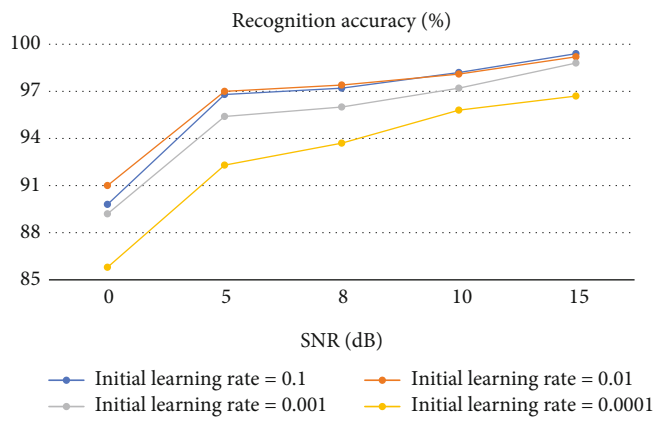

Figure 12: Comparative experiments with different initial learning rates.

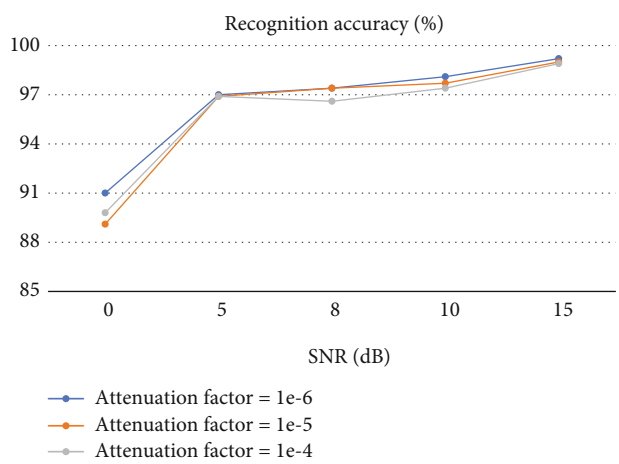

Figure 13: Comparative experiments with different attenuation factors.

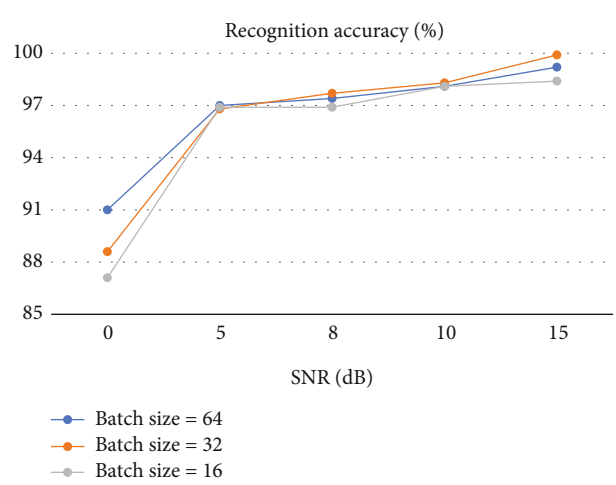

Figure 14: Comparative experiments with different batch sizes.

conditions. Since the autocorrelation denoising method can effectively eliminate noise; our algorithm can significantly improve recognition accuracy. Even if the SNR is 0 dB, the accuracy can still reach 91%. When the SNR is 5 dB, 8 dB, and 10 dB, the accuracy of the algorithm in this letter can increase by 23.8%, 15.9%, and 3.6%, respectively, compared to the algorithm in literature [33]. When the SNR is 15 dB, the influence of noise can be ignored, and the autocorrelation method to reduce noise will cause the loss of information from the original signals, which results in the loss of features. This part of the loss offsets the influence of noise, making the accuracy slightly lower than in the literature [33], but it can still reach 99.2%.

Table 4: Training time for a single epoch.

Batch size	Time(s)
64	4.079
32	5.055
16	8.044

If we extract the autocorrelation spectrogram features and select the network model in the literature [33], the recognition accuracy under low SNR conditions can still be effectively improved. When the SNR is 0 dB, 5 dB, 8 dB, and 10 dB, the recognition accuracy can increase by 43.6%,23.0%, 15.9%, and 3.4%, respectively. When the SNR is 15 dB, due to the loss of features caused by the denoising method, the recognition accuracy is lower than that of literature [33]. Compared with the method in this paper, the recognition accuracy is also lower due to the simple network.

In addition, when the extracted features are autocorrelation spectrogram features, the recognition accuracy can be further improved by using the network in this paper.

4.3. Comparison of Different Network Models. This experiment compares the recognition accuracy of several classical convolutional neural networks. First, as representatives of simple convolutional neural networks, AlexNet and LeNet are chosen as comparison objects. Classic network models such as VGG-19 and ResNet34 are also compared. When the network tends to be stable, the experimental results of different network models are shown in Figure 16.

AlexNet itself is easy to implement due to its simple structure, and its experimental results are better than those of LeNet and VGG-19, and slightly inferior to ResNet34.

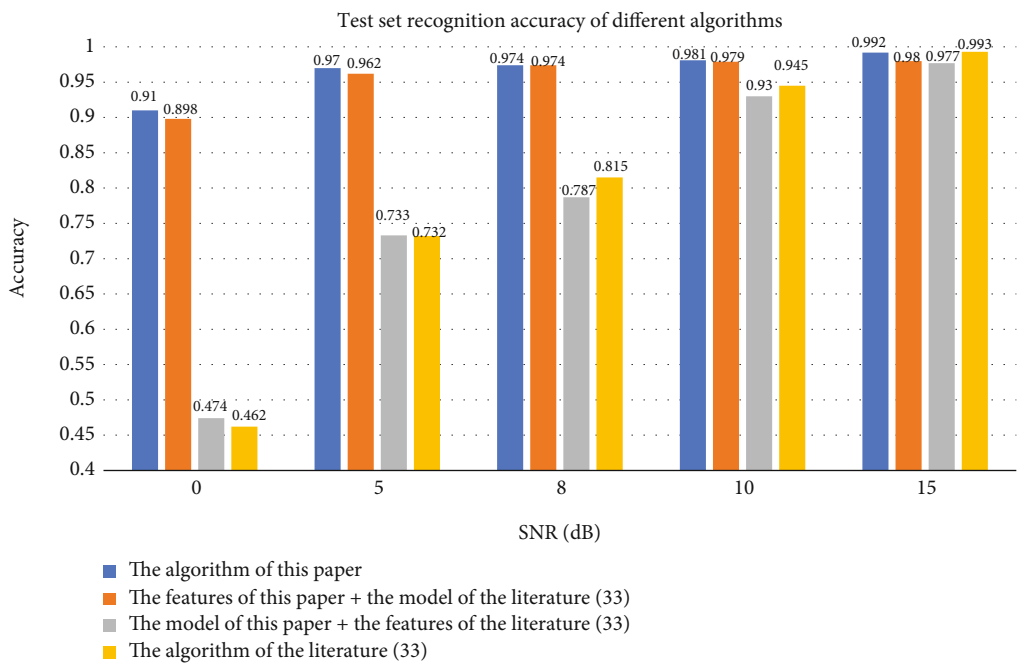

Figure 15: Comparison of different algorithms.

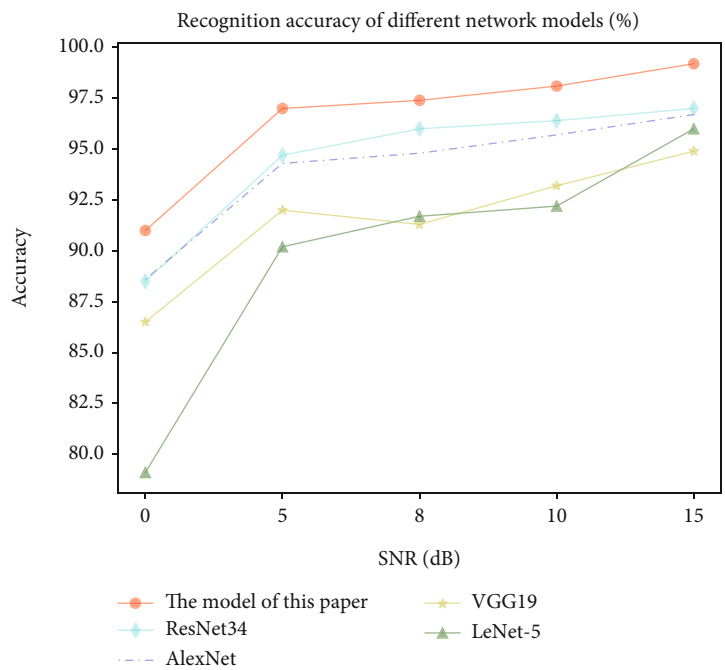

Figure 16: Recognition results of different network models.

When the SNR ranges from 0 to 15 dB, our network model can perform better recognition, which is superior to traditional CNNs.

5. Conclusions

In this paper, we carry out research on the identification of shortwave radio communication behavior, starting from five types of burst waveforms in the physical layer. A signal feature extraction method based on autocorrelation spectrogram features is proposed. A neural network model is improved to further optimize the algorithm. The experimental results prove that the autocorrelation spectrogram features are not easily affected by noise, and the proposed network can further improve the recognition results. Our proposed algorithm can dramatically improve recognition results under low SNR conditions. Behavioral learning is increasingly important in communications, as a typical CRS, shortwave radio is just the first research object in a series of relevant works. Our subsequent work will continue

to focus on behavior recognition research on the CRS. In the future, we aim to expand related research to more types of CRS and wider communication scenarios, and consider more environmental factors, which is quite meaningful for communication confrontation.

Data Availability

Each burst waveform is generated according to the third-generation shortwave communication protocol standard. The dataset we use is made according to the feature extraction process mentioned in this paper. You can also ask for the data by contacting lihaitao_01@163.com.

Conflicts of Interest

The authors declare that they have no conflicts of interest.

Acknowledgments

We would like to thank the National Natural Science Foundation of China, for the research on several key technologies for the individual identification of communication radiation sources in complex electromagnetic environments. (Grant 62071479).

References

[1] I. Lee, D. Kim, and S. Lee, "3-D human behavior understanding using generalized TS-LSTM networks," *IEEE Transactions on Multimedia*, vol. 23, pp. 415–428, 2021.

[2] Z. Zhigang, D. Guangxue, L. Huan, Z. Guangbing, W. Nan, and Y. Wenjie, "Human behavior recognition method based on double-branch deep convolution neural network," in *2018 Chinese Control And Decision Conference (CCDC)*, pp. 5520–5524, Shenyang, China, 2018.

[3] Z. Shi, L. Cao, Y. Han, H. Liu, F. Jiang, and Y. Ren, "Research on recognition of motion behaviors of copepods," *IEEE Access*, vol. 8, pp. 141224–141233, 2020.

[4] S. Mukhopadhyay and H. Leung, "Recognizing human behavior through nonlinear dynamics and syntactic learning," in *Conference Proceedings - IEEE International Conference on Systems, Man and Cybernetics*, pp. 846–850, Seoul, Korea, 2012.

[5] H.-L. Chen, M. J. Tsai, and C. C. Chan, "A hidden Markov model-based approach for recognizing swimmer's behaviors in swimming pool," in *2010 International Conference on Machine Learning and Cybernetics*, pp. 2459–2465, Qingdao, China, 2010.

[6] Z. Jiang, D. Crookes, B. D. Green et al., "Context-aware mouse behavior recognition using hidden Markov models," *IEEE Transactions on Image Processing*, vol. 28, no. 3, pp. 1133–1148, 2019.

[7] M. Quaid and A. Jalal, "Wearable sensors based human behavioral pattern recognition using statistical features and reweighted genetic algorithm," *Multimedia Tools and Applications*, vol. 79, no. 9-10, pp. 6061–6083, 2020.

[8] K. Wu, H. Jiang, and C. Tellambura, "Cooperative sensing with heterogeneous spectrum availability in cognitive radio," *IEEE Transactions on Cognitive Communications and Networking*, vol. 8, no. 1, pp. 31–46, 2022.

[9] M. Alaee-Kerahroodi, E. Raei, S. Kumar, and M. Bhavani Shankar, "Cognitive radar waveform design and prototype for coexistence with communications," *IEEE Sensors Journal*, vol. 22, no. 10, pp. 9787–9802, 2022.

[10] W. Lu, P. Si, G. Huang, H. Han, and L. Qian, "SWIPT cooperation spectrum sharing for 6G-enabled cognitive IoT network," *IEEE Internet of Things Journal*, vol. 8, no. 20, pp. 15070–15080, 2020.

[11] H. Li, Y. Li, C. He, J. Zhan, and H. Zhang, "Cognitive electronic jamming decision-making method based on improved-learning algorithm," *International Journal of Aerospace Engineering*, vol. 2021, Article ID 8647386, 12 pages, 2021.

[12] A. Darpa, "Behavioral learning for adaptive electronic warfare," in *Darpa-BAA-10-79, Defense Advanced Research Projects Agency*, Arlington, USA, 2010.

[13] Y. Wu, X. Li, and J. Fang, "A deep learning approach for modulation recognition via exploiting temporal correlations," in *2018 IEEE 19th International Workshop on Signal Processing Advances in Wireless Communications (SPAWC)*, pp. 1–5, Kalamata, Greece, 2018.

[14] G. Liu and J. Cao, "Research on modulation recognition of OFDM signal based on hierarchical iterative support vector machine," in *2020 International Conference on Communications, Information System and Computer Engineering (CISCE)*, pp. 38–44, Kuala Lumpur, Malaysia, 2020.

[15] S. Ansari, K. A. Alnajjar, S. Abdallah, and M. Saad, "Automatic digital modulation recognition based on machine learning algorithms," in *2020 International Conference on Communications, Computing, Cybersecurity, and Informatics (CCCI)*, pp. 1–6, Sharjah, United Arab Emirates, 2020.

[16] F. Liu, Z. Zhang, and R. Zhou, "Automatic modulation recognition based on CNN and GRU," *Tsinghua Science and Technology*, vol. 27, no. 2, pp. 422–431, 2022.

[17] X. Li and Y. Lei, "Radiation source individual identification using machine learning method," in *2019 IEEE 8th Joint International Information Technology and Artificial Intelligence Conference (ITAIC)*, pp. 1001–1005, Chongqing, China, 2019.

[18] Y. Chen, L. Yu, Y. Yao, and L. Zhu, "Individual identification technology of communication radiation sources based on deep learning," in *2020 IEEE 20th International Conference on Communication Technology (ICCT)*, pp. 1301–1305, Nanning, China, 2020.

[19] L. Ying, J. Li, and B. Zhang, "Differential complex-valued convolutional neural network-based individual recognition of communication radiation sources," *IEEE Access*, vol. 9, pp. 132533–132540, 2021.

[20] S. Yang, H. Peng, M. Xu, Y. Pan, and X. Hou, "Ultra-shortwave specific signal spectrogram recognition based on convolution neural network," *Journal of Systems Engineering and Electronics*, vol. 47, no. 4, pp. 744–751, 2019.

[21] X. Cha, M. Xu, H. Peng, X. Qin, and T. Li, "Specific protocol signal recognition based on deep residual network," *Acta Electronica Sinica*, vol. 47, no. 7, pp. 1532–1537, 2019.

[22] Q. Jin, X. Gou, W. Jin, and N. Wu, "Intention recognition of aerial targets based on Bayesian optimization algorithm," in *2017 2nd IEEE International Conference on Intelligent Transportation Engineering (ICITE)*, pp. 356–359, Singapore, Singapore, 2017.

[23] X. Gou and N. Wu, "Air group situation recognition method based on GRU-attention neural network," *Computer and Modernization*, vol. 35, no. 10, pp. 11–16, 2019.

[24] C. Liu, X. Wu, C. Yao, L. Zhu, Y. Zhou, and H. Zhang, "Discovery and research of communication relation based on communication rules of ultrashort wave radio station," in *2019 IEEE 4th International Conference on Big Data Analytics (ICBDA)*, pp. 112–117, Suzhou, China, 2019.

[25] C. Liu, X. Wu, L. Zhu et al., "The communication relationship discovery based on the spectrum monitoring data by improved DBSCAN," *IEEE Access*, vol. 7, pp. 121793–121804, 2019.

[26] C. Liu, X. Wu, L. Zhu et al., "Research on communication network structure mining based on spectrum monitoring data," *IEEE Access*, vol. 8, pp. 3945–3959, 2020.

[27] C. Liu, X. Wu, C. Yao et al., "Research on discovery of radio communication relationship based on correlation analysis," *IOP Conference Series: Earth and Environmental Science*, vol. 440, no. 4, article 042006, 2020.

[28] T. Pan, X. Wu, C. Yao, Y. Zhou, and X. Lu, "Communication behavior structure mining based on electromagnetic spectrum analysis," in *2019 IEEE 8th Joint International Information Technology and Artificial Intelligence Conference (ITAIC)*, pp. 1611–1616, Chongqing, China, 2019.

[29] K. Cheng, L. Zhu, C. Yao et al., "DCGAN based spectrum sensing data enhancement for behavior recognition in self-organized communication network," *China Communications*, vol. 18, no. 11, pp. 182–196, 2021.

[30] J. Zhang, M. Tan, F. Shi, Y. Yang, and Z. Yang, "A novel approach of protocol behavior identification for TDMA-based frequency hopping communication," *Wireless Communication and Mobile Computing*, vol. 2022, article 7941367, pp. 1–14, 2022.

[31] X. You and W. Ge, "Protocol identification and multi-conversation relationship extraction in Fetion," *Modern Electronics Technique*, vol. 37, no. 21, pp. 19–23, 2014.

[32] H. Zhou, L. Yang, and Z. Wu, "Feasibility analysis of tactical radio station communication behaviors cognition," in *2021 Asia-Pacific Conference on Communications Technology and Computer Science (ACCTCS)*, pp. 160–166, Shenyang, China, 2021.

[33] Z. Wu, H. Chen, and Y. Lei, "Recognizing non-collaborative radio station communication behaviors using an ameliorated LeNet," *Sensors*, vol. 20, no. 15, pp. 1–20, 2020.

[34] Z. Wu, H. Chen, Y. Lei, and H. Xiong, "Recognizing automatic link establishment behaviors of a short-wave radio station by an improved unidimensional DenseNet," *IEEE Access*, vol. 8, pp. 96055–96064, 2020.

[35] Z. Wu, H. Chen, and Y. Lei, "Visualization research on improved DenseNet applied to recognize a radio station's link establishment behavior," *Journal of Systems Engineering and Electronics*, vol. 43, no. 5, pp. 1371–1381, 2021.

[36] Z. Wu, H. Chen, and Y. Lei, "Unidimensional ACGAN applied to link establishment behaviors recognition of a short-wave radio station," *Sensors*, vol. 20, no. 4270, pp. 1–19, 2020.

[37] Y. Xie and H. Deng, "A radio frequency fingerprinting identification method based on improved ResNet," *Telecommunication Engineering*, vol. 62, no. 4, pp. 416–423, 2022.

[38] J. Jia and L. Qi, "RF fingerprint extraction method based on bispectrum," *Journal of Terahertz Science and Electronic Information Technology*, vol. 19, no. 1, pp. 107–111, 2021.

Hindawi
Wireless Communications and Mobile Computing
Volume 2022, Article ID 4748519, 15 pages
https://doi.org/10.1155/2022/4748519

Research Article

Specific Emitter Identification Based on a Hybrid Deep Neural Network for ACARS Authentication

Liyan Yin, Xin Xiang, Kun Liu, and Yuan Liang

Aviation Engineering College, Air Force Engineering University, Xi'an 710038, China

Correspondence should be addressed to Liyan Yin; 13379547517@126.com

Received 24 April 2022; Accepted 10 August 2022; Published 22 September 2022

Academic Editor: Yunfei Chen

With the increasing variety and quantity of aircraft, there is a potential threat to the security of the Aircraft Communications Addressing and Reporting System (ACARS) due to the lack of reliable authentication measures. This paper proposes a novel specific emitter identification (SEI) algorithm based on a hybrid deep neural network (DNN) for ACARS authentication. Our deep learning architecture is a combination of Deep Residual Shrinkage Network (DRSN), Bidirectional-LSTM (Bi-LSTM), and attention mechanism (AM), which perform the functions of local and global feature learning and feature focusing, respectively, so that the individual information hidden in the signal waveform can be thoroughly mined. We introduce soft thresholding as a nonlinear transformation in the DSRN to enhance robustness against noise and adopt a low-cost training strategy for new data using transfer learning. The proposed SEI algorithm is optimized and evaluated based on real-world ACARS signals captured in the Xianyang airport. Experimental results demonstrate that our algorithm can distinguish authorized entities from unauthorized entities and obtain an identification accuracy of up to 0.980. In addition, the design rationality and the superiority over other algorithms are verified through the experiments.

1. Introduction

Aircraft Communications Addressing and Reporting System (ACARS) is a datalink communication system established between aircraft and ground stations via the very high frequency/high frequency (VHF/HF) channel, which enables real-time transmission of crucial information, including aircraft registration number, planned track, position coordinates, health conditions [1], etc. The ACARS is widely used in civil aviation due to its long-term operation and adequate surface infrastructure. However, ACARS is transmitted in clear text over the open radio frequency channel [2]. Therefore, it is vulnerable to threats posed by unauthorized entities that may disguise and tamper with information using low-cost transceivers. In particular, active attackers try to attempt to exploit avionic systems or create confusion for air traffic control (ATC), thereby jeopardizing flight security [3, 4].

Commercial airlines have adopted some authentication measures based on bit-level security mechanism, such as the ACARS message security (AMS) protocol defined in ARINC Specific 823 [5], which run above the physical layer of the Open System Interconnection (OSI) reference model. But they are still at risk of being cracked by using compromised or broken encryption keys, or by impersonating an authorized device's identity [6]. Fortunately, it is almost impossible for unauthorized entities to imitate the intrinsic characteristics at the physical layer, i.e. radio frequency fingerprints (RFFs). The technique for identifying individual emitters using RFFs is called SEI [7], enabling the authentication system to work without large-scale infrastructure modification or protocol update, as shown in Figure 1. Besides, SEI provides an additional guarantee of security to detect unauthorized entities; therefore it can be used as a low-cost complement to traditional authentication schemes.

In the past years, machine learning (ML) has been proved to be an effective and efficient approach to realizing SEI [8]. Feature engineering is one of the most critical aspects of ML, which determines the upper bound of the SEI. ML relies on manually extracted features, including

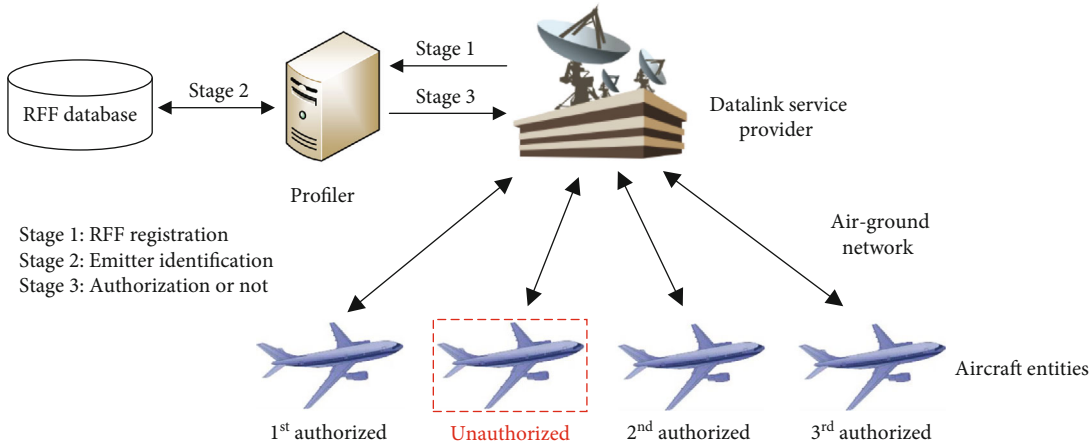

Figure 1: The SEI-aided ACARS authentication system, which contains RFF registration, emitter identification and authorization.

frequency and phase offset [9], IQ imbalance [10], discrete wavelet transformation (DWT) [11], nonlinear characteristics [12], etc. However, these features must be extracted for the specific transient period or steady-state period of a complete transmission, thereby undermining the generality of SEI [13]. At the same time, due to the short duration of the transient period, it is difficult to accurately extract the features of the transient signal. Steady state signals are also vulnerable to the impact of the acquisition environment, resulting in the distortion of the features. Furthermore, fine feature engineering consumes high computational costs and depends on professional experience and domain knowledge. Therefore, researchers tend to find more intelligent means to replace ML for implementing SEI [14].

Thanks to advances in computer hardware and algorithms, deep learning (DL), as a particular version of ML, has achieved great success in the field of image and natural language processing [15, 16], etc. Recently, various deep architectures including convolutional neural network (CNN), long short-term memory (LSTM), and residual network (ResNet) have illustrated the outstanding potential for radio signal classification. Quite a few SEI approaches still use the manually extracted features as the inputs of the DNN, such as Bispectrum [17], Hilbert-Huang transform (HHT) [18], and differential constellation trace figure (DCFT) [19]. However, the most significant advantage of DL, namely automatic feature extraction, has not been exploited to the full. In other works, traditional features are abandoned, and deep features are extracted directly from the raw time-series signal. Merchant et al. developed a framework for training a CNN using time-domain complex baseband error signals of the ZigBee devices [20]. Wang et al. designed an efficient SEI method for the Internet of things (IoT) based on a novel complex-valued neural network (CVNN) [21]. Wu et al. proposed an LSTM-based recurrent neural network (RNN) model that captures hardware-specific features of IQ data at the output of the analog-to-digital (ADC) of the USRP transmitter [22]. Of course, there are also a few works that discuss the application of deep learning to aircraft radio fingerprint identification. Zha et al. converted ADS-B signals to Contour Stellar Images (CSI) and applied the architectures of AlexNet and GoogleNet to SEI [23]. Jian et al. used a deep architecture named ResNet-50-1D to capture salient, discriminative features from IQ samples transmitted by ADS-B radios [24]. Chen et al. used the inception-residual neural network model structure for large-scale ACARS and ADS-B radio signal classification [25]. These works focus on designing suitable network structures for a stronger capability of feature learning. Nevertheless, these deep architectures are designed for their respective target signals, and it is necessary to perform specific preprocessing in front of the network to guarantee the proper identification performance of the ACARS signals.

In this paper, we propose a novel SEI algorithm under an end-to-end DL architecture for ACARS authentication. First, the valid part of the raw signal is intercepted through preprocessing. Then, the inputs are propagated into a hybrid architecture composed of DRSN, Bi-LSTM, and AM, which perform the functions of local feature learning, global feature learning, and feature focusing, respectively. To the best of our knowledge, this is the first attempt to use a joint CNN and RNN-based architecture on SEI in the authentication system. Among them, DSRN uses a structure with soft thresholding to enhance the noise elimination capability. Based on the real-world captured ACARS signals from seven civil aircraft in Xianyang airport, a series of trials and experiments are carried out for hyperparameter selection and performance validation. Through discussions of the experimental results, the feasibility and superiority of the SEI algorithm are adequately studied. Our main contributions are as follows:

(i) According to the ACARS protocol, the method of signal preprocessing is studied, in which we mainly discuss how to intercept the valid signal. This will enhance the efficiency and accuracy of our algorithm

(ii) A hybrid DRSN-BiLSTM-AM deep architecture is proposed for the SEI of the ACARS authentication system. The hyperparameters of the model are

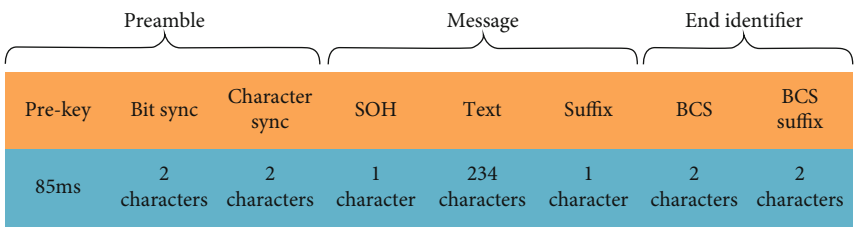

Figure 2: Frame structure of the transmission packet in ACARS.

Table 1: Character structure of transmission packet in ACARS.

Component	Length	Value
Pre-key	85 ms	All binary "ones"
Bit sync	2 characters	<+> (0x2B), <*> (0x2A)
Character sync	2 characters	<+ > (0x2B), <* > (0x2A)
Start of header	1 character	<SOH> (0x01)
Text	234 characters maximum	\
Suffix	1 character	<ETX> (0x03) or < ETB> (0x17)
BCS	2 characters	\
BCS suffix	1 character	<DEL> (0x7F)

adjusted to the optimization through trials. In this way, the computational complexity and identification accuracy are balanced well

(iii) Soft thresholding acts as a layer of the DRSN that performs a nonlinear transformation, and the branch of adaptive threshold selection is added simultaneously. This will make our DNN model insensitive to noise

(iv) The strategy of transfer learning is introduced using limited training samples. This will greatly reduce the cost of training of our algorithm on new data

The remainder of this paper is organized as follows: Section 2 briefly describes the ACARS protocol and the corresponding preprocessing technique. Section 3 proposes the hybrid DNN model. Section 4 illustrates the implementation of the proposed algorithm. The comparative experimental results on a real-world dataset are covered in Section 5. And, the conclusion is given in Section 6.

2. Brief Description of ACARS and Signal Preprocessing

2.1. Brief Description of ACARS. The research content of this paper is limited to the downlink signal in VHF band of ACARS, whose protocol is defined in the Specification 618 by Aeronautical Radio, Inc. (ARINC) [26]. The protocol aims to create character-oriented data connectivity between aircraft and ground service providers. The encoding scheme of ACARS adopts non-return-zero inverse (NRZI) with a bit rate of 2400 bps. Besides, ACARS adopts amplitude modulation-minimum shift keying (AM-MSK) composite modulation, and its carrier frequency operates around 131.55 MHz.

The default format of the transmission packet in ACARS is depicted in Figure 2, which is made up of three parts: Preamble, Message, and End Identifier. The Preamble consists of Pre-key, Bit sync, and Character Sync. The Message consists of Start of Header (SOH), Text, and Suffix. The End Identifier consists of Block Check Sequence (BCS) and BCS Suffix. Table 1 summarizes the detailed character structure of the transmission packet.

2.2. Signal Preprocessing. In this subsection, we investigate which part of the captured signal is considered as valid. As depicted in Table 1, pre-key is of indefinite length consisting of all binary "ones". Its role concludes with receiver AGC settling, transmitter power output stabilization, and local oscillator synchronization [26]. The bit sync, character sync, and the start of heading specify their respective character formats. These four components, namely Pre-key, Bit Sync, Character Sync, and the Start of Header are the most distinguishing part of the received signal. Furthermore, they conform to the standard message format and are not affected by the different transmitted content. Therefore, these three components best represent individual characteristics, and the other components are discarded.

Next, we discuss how to locate and intercept the valid signal using the synchronization sequences, including the Bit Sync and Character Sync. Figure 3 depicts the preprocessing framework proposed in this paper, and Figure 4 shows the output waveforms of several important steps.

As depicted in Figure 4(a), the received ACARS signal $r(t)$ is given by,

$$r(t) = R(t)\cos\left(2\pi f_c t + \varphi(t)\right) + n(t), \tag{1}$$

where $R(t)$, $\varphi(t)$, f_c and $n(t)$ is the envelope, phase shift,

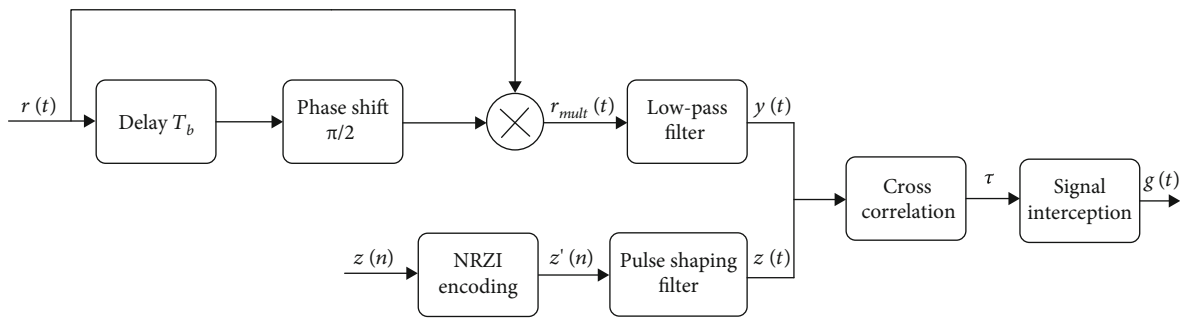

Figure 3: Framework of the preprocessing for the ACARS signal.

carrier frequency, and additive white Gaussian noise (AWGN), respectively.

In order to obtain accurate timing information, we adopt a method based on 1-bit differential noncoherent demodulation [27], which does not require precise carrier recovery and has a simple structure.

The delay-multiply signal is obtained with delay of T_b and shifted-phase of $\pi/2$,

$$r_{mult}(t) = R(t)\cos[2\pi f_c t + \varphi(t)]R(t-T_b)\cos[2\pi f_c(t-T_b) + \varphi(t-T_b)] + n'(t). \tag{2}$$

After low pass filtering, the high-frequency components are removed. We can obtain,

$$y(t) = \frac{1}{2}R(t)R(t-T_b)\sin[2\pi f_c T_b + \varphi(t) - \varphi(t-T_b)] + n''(t), \tag{3}$$

where $T_b = 1/2400\text{s}$ is the bit width, and $n''(t)$ denotes the noise component. According to the characteristics of MSK modulated signal, we have $f_c T_b = k, k = 1, 2, 3, \cdots$, then $y(t)$ can be rewritten as,

$$y(t) = \frac{1}{2}R(t)R(t-T_b)\sin[\varphi(t) - \varphi(t-T_b)] + n''(t). \tag{4}$$

Since $R(t)$ and $R(t-T_b)$ is always positive, $y(t)$ has the same polarity as$\varphi(t) - \varphi(t-T_b)$. Therefore, when the transmission bit is 1, $y(t)$ is positive; when the transmission bit is 0, $y(t)$ is negative. To estimate starting time τ of the synchronization sequence, we do not perform sampling and decision. Instead, we correlate the ideal synchronization waveform $z(t)$ and the received signal $y(t)$. As depicted in Table 1, the synchronization sequence $z(n)$ consists of 4 characters, which is generated through ASCII encoding by a bit sequence as, 00101011001010100001011000010110. After NRZI encoding for $z(n)$, we obtain $z'(n)$ as,

$$z'(n) = -111-1-1111-111-1-111-11-111 -1-1-11-11-1-1111-1. \tag{5}$$

Thereafter, the continuous training signal is given by,

$$z(t) = \sum_{n=1}^{32} z'(n)\cdot\left(\delta\left(t - \frac{n}{R_b}\right) * g(t)\right), \tag{6}$$

where $*$ is the convolution operation, and $g(t)$ is the pulse shaping filter, which is given by,

$$g(t) = \begin{cases} 1 & t \in (0, T_b] \\ 0 & \text{otherwise} \end{cases}. \tag{7}$$

The cross-correlation between $z(t)$ and $y(t)$ is given by,

$$corr(\tau) = \int_0^{T_z} z^*(t)y(t-\tau)dt, \tau \in (0, T_z], \tag{8}$$

where T_z is the time span of $z(t)$. As depicted in Figure 4(b), the starting of the synchronization sequence τ is given by

$$\tau = \arg\max_{\tau} corr(\tau). \tag{9}$$

Once τ is determined, we can locate the valid signal in $r(t)$. Marked by τ in the received ACARS signal $r(t)$, signals of lengths $T_p = 85\text{ms}$ and $T_q = 40T_b = 16.67\text{ms}$ are intercepted at the forward and backward directions, respectively, which is shown in Figure 4(c). In fact, in order to ensure that there are no redundant sampling points during signal segmentation in the subsequent operation, 1.83 ms at the end of the signal is discarded. Thus, the duration of the valid signal $v(t)$ is $T_v = 99.84\text{ms}$, as shown in Figure 4(d). Note that the objects described above are continuous signals, but the captured signals are processed in a discrete form. We collect signals at the sampling rate of 400 kHz in the experiments. Therefore, the signal of T_v is discretized into 39936 sampling points. For the sake of presentation, we use the raw and original data to represent the ACARS signals before and after the signal interception.

The original signal is then divided into 39 nonoverlapping segments and each segment contains 1024 complex sampling points. The segments are randomly grouped into training dataset and testing dataset by the ratios of 80% and 20%. It should be noted that all the segments in one sample belong to the same dataset. For the training dataset, the segments are labeled with the true emitter category, and then the order of them is randomly shuffled.

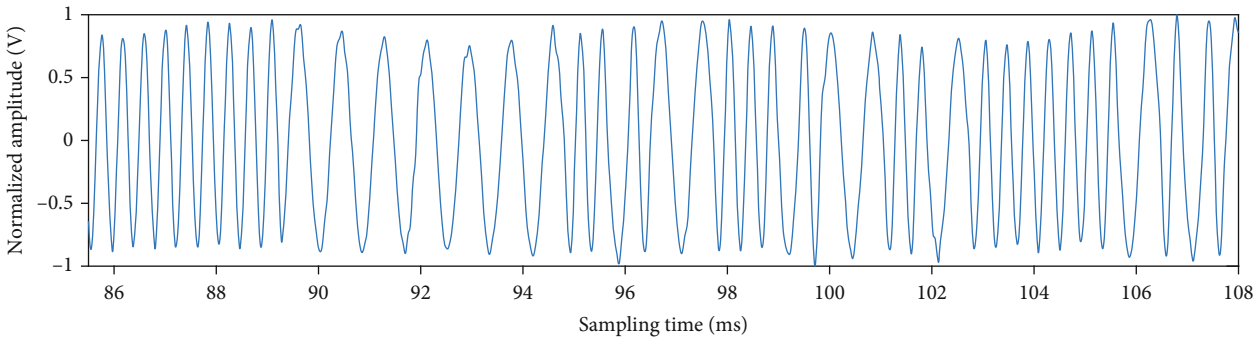

(a) Received ACARS signal $r(t)$

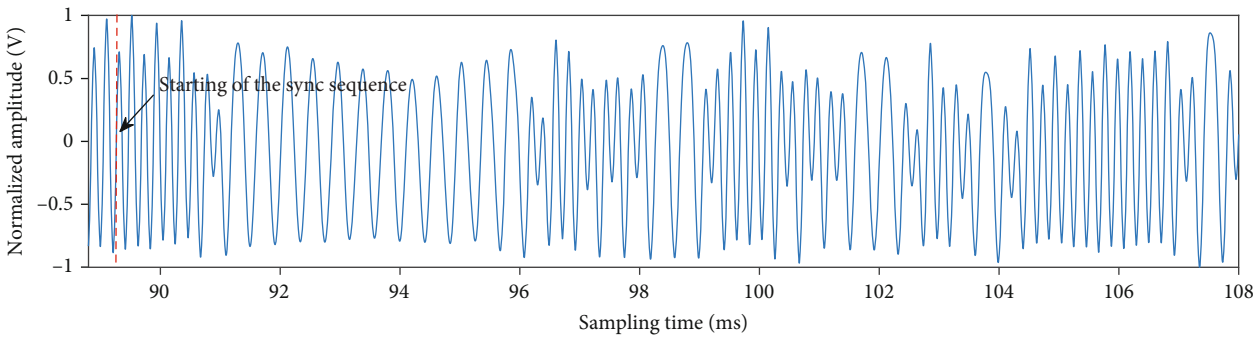

(b) Timing estimation τ in the output of MSK demodulation $y(t)$

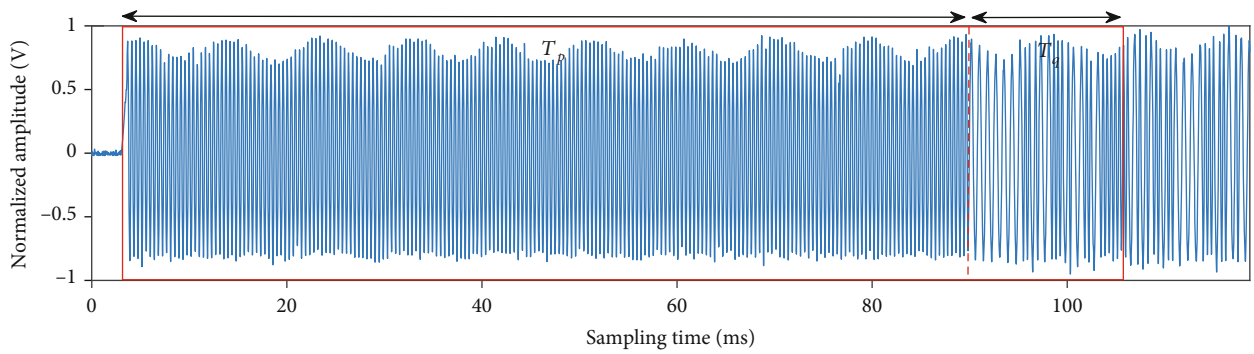

(c) τ, forward-intercepted T_p and backward-intercepted T_q in $r(t)$

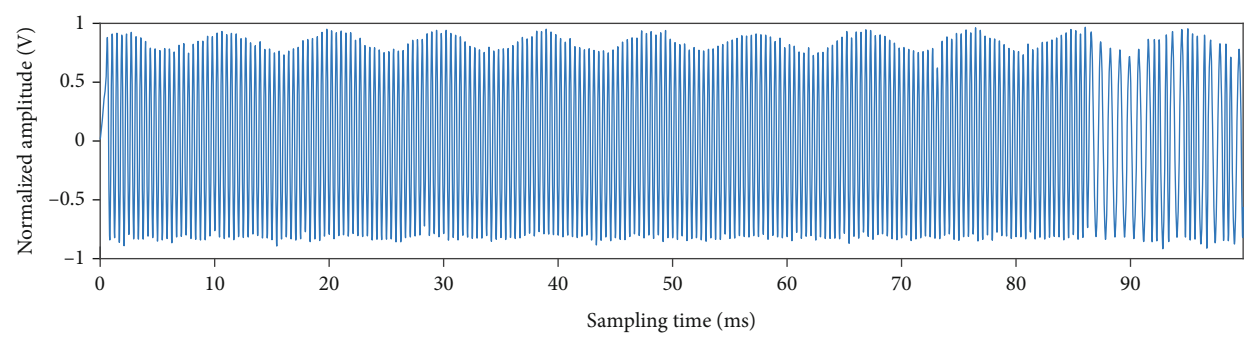

(d) Valid signal v(t)

Figure 4: Waveform diagrams of several key steps in signal preprocessing.

3. The Hybrid DNN Model

This section describes the deep learning architecture and its main components of our algorithm. In order to extract features more effectively and improve identification performance, DRSN, Bi-LSTM, and AM are integrated into a hybrid DNN model. As depicted in Figure 5, the proposed architecture consists of four essential blocks: local feature learning block, global feature learning block, attention block, and identification block. At first, DRSN is used to extract

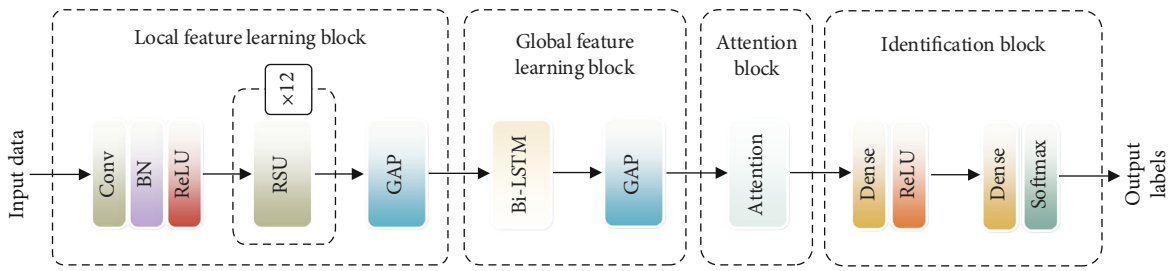

Figure 5: Architecture of the proposed network.

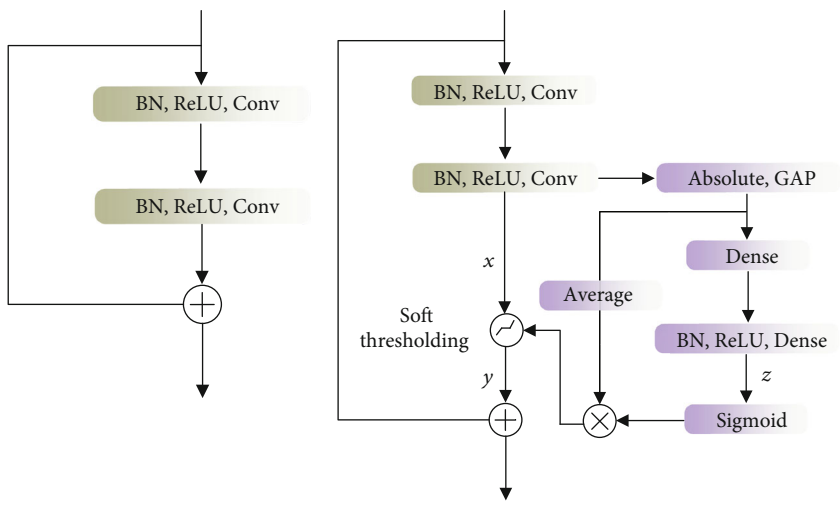

(a) Structure of standard RU (b) Structure of RSU

Figure 6: Comparison on two structures of residual unit.

Table 2: Local feature learning network parameters.

Unit (number)	Number/size/stride of kernels	Output dimension
Input	—	1024 × 2
Conv	4/5 × 1/1	4 × 1024 × 2
RSU	4/5 × 1/2	4 × 512 × 2
RSU (×3)	4/5 × 1/1	4 × 512 × 2
RSU	8/3 × 1/2	8 × 256 × 2
RSU (×3)	8/3 × 1/1	8 × 256 × 2
RSU	16/3 × 1/2	16 × 128 × 2
RSU (×3)	16/3 × 1/1	16 × 128 × 2
GAP	—	16

local features from the time series segments in the local feature learning block. These local features are then transferred in sequence to the Bi-LSTM layer to learn global features. In the attention block, AM assigns various attention scores, accentuating the influence of the more significant element of the feature map, and aids in making more correct determinations. Finally, we stack the dense and output layer in the identification block to perform the final identification. Each block of the proposed DNN model is demonstrated in detail below.

3.1. Local Feature Learning Block. In this block, we hope to obtain deep and invariant local features. The deep mining of features can be realized through the Deep Residual Network (DRN), which is composed of the stacked standard residual units (RUs). As shown in Figure 6(a), a standard RU consists of two batch normalization layers, two Rectified Linear Units (ReLUs) of activation layer and two convolutional layers. The input and output of RU is connected via shortcut, so as to solve the degradation problem in deep network. Noise interference will introduce variance to the features. In order to suppress the interference, the RUs in the DRN are replaced with the residual shrinkage units (RSUs), thus forming the residual shrinkage network (DRSN) [28]. Based on RU, soft thresholding is introduced as a nonlinear activation layer to eliminate noise-related features, which is calculated as,

$$y = \begin{cases} x - \kappa & x \geq \kappa \\ 0 & -\kappa \leq x < \kappa \\ x + \kappa & x < \kappa \end{cases}, \tag{10}$$

where x is the input feature map, y is the output feature map, and κ is the threshold, i.e., a positive parameter. Unlike ReLU setting the negative features to zero, soft thresholding

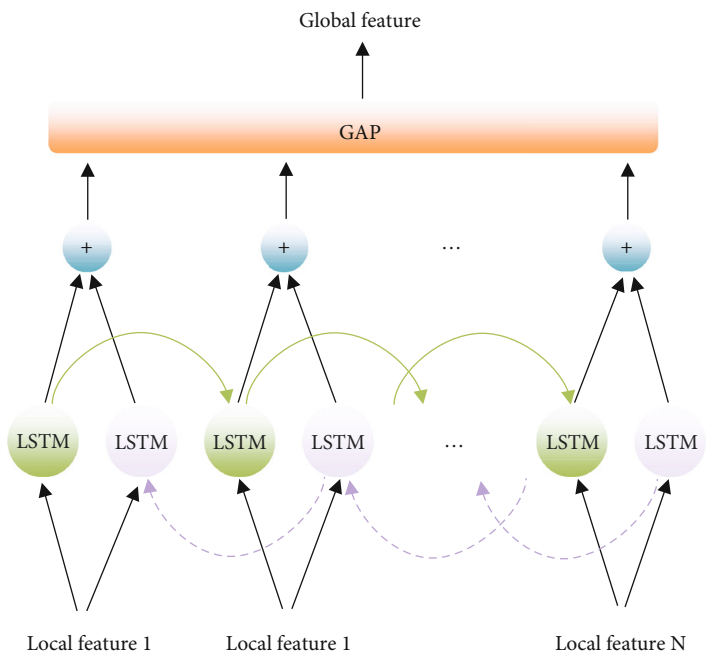

Figure 7: Schematic diagram of global feature extraction block.

sets the near-zero features to zeros to retain the useful negative features [28].

An additional branch of adaptive threshold calculation is added in RSU, as shown in the violet part of Figure 6(b). First, we use a global average pooling (GAP) layer to compress the absolute values of x into a one-dimensional (1D) vector, which is fed into a two-layer dense network to obtain the intermediate variable z [29]. z is then scaled to the range of (0, 1) using the sigmoid function, which is given by,

$$\alpha = \frac{1}{1 + e^{-z}}. \tag{11}$$

After that, the scaling parameter α is multiplied by the average value of $|x|$ to obtain the threshold. This is motivated by the fact that the threshold needs to be positive and cannot be too large. Thus, the threshold used in the RSU is given by,

$$\kappa = \alpha \cdot \underset{i,j,c}{average} \left| x_{i,j,c} \right|, \tag{12}$$

where i, j, and c are the indexes of width, height, and channel of x, respectively. In this way, the threshold is controlled in a reasonable range with respect to the input feature map.

In the local feature block, we stack several RSUs to achieve the following objectives: (a) extract deeper-level features, which aids in better representation of the input data; (b) gradually eliminate the noise-related features layer-by-layer. The number of RSU stackings is 12, the rationality of which is discussed later. Since the input of the Bi-LSTM layer must be a 1D array, the output of the local feature block is flattened into 1D data by the global average pooling (GAP) layer. The DRSN parameters are shown in Table 2.

3.2. Global Feature Learning Block. As the original inputs and the learned local feature maps represent the time course of electromagnetic activity of ACARS emitters, a RNN-based structure can be used to learn from the input along the time sequence in a parameter-sharing manner and memorize the context through their internal states [30]. An improved variant of RNN is LSTM, whose advantage is that it solves the problems of long-term memory and gradient disappearance in RNN while remaining computational cheap. In this paper, we adopt the structure of Bi-LSTM which has a forward and a backward LSTM layer. The forward one can process the past data information, whereas the reverse one can obtain the future data information. As shown in Figure 7, the local feature vectors are propagated into the Bi-LSTM layer in sequence, and the outputs are summed into a local-focused global feature vector, which encapsulates features from the context of the current step in both forward and backward directions. Both LSTM layers have 128 units, so the length of each local-focused global feature vector is 128. Finally, we use GAP to obtain a single output vector for the identification block.

3.3. Attention Block. Different kinds of information related to the emitter individual have different influence on the identification results. AM selectively focuses on some more influential information, so as to boost the expected information. The essence of AM is a mapping from a query to a sequence of key-value pairs, as depicted in Figure 8. The calculation of AM involves the following three stages.

At the first stage, the preliminary attention score is given by,

$$s_t = \tanh\left(W_h h_t + b_h\right), \tag{13}$$

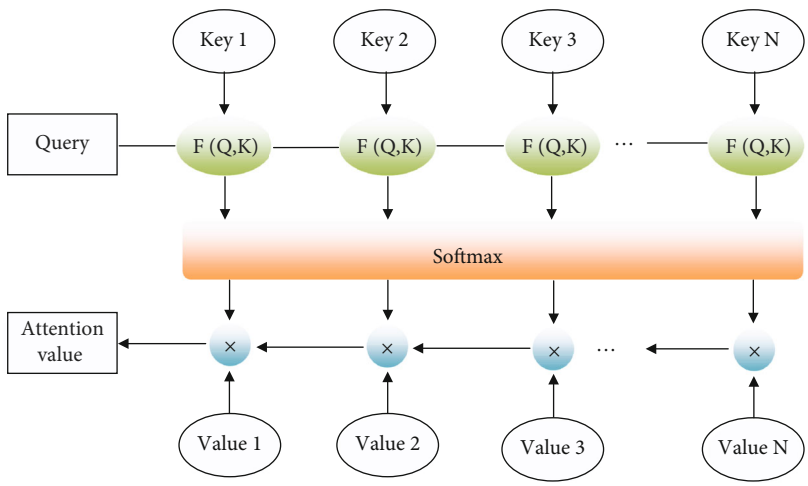

Figure 8: Schematic diagram of attention block.

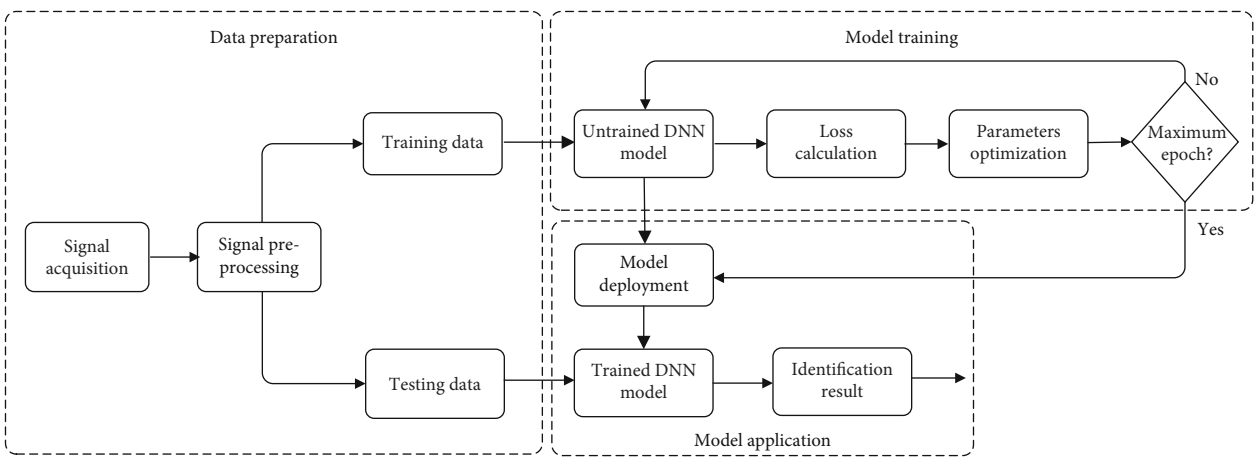

Figure 9: Flow chart of the proposed algorithm based on the DNN model.

where W_h, b_h are the weight and bias of AM, respectively, and h_t is the input vector. Then, the score is normalized using the softmax function,

$$a_t = \frac{\exp(s_t)}{\sum_t \exp(s_t)}, \tag{14}$$

regarding the score coefficient, the final attention score is obtained by weighted summation as shown,

$$c = \sum_t a_t q_t. \tag{15}$$

The above process shows that AM determines the most significant information by allocating higher scores to the feature map [31]. Thus, it has a positive optimization impact on our DNN model, and thus improves identification accuracy.

3.4. Identification Block. The dense layers map the distributed feature representation to the sample tag space via nonlinear transformations. We have two dense layers in the final block, and the first one has 128 neurons, while the second one has 7 neurons (corresponding to 7 categories). The first activation function uses ReLU to accelerate the back-propagation of gradients. The second activation function uses softmax to predict the probability distribution over the 7 categories.

4. Implementation of the Proposed SEI Algorithm

4.1. Overall Procedure of the Proposed Algorithm. In this paper, our proposed SEI algorithm contains three main steps: data preparation, model training, and model application, shown in Figure 9. In data preparation, the ACARS signals are collected in the out-field of the Xi 'an Xianyang airport emitted by seven civil aircraft, whose registration numbers are B1867, B30ER, B3229, B5180, B6469, B6695, and B9936. 1250 samples are collected from each aircraft. Subsequently, all samples are pre-processed in the same manner as section 2 described. The inputs are divided into training and testing data, which have a size of 1000 samples

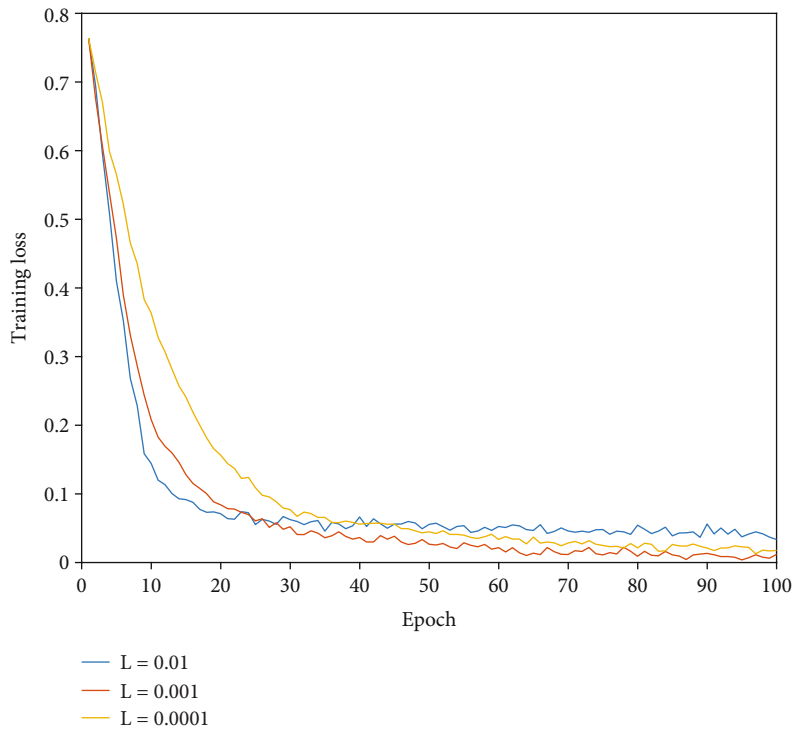

Figure 10: Training loss curve concerning different learning rate.

and 250 samples, respectively. We set the mini-batch size of the input data to 30. In model training, all aircraft that require certification must be registered offline. First, we construct the proposed DNN model with the determined initial parameters, and the training data from authorized entities are fed into the network to achieve forward propagation. We use cross-entropy as the loss function and the Adam algorithm as the optimizer. This training process will continue until the maximum epoch 200 is achieved. In model application, the online authentication system realizes the identification of the testing data through the trained DNN and finally outputs the probability distribution of the predicted emitter category. Through these three steps, SEI is implemented using the proposed algorithm.

The overall algorithm is run on a Linux machine with Nvidia K80 GPU, Intel Xeon W2155 CPU and 64 GB RAM. The signal acquisition is implemented by TI ADC32RF82 RF-sampling wideband receiver and the preprocessing of the captured signals is performed on Matlab 2020b. The framework of the DNN model is constructed in Keras 2.0.8 with Tensorflow 1.7 backend.

4.2. Hyperparameters Selection of the DNN Model. The adjustments of model parameters are data-driven, but hyperparameters need to be selected manually. Here, we select several hyperparameters for balancing the performance and computational cost through a few trials.

(a) Learning Rate: Learning rate controls the speed at which the loss function descends along the gradient. As shown in Figure 10, the curves of training loss concerning various learning rates exhibit significant differences. We have the minimum training loss and the fastest convergence speed when we set the learning rate to 0.001. Thus, our DNN model selects the learning rate of 0.001 in the training process

(b) Hyperparameters of Local Features Learning Block: As mentioned in Section 3, DRSN is designed to address the problem of performance degradation as the network deepens. Generally speaking, the deeper the residual network, the better the performance of feature learning. However, since an RSU occupies many computing resources, increasing the residual network depth will lead to the burden of computational complexity. Table 3 shows the identification accuracy and computational complexity concerning various numbers of RSUs. Note that the identification accuracy described here and below is for testing data. We can see that compared with image processing which requires dozens or even hundreds of layers of RSUs, feature learning for the signal can achieve good performance without stacking so many RSUs. The performance of feature learning hardly increases when the number of RUs is more than 12, but the computational complexity increases by 0.83 MFLOPs. Thus, we select 12 RSUs as the main body of the local feature learning block

(c) Hyperparameters of Global Features Learning Block: We use dropout regularization in LSTM to prevent

Table 3: Identification accuracy and computational complexity concerning various hyperparameter settings for local feature learning.

Number of RSUs	Identification accuracy	Computational complexity (MFLOPs)
4	0.937	0.83
8	0.968	1.66
12	**0.980**	**2.50**
16	0.982	3.33
20	0.982	4.16

Table 4: Identification accuracy concerning various hyperparameter combination settings for global feature learning.

No. of LSTM units	Dropout rate	Recurrent dropout rate	Identification accuracy (%)
128	0.4	0.2	0.973
128	0.5	0.1	0.978
128	**0.5**	**0.2**	**0.980**
64	0.5	0.2	0.962
256	0.5	0.2	0.967

Table 5: Average time cost with raw and original ACARS signals as inputs of the DNN model.

Input ACARS signals	Raw	Original
Average training time (s)	48.2	14.7
Average testing time (s)	0.56	0.15

model over-fitting. Therefore, the hyperparameters closely related to model performance in the global feature learning block include LSTM unit number, dropout rate, and recurrent dropout rate. Table 4 shows the identification accuracy of various combinations of the above hyperparameters. We obtain the best performance when we have LSTM 128 units, 0.5 dropout rate, and 0.2 recurrent dropout rate

4.3. Complexity Analysis of the DNN Model. Next, we analyze the complexity of the proposed DNN model from time and space dimensions. The time complexity can be calculated by the FLoating-Point Operations (FLOPs), and our model has 12.6MFLOPs; the space complexity can be calculated by the total weight parameters of the model, and our model has 4.7Mparas. Compared with the classical deep ResNet-50 network for image processing, which has 410 MFLOPs and 25.5Mparas, our model has low complexity. This is because we use the time series of signals as input, thus reducing the dimension of features and the complexity of the FC layer is greatly reduced due to fewer classification categories.

We then analyze the average time cost by dividing the total training and testing time by the dataset size. It can be seen from Table 5 that using original ACARS signals as inputs costs much more time than those using raw ACARS signals as inputs. The size of the original signal is several times smaller than that of the raw signal due to the preprocessing. Thus, there are fewer segments in a sample that corresponds to the raw signal, which greatly reduces the time overhead.

5. Experiments and Discussions

5.1. Basic Identification Results. First, we conducted RF fingerprint registration for all 7 aircrafts, that is, training the collected samples through the network. The confusion matrix is shown in Figure 11(a), from which we can see that our algorithm is highly discriminative for the authorized aircraft. Next, we treated the aircraft with registration number B9936 as an unauthorized entity; namely, the corresponding samples are tested directly without training. The confusion matrix is shown in Figure 11(b), from which we can see that the probability distribution of the identification results of the unauthorized entity is scattered. Thus, we can set a threshold on the diagonal of the confusion matrix, such as 0.6, to distinguish between the authorized and unauthorized entities. We define the identification accuracy of the SEI algorithm as the average of the correct identification probability of all registered categories. In the case of Figure 11(a), the identification accuracy is 0.980, while in the case of Figure 11(b), the identification accuracy is 0.977. Generally speaking, the higher the proportion of registered entities in all categories, the higher the identification accuracy. Samples of unauthorized entities are untrained, leading to possible confusion with authorized entities. The identification accuracy involved below corresponds to the case where all seven aircraft have been registered.

Then, we evaluate the effect of valid signal interception in preprocessing. As Section 3 highlighted, we use the terms "raw ACARS signals" and "original ACARS signals" to represent the signals before and after the interception. As shown in Figure 12, the use of the original data shows better identification accuracy than that of the raw data. This is because we intercept the most representative part of the signal that best characterizes the individual information of each emitter in the preprocessing; on the other hand, the remainder of the raw data may contain differences in the message content, thus affecting the features learned by the network. According to the discussion in Section 4(c), the preprocessing makes our algorithm more competitive in identification accuracy and computational complexity.

5.2. Comparison with Other State-of-the-Art Algorithms. As our algorithm is based on the end-to end learning, we select three DL algorithms which learn deep features directly from time series signals, namely CNN [20], LSTM [22, 32], and ResNet-50-1D [24]. Besides, we also use three manual feature-based machine learning algorithms for comparison, namely Bispectrum-CNN [17], HHT-DRN [18], and DCFT-CNN [19]. The identification results for various algorithms are shown in Figure 13. It can be observed that DL algorithms have better performance than ML algorithms, which indicates that the deep features are more reliable than the manual features. This may be due to the loss of information in the process of signal transformation. Moreover, manual feature extraction as an

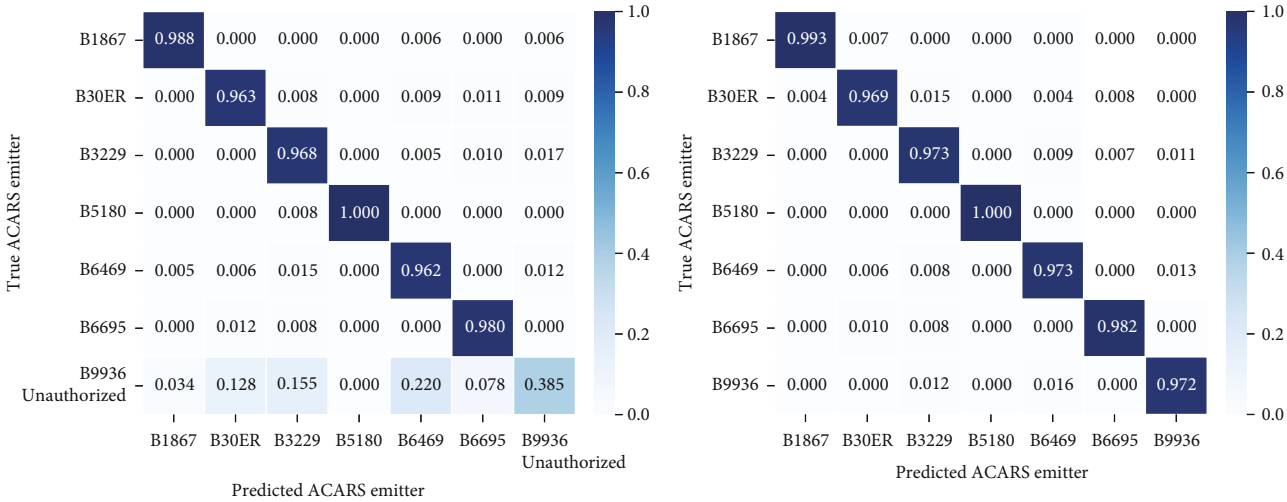

(a) All aircraft registered offline

(b) B9936 unregistered offline

Figure 11: Confusion matrix for the SEI of ACARS authentication (The color depth of the color bar on the right of the picture represents the identification probability. The darker the color, the greater the identification probability).

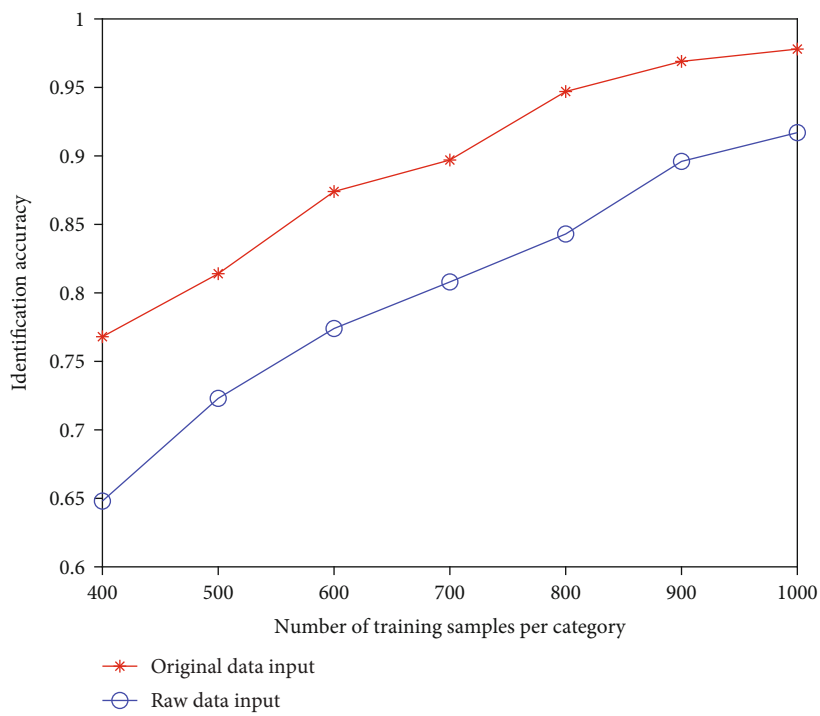

Figure 12: Identification results with original data and raw data as inputs.

additional operation will lead to a sharp rise in computational complexity, which is unfavorable to the practical application. We find that the Bispectrum-CNN performs the worst. For the local feature, the learning ability of the ResNet is stronger than that of the CNN, as the shortcut connections help the gradients propagate. The RNN-based structure, namely, LSTM in this paper, does well in characterizing temporal behavior but is poor at dealing with very long sequences. The length of the sequence is compressed after the local feature learning block, which enhances the effectiveness and efficiency of RNN-based structure to learn global features. Among all DL algorithms, our DNN model based on DRSN and Bi-LSTM has the highest identification accuracy, which indicates that our hybrid deep architecture is competitive.

In addition, we also consider the role of AM in the proposed DNN model. The result shows that the absence of AM will lead to a decline in identification accuracy, which indicates that AM indeed enhances feature learning. Moreover, our pre-processing does not distinguish the

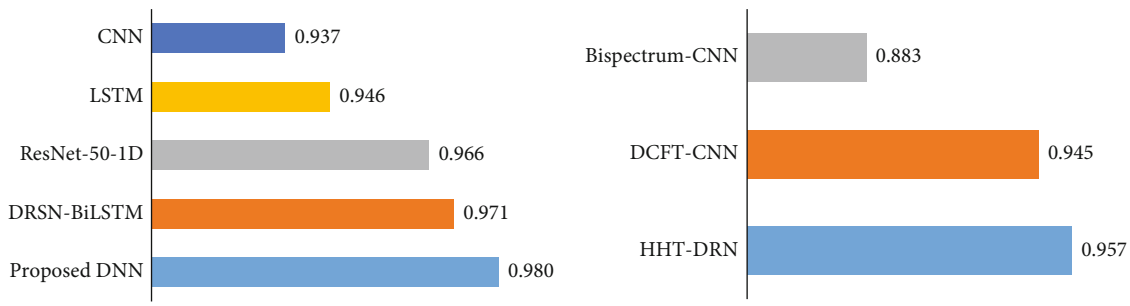

(a) DL algorithm (b) ML algorithm

Figure 13: Identification accuracy of various state-of-the-art algorithms.

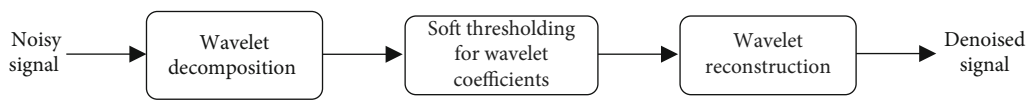

Figure 14: Wavelet denoising in the preprocessing.

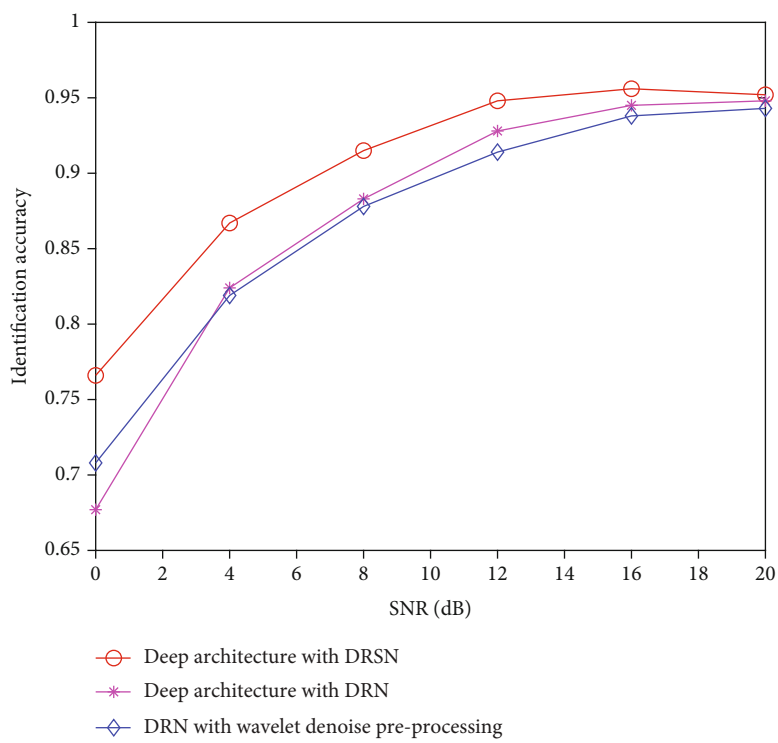

Figure 15: Performance on the noise sensitivity test under different deep architecture.

transient signal from the steady-state signal, AM aids to give different attention to the different signal periods to improve the accuracy of identification.

5.3. Noise Sensitivity Test. Next, we judge the identification performance of our algorithm under various signal qualities. Due to the limitation of acquisition conditions, we adopt the method of superimposing noise on the baseband signals. AWGN is injected with signal-to-noise ratio (SNR) ranging from 5 dB to 20 dB. It should be noted that the original signal is regarded as the unnoisy signal, so the actual SNRs are more miniature than the settings. For comparison, we use the DRN composed of standard RU and the wavelet denoise preprocessing. The wavelet denoising process is depicted in Figure 14. The 'db4' wavelet is used to decompose the noise signal in the 4th order. We then use soft thresholding to filter the wavelet coefficients and perform inverse wavelet transformation to reconstruct the target signal [33].

Figure 15 compares the identification performance of ACARS signals for different deep architecture at various

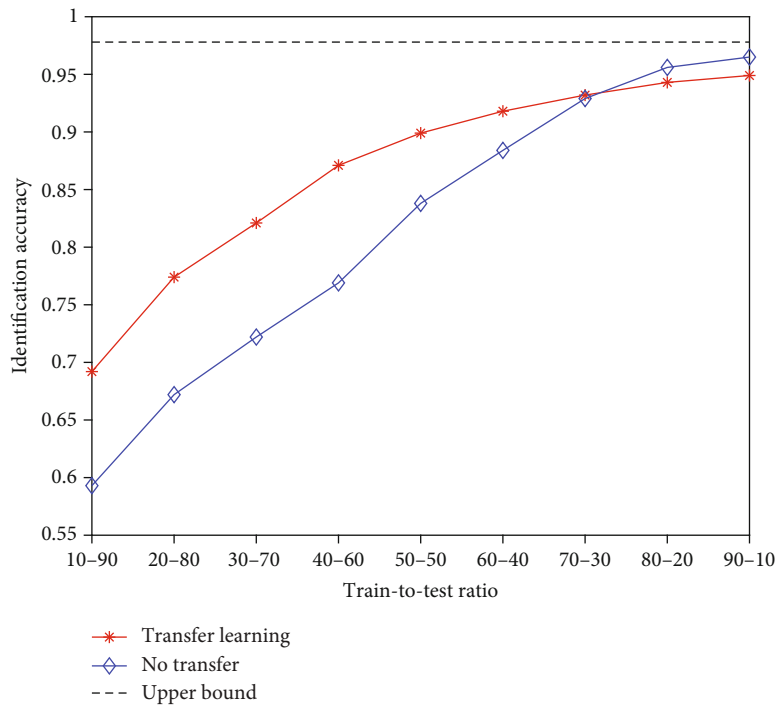

Figure 16: Performance on the robustness test for new data.

noise levels. It can be seen that compared with DRN, DRSN can enhance the resistance of the algorithm to noise disturbance, which is attributed to the stackings of several RSUs. Besides, the algorithm with denoise preprocessing performs with that without denoise preprocessing. The result suggests that denoising is not required in the preprocessing since part of the subtle characteristics representing individual differences may be removed simultaneously.

5.4. Robustness Test for New Data. At last, a new signal acquisition process was carried out a month after the first acquisition to test the robustness of our algorithm. In this experiment, we collected 1000 samples from each aircraft and divide training data and testing data according to a variable range. There are two strategies for the training process of the new data: transfer learning or no transfer. For transfer learning, the parameters are frozen in the local feature learning block, global feature learning block, and attention block, and the new data is used to re-train the dense layers in the identification block. This process can be called fine-tuning [34]. For the no transfer method, the new data is directly used to train the DNN model. In addition, the experiment uses the identification performance of a sufficient training set (containing 2000 samples) as the upper bound.

In Figure 16, we compare the two training strategies concerning the ratio of the sample number of train-to-test. It can be concluded that the performance will decrease with the shrinkage of the size of the training dataset, but using the transfer training strategy can significantly reduce the need for the number of training samples when the train-to test ratio is less than "60-40". Since feature extraction is the most time-consuming part of the training process, transfer learning can also accelerate training [34]. However, as the number of training samples increases gradually, transfer learning even inhibits the optimization of the model, leading to the decline of the identification accuracy. Therefore, we recommend using 500-600 samples for transfer learning, which can conduct the training process of new data in a relatively short time and achieve an identification accuracy of 0.90 or so, which is close to the upper bound.

6. Conclusions

This paper proposed a novel SEI algorithm based on a hybrid DNN for ACARS authentication. The deep architecture combined DRSN, Bi-LSTM, and AM so that the hybrid network has a strong ability for feature learning and focusing. First, we preprocessed the captured signal to intercept the valid part according to the ACARS protocol. Then, the inputs were propagated into the hybrid DNN to obtain the probability distribution of the predicted emitter category. We introduced soft thresholding in DRSN to enhance the robustness against noise interference and adopted the transfer learning strategy to train new data in a low-cost manner. The hyperparameters of the model were determined through various trials. Finally, we performed a series of experiments under the condition of real-world signal acquisition. The results verify the rationality of the design and show considerable advantages of our algorithm in terms of accuracy and efficiency. The superior performance of the SEI algorithm shows its tremendous potential for practical application in ACARS authentication, thus providing a reliable guarantee for aviation information security. However, our signal acquisition process is all done on the ground, and the dataset is limited in size. In future work, we will

investigate the effect of transmission channels and consider applying large-scale datasets for validation.

Data Availability

The experimental data used to support the findings of this study are available from the corresponding author upon request.

Conflicts of Interest

The authors declare that they have no conflicts of interest regarding this work.

Acknowledgments

This research was supported in part by the Natural Science Foundation of Shaanxi Province under Grant 2021JM-220, and in part by the Aeronautical Science Foundation of China under Grant ASFC-202055096001.

References

[1] A. Roy, "Secure aircraft communications addressing and reporting system (ACARS)," in *20th DASC. 20th Digital Avionics Systems Conference (Cat. No.01CH37219)*, vol. 2, pp. 7A2/1–7A2/11, Daytona Beach, FL, USA, 2001.

[2] M. Smith, M. Strohmeier, V. Lenders, and I. Martinovic, "On the security and privacy of ACARS," *Integrated Communications Navigation and Surveillance (ICNS)*, vol. 2016, pp. 1–27, 2016.

[3] C. Bresteau, S. Guigui, P. Berthier, and J. M. Fernandez, "On the security of aeronautical datalink communications: problems and solutions," in *2018 Integrated Communications, Navigation, Surveillance Conference (ICNS)*, Herndon, VA, USA, 2018.

[4] C. Perner and C. Schmitt, "Security concept for unoccupied aerial systems," in *2020 AIAA/IEEE 39th Digital Avionics Systems Conference (DASC)*, pp. 1–8, San Antonio, TX, USA, 2020.

[5] Aeronautical Radio, Incorporated, "ARINC 823 part 1 ACARS message security (AMS)," 2007, https://www.sae.org/standards/content/arinc823p1/.

[6] H. Xu, X. Chen, F. Zhu, and P. Li, "A novel security authentication protocol based on physical unclonable function for RFID healthcare systems," *Wireless Communications and Mobile Computing*, vol. 2021, Article ID 8844178, 14 pages, 2021.

[7] H. Zhou, L. Jiao, S. Zheng, L. Yang, W. Shen, and X. Yang, "Generative adversarial network-based electromagnetic signal classification: a semi-supervised learning framework," *China Communications*, vol. 17, no. 10, pp. 157–169, 2020.

[8] N. Soltanieh, Y. Norouzi, Y. Yang, and N. C. Karmakar, "A review of radio frequency fingerprinting techniques," *IEEE Journal of Radio Frequency Identification*, vol. 4, no. 3, pp. 222–233, 2020.

[9] L. Peng, A. Hu, J. Zhang, Y. Jiang, J. Yu, and Y. Yan, "Design of a hybrid RF fingerprint extraction and device classification scheme," *IEEE Internet of Things Journal*, vol. 6, no. 1, pp. 349–360, 2019.

[10] L. J. Wong, W. C. Headley, and A. J. Michaels, "Specific emitter identification using convolutional neural network-based IQ imbalance estimators," *IEEE Access*, vol. 7, pp. 33544–33555, 2019.

[11] C. Bertoncini, K. Rudd, B. Nousain, and M. Hinders, "Wavelet fingerprinting of radio-frequency identification (RFID) tags," *IEEE Transactions on Industrial Electronics*, vol. 59, no. 12, pp. 4843–4850, 2012.

[12] G. Huang, Y. Yuan, X. Wang, and Z. Huang, "Specific emitter identification based on nonlinear dynamical characteristics," *Canadian Journal of Electrical and Computer Engineering*, vol. 39, no. 1, pp. 34–41, 2016.

[13] D. Sun, Y. Li, Y. Xu, and J. Hu, "A novel method for specific emitter identification based on singular spectrum analysis," *In IEEE Wireless Communications and Networking Conference (WCNC)*, pp. 1–6, 2017.

[14] A. Jagannath, J. Jagannath, and P. S. Kumar, "A comprehensive survey on radio frequency (RF) fingerprinting: traditional approaches, deep learning, and open challenges," 2022, https://arxiv.org/abs/2201.00680.

[15] Z. Zhang, P. Cui, and W. Zhu, "Deep learning on graphs: a survey," *IEEE Transactions on Knowledge and Data Engineering*, vol. 34, no. 1, pp. 249–270, 2022.

[16] T. Young, D. Hazarika, S. Poria, and E. Cambria, "Recent trends in deep learning based natural language processing [review article]," *IEEE Computational Intelligence Magazine*, vol. 13, no. 3, pp. 55–75, 2018.

[17] L. Ding, S. Wang, F. Wang, and W. Zhang, "Specific emitter identification via convolutional neural networks," *IEEE Communications Letters*, vol. 22, no. 12, pp. 2591–2594, 2018.

[18] Y. Pan, S. Yang, H. Peng, T. Li, and W. Wang, "Specific emitter identification based on deep residual networks," *IEEE Access*, vol. 7, pp. 54425–54434, 2019.

[19] L. Peng, J. Zhang, M. Liu, and A. Hu, "Deep learning based RF fingerprint identification using differential constellation trace figure," *IEEE Transactions on Vehicular Technology*, vol. 69, no. 1, pp. 1091–1095, 2020.

[20] K. Merchant, S. Revay, G. Stantchev, and B. Nousain, "Deep learning for RF device fingerprinting in cognitive communication networks," *IEEE Journal of Selected Topics in Signal Processing*, vol. 12, no. 1, pp. 160–167, 2018.

[21] Y. Wang, G. Gui, H. Gacanin, T. Ohtsuki, O. A. Dobre, and H. V. Poor, "An efficient specific emitter identification method based on complex-valued neural networks and network compression," *IEEE Journal on Selected Areas in Communications*, vol. 39, no. 8, pp. 2305–2317, 2021.

[22] Q. Wu, C. Feres, D. Kuzmenko et al., "Deep learning based RF fingerprinting for device identification and wireless security," *Electronics Letters*, vol. 54, no. 24, pp. 1405–1407, 2018.

[23] H. Zha, Q. Tian, and Y. Lin, "Real-world ADS-B signal recognition based on radio frequency fingerprinting," in *2020 IEEE 28th international conference on network protocols (ICNP)*, pp. 1–6, Madrid, Spain, 2020.

[24] T. Jian, B. C. Rendon, E. Ojuba et al., "Deep learning for RF fingerprinting: a massive experimental study," *IEEE Internet of Things Magazine*, vol. 3, no. 1, pp. 50–57, 2020.

[25] S. Chen, S. Zheng, L. Yang, and X. Yang, "Deep learning for large-scale real-world ACARS and ADS-B radio signal classification," *IEEE Access*, vol. 7, pp. 89256–89264, 2019.

[26] Aeronautical Radio, Incorporated, "ARINC 618-8 air/ground character-oriented protocol specification," 2016, https://www.sae.org/standards/content/arinc618-8.

[27] Y. Qian, J. Qi, X. Kuai, G. Han, H. Sun, and S. Hong, "Specific emitter identification based on multi-level sparse representation in automatic identification system," *IEEE Transactions on Information Forensics and Security*, vol. 16, pp. 2872–2884, 2021.

[28] M. Zhao, S. Zhong, X. Fu, B. Tang, and M. Pecht, "Deep residual shrinkage networks for fault diagnosis," *IEEE Transactions on Industrial Informatics*, vol. 16, no. 7, pp. 4681–4690, 2020.

[29] Z. Wang, W. Yan, and T. Oates, "Time series classification from scratch with deep neural networks: a strong baseline," in *2017 International Joint Conference on Neural Networks (IJCNN)*, pp. 1578–1585, Anchorage, AK, USA, 2017.

[30] R. He, Y. Liu, K. Wang et al., "Automatic cardiac arrhythmia classification using combination of deep residual network and bidirectional LSTM," *IEEE Access*, vol. 7, pp. 102119–102135, 2019.

[31] P. Kavianpour, M. Kavianpour, E. Jahani, and A. Ramezani, "A CNN-BiLSTM model with attention mechanism for earthquake prediction," 2021, https://arxiv.org.abs/2112.13444.

[32] J. Ma, H. Liu, C. Peng, and T. Qiu, "Unauthorized broadcasting identification: a deep LSTM recurrent learning approach," *IEEE Transactions on Instrumentation and Measurement*, vol. 69, no. 9, pp. 5981–5983, 2020.

[33] D. L. Donoho, "De-noising by soft-thresholding," *IEEE Transactions on Information Theory*, vol. 41, no. 3, pp. 613–627, 1995.

[34] F. Zhuang, Z. Qi, K. Duan et al., "A comprehensive survey on transfer learning," *Proceedings of the IEEE*, vol. 109, no. 1, pp. 43–76, 2021.

Hindawi
Wireless Communications and Mobile Computing
Volume 2022, Article ID 8008460, 8 pages
https://doi.org/10.1155/2022/8008460

Research Article

A Novel Approach Based on Generative Adversarial Network for Signal Enhancement in Wireless Communications

Shoushuai He,[1] **Lei Zhu**,[1] **Changhua Yao**,[2] **Lei Wang**,[1] **and Zhen Qin**[1]

[1]*College of Communications Engineering, Army Engineering University, Nanjing 210007, China*
[2]*School of Electronic and Information Engineering, Nanjing University of Information Science and Technology, Nanjing 210044, China*

Correspondence should be addressed to Lei Zhu; zhulei_paper@126.com and Changhua Yao; ych2347@163.com

Received 1 May 2022; Revised 1 August 2022; Accepted 4 August 2022; Published 16 September 2022

Academic Editor: Mingqian Liu

Wireless communication signals are often affected by noise and interference in the channel during transmission, which makes it difficult for the receiver to analyze. The signal enhancement technology can suppress the noise and interference in the signal, so as to improve the communication quality. It is one of the main research directions of signal processing. Classical enhancement methods separate the signals through separable transform domain. Artificial construction of the corresponding separable transform domain requires prior information of noise and interference, but they have the characteristics of randomness. Further, these methods usually use high-level features and rely on statistics, so they can only deal with specific noise conditions. At present, deep learning is increasingly applied in the field of wireless communications due to its powerful feature extraction ability for large sample sets. In this paper, a communication signal enhancement model based on generative adversarial network (GAN) is proposed. Compared with classical methods, the signal is operated directly and the model is trained end-to-end. It can adapt to different noise conditions and avoid the above problems. An independent and invisible test set is used to evaluate several comparative methods. The experimental results confirm the effectiveness of the proposed model.

1. Introduction

Cognitive radio technology has shown superior performance in the field of wireless communications [1]. In the transmission process, however, the signal cannot avoid the influence of noise and interference due to the limited transmission bandwidth and the multipath effect of the channel. It increases the difficulty of demodulation and reduces the ability of spectrum sensing. Since it is meaningful to process and analyze high-quality signals, it is necessary to eliminate noise and interference in the received signals. Signal enhancement attempts to improve the signal quality in noisy environments, which can promote the development of communication technology. In addition, it can also be used in the preprocessing stage of wireless communications.

A variety of signal enhancement methods have been proposed, mainly divided into two categories: linear method and nonlinear method [2]. Based on the assumption that the signal is stationary, the linear method is relatively simple, but it may not find the global optimal solution to eliminate noise and interference. The actual communication signal usually has nonstationary statistical characteristics, so the nonlinear method has more advantages, which uses the time and spectrum information in the signal. Traditional methods need prior information of noise and interference, and then map them into separable transform domain for separation. However, the randomness of noise and interference makes it difficult to construct the corresponding separable transform domain. So these methods fail to adaptively complete real-time signal enhancement.

In terms of frequency domain, nonstationary interference can be eliminated by using band-pass filters, then the signal in the required frequency band can be obtained. In the ideal case, once the corresponding index is given, the filter can be designed to meet the requirements [3]. But in the general case, the parameters of the signal to be identified may be unknown, such as bandwidth and center frequency. And the influence of the external environment on the

statistical characteristics of the received signal is unpredictable. These make the performance of the predesigned filter degrade, or even fail to work. Consequently, adaptive filters are proposed to solve these problems [4]. Their optimization process is adjusted according to the changes of the external environment. Since the response is relatively lagging, it is difficult for them to deal with the interference signal whose statistical characteristics change rapidly. In brief, classical enhancement methods use filters or transform domains to eliminate noise and interference, and they cannot adaptively learn signal features.

In recent years, deep learning has been used to solve many classical communication problems. Compared with machine learning algorithm, the deep learning model has better ability of feature extraction and adaptive learning for complex and dynamic data distribution. It has made great progress in the field of wireless communications [5, 6]. These valuable researches provide some references for communication signal enhancement. For the method based on deep learning, there is no need to make clear assumptions about the original data, and its application in electromagnetic signal anti-interference, which means the reduction and suppression of interference existing in the signal will become a development trend [7–9].

Generative model is a learning framework [10], whose purpose is to generate fake samples like real ones. An important breakthrough of deep learning in generative model is generative adversarial network (GAN) [11]. GAN has shown excellent performance in the field of computer vision. It can generate realistic images and learn complex high-dimensional distributions. For wireless communications, it is also applied to spectrum sensing tasks [12].

Inspired by SEGAN [13], a communication signal enhancement model based on generative adversarial network is constructed in this paper. The model avoids complex transformation of the original signal. And its end-to-end structure is different from the traditional method. It adaptively eliminates dynamic noise and interference, thus has better robustness. The generator in the model learns the distribution characteristics of the original signal in an adversarial way. And the original signal is used as conditional information to generate an enhanced signal. Even if the external environment changes, the model can effectively achieve the goal of signal enhancement. The training process is independent of the specific application, so it can be embedded into the wireless communication system as a preprocessing module.

The proposed communication signal enhancement model is universal and real-time. Its main advantages include: (1) it adopts an end-to-end mode and operates signals directly. The model avoids extracting artificial features through intermediate transformation and making clear assumptions on the original data, which is quite different from the common pipeline. (2) It provides a fast enhancement process. The model excludes causality and recursive operations like recurrent neural network (RNN) [14]. (3) It learns from different types of signals and interferences. The model has good adaptive ability. Although the statistical characteristics of the external environment are variable and unpredictable, the performance of the model is not affected.

The specific contents of this paper are summarized as follows: next, the principle and structure of generative adversarial network are introduced. In Section 3, the proposed model is described in detail. The parameter settings are described and the experimental results are discussed in Section 4. Finally, this paper is concluded in Section 5.

2. Generative Adversarial Network

GAN is a generative model, which generates new samples according to the real data distribution through adversarial training. It consists of two components: a generator G and a discriminator D. The task of G is to learn an effective mapping that simulates the real data distribution and generates new samples. G learns by mapping the distribution characteristics to a predefined manifold, rather than by memorizing input-output pairs. D is a typical binary classifier. Its purpose is to classify the samples from the original data as real and the samples generated by G as fake.

The adversarial behavior is that G generates fake samples, while D distinguishes between real samples from original data and fake samples generated by G. G tries to trick D into classifying the fake samples as real. In the process of back propagation, D gets better in finding the real distribution characteristics. In turn, G adjusts its parameters to make the fake samples closer to the real data manifold. Through alternate training, G and D form a dynamic game process, as shown in Figure 1. According to the feedback of D, G gradually generates fake samples similar to real samples. When the training balance is reached, D can only randomly discriminate whether the samples generated by G are real or fake. It means that the discrimination accuracy of D is about 50 percent. The objective function of GAN is expressed in the following as a min-max game between G and D:

$$\min_G \max_D V(D, G) = E_{x\sim p_X(x)}[\log D(x)] + E_{z\sim p_Z(z)}[\log (1 - D(G(z)))]. \tag{1}$$

3. Communication Signal Enhancement Model

3.1. Objective Function. The original GAN is difficult to control with the generated samples, which leads to the mismatch between the enhanced signal and the noisy signal. In order to solve this problem, conditional generative adversarial network (CGAN) is introduced in this paper. In CGAN, conditional variables guide the data generation process [15]. The additional information helps G and D perform mapping and classification. In this way, the model is ensured to generate a corresponding enhanced signal. In the proposed model, the clean signal is used as a conditional variable, and the objective function is changed to the following:

$$\begin{aligned}\min_G \max_D V(D, G) = {} & E_{x,x_c\sim p_X(x,x_c)}[\log D(x, x_c)] \\ & + E_{z\sim p_Z(z),x_c\sim p_X(x_c)}[\log (1 - D(G(z, x_c), x_c))].\end{aligned} \tag{2}$$

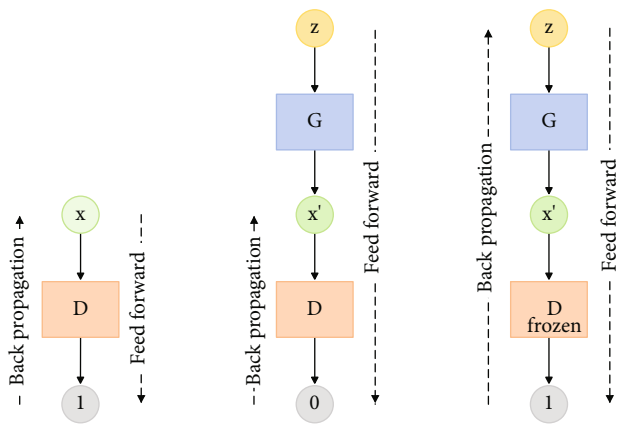

Figure 1: Dynamic game of GAN.

The classical GAN suffers from gradient disappearance due to the cross entropy loss used for training. In view of this problem, least square generative adversarial network (LSGAN) uses the least square function to replace the sigmoid cross entropy [16]. This improvement can stabilize the training and improve the quality of the generated samples. The proposed model adopts a binary form of the least square function, where 1 and 0 represent real and fake, respectively. Therefore, the above equation is changed to the following form:

$$\min_D V(D) = E_{x,x_c\sim p_X(x,x_c)}\left[(D(x,x_c)-1)^2\right] + E_{z\sim p_Z(z),x_c\sim p_X(x_c)}\left[D(G(z,x_c),x_c)^2\right], \tag{3}$$

$$\min_G V(G) = E_{z\sim p_Z(z),x_c\sim p_X(x_c)}\left[(D(G(z,x_c),x_c)-1)^2\right]. \tag{4}$$

In order to minimize the distance between the generated sample and the original sample, a minor component should be added to the loss of generator G. In the proposed model, L_1 norm is selected to represent the distance, which has been proved to be effective in the field of image processing [17]. In this way, G can generate more fine-grained samples and approximate the original signal waveform. The magnitude of L_1 norm is controlled by hyperparameter α, and the loss function of G is further changed to:

$$\min_G V(G) = E_{z\sim p_Z(z),x_c\sim p_X(x_c)}\left[(D(G(z,x_c),x_c)-1)^2\right] + \alpha\|G(z,x_c)-x\|_1. \tag{5}$$

3.2. Generator Structure. The structure of generator G is similar to that of auto-encoder [18], as shown in Figure 2. In the encoding stage, the input signal is compressed through multiplestrided convolutional layers, followed by Leaky ReLU. For the training of GAN, strided convolution is proved to be more stable than other pooling methods [19], so it is selected to calculate the convolution results. Compression is performed until the representation vector c is obtained, which is connected to the latent vector z. The encoding process is reversed by deconvolution in the decoding stage, also followed by Leaky ReLU.

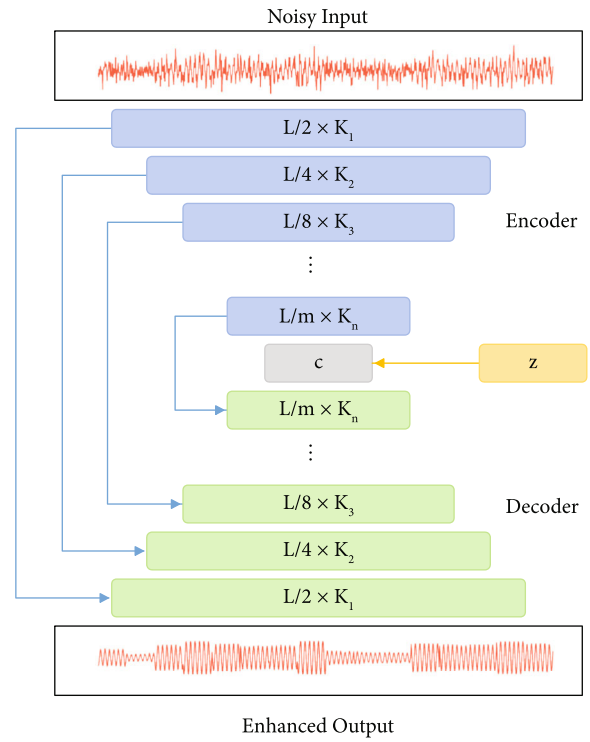

Figure 2: Structure of G.

The structure of generator G also includes skip connections, as shown in Figure 2. They connect each encoding layer to its corresponding decoding layer and bypass the compression performed in the middle of the structure. In this way, the inputs and outputs of the network share the same features. On the contrary, if all the information is forced through the compression, many low-level details used to accurately reconstruct the signal may be lost. The skip connections directly transfer the fine-grained information of the signal to the decoding stage. In addition, they can provide better training behavior, because gradients can pass deeper through the entire structure [20].

3.3. Convolutional Layer. Both generator G and discriminator D are composed of convolutional layers, without fully connected layers. It makes the model focus on the correlation in the input signal. In addition, it reduces the training parameters, thus reduces the training time.

The encoding-decoding structure of G is composed of strided convolutional layers and corresponding deconvolutional layers. In the encoding stage, the number of filters in each layer increases compared with the previous layer. Therefore, the depth gets larger as the width gets smaller. As described above, the decoding stage is symmetrical to the encoding stage, with the same number and size of filters per layer. Skip connections and additional latent vectors double the number of feature maps in each layer. Finally, the generated signal can be restored to the same width as the input signal.

D follows almost the same convolution structure as the encoding stage of G. The difference is that it has dual input channels and an extra convolutional layer for classification.

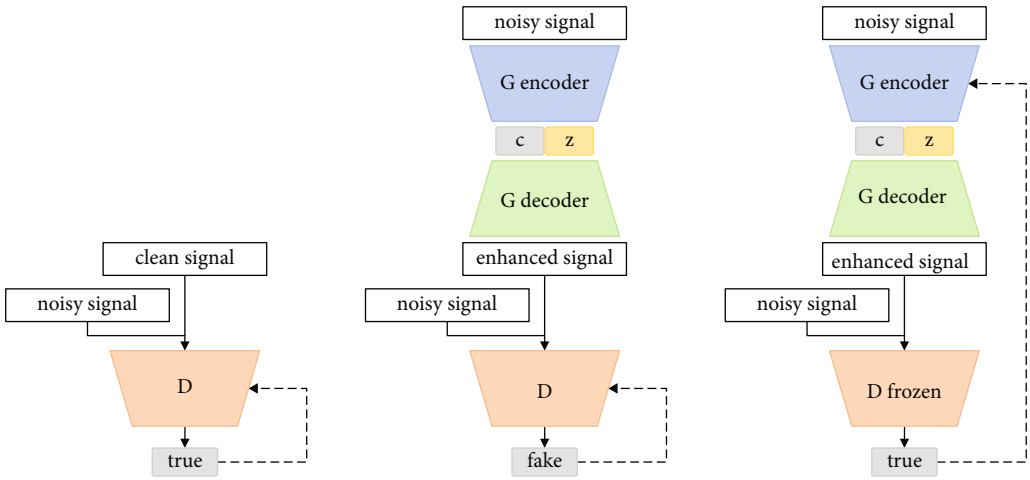

Figure 3: Adversarial training of the proposed model.

The extra convolutional layer is connected after the last activation layer, in which the filter width is 1. It further reduces the number of parameters required for classification.

In the proposed model, virtual batch normalization (VBN) is performed after the convolutional layer, which normalizes the input of each neuron and adds a bias term [21]. VBN can not only solve the problem of unstable training caused by poor initialization but also avoid the problem in which generator G maps the generated samples to a single point.

For the problem of communication signal enhancement, the noisy signal is processed to obtain an enhanced signal. Based on generative adversarial network, a communication signal enhancement model is proposed in this paper. The adversarial training of the proposed model is shown in Figure 3, which can be regarded as a game process between G and D. The generator G performs enhancement, its input is a noisy signal and a latent representation, and its output is an enhanced signal. The discriminator D performs classification, its input is a real pair composed of a noisy signal and a clean signal, or a fake pair composed of a noisy signal and an enhanced signal. According to the characteristics of communication signals, the conditional generative adversarial network is adopted, the loss function is improved, and the model structure is established. On this basis, the proposed model can eliminate the noise and interference in the signal without extracting artificial features.

4. Evaluation

4.1. Parameter Setup. In order to verify the validity of the proposed model, a simulated communication dataset is used in this paper. For signal types, several modulation modes with wide application and high spectral efficiency are selected in the experiment, including BPSK, QPSK, 8PSK, 16QAM, and 32QAM. There are two sets of signals: the original clean signal and the noisy signal with noise and interference. The noisy signal to be enhanced is composed of clean signal, Gaussian white noise, and other interference signals. In the training phase, the clean signal and the corresponding noisy signal are connected then fed to the model, where the clean signal is used as a condition. In order to further prove the adaptability of the proposed model, the test set is set to be different from the training set, the noise and interference in the test set are also set to be different from those in the training set.

In the experiment, the signal is down-sampled at a sampling rate of 2 MHz, and a sliding window is used to segment the signal into a fixed length of 1024 sampling points. The total number of signals in the training set and the test set for each condition is 9000 and 1000, respectively. Adam optimizer is adopted to optimize network parameters. The learning rate is set to 0.0002, the epoch is set to 20, and the batch size is set to 100. For the network structure, the generator G is composed of 14 convolutional layers, with a filter width of 31 and a stride of 2. All hyperparameters are determined by a large number of experiments.

4.2. Experimental Results. In order to evaluate the quality of the enhanced signal, signal-to-noise ratio (SNR) and root mean square error (RMSE) are selected as evaluation metrics in the experiment. Three typical enhancement systems based on deep learning are constructed as the baseline method, which further demonstrates the superiority of the proposed model. The first one uses deep auto-encoder (DAE) [22], which is a network structure commonly used for denoising. The second one uses convolutional neural network (CNN) for enhancement [23]. The third one is a modification of GAN [24].

The goal of alternate training is to get a generative network, which removes noise and interference, then realizes signal enhancement. After the training is completed, the noisy signal is fed into the generative network to obtain an enhanced signal. Figures 4–6 show the clean signal, the noisy signal, and the enhanced signal generated by the proposed model, respectively, when the modulation mode is 16QAM and the SNR is 0 dB. The signals before and after enhancement are compared in terms of waveforms. It can be seen that the enhanced signal is similar to the original clean signal.

In the first part of the experiment, a specific modulation signal is optimized, which is only overlapped by noise. The

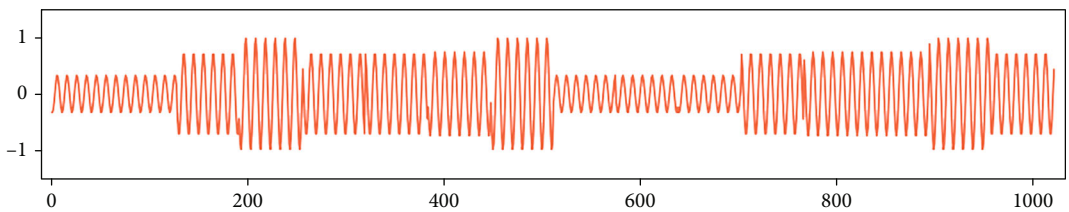

Figure 4: Clean signal.

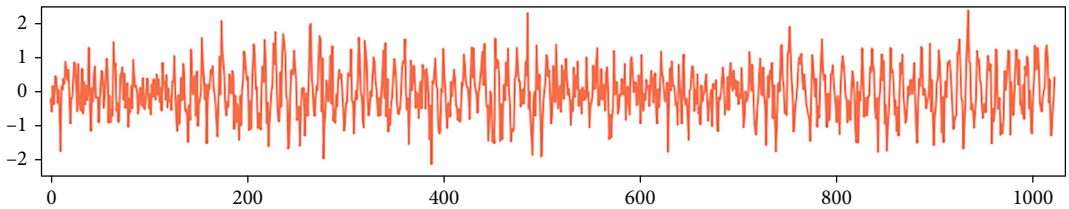

Figure 5: Noisy signal.

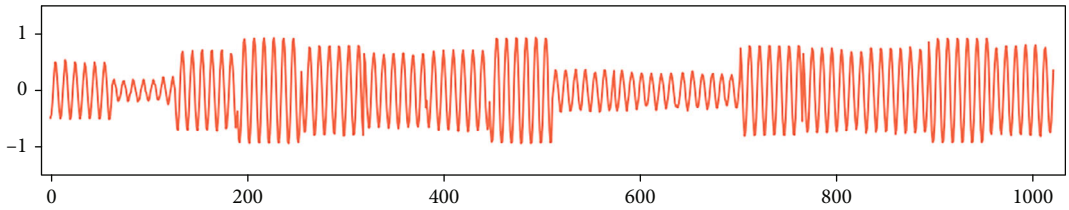

Figure 6: Enhanced signal generated by the proposed model.

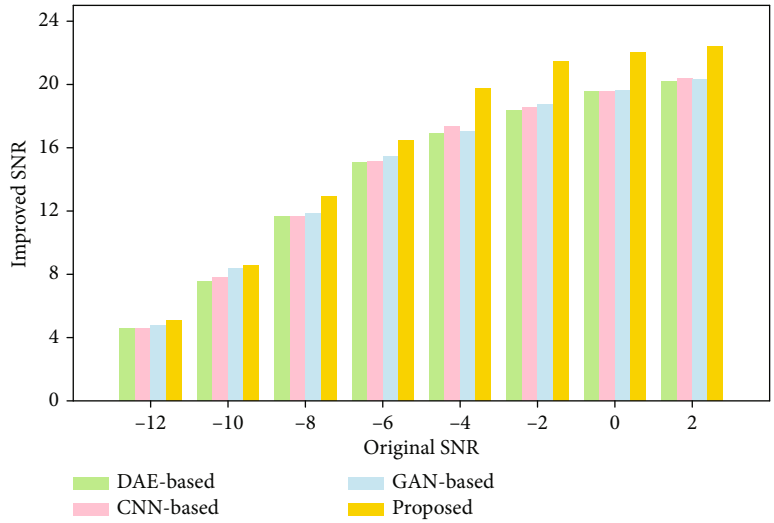

Figure 7: Improvement of SNR in QPSK scene.

improved SNR is calculated, the higher the better. In order to intuitively reflect the enhancement effect in QPSK scene, Figure 7 depicts the improvement comparison of four methods for noisy signals with different original SNR. As can be seen, all methods can solve the problem of signal enhancement, and the proposed model performs better. Whether in the case of high or low SNR, it provides better results than other methods.

The enhancement model should not be limited to certain types of wireless signals, but should be suitable for most types. Therefore, a signal dataset composed of other modulation modes is also tested, in which the original signal is

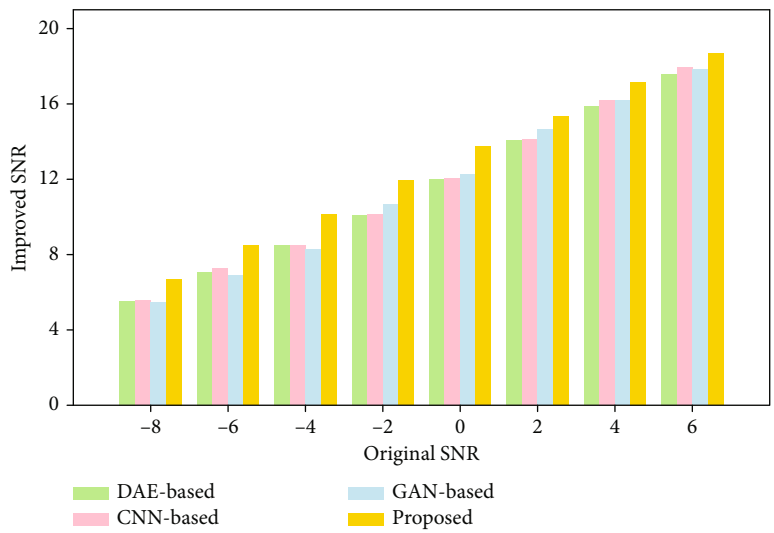

Figure 8: Improvement of SNR in 16QAM scene.

Table 1: RMSE for specific SNR in 16QAM scene.

Methods	-8	-6	-4	-2	0	2	4	6
DAE-based	0.2940	0.2467	0.2068	0.1721	0.1412	0.1164	0.0938	0.0815
CNN-based	0.2957	0.2520	0.2082	0.1752	0.1412	0.1183	0.0961	0.0809
GAN-based	0.2943	0.2517	0.2066	0.1655	0.1365	0.1094	0.0966	0.0791
Proposed	**0.2580**	**0.2140**	**0.1821**	**0.1487**	**0.1245**	**0.1031**	**0.0885**	**0.0782**

Table 2: RMSE for various SNR in 16QAM scene.

Methods	-8	-6	-4	-2	0	2	4	6
DAE-based	0.2960	0.2430	0.2000	0.1659	0.1395	0.1195	0.1047	0.0940
CNN-based	0.2957	0.2430	0.2004	0.1665	0.1402	0.1205	0.1057	0.0953
GAN-based	0.2893	0.2383	0.1972	0.1648	0.1399	0.1212	0.1076	0.0980
Proposed	**0.2393**	**0.1985**	**0.1662**	**0.1415**	**0.1229**	**0.1093**	**0.0996**	**0.0929**

set to different amplitude and carrier frequency. For 16QAM modulation signal, the same experiment is carried out to prove the universality of the proposed model. The experimental results are presented in Figure 8. Obviously, the proposed model can still achieve the ideal enhancement effect. It indicates that the proposed model can adapt to various changes in the characteristics of the original signal.

For the case that the clean signal is overlapped by noise and other types of interference signals with the same or similar carrier frequency, the RMSE of the enhanced signal is calculated, the lower the better. Table 1 lists the experimental results for specific SNR and interference type in 16QAM scene. It can be seen that RMSE is significantly reduced by the proposed model. It verifies that the proposed model can not only effectively eliminate the noise, but also moderately reduce the interference with the same frequency.

The enhancement performance of the proposed model for various SNR and unknown interference is evaluated in the last part of the experiment. Specifically, the clean signal in the training set is overlapped by noise with a specific SNR and interference with a specific type. But the SNR range and interference type of noisy signals in the test set are quite different from those in the training set. Table 2 shows the enhancement performance in 16QAM scene. The training set contains noisy signals whose SNR is only 0 dB. For other conditions, noise and interference can still be reduced, which reflects the strong robustness of the proposed model.

The analysis of the above experimental results indicates that the proposed model has better enhancement performance among the competitive methods.

5. Conclusion

Signal enhancement can be embedded into practical applications in the field of wireless communications as a preprocessing module. Traditional enhancement methods usually have some disadvantages, such as the lack of universality for noise and interference and lack of adaptive learning ability for signal features. When the external environment changes, they are difficult to distinguish between the signal

and the noise, resulting in the decline of the enhancement effect. In this paper, an end-to-end communication signal enhancement model is proposed to solve the above problems. In the framework of generative adversarial network, the model adopts the encoding-decoding structure based on convolutional layer. It aims to rapidly eliminate noise and interference in the signal. Moreover, the improvement process of the objective function is analyzed, the design structure of the model is provided, and the feasibility of the model is verified by a large number of experiments. The experimental results confirm that the proposed model is more effective for communication signal enhancement than other deep learning-based methods.

Data Availability

The simulated dataset used to support the findings of this study are available from the corresponding author upon request.

Conflicts of Interest

The authors declare that there is no conflict of interest regarding the publication of this paper.

Acknowledgments

This work is supported by the National Natural Science Foundation of China No. 61702543 and No. 61971439, the Natural Science Foundation of Jiangsu Province No. BK20191329, the China Postdoctoral Science Foundation No. 2019T120987, and the Startup Foundation for Introducing Talent of Nanjing University of Information Science and Technology No. 2020r100.

References

[1] M. Hajiabadi, H. Khoshbin, and H. G. Abed, "Cooperative spectrum estimation over large-scale cognitive radio networks," *IET Signal Processing*, vol. 11, no. 8, pp. 1006–1014, 2017.

[2] B. Bilgehan, "Efficient approximation for linear and non-linear signal representation," *IET Signal Processing*, vol. 9, no. 3, pp. 260–266, 2015.

[3] X.-P. Mao, Y.-L. Yang, H. Hong, and W. B. Deng, "Multi-domain collaborative filter for interference suppressing," *IET Signal Processing*, vol. 10, no. 9, pp. 1157–1168, 2016.

[4] S. M. Jung and P. Park, "Normalised least-mean-square algorithm for adaptive filtering of impulsive measurement noises and noisy inputs," *Electronics Letters*, vol. 49, no. 20, pp. 1270–1272, 2013.

[5] X. Zhou, Z. Sun, H. Wu, and Q. Wu, "Embeddable convolutional layer-based filter for wireless signal detection," in *2019 IEEE Wireless Communications and Networking Conference Workshop (WCNCW)*, pp. 1–6, Marrakech, Morocco, 2019.

[6] Z. Sun, J. Li, and J. Fan, "Convolutional neural filtering for intelligent communications signal processing in harsh environments," *IEEE Access*, vol. 9, pp. 8212–8219, 2021.

[7] H. Ye, G. Y. Li, and B.-H. Juang, "Power of deep learning for channel estimation and signal detection in OFDM systems," *IEEE Wireless Communications Letters*, vol. 7, no. 1, pp. 114–117, 2018.

[8] Y. Wang, L. Tu, J. Guo, and Z. Wang, "Residual learning based RF signal denoising," in *2018 IEEE International Conference on Applied System Invention (ICASI)*, pp. 15–18, Chiba, Japan, 2018.

[9] T. Xu, T. Xu, and I. Darwazeh, "Deep learning for interference cancellation in non-orthogonal signal based optical communication systems," in *2018 Progress in Electromagnetics Research Symposium (PIERS-Toyama)*, pp. 241–248, Toyama, Japan, 2018.

[10] M. Wu, Z. He, X. Zhao, and S. Zhang, "General generative model-based image compression method using an optimisation encoder," *IET Image Processing*, vol. 14, no. 9, pp. 1750–1758, 2020.

[11] I. Goodfellow, J. Pouget-Abadie, M. Mirza et al., "Generative adversarial nets," in *Proceedings of the 27th International Conference on Neural Information Processing Systems*, pp. 2672–2680, 2014.

[12] K. Davaslioglu and Y. E. Sagduyu, "Generative adversarial learning for Spectrum sensing," in *2018 IEEE International Conference on Communications (ICC)*, pp. 1–6, Kansas City, MO, USA, 2018.

[13] S. Pascual, A. Bonafonte, and J. Serrà, "SEGAN: speech enhancement generative adversarial network," 2017, https://arxiv.org/abs/1703.09452.

[14] F. Weninger, H. Erdogan, S. Watanabe et al., "Speech enhancement with LSTM recurrent neural networks and its application to noise-robust ASR," *Latent Variable Analysis and Signal Separation*, pp. 91–99, 2015.

[15] P. Isola, J. Y. Zhu, T. Zhou, and A. A. Efros, "Image-to-image translation with conditional adversarial networks," in *2017 IEEE Conference on Computer Vision and Pattern Recognition (CVPR)*, pp. 5967–5976, 2017.

[16] X. Mao, Q. Li, H. Xie, R. Y. Lau, Z. Wang, and S. Paul Smolley, "Least squares generative adversarial networks," in *2017 IEEE International Conference on Computer Vision (ICCV)*, pp. 2813–2821, 2017.

[17] D. Pathak, P. Krahenbuhl, J. Donahue, T. Darrell, and A. A. Efros, "Context encoders: feature learning by Inpainting," in *2016 IEEE Conference on Computer Vision and Pattern Recognition (CVPR)*, pp. 2536–2544, 2016.

[18] V. Badrinarayanan, A. Kendall, and R. Cipolla, "SegNet: a deep convolutional encoder-decoder architecture for image segmentation," *IEEE Transactions on Pattern Analysis and Machine Intelligence*, vol. 39, no. 12, pp. 2481–2495, 2017.

[19] A. Radford, L. Metz, and S. Chintala, "Unsupervised representation learning with deep convolutional generative adversarial networks," in *4th International Conference on Learning Representations, ICLR 2016*, 2016.

[20] K. He, X. Zhang, S. Ren, and J. Sun, "Deep residual learning for image recognition," in *2016 IEEE Conference on Computer Vision and Pattern Recognition (CVPR)*, pp. 770–778, 2016.

[21] T. Salimans, I. Goodfellow, W. Zaremba, V. Cheung, A. Radford, and X. Chen, "Improved techniques for training GANs," in *Proceedings of the 30th International Conference on Neural Information Processing Systems*, pp. 2234–2242, 2016.

[22] H. Li, S. Chen, S. Xu, Z. Song, J. Chen, and D. Zhao, "EMI signal feature enhancement based on extreme energy difference and deep auto-encoder," *IET Signal Processing*, vol. 12, no. 7, pp. 852–856, 2018.

[23] Y. Dai, T. Jin, Y. Song, H. du, and D. Zhao, "CNN-based multiple-input multiple-output radar image enhancement method," *The Journal of Engineering, The Institution of Engineering and Technology*, vol. 2019, no. 20, pp. 6840–6844, 2019.

[24] F. Li, J. Zheng, and Y. Zhang, "Generative adversarial network for low-light image enhancement," *IET Image Processing*, vol. 15, no. 7, pp. 1542–1552, 2021.

Hindawi
Wireless Communications and Mobile Computing
Volume 2022, Article ID 9167017, 15 pages
https://doi.org/10.1155/2022/9167017

Research Article

Optimization of Rolling Schedule for Single-Stand Reversible Cold Rolling Mill Based on Multiobjective Artificial Fish Swarm Algorithm

Zhe Yang,[1,2] Ding Liu,[1,2] Xinyu Zhang,[1,2] Weichao Huang,[1,2] and Gang Zheng[1,2]

[1]*Faculty of Automation and Information Engineering, Xi'an University of Technology, Xi'an 710048, China*
[2]*Shaanxi Key Laboratory of Complex System Control and Intelligent Information Processing, Xi'an University of Technology, Xi'an 710048, China*

Correspondence should be addressed to Zhe Yang; yangzhex@126.com

Received 5 August 2022; Revised 29 August 2022; Accepted 30 August 2022; Published 16 September 2022

Academic Editor: Mingqian Liu

The single-stand reversible cold rolling mill is important equipment in the production of steel strips. The rolling schedule is the core technological content in the strip production of the single-stand reversible cold rolling mill. The scientific rolling schedule is the fundamental guarantee for the production capacity of the rolling mill, product quality, accuracy, shape quality, energy saving, and consumption reduction. This paper takes the dynamic rolling process of single-stand cold rolling as the research object, the purposes of increasing production capacity, saving energy, and reducing consumption are achieved by optimizing the rolling schedule. Based on the study of the mechanism model and the analysis of a large number of field measured data, a slice of mathematical models of the rolling process suitable for engineering calculation are proposed, and a few objective functions suitable for the single-stand reversible cold rolling process are designed. On this basis, the artificial fish swarm algorithm is improved into a multiobjective optimization algorithm for the optimization of rolling schedule, and the optimal rolling load distribution scheme is obtained. Finally, the optimization method of rolling schedule proposed in this paper is applied to the actual rolling production. The results show that the proposed method can improve productivity and save energy compared with the empirical rolling schedule, and the feasibility and validity of the proposed algorithm are verified.

1. Introduction

The cold-rolled sheets and strips are an important steel product for iron and steel enterprises, and it is also the product with the highest technical content in iron and steel products. It is widely used in automobiles, ship, construction, home appliances, light industry, machinery manufacturing, chemicals, hardware products, and packaging industries. The single-stand reversible cold rolling mill is important equipment for steel sheet and strip production. Although, compared with the tandem cold rolling mill, the single-stand reversible cold rolling mill has the disadvantages of low production efficiency and low yield, but the advantage of it is that the production method is relatively flexible, suitable for the production of ultrathin strip steel, low investment, and can produce a variety of small batches of products of different specifications. Therefore, the single-stand reversible cold rolling mill has an irreplaceable role. With the continuous improvement of the quality requirements of cold-rolled products and the pressure of cost, environmental protection, market, and other aspects, the production of modern single-stand reversible cold-rolling mills has the extreme pursuit of high precision, high yield, high production efficiency, and low production cost. In this case, for the single-stand cold rolling mill, in addition to improving the control accuracy of the automatic control system through advanced control methods, the rolling process is also put forward with higher requirements. Rolling

schedule is the core process technology in rolling production, which has a significant impact on production, quality, cost, production safety, and process control accuracy. Reasonable rolling schedule can not only improve the productivity of strip steel, reduce energy consumption but also ensure product quality, improve process control accuracy, response speed, equipment utilization efficiency, and bring great economic benefits.

The cold rolling process has a complex mechanism, with typical characteristics of multivariable, strong coupling, nonlinear, and time-varying, it is very difficult to calculate accurately. Therefore, the traditional main methods of rolling schedule design are empirical form method, energy consumption curve method, and load distribution method based on rolling theory.

The empirical form method refers to the method of directly assigning the reduction amount and thickness of each pass or stand through the operator's production experience, and recording this experience through a table to form a standard rolling specification table as the basis for load distribution. The most significant advantage of the empirical form method is that it is easy to use and does not require complex theoretical calculations and machine operations [1]. At present, this method is still used in many steel companies. However, the empirical form method completely relies on the operator's experience, and it may not be optimal with the change of production conditions.

The energy consumption curve method is drawing the relationship between the power required for rolling a unit mass of rolled pieces and the thickness or elongation according to the historical rolling data. Since the inlet thickness and target thickness of the rolled piece have been determined, the total rolling power can be calculated from the energy consumption curve. On the premise that the load distribution ratio of each pass is known, the intermediate thickness of each pass can be derived according to the energy consumption curve, it means the reduction amount distribution scheme can be determined. This method has a long history of application and has been applied in hot tandem rolling as early as 1964 [2]. This method is effective when rolling strips of the same specification, but it is difficult to guarantee the rolling accuracy once the specification is changed, and it is necessary to repeat the experiment to draw the curve.

The load distribution method based on the rolling theory is to give full play to the production capacity of the rolling mill and prevent the overload of the mill load, so that the ratio between the production load and the limit load of each pass is constant, which is also called the load proportionality principle. The load value (reduction rate, rolling force, and motor power) of each pass can be calculated according to the relevant rolling mathematical model. Furthermore, the target thickness for each pass is obtained by solving a set of nonlinear equations. The Newton-Raphson method was used to solve the nonlinear equation system [3], but this method needs to solve the inverse of the Jacobian matrix and the reciprocal of the rolling load to the thickness, which is complicated to calculate and sensitive to the initial value [4]. Many scholars have improved this method and reduced the amount of computation [5, 6]. However, the load distribution method based on rolling theory still cannot get rid of the dependence of artificial experience.

To get rid of the influence of empirical values, optimization techniques are introduced into rolling schedule optimization. Especially, with the improvement of industrial computer performance, many single-objective and multiobjective intelligent optimization algorithms have been applied to rolling schedule design in recent years, and various objective functions have been established for different technological objectives. Because of the high efficiency and fast running speed, the rolling schedule design based on single objective optimization algorithm has been widely used in practical production. Jin et al. designed the load distribution using a genetic algorithm method with excellent flatness as the objective function [7]. Cao et al. used the self-adaptive particle swarm optimization algorithm to design the load distribution model [8]. With the increasing requirements of rolling production, the increasing factors need to be considered, and the results of load distribution according to a single objective function are difficult to fully meet the various requirements of the rolling process. Therefore, multiobjective optimization methods are gradually introduced into rolling schedule design. The optimization method of multiobjective rolling schedule is divided into a priori method and a posteriori method. In the priori method, the multiobjective optimization problem is transformed into a single-objective optimization problem by means of a weighted sum. Yang et al. used a set of fixed weight coefficients to convert the motor power consumption objective function and the slip prevention objective function into a comprehensive objective function and optimized the rolling schedule through an improved artificial bee colony algorithm based on chaos theory [9]. Chen et al. proposed a schedule optimization model based on cost functions, which take rolling force, motor power, interstand tension, and stand reduction into consideration, and the Nelder-Mead simplex method was used to optimize the rolling schedule [10]. Bu et al. transformed the power objective function, tension objective function, and flatness objective function into a comprehensive objective function through the influence function, and the Tabu search algorithm was used to optimize the rolling schedule [11]. Wang et al. designed a dynamic adjustment model for the weight coefficients of objectives based on rolling length and used NSGA-II to optimize the rolling schedule [12]. The difficulty of the a priori method lies in the determination of the weight coefficient, and the choice of the weight coefficient directly affects the optimization effect. Compared with the prior method, the posterior method is more suitable for practical applications. The posterior method obtains a set of complementary dominant Pareto solution set for selecting according to the actual requirements without setting weight coefficients. Che et al. used the chaotic multiobjective quantum genetic algorithm to optimize the rolling schedule with the equal relative load and flatness of the last stand as the objective functions [13]. Li and Fang designed a robust multiobjective optimization model of rolling schedule for tandem cold rolling and proposed a differential evolution algorithm based on the evolutionary direction [14]. Wei et al. used an improved

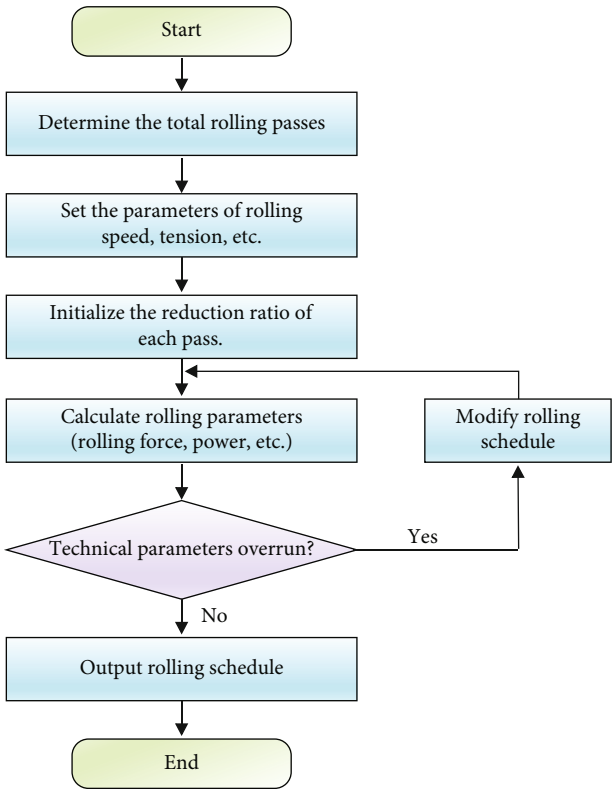

Figure 1: The flow chart of rolling schedule design of single-stand reversible cold rolling mill.

multiobjective particle swarm algorithm to optimize the objective functions of equal relative load and slip rate, and the method was applied to a five-stand tandem mill [15]. Wang et al. proposed a multiobjective particle swarm optimizer with dynamic opposition-based learning to optimize the rolling schedule with the objectives of minimum energy consumption, relative power margin, and slippage preventing [16]. Hu et al. selected five objectives as optimization objectives and used a multiobjective evolutionary algorithm based on decomposition and Gaussian mixture model to design the rolling schedule [17]. Taking the practical engineering application as the starting point, Zoheir et al. used the NSGA-II algorithm to realize the optimization of the rolling schedule of the tandem mill, and fully compared with the optimization results of the single-objective rolling schedule and the original rolling schedule [18]. At present, the main research is on the optimization of rolling schedule for continuous rolling mills, and the optimization of multiobjective rolling schedules for single-stand cold rolling mills is less. How to give full play to the advantages of the multiobjective optimization algorithm in the optimization of the rolling schedule of the single-stand rolling mill still needs to be further research.

In this paper, a rolling schedule optimization method based on multiobjective artificial fish swarm algorithm is developed to solve the rolling schedule optimization problem of single stand reversing cold mill. The major works of this paper are as follows:

(1) The related problems of multiobjective optimization of rolling schedule for single-stand cold rolling mill are discussed

(2) A few of the mathematical models of the rolling process of single-stand cold rolling mill suitable for practical engineering applications are proposed

(3) The artificial fish swarm algorithm is improved into a multiobjective optimization method and applied to the rolling schedule optimization

(4) The proposed method is verified by practical engineering application, and the results are satisfactory

The remainder of this paper is organized as follows: Section 2 discusses the related problems of the design of rolling schedule and gives a mathematical model of rolling process suitable for engineering applications. The basic theory of artificial swarm algorithm and the detail of the proposed method are introduced in Section 3. Section 4 makes the application and verification of the proposed method in the practical rolling project. Section 5 contains some conclusions plus some ideas for further work.

2. Problems Related to the Optimization of Rolling Schedule

The technological characteristic of rolling production of single-stand reversible cold rolling mill is that the raw material of the steel strip undergoes reciprocating rolling in multiple passes and finally reaches the finished product thickness. The design of rolling schedule is assigning the rolling technological parameters according to the rolling strategy and the rolling mathematical model, including rolling pass, pass reduction, rolling force, front and back tension, and rolling speed. For a single-stand reversing cold rolling mill, the pass reduction is the most important technological parameter. The distribution of the rolling reduction of each pass constitutes the load distribution scheme. After the load distribution scheme is determined, it will directly lead to the determination of rolling force, rolling power, and rolling speed according to the rolling mathematical model. Therefore, the optimization of the rolling schedule of the single-stand reversing cold rolling mill is mainly the optimization of the load distribution. According to setting the specific optimization objective, the optimal load distribution scheme is obtained by the optimization algorithm, and other rolling technological parameters are then calculated. Figure 1 shows the flow chart of the design of the rolling schedule for a single-stand reversing cold mill. The design and optimization of the rolling schedule is also one of the core functions of the rolling process automation system, and its role is to provide the reasonable preset values for the basic automation system. It can be seen that the optimization of the rolling schedule involves three problems: the mathematical model of the rolling process, the objective functions, and the optimization method.

2.1. The Main Mathematical Model of the Rolling Process. Mathematical models are the basis for rolling schedule design and the important basis for calculating the objective functions. The mathematical models required for the design of the rolling schedule of single-stand reversible rolling mill include rolling force model, deformation resistance model, friction coefficient model, forward slip model, tension model, rolling torque and power model, and rolling pass model. Among them, the most important is the rolling force model and the model related to the rolling force.

2.1.1. Rolling Force Model. The cold rolling process has a complex mechanism, with typical characteristics of multivariable, strong coupling, nonlinear, and time-varying, it is very difficult to obtain an accurate rolling force model. For decades, many scholars have conducted very detailed research and analysis on the cold rolling force model and obtained many cold rolling force models. Combined with the real-time calculation and practical engineering application experience, this paper chooses the Bland-Ford-Hill formula to calculate the rolling force.

$$\begin{cases} F = Bl' K_T Q_P K, \\ l' = \sqrt{R'\Delta h}, \\ R' = R\left(1 + 2.11 \times 10^{-5} \dfrac{F}{B\Delta h}\right), \\ Q_P = 1.08 + 1.79\mu\varepsilon\sqrt{1-\varepsilon}\sqrt{R'/h_1} - 1.02\varepsilon, \\ K_T = 1 - \dfrac{\tau_b + \tau_f}{2K}, \end{cases} \tag{1}$$

where F is the rolling force; B is the width of the steel strip; l' is the contact arc length of the rolled piece in the deformation zone during rolling; R is the roll radius; R' is the roll flattening radius; Q_P is the external friction stress state coefficient after flattening; K_T is the tension influence coefficient; K is the deformation resistance of steel strip; μ is friction coefficient; Δh is absolute reduction; τ_f is front tensile stress; τ_b is back tensile stress; ε is the reduction rate, i.e., the reduction rate $\varepsilon = (h_0 - h_1)/h_0$; h_1 is outlet thickness per pass; and h_0 is inlet thickness per pass. Friction coefficient μ and deformation resistance K are variables that cannot be measured by sensors, the calculation methods of these two parameters will be introduced in subsequent chapters.

2.1.2. Friction Coefficient Model. Because of constantly changing during the production process, the friction coefficient is very difficult to be calculated directly. In this paper, a friction coefficient calculation formula is proposed by analyzing and regressing the actual production data.

$$\mu = \mu_{basic} + \mu_{vl}, \tag{2}$$

where μ_{basic} is the basic friction coefficient model obtained by inversion of the Stone rolling force formula; and μ_{vl} is the correction factor related to the rolling speed and the rolling length of the roll.

$$\mu_{basic} = \frac{1/2\sqrt{\Delta h/R'}}{1 - 2\sqrt{(1-\varepsilon)(f/\varepsilon)}}, \tag{3}$$

where f is the forward slip, the calculation model of which is as follows:

$$f = \frac{R}{h_1}\gamma^2,$$
$$\gamma = \sqrt{\frac{h}{R}} \tan\left[\frac{1}{2}\arctan^{-1}\sqrt{\frac{\varepsilon}{1-\varepsilon}} + \frac{\pi}{8}\ln(1-\varepsilon)\sqrt{\frac{h}{R}}\right], \tag{4}$$

where γ is the neutral angle of which is as follows:

$$\mu_{vl} = \frac{f(v)}{1 + g \cdot L/L_0},$$
$$f(v) = av + bv^2 + cv^3 + dv^4 + ev, \tag{5}$$

where L_0 is the benchmark rolling length$(1000m)$; v is the rolling speed; L is the cumulative rolling length after roll change; $f(v)$ is a predicted value of the friction coefficient depending on the speed, a, b, c, d, e are polynomial regression coefficients; and g is a coefficient related to rolling mileage, obtained by least squares fitting method.

This friction coefficient model considers the two factors of rolling speed and rolling length, while reducing the sensitivity of the model to the speed when the speed is too large.

2.1.3. Deformation Resistance Model. According to the characteristics of the cold rolling production process, the deformation resistance of the cold rolling process is mainly related to the deformation speed, the deformation temperature, and the cumulative deformation degree. Among them, the cumulative deformation degree is the main factor affecting the deformation resistance of the material. Based on the data analysis of a large number of practical productions, the third-order polynomial model is chosen to predict the deformation resistance.

$$K = 1.15\sigma_s, \tag{6}$$

$$\sigma_s = a + b\varepsilon_{\sum}^1 + c\varepsilon_{\sum}^2 + d\varepsilon_{\sum}^3, \tag{7}$$

$$\varepsilon_{\sum} = \frac{1}{3}\frac{H - h_0}{H} + \frac{2}{3}\frac{h_1}{H}, \tag{8}$$

where K is the deformation resistance; σ_s is the yield stress of the strip; $\varepsilon_{\sum}$ is the cumulative degree of deformation of the rolled piece; H is the thickness of the raw material; and a, b, c, d are undetermined coefficients of the polynomial model.

2.1.4. Rolling Pass Model. The number of rolling passes can be determined by

$$n = Int\frac{\ln(h_i/H)}{\ln(1-\varepsilon_m)}, \tag{9}$$

where n is the number of rolling passes; ε_m is the maximum reduction rate; and h_i is the target thickness. For a single stand reversing cold rolling mill, $\varepsilon_m \leq 40\%$.

2.1.5. Rolling Torque and Rolling Power. During normal rolling, the rolling torque M_F required by the roll is as follows:

$$M_F = Fl' + (\tau_b - \tau_f)R. \tag{10}$$

The rolling power of the motor is determined by the rolling torque and the rotational speed of the roll, which can be calculated by the following formula:

$$P = M_{\sum}\omega, \tag{11}$$

$$M_{\sum} = M_F/i + M_f + M_x \pm M_d, \tag{12}$$

where P is the rolling power of the motor; $M_{\sum}$ is the main motor total torque; ω is the angular velocity of the motor. M_f is the additional friction torque; M_x is the idling torque; M_d is dynamic torque; and i is gear ratio.

2.2. Objective Functions. To increase the utilization rate of machinery, equipment, and motors and improve the quality of rolling products, the load distribution of rolling schedule needs to be optimized according to different objectives. The objectives of optimization under different conditions are different, so it is necessary to establish objective functions under various conditions from different viewpoints.

2.2.1. Energy Consumption Objective Function. Due to the different reduction of each pass, the rolling energy consumption of each pass is also different. After optimizing the reduction of each pass, a set of load distribution schemes can always be found, so that the total energy consumption of each pass is the lowest. Therefore, the minimum energy consumption objective function is established as follows:

$$\min P_t = \sum_{i=1}^{n} P_i(\varepsilon_i). \tag{13}$$

where P_t is the total energy consumption of rolling; P_i is the rolling power of the i_{th} pass; n is the number of rolling passes; and ε_i is the reduction rate of the i_{th} pass.

2.2.2. Equal Power Margin Objective Function. To give full play to the performance of the rolling mill motor and improve the production efficiency of the rolling mill as much as possible, it is hoped that the rolling power of each pass has the same relative power margins. It means that not only the difference of rolling power between adjacent passes is desired to be minimized but also the difference of rolling power between a certain pass and other passes is desired to be minimized. Therefore, the objective function of equal power margin is constructed as follows:

$$S_i = \frac{P_r - P_i}{P_r}, \tag{14}$$

$$\min S = \sum_{i=1}^{n}\sum_{j>i}^{n}\left|S_i - S_j\right|, \tag{15}$$

where P_r is the rated power of the main motor; and S_i is the power margin factor of the i_{th} pass.

2.2.3. Good Flatness Objective Function. Good flatness means that under the condition of a certain roll-shape system, it is ensured that the section geometry of the rolling stock before and after rolling is similar. Considering that the main influence of the exit crown is the rolling force, the objective function can be written as [7]:

$$\min G = \sum_{i=1}^{n}(F_i - Fo_i)^2, \tag{16}$$

where F_i is the rolling force of the i_{th} pass; and Fo_i is the rolling force to make the best plate shape of the i_{th} pass.

2.3. Constraint Conditions. When optimizing the rolling schedule, it is necessary to constrain the technological parameters of each pass, so that the parameters of each pass are less than the maximum allowed by the equipment capacity and technological conditions. Constraint conditions include technological constraints and equipment constraints. The major technological constraints are as follows:

$$\begin{aligned} \varepsilon_{\min i} \leq \varepsilon_i \leq \varepsilon_{\max i}, \\ h_{\min i} \leq h_i \leq h_{\max i}, \\ v_{\min i} \leq v_i \leq v_{\max i}, \\ t_{\min i} \leq t_i \leq t_{\max i}, \end{aligned} \tag{17}$$

where $\varepsilon_{\min i}$, $\varepsilon_{\max i}$ are, respectively, the minimum and maximum reduction rates allowed for the i_{th} pass; h_i is the outlet thickness of the i_{th} pass; $h_{\min i}$, $h_{\max i}$ are, respectively, the minimum and maximum outlet thickness allowed for the i_{th} pass; v_i is the rolling speed of the i_{th} pass; $v_{\min i}$, $v_{\max i}$ are, respectively, the minimum and maximum rolling speed allowed for the i_{th} pass; t_i is the tensile stress of the i_{th} pass; and $t_{\min i}$, $t_{\max i}$ are, respectively, the minimum and maximum tensile stress allowed for the i_{th} pass.

The constraints of the rolling mill are as follows:

$$\begin{aligned} F_i \leq F_{\max}, \\ P_i \leq P_{\max}, \\ M_i \leq M_{\max}, \end{aligned} \tag{18}$$

where F_i, P_i, M_i are, respectively, the rolling force, the total power and roll torque of the i_{th} pass; and $F_{\max}$, $P_{\max}$, $M_{\max}$

are, respectively, the maximum rolling force, the rated power of the motor and the maximum roll torque.

2.4. Multiobjective Optimization Model of Rolling Schedule. It can be seen from the above analysis that the process parameters related to the optimization of the rolling schedule can be obtained from the mathematical model of the rolling process through the reduction of each pass. Therefore, the reduction rate of each pass is selected as the variable of the optimization model. For the rolling production of single-stand cold rolling mills, more attention is paid to reducing production cost and improving production efficiency. For this reason, a multiobjective optimization model of rolling schedule for single-stand reversible cold rolling mill is constructed with minimum energy consumption and equal power margin as objective functions. The optimization model of rolling schedule based on two objective functions is as follows:

$$\begin{aligned} &\min F(X) = (f_1(X), f_2(X)), \\ &\quad s.t. \qquad g_i(X) \in \Omega \; i = 1, 2 \cdots, n, \end{aligned} \tag{19}$$

where $f_1(X)$ is the energy consumption objective function; $f_2(X)$ is the equal power margin objective function; X is the set of reduction ratios of each pass. $g_i(X)$ are the i_{th} constraint conditions.

3. Multiobjective Artificial Fish Swarm Algorithm

Aiming at the multiobjective optimization problem of rolling schedule, a solution strategy based on multiobjective artificial fish swarm algorithm (MOAFSA) is proposed. The basic artificial fish swarm algorithm (AFSA) is a single objective swarm intelligent optimization algorithm. The artificial fish swarm algorithm is improved into a multiobjective optimization algorithm by designing a fast search Pareto optimal solution method, constructing a Pareto optimal solution set method, designing an artificial fish state update method and a bulletin board maintenance strategy. In this section, the basic artificial fish swarm algorithm is introduced firstly. Next, the specific methods of each link of the multiobjective artificial fish swarm algorithm and the application steps in the optimization of the rolling schedule are introduced.

3.1. Review of AFSA. The basic idea of AFSA is searching for an optimal solution by simulating the preying behavior of artificial fish [19]. The artificial fish corresponds to the optimal solution of the optimization problem, the water area corresponds to the solution space of the optimization problem, and the food concentration corresponds to the objective function of the optimization problem. Some parameters of AFSA are defined as follows [20]. There are N artificial fishes in a D-dimensional space. The state vector of the i_{th} artificial fish is $X_i = [x_{i1}, x_{i2}, \cdots, x_{iD}]$, $i = 1, \cdots, N$, and $Y_i = f(X_i)$ is the food concentration of artificial fish. The distance from the i_{th} artificial fish to the j_{th} artificial fish is $d_{ij} = \|X_i - X_j\|$. δ, Visual, Step, L, N_f are, respectively, the congestion factor of artificial fish swarm, the perceived range of artificial fish, moving step of artificial fish, maximum preying time, and the number of artificial fish within the perceived range. The artificial fish mainly updates its state through four behaviors [21, 22]: preying, following, swarming, and random. The four behaviors are described as follows:

(1) Preying behavior: assuming that the current state of the artificial fish is X, a new state X_{next} is obtained firstly according to Equation (20) and Equation (21). Then, the food concentration functions Y and Y_{next} for X and X_{next} are calculated, respectively. Determining whether Y_{next} is superior to Y. If Y_{next} is superior to Y, X will be moved to X_{next} according to Equation (21). Otherwise, the new state of artificial fish will continue to be obtained according to Equation (20) and Equation (21). If the artificial fish acquires new states more than L times and Y_{next} is still worse than Y, the artificial fish performs random behavior

$$X' = X + \text{Visual} \cdot \text{rand}\,(\,), \tag{20}$$

$$X_{next} = X + \frac{X' - X}{X' - X} \cdot \text{step} \cdot \text{rand}\,(\,), \tag{21}$$

where rand () is the random number between 0-1; X_{next} is the next state of artificial fish

(2) Following behavior: assuming that the current state of the artificial fish is X, the optimal state of the artificial fish within the perceived range is X_{gbest}. If the food concentration X_{gbest} corresponding to Y_{gbest} is superior to Y, and $Y_{gbest}/N_f < \delta \bullet Y$, then, X moves to X_{gbest} according to Equation (22), otherwise the swarming behavior is performed as

$$X_{\text{next}} = X + \frac{X_{\text{gbest}} - X}{\|X_{\text{gbest}} - X\|} \bullet \text{step} \bullet \text{rand}\,() \tag{22}$$

(3) Swarming behavior: assuming that the current state of the artificial fish is X, the central position of the artificial fish within the perceived range is X_c. If the food concentration X_c corresponding to Y_c is superior to Y, and $Y_c/N_f < \delta \bullet Y$, then, X moves to X_c according to Equation (23), otherwise the preying behavior is performed as

$$X_{next} = X + \frac{X_c - X}{\|X_c - X\|} \bullet step \bullet \text{rand}\ () \tag{23}$$

(4) Random behavior: the artificial fish moves to a new state randomly according to Equation (20) within the perceived range

3.2. MOAFSA. According to the ideas of multiobjective evolutionary algorithm and multiobjective particle swarm algorithm [23–27], to improve the basic artificial fish swarm algorithm to multiobjective artificial fish swarm algorithm, the following three issues need to be addressed. (1) Fast searching Pareto optimal solutions and constructing Pareto optimal solution set; (2) determining the moving direction of artificial fish under multiobjective conditions; and (3) maintaining and updating the bulletin board (external archives) of artificial fish swarm.

(1) Fast searching Pareto optimal solutions and constructing Pareto optimal solution set

Searching for the Pareto optimal solution quickly and constructing the Pareto optimal solution set are the key points in multiobjective optimization problems [28]. Kong et al. proposed a method of fast searching for Pareto optimal solutions and constructing Pareto optimal solution set [29]. This method greatly improves the speed of searching for the Pareto optimal solution and the speed of constructing the Pareto optimal solution set, but it does not consider the situation of an existing multiple first objective functions with the same value when searching for the Pareto optimal solution. On the basis of this method, in this section, an improved method of fast searching Pareto optimal solutions and constructing Pareto optimal solution set is introduced [30]. According to the optimization problem required in this paper, the number of objective functions is defined as 2, and the optimization objective is to minimize the objective function. There are M total artificial fishes as alternative solutions. The steps of searching for Pareto optimal solutions and constructing Pareto optimal solution set are as follows:

(2) Status update of MOAFSA

Step 1. M alternative solutions are sorted rapidly in ascending order according to the first objective function; the sorted artificial fish are numbered 1 to M. At the same time, the artificial fishes with the same first objective function value are marked. The first alternative solution is selected temporarily as the Pareto optimal solution, and this alternative solution is added to the Pareto optimal solution set temporarily. Then, the second objective function of this alternative solution is set as the reference value, let $i = 2$.

Step 2. Determining whether the first objective function of the i_{th} artificial fish is the same as the first objective function corresponding to the current reference value, if it is the same, execute step 3, otherwise execute step 4.

Step 3. Compare the second function value of the i_{th} artificial fish with the reference value, if it is smaller than the reference value, remove this solution corresponding to the current reference value from the Pareto optimal solution set, and the i_{th} artificial fish is added to the Pareto optimal solution set temporarily, the second objective function value of this artificial fish is set as the reference value, and then, execute step 5, otherwise directly execute step 5.

Step 4. Compare the second function value of the i_{th} artificial fish with the reference value, if it is smaller than the reference value, and the i_{th} artificial fish is added to the Pareto optimal solution set temporarily, the second objective function value of this artificial fish is set as the reference value, and then, execute step 5, otherwise directly execute step 5.

Step 5. Let $i = i + 1$, determining whether i is greater than M, if i is greater than M, the comparison is stop, and the final, Pareto optimal solution sets are outputted, otherwise go to Step 2.

Since the Pareto optimal definition of the multiobjective optimization algorithm is introduced, the congestion factor δ of the AFSA is no longer applicable, and the congestion factor δ is replaced by defining a congestion distance *Dis* [31]. When determining the movement of the artificial fish, the congestion distance and the Pareto dominance rule are considered. After improvement, the status of artificial fish of the MOAFSA can be updated by the three behaviors of preying, following, and swarming.

Assuming that there are N_f artificial fish in the perceived range of the artificial fish, the steps for calculating the congestion distance *Dis* are as follows:

Step 1. The congestion distance of each artificial fish is initialized to 0, and the number of current objectives j is set to 1.

Step 2. The j_{th} objective is sorted in ascending order, and the sorted artificial fishes are remarked. Assuming that the i_{th} artificial fish is remarked as i', let the congestion distance of the artificial fish with $i' = 1$ and $i' = N_f$ be infinite, and let $i = 2$.

Step 3. The congestion distance of the i_{th} artificial fish is calculated according to .

$$Dis(i) = Dis(i) + \left| \frac{f_j\left(i' + 1\right) - f_j\left(i' - 1\right)}{\max\left(f_j\right) - \min\left(f_j\right)} \right|. \tag{24}$$

Step 4. Let $i = i + 1$, if $i > N_f$, go to step 5, otherwise go to step 3.

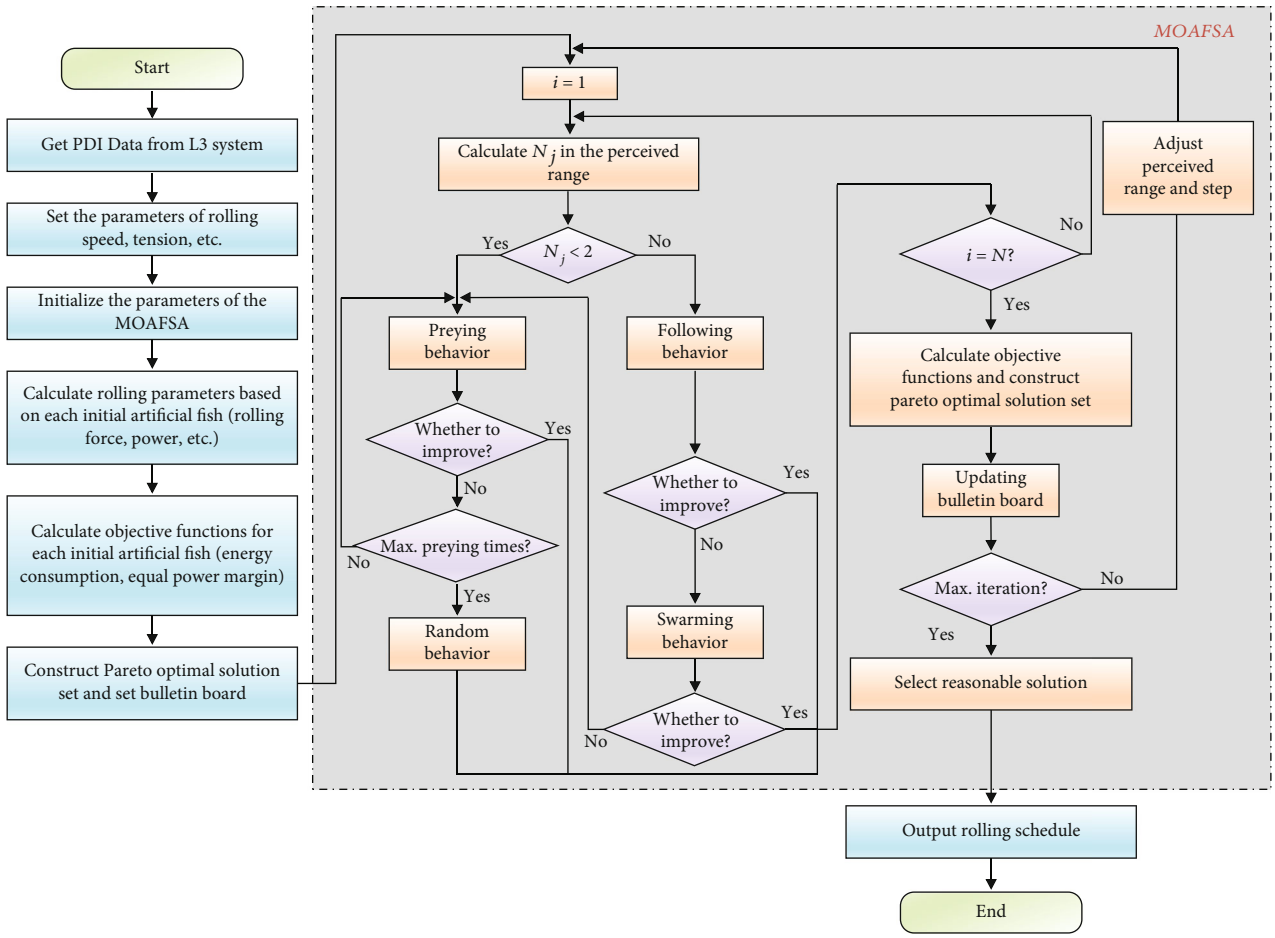

Figure 2: The flow chart of optimization of rolling schedule based on MOAFSA.

Step 5. Let $j = j + 1$, if $j > 2$, the final result is outputted and the calculation is stopped, otherwise go to step 2.

After the introduction of the Pareto dominance rule and the congestion distance, the three behaviors of preying, following, and swarming have also been improved accordingly. The specific improvements are as follows:

(a) Preying behavior: assuming that the current state of the artificial fish is X, a new state X_{next} is obtained firstly according to Equation (20) and Equation (21). Since the food concentration function is no longer a value, but a vector, the basis for determining whether X moves to X_{next} is whether $F(X_{next})$ dominates $F(X)$. If $F(X_{next})$ dominates $F(X)$, then, X moves to X_{next}, otherwise continue generating a new solution according to Equation (20) and Equation (21) until exceeding L times, and then, performs random behavior

(b) Following behavior: assuming that the current state of the artificial fish is X, the artificial fish searches for nondominated solutions within its perceived range according to the Pareto dominance rule, then, calculate the congestion distance of each artificial fish is calculated, and the solution X_{gbest} with the largest congestion distance is obtained. If $Dis(X_{gbest}) < Dis(X)$, X moves to X_{gbest} according to Equation (22), otherwise the swarming behavior is performed

(c) Swarming behavior: assuming that the current state of the artificial fish is X, the central position of the artificial fish within the perceived range is X_c. If $F(X_c)$ dominates $F(X)$ and $Dis(X_c) < Dis(X)$, X moves to X_c according to Equation (23), otherwise the preying behavior is performed

(3) Maintenance strategy of bulletin board for MOAFSA

In the AFSA, the bulletin board is used to record the position of the optimal artificial fish and the food concentration function in each iteration process. With the introduction of Pareto optimal definition in multiobjective optimization, the bulletin board no longer only records the position and food concentration function of an artificial fish, but it is equivalent to the external file set of multiobjective evolutionary algorithm and multiobjective particle swarm optimization algorithm, and becomes Pareto optimal

solution set [32]. Therefore, the maintenance and update of the bulletin board is a necessary link for the artificial fish to obtain a Pareto front with better diversity and distribution when moving. In this paper, the maintenance strategy based on grid density commonly used in multiobjective evolutionary algorithm and multiobjective particle swarm algorithm is adopted [29]. When the bulletin board is updating, the Pareto optimal solution set obtained in this iteration process is merged with the bulletin board firstly, and the dominated artificial fish is eliminated according to the above method. Then, determine whether the number of artificial fish in the bulletin board is greater than the maximum number of artificial fish K_m in the bulletin board. If it is greater than K_m, the target space of each dimension of the bulletin board is divided into 10 parts equally; then, the entire target space is evenly divided into 100 blocks. The number of all artificial fish in the area where each artificial fish is located is defined as the grid density of this artificial fish, and finally, the artificial fish with the largest grid density is removed one by one until the number of artificial fish is equal to K_m.

Therefore, the implementation steps of the MOAFSA are summarized as follows:

$$\phi = \exp\left(-30\bullet\left(\frac{t}{T)^{10}}\right)\right., \tag{25}$$

$$\text{Step} = \text{Step}\bullet\phi + \text{Step}_{\min}, \tag{26}$$

$$\text{Visual} = \text{Visual}\bullet\phi + \text{Visual}_{\min}. \tag{27}$$

Step 1. Initializing all parameters of the MOAFSA.

Step 2. Calculating the objective functions, searching for the Pareto optimal solution, and constructing the Pareto optimal solution set, and the Pareto optimal solution set is merged with the bulletin board.

Step 3. Calculating the number of other artificial fish N_f in the perceived range of each artificial fish, if $N_f < 2$, executing preying behavior, otherwise execute the following behavior.

Step 4. Calculating the objective functions, searching for the Pareto optimal solution, and constructing the Pareto optimal solution set of this iteration process, and the Pareto optimal solution set is merged with the bulletin board.

Step 5. To improve the convergence speed and convergence accuracy, the perceived range and moving step of artificial fish are updated according to, [33] and are as follows:

Step 6. Determining whether the number of iterations is greater than the maximum number of iterations T, if it is greater than T, outputting the bulletin board, and outputting the artificial fish with the smallest grid density as the optimal solution, otherwise go to Step 3.

3.3. MultiObjective Optimization Process of Rolling Schedule Based on MOAFSA. MOAFSA will be applied to the optimization of rolling schedule to search a load distribution scheme which considers two objectives. First, the product specification to be optimized needs to be obtained, which is usually obtained from the L3 production management system. Second, according to finished product specifications, the production constraints are set, such as tension limit values, and rolling speed limits. Then, the parameters of the MOAFSA are initialized, and the initial value of rolling parameters and the initial value of the objective function are calculated. After that, the iterative process of MOAFSA is entered, and the result of load distribution is obtained after reaching the maximum number of iterations. The detailed optimization flow of the rolling schedule based on MOAFSA is shown in Figure 2.

Table 1: Mechanical and electrical parameters of the rolling mill.

Parameters	Value
Power [KW]	6000
Max. Rolling force [KN]	12000
Max. Rolling speed [m/min]	1300
Max. Diameter of work roll [mm]	397
Mill rigidity coefficient [KN/mm]	3500
Max. Tension [KN]	170

4. Engineering Implementation and Validation

In the practical cold rolling project, the optimization of the rolling schedule is realized in the L2 process automation system. After the L2 process automation system receives the production plan and raw material information from the L3 production management system, the rolling technological table consisting of a set of detailed basic automation settings according to the rolling process mathematical model and the rolling schedule optimization method is calculated. According to the control sequence, the rolling technological table of the corresponding raw material is sent to the basic automation level for precise control. In this section, to verify the validity and feasibility of the rolling schedule optimization method based on MOAFSA in the practical system, the proposed method was tested in the practical system and compared with the rolling schedule based on experience.

4.1. Description of Plant. The platform of the verification experiment adopts the self-developed 1380 mm single-stand six-high reversible cold rolling mill automation system. The automation system adopts a two-level automation control system structure, which consists of a process automation system (L2) and a basic automation system (L1). And the system has a communication interface with production management automation system (L3), which can communicate with the L3 in real time. The rolling mill equipment uses two independent hydraulic cylinders to generate rolling force, and the rolls are driven by AC motors. The mechanical and electrical parameters of the rolling mill

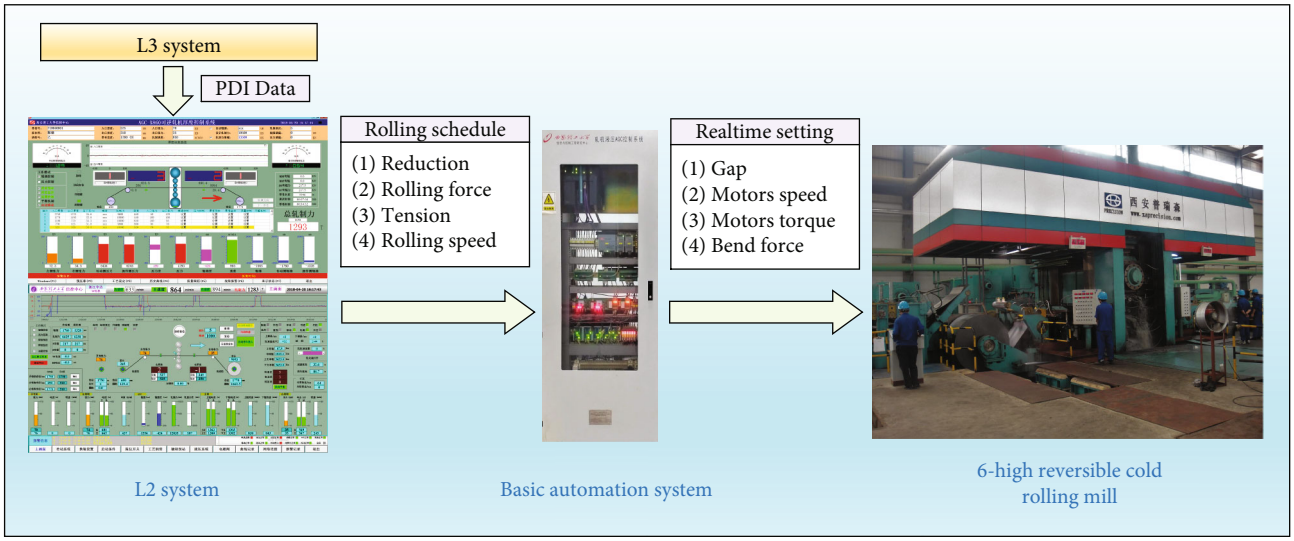

Figure 3: Single stand reversible cold rolling mill and automa1tion system.

Table 2: Parameters and production requirements of the tested steel coils.

Parameters	No.1 SPEC.	No.2 SPEC.
Steel grade	SPHC	Q195
Width [mm]	1075	1225
Weight [T]	19.35	22.05
Initial thickness [mm]	2.75	3
Target thickness [mm]	0.16	0.25
Total pass	6	6

are shown in Table 1. The practical rolling mill and automation system are shown in Figure 3.

4.2. Experimental Results and Analysis. To verify the rolling schedule optimization method proposed in this paper, two product specifications with the largest output selected from the product outline of this cold rolling mill were tested, respectively. The specific parameters and production requirements of these two product specifications are shown in Table 2. For No.1 SPEC., the optimal rolling schedule and the empirical rolling schedule use the same tension coefficient and rolling speed. For No.2 SPEC., the optimal rolling schedule and the empirical rolling schedule use the same tension coefficient, but the rolling speed is set according to the limit of rolling power and the maximum speed of motor. The rolling schedules obtained by both methods are sent to the basic automation system for production, and the application effects of the rolling schedules are compared through the collected practical production data.

According to the rolling characteristics, the reduction ratios of each pass were randomly generated within a reasonable range to constitute the initial position of the artificial fishes. The initial value of Step is 0.02. The initial state of the bulletin board is empty. The other parameters of MOAFSA are as follows:

(1) The number of artificial fishes N: 30

(2) The maximum preying time L: 10

(3) The perceived range of artificial fish Visual: 0.05

(4) The minimum perceived range of artificial fish $\text{Visual}_{\text{min}}$: 0.01

(5) The minimum moving step of artificial fish Step_{min}: 0.005

(6) The maximum number of iterations T: 100

(7) The maximum number of bulletin boards K_m: 100

Taking the minimum energy consumption and equal power margin as the objective function, the approximate Pareto optimal solution set after the normalization of the two specifications is obtained through the optimization calculation, as shown in Figure 4.

The optimization method proposed in this paper is repeated independently for 20 times, and the experimental results are taken as the average value of the 20 experiments. The artificial fish with the smallest lattice density was selected as the optimal solution and sent to the basic automation system for production. Tables 3 and 4 show the comparison of the load distribution and practical production data of the two specifications of strip with the optimized rolling schedule and the empirical rolling schedule.

The power distribution of each pass of two specifications based on empirical and optimized method is shown in Figure 5.

Figure 5(a) shows the power distribution of No.1 SPEC., compared with the empirical rolling schedule, the total energy consumption of the rolling schedule obtained by the proposed method is almost the same as that of the

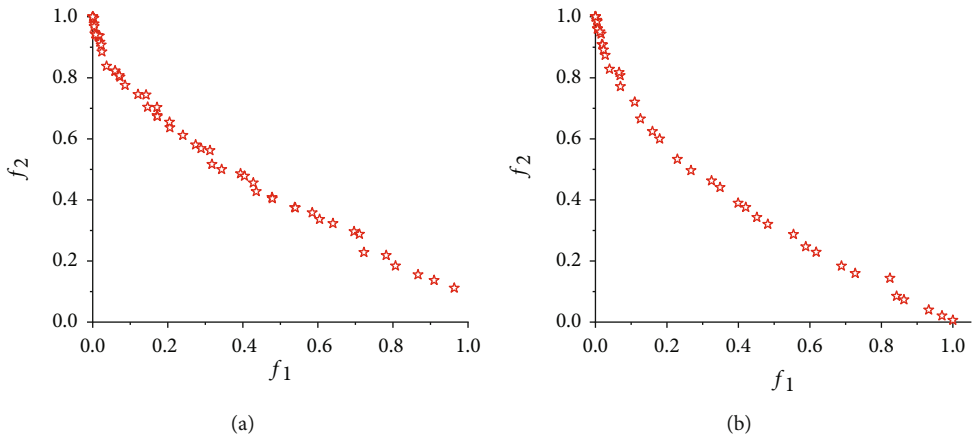

Figure 4: Pareto optimal set. (a) No.1 SPEC. (b) No.2 SPEC.

Table 3: Comparison of optimized schedule (Opt.) and empirical schedule (Emp.) for No.1 SPEC.

Pass	Method	Outlet thickness [mm]	Reduction rate	Rolling force [KN]	Power [KW]	Rolling speed [m/min]	Rolling time [min]
1	Opt.	1.73	0.37091	8242	4449	500	2.932
	Emp.	1.92	0.30	6550	3184	500	2.67
2	Opt.	1.07	0.38150	8521	4618	600	3.909
	Emp.	1.16	0.395	8967	5169	600	3.632
3	Opt.	0.65	0.39252	8636	4609	700	5.433
	Emp.	0.70	0.395	8807	4870	700	5.073
4	Opt.	0.390	0.40	8749	4566	800	7.799
	Emp.	0.42	0.40	8717	4650	800	7.274
5	Opt.	0.235	0.39744	8396	4713	1000	10.32
	Emp.	0.255	0.39	8177	4631	1000	9.554
6	Opt.	0.16	0.31915	8717	5150	1200	12.617
	Emp.	0.16	0.37	9342	5856	1200	12.615

empirical rolling schedule, but the proposed method can obtain a more uniform power distribution. The power margins of the empirical rolling schedule and the optimized rolling schedule are 1.1530 and 0.0053, respectively, which means that the optimized rolling schedule still has the potential to increase the rolling speed in the middle several passes, which can further improve the production efficiency. To verify the ability of the proposed algorithm in improving productivity, during the production of the No.2 SPEC, the rolling speed is only limited by the motor power and the maximum rotate speed, regardless of the experience rolling schedule or the optimized rolling schedule. Figure 5(b) shows a comparison of the power distribution for the empirical and optimized rolling schedules of the No.2 SPEC. The power margins of the empirical rolling schedule and the optimized rolling schedule are 0.9910 and 0.4884, respectively. It can be seen from Figure 5(b) that the two design methods of rolling schedule try to maximize the power capability of the motor, compared with the empirical rolling schedule, the power distribution of each pass of the optimized rolling schedule is more uniform, and the rolling power of more passes can approach the limit value of the rolling power. It means that the optimized rolling schedule can better utilize capacity of the rolling mill. Figure 6 shows the comparison of the rolling efficiency for the No.2 SPEC between the optimized rolling schedule and the empirical rolling schedule.

Figure 6(a) shows the comparison of rolling speed for No.2 SPEC. It can be clearly seen from Figure 6(a) that the rolling speed of the optimized rolling schedule has been significantly improved in the middle three passes, and the production efficiency has been significantly improved. Figure 6(b) shows the comparison of rolling time, which also confirms the advantages of the optimized rolling schedule in improving the production efficiency in the middle three passes. Using the optimized rolling schedule, the production time of each coil can save 1.308 min, which is also a very meaningful improvement for mass production. As shown

Table 4: Comparison of optimized schedule (Opt.) and empirical schedule (Emp.) for No.2 SPEC.

Pass	Method	Outlet thickness [mm]	Reduction rate	Rolling force [KN]	Power [KW]	Rolling speed [m/min]	Rolling time [min]
1	Opt.	2.01	0.33	8493	4496	500	2.563
	Emp.	2.10	0.30	7663	3866	500	2.465
2	Opt.	1.33	0.33831	8770	5876	740	2.764
	Emp.	1.37	0.35	9284	5897	678	2.850
3	Opt.	0.87	0.34586	8738	5831	860	3.548
	Emp.	0.87	0.36	9429	5868	770	3.856
4	Opt.	0.60	0.31034	7761	5876	1200	3.859
	Emp.	0.56	0.36	8598	5894	1020	4.588
5	Opt.	0.39	0.35	8246	5829	1200	5.839
	Emp.	0.37	0.34	8100	5540	1200	6.519
6	Opt.	0.25	0.35897	8779	5644	1200	8.220
	Emp.	0.25	0.32	8279	5054	1200	8.318

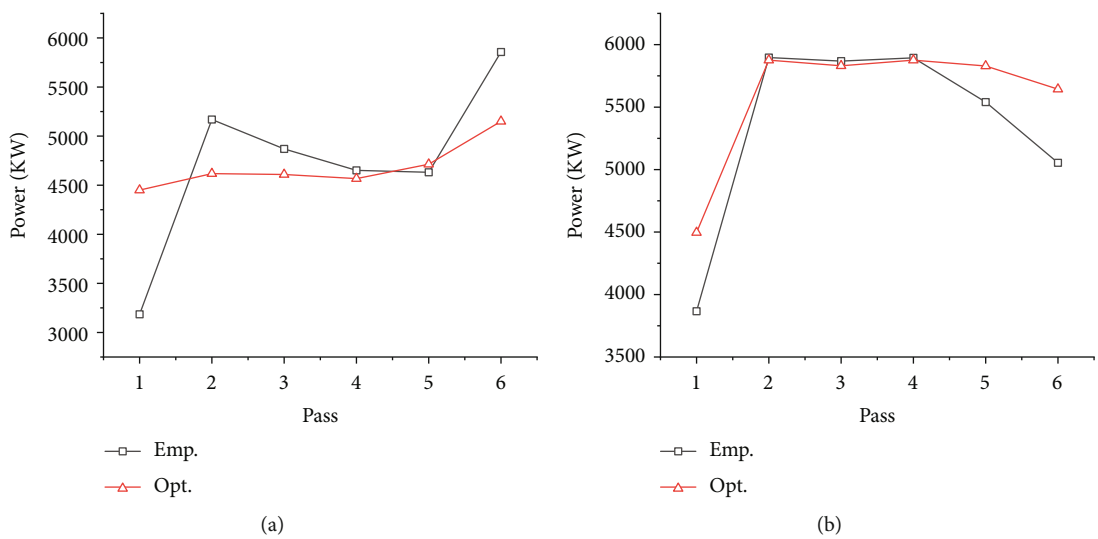

Figure 5: Power distribution of the two methods. (a) No.1 SPEC. (b) No.2 SPEC.

in Figure 7, the total power consumption of the rolling schedule obtained by the optimized method is almost the same as that of the empirical rolling schedule, which is also determined by the production characteristics of the single-stand cold rolling mill.

However, the empirical rolling schedule design method does not consider the influence of changes in production parameters, and the results on production efficiency are completely unknown. In applying the empirical rolling schedule, the operator needs to modify the technological setting parameters repeatedly, which is easy to cause unstable product quality and affect production efficiency. The significance of the optimization method of rolling schedule based on MOAFSA is that the setting value of technological parameter which takes into account some objectives can be automatically calculated without relying on personal experience. In practical application, compared with the empirical rolling schedule, the operator does not need to modify the technological setting parameters frequently, the product quality is more stable, and the production efficiency is higher. When the production parameters change, the results of the optimized rolling schedule will change accordingly, i.e., the optimization method of rolling schedule based on MOAFSA has better adaptability. As can be seen from the above experimental results, the optimization method of rolling schedule based on MOAFSA can obtain a result that takes into account the total rolling power consumption and rolling efficiency, and can effectively improve the production efficiency without consuming too much power consumption. The experimental results also show the feasibility and effectiveness of the proposed algorithm.

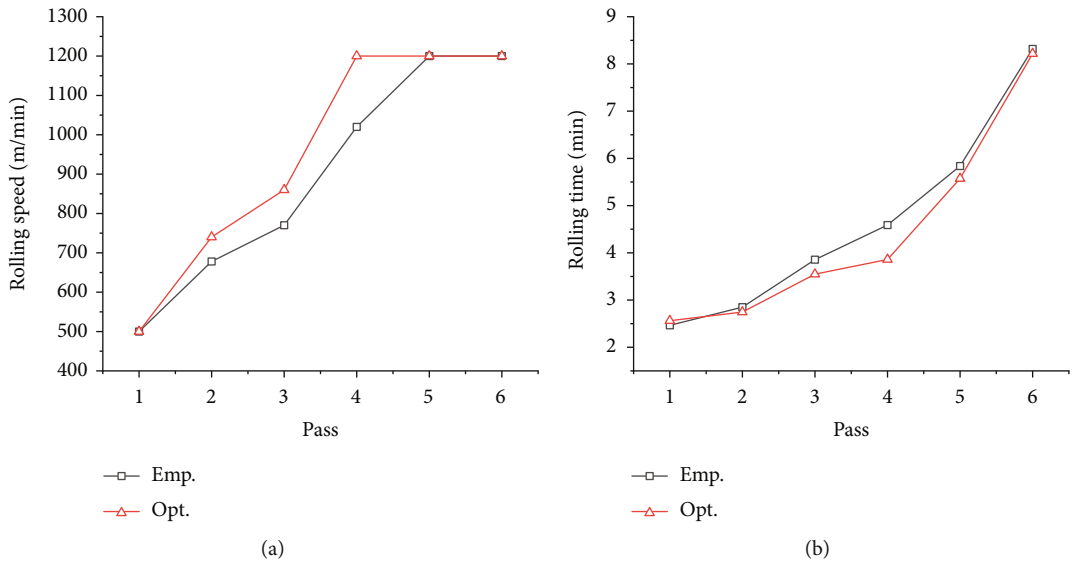

Figure 6: The comparison of rolling efficiency for NO.2 SPEC. (a) Rolling speed comparison. (b) Rolling time comparison.

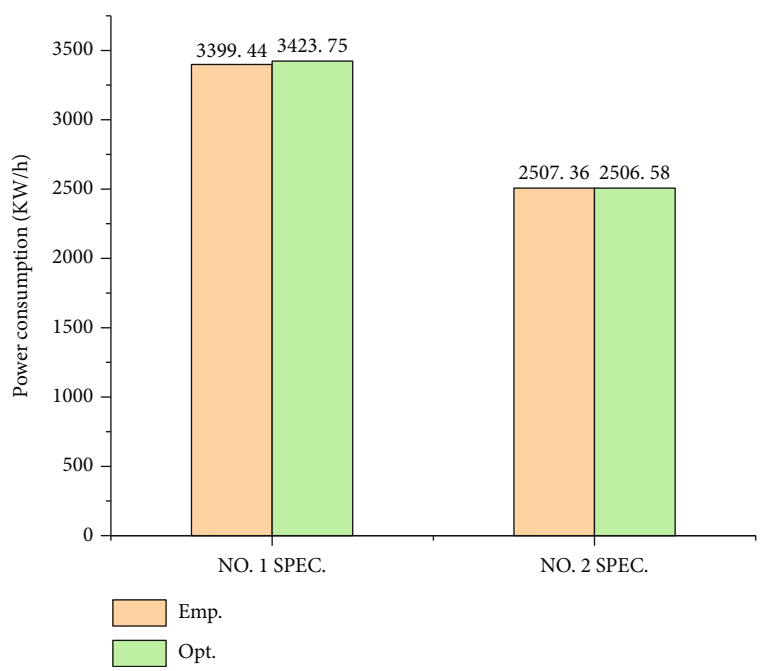

Figure 7: The comparison of rolling power consumption.

5. Conclusions

In this work, a rolling schedule optimization method based on MOASFA was proposed for the single-stand reversible cold rolling process. First, a multiobjective optimization model composed of an energy consumption function and equal power margin function was designed, and these objective functions were calculated based on the proposed mathematical model of the rolling process of single-stand cold rolling mill suitable for practical engineering applications. Then, the AFSA was improved into a multiobjective optimization method, and the method of quickly constructing Pareto optimal solution set was improved. At the same time, the four behaviors of artificial fish are improved under the framework of multiobjective optimization, and the maintenance strategy for the bulletin board of artificial fish swarm algorithm in the multiobjective optimization algorithm is added. The practical industrial verification of rolling scheduling optimization based on MOASFA proves the effectiveness and feasibility of the proposed algorithm. On the basis of roughly the same energy consumption, the rolling schedule optimization method proposed in this paper can

improve the production efficiency by 4.6% compared with the experience rolling schedule. This study provides a useful exploration for the application of optimized rolling schedules in practical engineering. When there are many objective functions, the method of constructing Pareto optimal solution set adopted in this paper still has high algorithm complexity, which limits the introduction of more objective functions. Therefore, it is necessary to further study the method of rapidly constructing Pareto optimal solution set. At the same time, more objective functions will be introduced in the optimization of rolling schedule.

Data Availability

The data used to support the findings of this study are available from the corresponding author upon request.

Conflicts of Interest

The authors declare that they have no conflict of interest.

Acknowledgments

This work was supported by the National Natural Science Foundation (NNSF) of China [grant numbers 62003261 and 62073258].

References

[1] Z. Hu, Z. Wei, H. Sun, J. Yang, and L. Wei, "Optimization of metal rolling control using soft computing approaches: a review," *Archives of Computational Methods in Engineering*, vol. 28, no. 2, pp. 405–421, 2021.

[2] I. Imai, "Continuous rolling theory in hot strip mill and its application," *Bulletin of JSME*, vol. 7, no. 26, pp. 430–436, 1964.

[3] M. Kamata, *Continuous Rolling of Sheet Products Footsteps of Engineers Who Have Persued the world's Most Advanced Technology*, Metallurgical Industry Press, Beijing, 2002.

[4] K. Sekiguchi, Y. Seki, N. Okitani et al., "The advanced set-up and control system for Dofasco's tandem cold mill," *IEEJ Transactions on Industry Applications*, vol. 32, no. 3, pp. 608–616, 1996.

[5] H. Li, J. Xu, G. Wang, and X. H. Liu, "Improvement on conventional load distribution algorithm in hot tandem mills," *Journal of Iron and Steel Research International*, vol. 14, no. 2, pp. 36–41, 2007.

[6] J. Sheng, Z. Jiao, and G. Wang, "Simple iteration method of calculating load distribution for reversible cold mill," *Journal of Iron and Steel Research*, vol. 19, no. 3, pp. 35–37, 2007.

[7] X. Jin, C. Li, Y. Wang, X. Li, Y. Xiang, and T. Gu, "Investigation and optimization of load distribution for tandem cold steel strip rolling process," *Metals - Open Access Metallurgy Journal*, vol. 10, no. 5, p. 677, 2020.

[8] Y. Cao, J. Cao, T. Wang et al., "The cold rolling load distribution of the nuclear power zirconium alloy based on the self-adaptive particle swarm optimization algorithm," *The International Journal of Advanced Manufacturing Technology*, vol. 119, no. 9-10, pp. 6007–6016, 2022.

[9] J. Yang, C. Wang, H. Che, and L. Zhao, "Improved ABC algorithm based on aluminum hot strip mill rolling schedule optimization design," *Journal of Plasticity Engineering*, vol. 20, no. 5, pp. 91–96, 2013.

[10] S. Chen, X. Zhang, L. G. Peng, D. H. Zhang, J. Sun, and Y. Z. Liu, "Multi-objective optimization of rolling schedule based on cost function for tandem cold mill," *Journal of Central South University*, vol. 21, no. 5, pp. 1733–1740, 2014.

[11] H. N. Bu, Z. W. Yan, D. H. Zhang, and S. Z. Chen, "Rolling schedule multi-objective optimizationbased on influence function for thin gauge steel strip in tandem cold rolling," *Scientia Iranica*, vol. 23, no. 6, pp. 2663–2672, 2016.

[12] Y. Wang, C. Li, X. Jin, Y. Xiang, and X. Li, "Multi-objective optimization of rolling schedule for tandem cold strip rolling based on NSGA-II," *Journal of Manufacturing Processes*, vol. 60, pp. 257–267, 2020.

[13] H. Che, L. Wang, J. Gu, L. Huo, H. Sun, and J. Yang, "Rolling schedule optimization based on adaptive grid multi-objective quantum genetic algorithm," *Journal of Plasticity Engineering*, vol. 23, no. 6, pp. 79–86, 2016.

[14] Y. Li and L. Fang, "Robust multi-objective optimization of rolling schedule for tandem cold rolling based on evolutionary direction differential evolution algorithm," *Journal of Iron and Steel Research International*, vol. 24, no. 8, pp. 795–802, 2017.

[15] L. Wei, L. Wang, M. Ma, H. Che, and J. Yang, "Optimization of tandem cold rolling schedule based on improved multi-objective particle swarm optimization algorithm," *China Mechanical Engineering*, vol. 26, no. 9, pp. 1239–1242, 2015.

[16] Y. Wang, J. Wang, C. Yin, and Q. Zhao, "Multi-objective optimization of rolling schedule for five-stand tandem cold mill," *IEEE Access*, vol. 8, pp. 80417–80426, 2020.

[17] Z. Hu, Z. Wei, X. Ma, H. Sun, and J. Yang, "Multi-parameter deep-perception and many-objective autonomous-control of rolling schedule on high speed cold tandem mill," *ISA Transactions*, vol. 102, pp. 193–207, 2020.

[18] Z. Babajamali, M. K. khabaz, F. Aghadavoudi, F. Farhatnia, S. A. Eftekhari, and D. Toghraie, "Pareto multi-objective optimization of tandem cold rolling settings for reductions and inter stand tensions using NSGA-II," *ISA Transactions*, 2022.

[19] X. L. Li, Z. J. Shao, and J. X. Qian, "An optimizing method based onautonomous animats: fish-swarm algorithm," *Institute of Sy stems Engineering*, vol. 11, pp. 32–38, 2002.

[20] J. Huang, J. Zeng, Y. Bai et al., "Layout optimization of fiber Bragg grating strain sensor network based on modified artificial fish swarm algorithm," *Optical Fiber Technology*, vol. 65, article 102583, 2021.

[21] Y. Zhu, W. Xu, G. Luo, H. Wang, J. Yang, and W. Lu, "Random forest enhancement using improved artificial fish swarm for the medial knee contact force prediction," *Artificial Intelligence In Medicine*, vol. 103, article 101811, 2020.

[22] Y. Gao, L. Xie, Z. Zhang, and Q. Fan, "Twin support vector machine based on improved artificial fish swarm algorithm with application to flame recognition," *Applied Intelligence*, vol. 50, no. 8, pp. 2312–2327, 2020.

[23] K. Alkebsi and W. L. Du, "A fast multi-objective particle swarm optimization algorithm based on a new archive updating mechanism," *IEEE Access*, vol. 8, pp. 124734–124754, 2020.

[24] J. Meza, H. Espitia, C. Montenegro, and R. G. Crespo, "Statistical analysis of a multi-objective optimization algorithm based on a model of particles with vorticity behavior," *Soft Computing*, vol. 20, no. 9, pp. 3521–3536, 2016.

[25] M. L. Yang, Y. M. Liu, and J. Yang, "A hybrid multi-objective particle swarm optimization with central control strategy," *Computational Intelligence and Neuroscience*, vol. 2022, Article ID 1522096, 23 pages, 2022.

[26] Z. Liu, Z. Qin, P. Zhu, and H. Li, "An adaptive switchover hybrid particle swarm optimization algorithm with local search strategy for constrained optimization problems," *Engineering Applications of Artificial Intelligence*, vol. 95, article 103771, 2020.

[27] H. F. Wang, Y. P. Fu, M. Huang, G. Huang, and J. W. Wang, "A hybrid evolutionary algorithm with adaptive multi-population strategy for multi-objective optimization problems," *Soft Computing*, vol. 21, no. 20, pp. 5975–5987, 2017.

[28] X. Y. Zhang, X. T. Zheng, R. Cheng, J. Qiu, and Y. Jin, "A competitive mechanism based multi-objective particle swarm optimizer with fast convergence," *Information Sciences*, vol. 427, pp. 63–76, 2018.

[29] W. Kong, T. Chai, J. Ding, and Z. Wu, "A real-time multiobjective electric energy allocation optimization approach for the smelting process of magnesia," *Acta Automatica Sinica*, vol. 30, no. 1, pp. 51–61, 2014.

[30] D. Liu, X. Zhang, and Y. Chen, "Monocrystalline silicon diameter detection image threshold segmentation method using multi-objective artificial fish swarm algorithm," *Acta Automatica Sinica*, vol. 42, no. 3, pp. 431–442, 2016.

[31] Z. Zhang, K. Wang, L. Zhu, and Y. Wang, "A Pareto improved artificial fish swarm algorithm for solving a multi-objective fuzzy disassembly line balancing problem," *Expert Systems with Applications*, vol. 86, pp. 165–176, 2017.

[32] Y. Liu, X. Feng, L. Zhang, W. Hua, and K. Li, "A Pareto artificial fish swarm algorithm for solving a multi-objective electric transit network design problem," *Transportmetrica A: Transport Science*, vol. 16, no. 3, pp. 1648–1670, 2020.

[33] X. Zhang, L. Lian, and F. Zhu, "Parameter fitting of variogram based on hybrid algorithm of particle swarm and artificial fish swarm," *Future Generation Computer Systems*, vol. 116, no. 1, pp. 265–274, 2021.

Hindawi
Wireless Communications and Mobile Computing
Volume 2022, Article ID 5265038, 14 pages
https://doi.org/10.1155/2022/5265038

Research Article

A Novel Path Planning and Node Selection Method Using Reinforcement Learning in NTN IoT Networks

Siming Yang,[1] Zheng Shan,[1] Jiang Cao,[2] Yuan Gao,[2] Yang Guo,[2] Ping Wang,[2] Jing Wang,[2] and Xiaonan Wang[2]

[1]*State Key Laboratory of Mathematical Engineering and Advanced Computing, Zhengzhou, Henan 450001, China*
[2]*Academy of Military Science of the PLA, 100091, China*

Correspondence should be addressed to Siming Yang; 972856350@qq.com

Received 16 May 2022; Accepted 25 August 2022; Published 16 September 2022

Academic Editor: Mingqian Liu

With the rapid deployment of 5G networks in recent years, the characteristics of high bandwidth, low latency, and low energy consumption of 5G networks have enabled the rapid development of IoT (Internet of things) technology. However, 5G networks cannot provide high-quality wireless coverage for many IoT devices in border areas and hotspots with a high signal density that lack fixed infrastructure. Therefore, this paper uses the UAV (unmanned aerial vehicle) to carry the communication platform to build the NTN (nonterrestrial network) to provide wireless coverage for terrestrial fixed and mobile IoT devices. Meanwhile, since the NTN needs to provide wireless coverage for many IoT devices, we use deep reinforcement learning to provide path planning for the UAV communication platform to improve the efficiency of wireless coverage. We build a simulation environment to evaluate the performance of the NTN network for wireless coverage of IoT devices in urban hotspot areas. Experimental results show that the method proposed in this paper can provide higher downlink rates for more IoT devices than NB-IoT (narrowband Internet of things).

1. Introduction

In recent years, IoT technology has made great progress with the advent of 5G networks. Stable, high-quality, and wide wireless coverage are necessary prerequisite for the development and application of IoT technology. The widely used NB-IoT (narrowband Internet of things) [1] technology is mainly used in applications with small data volumes and low rates. The advantage of NB-IoT is lower power consumption and cost. At present, with the rise of video and audio applications, the low rate of NB-IoT technology limits the development of the IoT. The high-speed and low-latency characteristics of the 5G network make up for the low transmission rate. On the other hand, the massive MIMO (multiple input multiple output) technology proposed by the 5G network utilizes the spatial independence of users to provide independent narrow-beam coverage for different users in space and simultaneously transmit data of different users to improve system throughput [2]. The generation of this technology makes it possible to increase the capacity of the system while ensuring a high transmission rate. However, 5G networks cannot provide high-quality wireless coverage in border areas and hotspots with a high signal density and that lack fixed infrastructure. The IoT has two characteristics. One is that the number of connected devices is large, and the other is that the services of IoT devices are mainly burst services. Therefore, how to reasonably provide high-quality wireless coverage for a large number of IoT devices is a crucial problem to be solved at present. In order to promote the development and application of IoT in border areas and hotspot areas, many countries are now discussing the realization of high-quality signal coverage for IoT through NTN (nonterrestrial networks) [3] under the 6G standard.

Compared with traditional terrestrial base station networking, NTN uses HAP (high-altitude platform) for networking. Taking advantage of the maneuverability of HAP and the characteristics of line-of-sight communication,

NTN can provide high-quality signal coverage for border areas without ground base station coverage and disaster areas where ground base stations are damaged due to disasters. At the same time, in urban hot spots, NTN can assist ground base stations in solving the problem of wireless network congestion. The current challenge is that the NTN communication platform needs to serve many IoT devices and the distance from the NTN platform to the terminal is significantly larger than that of the ground base station. In addition, the Doppler frequency shift caused by the relative motion between the NTN platform and the IoT device can lead to fast fading. Therefore, avoiding fast fading while enabling the NTN platform to efficiently provide wireless coverage for terrestrial fixed and mobile IoT devices is an urgent problem to be solved.

This paper adopts a UAV (unmanned aerial vehicle) equipped with a base station called UAV-AP (unmanned aerial vehicle-aerial platform) as the NTN high-altitude platform to provide wireless coverage for urban IoT devices. We design a path planning algorithm based on deep reinforcement learning for the NTN communication platform. The algorithm enables the NTN platform to adjust its flight trajectory in real time according to the terrain characteristics and the IoT device's location information. With the support of algorithms, the NTN platform can provide services for as many IoT devices as possible and maximize the sum of the downlink rates of ground IoT devices while avoiding rapid fading.

The path planning method based on deep reinforcement learning has been widely used in scenarios where a UAV is used as a base station platform. Guo et al. and Bayerlein et al. [4, 5] used DQN [6] to solve the trajectory optimization problem to maximize the communication rate of transmission. However, DQN can only be applied to tasks in discrete action spaces and have a defect of overestimating the value function. Wang et al. [7] studied the optimal deployment of UAVs to maximize the real-time downlink capacity by using the double DQN algorithm [8]. Double DQN revises the defect of overestimation, but it is still unable to control the agent's actions in the continuous action space task. Liu et al. and Qi et al. [9, 10] adopted the DDPG algorithm [11] to maximize the geographical fairness of all considered points of interest (PoIs) and minimized the total energy consumptions. The DDPG (deep deterministic policy gradient) algorithm has successfully applied the algorithm to continuous action space tasks. However, the DDPG algorithm has too many hyperparameters that need to be adjusted, leading to slow and unstable agent training.

The main contributions of this paper are as follows:

(1) This paper proposes a UAV-AP air-to-ground urban propagation model. Meanwhile, we summarize the task as an optimization problem by combining the air-to-ground channel model and requirements of the UAV-AP communication support task

(2) We built a simulation environment that meets the task requirements based on the OpenAI Gym environment. The simulation environment reserves an interface for the interaction of reinforcement learning algorithms, which can efficiently train the agent

(3) This paper proposes an intrinsic reward reinforcement learning algorithm based on a parallel architecture. The algorithm can not only be used for policy optimization in continuous action space but also has a higher learning speed and better performance than previous reinforcement learning algorithms. The algorithm enables the NTN platform to perform real-time path planning based on multiple static and mobile IoT devices in a simulated environment, efficiently providing wireless coverage for IoT devices

The rest of this paper is organized as follows. Section 2 describes the NTN IoT network and generalizes the wireless coverage task as an optimization problem. In Section 3, we give a brief introduction to deep reinforcement learning and provide an analysis of our proposed algorithm. Then, we built a simulation environment, carried out related experiments, and analyzed the experimental results. Finally, Section 5 concludes the paper and looks forward to future work.

2. Problem Formulation

In this chapter, we will analyze the task of the NTN communication platform to provide wireless coverage for terrestrial IoT devices. Then, we introduce an air-to-ground channel model to estimate the path loss between NTN platforms and mobile IoT devices in urban environments. At the same time, we define the symbols used in subsequent articles and obtain the mathematical expression of the NTN platform signal coverage task.

The use of the NTN communication platform efficiently protects the burst services of a large number of static or mobile IoT devices on the ground. For example, in the rescue operation of the Henan flood in 2021, the NTN communication platform has achieved long-term stable continuous mobile signal coverage in the disaster area of about 50 square kilometers. The NTN communication platform has connected 2,572 users, generating 1,089.89 M of traffic, with a maximum of 648 users accessing a single time. The NTN communication platform restored the mobile public network signal for residents in the disaster area to promptly report the disaster situation and location information and also provided communication support for the rescue team.

As shown in Figure 1, the NTN communication platform can rely on its mobility to efficiently provide wireless connections for burst communications in multiple areas.

When providing wireless coverage for IoT devices in the target area, the NTN platform needs to comprehensively consider the signal attenuation caused by the building and the location information of the IoT device to adjust its flight trajectory in real time. The NTN platform needs to ensure that the downlink rate of all IoT devices is higher than the minimum threshold rate and avoid fast fading caused by relative motion.

2.1. Modeling of the Air-to-Ground Channel. We introduce an air-to-ground channel path loss model based on the

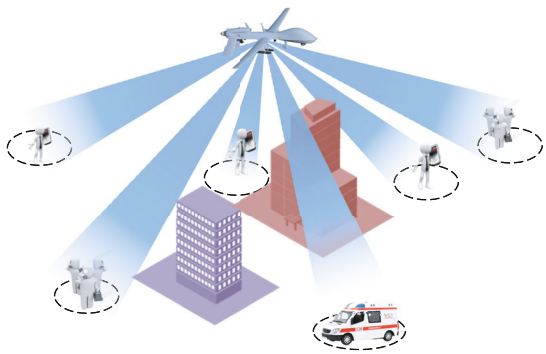

Figure 1: Schematic diagram of the NTN network wireless coverage task.

urban environment, mainly considering the path loss caused by the signal blocking by urban buildings. The International Telecommunication Union (ITU) proposes a general model based on the loss of radio signal transmission caused by the occlusion of buildings in its official standard. The model can be applied to a variety of urban environments. The transmission probability of line-of-sight communication and non-line-of-sight communication between the transmitter and the receiver is defined as a function of elevation angle and environmental parameters. Through mathematical derivation, the formula is achieved, which is gradually evolved and simplified by SIGMOD.

The International Telecommunication Union (ITU) [12] proposed an air-to-ground channel model that can be used in a variety of urban environments to measure the geometric probability of LoS transmission between the transmitter and the receiver. This model summarizes the probability of LoS (line of sight) and NLoS (nonline of sight) as a function of elevation angle and several environmental parameters. The formula can be fitted by the SIGMOD function which can be written as follows:

$$\mathbf{P}(\mathbf{LoS}, \theta) = \frac{1}{1 + a \exp\left(-b[\theta - a]\right)}. \tag{1}$$

Parameters "a" and "b" are called S-curve parameters, which can be queried in literature [12] according to the corresponding city type.

According to the obtained LoS probability, the NLoS probability is written as follows:

$$\mathbf{P}(\mathbf{NLoS}, \theta) = 1 - \mathbf{P}(\mathbf{LoS}, \theta). \tag{2}$$

Therefore, the path loss of the propagation can be modeled as follows:

$$\mathbf{PL}_{\xi} = \mathbf{FSPL} + \eta_{\xi}, \tag{3}$$

where **FSPL** represents the free space pathloss [13] between the NTN platform and an IoT device. η_{ξ} is the excessive path loss which is determined by the environment, and ξ refers to the propagation group. In this paper, we divide the propagation model into LoS and NLoS, which means that $\xi \in \{\mathrm{LoS}, \mathrm{NLoS}\}$, and the total path loss can be modeled as the following:

$$\mathbf{PL} = \mathbf{P}(\mathbf{LoS}, \theta) \times \mathbf{PL}_{\mathrm{LoS}} + \mathbf{P}(\mathbf{NLoS}, \theta) \times \mathbf{PL}_{\mathrm{NLoS}}, \tag{4}$$

where PL is the total path loss of the channel model and the downlink rate of each device can be calculated according to the path fading formula. Using the general model, we can obtain the path loss values of the UAV and the ground target at different elevation angles under the premise of free space loss. The general path loss calculation method for air-to-ground channels is the basis for generalizing the UAV-AP communication coverage task as an optimization problem.

2.2. Mathematical Expression of the Problem. We define the signal path loss from the NTN platform to an IoT device $m(m \in M)$ as PL_m, speed of light as c, signal frequency as f, NTN platform's base station transmit power as P_s, the bandwidth as W, and the position vector from the NTN platform to the IoT device m as $\vec{d}_m$. Besides that, we set the velocity vectors of the NTN platform and an IoT device to be $\vec{v}_f$ and $\vec{v}_m$, respectively. The Gaussian white noise power on the bandwidth is set to N, and the minimum threshold rate of IoT device m is D_m. Figure 2 is a schematic diagram of the relationship between the NTN platform and a mobile IoT device.

The frequency of the signal received by the device m at time t can be written as follows:

$$f_{mt} = f \times \left(\frac{c - \vec{v}_m \cdot \vec{d} / \left| \vec{d} \right|}{c - \vec{v}_f \cdot \vec{d} / |d|} \right). \tag{5}$$

The IoT device m that received power at time t is shown as follows:

$$\mathbf{Pr}_{\mathbf{mt}} = 10 \lg \left(1000 \times P_s\right) - PL. \tag{6}$$

We can get the theoretical maximum downlink rate from Shannon's formula [13], which can be written in the following form:

$$\mathbf{C}_{\mathbf{mt}} = W \log_2 \left(1 + \frac{\mathbf{Pr}_{\mathbf{mt}}}{N}\right), \tag{7}$$

where $\mathbf{C}_{\mathbf{mt}}$ is the downlink rate of the device m at time t. The NTN communication platform continues to provide wireless coverage for terrestrial IoT devices during time T. During this period, the time for device m to perform burst service is T_m. Under the condition that each IoT device does not produce fast fading and the downlink rate is higher than the threshold rate, our goal is to maximize the average downlink rate of M devices under the effective communication time in a period T. In time T, we set the time set of user

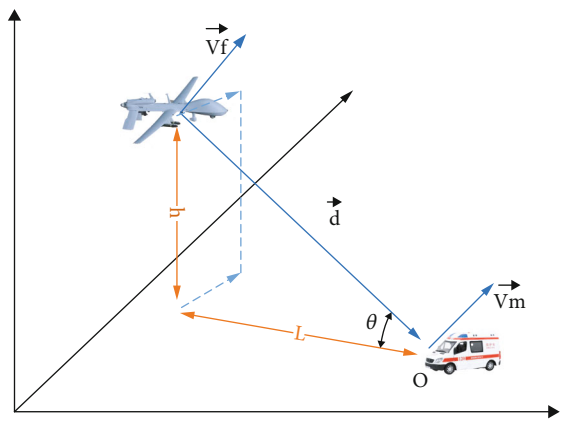

Figure 2: Relative position relationship between an NTN platform and a ground mobile IoT device in a certain time slot.

m to perform burst service as G_m. In order to avoid the fast fading of IoT devices, it is necessary to ensure that the symbol time is longer than the coherence time when the device performs burst communication, which means that when $t \in G_m$, $C_{mt} f_{mt}$. So, our problem can be summarized as the following optimization problem:

$$\begin{aligned} &\text{maximum} \frac{1}{M} \times \sum_{m}^{M} \left(\frac{1}{T_m} \times \sum_{t=0}^{T} C_{mt} \right) \\ &\text{subject to } C_{mt} f_{mt}, \quad \text{when } t \in G_m, \\ &C_{mt} \geq D_m, \quad \text{when } t \in G_m. \end{aligned} \tag{8}$$

It can be seen that the UAV-AP wireless coverage task is an optimization problem with many unknowns. Such problems are difficult to solve using optimization theory, so we use deep reinforcement learning to optimize the policy in the interaction between the agent and the environment. The optimization objective in equation (8) is the expected return of the DRL algorithm, and the constraints limit the form of the algorithm's reward function.

3. Algorithm Analysis

From the conclusions of Section 2, we can see that the task of an NTN communication platform to provide wireless coverage for terrestrial multi-IoT devices involves many variables. It is difficult to find the optimal solution with traditional optimization methods for this problem. Therefore, we intend to use reinforcement learning methods to improve the policy using the experience generated by the agent (i.e., the NTN communication platform) interacting with the environment. Eventually, the agent can learn a near-optimal policy that satisfies our goal.

In this section, we first introduce deep reinforcement learning and then propose our improved method for the slow learning speed of the current algorithms.

3.1. Introduction of DRL. RL (reinforcement learning) [14] originated from the optimal control theory in cybernetics. It is mainly used to solve sequential decision-making problems. Through continuous interaction and trial and error with the environment, the agent finally learns a near-optimal strategy and maximizes the expected revenue. DRL (deep reinforcement learning) is a combination of DL (deep learning) [15] and reinforcement learning. With the help of deep neural networks' powerful feature representation capabilities, it can fit various functions in reinforcement learning well, enhance the fitting ability of reinforcement learning, and expand the RL application scenarios.

Our research sets the NTN communication platform as the agent and sets up a simulated environment to interact with the agent. Using the empirical data generated by the interaction between the agent and the environment, the agent can finally learn a near-optimal path planning strategy. The NTN communication platform makes real-time decisions according to the strategy obtained by training, maximizing the average downlink rate of the ground IoT devices under adequate communication time.

A drawback of the current DRL is that the algorithm learns slowly, especially when dealing with tasks with ample state space and action space. Therefore, we need to design an algorithm that can efficiently process a large amount of empirical data and rapidly improve the strategy's performance. The training process of reinforcement learning can be divided into the empirical data collection stage and the agent training stage. The former is responsible for collecting interaction data between the agent and the environment, and the latter is responsible for training strategies using the collected data. When we discuss the acceleration of the algorithm, both stages need to be considered in detail. Methods to improve the learning speed of the agent refer to Figure 3.

In the empirical data collection stage, the primary methods to accelerate the learning rate are to improve the quality of empirical data or improve the efficiency of data collection. In order to improve the sample quality, we can use the algorithms which can guide the agent to explore the unknown environment efficiently, thereby increasing the diversity of the collected data. In order to improve the efficiency of data collection, the current mainstream method is to combine reinforcement learning algorithms with parallel architectures.

The main methods to improve the learning speed in the strategy training phase can be summarized as follows. The first type of method balances the deviation and variance of the value function estimation. The second type of method is to utilize the information of value distribution. The third type of method is to stabilize the training process of the agent and avoid excessive fluctuations that affect the convergence speed and results. The fourth method is to improve data utilization efficiency, which can replay critical empirical data to accelerate algorithm convergence.

3.2. Algorithm. In order to improve the learning speed of the algorithm, we refer to the RND algorithm [17] and introduce intrinsic rewards in order that the agent can make the training process stable and improve exploration efficiency to obtain high-quality data. RND innovatively uses intrinsic reward to measure the novelty of the current state,

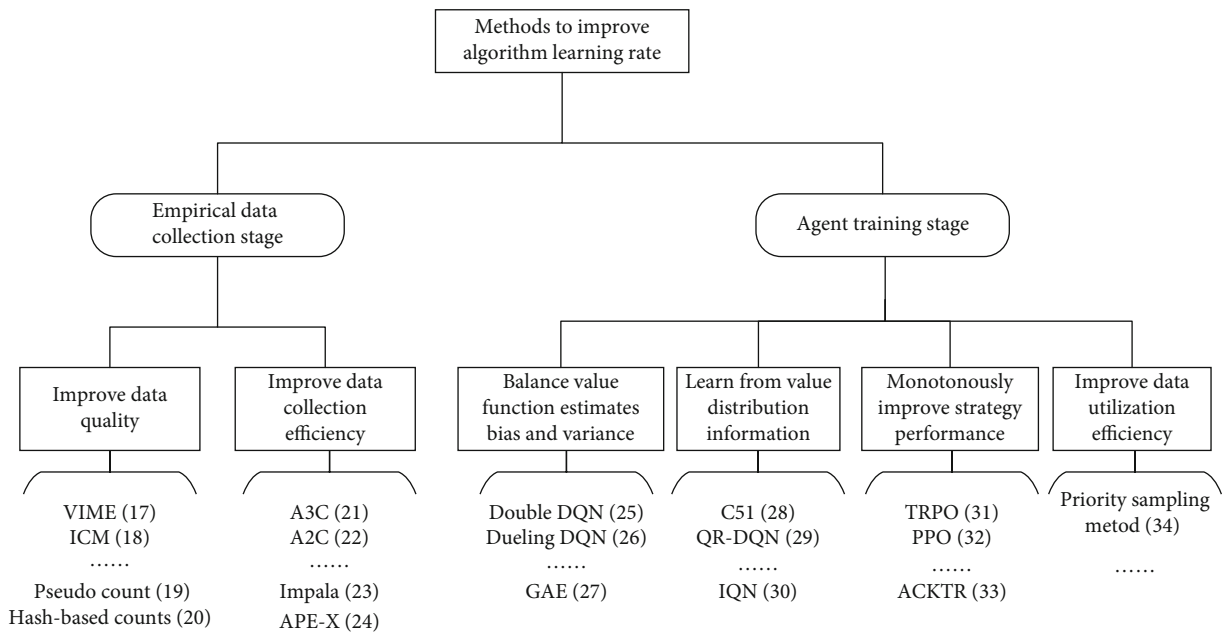

Figure 3: Methods to improve algorithm learning speed.

which encourages the agent to explore the strange state action combination of the simulation environment. In addition, the RND algorithm incorporates the idea of the PPO [16] algorithm and achieves a monotonous increase in agent performance during the training process, which improves the stability of the training process. Based on the RND algorithm, our proposed algorithm integrates it into a parallel architecture to accelerate the learning rate of the algorithm by improving the efficiency of data collection.

Next, we briefly introduce the adopted architecture and then propose solutions for the problem of bias caused by strategy learning.

3.2.1. Architecture Introduction. The architecture of the RND algorithm is summarized in Figure 4. The problem of the algorithm is that the data collection efficiency is too low.

In order to further improve the data sampling efficiency, we refer to the idea of Impala architecture. The Impala architecture contains multiple workers and one or more learners. The worker is responsible for interacting with the independent environment and collecting experience data. The learner is responsible for updating the strategy with aggregated data. Figure 5 shows the architecture diagram with multiple workers and one learner.

Each worker is independent. In Figure 5, worker i completes an episode of data interaction, stores the collected experience data in the cache, then synchronizes the current latest strategy from the learner, and starts a new round of interaction. The learner will use the collected data from multiepisode to update the strategy. After completing an episode of interaction and the experience data is saved in the cache, worker i will synchronize the latest strategy of the learner instead of waiting for the strategy update of the learner. This architecture completely decouples the learner and the worker, saves the worker's waiting time, and dramatically accelerates the speed of data collection. Figure 6 shows the timeline comparison between the learner and the worker in Impala, A3C, and A2C algorithms.

It is shown that each worker of the A3C architecture needs to wait for the strategy update of the learner to synchronize its latest strategy and uses the new policy to start the next episode of interaction. In A2C architecture, the learner needs to wait for all workers to complete the interaction task and uses data to update policy and then synchronize policy to all workers. Compared to the above architectures, workers and learners of the Impala architecture are entirely decoupled. With the simple architecture, the learner can conveniently use the GPU for acceleration and the workers can be easily distributed on many machines.

3.2.2. Intrinsic Reward RL Algorithm Based on Parallel Architecture. Because the behavior strategy is inconsistent with the target strategy, which makes the algorithm become an off-policy algorithm. Therefore, the collected data needs to be processed before learning; otherwise, the training process will generate a large deviation resulting in performance degradation. In order to solve this problem, we use the V-trace method to process the sampled intrinsic rewards and extrinsic rewards and obtain the estimated value function that the learner can utilize to update policy.

According to behavior policy μ, a worker interacts with the environment and collects an episode of data. We define the n-step V-trace value of state x_s as follows:

$$v_s = V(x_s) + \sum_{t=s}^{s+n-1} \gamma^{t-s} \left(\prod_{i=s}^{t-1} c_i \right) \sigma_t V, \tag{9}$$

where $\sigma_t V = \rho(r_t + \gamma V(x_{t+1}) - V(x_t))$ is the temporal difference value of V estimated from data sampled by the worker.

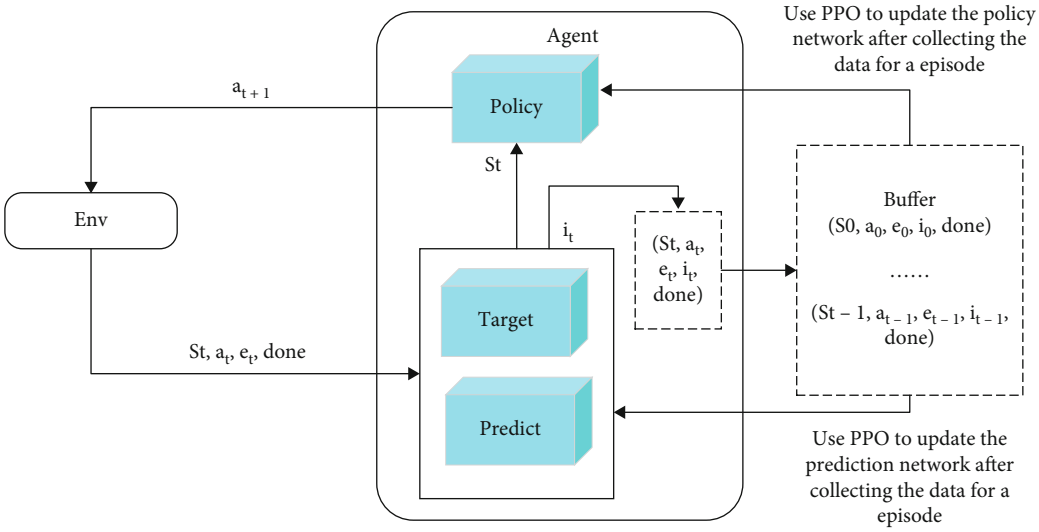

Figure 4: Architecture diagram of the reinforcement learning algorithm based on intrinsic reward.

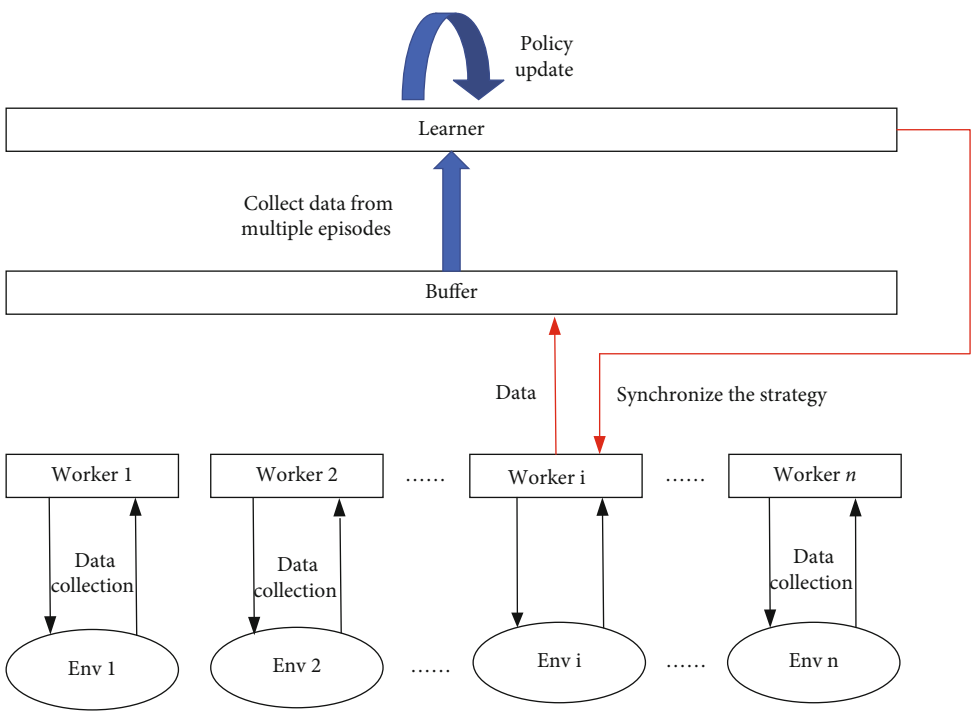

Figure 5: Architecture diagram of Impala.

Parameter $\rho_t = \min(\rho, (\pi(a_t|x_t)/\mu(a_t|x_t)))$ and parameter $c_i = \min(c, (\pi(a_t|x_t)/\mu(a_t|x_t)))$. ρ_t and c_i have different roles in the equation. The former is used in the definition of $\sigma_t V$ and according to the fixed point theory, the estimated value function of the above formula is the value function V^{π_ρ} under the strategy π_ρ. The policy π_ρ can be written as follows:

$$\pi_\rho(a|x) = \frac{\min(\rho\mu(a|x), \pi(a|x))}{\sum_{b\in A} \min(\rho\mu(b|x), \pi(b|x))}. \quad (10)$$

The above formula shows that when ρ is infinite, policy π_ρ is the target policy and V^{π_ρ} is the value function of the target policy π. If ρ is close to zero, we obtain the value function of the behavior policy V^{π_μ}. When we choose a truncation level $\rho < \infty$, our fixed point is the value function V^{π_ρ} which is somewhere between μ and π. The weights $c_s \cdots c_{t-1}$ quantitatively assess the impact of temporal difference $\sigma_t V$ observed at time t on the update of the value function at a previous time s. Thus, in the formula, ρ impacts the convergence fixed point of the value function and c impacts the coverage speed.

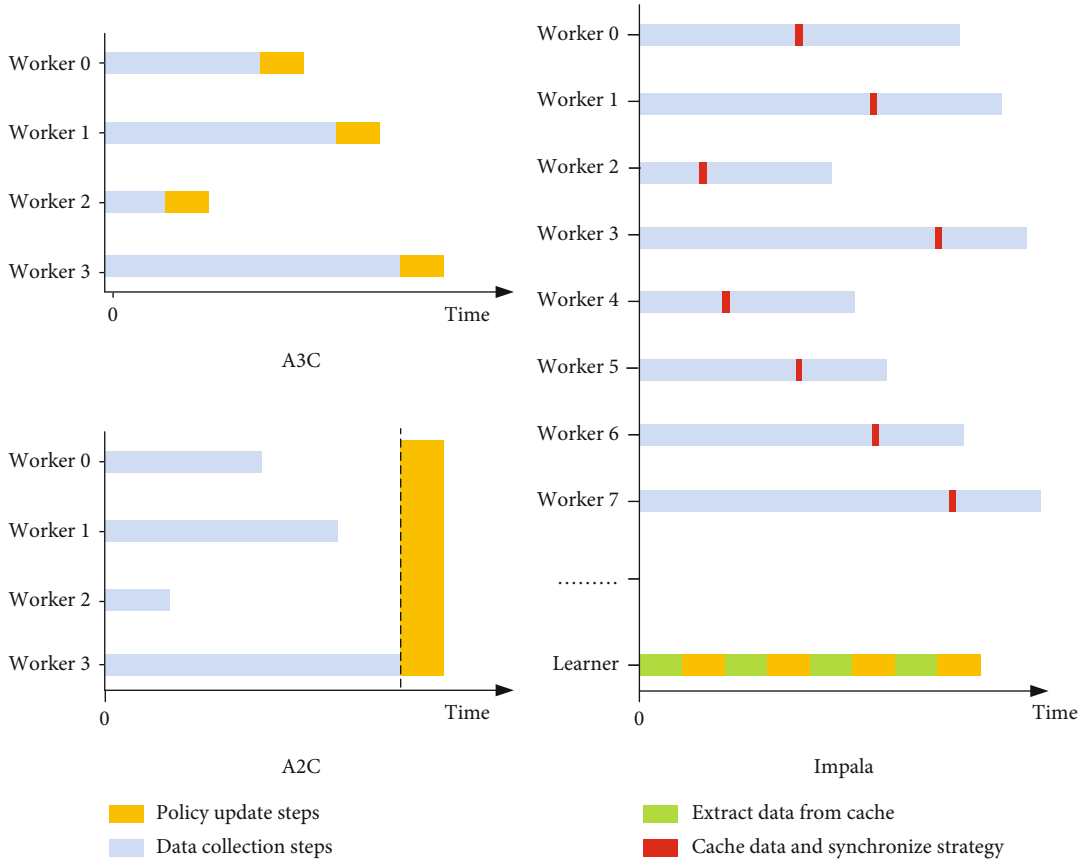

Figure 6: Timeline comparison chart.

Finally, we propose the intrinsic reward RL algorithm under the parallel framework and the flow chart is shown in Figure 7. It is shown that each worker independently interacts with its environment to collect data and store it in the buffer. Then, the worker synchronizes the current latest policy from the learner and starts the next round of interaction. The learner will periodically fetch data from the buffer for policy updates. The data collected by different behavior strategies will be processed through the V-trace method. Then, the value function of the intrinsic reward and the value function of the extrinsic reward will be calculated. Finally, the policy network and the value function evaluation network are updated by using the PPO algorithm. Our proposed algorithm can be divided into two parts, worker and learner. The worker is mainly responsible for the data acquisition function, and its pseudocode can be found in Algorithm 1. Learner is mainly used for policy training, and its pseudocode can be used in Algorithm 2.

4. Experiments

In this section, we will set the parameters used in the experiments and define the agent's action space, state space, and reward function. We will then analyze the experimental results.

4.1. Parameter Settings. We use OpenAI Gym [18] to build the simulation environment. We assume a communication assurance task, and the task is set as follows. In a three-dimensional map with the size of 50 km × 50 km × 5 km, there are randomly distributed buildings with the height of 50 m ~ 150 m. The NTN platform provides wireless coverage for ten moving IoT devices and ten static IoT devices randomly distributed on the ground. We set all IoT devices to perform burst traffic with a probability of 0.01 every time slot. It can also be regarded as a Poisson distribution with a λ of 1 in 100 seconds. The NTN platform can adjust the flight direction within the range of 0–360 Â°, the flight elevation angle within the range of 0–180 Â°, and the flying speed within the range of 180 ~ 300 km/h. Then, we will define the state space, action space, and reward function in the reinforcement learning process.

4.1.1. The State Space. The agent's state space is the combination of the NTN platform and 20 IoT devices' states. The reason why we only set up 20 devices in the experiment is because it is limited by the performance of individual experimental devices. More users means that UAV-APs need to cover more locations and actively adjust their flight status to provide users with high-quality services. In this experiment, since the starting positions and flight trajectories of each user are random, the positions are scattered and the trajectories are uncertain, which ensures the validity of the experimental results to a certain extent. In the future, we will add more users to test the performance of the algorithm. The NTN platform state can be defined as a 7-

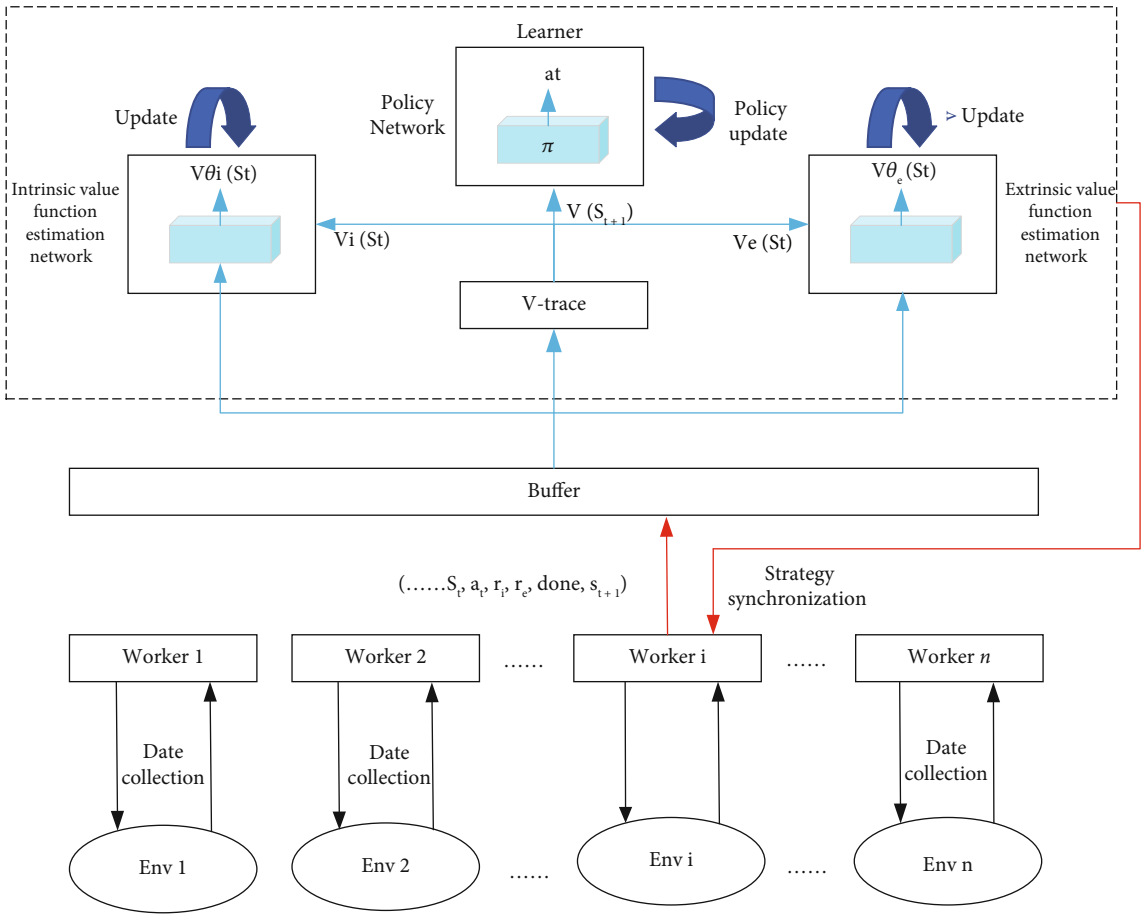

Figure 7: Algorithm flow chart.

element vector that includes the NTN platform's location coordinates in the map, the flight angle, flight elevation angle, speed of NTN platform, and base station transmit power. The IoT device state is a 4-dimensional vector including the device's coordinates on the map, moving angle, and speed of IoT device. In order to ensure the consistency of the matrix form, the remaining elements are set to 0. So, the state space of the agent is the 21×7 matrix.

4.1.2. The Action Space. The action space of the agent is a vector containing four continuous elements, including speed, flight angle, flight elevation angle of the NTN platform, and base station transmit power. We need to standardize these variables, and then, the agent will execute these actions in a simulated environment and get the reward at this time slot.

4.1.3. The Reward. The NTN platform needs to ensure that the downlink rate of each IoT device is greater than the threshold rate while preventing fast fading caused by the Doppler frequency shift. Under this premise, the goal of the task is to maximize the average downlink rate of the device under adequate communication time. We set the reward value for each time slot as the average downlink rates of IoT devices performing bursty services in that time slot. However, if a device is affected by fast fading or the downlink rate is lower than a threshold, the downlink speed of that device is considered to be is 0. Besides, if the NTN platform hits the building, we terminate the experiment and return −100 as the reward value for this round. If the problems mentioned above do not occur during the communication guarantee task, the reward value of 100 is returned. If the experiment termination condition has not been triggered within time t, we terminate the experiment and return the reward value 100.

The algorithm code is written in Python 3.8, mainly using libraries such as PyTorch, Gym, and NumPy. The training environment is the simulation environment introduced in Section 3, built on the Windows 10 system with 2 NVIDIA 3090 graphic cards and 64 g RAM. In the experiments, we tested the proposed algorithm with the current mainstream reinforcement learning algorithms and algorithms under different parallel architectures in a simulation environment. Each experiment ran on 2 K rollouts with 32 parallel environments, and the hyperparameters used in the algorithm are shown in Table 1. The parameters of the communication metrics have been introduced in Section 2 and the introduction of algorithm hyperparameters in Section 3. We utilize 32 parallel environments for data collection to improve the training speed. At the same time, we

```
T←numbers of parallel environments; K←→initial length of rollout;
D←number of initial steps for initializing observation;
t=0
Sample state s_0 ~ P_0(s_0)
For d=1 to D do
   Sample a_t ~ Normalized(a_t)
   Sample s_{t+1} ~ p(s_{t+1}|s_t, a_t)
   Update observation normalization parameters using s_{t+1}
   t += 1
End for
While true
t=0
   For j=1 to K do
      For h=1 to T do
         Sample a_t ~ Normalized π(a_t|s_t)
         Sample s_{t+1}, e_t ~ p(s_{t+1}, e_t|s_t, a_t)
         Caculate intrinsic reward i_t = ||f^(s_{t+1}) − f(s_{t+1})||^2
         Add s_t, s_{t+1}, a_t, e_t, i_t to optimization batch B_h
         Update reward normalization parameters using i_t
         t +=1
      End for
      Collect data,put B_h into the global buffer B
   End for
   Synchronize the strategy from the learner
```

Algorithm 1:Data acquisition module pseudocode.

```
L←the length of the data extracted; N_opt←→initial number of optimization steps;
K←initial length of rollout; N^_opt←→number of optimization steps in later stages;
K^ ←→new length of rollout in later stages;
While true
   Extract data from the buffer
   Normalize the intrinsic rewards contained in B
   For j=1 to L do
      Caculate returns R_{I,i} and advantages A_{I,i} for intrinsic reward
      Caculate returns R_{E,i} and advantages A_{E,i} for extrinsic reward
      Utilize A_{I,i} and A_{E,i} by using V-trace and obtain value function A^_{I,i} and A^_{E,i} of π_ρ
      Caculate combined advantages A_i = A^_{I,i} + A^_{E,i}
      Update observation normalization parameters
   End for
   For j=1 to N_opt do
         Optimize θ_π wrt PPO loss on batch B, A_i using AdamW
         Optimize θ_f wrt distillation loss on B using AdamW
   End for
   Check recent data if meet the conditions of adjusting parameters
      Then set K = K^, N_opt = N^_opt
```

Algorithm 2: Policy training module pseudo code.

set the initial rollout length to 2,500 and the initial optimization step to 4 to pretrain the parameters of the model. We set the learning rate to 0.0003 to avoid overfitting and set the discount values for internal and external rewards to 0.99 and 0.999 to ensure that the agent is not affected by reward values that are too old. The design of GAE and PPO parameters is to avoid that the optimization step size is too large, resulting in failure to converge to a better result.

Figure 8 shows the number of IoT devices that can operate normally after adopting the NB-IoT method or the method based on the NTN communication platform. Since an IoT device obeys a Poisson distribution with a λ of 1 within 100 seconds, the data are counted in units of 100 seconds and all are rounded.

The blue bar in represents the number of mobile IoT devices that successfully performed burst services within

Table 1: The value of parameter used in the algorithm.

Hyperparameter	Value
Number of users (M)	10
Threshold rate (C_{th})	5 M/s
Bandwidth (W)	10 MHz
Transmit power (P_s)	200 W
Path loss parameter (PL_{LoS}/PL_{NLOS})	0.1/21.0
Environment parameters (a, b)	0.1750
Parallel environments (T)	32
Number of rollouts (N)	2000
Initial rollout length (K)	2500
Initial optimization steps (N_{opt})	4
Initial learning rate	0.0003
Initial number of minibatches	8
Intrinsic discount factor	0.99
Extrinsic discount factor	0.999
Optimization algorithm	AdamW
GAE factor λ	0.95
PPO clip range	[0.9,1.1]
Coefficient of extrinsic reward	1
Coefficient of intrinsic reward	1
ρ	1
c	1

100 s. The orange bar represents the number of static IoT devices that successfully performed burst services within 100 s. According to the probability calculation, both static IoT devices and dynamic IoT devices will perform an average of 10 burst services within 100 s. It shows the results using the NB-IoT method. It can be seen that the static IoT device and the mobile device can successfully execute the burst service six times and three times, respectively, every 100 seconds, which is far less than the estimated execution times. The reason is that NB-IoT relies on fixed base stations, the signal strength will attenuate as the distance increases, and buildings will also block the signal. Attenuation of the signal makes the downlink rate of static and mobile IoT devices far away from the base station too low to perform services typically. At the same time, the fixed base station cannot effectively handle the fast fading caused by the Doppler effect, so the support for mobile IoT devices is even worse.

The lower diagram in Figure 8 represents the use of the NTN communication platform to provide wireless coverage for IoT devices. It can be seen that the static IoT device and the mobile device can successfully execute 10 and 8 burst services, respectively, every 100 seconds, which is relatively close to the estimated execution times. This is because the NTN platform can adjust its flight status according to the learned strategy based on the current status information and IoT devices. Learned strategies enable the NTN platform to take into account both static devices and mobile devices and maximize the average downlink rate of all IoT devices on the premise of avoiding fast fading. On the other hand, in the experiment, the method based on the NTN communication platform can make the average downlink speed of IoT devices reach 10 Mbps. In contrast, the NB-IoT method can only provide a maximum downlink rate of 250 Kbps. Therefore, the method based on the NTN platform can provide services for more IoT devices and significantly increase the downlink rate of the device.

Figure 9 shows the performance comparison between our algorithm and current mainstream reinforcement learning algorithms in the NTN platform path planning task. The results show that the algorithm performs poorly in the early stage. This is because the agent needs to fully explore the environment under the guidance of internal rewards in the early stage and accumulate more valuable experience data. Therefore, in the early stage of training, the agent tends to explore rather than improve the policy performance. We can see that after training to nearly 700 scenes of data, the algorithm's performance will increase exceptionally quickly. This is because the agent has conducted a comprehensive exploration of the environment and has begun to use the collected experience data to make targeted improvements. At this stage, the agent is more inclined to improve the policy performance. It can be seen that compared with the current mainstream algorithms, our algorithm has a faster convergence speed and a higher final score.

On the other hand, the learning rate of the proposed algorithm is much faster than other algorithms. When the agent is trained to 1,000 episodes, the algorithm's performance decreases. This may be due to overfitting caused by the large update step size. Subsequently, the algorithm finally completed the convergence at 1,200 episodes with the policy iteration. It can be seen that our algorithm has a higher final score than several other mainstream algorithms. This is because the agent collects diverse empirical data in the early stage, preventing the algorithm from converging to a locally optimal solution. On the other hand, our proposed algorithm also has the fastest convergence speed. This benefits from the improved efficiency of agent-environment interaction brought by the decoupled parallel architecture.

Figure 10 shows the performance comparison results of the proposed algorithm. It can be seen that the proposed algorithm has better performance than the algorithms based on A2C and A3C architecture. Among them, the performance of the A3C algorithm is the worst. Due to the asynchronous update method, each worker uses a different strategy leading to accumulation of deviations in the update process. This makes the algorithm based on A3C have poor performance and significant fluctuation during the training process. Compared to the algorithm based on the A2C architecture, the final performance is close but our algorithm allows the algorithm to reach the target score faster. The reason is that the worker and the learner are wholly decoupled, which makes the worker not need to wait for the learner to update the strategy improving the sampling efficiency. Comparing the algorithm without V-trace correction, it can be found that the algorithm without V-trace correction has significant fluctuation and hardly learns effect policy. The target policy will have a significant deviation if the learner uses data that V-trace has not corrected to update the

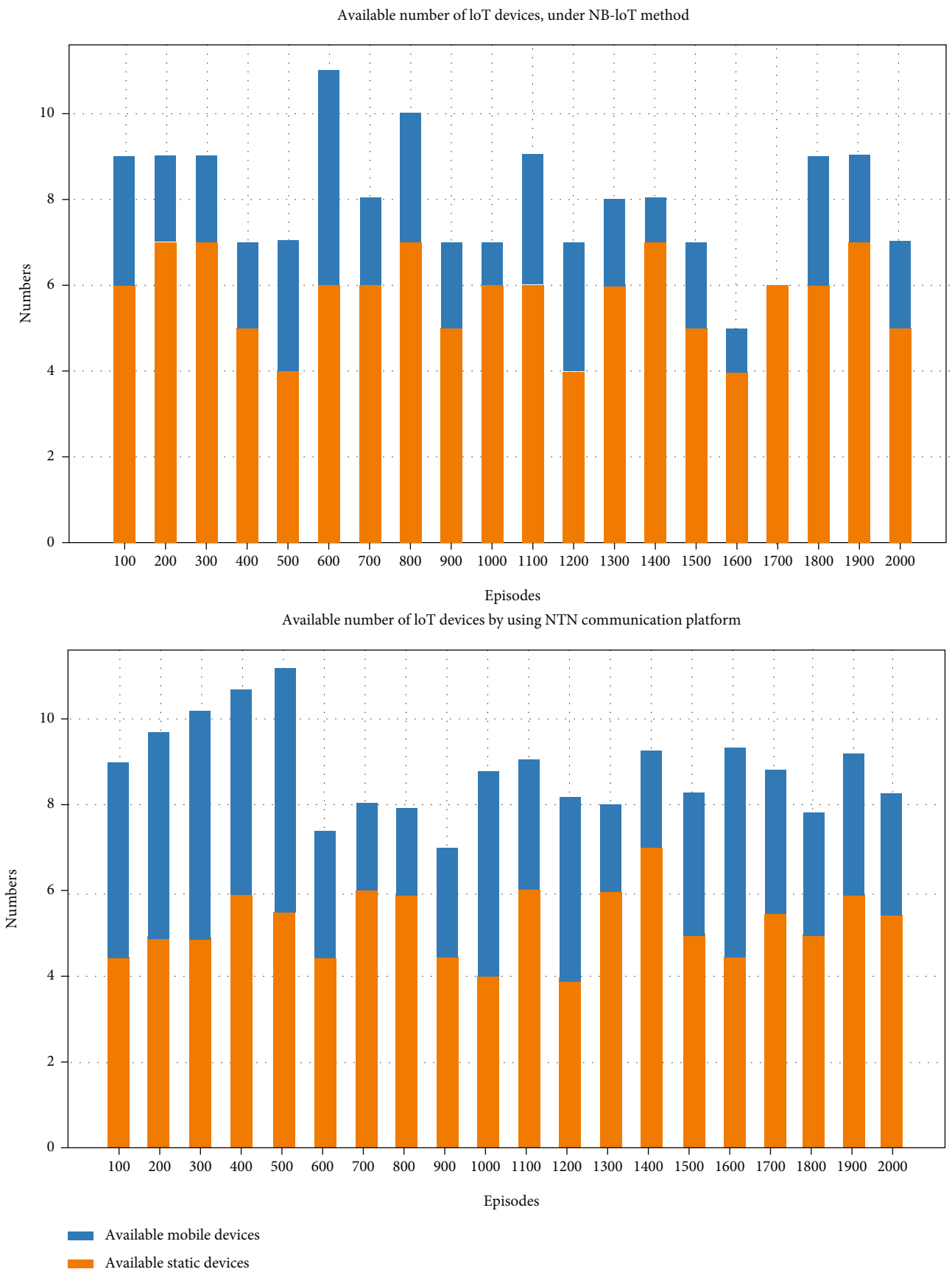

Figure 8: Comparison of the number of available IoT devices.

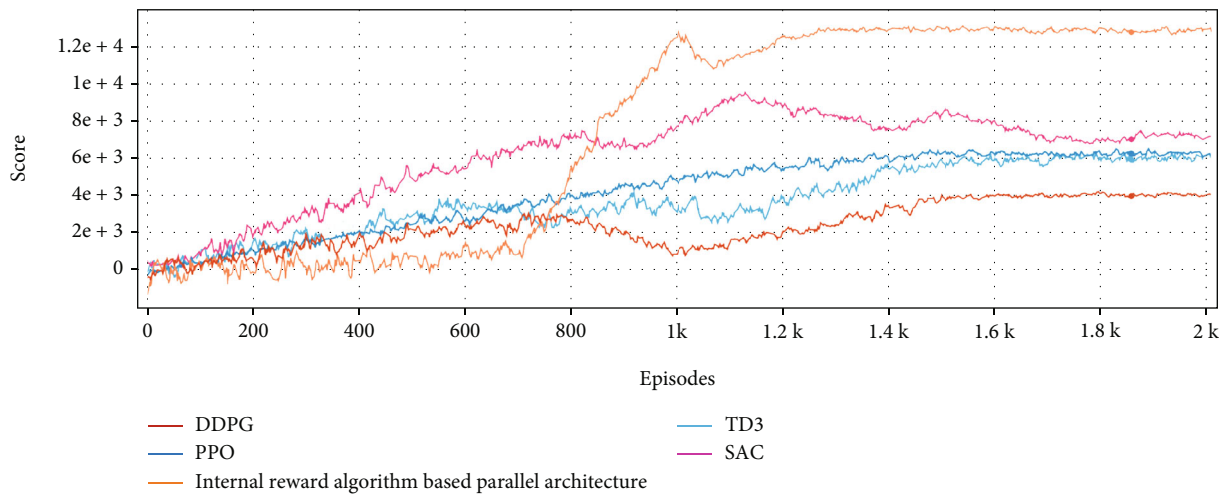

Figure 9: Performance comparison between the proposed algorithm and mainstream reinforcement learning algorithms.

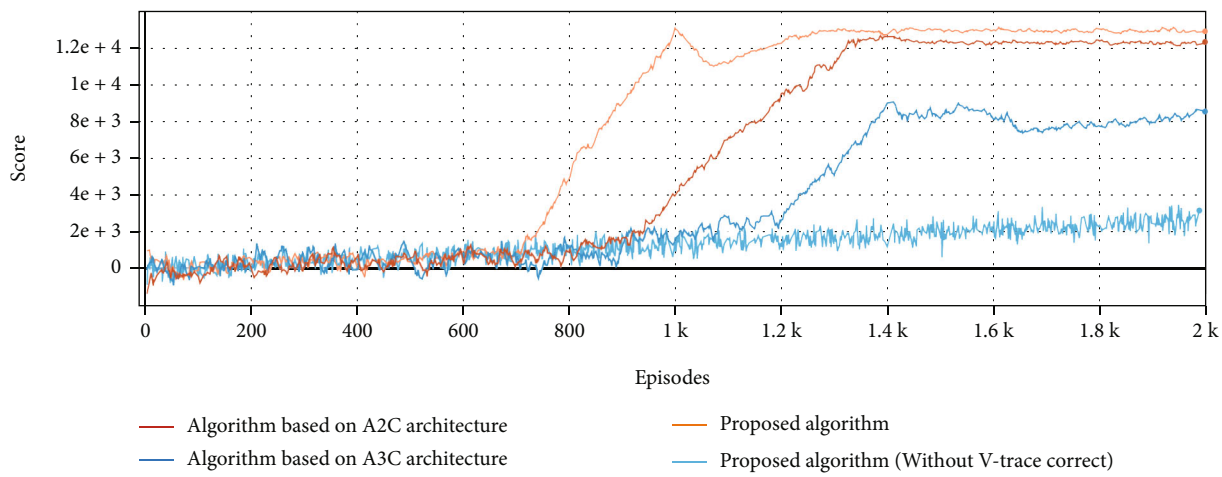

Figure 10: Performance comparison between the proposed algorithm and algorithms under other parallel architectures.

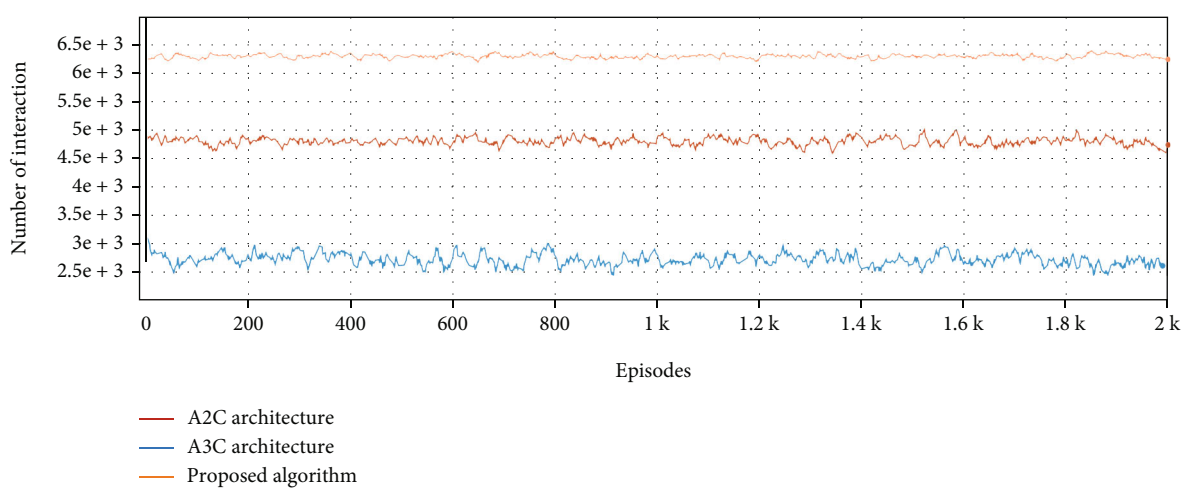

Figure 11: Comparison of the number of interactions between the agent and the environment per second in one episode.

strategy. The accumulation of deviation will reduce the accuracy of the agent's prediction of the value function, eventually leading to poor performance. So, the experiment proves that the V-trace correction is significant for the off-policy algorithm.

Figure 11 shows the average number of interactions between the agent and the environment per second in an episode of data during the training process. Our algorithm has the most significant number of interactions per second and has a minor variance during the training process, which means that the interaction is stable. The difference in the interaction time of different algorithms mainly depends on when the worker waits for the learner to update the strategy and synchronize the strategy. In A3C, each worker needs to wait for the learner to update its policy using collected data. Multiple workers queue up so that congestion occurs and the speed of interaction decreases. In A2C architecture, the learner needs to wait for all workers to complete the interaction and store the data in the buffer before starting the policy update. The main reasons for the weak interaction are the time that the learner waited for the workers and the time that the worker waited for the learner to process large-scale data. In our algorithm, the learner and workers are entirely decoupled and work asynchronously. Therefore, the learning speed of the learner does not affect the interaction between the workers and the environment. This is why our algorithm has the most significant number of interactions per second and the most stable interaction process.

5. Conclusion

This paper mainly explores the possibility of using a nonterrestrial IoT network built with the NTN platform to provide high-quality wireless coverage for terrestrial mobile IoT devices. The real-time path planning of the NTN platform is realized by using the reinforcement learning algorithm, which effectively improves the downlink rate of ground mobile IoT devices. Experimental results showed that our algorithm significantly improved the final performance and learning rate compared to mainstream reinforcement learning algorithms. Our architecture has higher data collection efficiency than commonly used parallel architectures. In summary, the NTN IoT network has the potential to make up for the shortage of fixed base stations that cannot provide high-quality signal coverage for ground IoT devices in border areas and urban hotspots. At the same time, this will further promote the development and application of IoT. In order for the algorithm to be applied in a practical environment, we need to solve the following problems in the future. First, the impact of signal interference on the NTN platform needs to be resolved. Secondly, the NTN platform needs to find a method that can quickly and accurately locate moving targets. According to the research, Liu et al. use federated learning to train a distributed network to identify signal disturbances [19]. Simulation results show that the method leads to excellent recognition performance with a small dataset. On the problem of moving target localization, Liu et al. propose a passive position parameter estimator for estimating moving aerial targets using multiple satellites [20] and an intelligent passive detection method based on reservoir computing networks [21]. The simulation results show that the method can accurately estimate the position parameters of moving objects and achieve efficient detection of moving objects. We will refer to the content of the above articles in the future and improve the algorithm proposed in this article to adapt to practical application scenarios.

Data Availability

This article uses the OpenAI Gym framework to build a reinforcement learning simulation environment. All experimental analysis data were obtained from this platform. The simulation platform has been applied for the corresponding software copyright, numbered 2021SR1463151. Since the research results are supported by the Academy of Military Science of the PLA, all experimental data and results are kept by the institution. You can contact Mr. Zhang at lanyangyang_1994@sina.com to apply for the experimental data.

Conflicts of Interest

The authors declare that they have no conflicts of interest.

Acknowledgments

This study is supported by the National Natural Science Foundation of China (61971092).

References

[1] M. Chen, Y. Miao, Y. Hao, and K. Hwang, "Narrow band internet of things," *IEEE Access*, vol. 5, pp. 20557–20577, 2017.

[2] H. Han, L. Fang, W. Lu, W. Zhai, Y. Li, and J. Zhao, "A gcica grant-free random access scheme for m2m communications in crowded massive mimo systems," *IEEE Internet of Things Journal*, vol. 9, no. 8, pp. 6032–6046, 2022.

[3] "TR 38.821-V0.4.0. "Solutions for NR to support non-terrestrial networks (NTN)"," https://www.3gpp.org/DynaReport/38821.html, 2019.

[4] J. Guo, Y. Huo, X. Shi et al., "3D aerial vehicle base station (UAV-BS) position planning based on deep Q-learning for capacity enhancement of users with different QoS," *Requirements[C]// 2019 15th International Wireless Communications and Mobile Computing Conference (IWCMC)*, p. 23, 2019.

[5] H. Bayerlein, P. D. Kerret, and D. Gesbert, "Trajectory Optimization for Autonomous Flying Base Station via Reinforcement Learning[C]," in *2018 IEEE 19th International Workshop on Signal Processing Advances in Wireless Communications (SPAWC)*, p. 24, IEEE, 2018.

[6] V. Mnih, K. Kavukcuoglu, D. Silver et al., "Playing Atari with deep reinforcement learning," *Computer Science*, vol. 25, 2013.

[7] Q. Wang, W. Zhang, Y. Liu, and Y. Liu, "Multi-UAV dynamic wireless networking with deep reinforcement learning," *IEEE Communications Letters*, vol. (99), pp. 1–22, 2019.

[8] H. V. Hasselt, A. Guez, and D. Silver, "Deep reinforcement learning with double Q-learning," *Computer Ence*, vol. 26, 2015.

[9] C. H. Liu, X. Ma, X. Gao, and J. Tang, "Distributed energy-efficient multi-UAV navigation for long-term communication coverage by deep reinforcement learning," *IEEE Transactions on Mobile Computing*, vol. 19, no. 6, pp. 1274–1285, 2020.

[10] H. Qi, Z. Hu, H. Huang, X. Wen, and Z. Lu, "Energy efficient 3-D UAV control for persistent communication service and fairness: a deep reinforcement learning approach," *IEEE Access*, vol. 8, no. 53172-53184, pp. 53172–53184, 2020.

[11] T. P. Lillicrap, J. J. Hunt, A. Pritzel et al., "Continuous control with deep reinforcement learning," *Computer Ence*, vol. 27, 2015.

[12] ITU-R, *Rec. P. 1410-2 Propagation Data and Prediction Methods for the Design of Terrestrial Broadband Millimetric Aadio Access Systems, P Series*, Radiowave propagation, 2003.

[13] A. Saakian, *Radio Wave Propagation Fundamentals, LI Ji-Jun; CHEN Hai-yan*, Propagation properties of metal clad waveguide at communication frequency, 2020.

[14] R. S. Sutton and A. G. Barto, "Reinforcement learning," *A Bradford Book*, vol. 15, no. 7, pp. 665–685, 1998.

[15] Y. Li, "Deep reinforcement learning: an overview," https://arxiv.org/abs/1701.07274, 2017.

[16] J. Schulman, F. Wolski, P. Dhariwal, A. Radford, and O. Klimov, *Proximal Policy Optimization Algorithms*, 2017.

[17] Y. Burda, H. Edwards, A. Storkey, and O. Klimov, *Exploration by Random Network Distillation*, 2018.

[18] G. Brockman, V. Cheung, L. Pettersson et al., *OpenAI Gym*, 2016.

[19] M. Liu, Z. Liu, W. Lu, Y. Chen, X. Gao, and N. Zhao, "Distributed few-shot learning for intelligent recognition of communication jamming," *IEEE Journal of Selected Topics in Signal Processing*, vol. 16, no. 3, pp. 395–405, 2022.

[20] M. Liu, B. Li, Y. Chen et al., "Location parameter estimation of moving aerial target in space–air–ground-integrated networks-based iov," *IEEE Internet of Things Journal*, vol. 9, no. 8, pp. 5696–5707, 2022.

[21] M. Liu, C. Liu, M. Li, Y. Chen, S. Zheng, and N. Zhao, "Intelligent passive detection of aerial target in space-air-ground integrated networks," *China Communications*, vol. 19, no. 1, pp. 52–63, 2022.

Hindawi
Wireless Communications and Mobile Computing
Volume 2022, Article ID 2254077, 17 pages
https://doi.org/10.1155/2022/2254077

Research Article

Structures Guided Dynamic Scene Deblurring Method

Qing Qi

Department of Physics and Electronics Information Engineering, Qinghai Minzu University, Xining, China

Correspondence should be addressed to Qing Qi; qiqing@tju.edu.cn

Received 17 May 2022; Accepted 30 July 2022; Published 15 September 2022

Academic Editor: Mingqian Liu

In this paper, we integrate image gradient priors into a generative adversarial networks (GANs) to deal with the dynamic scene deblurring task. Even though image deblurring has progressed significantly, the deep learning-based methods rarely take advantage of image gradients priors. Image gradient priors regularize the image recovery process and serve as a quantitative evaluation metric for evaluating the quality of deblurred images. In contrast to previous methods, the proposed model utilizes a data-driven way to learn image gradients. Under the guidance of image gradient priors, we permeate it throughout the design of network structures and target loss functions. For the network architecture, we develop a GradientNet to compute image gradients via horizontal and vertical directions in parallel rather than adopt traditional edge detection operators. For the loss functions, we propose target loss functions to constrain the network training. The proposed image deblurring strategy discards the tedious steps of solving optimization equations and taking further advantage of learning massive data features through deep learning. Extensive experiments on synthetic datasets and real-world images demonstrate that our model outperforms state-of-the-art (SOAT) methods.

1. Introduction

In the field of computer vision, image deblurring is a crucial and challenging task. Object motion, camera shake, and other complicated circumstances invariably result in blurry observations during the image acquisition process. Clean and fine image details are required for postprocessing applications such as traffic surveillance, object recognition, and image segmentation. Therefore, the importance of image deblurring is particularly prominent. Blind image deblurring aims at recovering deblurred images from a known blurry degraded image. The mathematical expression of the image deblurring modeling process can be expressed as

$$b = s * k + n, \tag{1}$$

where s, k, n, and b denote clean images, kernels, noise, and blurry images, respectively.

According to Equation (1), we can derive that estimating kernels and computing clean images is a tough task. In traditional image deblurring methods [1–7], the blurry kernel is usually determined by estimating significant structures of the image, and then nonblind deconvolution is computed to obtain the deblurred image. However, these methods have the following limitations: (1) these methods can only extract features from a limited number of images. It may not stimulate realistic dynamic blurry scene; (2) these methods obtain deblurred images by computing optimization equations, which is time-consuming, and the algorithm is less real-time.

With the development of deep learning, convolutional neural networks (CNNs) are exploited in methods [8–11] to learn blur kernels at the pixel level. Subsequently, nonblind deconvolution operations are employed to generate latent images. Although this strategy combines classic and learning-based methods, accumulated errors are derived by blending separately estimated kernels and deblurred images. To overcome the limitations of the isolated image deblurring strategy of "kernel estimation-deconvolution," methods [12–14] followed an end-to-end manner to directly investigate the underlying relationship between blurry and deblurred images. The multiscale deblurring methods [15, 16] followed the image deblurring strategy of "coarse-to-fine" to achieve deblurring. However, it has some limitations: first, at some

scales, the multiscale network structure tends to be overfitting. Second, multiscale networks focus on the relationships between scales rather than the relationship between the original input and the clean counterpart. Although deep learning-based methods alleviate the limitations of handcraft feature extraction methods, the lack of image prior guidance makes the network difficult to optimize and converge.

According to the mechanism of the human visual system, human eyes are the most sensitive to image structures compared to other components [17]. In other words, the human eye is the most intuitive in observing whether the image has clean and significant structures. On the one hand, structures of the image can be exploited as a priori for regularizing the image recovery process. On the other hand, image structures can be served as a quantitative evaluation metric for evaluating the quality of deblurred images. Few works focus on integrating image structure priors to CNN-based methods. Qi et al. [18] designed an edge adversarial mechanism for tackling dynamic scene deblurring. However, the processing of adaptively learning image structures is neglected.

Inspired by the image super-resolution method of [19], we propose an image deblurring method based on image gradients priors for tacking the dynamic scene deblurring task. Meanwhile, image gradient priors permeate the design of network structure and target loss function. For the loss functions, we propose objective loss functions aim to supervise the generator such that generated images have significant structure information. For the network topology, we propose a subnetwork of GradientNet. First, we introduce a recurrent gradient convolutional layer (RGCL) to localize and represent image gradient features rather than a conventional edge detector. Second, multibranch reuse blocks (MBRBs) are proposed to learn high-dimension local features in a multipath reuse way; third, recalibrated channels of these accumulated and enhanced nonlocal features are highlighted by the non-local SENet module [20]. Finally, we arrange several MBRBs in a cascaded manner to enhance and aggregate the relationship of structural features. Extensive experiments on synthetic datasets and real-world images confirm the effectiveness of the proposed model, which achieves decent performance and is comparable to or better than SOTA methods.

The main contributions of this paper are presented as follows:

First, we propose a GAN, which has decent performance in restoring clean images for tackling the dynamic scene deblurring task.

Second, we introduce a GradientNet to compute image gradients via horizontal and vertical directions in parallel.

Third, we develop multiterm target loss functions to drive the generator to generate images with salient structures.

2. Related Works

In recent years, many image deblurring methods have been proposed. We mainly introduce image deblurring methods from aspects of traditional segmentation-based methods and learning-based methods.

2.1. Traditional Segmentation-Based Methods. Dynamic blurry scenes are spatially varied in pixel level, and solutions for the uniform blurry task may not fit the complicated dynamic scene task. According to blurry regions in a dynamic scene, Kim et al. [21] adopted an image segmentation method to separate blurry regions and then deal with each of them, respectively. However, motion segmentation cannot accurately separate blurry regions. Kim and Lee [22] proposed an alternative segmentation-free method by exploiting the deblurring strategy to solve this challenging task. This scheme avoids drawbacks brought by inaccurate segmentation. However, the dynamic blurry scene is spatially varied in pixel level in extreme cases. Especially, when object motion and camera shake simultaneously occur in the imaging process. As a compromise, Pan et al. [23] proposed a method based on the segmentation confidence map for enhancing the segmentation accuracy of different regions of the degraded images.

2.2. Learning-Based Methods. CNNs are commonly used in image processing fields [24–28], due to their extremely robust feature extraction capabilities. Schuler et al. [11] and Xu et al. [29] employed multiple CNNs to implement image features extraction, blur kernels estimation, and deblurred image reconstruction separately. Chakrabarti [10], Sun et al. [8], and Gong et al. [9] exploited CNNs to estimate nonuniform blur kernels; then, they used existing nonblind deconvolution methods to generate deblurred images, following the image deblurring strategy that involves kernel estimation and nonblind deconvolution algorithms. Li et al. [30] and Ren et al. [31] adopted image priors with the benefits of CNN to achieve image deblurring. These methods make use of deconvolution algorithms and CNNs. Nonetheless, this isolated deblurring strategy causes cumulative errors, resulting in blurred details in the recovered images.

To overcome the limitations of the above algorithms, researchers further propose deblurring methods [12–14] to directly construct the essential relationship between blurry and clean images in an end-to-end manner. Nah et al. [15] followed the "coarse-to-fine" image deblurring strategy and propose a multiscale deblurring method. Although the multiscale network reduces the difficulty of image deblurring in a divide-and-conquer manner, the weight parameters of multiple scales are independent. And each scale of the network only deals with the image of the current resolution. Based on the literature [15], Tao et al. [16] proposed a multiscale CNN with shared parameters. On the one hand, this network takes advantage of the dependence of weight parameters between multiscales; on the other hand, it can reduce network parameters and stabilize network optimization. To acquire high-dimensional feature representations, Gao et al. [32] proposed an image deblurring method based on selective parameter sharing and nested connections, which can effectively extract high-order nonlinear features. Furthermore, Zhang et al. [33] introduced an image

deblurring method based on a recurrent neural network to learn the high-dimensional features by indirectly expanding receptive fields for image reconstruction and deblurring. However, image deblurring methods based on CNN do not consider the semantic information between blurry images and clean images.

GAN [34] is a machine learning architecture proposed by Goodfellow et al. in 2014. GAN has been applied in the computer vision community. Inspired by CycleGAN [35], image deblurring can be considered as an image translation task by translating blurry degraded input to the blurry-free one. Since the highly unstable property of GAN, it is difficult to simultaneously train two pairs of GAN models. Furthermore, directly transferring this recycling framework to image deblurring task unsurprisingly generates poor results. Nimisha et al. [36] proposed a GAN for tackling class-specific image deblurring task in an unsupervised fashion. Due to a lack of ground truths, they utilize blurry images themselves to guide the network to acquire image color information. Kupyn et al. [37] developed a conditional GAN named DeblurGAN. They propose a content loss to capture the semantic correspondence difference between blurry images and corresponding ground truths. Lately, to satisfy the different requirements of real-time processing and deblurring performance, Kupyn et al. [38] proposed three models with feature pyramid network architecture. Qi et al. [18] introduced a method based on an edge adversarial mechanism to narrow the difference in image structure between deblurred images and ground truths. To further facilitate the quality of deblurred image structures, we propose an image gradient-driven dynamic scene deblurring method to constrain image recovery. Specifically, we design a GradientNet to investigate the relationship between image gradients and dynamic scene deblurring in a data-driven way rather than adopt classic image edge detectors.

3. Proposed Method

In this section, we introduce specific illustrations of the overall network architecture, GradientNet, and target loss functions.

3.1. Network Architecture. We tailor a deep learning framework specifically for the challenging dynamic scene deblurring task. Figure 1 depicts the overall pipeline of the proposed network. The generator is designed to generate deblurred images with clean appearances and salient structures in an end-to-end fashion, while the discriminator is designed to assign correct labels to the fake and real images. Furthermore, the discriminator supervises the generator to ensure that it produces images infinitely close to being clean.

3.1.1. Generator. As shown in Figure 2, the generator is employed to map deteriorated blurry images to their clean counterparts. At the stage of the encoder, the blurry degraded inputs are spatially compressed and encoded. At the bottle of the U-Net, we introduce a GradientNet to investigate and preserve significant structures in a multi-branch reuse fashion. Correspondingly, at the stage of the decoder, decoded feature representations of blurry images are accessible for recovering deblurred images. Specific network framework and parameters configuration of the developed model are marked in Figure 2. Furthermore, skip connections are exploited to bridge the semantic gap between encoded features and their decoded counterparts. Following that, we introduce the backbones of GradientNet in detail.

3.1.2. GradientNet. In this paper, we propose a GradientNet to investigate the relationship between gradient representations and dynamic scene deblurring in a data-driven way. As shown in Figure 2, GradientNet consists of a prepositional feature transition module (PRFTM) and a multi-branch reuse unit (MBRU). Next, we introduce PRFTM and MBRU in detail, respectively.

(1) PRFTM. PRFTM is employed to extract higher-dimensional features by acting as partitions and buffers. In particular, PRFTM consists of two cascaded convolutional layers with kernels of 3×3. The following is the mathematical expression:

$$U_{-1} = f_{\mathrm{FE1}}(U_{n-1}), \tag{2}$$

$$U_0 = f_{\mathrm{FE2}}(U_{-1}), \tag{3}$$

where f_{FE1} and f_{FE2} denote the first and second convolutional layer in PRFTM, respectively. U_{n-1} implicates the input feature that delivers to PRFTM. U_{-1} represents the output feature from f_{FE1}. U_0 implies the output feature from f_{FE2}. Convolutional layers increase the number of channels of the input image and maps it to a space with more potential features.

(2) MBRU. As shown in Figure 2, MBRU consists of 10 MBRBs and a CA module [20]. Features of an image are usually obtained from local receptive fields that reflect spatial relationships within the image domain. For the dynamic scene deblurring task, it is essential to capture features that represent the overall data distributions of images. Therefore, we first learn high-order local features from MBRBs; then, recalibrated channels of these accumulated and enhanced nonlocal features are highlighted by the CA module. Indirectly, the proposed MBRU constructs the interdependencies between pixels and channels. Assuming there are n MBRBs, the n-th output U_n can be expressed as

$$U_n = \mathrm{MBRBs}_n(U_0), \tag{4}$$

where U_0 denotes input features from PRFTM, and U_n implicates output features processed by MBRU.

(3) MBRBs. It is essential to tightly correlate the learned features among the proposed network for addressing the image deblurring task. Therefore, we adopt the multipath reuse manner to enhance gradient features obtained by RGCL.

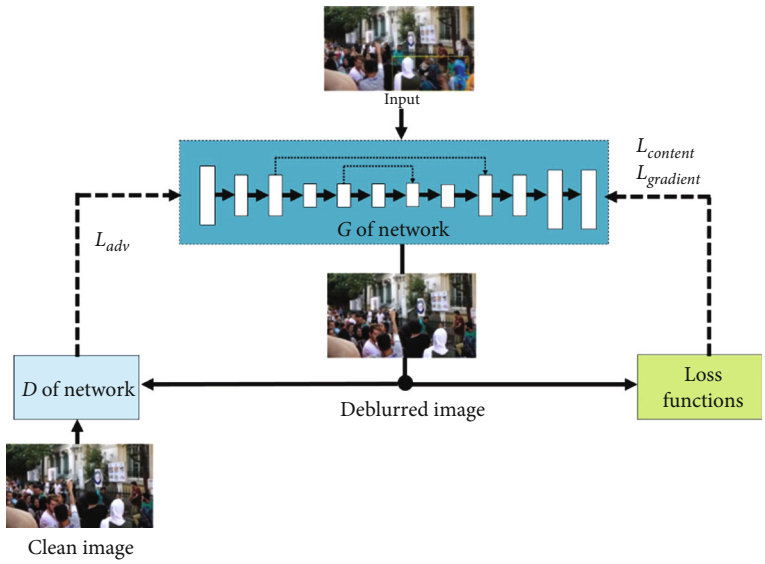

Figure 1: The entire framework of the proposed model comprises target loss functions and the network training process. The generator aims to generate deblurred images with clear appearances and discernible structures, while the discriminator is designed to assign correct labels to the fake and real images. Solid lines represent forward propagations, while dashed lines implicate back propagations.

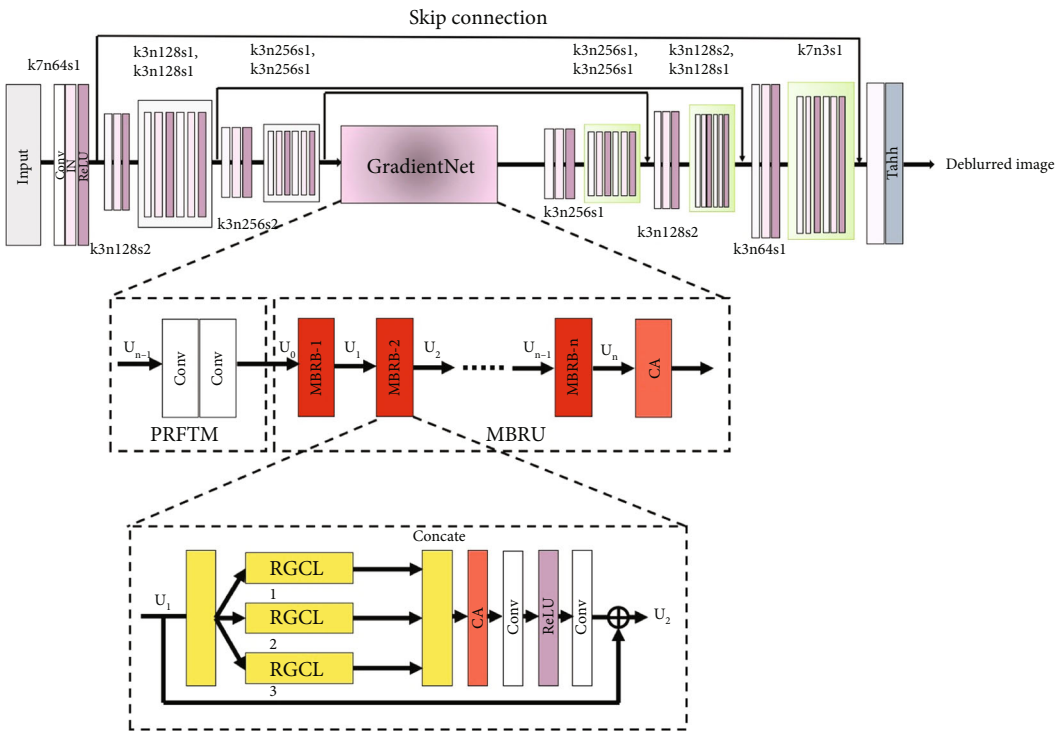

Figure 2: The overall structure of the generator in the proposed network, where IN standards for instance normalization, k implies kernel size, n expresses the number of feature maps, s indicates stride, Tanh represents Tanh function, and CA denotes channel attention module.

Reasons for not adopting a multiscale structure are (1) multiscale methods of [15, 16] follow the image deblurring strategy of "coarse-to-fine" to generate deblurred image gradually. Unlike [15, 16], we capture image gradient features in a multipath reuse manner simultaneously; (2) for blurry images, the images at multiple scales have different degrees of blurry. When the image features at different scales are fused, it is easy to produce blurry appearances; (3) this is not conducive to achieve gradient features enhancement. The specific network architecture of MBRBs is displayed in Figure 2. Each MBRB contains following steps: first, we arrange three RGCL in multipath reuse mode; second, these reused features are fused by a concatenate operation; third, the CA module is also employed to recalibrate essential channel features; fourth, two convolutional layers and ReLU activation function [39] are followed as a buffer to obtain

processed features; finally, building a residual connection between the input and output. The mathematical expression of MBRB can be formulated as

$$f_n = \mathrm{Con}((\mathrm{RGCL}_1(U_0) + \mathrm{RGCL}_2(U_0) + \mathrm{RGCL}_3(U_0))), \tag{5}$$

$$f_n = f_{\mathrm{FE4}}(\mathrm{ReLU}(f_{\mathrm{FE3}}(\mathrm{CA}(f_n)))) + U_0, \tag{6}$$

where RGCL denotes recurrent gradient convolutional layer, Con implicates a concatenate operation, f_{FE3} and f_{FE4} denote two convolutional layers in MBRB, and f_n implies processed features.

(4) RGCL. Classic edge detectors, such as Sobel and Laplace, can only calculate edges of a certain intensity. Given the above limitations, we introduce a RGCL that deals with image gradients in horizontal and vertical directions in parallel, as shown in Figure 3. Compared to plain convolutional layers, the idea of this rectangle convolution kernel design is based on the following: first, reducing network parameters and algorithmic complexity of the proposed network; second, dedicating to dealing with a certain dimension (vertical or horizontal) structures information. The parallel investigation can conserve more information than sequential design. In general, RGCL has the following advantages: (1) RGCL emphasizes image structures information by using the vertical and horizontal gradient information in parallel; (2) kernels of plain convolutional layers with the same receptive field have more computing complexity and parameters; (3) the recurrent mechanism is adopted to continuously enhance significant image structures obtained by gradient convolutional layers.

In order to implement the "parallel" processing strategy, inspired by cascaded several convolutional layers, we reconsider the traditional convolutional layer as two convolutional layers with asymmetrical kernels in horizontal and vertical directions, as shown in Figure 3. We specifically develop asymmetrical convolutional kernels with sizes of 3×1 and 1×3 rather than the generally square kernels. Furthermore, the recurrent number of gradient convolutional layers is configured as 3. The mathematical expression of GCL is as follows:

$$U_{\mathrm{RGCL}} = \mathrm{CA}\left(\mathrm{Sigmoid}\left(\mathrm{Conv}\left(\mathrm{LR}(k_{1\times n} \otimes U_0 + k_{n\times 1} \otimes U_0)_r\right)\right)\right) + \mathrm{Input}, \tag{7}$$

where k implies convolution kernels, n standards for kernel sizes, $\otimes$ denotes convolutional operations, r denotes the recurrent times, and U_{RGCL} expresses gradients information processed by RGCL.

Figure 4 depicts a sample of structural textures obtained using various filters. Compared to the Sobel operator, RGCL identifies edges in both vertical and horizontal directions. The results of Sobel and RGCL are shown in Figures 4(b) and 4(e), respectively. Gradient maps obtained by the filters

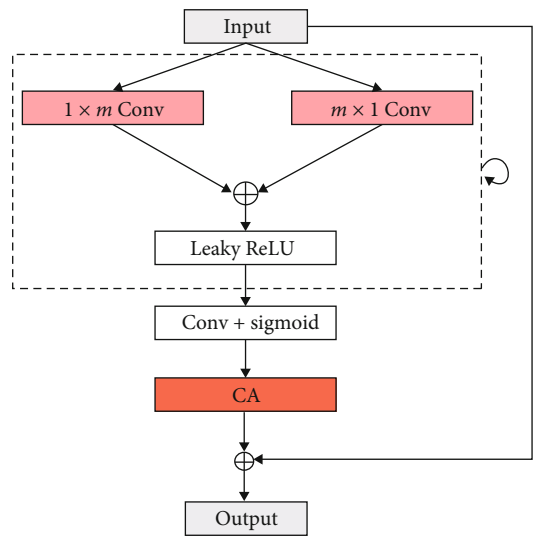

Figure 3: The pipeline of the proposed RGCL. Unlike normal convolution, RGCL aims at processing images parallel in vertical and horizontal directions by the rectangular kernel size.

of Sobel are rough outlines. In contrast, our method is able to extract and preserve significant structural features of the image, thus validating the possibility of the proposed RGCL to successfully investigate image structures. In particular, in Figures 4(c) and 4(d), we compare the produced edge maps with horizontal and vertical filters demonstrating that RGCL may extract more edge information than other edge detect operators.

3.1.3. Discriminator. The discriminator receives a generated image or a real image as input. The discriminator returns a probability in the range of [0,1] that indicates how real the input image is. Unlike the high-level task, deblurred image clarity is heavily influenced by local attributes rather than overall assessment. As a result, we use PatchGAN [40] as the discriminator in this paper.

3.2. Loss Functions. Throughout the design of network structures and target loss functions, we use image gradient priors. The proposed network's objective loss functions include (1) the semantic content loss L_{content}, which drives the image semantic coherence between generated images and clean ones; (2) the structure loss L_{gradient}, which facilitates generated images to retain salient structures; and (3) the adversarial loss L_{adv}, which supervises generated results to toward sharp counterparts.

3.2.1. Content Loss Function. Johnson et al. [41] propose a VGG19-based [42] semantic loss that has been pretrained on the ImageNet dataset to meet the visual perception of human eyes. For network optimization, we apply content loss [41] to drive perceptual similarity between generated images and corresponding ground truths at the feature level. Accordingly, the following is the mathematical expression of L_{content}:

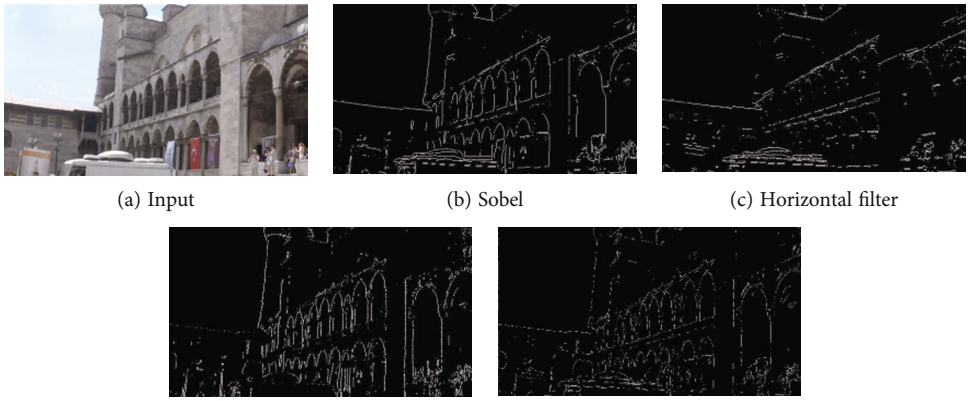

(a) Input (b) Sobel (c) Horizontal filter

(d) Vertical filter (e) RGCL

Figure 4: Gradient maps are visualized. Gradient maps of input have distinct structures, whereas gradient maps obtained by filters of Sobel are rough outline. Our method is capable of regenerating gradient maps with distinct outlines.

$$L_{\text{content}} = \frac{1}{\text{CWH}} \sum_{x=1}^{W} \sum_{y=1}^{H} \left\| \phi_{i,j}(s_k)_{x,y} - \phi_{i,j}(G(b_k))_{x,y} \right\|_2, \quad (8)$$

where s_k represents the ground truth, $G(b_k)$ denotes the generated image, C, W, and H imply the number, height, and width of feature maps, respectively. Following [41], we restrict the content difference of s_k and $G(b_k)$ via $\|\phi_{i,j}(s_k)_{x,y} - \phi_{i,j}(G(b_k))_{x,y}\|_2$. Let $\phi_{i,j}$ be the feature map obtained by the j-th convolutional after activation and before the i-th pooling layer within the pretrained VGG19 network ϕ. Here, we experimentally select the "ReLU4-3" layer in the pretrained VGG19 model to extract semantic feature representations of generated images and sharp ones, respectively.

3.2.2. Gradient Loss Function. We introduce a gradient loss function to supervise the generator that learns image structure information because gradient maps are capable of reflecting salient structures of images. We adopt a gradient loss to narrow the gap between blurry images and ground truths in horizontal and vertical gradient directions. Accordingly, the following is the mathematical expression of L_{gradient}:

$$\begin{aligned} L_{\text{gradient}} = \frac{1}{\text{WH}} \sum_{x=1}^{W} \sum_{y=1}^{H} & \left[\left\| \nabla_h(s_k)_{x,y} - \nabla_h(G(b_k))_{x,y} \right\| \right] \\ & + \left[\left\| \nabla_v(s_k)_{x,y} - \nabla_v(G(b_k))_{x,y} \right\| \right], \end{aligned} \quad (9)$$

where ∇_h and ∇_v represent gradient operations in the horizontal and vertical directions, respectively. We supervise the structure difference of s_k and $G(b_k)$ along the horizontal direction and vertical direction via $\|\nabla_h(s_k)_{x,y} - \nabla_h(G(b_k))_{x,y}\|_1$ and $\|\nabla_v(s_k)_{x,y} - \nabla_v(G(b_k))_{x,y}\|_1$.

3.2.3. Adversarial Loss. The purpose of adversarial loss optimization is to lead image feature maps from the blurry image domain B to the clean image domain S. We also employ WGAN-GP [43] as a network optimization critique function. L_{adv} can be expressed mathematically as follows of L_{adv}:

$$\begin{aligned} L_{\text{adv}} = & E_{G(b_k)\sim P_{\text{data}}(b)}[D(G(b_k))] - E_{s_k\sim P_{\text{data}}(s)}[D(s_k)] \\ & - \lambda E_{\hat{x}\sim P_{\hat{x}}}\left[\left(\|\nabla_{\hat{x}} D(\hat{x})\|^p \right) \right], \end{aligned} \quad (10)$$

where $\lambda E_{\hat{x}\sim P_{\hat{x}}}[(\|\nabla \hat{x} D(\hat{x})\|_2 - 1)^2]$ represents a sample uniformly sampled on the line between s_k and b_k, $G(b_k)$ signifies the generated image, s_k expresses the clean one, $E_{G(b_k)\sim P_{\text{data}}(b)}[D(G(b_k))]$ and $E_{s_k\sim P_{\text{data}}(s)}[D(s_k)]$ denote the expectation of D allocate the correct label to $G(b_k)$ and s_k, respectively.

Finally, we use multiterm loss functions to optimize the proposed model from the perspectives of L_{content}, L_{gradient}, and L_{adv}. The following is the definition of our network's overall loss function:

$$L(G, D) = \alpha L_{\text{content}} + \beta L_{\text{gradient}} + \gamma L_{\text{adv}}, \quad (11)$$

we adopt the following weight coefficients for each constraint item: $\alpha = 10$, $\beta = 1$, and $\gamma = 1$, respectively.

4. Experiments

In this part, we first introduce datasets and implementation details. The results of the proposed method are compared with SOTA methods subjectively and objectively on synthetic and real datasets. Then, we perform user study and computational complexity. Finally, we conduct ablation investigations to evaluate the relationship between image deblurring performance and loss functions as well as building blocks.

4.1. Datasets. In this paper, standard benchmarks of GOPRO [15], Köhler et al. [44], and Lai et al. [45] are utilized to train and test the proposed network. To train the network model, we select the training dataset of GOPRO [15]. The datasets of Köhler et al. [44] and Lai et al. [45] are adopted as test datasets to evaluate the deblurring performance of the

Figure 5: The blurry sample images of GOPRO [15].

Figure 6: The blurry sample images of [44].

Figure 7: The blurry sample images of the real-world subdataset of Lai [45].

proposed model. Next, we further present these datasets as follows:

4.1.1. GOPRO. The GOPRO dataset was introduced by Nah et al. in 2017 as a standard dataset for training neural networks for image deblurring. A GoPro4 Hero Black camera is used to shoot the video sequence of the dataset, and blurry images are processed by averaging clear frames. The GOPRO collection has 3214 pairs of blurry and clear images with a total resolution of 1280×720 pixels. The 2103 pairs of images are employed for training, and the remaining 1111 pairs of images are utilized for testing. An example of the dataset of GOPRO is shown in Figure 5.

4.1.2. Köhler. Köhler et al. [44] put up an experimental environment for recording and sampling the six-dimensional camera's motion trajectory to capture a series of clear images. Köhler consists of four clean images that correspond to 12 blurry images of a different blur. The dataset contains a total of 48 blurry images. An example of the dataset of Köhler is shown in Figure 6.

4.1.3. Lai. In 2016, Lai et al. presented a dataset [45] for evaluating image deblurring algorithms. The dataset contains two synthetic datasets and one real dataset. The dataset includes natural images, text images, face images, and other images. An example of the dataset of Lai is shown in Figure 7.

4.2. Training Strategy and Implementation Details. This section delves into the training process for the entire framework. We use the GOPRO dataset to train the proposed model in order to obtain deblurred images in a data-driven manner. The generator is fed blurry inputs that have been randomly cropped to 256×256 pixel sizes for training. To optimize the network, target loss functions reduce the distance between the learned picture and the label image. The discriminator receives the deblurred image or a real image at random, and it generates a probability in the range of [0, 1] that shows how real the input image is. The discriminator is used to supervise the training of the generator, which is used to learn deblurred images with distinct structures and clean appearances.

The experimental software configurations for our network are as follows: the operating system is Ubuntu 14.04, and the deep learning framework is Pytorch. The graphics card is an NVIDIA 1080Ti, and the processor is an Intel(R) Core(TM) I7 (16 GB RAM). The network is trained using 150 epochs in total. We set the generator and discriminator learning rates to 0.0001 and the batch size to 4. The Adam optimizer [46] is used for optimization training, with the parameters $\beta_1 = 0.5$ and $\beta_2 = 0.999$. During training, the generator is updated once, and the discriminator is upgraded

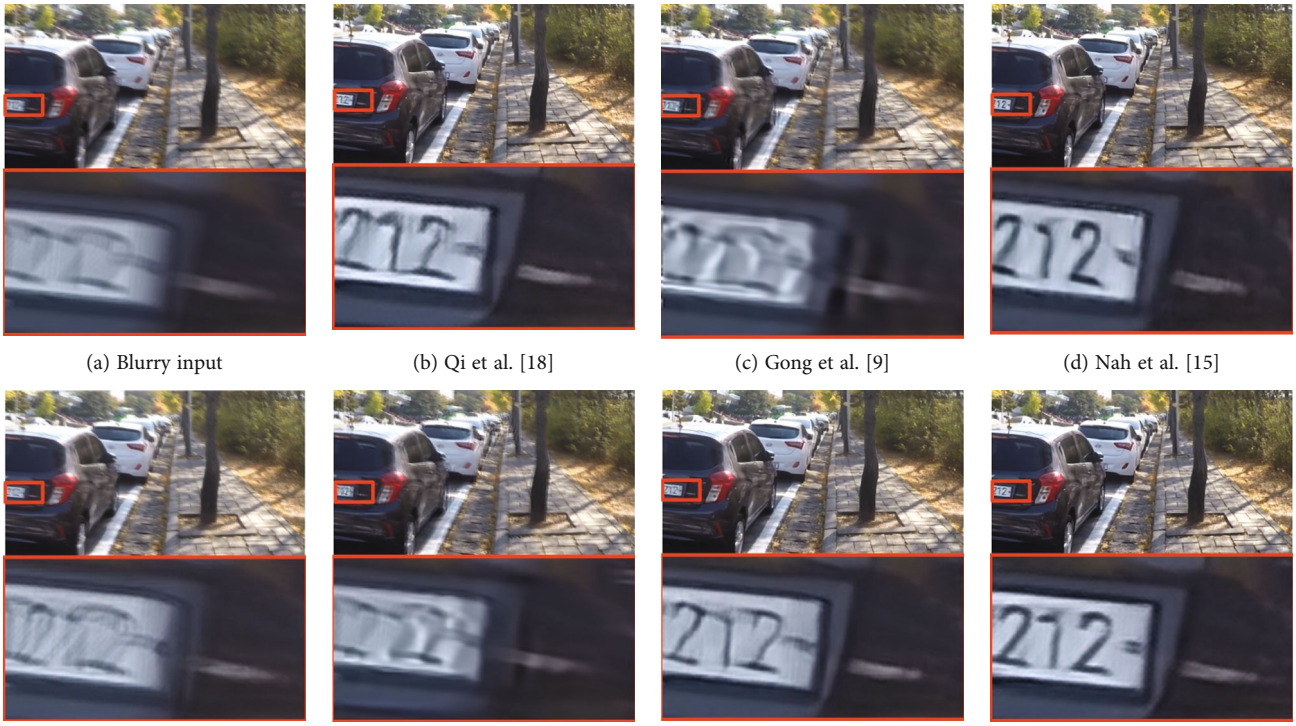

(a) Blurry input (b) Qi et al. [18] (c) Gong et al. [9] (d) Nah et al. [15]

(e) Kupyn et al. [37] (f) Mustaniemi et al. [47] (g) Kupyn et al. [38] (h) Ours

Figure 8: The visual effect of comparison methods and the proposed model on the synthetic dataset of GOPRO [15]. Our method has satisfactory visual effects and good details.

5 times. When the network has converged, original blurry inputs are conveyed to the pretrained generator to obtain deblurred images.

4.3. Experiments on Synthetic Data. Subjective and objective comparison studies using simulated blurry datasets are used to validate the proposed network's efficiency and effectiveness. Several typical learning-based methods are selected for comparing image deblurring performance on the test datasets of GOPRO [15] and Köhler et al. [44]. In the conventional maximum a posteriori framework, Gong et al. [9] adopted a data-driven method to replace the kernel estimate operator. Nah et al. [15] is a multiscale CNN in the traditional sense. GAN-based methods of [37, 38] are also considered. In addition, the image deblurring method based on the edge adversarial mechanism [18] is also compared. To be fair, we recurrent these methods by conducting their official implementations with default settings and parameters. Deblurred results on these synthetic test datasets are shown in Figures 8–10.

Figure 8 displays some deblurred outcomes as a result of severe camera shake. From degraded observations with substantial blur, the developed network is capable of recovering clean appearances and significant structures. CNN is used by Gong et al. [9] to estimate blur kernels in an end-to-end manner. Due to the operator's erroneous kernel estimation, the outcomes are indiscriminately blurry. Even though receptive fields are enlarged on 120 convolution layers, the method of [15] is disabled to solve blur caused by significant camera motion. The nonuniform image deblurring difficulty is insurmountable for GAN-based methods [37, 38]. Using only a semantic content loss function, for example [37], the image deblurring method may not be penalized.

Figure 9 depicts a case caused by object motion. Methods [9, 37, 38, 47] fail to recover blurry local areas even though the fraction of blurry regions in the overall image is minimal. The deblurred image generated by the proposed method contains distinct structures as shown in Figure 9(h).

Figure 10 shows some deblurred results from complex blurring settings involving considerable camera shake and object motion. Methods [9] do not yield good outcomes. Although stacking numerous convolutional layers can increase receptive fields, Nah et al. [15] produce underlying results without sharp edges, such as person motion outlines. Because content loss functions can only attempt to capture semantic correspondences between high-level representations, semantic content loss functions may not be able to deal with complex non-uniform scenarios. Therefore, methods of [37, 38, 47] are unable to restore substantial edges and fine details. To some extent, the results of methods [18] can recover image appearances. However, the background and pedestrian movement trajectory are not clean enough. The proposed network has a robust capacity for producing deblurred images with conspicuous structure and fine features when compared to SOTA methods.

We conduct several experiments on the synthetic datasets of Köhler et al. [44] to further demonstrate the generalization of the proposed network. Figure 11 shows some

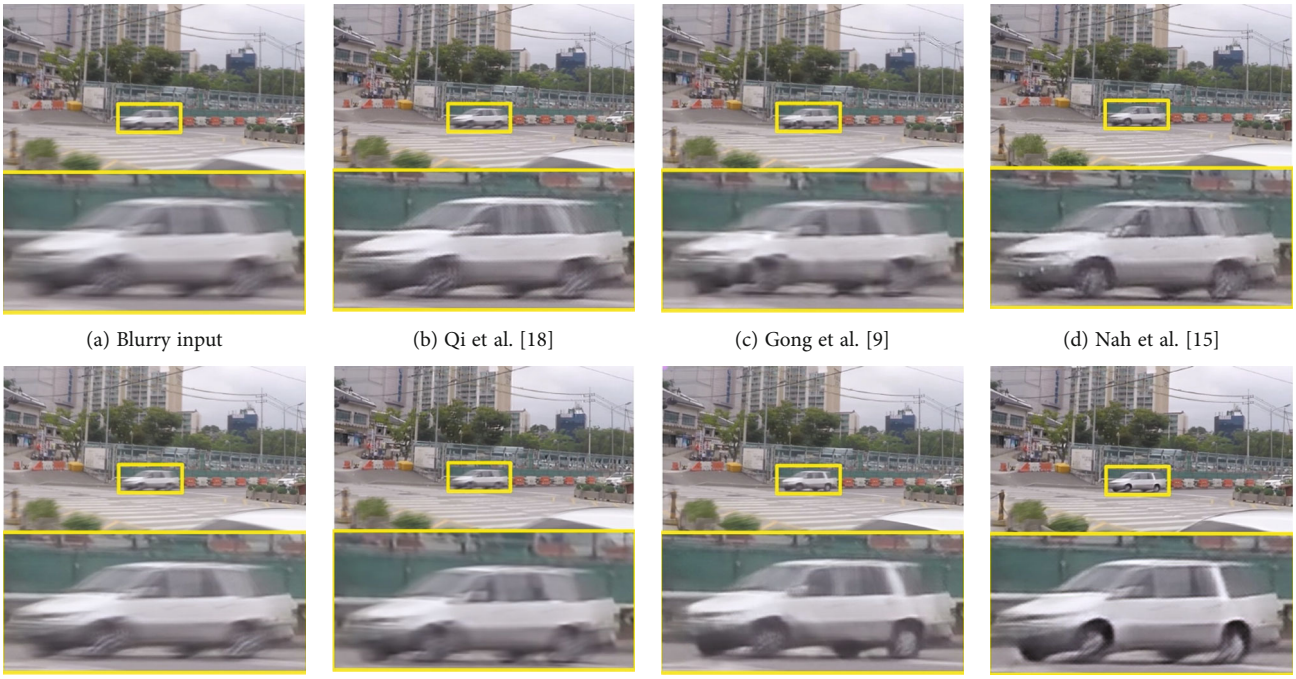

(a) Blurry input (b) Qi et al. [18] (c) Gong et al. [9] (d) Nah et al. [15]

(e) Kupyn et al. [37] (f) Mustaniemi et al. [47] (g) Kupyn et al. [38] (h) Ours

Figure 9: The visual effect of comparison methods and the proposed model on the synthetic dataset of GOPRO [15]. Our method has satisfactory visual effects and good details.

(a) Blurry input (b) Qi et al. [18] (c) Gong et al. [9] (d) Nah et al. [15]

(e) Kupyn et al. [37] (f) Mustaniemi et al. [47] (g) Kupyn et al. [38] (h) Ours

Figure 10: The visual effect of comparison methods and the proposed model on the synthetic dataset of GOPRO [15]. Our method has satisfactory visual effects and good details.

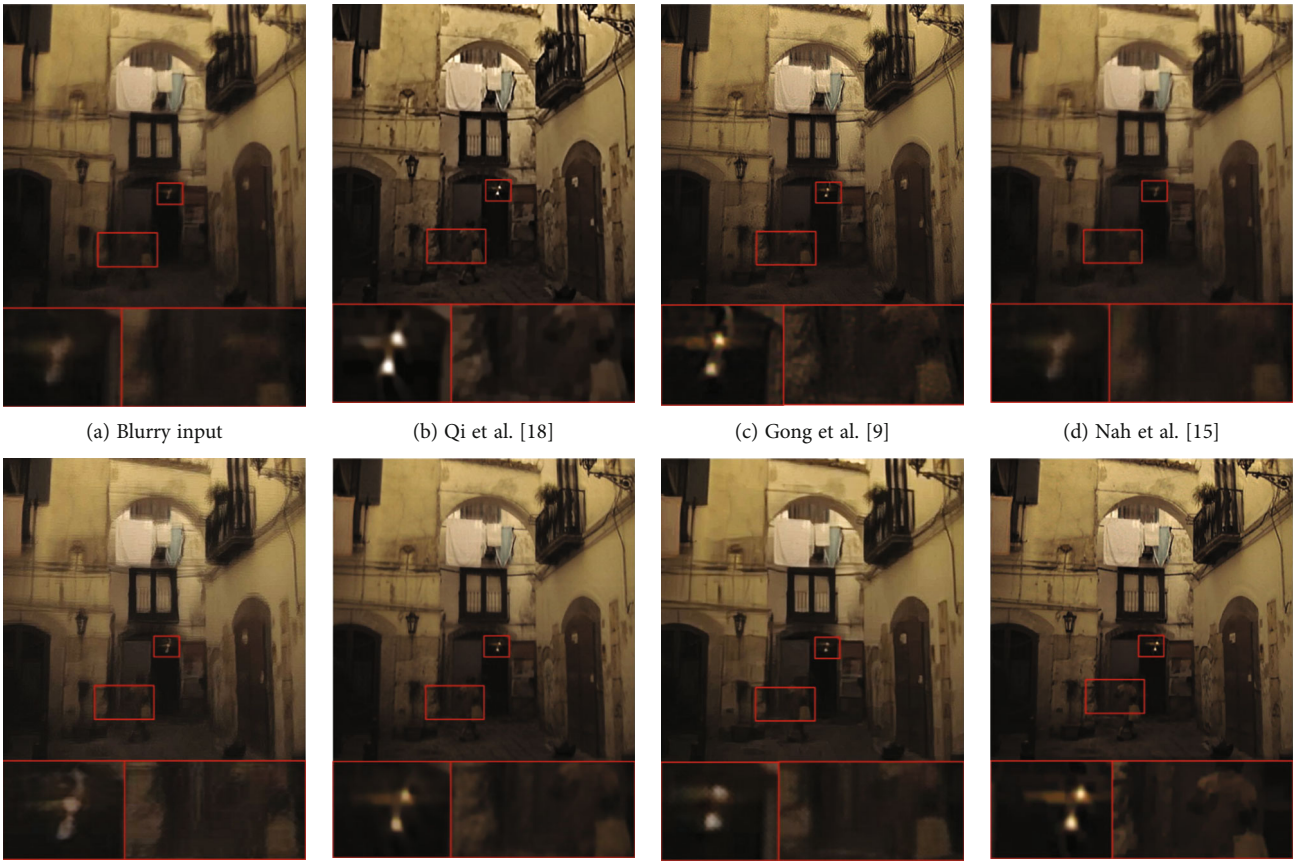

(a) Blurry input (b) Qi et al. [18] (c) Gong et al. [9] (d) Nah et al. [15]

(e) Kupyn et al. [37] (f) Mustaniemi et al. [47] (g) Kupyn et al. [38] (h) Ours

Figure 11: Visual comparison on the dataset of Köhler et al. [44], zoom in for the best view. The proposed method has a photo-realistic effect and generates much clearer details.

recovered results from SOTA methods and our model. Because methods [15, 18, 37, 38] are trained on the GOPRO dataset, they have some deblurring performance on the same test dataset. Their methods exhibit weak robustness on different datasets according to their over smoothed results on the Köhler dataset. In comparison to SOTA results, the proposed network has good generalization and generates deblurred images with significant structure and fine details.

To objectively evaluate the proposed method and SOTA methods on synthetic datasets, we use two quantitative assessment metrics: peak signal to noise ratio (PSNR) and structural similarity index (SSIM) [48]. Table 1 provides average PSNR and SSIM values from GOPRO and Köhler test datasets. Our network outperforms the competition in terms of PSNR and SSIM. The highest PSNR score indicates that there are the fewest similarities in content between the deblurred image and the matching ground truth. The SSIM value increases as the structural similarity difference between the deblurred image and the matching ground truth decreases. Because (1) the developed network directly narrows differences by various restrictions, resulting in greater pixel-wise coherence; and (2) image appearances are aided by primary building blocks, which contribute to structural similarity.

4.4. Experiments on Real Datasets. The evaluation of image deblurring performance is carried out on synthetic datasets, as mentioned in the preceding subsection, and satisfactory results are obtained. Real-world blurry images are frequently the result of more convoluted scenarios. This section uses the dataset of Lai [45] as a test dataset to confirm the effectiveness and generalization of the proposed network. Figures 12–14 show three groups of results from our network and comparison methods, respectively.

Figure 12 illustrates a blurry image under low-light situations. Gong et al. [9] adopt a data-driven way to estimate kernels and then adopt existing nonblind deconvolution algorithms to yield deblurred images. Because the kernel estimation and deblurred image computation are carried out independently, the "two-step" method rarely yields satisfactory results. Kupyn et al. [37] have low compatibility with real-world blurry images. The method [38] is an enhanced version of DeblurGAN that can restore appearances on synthetic blurry images. Because synthetic datasets cannot stimulate the true blur imaging process, methods of [15, 38] have limited generalization on real datasets, as seen in Figures 12(d) and 12(g). Although the developed network does not use low-light training samples, it still performs well on synthetic datasets.

Table 1: Performance comparison with SOTA methods evaluated by quantitative assessment of PSNR (dB) and SSIM. We calculate average values on synthetic datasets of GOPRO [15] and Köhler et al. [44].

Methods	GOPRO PSNR	GOPRO SSIM	Köhler PSNR	Köhler SSIM
Qi et al. [18]	28.9019	0.8694	21.3521	0.6521
Gong et al. [9]	27.2778	0.8187	21.2371	0.6490
Nah et al. [15]	28.3225	0.8588	20.8507	0.6340
Kupyn et al. [37]	25.2363	0.7773	19.0843	0.5838
Mustaniemi et al. [47]	25.9563	0.8285	20.4833	0.6442
Kupyn et al. [38]	27.8086	0.8664	21.2987	0.6544
Ours	29.2252	0.8714	21.3728	0.6602

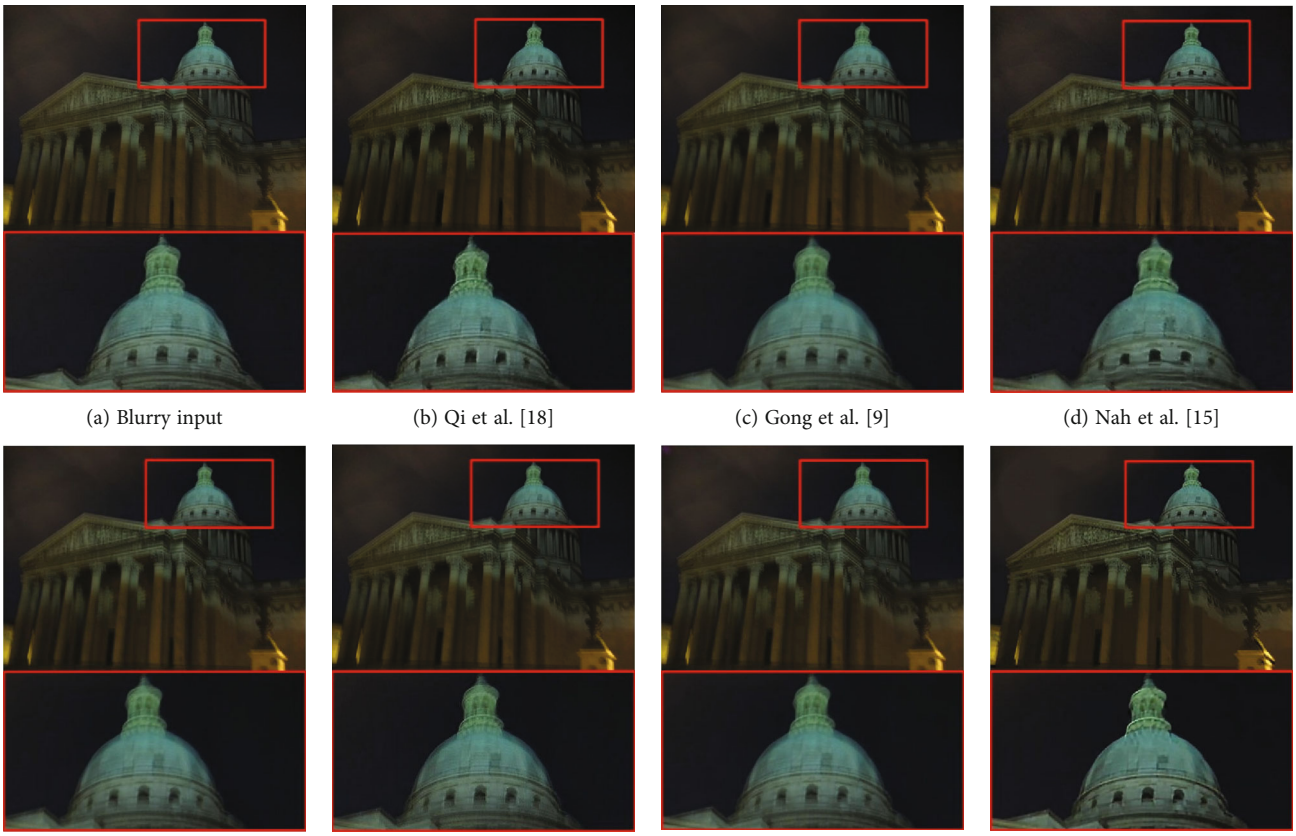

(a) Blurry input (b) Qi et al. [18] (c) Gong et al. [9] (d) Nah et al. [15]

(e) Kupyn et al. [37] (f) Mustaniemi et al. [47] (g) Kupyn et al. [38] (h) Ours

Figure 12: Visual comparison on the real-world images of Lai et al. [45]. Our network has satisfactory visual effects and good details.

Figures 13, 13(d), 13(e), 13(f), and 13(g) show that the class-specific blurry image has a light blur effect, but no high-quality deblurred results. This is because the methods of [9, 15, 37, 38, 47] fail to stimulate the real-world image blurring process. Figure 14 displays a blurry image under low-light conditions. Our method can restore blurred text and image background decently.

In conclusion, the proposed network is trained on simulated datasets and then tested on real-world images, confirming the model's efficiency and generalization that surpass SOTA methods. It takes advantage of the training data as well as the elaborately constructed network.

4.5. User Study. We randomly select 10 blurry images from datasets of Lai et al. [45] and GOPRO [15] for user study to perform an objective visual comparison. The results processed by various methods are displayed randomly and compared to the corresponding blurry input. Following that, we invite 5 participants with image processing experience to score the results. Furthermore, the participants have no idea which results are generated by ours. The scores range from 1 (worst) to 10 (best). We set the raw underwater image scores to 5 as a baseline. We anticipated that the good result has visual pleasant effects and abundant details, particularly the edge information.

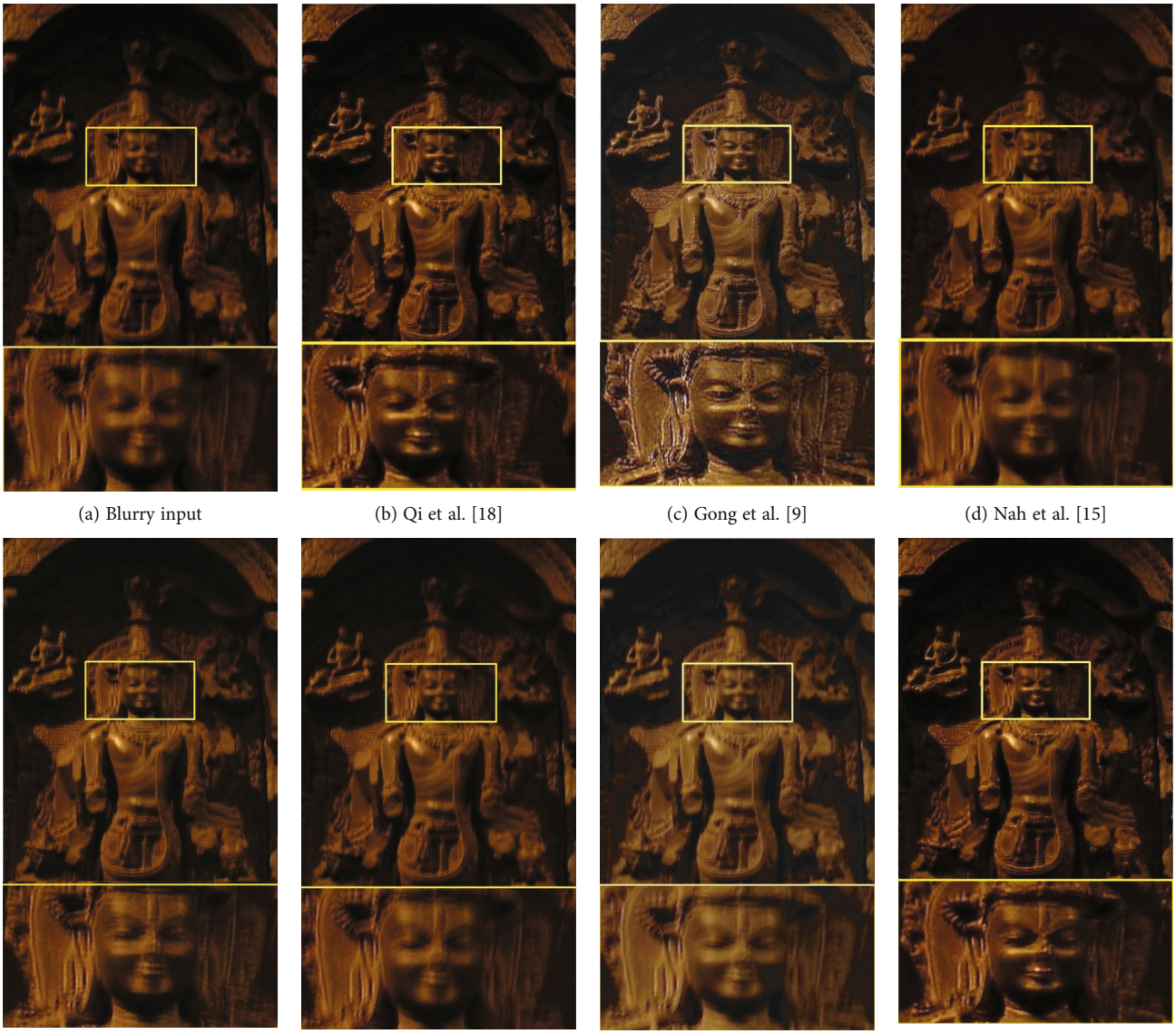

(a) Blurry input (b) Qi et al. [18] (c) Gong et al. [9] (d) Nah et al. [15]

(e) Kupyn et al. [37] (f) Mustaniemi et al. [47] (g) Kupyn et al. [38] (h) Ours

Figure 13: Visual comparison on the real-world images of Lai et al. [45]. Our network has satisfactory visual effects and good details.

Table 2 displays the average visual quality scores of 10 test images. In Table 2, our results get the highest score. It indicates that our results are more consistent with human visual perception. In addition, the image deblurring methods also achieve decent scores. For blurry input, Qi et al. [18], Gong et al. [9], Nah et al. [15], Kupyn et al. [37], Mustaniemi et al. [47], Kupyn et al. [38], and ours, the average visual quality scores for the selected 20 blurry images are 5, 6.3, 5.3, 6.4, 5.4, 6.0, 5.6, and 7.2.

4.6. Execution Time and Computational Complexity. We show the developed method's efficiency by comparing it to SOTA methods in terms of execution time and computational complexity. The results of calculating floating point operations per second (FLOPs) and average execution time on images with a resolution of 1280×720 pixels are shown in Table 3. Because the deblurring method [9] involves a nonblind deconvolution procedure, they encounter computational difficulties. Nah et al. [15] use a multiscale CNN to expand the receptive fields for image deblurring performance. Because multiscale networks are independent between scales, the method [15] takes longer than Kupyn et al. [37] and Kupyn et al. [38]. Mustaniemi et al. [47] construct a U-Net-based CNN to optimize the network for image recovery. Mustaniemi et al. [47] increase the receptive fields by constructing the feature pyramid network. Qi et al. [18] propose a partial weight sharing network by building several blocks for achieving image deblurring. Unlike the previously described methods for image deblurring, the proposed method involves the formation of GradientNet, which saves a little more time than Kupyn et al. [38].

4.7. Investigation of the Impact of Loss Functions. To demonstrate the efficiency of each loss function in our model, we conduct ablation experiments, which include the following three experiments:

(a) Blurry input (b) Qi et al. [18] (c) Gong et al. [9] (d) Nah et al. [15]

(e) Kupyn et al. [37] (f) Mustaniemi et al. [47] (g) Kupyn et al. [38] (h) Ours

Figure 14: Visual comparison on the real-world images of Lai et al. [45]. Our network has satisfactory visual effects and good details.

Table 2: The average visual quality scores of test images.

Methods	I1	I2	I3	I4	I5
Inputs	5	5	5	5	5
Qi et al. [18]	6.3	6.5	6.9	6.0	6.0
Gong et al. [9]	5.0	5.2	5.6	5.9	5.0
Nah et al. [15]	6.8	6.9	6.3	5.5	6.5
Kupyn et al. [37]	5.1	5.5	5.3	5.4	5.6
Mustaniemi et al. [47]	5.5	6.1	6.3	5.5	6.5
Kupyn et al. [38]	5.4	5.7	5.3	6.5	5.0
Ours	7.5	7.7	7.2	6.9	6.8

Table 3: The efficiency of comparison image deblurring methods and the proposed method. We calculate algorithmiccomplexity and the average execution time on images with the size of 1280 × 720 of the test dataset of GOPRO.

Methods	FLOPs	Seconds
Qi et al. [18]	468.54G	0.8
Gong et al. [9]	4.12G	1300
Nah et al. [15]	1760.04G	8.1
Kupyn et al. [37]	678.29G	1.1
Mustaniemi et al. [47]	128.13G	4.5
Kupyn et al. [38]	411.34G	0.6
Ours	446.98G	0.7

(1) The proposed network without L_{content} (w/o cont)

(2) The proposed network without L_{gradient} (w/o gradient)

(3) The proposed network

Parameter setting and training methods consistent with the proposed network are used in the ablation experiments. The quantitative evaluation is performed on the dataset of GORPO. Figure 15 exhibits the visual results obtained from the ablation experiments performed on each module of the proposed network. The blurred image is presented in Figure 15(a). As illustrated in Figure 15(b), the network without L_{content} generates visually unpleasant results. Such findings demonstrate that the performance of the proposed network has a positive correlation with L_{content}. In comparison, L_{content} measures image semantic content coherence more robust. As shown in Figure 15(c), without the restrictions of L_{gradient}, the visual quality of the deblurred image significantly declined. Finally, an ablation investigation of proposed loss functions demonstrates that L_{content} and

(a) (b) (c) (d)

Figure 15: Visual results for the ablation study of loss functions on the nonuniform dataset GOPRO. (a) Blurry input, (b, c) are the results of the components of w/o content loss function and w/o gradient loss function, respectively. (d) The result of the proposed method. The proposed method generates clearer images with fine details and salient structures.

Table 4: Quantitative evaluations on the dataset of GOPRO for the ablation study of loss functions.

Loss	PSNR	SSIM
W/o content	26.3751	0.7921
W/o gradient	28.7011	0.8617
Ours	29.2252	0.8714

L_{gradient} make significant improvements to deblurring performance. This confirms that it is feasible to exploit image structures as the target loss function to optimize network training.

In addition, the PSNR and SSIM objective evaluations are employed to assess the outcomes achieved from each ablated part, and the average results of the above networks tested on the GOPRO dataset are shown in Table 4. We observed that (1) when L_{content} is removed, quantitative metrics of PSNR and SSIM sharply decrease; (2) when L_{gradient} is ablated, the deblurring performance of our model also decreases. The quantitative evaluation results are compatible with the subjective visual effects, validating the efficiency of the image deblurring method based on image gradient priors.

4.8. Ablation Study on the Effectiveness of Building Blocks. To validate that the proposed network's image deblurring performance has a positive correlation with the constructed building blocks of RGCL, MBRBs, and GradientNet, we conduct ablation experiments, which involve the following four experiments:

(1) Our model without RGCL (w/o RGCL)

(2) Our model without (w/o MBRBs)

(3) Our model without GradientNet (w/o GradientNet)

(4) Our model

The first experiment denotes we replace RGCL with normal convolution layers in MBRBs. The purpose of the second experiment is to replace the multipath reuse module with a single path. The third experiment is to ablate GradientNet and validate how important the GradientNet is to generating salient structures.

We adopt the identical training strategy, parameter values, loss functions, and training datasets as in Section 4 in these experiments unless otherwise stated. Figure 16 displays the visual results obtained from the ablation experiments performed on each block of the proposed network. As exhibited in Figure 16(b), without the proposed RGCL, the letters that could not be recovered are dense with each other and difficult to identify. As shown in Figure 16(c), without the assistance of MBRBs, the visual quality of the deblurred image has a slight improvement to Figure 16(b). As illustrated in Figure 16(d), without GradientNet, the visual quality of the deblurred image significantly declined. Such finding validates that the performance of the proposed network has a positive correlation with GradientNet. Finally, an ablation investigation of proposed building blocks validates that RGCL, MBRBs, and GradientNet make considerable improvements to deblurring performance.

To evaluate the effectiveness of building blocks in our model, quantitative evaluation indicators of PSNR and SSIM are also employed. As displayed in Table 5, the average results of the above building blocks are tested on the GOPRO dataset. We can indicate that our model achieves the best quantitative assessment results. When RGCL, MBRBs, and GradientNet are removed, respectively, the quantitative metrics of the corresponding networks have different degrees of decrease. The quantitative evaluation results match the subjective visual effects, indicating that the image deblurring method based on image gradient priors is effective.

In conclusion, (1) instead of using plain convolutional layers, RGCL is developed to investigate and preserve the majority of image structures in a parallel manner; (2) MBRBs achieve structural feature correlations in a multipath reuse manner, then, recalibrated channels of these accumulated and enhanced nonlocal features are highlighted by implementing SENet module; (3) the structure-preserving subnetwork named GradientNet reinforces structural feature correlations by arranging many MBRBs in a cascade

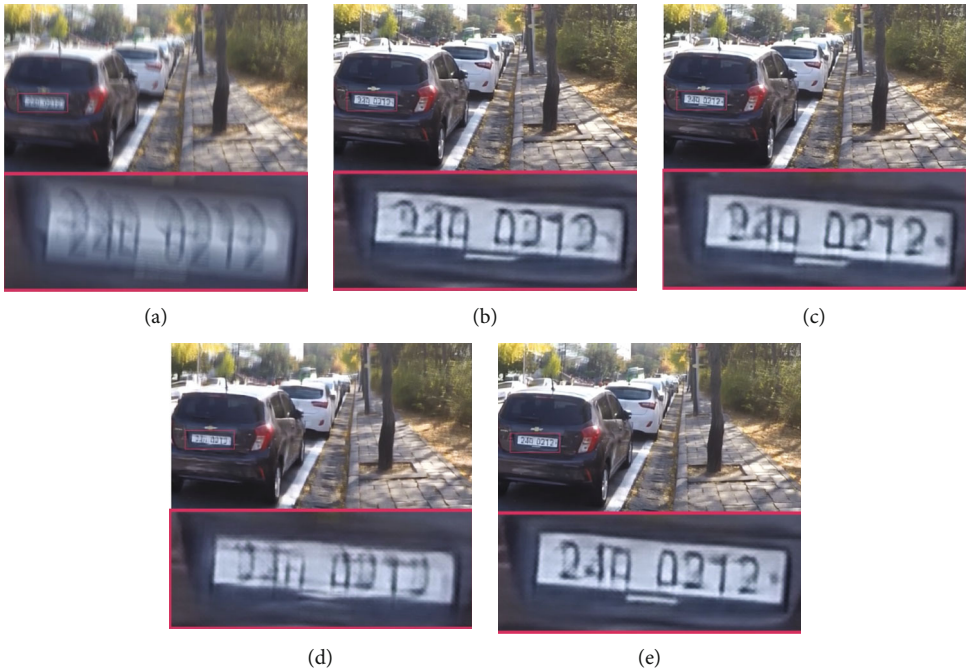

Figure 16: Visual results for ablation studies of building blocks on the dataset GOPRO. (a) Blurry input. (b–d) The results of network w/o RGCL, w/o MBRBs, and w/o GradientNet, respectively. (e) The result of the proposed method. Our network has satisfactory visual effects and good details.

Table 5: Quantitative evaluations on the dataset of GOPRO for the ablation study of building blocks.

Loss	PSNR	SSIM
W/o RGCL	29.0429	0.8691
W/o MBRBs	29.0859	0.884
W/o GradientNet	27.8708	0.8324
Ours	29.2252	0.8714

manner. It achieves the dynamic scene deblurring task under the guidance of image gradient features.

5. Conclusions

In this paper, we integrate image gradients in the proposed GAN-based network to generate images with clean appearances and conspicuous structures dynamically. We permeate image gradient priors to the design of network structures and loss functions. We develop a structure-preserving subnetwork named GradientNet, which contains the building blocks of RGCL and MBRBs. It investigates the relationship between image gradients and dynamic scene deblurring in a data-driven way. Subjective and objective comparison experiments on several synthetic datasets and real images are conducted to demonstrate the efficiency of the developed GradientNet. However, the proposed method has weak generalization on blurry images containing fewer structures and fruitful textures. Recovered images of those inputs are not smooth and have a strong coarse-grained visual perception. In the future, we consider extending and upgrading our model to mitigate the above limitations.

Data Availability

No data were used to support this study.

Conflicts of Interest

The author declares no conflicts of interest.

Acknowledgments

This work was supported in part by the Foundation of Grant 2022TQ04.

References

[1] S. Cho and S. Lee, "Fast motion deblurring," in *ACM SIGGRAPH Asia 2009 papers*, pp. 1–8, Yokohama, Japan, 2009 Dec 1.

[2] L. Xu and J. Jia, "Two-phase kernel estimation for robust motion deblurring," in *European conference on computer vision*, pp. 157–170, Springer, Berlin, Heidelberg, 2010.

[3] L. Xu, S. Zheng, and J. Jia, "Unnatural L_0 sparse representation for natural image deblurring," in *Proceedings of the IEEE conference on computer vision and pattern recognition*, pp. 1107–1114, Portland, OR, USA, 2013.

[4] J. Pan, D. Sun, H. Pfister, and M. H. Yang, "Blind image deblurring using dark channel prior," in *Proceedings of the IEEE conference on computer vision and pattern recognition*, pp. 1628–1636, Las Vegas, Nevada, USA, 2016.

[5] W. Ren, X. Cao, J. Pan, X. Guo, W. Zuo, and M. H. Yang, "Image deblurring via enhanced low-rank prior," *IEEE Transactions on Image Processing*, vol. 25, no. 7, pp. 3426–3437, 2016.

[6] L. Sun, S. Cho, J. Wang, and J. Hays, "Edge-based blur kernel estimation using patch priors," in *IEEE International Conference on Computational Photography (ICCP)*, pp. 1–8, Cambridge, MA, USA, 2013.

[7] H. Zhang, J. Yang, Y. Zhang, and T. S. Huang, "Sparse representation based blind image deblurring," in *2011 IEEE International Conference on Multimedia and Expo*, pp. 1–6, Barcelona, Spain, 2011.

[8] J. Sun, W. Cao, Z. Xu, and J. Ponce, "Learning a convolutional neural network for non-uniform motion blur removal," in *Proceedings of the IEEE conference on computer vision and pattern recognition*, pp. 769–777, Boston, MA, USA, 2015.

[9] D. Gong, J. Yang, L. Liu et al., "From motion blur to motion flow: a deep learning solution for removing heterogeneous motion blur," in *Proceedings of the IEEE conference on computer vision and pattern recognition*, pp. 3806–3815, Honolulu, Hawaii, USA, 2017.

[10] A. Chakrabarti, "A neural approach to blind motion deblurring," in *14th European Conference*, pp. 221–235, Amsterdam, The Netherlands, 2016.

[11] C. J. Schuler, M. Hirsch, S. Harmeling, and B. Schölkopf, "Learning to deblur," *IEEE transactions on pattern analysis and machine intelligence*, vol. 38, no. 7, pp. 1439–1451, 2016.

[12] M. Hradiš, J. Kotera, P. Zemck, and F. Šroubek, "Convolutional neural networks for direct text deblurring," in *Proceedings of BMVC*, vol. 10, Swansea, UK, 2015no. 2.

[13] M. Jin, M. Hirsch, and P. Favaro, "Learning face deblurring fast and wide," in *Proceedings of the IEEE Conference on Computer Vision and Pattern Recognition Workshops*, pp. 745–753, Salt Lake City, Utah, USA, 2018.

[14] X. Mao, C. Shen, and Y. B. Yang, "Image restoration using very deep convolutional encoder-decoder networks with symmetric skip connections," *Advances in neural information processing systems*, vol. 29, pp. 2802–2810, 2016.

[15] S. Nah, T. H. Kim, and K. M. Lee, "Deep multi-scale convolutional neural network for dynamic scene deblurring," in *Proceedings of the IEEE conference on computer vision and pattern recognition*, pp. 257–265, Honolulu, Hawaii, USA, 2017.

[16] X. Tao, H. Gao, X. Shen, J. Wang, and J. Jia, "Scale-recurrent network for deep image deblurring," in *Proceedings of the IEEE conference on computer vision and pattern recognition*, pp. 8174–8182, Salt Lake City, Utah, USA, 2018.

[17] X. Ran and N. Farvardin, "A perceptually motivated three-component image model-part i: description of the model," *IEEE Transactions on Image Processing*, vol. 4, no. 4, p. 401, 1995.

[18] Q. Qi, J. Guo, and W. Jin, "EGAN: non-uniform image deblurring based on edge adversarial mechanism and partial weight sharing network," *signal processing: image communication*, vol. 88, p. 115952, 2020.

[19] Y. Liu, Q. Jia, X. Fan, S. Wang, S. Ma, and W. Gao, "Cross-SRN: structure-preserving super-resolution network with cross convolution," *IEEE Transactions on Circuits and Systems for Video Technology*, vol. 32, no. 8, pp. 4927–4939, 2022.

[20] J. Hu, L. Shen, and G. Sun, "Squeeze-and-excitation networks," in *Proceedings of the IEEE conference on computer vision and pattern recognition*, pp. 7132–7141, Salt Lake City, Utah, USA, 2018.

[21] T. Kim, B. Ahn, and K. Lee, "Dynamic scene deblurring," in *Proceedings of the IEEE international conference on computer vision*, pp. 3160–3167, Sydney, Australia, 2013.

[22] T. Kim and K. Lee, "Segmentation-free dynamic scene deblurring," in *Proceedings of the IEEE conference on computer vision and pattern recognition*, pp. 2766–2773, Columbus, OH, USA, 2014.

[23] J. Pan, Z. Hu, Z. Su, H. Y. Lee, and M. H. Yang, "Soft-segmentation guided object motion deblurring," in *Proceedings of the IEEE conference on computer vision and pattern recognition*, pp. 459–468, Las Vegas, Nevada, USA, 2016.

[24] C. Li, R. Cong, J. Hou, S. Zhang, Y. Qian, and S. Kwong, "Nested network with two-stream pyramid for salient object detection in optical remote sensing images," *IEEE Transactions on Geoscience and Remote Sensing*, vol. 57, no. 11, pp. 9156–9166, 2019.

[25] C. Li, J. Guo, and C. Guo, "Emerging from water: underwater image color correction based on weakly supervised color transfer," *IEEE Signal processing letters*, vol. 25, no. 3, pp. 323–327, 2018.

[26] C. Li, C. Guo, J. C. Guo, P. Han, H. Z. Fu, and R. Cong, "PDR-net: perception-inspired single image dehazing network with refinement," *IEEE Transactions on Multimedia*, vol. 22, no. 3, pp. 704–716, 2020.

[27] C. Li, S. Anwar, and F. Porikli, "Underwater scene prior inspired deep underwater image and video enhancement," *Pattern Recognition*, vol. 98, article 107038, 2020.

[28] C. Li, C. Guo, J. Guo, P. Han, H. Fu, and R. Cong, "Underwater image enhancement by dehazing with minimum information loss and histogram distribution prior," *IEEE Transactions on Image Processing*, vol. 25, no. 12, pp. 5664–5677, 2016.

[29] L. Xu, J. S. Ren, C. Liu, and J. Jia, "Deep convolutional neural network for image deconvolution," in *Proceedings of the Advances in Neural Information Processing Systems (NIPS)*, pp. 1790–1798, Montreal, Canada, 2014.

[30] L. Li, J. Pan, W. S. Lai, C. Gao, N. Sang, and M. H. Yang, "Learning a discriminative prior for blind image deblurring," in *Proceedings of the IEEE conference on computer vision and pattern recognition*, pp. 6616–6625, Salt Lake City, USA, 2018.

[31] D. Ren, K. Zhang, Q. Wang, Q. Hu, and W. Zuo, "Neural blind deconvolution using deep priors," in *Proceedings of the IEEE/CVF Conference on Computer Vision and Pattern Recognition*, pp. 3341–3350, 2020.

[32] H. Gao, X. Tao, X. Shen, and J. Jia, "Dynamic scene deblurring with parameter selective sharing and nested skip connections," in *Proceedings of the IEEE/CVF conference on computer vision and pattern recognition*, pp. 3848–3856, Long Beach, USA, 2019.

[33] J. Zhang, J. Pan, J. Ren et al., "Dynamic scene deblurring using spatially variant recurrent neural networks," in *Proceedings of the IEEE Conference on Computer Vision and Pattern Recognition*, pp. 2521–2529, Salt Lake City, USA, 2018.

[34] I. Goodfellow, J. Pouget-Abadie, M. Mirza et al., "Generative adversarial nets," in *NIPS*, pp. 2672–2680, Montreal, Canada, 2014.

[35] J. Y. Zhu, T. Park, P. Isola, and A. A. Efros, "Unpaired image-to-image translation using cycle-consistent adversarial networks," in *Proceedings of the IEEE international conference on computer vision*, pp. 2223–2232, Venice, Italy, 2017.

[36] T. M. Nimisha, K. Sunil, and A. Rajagopalan, "Unsupervised class-specific deblurring," in *Proceedings of the European Conference on Computer Vision (ECCV)*, pp. 353–369, Munich, Germany, 2018.

[37] O. Kupyn, V. Budzan, M. Mykhailych, D. Mishkin, and J. Matas, "Deblurgan: blind motion deblurring using conditional adversarial networks," in *Proceedings of the IEEE conference on computer vision and pattern recognition*, pp. 8183–8192, Salt Lake City, Utah, USA, 2018.

[38] O. Kupyn, T. Martyniuk, J. Wu, and Z. Y. Wang, "DeblurGAN-v2: deblurring (orders-of-magnitude) faster and better," in *Proceedings of the IEEE/CVF International Conference on Computer Vision*, pp. 8878–8887, Seoul,Korea, 2019.

[39] A. L. Maas, A. Y. Hannun, and A. Y. Ng, "Rectifier nonlinearities improve neural network acoustic models," in *Proceedings of International Conference on International Conference on Machine Learning*, vol. 30no. 1, p. 3, Atlanta, USA, 2013.

[40] P. Isola, J. Y. Zhu, T. Zhou, and A. A. Efros, "Image-to-image translation with conditional adversarial networks," in *Proceedings of the IEEE conference on computer vision and pattern recognition*, pp. 1125–1134, Honolulu, Hawaii, USA, 2017.

[41] J. Johnson, A. Alahi, and L. Fei-Fei, "Perceptual losses for real-time style transfer and super-resolution," in *14th European Conference*, pp. 694–711, Amsterdam, The Netherlands, 2016.

[42] K. Simonyan and A. Zisserman, "A very deep convolutional networks for large-scale image recognition," 2014, https://arxiv.org/abs/1409.1556.

[43] I. Gulrajani, F. Ahmed, M. Arjovsky, V. Dumoulin, and A. C. Courville, "Improved training of wasserstein gans," *Advances in neural information processing systems*, vol. 30, 2017.

[44] R. Köhler, M. Hirsch, B. Mohler, B. Schölkopf, and S. Harmeling, "Recording and playback of camera shake: benchmarking blind deconvolution with a real-world databaseEuropean conference on computer vision," Springer, Berlin, Heidelberg, 2012.

[45] W. S. Lai, J. B. Huang, Z. Hu, N. Ahuja, and M. H. Yang, "A comparative study for single image blind deblurring," in *Proceedings of the IEEE Conference on Computer Vision and Pattern Recognition*, pp. 1701–1709, Las Vegas, Nevada, USA, 2016.

[46] D. P. Kingma and J. Ba, "Adam: a method for stochastic optimization," 2014, https://arxiv.org/abs/1412.6980.

[47] J. Mustaniemi, J. Kannala, S. Särkkä, J. Matas, and J. Heikkila, "Gyroscope-aided motion deblurring with deep networks," in *2019 IEEE Winter Conference on Applications of Computer Vision (WACV)*, pp. 1914–1922, Waikoloa, HI, USA, 2019 Jan 7.

[48] Z. Wang, A. C. Bovik, H. R. Sheikh, and E. P. Simoncelli, "Image quality assessment: from error visibility to structural similarity," *IEEE transactions on image processing*, vol. 13, no. 4, pp. 600–612, 2004.

Hindawi
Wireless Communications and Mobile Computing
Volume 2022, Article ID 1648244, 9 pages
https://doi.org/10.1155/2022/1648244

Research Article

Sparse Spatial Spectral Fitting with Nonuniform Noise Covariance Matrix Estimation Based on Semidefinite Optimization

Tuo Guo,[1] **Yang Bi**,[2] **Xian Feng**,[3] **and Luoheng Yan**[3]

[1]*School of Electronic Information and Artificial Intelligence, Shaanxi University of Science & Technology, Xi'an, Shaanxi 710021, China*
[2]*School of Electronic Engineering, Xi'an Aeronautical University, Xi'an, Shaanxi 710077, China*
[3]*School of Marine Science and Technology, Northwestern Polytechnical University, Xi'an 710072, China*

Correspondence should be addressed to Yang Bi; 200707002@xaau.edu.cn

Received 14 June 2022; Accepted 11 August 2022; Published 15 September 2022

Academic Editor: Mingqian Liu

In general, the azimuth estimation in array signal processing is derived under the assumption of uniform white noise, whose covariance matrix is a scaled identity matrix. However, in practice, the noise can be nonuniform with an arbitrary unknown diagonal covariance matrix. In this paper, the estimation of the noise covariance matrix is formulated into a solution to the semidefinite optimization problem which can obtain a more accurate sensor noise covariance matrix. In the proposed algorithm, the estimated nonuniform noise is subtracted from the sample covariance matrix. The simulation results show that the proposed algorithm can significantly improve the performance of the sparse spectrum fitting algorithm in nonuniform noise case, while the classic SpSF algorithm is used under uniform white noise assumption. The water pool experiments show that there are indeed significant differences in the noise covariance of the sensors.

1. Introduction

Determining the direction-of-arrival (DOA) of incoming signals is an important research problem in array signal processing, which is widely used in radar, sonar, navigation, wireless communications, and acoustics [1–7]. Under the uniform white noise assumption, several high resolution DOA estimation approaches are well known to provide high accuracy and excellent asymptotic performance, such as multiple signal classification (MUSIC) [8] and estimation of signal parameters via rotational invariance technique (ESPRIT) [9]. According to the assumption, sensor noises are presumed to be a zero-mean Gaussian process with the covariance matrix $\sigma^2 I$, which is the unknown uniform noise variance, and I is the identity matrix [10].

The sparse spectrum fitting (SpSF) [11] algorithm is another high resolution DOA estimation algorithm, which is based on the sparse signal model of the array and compressive sensing theory. SpSF is formulated by applying L_1-norm penalization to the spatial sparse model of the sample covariance matrix. It is similar to Lasso-type algorithms [12–15] which utilize compressive sensing theory with L_1-norm replacing L_0-norm. However, the SpSF algorithm still assumes the sensors noise is uniform Gaussian white noise. In fact, the sensor noise may be nonuniform [16–18], spatially correlated [19–24], or block-correlated [25–28]. In particular, in the field of underwater acoustic signal processing, the noise of different hydrophones tends to be nonuniform due to inaccuracy in the manufacture of hydrophones.

In this paper, as usual, we still assume that the noise entering the sensor is Gaussian noise, but the noise variances of sensor are nonidentical across the array, and then we propose a new DOA estimation algorithm with sparse spatial spectral fitting based on nonuniform noise estimation (NN-SpSF). The NN-SpSF algorithm significantly improves

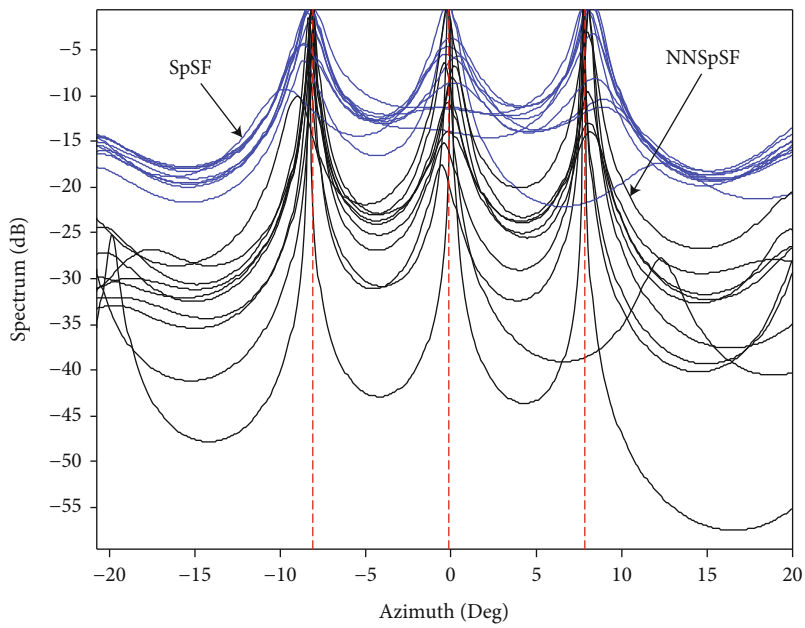

Figure 1: Comparisons of SpSF and NN-SpSF for DOA estimation.

the performance of DOA estimation under nonuniform noise compared with the SpSF algorithm.

The paper is organized as follows. The signal model is formulated in Section 2. The SpSF algorithm based on nonuniform noise estimation is developed in Section 3. Simulation results are presented in Section 4. The results of the water pool experiment are shown in Section 5. Conclusions are provided in Section 6.

2. Signal Model

Consider a uniform linear hydrophone array of M elements with its steering vector denoted by $\boldsymbol{a}(\theta)$. Suppose that $K(K < M)$ far-field narrow-band signals impinge on the array from the unknown DOAs $\theta = (\theta_1, \cdots, \theta_K)$, then the signal observed of the array at time t is given as

$$x(t) = A(\theta)s(t) + e(t), t = 1, \cdots, L, \tag{1}$$

where $A(\theta) = [a(\theta_1), \cdots, a(\theta_K)]$ is the steering matrix of the array, and $a_m(\theta) = [1, e^{j\varphi} \cdots, e^{j(M-1)\varphi}]^T$ is the steering vector [29]. In a uniform linear array (ULA) with half-wavelength interelement spacing, the mth entry of $a_m(\theta)$ is given by

$$\varphi = \frac{2\pi\Delta}{\lambda} \sin\theta, \tag{2}$$

where $\boldsymbol{s}(t) = [s_1(1), \cdots, s_K(n)]$ and $e(t)$ are the signal and noise vectors, respectively. They are assumed to be uncorrelated. L is the number of snapshots. Then, the array output covariance matrix can be expressed as

$$R = E\{x(t)x^{\mathrm{H}}(t)\} = \mathrm{APA}^{\mathrm{H}} + Q, \tag{3}$$

where $E\{\cdot\}$ and $(\cdot)$ represent the mathematical expectation and Hermitian transpose, respectively. $P = E\{s(t)s^H(t)\}$ is the signal covariance matrix, and $Q = E\{e(t)e^H(t)\}$ is the noise covariance matrix. For uncorrelated sources, P is a diagonal matrix. In this paper, the sensor noise is considered to be nonuniform and can be modeled as a spatially and temporally uncorrelated zero-mean random process, and then Q is also a diagonal matrix having the form

$$Q = \mathrm{diag}\ \{\sigma_1^2, \cdots, \sigma_M^2\}, \tag{4}$$

where $\sigma_1^2, m = 1, \cdots, M$ are the sensor noise variances, and diag $\{\cdot\}$ denotes a diagonal matrix. In practical applications, the array covariance matrix is usually estimated as $\widehat{R} = 1/L \sum_{t=1}^{L} x(t)x^H(t)$.

3. The Proposed SpSF Algorithm with Nonuniform Noise Estimation (NN-SpSF)

The SpSF algorithm is formulated by applying l_1-norm penalization of fitting the source covariance model to the estimated spatial covariance, which applies the vectorization operation [30–32] to $\widehat{R}$, and it can obtain the following relation:

$$r = A_{N_\theta} p^\circ + \sigma^2 \mathrm{vec}(I), \tag{5}$$

where $r = \mathrm{vec}(\widehat{R})$, vec(), is the vectorization operation; $A_{N_\theta} = [a_v(\theta_1) a_v(\theta_2) \cdots a_v(\theta_{N_\theta})]$ is the array manifold matrix, in which $a_v(\theta) = \mathrm{vec}(a(\theta)a^{\mathrm{H}}(\theta))$, and N_θ is the number of search angles for θ. According to the Formula (5), the noise entering the array is assumed to be uniform Gaussian white noise. However, if the noise is nonuniform, (5) can be

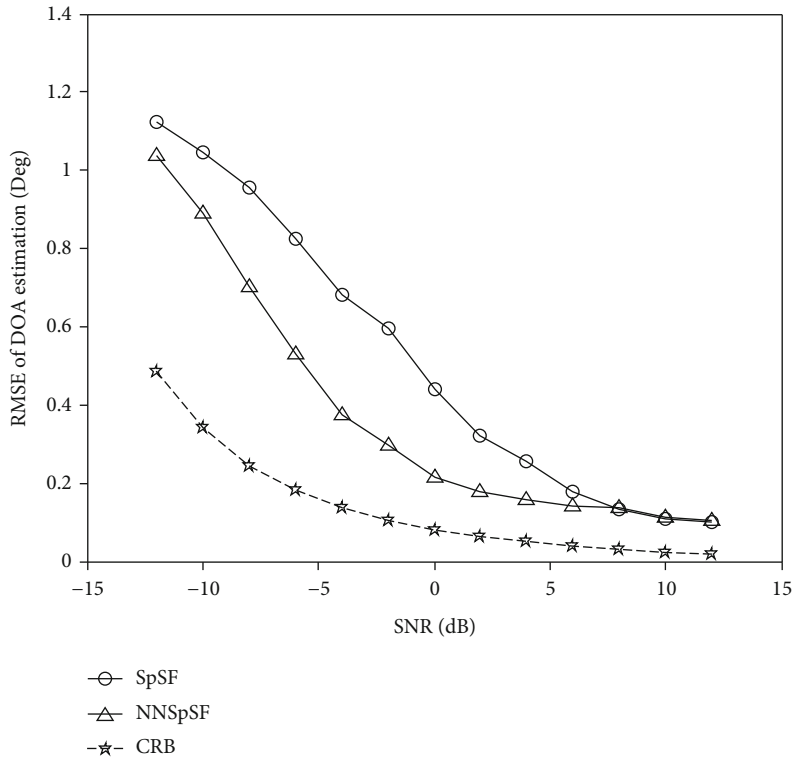

Figure 2: Comparison of the DOA estimation RMSEs versus SNR.

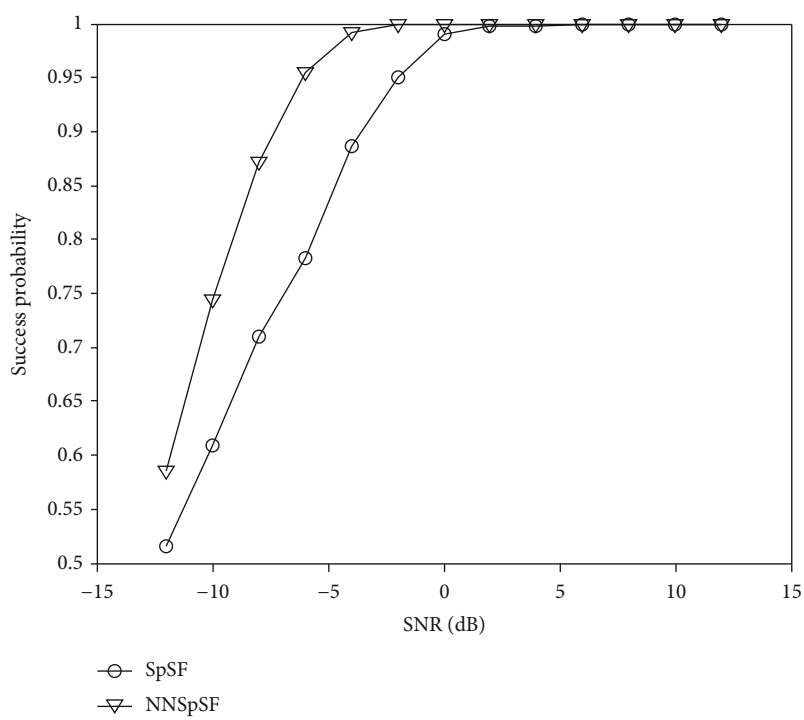

Figure 3: Comparison of the success probability of DOA estimation versus SNR.

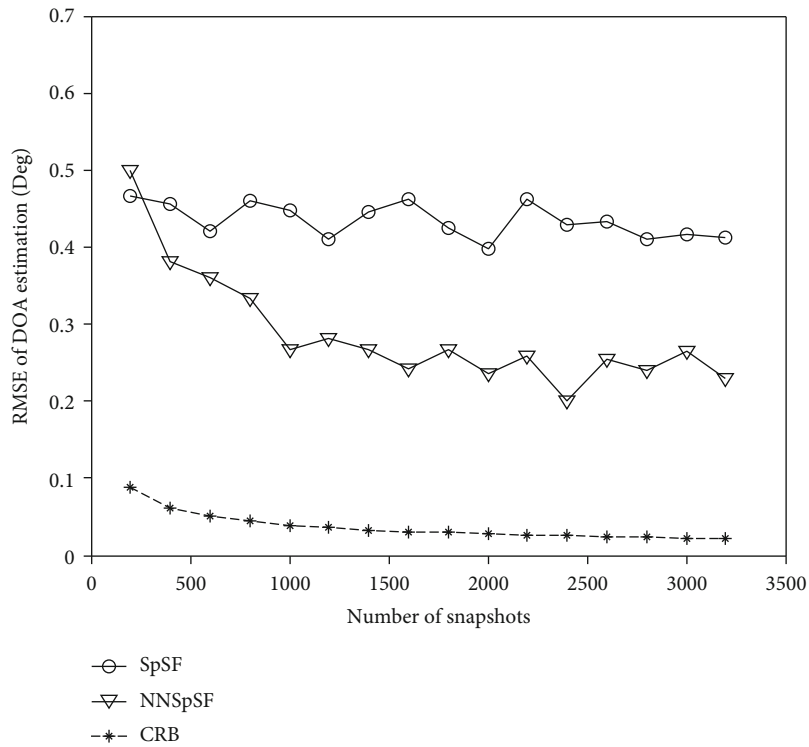

Figure 4: Comparison of the DOA estimation RMSEs versus the number of snapshots.

rewritten as

$$r = A_{N_\theta} p^{\circ} + \mathrm{vec}(Q), \tag{6}$$

where Q is a diagonal matrix, but the elements are not equal; therefore, the bearing estimation performance of the SpSF algorithm will be significantly reduced. In the case of nonuniform Gaussian white noise, we need to remove the nonuniform noise information from Q by the following operations:

$$(Q\text{-}Q_N) \longrightarrow \lambda \cdot I. \tag{7}$$

To get the nonuniform diagonal matrix $Q_N = \mathrm{diag}\,\{\sigma'^2_1, \cdots, \sigma'^2_M\}$, and $\sigma'^2_1 \neq \sigma'^2_2 \neq \cdots \neq \sigma'^2_M$, we can convert it to the following semipositive definite optimization problem, as shown in Formula (8):

$$\begin{aligned} &\max \sum_{m=1}^{M} \sigma'^2_m, \\ &s.t. \left|\widehat{R}\right| - Q_N \geq \eta \cdot I, \\ &Q_N \geq 0, \\ &\eta = \min\left(\mathrm{diag}\left(\widehat{R}\right)\right). \end{aligned} \tag{8}$$

When Q_N is obtained, the DOA estimator of the SpSF algorithm in the nonuniform noise situation (written as NN-SpSF) can be given as

$$\begin{aligned} p^* = \arg \min_{p,\mu} \left\|\mathrm{vec}\left(\widehat{R} - Q_N\right)\text{-}A_{N_\theta} p\right\|_2^2 + \mu \|p\|_1, \\ s.t. p_i \geq 0, i = 1, \cdots, N_\theta. \end{aligned} \tag{9}$$

Formula (8) and (9) can be solved with the convex optimization tool like CVX [33], which is used to solve the semipositive definite optimization problem. Here in formula (9), the variable μ takes the value of 0.8.

4. Simulations

In this section, a series of numerical experiment results under different conditions are conducted to validate the performance of the proposed NN-SpSF algorithm. The experiments are performed with a uniform linear array (ULA) with $M = 12$ sensors and half-wavelength space. Three equally powered independent narrowband signals impinge on the array from directions -8°, 0°, and 8° respectively. The noise is assumed spatially nonuniform and independent, which has the following covariance matrix:

$$Q = \mathrm{diag}\,[10.2\ 5.6\ 8.5\ 11.2\ 7.8\ 9.5\ 8\ 4.8\ 9\ 6.1\ 7.2\ 2]. \tag{10}$$

The signal-to-noise ratio (SNR) is defined as

$$\mathrm{SNR} = 10 \log 10 \left(\sigma_n^2 \frac{\sigma_s^2}{\sum_{i=1}^{M} \sigma_i^2}\right), \tag{11}$$

where σ_s^2 denotes the power of source signal.

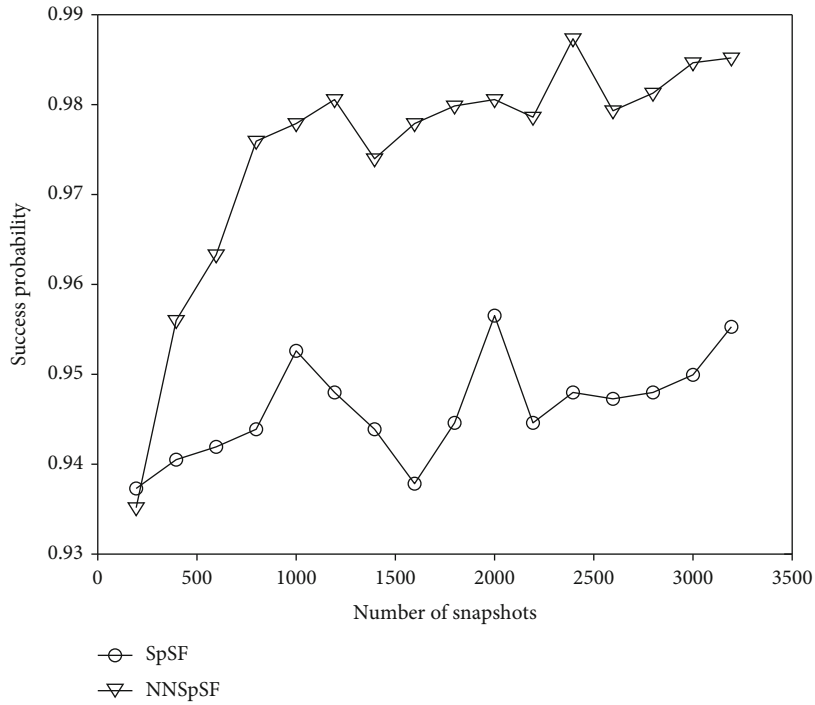

Figure 5: Success probability of DOA estimation versus the number of snapshots.

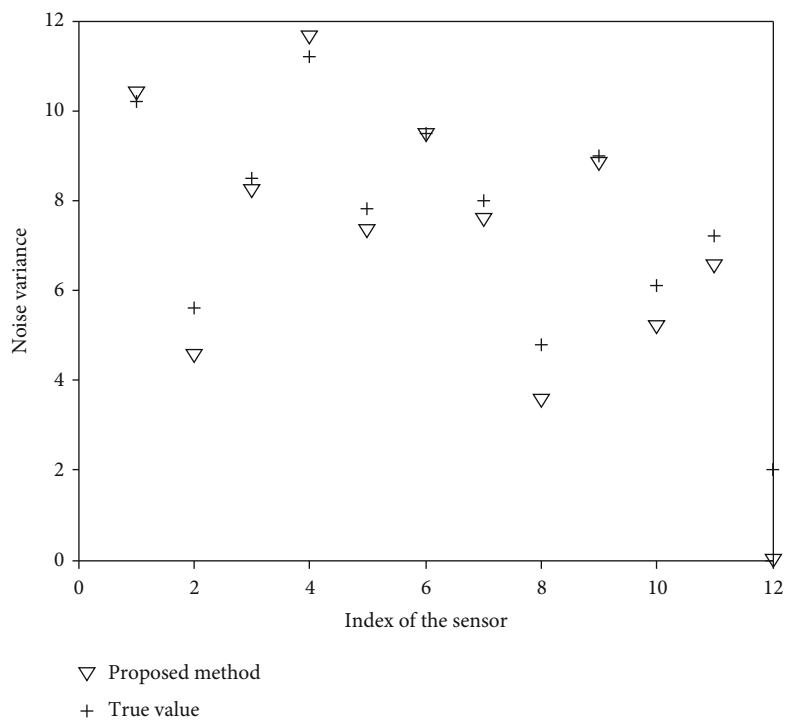

Figure 6: Averaged noise variances of sensors.

In the first simulation, the number of snapshots is 500, and 10 independent experiment runs for SNR = 0dB are performed. The comparison performance of the proposed NN-SpSF algorithm with the SpSF algorithm is shown in Figure 1.

As can be seen from Figure 1, the NN-SpSF algorithm has higher accuracy of azimuth estimation and lower sidelobe in nonuniform noise case.

Next, we set the number of snapshots to 800 and evaluate the performances of the proposed algorithms at different

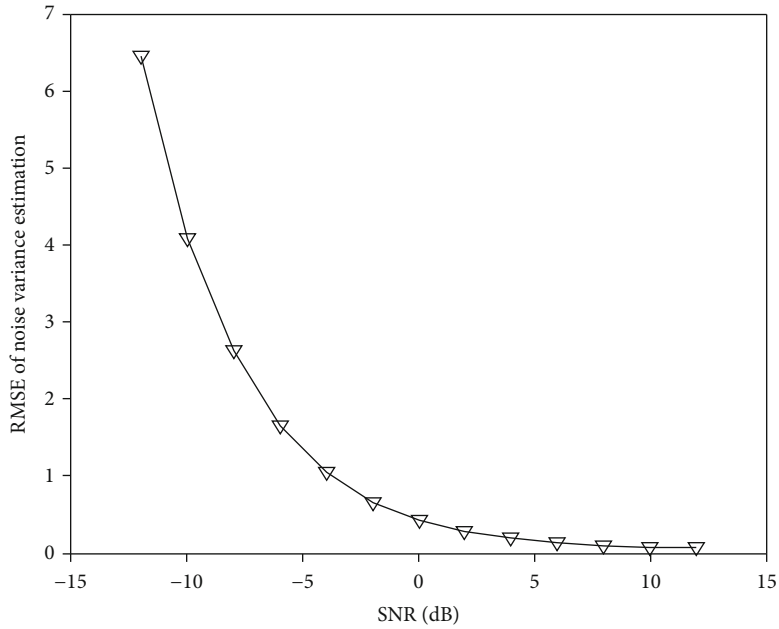

Figure 7: RMSE versus SNR for noise variance estimation.

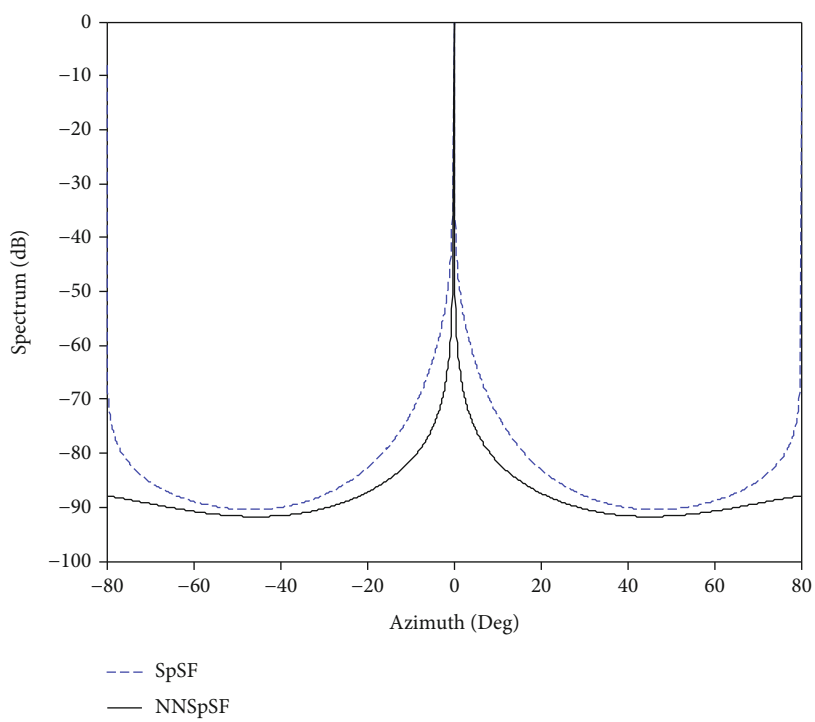

Figure 8: Comparison of SpSF and NN-SpSF algorithm for DOA estimation of pool experiment.

SNR levels. The root-mean-square error (RMSE) of the estimated DOA of the sources is defined as

$$\mathrm{RMSE} = \sqrt{\frac{1}{K * N_m} \sum_{p=1}^{N_m} \sum_{k=1}^{K} \left(\widehat{\theta}_k(p) - \theta_k \right)^2}, \qquad (12)$$

where $\widehat{\theta}_k(p)$ is the estimate of θ_k for the pth Monte Carlo trial, K is the number of sources, N_m is the number of the Monte Carlo trials, and $N_m = 200$ in all the following simulations. The RMSE and success probability of DOA estimation versus SNR are shown in Figures 2 and 3. The SNR varies from -12 dB to 12 dB with 2 dB step size.

It can be seen from Figures 2 and 3 that the NN-SpSF algorithm has lower RMSE and higher success probability

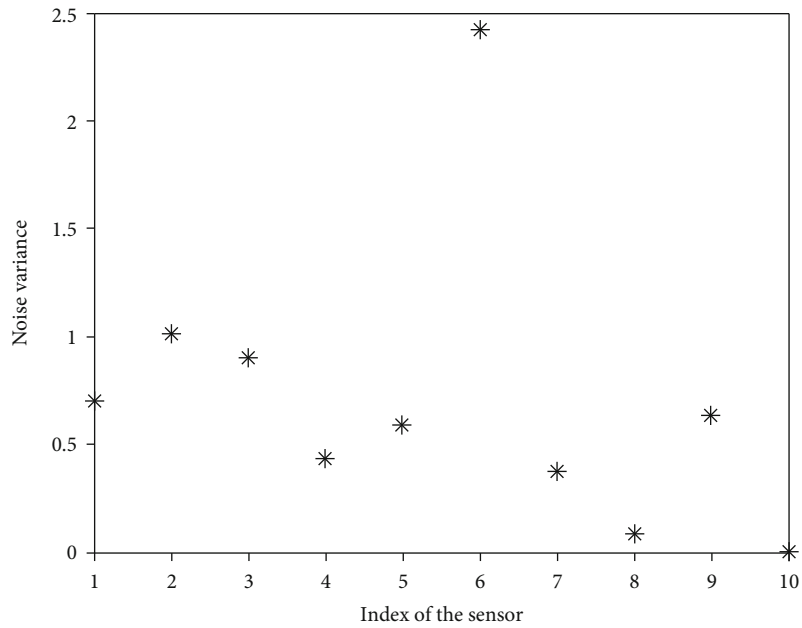

Figure 9: Noise variance estimation of the all sensors.

than the SpSF algorithms when the signal-to-noise ratio changes. Figures 4 and 5 show the RMSE and success probability of DOA estimation versus snapshots, which varies from 200 to 3200 with 200 step sizes.

It can be found that, as the snapshots increasing, the NN-SpSF algorithm has the similar performance with Figures 2 and 3. Besides the performance of DOA estimation, we also evaluate the performance of the proposed NN-SpSF and SpSF algorithm for noise variance estimation. Figure 6 depicts the estimated noise variances averaged from 500 Monte Carlo trials at SNR = −8 dB. Figure 7 shows the RMSE of noise variance estimation of all sensors versus SNR; the SNR varies from -12 dB to 12 dB with 2 dB step size.

It can be seen that the RMSE of noise variance decreases rapidly with the increase of the SNR, and the proposed algorithm can still estimate the nonuniform noise with a lower deviation at a lower SNR, such as the -8 dB case in Figure 6.

5. Water Pool Experiment

The algorithm in this paper was verified by pool experiments in an anechoic pool. The water pool is 20 m long, 8 m wide, and 7 m deep. The receiving array is a vertical uniform linear array with 10 array elements, and the first hydrophone was placed at a depth of 0.7 m. The transmitting transducer is 7 m away from the receiving array, and its transmitting signal is a CW pulse with a frequency of 3 kHz. The CW pulse signal has a length of 400 ms and a period of 1 s.

The results of the DOA estimation of the water pool experiment for the NN-SpSF algorithm is shown in Figure 8, and it can be observed that the NN-SpSF algorithm has lower sidelobe. The noise variance estimation of all sensors of the array is shown in Figure 9. In the actual situation, there are indeed some differences in the noise background of the sensors in the array due to manufacturing, installation, and other reasons.

6. Conclusion

In this paper, a new noise variance estimation algorithm of all sensors in an array in nonuniform noise for DOA estimation is proposed. The estimation of the noise covariance matrix is formulated into a solution to the semidefinite optimization problem which can obtain a more accurate sensor noise covariance matrix. Simulation results show that subtracting the estimated nonuniform noise from the sample covariance matrix can significantly improve the performance of the SpSF algorithm. The water pool experiments show that due to manufacturing and other reasons, nonuniform noise of the sensor does exist, but independent nonuniform noise in the sensor array is the simplest assumption. In future, we will study the noise covariance matrix estimation algorithm closer to the real situation to improve the performance of azimuth estimation.

Data Availability

The data that support the findings of this study are available from the corresponding author upon reasonable request.

Conflicts of Interest

The authors declared that they have no conflicts of interest regarding this work.

Acknowledgments

This work is support in part by the National Natural Science Foundation of China (Grant No. 12004293, No. 61671378, No. 62031021), Special Scientific Research Project of

Shaanxi Provincial Department of Education (Grant No. 20JK0533), and Aviation Science Foundation (Grant Nos. 201809T7001, 2019ZH0T7001).

References

[1] F. Wang, Z. Tian, G. Leus, and J. Fang, "Direction of arrival estimation of wideband sources using sparse linear arrays," *IEEE Transactions on Signal Processing PP.*, vol. 69, pp. 4444–4457, 2021.

[2] M. Liu, Z. Liu, W. Lu, Y. Chen, X. Gao, and N. Zhao, "Distributed few-shot learning for intelligent recognition of communication jamming," *IEEE Journal of Selected Topics in Signal Processing*, vol. 16, no. 3, pp. 395–405, 2022.

[3] M. Liu, B. Li, Y. Chen et al., "Location parameter estimation of moving aerial target in space–air–ground-integrated networks-based IoV," *IEEE Internet of Things Journal*, vol. 9, no. 8, pp. 5696–5707, 2022.

[4] M. Liu, C. Liu, M. Li, Y. Chen, S. Zheng, and N. Zhao, "Intelligent passive detection of aerial target in space-air-ground integrated networks," *China Communications*, vol. 19, no. 1, pp. 52–63, 2022.

[5] Q. Fang, M. Jin, W. Liu, and Y. Han, "DOA estimation for sources with large power differences," *International Journal of Antennas and Propagation*, vol. 2021, Article ID 8862789, 12 pages, 2021.

[6] M. Liu, J. Wang, N. Zhao, Y. Chen, H. Song, and R. Yu, "Radio frequency fingerprint collaborative intelligent identification using incremental learning," *IEEE Transactions on Network Science and Engineering*, vol. 9, no. 5, pp. 3222–3233, 2021.

[7] X. M. Shi and Z. Liu, "Electromagnetic Vector-Sensor Array Processing for Distributed Source Localization," *Progress in Electromagnetics Research B*, vol. 39, pp. 281–299, 2012.

[8] R. O. Schmidt, "Multiple emitter location and signal parameter estimation," *IEEE Transactions on Antennas and Propagation*, vol. 34, no. 3, pp. 276–280, 1986.

[9] R. Roy and T. Kailath, "ESPRIT-estimation of signal parameters via rotational invariance techniques," *IEEE Trans. Acoust., Speech, Signal Process.*, vol. 37, no. 7, pp. 984–995, 1989.

[10] B. Liao, S. C. Chan, L. Huang, and C. Guo, "Iterative methods for subspace and DOA estimation in nonuniform noise," *IEEE Transactions on Signal Processing*, vol. 64, no. 12, pp. 3008–3020, 2016.

[11] J. Zheng and M. Kaveh, "Sparse spatial spectral estimation: a covariance fitting algorithm, performance and regularization," *IEEE Transactions on Signal Processing*, vol. 61, no. 11, pp. 2767–2777, 2013.

[12] C. F. Mecklenbräuker, P. Gerstoft, and E. Zochmann, "c-LASSO and its dual for sparse signal estimation from array data," *Signal Processing*, vol. 130, pp. 204–216, 2017.

[13] A. Panahi and M. Viberg, "Fast LASSO based DOA tracking," in *2011 4th IEEE International Workshop on Computational Advances in Multi-Sensor Adaptive Processing (CAMSAP)*, pp. 397–400, San Juan, PR, USA, 2011.

[14] R. Tibshirani, "Regression shrinkage and selection Via the lasso," *Journal of the Royal Statistical Society Series B, Statistical Methodology*, vol. 58, no. 1, pp. 267–288, 1996.

[15] A. Panahi and M. Viberg, "Fast candidate points selection in the LASSO Path," *IEEE Signal Processing Letters*, vol. 19, no. 2, pp. 79–82, 2012.

[16] C. Chen, F. Lorenzelli, R. Hudson, and K. Yao, "Stochastic maximum-likelihood DOA estimation in the presence of unknown nonuniform noise," *IEEE Transactions on Signal Processing*, vol. 56, no. 7, pp. 3038–3044, 2008.

[17] Y. Wu, C. Hou, G. Liao, and Q. Guo, "Direction-of-Arrival Estimation in the Presence of Unknown Nonuniform Noise Fields," *IEEE Journal of Oceanic Engineering*, vol. 64, no. 12, pp. 504–510, 2006.

[18] B. Liao, L. Huang, C. Guo, and H. C. So, "New approaches to direction-of-arrival estimation with sensor arrays in unknown nonuniform noise," *IEEE Sensors Journal*, vol. 16, no. 24, pp. 8982–8989, 2016.

[19] M. Esfandiari, S. A. Vorobyov, S. Alibani, and M. Karimi, "Non-iterative subspace-based DOA estimation in the presence of nonuniform noise," *IEEE Signal Processing Letters*, vol. 26, no. 6, pp. 848–852, 2019.

[20] P. Stoica, K. M. Wong, and Q. Wu, "On a nonparametric detection method for array signal processing in correlated noise fields," *IEEE Transactions on Signal Processing*, vol. 44, no. 4, pp. 1030–1032, 1996.

[21] P. Stoica, M. Viberg, Kon Max Wong, and Qiang Wu, "Maximum-likelihood bearing estimation with partly calibrated arrays in spatially correlated noise fields," *IEEE Transactions on Signal Processing*, vol. 44, no. 4, pp. 888–899, 1996.

[22] P. Stoica, M. Agrawal, and P. Hgren, "Array processing for signals with non-zero means in colored noise fields," *Digital Signal Processing*, vol. 14, no. 4, pp. 296–311, 2004.

[23] M. Malek-Mohammadi, M. Jansson, A. Owrang, A. Koochakzadeh, and M. Babaie-Zadeh, "DOA estimation in partially correlated noise usinglow-rank/sparse matrix decomposition," in *2014 IEEE 8th Sensor Array and Multichannel Signal Processing Workshop (SAM)*, pp. 373–376, A Coruna, Spain, 2014.

[24] C. Gu, J. He, X. Zhu, and Z. Liu, "Efficient 2D DOA estimation of coherent signals in spatially correlated noise using electromagnetic vector sensors," *Multidimensional Systems and Signal Processing*, vol. 21, no. 3, pp. 239–254, 2010.

[25] Z. Zhang and B. D. Rao, "Extension of SBL algorithms for the recovery of block sparse signals with intra-block correlation," *IEEE Transactions on Signal Processing*, vol. 61, no. 8, pp. 2009–2015, 2013.

[26] L. Yang, J. Fang, H. Li, and B. Zeng, "Localized low-rank promoting for recovery of block-sparse signals with intrablock correlation," *IEEE Signal Processing Letters*, vol. 23, no. 10, pp. 1399–1403, 2016.

[27] Z. Zhilin and B. D. Rao, "Iterative reweighted algorithms for sparse signal recovery with temporally correlated source vectors," in *2011 IEEE International Conference on Acoustics, Speech and Signal Processing (ICASSP)*, pp. 3932–3935, Prague, Czech Republic, 2011.

[28] L. Yang and Z. Song, "An improved IRLS algorithm for sparse recovery with intra-block correlation," *Optik - International Journal for Light and Electron Optics*, vol. 126, no. 7-8, pp. 850–854, 2015.

[29] H. Van Trees, "Van Trees," *Optimum Array Processing*, 2002.

[30] P. Pal and P. P. Vaidyanathan, "DOA estimation of quasi-stationary signals with less sensors than sources and unknown spatial noise covariance: a Khatri–Rao subspace approach," *IEEE Transactions on Signal Processing*, vol. 58, no. 4, pp. 2168–2180, 2010.

[31] S. Zhao, C. Tuna, T. N. Nguyen, and D. L. Jones, "Large-region acoustic source mapping using a movable array and sparse covariance fitting," *The Journal of the Acoustical Society of America*, vol. 141, no. 1, pp. 357–372, 2017.

[32] J. W. Paik, W. Hong, J. K. Ahn, and J. H. Lee, "Statistics on noise covariance matrix for covariance fitting-based compressive sensing direction-of-arrival estimation algorithm: for use with optimization via regularization," *Journal of the Acoustical Society of America*, vol. 143, no. 6, pp. 3883–3890, 2018.

[33] M. Grant and S. Boyd, *CVX: Matlab software for disciplined convex programming, version 2.0 beta*, 2013, http://cvxr.com/cvx.

Hindawi
Wireless Communications and Mobile Computing
Volume 2022, Article ID 3233789, 15 pages
https://doi.org/10.1155/2022/3233789

Research Article

An Information-Entropy-Based Hierarchical Serialization Allocation Method for UAV Tracking in 6G Networks

Yuhao Zhong,[1] **Zhihao Yang**,[2] **Ting Li**,[3] **and Yuting Zhang**[4]

[1]*College of Computer and Network Security (Oxford Brookes College), Chengdu University of Technology, Chengdu, Sichuan, China*
[2]*School of Computer and Information Science, Southwest University, Chongqing, China*
[3]*Department of Information and Software Engineering, University of Electronic Science and Technology of China, Chengdu, China*
[4]*International College of CQUPT, Chongqing University of Posts and Telecommunications, Chongqing, China*

Correspondence should be addressed to Ting Li; 2018091617029@std.uestc.edu.cn

Received 18 July 2022; Revised 6 August 2022; Accepted 22 August 2022; Published 7 September 2022

Academic Editor: Ning Zhang

Unmanned aerial vehicles (UAVs) play an important role in future 6G networks, which can be used to assist cellular networks in setting up temporary networks to provide communication services when network access demand is intense. It is critical to design a UAV tracking method with high efficiency and high precision under active sensor radiation control to build a reliable network of UAVs. Multisensor cooperative multitarget tracking for UAVs with high accuracy is an alternative solution to meet the performance requirements of 6G. In this paper, an information-entropy-based multisensor to multitarget allocation method under low-radiation control is proposed for UAV tracking. Specifically, the knowledge-map-based demand assessment of integrated track detection is first present; and then, fuzzy-decision-tree-based generation of sensor management plan is given; the next, the basic linear programming model for multitarget to multi-UAV allocation is utilized based on cooperative tracking under radiation control; finally, extensive experiments are conduct, and the experimental results show that the proposed method has a good performance.

1. Introduction

With the rise of emerging technologies, e.g., AI [1–3], unmanned aerial vehicle (UAV) communication [4, 5], and D2D communication [6, 7], the future 6G network is expected to connect everything and meet different communication needs [8, 9]. Actually, UAVs play an important role in future 6G networks, which can be used to assist cellular networks in setting up temporary networks to provide communication services when network access demand is intense. It is critical to design a UAV tracking method under active sensor radiation control to build a reliable network of UAVs [10]. Sensor-based detection and tracking is one of the mainstream UAV tracking approaches, which can realize the tasks of formation coordination to build a reliable UAV network [11–13].

Through the cooperative action of two or three unmanned aerial vehicles (UAVs) equipped with passive detection sensors in formations, coordinated target positioning and silent attack can be realized. Under the premise of high precision for tracking targets, the coordinated guidance and tracking of the active and passive sensors of the UAVs can reduce the electromagnetic radiation time, power, and airspace of the active sensors and improve the overall performance of UAV communication. In addition, it is possible to realize decentralized optimization and coordinated control of heterogeneous multimotion platforms through the coordination of aircraft formations with active and passive sensors. However, there are two main constraints for sensor cooperative tracking. The first constraint is the capability of a single sensor. In a complex battlefield environment, each sensor unit can only track a limited number of targets with fixed detection accuracy. The second constraint is the resources contained in a single aircraft. Limited by transmission bandwidth and computing power, a single aircraft can only fuse and process measurement information from a small number of sensors. Therefore, it is necessary to focus on solving the problem of optimal pairing of sensors and

targets, rather than choosing as many sensors as possible. Moreover, it is also necessary to select the optimal sensor combination for each target and select the optimal tracking object for each sensor, so as to achieve the optimal tracking performance of multisensor to multitarget.

In this paper, a multi-UAV multitarget assignment method based on low-radiation control active sensors is proposed to meet the performance requirements of the tracking task. In the method, a mathematical model of multi-UAV to multiobjection allocation decision is established, in which, one sensor is equipped on one UAV. First of all, the interval between active sensors' radiation duration periods is calculated. According to the current situation of active sensors, it is divided into two modes: active and passive coordinated tracking and passive sensor coordinated tracking. Then, based on the information entropy and target threat degree, a multi-UAV cooperative allocation scheme for multitarget tracking is given. To verify the effectiveness of the multitarget and multisensor allocation method in this paper, the simulation experiments are carried out according to the following scenarios. A single UAV platform with multiple sensors is used to track four target UAVs. The experimental result demonstrates that our method has a high efficiency and high accuracy.

2. Related Work

Regarding target allocation, many scholars have conducted research, mainly focusing on multi-UAV (unmanned aerial vehicle) task allocation as the research background [14]. In recent years, the research on the model of multisensor to multitarget allocation mainly includes two aspects: one is the target-priority, and the other is the matching algorithm of the sensors (or combination) to the targets [15–17]. Among them, the matching algorithm is difficult to express with a specific mathematical formula, and most of them use the method of directly assigning values to the existing parameter table. However, such methods cannot quantify the matching algorithm scientifically and reasonably, making the allocation result inaccurate. In [18], a sensor management method is proposed based on the efficiency function, in which, the efficiency function is established through the pairing function of the sensor and the target and the target priority function to realize the reasonable allocation of sensor resources.

In [19], the target-to-sensor allocation efficiency function is defined as a value function and a loss function in the target-to-sensor allocation model, but it does not consider the impact of the diversification of target characteristics on the efficiency. In [20], the target priority function and the sensor's effectiveness function are considered to establish a multisensor resource preallocation mathematical model, in which, the preallocation of the three tasks of target detection, target tracking, and target recognition is unified into one framework. Moreover, an improved Hungarian algorithm is used in [20] to solve the objective function. However, the disadvantage is that the task-based matching efficiency is not determined in the actual simulation. In [21], an allocation model is proposed based on the reconnaissance resolution of the sensors, where the UAV carries and the constraints of the targets' appearance time window. A set of UAVs with different reconnaissance payload capabilities to conduct information reconnaissance in multiple mission areas in a mission scenario is studied in [22]. In [23], Spyridis et al. studied target tracking of mobile IoT devices at unknown locations with a set of UAVs equipped with received signal strength indicator (RSSI) sensors in 6G network. In the proposed method, it preserves the swarms that approach the radio frequency (RF) source more efficiently, removing the rest of the drones that return to base.

In [24], a distributed reinforcement learning (RL) approach is proposed with an algorithmic framework that relies on the possibility of drones exchanging some information through communication channels to achieve context awareness and implicitly coordinate the actions of UAV swarms. In [25], an end-to-end collaborative multiagent reinforcement learning (MARL) scheme is presented that enables UAVs to make intelligent flight decisions for collaborative target tracking based on the past and current state of the target. In [26], a multi-UAV intelligent maritime task assignment and route planning scheme is designed based on improved particle swarm optimization combined with genetic algorithm (GA-PSO). In the proposed scheme, the traditional particle swarm optimization (PSO) is improved by introducing partial matching crossover and quadratic transposition variation based on the simulation of the intelligent ship control system. Moreover, the improved GA-PSO is used in [26] to solve the stochastic task assignment problem of multiple UAVs and the two-dimensional path planning problem of a single UAV. In [27], a multitarget tracking algorithm is proposed, in which trajectories evolve over a special Euclidean group SE(2). Applications include tracking ground targets using cameras on hovering multirotor drones. The method extends the recursive random sample consensus (R-RANSAC) algorithm to nonlinear motion models. Other related works also include security techniques for IoT and 6G [28–30] and AI for UAV communication [31–33].

In summary, these studies focus on the multiplatform and multitarget allocation of a single sensor without considering radiation control conditions. However, the development of formation coordination has not been analyzed, and the influence of these factors on target allocation has not been considered. It lacks comprehensive consideration of the influence of multiple factors such as formation coordination, active sensor low-radiation control, and heterogeneous multisensors.

3. Allocation Method Based on Information Entropy

According to the sensor scheduling instructions of the operator and the results received from the information fusion calculation, the sensor allocation results and management plans are generated, and the specific sensors are called to perform the actual measurement tasks.

First of all, it is necessary to carry out a comprehensive track detection requirements assessment, clarify the detection requirements, and then generate a sensor plan. On this basis, it is necessary to realize the sensor target pairing and dispatch the corresponding sensors. Due to the fact that the information gain in UAV allocation refers to the reduction of information entropy (uncertainty about target state) before and after each tracking [34], the UAV resources can be scheduled according to the value of the information gain, and then, the resource allocation and pairing of multitarget and multi-UAV can be completed.

3.1. Knowledge-Map-Based Demand Assessment of Integrated Track Detection. The integrated track detection demand assessment is to undertake the track information and track evaluation information from the information fusion system and make decisions to generate the current sensor task demand in combination with the actual task and aircraft platform status, including the demand for supplementing dimension detection when the target detection dimension is missing and the demand for improving target accuracy when the target accuracy is low. The sensor usage plan generation algorithm is utilized to obtain the usage and allocation of multisensor based on the detection requirements from the sensor detection requirements, as well as the sensor status, task, and carrier platform status.

Figure 1 shows the basic process of track integrated detection demand assessment. The track integrated detection demand assessment is mainly based on the system track quality assessment results and the actual task, platform status, and other information, making comprehensive decisions to generate the track integrated detection demand such as dimension supplement and accuracy improvement.

The core of the track integrated detection demand assessment is to build a knowledge map generated by the detection demand. Based on the map, the demand reasoning is carried out to generate the basic sensor use requirements, which is the basic constraint for the next multitarget and multisensor allocation. Figure 2 shows the entity relationship diagram of airborne sensor detection demand knowledge map, which describes the association relationship between airborne sensor detection demand entities. Here, the macro association relationship is described, and only the possible coupling relationship between entities is described.

The track integrated detection demand entity, as the output node, combined with the system cross-linking relationship, concludes that the track integrated detection demand entity has a direct one-step inference relationship with the fusion situation, basic task type, and sensor equipment. There is a direct one-step inference relationship between the aircraft platform and the sensor equipment, which represents the sensor load configuration of a specific flight platform. There is a direct one-step inference relationship between the aircraft platform and the fusion situation, which is used to express the relationship between the attitude of the aircraft platform and the fusion situation. The indirect relationship between flight platform and track integrated detection demand entity is multistep inference, which indicates the impact of different aircraft platform states on detection demand generation, such as health status. There is a direct one-step inference relationship between the basic task type and the sensor equipment, which indicates the constraints of different task types and stages on the available sensor modes, parameters, etc. In addition to the direct relationship between the basic task type and the sensor equipment, there is also an indirect relationship through multistep inference of the sensor equipment. The knowledge map should be continuously expanded and improved based on experience and knowledge.

3.2. Fuzzy-Decision-Tree-Based Generation of Sensor Management Plan. By receiving the integrated detection demand generated from the track integrated detection demand estimation, combined with the mission stage information, platform status information, etc., the comprehensive decision-making is how to generate specific parameters to guide the sensor work and generate the sensor management plan.

On the basis of obtaining the demand of track integrated detection, considering that the types of airborne sensors, multisensor control methods, and controllable parameters are basically clear, and the requirements for real-time decision-making are relatively high, the fuzzy decision tree method is selected to generate specific sensor equipment types and sensor control parameter sequences. The construction of fuzzy decision tree is to introduce fuzzy inference system (FIS) into the structure of traditional decision tree to form a fuzzy tree structure and fuzzify the fixed rule parameters, so that it has the ability to be optimized, and it is convenient to optimize the parameters of decision tree on its basis.

The purpose of the sensor management plan generation technology is to effectively use the existing sensor resources to collect information, meet the requirements of targets and scanning space, and effectively perform specific tasks. Its core problem is to determine which sensor to choose to monitor and track the target of concern, as well as the type, configuration, working mode, parameters, and measurement process of sensors according to certain rules or optimization criteria (such as track accuracy and detection probability). Mutual cooperation among sensors, etc., because different sensors have different characteristics, undertake different tasks, have different requirements for sensors, and have more practical information requirements, the generation of sensor management plan usually includes the following contents.

(i) *Switch State Management*. When the active sensor emits energy, it will expose itself and then be attacked. In order to hide or protect itself, it is necessary to control the switch state of the active sensor and reduce the radiation times of the sensor. On the premise of meeting the basic task, the active sensor should be in a silent state as far as possible. For the sensor with limited energy, controlling the switch state of the sensor can also prolong the working time and service life of the sensor

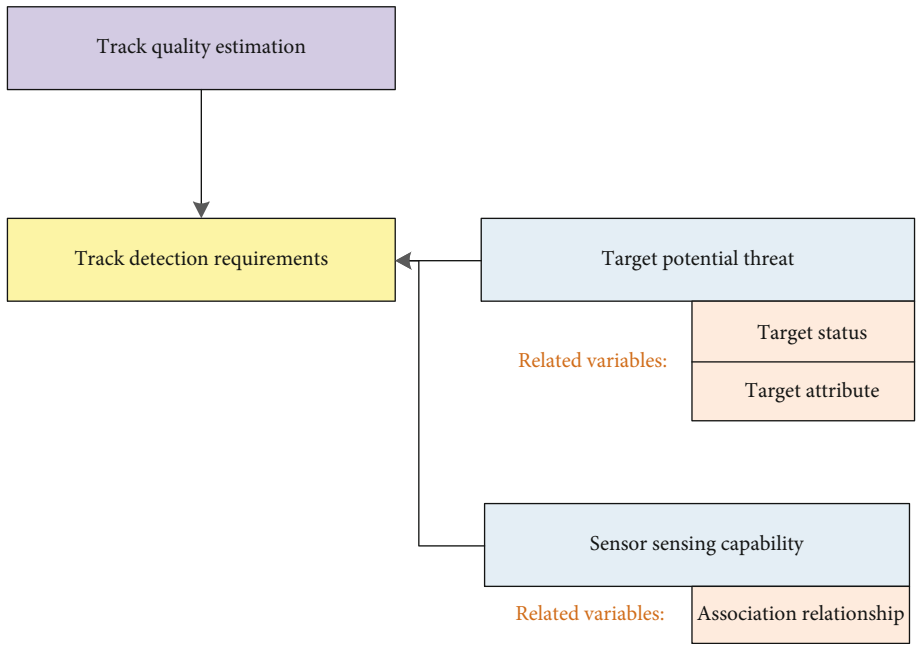

Figure 1: Flowchart of track integrated detection demand assessment.

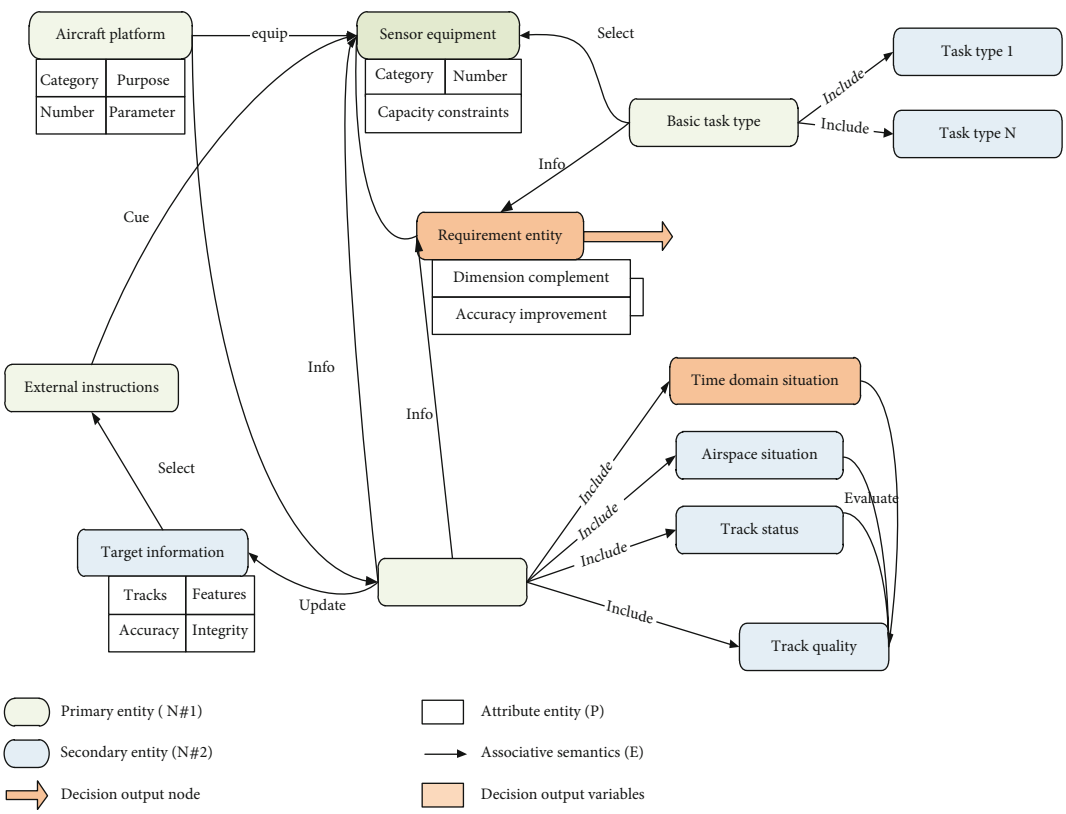

Figure 2: Schematic diagram of entity relationship of sensor detection demand knowledge map.

(ii) *Working Mode Management.* Some sensors have different working modes. Choosing different working modes can complete different tasks, and the working modes of sensors can be flexibly selected according to task requirements

(iii) *Working Parameter Control.* The working parameters of some sensors can be controlled, which will affect the task execution of the sensor. For example, for radar, the main operating parameters include operating carrier frequency, transmission power,

beam direction, and revisit frequency. By controlling these parameters, the target detection and tracking performance of radar can be optimized

(iv) *Time Management*. In a multisensor system, for different tasks or observation objects, only a part of the sensors may be required to work at a certain time. Therefore, it is necessary to plan the tasks of each sensor in the time series. In addition, when some sensors or certain things in the target environment maintain synchronization or relationship in time (such as moving target detection, track loss, etc.), it is required to manage the time of sensor operation

(v) *Space Management*. The main task of space management is to determine the spatial direction of each sensor, so as to better complete the detection and tracking tasks of single target and multitarget. In addition, many sensors do not work in an omnidirectional way, which requires that the spatial orientation of multiple sensors can ensure the coverage of the entire airspace and the continuity of task execution, such as the indication and handover of sensors to targets, while requiring time and space management

(vi) *Sensor Task Coordination*. Multiple sensors in sensor networks usually need different sensing capabilities and can obtain different sensing information. By realizing information sharing among sensors, they can cooperate with the tasks of each sensor on this basis, drive the actions of sensors with tasks, and enable multisensor cooperation to complete battlefield sensing tasks. Through the decomposition of the above management purpose, the whole multisensor information fusion system becomes a closed-loop system, so that the working state and tasks of the sensors can be adjusted in real time according to the needs of the task and the changes of the target and environment, so as to give full play to the advantages of each sensor, better complete the target and environment sensing tasks, improve performance, improve their own viability, automate the process, and reduce the burden of operation

As shown in Figure 3, the decision tree based on tree structure is suitable for most of the clear correspondence between input and output and can give more accurate prior expert knowledge. It can express the related knowledge through the multitree structure, expand the knowledge conveniently through the construction of subtree, and realize the reasoning ability with fuzzy attributes or Bayesian probability by setting the fuzzy system on the tree node or the state transition probability on the opposite side. On the basis of prior expert knowledge, genetic algorithm and small neural network can be used to optimize the combination relationship of knowledge structure and even the parameters in knowledge structure, which can produce more reasonable and high-quality decisions.

On the basis of obtaining the demand of track integrated detection, considering that the multisensor control mode is basically clear, the fuzzy decision tree method is selected to generate specific sensor equipment types and sensor control parameter sequences. The construction of fuzzy decision tree is to introduce fuzzy inference system (FIS) into the structure of traditional decision tree to form a fuzzy tree structure and fuzzify the fixed rule parameters, so that it has the ability to be optimized, and it is convenient to optimize the parameters of decision tree on its basis.

As shown in Figure 3, by obtaining the time domain situation, airspace situation, measurement dimension requirements, and measurement performance requirements with the detection demand assessment, two state measurement nodes can be set: (1) situation assessment node and (2) status evaluation node. Note that, the situation assessment node completes the measurement parameter demand analysis of all targets in the airspace within a certain period; and the status evaluation node completes the performance demand analysis of all measured parameters. These two state nodes correspond to two decision points, which are sensor type decision and sensor working parameter decision.

The fuzzy reasoning mode based on fuzzy inference engine is suitable for the knowledge expression mode of tree structure. By introducing the fuzzy reasoning system into the decision tree node, it has the ability of generalization and optimization under the guidance of certain prior knowledge and has a wide range of applications. As shown in Figure 4, taking radar mode management as an example, drawing on the knowledge of domain experts, multiple target attribute values and corresponding radar mode selection results are selected as training samples to learn the fuzzy decision tree and establish the fuzzy decision tree of radar mode management. The established fuzzy decision tree is used as the reasoning rule, and the real-time target is used as the test data to reason and classify it. The classification results are expressed with confidence as the real-time radar mode management results. For fuzzy decision tree, the most important reasoning mechanism depends on the design of fuzzy system. The membership function and the design of membership function are introduced. For details of the fuzzy attribute membership values of enemy target attributes, please refer to Table 1.

As shown in Figure 5, the selection of the attribute with the smallest fuzzy information entropy among all attributes to be the current test attribute node and the specific tree building algorithm is as follows.

Let the data set (e.g., instance set) $D = \{e_1, e_2, \cdots, e_N\}$ be the example set defined on the discrete value universe x, the fuzzy attribute set be $\{A_1, A_2, \cdots, A_M\}$, the attribute value of attribute A_i be $T(A_i) = \{a_{i_1}, a_{i_2}, \cdots, a_{i_k}\} (1 \le i \le M)$, and the class $C = \{C_1, C_2, \cdots, C_K\}$ to be divided. In the i example, the value of e_i about the j attribute is represented by the corresponding membership degree μ_{IJ}, which is a fuzzy subset defined on $T(A_i)$. If the attribute A_i is a symbolic value attribute, the value of μ_{IJ} is 0 or 1. Let D^{C_k} be the data subset of category C_k, and $|D|$ be the cardinality of D.

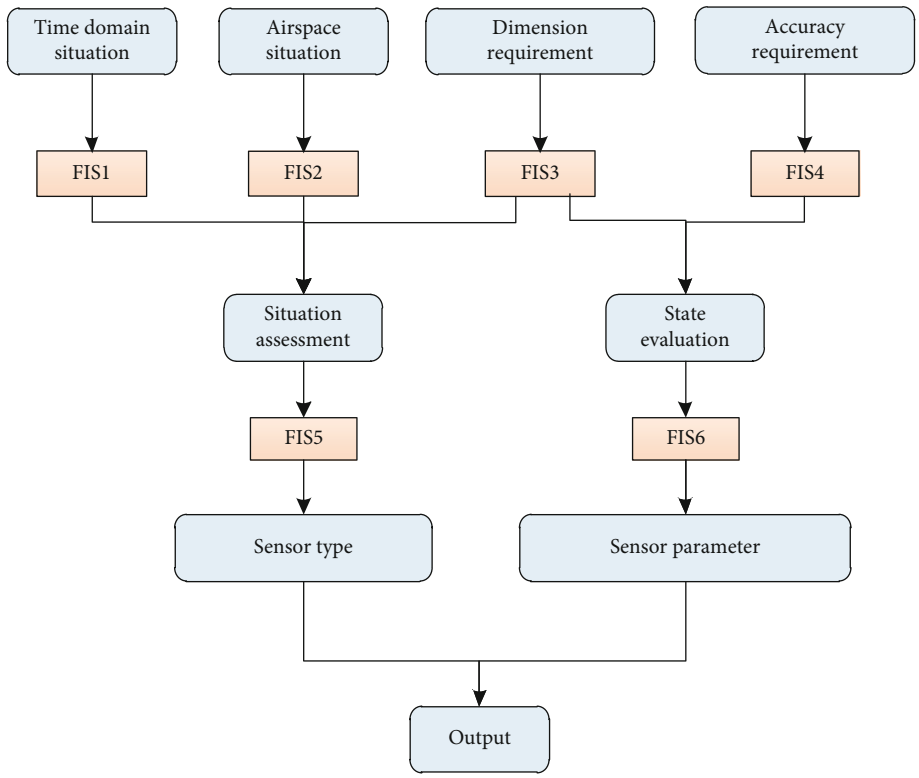

Figure 3: Decision tree model with fuzzy inference system.

Step 1. Initialize and create a root node.

Step 2. The node is a leaf node, if the current node meets one of the following conditions.

(1) All attributes are used up

(2) $D^{C_k}/D > \theta$

(3) $|D| < \beta$

Among them, θ is the level of importance, and β is the confidence level.

Step 3. If the current node does not meet the above conditions, perform fuzzy segmentation on the node. The segmentation steps are as follows.

(1) Calculate the information gain $G(A_i, D)$ of each attribute, and select the attribute $A_{\max}$ with the largest information gain as the test attribute of the current node

(2) Divide d according to the fuzzy attribute value of $A_{\max}$, get a new fuzzy subset $D_1, D_2 \cdots, D_m$, and generate a new node $t_1, t_2, \cdots, t_m$

(3) Replace d with $D_1, D_2, \cdots, D_m$ in turn, and return to Step 2 for iteration

Using the above method, the attribute with the largest information gain is selected as the test attribute each time, and the data set is divided, so as to generate a fuzzy decision tree. The resulting decision leaf node is not a unique class, but a class calibrated by trust. Thus, a reference fuzzy decision tree for radar air mode management can be obtained, as shown in the above figure, in which $M_1 \sim M_5$ represent different RD working modes, including passive detection mode, side scan tracking mode, continuous tracking mode, follow-up detection mode, and active jamming mode. Reasoning based on the fuzzy decision tree is constructed above. The target data searches down multiple branches with its confidence (membership) of each branch (fuzzy subset) of the corresponding test attribute and finally reaches multiple leaf nodes and then calculates the confidence of each mode. The specific calculation process is as follows.

Step 1. Path confidence calculation. Fuzzificate the current target data, obtain the confidence of the target data to each branch of the fuzzy subset of the test attribute, and calculate the path confidence with the minimum operator. As shown in Figure 5, if the leftmost path has distance $\longrightarrow \mathrm{F}(\mu_F = 0.8)$, and Entry angle $\longrightarrow H(\mu_H = 0.5)$, the confidence of the path is $\min(\mu_F, \mathrm{I}_H) = \min(0.8, 0.5) = 0.5$.

Step 2. Confidence calculation of each mode. Calculate the trust degree of each mode on all leaf nodes with the product operator, as shown in the leftmost leaf node in Figure 5. The trust degree of $D = M_1 = 0.83 \cdot \min(\mu_F, H) = 0.83 \cdot 0.5 =$

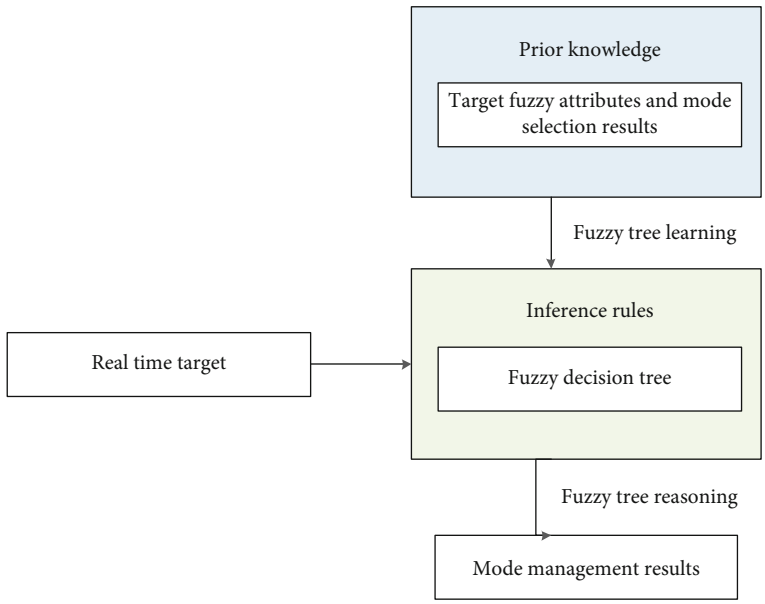

Figure 4: Radar mode management system based on fuzzy decision tree.

Table 1: Fuzzy attribute membership value table of target attribute.

Fuzzy attribute	Attribute value
Target distance	Far (F), middle (M), and near (N)
Target entry angle	Head on (H) and tail rear (T)
Lock status	Lock (L) and unlock (U)

0.415. And then, combine the confidence of the same mode on all leaf nodes and calculate with the maximum operator. If the confidence of $D = M_1$ of each leaf node is $\{0.42, 0.8, 0.6, 0.36, 0.92, 0.5, 0.83\}$, the confidence of $D = M_1$ after combination is $\mu_D = M_1 = \max(0.42, 0.8, 0.6, 0.36, 0.92, 0.5, 0.83) = 0.92$; finally, normalize the confidence of the merged model as follows.

$$\bar{\mu}_D = \frac{\mu_D = M_i}{\sum_{j=1}^{5} \mu_D = M_j}. \tag{1}$$

The confidence of each mode obtained in the above steps is used as the reasoning result to characterize the demand degree of RD for each mode. When nonnumerical reasoning results are needed, the mode with the greatest confidence is selected as the result of RD empty mode management. In addition, for the fuzzy membership parameters of fuzzy tree, genetic algorithm can be constructed to form genetic fuzzy tree for parameter optimization, and then, the decision-making process can be optimized more carefully and flexibly.

3.3. Basic Linear Programming Model for Multitarget to Multi-UAV Allocation Based on Cooperative Tracking. Generally, we assume that a sensor-to-target pairing system includes a set of basic sensors $\{s_1, s_2, \cdots, s_n\}$ and a set of targets $\{tar_1, tar_2, \cdots, tar_m\}$, where n and m, respectively, refer to the numbers of sensors and targets. For n basic sensors are able to form $2^n - 1$ sensors' combinations which are named tracking unit. The basic sensors are signed from 1 to n, and the combinations are signed from $n + 1$ to $2^n - 1$. Therefore the m targets are tracked by $2^n - 1$ sensors' combination. Here, the symbol S_i is used to present the combinations. For an example, 3 sensors are able to form a set of 7 tracking units named, contained $S_1 = \{s_1\}, S_2 = \{s_2\}, S_3 = \{s_3\}, S_4 = \{s_1, s_2\}, S_5 = \{s_2, s_3\}, S_6 = \{s_1, s_3\}, S_7 = \{s_1, s_2, s_3\}$.

An integer set $J(b) = \{j | s_b \in S_j\} (b = 1, 2, \cdots, n)$ refers to the numbers of the tracking unit which the bth basic sensor belongs to. The assignment decision mathematical model of target tracking under low radiation control can be expressed as a multiobjective optimization linear programming model with multiple constraints. The objective functions are composed of total tracking benefit and active sensors' radiation interval. The first optimal solution set D_1 is obtained for maximizing for the active sensor radiation interval, and the second optimal solution set D_2 is obtained for maximizing the total tracking benefit. The total tracking benefit can be expressed as a function of target tracking priority index, tracker coordination coefficient, information gain, and sensor-target pairing matrix. The objective functions are as follows

$$\max \begin{cases} C = \sum_{i=1}^{m} \left(R_j \cdot \left(\sum_{i=1}^{2^n - 1} F_i \cdot I_{ij} \cdot X_{ij} \right) \right), \\ \Delta t_k, \end{cases} \tag{2}$$

$$\text{s.t.} \sum_{i \in J(b)} \sum_{j} X_{ij} \le \tau_b, b = 1, 2, \cdots, n, \tag{3}$$

$$\sum_{i=1}^{2^n - 1} X_{ij} = 1, j = 1, 2, \cdots, m, \tag{4}$$

$$X_{ij} \in \{0, 1\}, \forall i, j, \tag{5}$$

$$P(k) = f(\Delta t_k, R[P_T(k), T_{OT}(k)], POF) \leq P_{ex}. \tag{6}$$

In Eq. (2), the first equation refers to the maximum matching matrix C of the total tracking benefit of the sensor and target pairing. In this equation, R_j refers to the priority indicators for tracking targets. From [35, 36], we have the following property: the larger R_j is, the higher the priority indicator of the target j is. F_i refers to the coefficient of the ith tracking unit which is according to the sensor coefficient function. I_{ij} refers to the information gain between the ith tracking unit and the jth target. X_{ij} is an element of the solution matrix, whose value is only 0 or 1. If the value of X_{ij} is 1, the ith tracking unit tracks the jth target, and if the value is 0, the ith unit does not track the jth target. Δt_k represents the covariance of the track filter and the recurrence rate of the active sensors' radiation discontinuity required to achieve the specified tracking accuracy.

In constraints, τ_b in Eq. (3) refers to the maximum number of tracking targets of the bth basic sensor. Eq. (4) ensures that the number of targets tracked by the tracking unit will not exceed the maximum tracking number of each basic sensor. Equation (5) ensures that one target is tracked by one tracking unit at most. In Eq. (6), $P(k)$ is the targets' state covariance matrix at the moment t_k and related to the sensor measurement noise covariance function $R(\cdot)$. P_{ex} is the given expected covariance matrix which is the specified target tracking accuracy of the sensors, and the value of P_{ex} can be selected according to different control measurements.

3.4. Multitarget and Multi-UAV Allocation Method for Cooperative Tracking. In order to solve the model introduced in Section II-A, a hierarchical sequence optimization method is proposed in this paper. First, the stealth control model is solved by taking the active sensor radiation time as the target and the coordinated tracking accuracy as the constraint. Then, on the basis of this solution set, the allocation optimization model is solved by taking the synergy coefficient and the target priority to weight the information entropy as the goal. The hierarchical sequence optimization effectively reduces the dimensionality of the optimization problem and the probability of falling into a local optimum. According to the output state estimation and covariance estimation of the active and passive sensors' cooperative tracking algorithm, the predicted covariance is compared with the previous covariance to control the radar radiation. When the predicted covariance is less than the threshold which means $P_{k|k-1} \leq P_{ex}$, the radar does not radiate; when the predicted covariance exceeds the threshold, the radar radiates, where $P_{k|k-1}$ refers to the predicted position error for the moment k at the moment $k-1$.

3.5. UAV and Target Pairing Algorithm Based on Information Entropy. Pseudocode based on multiaircraft cooperative tracking sensor and target pairing algorithm is proposed by using traversal target list method to achieve. Consider a scenario that there is a formation networked sensor system with S sensors, and the number of tracked targets is N. At the moment k, it needs to be tracked according to the estimated accuracy of $N(k)$ targets. First, the predicted covariance matrix of each target is calculated and used to compare with the preset expected covariance to determine whether the active sensor will participate in the collaboration at the next moment. Then, according to whether the active sensor participates in the next moment of coordination, it traverses the optional tracking units and constructs a feasible target tracking scheme based on the maximum total tracking benefit. Note that the scheme must meet the constraints of the model. Its main functions are described in Table 2.

4. Experimental Results

Consider the following scenario for simulation experiments: a single UAV to track four target UAVs, and the UAV is equipped with three types of space-based platform sensors, i.e., the first sensor S_1, the second sensor S_2, and the third sensor S_3. Build a 1-to-4 oriented digital simulation platform to support simulation verification. Figure 6 shows the deployment diagram of the digital simulation platform, which supports the 1-to-4 confrontation scenario. One computing node on the red side simulates one aircraft, four computing nodes on the blue side simulate four aircraft, and the middle station is the white node (integrated with the red node) for comprehensive evaluation, where the computer adopts PC and is connected through Ethernet. The PCs used in the experiments are desktop computer with Win7 operation system, Intel (R) Core (TM) i7-7700T CPU, and 16 GB of RAM.

4.1. Simulation of Fuzzy Decision Tree Algorithm. Take the following scenario as an example to demonstrate the implementation process of sensor management plan generation technology. The scene is shown in Figure 7. First, the scene is defined, and the airborne photoelectric sensor is used. Its visual range is 20 km, the detection probability is set to 90%, the field of view (FOV) range is 15 degrees, and the scanning angle is 120 degrees to track the moving target. The target moves in a two-dimensional horizontal plane, and its starting position is located at $(500\text{m}, 2000\text{m})$ and moves at a speed of 20 m/s in the X direction and 1.35 m/s in the Y direction within $[0, 20]$ time steps. Within $[21, 50]$ time steps, it provides an acceleration of 5 m/s in the X direction, and the speed in the Y direction remains unchanged. Within $[51, 65]$ time steps, it provides an acceleration of -5 m/s in the X direction, and the speed in the Y direction remains unchanged. Within $[66, 73]$ time steps, it performs steering operation, in which the speed in the X direction is $(v_{x_{T_{\text{step}}-1}} - 5) * (T_{\text{step}} - 73)^2/15$, and the speed in the Y direction is $v_{x_{T_{\text{step}}-1}} * (T_{\text{step}} - 65)^2/80$, within $[73, 90]$ time steps, the speed in X direction remains unchanged, and the deceleration in Y direction is -5 m/s.

Set up a control group, and compare the azimuth error of beam pointing under the two ways of not using sensor control feedback technology and using sensor control

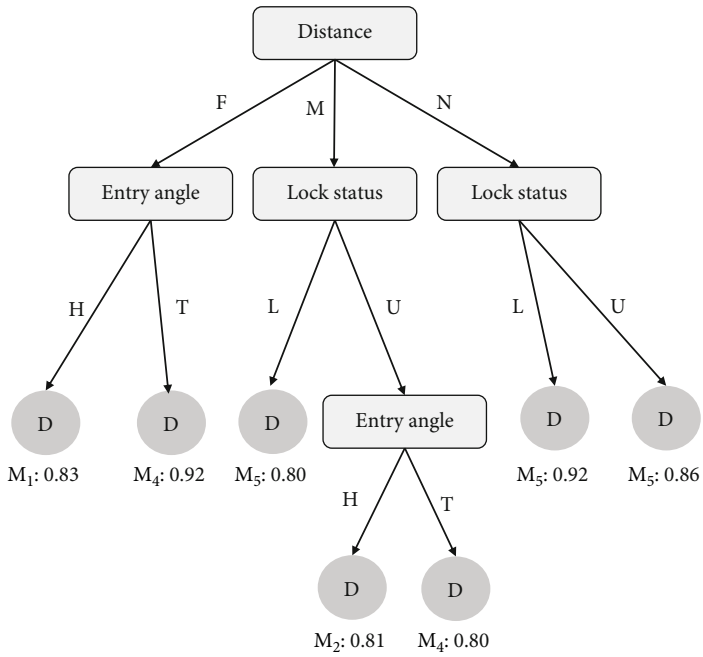

Figure 5: Fuzzy decision tree of RD to empty pattern management.

Table 2: The list of main functions.

Number	Software name	Function description
1	Sensor usage plan	Provide automatic start and stop control for sensor usage and status maintenance; provide control management based on stealth level.
2	Sensor scheduling	Provide the ability to control all sensor functional models; provide sensor active state maintenance function.
3	Display control	Provides control and monitoring of sensors; provide the display function of two-dimensional situation map (red/blue platform running track display)
4	Simulation model	Provide sensors' function model; provide communication function model.
5	Simulation operation configuration management	Configuration management of environment parameters required for system operation; graphical configuration management of simulation model interaction.
6	Evaluation software	Provide real-time analysis and evaluation of measurement error.

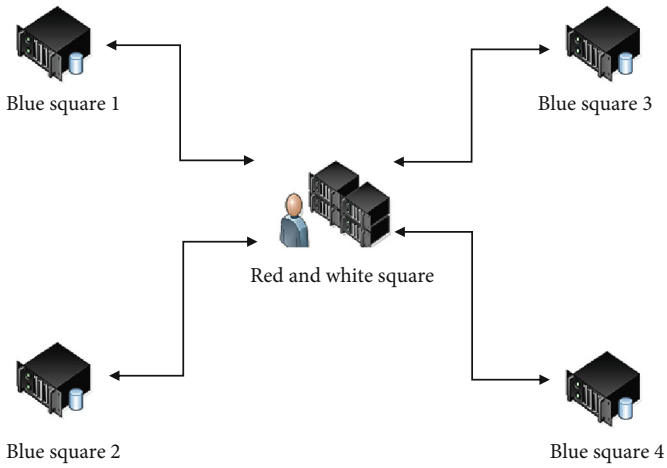

Figure 6: Digital simulation deployment diagram.

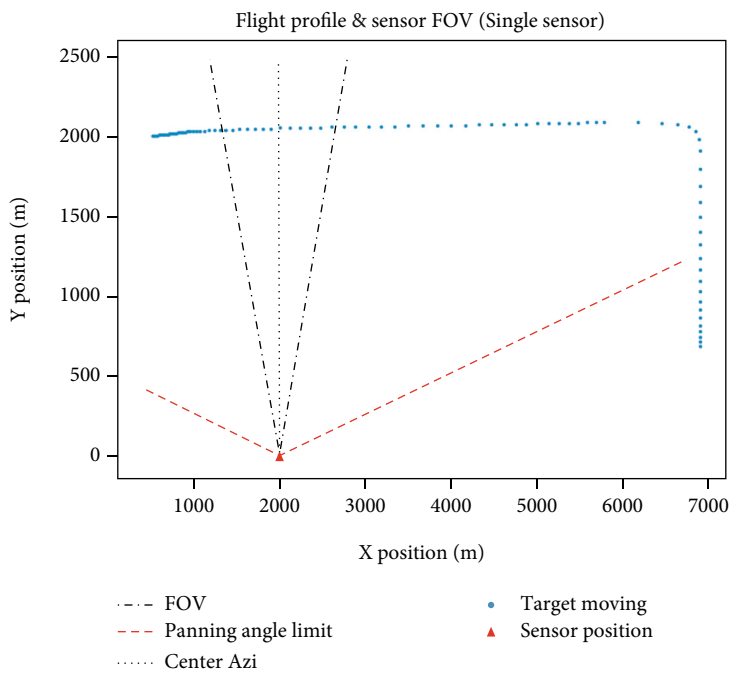

Figure 7: Basic setting diagram of scene.

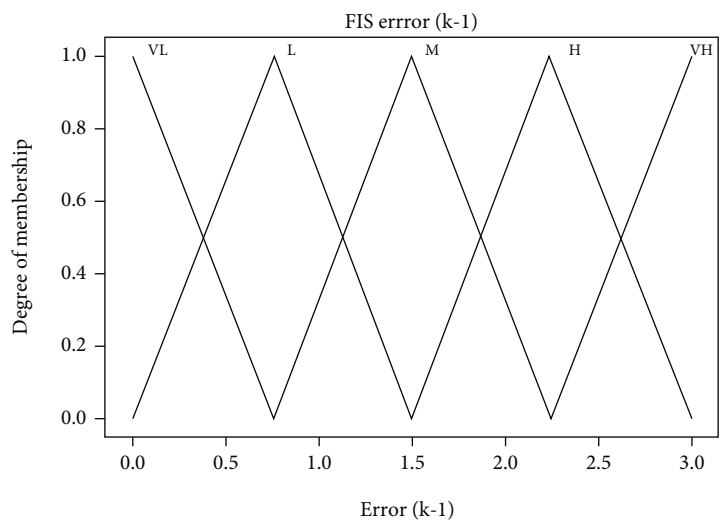

Figure 8: Input fuzzy controller.

feedback technology. For multisensor fusion, this index is reflected by track quality evaluation. The data fusion in the process of target tracking is carried out through the IMM Kalman filter. According to the fused data information, the beam pointing azimuth errors (i.e., error k and error $k-1$ between the current time and the previous time) are calculated and sent to the sensor using the plan generation module. The sensor uses the plan generation module to request the azimuth error from the data fusion system as the input.

By constructing the prior knowledge, the prior knowledge is modeled into a fuzzy system to generate a fuzzy controller. As shown in Figures 8 and 9, the fuzzy controller takes error (k) and error ($k-1$) as inputs for discrete fuzzification and constructs five levels of language values, VL (very low error), L (low error), M (medium error), H (high error), and VH (very high error). Each language value corresponds to a specific triangular membership function. The output of the fuzzy system is constructed. The decision outputs the scanning frequency and fuzzy nodes, which are divided into 13 levels of language values, VL (very low), MVL (very low), L (low), ML (medium low), M (medium), MH (medium high), H (high), MVH (very high), VH (particularly high), MVVH (extremely high), VVH (very, very high), MVVVH (sky-high), and VVVH (most high).

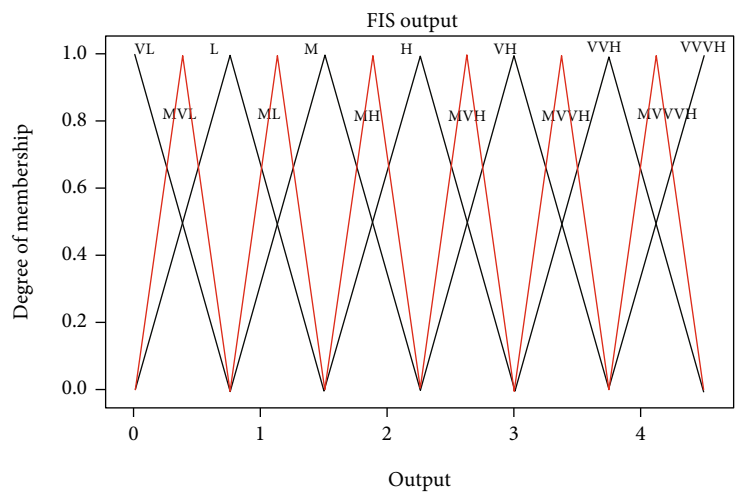

Figure 9: Output fuzzy controller.

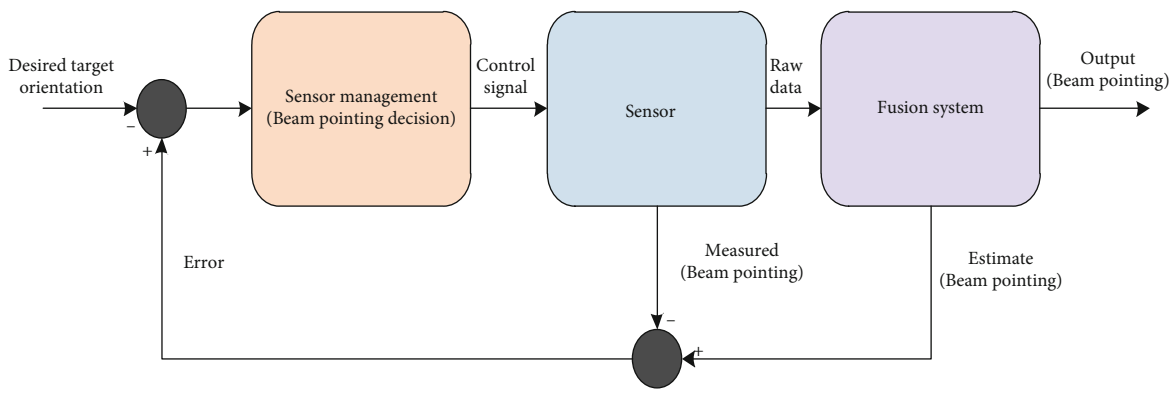

Figure 10: Sensor feedback closed loop control block diagram.

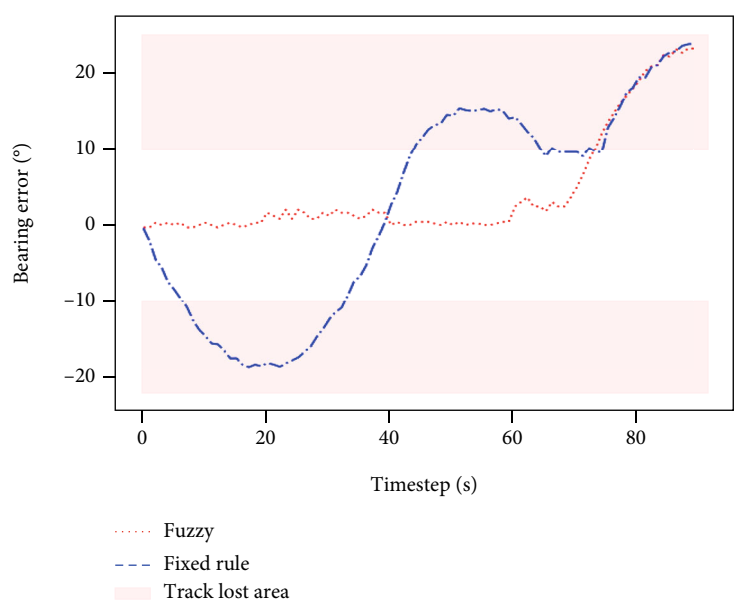

Figure 11: Comparison between single sensor based on fuzzy control and fixed rules.

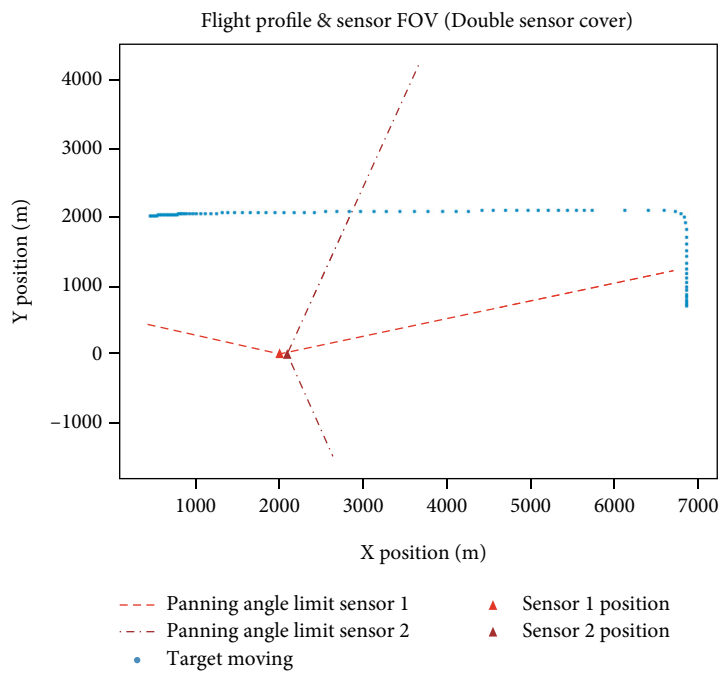

Figure 12: Dual sensor configuration scenario.

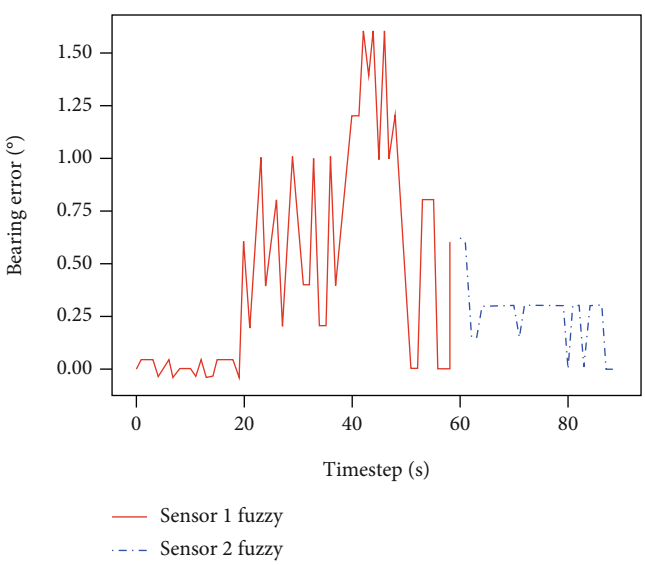

Figure 13: Error under dual sensor configuration.

Table 3: Initial parameter setting of tracking units.

Tracking units	Coefficient	(Distance (m), angle)
S_1	1	(100, 0.2292°, 0.2292°)
S_2	1	(0.4°, 0.7°)
S_3	1	(100,0.2292°, 0.2292°)
$\{S_1, S_2\}$	1.526	–
$\{S_1, S_3\}$	1.607	–
$\{S_2, S_3\}$	1.219	–
$\{S_1, S_2, S_3\}$	2.713	–

Trigonometric membership functions are also used to define specific values.

The closed-loop flow chart of the whole simulation example is as shown in Figure 10. Case 1: Figure 11 plots the comparison diagram of sensor tracking error based on the above scenario using sensor control feedback technology (fuzzy system) and not using sensor control feedback technology (fixed rules). Without using the sensor control feedback technology, the method of changing 1° per time step is adopted. It can be seen that based on the fixed rule, the azimuth error is out of tolerance at about 10 s and 50 s, resulting in the loss of tracking, while based on the feedback control, the tracking is lost only at about 70 s, because the target at this time has exceeded the scanning range of the sensor (set the scanning area of the sensor unchanged). Case 2: based on the above simulation scenario, it is added a sensor, located at (2100,0), pointing at 85 to form a complete coverage of the target (as shown in Figure 12). For the sensor configuration at this time, the simulation results are shown in Figure 13. At about 60 s, the sensor is switched and tracked by sensor 2. The error is small and relatively stable.

To sum up, take the above scenario as an example to build the basic closed-loop process of sensor control feedback technology. For future practical application scenarios, it is necessary to reasonably complicate the scenario and cover the fusion decision of multiple sensors. Accordingly, for the fuzzy control system and fuzzy rules used in simple simulation, and for the complexity of specific scenes, the knowledge base and corresponding reasoning algorithm described above are used to build a comprehensive model.

Table 4: One-step information gain/pair tracking benefit of the active sensor S_1 involved in the tracking unit to the target.

Tracking units	tar_1	tar_2	tar_3	tar_4
S_1	1.4946/0.7473	1.5011/0.7505	1.5087/1.5087	1.5163/0.5054
$\{S_1, S_2\}$	2.5668/1.9585	2.4477/1.8676	2.2843/3.4858	2.1051/1.0708
$\{S_1, S_3\}$	2.5802/2.0732	2.4564/1.9737	2.2919/3.6832	2.1153/1.1331
$\{S_1, S_2, S_3\}$	2.6371/2.6073	2.5055/2.5271	2.3318/3.8425	2.1453/1.8717

Table 5: One-step information gain/pair tracking benefit of the passive sensor S_2 and S_3 involved in the tracking unit to the target.

Tracking units	tar_1	tar_2	tar_3	tar_4
S_2	0.1411/0.0470	0.9328/0.9328	0.1538/0.0769	0.1307/0.0653
S_3	1.6350/0.5450	1.4780/1.4780	1.7198/0.8599	1.4046/0.7023
$\{S_2, S_3\}$	1.6371/1.4805	2.4389/2.9037	1.7280/2.3441	1.4123/1.9158

Table 6: One-step information gain/pair tracking benefit of the active sensor S_1 involved in the tracking unit to the target.

Tracking units	tar_1	tar_2	tar_3	tar_4	Tracking capacity
S_1	1	0	0	0	3
S_2	0	0	0	0	2
S_3	0	0	0	0	2
$\{S_1, S_2\}$	0	0	0	0	≤2
$\{S_1, S_3\}$	0	0	0	0	≤2
$\{S_2, S_3\}$	0	1	0	1	≤2
$\{S_1, S_2, S_3\}$	0	0	1	0	≤2

4.2. Simulation of Multitarget and Multisensor Allocation Algorithm. To verify the effectiveness of the multitarget and multisensor allocation method in this paper, the simulation experiments are carried out according to the following scenarios. A single UAV platform with multiple sensors is used to track four target UAVs. The sensor target allocation of four target tracking processes in the air is simulated. The airborne radar ranging function completes the angle measurement functions of ESM and infrared search and tracking, respectively, forming a high synergy coefficient. The parameter settings of the tracking unit are shown in Tables 3–5. A total of 7 tracking units (including four combinations) and 4 UAV platforms are set. Assuming that the current moment is in the hth management period, the data sampling rate of each sensor is the same. Tables 4 and 5 show the one-step information gain of the tracking unit to the target and the total tracking benefit after pairing. Table 6 is based on the data in Tables 4 and 5 combined with the final distribution results of the model algorithm. When considering the target threat and the detection capacity of each sensor, the result of the optimal allocation is following: the first radar sensor S_1 tracks the target tar_1. Sensors' combination $\{S_2, S_3\}$ tracks the target tar_2 and tar_4. Sensors' combination $\{S_1, S_2, S_3\}$ tracks the target tar_3. The total tracking benefit is 9.4093.

5. Conclusion

To make full use of the sensors in the formation and improve the overall tracking performance, it is necessary to allocate the targets for coordinated tracking units of multisensors while active sensor radiation is controlled. This paper proposes an allocation decision model and a matching algorithm based on multisensor and multitarget cooperative tracking under low radiation intensity. The first situation with the active sensors turned on, the radiation of the active sensors is controlled according to the tracking accuracy requirements of task performance, and the active sensors are used to participate in the radiation interval of the active sensor. Another situation with the active sensors turned off, the passive combined sensors are used to perform angle tracking or coordinated positioning of targets. These two situations are combined separately and alternately performed. Through intermittent passive sensor data and interval active sensor data for sequential coordinated tracking, a continuous target tracking trajectory is formed, which completes multisensors rationality for multitargets. The coordinated formation of UAV swarms based on 6G communication guarantees the realization of the method proposed in this paper. Finally, the optimization model and the matching algorithm are proved to be reasonableness and effectiveness.

Data Availability

No data were used to support this study.

Conflicts of Interest

The authors declare that they have no conflicts of interest.

References

[1] W. Wu, C. Zhou, M. Li et al., "AI-native network slicing for 6G networks," *IEEE Wireless Communications*, vol. 29, no. 1, pp. 96–103, 2022.

[2] L. Ale, N. Zhang, H. Wu, D. Chen, and T. Han, "Online proactive caching in mobile edge computing using bidirectional deep recurrent neural network," *IEEE Internet of Things Journal*, vol. 6, no. 3, pp. 5520–5530, 2019.

[3] D. Chen, Z. Zhao, X. Qin et al., "MAGLeak: a learning-based side-channel attack for password recognition with multiple sensors in IIoT environment," *IEEE Transactions on Industrial Informatics*, vol. 18, no. 1, pp. 467–476, 2022.

[4] H. Nawaz, H. M. Ali, and A. A. Laghari, "UAV communication networks issues: a review," *Archives of Computational Methods in Engineering*, vol. 28, no. 3, pp. 1349–1369, 2021.

[5] J. Huang, F. Zan, X. Liu, and D. Chen, "UAV routing protocol based on link stability and selectivity of neighbor nodes in ETX metrics," *Wireless Communications and Mobile Computing*, vol. 2022, Article ID 5428280, 12 pages, 2022.

[6] C. Lou, M. Cao, R. Wu, D. Chen, and H. Xu, "A lightweight key generation scheme for secure device-to-device (D2D) communication," *Wireless Communications and Mobile Computing*, vol. 2021, Article ID 6642605, 17 pages, 2021.

[7] G. Wang, C. Wu, T. Yoshinaga et al., "Coexistence analysis of D2D-unlicensed and Wi-Fi communications," *Wireless Communications and Mobile Computing*, vol. 2021, Article ID 5523273, 11 pages, 2021.

[8] N. Zhang, P. Yang, J. Ren, D. Chen, L. Yu, and X. Shen, "Synergy of big data and 5G wireless networks: opportunities, approaches, and challenges," *IEEE Wireless Communications*, vol. 25, no. 1, pp. 12–18, 2018.

[9] X. Shen, J. Gao, W. Wu, M. Li, C. Zhou, and W. Zhuang, "Holistic network virtualization and pervasive network intelligence for 6G," *IEEE Communications Surveys and Tutorials*, vol. 24, no. 1, pp. 1–30, 2022.

[10] Y. Li, C. Fu, F. Ding, Z. Huang, and G. Lu, "AutoTrack: towards high-performance visual tracking for UAV with automatic spatio-temporal regularization," in *IEEE/CVF Conference on Computer Vision and Pattern Recognition*, pp. 11923–11932, Seattle, WA, USA, 2020.

[11] Z. Wang, W. J. Chen, and K. Y. Qin, "Dynamic target tracking and ingressing of a small UAV using monocular sensor based on the geometric constraints," *Electronics*, vol. 10, no. 16, p. 1931, 2021.

[12] J. Yang, Y. Khedar, M. K. Ben-Larbi et al., "Concept and feasibility evaluation of distributed sensor-based measurement systems using formation flying multicopters," *Atmosphere*, vol. 12, no. 7, p. 874, 2021.

[13] S. Pardoel, J. Kofman, J. Nantel, and E. D. Lemaire, "Wearable-sensor-based detection and prediction of freezing of gait in Parkinson's disease: a review," *Sensors*, vol. 19, no. 23, p. 5141, 2019.

[14] I. Tkach and Y. Edan, *Distributed Heterogeneous Multi Sensor Task Allocation Systems*, Springer International Publishing, 2020.

[15] F. Yang, P. Wang, and Y. Zhang, "Multi-frame multi-sensor multi-target task allocation method based on improved wolf colony algorithm," in *2018 International Conference on Control, Automation and Information Sciences (ICCAIS)*, pp. 84–89, Hangzhou, China, 2018.

[16] D. E. Clark, "Multi-sensor network information for linear-Gaussian multi-target tracking systems," *IEEE Transactions on Signal Processing*, vol. 69, no. 2021, pp. 4312–4325, 2021.

[17] P. Wang, F. Yang, Y. Zhang, and L. Zhang, "Multi-sensor and multi-target task allocation method based on improved firefly algorithm," in *Global Intelligence Industry Conference (GIIC 2018)*, pp. 148–153, Beijing, China, 2018.

[18] J. Tong and G. L. Shan, "Modeling and solution of task oriented multi-sensor resources preallocation," *Systems Engineering and Electronics*, vol. 34, no. 10, pp. 2036–2044, 2012.

[19] J. Tong and G. L. Shan, "Study of multi-sensor allocation based on modified Riccati equation and Kuhn-Munkres algorithm," *Control and Decision*, vol. 27, no. 5, p. 885, 2012.

[20] F. Liu, X. Wang, A. Li, F. Wan, and L. Liu, "Improved multi-sensor management based on linear programming," *Computer Automated Measurement & Control*, vol. 10, 2005.

[21] J. Sun, H. Liu, and Q. Xi, "Cooperative reconnaissance mission plan- ning for multiple UAVs based on improved PSO algorithm," *Modern Electronic Technology*, vol. 35, no. 7, pp. 12–15, 2012.

[22] Y. Zhang, Y. Xie, L. Zhang, and J. Zhang, "Optimal task decision-making for heterogeneous multi-UAV cooperation econnaissance," *Journal of Northwestern Polytechnical University*, vol. 35, no. 3, p. 8, 2017.

[23] Y. Spyridis, T. Lagkas, P. Sarigiannidis et al., "Towards 6G IoT: tracing mobile sensor nodes with deep learning clustering in UAV networks," *Sensors*, vol. 21, no. 11, p. 3936, 2021.

[24] F. Venturini, F. Mason, F. Pase et al., "Distributed reinforcement learning for flexible and efficient uav swarm control," *IEEE Transactions on Cognitive Communications and Networking*, vol. 7, no. 3, pp. 955–969, 2021.

[25] Z. Xia, J. Du, J. Wang et al., "Multi-agent reinforcement learning aided intelligent UAV swarm for target tracking," *IEEE Transactions on Vehicular Technology*, vol. 71, no. 1, pp. 931–945, 2022.

[26] M. Yan, H. Yuan, J. Xu, Y. Yu, and L. Jin, "Task allocation and route planning of multiple UAVs in a marine environment based on an improved particle swarm optimization algorithm," *EURASIP Journal on Advances in Signal Processing*, vol. 2021, p. 94, 2021.

[27] M. E. Petersen and R. W. Beard, "Multiple target tracking on SE(2) using recursive-RANSAC," in *2021 60th IEEE Conference on Decision and Control (CDC)*, pp. 4460–4465, Austin, TX, USA, 2021.

[28] D. Chen, H. Wang, N. Zhang et al., "Privacy-preserving encrypted traffic inspection with symmetric cryptographic techniques in IoT," *IEEE Internet of Things Journal*, 2022.

[29] X. Sun, D. W. Ng, Z. Ding, Y. Xu, and Z. Zhong, "Physical layer security in UAV systems: challenges and opportunities," *IEEE Wireless Communications*, vol. 26, no. 5, pp. 40–47, 2019.

[30] D. Chen, N. Zhang, N. Cheng, K. Zhang, Z. Qin, and X. Shen, "Physical layer based message authentication with secure channel codes," *IEEE Transactions on Dependable and Secure Computing*, vol. 17, no. 5, pp. 1079–1093, 2020.

[31] Z. Yang, M. Chen, X. Liu et al., "AI-driven UAV-NOMA-MEC in next generation wireless networks," *IEEE Wireless Communications*, vol. 28, no. 5, pp. 66–73, 2021.

[32] K. Sheth, K. Patel, H. Shah, S. Tanwar, R. Gupta, and N. Kumar, "A taxonomy of AI techniques for 6G communication networks," *Computer Communications*, vol. 161, pp. 279–303, 2020.

[33] J. Kusyk, M. U. Uyar, K. Ma et al., "AI based flight control for autonomous uav swarms," in *The 2018 International Conference on Computational Science and Computational Intelligence (IEEE CSCI)*, pp. 1155–1160, Las Vegas, NV, USA, 2018.

[34] W. A. Jundi, X. U. Yunshan, X. I. Bingsong, and X. I. Haibao, "Sensor-target assignment algorithm based on complementary principle," in *2018 Chinese Automation Congress (CAC)*, pp. 1774–1777, Xi'an, China, 2018.

[35] C. Kreucher, A. O. Hero, and K. Kastella, "A comparison of task driven and information driven sensor management for target tracking," in *The 44th IEEE Conference on Decision and Control*, pp. 4004–4009, Seville, Spain, 2005.

[36] C. W. Ju, X. Z. Yang, R. Wang, and H. S. Wang, "Sorting of multi-target's threat in multi-sensor management system," *Electronics Optics & Control*, vol. 3, pp. 8–12, 2001.

Hindawi
Wireless Communications and Mobile Computing
Volume 2022, Article ID 7916305, 10 pages
https://doi.org/10.1155/2022/7916305

Research Article

Space Deployment Algorithm for UAV-IRS-Based Systems Using a Ck++ Optimizer

Hao Lu, Minghe Mao, and Jianjun Sun

School of Computer and Information, Hohai University, Nanjing 211100, China

Correspondence should be addressed to Minghe Mao; maominghe@hhu.edu.cn

Received 26 May 2022; Accepted 20 August 2022; Published 5 September 2022

Academic Editor: Mingqian Liu

With the popularity of 5G mobile communication services, the number of users has increased dramatically, as well as the nonuniformity of user density distribution; many users are in nonideal channel conditions, so unmanned aerial vehicle (UAV) as a passive relay equipment platform has gradually entered people's vision. Intelligent reflective surfaces (IRSs) capable of reconfiguring electromagnetic absorption and reflection properties in real-time are offering unprecedented opportunities to enhance wireless communication experience in challenging environments. In this paper, we start from the point of minimizing the energy consumption and nodes of UAV passive relay; the paper proposes to install intelligent reflecting surface (IRS) on UAV as a new passive relay and establish the communication coverage model of UAV-IRS. Then, the main relationship between the coverage radius and hover height of UAV-IRS is verified. In view of different distribution densities of target users, a CK++ (cyclic *k*-means++) is proposed to solve the spatial deployment problem of UAV-IRS, where the optimal solution of the system is obtained through cyclic clustering. And the algorithm is verified to effectively improve the performance of urban mobile communication and user communication service quality through numerical stimulation.

1. Introduction

Today, the communication network is increasingly developed. Especially with the maturity of 5G technology, higher requirements are placed on the communication network. Wireless relay, as an effective means to expand the transmission range and an important way to improve the transmission capacity, can be achieved by using fixed relay nodes or mobile relay platforms. With the diversified development of relay network scenarios, unmanned aerial vehicles (UAVs) appear more and more in wireless relay scenarios in recent years [1–4]. Due to UAVs having the advantages of low cost, high flexibility, and rapid deployment [5], installing the relay equipment on them to form UAV-IRSs can provide more effective communication services. UAV-assisted wireless communication networks also face many challenges, such as how to improve energy efficiency, ensure lower latency, improve resource utilization, and optimize mobility management strategies, so UAV-assisted wireless communication networks require further research. As an aerial relay platform, UAV has some differences from fixed ground relay deployment:

(1) Deployment can be more convenient owing to the flexibility of UAV-IRS. After obtaining the deployment location, UAV-IRS can reach the specified location quickly to complete the deployment, and the deployment location of UAV-IRS can be changed at any time. However, the fixed relay has a fixed deployment location, a long deployment period, and a confined service range

(2) The link between UAV-IRSs is different from that between fixed relay nodes. UAV is above the user, and it is very easy to build a line-of-sight link, while the link between fixed relay nodes will experience various fading and various line-of-sight obstacles, and most of the links are non-line-of-sight links

(3) The load, airborne time, power, and energy supply of the UAV-IRS are limited, and the height of the UAV

directly affects the size of the communication coverage, while the fixed relay node does not need to consider the energy problem when deploying

The flexibility of UAV-IRS can make the deployment more convenient. However, due to the deficiency of the current battery technology, the load, airborne time, and power of the UAV-IRS are also restricted, and for the height of UAV directly affecting the coverage range of communication, energy efficiency needs to be considered in the deployment of UAV-IRS network. Therefore, this paper considers studying the minimum number of UAV-IRS deployment, which could both ensure real-time communication of users and minimize the total energy consumption of UAV.

To address the technical problem of limited onboard energy due to UAV battery limitations, an intuitive approach is to use lightweight, low-power relay devices on UAVs; another effective energy-saving solution is to use an intelligent reflecting surface [6]: IRS only reflects incident signals and meets the requirement of passive relay. By adjusting the reflection coefficient, the IRS changes the phase difference of the incident electromagnetic wave, which can subtly reconfigure the signal transmission environment, improve the power of the received signal, or suppress the interference signal [7]. Since all of these surfaces used to reflect signals are passive, a small amount of energy is consumed only when the reflective surface controller needs to intelligently control the orientation of the surface. Besides, combined with its lightweight and passive nature [8], it will significantly reduce the power consumption of the UAV, thereby greatly extending the runtime of the UAV-IRS.

At present, some research has been carried out on the deployment of UAV-IRS at home and abroad. In existing studies, the convex hull algorithm [9], deep Q network particle [10], swarm optimization [11], and BRB-DA [12] are used to deploy UAVs, but most of them do not consider the user's receiving power interference. In addition, some literatures consider the special situation of interference. For example, the literature [13] only considers the deployment of two UAVs under interference conditions, but the number of UAVs is too small to be universal. Although another literature [14] considers various situations, it is assumed that the distribution of ground users is set as uniform distribution, which is not universal.

To get closer to practical applications, this paper examines a spatial deployment algorithm of UAV-IRS based on the cyclic k-means++ algorithm. This paper mainly considers deploying multiple UAV-IRSs in one region. Due to the difference in user density, the quality of communication varies in different hotspot areas. Therefore, UAV-IRSs need to be deployed through changes in horizontal position and height, as well as increase or reduce the number to improve the communication quality of different hotspot users. Therefore, in order to minimize UAV-IRS energy consumption and minimum relay nodes, the cyclic k-means++ algorithm is adopted; that is, given the number and location information of ground users and the maximum load number of each UAV-IRS, use the cyclic k-means++ algorithm to deduce the optimal two-dimensional position of the UAV and output the required number of UAV-IRSs and each UAV-IRS. The coverage radius of the UAV-IRS unit can be extended. In the second subproblem, the optimal altitude of the UAV is determined by optimizing the total transmission power of the UAV-IRS, and finally, the space deployment of the UAV-IRS is completed.

2. System Model

In the IRS-assisted cellular network system of UAV, 5G base station, UAV-IRS, and user equipment with nonideal channel conditions are regarded as communication nodes in the IRS-assisted cellular network of UAV, and UAVs in the system all carry IRS relay components. Since the location of 5G base station is known and fixed and users with nonideal channel conditions are disorderly and random, the deployment location of UAV-IRS node needs to be reasonably designed according to the location information of 5G base station and user equipment with nonideal channel conditions.

As shown in Figure 1, under the problem of performance degradation during communication dead zones or peak user periods, weak signals from the base station will cause connection interruption or force the user device to increase its transmitting power. To solve this problem, UAV-IRSs are deployed to provide communication services to target users and restore target user communications. In this case, the UAV carrying the IRS relaying component is positioned within the coverage of the base station as a passive aerial relay for users with nonideal channel conditions.

3. Analysis of UAV Optimal Hover Height

Different from the traditional fixed relay, the radio signal is reflected by UAV-IRS travels in a free space. From the most widely used air-ground communication models [15], it can be seen that the main propagation of communication signals is the line of sight or equivalent line of sight, and some are non-line-of-sight propagation through reflection and diffraction. In this paper, the model is adopted, and the expected value of the spatial path loss can be expressed as

$$E = P_{\mathrm{LoS}} \bullet L_{\mathrm{LoS}} + P_{\mathrm{NLoS}} \bullet L_{\mathrm{NLoS}}. \tag{1}$$

In the formula, L_{LoS} and L_{NLoS} are the average spatial path loss of line-of-sight propagation and non-line-of-sight propagation, respectively. According to the hypothesis of Friis equation, it can be expressed as

$$\begin{aligned} L_{\mathrm{Los}} &= 20 \log_{10} \frac{4\pi d}{\lambda} + \eta_{\mathrm{Los}}, \\ L_{\mathrm{NLos}} &= 20 \log_{10} \frac{4\pi d}{\lambda} + \eta_{\mathrm{NLos}}. \end{aligned} \tag{2}$$

In the formula, d is the straight-line distance between UAV-IRS and user, $d = \sqrt{h^2 + r^2}$; λ is electromagnetic wave length, $\lambda = c/f$; c is the speed of light; f is the carrier frequency; η_{Los} and η_{NLos} are the path loss under line-of-sight propagation and non-line-of-sight propagation, respectively.

Figure 2 shows the path loss relation diagram corresponding to different elevation angles of users in different urban environments.

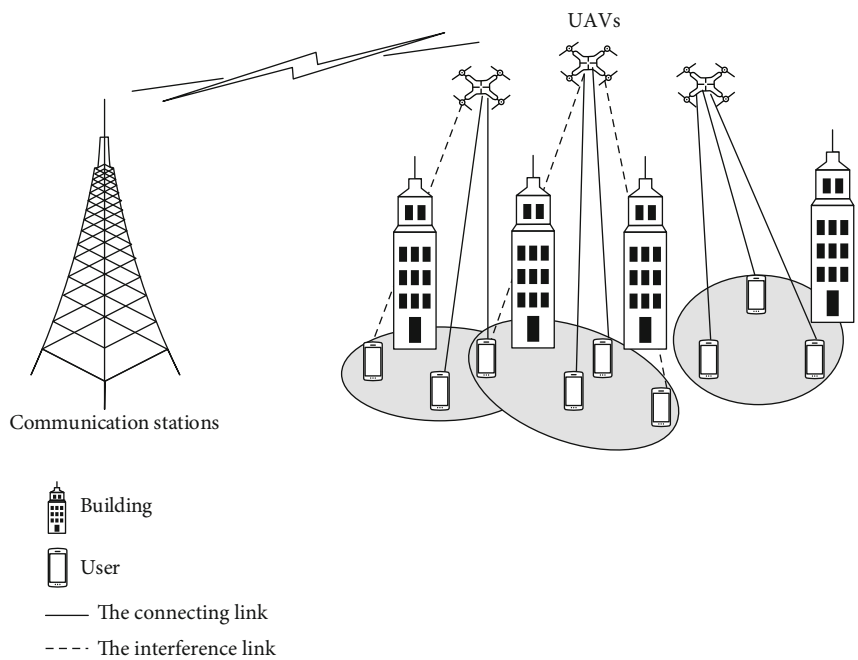

Figure 1: The map of system model.

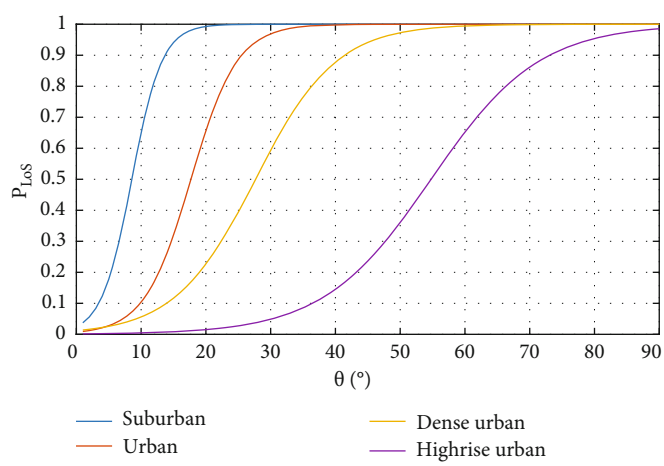

Figure 2: The calculated line-of-sight probabilities, with their related S-curve fitting for different urban environments.

P_{LoS} and P_{NLoS} are the probability of line-of-sight propagation and non-line-of-sight propagation, respectively, which are related to the propagation environment coefficient and elevation angle. The probability of line-of-sight propagation can be fitted by sigmoid function and can be expressed as

$$P_{\mathrm{LoS}} = P(\mathrm{LoS}, \theta) = \frac{1}{1 + ae^{-b(\theta - a)}}, \qquad P_{\mathrm{NLoS}} = 1 - P_{\mathrm{LoS}}. \tag{3}$$

In the formula, a and b are arguments to the sigmoid function; θ is the elevation angle of the user and UAV-IRS, $\theta = \tan^{-1} h/r$, h is the vertical flight height of the UAV-IRS, and r is the distance from the user to the projection point of the horizontal position of the UAV-IRS. When the frequency of a and b is 2000 MHz, the parameters in different geographical environments can be found in Table 1.

According to the literature [16], the higher the height of UAV-IRS, the larger the communication coverage area:

$$\theta = \tan^{-1} \frac{h}{r}. \tag{4}$$

Substitute the above formula to obtain

$$E = \frac{\eta_{\mathrm{Los}} - \eta_{\mathrm{NLos}}}{1 + ae^{-b(\tan^{-1}(h/r) - a)}} + 10 \log_{10}\left(h^2 + r^2\right) + 20 \log_{10} \frac{4\pi f}{c} + \eta_{\mathrm{NLos}}. \tag{5}$$

According to the analysis of the formula, the average spatial path loss function of signals transmitted in air-

Table 1: Different environmental parameters.

Urban environments	a	b	η_{Los}	η_{NLos}
Suburban	4.88	0.43	0.1	21
Urban	9.61	0.28	1.0	20
Dense urban	12.08	0.16	1.6	23
Highrise urban	27.23	0.12	2.3	34

ground channel is a nonlinear function about h and r, according to which the signal intensity received by ground users is strictly dependent on h and r. In order to ensure the communication quality of users on the ground, it is assumed that the received power P must exceed a certain threshold $P_{\min}$, which is equivalent to the path loss of the UAV-IRS to any user must be less than or equal to a certain threshold L_{th}, so as to ensure the basic communication of users. When the path loss between the UAV-IRS and the user exceeds the threshold, the link is interrupted. By solving $\partial r/\partial h = 0$, the maximum coverage radius $r_{\max}$ and the optimal flight height $h^* = r_{\max} \bullet \tan\theta$ can be obtained. The optimal flight height of UAV-IRS corresponding to different path losses is shown in Figure 3. And the relationship between the height and the coverage radius is shown in Figure 4.

4. System Energy Consumption Analysis

In this section, the power consumption model of UAV-IRS auxiliary communication system is proposed. The total power consumption of the system consists of the reflected power of the base station, the power consumption of the base station hardware equipment P_{BS}, the power consumption P_{IRS} of IRS, and the power consumption P_{UAV} of the UAV.

Therefore, total power consumption of the system can be expressed as

$$P_t = P_S + P_{\mathrm{BS}} + P_{\mathrm{IRS}} + P_{\mathrm{UAV}}. \tag{6}$$

The power consumption of IRS depends on the nature and resolution of the reflector for effective phase shift of the incident signal. Assuming that each reflector is I phase shifter, the power consumption of IRS composed of a reflector $P_{\mathrm{IRS}} = NP_i(b), i \in \{1, 2, \cdots, I\}$ is given, representing the power consumed by the circuit for a phase shifter with bit resolution. Reference [17] provides some typical values for IRS.

P_{UAV} includes the energy consumed by the UAV in flight and hovering. According to Reference [18], the power of the UAV can be expressed as

$$P_{UAV} = a_1 v^3 + \frac{a_2}{v}, \tag{7}$$

where a_1 and a_2 are constants, depending on the UAV's weight, wing size, and air density, representing the average flight speed of the UAV. Therefore, the minimum power consumption of UAV is [18]

$$P_{\mathrm{UAV}\min} \triangleq \left(3^{-3/4} + 3^{1/4}\right) a_1^{1/4} a_2^{3/4}. \tag{8}$$

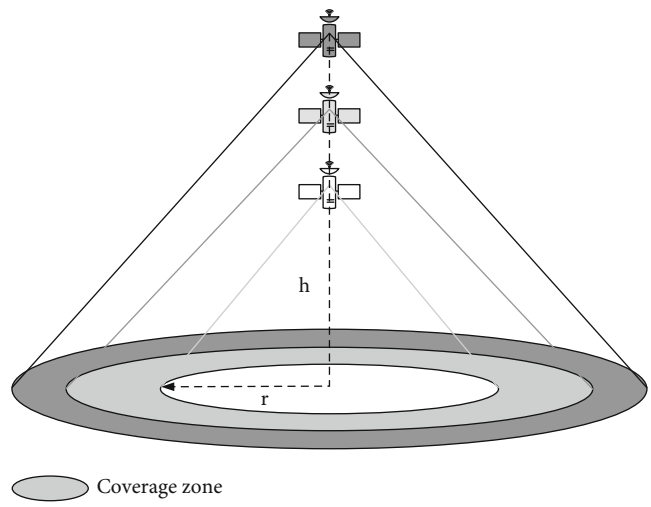

Figure 3: The coverage zone by a low altitude platform.

5. Description of Algorithm

Under the assumption that users are randomly distributed and their positions are known, the path loss of downlink is taken into account, and the UAV-IRS should be in the optimal working state as far as possible under the premise of satisfying user communication quality. In this paper, since the distance between the 5G base station and UAV-IRS is much larger than that between the user and UAV-IRS, it can be assumed that the signal power reflected by each UAV-IRS is equal. This article innovatively considers capacity constraints when deploying relays. Since the working bandwidth of a single UAV-IRS is limited, in order to meet the communication quality requirements of users, each UAV-IRS serves a fixed number of users. It is assumed that the upper limit of users covered by UAV-IRS is L.

According to the above situation, adjusting the flight height of UAV-IRS to h^* allows the UAV-IRS to reach the maximum coverage radius $r_{\max}$ of the ground user. If the communication coverage is carried out with the maximum coverage radius, more users will be served. In the coverage area with higher user density, UAV-IRS overload will be caused; Through theoretical analysis [16], the energy loss of UAV is closely related to its coverage radius and flight altitude. Based on the above, the UAV-IRS coverage problem is transformed into an optimal coverage problem with minimum energy loss.

5.1. UAV Deployment Positioning Analysis. There is a horizontal projection relative distance between the relays of each UAV. If the horizontal projection relative distance between the relays of adjacent UAVs is less than the preset threshold, the UAV will move away from its neighbor UAV in order to ensure that UAVs will not excessively gather in one area and repeatedly cover a certain area. If the distance between two

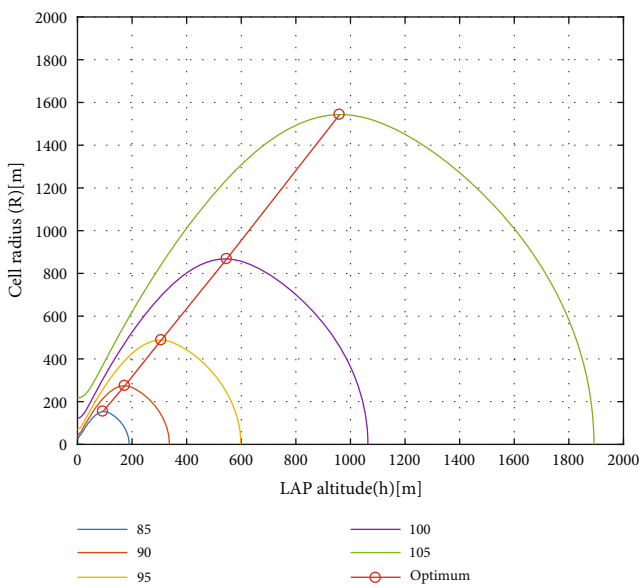

Figure 4: Relationship between the height and the coverage radius of UAV-IRS.

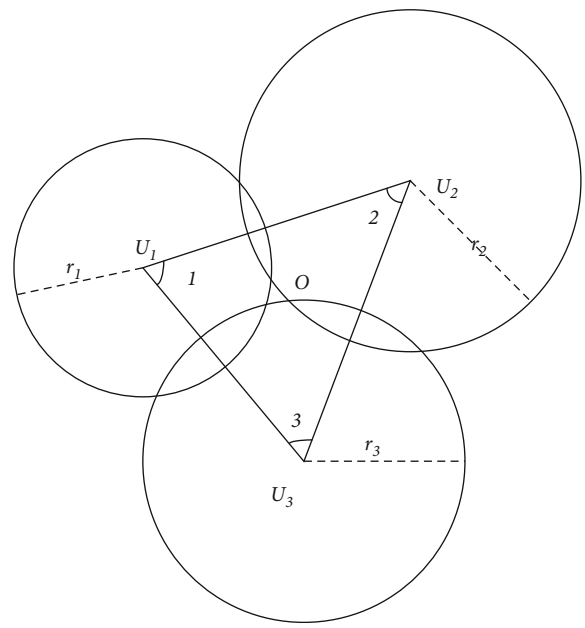

Figure 5: Schematic diagram of multiple UAV relay deployment technology.

adjacent UAVs is greater than the threshold and smaller than the communication radius, the UAVs move to the neighbor UAV to minimize the coverage of the blind area. If the distance between two UAVs is equal to the threshold or greater than the communication radius, the relative distance between two UAVs will not affect the movement of UAVs. The deployment mode of three UAVs relay is shown in Figure 5.

Theoretically, when the three UAVs relay U_1, U_2 and U_3 want to achieve optimal coverage, the area of coverage blind area O is 0 and the coverage area can be expressed as

$$S = 2 \bullet S_{\Delta U_1 U_2 U_3} + S_{U_1(2\pi - 2 \bullet \angle 1)} + S_{U_2(2\pi - 2 \bullet \angle 2)} + S_{U_3(2\pi - 2 \bullet \angle 3)}. \tag{9}$$

When the coverage area is the largest, the relation can be deduced as

$$\angle 1 : \angle 2 : \angle 3 = \frac{1}{r_1^2} : \frac{1}{r_2^2} : \frac{1}{r_3^2}. \tag{10}$$

5.2. k-Means++ Algorithm. At present, the static coverage deployment of UAV-IRS assumes that global information such as location service requirements of ground users is known, and the location of the UAV-IRS is adjusted by a centralized deployment optimization method. According to the summary of the UAV static deployment method of relay, it can be seen that most static deployment methods do not consider the load capacity of UAV-IRS and the transmission rate of a certain bandwidth; at the same time, the number of users is certain, so the load capacity is one of the important factors affecting relay deployed drones. In order to optimize transmission power, this paper investigates the spatial deployment of multiple UAVs as aerial relays considering the load capacity of UAVs.

Assuming that the user distribution and location are known and considering the downlink situation, the goal is to minimize the total transmission power of UAV-IRS while meeting the quality of service requirements of the user. In addition, under the premise of user service quality and load capacity of UAV-IRS, multiple UAV-IRSs are deployed in a three-dimensional space and the height and horizontal position of each UAV are obtained. In order to determine the optimal position and coverage radius of each UAV, the 3D deployment problem was decomposed into two subproblems. In the first subproblem, given the number of ground users and location information and the maximum load number of each UAV-IRS, the circular k-means algorithm is used to deduce the optimal two-dimensional position of UAV and calculate the coverage radius of each UAV unit. In the second subproblem, the optimal height of UAV is determined by optimizing the total transmission power of UAV-IRS, and finally, the spatial deployment of UAV-IRS is completed.

The k-means algorithm is a typical distance-based clustering algorithm. Typically using Euclidean distance as the similarity index of clusters, data point objects are divided into K clusters, and each object is divided into the cluster nearest to the center of the cluster. The k-means algorithm first randomly determines the location of k cluster centers and then connects each user to the nearest center of mass. The centroid position is then updated by getting the Euclidean distance value for the user position connected to each centroid. Repeat this operation until the cluster center position does not change or the maximum number of iterations is reached.

However, the number k of k-means algorithm's clustering centers needs to be given in advance, but in practice, the selection of k value is difficult to estimate. In many cases, it is not known in advance how many categories a given dataset should be divided into. The k-means require manual determination of initial cluster centers, and different initial cluster centers can lead to completely different cluster results.

Therefore, according to the scenario in this paper, the k-means algorithm is improved and the k-means++ algorithm is adopted. The basic idea of selecting seeds in the k-means++ algorithm is that the distance between the initial clustering centers should be as far as possible. The deployment algorithm is described in Algorithm 1.

5.3. Optimal Height of UAV-IRS. After the above circular k-means++ algorithm is used to determine the projection position of UAV-IRS on the horizontal plane, the height of each UAV-IRS is determined. To minimize power, you can minimize path losses. Then, the optimization function is as follows:

$$\min \sum_{i \epsilon K} \left| 20 \log \left(\frac{4\pi f_c \sqrt{r_i^2 + h_i^2}}{c} \right) + P_{\mathrm{LoS}}(\eta_{\mathrm{LoS}} - \eta_{\mathrm{NLoS}}) + \eta_{\mathrm{NLoS}} \right|. \tag{11}$$

Figure 6 simulates the relationship between coverage radius and height when UAV-IRS $f_c = 2$ GHz and path loss is 120 dB in different environments. It can be seen from Figure 4, with the increase of UAV height, coverage radius increases after the first decreases and is not a monotonic function; for a particular user, when the service environment with the UAV-IRS is determined, there is maximum coverage radius; the tow corresponding heights—the maximum and minimum height—were referred to as high domain. For a user of UAV-IRS service, each user has a height domain, and the intersection of the height domain of all users is called the total height domain. In this paper, the method of rising in the total height domain is adopted to determine the UAV-IRS height, and the height corresponding to the minimum value found is the optimal height.

5.4. Steps of Algorithm. The main idea of unmanned aerial vehicle passive relay spatial deployment algorithm based on k-means++ is to use the k-means++ algorithm to divide ground users into K clusters according to the load capacity of UAV-IRS to obtain the horizontal position coordinates of UAV-IRS and then optimize the height of each UAV-IRS in order to minimize transmission power and finally obtain the 3D coordinates of each UAV-IRS.

The specific steps of UAV-IRS spatial deployment algorithm based on k-means++ are as follows:

(Step 1) Enter the number of users and their location information; the maximum load number of UAV-IRS is L.

(Step 2) Use the k-means++ algorithm to divide all users into k clusters, and detect the number of users in each cluster.

(Step 3) If the number of users in the cluster is greater than L, $k = k + 1$, go to Step 1. If no, go to Step 4.

(Step 4) Calculate the coverage radius of each UAV-IRS; that is, the horizontal distance between the cluster center and the furthest user in the class.

(Step 5) Formula (8) is used to calculate the optimal height of each UAV-IRS.

(Step 6) Get the 3D position of each UAV-IRS.

6. Results and Discussion

In this chapter, Python software is adopted to simulate the spatial deployment algorithm of UAV-IRS based on k-means++. The task area is a square area with side length of 1 km. Two different users are distributed in different ways in this area, and the simulation experiment of UAV-IRS deployment is carried out. Table 2 shows some experimental parameters.

6.1. Analysis of Simulation Results of CK++. In this section, it is assumed that mobile users are randomly distributed on the ground, and 400 groups of 2D ground movement coordinates are generated within 1 km ∗ 1 km by random function. The Ck++ algorithm is used to calculate this data set, as shown in Figure 7, and the algorithm deployment result is obtained. The ground mobile users are represented by different colored dots, and different colors represent different clusters. The multicolored pentagonal star in the center represents the two-dimensional deployment position of UAV-IRS, and the coverage area of each UAV-IRS is represented by a red circle.

The theoretical initial K value for UAV-IRS deployment is 8, but the actual result is that 14 UAV-IRSs are required in the area to provide communications services. It can be seen that the service coverage radius of each UAV-IRS is not equal, because the total number of users aggregated by each cluster after clustering is different and the two-dimensional distribution position is different. Each user is provided relay service by the nearest UAV-IRS. The number of UAV-IRS deployments in the areas with higher user density is significantly higher than that in the areas with lower user density. This is because when the user density is higher, the resources of UAV-IRS are already utilized by the nearest users, resulting in its inability to serve further users. In addition, in the left side of the low-density area, the higher the height, the more users can improve the relay service.

6.2. Compared with Traditional k-Means Clustering Algorithm. In this section, it is assumed that mobile users are randomly distributed on the ground, and 300 groups of coordinates are generated within 1 km ∗ 1 km by random function. The dataset was calculated by the k-means

Initialization:
Initialize the initial position of the user node, and calculate the number of UAV-IRS in theory;
1. A random point is selected from the input user node location and then it will be set as the first cluster center;
2. For each point x in the data set, calculate its distance $D(x)$from the nearest cluster center (selected cluster center);
3. A new data point is selected as the new clustering center, and the selection principle is as follows: the point with larger $D(x)$ has a higher probability of being selected as the clustering center;
4. Repeat steps 2 and 3 until k cluster centers are selected.
5. The k initial clustering centers are used to run the standard K-means algorithm.
Step 3 Reflect $D(x)$ to the probability of point selection. The specific algorithm is as follows:
1. Let us start with a random seed from our database;
2. For each point, we calculate its straight-line distance $D(x)$ from the nearest seed point and store it in an array. Then we add up the distances to get $Sum(D(x))$;
3. Then, a random value is taken and the next seed point is calculated in the way of weight. The algorithm is realized by taking a random value "*Random*" that can fall in $Sum(D(x))$ and then using $Random = -Sum(D(x))$ until it is not greater than 0, at which point the next seed point is taken;
4. Repeat steps 2 and 3 until k cluster centers are selected;
5. These k initial clustering centers are used to run the standard k-means++ algorithm.

Algorithm 1: Deployment Algorithm.

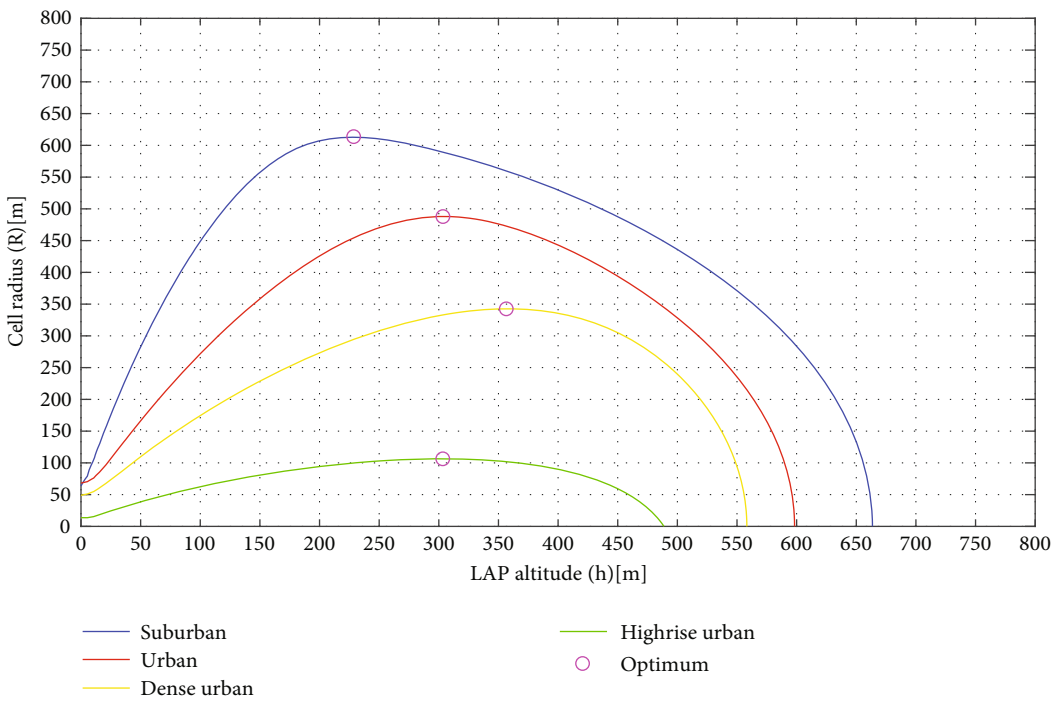

Figure 6: Relationship between the height and coverage radius of UAV-IRS.

Table 2: Simulation parameters.

Parameters	Value
a	9.61
b	0.28
η_{Los}	1.0 dB
η_{NLos}	20 dB
C (m/s)	3.0e+8
Iterations	1000
Maximum number of UAV-IRS service users	50

clustering algorithm and Ck++ algorithm, respectively, as shown in Figures 8 and 9, two different algorithm deployment results are obtained, and the 2D coordinates of UAV-IRS deployment as well as the 3D deployment coordinates of coverage and UAV-IRS are drawn, respectively. The black dots in Figure 8(a) represent edge users not covered by UAV-IRS.

As can be seen from Figure 8, the number of UAV-IRS deployed using the Ck++ algorithm is 6, and the coverage rate is less than 100%. As the k value of the k-means algorithm is fixed, the relay service for edge users cannot be provided, so some users still cannot communicate normally.

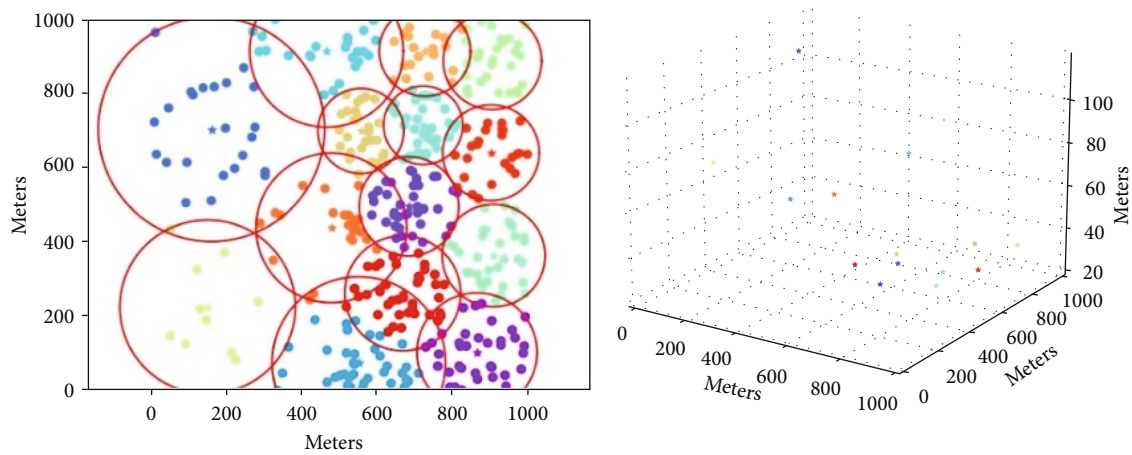

(a) (b)

Figure 7: 400 users are distributed in the task area. (a) 2D position of UAV-IRSs and ground user. (b) The space position of UAV-IRSs.

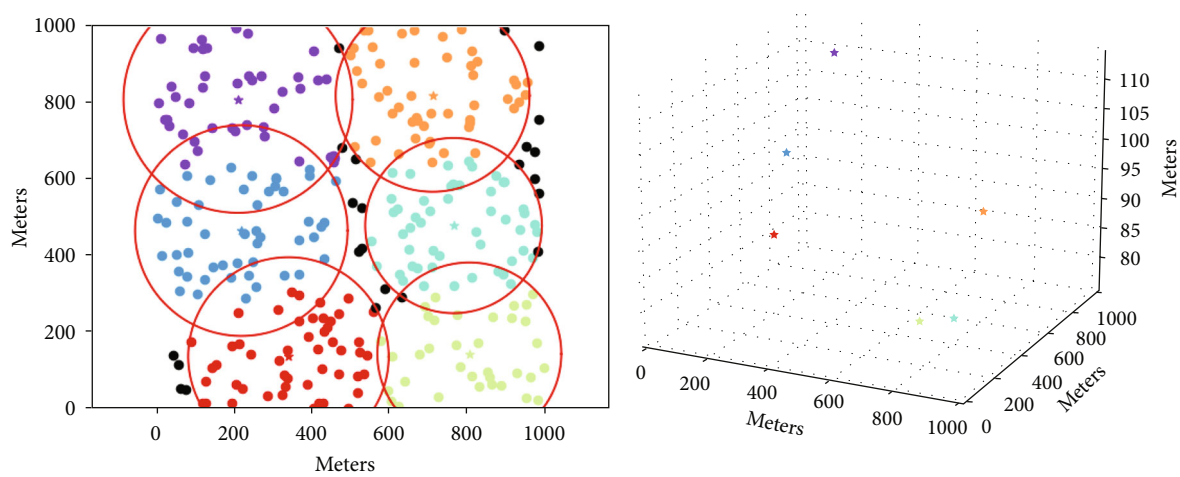

(a) (b)

Figure 8: k-means algorithm results. (a) 2D position of UAV-IRSs and ground user. (b) The space position of UAV-IRSs.

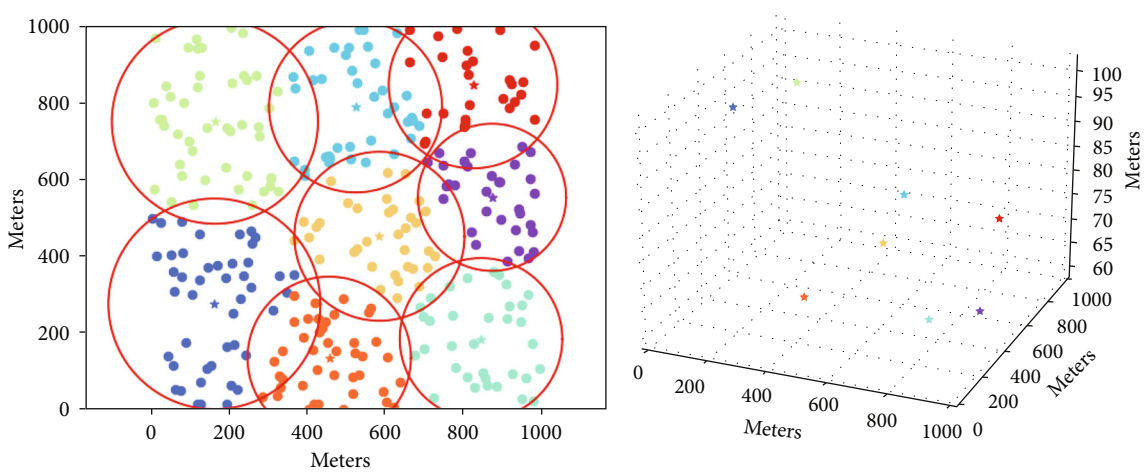

(a) (b)

Figure 9: CK++ algorithm results. (a) 2D position of UAV-IRSs and ground user. (b) The space position of UAV-IRSs.

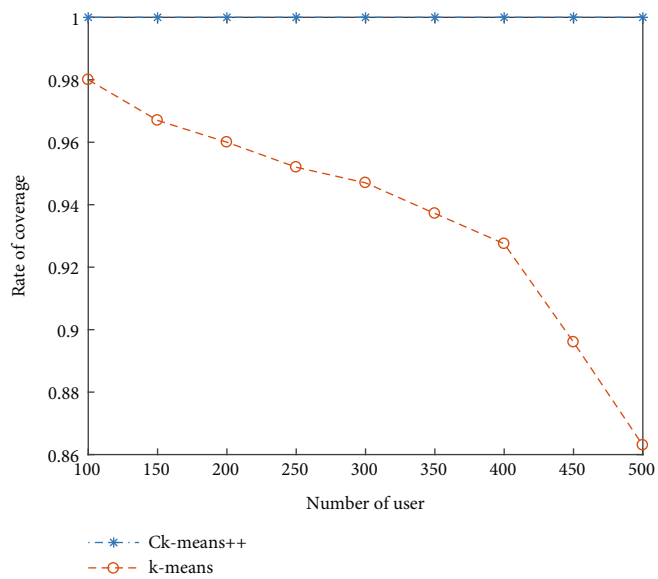

Figure 10: Comparison of coverage between k-means and CK++.

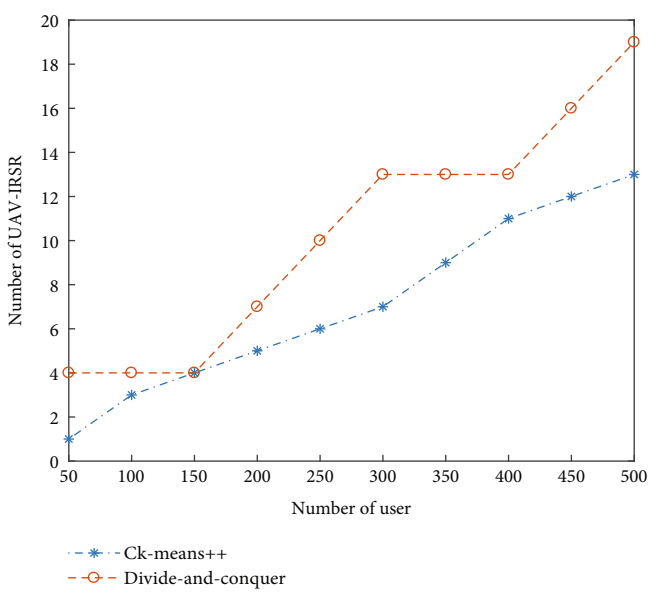

Figure 11: Relationship between the number of USERS of divide-and-conquer and CK++ and the number of UAV-IRS deployments.

As it can be seen from Figure 9, the number of UAV-IRS deployed using the Ck++ algorithm is two more than the k-means, but the coverage rate reaches 100%. This is because the Ck++ algorithm optimizes the initial clustering center during initialization and circulates clustering by increasing k value when the UAV-IRS service is found to be full.

As can be seen from Figure 10, the relation curves between user density and coverage of the two algorithms are drawn. As the number of users gradually increases, that is, the coverage of the k-means clustering algorithm is getting lower and lower. It can be seen that in the scenario of high user density, the coverage of the Ck++ algorithm is better than that of the traditional k-means clustering algorithm.

6.3. Compared with Divide-and-Conquer Algorithm. In this section, it is assumed that mobile users are randomly distributed on the ground, and different numbers of user coordinates are generated within $1\,\text{km} * 1\,\text{km}$ through random functions. The divide-and-conquer algorithm proposed in this paper and the drone based on the Ck++ algorithm also consider the trunk deployment method under the premise that the UAV relay load capacity and ground users are fully covered. The basic idea of the divide-and-conquer algorithm is that when the total number of users in a cluster is detected to be greater than the maximum load number of UAV-IRS, it is similar to dividing the cluster into four clusters by cell division. As can be seen from Figure 11, with the gradual increase of the number of users, namely, the increasing user density, both algorithms meet the communication requirements of ground mobile users by increasing the number of UAV-IRS deployment. However, the number of UAV-IRS deployed by the Ck++ algorithm proposed in this paper is always less than that of the divide-and-conquer algorithm. In terms of saving the number of UAV-IRS deployments, the Ck++ algorithm proposed in this chapter is superior to the divide-and-conquer algorithm in the same case.

7. Conclusion

In this paper, the optimal space deployment of UAV passive relay is solved under the premise of considering UAV relay load capacity. Firstly, a multi-UAV-IRS network coverage user system model was established, and an unmanned aerial vehicle passive relay spatial deployment algorithm based on Ck++ was proposed. Then, based on the deficiency of the traditional k-means clustering algorithm, the Ck++ algorithm was proposed to obtain the two-dimensional coordinates and coverage radius of each UAV, and then the optimal hovering height of UAV-IRS was calculated with the coverage radius. Finally, being compared with the traditional k-means clustering algorithm, it was shown that the

proposed algorithm had a better coverage. Then, on the premise of all users being covered, the UAV load ability of the proposed algorithm with the same partition algorithm on the basis of the comparison was considered. After using the deployment of less UAV, the feasibility of the partition algorithm was proved.

Data Availability

The data mainly comes from simulation experiments.

Conflicts of Interest

The authors declare that they have no conflicts of interest.

Acknowledgments

This work was supported by the Jiangsu Province Science and Technology Support Project (Social Development Projects, General Program) under Grant BE2020714.

References

[1] M. Mozaffari, W. Saad, M. Bennis, and M. Debbah, "Efficient deployment of multiple unmanned aerial vehicles for optimal wireless coverage," *IEEE Communications Letters*, vol. 20, no. 8, pp. 1647–1650, 2016.

[2] Q. Wu, Y. Zeng, and R. Zhang, "Joint trajectory and communication design for multi-UAV enabled wireless networks," *IEEE Transactions on Wireless Communications*, vol. 17, no. 3, pp. 2109–2121, 2018.

[3] C. Liu, W. Feng, Y. Chen, C.-X. Wang, and N. Ge, "Cell-free satellite-UAV networks for 6G wide-area internet of things," *IEEE Journal on Selected Areas in Communications*, vol. 39, no. 4, pp. 1116–1131, 2021.

[4] Y. Wang, W. Feng, J. Wang, and T. Q. S. Quek, "Hybrid satellite-UAV-terrestrial networks for 6G ubiquitous coverage: a maritime communications perspective," *IEEE Journal on Selected Areas in Communications*, vol. 39, no. 11, pp. 3475–3490, 2021.

[5] T. Zhao, H. Wang, and Q. Ma, "The coverage method of unmanned aerial vehicle mounted base station sensor network based on relative distance," *International Journal of Distributed Sensor Networks*, vol. 16, no. 5, Article ID 155014772092022, 2020.

[6] E. Basar, "Transmission through large intelligent surfaces: a new frontier in wireless communications," in *2019 European Conference on Networks and Communications (EuCNC)*, pp. 112–117, Valencia, Spain, 2019.

[7] G. Zhou, C. Pan, H. Ren, K. Wang, and A. Nallanathan, "Intelligent reflecting surface aided multigroup multicast MISO communication systems," *IEEE Transactions on Signal Processing*, vol. 68, pp. 3236–3251, 2020.

[8] J. W. Yao and N. Wang, "Intelligent surfaces: promising 6G technology," *Telecommunications Information*, vol. 4, no. 7, pp. 8–13, 2020.

[9] Z. Zhu, L. Li, and W. Zhou, "QoS-aware 3D deployment of UAV base stations," in *2018 10th International Conference on Wireless Communications and Signal Processing (WCSP)*, pp. 1–6, Hangzhou, China, 2018.

[10] J. Guo, Y. Huo, X. Shi et al., "3D aerial vehicle base station (UAV-BS) position planning based on deep Q-learning for capacity enhancement of users with different QoS requirements," in *2019 15th International Wireless Communications & Mobile Computing Conference (IWCMC)*, pp. 1508–1512, Tangier, Morocco, 2019.

[11] Y. Chen, H. Wang, F. Xiong, A. Li, Z. Qin, and J. Yuan, "Relay selection based on trajectory prediction for UAV networks," in *2020 International Conference on Wireless Communications and Signal Processing (WCSP)*, pp. 1212–1217, Nanjing, China, 2020.

[12] X. Zhong, Y. Guo, N. Li, and S. Li, "Deployment optimization of UAV relays for collecting data from sensors: a potential game approach," *IEEE Access*, vol. 7, pp. 182962–182973, 2019.

[13] M. Mozaffari, W. Saad, M. Bennis, and M. Debbah, "Drone small cells in the clouds: design, deployment and performance analysis," in *2015 IEEE global communications conference (GLOBECOM)*, pp. 1–6, San Diego, CA, USA, 2015.

[14] Y. Huang, W. Mei, J. Xu, L. Qiu, and R. Zhang, "Cognitive UAV communication via joint maneuver and power control," *IEEE Transactions on Communications*, vol. 67, no. 11, pp. 7872–7888, 2019.

[15] A. Al-Hourani, S. Kandeepan, and S. Lardner, "Optimal LAP altitude for maximum coverage," *IEEE Wireless Communications Letters*, vol. 3, no. 6, pp. 569–572, 2014.

[16] Y. Zeng, Q. Wu, and R. Zhang, "Accessing from the sky: a tutorial on UAV communications for 5G and beyond," *Proceedings of the IEEE*, vol. 107, no. 12, pp. 2327–2375, 2019.

[17] C. Huang, A. Zappone, G. C. Alexandropoulos, M. Debbah, and C. Yuen, "Reconfigurable intelligent surfaces for energy efficiency in wireless communication," *IEEE Transactions on Wireless Communications*, vol. 18, no. 8, pp. 4157–4170, 2019.

[18] J. Yang, J. Chen, and Z. Yang, "Energy-efficient UAV communication with trajectory optimization," in *2021 2nd International Conference on Big Data & Artificial Intelligence & Software Engineering (ICBASE)*, pp. 508–514, Zhuhai, China, 2021.

Hindawi
Wireless Communications and Mobile Computing
Volume 2022, Article ID 8681599, 8 pages
https://doi.org/10.1155/2022/8681599

Research Article

Conventional Neural Network-Based Radio Frequency Fingerprint Identification Using Raw I/Q Data

Tian Yang, Su Hu, Weiwei Wu, Lixin Niu, Di Lin, and Jiabei Song

University of Electronic Science and Technology of China, China

Correspondence should be addressed to Su Hu; husu@uestc.edu.cn

Received 12 June 2022; Accepted 26 July 2022; Published 22 August 2022

Academic Editor: Mingqian Liu

Radio frequency (RF) fingerprint identification is a nonpassword authentication method based on the physical layer of communication devices. Deep learning methods have thrown new light on RF fingerprint identification. In this paper, a conventional neural network- (CNN-) based RF identification model is proposed. The CNN models are designed to be lightweight. Raw data that reflects the characteristics of the I channel, the Q channel, and the 2-dimensional $I+Q$ data is successively fed into a CNN model. Therefore, three submodels are generated. The final predictive labels are determined by the results of the three submodels through a voting scheme. Experimental results have demonstrated that in the SNR setting at 5 dB, the final recognition accuracy of four transmit devices could achieve as high as 97.25%, while the identification accuracies based on the I channel data, Q channel data, and $I+Q$ channel data are 94.5%, 95%, and 94.5%, respectively. The training time for the 4 devices is around 30 seconds.

1. Introduction

By analysing the subtle differences of transmitters' RF fingerprints, RF fingerprint-based learning models could distinguish varieties of devices, thereby being difficult to clone and fake [1–4]. These subtle differences of transmitters are normally hard to be identified, and artificial intelligence (AI) methods could be appropriate to mitigate this problem [5–7].

AI models are divided into two main categories, including machine learning and deep learning. Machine learning (ML) needs first to extract the features of data samples and then select an appropriate model to train the samples to get model parameters. The ML methods include decision tree, naive Bayesian, K-nearest neighbor, and support vector machine. For communication signals, the extracted features include carrier frequency, phase noise, constellation, high-order moments, power spectrum, and fractal features. In [8], Hu et al. extracted primary features, such as information dimension, constellation feature, and phase noise spectrum of the transmitted signal. The ML models, including the support vector machine, bagged tree, and weighted K-nearest neighbor, were used for RF fingerprinting recognition.

The feature extraction process requires professional knowledge. Moreover, specific information in original data might be lost after feature extraction. To mitigate the issues, unlike ML models, deep learning (DL) models could directly process raw data, transform the original data into higher-level representations, and automatically learn better feature representations. The automatic learning process could replace feature extraction, thus avoiding the procedure of feature engineering that may be at the cost of extracomputing resources. Examples of DL methods include feedforward neural networks [9], CNN, and recurrent neural networks [10, 11]. Particularly, the CNN has widely been applied in signal processing. In [12], Merchant et al. developed a framework for training a CNN algorithm using the time-domain complex baseband error signal. Building on seven 2.4 GHz commercial Zigbee devices, the experimental results demonstrated 92.29% identification accuracy. The robustness of the method over a wide range of signal-to-noise ratios (SNRs) was also illustrated. In [13], raw I/Q data

was used as a 2-dimensional input dataset into the CNN model to perform modulation classifications. In [14], raw I/Q data was used as a complex dataset and an RF-based deep complex residual network model that effectively extracts the I/Q-related information in the electromagnetic signal waveform was proposed. The authors showed that the recognition accuracy of the proposed method was 99.56%, compared with the contour stellar-based method 90.4%, and the deep complex CNN-based method 94.8%. However, the complex-valued method is complicated and not widely generalized.

In our paper, the raw data directly sampled from the I channel and the Q channel and a new 2-dimensional $I+Q$ data are fed into a CNN model. The final identification result depends on the aggregated results of the three submodels. Specifically, if two or three predictive results of the three submodels are the same, the final result is determined by the two or three submodels. On the other hand, if all the results from the three submodels are different, the final result is determined purely by the result that is obtained from $I+Q$ data.

The main contributions of this paper are as follows:

(i) The raw sampled data from the I channel and the Q channel and a new 2-dimensional $I+Q$ data are trained by a typical CNN structure like LeNet-5 [15]. The identification accuracies for 4 transmit devices by the three CNN submodel are compared under 0 dB, 5 dB, and 10 dB SNRs

(ii) The CNN submodel is designed to be lightweight. A small number (32 or 64) of sample points are used for training. Only two conventional layers are included in the CNN structure. The output size of each layer is decreased to a half of the input size. The training time for the 4 devices is about 30 seconds. This is useful to extract the RF fingerprint in real time

(iii) A voting scheme is proposed to synthesize the above three identifications, which further improves the identification accuracy

2. CNN-Based RF Fingerprint Identification Method

2.1. RF Fingerprint Identification and CNN Introduction. The RF fingerprints refer to the hardware features of wireless devices based on the signals transmitted by the devices. The hardware features for RF fingerprint identification attribute to the differences between wireless devices due to the tolerances of electronic components [16]. The CNN is a feedforward neural network that includes convolutional computation and has a deep structure. A CNN model can classify the categories of input information, which is also called "a translation-invariant artificial neural network." The relevant research began from the 1980s. With the introduction of deep learning theory and the improvement of computing equipment, CNN models have been rapidly developed and widely used in computer vision, natural language processing, and other fields.

2.2. CNN-Based RF Fingerprint Identification Method. The CNN-based RF fingerprint identification method is shown in Figure 1. A small slice is selected from the original raw I/Q data to reduce computation time. For each transmitter, 200 out of 10000 transmission records and 32 or 64 out of 8000 sample points are extracted for the following signal processing. The selected samples are then normalized to eliminate the amplitude differences due to the distances between the transmitter and receiver. The normalization method is illustrated in the following equations.

$$X_{Imn} = \frac{N \bullet x_{Imn}}{\sqrt{\sum_{n=1}^{N}\left(x_{Imn}^2 + x_{Qmn}^2\right)}}, \quad X_{Qmn} = \frac{N \bullet x_{Qmn}}{\sqrt{\sum_{n=1}^{N}\left(x_{Imn}^2 + x_{Qmn}^2\right)}}, \tag{1}$$

where x_{Imn} is the sample data at the I channel of the nth sample point of the mth transmission, x_{Qmn} is the sample data at the Q channel of the nth sample point of the mth transmission, X_{Imn} is the normalized result of x_{Imn}, X_{Qmn} is the normalized result of x_{Qmn}, and N is the total sample points, which equals to 32 or 64.

Additive White Gaussian noise is then added to the normalized sample data by employing MATLAB function "awgn." For each case, 200 transmissions are equally split into a training dataset and a testing dataset. The training process is then carried out by CNN models. Three predicted results by the I channel data, Q channel data, and $I+Q$ channel data are obtained and denoted as pI, pQ, and pIQ, respectively. The final identification is voted by the three predicted results, which means that the final predicted device is the one receiving the most votes among the three predicted results. For example, if the predicted results of RF fingerprint identification by the I channel data and the Q channel data are both device 1, while the predicted result by the $I+Q$ channel data is device 2, that means that device 1 receives 2 notes, device 2 receives 1 note, and device 3 and device 4 receive 0 notes, so the voted result, denoted as pV, is device 1. If all the three predicted results are different from each other, the final identification is the same as the predicted result by the $I+Q$ channel data, because $I+Q$ channel data contains more information. For example, if the predicted result by the I channel data is device 1, the predicted result by the Q channel data is device 2 and the predicted result by the $I+Q$ channel data is device 3; then, the final identification is device 3. The voting scheme can be simply summarized as Figure 2.

A CNN structure like LeNet-5 is applied to carry out the RF fingerprint identification. The structure consists of 10 layers. The CNN model is designed to be lightweight. Only two conventional layers are included in the CNN structure. The output size of each layer is decreased to a half of the input size. The parameters of each layer are given as follows.

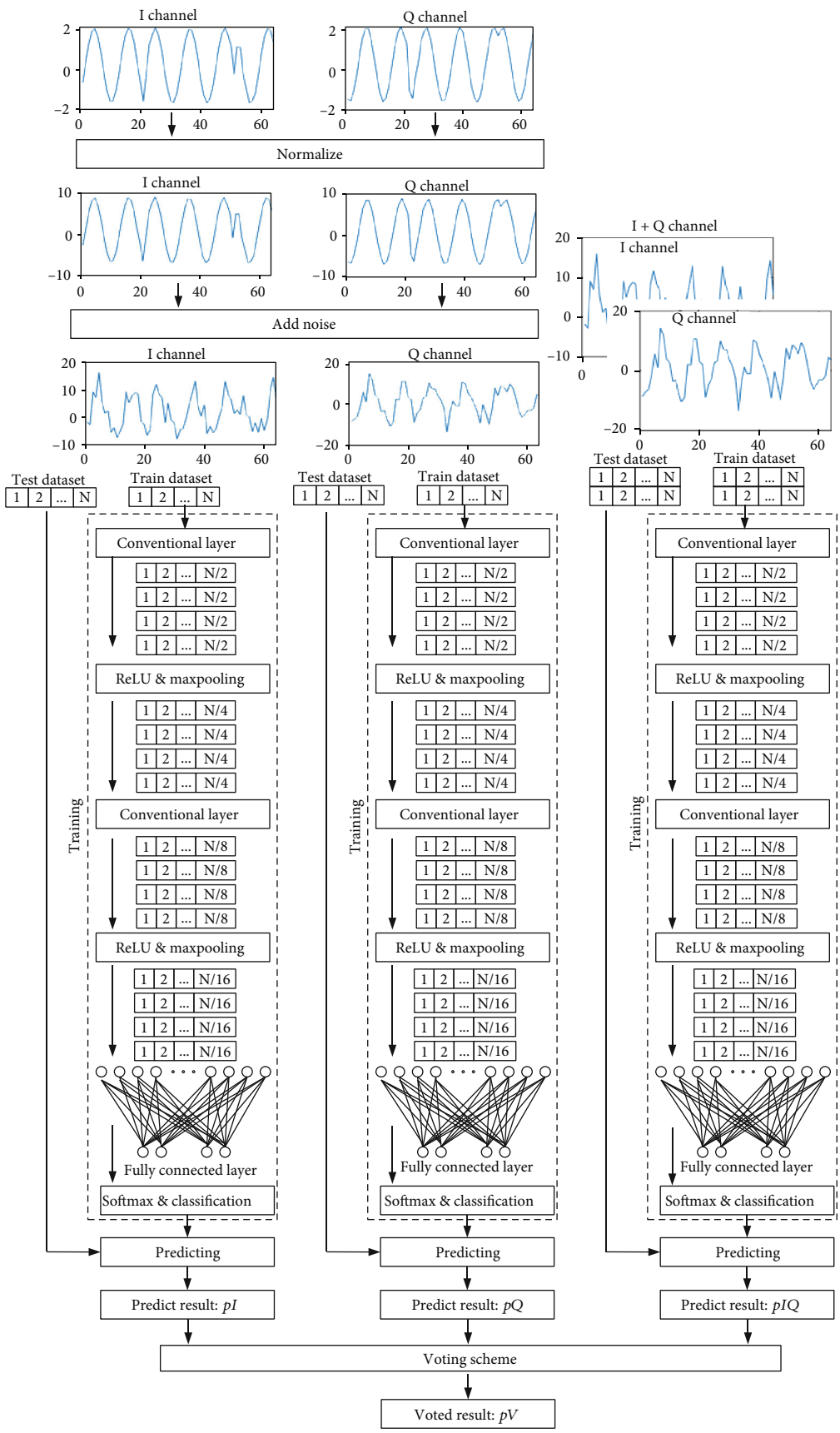

Figure 1: A radio frequency fingerprint identification method based on CNN.

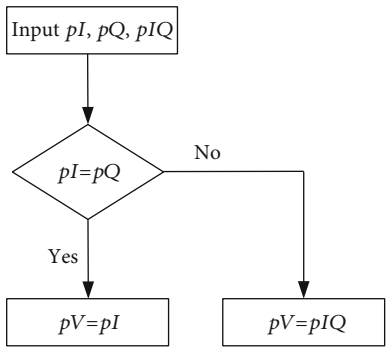

Figure 2: Algorithm flow of voting scheme.

The first layer is the data input layer. The size is $[L \times N \times 1]$, where $L = 1$ for the I channel data or the Q channel data, $L = 2$ for the $I + Q$ channel data, and N is the number of sample points that equals 32 or 64, which denotes that a segment of 32 data points can represent one signal transmission. The second layer is a 2D convolutional layer which is the major building block in the CNN. The convolutional layer performs a convolutional operation that involves the multiplication of a set of weights with the input to simulate a traditional neural network. The filter size is $[L \times 2 \times 1]$. The number of filters is 4. The stride is set as 2. The output data size is $[4 \times N/2 \times 1]$. The third layer is a rectified linear unit (ReLU) layer that performs a threshold operation to each element of the input, where any value less than zero is set to zero. The fourth layer is a 2D max pooling layer that manipulates downsampling by dividing the input into rectangular pooling regions and computing the maximum of each region. The pool size is $[1 \times 2]$. The stride is also set as 2. The output data size is $[4 \times N/4 \times 1]$. The fifth layer is a 2D convolutional layer. The filter size is $[1 \times 2 \times 1]$. The number of filters is 16. The stride is still set as 2. The output data size is $[4 \times N/8 \times 1]$. The sixth layer is a ReLU layer. The seventh layer is a 2D max pooling layer. The pool size is $[1 \times 2]$. The stride is 2. The output data size is $[4 \times N/16 \times 1]$. The eighth layer is a fully connected layer that compiles the data extracted by previous layers to form the final output. The output size is flattened to be 4, corresponding to the classifications of 4 devices. The ninth layer is a softmax layer that turns arbitrary real values into probabilities. The tenth layer is a classification layer that computes the cross-entropy loss for classification. A flow chart of the CNN structure is shown in Figure 3.

The CNN training models are implemented by the MATLAB deep learning toolbox. The MATLAB program is run by the Intel Xeon CPU E5-2678 v3 @ 2.5 GHz of a Dell PowerEdge T430 computer with a RAM size of 128 GB.

3. Results and Discussion

An experimental hardware platform consisting of four transmitters and one receiver is built and shown in Figure 4. Three low-cost USRP RIO-1082 (universal software radio peripheral-radio reconfigurable input/output) devices are used. Each USRP RIO-1082 device contains 2 radio frequency transmitting channels and 2 radio frequency receiving channels. The four transmitters are comprised of two USRP RIO-1082 devices and four antennas. The receiver is comprised of a USRP RIO-1082 device and an antenna. An NI-PXIe 1085 device is used to collect and store the signal data. The QPSK-modulated signals are transmitted with the carrier frequency of 2 GHz and symbol rate 10 kbps. The sample rate of the receiver is 1 MHz.

During the experiment, each transmitter separately transmitted 10000 times. Each transmission was sampled at the I channel and Q channel simultaneously. After an synchronization, 8000 sample points of each transmission were stored. Therefore, we obtained four $10000 \times 8000 \times 2$ arrays of raw I/Q data corresponding to the four transmitters.

The influences of the sample size and SNR on the accuracy of RF fingerprint identification have been observed. Figure 5 shows the training progresses of the CNN with the I channel data, Q channel data, and $I + Q$ channel data under 0 dB SNR and 32 sample points. After 1400 iterations, the accuracies of the I channel data and $I + Q$ channel data are both about 90%, while the accuracy of the Q channel data is about 80%.

Figure 6 shows the training progresses of the CNN with the I channel data, Q channel data, and $I + Q$ channel data under 5 dB SNR and 32 sample points. After 1400 iterations, the accuracies of the I channel data and Q channel data are both about 95%, while the accuracy of the $I + Q$ channel data is about 97%.

Figure 7 shows the training progresses of the CNN with the I channel data, Q channel data, and $I + Q$ channel data under 10 dB SNR and 32 sample points. The accuracy of the I channel is about 95% after 1400 iterations, while the accuracies of the Q channel data and $I + Q$ channel are nearly 100% after 1000 iterations, which means that the CNN model is overfitting during the late stages of training.

Figure 8 shows the training progresses of the CNN with the I channel data, Q channel data, and $I + Q$ channel data under 0 dB SNR and 64 sample points. After 1400 iterations, the accuracies of the I channel data, Q channel data, and $I + Q$ channel data are about 97%, 95%, and 99%, respectively.

Figure 9 shows the training progresses of the CNN with the I channel data, Q channel data, and $I + Q$ channel data under 5 dB SNR and 64 sample points. The accuracy of the I channel is about 95% after 1400 iterations, while the accuracies of the Q channel data and $I + Q$ channel are nearly 100% after 1000 iterations, which means that the CNN model is overfitting during the late stages of training.

Figure 10 shows the training progresses of the CNN with the I channel data, Q channel data, and $I + Q$ channel data under 10 dB SNR and 64 sample points. The accuracies of the three CNN models are all near 100% after 600 iterations, which means that the CNN model is overfitting during the late stages of training.

Table 1 shows the elapsed time of the training progress when the I channel data, Q channel data, and the $I + Q$ channel data are input into the CNN model under 0 dB, 5 dB, and 10 dB SNRs, respectively, and 32 and 64 sample

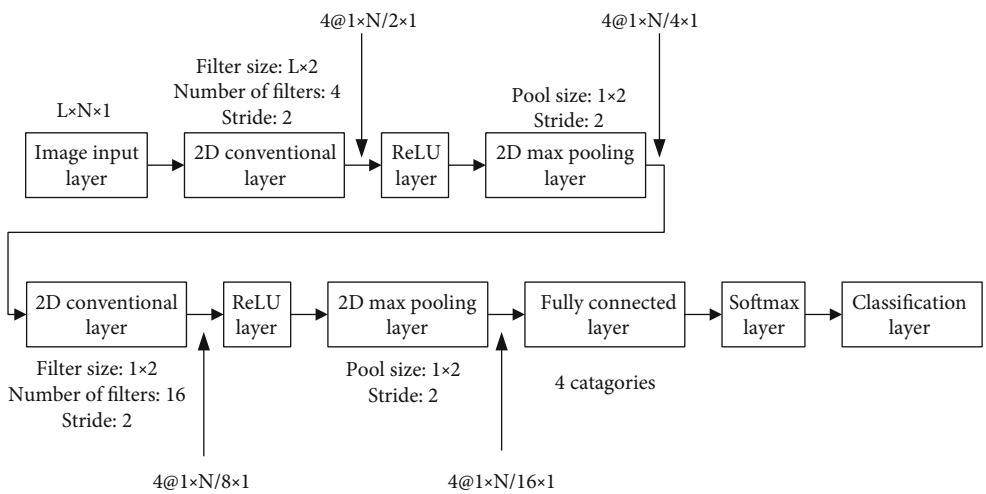

Figure 3: A flow chart of the CNN structure.

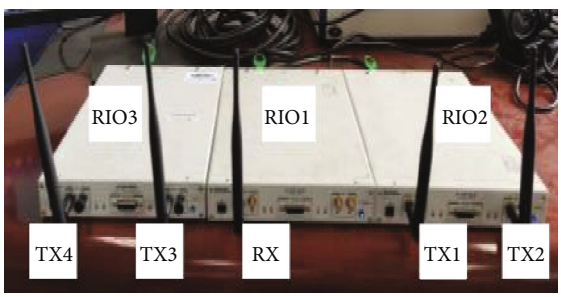

Figure 4: Experimental setup: four transmitters and one receiver.

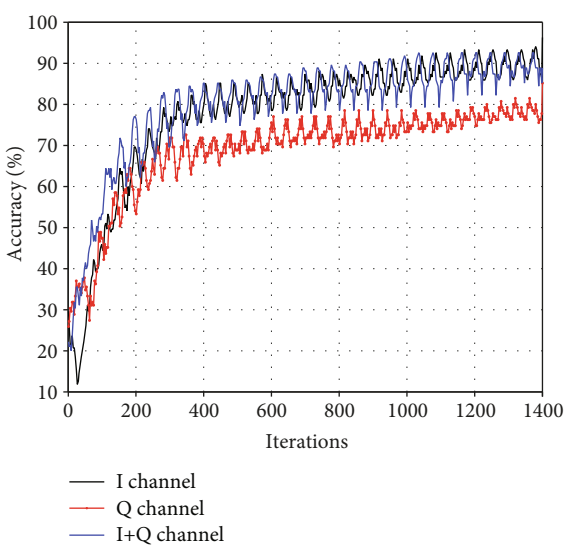

Figure 5: The training progresses of the CNN under 0 dB SNR and 32 sample points.

points. The elapsed time is between 24 s and 35 s, which is capable to extract the RF fingerprint in real time.

Table 2 shows the model accuracy rates of the submodel based on the I channel data, the submodel based on the Q channel, the submodel based on the $I+Q$ data, and the final aggregated model. Generally, it can be seen

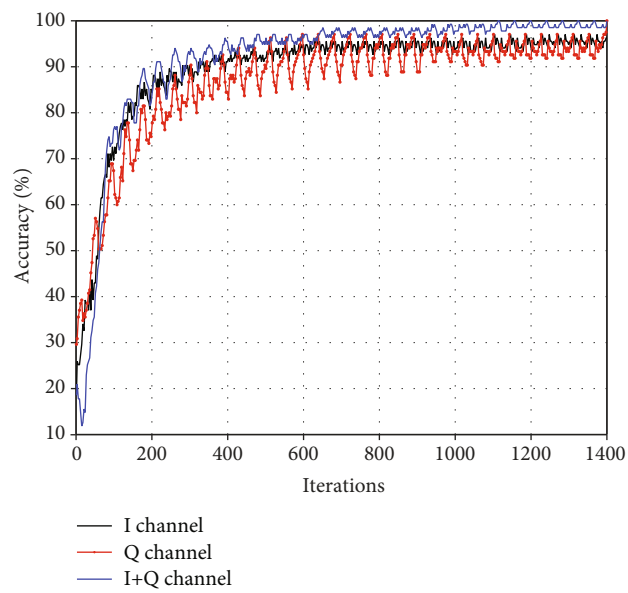

Figure 6: The training progresses of the CNN under 5 dB SNR and 32 sample points.

that the identification accuracy of the final model is higher than that of all the other three ones. Under the same SNR, the model accuracy with 64 sample points is higher than with 32 sample points. When the sample points are set as 32, the model accuracy rates are 87.25%, 93.75%, and 98.25% under SNR 0 dB, 5 dB, and 10 dB, respectively. When the sample points are set as 64, the model accuracy rates are 93%, 97.25%, and 99.5% under SNR 0 dB, 5 dB, and 10 dB, respectively.

Tables 3–8 show the confusion matrices of the voted results for the four device identification problems in consideration of different sample sizes and SNRs. The sum of every row in the confusion matrices is 100, which is the total number of running epochs. The diagonal numbers are the numbers of iterations for correct predictions, while the other numbers are the numbers of iterations for wrong predictions.

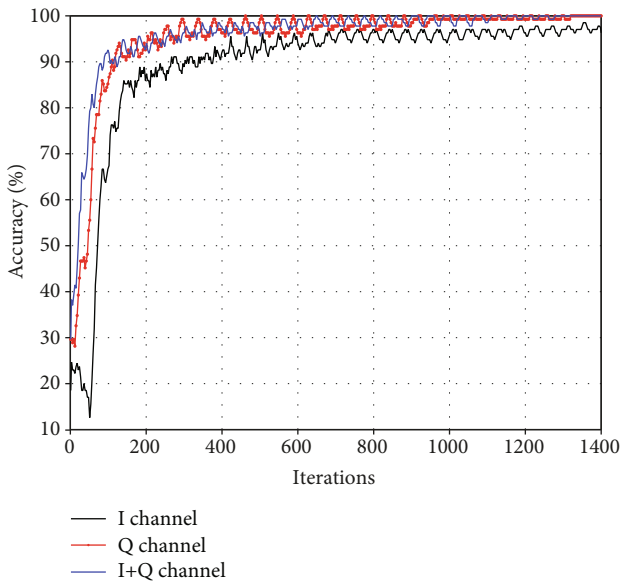

Figure 7: The training progresses of the CNN under 10 dB SNR and 32 sample points.

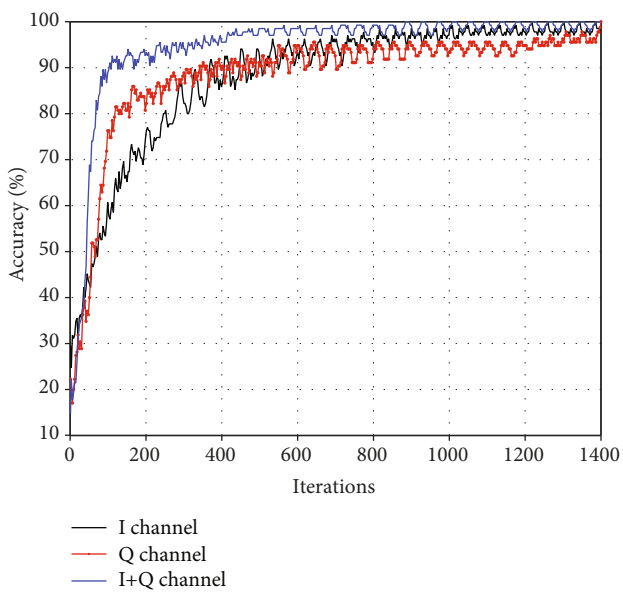

Figure 8: The training progresses of the CNN under 0 dB SNR and 64 sample points.

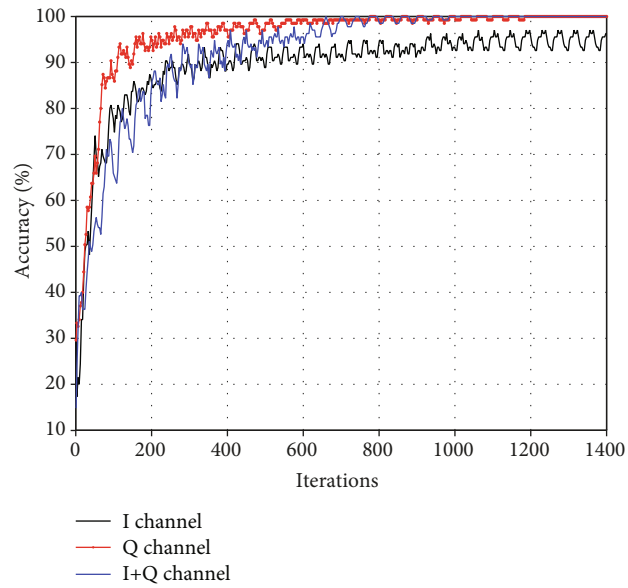

Figure 9: The training progresses of the CNN under 5 dB SNR and 64 sample points.

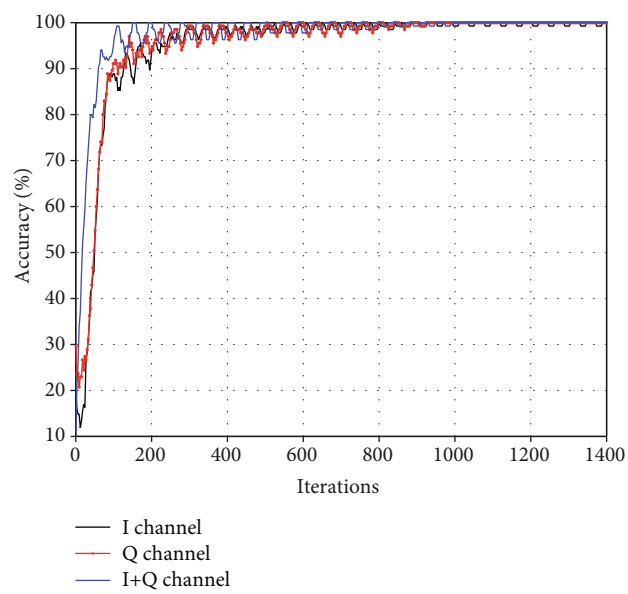

Figure 10: The training progresses of the CNN under 10 dB SNR and 64 sample points.

Table 3 shows the confusion matrix when the number of sample points is 32 and the SNR is 0 dB. Out of 100 epochs, device 1 is predicted to be device 1 for 89 times, device 2 for one time, and device 3 for 10 times. Device 2 is predicted to be device 1 for one time, device 2 for 98 times, and device 4 for one time. Device 3 is predicted to be device 1 for 5 times, device 2 for 2 times, device 3 for 74 times, and device 4 for 19 times. Device 4 is predicted to be device 3 for 12 times and device 4 for 88 times.

Table 4 shows the confusion matrix when the number of sample points is 32 and the SNR is 5 dB. Out of 100 epochs, device 1 is predicted to be device 1 for 98 times and device 3 for 2 times. Device 2 is predicted to be device 1 for one time and device 2 for 99 times. Device 3 is predicted to be device 1 for 3 times, device 3 for 81 times, and device 4 for 16 times. Device 4 is predicted to be device 3 for 3 times and device 4 for 97 times.

Table 5 shows the confusion matrix when the number of sample points is 32 and the SNR is 10 dB. Device 1, device 2, and device 4 are correctly predicted for all 100 times. Out of 100 epochs, device 3 is predicted to be device 1 for one time, device 3 for 93 times, and device 4 for 6 times.

Table 6 shows the confusion matrix when the number of sample points is 64 and the SNR is 0 dB. Out of 100 epochs,

Table 1: Elapsed time of the training progress.

	$N = 32$, SNR = 0 dB	$N = 32$, SNR = 5 dB	$N = 32$, SNR = 10 dB	$N = 64$, SNR = 0 dB	$N = 64$, SNR = 5 dB	$N = 64$, SNR = 10 dB
I channel	28 s	27 s	33 s	30s	33 s	26 s
Q channel	29 s	25 s	30s	29 s	34 s	26 s
$I + Q$ channel	27 s	25 s	33 s	28 s	35 s	24 s

Table 2: Accuracy of RF fingerprint identification under different conditions.

	$N = 32$, SNR = 0 dB	$N = 32$, SNR = 5 dB	$N = 32$, SNR = 10 dB	$N = 64$, SNR = 0 dB	$N = 64$, SNR = 5 dB	$N = 64$, SSNR = 10 dB
I channel	0.79	0.8675	0.965	0.8	0.945	0.985
Q channel	0.7725	0.9225	0.965	0.8025	0.95	0.98
$I + Q$ channel	0.7875	0.93	0.965	0.92	0.945	0.9825
Voted results	0.8725	0.9375	0.9825	0.93	0.9725	0.995

Table 3: Confusion matrix of the voted RF fingerprint identification. $N = 32$, SNR = 0 dB.

		Predicted devices			
		1	2	3	4
Actual devices	1	89	1	10	0
	2	1	98	0	1
	3	5	2	74	19
	4	0	0	12	88

Table 4: Confusion matrix of the voted RF fingerprint identification. $N = 32$, SNR = 5 dB.

		Predicted devices			
		1	2	3	4
Actual devices	1	98	0	2	0
	2	1	99	0	0
	3	3	0	81	16
	4	0	0	3	97

Table 5: Confusion matrix of the voted RF fingerprint identification. $N = 32$, SNR = 10 dB.

		Predicted devices			
		1	2	3	4
Actual devices	1	100	0	0	0
	2	0	100	0	0
	3	1	0	93	6
	4	0	0	0	100

Table 6: Confusion matrix of the voted RF fingerprint identification. $N = 64$, SNR = 0 dB.

		Predicted devices			
		1	2	3	4
Actual devices	1	94	0	6	0
	2	1	98	0	1
	3	9	0	85	6
	4	0	0	5	95

Table 7: Confusion matrix of the voted RF fingerprint identification. $N = 64$, SNR = 5 dB.

		Predicted devices			
		1	2	3	4
Actual devices	1	99	0	1	0
	2	0	100	0	0
	3	4	0	93	3
	4	0	0	3	97

Table 8: Confusion matrix of the voted RF fingerprint identification. $N = 64$, SNR = 10 dB.

		Predicted devices			
		1	2	3	4
Actual devices	1	100	0	0	0
	2	0	100	0	0
	3	2	0	98	0
	4	0	0	0	100

device 1 is predicted to be device 1 for 94 times and device 3 for 6 times. Device 2 is predicted to be device 1 for one time, device 2 for 98 times, and device 4 for one time. Device 3 is predicted to be device 1 for 9 times, device 3 for 85 times, and device 4 for 6 times. Device 4 is predicted to be device 3 for 5 times and device 4 for 95 times.

Table 7 shows the confusion matrix when the number of sample points is 64 and the SNR is 5 dB. Out of 100 epochs,

device 1 is predicted to be device 1 for 99 times and device 3 for 1 time. Device 2 is correctly predicted for all 100 times. Device 3 is predicted to be device 1 for 4 times, device 3 for 93 times, and device 4 for 3 times. Device 4 is predicted to be device 3 for 3 times and device 4 for 97 times.

Table 8 shows that the confusion matrix when the number of sample points is 64 and the SNR is 10 dB. Device 1, device 2, and device 4 are correctly predicted for all 100 times. Out of 100 epochs, device 3 is predicted to be device 1 for 2 times and device 3 for 98 times.

4. Conclusions

The CNN-based RF identification models on the I channel-related data, the Q channel-related data, and the $I+Q$ -related data are used to recognize four transmitters. The final identification labels are determined by a voting scheme of the three submodels. It has been shown that the accuracy of the final model is higher than those of all the three submodels. Additionally, experimental results illustrate that the recognition accuracy with 64 sample points is higher than that of 32 sample points in the same settings of SNRs. The model accuracy is more than 90% under 32 sample points in the setting of SNR at 5 dB. The elapsed time of training the CNN model is between 24 s and 35 s, which proves that the model is capable to extract the RF fingerprint in real time.

Data Availability

The data used to support the findings of this study are available from the corresponding author upon request.

Conflicts of Interest

The authors declare that there is no conflict of interest regarding the publication of this paper.

Acknowledgments

This work is partially supported by the National Natural Science Foundation of China (no. 61971092), Sichuan Province Foundation for Distinguished Young Scholars (no. 2020JDJQ0023), and Fundamental Research Funds for the Central Universities (nos. ZYGX2020ZB045 and ZYGX2019J123).

References

[1] G. Shen, J. Zhang, A. Marshall, and J. R. Cavallaro, "Towards scalable and channel-robust radio frequency fingerprint identification for LoRa," *IEEE Transactions on Information Forensics and Security*, vol. 17, pp. 774–787, 2022.

[2] A. Al-Shawabka, F. Restuccia, S. D'Oro et al., "Exposing the fingerprint: dissecting the impact of the wireless channel on radio fingerprinting," in *IEEE INFOCOM 2020-IEEE Conference on Computer Communications*, pp. 646–655, Toronto, ON, Canada, 2020.

[3] K. Youssef, L. Bouchard, K. Haigh, J. Silovsky, B. Thapa, and C. V. Valk, "Machine learning approach to RF transmitter identification," *IEEE Journal of Radio Frequency Identification*, vol. 2, no. 4, pp. 197–205, 2018.

[4] A. Jagannath, J. Jagannath, and P. S. P. V. Kumar, "A comprehensive survey on radio frequency (RF) fingerprinting-traditional approaches, deep learning, and open challenges," 2022, http://arxiv.org/abs/2201.00680.

[5] M. Liu, Z. Liu, L. Weidang, Y. Chen, X. Gao, and N. Zhao, "Distributed few-shot learning for intelligent recognition of communication jamming," *IEEE Journal of Selected Topics in Signal Processing*, vol. 16, no. 3, pp. 395–405, 2022.

[6] M. Liu, B. Li, Y. Chen et al., "Location parameter estimation of moving aerial target in space–air–ground-integrated networks-based IoV," *IEEE Internet of Things Journal*, vol. 9, no. 8, pp. 5696–5707, 2022.

[7] M. Liu, C. Liu, M. Li, Y. Chen, S. Zheng, and N. Zhao, "Intelligent passive detection of aerial target in space-air-ground integrated networks," *China Communications*, vol. 19, no. 1, pp. 52–63, 2022.

[8] S. Hu, P. Wang, Y. Peng et al., "Machine learning for RF fingerprinting extraction and identification of soft defined radio devices," in *Artificial Intelligence in China*, Lecture Notes in Electrical Engineering, Springer, Singapore, 2020.

[9] A. Hirose and S. Yoshida, "Generalization characteristics of complex-valued feedforward neural networks in relation to signal coherence," *IEEE Transactions On Neural Networks And Learning Systems*, vol. 23, no. 4, pp. 541–551, 2012.

[10] Q. Wu, C. Feres, D. Kuzmenko et al., "Deep learning based RF fingerprinting for device identification and wireless security," *Electronics Letters*, vol. 54, no. 24, pp. 1405–1407, 2018.

[11] W. Lee, S. Y. Baek, and S. H. Kim, "Deep-learning-aided RF fingerprinting for NFC security," *IEEE Communications Magazine*, vol. 59, no. 5, pp. 96–101, 2021.

[12] K. Merchant, S. Revay, G. Stantchev, and B. Nousain, "Deep learning for RF device fingerprinting in cognitive communication networks," *IEEE Journal of Selected Topics in Signal Processing*, vol. 12, no. 1, pp. 160–167, 2018.

[13] T. J. O'Shea, T. Roy, and T. C. Clancy, "Over-the-air deep learning based radio signal classification," *IEEE Journal of Selected Topics in Signal Processing*, vol. 12, no. 1, pp. 168–179, 2018.

[14] S. Wang, H. Jiang, X. Fang, Y. Ying, J. Li, and B. Zhang, "Radio frequency fingerprint identification based on deep complex residual network," *IEEE Access*, vol. 8, pp. 204417–204424, 2020.

[15] Y. Lecun, L. Bottou, Y. Bengio, and P. Haffner, "Gradient-based learning applied to document recognition," *Proceedings of the IEEE*, vol. 86, no. 11, pp. 2278–2324, 1998.

[16] V. R. Pagán and T. E. Murphy, "Electrooptic millimeter-wave downconversion and vector demodulation using phase-modulation and optical filtering," in *2014 IEEE Avionics, Fiber-Optics and Photonics Technology Conference (AVFOP)*, Atlanta, GA, USA, Nov.2014.

Hindawi
Wireless Communications and Mobile Computing
Volume 2022, Article ID 8280428, 10 pages
https://doi.org/10.1155/2022/8280428

Research Article

An Improved Kalman Filter Based on Long Short-Memory Recurrent Neural Network for Nonlinear Radar Target Tracking

Fei Song,[1,2] **Yong Li**,[1] **Wei Cheng**,[1] **Limeng Dong**,[1] **Minqi Li**,[3] **and Junfang Li**[2]

[1]*School of Electronic Information, Northwestern Polytechnical University, Xi'an 710072, China*
[2]*School of Electronic Engineering, Xi'an Aeronautical Institute, Xi'an 710077, China*
[3]*School of Electronic Information, Xi'an Polytechnic University, Xi'an 710048, China*

Correspondence should be addressed to Yong Li; ruikel@nwpu.edu.cn

Received 26 May 2022; Accepted 25 July 2022; Published 21 August 2022

Academic Editor: A.H. Alamoodi

The target tracking of nonlinear maneuvering radar in dense clutter environments is still an important but difficult problem to be solved effectively. Traditional solutions often rely on motion models and prior distributions. This paper presents a novel improved architecture of Kalman filter based on a recursive neural network, which combines the sequence learning of recurrent neural networks with the precise prediction of Kalman filter in an end-to-end manner. We employ three LSTM networks to model nonlinear motion equation, motion noise, and measurement noise, respectively, and learn their long-term dependence from a large amount of training data. They are then applied to the prediction and update process of Kalman filter to calculate the estimated target state. Our approach is able to address the tracking problem of nonlinear maneuvering radar target online end-to-end and does not require the motion models and prior distributions. Experimental results show that our method is more effective and faster than the traditional methods and more accurate than the method with LSTM network alone.

1. Introduction

Target tracking is an important support for radar, sonar, satellite, optical sensor, and other systems to realize monitoring, positioning, navigation, and other applications. Its working mechanism is to fuse the prior information of the target and the online measurement information of the sensor and estimate the number, position, and motion state of the target online under the background of noise. In general, there are two key difficulties in target tracking, namely, target dynamic state uncertainty and measurement data uncertainty. This paper only focuses on the dynamic state uncertainty in radar target tracking.

For the single target tracking of approximately uniform motion, it is basically solved based on Bayesian theory. The essence of Bayesian theory is to seek the solution of the posterior probability density of motion state according to the prior probability density and observation likelihood function of dynamic parameters. Kalman filter (KF) [1] is an unbiased optimal estimation in the recursive form of Bayesian theory, which is applicable to target tracking of linear Gaussian motion in many fields. For nonlinear object tracking, the common improvement method is the Extended Kalman filter (EKF) [2], which approximately linearizes the system near the working point. The Unsensitive Kalman filter (UKF) [3] makes an approximate Gaussian distribution after projection of a few deterministic sample points. The Particle filtering (PF) [4] approximates the posterior probability density of the nonlinear functions by a large number of random discrete samples. These methods all approximate the posterior probability distribution from different directions. And their computational accuracy is limited by the model approximation effectiveness, or they need to balance the effectiveness and computational efficiency.

For target tracking with strong maneuverability, target maneuvering leads to the change of target dynamic characteristics. The commonly used solutions are the Markov jump multimodel algorithms, e.g., the interactive multimodel (IMM) algorithm and the variable structure multimodel algorithm (VSMM) algorithm [5, 6]. In essence, this kind of algorithms applies multiple motion models for matching the motion patterns of maneuvering target, with the models

transferred by Markov matrix. The disadvantage is that the model structure and quantity need to be determined in advance, leading to limited statistical accuracy due to model mismatch and insufficient estimation data.

For the nonlinear maneuvering radar target, its motion equation is often unpredictable, and the distribution of the motion process noise and measurement noise is also uncertain. These problems are difficult to solve using the traditional methods mentioned above. We analyze, in essence, the target tracking is to estimate the nonlinear mapping from the observation sequence to the real state of the target in time dimension. Considering the rapid development of deep neural networks (DNN) [7–11] in recent years, relying on its strong expression ability, it is possible to find a deterministic map to approximate the conditional density from a given input to an output in a mathematically optimal way by learning from a large amount of data [12]. Recurrent neural network (RNN) plays an important role in processing time series as a vital branch of DNN. Its main specialities are able to process historical data cyclically and recursively and model the historical memory information. With this help, RNN is good at dealing with the time series, which have tight correlation sequence information and uncertain length. Theoretically, as long as there is enough training data covering the possible motion path of the tracked object and an appropriate network structure, RNN is able to output the target state condition density of a given available observation value at each time step [13]. This coincides with the needs of target tracking. Inspired by this, we integrate the deep neural network with the traditional target tracking method, giving full play to their advantages, so as to effectively solve the above complex target tracking problems.

The contributions of this paper are summarized in the following items:

(1) In order to overcome the problems of nonlinear maneuvering radar target tracking, inspired by deep learning ideas, we propose a novel target tracking architecture combing Kalman filter and LSTM network. We model three LSTM networks separately for the uncertainty of the nonlinear motion equation, motion process noise distribution, and measurement noise distribution in Kalman filter. Relying on the powerful learning ability of LSTM network, the long-term dependent characteristics of target motion and measurement can be learned from the training of abundant training data and uniformly applied to the motion state prediction of Kalman filter. The advantages of this architecture are that it requires no approximation and no prior distribution, and it can carry out the nonlinear maneuvering radar target tracking end-to-end online

(2) We generate a large amount of training data using model sampling, based on widely used nonlinear maneuvering radar target time series model

(3) The qualitative and quantitative simulation results show that the proposed architecture is stronger than the traditional nonlinear target tracking methods in both the estimation error and computational speed in nonlinear maneuvering target tracking task

2. Related Work

In recent literatures, the application of DNN network in target estimation and prediction has been widely studied. In this section, we introduce those works that explicitly use LSTM in combination with traditional methods to infer time correlation in chronological order.

Early, Haarnoja et al. [14] used the one-time estimation as the measured value inputting into the Kalman filter. And the estimator is required to provide the prediction of noise covariance, which is often inaccurate without a learning process. Coskun et al. [15] proposed a method to human image pose regularization, which uses the LSTM estimator fused with a KF. However, it is only applicable to the estimation of slowly changing human image posture, and it does not fully explain the use performance of target tracking problem with rapidly changing state. Recently, Gao et al. [16] proposed two LSTM networks to receive the observation results and output the real state in a continuous manner. They complete the process of prediction and filtering, respectively. However, the two processes are independent and not related. The accuracy of the estimate will be limited. Moreover, they use an overall LSTM structure for estimation, which makes it more difficult to fit. Llerena et al. [17] used the LSTM unit to estimate the motion state through the encoder decoder architecture. However, only the performance comparison with EKF algorithm, and only under several linear and specific motion paths, cannot fully explain the superiority of this algorithm. Zhang et al. [18] used a Kalman filter based on LSTM for data assimilation of a two-dimensional spatiotemporal depth average ocean flow field and path planning of underwater glider. The LSTM network only models the spatial basis function in the nontidal flow field. The output of LSTM and the observation results obtained from the glider flow estimation data both are inputted to the Kalman filter. LSTM does not estimate all motion equations, process noise, and measurement noise, so the accuracy of estimation effect is limited.

In [19], we proposed to use of the LSTM network commonly used in RNN to extract the features of continuous data. Thus, it is able to fit the nonlinear mapping between noisy observations and target state under the conventional motion model. However, for nonlinear maneuvering radar target tracking, the ability of this method is limited. Therefore, we propose a new architecture combining LSTM network and Kalman filter, which strengthens the extraction of target motion history features, prediction accuracy, and noise resistance.

Our architecture is somewhat similar to [16], but is different in three key ways: First, motion state prediction and filtering in [16] are independently completed, while we integrate the results of the LSTM prediction into the Kalman filter state prediction to enhance the accuracy of the target prediction. Secondly, a whole RNN is used in [16] for learning and estimation, while we use three LSTMs: motion state, motion process noise, and measurement noise for learning and estimation. In this way, the learned historical information is more comprehensive and has stronger anti-interference ability. Thirdly, due to the different network architecture, we also use different loss functions.

3. Background

The Bayesian principle is applied as a basic theoretical framework for dealing with the observation data and its sequential characteristics uncertainty. The Bayesian method uses the prior estimation of motion state and the likelihood function of observation value to accurately estimate the motion state. We assume the motion model of the system is as follows:

$$\begin{aligned} \text{State equation}: x_k &= f(x_{k-1}) + v_k, \\ \text{Observation equation}: y_k &= h(x_k) + w_k, \end{aligned} \tag{1}$$

where x_k is the motion state at k step, v_k is the prediction process noise, which obeys the Gaussian distribution $v_k \sim N(0, Q)$, and $f()$ is the motion equation, y_k is the observation data at the k step, w_k is the observation noise, which obeys the Gaussian distribution $w_k \sim N(0, R)$, and h is the observation equation.

The best solution of Bayesian filtering on the math from the classical Bayesian theory is the following:

$$p(x_k|y_{k-1}) = \int p(x_k|x_{k-1})p(x_{k-1}|y_{k-1})dx_{k-1}, \tag{2}$$

$$p(x_k|y_k) = \frac{1}{p(y_k|y_{k-1})} p(y_k|x_k)p(x_k|y_{k-1}). \tag{3}$$

From these, the Bayesian filtering consists chiefly of two stages: prediction stage as Equation (2) and filtering stage as Equation (3). We are able to accurately acquire the posterior probability density of the two stages. The Kalman filter algorithm is the recursive form to realize this accurate solution.

3.1. Kalman Filter. If we use x_t to represent the motion state and y_t to represent the measurement, we can change the model to

$$x_t = Ax_{t-1} + w \; w \sim N(0, Q), \tag{4}$$

$$y_t = Hx_t + v \quad v \sim N(0, R), \tag{5}$$

where A is the motion matrix, x_{t-1} is the motion state at time $t-1$, and w is process noise, which is a Gaussian white noise with zero mean and covariance matrix Q. H is the observation matrix, and v is measurement noise, which is a Gaussian white noise with zero mean and covariance matrix R.

The Kalman filter algorithm is divided into two stages: prediction and update.

The prediction stage calculates the state prior estimation and the error covariance prior estimation at current time according to the state estimate at previous time, as follows:

$$\hat{x}_t' = A\hat{x}_{t-1}, \tag{6}$$

$$\hat{P}_t' = A\hat{P}_{t-1}A^T + Q. \tag{7}$$

The update stage combines the prior estimations with new measurement data to calculate the improved posteriori estimations. K_t is the calculated filter gain matrix and the intermediate calculation result of filtering. The Kalman filter algorithm is a recursive prediction update method.

$$K_t = \hat{P}_t' H^T \left(H\hat{P}_t' H^T + R\right)^{-1}, \tag{8}$$

$$\hat{x}_t = \hat{x}_t' + K_t\left(\hat{y}_t - H\hat{x}_t'\right), \tag{9}$$

$$\hat{P}_t = (I - K_T H)\hat{P}_t'. \tag{10}$$

3.2. Long Short-Term Memory. With the help of RNN's characteristics as mentioned above, RNN is best adapted for dynamic scenes, hardly characterized by a fixed number of parameters. It is adequate for handling strongly correlated information in time and space series such as target tracking.

However, the traditional RNN is bad at storing the long-term memory of sequence information and may cause serious gradient disappearance or gradient explosion [20]. The main method to solve this problem is to use long-term memory network (LSTM), which is able to overcome the above shortcomings effectively.

LSTM is an improved RNN adding special memory function. It is able to compute the state of hidden layer neurons in various ways. The memory unit is mainly composed of four components: input gate, forgotten gate, output gate, and self-circulation connection. The LSTM protects and controls the status of the memory units by dominating the gates outputs. They work together to make LSTM get the ability to store and transmit sequence information for a long time and then reducing the problem of gradient disappearance.

In this paper, we use a general variant of forgetting gate [21], which is good for improving performance [22]. The LSTM variants are described below:

$$f_t = \sigma\left(W_{fh}h_{t-1} + W_{fx}x_t + b_f\right), \tag{11}$$

$$i_t = \sigma(W_{ih}h_{t-1} + W_{ix}x_t + b_i), \tag{12}$$

$$o_t = \sigma(W_{oh}h_{t-1} + W_{ox}x_t + b_o), \tag{13}$$

$$\tilde{c}_t = \tanh\,(W_{ch}h_{t-1} + W_{cx}x_t + b_c), \tag{14}$$

$$c_t = f_t \otimes c_{t-1} + i_t \otimes \tilde{c}_t, \tag{15}$$

$$h_t = o_t \otimes \tanh\,(c_t), \tag{16}$$

where σ represents sigmoid function and $\bigotimes$ represents element level multiplication. From these equations, it can be seen that the LSTM applies the forgotten gate f_t to reset the memory, uses the input gate i_t to write to the memory, employs the output gate o_t to read from the memory, and finally forms the output or hidden state h_t. The values of the intermediate storage unit $\tilde{c}_t$ and all gates are determined by the input x_t and all kinds of W and b parameters, which are learned in a training process. For multilayer LSTM, the first layer hidden states h_t are regarded as the input x_t of the second layer, and so on.

4. Kalman Filter Fusing LSTM for Nonlinear Target Tracking

It can be seen from the above analysis that Kalman filter algorithm requires the linear equation of motion state, and the motion process noise and measurement noise are both Gaussian white noise with 0 mean. However, for nonlinear maneuvering targets, their motion state is often irregular, and the distribution of motion process noise and measurement noise is also a priori unknown. To address these problems, we present the Kalman filter fusing LSTM (KFFLSTM), a novel structure for the nonlinear target tracking. Specifically, we make use of three different LSTM networks to model the nonlinear process function, process noise, and measurement noise in Kalman filter, respectively. Through the deep learning process from massive training data, we are able to achieve the best coefficient representation of the three networks. Then, it is applied to the Kalman filter calculation to obtain a more accurate target state prediction.

4.1. System Description. In essence, our network model is a kind of Kalman filter technology based on deep learning. With the continuous refinement of the measured values, it can regularize the nonlinear target motion state without manually setting the process and measurement models.

Theoretically, by setting the receiving vector sequence of the LSTM network, from Equations (11)–(16), the hidden state of the t-th time step of the LSTM is summarized as

Theoretically, by setting the receiving vector sequence $X = (x_1, x_2, \cdots, x_T)$ of the LSTM network, from Equations (11)–(16), the hidden state of the t-th time step of the LSTM is summarized as

$$h_t = f_{\theta_h}(x_t, h_{t-1}), \tag{17}$$

where h_{t-1} is the hidden state of the previous step and f_{θ_h} is a deterministic gated activation function through the parameter set θ_h determined. The corresponding output at time t can also be summarized as

$$o_t = f_{\theta_o}(x_t, h_{t-1}), \tag{18}$$

where f_{θ_o} is a deterministic gated activation function through the parameter set θ_o determined.

Through the training process of LSTM network, we achieve the optimal parameter set θ^* (θ_h and θ_o are its subsets) in statistical sense, with the error function minimized. With its help, the LSTM deterministically approximate the conditional probability density $p(y_1, \cdots, y_t | x_1, \cdots, x_t)$ and complete the deterministic mapping from input to output. This is expressed as

$$p(y_1, \cdots, y_T | x_1, \cdots, x_T) = \prod_{t=1}^{T} p(y_t | x_t), \tag{19}$$

where each of $p(y_t | x_t)$ is parameterized by a cyclic module, which defines a deterministic function.

Through LSTMs, we can learn the mapping relationship from input to output from abundant training data and apply them to the estimation of key parameters in Kalman filter. Compared with the traditional model-based methods, this new one's advantages will be very significant. In traditional methods, these parameters are often determined by fixed models or obtained by experience, which limits their application in nonlinear and non-Gaussian target tracking. The fusion of LSTM networks and Kalman filter not only makes the Kalman filter algorithm break through the original limitation of linear Gaussian but also helps the updating process of Kalman filter to combine the estimation obtained by LSTM and measurement, which is expected to make the nonlinear target tracking more effective than that of Kalman or LSTM alone.

Specifically, our network model divides the tracking task into three different LSTM networks according to their function. Each LSTM estimates the undetermined matrix in the Kalman filter: the LSTM-A estimates the process state transition matrix A (Equation (6)), the LSTM-Q estimates the process noise covariance matrix Q (Equation (7)), and the LSTM-R estimates the measurement noise covariance matrix R (Equation (8)). The three networks are organically combined by the prediction and update process of the Kalman filter. Compared with one whole LSTM [23] learning process, this arrangement is able to make the learning task of each LSTM simpler, converge faster, and improve the effect of overall estimation.

The system structure is shown in Figure 1. In the time step t, LSTM-A takes the prediction of the previous step $\hat{x}_{t-1}$ as the input to generate the intermediate state of process estimation $\hat{x}_t'$. Then, it is input to LSMT-Q to generate the estimation of process noise covariance $\hat{Q}_t$. Meanwhile, the observed value y_t of this time step is input to LSTM-R to generate the estimation of the measurement noise covariance $\hat{R}_t$. Finally, the $\hat{x}_t'$, $\hat{y}_t$, $\hat{Q}_t$, and $\hat{R}_t$ are inputted to the above update Equations (8)–(10) of Kalman filter to obtain the final state prediction value $\hat{x}_t$ of this time step. Each time step in the whole prediction process is iterated according to this step, and finally a whole tracking prediction results can be obtained.

4.2. Model Prediction and Update Steps. Assuming that the measured value is a noisy estimation of the basic state, it can be simplified to make $H = I$ in above Equation (5). The original model updates as

$$\begin{aligned} x_t &= Ax_{t-1} + w \quad & w &\sim N\left(0, \hat{Q}_t\right), \\ \hat{y}_t &= x_t + v & v &\sim N\left(0, \hat{R}_t\right), \end{aligned} \tag{20}$$

where the process equation A in the prediction step is modeled by LSTM-A network, $\hat{Q}_t$ is output by LSMT-Q and $\hat{R}_t$ is output by LSTM-R. $\hat{y}_t$ is the measurement observed at time t as the input to the filter. The formula of

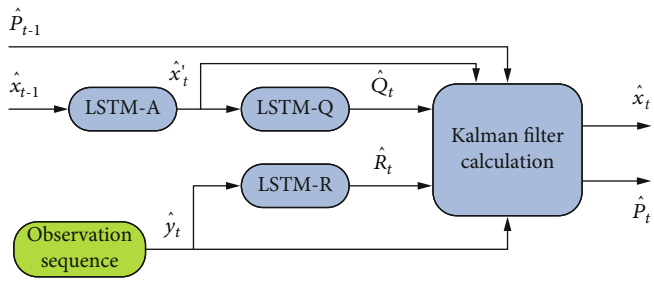

Figure 1: Overview of the KFFLSTM. In a time step t, the architecture of the KFFLSTM is composed of three LSTM modules and Kalman filter calculation modules.

Kalman filter process is modified to

$$\hat{x}'_t = A\hat{x}_{t-1}, \tag{21}$$

$$\hat{P}'_t = A\hat{P}_{t-1}A^T + \hat{Q}_t, \tag{22}$$

$$K_t = \hat{P}'_t\left(\hat{P}'_t + \hat{R}_t\right)^{-1}, \tag{23}$$

$$\hat{x}_t = \hat{x}'_t + K_t\left(\hat{y}_t - \hat{x}'_t\right), \tag{24}$$

$$\hat{P}_t = (I - K_t)\hat{P}'_t, \tag{25}$$

where $\hat{x}_t$ and $\hat{x}_{t-1}$ represent the posteriori state estimation values at time t and time $t-1$, respectively, which are part of the filtering results. Other filtering results are $\hat{P}_t$ and $\hat{P}_{t-1}$, which represent the a posteriori estimation covariance at time t and time $t-1$, respectively. Next section, we give a detailed description of the LSTM networks.

4.3. LSTM Network Architecture. We use LSTM-A, LSTM-Q, and LSTM-R to represent the three LSTM networks. Each network is described in Figure 2.

Specifically, the estimation task of nonlinear process function is the most important, in which a large of features need to be extracted from the training data. Therefore, the LSTM-A is designed consisting of four stacked LSTM layers; each layer has 1024 hidden units. There are three fully connected (FC) layers, whose hidden units are set 1024, 1024, and 2, respectively. The process noise estimation task is relatively easy. The LSTM-Q is designed as a single layer LSTM with 256 hidden units, adding a full connection layer of 2 hidden units. The measurement noise is relatively fixed, and the estimation is easier. The LSTM-R is designed as a single-layer LSTM network with 128 hidden units and a full connection layer connecting 2 hidden units. Behind each LSTM layer in the design, there is a loss layer with a retention probability of 0.8. The activation function of each fully connected layer is the nonlinear function Relu (except the last layer).

It should be noted that in order to ensure the invertibility of the matrix generated when calculating the Kalman gain, the $\hat{Q}_t$ and $\hat{R}_t$ are limited to diagonal matrices and positive definite by exponentiation of the outputs of LSTM-Q and LSTM-R.

4.4. Loss Function. In practice, we first used the commonly used sum of squares of residuals (SSR) loss function:

$$L(\theta) = \frac{1}{T}\sum_{t=1}^{T}\|x_t - \hat{x}_t(\theta)\|^2. \tag{26}$$

However, the value of the loss function did not converge during the training process. After the problem locating, we found that the LSTM-A module cannot learn any reasonable mapping. Therefore, a regular term is added to the loss function to strengthen the gradient flow to LSTM-A. So the modified loss function is as follows:

$$L(\theta) = \frac{1}{T}\sum_{t=1}^{T}\|x_t - \hat{x}_t(\theta)\|^2 + \lambda\left\|x_t - \hat{x}'_t(\theta)\right\|^2, \tag{27}$$

where x_t the real target motion state at time t, $\hat{x}_t(\theta)$ is the result of state estimation values at time t, and $\hat{x}'_t(\theta)$ is the intermediate result estimated by LSTM-A. The super parameter λ is empirically set to 0.7.

4.5. Training Optimization. Our goal is to find the optimal fixed parameter sets, which are able to make the loss caused by all free parameters in the complex loss function minimized. These parameters are the sum of all weight and bias parameters of all three LSTM modules. The optimization process is often nonconvex. Facing many local minima, we only need to achieve a small enough local minimum. That is adequate for our practice [24].

To train the model, we use the back propagation time algorithm [25] to obtain the gradient. The gradient update is performed according to the commonly used Adam [26] optimizer.

The huge training data set may increase the computational complexity of gradient calculation. In order to overcome this problem, we only use a small batch of training data to update the parameters in each iteration. The benefits are selecting the descent direction accurately for every gradient descent and reducing the training shock, within a certain range. However, the defects are increasing the number of iterations, rising the operation time and slowing parameters modification. There is no final conclusion on how to select the batch size. Too small batch will introduce more noise, and too large batch will increase the training shock [27, 28].

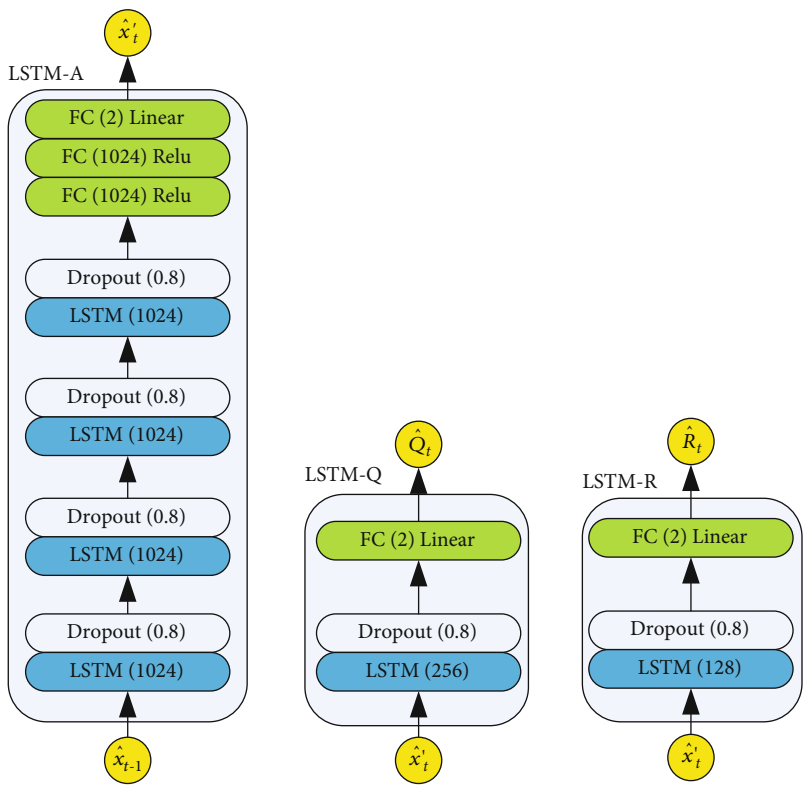

Figure 2: LSTM-A, LSTM-Q, and LSTM-R architecture. As detailed below, the LSTM-A, LSTM-Q, and LSTM-R are composed of different neuron layers in KFFLSTM.

For the sake of suppressing the problem of gradient explosion, the gradient clipping mechanism is introduced. When the weight is updated too quickly in the iteration, it is easy to lead to loss divergence. Therefore, we need to cut the gradient. By controlling the maximum normal form of the gradient, we limit the weight to update in an appropriate range, which effectively restrain the gradient problem.

5. Experiments

In this section, in order to show the tracking performance of the designed KFFLSTM structure for nonlinear targets, we compare the performance with a series of common nonlinear target tracking algorithms, including EKF, UKF, PF, IMM, and B-LSTM structure. This B-LSTM structure, proposed in [19], is the representative of a kind of model, whose feature is using two whole LSTMs to learn the prediction step and measurement update step from the training data, respectively.

5.1. Dataset. Specifically, we use a typical nonlinear time series model. This model is widely used in the literature as a benchmark numerical filtering technique to demonstrate performance improvement [29, 30]. The state space equation is as follows:

$$x_k = \frac{x_{k-1}}{2} + 25\frac{x_{k-1}}{1+x_{k-1}^2} + 8\cos(1.2k) + u_k,$$
$$z_k = \frac{x_k^2}{2} + v_k, \tag{28}$$

where the process noise distribution is $u_k \sim N(0, \sigma_u^2)$, $\sigma_u^2 = 10$. The observed noise distribution is $v_k \sim N(0, \sigma_v^2)$, $\sigma_v^2 = 1$. The initial state distribution is $x_0 \sim N(0, 10)$.

Through the simulation of the model, the training data set can be obtained. Specifically, the random observation target was generated within a certain observation time, and the initial position was randomly set within a certain range. We produced 64 random path observation data, respectively, by simulating the target state sequence and the corresponding observation sequence, resulting in a total of 65536×2 observation data. It was assumed that the data variable of interest was set as the position state of the observation target.

In the implementation of LSTM network structure, adopting the network structure mentioned above, the scale of network parameters is nearly 307460 parameters, whose best values need to be achieved by training process using the loss function and optimization method described in Section 3. The initial learning rate of training KFFLSTM structures is set to $1e-5$ and attenuates to 0.9 from the second cycle. For this training, we use reduced time back propagation to propagate gradients of 64 time steps, and the batch size is set to 16. In the test stage, we simulated the test data set containing 1024 target state sequences and corresponding observation sequences to verify the enhancement of performance.

5.2. Performance Comparison. In the test, we selected some traditional methods, widely used to solve the nonlinear target tracking problem [29], EKF, UKF, IMM, PF, and the single LSTM method B-LSTM as the baseline to compare

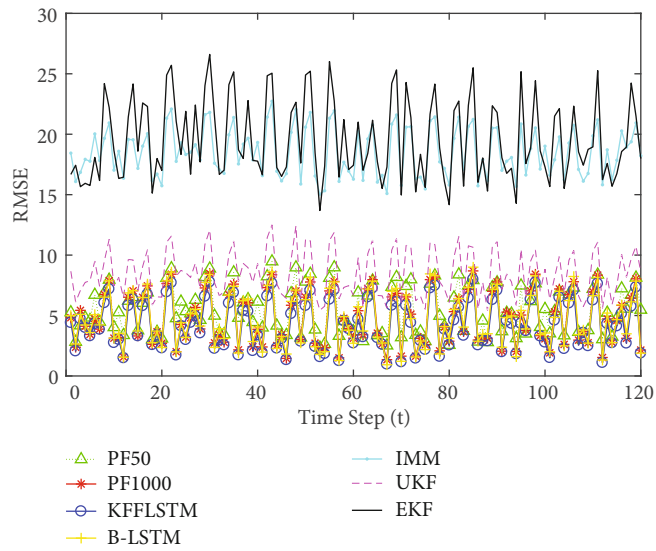

Figure 3: The RMSE of KFFLSTM compared with other baseline methods. Our method performs better than the traditional method and single LSTM method.

with the designed KFFLSTM structure. The IMM method selected CV and CT models to switch. The PF method simulated the performance of 50 particles and 1000 particles, respectively. These above algorithms all have performed 500 Monte Carlo calculations and obtained the root mean square error (RMSEs) of each time step, as shown in Figure 3.

As shown in Figure 3, for this typical nonlinear time series target tracking, EKF performs worse than sampling methods (UKF and PF) and LSTM-based methods. The multimodel method IMM only selects the commonly used CV and CT models for switching, so its performance is similar to EKF. For the PF method, the performance of 1000 particles is slightly worse than that of B-LSTM method. Our proposed KFFLSTM performs better than B-LSTM. It is worth noting that although the traditional methods are very different from the proposed LSTM network methods in solving the nonlinear target tracking problem, the fluctuation of RMSE curve is similar. This shows that these methods can achieve the purpose of tracking, but the accuracy is different.

In addition, we also compared the average running time and average RMSE of each iteration of various methods under the condition of using the same CPU, as shown in Table 1.

Because the estimation accuracy of EKF, UKF, and IMM is far from that of other methods, we focus on the comparison between PF and LSTM methods. It can be seen that our proposed KFFLSTM can provide accurate estimation in a short calculation time. Compared with PF with 50 particles, the accuracy is improved by 27.3% and the calculation time is shortened by 45.5%. Compared with 1000 particle PF, the accuracy is improved by 14.5%, and the calculation time is reduced by 96.8%. Compared with the B-LSTM method, this method improves the accuracy by 13.2%, but the running time is slightly longer. This may be because KFFLSTM not only needs to calculate a similar number of gradients but also has to calculate many matrix operations, including the inversion of the square matrix in Equation (23), at each time step.

Table 1: Table of the main algorithms, RMSE values, and runtimes at each iteration.

Algorithms	RMSE	Run times
PF (50 particles)	5.532	1.424 ms
PF (1000 particles)	4.758	24.32 ms
KFFLSTM	4.235	0.775 ms
B-LSTM	4.732	0.453 ms

5.3. Influence of Different Noise Variances. In order to carry out this experiment, we change the observation noise variance and motion noise variance, respectively, to dynamically simulate the impact of mobility change or measurement error change on the estimation effect of these methods.

Firstly, our simulation uses the same initial state and fixed motion noise variance to calculate the average RMSE of PF50, PF1000, B-LSTM, and KFFLSTM methods, when the observed noise distribution variance is set to the typical value of 1, 10, 50, and 100, as shown in Figure 4.

As shown in Figure 4, when the observation variance increases by order of magnitude, the RMSE of PF1000 changes a little and increases slightly, while the RMSE of PF50 changes greatly and increases significantly. The RMSE of B-LSTM and KFFLSTM nearly remain the same.

Secondly, our simulation uses the same initial state and fixed the observation noise distribution variance to calculate the average RMSE of PF50, PF1000, B-LSTM, and KFFLSTM methods, when the motion noise variance is set to the typical value of 1, 10, 50, and 100, as shown in Figure 5.

As shown in Figure 5, when the motion variance increases by order of magnitude, the RMSE change of PF1000 and PF50 increases significantly. The RMSE of B-LSTM increases slowly, and KFFLSTM increases slightly.

This shows that the two LSTM-based methods are insensitive to the mobility change of nonlinear tracking target and the change of measurement error compared with the

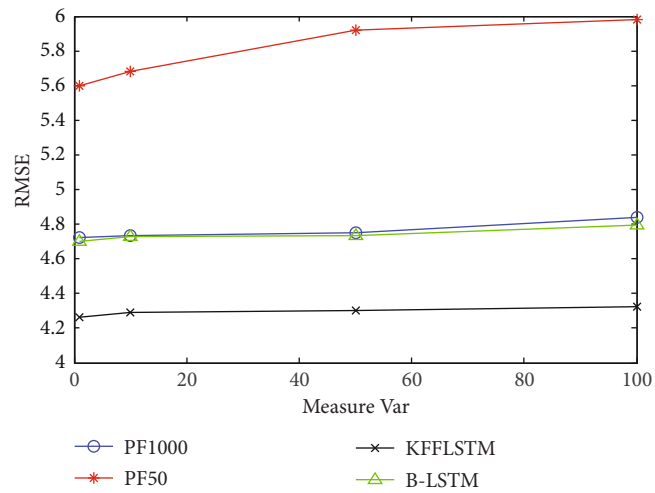

Figure 4: The RMSE of KFFLSTM with different measure noise variance. RMSE curve of our method and B-LSTM increases slightly.

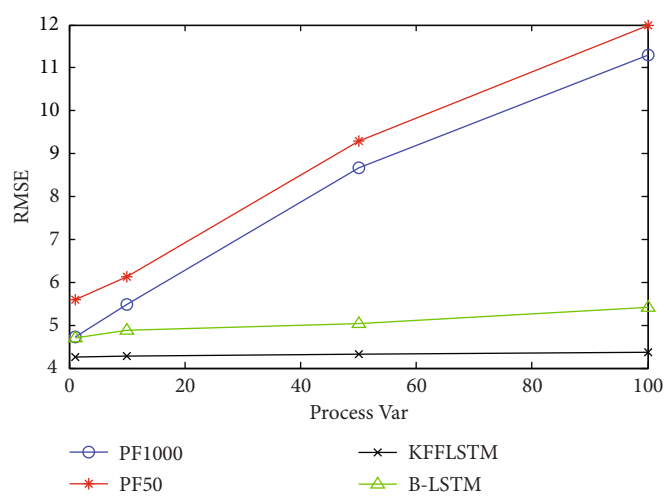

Figure 5: The RMSE of KFFLSTM with different process noise variance. Our method's RMSE curve basically remained unchanged.

traditional methods. Especially, the antisensitivity of KFFLSTM described in this paper is stronger than that of LSTM alone method.

5.4. Influence of Initial a Prior. In our experiment, we assumed that the initial a priori motion state of the target is known, that was to say, the initial a priori of the test data and the training data were considered to be the same. However, in practice, the initial state of the actual target is often unexpected. Once it is out of the distribution range of training data, this will lead to poor tracking effect of the model on test data [30]. In order to solve this problem, we may increase the support range of the initial a priori of training data theoretically, but the price is more training data required.

To verify this, we simulated the training data with different initial state distribution range and the same test data set and calculated the RMSE of the KFFLSTM, respectively, as shown in Table 2. The results show that the estimation accuracy of the model remains almost unchanged as long as the initial prior distribution of the training data can cover the initial prior distribution of the test data.

Table 2: RMSE of the KFFLSTM trained with different initial prior data sets.

Training data initial prior distribution	Test data initial prior distribution	RMSE of KFFLSTM
N (0, 10)	N (0, 10)	4.235
N (0, 100)	N (0, 10)	4.238
N (0, 500)	N (0, 10)	4.237
N (0, 1000)	N (0, 10)	4.239

6. Conclusion

Against nonlinear moving target tracking, KFFLSTM structure combining LSTM and Kalman filter is proposed in this

paper. This creative structure is able to learn the nonlinear motion process, motion noise, and measurement noise from massive training data and then apply it to the Kalman filter equations to complete the accurate estimation of the target motion states. It not only does not need to specify the motion model and noise model in advance but also is capable of learning the nonlinear motion model through the data, which is very difficult to record explicitly. The experimental data indicate that compared to the traditional methods, this method estimates the states more accurately within a shorter calculation time and also performs better than the single LSTM method.

What this paper provides is only a preliminary algorithm. In the future, with the continuous development of LSTM or RNN, its performance in the field of nonlinear tracking will be continuously improved.

Data Availability

The experimental data used to support the findings of this study are available from the corresponding author upon request.

Conflicts of Interest

The authors declare that there are no conflicts of interest regarding the publication of this article.

Acknowledgments

This research was supported by the Fundamental Research Funds for the Central Universities under Grant 3102019ZX015, the Aeronautical Science Foundation of China under Grant 2019ZH0T7001, the Scientific Research Foundation of Xi'an Aeronautical University under Grant 2019KY0207, and the Fundamental Research Funds for the Central Universities under Grant D5000220131.

References

[1] R. E. Kalman, "A new approach to linear filtering and prediction problems," *Journal of Basic Engineering*, vol. 82, no. 1, pp. 35–45, 1960.

[2] H. Kushner, "Approximations to optimal nonlinear filters," *IEEE Transactions on Automatic Control*, vol. 12, no. 5, pp. 546–556, 1967.

[3] S. J. Julier, J. K. Uhlmann, and H. F. Durrant-Whyte, "A new approach for filtering nonlinear systems," in *Proceedings of 1995 American Control Conference-ACC'95. IEEE*, pp. 1628–1632, Seattle, WA, USA, 1995.

[4] A. Doucet, S. Godsill, and C. Andrieu, "On sequential Monte Carlo methods for Bayesian filtering," *Statistics and Computing*, vol. 10, no. 3, pp. 197–208, 2000.

[5] X. R. Li, X. Zhi, and Y. Zhang, "Multiple-model estimation with variable structure. V. likely-model set algorithm," *IEEE Transactions on Aerospace and Electronic Systems*, vol. 36, no. 2, pp. 448–466, 2000.

[6] X. Wang, S. Challa, R. J. Evans, and X. R. Li, "Minimal submodel-set algorithm for maneuvering target tracking," *IEEE Transactions on Aerospace and Electronic Systems*, vol. 38, no. 4, pp. 1218–1231, 2003.

[7] P. Ondruska and I. Posner, "Deep tracking: seeing beyond seeing using recurrent neural networks," in *Proceedings of the Thirtieth AAAI Conference on Artifificial Intelligence*, pp. 3361–3367, Phoenix, Arizona, 2016.

[8] M. Q. Liu, Z. L. Liu, W. D. Lu, Y. Chen, X. Gao, and N. Zhao, "Distributed few-shot learning for intelligent recognition of communication jamming," *IEEE Journal of Selected Topics in Signal Processing*, vol. 16, no. 3, pp. 395–405, 2022.

[9] M. Q. Liu, B. Li, Y. F. Chen et al., "Location parameter estimation of moving aerial target in space-air-ground integrated networks-based IoV," *IEEE Internet of Things Journal*, vol. 9, no. 8, pp. 5696–5707, 2022.

[10] M. Q. Liu, C. H. Liu, M. Li, Y. Chen, S. Zheng, and N. Zhao, "Intelligent passive detection of aerial target in space-air-ground integrated networks," *China Communications*, vol. 19, no. 1, pp. 52–63, 2022.

[11] M. Q. Liu, J. K. Wang, N. Zhao, Y. Chen, H. Song, and R. Yu, "Radio frequency fingerprint collaborative intelligent identification using incremental learning," *IEEE Transactions on Network Science and Engineering*, 2021.

[12] Y. LeCun, Y. Bengio, and G. Hinton, "Deep learning," *Nature*, vol. 521, no. 7553, pp. 436–444, 2015.

[13] C. Gao, H. Liu, S. Zhou et al., "Maneuvering target tracking with recurrent neural networks for radar application," in *2018 International Conference on Radar (RADAR)*, pp. 1–5, Brisbane, QLD, Australia, 2018.

[14] T. Haarnoja, A. Ajay, S. Levine, and P. Abbeel, "Backprop KF: learning discriminative deterministic state estimators," *Advances in Neural Information Processing Systems*, vol. 29, pp. 1132–1143, 2016.

[15] H. Coskun, F. Achilles, R. DiPietro, N. Navab, and F. Tombari, "Long short-term memory Kalman filters: recurrent neural estimators for pose regularization," in *Proceedings of the 2017 IEEE International Conference on Computer Vision*, pp. 5525–5533, Venice, Italy, 2017.

[16] C. Gao, J. Yan, S. Zhou, B. Chen, and H. Liu, "Long short-term memory-based recurrent neural networks for nonlinear target tracking," *Signal Processing*, vol. 164, pp. 67–73, 2019.

[17] J. P. Llerena Caña, J. García Herrero, and J. M. Molina López, "Forecasting nonlinear systems with LSTM: analysis and comparison with EKF," *Sensors*, vol. 21, no. 5, pp. 1805–1820, 2021.

[18] Z. Zhang, M. Hou, F. Zhang, and C. R. Edwards, "An LSTM based Kalman filter for spatio-temporal ocean currents assimilation," in *Proceedings of the International Conference on Underwater Networks & Systems*, pp. 1–7, Atlanta, GA, USA, 2019.

[19] F. Song, Y. Li, Y. Bi, and M. Li, "Radar maneuvering target tracking based on LSTM network," in *Advances in Natural Computation, Fuzzy Systems and Knowledge Discovery*, pp. 1780–1791, Springer, Cham, 2021.

[20] S. Hochreiter and J. Schmidhuber, "Long short-term memory," *Neural Computation*, vol. 9, no. 8, pp. 1735–1780, 1997.

[21] F. A. Gers, J. Schmidhuber, and F. Cummins, "Learning to forget: continual prediction with LSTM," *Neural Computation*, vol. 12, no. 10, pp. 2451–2471, 2000.

[22] K. Greff, R. K. Srivastava, J. Koutník, and R. Bas, "LSTM: a search space odyssey," *IEEE Transactions on Neural Networks and Learning Systems*, vol. 9, no. 7, pp. 1031–1047, 2016.

[23] R. G. Krishnan, U. Shalit, and D. Sontag, "Deep kalman filters," 2015, https://arxiv.org/abs/1511.05121.

[24] A. Tarsauliya, S. Kant, R. Kala, R. Tiwari, and A. Shukla, "Analysis of artificial neural network for financial time series forecasting," *International Journal of Computer Applications*, vol. 9, no. 5, pp. 16–22, 2010.

[25] P. J. Werbos, "Backpropagation through time: what it does and how to do it," *Proceedings of the IEEE*, vol. 78, no. 10, pp. 1550–1560, 1990.

[26] D. Kingma and J. Ba, "Adam: a method for stochastic optimization," 2014, https://arxiv.org/abs/1412.6980.

[27] N. S. Keskar, D. Mudigere, J. Nocedal, M. Smelyanskiy, and P. T. P. Tang, "On large-batch training for deep learning: generalization gap and sharp minima," 2017, https://arxiv.org/abs/1609.04836.

[28] S. L. Smith, P. J. Kindermans, C. Ying, and Q. V. Le, "Don't decay the learning rate, in crease the batch size," *Proceedings of the International Conference on Learning Representations*, vol. 1, pp. 1280–1293, 2018.

[29] M. S. Arulampalam, S. Maskell, N. Gordon, and T. Clapp, "A tutorial on particle filters for online nonlinear/non-Gaussian Bayesian tracking," *IEEE Transactions on Signal Processing*, vol. 50, no. 2, pp. 174–188, 2002.

[30] S. Ben-David, J. Blitzer, K. Crammer, A. Kulesza, F. Pereira, and J. W. Vaughan, "A theory of learning from different domains," *Machine Learning*, vol. 79, no. 1-2, pp. 151–175, 2010.

Hindawi
Wireless Communications and Mobile Computing
Volume 2022, Article ID 9680479, 10 pages
https://doi.org/10.1155/2022/9680479

Research Article

Deep Learning-Based Localization with Urban Electromagnetic and Geographic Information

Wenyu Wang,[1] **Baozhu Li**,[2] **Zhen Huang**,[2] **and Lei Zhu**[1]

[1]*College of Communications Engineering, Army Engineering University of PLA, Nanjing 210001, China*
[2]*Beijing National Research Center for Information Science and Technology, Tsinghua University, Beijing 100089, China*

Correspondence should be addressed to Zhen Huang; huangzhen@tsinghua.edu.cn and Lei Zhu; zhulei_paper@126.com

Received 12 May 2022; Revised 1 August 2022; Accepted 11 August 2022; Published 21 August 2022

Academic Editor: Mingqian Liu

There is a growing demand for localization of illegal signal sources, aiming to guarantee the security of urban electromagnetic environment. The performance of traditional localization methods is limited due to the non-line-of-sight (NLOS) propagation and sparse layouts of sensors. In this paper, a deep learning-based localization method is proposed to overcome these issues in urban scenarios. Firstly, a model of electromagnetic wave propagation considered with geographic information is proposed to prepare reliable datasets for intelligent cognition of urban electromagnetic environment. Then, this paper improves an hourglass neural network which consists of downsampling and upsampling layers to learn the propagation features from sensing data. The core modules of VGG and ResNet are, respectively, utilized as feature extractors in downsampling. Moreover, this paper proposes a weighted loss function to expand the attention on position features, in order to improve the performance of localization with sparse layouts of sensors. Representative numerical results are discussed to assess the proposed method. ResNet-based extractor performs more efficiently than VGG-based extractor, and the proposed weighted loss function increases the localization accuracy by more than 50%. Additionally, the established geographic model supports qualitative and quantitative evaluation of the robustness with varied degree of NLOS propagation. Compared with other deep learning-based algorithms, the proposed method presents the more robust and superior performance under severe NLOS propagation and sparse sensing conditions.

1. Introduction

Along with the acceleration of social urbanization and informatization progresses, human activities have been concentrated in urban areas. The urban electromagnetic environment has become much more complex as well. Illegal signal sources in the cities encroach the spectrum resources without a valid license or even cause harmful interference, which probably leads to the loss of data and other critical faults in the communication systems [1]. As a result, localization of illegal signal sources is significant to guarantee the security of the urban electromagnetic environment. Wireless sensor networks (WSN) [2] utilize a set of sensors to monitor the electromagnetic activities in the target area. These sensors are characterized by small volume and low power, working in concert for localization by collecting and processing the signal parameters such as time of arrival (TOA), time difference of arrival (TDOA), angle of arrival (AOA), and received signal strength (RSS) [3].

However, it is unavoidable for the reflections and diffractions of electromagnetic wave to create non-line-of-sight (NLOS) propagation due to the dense buildings in urban scenarios. Compared with line-of-sight (LOS) propagation, it results in longer propagation distance and time, so that the localization errors reach to hundreds of meters [4]. In this case, traditional geometry-based positioning methods require at least three LOS paths between sensors and signal sources to solve nonlinear equations (such as TOA-based, TDOA-based, AOA-based, and RSS-based equations) which are susceptible to severe NLOS propagation conditions [5–8].

Addressing the challenges of localization in urban environment, researchers focus on the reduction of the estimation errors for signal parameters by identifying and discarding the sensing data of NLOS or changing the weight of NLOS data

[9–13]. These solutions, in essence, still apply LOS paths for localization as much as possible, but LOS paths are not available in complex urban scenarios. Furthermore, there are also some approaches (e.g., [14–16]) mitigating the NLOS errors by nonlinear optimization, convex relaxation, and other algorithms with prior information. A solution based on robust least squares and semidefinite relaxation is suggested in [16]. It is able to carry out the localization with only one LOS path but requires prior knowledge of the upper bound loss in NLOS propagation. However, the prior knowledge is difficult to obtain in the complex electromagnetic environment. Additionally, with the development of modern geographic information system (GIS) techniques, geographic models are introduced into relevant field [17, 18]. A floor map [19] is used to initialize and update the landmark graph for indoor localization with the aid of multifunction sensing components. In [20], the environmental information is imported into the proposed quasi 3D ray-tracing model to construct the synthetic radio map, and then, the refined radio map is used to prepare the training datasets for the indoor intelligent target intrusion sensing and localization. Focusing on the localization under NLOS conditions, Zhang et al. [21] correct the NLOS errors with the aid of 3D mapping database and employ factor graph optimization for the positioning calculation in global navigation satellite system. Perez-Cruz et al. [22] propose a probabilistic algorithm to learn and correct the NLOS biases. The above approaches are all generalized by two steps, i.e., calibrate the parameter estimation errors caused by NLOS propagation and solve the positioning equations by various optimization algorithms. Undeniably, such solutions are mathematically intractable and faced with double challenges from parameter estimation errors and localization errors.

From another perspective, since the NLOS propagation channels are relatively stable in a certain urban area with known geographic information, solutions of localization can be formulated to seek for the mapping of signal positions with sensing data by learning the NLOS propagation features in the target area, which offers an end-to-end intelligent cognition service. Deep learning has been proved to be an efficient tool in a wide range of fields due to its outstanding capability to capture the features and learn the mapping of data [23, 24]. Recently, several researches [25–27] apply deep neural networks (DNN) for end-to-end localization and gain some improvement. A long short-term memory (LSTM) network is used in [25] for small-scale indoor localization. Lin et al. [26] suggest a heatmap regression-based HMTLNet, revealing the active role of ResNet in a fully convolutional network (FCN) for localization. Zhan et al. [27] present a convolutional neural network (CNN) to solve localization problems from a view of computer vision. However, there are mainly two challenges of these methods.

(1) The empirical and statistical propagation model used in simulated validation (e.g., [25, 26]) is far from the actual electromagnetic propagation data, without considering the geographical distribution in urban areas

(2) The existing deep learning-based localization methods require massive data and dense deployment of sensors for perception of the target area. For example, the density of sensors in DeepMTL method [27] is 2 percent, with the number of sensors reaching to 200 in a $1\,\mathrm{km} \times 1\,\mathrm{km}$-sized area, which is costly in practice

To adapt to the NLOS propagation and sparse layouts of sensors, a localization method based on the intelligent cognition of urban electromagnetic environment is proposed in this paper. The main contribution is that geographic information is considered in the electromagnetic wave propagation model. The model prepares datasets which are closer to actual electromagnetic propagation. More specifically, an hourglass neural network and a weighted loss function are proposed to predict the position probability distribution with the sparse sensing data in urban electromagnetic environment. Finally, the performance of the proposed method is verified on the reliable datasets with extremely sparse sensors.

The rest of this paper is organized as follows. In Section 2, reliable datasets are prepared with the aid of geographic information. In Section 3, the proposed deep learning-based localization method is depicted in detail. In Section 4, the comparative simulations with different density of sensors are presented and discussed. Finally, conclusions are stated in Section 5.

2. Data Preparation

In this section, we introduce the urban propagation model considered with geographic information and the prepared datasets for intelligent cognition.

2.1. The Urban Propagation Model with Geographic Information. NLOS propagation is mainly caused by ray blocking from varied objects in urban scenarios. The layouts and positions of urban objects are essential on the analysis of NLOS propagation. Generally, the GIS data are open access, which contains the distribution of buildings, vegetation, rivers, and other objects. Based on the GIS information, the geographic model G is established. This paper is aimed at learning features in NLOS propagation with the aid of geographic information, demanding of massive data. Calculating accurate electromagnetic wave propagation is the core step to prepare effective datasets for deep learning-based localization. Empirical or statistical electromagnetic propagation models (e.g., COST 231 Walfisch-Ikegami propagation model [28]) only consider statistical features of different geographic scenarios roughly but take no account of the specific geographic models of the study area. Hence, they are prone to deviate a lot from practical propagation. According to the interactions between electromagnetic waves and urban geographical objects, ray-tracing model [29] is able to track hundreds of propagation paths for each receiving sensor but is susceptible to small errors in geographic models. Considering geographic information, Wahl et al. [30] propose dominant path model (DPM). In [31], DPM has been proved as a more accurate and robust electromagnetic propagation model than intelligent ray tracing

(IRT) model and the COST 231 Walfisch-Ikegami model in complex urban scenarios. Therefore, in this paper, DPM is utilized to calculate the propagation loss based on the established geographic model G.

Assume that the illegal signal source is located at $s_i = (x_i, y_i)$, and coordinates of all receiving points (different from the definition of sensor positions) in G are collected in the set $M = \{m_1, m_2, \cdots, m_Q\}$. Then, the length of the propagation path between the signal source and a receiving point is formulated as $d(s_i, m_j \in M(s_i))$, which also includes the case that the direction of propagation is changed by blocking. The function $f(\varphi, k)$ in dB means the kth interaction loss with the new propagation direction φ. Therefore, the predicted loss in G is calculated as

$$L(s_i, m_j) = -27.56 + 20 \log (f) + 10p \log (d(s_i, m_j)) + \sum_{k=0}^{n} f(\varphi, k) - \frac{1}{c} \sum_{u=0}^{c} w_u. \quad (1)$$

Here, f is the electromagnetic wave frequency in MHz. The factor p depends on the LOS or NLOS condition of the propagation path. And w is the waveguiding factor which represents the effect of reflection along the walls in dominant path.

Since RSS is easily acquired in receiving sensors, we collect RSS as sensing parameters. The RSS at m_j is expressed as

$$P_r(s_i, m_j) = P_t(s_i) - L(s_i, m_j), \quad (2)$$

where $P_r(s_i)$ means the transmission power of the signal source at s_i. For the whole target area, the RSS from each receiving point is collected into the set $H_{\text{full}} = \{P_r(s_i, m_j)\}$. However, it is impractical to deploy sensors densely. This paper focuses on the localization solutions by learning the propagation features from sparse sensing data. The following is the generation of sparse sensing datasets for deep learning.

2.2. Dataset Preparation. Intelligent cognition of the mapping between sparse sensing data and signal positions is driven by the calculation of electromagnetic data with geographic model. Toward this end, there are three steps to generate the datasets.

Step 1. Calculate the H_{full} of the target area with fixed signal source position s_i, and then extract RSS for sparse sensors from H_{full}. The set of sensor positions is expressed as $V = \{v_1, v_2, \cdots, v_N\}$ with $N \ll Q$ and $V \subseteq M$. Therefore, the RSS of sensors is

$$P_r(V) = P_r(s_i, m_j), m_j \in V. \quad (3)$$

Step 2. Convert RSS data of sensors into an image matrix where the sensing data are combined with sensor positions. Corresponding to the size of target area, the image matrix is established as

$$I(x, y) = \begin{cases} P_r, & (x, y) \in V, \\ 0, & (x, y) \notin V. \end{cases} \quad (4)$$

There are RSS values at the sensor positions, while others are zeros. The DNN is aimed at capturing both geographic and propagation features from the input matrix I.

Step 3. Predict the signal source position in terms of probability distribution. Different from conventional datasets labeled with two-dimensional coordinates, the labels in our dataset are expressed in the image matrix Y with the same size as I. The maximum probability value in Y is 1, located at the true position, and others are zeros. The output $\hat{Y} = f_{\text{DNN}}(I)$ of the neural network is expected as a probability matrix where the higher the probability is predicated, the closer to the true position.

Then, a fusion dataset is obtained with fixed sensor positions. Its size depends on the number of samples with varied signal positions. In the training dataset, positions of signal sources traverse the target area by gird. In the validation and testing dataset, positions of signal sources are randomly generated in the target area. In addition, different datasets are created by changing the positions and number of sensors. Consequently, there are two advantages of the proposed fusion datasets.

(1) In content, the fusion datasets are collected based on the electromagnetic propagation calculation fused with geographic models, and the datasets are more effective than other simulation datasets based on the empirical or statistical propagation models. Hence, it is more persuasive to verify the validity of proposed localization method by applying the effective datasets

(2) On structure, the fusion datasets are framed in image matrices including position features of sensors and signal sources, highlighting the propagation characteristic from different positions. Besides, compared with the datasets based on the practical measurement, it is more flexible for the proposed datasets to adjust sensor distribution to satisfy the requirements of researches

In conclusion, the proposed method can be used to generate authentic datasets flexibly and efficiently with accessible geographic models.

3. Deep Learning-Based Localization Method

The deep learning-based localization works in two stages, i.e., training stage and localization stage. During the training stage, DNN is driven by fusion datasets to minimize the errors between the predicated matrix $\hat{Y}$ and the label Y, in order to boost the cognition for the NLOS propagation channels. During the localization stage, the sensing image

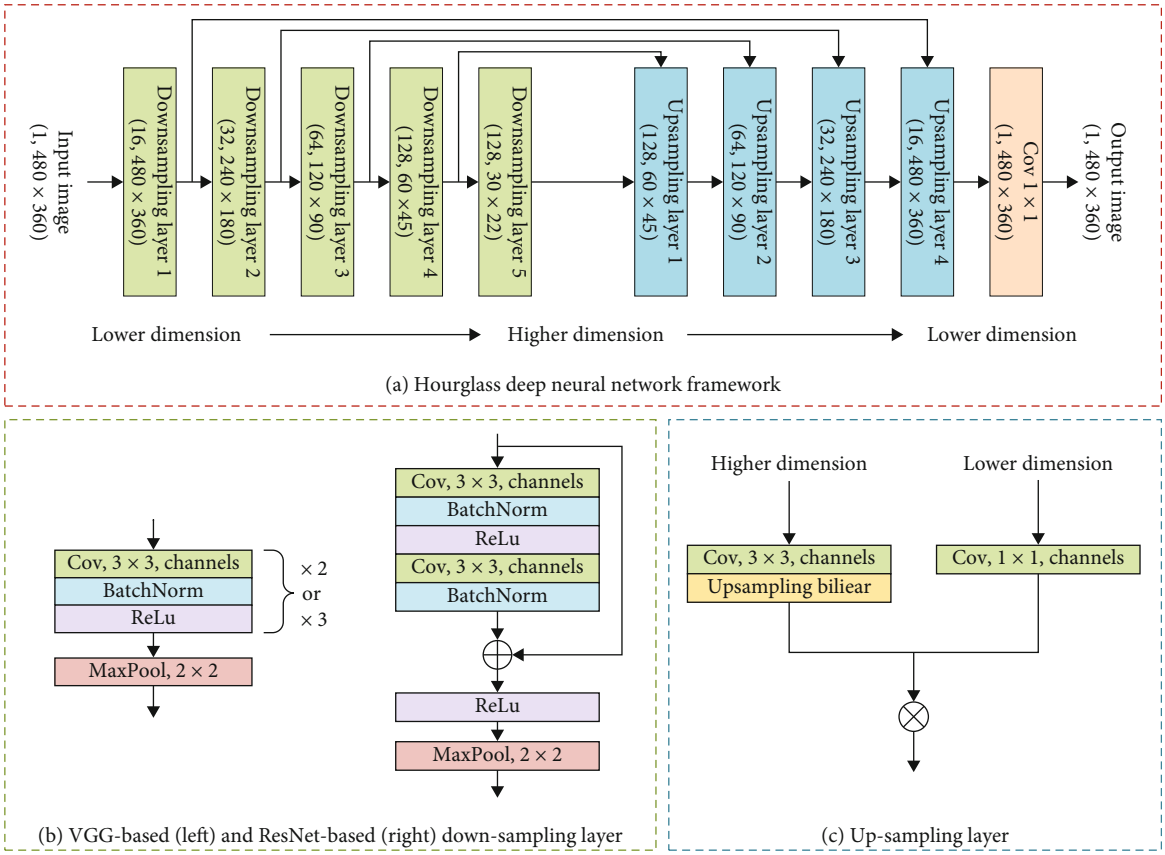

Figure 1: The structure and core modules of hourglass deep neural network.

matrix is sent into the trained network to output the probability matrix. The pixel with the peak value in the output matrix is predicted as the position of single signal source.

In order to improve localization under the sparse layout of sensors, an hourglass architecture is applied to capture multiscale features from the sparse input I. In addition, a weighted loss function is proposed to help the hourglass network pay more attention to the position feature from the sparse label Y.

3.1. The Hourglass Architecture in DNN. Most neural networks extract and learn the features via downsampling, whereas hourglass networks [32] carry out the upsampling after downsampling. In this paper, the upsampling is used to learn the position probability distribution from the multidimensional features extracted by the downsampling. Specifically, the higher-dimensional and lower-dimensional features are combined in the upsampling layers to generate the probability matrix, and the output is restored into the original size of input image gradually. As shown in Figure 1, the hourglass network in this paper contains five downsampling layers and four upsampling layers.

During the downsampling in this paper, the core modules of VGG [33] and ResNet [34] are taken as the feature extractors, respectively. VGG is a convolutional deep neural network proposed in 2014. Each convolutional module consists of a convolutional layer with the kennel of 3×3, a batch normalization layer, and an activation layer with the ReLu function, which leads a deep capture for features. ResNet-based extractor is motivated by the residual module, which has a skip connection between the input and output of a stack of two convolutional layers. And then, the fusion feature is activated by the ReLu function. Moreover, thanks to the max pooling layer after the convolutional module or the residual module, the feature maps become smaller from the lower dimension to the higher dimension.

During the upsampling, the higher-dimensional features and the lower-dimensional features are, respectively, unified in channels by the 3×3 convolutional layer and the 1×1 convolutional layer at first. Next, the bilinear interpolation is adopted to scale up the higher-dimensional feature maps. Then, multiply the higher-dimensional feature maps and the lower-dimensional to realize the fusion of different feature dimensions. Progressively, the size of data turns back to the same as input. Finally, an output matrix $\widehat{Y}$ is obtained through a convolutional layer.

3.2. The Proposed Weighted Loss Function. The training stage is intended to minimize the loss between the output $\widehat{Y}$ and the label Y. The loss function is expressed in mean square error (MSE) as follows:

$$L_{\mathrm{MSE}} = \frac{1}{n}\sum_{i=1}^{n}\left(\widehat{\mathrm{Y}}_i - \mathrm{Y}_i\right)^2. \tag{5}$$

The label Y is extremely sparse, which is intractable for the hourglass network to concentrate on the features around the signal position. Therefore, a weighted loss function is proposed in this section. Without any prior information of illegal signal sources, it is difficult to calculate the weight at each pixel of the matrix precisely. However, we cannot overlook the fact that a higher number of weight should be assigned if it is closer to the true position. Assume that the weight distribution is centered on the label position and decreases around with the two-dimensional normal distribution probability density function. The weight matrix W with the same size as the input and output is expressed as

$$W_i(x, y) = \frac{1}{2\pi\sigma^2} \exp\left\{-\frac{1}{2\sigma^2}\left[(x - x_i)^2 + (y - y_i)^2\right]\right\}, \quad (6)$$

where (x_i, y_i) means the coordinate of the illegal signal source s_i, as well as the weighted center. Weighted radius is set as $R = 3\sigma$, which means there is a 99.7 percent chance that the signal source is located in the weighted area. More specifically, the hourglass network expands the attention on the position feature from single pixel to an area of the radius R via the weighted method. The weighted loss function is determined as follows:

$$L_{\mathrm{WMSE}} = \frac{1}{n}\sum_{i=1}^{n} \mathrm{W}_i\left(\widehat{\mathrm{Y}}_i - \mathrm{Y}_i\right)^2. \quad (7)$$

The RMSProp optimizer and backpropagation algorithm are used for training until the loss falls below a threshold or the iteration reaches to a certain number.

In the stage of localization, the RSS data are collected from sensors and converted into the image data. Successively, the trained hourglass network is expected to predict the probability matrix from the sensing image. For the localization task with single signal source, the predicted position is calculated as

$$\widehat{s}_i(\widehat{x}_i, \widehat{y}_i) = \underset{\widehat{x}_i, \widehat{y}_i}{\mathrm{argmax}}\left(\widehat{Y}\right). \quad (8)$$

4. Results and Discussion

4.1. Simulation Setup. As is shown in Figure 2, the geographic model of Tsinghua University is established for the following simulations. A study area with the size of 480 m × 360 m is marked in the red box. Accordingly, the input and output data are 480 ×360-sized image matrices. Based on the geographic model, the RSS set H_{full} is obtained by a software called WinProp [35] which supports the calculation for DPM. The calculation resolution is set to 1 m, representing the interval between receiving points in H_{full} is 1 m. The frequency of signal source is set to 1800 MHz, and the transmission power is 43 dBm, which are unknown for DNN. All simulation parameters are set in detail according to Table 1. Figure 3(a) shows the RSS distribution in the whole study area, which reveals the nonuniform attenuation of radio wave propagation to the surrounding due to the blocking of buildings etc. In Figure 3(b) about the LOS/NLOS distribution, the NLOS propagation paths account for a huge proportion in the urban scenario.

Figure 2: The established three-dimensional geographic model of Tsinghua University (grey, green, and blue objects, respectively, represent buildings, vegetation, and rivers).

Four groups of datasets are set up with varied number of sensors, i.e., 48, 12, 8, and 4. The sensors are uniformly deployed as shown in Figure 4. Compared with most datasets in deep learning-based localization methods [26, 27], the sensor density in our datasets is extremely sparse. For the training datasets, the traversal gird of signal source positions is set into a size of 3 m × 3 m, generating 19200 samples to learn the propagation features of the whole study area. The learning rate is set to 0.001, and the training epoch is 20. To evaluate the performance of the localization in the testing stage, the mean positioning error of the $n_s = 2400$ samples are calculated by

$$e = \frac{1}{n_s}\sum_{i}^{n_s} \sqrt{(x_i - \widehat{x}_i)^2 + (y_i - \widehat{y}_i)^2}. \quad (9)$$

Additionally, in this paper, PyTorch is the basis of the deep learning algorithm framework. All simulations are implemented on an RTX2080ti GPU with 96 GB of RAM.

4.2. Results and Evaluation

4.2.1. Comparison of VGG-Based and ResNet-Based Extractor. In this paper, VGG and ResNet are, respectively, applied as feature extractors in downsampling of the hourglass network. From Figure 5, the two extractors achieve satisfactory localization results with the errors of about 2 m when the total number of sensors is 48. With the reduction of sensors, the positioning errors present an upward trend, whereas the ResNet-based extractor suffers less severe degradation than VGG-based extractor. It is indicated that the residual module plays an active part to extract features from sparse input image, which benefits from the fusion of multiscale features though the skip connections. Nonetheless, when there are only 4 sensors, ResNet-based extractor performs worse.

4.2.2. Evaluation of the Weighted Loss Function. To alleviate the hardships of localization from sparse sensing data, the weighted loss function is proposed to enhance the attention on the position features. As the number of sensors decreases,

Table 1: Simulation parameters.

Study area	Size	480 m × 360 m
Buildings	Materials	Concrete
	Thickness of walls	10 cm
	Permittivity	4
	Permeability	1
	Conductivity	0.01 S/m
Water	Permittivity	81
	Permeability	1
	Conductivity	0.5 S/m
Vegetation	Additional loss	10 dB
	Additional attenuation or rays	0.05 dB/m
Signal source	Frequency	1800 MHz
	Power	43 dB
DPM	Resolution	1 m
	Interaction loss	11 dB
	Building penetration loss	20 dB
	LOS path loss exponent	Before/after breakpoint: 2.3/3.3
	NLOS path loss exponent	Before/after breakpoint: 2.5/3.6
	Wave guiding weighting factor	1

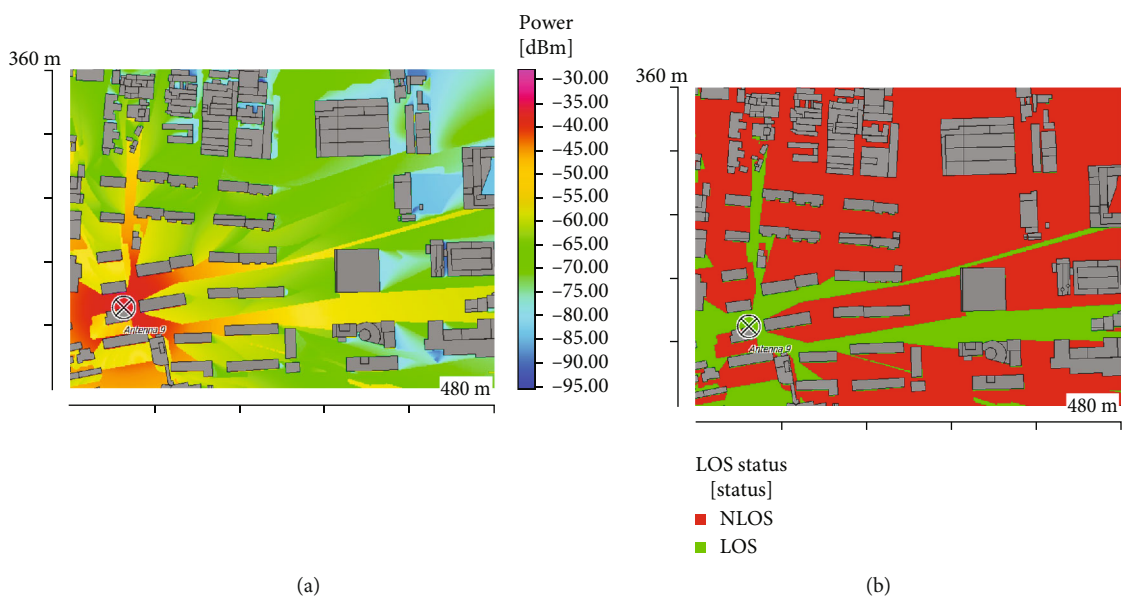

Figure 3: Visual implementation of (a) RSS distribution and (b) LOS/NLOS distribution in the study area of 480 m × 360 m.

the hourglass deep neural network requires wider attention on the position features, leading to a larger weighted radius. However, if the weighted radius is too large, the network has to pay attention to more extra features in the whole weighted area and reduce the attention to the true position. There is a balance between larger weighted area and the better accuracy. Varied from 65 m to 145 m with the interval of 20 m, an appropriate weighted radius is determined via several purposeful setting and numerous tests. Finally, considering the overall positioning performance with different number of sensors, the weighted radius is set to 105 m.

Figure 6 gives the effect of the weighted loss function with a 105 m radius on the localization results, which reveals that the proposed weighted loss method provides a significant enhancement over the original loss function. The localization errors are limited in 10 m with a total of 8 sensors. And the weighted loss function improves the performance of localization more than 50% with a total of 4 sensors.

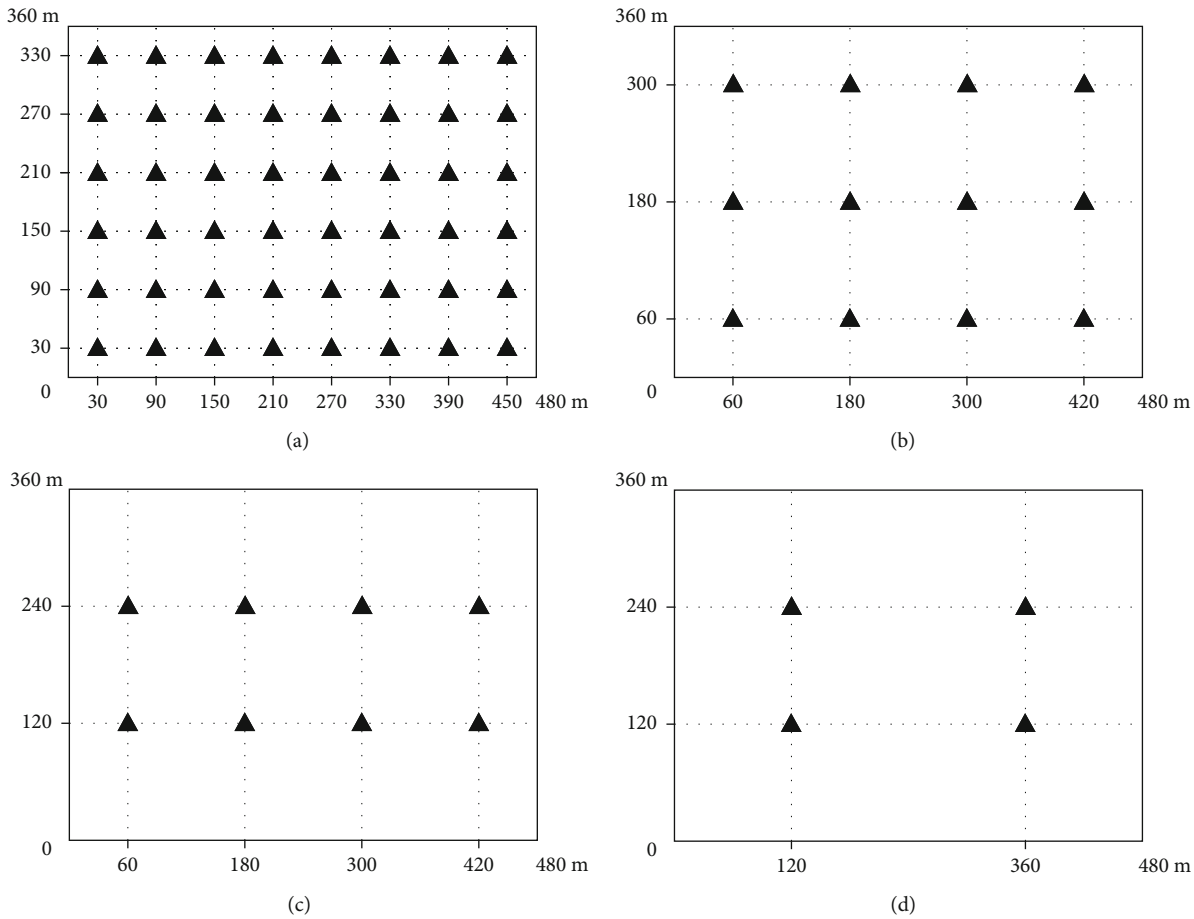

Figure 4: Visual implementation of the distribution of (a) 48 sensors, (b) 12 sensors, (c) 8 sensors, and (d) 4 sensors (which are represented as black triangles).

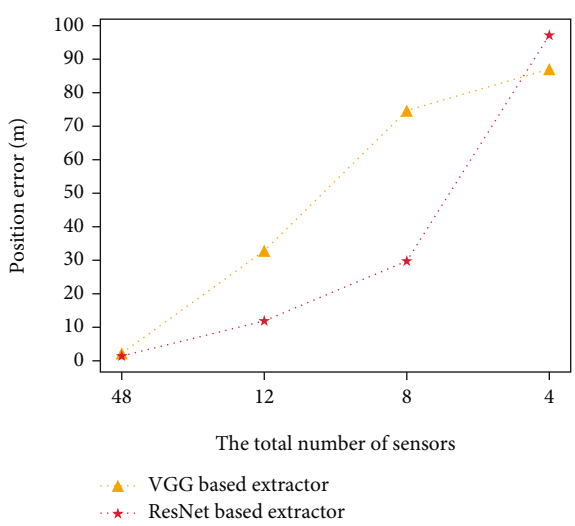

Figure 5: Comparative localization results of VGG-based and ResNet-based extractor with different number of sensors.

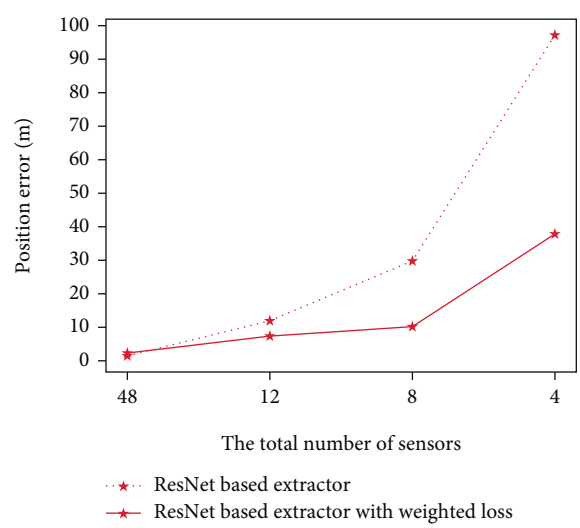

Figure 6: Effect of the weighted loss function on the localization results.

4.2.3. Analysis of LOS/NLOS Propagation. It is rarely possible to count the number of LOS or NLOS sensors without geographic information, so that the sensors with NLOS propagation paths are generally assumed in most simulations of other researches (e.g., [16]). On the other hands, dense layouts of hundreds of sensors in traditional deep learning-

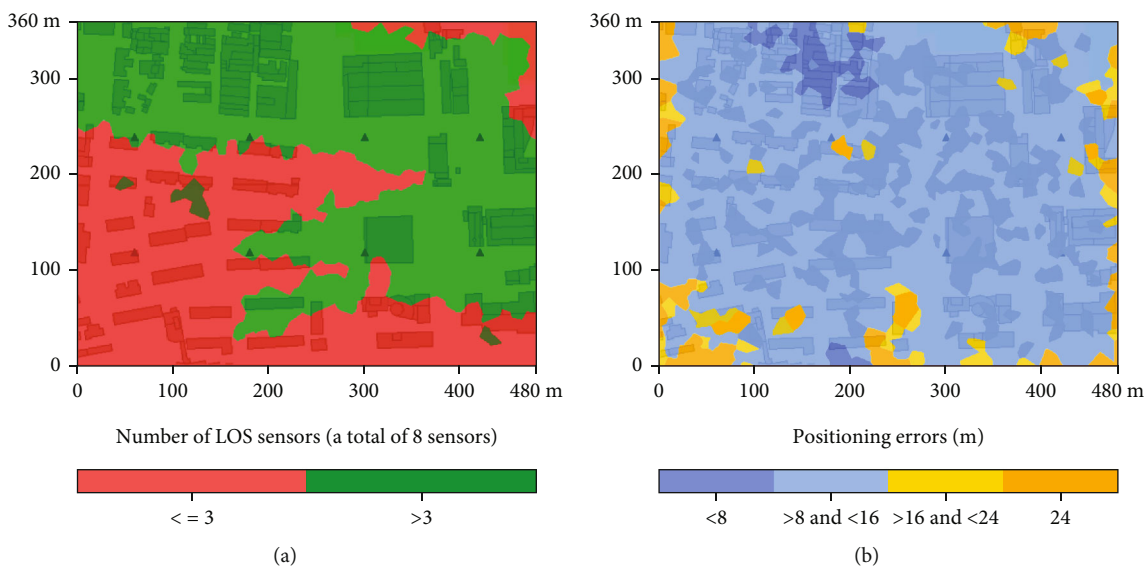

Figure 7: Visual implementation of (a) LOS/NLOS distribution and (b) positioning errors with a total of 8 sensors (which are represented as black triangles).

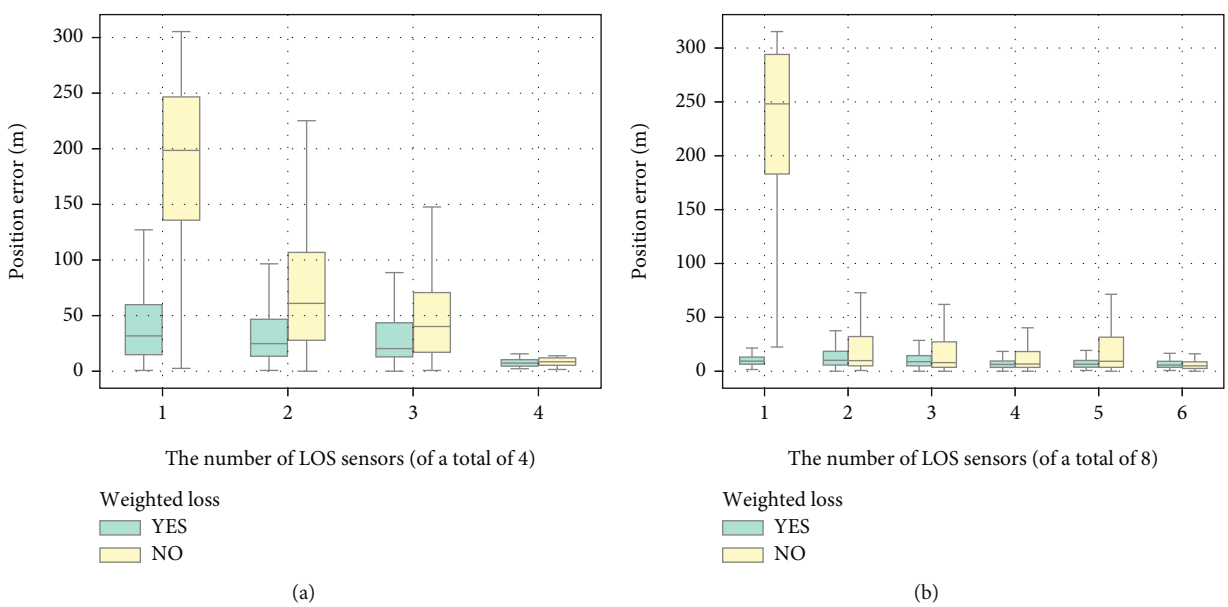

Figure 8: The positioning errors with different number of LOS sensors. (a) The total number of sensors is 4. (b) The total number of sensors is 8.

based localization methods inevitably provide sufficient LOS paths for accurate localization. Differently, this paper applies the geographic model to offer LOS and NLOS information and focuses on the localization with sparse distribution of sensors. As a result, the LOS and NLOS sensors are distinguished to evaluate their influences on the localization.

As a qualitative analysis, Figure 7 is the visual implementation of LOS/NLOS distribution and positioning errors against a backdrop of urban buildings. In Figure 7(a), when an illegal signal source is located in the red area, there are less than 4 LOS sensors with a total of 8 sensors, which means it suffers from severe NLOS propagation. In contrast, Figure 7(b) shows that localization results calculated by the proposed method are less affected by NLOS propagation in the corresponding area, indicating that the NLOS propagation features are well captured for robust localization. And the worse performance at the edge of the study area can be interpreted by the poor sensing.

As a quantitative analysis, Figure 8 gives the positioning errors with different number of LOS sensors, representing that the more LOS sensors there are, the better performance the proposed method offers. With a total of 4 sensors, Figure 8(a) shows that the error fluctuations of the localization method with weighted loss function decrease 85% as the number of LOS sensors increases from 1 to 4. In addition, with a total of 8 sensors in Figure 8(b), the weighted method

Table 2: Comparative results of different algorithms.

Algorithms	Positioning errors (m) with varied number of sensors			
	48	12	8	4
DeepMTL	19.00	203.08	223.53	222.59
U-net	5.48	35.95	100.69	140.13
VGG-based proposed method	2.36	9.92	16.40	50.87
ResNet-based proposed method	2.28	7.34	10.16	37.81

achieves the robust localization performance of median errors below 10 m, especially as the original method fails to localize with single LOS sensor.

4.2.4. Comparison with Other Algorithms. The proposed method is compared with DeepMTL localization [27] and another network structure, i.e., U-net [36]. DeepMTL primarily converts the RSS value into image data and predicts the positions of multiple transmitters by CNN. In this paper, apply DeepMTL for localization of single signal source to evaluate its performance under the condition of NLOS propagation and sparse sensor distribution. Besides, a typical U-net that consists of four downsampling and four upsampling layers is considered for comparisons.

Table 2 shows the comparative results. DeepMTL performs worst due to the sparse layouts of sensors. Its original performance is based on the dense sensors and the ideal or statistical propagation data which are easy to learn the localization features. Driven by our datasets that is closer to the practical electromagnetic environment, its localization errors of single signal source are up to 200 meters, illustrating that DeepMTL is not suitable for the severe NLOS propagation conditions. On the other hand, the VGG-based and ResNet-based hourglass networks with weighted loss function have a 63.7% and 73.0% improvement over U-net with a total of 4 sensors, respectively. The comparisons express the fusion of multiscale features in hourglass network which is more efficient to predict probability distributions of positions than U-net, and the weighted loss function improves the attention on true positions. Therefore, it is concluded that the proposed method is more qualified for localization in large-scale urban scenarios.

5. Conclusions

For the challenges of severe NLOS propagation and sparse layouts of sensors in urban scenarios, this paper proposes a deep learning-based localization method which learns the NLOS propagation features with the aid of urban geographic model. The proposed method fully considers the fusion of geographic information and electromagnetic wave propagation. The reliable urban propagation model prepares the datasets close to practical electromagnetic environment and motivates neural networks. Moreover, the improved hourglass networks with two typical feature extractors, i.e., VGG and ResNet, are trained for localization. In comparative simulations, the ResNet-based hourglass network outperforms the VGG-based, but huge positioning errors still exist when there are only 4 sensors. With the assistance of the proposed weighted loss function, the localization performance is enhanced by over 50%. Furthermore, geographic information supports for the distinction between LOS and NLOS paths in order to evaluate the robustness of the method with different number of LOS sensors. Compared with other deep learning-based algorithms, the proposed method keeps obviously reliable and superior performance as the total number of sensors decreases. The results present the validity and robustness of the proposed deep learning-based localization method under the severe NLOS propagation and sparse sensing conditions in urban scenarios.

Data Availability

The original data used in this work is generated by simulation via WinProp. The method of dataset generation is included within the article.

Conflicts of Interest

The authors declare that there is no conflict of interest regarding the publication of this article.

Acknowledgments

This work was funded by the National Natural Science Foundation of China (grant numbers 61971439 and 61702543).

References

[1] A. Haniz, G. K. Tran, K. Saito et al., "A novel phase-difference fingerprinting technique for localization of unknown emitters," *IEEE Transactions on Vehicular Technology*, vol. 66, no. 9, pp. 8445–8457, 2017.

[2] B. Kaur and D. Prashar, *Analysis and Comparison of Localization Approaches in WSN: A Review*, Springer, Singapore, 2019.

[3] I. Javed, X. Tang, M. A. Saleem, M. U. Sarwar, M. Tariq, and C. S. Shivachi, "3D localization for mobile node in wireless sensor network," *Wireless Communications and Mobile Computing*, vol. 2022, 12 pages, 2022.

[4] J. Pospisil, R. Fujdiak, and K. Mikhaylov, "Investigation of the performance of TDoA-based localization over LoRaWAN in theory and practice," *Sensors*, vol. 20, no. 19, article 5464, 2020.

[5] Y. Chen, Z. Yao, and P. Zheng, "A novel method for asynchronous time-of-arrival-based source localization: algorithms, performance and complexity," *Sensors*, vol. 20, no. 12, p. 3466, 2020.

[6] C. Xu, Z. Wang, Y. Wang, Z. Wang, and L. Yu, "Three passive TDOA-AOA receivers-based flying-UAV positioning in

extreme environments," *IEEE Sensors Journal*, vol. 20, no. 16, pp. 9589–9595, 2020.

[7] Y. Li, F. Shu, B. Shi, X. Cheng, Y. Song, and J. Wang, "Enhanced RSS-based UAV localization via trajectory and multi-base stations," *IEEE Communications Letters*, vol. 25, no. 6, pp. 1881–1885, 2021.

[8] S. Tomic, M. Beko, and R. Dinis, "3-D target localization in wireless sensor networks using RSS and AoA measurements," *IEEE Transactions on Vehicular Technology*, vol. 66, no. 4, pp. 3197–3210, 2017.

[9] L. Cheng, M. Xue, Y. Wang, Y. Wang, and Y. Bi, "A robust tracking algorithm based on modified generalized probability data association for wireless sensor network," *IEEE Transactions on Industrial Electronics*, vol. 69, no. 2, pp. 2136–2146, 2022.

[10] J. Hua, Y. Yin, W. Lu, Z. Yu, and F. Li, "NLOS identification and positioning algorithm based on localization residual in wireless sensor networks," *Sensors*, vol. 18, no. 9, p. 2991, 2018.

[11] C. L. Sang, B. Steinhagen, J. D. Homburg, M. Adams, M. Hesse, and U. Rückert, "Identification of NLOS and multi-path conditions in UWB localization using machine learning methods," *Applied Sciences*, vol. 10, no. 11, p. 3980, 2020.

[12] Y. Yuan, F. Shen, and X. Li, "GPS multipath and NLOS mitigation for relative positioning in urban environments," *Aerospace Science and Technology*, vol. 107, article 106315, 2020.

[13] J. Bordoy, C. Schindelhauer, R. Zhang, F. Hoflinger, and L. M. Reindl, "Robust extended Kalman filter for NLOS mitigation and sensor data fusion," in *2017 IEEE International Symposium on Inertial Sensors and Systems (INERTIAL)*, pp. 117–120, Kauai, HI, USA, March 2017.

[14] S. Tomic and M. Beko, "A robust NLOS bias mitigation technique for RSS-TOA-based target localization," *IEEE Signal Processing Letters*, vol. 26, no. 1, pp. 64–68, 2019.

[15] C. Geng, X. Yuan, and H. Huang, "Exploiting channel correlations for NLOS ToA localization with multivariate Gaussian mixture models," *IEEE Wireless Communications Letters*, vol. 9, no. 1, pp. 70–73, 2020.

[16] Y. Sun, S. Yang, G. Wang, and H. Chen, "Robust RSS-based source localization with unknown model parameters in mixed LOS/NLOS environments," *IEEE Transactions on Vehicular Technology*, vol. 70, no. 4, pp. 3926–3931, 2021.

[17] S. Miura, L.-T. Hsu, F. Chen, and S. Kamijo, "GPS error correction with pseudorange evaluation using three-dimensional maps," *IEEE Transactions on Intelligent Transportation Systems*, vol. 16, no. 6, pp. 3104–3115, 2015.

[18] D. Acharya, M. Ramezani, K. Khoshelham, and S. Winter, "BIM-Tracker: a model-based visual tracking approach for indoor localisation using a 3D building model," *ISPRS Journal of Photogrammetry and Remote Sensing*, vol. 150, pp. 157–171, 2019.

[19] G. Fuqiang, S. Valaee, K. Khoshelham, J. Shang, and R. Zhang, "Landmark graph-based indoor localization," *IEEE Internet of Things Journal*, vol. 7, no. 9, pp. 8343–8355, 2020.

[20] M. Zhou, Y. Lin, N. Zhao, Q. Jiang, X. Yang, and Z. Tian, "Indoor WLAN intelligent target intrusion sensing using ray-aided generative adversarial network," *IEEE Transactions on Emerging Topics in Computational Intelligence*, vol. 4, no. 1, pp. 61–73, 2020.

[21] G. Zhang, H.-F. Ng, W. Wen, and L.-T. Hsu, "3D mapping database aided GNSS based collaborative positioning using factor graph optimization," *IEEE Transactions on Intelligent Transportation Systems*, vol. 22, no. 10, pp. 6175–6187, 2021.

[22] F. Perez-Cruz, P. M. Olmos, M. M. Zhang, and H. Huang, "Probabilistic time of arrival localization," *IEEE Signal Processing Letters*, vol. 26, no. 11, pp. 1683–1687, 2019.

[23] I. Nirmal, A. Khamis, M. Hassan, H. Wen, and X. Zhu, "Deep learning for radio-based human sensing: recent advances and future directions," *IEEE Communications Surveys Tutorials*, vol. 23, no. 2, pp. 995–1019, 2021.

[24] Y. Liu, C. Lyu, X. Liu, and Z. Liu, "Automatic feature engineering for bus passenger flow prediction based on modular convolutional neural network," *IEEE Transactions on Intelligent Transportation Systems*, vol. 22, no. 4, pp. 2349–2358, 2021.

[25] A. Poulose and D. S. Han, "UWB indoor localization using deep learning LSTM networks," *Applied Sciences*, vol. 10, no. 18, p. 6290, 2020.

[26] M. Lin, Y. Huang, B. Li, and Z. Huang, "Heatmap-basedmultiple co-channel transmitter localization with fully convolutional network," in *2021 International Applied Computational Electromagnetics Society (ACES-China) Symposium*, pp. 1-2, Chengdu, China, 2021.

[27] C. Zhan, M. Ghaderibaneh, P. Sahu, and H. Gupta, "DeepMTL: deep learning based multiple transmitter localization," in *2021 IEEE 22nd International Symposium on a World of Wireless, Mobile and Multimedia Networks (WoWMoM)*, pp. 41–50, Pisa, Italy, June 2021.

[28] L. M. Correia, "A view of the COST 231-Bertoni-Ikegami model," in *2009 3rd European Conference on Antennas and Propagation*, pp. 1681–1685, Berlin, Germany, 2009.

[29] B. Friebel, M. Schweins, N. Dreyer, and T. Kurner, "Simulation of GPS localisation based on ray tracing," *Advances in Radio Science*, vol. 19, pp. 85–92, 2021.

[30] R. Wahl, G. Wolfle, P. Wertz, P. Wildbolz, and F. Landstorfer, "Dominant path prediction model for urban scenarios," in *14th IST Mobile and Wireless Communications Summit*, pp. 1–5, Dresden, Germany, 2005.

[31] A. Aschrafi, P. Wertz, M. Layh, F. M. Landstorfer, G. Wolfle, and R. Wahl, "Impact of building database accuracy on predictions with wave propagation models in urban scenarios," in *2006 IEEE 63rd Vehicular Technology Conference*, vol. 6, pp. 2681–2685, Melbourne, VIC, Australia, 2006.

[32] H. Law and J. Deng, "CornerNet: detecting objects as paired keypoints," in *Proceedings of the European Conference on Computer Vision (ECCV)*, pp. 734–750, Munich, Germany, September 2018.

[33] K. Simonyan and A. Zisserman, "Very deep convolutional networks for large-scale image recognition," 2014, https://arxiv.org/abs/1409.1556.

[34] K. He, X. Zhang, S. Ren, and J. Sun, "Deep residual learning for image recognition," in *Proceedings of the IEEE Conference on Computer Vision and Pattern Recognition (CVPR)*, pp. 770–778, Las Vegas, NV, USA, June 2016.

[35] R. Hoppe, G. Wolfle, and U. Jakobus, "Wave propagation and radio network planning software. WinProp added to the electromagnetic solver package FEKO," in *2017 International Applied Computational. Electromagnetics Society Symposium - Italy (ACES)*, pp. 1-2, Firenze, Italy, March 2017.

[36] Z. Wang, Y. Zhou, F. Wang, S. Wang, and X. Zhiyu, "SDGH-Net: ship detection in optical remote sensing images based on Gaussian heatmap regression," *Remote Sensing*, vol. 13, no. 3, p. 499, 2021.

Hindawi
Wireless Communications and Mobile Computing
Volume 2022, Article ID 3463438, 10 pages
https://doi.org/10.1155/2022/3463438

Research Article

Polarimetric Direction of Arrival Estimations Based on Adaptive Linear Time-Frequency Transforms

Shao Shuai, Liu Aijun, Wang Xiuhong, and Yang Hongjuan

School of Information Science and Engineering, Harbin Institute of Technology at Weihai, Weihai 264209, China

Correspondence should be addressed to Yang Hongjuan; hjyang@hit.edu.cn

Received 23 June 2022; Revised 15 July 2022; Accepted 21 July 2022; Published 8 August 2022

Academic Editor: Mingqian Liu

A spatially polarized time-frequency distribution (SPTFD) based on dual-polarized double-fed antenna arrays is adapted to deal with polarization-unstable signals. A linear time-frequency (TF) representation was used for an instantaneous frequency (IF) estimate, primarily due to its simplicity and immunity to cross-interference. Using a set of linear TF transformations using Gaussian windows and Fourier oscillation kernels, the IF estimated window widths of multiple unstable signals are obtained. This paper introduces a new method for estimating the direction of arrival (DOA) of polarized waves using adaptive linear time-frequency transforms. In this paper, a narrowband far-field point source on the receiving array is analyzed. The source signal is split into two orthogonally polarized components. The optimal window is determined by the first derivative of the IF; for this purpose, we take a simple algorithm for solving the derivative and optimize it. In developing TF-adaptive and fully automatic TF display technology, the first method is to use the time-adaptive window for minimizing the IF estimate mean square error (MSE) sum at each moment, while the second procedure is to adjust according to time and frequency and minimize estimate MSE sum at each position in the TF region. Due to its combination with signal polarization, the spatial time-frequency distribution (STFD) gains more freedom and thus perfects the phonon space estimation of noise and signal. On the SPTFD platform, polarized time-frequency multiple signal classification (PTF-MUSIC) is used for the estimation of signal direction of arrival, which outperforms conventional time-frequency MUSIC. Using the example of a synthesized signal, this method outperforms conventional techniques in DOA estimation.

1. Introduction

In many aspects of technology, we are studying changes in the spectrum. Descriptive information for such a signal can be obtained from a time-frequency representation (TFR), which projects the signal into the time-frequency region, exposing momentary changes in its spectral content [1]. In recent decades, various TFRs have been developed and used in a wide range of applications [2, 3]. These techniques have taken advantage of signal sparseness inside TF regions [4]. Time-frequency analysis is an effective method for DOA estimation of unstable signals. To improve the performance of DOA, [5–7] propose new DOA estimation methods.

In TFR, the linear transform can be viewed as a window to the Fourier transform; prominent examples of this type are the short-time Fourier transform (STFT) and the S transform (ST) [8]. Cohen's TF distribution is based on a generalized instantaneous autocorrelation function. During the analysis, these signals can generate unwanted error signals, which can be hidden, so it is necessary to have a suitable core [9]. The instantaneous frequency (IF) is the most fundamental concept in TF, reflecting the instantaneous change rate of the signal phase function, a simple and well-known instantaneous frequency estimation method by the maxima location of the TFR [10]. To accurately express the frequency law of the signal, TFR is generally required according to the design of the signal because no TFR can optimize all signals like all fixed graphs. Therefore, much research has been devoted to adaptive TFRs whose parameters can be changed with the signal without being disturbed by the user. In this case, energy concentration measurement (ECM) is widely used to determine the energy distribution over the signal components to automatically select good TFR criteria [11, 12]. A multiview approach to adaptive TFR is to build multiple

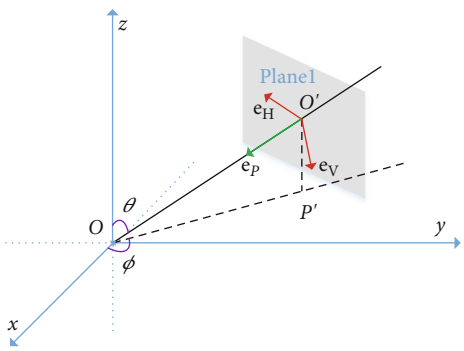

Figure 1: Dual-polarized array.

TFRs and combine them according to predetermined criteria [13–15].

The accuracy of IF is a primary measure of TF, so we can use it to measure the statistical performance of IF to get a more accurate TFR. In several works [16, 17], the accuracy of IF estimation for TFR was investigated, where the accuracy of the estimate depends on the width of the window and optimizing for this requires optimizing for unknown first derivatives of information. Because of this limitation, this paper uses the intersection of confidence intervals (ICI) to approximate the optimal width in [18]. In [19], a three-stage adaptive algorithm was proposed to reduce the computational complexity required to obtain the linear TFR improved in [20]. However, the optimal width depends on the statistical performance of the IF estimation. [21] utilized a new general formula that describes the error and variation of IF estimation in noisy environments, resulting in the optimal window width for linear TFR. Meanwhile, in [22, 23], polarization information is adopted, which further improves the estimation performance of DOA. Then, an adaptive method based on the combination of polarization and time-frequency domain information is proposed.

In Materials and Methods, we will discuss the time-frequency distribution patterns of spatial polarization and two automation linear TFRs. The one utilizes a time-adaptive window for minimizing the MSE sum values. In another TFR, a TF-adaptive window is used to minimize the location of the estimated MSE in the TF region. The part also introduces the polarized time-frequency MUSIC. The method in this paper is evaluated in the Results and Discussion. Through numerical calculation, it is proved that the procedure is superior to general and complex algorithms.

2. Materials and Methods

2.1. Spatial Polarimetric Time-Frequency Distributions. In Figure 1, a electromagnetic wave incident into the array can be described as

$$\begin{aligned}\mathbf{E}(t) = E_\theta(t)\boldsymbol{\theta} + E_\phi(t)\boldsymbol{\phi} = [&E_\theta(t)\cos(\theta)\cos(\phi) \\ &- E_\phi(t)\sin(\phi)]\mathbf{x} + [E_\theta(t)\cos(\theta)\sin(\phi) \\ &+ E_\phi(t)\cos(\phi)]\mathbf{y} + E_\theta(t)\sin(\theta)\mathbf{z},\end{aligned} \tag{1}$$

where $\boldsymbol{\phi}$ and $\boldsymbol{\theta}$ are the spherical azimuth and elevation unit vectors observed by the source. The $\mathbf{x}$, $\mathbf{y}$, and $\mathbf{z}$ are unit vectors along the x, y, and z directions, respectively. For generality and simplicity, we assumed that the signal is located in the $x-y$ plane and the array is in the $y-z$ plane. Accordingly $\theta = 90^\circ$ ($\boldsymbol{\theta} = -\mathbf{z}$),

$$\mathbf{E}(t) = -E_\phi(t)\sin(\phi)\mathbf{x} + E_\phi(t)\cos(\phi)\mathbf{y} + E_\theta(t)\mathbf{z}. \tag{2}$$

We express $s(t)$ in terms of the amplitude of the source measured by the receiving reference sensor, which has a polarization angle $\gamma \in [0, \pi/2]$ and a polarization phase difference $\eta \in (-\pi, \pi]$. $s^{[v]}(t)$ and $s^{[h]}(t)$ are the source horizontal and vertical polarization part components, which can be described by spherical fields, $E_\theta(t)$ and $E_\phi(t)$, as

$$\begin{aligned}E_\theta(t) &= s^{[v]}(t) = s(t)\cos(\gamma), \\ E_\phi(t) &= s^{[h]}(t) = s(t)\sin(\gamma)e^{j\eta}.\end{aligned} \tag{3}$$

A signal is linearly polarized if $\eta = 0^\circ$ or $\eta = 180^\circ$. Replacing (3) into (2) gets

$$\mathbf{E}(t) = s(t)\left[-\cos(\gamma)\sin(\phi)\mathbf{x} + \cos(\phi)\sin(\gamma)e^{j\eta}\mathbf{y} + \cos(\gamma)\mathbf{z}\right]. \tag{4}$$

We assume that N signals enter on the array of M dual-polarized antennas. The distance between sensors is d, and d is not more than $\lambda/2$ for ensuring that there is no array ambiguity. In another word, the expected direction of the incident signal is only one. When d is $\lambda/2$, there are high array sensor utilization rate and effect guarantee. The nth source vertical and horizontal components are

$$\begin{aligned}s_n^{[v]}(t) &= s_n(t)\cos(\gamma_n) \triangleq c_{n1}s_n(t), \\ s_n^{[h]}(t) &= s_n(t)\sin(\gamma_n)e^{j\eta_n} \triangleq c_{n2}s_n(t),\end{aligned} \tag{5}$$

where the parameters $c_{n1} = \cos(\gamma_n)$ and $c_{n2} = \sin(\gamma_n)e^{j\eta_n}$ represent the vertical and horizontal polarization coefficients. The signal entering on the mth dual-polarized antenna is

$$\begin{aligned}\underline{y}_m(t) &= \left[y_m^{[v]}(t), y_m^{[h]}(t)\right]^{\mathrm{T}} = \sum_{n=1}^{N}\left[a_{nm}^{[v]}\mathbf{E}_n\cdot\mathbf{z}, a_{nm}^{[h]}\mathbf{E}_n\cdot\mathbf{y}\right]^{\mathrm{T}} \\ &= \sum_{n=1}^{N}\left[a_{nm}^{[v]}s_n^{[v]}(t), a_{nm}^{[h]}s_n^{[h]}(t)\cos(\phi_n)\right]^{\mathrm{T}},\end{aligned} \tag{6}$$

where "$\cdot$" denotes the dot product, $\mathbf{E}_n$ represents the nth source electric field vector, and $a_{nm}^{[v]}$ and $a_{nm}^{[h]}$, respectively, denote the mth elements of the vertically and horizontally polarized array vectors, $\mathbf{a}^{[v]}(\phi_n)$ and $\mathbf{a}^{[h]}(\phi_n)$. We assume that both $\mathbf{a}^{[v]}(\phi)$ and $\mathbf{a}^{[h]}(\phi)$ are known and normalized ($\|\mathbf{a}^{[v]}(\phi)\|^2 = \|\mathbf{a}^{[h]}(\phi)\|^2 = M$) and the array has been calibrated. It should be pointed out that in the array calibration of the relevant area, the $\cos(\phi_n)$ term in the horizontally

polarized array manifold can be introduced, so it will not be considered. Then, the above equation is simplified as

$$\begin{aligned}\underline{y}_m(t) &= \left[a_{nm}^{[v]}s_n^{[v]}(t), a_{nm}^{[h]}s_n^{[h]}(t)\right]^{\mathrm{T}} \\ &= s_n(t)\left(\begin{bmatrix} a_{nm}^{[v]} & a_{nm}^{[h]}\end{bmatrix}^{\mathrm{T}} \odot \begin{bmatrix} c_{n1} & c_{n2}\end{bmatrix}^{\mathrm{T}}\right) \\ &\triangleq s_n(t)\mathbf{a}_{nm} \odot \mathbf{c}_n,\end{aligned} \tag{7}$$

where the vector $\mathbf{c}_n = [c_{n1}, c_{n2}]^{\mathrm{T}} = [\cos(\gamma_n), \sin(\gamma_n)e^{j\eta_n}]^{\mathrm{T}}$ is the nth source polarization signature.

For a dual-polarized sensor, we define the general short Fourier transform (GSFT) as

$$D_{x^{[i]}}(t,f) = \int_{-\infty}^{+\infty} w(t-\tau, \sigma(t,f))x^{[i]}(t)e^{-j2\pi f\tau}d\tau, \tag{8}$$

where the Gaussian window is defined as

$$w(t,\sigma(t,f)) = \frac{1}{\sqrt{2\pi}\sigma(t,f)} \exp\left(\frac{-t^2}{2\sigma^2(t,f)}\right). \tag{9}$$

Formulas (1)–(9) correspond to the single dual-polarization sensor case. With an M-sensor array, for each polarization i, $i = v$ or h, the data vector is

$$\begin{aligned}\mathbf{x}^{[i]}(t) &= \left[x_1^{[i]}(t), x_2^{[i]}(t), \cdots, x_M^{[i]}(t)\right]^{\mathrm{T}} \\ &= \mathbf{y}^{[i]}(t) + \mathbf{n}^{[i]}(t) = \mathbf{A}^{[i]}(\mathbf{\Phi})\mathbf{s}^{[i]}(t) + \mathbf{n}^{[i]}(t).\end{aligned} \tag{10}$$

Using formula (10), the case of extending the polarization time-frequency distribution of a single sensor to multiple sensors is obtained. Instead of the scalar TFD of (8), we define the polarization STFD matrix of the data vector

$$\mathbf{D}_{\mathbf{x}^{[i]}}(t,f) = \int_{-\infty}^{+\infty} w(t-\tau, \sigma(t,f))\mathbf{x}^{[i]}(t)e^{-j2\pi f\tau}d\tau, \tag{11}$$

which, for the no-noise case, can be represented as

$$\mathbf{D}_{\mathbf{x}^{[i]}}(t,f) = \mathbf{A}^{[i]}(\mathbf{\Phi})\mathbf{D}_{\mathbf{s}^{[i]}}(t,f)\left(\mathbf{A}^{[i]}(\mathbf{\Phi})\right)^{\mathrm{H}}. \tag{12}$$

According to (10), the double polarization data vectors can be built as follows:

$$\begin{aligned}\mathbf{x}(t) &= \begin{bmatrix}\mathbf{x}^{[v]}(t) \\ \mathbf{x}^{[h]}(t)\end{bmatrix} = \begin{bmatrix}\mathbf{A}^{[v]}(\mathbf{\Phi}) & \mathbf{0} \\ \mathbf{0} & \mathbf{A}^{[h]}(\mathbf{\Phi})\end{bmatrix}\begin{bmatrix}\mathbf{s}^{[v]}(t) \\ \mathbf{s}^{[h]}(t)\end{bmatrix} \\ &+ \begin{bmatrix}\mathbf{n}^{[v]}(t) \\ \mathbf{n}^{[h]}(t)\end{bmatrix} = \begin{bmatrix}\mathbf{A}^{[v]}(\mathbf{\Phi}) & \mathbf{0} \\ \mathbf{0} & \mathbf{A}^{[h]}(\mathbf{\Phi})\end{bmatrix}\begin{bmatrix}\mathbf{Q}^{[v]} \\ \mathbf{Q}^{[h]}\end{bmatrix}\mathbf{s}(t) \\ &+ \begin{bmatrix}\mathbf{n}^{[v]}(t) \\ \mathbf{n}^{[h]}(t)\end{bmatrix} = \mathbf{B}(\mathbf{\Phi})\mathbf{Q}\mathbf{s}(t) + \mathbf{n}(t),\end{aligned} \tag{13}$$

where

$$\mathbf{B}(\mathbf{\Phi}) = \begin{bmatrix}\mathbf{A}^{[v]}(\mathbf{\Phi}) & \mathbf{0} \\ \mathbf{0} & \mathbf{A}^{[h]}(\mathbf{\Phi})\end{bmatrix}, \tag{14}$$

represents block diagonal, and

$$\mathbf{Q} = \begin{bmatrix}\mathbf{Q}^{[v]} \\ \mathbf{Q}^{[h]}\end{bmatrix}, \tag{15}$$

represents the signal polarization characteristic vector, where

$$\begin{aligned}\mathbf{q}^{[v]} &= [\cos(\gamma_1), \cdots, \cos(\gamma_N)]^{\mathrm{T}}, \\ \mathbf{Q}^{[v]} &= \mathrm{diag}\left(\mathbf{q}^{[v]}\right),\end{aligned} \tag{16}$$

$$\begin{aligned}\mathbf{q}^{[h]} &= \left[\sin(\gamma_1)e^{j\eta_1}, \cdots, \sin(\gamma_N)e^{j\eta_N}\right]^{\mathrm{T}}, \\ \mathbf{Q}^{[h]} &= \mathrm{diag}\left(\mathbf{q}^{[h]}\right).\end{aligned} \tag{17}$$

Correspondingly,

$$\begin{aligned}\mathbf{B}(\mathbf{\Phi})\mathbf{Q} &= \begin{bmatrix}\mathbf{a}^{[v]}(\phi_1)\cos(\gamma_1) & \cdots & \mathbf{a}^{[v]}(\phi_n)\cos(\gamma_N) \\ \mathbf{a}^{[h]}(\phi_1)\sin(\gamma_1)e^{j\eta_1} & \cdots & \mathbf{a}^{[h]}(\phi_n)\sin(\gamma_N)e^{j\eta_N}\end{bmatrix} \\ &= [\tilde{\mathbf{a}}(\phi_1) \ \cdots \ \tilde{\mathbf{a}}(\phi_N)].\end{aligned} \tag{18}$$

The matrix (18) can be considered as the extended mixing matrix, within $\tilde{\mathbf{a}}(\phi_n)$ denoting the nth signal joint spatial polarization characteristic. For the nth signal, the extended spatial polarization characteristic vector is

$$\tilde{\mathbf{a}}(\phi_n) = \begin{bmatrix}\mathbf{a}^{[v]}(\phi_n)\cos(\gamma_n) \\ \mathbf{a}^{[h]}(\phi_n)\sin(\gamma_n)e^{j\eta_n}\end{bmatrix}. \tag{19}$$

Obviously, the double polarization array can double the spatial dimension of the vector.

The polarization, spatiality, and time-frequency characteristics can be combined with the source signal incident on the receiver array. The STFD of a dual-polarization data vector $\mathbf{x}(t)$ can be as follows:

$$\mathbf{D}_{\mathbf{x}}(t,f) = \int_{-\infty}^{+\infty} w(t-\tau, \sigma(t,f))\mathbf{x}(t)e^{-j2\pi f\tau}d\tau. \tag{20}$$

$\mathbf{D}_{\mathbf{x}}(t,f)$ is called the SPTFD matrix. This matrix is a general method that can solve some common problems in array processing, as described in the following.

When the noise effect is neglectful, the SPTFD matrix is connected with the signal TFD matrix by

$$\mathbf{D}_{\mathbf{xx}}(t,f) = \mathbf{B}(\mathbf{\Phi})\mathbf{Q}\mathbf{D}_{\mathbf{s}}(t,f)\mathbf{Q}^{\mathrm{H}}\mathbf{B}^{\mathrm{H}}(\mathbf{\Phi}). \tag{21}$$

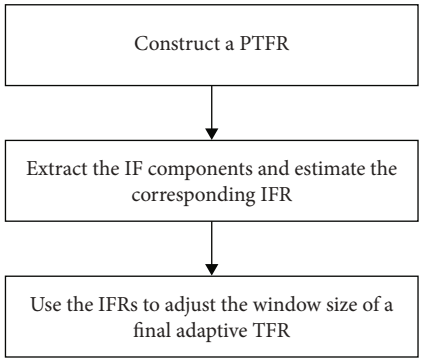

Figure 2: Flowchart of adaptive TFRs based on linear TF transforms.

Firstly, the time-frequency points are selected by the algorithm in the next section to construct the matrix. Then, eigenvectors are obtained by eigendecomposition of formula (21). Finally, the noise subspace U_n constructed by eigenvectors is used for subsequent spatial spectrum estimation.

2.2. Three-Step Method for IF Estimation. Abdoush et al. [21] gave a general expression relating the error and variance of the IF estimate to the smoothness of the observation window and the IF. The correct IF estimation demands a data-based approach to choose at least reasonable window width. Therefore, the paper summarizes and extends the "low complexity" described in [19, 20]; the method includes three processes, as shown in Figure 2, which will be explained in this section. On this basis, this paper proposes a new linear TFR method based on estimation error and variance. The one uses a time-varying window for minimizing the MSE sum value estimated by IF at each moment, while in the latter TFR, the TF value is adjustable to minimize the MSE of each point in the TF region.

For practical application, we will limit ourselves to a discrete version of GSFT, which we define as

$$D_x\left[k_t, k_f\right] = \sum_{n=0}^{N-1} x[l] w\left[k_t - l, \sigma\left[k_t, k_f\right]\right] e^{-j2\pi k_f (l/N)}, \quad (22)$$

where $x[k_t]$ represents a length K_t discrete time series corresponding to $x(k_t T_s)$ by sampling interval T_s and $k_f = -K_t/2, \cdots, K_t/2 - 1$ denoting frequency index.

2.2.1. Preliminary TFR. For any TFR, the optimized formula (22) requires an understanding of the IF. So, in adaptation, the first step is to create a preliminary TFR (PTFR) that roughly estimates the IF orbit. Although this stage can tolerate minor estimation errors, however, more significant estimation errors are propagated to the after step, so the final IF estimation accuracy decreases. To this end, Pei and Huang in [20] adopted an STFT of optimizing window width according to the ECM. While it performed well, when we used different multicomponent signals to detect this ECM, we found that the approach was beneficial for a noisy element and detrimental for a rapidly changing part. That is, in TFR, only quasistable components are selected. In this paper, we design an STFT based on the standard deviation of conventional rates based on PTFR. The rate is defined as the ratio of the effectivity bandwidth B_{eff} to the effectivity duration T_{eff} of the signal being analyzed.

$$\nu_0 = \frac{B_{\text{eff}}}{T_{\text{eff}}} = \left[\frac{1}{N} \frac{\sum_{k=-K_t/2}^{K_t/2-1} (k - k_0)^2 |X[k]|^2}{\sum_{k_t=0}^{K_t-1} (k_t - k_{t0})^2 |x[k_t]|^2}\right]^{1/2}, \quad (23)$$

where $X[k]$ represents the discrete Fourier transform of $x[k_t]$:

$$\begin{aligned} k_0 &= \frac{\sum_{k=-K_t/2}^{K_t/2-1} k |X[k]|^2}{\sum_{k=-K_t/2}^{N/2-1} |X[k]|^2}, \\ k_{t0} &= \frac{\sum_{k_t=0}^{K_t-1} k_t |x[k_t]|^2}{\sum_{k_t=0}^{K_t-1} |x[k_t]|^2}. \end{aligned} \quad (24)$$

If the normalized power spectral density (that is, the normalized unit) of a signal is regarded as a function of probability mass, the second central moment of the signal B_{eff}^2 is the second central moment of its frequency, B_{eff} is its standard deviation, and it represents the bandwidth of the signal. We can think of T_{eff} as the time width of a signal, as before. In this way, the conventional ratio ν_0 can be understood as the linear chirp scanning the frequency range B_{eff} throughout T_{eff}. We use the regular rate to determine the overall constant change rate of the signal IF regularity, which can be used as a fixed observation window for the PTFR to set the standard deviation of the STFT according to $\sigma = (3/7)^{1/4}/\sqrt{2\pi\nu_0}$.

2.2.2. IF Rate Estimation. In stage 2 of the adaptive algorithm, we get a rough estimate of IFR (IFR: IF rate, that is first derivative of IF). For this end, the IF is estimated by the main trajectory of PTFR. On this basis, the IFR is obtained by the IF first derivative. If the signal is multicomponent, each component must be found before differentiating each IF ridge. Here, the IF component separation is implemented according to the image processing algorithm described in [24]. It involves converting the TFR to a binary image and then performing a component connection process, in the case of TFR longer than a predetermined threshold, according to the adjacent connection criterion, extracting the connection peak from the TFR. This approach does not require prior knowledge of the relevant components but instead assumes that the IF ridge can be distinguishable in the TFR, which are many real-world signals, including most signals [25–27].

For the derivation, [19] adopted the conventional difference operator. However, we know that this method is very sensitive to identifying discrete signals with noise. Therefore, the signal-to-noise ratio of the differential signal is usually lower than that of the original signal. Thus, in [20], the difference operator is replaced by principal component analysis, which executes eigenvalue decomposition for the 2L estimations neighbouring $\hat{f}_I[k_t]$ to approximate $f_I{}'[k_t]$. In

this article, we use a more straightforward way to find first-order differentials. First, the estimates $\widehat{f}_I[k_t]$ are smoothed according to

$$\widetilde{\widehat{f}}_I[k_t] = \frac{1}{2L+1}\sum_{k_t-L}^{k_t+L}\widehat{f}_I[k_t], \quad k_t = L, \cdots, K_t - L, \tag{25}$$

where L represents a positive integer. The above smoother represents a simple average moving filter used to improve the SNR of the differential signal [28]. After above smoothing the signal, the IFR is estimated using a traditional difference operator. As L increases, the degree of noise reduction increases, but the attenuation of the differential amplitude also becomes more remarkable. In addition, filtering the IF estimates according to (25) can help exclude possible outliers before derivation. Still, the accuracy of this method is limited because there is a certain relation between consecutive sampling errors in TFR [10]. Therefore, be careful when choosing L. Here, the smoothing width is 11.

2.2.3. Optimizing Window Width. After extracting the IF and IFR, they can be optimized for appropriate window widths. At this step, two ways adjust the TFR window width. In one case, the window width can be set in terms of time or frequency. For all signals, the primary purpose of this width optimization is to perform an optimal tradeoff at each moment or frequency. Therefore, when the window width is optimal, its cost function is the smallest. Since both adaptivity STFT (ASTFT) and ST can be done rapidly with FFT, the advantage of this method is that its complexity is slight. On the other hand, you can set a window to change at different times and frequencies. Within the TF region, width adjustment is allowed, and the second method requires more flexibility; however, since $\sigma[k_t, k_f]$ is related to k_t and k_f, in (22), GSFT cannot be implemented with FFT.

We design an ASTFT that minimizes the IF estimation MSE sum at any moment. Because the TFRs generated by ASTFTs generally do not have crossterms, the TFRs can be approximated to the TFRs corresponding to the individual components of the overall signal. In this example, the formula can be generalized to the case of multicomponent signals with TF regions. That is, with ASTFT, an estimate of the IF with no offset can be obtained, and the total MSE can be obtained:

$$\mathrm{MSE}_{\mathrm{tot}}[k_t, \sigma[k_t]] = \sum_{l=1}^{L_n}\frac{\left[\left(2\pi f_{Il}'[k_t]\sigma^2[k_t]\right)^2 + 1\right]^{5/2}}{32\pi^{5/2}\sigma^3[k_t]C_0}, \tag{26}$$

where L_n represents the signal component number at the moment instant k_tT_s and $f_{Il}{}'[k_t]$ represents the lth single IF component IFR. The optimal window width is defined by minimizing $\mathrm{MSE}_{\mathrm{tot}}[k_t, \sigma[k_t]]$, which may be approximated by

$$\sigma_{\mathrm{opt}}[k_t] \approx \arg\ \min_{\sigma[k_t]}\sum_{l=1}^{L_n}\frac{\left[\left(2\pi\widehat{f}_{Il}'[k_t]\sigma^2[k_t]\right)^2 + 1\right]^{5/2}}{\sigma^3[k_t]}. \tag{27}$$

Note that $\mathrm{MSE}_{\mathrm{tot}}[k_t, \sigma[k_t]]$ represents the summation of all functions, each of which is completely convex and has an overall minimum value on $\sigma_l[k_t]$, and there also is an overall minimum value for $\mathrm{MSE}_{\mathrm{tot}}[k_t, \sigma[k_t]]$. Therefore, it is contained in the following range:

$$\sigma_{\mathrm{opt}}[k_t] \in \left[\min\left\{\sigma_1[k_t], \cdots, \sigma_{L_n}[k_t]\right\}, \max\left\{\sigma_1[k_t], \cdots, \sigma_{L_n}[k_t]\right\}\right]. \tag{28}$$

A good approximation of $\sigma_{\mathrm{opt}}[k_t]$ is obtained in two steps: first, $\sigma_l[k_t]$ is found corresponding to the estimated IFR minimum and maximum; thus, for width between the above two limits, the optimal candidates depend on the objective function form (27). The TFR we obtained is called optimal ASTFT (OASTFT).

To reduce the sum of MSE estimated by IF, the width of the frequency domain correlation window in ST is optimized. It is required to obtain the 1st- and 2nd-order frequency derivative information of the window widths. Not knowing the nature of the differential equation, it has to be designed accordingly, making the method impractical; therefore, we cannot go on like this.

The previous OASTFT algorithm has achieved a good balance among the signal components in the TF region, but it needs to be adjusted more to make it more adaptable. If the IF ridges can be separated within the TF region, then the window width of the GSFT can be adjusted individually. We can roughly estimate the IFs and IFRs, so the problem is how to defend the standard deviation of a window about the on-ridge and off-ridge time-frequency points. At IF, the first and second derivatives of the standard deviation and frequency are 0, and then, window width is optimal. Therefore, we define a window width interval Δ_f determined by the following formula on each upper ridge point of the IF component according to

$$\sigma\left[k_t, k_f\right] = \frac{(3/7)^{1/4}}{\sqrt{2\pi\left|\widehat{f}_{Il}'[k_t]\right|}}, \quad 0 \le \left|k_f - \widehat{f}_{Il}[k_t]\right| \le \frac{\Delta_f}{2}, \tag{29}$$

whereas outside the section, the window width is achieved by two-dimensional linear interpolation in [20]. The last interpolation ensures that the $\sigma[k_t, k_f]$ 1st- and 2nd-order frequency derivatives are close to 0 neighbouring $\widehat{f}_{Il}[k_t]$, so the width chosen is best for MSE. Also, the coarse IF estimate can be far from its actual value due to noise. Therefore, preferably, not only the width of (29) is specified for $\widehat{f}_{Il}[k_t]$ but also for adjacent frequencies. In experiments, we found that several frequency bands are wide enough to obtain accurate IF estimates. The resulting transformation is expressed by optimal GSFT (OGSFT).

The adaptation plan adopted consists of the three phases mentioned above. Its main work is to realize PTFR, extract and track IF components, thus obtain the corresponding IFR value, and realize adaptive TFR. The PTFR designed in this paper is STFT, and its computational complexity is $O(N^2 \log N)$. The chosen IF component extraction and tracking algorithm is presented in [24]; the computational cost for this analysis procedure is outside the scope of this work. The final TFR can be a time-adaptive ASTFT or a TF-adaptive GSFT. OASTFT can be done by FFT. That is, OASTFT needs to operate on the order of $O(N^2 \log N)$. The TF-adaptive GSFT algorithm has high adaptability, but because the FFT program cannot complete the conversion, it will lead to $O(N^3)$ level of computational complexity.

2.3. Polarimetric Time-Frequency Music and Spatial Polarimetric Correlations. For improving the signal spatial resolution with well-defined time-frequency characteristics, time-frequency multiple signal classification (TF-MUSIC) has recently been proposed [29]. This method provides an essential summary for applying MUSIC to polarization arrays, which searches for the minimum of the array vector derived from the SPTFD matrix defined in the combined space and polarization domains. The advantages of the algorithm mainly include the following two points: the algorithm integrates polarization information and time-frequency information to increase the utilization rate of multidimensional information. The algorithm adaptively recognizes the time-frequency points of autoterms and avoids the trouble of manual selection.

Consider the following spatial signature matrix:

$$\mathbf{F}(\phi) = \frac{1}{\sqrt{M}} \begin{bmatrix} \mathbf{a}^{[v]}(\phi) & \mathbf{0} \\ \mathbf{0} & \mathbf{a}^{[h]}(\phi) \end{bmatrix}. \tag{30}$$

Because $\|\mathbf{a}^{[i]}(\phi)\|^2 = M$, $\mathbf{F}^{\mathrm{H}}(\phi)\mathbf{F}(\phi)$ represents the identity matrix. For searching from the spatial and polarization joint domains, the spatial polarization vector is defined as

$$\mathbf{f}(\phi, \mathbf{c}) = \frac{\mathbf{F}(\phi)\mathbf{c}}{\|\mathbf{F}(\phi)\mathbf{c}\|} = \mathbf{F}(\phi)\mathbf{c}, \tag{31}$$

where the vector $\mathbf{c} = [c_1\ c_2]^{\mathrm{T}}$ represents an unknown unit norm vector of polarization coefficients. In (31), $\|\mathbf{F}(\phi)\mathbf{c}\| = [\mathbf{c}^H\mathbf{F}^H(\phi)\mathbf{F}(\phi)\mathbf{c}]^{1/2} = (\mathbf{c}^H\mathbf{c})^{1/2} = 1$.

The PTF-MUSIC spectrum is provided from the following function:

$$\begin{aligned} P(\phi) &= \left[\min_{\mathbf{c}} \mathbf{f}^{\mathrm{H}}(\phi, \mathbf{c})\mathbf{U}_n\mathbf{U}_n^{\mathrm{H}}\mathbf{f}(\phi, \mathbf{c})\right]^{-1} \\ &= \left[\min_{\mathbf{c}} \mathbf{c}^{\mathrm{H}}\mathbf{F}^{\mathrm{H}}(\phi)\mathbf{U}_n\mathbf{U}_n^{\mathrm{H}}\mathbf{F}(\phi)\mathbf{c}\right]^{-1}, \end{aligned} \tag{32}$$

where $\mathbf{U}_n$ represents the noise subspace from the SPTFD matrix of (20) utilized the selected time-frequency points. For DOA estimation, different STFD or SPTFD matrices can be combined using TF average and joint block diagonalization techniques [29]. Picking these points from regions of high energy concentration associated with global or local sources can improve the signal-to-noise ratio and make the MUSIC algorithm more noise-robust than its traditional MUSIC counterpart [30]. In (32), by acquiring the smallest eigenvalue for the matrix $\mathbf{F}^{\mathrm{H}}(\phi)\mathbf{U}_n\mathbf{U}_n^{\mathrm{H}}\mathbf{F}(\phi)$, this method can perform simple eigendecomposition on the 2×2 matrix, thus avoiding performing a large number of operations in the polarization region. In this way, the spectrum of PTF-MUSIC can be described as

$$P(\phi) = \lambda_{\min}^{-1}\left[\mathbf{F}^{\mathrm{H}}(\phi)\mathbf{U}_n\mathbf{U}_n^{\mathrm{H}}\mathbf{F}(\phi)\right], \tag{33}$$

where $\lambda_{\min}[\cdot]$ represents the smallest eigenvalue solution. The DOA value of the source is the highest in the spectrum. Corresponding to each angle ϕ_n of arrival of N signals, $n = 1, 2, \cdots, N$, each polarized signal parameter can be estimated as follows:

$$\hat{\mathbf{c}}(\phi_k) = \mathbf{v}_{\min}\left[\mathbf{F}^{\mathrm{H}}(\phi_k)\mathbf{U}_n\mathbf{U}_n^{\mathrm{H}}\mathbf{F}(\phi_k)\right], \tag{34}$$

where $\mathbf{v}_{\min}[\cdot]$ represents the eigenvector corresponding to the minimality eigenvalue $\lambda_{\min}[\cdot]$.

The spatial resolution capability of the array has a lot to do with the propagation characteristics of the signal [30]. This depends on the manifold vector normalized inner product of each array. For potential problems involving spatial and polarization dimensions, the extended array manifold $\tilde{\mathbf{a}}(\phi)$ is used to define the joint spatial polarization correlation coefficient between the source n_l and n_k, that is,

$$\begin{aligned} \beta_{n_l,n_k} &= \frac{1}{M}\tilde{\mathbf{a}}^{\mathrm{H}}\left(\phi_{n_k}\right)\tilde{\mathbf{a}}\left(\phi_{n_l}\right) = c_{n_k1}^* c_{n_l1}\beta_{n_l,n_k}^{[v]} + c_{n_k2}^* c_{n_l2}\beta_{n_l,n_k}^{[h]} \\ &= \frac{1}{M}\left(c_{n_k1}^* c_{n_l1}\left(\mathbf{a}^{[v]}\left(\phi_{n_k}\right)\right)^{\mathrm{H}}\mathbf{a}^{[v]}\left(\phi_{n_l}\right)\right. \\ &\quad \left. + c_{n_k2}^* c_{n_l2}\left(\mathbf{a}^{[h]}\left(\phi_{n_k}\right)\right)^{\mathrm{H}}\mathbf{a}^{[h]}\left(\phi_{n_l}\right)\right), \end{aligned} \tag{35}$$

where $\beta_{n_l,n_k}^{[i]} = (1/M)(\mathbf{a}^{[i]}(\phi_{n_k}))^H\mathbf{a}^{[i]}(\phi_{n_l})$ represents the spatial relation coefficient.

An interesting case phenomenon occurs with the identical array manifolds between vertically and horizontally polarization, i.e., $\mathbf{a}^{[v]}(\phi) = \mathbf{a}^{[h]}(\phi)$. For the condition, $\beta_{n_l,n_k}^{[v]} = \beta_{n_l,n_k}^{[h]}$, and the spatial polarization joint relation coefficient is the individual spatial polarimetric correlations product:

$$\beta_{n_l,n_k} = \beta_{n_l,n_k}^{[v]}\rho_{n_l,n_k}, \tag{36}$$

within

$$\begin{aligned} \rho_{n_l,n_k} = \mathbf{c}_{n_k}^{\mathrm{H}}\mathbf{c}_{n_l} &= \cos\left(\gamma_{n_l}\right)\cos\left(\gamma_{n_k}\right)e^{j\left(\eta_{n_l}-\eta_{n_k}\right)} \\ &\quad + \sin\left(\gamma_{n_l}\right)\sin\left(\gamma_{n_k}\right), \end{aligned} \tag{37}$$

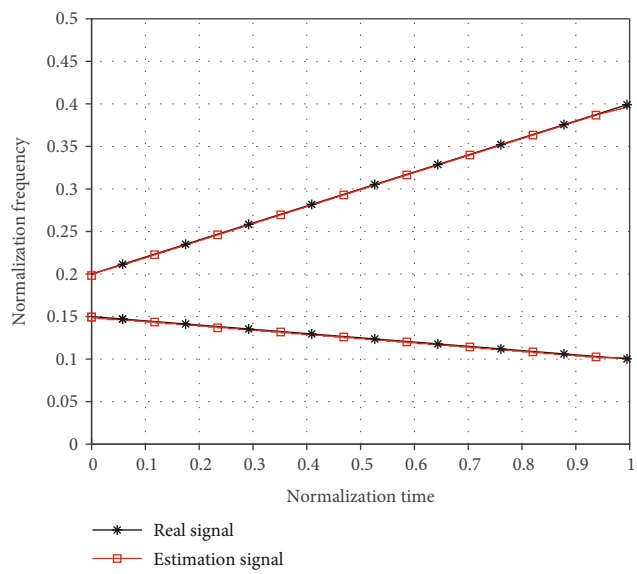

Figure 3: The results of time-frequency analysis.

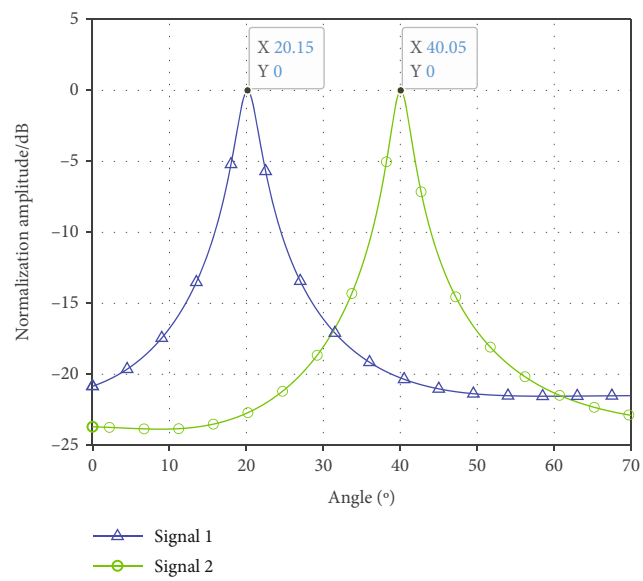

Figure 4: The spatial spectrum estimation.

denoting the polarization correlation coefficient. Particularly, for linear polarization, $\eta_{n_l} = \eta_{n_k} = 0$, and (37) reduces to

$$\rho_{n_l,n_k} = \cos\left(\gamma_{n_l} - \gamma_{n_k}\right). \tag{38}$$

Since $|\rho_{n_l,n_k}| \leq 1$, the equality holds only when the polarization states of the two light sources are the same; compared with the single spatial correlation coefficient, the spatial polarization correlation coefficient is small. Due to the polarization diversity dropping correlation value, the introduced method ρ_{n_l,n_k} was adopted, which was converted into enhanced signal source identification. In this way, it is difficult to resolve the two sources with a single monopolar spatial array manifold $\mathbf{a}^{[v]}(\phi)$ or $\mathbf{a}^{[h]}(\phi)$ with an extended spatial polarized array manifold, defined by $\tilde{\mathbf{a}}(\phi)$, which can be easily separated. This improvement is more pronounced when the signal spatial relation coefficient is large, but the individual polarization correlations are low.

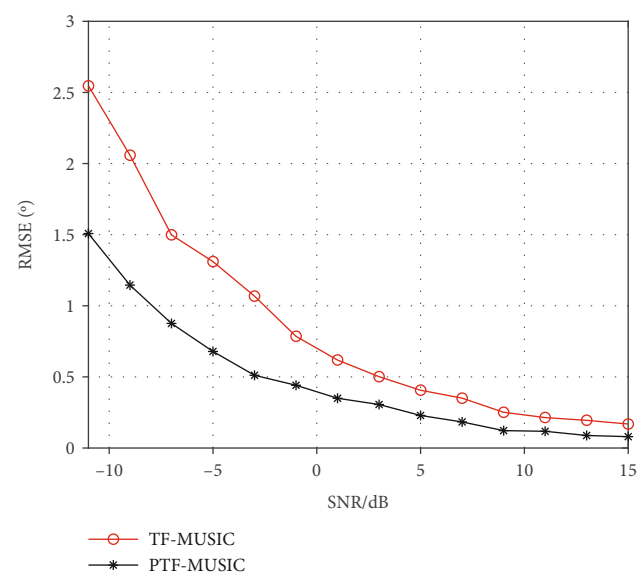

Figure 5: The curve between RMSE and SNR.

3. Results and Discussion

This paper focuses on the improvement of the adaptive time-frequency analysis algorithm, so the polarization parameters are assumed to be known prior parameters in the simulation process. The results of the three-step adaptive time-frequency analysis are analyzed by simulation. Simulation conditions are as follows: the signal component 1 normalized frequency is from 0.15 to 0.1; the signal component 2 normalized frequency is from 0.2 to 0.4; the number of sampling points is 1024; the SNR is 0 dB. The simulation results are shown in Figure 3. The black asterisk line in the figure represents the truth value; the red box line represents the estimated result. It can be seen that the algorithm can accurately estimate the instantaneous frequency of the signal. It is possible to select time-frequency points to construct the spatially polarized time-frequency distribution matrix. Then, the spatial spectrum estimation algorithm is simulated and analyzed under the following conditions: the normalized frequency of the two signal components is the same as before; the incidence angles are 20 degrees and 40 degrees, respectively. The number of snapshots is 512; the SNR is 0 dB. Simulation results of spatial spectrum estimation of polarization time-frequency MUSIC algorithm based on adaptive time-frequency analysis algorithm are shown in Figure 4. The blue triangle curve is the spatial spectrum estimation result of signal component 1. The green circle curve is the result of spatial spectrum estimation of signal component 2. It can be seen from the marked DOA estimation

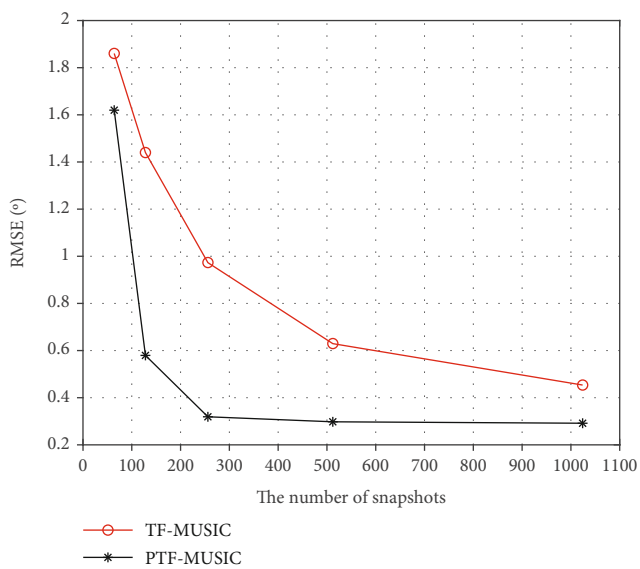

Figure 6: The curve between RMSE and snapshot number.

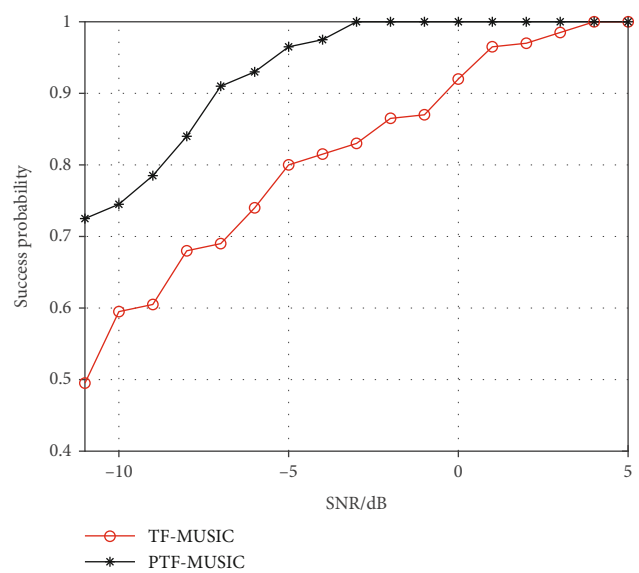

Figure 7: The curve between the estimation success probability and SNR.

results of the figure that the algorithm can accurately distinguish and estimate the angle of the incident signal.

Finally, the performance of the proposed algorithm is simulated and analyzed. The relationship between RMSE and SNR and snapshot number is analyzed, and the time-frequency MUSIC algorithm based on traditional time-frequency analysis is compared. The simulation analysis conditions of RMSE and SNR are as follows: the normalized frequency and incident angle of the two signals are the same as before; the number of snapshots is fixed at 512. The SNR increased from -11 dB to 15 dB with a step size of 1 dB. The simulation results are shown in Figure 5. In the figure, the black star curve is the estimation result of the proposed algorithm, and the red circle curve is the result of the traditional algorithm. The results show that the RMSE of both methods decreases in the case of SNR increasing, and the proposed algorithm is significantly better than the traditional algorithm. The effect is more evident at low SNR. At about 0 dB, there is still about 0.2 degree of improvement. The simulation analysis conditions of RMSE and snapshot number are as follows: the normalized frequency and incident angle of the two signals are the same as before; the SNR is fixed at 0 dB; the number of snapshots increases gradually from 64 to 1024, taking the whole power of 2. The simulation results are shown in Figure 6. In the figure, the black star curve is the estimation result of the proposed algorithm, and the red circle curve is the result of the traditional algorithm. The results show that the RMSE of both methods decreases in the case of snapshot number increasing, and the proposed algorithm is obviously better than the traditional algorithm. When the number of snapshots is low, due to the small number of samples, the results of the two algorithms are relatively close, but the proposed algorithm is still better than the traditional algorithm. As the number of snapshots increases, the RMSE of the proposed algorithm decreases rapidly compared with the traditional algorithm. In practice, considering the actual finite length received data, the spatially polarized time-frequency distribution matrix is estimated according to the received data obtained by many snapshot number. As the snapshot number increases, the matrix estimation is more accurate. After the eigendecomposition, the noise subspace estimation is more accurate, thus improving DOA estimation performance.

Additionally, the relationships between the estimation success probability and SNR and snapshot number are analyzed, and the time-frequency MUSIC algorithm based on traditional time-frequency analysis is compared. The simulation analysis conditions of the estimation success probability and SNR are as follows: the normalized frequency and incident angle of the two signals are the same as before; the number of snapshots is fixed at 512. The SNR increased from -11 dB to 5 dB with a step size of 1 dB. When the estimation error is less than 1.5 degrees, the estimation is judged to be successful. The simulation results are shown in Figure 7. In the figure, the black star curve is the estimation result of the proposed algorithm, and the red circle curve is the result of the traditional algorithm. The results show that the estimation success probability of both methods increases with SNR increasing, and the proposed algorithm is significantly better than the traditional algorithm. The improvement of the estimation success probability is more evident at low SNR. The simulation analysis conditions of the estimation success probability and the snapshot number are as follows: the normalized frequency and incident angle of the two signals are the same as before; the SNR is fixed at -2 dB; the number of snapshots increases gradually from 64 to 1024, taking the whole power of 2. When the estimation error is less than 1.5 degrees, the estimation is judged to be successful. The simulation results are shown in Figure 8. In the figure, the black star curve is the estimation result of the proposed algorithm, and the red circle curve is the result of the traditional algorithm. The results show that the estimation success probability of both methods increases with snapshot number increasing, and the proposed algorithm

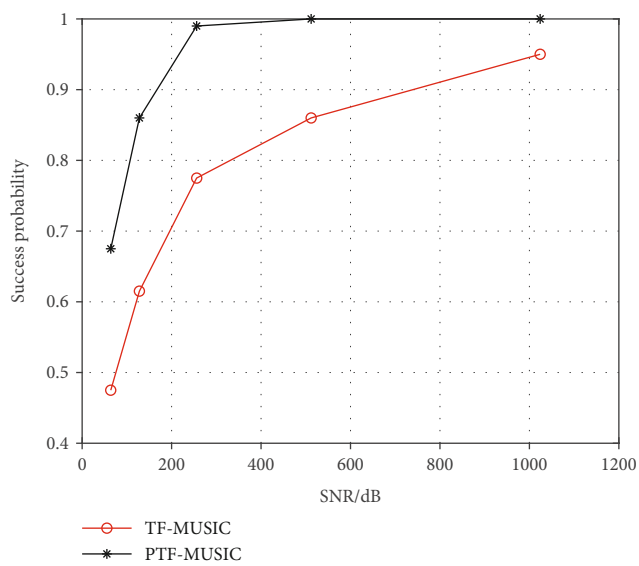

Figure 8: The curve between the estimation success probability and snapshot number.

is obviously better than the traditional algorithm. When the number of snapshots is low, due to the small number of samples, the results of the two algorithms are general, but the proposed algorithm is still better than the traditional algorithm. As the number of snapshots increases, the estimation success probability of the proposed algorithm increases rapidly compared with the traditional algorithm. From many aspects, the performance of the proposed algorithm is obviously due to the traditional algorithm. The polarization spatial time-frequency DOA estimation algorithm combines the three-step adaptive time-frequency analysis algorithm to achieve good results.

4. Conclusions

This paper introduces a new method for estimating the direction of arrival of polarized waves using time-frequency adaptive linear time-frequency transforms. A linear TFR was used as an IF estimate, primarily due to its simplicity and immunity to cross-interference. The optimal window relies on the IF 1st-order derivative. Therefore, a simple algorithm is used for deriving the derivative and optimizing it accordingly. Due to its combination with signal polarization, STFD gains more freedom and thus promotes the estimation of the signal and noise phonon space. On the SPTFD platform, PTF-MUSIC is used for the estimation of signal DOA, which outperforms conventional time-frequency MUSIC. Through the analysis of the simulation results in the previous section, it is proved that the proposed algorithm is superior to the traditional algorithm in many aspects. Compared with the traditional algorithm, the improvement is more significant.

Data Availability

The data used to support the findings of this study are available from the corresponding author upon request.

Conflicts of Interest

The authors declare that there is no conflict of interest regarding the publication of this paper.

Acknowledgments

The research and publication of the article were funded by the National Natural Science Foundation of China (Nos. 62031015, 61971159, 61971156, and 62171154), the Natural Science Foundation of Shandong Province (Nos. ZR2020MF007 and ZR2020MF013), and the Research Fund Program of Guangdong Key Laboratory of Aerospace Communication and Networking Technology (No. 2018B030322004).

References

[1] B. Boashash, *Time-Frequency Signal Analysis and Processing: A Comprehensive Reference*, Academic press, 2015.

[2] B. Boashash and S. Ouelha, "Automatic signal abnormality detection using time-frequency features and machine learning: a newborn EEG seizure case study," *Knowledge-Based Systems*, vol. 106, pp. 38–50, 2016.

[3] M. Liu, Z. Liu, W. Lu, Y. Chen, X. Gao, and N. Zhao, "Distributed few-shot learning for intelligent recognition of communication jamming," *IEEE Journal of Selected Topics in Signal Processing*, vol. 16, no. 3, pp. 395–405, 2022.

[4] S. H. Liu, Y. D. Zhang, T. Shan, and R. Tao, "Structure-aware Bayesian compressive sensing for frequency-hopping spectrum estimation with missing observations," *IEEE Transactions on Signal Processing*, vol. 66, no. 8, pp. 2153–2166, 2018.

[5] R. Zhagypar, K. Zhagyparova, and M. T. Akhtar, "Spatially smoothed TF-root-MUSIC for DOA estimation of coherent and non-stationary sources under noisy conditions," *IEEE Access*, vol. 9, pp. 95754–95766, 2021.

[6] M. Liu, B. Li, Y. Chen et al., "Location parameter estimation of moving aerial target in space–air–ground-integrated networks-based IoV," *IEEE Internet of Things Journal*, vol. 9, no. 8, pp. 5696–5707, 2022.

[7] R. Zhagypar, K. Zhagyparova, and M. T. Akhtar, "Exploiting the rules of the TF-MUSIC and spatial smoothing to enhance the DOA estimation for coherent and non-stationary sources," in *2020 Asia-Pacific Signal and Information Processing Association Annual Summit and Conference (APSIPA ASC), IEEE*, pp. 236–241, Auckland, New Zealand, 2020.

[8] R. G. Stockwell, L. Mansinha, and R. P. Lowe, "Localization of the complex spectrum: the S transform," *IEEE Transactions on Signal Processing*, vol. 44, no. 4, pp. 998–1001, 1996.

[9] B. Boashash, N. A. Khan, and T. Ben-Jabeur, "Time-frequency features for pattern recognition using high-resolution TFDs: a tutorial review," *Digital Signal Processing*, vol. 40, pp. 1–30, 2015.

[10] L. Stanković, I. Djurović, S. Stanković, M. Simeunović, S. Djukanović, and M. Daković, "Instantaneous frequency in time-frequency analysis: enhanced concepts and performance of estimation algorithms," *Digital Signal Processing*, vol. 35, pp. 1–13, 2014.

[11] E. Sejdić, I. Djurović, and J. Jiang, "A window width optimized S-transform," *EURASIP Journal on Advances in Signal Processing*, vol. 2008, 13 pages, 2007.

[12] W. Lu, Y. Ding, Y. Gao et al., "Resource and trajectory optimization for secure communications in dual unmanned aerial vehicle mobile edge computing systems," *IEEE Transactions on Industrial Informatics*, vol. 18, no. 4, pp. 2704–2713, 2022.

[13] N. A. Khan and B. Boashash, "Instantaneous frequency estimation of multicomponent nonstationary signals using multiview time-frequency distributions based on the adaptive fractional spectrogram," *IEEE Signal Processing Letters*, vol. 20, no. 2, pp. 157–160, 2013.

[14] M. Liu, C. Liu, M. Li, Y. Chen, S. Zheng, and N. Zhao, "Intelligent passive detection of aerial target in space-air-ground integrated networks," *China Communications*, vol. 19, no. 1, pp. 52–63, 2022.

[15] Y. Xu, J. Tang, B. Li, N. Zhao, D. Niyato, and K.-K. Wong, "Adaptive aggregate transmission for device-to-multi-device aided cooperative NOMA networks," *IEEE Journal on Selected Areas in Communications*, vol. 40, no. 4, pp. 1355–1370, 2022.

[16] V. N. Ivanovic, M. Dakovic, and L. Stankovic, "Performance of quadratic time~frequency distributions as instantaneous frequency estimators," *IEEE Transactions on Signal Processing*, vol. 51, no. 1, pp. 77–89, 2003.

[17] E. Sejdic, L. J. Stankovic, M. Dakovic, J. Jiang, and E. Sejdic, "Instantaneous frequency estimation using the S-transform," *IEEE Signal Processing Letters*, vol. 15, pp. 309–312, 2008.

[18] V. Katkovnik and L. J. Stankovic, "Instantaneous frequency estimation using the Wigner distribution with varying and data-driven window length," *IEEE Transactions on Signal Processing*, vol. 46, no. 9, pp. 2315–2325, 1998.

[19] J. Zhong and Y. Huang, "Time-Frequency representation based on an adaptive short-time Fourier transform," *IEEE Transactions on Signal Processing*, vol. 58, no. 10, pp. 5118–5128, 2010.

[20] S. C. Pei and S. G. Huang, "STFT with adaptive window width based on the chirp rate," *IEEE Transactions on Signal Processing*, vol. 60, no. 8, pp. 4065–4080, 2012.

[21] Y. Abdoush, G. Pojani, and G. E. Corazza, "Adaptive instantaneous frequency estimation of multicomponent signals based on linear time–frequency transforms," *IEEE Transactions on Signal Processing*, vol. 67, no. 12, pp. 3100–3112, 2019.

[22] Y. Zhang, B. A. Obeidat, and M. G. Amin, "Spatial polarimetric time-frequency distributions for direction-of-arrival estimations," *IEEE Transactions on Signal Processing*, vol. 54, no. 4, pp. 1327–1340, 2006.

[23] S. Shuai, L. Aijun, Y. Changjun, and Z. Quanrui, "Polarization quaternion DOA estimation based on vector MISC array," *Journal of Systems Engineering and Electronics*, vol. 32, no. 4, pp. 764–778, 2021.

[24] L. Rankine, M. Mesbah, and B. Boashash, "IF estimation for multicomponent signals using image processing techniques in the time–frequency domain," *Signal Processing*, vol. 87, no. 6, pp. 1234–1250, 2007.

[25] S. Dong, G. Azemi, B. Lingwood, P. B. Colditz, and B. Boashash, "Performance evaluation of multi-component instantaneous frequency estimation techniques for heart rate variability analysis," in *2012 11th International Conference on Information Science, Signal Processing and their Applications (ISSPA), IEEE*, pp. 1211–1216, Montreal, QC, Canada, 2012.

[26] Y. Xu, B. Li, N. Zhao et al., "Coordinated direct and relay transmission with NOMA and network coding in Nakagami-m fading channels," *IEEE Transactions on Communications*, vol. 69, no. 1, pp. 207–222, 2021.

[27] W. Lu, P. Si, G. Huang et al., "SWIPT cooperative spectrum sharing for 6G-enabled cognitive IoT network," *IEEE Internet of Things Journal*, vol. 8, no. 20, pp. 15070–15080, 2021.

[28] P. O'Shea, "On refining polynomial phase signal parameter estimates," *IEEE Transactions on Aerospace and Electronic Systems*, vol. 46, no. 3, pp. 978–987, 2010.

[29] A. Belouchrani and M. G. Amin, "Time-frequency MUSIC," *IEEE Signal Processing Letters*, vol. 6, no. 5, pp. 109-110, 1999.

[30] Y. Zhang, W. Ma, and M. G. Amin, "Subspace analysis of spatial time-frequency distribution matrices," *IEEE Transactions on Signal Processing*, vol. 49, no. 4, pp. 747–759, 2001.

Hindawi
Wireless Communications and Mobile Computing
Volume 2022, Article ID 4139345, 13 pages
https://doi.org/10.1155/2022/4139345

Research Article

Cognitive-Based High Robustness Frequency Hopping Strategy for UAV Swarms in Complex Electromagnetic Environment

Rui Xue and Mingfei Zhao

Harbin Engineering University, Harbin 150001, China

Correspondence should be addressed to Mingfei Zhao; zhaomingfei0825@hotmail.com

Received 17 May 2022; Revised 19 June 2022; Accepted 7 July 2022; Published 31 July 2022

Academic Editor: Mingqian Liu

Unmanned aerial vehicles (UAVs) confront various interference in the process of missions, and frequency hopping (FH) technology is one of the effective means of anti-interference for UAV. The FH system can avoid interference frequency points and possess certain anti-interference ability by making the carrier frequency continuously popping. However, the increasingly complex electromagnetic environment of UAV swarms requires more efficient anti-interference measure. To further improve the anti-interference ability of UAVs, this paper proposes a cognitive-based high robustness FH strategy. By adding a cognitive module to FH system, UAVs can avoid the interference frequency points adaptively and sensitively. The proposed system can identify typical suppressed interference and filter the interference frequency points. Cognitive FH system can avoid interference points completely with accurate detections and enhance the robustness for UAV swarms in complex electromagnetic environment compared to conventional FH system. Simulation results have shown that BER performance of proposed cognitive FH strategy is better than conventional FH strategy for typical suppressed interference.

1. Introduction

The applications of unmanned aerial vehicles (UAVs) become more and more extensive in both civil and military fields due to advantages such as low cost, light weight and ease of deployment [1–5]. As the missions become more intricate, multiple UAVs as a swarm instead of one single UAV obtain wider applications [6–8]. However, as information technology and communication network are developing rapidly [9], the electromagnetic environment confronted by UAV swarms for wireless communication is more complex [10]. Multiple drones will face different geographical environment, weather environment, and electromagnetic environment when performing tasks [11]. Therefore, a high robustness system is the key of information transmission for UAV swarms. To guarantee the reliability and security of data transmission, the anti-interference ability of UAV swarm is increasingly required [12].

The data link of UAV swarms can be divided into uplink, downlink, and relay link due to the direction of information transmission, as shown in Figure 1. Uplink is mainly used to send control and command information. The amount of uplink information is small, and the time of transmission is short, which makes uplink data difficult to interfere [13]. Different from the uplink, the transmission of downlink data is easily interfered because downlink is primarily used to transmit multimedia information from UAVs such as high-definition images and videos, which occupy more transmission time. Specially, remote UAVs employ satellite relays to transmit data, which increases the risk of interference. For example, RQ-170 Sentinel UAV was captured by Iranian forces due to the interference signal on December 4, 2011 [14]. The external interference faced by UAVs can be divided into suppressed interference and deceptive interference [15]. Suppressed interference suppresses the source information by sending high-power

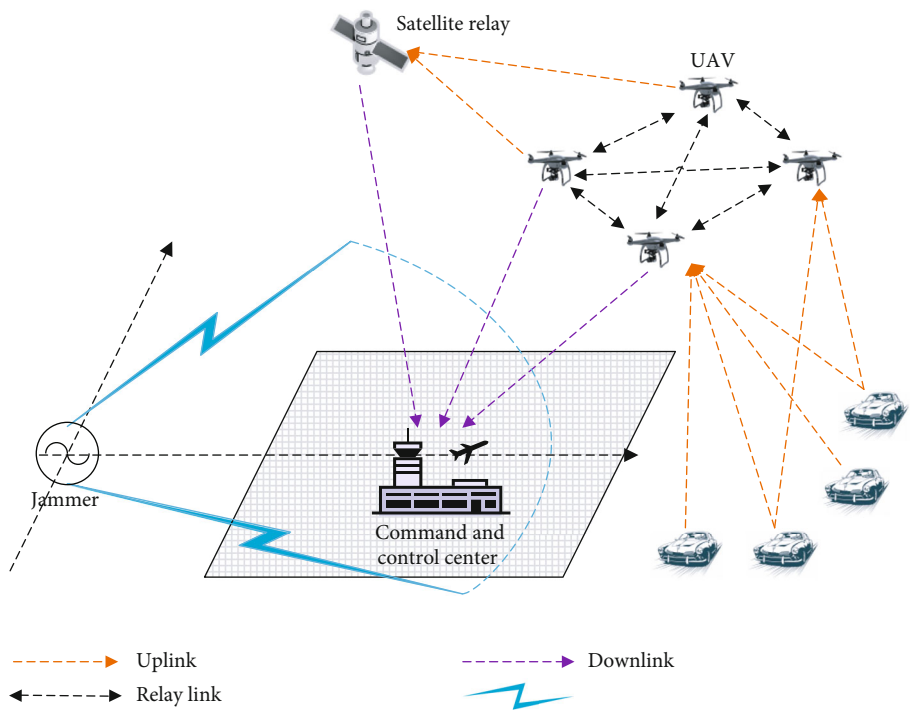

Figure 1: Types of UAV communication links.

interference, which is simple in implementation and has become a widely applied interference method recently. Therefore, the interference faced by downlink data of UAVs is mostly suppressed interference, including broadband noise (BN) interference [16], single-tone (ST) interference, multitone (MT) interference [17], narrowband noise (NN) interference [18], and linear frequency modulation (LFM) interference [19].

The anti-interference of UAVs is to taking certain measures to eliminate the influence of interference sources on UAV communications, so that UAV can complete data transmission [20]. Each anti-interference technology is effective to one or several certain interferences, and no existing anti-interference technology can resist all types of interference [21]. The anti-interference methods of UAVs mainly include direct sequence spread spectrum technology, frequency hopping (FH) technology, time hopping technology, hybrid spread spectrum technology, and adaptive antenna nulling technology [22]. Among them, FH technology is generally applied due to its excellent anti-interference performance and covert communication capability by continually changing the frequency point to avoid interference. Identification and detection of interference signals is the foundation of FH system. Improving the performance of detection and identification can enhance the anti-interference ability of the system [23, 24]. The authors in [25] employ a differential FH communication system for UAVs to confront interference and verify the performance of the system in Rician channels. However, the Rician channel model is not universal in UAV systems. The authors in [26] propose a reinforcement learning approach for antijamming communications in UAV swarms. This method has improved the communication quality, but the application of the scheme is limited due to its high complexity. The authors in [27] present a local reaction antijamming scheme based on adaptive frequency hopping. The FH strategy of the scheme is selected based on the node type without considering the type of interference.

We can observe that FH technology is an effective method for the anti-interference ability of one single drone. However, the advantages of FH diminish as the increasing number of UAVs due to the more complex electromagnetic environment. Conventional FH system simply carries out according to established rules without the ability of interference detecting. To further promote the robustness of UAV swarms, we propose a cognitive-based FH strategy for anti-interference in complex electromagnetic environment. The proposed strategy adds cognitive decision module compared to the conventional FH system and avoid the interference point in advance by interference detection algorithms. Cognitive FH strategy conforms to the development trend of UAV and provides crucial guarantee for the robustness of information transmission, which can meet communication requirements in complex electromagnetic environments.

The rest of the paper is organized as follows. Section 2 describes the interference detection algorithm, which is the basis of cognitive FH strategy. Section 3 expresses the cognitive FH strategy for UAV swarms, including the system model and functional module. Section 4 introduces the numerical results and analysis. Section 5 is the conclusions.

2. Interference Detection Algorithm

The interference of UAVs mainly comprises suppressed interference and deceptive interference. Suppressed interference is simpler to implement and becomes a common means

of interference, including BN interference, ST interference, MT interference, NN interference, and LF interference. For the five kinds of interference above, the interference signal model and interference recognition algorithm are introduced in this section.

2.1. Interference Signal Model. BN interference generates interference signals by employing random noise and applies them to all hopping subchannels. Therefore, additive white Gaussian noise (AWGN) is required to generate BN interference, which is shown as follows:

$$x_{\mathrm{BN}}(t) \sim N\left(0, \frac{P_J}{2W_s}\right), \tag{1}$$

where W_s and P_J present the bandwidth of the system and interference power. BN interference can be obtained by filtering Gaussian white noise as follows:

$$J_{\mathrm{BN}}(t) = \int_{-\infty}^{\infty} x(\tau)h(t-\tau)d\tau, \tag{2}$$

where the filter function is $h(t)$ and the Fourier transform of $h(t)$ is $H_{\mathrm{BN}}(j2\pi f)$, which can be expressed as follows:

$$H_{\mathrm{BN}}(j2\pi f) = \begin{cases} 1, & |f| \le W_s, \\ 0, & \text{else}. \end{cases} \tag{3}$$

Then, an amplifier is employed to generate BN interference, which is used to suppress the entire frequency band of the target system. The time domain diagram and frequency domain diagram of BN interference is shown in Figure 2 when the interference power is 8 dBW. BN interference is applied to the entire frequency band. Therefore, it is necessary to expand the bandwidth to improve the anti-interference performance.

NN interference uses narrowband filters to process Gaussian white noise, which is the difference between NN interference and BN interference. Gaussian white noise of NN interference can be expressed as follows:

$$x_{\mathrm{NN}}(t) \sim N\left(0, \frac{P_J}{2W_J}\right), \tag{4}$$

where W_J is the interfered bandwidth of the system. After the filter, NN interference is depicted as follows:

$$J_{\mathrm{NN}}(t) = \int_{-\infty}^{\infty} x(\tau)h(t-\tau)d\tau. \tag{5}$$

$H_{\mathrm{NN}}(j2\pi f)$ is the Fourier transform of $h(t)$, and $H_{\mathrm{BN}}(j2\pi f)$ is related to the bandwidth of the interference signal. $H_{\mathrm{BN}}(j2\pi f)$ can be expressed as follows:

$$H(j2\pi f) = \begin{cases} 1, & \left|f \pm f_J\right| \le \dfrac{W_J}{2}, \\ 0, & \text{else}, \end{cases} \tag{6}$$

where f_J and W_J denote the centre frequency and the bandwidth of the interference, respectively. The time domain diagram and frequency domain diagram of NN interference are depicted in Figure 2 when interference power is 8 dBW and the value of interference factor $k = 1$. Inaccuracy of threshold setting for forward consecutive mean excision (FCME) with single thresholds will affect the detection performance and FCME with double thresholds can avoid high probability of false alarm. Therefore, FCME with double thresholds is selected for NN interference.

ST interference and MT interference are both tone interference. The domain expression of the ST interference is as follows:

$$J_{\mathrm{ST}}(t) = \sqrt{2P_J}\cos\left(2\pi f_J t + \varphi\right), \tag{7}$$

where f_J and φ denote interference frequency and initial phase. ST interference imposes all power on the frequency point f_J with energy concentration but limited interference range. The time domain diagram and frequency domain diagram of ST interference when the interference power is 1 dBW are shown in Figure 2.

MT interference is the application of interference signal to some specific frequency points in the frequency hopping band. The domain expression of the MT interference is as follows:

$$J_{\mathrm{MT}}(t) = \sum_{i=1}^{N_J} \sqrt{2P_i}\cos\left(2\pi f_i t + \varphi_i\right), \tag{8}$$

where N_J is the number of interference points. The range of MT interference is larger than ST interference, and its interference frequency is more concentrated than NN interference. The time domain diagram and frequency domain diagram when interference is 1 dBW are shown in Figure 2.

In addition, the domain expression of LFM interference is shown as follows:

$$J_{\mathrm{LFM}}(t) = A\exp\left[j\left(2\pi f_j t + \pi K t^2 + \varphi\right)\right], \quad 0 \le t \le T, \tag{9}$$

where A is the signal amplitude, f_j is the centre frequency, φ is the initial phase, T is the signal duration, B_{LFM} is the frequency modulation interference bandwidth, and $K = B_{\mathrm{LFM}}/T$. The time domain diagram and frequency domain diagram are shown in Figure 2. The sampling frequency $f_s =$ 1000Hz, the interference power is 1 dBW, and the sweep bandwidth is frequency domain diagram of LFM interference with 100M. For ST, MT, and LFM interference, to reduce the detection delay and improve the real-time performance of the detection algorithm, the single-threshold FCME algorithm is selected.

2.2. Interference Detection Algorithm. The interference detection algorithm is the basis and premise of FH. Rapid detection and accurate judgment of interference signal types can improve the efficiency of cognitive module. Time domain energy detection algorithm can quickly detect the

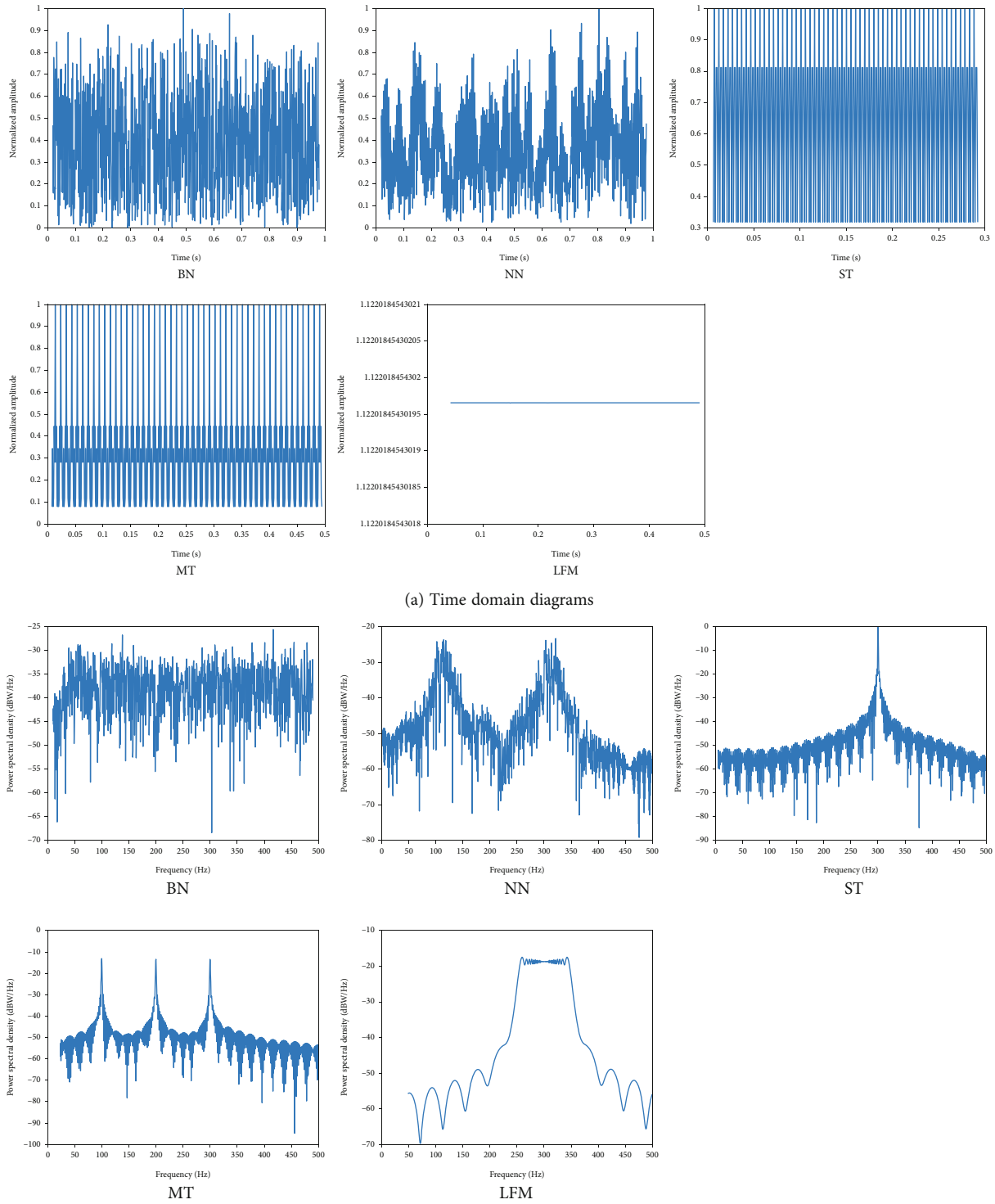

(a) Time domain diagrams

(b) Frequency domain diagrams

Figure 2: Time domain and frequency domain diagrams of typical interference.

presence of interference without the requirement of any prior information, which is easy to implement and widely applied. However, in addition to detecting the existence of interference, no more information can be obtained for time domain energy detection algorithm. Therefore, we adopt frequency domain detection algorithm to detect interference in this paper, which can locate interference frequency accurately.

The schematic diagram of frequency domain detection algorithm is shown in Figure 3. The signal was processed by A/D sampling and fast Fourier transform (FFT). Then, the sum square of the amplitude modulus of the frequency point is calculated and compared with the judgment threshold, in which way the position of interference frequency can be obtained. The judgment threshold is obtained by

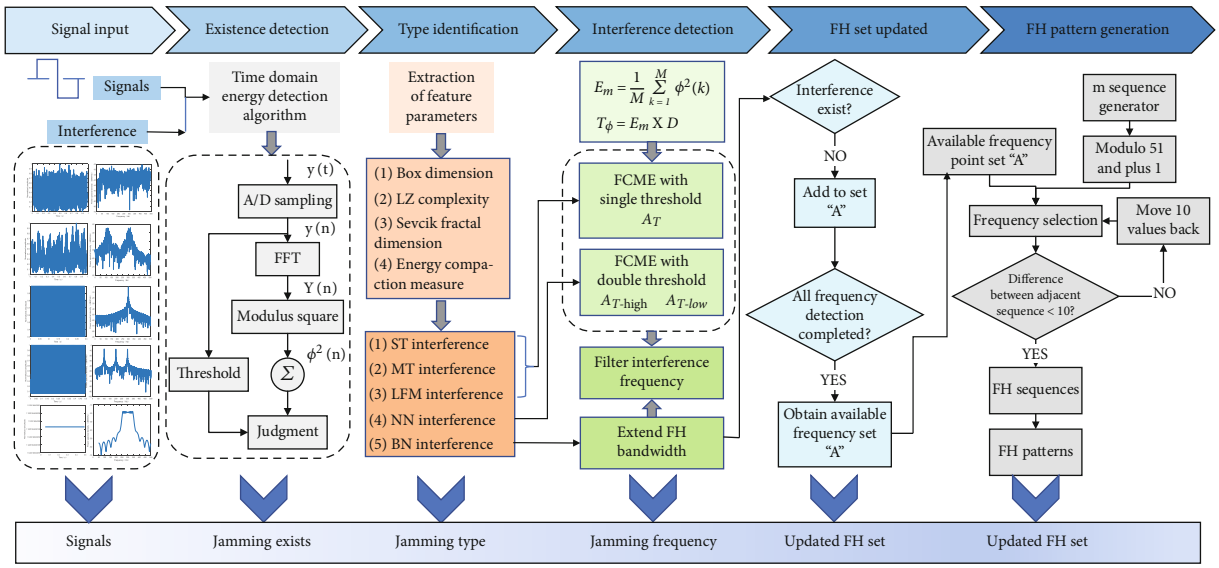

Figure 3: Data processing flow chart of cognitive FH system.

multiplying the threshold factor by the mean value of the noise spectral amplitude. However, the mean value of noise amplitude contains interference signals, which leads to an excessive threshold because the noise mean contains the interference signal. FCME algorithm can eliminate interference frequency points and constantly update the threshold to obtain the final judgment threshold. FCME algorithm improves the disadvantage of excessive threshold of frequency domain energy detection algorithm. We illustrate the detection performance of FCME algorithm with single threshold and double thresholds, respectively.

When calculating the detection threshold for the first time, FCME algorithm only considers a small part of the frequency points with small amplitude as noninterference signals. In this way, noise estimation accuracy is improved, and the value of threshold is more accurate. A/D sampling is performed on the received signal $y(t)$ to obtain $y(n)$, and FFT is performed to obtain $Y(n)$. The square of amplitude modulus at each frequency point of received signal can be expressed as follows:

$$\phi^2(n) = R_e^2|Y(n)| + I_m^2|Y(n)|, n = 0, 1, \cdots, N-1, \quad (10)$$

where the minor M values of $\phi^2(n)$ are noise frequency points, and the mean value is as follows:

$$E_m = \frac{1}{M}\sum_{k=1}^{M}\phi^2(k). \quad (11)$$

The judgment threshold T_ϕ is obtained by multiplying E_m with the threshold factor D as follows

$$T_\phi = E_m \times D. \quad (12)$$

The square of amplitude modulus $\phi^2(n)$ of remaining frequency points are compared with T_ϕ, and the frequency points greater than T_ϕ are considered to be interference frequency points. After eliminating the interference frequency points, the residual noise frequency points form a new set of noise frequency points. Repeating the algorithm above can continuously update the judgment threshold until no new interference frequency is removed. Therefore, the value of final detection threshold A_T is obtained. When the value of $\phi^2(n)$ is greater than A_T, it is determined as interference points. However, when FCME algorithm with single threshold detects discontinuous signals, such as NN interference, false alarm probability will be high or misjudged due to inappropriate threshold factors. Therefore, FCME algorithm with double thresholds is applied to NN interference detections.

FCME algorithm with double thresholds adopts two different threshold factors. The minor threshold factor is employed to detect all frequency points so that possible interference frequency points can be screened out. The set of selected interference frequency points is defined as cluster, using the larger threshold factor to detect the possible interference frequency in the cluster and ultimately determine whether there is interference. Specifically, $Y(n)$ is obtained by FFT of $y(t)$. Square of amplitude modulus $\phi^2(n)$ at each frequency point of received signal are expressed as follows:

$$\phi^2(n) = R_e^2|Y(n)| + I_m^2|Y(n)|, n = 0, 1, \cdots, N-1. \quad (13)$$

The minor M points are considered as frequency points which contain only noise and the average E_{m1} as follows:

$$E_{m1} = \frac{1}{M}\sum_{k=1}^{M}\phi^2(k). \quad (14)$$

The minor judgment threshold $T_{\phi 1}$ is obtained by multiplying the threshold factor D_1 with the mean value E_{m1} as follows:

$$T_{\phi 1} = E_{m1} \times D_1. \tag{15}$$

As mentioned above, the judgment threshold is continuously updated until no new interference frequency points are eliminated. The final judgment threshold is obtained as $A_{T-\text{low}}$. The higher threshold $A_{T-\text{high}}$ is obtained by multiplying the larger threshold D_2 with the mean square of the final amplitude modulus. Comparing the maximum value of each cluster with $A_{T-\text{high}}$, if it is greater than A, it is considered that this cluster is an interference frequency band.

3. Cognitive FH Strategy for UAV Swarms

As demonstrated above, frequency points which are interference can be screened out by FCME algorithms. Based on interference detection technology, we apply cognitive FH technology to the data link of UAV swarm. For UAV swarms, different communication channels for each UAV result in different and irregular interference frequency points. Conventional FH technology is difficult to meet the anti-interference requirements of each UAV. Cognitive FH technology can avoid interference frequency actively and possess excellent anti-interference effect. For cognitive FH strategy of UAV swarms, the system model and functional module will be introduced, respectively, in this section. The data processing flow chart of cognitive FH system is shown in Figure 3, including interference existence detection, interference type detection, interference frequency detection, FH set update, and FH pattern generation. In recent years, signal recognition based on deep learning has become a research hotspot [28, 29]. In addition, the complexity of signal recognition can be reduced by feature extraction [30]. Recognition algorithm based on Sevcik fractal dimension and energy aggregation degree obtains obvious advantages at low values of JNR, such as the fast recognition speed and high recognition rate [12]. The selection of FCME algorithm with single/double thresholds requires accurate interference identification results. Therefore, we adopt and we select two-dimensional feature interference recognition algorithm based on Sevcik fractal dimension and energy aggregation degree for the identification of signal type.

3.1. System Model. Cognitive FH strategy draws on the idea of cognitive radio and adds cognitive units to the conventional FH system. The data link employed for UAV swarms in this paper refers to link16 data link, and the system model for data link of UAV swarm based on cognitive FH is shown in Figure 3. Information from the transmitter is processed by Reed Solomon (RS) encoding, interleaving, cyclic code shift keying (CCSK) spread spectrum, and minimum shift keying (MSK) modulation. FH modulation is acquired by mixing frequency with frequency synthesizer output controlled by pseudorandom sequence. At the receiving terminal, compared with conventional FH technology, cognitive FH technology adds cognitive units for anti-interference. Therefore, the receiver can filter out the interference frequency by cognitive unit and update FH set. In addition, the receiver will decode, demodulate, despread, and deinterleave the received signal to get the original information.

As shown in Figure 3, the cognitive unit consists of interference cognitive module, cognitive decision module, and spectrum dynamic allocation module. Interference cognition module consists of interference detection and interference type recognition, which requires rapid and effective detection of interference signals from complex electromagnetic environment. Then, the interference type is determined and submitted to the cognitive decision module. Cognitive decision module makes corresponding anti-interference strategy based on interference information and filter interference frequency points. After obtaining the available FH points, they are transmitted to the dynamic spectrum allocation module to generate the available frequency hopping set. Finally, the updated FH frequency set is transmitted to the transmitter and receiver to optimize the FH system.

For the cognitive unit, the flow chart of signal processing is shown in Figure 4. First of all, energy detection algorithm is adopted to detect the presence of interference. Energy detection algorithm possesses high detection efficiency for preliminary screening of interference signals. Two characteristic parameters are extracted to form two-dimensional feature vector $\mathbf{T}$ when interference exists. $\mathbf{T}$ consists of frequency domain Sevcik fractal dimension and fractional Fourier domain energy aggregation degree, which is considered as the basis for interference identification. Then, recognition results are passed to the cognitive decision module. Cognitive decision module selects corresponding transmission strategy by interference type. When ST, MT, and LFM interference are identified, FCME with double thresholds obtains no obvious improvement compared to FCME with single threshold. Therefore, to reduce the detection delay and improve the real-time performance of the detection algorithm, FCME, the single threshold algorithm is selected to filter interference frequency. Similarly, when NN interference and BN interference are identified, FCME algorithm with double thresholds and FH bandwidth extension are adopted, respectively.

3.2. Functional Module. In this paper, 51 frequency points are selected and numbered as $1, 2, L \cdots, 51$ to constitute the initial frequency set. In addition, FH frequency range is set as 969~1008 MHz, 1053~1065 MHz, and 1113~1206 MHz, and frequency interval is set as 3 MHz.

When interference is detected, including ST, MT, LFM, NN, and BN interference, the system selects available frequency points from all frequency points for FH and updates the hopping frequency set. The flow chart of adaptive update for cognitive FH strategy can be seen in Figure 3. According to the results of interference identification, FCME algorithm with single or double thresholds is adopted to detect whether there is interference at each frequency point. If no interference exists, the frequency point number is added to set A. After all subband detection is completed, the FH frequency set is updated adequately.

The flow chart of FH pattern generation is demonstrated in Figure 5. Signals sent at the transmitter $s(t)$ can be expressed as follows:

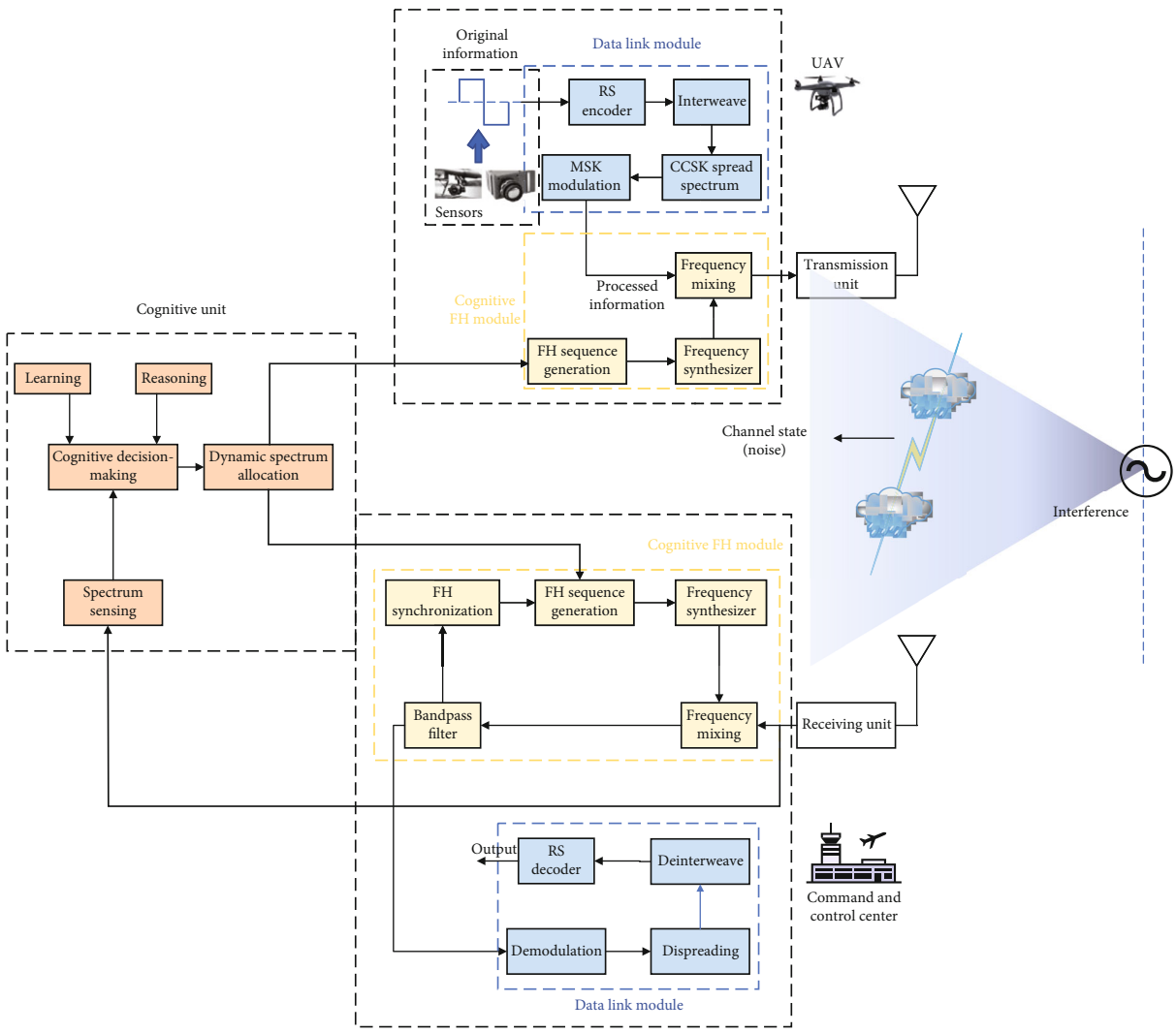

Figure 4: System model for data link of UAV swarm based on cognitive FH.

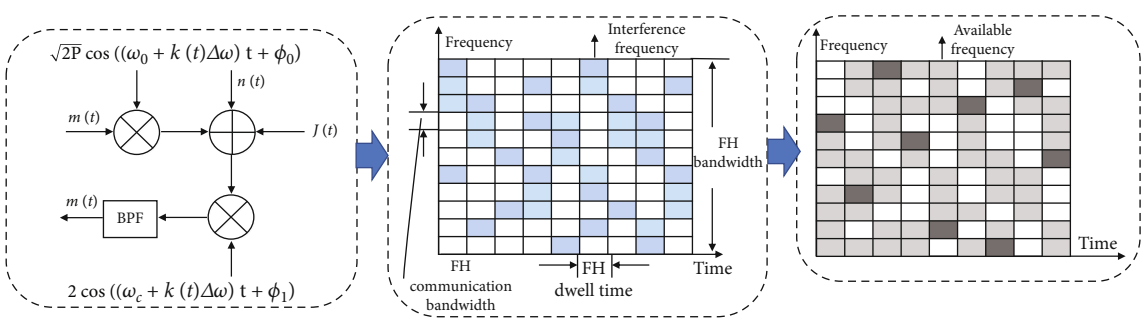

Figure 5: Flow chart of FH pattern generation.

$$s(t) = \sqrt{2P}m(t)\cos[(\omega_0 + k(t)\Delta\omega)t + \varphi_0], \quad (16)$$

$$r(t) = \sqrt{2P_i}m(t)\cos[(\omega_0 + k(t)\Delta\omega)t + \varphi(t)] + J(t) + n(t), \quad (17)$$

where $s(t)$ is modulated signals, ω_0 is minimum angular frequency, $\Delta\omega$ is the minimum interval of angular frequency, φ_0 is the initial phase, and $k(t)$ varies with pseudorandom sequence. In addition, signals received at the receiving terminal $r(t)$ can be expressed as follows:

where $J(t)$ and $n(t)$ represent interference signals and noise signals in channels, respectively. P_i is the power of the receiving signal, and $\varphi(t)$ represents the phase of the receiving signals.

When the FH synchronization is completed, the output of the mixer unit $r'(t)$ can be expressed as follows:

$$\begin{aligned} r'(t) &= r(t) \times 2\cos\{[(\omega_c + k(t)\Delta\omega)t + \varphi_1]\} \\ &= 2\sqrt{2P_i}m(t)\cos[(\omega_0 + k(t)\Delta\omega)t + \varphi(t)]\cos \\ &\quad \cdot [(\omega_c + k(t)\Delta\omega)t + \varphi_1] + 2[J(t) + n(t)]\cos \\ &\quad \cdot [(\omega_c + k(t)\Delta\omega)t + \varphi_1] \\ &= \sqrt{2P_i}m(t)\cos[\omega_I t + \varphi(t) - \varphi_1] \\ &\quad + \sqrt{2P_i}m(t)\cos\{[\omega_0 + \omega_c + 2k(t)\Delta\omega]t + \varphi(t) + \varphi_1\} \\ &\quad + 2[J(t) + n(t)]\cos[(\omega_c + k(t)\Delta\omega)t + \varphi_1], \end{aligned} \tag{18}$$

where $2\cos\{[(\omega_c + k(t)\Delta\omega)t + \varphi_1]\}$ is output of the frequency synthesizer, ω_c is the central angular frequency, φ_1 is phase deviation, ω_I is intermediate frequency angular frequency, and $\omega_I = \omega_c - \omega_0$. The output signal of band-pass filter (BPF) $m'(t)$ can be expressed as follows:

$$m'(t) = \sqrt{2P_i}s(t)\cos[\omega_I t + \varphi(t) - \varphi_1] + J'(t) + n'(t), \tag{19}$$

where $J'(t)$ and $n'(t)$ represent interference and noise at the output end.

Different from the conventional FH technology which selects the FH carrier frequency from all frequency points, cognitive FH adopts frequency points from the updated available hopping frequency set according to the results of interference frequency selections. In addition, the interval between adjacent frequency points is more than 30 MHz. As depicted in Figure 5, the blue part, grey part, and black part represent interference frequency, available frequency, and the selected frequency. The available frequency set A can be expressed as follows:

$$A = A_E - A_I = \{f_i | f_i \in A_E, f \notin A_I\}, \tag{20}$$

where A, A_E, and A_I express the available frequency set, the entire frequency set, and the removed frequency set. After completing the adaptive update of the FH set, a set of available frequency hopping points A is obtained. Then, the FH sequence is generated by employing m sequence with length of 63. The obtained FH sequence is taken as modulus 51 and add 1, in which way the FH sequence between 1 and 51 can be acquired. In order to make the interval between adjacent FH points not less than 30 MHz, the difference between adjacent FH sequences should be guaranteed more than 10.

At the receiving terminal, cognitive unit of cognitive FH strategy obtains the available FH set through perception, analysis, and decision-making. Then, cognitive FH transmits relevant information to both transmitter and receiver through a reliable public communication channel. Therefore, the transmitter and the receiver obtain the same spectrum information and realize FH synchronization and communication parameters adjustment.

4. Numerical Results and Analysis

In the cognitive FH strategy data link of this paper, transmission slots of the system are divided into data transmission slot and interference cognitive time slots, which are carried out alternately. The interference cognition takes up one FH time slot, and the data transmission occupies 93 FH time slots. We assume that the cognitive FH strategy of UAV swarm is applied in open plains with less obstacles, such as mountains and buildings. Therefore, the Nakagami-m channel fading model is selected for simulations, where the value of parameter m represents the severity of fading. Specifically, it can be considered as Rayleigh fading channel when $m = 1$, Rice channel when $m > 1$, and AWGN channel when $m \longrightarrow \infty$. Considering that the scenario for UAV data link in this paper is a broad plain environment, the value of m is set to 2. Other simulation parameters refer to link 16 in this paper, and specific parameter settings are shown in Table 1.

We have simulated BER performance of five typical types of interference of different values of JNR, including BN interference, NN interference, ST interference, MT interference, and LFM interference. We adopt JNR = 12dB , JNR = 8dB, JNR = 4dB, and JNR = 0dB for simulations. BER performance of different values of JNR for BN interference is shown in Figure 6. BN interference is realized by applying interference to the whole bandwidth of FH communications. It can be seen that at the same value of SNR, larger value of JNR leads to worse BER performance. Larger values of JNR lead to greater interference power and the interference power allocated to each frequency point is greater, which generate greater damage to the communication system. Therefore, countering BN interference can be achieved by extending hopping bandwidth because wider bandwidth increases the difficulty of interference. In addition, BER performance of cognitive FH strategy is superior to conventional FH system. For example, when BER = 10^{-3} and JNR = 8dB, cognitive FH strategy obtains 1 dB gains compared to conventional FH system. Hence, cognitive FH system improves the ability of UAV data link against BN interference.

As mentioned above, FCME with double thresholds obtains better detection performance for NN interference. Therefore, FCME with double thresholds is selected to remove the frequency points with interference and update FH set for NN interference system. The BER performance of different JNR for NN interference system is shown in Figure 7. NN interference in simulations contains two interference bands. It can be seen that cognitive FH attains better BER performance compared to conventional FH systems when the value of JNR is fixed. Specifically, when the values of BER and JNR are 10^{-4} and 4 dB, cognitive FH strategy obtains approximately 0.2 dB gains compared to conventional FH system.

Tone interference includes ST interference and MT interference. FCME with single threshold achieves satisfactory detection results and filter out interference. Since FCME with double thresholds does not obviously improve detection performance compared to FCME with single threshold,

Table 1: Parameters for simulations.

Frequency range	969~1008 MHz, 1053~1065 MHz, 1113~1206 MHz
Coding mode	RS (31, 15)
Modulation mode	MSK
Spread Spectrum mode	CCSK (32, 5)
Frequency interval	3 MHz
FH interval	30 MHz
FH points	51

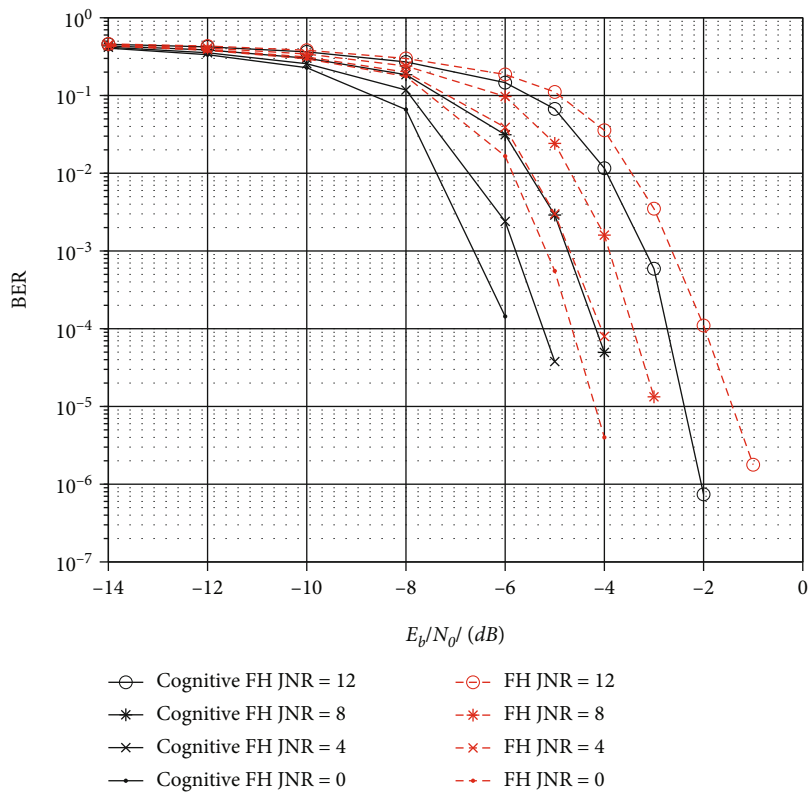

Figure 6: BER performance of different JNR for BN interference.

to reduce the detection delay and enhance the real-time performance of the detection algorithm, FCME with single threshold is adopted. BER performance of different JNR for ST interference is depicted in Figure 8. For conventional FH system, BER performance reduces as the value of JNR decreases because it cannot avoid interference points. However, BER performance of cognitive FH strategy has no obvious change with the different values of JNR. As a routine means of interference, tone interference can be detected by FCME algorithm, and interference can be filtered out easily. Therefore, cognitive FH strategy obtains better BER performance compared to conventional FH system for ST interference.

BER performance of different JNR for MT interference is depicted in Figure 9. Similar to ST interference, MT interference can also find interference frequency points accurately through FCME algorithm and eliminate interference frequency points. Simulation results indicate that cognitive FH strategy attains better BER performance than conventional FH system especially when the value of JNR is high. Therefore, cognitive FH can obviously improve BER performance for MT interference.

LFM interference is to scan the entire communication frequency band with a signal with relatively narrow bandwidth within a certain time. The instantaneous state of LFM can be regarded as NN interference. Therefore, we adopt FCME algorithm to detect and update FH set. BER performance of different JNR for LFM interference is shown in Figure 10, and the interference bandwidth is set to 30 MHz. BER performance of different JNR values is obviously different for cognitive FH strategy because FCME algorithm cannot detect all interference frequency points. Cognitive FH obtains better performance compared to conventional FH, but cognitive FH strategy cannot remove all interference frequency since LFM is a sweep interference.

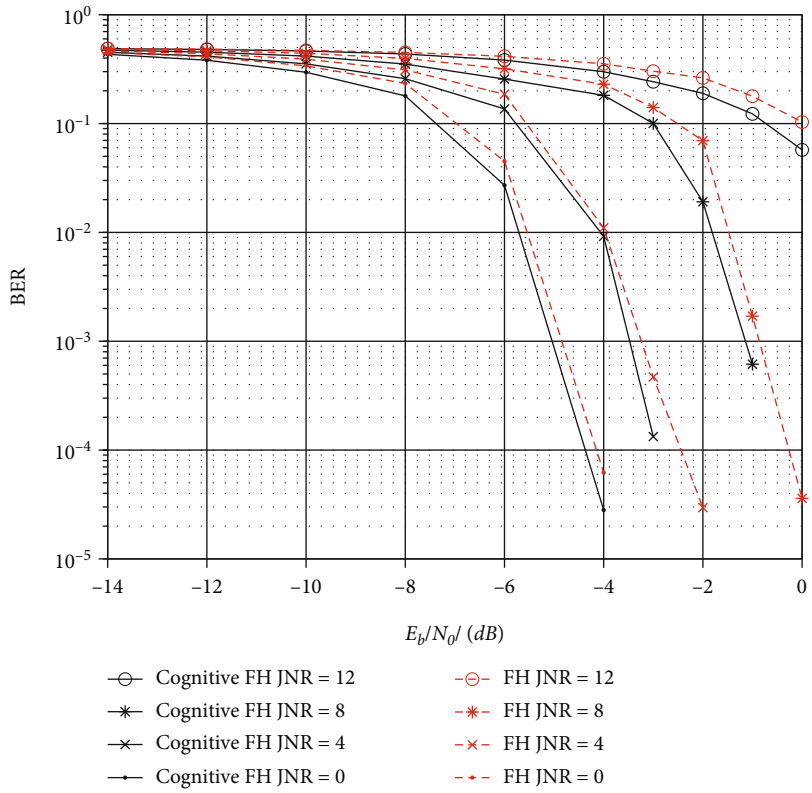

Figure 7: BER performance of different JNR for NN interference.

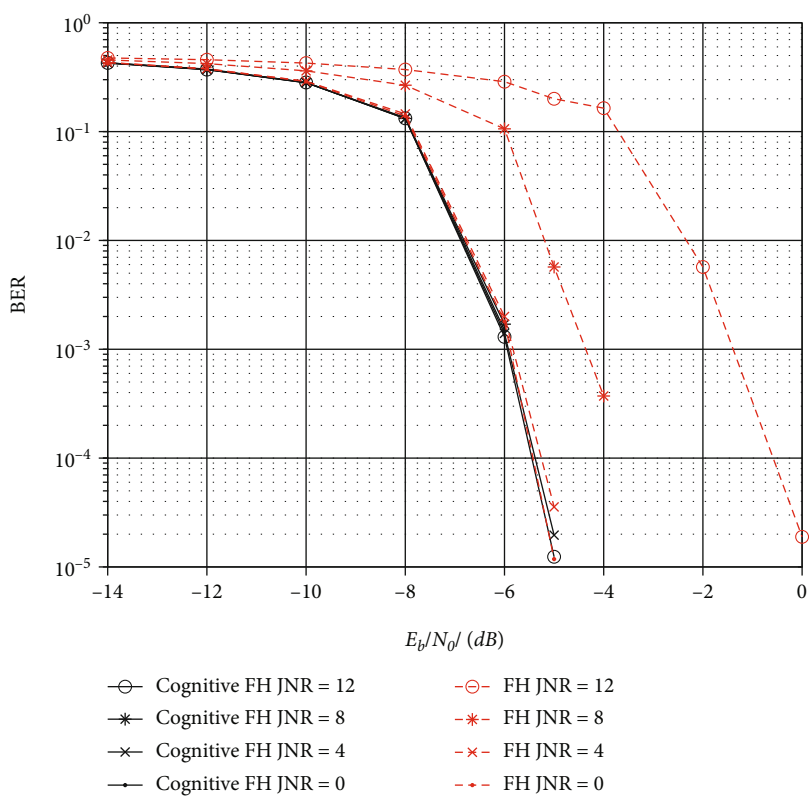

Figure 8: BER performance of different JNR for ST interference.

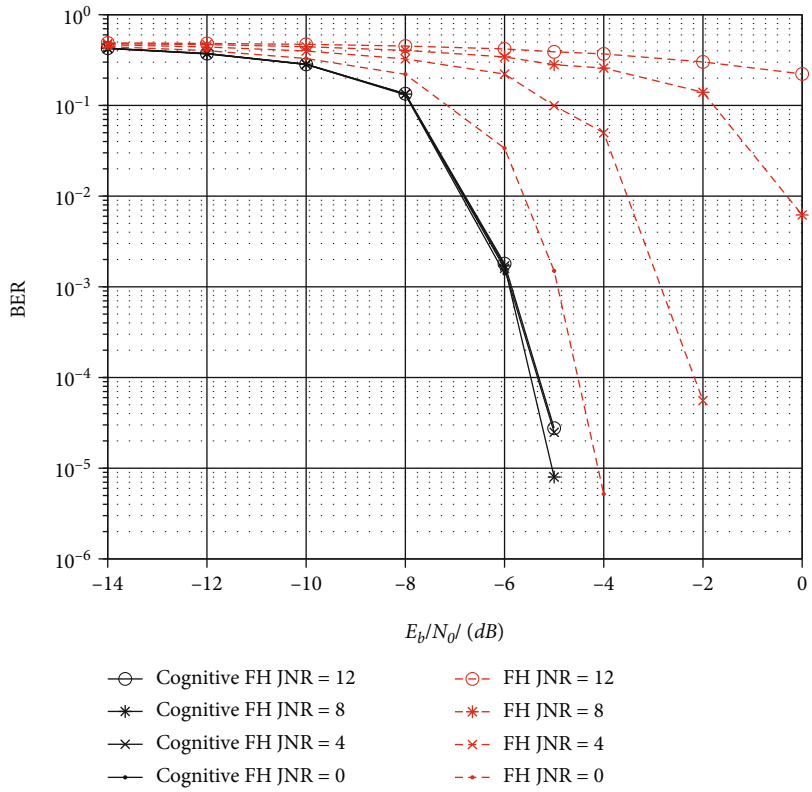

Figure 9: BER performance of different JNR for MT interference.

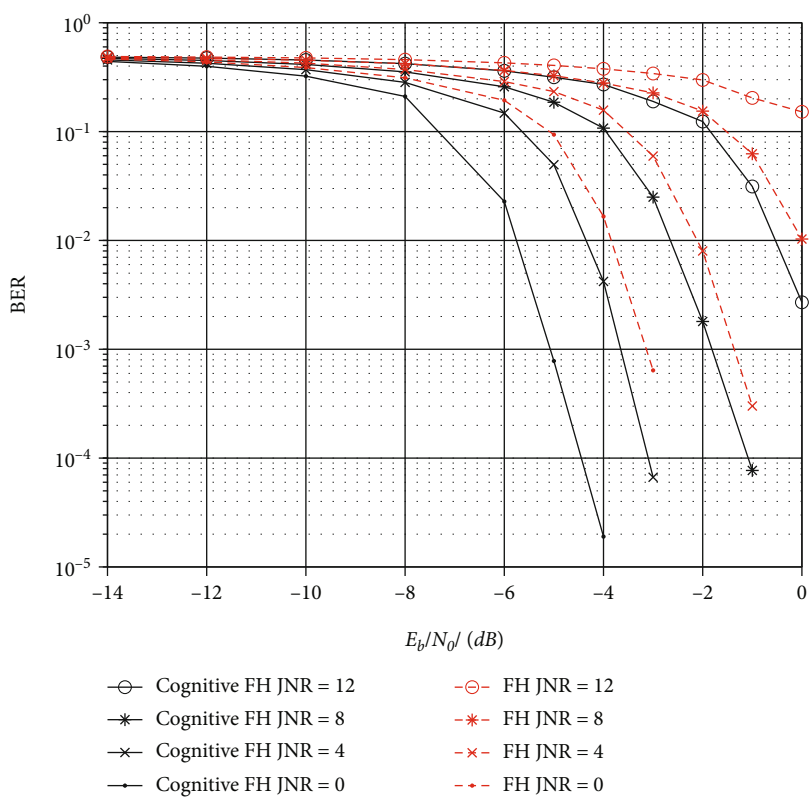

Figure 10: BER performance of different JNR for LFM interference.

5. Conclusions

To improve the robustness for data link of UAV swarm, this paper proposed cognitive-based high robustness frequency hopping strategy in complex electromagnetic environment. Through detecting and identifying the interference, the proposed cognitive FH strategy can obtain the type of interference and interference frequency points. Afterwards, the cognitive FH strategy can actively avoid the interference frequency points by updating the FH frequency set. Simulation results show that BER performance of cognitive FH strategy is improved compared to conventional FH system for five different types of interference, including BN interference, NN interference, ST interference, MT interference, and LFM interference. For example, when the value of target BER is 10^{-3}, cognitive FH strategy obtains approximately 0.5 dB gains of NN interference for different JNR values compared to conventional FH system. Cognitive FH strategy can adaptively select anti-interference strategy according to actual conditions, which enhances robustness for UAV swarms. In the future, electromagnetic environment faced by UAV swarms will be more complicated, which leads to an increasing requirement for anti-interference ability of the system. Therefore, cognitive FH strategy will become an important component for the data link of UAV swarms.

Data Availability

No data were used to support this study.

Conflicts of Interest

The authors declare that there are no conflicts of interest regarding the publication of this paper.

Acknowledgments

This paper was supported in part by the National Natural Science Foundation of China (No. 61873070), the Heilongjiang Provincial Natural Science Foundation of China (No. LH2020F018), and the Fundamental Research Funds for the Central Universities (No. 3072022QBZ0803).

References

[1] J. Liu, N. Sha, W. Yang, J. Tu, and L. Yang, "Hierarchical q-learning based uav secure communication against multiple UAV adaptive eavesdroppers," *Wireless Communications and Mobile Computing*, vol. 2020, Article ID 8825120, 15 pages, 2020.

[2] H. Niu, X. Zhao, L. Hou, and D. Ma, "Energy efficiency maximization for UAV-assisted emergency communication networks," *Wireless Communications and Mobile Computing*, vol. 2021, Article ID 7595347, 15 pages, 2021.

[3] R. Xue, M. Zhao, and H. Tang, "Information transmission schemes based on adaptive coded modulation for UAV surveillance systems with satellite relays," *IEEE Access*, vol. 8, no. 8, pp. 191355–191364, 2020.

[4] B. Li, Z. Fei, and Y. Zhang, "UAV communications for 5G and beyond: recent advances and future trends," *IEEE Internet of Things Journal*, vol. 6, no. 2, pp. 2241–2263, 2018.

[5] M. M. Azari, G. Geraci, A. Garcia-Rodriguez, and S. Pollin, "UAV-to-UAV communications in cellular networks," *IEEE Transactions on Wireless Communications*, vol. 19, no. 9, pp. 6130–6144, 2020.

[6] A. Mukherjee, S. Misra, A. Sukrutha, and N. S. Raghuwanshi, "Distributed aerial processing for IoT-based edge UAV swarms in smart farming," *Computer Networks*, vol. 167, article 107038, 2020.

[7] X. Chen, J. Tang, and S. Lao, "Review of unmanned aerial vehicle swarm communication architectures and routing protocols," *Applied Sciences*, vol. 10, no. 10, article 3661, 2020.

[8] J. Wang, Y. Liu, S. Niu, and H. Song, "Extensive throughput enhancement for 5G-enabled UAV swarm networking," *IEEE Journal on Miniaturization for Air and Space Systems*, vol. 2, no. 4, pp. 199–208, 2021.

[9] M. Liu, Z. Liu, W. Lu, Y. Chen, X. Gao, and N. Zhao, "Distributed few-shot learning for intelligent recognition of communication jamming," *IEEE Journal of Selected Topics in Signal Processing*, vol. 16, no. 3, pp. 395–405, 2022.

[10] Z. Bao, Y. Lin, S. Zhang, Z. Li, and S. Mao, "Threat of adversarial attacks on DL-based IoT device identification," *IEEE Internet of Things Journal*, vol. 9, no. 11, pp. 9012–9024, 2022.

[11] L. Lin, C. Chen, K. Su, B. Chen, and H. Li, "Design of anti-interference system for fully autonomous UAV based on ADRC-EKF algorithm," in *2019 IEEE 2nd International Conference on Electronics and Communication Engineering (ICECE)*, pp. 428–433, Harbin, China, 2019.

[12] R. Xue, J. Liu, and H. Tang, "Two-dimensional jamming recognition algorithm based on the Sevcik fractal dimension and energy concentration property for UAV frequency hopping systems," *Information*, vol. 11, no. 11, p. 520, 2020.

[13] W. Wang, B. Jiang, X. Tan, and C. Li, "UAV communication interference analysis and anti-interference methods," in *Proceedings of the 2020 International Conference on Cyberspace Innovation of Advanced Technologies*, pp. 197–201, Guangzhou, China, 2020.

[14] H. Baek and J. Lim, "Design of future UAV-relay tactical data link for reliable UAV control and situational awareness," *IEEE Communications Magazine*, vol. 56, no. 10, pp. 144–150, 2018.

[15] Y. Zheng, S. Li, K. Xing, and X. Zhang, "Unmanned aerial vehicles for magnetic surveys: a review on platform selection and interference suppression," *Drones*, vol. 5, no. 3, p. 93, 2021.

[16] S. Yan, M. Peng, and X. Cao, "A game theory approach for joint access selection and resource allocation in UAV assisted IoT communication networks," *IEEE Internet of Things Journal*, vol. 6, no. 2, pp. 1663–1674, 2018.

[17] S. Popli, R. K. Jha, and S. Jain, "Green NOMA assisted NB-IoT based urban farming in multistory buildings," *Computer Networks*, vol. 199, article 108410, 2021.

[18] M. Shalaby, M. Shokair, and N. W. Messiha, "Modelling and simulation of narrow band electromagnetic interference in millimeter wave massive MIMO systems," in *2018 35th National Radio Science Conference (NRSC)*, pp. 149–156, Cairo, Egypt, 2018.

[19] Y. He, D. Zhai, R. Zhang, X. du, and M. Guizani, "An anti-interference scheme for UAV data links in air–ground integrated vehicular networks," *Sensors*, vol. 19, no. 21, p. 4742, 2019.

[20] Z. Wang, R. Liu, Q. Liu, L. Han, and J. S. Thompson, "Feasibility study of UAV-assisted anti-jamming positioning," *IEEE Transactions on Vehicular Technology*, vol. 70, no. 8, pp. 7718–7733, 2021.

[21] G. Shichao, G. Dandan, Z. Qiongyu, W. Nankai, and D. Jiaxin, "Research progress of anti-jamming technology of unmanned aerial vehicle (UAV) data link," *IOP Conference Series: Materials Science and Engineering*, vol. 816, article 012011, 2020.

[22] B. M. Todorovic and V. D. Orlic, "Direct sequence spread spectrum scheme for an unmanned aerial vehicle PPM control signal protection," *IEEE Communications Letters*, vol. 13, no. 10, pp. 727–729, 2009.

[23] Y. Tu, Y. Lin, H. Zha et al., "Large-scale real-world radio signal recognition with deep learning," *Chinese Journal of Aeronautics*, 2021.

[24] M. Liu, C. Liu, M. Li, Y. Chen, S. Zheng, and N. Zhao, "Intelligent passive detection of aerial target in space-air-ground integrated networks," *China Communications*, vol. 19, no. 1, pp. 52–63, 2022.

[25] S. Xie and B. Qian, "Performance analysis of differential frequency hopping communication system over Rician channel," in *2018 IEEE 4th Information Technology and Mechatronics Engineering Conference (ITOEC)*, pp. 1015–1019, Chongqing, China, 2018.

[26] J. Peng, Z. Zhang, Q. Wu, and B. Zhang, "Anti-jamming communications in UAV swarms: a reinforcement learning approach," *IEEE Access*, vol. 7, pp. 180532–180543, 2019.

[27] K. Li, C. Wang, M. Lei, M.-M. Zhao, and M.-J. Zhao, "A local reaction anti-jamming scheme for UAV swarms," in *2020 IEEE 92nd Vehicular Technology Conference (VTC2020-Fall)*, pp. 1–6, Victoria, BC, Canada, 2021.

[28] Y. Lin, H. Zhao, X. Ma, Y. Tu, and M. Wang, "Adversarial attacks in modulation recognition with convolutional neural networks," *IEEE Transactions on Reliability*, vol. 70, no. 1, pp. 389–401, 2021.

[29] Y. Lin, Y. Tu, and Z. Dou, "An improved neural network pruning technology for automatic modulation classification in edge devices," *IEEE Transactions on Vehicular Technology*, vol. 69, no. 5, pp. 5703–5706, 2020.

[30] M. Liu, J. Wang, N. Zhao, Y. Chen, H. Song, and R. Yu, "Radio frequency fingerprint collaborative intelligent identification using incremental learning," *IEEE Transactions on Network Science and Engineering*, 2021.

Hindawi
Wireless Communications and Mobile Computing
Volume 2022, Article ID 8431967, 11 pages
https://doi.org/10.1155/2022/8431967

Research Article

Spectrum Sensing of Noncooperative Beam Signals

Xieda Song, Jinghua Li, Jiteng Liu, Yan Li, and Guoru Ding

Army Engineering University of PLA, China

Correspondence should be addressed to Jinghua Li; chinghwali@126.com

Received 10 April 2022; Revised 13 June 2022; Accepted 16 June 2022; Published 30 July 2022

Academic Editor: Mingqian Liu

In this paper, we investigate the issue of spectrum sensing of noncooperative beam signals that are emitted by a multiantenna transmitter. When the sampling period of the sensing node includes the whole process of beam scanning, that is, spectrum sensing is performed in an ideal situation, we use the traditional energy detection algorithm for spectrum sensing and get good results; for multiantenna beam scanning spectrum sensing in nonideal situation, the performance of traditional energy detection algorithm is seriously degraded. To deal with this problem, a sensing period selection (SPS) algorithm is proposed. The simulation results show that the proposed algorithm can effectively improve the performance of spectrum sensing in the multiantenna array beam scanning scenario.

1. Introduction

With the rapid development of wireless communication technology, the spectrum resource demand is also increasing [1]. The ever-increasing demand for spectrum has led to a shortage of available spectrum resources [2]. Spectrum sensing, based on various signal detection approaches, is one key enabling technology for dynamic spectrum sharing [3]. Traditional spectrum sensing mainly detects omnidirectional signals, which include energy detection [4] matched filter detection [5], and cyclostationary detection [6]. As the 5G cellular communication technology emerges, spatial domain signal generated by beamforming technology provides more available bandwidth for people's daily spectrum needs, while meeting the ever-increasing transmission rate and throughput requirements [7, 8]. At the same time, the new generation of spectrum sensing technology has also changed from the detection of omnidirectional signals to the detection of directional signals, that is, spectrum sensing of beam signals. The beamforming technology uses complex digital signal processing technology to convert the regular excitation signal into the corresponding amplitude and phase of each beam by designing the antenna array to generate a high-gain directional beam [9]. Beamforming technology can not only effectively make up for the shortcoming of beam signal's rapid loss in spatial transmission but also exploit spectrum resources from the spatial angle dimension [10]. At present, the detection of spectral holes in the spatial angle dimension, that is, spectrum beam sensing technology, has become a new research trend [11].

In spectrum sensing, it is necessary not only to sense the status of spectrum resources by primary users but also to provide spatial angle information in the spectrum. In general, the end of spatial spectrum sensing is divided into two stages: detection and positioning [12]. The research of these two stages is generally independent of each other. In the detection stage of spatial spectrum sensing, the main purpose is to detect whether the primary user exists. In [13], the authors propose a spatial detection algorithm, using techniques such as interference alignment to explore spatial spectrum resources and improve detection performance; the work in [14] uses beamforming to sectorize the space and proposes a spatial spectrum sensing algorithm based on sector segmentation, which not only improves the detection performance but also provides information about spare sectors in space. In addition, direction-of-arrival (DOA) estimation is required in the positioning stage of spatial spectrum sensing. The multiple signal classification (MUSIC) algorithm is the most representative algorithm in the positioning stage of spatial spectrum sensing [15–17]. The work in [18] proposes combined detection and positioning algorithms, where the authors first use the traditional detection algorithm to perform

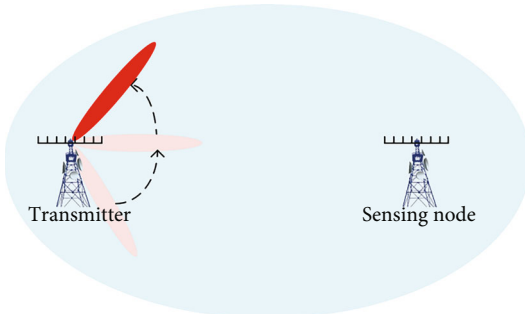

Figure 1: System model.

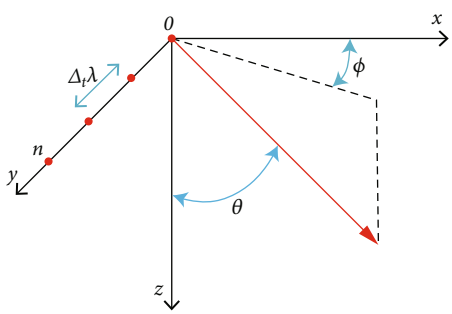

Figure 2: The deployment of antenna elements in linear array pattern.

spectrum sensing, then obtain the spatial information of spectrum holes through the angle-of-arrival (AOA) estimation algorithm to realize the function of spatial spectrum sensing.

This paper mainly studies the detection stage of spatial spectrum sensing in beam scanning scene. Specifically, this paper mainly studies spectrum sensing in multiantenna beam scanning scenarios, which is essentially spectrum sensing of beam signals. At this stage, there have been many papers on the spectrum sensing of multiantenna beamforming. The work in [19] proposes for multiantenna CR sensors a class of spectrum sensing methods, named the generalized likelihood ratio test (GLRT), that require no information about the primary users or the channels from the primary to the secondary users. The proposed methods utilize the eigenvalues of the sample covariance matrix of the received signal vector from multiple antennas and derive two new algorithms for spectrum sensing under different assumptions on the availability of the white noise power value at the CR receiver. The work in [20] designs a uniform circular array which uses a NC-α-MTG-MUSIC algorithm to sense the arrival signal. The NC-α-MTG-MUSIC includes an α-MTG algorithm to detect whether the primary signals exist and a MUSIC algorithm to estimate its DOA.

When a beamforming signal is sent to the receiver through the antenna array, the receiver's location information needs to be known. In other words, the beamforming direction needs to be determined. When the transmitter does not know the receiver's location, it generally determines the receiver's position information by beam scanning [21, 22], which provides an opportunity for sensing of noncooperative beam signals. There is no prior knowledge of beamforming arrays that can be obtained for noncooperative parties, which makes existing methods of spectrum sensing inapplicable. In this paper, a spectrum sensing method based on energy detection is proposed for the noncooperative beam scanning scenario. Since the noncooperative sensing party does not know any prior knowledge of the scanned signal, the energy detection method is the most effective spectrum sensing method in this scenario. Specifically, the main contributions of this paper are summarized as follows.

(1) Formulate a system model where the sensing node detects the presence of a beam scanning signal emitted by a noncooperative transmitter

(2) Derive the closed form expressions of the detection probability and the false alarm probability in beam scanning scenario

(3) Design an algorithm to improve spectrum sensing performance in nonideal situation of the beam scanning scenario by selecting the appropriate sensing time period

(4) Present in-depth simulation results which demonstrate the effectiveness of the proposed algorithm

The rest of the paper is organized as follows: Section 2 describes the system model, where we model the beam-scanning signal in the transmitter and the received signal in the receiver. Section 3 performs performance analysis of energy detection in beam scanning scenarios. In Section 4, a SPS algorithm is designed for spectrum sensing in nonideal situation. Section 5 presents the simulation results, including spectrum sensing results under ideal situation, spectrum sensing results under nonideal situation, and spectrum sensing results in nonideal situation after adding the proposed SPS algorithm. Section 6 concludes this paper.

2. Signal Model

In this paper, we consider a spectrum sensing system model as shown in Figure 1, which has a transmitter with a linear array to emit beam signals and a multiantenna sensing node to detect the presence of the beam signals. The transmitter is composed of a linear array of n_t antennas, which can generate a 0-180° scanning beam. The sensing node is located in the positive 90° direction of the beam generated by the noncooperative transmitter, where the beam starts to scan from 0°. Scanning beams ranging from 0° to 180° are generated by changing the phase of each transmit antenna. During the beam scanning process, the beam signal will cover the area where the sensing node is located. The sensing node is composed of a linear array composed of n_r antennas.

2.1. Transmitting Model. The transmitter consists of linear array antennas, and the number of antennas is n_t for a transmission channel from a transmitter to a sensing node. As shown in Figure 2, the azimuth and elevation angles are denoted by ϕ and θ, respectively, which obeys $\phi \in (-\pi, \pi]$ and $\theta \in (-\pi/2, \pi/2]$. Supposing that the path attenuation is the same for all antennas, the ith antenna transmit signal

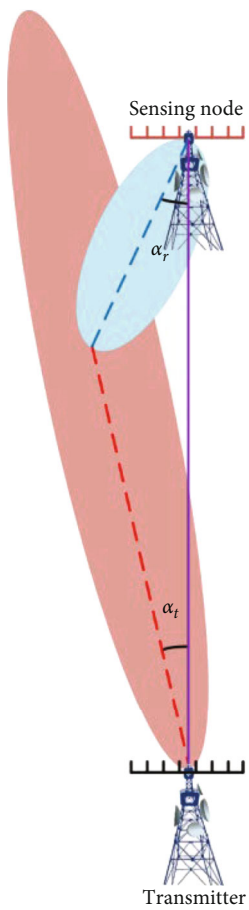

Figure 3: The beamforming gain with directional transmission and directional sensing node.

can be expressed as

$$y_i = Ae^{jd2\pi/\lambda}, \tag{1}$$

where A is the transmit power and d is the distance of signal propagation. λ is the carrier wavelength, and $\lambda = f/c$, where f is the carrier frequency and c is the speed of light. The distance between the two antennas is $\Delta_t\lambda$, the distance from the first antenna (the antenna that is closest to the receiver) to the sensing node is $d_1 = d_0$, the distance from the second antenna to the sensing node is $d_2 = d_0 + \Delta_t\lambda \sin\theta \cos\phi$, and the distance from the nth antenna to the sensing node is $d_n = d_0 + (n-1)\Delta_t\lambda \sin\theta \cos\phi$. Therefore, the beamforming vector can be expressed as

$$\mathbf{w_t} = \begin{bmatrix} 1 \\ \exp\left(j2\pi\Delta_t \sin\theta \cos\phi\right) \\ \exp\left(j2\pi 2\Delta_t \sin\theta \cos\phi\right) \\ \vdots \\ \exp\left(j2\pi(n_t-1)\Delta_t \sin\theta \cos\phi\right) \end{bmatrix}. \tag{2}$$

The channel vector can be obtained by

$$H = \exp\left(\frac{j2\pi d_0 \sin\theta \cos\phi}{\lambda}\right). \tag{3}$$

2.2. Sensing Model. The sensing node consists of a linear array of n_r antennas. When receiving the signal, the sensing node selects a direction to receive the signal. The sensing node is designed as a linear array to receive beam signals directionally. If the approximate direction of the transmit beam is known, interference from signals from other directions can be effectively reduced. The hypothesis is expressed by hyperparameters H_1 that the beam signal exists, and the absence of the beam signal is expressed by hyperparameters H_0 [23]. The received signal can be expressed as

$$y(n) = \begin{cases} \varepsilon(n), & H_0, \\ \mathbf{w_r^H H w_t} x(n) + \varepsilon(n), & H_1, \end{cases} \tag{4}$$

where $\mathbf{w_r}$ and $\mathbf{w_t}$ are the beamforming vector of the receiving beam and the beamforming vector of the transmitting beam, respectively. $\varepsilon(n)$ is additive noise following the zero mean additive white Gaussian noise (AWGN) distribution with variance δ_w^2. $x(n)$ is the symbol of the transmitted signal, denoted as $x_i(n) i = 1, 2, \cdots, n_t$, which is the output of the ith antenna, where n_t is the number of antennas. We define $|\mathbf{w_r^H H w_t}|^2$ as the beam alignment gain of the antenna G [23]:

$$G = G_r h G_t, \tag{5}$$

where G_r, G_t, and h denote the receive gain, transmit gain, and the channel gain, respectively, and their values depend on whether the beam is aligned. Here, we use the typical sector antenna model [24] expressing them as a function of the alignment angle:

$$G_n(\alpha) = \begin{cases} g_1 = \dfrac{2\pi - (2\pi - \varphi)g_2}{\varphi}, & \text{if} |\alpha_n| \le \dfrac{\varphi}{2}, \\ g_2, & \text{else}, \end{cases} \tag{6}$$

where n can be r or t. As shown in Figure 3, α_r and α_t represent the angle between the directional receiving beam and the optimal beam and the angle between the transmitting beam and the optimal transmitting beam, respectively. g_1 is the main beam gain, and g_2 is the sidelobe gain, which satisfies $0 \le g_1 \le 1 \le g_2$. φ is the bandwidth [25] of the beam in gain mode, which can be approximately expressed as

$$\varphi \approx 50.8 \frac{\lambda}{Nd \cos\beta}, \tag{7}$$

where β represents the angle between the beam pointing and the normal direction of the array.

3. Spectrum Sensing of Beam Signals

For noncooperative beam signals, the energy detection algorithm [26] can detect beam signals without prior information. The energy value of the received beam signal at the sensing node within a certain period of time is compared with a preset threshold, and if the received signal is higher than the threshold, it is determined that the beam signal exists [27].

Assuming that the channel is AWGN channel, the angular velocity of the transmitter to transmit the scanning beam is fixed. Note that x and ε both obey a Gaussian distribution. Therefore, we can conclude that the distribution of the received signal from formula (4) is

$$y(n) \sim \begin{cases} N\left(0, \delta_w^2\right) & H_0, \\ N\left(0, \delta_w^2 + G\delta_s^2\right) & H_1, \end{cases} \tag{8}$$

where G is the beam alignment gain; then, energy detection is used as a method for spectrum sensing. Let τ be the available sensing time and K be the number of samples (K is the maximum integer not greater than τf_s. For notation simplicity, we assume $K = \tau f_s$). The test statistic for energy detector is given by

$$\Lambda = \frac{1}{K}\sum_{n=1}^{K} |y(n)|^2, \tag{9}$$

where Λ, a random variable, is the energy detection statistic.

One key performance metric for energy detection is detection probability, which defines the probability that the detector detects the presence of a signal in H_1, which can be expressed as [28]

$$P_d = P(\Lambda > T|H_1). \tag{10}$$

Then, $p_1(x)$ is assumed to be expressed as the probability density function (PDF) of the energy detection statistic. Then, one key performance metric, named detection probability, can be further expressed as

$$P_d = \int_T^{\infty} p_1(x)dx. \tag{11}$$

Using central limit theorem (CLT), detection probability P_d can be given by

$$P_d = Q\left(\frac{T - \left(N\left(\delta_w^2 + G\delta_s^2\right)\right)}{\sqrt{(2/K)}\left(\delta_w^2 + G\delta_s^2\right)}\right), \tag{12}$$

where $Q(\cdot)$ is the complementary distribution function of the standard Gaussian,

$$Q(X) = \frac{1}{\sqrt{2\pi}}\int_x^{+\infty} e^{-t^2/2}dt. \tag{13}$$

Then, the missed detection probability can be expressed as

$$P_m = 1 - P_d. \tag{14}$$

Another key performance metric for energy detection is false alarm probability, which defines the probability that the detector detects the presence of a signal in H_0, which can be expressed as [28]

$$P_f = P(\Lambda > T|H_0). \tag{15}$$

Suppose $p_0(x)$ is represented as the PDF of the energy detection statistic Λ. Then, the probability of false warning can be given by

$$P_f = \int_T^{\infty} p_0(x)dx. \tag{16}$$

Using central limit theorem (CLT), false alarm probability P_f can be given by

$$P_f = Q\left(\frac{T - \delta_w^2}{\sqrt{2/K}\delta_w^2}\right). \tag{17}$$

4. Algorithm Design

In Section 3, we provide theoretical derivations for the performances of spectrum sensing in multiantenna beam scanning scenarios. As shown in Figure 4, the beam signal is scanned from 180° to 0°. The curves of different colors in Figure 4 represent the direction in which the transmitter emits the beam signal at different times, respectively. These performances can only be achieved under the ideal situation that the whole process of beam scanning is sampled by sensing nodes, and the sensing period is equal to the beam scanning period. In the actual situation, the process of beam scanning may not be completely sampled. Because the transmitter and the sensing node are noncooperative, it is difficult to set the sensing period to be the same as the beam scanning period. Therefore, for such a nonideal situation, we pay more attention to the sampling data of main lobe passing through the sensing node, where the time period is in t_s, as shown in Figure 4. We first assume that the sensing period t_s is the same as the time t_b for multiantenna beam scanning scenarios. In the spectrum sensing of beam scanning scenarios, we are more concerned about the energy detection statistics of the beam signal covering the sensing node, that is, the signal energy data in t_s time in Figure 4. If more data in the t_s can be sampled in the sensing cycle of the sensing node, the result of spectrum sensing will be greatly improved. Therefore, we propose an SPS algorithm to optimize the sensing results.

When the beam pattern covers the sensing node, the sensing node can detect a larger signal energy. Our goal is to collect the time period that the beam covers to the sensing node within the sensing period as much as possible. Therefore, the sensing performance will be greatly improved when the sensing node can collect more sampled data in the red area for spectrum sensing. In Figure 5, the transmitter starts

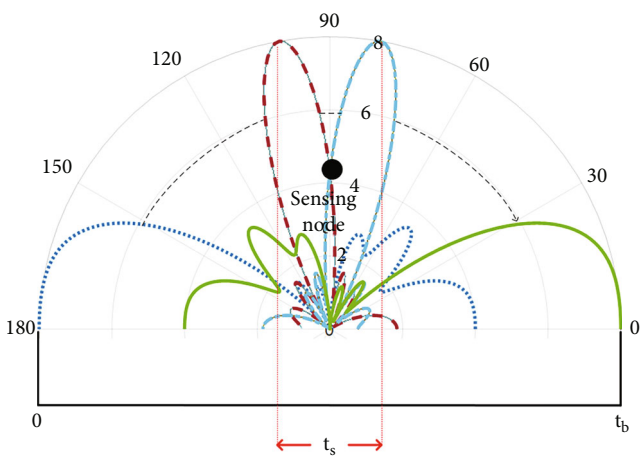

Figure 4: Important data sampling areas for spectrum sensing based on beam scanning.

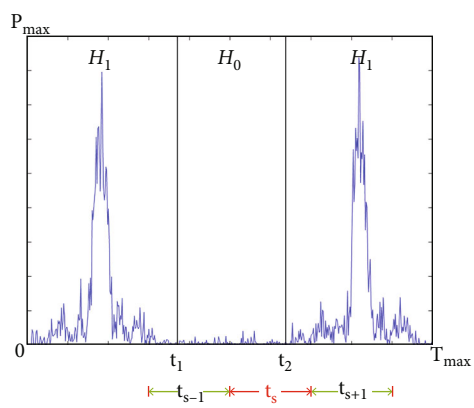

Figure 5: Signal energy data received by sensing node.

the first beam scanning at the time 0-t_1, the transmitter is off at the time t_1-t_2, and the transmitter starts the second round of beam scanning at the time t_2-T_{max}. We assume that the presence of the beam scanning signal in the t_s time period is to be sensed. The horizontal axis in the figure is a random period with a total time of T_{max}, including two complete beam scans of the transmitter. The longitudinal axis is the signal energy of the sensing node. In fact, during the t_s time period, the transmitter has started beam scanning. However, the time period in which the beam pattern covers the sensing node is not included in the t_s time, so the sensing node will mistakenly judge that the beam scanning signal does not exist. If we observe the sensing results in the t_{s+1} time period later, the sensing node will perceive the scanning signal correctly. Based on this idea, we design an SPS algorithm to improve the spectrum sensing performance in the case of nonideal beam scanning.

In nonideal situation, no matter when the sensing period starts, two sensing periods must contain the time for the whole beam scanning round. Suppose that the part of the process of beam scanning is sensed by the kth sensing cycle, then we need to compare the energy detection statistic Λ_k of the kth sensing cycle with the energy detection statistic Λ_{k-1} of the previous sensing cycle and the energy detection statistic Λ_{k+1} of the next sensing cycle. Comparing the largest energy detection statistic to a threshold, then the presence or absence of a beam scan signal will be given. The reason is we do not know whether the beam scanning process in the kth sensing period is the first half or the second half in t_b. Taking these three sensing periods can ensure that the whole beam scanning process is included. We can simplify this process by comparing these three energy detection statistics with the threshold. If they are all less than the threshold, the sensing result is H_0, otherwise, the perception result is H_1. When $t_s = t_b$, the algorithm is as follows.

When $t_s > t_b$, the whole beam scanning time must be included within 2 sensing cycles. Therefore, we can also use Algorithm 1 to optimize spectrum sensing. In this case, we cannot make the sensing time t_s too long. Because if the sensing time is too long, it will cause the sensing node to collect too many noise signals, which will eventually make the sensing result worse.

Then, we consider the case where the sensing period is smaller than the beam scanning period. We solve this problem by designing Algorithm 2. When $t_s < t_b$, we need to find an ideal integer i where $(i-1)t_s < t_b$ and $it_s > t_b$. Therefore, it can be ensured that the whole process of beam scanning must be included in i sensing cycles. Subsequently, similar to subsection C, the energy detection statistics for the first i and last i sensing cycles are compared to the threshold, respectively ($(2i+1)$ sensing cycles in total). If they are all less than the threshold, the sensing result is H_0, otherwise, the sensing result is H_1. In particular, we do not have to determine the ideal integer i. We need to estimate a small i where $it_s > t_b$, and we will get good results. The algorithm is as follows:

In addition, the case of $t_s \geq t_b$ can be regarded as the case of $i = 1$.

5. Simulation Results

In this section, we discuss the performance of the proposed energy detection method in the beam scanning scenario through numerical simulations and verify the theoretical analysis. Simulation results were investigated by running 10,000 iterations of Monte Carlo testing. The theoretical results are calculated using formulas (12) and (17). Considering the energy detection situation in the actual scene, we discussed the full process of beam scanning that sensing nodes are sampled and only part of the beam scan is sampled. The parameters in our simulation are shown in Table 1.

5.1. Sensing Results in Ideal Situation. In this subsection, we discuss the ideal case where the whole process of beam scanning is sampled by the sensing node and the sensing period t_s is the same as the time for one round of beam scanning t_b. In this case, the hyperparameter H_0 is defined as the transmitter which is not powered on during the sampling period of the sensing node; the hyperparameter H_1 is defined as the whole process of beam scanning which is sampled by the sensing node during the sensing period.

Input: threshold T, Energy detection statistics of the $(k-1)$-th sensing cycle Λ_{k-1}, Energy detection statistics of the k-th sensing cycle Λ_k, Energy detection statistics of the $(k+1)$-th sensing cycle Λ_{k+1}.
Output:H
1: If $\Lambda_{i-1} < T$ & $\Lambda_i < T$ & $\Lambda_{i+1} < T$
2: $H \leftarrow H_0$
3: Else
4: $H \leftarrow H_1$
5: End if

Algorithm 1: Equal period selection (EPS).

Input: threshold T, i, Energy detection statistics $\Lambda_{k-i} \ldots \Lambda_{k-1}$, Λ_k, $\Lambda_{k+1} \ldots \Lambda_{k+i}$.
Output:H
1: If $\Lambda_{k-i} < T$ & $\Lambda_{k-i+1} < T$ &…& $\Lambda_{k+i} < T$
2: $H \leftarrow H_0$
3: Else
4: $H \leftarrow H_1$
5: End if

Algorithm 2: Sensing period selection (SPS).

Table 1: Key simulation parameters.

Parameter	Value
Carrier frequency	$f_s = 28$ GHz
Maximum transmit power	$P_{\max} = 10$ W
Number of antennas	$n = 8$
Distance between antennas	$d_a = \lambda/2$
Distance between antenna array and receiver	$d = 10 \sim 50$ m
Loss	$\alpha = 2$

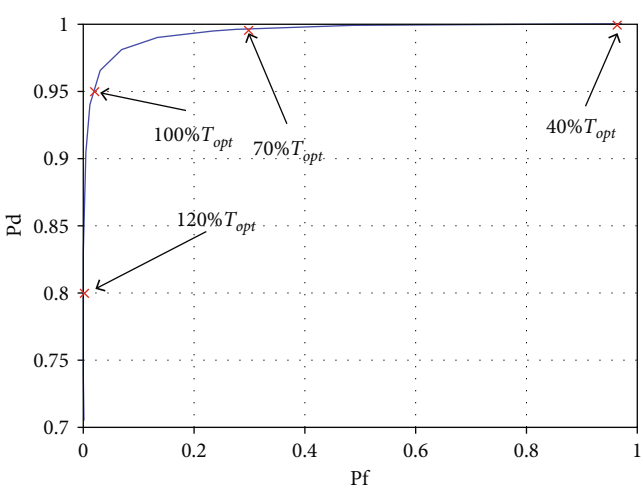

Figure 6: ROC curves of P_d and P_f in ideal situation.

Figure 6 shows the ROC curves of P_d and P_f at different thresholds. Setting different thresholds has a great impact on perceptual performance. If the threshold is set too large, some beam signals with weak energy may not be detected, resulting in reduced detection probability. If the threshold is set too small, the energy of some noise may have exceeded the threshold, resulting in an increase in the probability of false alarm probability. The threshold ranges from 40% T_{opt} with a step size of 5% to 100% T_{opt} which is defined as obtaining the optimum value of T_{opt} which results in target $P_d \geq 0.95$ while minimizing P_f.

Figure 7 shows the comparison between theoretical and simulated probabilities for P_d in different transmit powers with setting the threshold to make P_f as 0.01. It is seen that the probability of detection increases with the increase of the number of samples. As the transmit power increases, the signal power at each moment in the beam scanning process increases, too. It leads to an increase in SNR at any time in beam scanning process. So P_d will gradually become larger.

In Figure 8, we discussed the relationship between P_d and the change in the distance from the sensing node to the transmitter when the threshold is set to make P_f as 0.01. Figure 8 also shows the theoretical and simulated results of P_d. Obviously, when the distance increases to a certain extent, it decreases rapidly as the distance continues to increase. This is because the beam power in the wireless channel attenuates rapidly as the distance increases, and after the attenuation reaches a certain level, the power of beam signal is lower than noise.

5.2. Sensing Results in Nonideal Situation. In this subsection, we discuss a more realistic case where the part of the beam scanning process is sampled by the sensing nodes. In this case, the hyperparameter H_0 is defined as the transmitter which is not powered on during the sampling period of the sensing node; the hyperparameter H_1 is defined as the sampling period of the sensing node which contains the part of the beam scanning process.

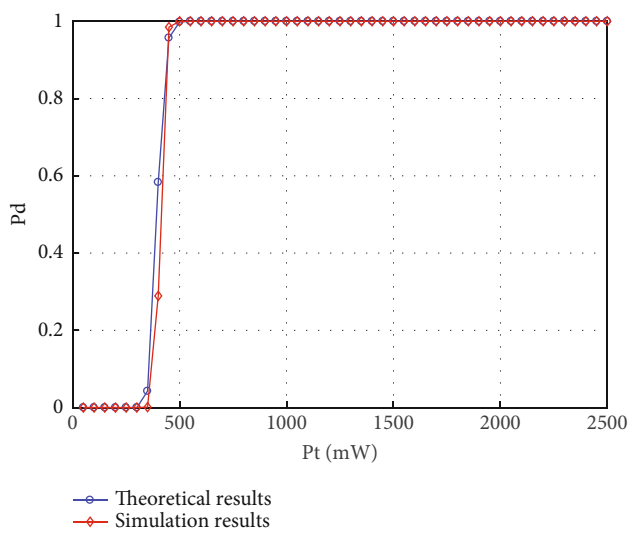

Figure 7: P_d as a function of power in ideal situation

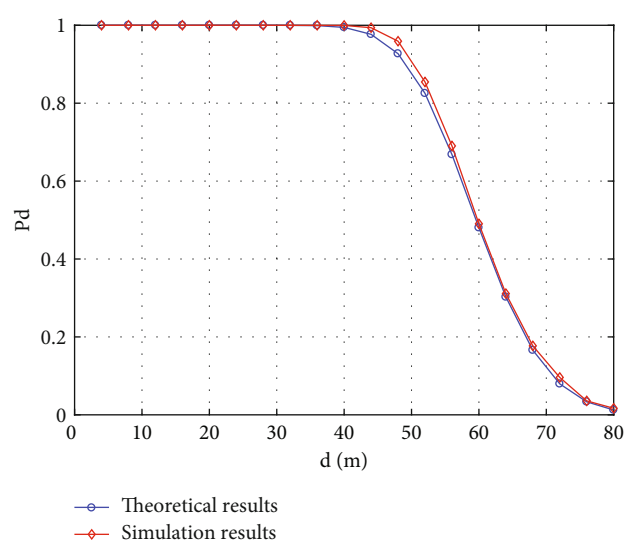

Figure 8: P_d as a function of distance in ideal situation.

The green curve in Figure 9 shows the ROC of P_d and P_f at different thresholds. Since the sensing node does not sample the whole process of beam scanning, the calculation results of equations (11) and (15) cannot be used to approximate the calculation results. In this case, simulation results were investigated by running 10,000 iterations of Monte Carlo testing.Comparing with Figure 6, the performance of the sampling partial scan process is significantly lower than that of the sampling full scan process.

The green curve in Figure 10 shows the variation of P_d in different transmit powers with setting the threshold to make P_f as 0.1. We find that with transmit power increased, P_d increases gradually. We found that using a larger transmit power, P_d may actually decrease compared to a smaller transmit power. Although a higher transmit power can obtain better SNR, the data collection process of sensing nodes is random. It is possible that only a short scan time

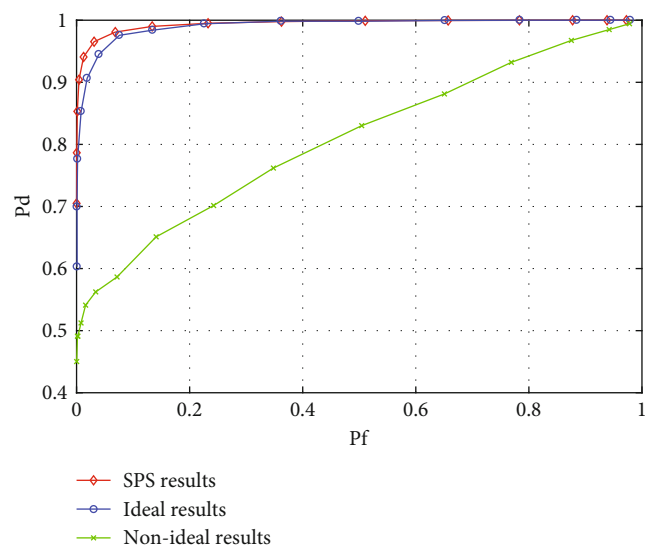

Figure 9: ROC curves of P_d and P_f in different situations.

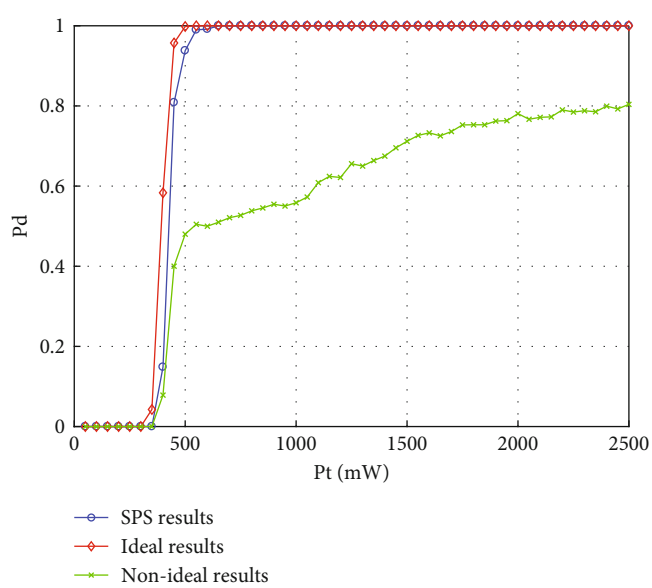

Figure 10: P_d as a function of power in the nonideal situation after using SPS algorithm in the nonideal situation

was acquired at higher transmit powers. In general, using larger transmit power can effectively improve the sensing results.

As shown in the green curve in Figure 11, when the threshold is set to make P_f as 0.01, we discuss the relationship between P_d and the change in the distance of the sensing node from the transmitter. Obviously, it keeps decreasing as the distance increases.

5.3. Sensing Results in Nonideal Situation Based on SPS Algorithm. In this subsection, we consider a more realistic situation. As in Subsection 5.2, the part of the beam scanning process is sampled by the sensing node. The definitions of hyperparameters H_0 and H_1 are the same as those in

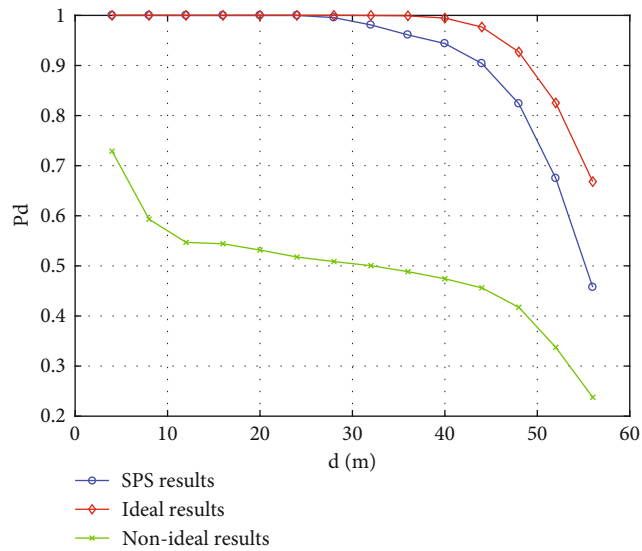

Figure 11: P_d as a function of distance in the nonideal situation after using SPS algorithm in the nonideal situation when the sensing node is in the 60° direction of the transmitter

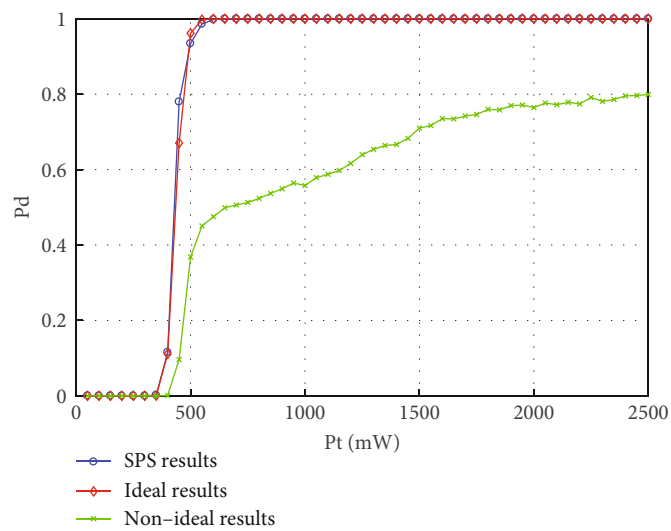

Figure 12: P_d as a function of power in the nonideal situation after using SPS algorithm in the nonideal situation when the sensing node is in the 60° direction of the transmitter

Subsection 5.2. When energy detection is implemented, the SPS algorithm is added to optimize the sensing results.

When the beam pattern covers the sensing node, the sensing node can detect a larger signal energy. Our goal is to collect the time period that the beam covers to the sensing node within the sensing period as much as possible. The purpose of adding SPS algorithm is to take the sampling data that the time of beam signal covers the sensing node as the sensing result.

Figure 9 shows the ROC curves of P_d and P_f at different thresholds. The threshold range is the same as the ROC curve in ideal and nonideal situation. In Figure 9, although the sensing node does not sample the whole process of beam scanning, the sensing performance is significantly better than the simulation result without adding the SPS algorithm. The reason is that the sensing result is closer to the situation where the whole process of beam scanning is sampled by sensing nodes, the ideal situation.

The variation of P_d in different transmit powers with setting the threshold to make P_f as 0.01 is shown in Figure 10. The blue curve is the relationship between P_d and power after adding the SPS algorithm. The blue curve is the relationship between P_d and power in the ideal situation, and the green curve is in the nonideal situation. After adding the SPS algorithm, the result is much better than that of traditional energy detection without using the SPS algorithm and even approaches the ideal result.

In Figure 11, when the threshold is set to make P_f as 0.01, we discuss the relationship between P_d and the change in the distance of the sensing node from the transmitter. The

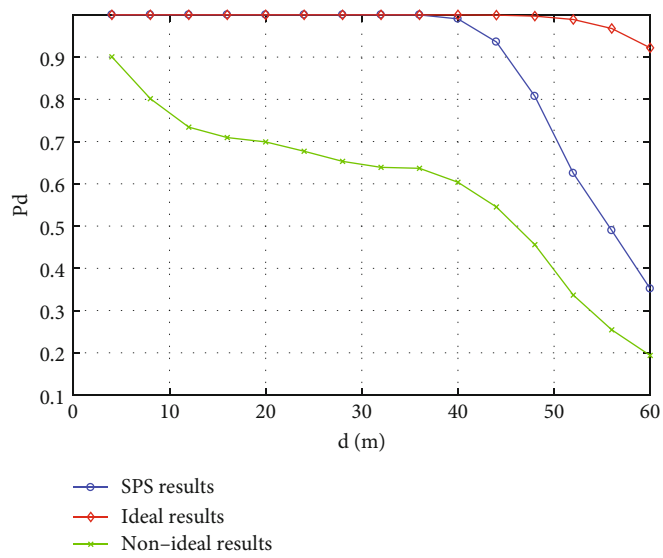

Figure 13: P_d as a function of distance in the nonideal situation after using SPS algorithm in the nonideal situation when the sensing node is in the 60° direction of the transmitter

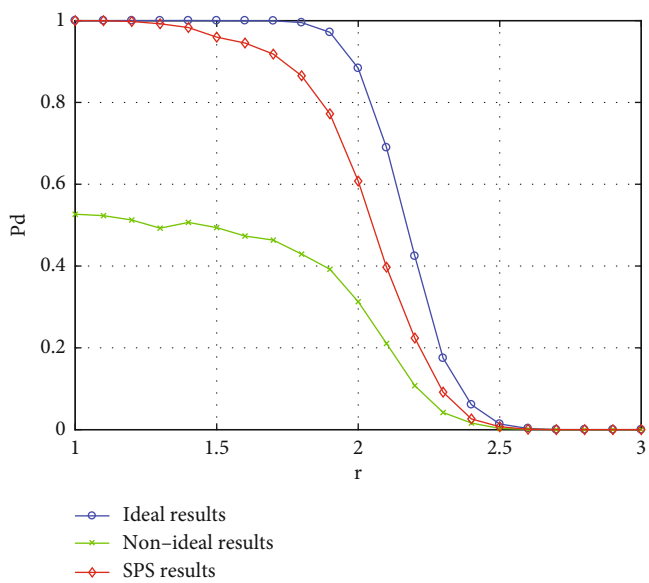

Figure 14: P_d as a function of distance sensing period duration

blue curve is the relationship between P_d and the distance between sensing node and transmitter after adding the SPS algorithm. The blue curve is the relationship between P_d and the distance between sensing node and transmitter in the ideal situation, and the green curve is in the nonideal situation. Obviously, when the distance increases to a certain extent, P_d decreases rapidly with the distance continues to increase. After adding the SPS algorithm, the sensing results are significantly better than the experimental results in the nonideal situation and approach the results in the ideal situation.

5.4. Sensing Results of Sensing Nodes in Other Locations. In this subsection, we discuss the sensing performance when the sensing node is in other positions in the ideal situation and nonideal situation and after adding SPS algorithm.

When the sensing node is in other locations, good sensing results can still be obtained after adding SPS algorithm. In Figures 12 and 13, the sensing results when the sensing node is located in the 60° direction of the transmitter are shown, respectively.

The variation of P_d in different transmit powers with setting the threshold to make $P_f$as 0.01 is shown in Figure 12. The blue curve is the relationship between P_d and power after adding the SPS algorithm. After adding SPS algorithm, the sensing result is slightly lower than the ideal red curve and significantly higher than the nonideal green curve. This is consistent with the case where the sensing node is located in the 90° direction of the receiver.

In Figure 13, when the threshold is set to make P_f as 0.01, we discuss the relationship between P_d and the change in the distance of the sensing node from the transmitter. The blue curve is the relationship between P_d and the distance between sensing node and transmitter after adding the SPS algorithm. After adding the SPS algorithm, the sensing result is slightly lower than the ideal red curve and significantly higher than the nonideal green curve. This is consistent with the case where the sensing node is located in the 90° direction of the receiver.

5.5. Setting Time of Sensing Period. The setting of the sensing time needs to be based on the estimation of the scanning period of the multiantenna beam. If the sensing time is set too large, it will result in the acquisition of too much noise.

As shown in Figure 14, where$r$is the ratio of the sensing period to the beam scanning period, we can see that $P_d$keeps decreasing as the sensing period increases. We consider the changes of P_d in the ideal case and nonideal case and after adding the SPS algorithm. In particular, the ideal situation here is defined as that the whole process of beam scanning is within the sensing time. In these three cases, P_d shows a

downward trend, but after adding the SPS algorithm, the performance of P_d is obviously close to the ideal situation.

When the sensing period is too long, there is only noise in most of the time period of sensing, and the time when the beam scans to the sensing node is very small. This results in the scanning signal being covered in long-term noise during the sensing phase.

If the sensing time is set too small, it will be difficult to sample the data that the scanning signal covers the sensing node. In these cases, we can optimize the perception results by using the SPS algorithm. However, if the difference between the sensing time and the beam scanning time is too large, the sensing result will become poor.

6. Conclusion

This paper has studied the issue of spectrum sensing of noncooperative beam signals. For the ideal case, the sensing period is equal to the time of one round of beam scanning and the sensing node collects all the data in the whole process of beam scanning. We use the theoretical derivation method and the Monte Carlo method to verify the performance indicators of spectrum sensing. The results show that in the ideal situation, the spectrum sensing performance indicators verified by the Monte Carlo method are almost consistent with the theoretically derived results and both have good sensing results. For the nonideal situation, that is, the situation closer to the actual situation, we use the traditional energy detection method and the energy detection method after adding the SPS algorithm to verify the performance of spectrum sensing. The experiment uses the Monte Carlo method. The results show that the application of the SPS algorithm in energy detection can effectively improve the performance of spectrum sensing.

Data Availability

Matlab simulation data is available.

Conflicts of Interest

The authors declare that they have no conflicts of interest.

Acknowledgments

This work was supported by the National Key R&D Program of China under Grant 2018YFB1801103 and the National Natural Science Foundation of China (No. 62171462, No. U20B2038, No. 61901520, No. 61931011, and No. 61871398).

References

[1] G. Ding, J. Wang, Q. Wu, Y. D. Yao, F. Song, and T. A. Tsiftsis, "Cellular-base-station-assisted device-to-device communications in TV white space," *IEEE Journal on Selected Areas in Communications*, vol. 34, no. 1, pp. 107–121, 2016.

[2] C. G. Tsinos and K. Berberidis, "Adaptive eigenvalue-based spectrum sensing for multi-antenna cognitive radio systems," *IEEE Transactions on Wireless Communications*, vol. 14, no. 3, pp. 1703–1715, 2013.

[3] J. L. Wang, G. Ding, Q. Wu, L. Shen, and F. Song, "Spatial-temporal spectrum hole discovery: a hybrid spectrum sensing and geolocation database framework," *Chinese Science Bulletin*, vol. 59, no. 16, pp. 1896–1902, 2014.

[4] H. Zhang and C. Guo, "Beam alignment-based mmWave spectrum sensing in cognitive vehicular networks," in *2019 IEEE Global Conference on Signal and Information Processing (GlobalSIP)*, pp. 1–5, Ottawa, ON, Canada, 2019.

[5] R. Rytel-Andrianik, "Efficient matched filtering and beamforming for coherent MIMO radar," in *2016 IEEE International Symposium on Phased Array Systems and Technology (PAST)*, pp. 1–6, Waltham, MA, USA, 2016.

[6] V. Prithiviraj, B. Sarankumar, A. Kalaiyarasan, P. P. Chandru, and N. N. Singh, "Cyclostationary analysis method of spectrum sensing for cognitive radio," in *2011 2nd International Conference on Wireless Communication, Vehicular Technology, Information Theory and Aerospace & Electronic Systems Technology (Wireless VITAE)*, pp. 1–5, Chennai, India, 2011.

[7] H. Kim, K. Granström, L. Gao, G. Battistelli, S. Kim, and H. Wymeersch, "5G mmWave cooperative positioning and mapping using multi-model PHD filter and map fusion," *IEEE Transactions on Wireless Communications*, vol. 19, no. 6, pp. 3782–3795, 2020.

[8] W. Lu, P. Si, G. Huang et al., "SWIPT cooperative spectrum sharing for 6G-enabled cognitive IoT network," *IEEE Internet of Things Journal*, vol. 8, no. 20, pp. 15070–15080, 2021.

[9] K. C. Ho and S. H. Tsai, "A novel multiuser beamforming system with reduced complexity and beam optimizations," *IEEE Transactions on Wireless Communications*, vol. 18, no. 9, pp. 4544–4557, 2019.

[10] F. Shen, G. Ding, Z. Wang, and Q. Wu, "UAV-based 3D Spectrum sensing in Spectrum-heterogeneous networks," *IEEE Transactions on Vehicular Technology*, vol. 68, no. 6, pp. 5711–5722, 2019.

[11] C. Liu, *Spatial Spectrum Based Spectrum Sensing in Cognitive Radio*, 2017.

[12] Y. H. Chen and Z. P. Shi, "A method of multi-antenna spatial spectrum sensing based on noncircular signals," in *2020 IEEE 20th International Conference on Communication Technology (ICCT)*, pp. 863–866, Nanning, China, 2020.

[13] A. Alizadeh, H. R. Bahrami, M. Maleki, and S. Sastry, "Spatial sensing and cognitive radio communication in the presence of a *K*-user interference primary network," *IEEE Journal on Selected Areas in Communications*, vol. 33, no. 5, pp. 741–754, 2015.

[14] T. Wilcoxd, A. Kortun, T. Ratnarajah, C. B. Papadias, and M. Sellathurai, "On spatial domain cognitive radio using single-radio parasitic antenna arrays," *IEEE Journal on Selected Areas in Communications*, vol. 31, no. 3, pp. 571–580, 2013.

[15] Y. Y. Wang, J. T. Chen, and W. H. Fang, "TST-MUSIC for joint DOA-delay estimation," *IEEE Transactions on Signal Processing*, vol. 49, no. 4, pp. 721–729, 2001.

[16] J. M. Kim, O. K. Lee, and J. C. Ye, "Compressive MUSIC: revisiting the link between compressive sensing and array signal processing," *IEEE Transactions on Information Theory*, vol. 58, no. 1, pp. 278–301, 2012.

[17] P. Vallet, X. Mestre, and P. Loubaton, "Performance analysis of an improved MUSIC DOA estimator," *IEEE Transactions on Signal Processing*, vol. 63, no. 23, pp. 6407–6422, 2015.

[18] J. Xie, Z. Fu, and H. Xian, "Spectrum sensing based on estimation of direction of arrival," in *International Conference on Computational Problem-Solving*, pp. 39–42, Li Jiang, China, 2010.

[19] R. Zhang, T. Lim, Y. C. Liang, and Y. Zeng, "Multi-antenna based spectrum sensing for cognitive radios: a GLRT approach," *IEEE Transactions on Communications*, vol. 58, no. 1, pp. 84–88, 2010.

[20] S. Lee, I. Nam, and D. Kim, "Electrical Beam Scan Antenna Using Miniaturized Frequency Selective Reflectors," *In 2018 International Symposium on Antennas and Propagation (ISAP)*, pp. 1-2, 2018.

[21] Q. Zeng, Z. Xue, W. Ren, and W. Li, "Dual-band beam-scanning antenna using rotatable planar phase gradient transmitarrays," *IEEE Transactions on Antennas and Propagation*, vol. 68, no. 6, pp. 5021–5026, 2020.

[22] C. X. Mao, S. Gao, and Y. Wang, "Broadband high-gain beam-scanning antenna array for millimeter-wave applications," *IEEE Transactions on Antennas and Propagation*, vol. 65, no. 9, pp. 4864–4868, 2017.

[23] D. Cabric, S. M. Mishra, and R. W. Brodersen, "Implementation issues in spectrum sensing for cognitive radios," in *Conference Record of the Thirty-Eighth Asilomar Conference on Signals, Systems and Computers*, pp. 772–776, Pacific Grove, CA, USA, 2004.

[24] J. Wildman, P. Nardelli, M. Latva-Aho, and S. Weber, "On the joint impact of beamwidth and orientation error on throughput in directional wireless Poisson networks," *IEEE Transactions on Wireless Communications*, vol. 13, no. 12, pp. 7072–7085, 2014.

[25] H. L. Van Trees, *Detection, Estimation, and Modulation Theory, Optimum Array Processing (Part IV), [M.S. thesis]*, John Wiley and Sons, Inc, New York, 2002.

[26] H. Urkowitz, "Energy detection of unknown deterministic signals," *Proceedings of the IEEE*, vol. 55, no. 4, pp. 523–531, 1967.

[27] F. F. Digham, M. S. Alouini, and M. K. Simon, "On the energy detection of unknown signals over fading channels," *IEEE Transactions on Communications*, vol. 55, no. 1, pp. 21–24, 2007.

[28] J. Gao, X. Yi, C. Zhong, X. Chen, and Z. Zhang, "Deep learning for spectrum sensing," *IEEE Wireless Communications Letters*, vol. 8, no. 6, pp. 1727–1730, 2019.

Hindawi
Wireless Communications and Mobile Computing
Volume 2022, Article ID 7228511, 13 pages
https://doi.org/10.1155/2022/7228511

Research Article

Abnormal Communication Signals Recognition Based on Image Enhancement and Improved Memory-Augmented Autoencoder

Tingyan Kuang,[1] Bo Zhou,[1] Jie Li,[1] Guoru Ding,[2] and Qihui Wu[1]

[1]*Key Laboratory of Dynamic Cognitive System of Electromagnetic Spectrum Space, Ministry of Industry and Information Technology, Nanjing University of Aeronautics and Astronautics, Nanjing 210016, China*
[2]*College of Communications Engineering, Army Engineering University, Nanjing 211106, China*

Correspondence should be addressed to Bo Zhou; b.zhou@nuaa.edu.cn

Received 14 June 2022; Revised 11 July 2022; Accepted 12 July 2022; Published 28 July 2022

Academic Editor: Mingqian Liu

Detecting increasing anomalous signals is critical to effective spectrum management due to the complexity of the use of electromagnetic spectrum. The anomaly recognition approach based on autoencoder (AE) heavily relies on the assumption that the reconstruction error of normal signals is generally lower than that of abnormal signals. Unfortunately, such an assumption does not necessarily hold due to the excessive generalization ability of the AE. The memory-augmented autoencoder model (MemAE) has been recently proposed to address this issue by introducing memory modules. Still, the standard MemAE model performs poorly on complex image datasets, and its performance for abnormal communication signals recognition is unknown. Therefore, we propose an image enhancement and improved memory-augmented autoencoder model (IIMemAE) to recognize abnormal communication signals. Specifically, we consider two key factors, i.e., the existence of redundant information in the time-frequency spectrogram and the low recognition accuracy of normal signals of the standard MemAE model. We introduce an image enhancement module and an anomaly determination module compared with the standard MemAE model. The proposed IIMemAE model can address the issue that the performance of anomaly recognition may be degraded due to the imbalanced communication signals in the real world. The simulation results show that IIMemAE can effectively recognize synthetic abnormal communication signals even at low signal-to-noise ratio (SNR) and jamming-to-signal ratio (JSR) conditions and outperform the standard MemAE model. Besides, the parametric Pauta criterion proposed can balance the recognition accuracy of normal and abnormal signals to meet the need for diverse recognition tasks.

1. Introduction

The electromagnetic spectrum is one of our most critical, widely used, and limited natural resources [1, 2]. With the advent of new wireless communication technologies, spectrum usage has become very complex, leading to radio wave congestion and other jamming issues [3]. Wireless spectrum anomalies may occur due to spectrum abuse or jamming. To effectively regulate the radio spectrum and improve the quality of service for wireless communications, it is crucial to analyze and detect anomalous behaviors in the electromagnetic spectrum.

Various communication antijamming technologies [4–6] and anomaly identification technologies [7, 8] have emerged to ensure the reliable transmission of information. In the wireless communication networks, the authors in [9] propose to detect interference by comparing the predicted packet delivery rate with the actual packet delivery rate. The authors in [10] focus on improving network performance under active jamming attacks to achieve jamming suppression. For spectrum anomaly identification, the characteristics of the communication signals can be exploited, as commonly done in the existing literature, such as [11–13]. The work in [11] proposes a cross-layer framework, which enables to detection of anomalous spectrum usage attacks (ASUA) in radio ad hoc networks by collecting the physical and network layer information. The authors in [12] propose a spectrum anomalous usage detection method using the

spatial distribution characteristics of the received signal strength. A typical spectrum is proposed based on feature extraction and a clustering algorithm to analyze spectral data in the broadcast bands [13].

However, these methods in [11–13] based on feature extraction could be of high computational complexity and consume lots of manpower and time [14]. In recent years, deep learning (DL) has achieved excellent performance in the radio field, such as interference identification [15] and spectrum anomaly detection [16]. A supervised learning-based scheme for signal detection and localization is proposed in [17], where a classification model is built by manually labeling each training sample. However, due to the complex electromagnetic spectrum situation and the unpredictable characteristics of anomalous signals, it is significantly difficult to collect and label a sufficient number of abnormal signals. Furthermore, communication signals in real-world systems are generally imbalanced. Abnormal communication signals can take many forms from the presence of unwanted signals in licensed bands to the absence of expected signals [18], which makes there are more abnormal signals than normal signals. Therefore, the performance of anomaly recognition methods based on supervised learning may be greatly degraded [19].

More recently, the unsupervised autoencoder (AE) learning model has emerged and has been adopted for anomaly detection with imbalanced data [20–25]. In network intrusion detection systems, the authors in [21] propose to employ a multimodal deep autoencoder (DAE) to detect abnormal traffic in the network and forward the anomaly to an attack classifier for classification. The authors in [22] use an ensemble of autoencoders to propose an online network traffic anomaly detection approach that can detect various attacks with performance comparable to offline anomaly detectors. In the anomaly recognition task, the AE is trained by minimizing the reconstruction error of normal signals, for which the reconstruction error is used as the anomaly metric. In [23], a deep autoencoder network is applied to detect the anomalies by reconstructing the spectrogram of the received signal. An unsupervised anomaly identification method based on the convolutional autoencoder (CAE) is studied in [24] to identify radio frequency interference. The authors in [25] propose a variational autoencoder- (VAE-) based spectral anomaly detection method for unlicensed bands, where the percentile (PER) score is introduced as a new measure of anomaly. Note that, the effectiveness of these AE models for anomaly recognition heavily relies on the assumption that the reconstruction error of normal signals is generally lower than that of abnormal signals.

However, this assumption does not necessarily hold as the abnormal signals may also be reconstructed well by the AE due to its strong generalization ability [26–28]. For example, if abnormal and normal signals share some common compositional features, a "strong" AE may also reconstruct the anomalies well. Thus, the reconstruction errors of the normal signals and some abnormal signals could be close to each other. Further, as there are generally no training samples of abnormal signals, it is impossible to predict the reconstruction results of abnormal signals. To address this issue, introduces a memory-augmented autoencoder (MemAE) to enlarge the reconstruction error of anomalous samples, thereby improving anomaly detection performance. However, the MemAE model does not achieve satisfactory performance for the anomaly recognition with complex image datasets (e.g., CIFAR-10), and its performance remains unknown for the datasets with abnormal communication signals. Moreover, the reconstruction error is used as the only criterion in [29] to determine whether a signal sample is normal or not. This, however, does not fully exploit the statistics (e.g., the mean and the variance) of the reconstruction error, which may be applied to define a more appropriate detection metric.

In this paper, we propose an unsupervised abnormal signal recognition algorithm based on image enhancement and improved memory-augmented autoencoder (IIMemAE). The main contributions can be described as follows:

(i) We consider an abnormal signal recognition model based on unsupervised learning. To the best of our knowledge, this work is the first attempt to apply the MemAE model in abnormal communication signals recognition

(ii) We propose an abnormal signal recognition algorithm based on image enhancement and improved memory-augmented autoencoder (IIMemAE). Specifically, we introduce an image enhancement module and an anomaly determination module to the standard MemAE model. Instead of using the reconstruction error directly, a parametric Pauta criterion is proposed to measure the anomaly of the reconstruction error of the signal

(iii) We evaluate the performance of various aspects of the IIMemAE model to verify its effectiveness and stability. The simulation results show that the average AUC (area under curve) value of the proposed method is greater than 80% even when the SNR is 2 dB and is close to 70% at the JSR is -5 dB. Compared to the standard MemAE model, the proposed IIMemAE model achieves better and more stable recognition performance, especially under low SNR and JSR conditions. Additionally, simulation results demonstrate that the anomaly determination module based on the parametric Pauta criterion proposed can balance the recognition accuracy of normal and abnormal signals and meet the need for different recognition tasks

The remainder of this paper is organized as follows. Section 2 introduces an abnormal signal recognition system model based on unsupervised learning. The function of each module of the IIMemAE model is presented in Section 3. Section 4 presents and analyzes the simulation results. Section 5 concludes the paper.

Notations: Matrices and vectors are in bold capital and bold lower cases, respectively. Number fields are in blackboard bold. The notations $|\bullet|$, $\|\bullet\|_1$, and $\|\bullet\|_2$ represent absolute value, ℓ_1-norm, and ℓ_2-norm, respectively.

2. System Model

As shown in Figure 1, we consider an abnormal signal recognition model in a wireless communication system. In addition to legitimate signals, there may be malicious or illegal signals in the signals received by the receiver in this system model. Then, the anomaly recognition module on the receiver accomplishes the reconstruction and anomaly recognition of the signal received.

We consider two ways to define abnormal signals. One is for unauthorized signals, that is, signals sent from illegal transmitters without the authorization of radio regulatory agencies. The other is an authorized signal, which suffered external malicious jamming or failures that occur on the receiver during transmission. In specific, for nonstationary signals, abnormal signals can be described as the following:

(i) The signal is legal, but the parameters such as the bandwidth and the center frequency of the signal are not within the specified range

(ii) This is one synthetic anomaly, where legal signals coexist with jamming signals and the jamming signal parameters are legal

The primary task of abnormal communication signals recognition is to identify whether the received signal is normal or abnormal. In this paper, we focus on the second type of anomaly (the abnormal signal recognition for the first type is left to future work.), and the abnormal signal is modeled as follows:

$$S_1(t) = S_0(t) + S_j(t), \tag{1}$$

where $S_0(t)$ denotes the normal signal received and $S_j(t)$ denotes the jamming.

The jamming-to-signal ratio (JSR) can be expressed as follows [30]:

$$\mathrm{JSR} = 10 \log_{10} \frac{P_j}{P_s}, \tag{2}$$

where P_j and P_s denote the jamming power and the signal power, respectively.

The problem of abnormal signal recognition can be formulated as a binary hypothesis test:

$$\begin{aligned} H_0 &: r(t) = S_0(t)C_0(t) + n(t), \\ H_1 &: r(t) = S_1(t)C_1(t) + n(t), \end{aligned} \tag{3}$$

where $r(t)$ denotes the received signal, $C_0(t)$ and $C_1(t)$ represent the channel of the normal signal and the channel of the abnormal signal, respectively, and $n(t)$ is the additive Gaussian white noise with zero mean and variance σ^2. The null hypothesis H_0 represents the absence of abnormal signals in the communication system operation, and the alternative hypothesis H_1 represents the presence of abnormal signals.

The variation of a signal in the time and frequency domains is the most crucial feature in spectrum usage. Time-frequency analysis can extract the characteristic information of communication signals at a specific time and frequency, accurately reflecting the relationship between the signal frequency and the time change. Therefore, the smooth pseudo Wigner-Ville distribution (SPWVD) [31] is performed to obtain a two-dimensional time-frequency spectrogram of the received signal as follows:

$$W_x(t,f) = \int g(u-t) \int h(\tau) s\left(t + \frac{\tau}{2}\right) s * \left(t - \frac{\tau}{2}\right) e^{-j2\pi f t} d\tau du, \tag{4}$$

where $g(u-t)$ and $h(\tau)$ are real symmetric window functions and s^* denotes the conjugate of s. In particular, $g(u-t)$ allows cross-terms oscillating parallel to the time axis to perform smoothing (i.e., time smoothing), and $h(\tau)$ allows smoothing of cross-terms oscillating parallel to the frequency axis (i.e., frequency smoothing). Since smoothing is performed in both the time and frequency domains, the cross-interference terms of multicomponent signals can be well suppressed.

3. IIMemAE-Based Abnormal Signal Recognition Algorithm

In this section, we introduce the structure of IIMemAE and its implementation in abnormal signal recognition.

3.1. Overview. As shown in Figure 2, the proposed IIMemAE model consists of five main components: an image enhancement module, an encoder, a decoder, a memory enhancement module, and an anomaly determination module. In specific, the image enhancement module first improves the contrast of the time-frequency spectrogram of the signal. The encoder encodes the time-frequency spectrogram of the signal and generates query terms. The memory enhancement module includes addressing operations for recording normal signal patterns and retrieving the memory items, which are then passed to the decoder for reconstruction. The IIMemAE model does not decode directly through the decoder like standard autoencoders. Instead, the encoded results are used as query terms to retrieve normal signal patterns in memory enhancement modules and update memory terms through attention-based addressing operations.

Finally, the query result is inputted into the decoder for reconstruction. In the training process, the IIMemAE model proposed is trained by minimizing the reconstruction error and the entropy loss of the query weight of memory items. In the test phase, the model performs reconstruction using only a limited number of normal signal patterns recorded in memory. The anomaly determination module quantifies the abnormality degree of the signal according to a parametric Pauta criterion.

3.2. Image Enhancement Algorithm. The time-frequency grayscale image converted from a communication signal has low contrast, and low-contrast images result from a lack

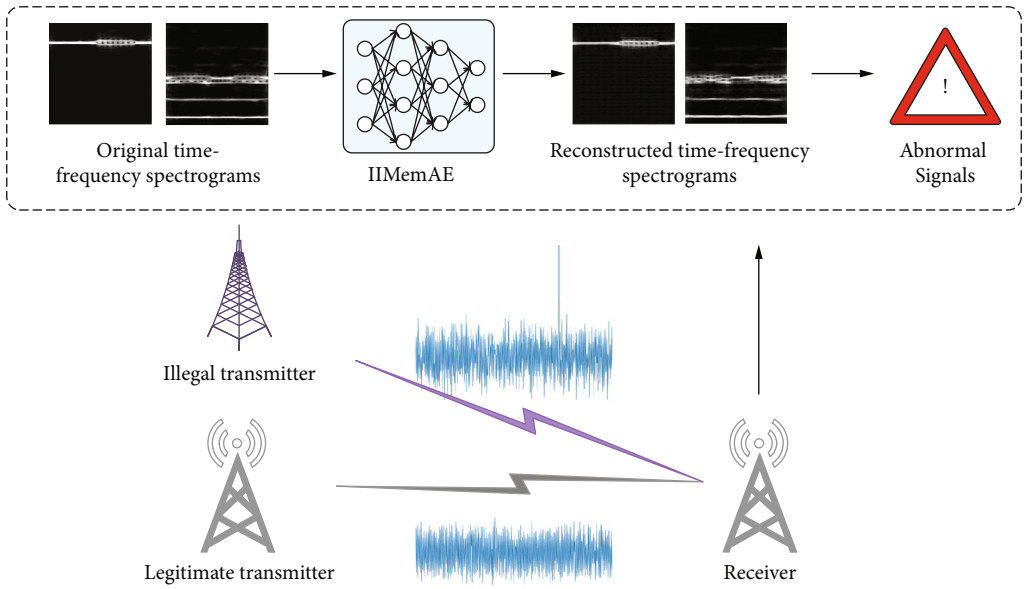

Figure 1: Abnormal signal recognition model structure.

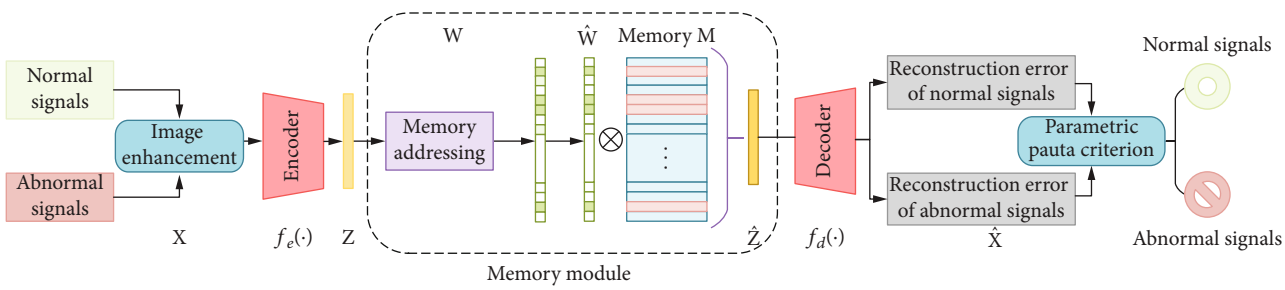

Figure 2: Diagram of the proposed IIMemAE.

of dynamic range in the imaging pixels, which may induce the model to extract incorrect features and false matches [32]. By contrast stretching, the effect of redundant pixels in image features is reduced. Hence, we introduce an image enhancement module and apply the classical image grayscale transformation to the time-frequency grayscale image. The basic principle of the image grayscale transformation is to map the gray value of the original grayscale image to a specified range of grayscale values of the output image. By saturating parts of the time-frequency grayscale image at the lowest and highest grayscales, the contrast of the output image can be improved. In this paper, the grayscale transformation of a time-frequency spectrogram can be expressed as follows:

$$\hat{o} = r\left(o, [p_1\, p_2], [q_1\, q_2]\right), \quad p_1 < p_2, q_1 < q_2, \tag{5}$$

where o denotes the original image, $\hat{o}$ denotes the image after grayscale transformation, and $r(\bullet)$ denotes the grayscale transformation function. The values of points (p_1, q_1) and (p_2, q_2) control the shape of the transformation function. In transforming the grayscale of the original image o to the new image $\hat{o}$, the grayscale value of the pixels in o whose grayscale value is lower than p_1 is assigned as q_1 in $\hat{o}$. Similarly, the gray value of the pixel in f whose gray value is higher than p_2 is also assigned as q_2 when it is transformed to $\hat{o}$.

For the gray value p of any pixel in the original image, the gray value $\hat{p}$ of the corresponding pixel in the new image is obtained after transformation. For example, the transformation processing can be given as follows:

$$\hat{p} = \begin{cases} 255p_1, & p < p_1, \\ \dfrac{q_2 - ql}{p_2 - p_1} \times (p - p_1) \times 255 + 255q_1, & p_1 < p < p_2, \\ 255p_2, & p < p_2. \end{cases} \tag{6}$$

3.3. Encoder and Decoder. The encoder and the decoder generally have a symmetrical structure. The input time-frequency spectrogram dataset sample space is represented as $\mathbb{X}$. When an input $\mathbf{x} \in \mathbb{X}$ is given, the encoder converts it into an encoded $\mathbf{z} \in \mathbb{Z}$ in the low-dimensional feature space. The decoder is trained to reverse map a latent

representation $\hat{\mathbf{z}} \in \mathbb{Z}$ to the domain $\mathbb{X}$. The above process can be expressed as follows:

$$\mathbf{z} = f_e(x; \theta_e), \tag{7}$$

$$\hat{x} = f_d(\hat{\mathbf{z}}; \theta_d), \tag{8}$$

where θ_e and θ_d denote the parameters of the encoder and the decoder, respectively. Here, $\mathbf{z}$ is used as a query to retrieve the relevant items in memory. Then, these items $\mathbf{z}$ are collected and fed to the decoder. Note that, for the standard AE model, $\mathbf{z}$ is set to be $\mathbf{z}$ [33].

3.4. Memory Enhancement Module. The memory enhancement module is designed as a matrix $\mathbf{M} \in \mathbb{R}^{N \times C}$, including N real-valued vectors of dimensions C. The dimension C of each memory item is the same as the dimension of the encoder encoding result $\mathbf{z}$. The hyperparameter N defines the maximum capacity of memory.

$$\hat{\mathbf{z}} = \mathbf{w}\mathbf{M} = \sum_{i=1}^{N} w_i m_i, \tag{9}$$

where $\mathbf{z}$ is obtained by soft addressing of weight vector $\mathbf{w} \in \mathbb{R}^{1 \times N}$ and memory $\mathbf{M}$. $\mathbf{w} = [w_i]_{i=1,2,\cdots,N}$ is a row vector with nonnegative entries that sum to one. The memory $\mathbf{M}$ records the various prototypical normal patterns during training. The weight vector $\mathbf{w}$ is obtained from $\mathbf{z}$ and calculated by the softmax operation in Equation (10), where d is the similarity measure, defined as cosine similarity.

$$w_i = \frac{\exp\left(d(\mathbf{z}, m_i)\right)}{\sum_{j=1}^{N} \exp\left(d\left(\mathbf{z}, m_j\right)\right)}. \tag{10}$$

In addition, the memory module can increase sparsity by hard shrinking the weight vector $\mathbf{w}$ in Equation (11). Sparse addressing encourages fewer but more relevant memory items to represent query results, improving the representation accuracy of memory items.

$$\hat{w}_i = h(w_i; \lambda) = \begin{cases} w_i, & \text{if } w_i > \lambda, \\ 0, & \text{otherwise}, \end{cases} \tag{11}$$

where λ denotes the shrinkage threshold and $\hat{\mathbf{w}}$ denotes the sparse weight vector. The elements in the weight vector $\mathbf{w}$ that are less than or equal to the threshold value are assigned as 0 to realize the sparsity of the vectors. However, it is not easy to calculate the backpropagation of discontinuous functions. To simplify the calculation, we employ the continuous ReLU function to realize the shrinking operation as follows:

$$\hat{w}_i = \frac{\max\left(w_i - \lambda, 0\right) \bullet w_i}{|w_i - \lambda| + \varphi}, \tag{12}$$

where φ is a very small constant. The standardized operation shall be carried out again when the shrinkage is completed as follows:

$$\hat{w}_i = . \tag{13}$$

3.5. Anomaly Determination Module. By querying the memory module, all prototype vectors are considered instead of the nearest prototype vectors, which solves the problem of the excessive generalization ability of the AE. This means that the reconstruction error for abnormal samples is enlarged, making recognition easier. The next phase is to design an appropriate threshold to separate the two classes instead of directly using the average reconstruction error as a metric. In the testing phase, the decoder outputs the reconstruction loss L_r for all test samples and compares it with a predefined threshold η, which can be expressed as follows:

$$L_r \underset{H_o}{\overset{H_1}{\gtrless}} \eta. \tag{14}$$

To design an appropriate threshold, the Pauta criterion [34] is introduced:

$$A_n = |e_n - \bar{e}| > 3\sigma, \tag{15}$$

where e_n denotes the reconstruction error and $\bar{e}$ and σ denote the mean and standard deviation of the reconstruction error of the normal signal. To make the Pauta criterion more accommodation for the abnormal signal recognition task, we modified the Pauta criterion as follows:

$$A_n > K\sigma, \tag{16}$$

where K denotes a positive constant. If the reconstruction error of the time-frequency spectrogram of the input signal satisfies the above formula, the signal is recognized as an abnormal signal. Otherwise, the signal is recognized as a normal signal.

3.6. Training. The training loss comprehensively considers the reconstruction loss and the entropy loss. Given a training dataset $D = \sum_{i=1}^{T} x_i$ containing T time-frequency spectrograms of normal signals, let $\hat{x}_i$ be the reconstruction time-frequency spectrogram corresponding the each training time-frequency spectrogram x_i. The minimized reconstruction error for each time-frequency spectrogram can be expressed as follows:

$$L_r(x_i, \hat{x}_i) = \|x_i, \hat{x}_i\|_2^2, \tag{17}$$

where the reconstruction error is replaced by ℓ_2-norm. The entropy loss improves the sparsity of the generated address weights during training. We minimize the entropy loss:

$$L_e(\hat{w}_i) = -\sum_{i=1}^{T} \hat{w}_i \log\left(\hat{w}_i\right). \tag{18}$$

Combining Equations (17) and (18), the training loss of IIMemAE is described as follows:

$$L = \frac{1}{T}\sum_{i=1}^{T}(L_r(x_i, \hat{x}_i) + \alpha L_e(\hat{w}_i)), \tag{19}$$

where α denotes a hyperparameter. The memory $\mathbf{M}$ is updated by backpropagation and gradient descent during training.

Specifically, there are three primary stages for the implementation of the abnormal communication signals recognition system:

(1) Signal reception: In the communication system operating, the receiver performs time-frequency processing on all received signals to obtain time-frequency spectrograms. The time-frequency spectrograms are then processed with an image enhancement algorithm

(2) Training IIMemAE: Since the normal communication signal is known to the system, the IIMemAE model can be pretrained by the time-frequency spectrogram of the normal communication signal, which is considered to memorize the characteristics of the normal communication signal. The time-frequency spectrogram used in training should also be processed via the image enhancement algorithm

(3) Anomaly recognition: All the time-frequency spectrograms obtained in (1) are used as the input of the IIMemAE model, which reconstructs all the time-frequency spectrograms. The parametric Pautu criterion measures the threshold. If the reconstruction error is larger than the threshold, it is considered an abnormal signal. Otherwise, it is considered to be a normal signal

4. Simulation Results and Discussion

In this section, the performance of the proposed IIMemAE model and its variants are evaluated through extensive simulations. The standard MemAE [29] serves as the baseline under identical conditions. All models are trained with the Adam optimizer of a learning rate of 0.01 for a maximum of 100 epochs. The hyperparameter α is 0.0002. All models are implemented based on the Pytorch framework and trained by using an NVIDIA GTX1080 GPU.

4.1. Simulation Setup. In this paper, the BPSK signal as the normal signal is obtained by simulation. Any remaining signal that is not a BPSK signal is considered anomalous, and we simulate six typical synthetic anomalies [35, 36]. (i) *Comb-spectrum*: the comb spectrum jamming consists of multiple identically modulated subjammings. It is a set of narrowband interferers modulated over a range of frequencies. Each subjamming is superimposed in the time domain and separated in the frequency domain. The jamming spectrum is comb-shaped. (ii) *Multitone*: the multitone jamming consists of multiple tones. Each frequency point is randomly distributed in a specific frequency band. (iii) *Pulse*: the pulse jamming transmitted at a random time on a fixed frequency band. (iv) *Single-tone*: single-tone jamming can affect the BPSK signal by generating high power. (v) *Sweeping*: it performs linear frequency sweep jamming on the BPSK signal, and the center frequency of the jamming is the same as the BPSK signal. (vi) *Noise-FM*: the noise FM jamming with a certain bandwidth and high power is added to the BPSK signal.

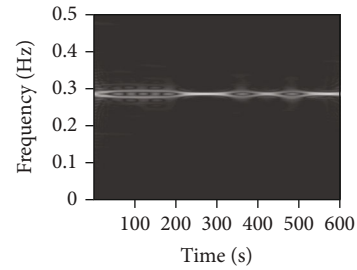

Figure 3: Time-frequency spectrograms of one normal signal.

The time-frequency spectrograms of one normal signal are shown in Figure 3 and six abnormal signals are shown in Figure 4. The training dataset contains 2000 normal time-frequency spectrograms, each of size 112×112. The testing dataset contains 1400 time-frequency spectrograms with 200 normal time-frequency spectrograms and 1200 anomalous time-frequency spectrograms. Each abnormal signal mentioned above has 200 time-frequency spectrograms, each of which is of size 112×112. The training and testing datasets are not duplicated. The test dataset's 200 time-frequency spectrograms of the normal signal are taken out as the validation dataset.

The implementation of the IIMemAE model to recognize abnormal signals can be described as follows:

(1) The training dataset and test dataset are processed by the image enhancement algorithm. Then, the training dataset is fed into the network to train. Only the time-frequency spectrogram of normal signals is trained during training. Figure 5 shows an example of the samples processed by the image enhancement algorithm

(2) Input the validation dataset into the trained network to obtain the reconstruction error of the normal signal timefrequency spectrogram. The threshold η is measured by the mean and variance of the reconstruction error

(3) Input the test dataset into the trained network and get the reconstruction error of each time-frequency spectrogram. Comparing the reconstruction error with the threshold η, if the reconstruction error of a time-frequency spectrogram satisfies the parametric Pauta criterion in Equation (16), it is considered an abnormal signal. On the contrary, it is considered a normal signal

As commonly done in the literature [20, 29], we use the AUC value as the evaluation index of all models, which is the area under the ROC (receiver operation characteristic)

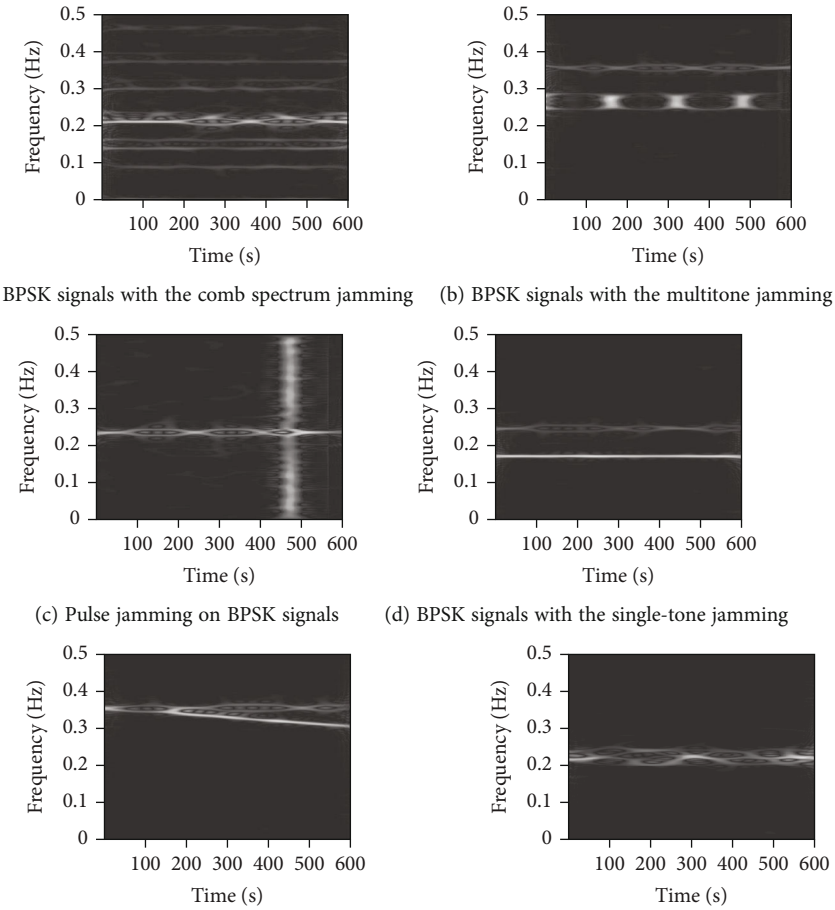

(a) BPSK signals with the comb spectrum jamming (b) BPSK signals with the multitone jamming

(c) Pulse jamming on BPSK signals (d) BPSK signals with the single-tone jamming

(e) Linear frequency sweeping jamming on BPSK signals (f) BPSK signals with the noise FM jamming

Figure 4: Time-frequency spectrograms of six abnormal signals.

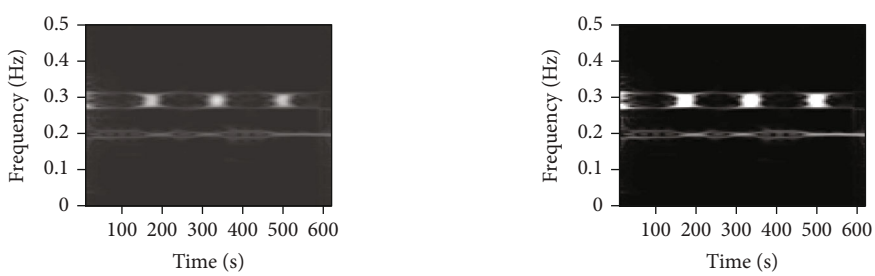

(a) The original time-frequency spectrogram (b) The time-frequency spectrogram after image enhancement processing

Figure 5: The time-frequency spectrogram of the *multitone* abnormal signal before and after image enhancement algorithm processing.

Table 1: Experimental results of different models.

Model	TP	TN	$F1$-score	AUC
MemAE	67.26	99.45	78.86	83.36
MemAE (IE)	59.83	99.47	73.36	79.65
MemAE ($K = 3$)	98.40	83.03	65.79	90.71
IIMemAE ($K = 3$)	**98.88**	92.10	80.31	**95.49**
IIMemAE ($K = 0.3$)	69.10	**99.54**	**80.40**	84.32

curve. We also consider the $F1$-score, which represents the harmonized average of precision and recall. It is a metric primarily used to assess imbalanced data accurately [37]. Table 1 shows the average AUC values for 20 tests on the signal dataset. The memory capacity N is 1000, the signal-to-noise ratio (SNR) is 10 dB, and the JSR is 5 dB.

As shown in Table 1, the proposed IIMemAE outperforms the standard MemAE. In particular, all evaluation metrics of IIMemAE at $K = 0.3$ outperform the standard MemAE.

Table 2: The computational complexity of the presented IIMemAE model, IIMemAE's variants, and the standard MemAE model.

	IIMemAE ($K = 0.3$)	IIMemAE ($K = 3$)	MemAE ($K = 3$)	MemAE (IE)	MemAE
Running time (s)	0.01599	0.01627	0.01524	0.01613	0.01495

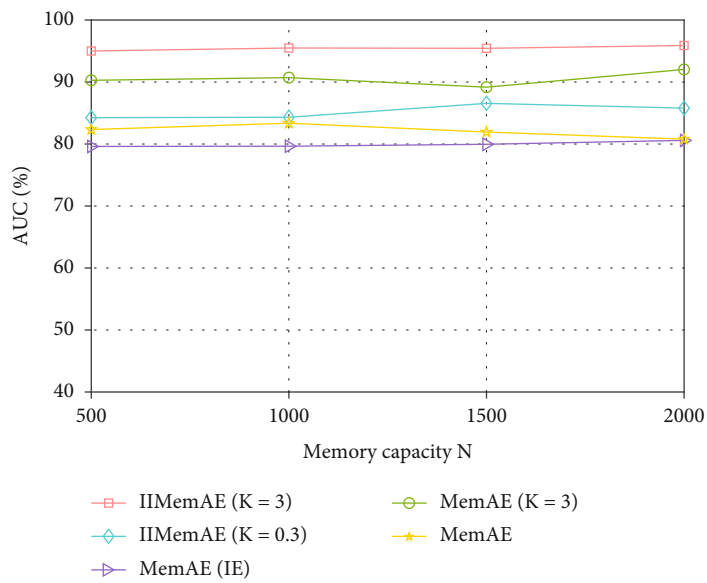

Figure 6: Robustness to the setting of memory capacity. The AUC values of IIMemAE and its variants for different memory capacities on the abnormal.

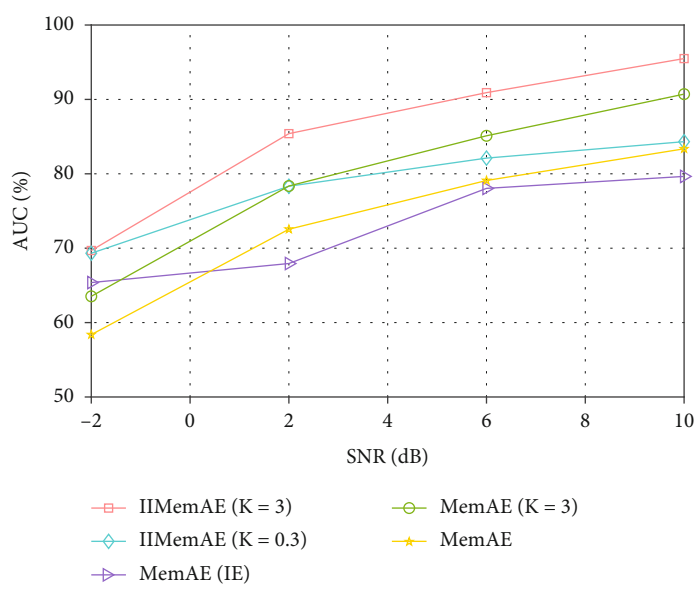

Figure 7: AUC of different SNRs for each model with the JSR of 5 dB.

Specifically, the model with anomaly determination module significantly outperforms MemAE without parametric Pauta criterion and exhibits higher TP (true positive). From the mean TN (true negative), MemAE (IE) can produce better results than the standard MemAE. We can conclude from Table 1 that the image enhancement module can improve the recognition accuracy of abnormal signals, and the abnormal judgment module can improve the recognition accuracy of normal signals. The IIMemAE proposed in this paper comprehensively considers the effect of the two modules on the overall recognition accuracy. Therefore, IIMemAE can yield better performance than the standard MemAE.

Moreover, we empirically study the computational complexity of the proposed method on the test dataset (i.e., contains 1400 time-frequency spectrograms) using NVIDIA GTX1080 GPU. As shown in Table 2, the proposed

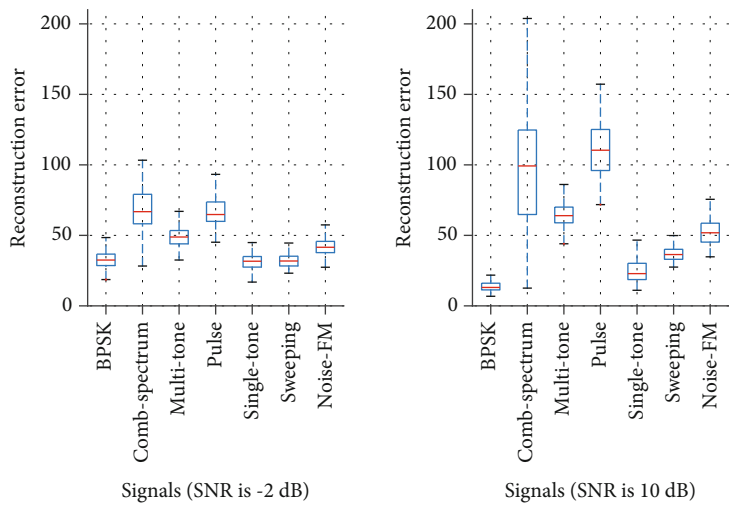

Figure 8: Boxplots of reconstruction error for each signal by the IIMemAE ($K = 3$) model. On the left is the reconstruction error distribution with an SNR of -2 dB. On the right is the reconstruction error distribution with an SNR of 10 dB.

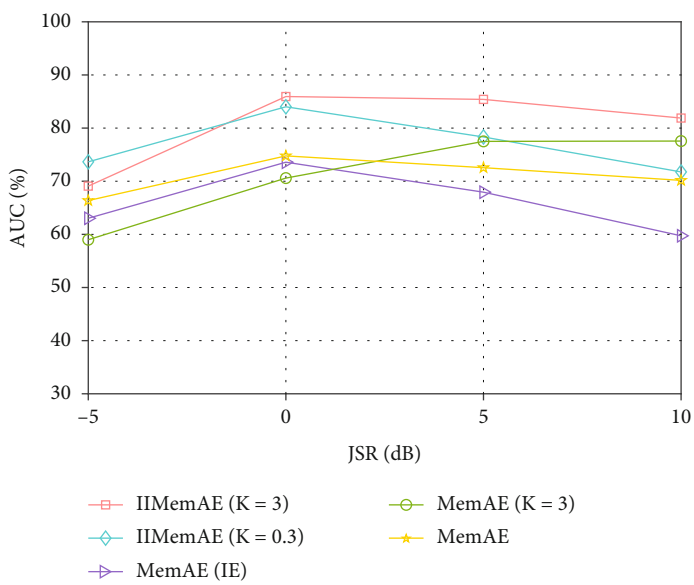

Figure 9: AUC of different JSRs for each model with the SNR of 2 dB.

IIMemAE ($K = 3$) averagely takes 0.01627 seconds to recognize a time-frequency spectrogram. Compared to the standard MemAE model that takes 0.01495 seconds for each time-frequency spectrogram, our image enhancement module and anomaly determination module induce little additional computational time (i.e., 1.32×10^{-3} seconds per time-frequency spectrogram).

4.2. Impact of Different Memory Capacities. We conduct experiments by setting different memory capacities, and the AUC values are shown in Figure 6. For the anomalous signal datasets, the AUC of the model is always stable even as the dimension of the memory matrix increases. It indicates that IIMemAE is insensitive to memory capacity N and can robustly produce credible results. In addition, simulation results of other models show that they are equally stable and robust. All models have AUC values of 80% and above, with IIMemAE ($K = 3$) performing the best. Compared with the standard MemAE, IIMemAE and MemAE ($K = 3$) can produce better AUC values. The MemAE (IE) does not perform well as the standard MemAE because it has worse TP values.

4.3. Impact of Different SNRs. As shown in Figure 7, with the increase of SNR, the AUC values of the five models increase. Overall, MemAE (IE) shows the worst performance, and IIMemAE ($K = 3$) offers the best performance. However, it is worth noting that the standard MemAE performs the worst at low SNR. These models with the image enhancement module and anomaly determination module can produce good recognition results even at low SNR.

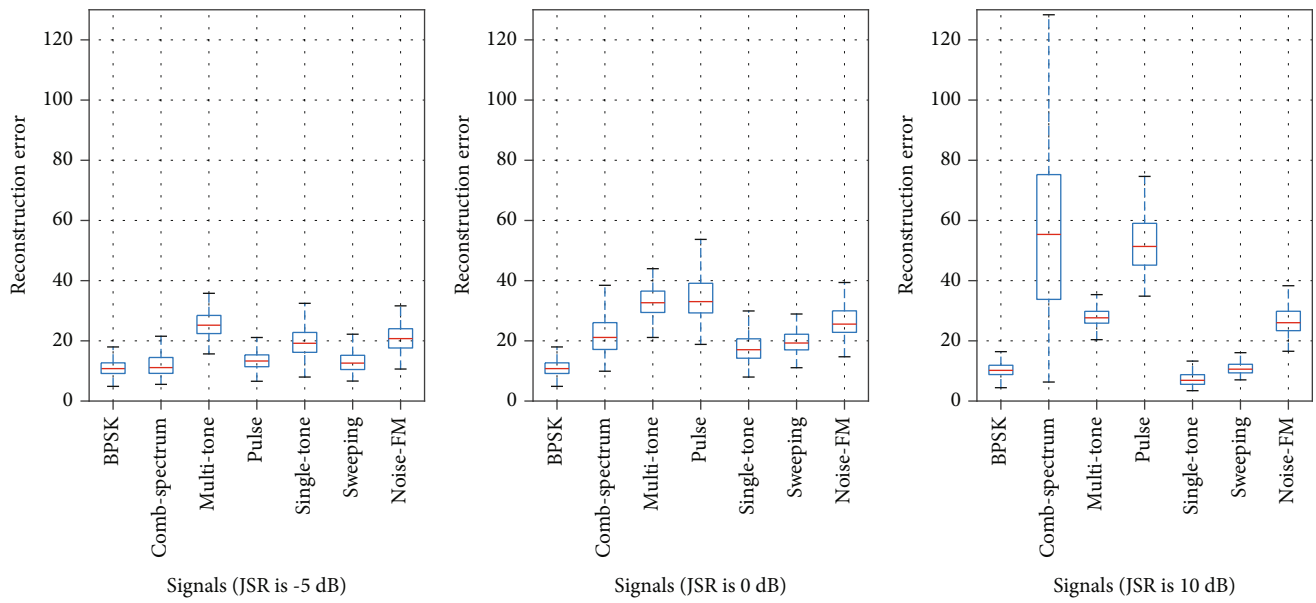

FIGURE 10: Boxplots of reconstruction error for each signal by the IIMemAE ($K = 3$) model. On the left is the reconstruction error distribution with a JSR of -5 dB. In the middle is the reconstruction error distribution with a JSR of 0 dB. On the right is the reconstruction error distribution with a JSR of 10 dB.

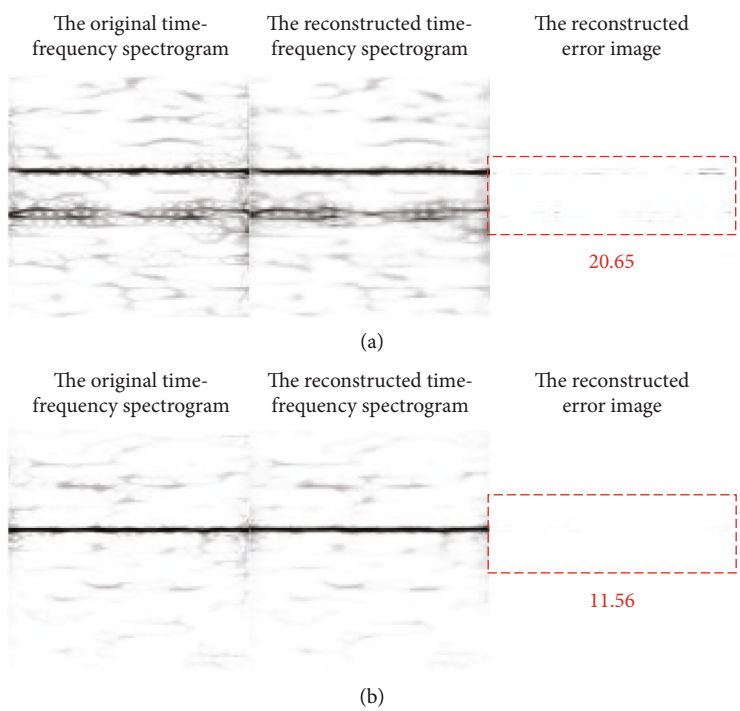

FIGURE 11: The reconstruction results of the abnormal signal single-tone by IIMemAE ($K = 3$). (a) The reconstruction results of IIMemAE ($K = 3$) with a JSR of 0 dB. (b) The reconstruction results of IIMemAE ($K = 3$) with a JSR of 10 dB.

Figure 8 shows the reconstruction error distribution for each signal under the IIMemAE ($K = 3$) model. In the boxplots, the upper and lower bounds of the box in blue are the upper and lower quartiles of one signal reconstruction error, respectively. Therefore, the width of the box reflects the degree of fluctuation in the reconstruction error of each signal. The red line segment in the middle of the box represents the median of each signal reconstruction error. SNR is -2 dB in the left boxplots, the average reconstruction error of the BPSK signal is 32.69, and the average reconstruction error of each abnormal signal is 71.69, 49.32, 66.80, 31.35, 32.75, and 42.88, respectively. SNR is 10 dB in the right boxplots, the average reconstruction error of the BPSK signal is 13.63, and the average reconstruction error of each

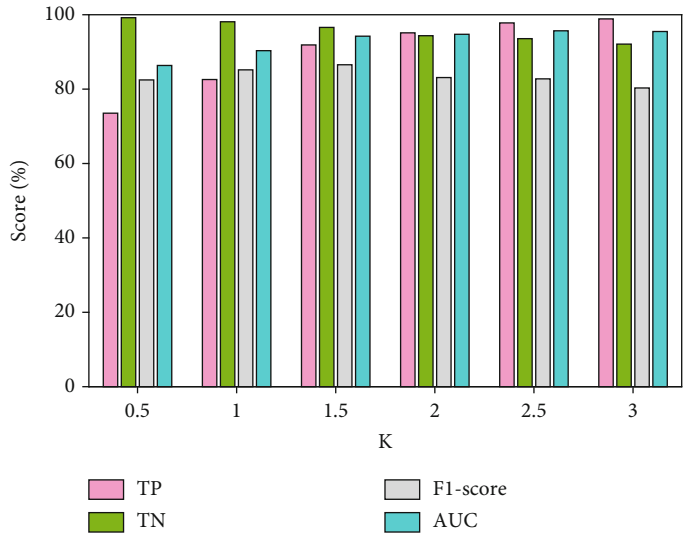

Figure 12: The influence of different parameters K in the IIMemAE model on the recognition performance of abnormal signals.

abnormal signal is 98.57, 64.27, 110.48, 26.09, 38.34, and 56.48, individually. As the SNR increases, the average reconstruction error of the BPSK signal decreases, while the average reconstruction error of the abnormal signal increases. Therefore, the larger the SNR, the IIMemAE model can better reconstruct normal signals and enlarge the reconstruction error of abnormal signals.

4.4. Impact of Different JSRs. Figure 9 shows the experimental results of setting different JSRs. Compared with the standard MemAE model, the IIMemAE ($K = 3$) model offers the best performance evaluated based on AUC. In particular, all models except MemAE ($K = 3$) perform best when JSR is 0 dB. Specifically, Figure 10 shows the reconstruction error distribution of each signal through the IIMemAE ($K = 3$) model at different JSRs. JSR is -5 dB in the left boxplots, the average reconstruction error of the BPSK signal is 11.06, and the average reconstruction error of each abnormal signal is 17.76, 25.75, 13.62, 19.86, 16.46, and 25.54, respectively. JSR is 0 dB in the middle boxplots, the average reconstruction error of the BPSK signal is 11.06, and the average reconstruction error of each abnormal signal is 26.74, 32.87, 34.71, 17.93, 22.15, and 28.71, individually. Since the parameter JSR is set based on the abnormal signal, it does not affect the reconstruction of the BPSK signal for the IIMemAE model. As the JSR increases, the IIMemAE model enlarges the reconstruction error of anomalous signals and thus can result in better performance.

However, when the JSR increases to a certain level, the performance of the IIMemAE model begins to decline. In Figure 10, JSR is 10 dB in the right boxplots, the average reconstruction error of each abnormal signal is 55.27, 27.97, 53.07, 7.47, 11.14, and 27.61, respectively. Compared with the middle boxplots at JSR of 0 dB, the reconstruction errors of abnormal signal *comb-spectrum* and *pulse* are enlarged. However, the reconstruction errors of abnormal signals *multitone*, *single-tone*, *sweeping*, and *noise-FM* are reduced instead. Particularly, the reconstruction errors of abnormal signal *single-tone* and *sweeping* are almost as same as the normal BPSK signal.

To see it more clearly, we further plot images for the experimental results, which are performed color reversion process in Figure 11. It shows the time-frequency spectrogram, the reconstructed time-frequency spectrogram, and the reconstructed error image of the abnormal signals *single-tone* with a JSR of 10 dB. Comparing the reconstructed error images at the JSR is 0 dB and 10 dB, the IIMemAE model can reconstruct the abnormal signal *single-tone* and *sweeping* well with the JSR of 10 dB. In Figure 11(a) and Figure 11(b), the reconstruction error is 20.65 and 11.56, respectively. Single-tone jamming and frequency sweeping jamming characteristics are similar to the BPSK signal characteristic. From the time-frequency spectrogram, they both look like a line segment. Therefore, the performance of the IIMemAE model begins to degrade at the JSR of 5 dB.

The synthetic abnormal signal in this paper is formed by the superimposition of the jamming signal on the normal recognition. Simulation results show that the IIMemAE model outperforms the standard MemAE model even at low SNR and JSR. Specifically, in the IIMemAE model, the image enhancement module can improve the recognition accuracy of abnormal signals, and the anomaly determination module can improve the recognition accuracy of normal signals. Moreover, the anomaly determination module with the parametric Pauta criterion can balance the recognition accuracy of normal and abnormal signals and adapt to diverse abnormal signal recognition tasks. Future works will investigate the image enhancement model to further improve the performance of the IIMemAE model for signals with similar features. Besides, more research work is needed to detect anomalies in real-time signal. When the JSR increases to a certain level, the time-frequency spectrogram of the synthetic abnormal signal will mainly display the characteristics of the jamming signal. If the characteristics

of the jamming signal are similar to the normal signal, the IIMemAE model will reconstruct the synthetic abnormal signal well, leading to its performance degradation. This issue also exists in the standard MemAE model and two variant models. We hope to address this issue in future work further.

4.5. Impact of Different K. Figure 12 shows the effect of different parameters K in the IIMemAE model on the recognition performance of abnormal signals with the SNR is 10 dB and the JSR is 5 dB. The evaluation indexes TP and AUC increase with the increase of K, and the $F1$-score fluctuates relatively stably within a certain range. However, the evaluation index TN decreases as K increases. It dictates that the size of K can balance the classification accuracy of positive samples and negative samples. In particular, TP and TN are above 94% when the parameter K is set to 2. Therefore, we can select an appropriate K value for the IIMemAE model to adapt to different abnormal signal recognition task requirements.

5. Conclusion

In this paper, we have proposed an IIMemAE model to improve the performance of abnormal communication signals recognition based on the MemAE model. The proposed IIMemAE model can address the issue that the performance of anomaly recognition may be degraded due to the imbalanced communication signals in the real world. We have considered two important issues, i.e., redundant information exists in the time-frequency spectrogram, and the recognition accuracy of normal signals based on the standard MemAE model is low. We have introduced an image enhancement module and an anomaly determination module. In particular, the image enhancement module can reduce the influence of redundant information in the time-frequency spectrogram, and the anomaly determination module based on the parametric Pauta criterion can be flexibly adjusted according to the need for anomaly or classify the detected anomalies.

Data Availability

The data that support the findings of this study are available from the corresponding author upon reasonable request.

Conflicts of Interest

The authors declare that they have no conflicts of interest.

Acknowledgments

This work is supported by the National Key R&D Program of China (No. 2018YFB1800800) and the National Natural Science Foundation of China (No. U20B2038, No. 61901520, No. 61931011, No. 61871398, No. 61827801, and No. 62101254).

References

[1] Q. Wu, G. Ding, J. Wang, and Y.-D. Yao, "Spatial-temporal opportunity detection for spectrum-heterogeneous cognitive radio networks: two-dimensional sensing," *IEEE Transactions on Wireless Communications*, vol. 12, no. 2, pp. 516–526, 2013.

[2] G. Ding, J. Wang, Q. Wu, Y.-D. Yao, F. Song, and T. A. Tsiftsis, "Cellular-base-station-assisted device-to-device communications in TV white space," *IEEE Journal on Selected Areas in Communications*, vol. 34, no. 1, pp. 107–121, 2016.

[3] S. Rajendran, V. Lenders, W. Meert, and S. Pollin, "Crowd-sourced wireless spectrum anomaly detection," *IEEE Transactions on Cognitive Communications and Networking*, vol. 6, no. 2, pp. 694–703, 2020.

[4] M. Liu, B. Li, Y. Chen et al., "Location parameter estimation of moving aerial target in space–air–ground-integrated networks-based IoV," *IEEE Internet of Things Journal*, vol. 9, no. 8, pp. 5696–5707, 2022.

[5] H. Pirayesh and H. Zeng, "Jamming attacks and anti-jamming strategies in wireless networks: a comprehensive survey," *IEEE Communications Surveys Tutorials*, vol. 24, no. 2, pp. 767–809, 2022.

[6] M. Liu, C. Liu, M. Li, Y. Chen, S. Zheng, and N. Zhao, "Intelligent passive detection of aerial target in space-air-ground integrated networks," *China Communications*, vol. 19, no. 1, pp. 52–63, 2022.

[7] M. Liu, J. Wang, N. Zhao, Y. Chen, H. Song, and R. Yu, "Radio frequency fingerprint collaborative intelligent identification using incremental learning," *IEEE Transactions on Network Science and Engineering*, p. 1, 2021.

[8] A. Moumena, "Abnormal behavior detection of jamming signal in the spectrum using a combination of compressive sampling and intelligent bivariate k-means clustering technique in wideband cognitive radio systems," in *2015 4th International Conference on Electrical Engineering (ICEE)*, pp. 1–4, Boumerdes, Algeria, 2015.

[9] M. Spuhler, D. Giustiniano, V. Lenders, M. Wilhelm, and J. B. Schmitt, "Detection of reactive jamming in DSSS-based wireless communications," *IEEE Transactions on Wireless Communications*, vol. 13, no. 3, pp. 1593–1603, 2014.

[10] D. Ciuonzo, A. Aubry, and V. Carotenuto, "Rician mimo channel- and jamming-aware decision fusion," *IEEE Transactions on Signal Processing*, vol. 65, no. 15, pp. 3866–3880, 2017.

[11] C. Sorrells, P. Potier, L. Qian, and X. Li, "Anomalous spectrum usage attack detection in cognitive radio wireless networks," in *2011 IEEE International Conference on Technologies for Homeland Security (HST)*, pp. 384–389, Waltham, MA, USA, 2011.

[12] S. Liu, L. J. Greenstein, W. Trappe, and Y. Chen, "Detecting anomalous spectrum usage in dynamic spectrum access networks," *Ad Hoc Networks*, vol. 10, no. 5, pp. 831–844, 2012.

[13] H. Yan, B. Zhou, J. Liu, M. Kong, and Z. Pei, "Radio signal recognition based on constructing typical spectrum," in *2016 2nd IEEE International Conference on Computer and Communications (ICCC)*, pp. 1889–1894, Chengdu, 2016.

[14] Q. Qu, S. Wei, S. Liu, J. Liang, and J. Shi, "JRNet: jamming recognition networks for radar compound suppression jamming signals," *IEEE Transactions on Vehicular Technology*, vol. 69, no. 12, pp. 15035–15045, 2020.

[15] P. Wang, Y. Cheng, B. Dong, and G. Gui, "Binary neural networks for wireless interference identification," *IEEE Wireless Communications Letters*, vol. 11, no. 1, pp. 23–27, 2022.

[16] H. Xu, X. Ma, C. Wang et al., "A neural network approach for wireless spectrum anomaly detection in 5G-unlicensed network," *CCF Transactions on Pervasive Computing and Interaction*, pp. 1–9, 2022.

[17] T. J. O'Shea, T. Roy, and T. Erpek, "Spectral detection and localization of radio events with learned convolutional neural features," in *2017 25th European Signal Processing Conference (EUSIPCO)*, pp. 331–335, Kos, Greece, 2017.

[18] S. Rajendran, W. Meert, V. Lenders, and S. Pollin, "Unsupervised wireless spectrum anomaly detection with interpretable features," *IEEE Transactions on Cognitive Communications and Networking*, vol. 5, no. 3, pp. 637–647, 2019.

[19] R. Longadge and S. Dongre, "Class imbalance problem in data mining review," *International Journal of Computer Science & Network*, vol. 2, no. 1, 2013.

[20] B. Min, J. Yoo, S. Kim, D. Shin, and D. Shin, "Network anomaly detection using memory-augmented deep autoencoder," *IEEE Access*, vol. 9, pp. 104695–104706, 2021.

[21] G. Bovenzi, G. Aceto, D. Ciuonzo, V. Persico, and A. Pescapé, "A hierarchical hybrid intrusion detection approach in IoT scenarios," in *GLOBECOM 2020 - 2020 IEEE Global Communications Conference*, pp. 1–7, Taipei, Taiwan, December 2020.

[22] Y. Mirsky, T. Doitshman, Y. Elovici, and A. Shabtai, "Kitsune: an ensemble of autoencoders for online network intrusion detection," 2018, http://arxiv.org/abs/1802.09089.

[23] Q. Feng, Y. Zhang, C. Li, Z. Dou, and J. Wang, "Anomaly detection of spectrum in wireless communication via deep auto-encoders," vol. 73, Tech. Rep. 7, Journal of Supercomputing, 2017.

[24] Y. Ghanney and W. Ajib, "Radio frequency interference detection using deep learning," in *2020 IEEE 91st Vehicular Technology Conference (VTC2020-Spring)*, pp. 1–5, Antwerp, Belgium, May 2020.

[25] Y. Tian, H. Liao, J. Xu, Y. Wang, S. Yuan, and N. Liu, "Unsupervised spectrum anomaly detection method for unauthorized bands," *Space: Science & Technology*, vol. 2022, article 9865016, pp. 1–10, 2022.

[26] C. Huang, Z. Yang, J. Wen et al., "Self-supervision-augmented deep autoencoder for unsupervised visual anomaly detection," *IEEE Transactions on Cybernetics*, pp. 1–14, 2021.

[27] B. Zong, Q. Song, M. R. Min et al., "Deep autoencoding Gaussian mixture model for unsupervised anomaly detection," in *International Conference on Learning Representations*, Vancouver, Canada, 2018.

[28] F. Ye, C. Huang, J. Cao, M. Li, Y. Zhang, and C. Lu, "Attribute restoration framework for anomaly detection," *IEEE Transactions on Multimedia*, vol. 24, pp. 116–127, 2022.

[29] D. Gong, L. Liu, V. Le et al., "Memorizing normality to detect anomaly: memory-augmented deep autoencoder for unsupervised anomaly detection," in *2019 IEEE/CVF International Conference on Computer Vision (ICCV)*, pp. 1705–1714, South Korea, 2019.

[30] L. Zhang, H. Wang, and T. Li, "Anti-jamming message-driven frequency hopping—part I: system design," *IEEE Transactions on Wireless Communications*, vol. 12, no. 1, pp. 70–79, 2013.

[31] Z. Chen and L. Wu, "Blind source separation of dual-carrier MPPSK signal based on smoothed pseudo wigner distribution," in *2014 9th International Symposium on Communication Systems, Networks Digital Sign (CSNDSP)*, pp. 664–667, Manchester, UK, July 2014.

[32] V. Bajaj, K. Rai, A. Kumar, and D. Sharma, "Time-frequency image based features for classification of epileptic seizures from EEG signals," *Biomedical Physics & Engineering Express*, vol. 3, no. 1, p. 015012, 2017.

[33] Y. Zhou, X. Song, Y. Zhang, F. Liu, C. Zhu, and L. Liu, "Feature encoding with autoencoders for weakly supervised anomaly detection," *IEEE Transactions on Neural Networks and Learning Systems*, vol. 33, no. 6, pp. 1–12, 2021.

[34] F. Wan, G. Guo, C. Zhang, Q. Guo, and J. Liu, "Outlier detection for monitoring data using stacked autoencoder," *IEEE Access*, vol. 7, pp. 173827–173837, 2019.

[35] T. Kuang, H. Chen, L. Han, R. He, W. Wang, and G. Ding, "Abnormal signal recognition with time-frequency spectrogram: a deep learning approach," 2022, http://arxiv.org/abs/2205.15001.

[36] M. Liu, Z. Liu, W. Lu, Y. Chen, X. Gao, and N. Zhao, "Distributed few-shot learning for intelligent recognition of communication jamming," *IEEE Journal of Selected Topics in Signal Processing*, vol. 16, no. 3, pp. 395–405, 2022.

[37] T. M. Barros, P. A. Souza Neto, I. Silva, and L. A. Guedes, "Predictive models for imbalanced data: a school dropout perspective," *Education Sciences*, vol. 9, no. 4, p. 275, 2019.

Hindawi
Wireless Communications and Mobile Computing
Volume 2022, Article ID 5312590, 10 pages
https://doi.org/10.1155/2022/5312590

Research Article

Multiobjective Optimization of Process Parameters of Silicon Single Crystal Growth

Weichao Huang,[1] **Ganggang Zhang**,[2] **and Jing Wang**[3]

[1]*Shaanxi Key Laboratory of Complex System Control and Intelligent Information Processing, Xi'an University of Technology, Xi'an 710048, China*
[2]*School of Automation and Information Engineering, Xi'an University of Technology, Xi'an 710048, China*
[3]*School of Printing, Packaging and Digital Media, Xi'an University of Technology, Xi'an 710048, China*

Correspondence should be addressed to Weichao Huang; huangweichao311@163.com

Received 1 June 2022; Accepted 7 July 2022; Published 27 July 2022

Academic Editor: Mingqian Liu

In order to obtain higher quality silicon single crystal, a hybrid strategy for modeling of Czochralski silicon crystal growth and optimizing of process parameters is presented in the paper. The hybrid strategy includes the computational fluid dynamics (CFD) method, neural network of group method of data handing (GMDH), and improved nondominated sorting genetic algorithm II (NSGA-II). The shape variable of solid-liquid interface h and the defect evaluation criteria V/G are set to objective functions according to engineering experience and process requirement. The polynomial of the objective functions is produced by GMDH and CFD. Ultimately, an improved elitist strategy and crowding distance NSGA-II is proposed in the paper to obtain the Pareto optimum solution by the objective functions identified by the GMDH. Compared with other optimization algorithms, the improved NSGA-II can increase the lateral diversity and the uniform distribution of the nondominated solutions. Engineering validation proved that the proposed hybrid strategy can effectively solve the complex uncertain multiobjective optimization problem of system and provides a new method for obtaining high-quality crystal growth process parameters.

1. Introduction

The vigorous development of integrated circuit industry promoted the development of silicon crystal in the direction of larger size and higher quality [1]. The process of silicon crystal growth is the key factor to measure the production level of semiconductor materials. The process parameters are usually set from numerical simulation methods or engineering experience. But the process parameters obtained by those methods are often not optimal. Therefore, it is a new direction to study the intelligent optimization method of crystal growth process parameters to improve the growth process and improve the crystal quality.

At present, there are two main research directions for process parameters in the field of silicon single crystal growth. One is the combination of empirical method and experimental method, the other is numerical simulation method based on computational fluid dynamics (CFD). Empirical and experimental methods rely on specific equipment, which requires experienced technicians and strong experimental funds. The production units often use the experimental method in the final verification stage. The experimental data and experience obtained are also confidential. Because of the advantages of fast, high efficiency, low cost, and flexible design, numerical simulation method has been widely used in the research of crystal growth.

In recent years, the study of crystal growth technology has expanded from two-dimensional global model to three-dimensional local model, from simple fluid-thermal coupling to impurity transport, and from fixed boundary to complex boundary conditions involving functional and chemical reactions [2–4]. At present, the researches on optimization of process parameters are still at the level of numerical simulation and mechanism analysis. Liu et al. studied the effect of temperature and external magnetic field on the deformation of solid-liquid interface [5]. Asadi et al. studied the change of

solid-liquid interface at different rotating speeds of crystals and crucibles [6]. Voronkov and Falster studied the effect of growth parameters on crystal quality from the factors of crystal defects and proposed a criterion V/G for evaluating the probability of vacancies and self-gap in crystals [7]. Neural networks and intelligent optimization methods have been applied more and more in the field of crystal growth. Qi et al. established a heat and mass transfer model to simulate the crystal growth process and verified the experimental data with neural network and genetic algorithm to obtain the optimal growth parameters [8]. Dang et al. established the heat transfer model and a thermal stress model in single crystalline silicon growth and studied the mapping relationship between optimization variables and targets [9]. The above researches based on numerical simulation can effectively explain the relationship between single process parameter and crystal quality, but these conclusions are limited to the basis of limited calculation results, which is helpless for multiobjective and multiprocess parameters cooperative optimization.

For parameter optimization problems, researchers always expect a clear mathematical model or objective function, in which CFD cannot achieve. However, the combination of CFD, model identification, and multiobjective optimization is a good strategy. This hybrid strategy has been applied in many industrial fields and has attracted more and more attention [10–12]. Wang et al. simulated the turbine model use CFD and provided training samples for BP neural network. The maximum efficiency and the minimum blocking quality were optimized by using NSGA-II with improved congestion distance [13]. Damavandi et al. established the models of maximum heat transfer efficiency and minimum pressure drop function of corrugated fin elliptical heat exchanger by combining CFD with the group method of data handing (GMDH) neural network. The improved nondominated sorting genetic algorithm II (NSGA-II) is used to optimize the structure design, and the optimal structural design scheme is obtained [14]. Jafari et al. modeling and calculation of DI diesel engine used CFD and response surface fitting Used Kriging interpolation method, and optimize the first efficiency law and the second efficiency law used multiobjective optimization algorithm [15]. Because it is difficult to establish the model of optimization objective and process parameters, the application of this hybrid strategy in the field of crystal growth has not been reported yet.

In the paper, the process of 300 mm silicon crystal growth by the Cz method is studied. The solid-liquid interface deformation h and V/G value, which represent the crystal quality, are taken as objective functions. Heating temperature T, crystal rotating velocity r_c, melt rotating velocity r_m, and pulling speed V are the process parameters to be optimized. Firstly, according to design variables, the three-dimensional local model of the Cz crystal growth was solved by CFD technology, and training samples for GMDH were provided. Then, the polynomial models of two objective functions are obtained by the GMDH algorithm. Finally, an improved NSGA-II is proposed to optimize the process parameters and obtain the Pareto frontier, which satisfies the requirements of two objective functions at the same time. This improved NSGA-II includes controlling elite strategy to limit the number of individuals on nondominated frontier, improving the congestion distance, and using dynamic crowding distance (DCD) to improve the Pareto frontier distribution. The effectiveness of the hybrid algorithm is verified by crystal growth experiments.

2. Crystal Growth Model and Numerical Solution

2.1. Mathematical Models. The Cz silicon crystal growth consists by high-temperature melt and crystal. The structure of the Cz silicon crystal is shown in Figure 1. The melt in crucible is kept liquid state by the high temperature. The crystal rises slowly at a certain pulling speed. In order to make the temperature in the melt evenly distributed, the crucible and the crystal rotate in the opposite direction at different speeds. The continuum equation, momentum conservation equation, and energy conservation equation of melt flow and heat transfer calculation are expressed as follows [16].

$$\nabla \times \vec{v} = 0, \tag{1}$$

$$\rho \vec{v} \times \nabla \vec{v} = -\nabla p + \nabla \times \left[\mu\left(\nabla \vec{v} + \nabla \vec{v}^{T}\right)\right] - \rho \vec{g} \beta_T \Delta T, \tag{2}$$

$$\rho c \vec{v} \times \nabla T = \nabla \times (k \nabla T), \tag{3}$$

where T, ρ, p, μ, $\vec{g}$, β_{T}, c, and k are temperature, density, pressure, melt viscosity, gravity acceleration, thermal expansion coefficient, thermal capacity, and thermal conductivity, respectively. The melt velocity $\vec{v}$ is mainly related to the rotational speed of crystals and melts. The last term in Equation (2) denotes thermal buoyancy, which is one of the main factors affecting the conservation of momentum.

At the solid-liquid interface, it is assumed that the temperatures of solid and liquid phases are equal, that is, $T_s = T_l$. The energy balance equation at the solid-liquid interface is as follows:

$$\rho_s L_a (V_I - V) = \lambda_s \frac{\partial T}{\partial n}\bigg|_s - \lambda_l \frac{\partial T}{\partial n}\bigg|_l, \tag{4}$$

where n is the normal vector of interface. V_I and V are interface moving speed and crystal lifting speed, respectively. L_a is latent heat. λ is thermal conductivity, and subscripts s and l indicate crystals and melts, respectively. The deformation position of solid-liquid interface at each moment can be obtained by calculating V in Equation (4).

2.2. Numerical Simulation. The Fluent software is used to simulate the Cz silicon single crystal growth 3D local model in the paper, which is an internationally popular commercial CFD software. Convection and diffusion terms are upwind of second order, and the SIMPLE algorithm [5] is used to solve the coupling between velocity and pressure fields. The two-equation realizable $k-\varepsilon$ turbulence model is selected, which ensures the continuity of turbulence and has a good performance for rotational flow and boundary layer flow.

In order to ensure the independence of the grid and minimize the computational cost, numerical analysis is carried out under three models with different mesh accuracy. The

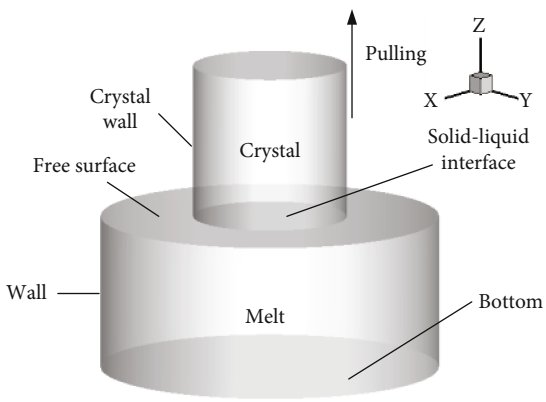

Figure 1: Three-dimensional local model and boundary description of the Cz crystal growth.

results of objective functions h and V/G on different grids are shown in Table 1, when the computational parameters are $T = 1720\text{K}$, $r_c = 10\text{rev/min}$, $r_m = 5\text{rev/min}$, and $V = 1.8\text{mm/min}$. The errors between the results of 232436 mesh models and those of the denser mesh models can be neglected. So, 232436 mesh models satisfy the requirement of independence precision. The meshing of the three-dimensional model of crystal growth and the result of numerical simulation are shown in Figures 2(a) and 2(b), respectively.

3. Design Variables and Objective Functions

Four design variables related to the objective function are selected in the paper, which are the heater temperature T, the crystal rotating velocity r_c, the melt rotating velocity r_m, and the lifting speed V. These variables and their value ranges are listed in Table 2. Many design points can be obtained by changing the value of the design variables, so the corresponding objective function values of these design points can be calculated by CFD.

The two objective functions are the deformation of solid-liquid interface h and the defect evaluation criteria V/G. Because of the change of heat transfer from melt to crystal, the convex deformation of solid-liquid interface is produced under the action of thermal stress. The larger the deformation h, the greater the probability of growth defects and the thermoelastic stress in the crystal. V/G is an important index for "self-gap" and "vacancy" in silicon wafers. Literature [17] shows that the range of lifting speed V is related to the size of crystal diameter within the required range of V/G. The perfect range of V/G values can be ensured when the lifting speed is set between 1mm/min and 1.8mm/min for 300 mm diameter silicon crystal. The larger the V/G, the larger lifting speed, and the more conducive to shortening the production cycle, saving energy consumption, and reducing costs. However, the increase of lifting speed will increase h and reduce the uniformity of crystal cross-section. The two objective functions are conflicting and constitute a multiobjective optimization problem in the process of silicon crystal growth. Therefore, the purpose of this study is to find the optimal solution which satisfies the two objective functions simultaneously.

Table 1: Result of grid independence.

Mesh number	h	V/G
141096	0.01127	$1.902e-3$
232436	0.01011	$1.885e-3$
754356	0.01007	$1.883e-3$

4. Object Function Modeling by GMDH

Although the approximate solutions of the two objective functions can be obtained by numerical calculation, the explicit mathematical expressions containing the four design variables mentioned above cannot be obtained. However, the accurate model of objective functions is necessary for system control and process parameter optimization. The artificial neural network cannot be restricted by the nonlinear model because it has the ability to approximate any nonlinear mapping by learning. So, the artificial neural network method is used to determine model has obvious advantages. GMDH is a relatively complete and widely used neural network structure [18]. The GMDH algorithm works by describing the model as the structure of a group of neurons. Each pair of neurons in each layer is connected by a quadratic polynomial and new neurons are created in the next layer. During modeling, the input-output mapping can be represented using this method.

The way to solve the problem of model identification is to establish a function $\widehat{f}$ that can approximately replace the actual model f, so as to minimize the error between the estimated output $\widehat{y}$ and the actual model output y when the input vector $X = (x_1, x_2, \cdots, x_n)$ is specified. Therefore, the M-estimated values include n inputs, and one output can be expressed as follows:

$$y_i = f(x_{i1}, x_{i2}, x_{i3} \cdots x_{\text{in}}). \tag{5}$$

Estimate of the target value $\widehat{y}_i$ of each input vector $X = (x_{i1}, x_{i2}, x_{i3} \cdots x_{\text{in}})$ by the GMDH neural network is as follows:

$$\widehat{y}_i = \widehat{f}(x_{i1}, x_{i2}, x_{i3} \cdots x_{\text{in}}). \tag{6}$$

The GMDH neural network can minimize the difference square between the actual value and the predicted value, which is

$$\sum_{i=1}^{M} [\widehat{y}_i - y_i]^2 \Rightarrow \min. \tag{7}$$

The overall relationship between input and output variables can be expressed as a complex discrete Volterra function:

$$y = a_0 + \sum_{i=1}^{n} a_i x_i + \sum_{i=1}^{n}\sum_{j=1}^{n} a_{ij} x_i x_j + \sum_{i=1}^{n}\sum_{j=1}^{n}\sum_{k=1}^{n} a_{ijk} x_i x_j x_k + \cdots. \tag{8}$$

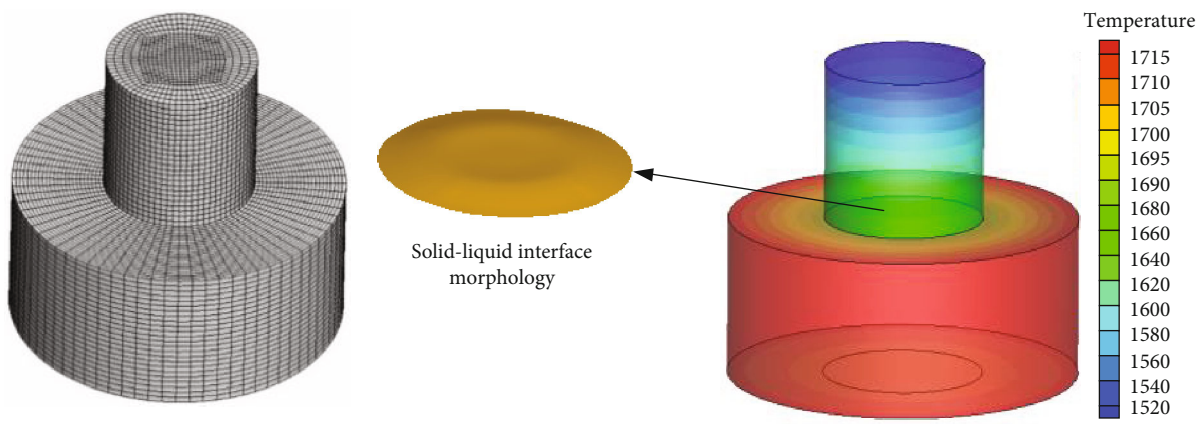

(a) (b)

Figure 2: The meshing of three-dimensional model of crystal growth (a) and the result of numerical simulation (b).

Table 2: Design variables and values ranges.

Design variables	Minimum	Maximum	Unit
T	1720	1750	K
r_c	5	25	rev/min
r_m	5	15	rev/min
V	1	1.8	mm/min

The above equation can be simplified to the composition form of a partial quadratic polynomial containing only two variables, namely

$$\hat{y} = G(x_i, x_j) = a_0 + a_1 x_i + a_2 x_j + a_3 x_i^2 + a_4 x_j^2 + a_5 x_i x_j. \quad (9)$$

The parameters a_i in the equation are calculated by the regression method.

Obviously, the greater the amount of input and output data used in the calculation, the more accurate and effective the GMDH method will be. In the paper, each set of input and output data is obtained by the CFD calculation. For each set of numerical simulation calculation, especially for three-dimensional model calculation with large number of grids, there is a certain calculation time cost, and the acquisition of these data cannot be infinite. Therefore, the limited amount of data should be reasonably optimized to obtain the maximum information. In this paper, 245 groups of effective CFD results are used as input and output data, of which 196 groups are training samples and 49 groups are used to test neural networks. The training set trains the neural network according to GMDH algorithm, and the test set is used to analyze the performance of the network. The inputs are four design variables T, r_c, r_m, and V. The outputs are objective functions h and V/G. The structure of GMDH neural network with two hidden layers is shown in Figures 3(a) and 3(b). The GMDH polynomial coefficients and equations of functions h can be expressed as follows:

$$\begin{aligned}
y1 &= -13.264 + 0.0146T - 0.0139r_m - 3.9973e-6T^2 + 2.3697e-5r_m^2 + 7.4065e-6Tr_m,\\
y2 &= -3.9785 + 0.0039T - 0.0045r_c - 9.12e-7T^2 + 1.2125e-5r_c^2 + 2.3085e-6Tr_c,\\
y3 &= 3.6691 - 0.0049T - 0.0442V + 1.6128e-6T^2 - 9.7088e-4V^2 + 2.8777e-5TV,\\
y4 &= -6.5822e-4 + 0.7795y1 + 0.2406y2 + 33.4405y1^2 + 37.2714y2^2 - 64.6788y1y2,\\
y5 &= 3.5224e-5 + 0.8606y1 + 0.1163y3 + 7.1862y1^2 + 7.0331y3^2 - 13.4094y1y3,\\
h &= y6 = 9.6574e-6 + 1.618y4 - 0.6166y5 - 69.7539y4^2 - 45.1352y5^2 + 114.8276y4y5.
\end{aligned} \quad (10)$$

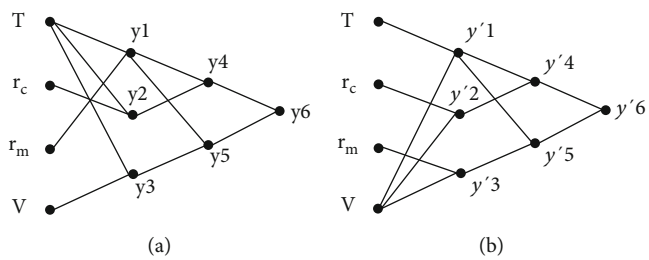

Figure 3: Evolved structures of objective function (a) h and objective function (b) V/G.

Similarly, the GMDH polynomial coefficients and equations of the objective function V/G can be expressed as follows:

$$\begin{aligned}
y'1 &= -0.1216 + 1.4e-4T + 0.0061V - 4.0303e-8T^2 + 1.0417e-6V^2 - 2.9295e-6TV,\\
y'2 &= -4.6869e-5 + 5.4857e-7r_c - 2.7376e-8r_c^2 + 0.0011V - 2.831e-5V^2 + 9.3239e-7r_cV,\\
y'3 &= -5.5267e-5 + 1.98e-6r_m - 2.0407e-7r_m^2 + 0.0011V - 3.4898e-5V^2 + 3.0291e-6r_mV,\\
y'4 &= 8.8019e-6 + 1.004y'1 - 0.0185y'2 + 212.8503y'1^2 + 262.4922y'2^2 - 470.8536y'1y'2,\\
y'5 &= 1.6033e-5 + 1.0715y'1 - 0.0972y'3 + 182.4942y'1^2 + 294.8509y'3^2 - 461.6831y'1y'3,\\
V/G = y'6 &= 1.2105e-5 + 8.1999y'4 - 7.2203y'5 - 4.6729e+5y'4^2 - 4.6164e+5y'5^2 + 9.2894e+5y'4y'5.
\end{aligned} \tag{11}$$

The comparison results of objective functions h and V/G obtained from CFD and GMDH are shown in Figures 4(a) and 4(b). At the same time, the backpropagation artificial neural network (BP-ANN) algorithm is used to calculate the objective function and compare with CFD results. The result comparisons are shown in Figures 5(a) and 5(b).

In order to evaluate the performance of the model established by GMDH, two statistical parameters are introduced, that is absolute variance fraction R^2 and mean absolute percentage error $MAPE$. The formulas were expressed as follows:

$$\begin{aligned}
R^2 &= 1 - \sum_{i=1}^{n} \frac{(y_{iGMDH} - y_{iCFD})^2}{y_{iCFD}^2},\\
MAPE &= \left(\frac{1}{n}\sum_{i=1}^{n} \frac{(y_{iGMDH} - y_{iCFD})}{y_{iCFD}}\right) \times 100.
\end{aligned} \tag{12}$$

The calculated results of the statistical parameters R^2 and $MAPE$ of the objective function by GMDH and BP-ANN are shown in Table 3. The results show that the GMDH model has high accuracy in predicting CFD data and the prediction accuracy is slightly higher than that of the BP-ANN algorithm.

5. Optimization Results of NSGA-II and Analysis

5.1. Improved NSGA-II. NSGA-II is a universally recognized multiobjective optimization algorithm with extensive applications and excellent effects [19]. It contains many advanced concepts, such as elite strategy, fast nondominant ranking, and diversity maintenance of the Pareto frontier. However, there are still deficiencies in NSGA-II in maintaining transverse diversity and uniform distribution of nondominant solutions [20]. The main reason for these defects is that they simply judge the individual distribution from the crowded distance but ignore the uneven distribution caused by the individual density, which is easy to fall into the local optimal. To overcome the shortcomings of NSGA-II, an improved scheme is proposed in the paper. This scheme is divided into two aspects. Firstly, to ensure the diversity of nondominant individuals by exert control on elite strategies. Secondly, the congestion distance formula is improved, and dynamic congestion distance (DCD) is used to improve the distribution of noninferior solutions.

Controlling elite strategy is to limit the number of individuals in the current best nondominant frontier and maintain the predistribution of the number of individuals in each

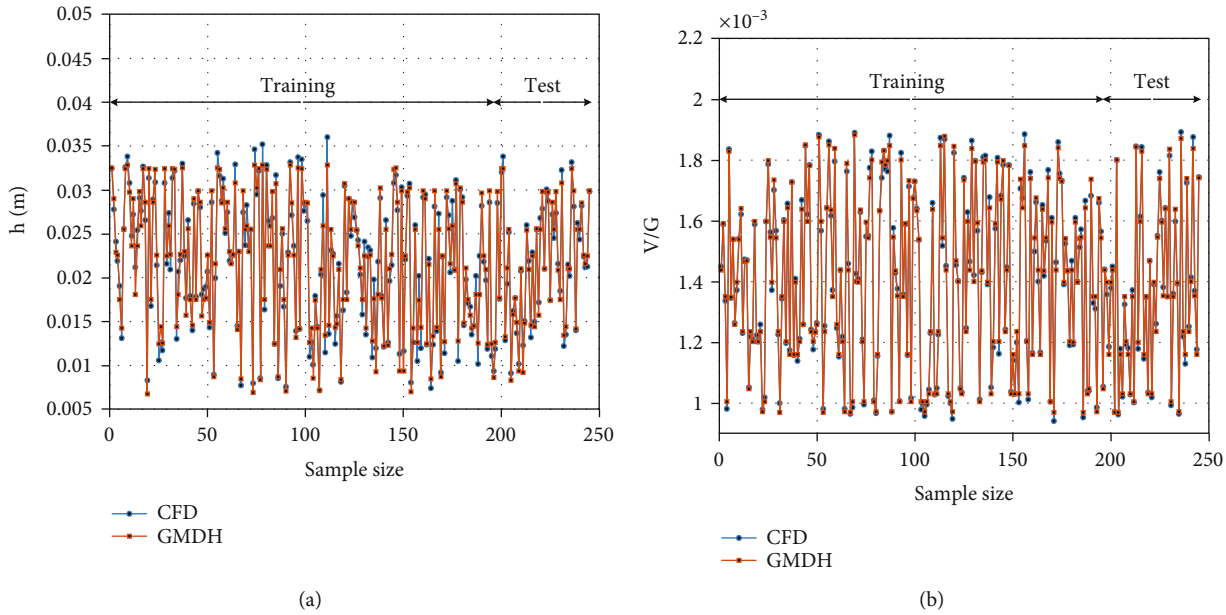

Figure 4: Result comparisons of CFD and GMDH for objective function (a) h and (b) objective function V/G.

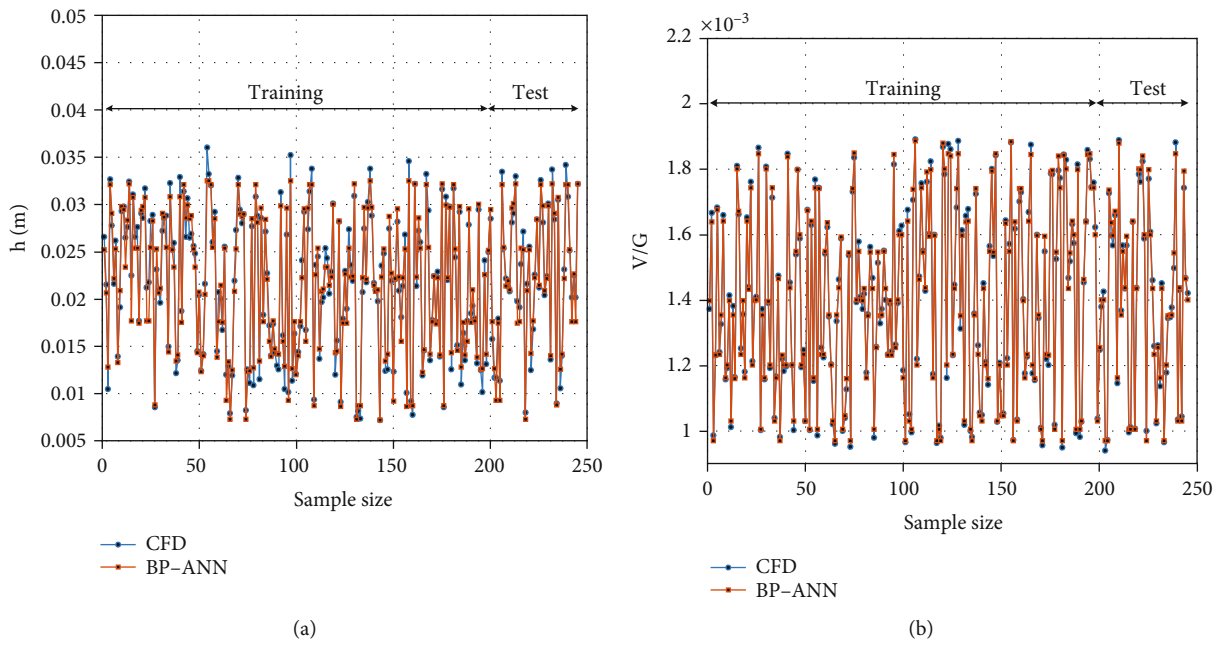

Figure 5: Result comparisons of CFD and BP-ANN for objective function (a) h and (b) objective function V/G.

Table 3: Results of R^2 and $MAPE$ of GMDH and BP-ANN on the objective function.

Algorithm	GMDH				BP			
Parameters	h		V/G		h		V/G	
	Training	Test	Training	Test	Training	Test	Training	Test
R^2	0.9121	0.9417	0.9674	0.9896	0.9104	0.9472	0.9620	0.9791
$MAPE(100\%)$	0.1841	0.2590	0.0977	0.0886	0.1912	0.2636	0.1017	0.0892

frontier. A new population $R(t)$ is ordered nondominated, which is formed by combining the parent population pop_t and the offspring population off_t. The nondominant frontier number of the merged population is named S. According to the geometric distribution, the number of individuals allowed at the jth frontier in the new population is the largest and the size of the population N_j is given by

$$N_j = N\frac{1-r}{1-r^S}r^{j-1}, \tag{13}$$

where $r \in (0, 1)$ is the decrease rate. So, the maximum number of individuals allowed on the first nondominant front is the maximum. The number of individuals allowed for each subsequent front is exponentially lower.

To eliminate the inhomogeneity of individual distribution and improve lateral diversity in the Pareto frontier, Luo et al. proposed a dynamic congestion distance (DCD) method [21]. This method deletes the individual with the lowest DCD value calculated each time and recalculates the DCD value for the remaining individual. Because the calculation of DCD value still depends on the crowding distance, the shortcomings of crowding distance calculation are not avoided. In the paper, a simple improvement of crowding distance is made, to allocate a characteristic coefficient to the crowding distance to balance the contribution of each target to the crowding distance.

$$\begin{aligned} C_j' &= \sigma_j C_j,\ C_j = \frac{1}{N}\sum_{i=1}^{N}\left|F_i^{j+1} - F_i^{j-1}\right|, \\ \sigma_j &= \prod_{i=0}^{N}\frac{F_i^{j+1} - F_i^{j-1}}{\left(F_i^j\right)_{\max} - \left(F_i^j\right)_{\min}}, \end{aligned} \tag{14}$$

where C_j' is the improved crowding distance for the jth individuals. σ_j and C_j are corresponding characteristic coefficients and original congestion distances, respectively. $(F_i^j)_{\max}$ and $(F_i^j)_{\min}$ are the maximum and minimum of the objective function i for all individuals on the same front. The improved individual dynamic congestion distance value is

$$DCD_j = \frac{C_j'}{\log\left(1/Var_j\right)}, \tag{15}$$

where Var_j is the variance of crowding distance between neighbors of the jth individual, which can be expressed as

$$Var_j = \frac{1}{N}\sum_{i=1}^{N}\left(\left|F_i^{j+1} - F_i^{j-1}\right| - C_j'\right)^2. \tag{16}$$

The population size is assumed as N, and the size of combined population of the t-generation nondominant set R is M. If $M > N$, $(M\text{-}N)$ individuals are removed from the nondominant concentration by DCD strategy. The process of DCD algorithm is briefly described as follows.

Step1: if $|R(t)| \le N$, go to Step5; otherwise, go to Step2

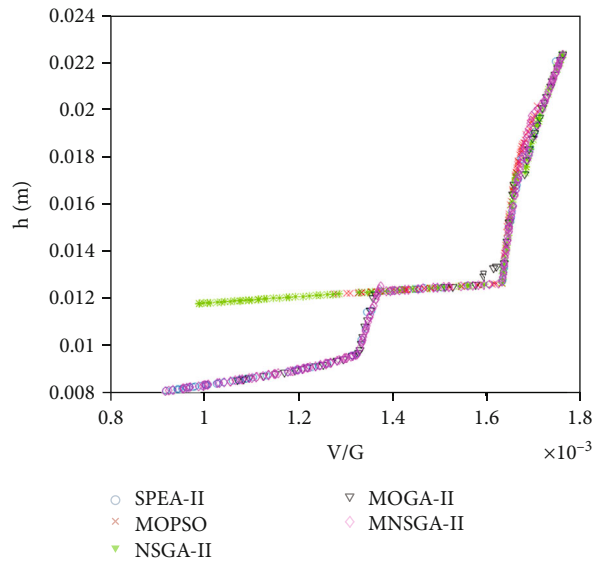

Figure 6: Pareto frontier of different algorithms.

Step2: calculating the DCD value of individuals in $R(t)$, use formula (15)

Step3: ranking nondominant set $R(t)$ based on DCD strategy

Step4: removing the individual of lowest DCD in $R(t)$

Step5: if $|R(t)| \le N$, stop population maintenance; otherwise, transfer to Step2 and continue execution

5.2. Implementation of the Improved NSGA-II Strategy. The steps of the improved NSGA-II proposed in the paper for the optimization of the above two objective functions in Cz crystal growth are described as follows.

Step1: set initial parameters, such as population size N, probability of crossover and mutation, index of crossover and mutation, iterations, and upper and lower bounds of design variables

Step2: generate random initial population pop_0 in the range of design variables and iteration numbers $t = 0$

Step3: evaluate the objective functions h and V/G with each individual of each generation pop_t

Step4: creating offspring population by the tournament selection, simulated binary crossover operator, and polynomial mutation

Step5: nondominant sequencing of merged population $R(t)$

Step6: to limit the number of individuals at the best nondominant frontier at present, use control elite strategy and maintain the predistribution of the number of individuals at each frontier use the formula (13). The decrease rate r is 0.5

Step7: if the numbers of nondominant set is larger than the numbers of population, then use the DCD strategy to remove $(M\text{-}N)$ individuals from nondominant sets, and then jump to Step4

Step8: the algorithm stopped when the iteration count reaches the maximum iterations; otherwise, the number of iterations increases 1 and then jumps to Step3

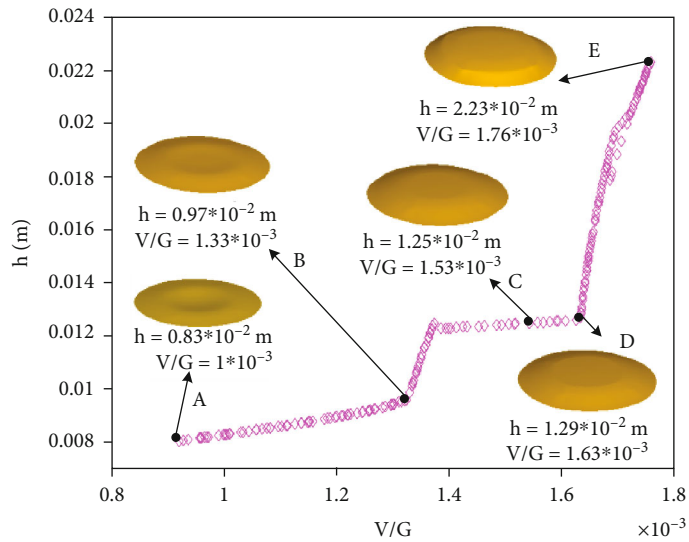

Figure 7: Pareto optimization point analysis and morphology of solid-liquid interface.

Table 4: Design variables and corresponding objective function values for selected points.

Optimization point	Design variable				Objective function	
	T	r_c	r_m	V	h	V/G
A	1750	5	15	1.1	0.0083	$1.002e-3$
B	1746.5	7.5	14.2	1.46	0.0097	$1.324e-3$
C	1728.5	10.3	6.2	1.61	0.0125	$1.544e-3$
D	1732.5	14.7	6.8	1.73	0.0129	$1.619e-3$
E	1725	25	5	1.8	0.0223	$1.786e-3$

5.3. Result Analysis. The ultimate goal of the paper is to obtain the optimum process parameters with the requirements of minimizing the interface deformation h and maximizing V/G. However, the objective functions cannot be optimally satisfied at the same time, so the feasible solution is to seek Pareto optimal sets. The optimization research for Cz crystal growth can be expressed in the following forms

$$\begin{aligned} &\textit{Maxmize} && V/G = f_1(T, r_c, r_m, V) \\ &\textit{Minmize} && h = f_2(T, r_c, r_m, V) \\ &\text{Subject to :} && 1720\text{K} \le T \le 1750\text{K} \\ & && 5\ \text{rev/min} \le r_c \le 25\ \text{rev/min} \\ & && 5\ \text{rev/min} \le r_m \le 15\ \text{rev/min} \\ & && 1\ \text{mm/min} \le V \le 1.8\ \text{mm/min}. \end{aligned} \tag{17}$$

In order to prove the validity and correctness of improved NSGA-II in optimizing the process parameters of crystal growth, four multiobjective optimization algorithms are selected to compared with the results of our algorithm, including NSGA-II, multiobjective particle swarm optimization algorithm (MOPSO) [22], second-generation multiobjective genetic algorithm (MOGA-II) [23], and second-generation strong Pareto evolutionary algorithm (SPEA-II) [24]. The Pareto frontier results of five algorithms are shown in Figure 6, and MNSGA-II is our algorithm. NSGA-II and MOPSO fall into local optimum easily and cannot get the optimum Pareto front. MOGA-II and SPEA-II have similar Pareto frontier trends, but there are obvious shortcomings. Although the MOGA-II algorithm maintains a good individual distance, there are some individuals are missed in the frontier. SPEA-II maintains the continuity of the frontier, but the individual distance is not good. The improved NSGA-II effectively avoids the shortcomings of MOGA-II and SPEA-II and obtains a relatively excellent Pareto frontier.

The Pareto frontier obtained by the improved NSGA-II is shown in Figure 7. Five characteristic optimization points, A, B, C, D, and E are selected. It is clear that each optimization point cannot be called absolute optimization for another point, that is to say, from one point to another, one objective function will become better, and the other one will become worse. The corresponding design variables are shown in Table 4. As can be seen in Figure 7, from point A to point E, the interface deformation increases gradually with the increase of V/G. From point A to point B, the increase of interface deformation is very small (about 10%), while the increase of V/G is very large (about 37.5%). Similarly, from point D to point E, the interface deformation increases significantly (about 67.1%), while V/G has little change (about 16.3%). In order to find the points that fully satisfy these two objective functions, the objective function values corresponding to these optimization points are normalized, and then the norms of these function values are calculated. Among them, the optimum point is the point with the highest norm value. The point C is the optimal point obtained by this method.

6. Experiments

The above research methods are verified by engineering experiments, and 300 mm silicon single crystal is employed as an experimental object. The C point on the Pareto frontier is

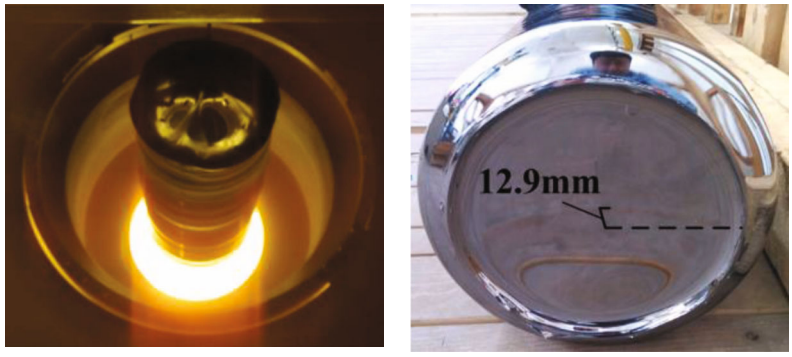

(a) (b)

Figure 8: (a) Experiment of crystal growth and (b) deformation of solid-liquid interface.

selected, and the corresponding process parameters are heating temperature $T = 1730$K, crystal rotation speed $r_c = 10$rev /min, melt rotation speed $r_m = 6$rev/min, and pulling speed $V = 1.6$mm/min. The experimental process of crystal growth is shown in Figure 8(a). From the start stage to the end of body stage of growth, the crystal growth is stable, which shows that the process parameters can meet the needs of large-size silicon single crystal growth. In order to measure the deformation of the solid-liquid interface, the end stage of crystal growth is abandoned. The crystal is pulled away from the silicon melt by rapid pulling, which ensures the visibility of the solid-liquid interface shape and facilitates the measurement of the deformation of the solid-liquid interface. The solid-liquid interface shape is shown in Figure 8(b). The deformation obtained by measuring the solid-liquid interface is about 12.9 mm. The relative error is only 3.1% compared to the optimized results. The actual engineering practice proves that the optimized result of the proposed hybrid strategy has higher precision and is more suitable for the optimization of high-quality silicon single crystal growth process parameters.

7. Conclusion

A hybrid strategy including CFD, GMDH, and improved NSGA-II for the process parameter optimization of Cz crystal growth is proposed in the paper. In order to obtain the optimal process parameters, the deformation of solid-liquid interface h and the defect evaluation criteria V/G are selected as the optimization functions. The polynomial model of objective function is identified by the CFD and GMDH neural network algorithm. An improved NSGA-II is proposed to obtain Pareto optimal solution of production process parameters. The hybrid strategy proposed in this paper combines the numerical simulation method with an advanced intelligent algorithm, which has the advantage of avoiding the limitation of numerical simulation results, transforming the complex crystal growth process model into a clear mathematical expression by the system identification strategy, and establishing the correspondence relationship between crystal quality and growth process parameters through the intelligent optimization. The experiments prove that the hybrid strategy is a new method to obtain accurate crystal growth process parameters, which can be applied to solve multiobjective optimization problems of other complex systems with uncertain models.

Data Availability

No data were used to support this study.

Conflicts of Interest

The authors declare that they have no conflicts of interest.

Acknowledgments

This work is supported by the National Natural Science Foundation (NNSF) of China (62073258, 62003261, and 62127809), Natural Science Basic Research Program of Shaanxi Province of China (No. 2020JQ-650), and Scientific Research Program Funded of Shaanxi Education Department (No. 20JK0788).

References

[1] L. Ding, *Process modeling and control of silicon crystal growth in Cz method*, Science Press, Beijing, 2015.

[2] A. D. Smirnov and V. V. Kalaev, "Analysis of impurity transport and deposition processes on the furnace elements during Cz silicon growth," *Journal of Crystal Growth*, vol. 311, no. 3, pp. 829–832, 2009.

[3] A. Sabanskis, K. Bergfelds, A. Muiznieks, T. Schröck, and A. Krauze, "Crystal shape 2D modeling for transient CZ silicon crystal growth," *Journal of Crystal Growth*, vol. 377, no. 7, pp. 9–16, 2013.

[4] H. Wei-Chao, L. Ding, J. Shang-Bin, and Z. Ni, "Thermo-fluid coupling of unsteady flow in Czochralski crystal growth," *Acta Physica Sinica*, vol. 64, no. 20, pp. 208102–208424, 2015.

[5] L. Liu and K. Kakimoto, "Effects of crystal rotation rate on the melt–crystal interface of a CZ-Si crystal growth in a transverse magnetic field," *Journal of Crystal Growth*, vol. 310, no. 2, pp. 306–312, 2008.

[6] X. Liu, L. Liu, Z. Li, and Y. Wang, "Effects of cusp-shaped magnetic field on melt convection and oxygen transport in an industrial CZ-Si crystal growth," *Journal of Crystal Growth*, vol. 354, no. 1, pp. 101–108, 2012.

[7] N. O. Asadi, M. Jomâa, and M. M'Hamdi, "Analysis of W-shape melt/crystal interface formation in Czochralski silicon

crystal growth," *Journal of Crystal Growth*, vol. 362, no. 1, pp. 77–82, 2013.

[8] V. V. Voronkov and R. Falster, "Properties of vacancies and self-interstitials in silicon deduced from crystal growth, wafer processing, self-diffusion and metal diffusion," *Materials Science and Engineering B*, vol. 134, no. 2–3, pp. 227–232, 2006.

[9] X. D. Wang, C. Hirsch, S. Kang, and C. Lacor, "Multi-objective optimization of turbomachinery using improved NSGA-II and approximation model," *Computer Methods in Applied Mechanics and Engineering*, vol. 200, no. 9–12, pp. 883–895, 2011.

[10] M. D. Damavandi, M. Forouzanmehr, and H. Safikhani, "Modeling and Pareto based multi-objective optimization of wavy fin-and- elliptical tube heat exchangers using CFD and NSGA-II algorithm," *Applied Thermal Engineering*, vol. 111, pp. 325–339, 2017.

[11] M. Jafari, M. J. Parhizkar, E. Amani, and H. Naderan, "Inclusion of entropy generation minimization in multi-objective CFD optimization of diesel engines," *Energy*, vol. 114, pp. 526–541, 2016.

[12] Z. Dong, F. Hu, and X. Peng, "Expansion design of interferometric aperture synthesis arrays based on multi-objective optimization," *IEEE Access*, vol. 7, pp. 16787–16794, 2019.

[13] M. Elarbi, S. Bechikh, A. Gupta, L. Ben Said, and Y. S. Ong, "A new decomposition-based NSGA-II for many-objective optimization," *IEEE Transactions on Systems, Man, and Cybernetics: Systems*, vol. 48, no. 7, pp. 1191–1210, 2018.

[14] M. Villalobos-Cid, M. Dorn, R. Ligabue-Braun, and M. Inostroza-Ponta, "A memetic algorithm based on an NSGA-II scheme for phylogenetic tree inference," *IEEE Transactions on Evolutionary Computation*, vol. 23, no. 5, pp. 776–787, 2019.

[15] L. Liu, X. Liu, and Y. Wang, "Large-eddy simulation of melt turbulence in a 300-mm Cz-Si crystal growth," *International Journal of Heat and Mass Transfer*, vol. 55, no. 1–3, pp. 53–60, 2012.

[16] J. Vanhellemont, "The v/G criterion for defect-free silicon single crystal growth from a melt revisited: implications for large diameter crystals," *Journal of Crystal Growth*, vol. 381, pp. 134–138, 2013.

[17] I. Ebtehaj, H. Bonakdari, A. H. Zaji, H. Azimi, and F. Khoshbin, "GMDH-type neural network approach for modeling the discharge coefficient of rectangular sharp-crested side weirs," *Engineering Science and Technology, an International Journal*, vol. 18, no. 4, pp. 746–757, 2015.

[18] A. G. Ivakhnenko, "Polynomial theory of complex systems," *IEEE Transactions on Systems, Man, and Cybernetics*, vol. -SMC-1, no. 4, pp. 364–378, 1971.

[19] K. Deb, A. Pratap, S. Agarwal, and T. Meyarivan, "A fast and elitist multiobjective genetic algorithm: NSGA-II," *IEEE Transactions on Evolutionary Computation*, vol. 6, no. 2, pp. 182–197, 2002.

[20] P. Zhou, M. Li, D. Guo, H. Wang, and T. Chai, "Modeling for output fiber length distribution of refining process using wavelet neural networks trained by NSGA II and gradient based two-stage hybrid algorithm," *Neurocomputing*, vol. 238, no. 17, pp. 24–32, 2017.

[21] B. Luo, J. Zheng, J. Xie, and J. Wu, "Dynamic crowding distance: a new diversity maintenance strategy for MOEAs," in *2008 Fourth International Conference on Natural Computation*, pp. 580–585, Jinan, China, 2008.

[22] J. Yang, J. Zhou, L. Liu, and Y. Li, "A novel strategy of pareto-optimal solution searching in multi-objective particle swarm optimization (MOPSO)," *Computers & Mathematics with Applications*, vol. 57, no. 11-12, pp. 1995–2000, 2009.

[23] P. Ranut, G. Janiga, E. Nobile, and D. Thévenin, "Multi-objective shape optimization of a tube bundle in cross-flow," *International Journal of Heat and Mass Transfer*, vol. 68, no. 1, pp. 585–598, 2014.

[24] A. Wahid, X. Gao, and P. Andreae, "Multi-objective clustering ensemble for high-dimensional data based on strength Pareto evolutionary algorithm (SPEA-II)," in *2015 IEEE International Conference on Data Science and Advanced Analytics (DSAA)*, pp. 734–795, Paris, France, 2015.

Hindawi
Wireless Communications and Mobile Computing
Volume 2022, Article ID 6951117, 9 pages
https://doi.org/10.1155/2022/6951117

Research Article

Online Gain-Phase Self-Calibration Method of MIMO Array Based on Statistical Characteristics of Target Angle Distribution

Linwei Wang,[1] **Bo Li**,[1] **Quanrui Zhao**,[2] **Xiaowei Ji**,[3] **and Changjun Yu**[1]

[1]*School of Information Science and Engineering, Harbin Institute of Technology at Weihai, Weihai 264209, China*
[2]*The 5th Research Department, Shanghai Radio Equipment Research Institute, Shanghai 201109, China*
[3]*School of Electronics and Information Engineering, Harbin Institute of Technology, Harbin 150001, China*

Correspondence should be addressed to Changjun Yu; yuchangjun@hit.edu.cn

Received 29 May 2022; Accepted 1 July 2022; Published 25 July 2022

Academic Editor: Liu Mingqian

As a hot research topic, the gain-phase error self-calibration in MIMO radar systems has been investigated for many years. In this paper, we proposed a novel array error self-calibration method, termed online errors self-calibration based on feature learning (OES-FL). This method regards the statistical characteristics of the detected targets' DOA as a prior knowledge and does not require the calibrated antenna subarray or external reference source to correct the array disturbances in real time. First, we analyse the monostatic MIMO signal model suffering gain-phase error. Then, we exploit the statistical characteristics of DOA of many targets for correcting gain-phase error of antenna array. Next, the gain-phase error estimation scheme based on LMS and the DOA deviation estimation method based on LSTM are proposed, respectively. Using real-life radar data collected at the integrated transportation hubs to generate simulation data, the proposed approach is shown to be effective in correcting gain-phase errors and, therefore, provides a promising model for online error self-calibration in monostatic MIMO radars.

1. Introduction

Direction-of-arrival (DOA) estimation has played an important role in array signal processing over the past few decades [1, 2]. Multiple-input multiple-output (MIMO) technology is first widely used in the field of communication [3–5] and is later introduced into the radar field [6–9]. MIMO radar has gained extensive interest owing to the capability of space diversity [6]. Many DOA estimation algorithms [10–14] have been proposed. Due to the production process, external environment factors, there is always inconsistency among the antenna array elements in practice. The accuracy of DOA estimation is constricted by this inevitable inconsistency [15–17]. As for MIMO radar, the errors of transmit and receive antennas are coupled with each other, thus significantly causes the performance degradation of DOA estimation [18]. Consequently, it is necessary to correct the errors of array, including mutual coupling error, position error, and gain-phase error. In this paper, we focus on developing the approach to mitigate the gain-phase error of MIMO radar array.

Due to the fact that the MIMO radar can generate virtual arrays, the array aperture is enlarged and the number of array elements is increased. Hence, the parameter estimation performance of MIMO radar system is superior than that of conventional phased array radar [7]. Many calibration approaches have been proposed in the literature, an estimating signal parameters via rotational invariance techniques- (ESPRIT-) like algorithm has been proposed by Guo et al. [18], which can provide closed-form solution for joint DOD and DOA estimation. Recently, Li et al. [19] proposed an eigenspace based algorithm for joint parameter estimation. This method initially uses the eigenvalue decomposition (EVD) of covariance matrix to acquire the coarse estimation results of DOA and then applies an improved multiple signal classification- (MUSIC-) based cost function to obtain more accurate estimation of DOA. The accurate estimated DOAs interfering with the noise subspace, the error vector of array gain-phase is achieved. Wen et al. [20] proposed a novel parallel factor (PARAFAC) estimator for estimating the DOD and DOA, and this method utilizes the combination of one-dimensional grid searching and least

squares (LS) fitting, which avoids the most of the costly computations generated by eigen decomposition or high-dimension spectrum searching. Li et al. [21] proposed a calibration method for coprime MIMO radar, this method estimates the gain-phase errors by trilinear decomposition, iteratively updated based on least squares, and has an ideal performance. Hu et al. [22] proposed an efficient compressed sensing based DOA method for bistatic MIMO radar with unknown gain-phase errors, which has a high computational efficiency and stability.

These recently proposed methods usually assume that several antennas in the array have been corrected or employ the auxiliary array as a reference. At times associated with complexity of scenario, these corrected antennas or auxiliary array cannot realize. Furthermore, correcting a limited number of antennas also increases the experiment cost, and the antenna array with large scale integration cannot be readily dismantled. Such a kind of self-calibration method would be unsuitable in many field experiments. Consequently, developing a self-calibration approach without any calibrated antennas is very necessary for MIMO radar system. It is the purpose of the present paper to develop a real-time self-calibration approach that accurately estimates the DOA of targets by learning the information acquired by itself.

With the development of machine learning, adaptive technology has made great progress in communication [22–24] and recognition [25, 26]. Real-time parameter optimization can be realized online in a large number of scenarios according to the environment. These experiment conditions in this paper based on a radar system are deployed for a very long period. Although the active calibrated has been carried out, the antenna array must be corroded and damaged after a long time of work, resulting in gain-phase error. Under this common phenomenon, we design an online gain-phase error self-calibration method by considering DOA statistical characteristics of the detected targets as a prior information. We design the gain-phase error estimation method based on LSM and the DOA offset estimation method based on LSTM, which realizes the real-time online error correction achieved without reference sources.

This paper is organized as follows. Section 2 presents a brief description of signal model with gain and phase errors in monostatic MIMO radar. Section 3 focuses on the concepts of the proposed calibration method and its way to achieve. In Section 4, we analyse the performance of the proposed approach using abundant real-life millimeter-wave radar data collected at the junction urban and suburb. Concluding remarks are given in Section 5.

2. Signal Model

Theoretical analysis and simulation results are exhibited for illustrating the superiority of the proposed scheme, including the ideal estimation accuracy and the robustness for correcting gain-phase errors. Assume that there is a monostatic MIMO radar system composed of the M transmit antenna elements and N receive antenna elements, and $\mathbf{A}_T(\theta)$ and $\mathbf{A}_R(\theta)$, respectively, represent the receive and transmit steering vectors without array gain-phase errors, respectively.

$$\begin{aligned}\mathbf{A}_T(\theta) &= \begin{bmatrix} 1 & e^{j2\pi d_T \sin(\theta)/\lambda} & \cdots & e^{j2\pi(M-1)d_T \sin(\theta)/\lambda} \end{bmatrix},\\ \mathbf{A}_R(\theta) &= \begin{bmatrix} 1 & e^{j2\pi d_R \sin(\theta)/\lambda} & \cdots & e^{j2\pi(N-1)d_R \sin(\theta)/\lambda} \end{bmatrix},\end{aligned} \tag{1}$$

where θ is the DOA of a target, the separation distance between the transmit antenna elements is d_{T}, and the d_{R} represents separation distance between the receive antenna elements. λ is the wavelength. Suppose that the error of each cell with respect to the first cell is

$$\begin{aligned}\mathbf{\Gamma}_T &= \begin{bmatrix} a_1^T e^{j\phi_1^T} & a_2^T e^{j\phi_2^T} & \cdots & a_M^T e^{j\phi_M^T} \end{bmatrix},\\ \mathbf{\Gamma}_R &= \begin{bmatrix} a_1^R e^{j\phi_1^R} & a_2^R e^{j\phi_2^R} & \cdots & a_N^R e^{j\phi_N^R} \end{bmatrix},\end{aligned} \tag{2}$$

where a_m^{T} represents the gain error of the mth transmit antenna element and ϕ_m^{T} represents the phase error of the mth transmit antenna element. Accordingly, the a_n^{R} and ϕ_n^{R} represent the gain error and phase error for nth receive antenna element, respectively. And particularly, $a_1 e^{j\phi_1^{\mathrm{T}}} = b_1 e^{j\phi_1^{\mathrm{R}}} = 1$. Then, the echo signal of the target can be expressed as

$$\mathbf{x}(\theta) = (\mathbf{\Gamma}_T \odot \mathbf{A}_T(\theta)) \otimes (\mathbf{A}_R(\theta) \odot \mathbf{\Gamma}_R), \tag{3}$$

where $\odot$ represents the Hadamard product, and $\otimes$ represents the Kronecker product. $\mathbf{x}(\theta)$ is a vector with a length of MN, and it can also be reshaped into a $M \times N$ dimensional matrix $\mathbf{X}(\theta)$. In the matrix $\mathbf{X}(\theta)$, the element $x(m, n)$ in mth row and nth column represents the echo signal transmitted from the mth transmit antenna, then reflected from the target and received by the nth receive antenna element. Hence, $x(m, n)$ can be expressed as

$$\begin{aligned}x(m,n) &= a_m^{\mathrm{T}} e^{j\phi_m^{\mathrm{T}}} e^{j2\pi(m-1)d_{\mathrm{T}} \sin(\theta)/\lambda} e^{j2\pi(n-1)d_{\mathrm{R}} \sin(\theta)/\lambda} a_n^{\mathrm{R}} e^{j\phi_n^{\mathrm{R}}}\\ &= a_m^{\mathrm{T}} a_n^{\mathrm{R}} e^{j\left(2\pi(m-1)d_{\mathrm{T}} \sin(\theta)/\lambda + 2\pi(n-1)d_{\mathrm{R}} \sin(\theta)/\lambda + \phi_m^{\mathrm{T}} + \phi_n^{\mathrm{R}}\right)}.\end{aligned} \tag{4}$$

When separating the amplitude and the phase, we can obtain

$$\begin{aligned}A(m,n) &= a_m^{\mathrm{T}} a_n^{\mathrm{R}},\\ \Phi(m,n) &= K(m,n) \sin(\theta) + \phi_m^{\mathrm{T}} + \phi_n^{\mathrm{R}},\end{aligned} \tag{5}$$

where $K(m,n) = [2\pi(m-1)d_{\mathrm{T}} + 2\pi(n-1)d_{\mathrm{R}}]/\lambda$ and the amplitude error can be obtained according to the previous $A(m,n)$. As for obtaining phase error, ϕ_1^{T} and ϕ_1^{R} are known, and the rest part of the antenna errors can be solved by the following equation.

$$\mathbf{\Phi} = \mathbf{HX}, \tag{6}$$

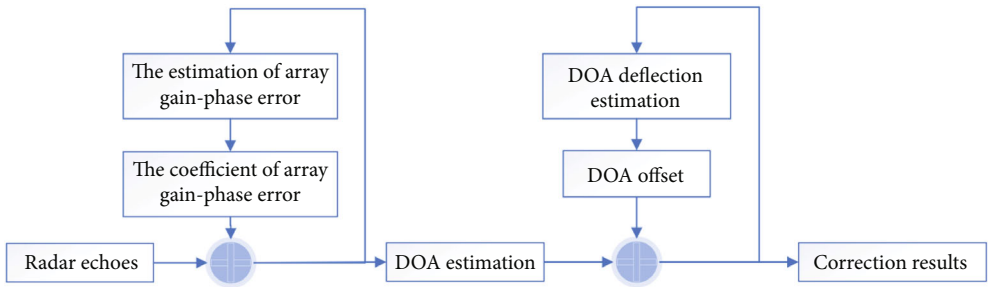

Figure 1: Flowchart diagram of proposed algorithm.

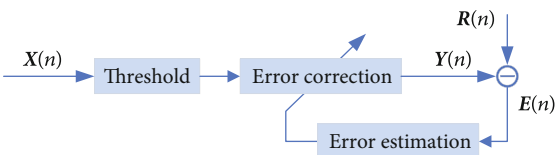

Figure 2: LMS algorithm processing scheme.

where $\mathbf{\Phi} = [\Phi(1,2) \quad \Phi(1,3) \quad \cdots \quad \Phi(1,N) \quad \Phi(2,1) \quad \cdots \quad \Phi(M,N)]$,

$$\mathbf{H} = \left[\begin{array}{ccc|ccc|c} & & & 1 & & & K(1,2) \\ & & & & \ddots & & \vdots \\ & & & & & 1 & K(1,N) \\ \hline 1 & & & & & & K(2,1) \\ 1 & & & 1 & & & K(2,2) \\ \vdots & & & & \ddots & & \vdots \\ 1 & & & & & 1 & K(2,N) \\ \hline & 1 & & & & & K(3,1) \\ & 1 & & 1 & & & K(3,2) \\ & \vdots & & & \ddots & & \vdots \\ & 1 & & & & 1 & K(3,N) \\ & & \ddots & & \vdots & & \vdots \\ & & 1 & & & 1 & K(M,N) \end{array}\right],$$

$$\mathbf{X} = \left[\phi_2^{\mathrm{T}} \quad \phi_3^{\mathrm{T}} \quad \cdots \quad \phi_M^{\mathrm{T}} \quad \phi_2^{\mathrm{R}} \quad \phi_3^{\mathrm{R}} \quad \cdots \quad \phi_N^{\mathrm{R}} \quad \sin\theta\right].$$

Equation (6) can be viewed as an equation set of multiple variables consisting of $MN - 1$ linear equations. Because the last column of $\mathbf{H}$ can be represented by a linear combination of the previous $M + N$ columns, the maximum rank of this matrix is $M + N - 2$. And the total number of unknowns is $M + N - 1$; obviously, this equation has multiple solutions, and the additional information is required to determine the value of each unknown. In the active calibration technology, where θ is known, that full rank can be satisfied, and the errors of each element can be solved. For the self-calibration algorithm, θ is unknown, as long as the error of any element is known, that is to say, one antenna is calibrated in this array, and the phase errors of each element can be obtained.

3. Error Calibration Method

3.1. Theoretical Model. The previous methods usually estimate the DOA of the targets by applying the calibrated antennas and then estimate the gain-phase errors of other elements in the array according to the DOA of targets. If the gain-phase errors of all antenna elements are unknown, Equation (6) has infinite number of solutions. In addition, if a phase error between two elements in array is ignored, a wrong DOA estimation result will be obtained by this pair of elements. When utilizing this wrong DOA estimation result to further estimate the error of other antenna elements, all the results are a function of the element that we ignored. And the DOA results of this array will also have a fixed phase deviation, which is the phase error of the ignored element. Using this correction result to estimate the DOA of targets again, all the obtained results will have a fixed deviation. In this scenario, when the distribution characteristics of targets' DOA are identified, the errors of DOA will be corrected. Therefore, we propose a calibration algorithm model as shown in Figure 1. The calibration algorithm model consists of two parts: error estimation and DOA deflection estimation.

In the error estimation, we first ignore the error of an antenna element, and anyone has opportunity to be tentatively ignored. For example, we ignore the error of the second transmit antenna element, $\hat{\phi}_2^{\mathrm{T}} = 0$, hence, the Equation (6) has only one unique solution as follows.

$$\begin{aligned} \hat{\phi}_m^{\mathrm{T}} &= \Phi(m,1) - (m-1)\Phi(2,1), \\ \hat{\phi}_n^{\mathrm{R}} &= \Phi(1,n) - (n-1)\Phi(2,1)\frac{d_R}{d_T}. \end{aligned} \tag{7}$$

As for another target with direction φ, the array echo calibrated by Equation (7) is as follows.

$$\begin{aligned} \Phi_\varphi(m,n) &= K(m,n)\sin(\varphi) + \phi_m^{\mathrm{T}} - \hat{\phi}_m^{\mathrm{T}} + \phi_n^{\mathrm{R}} - \hat{\phi}_n^{\mathrm{R}} \\ &= K(m,n)\sin(\varphi) + \left[(m-1) + (n-1)\frac{d_{\mathrm{R}}}{d_{\mathrm{T}}}\right]\phi_2^{\mathrm{T}} \\ &= K(m,n)\left[\sin(\varphi) + \frac{\lambda\phi_2^{\mathrm{T}}}{2\pi d_{\mathrm{T}}}\right]. \end{aligned} \tag{8}$$

In practice, there is a fixed phase offset $\Delta\varphi = \lambda\phi_2^{\mathrm{T}}/(2\pi d_{\mathrm{T}})$ when the DOA of target is estimated after correcting. If the distribution of real targets obeys a normal distribution and the mean of DOAs is 0°, the results will have a fixed deviation after the calibration. The mean is changed as arcsin ($\Delta\varphi$). The mean of DOAs can be obtained by applying a great

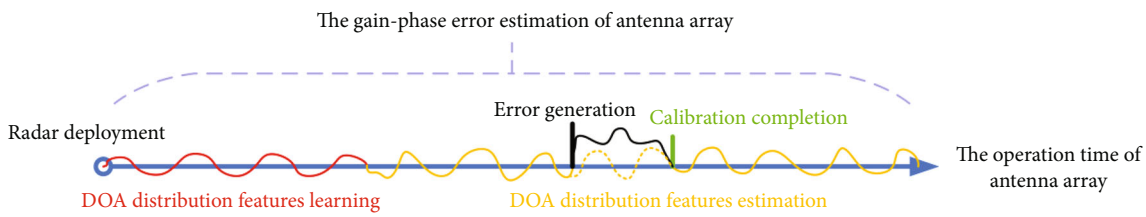

Figure 3: Proposed approach description and main steps.

deal of statistical information, so $\Delta\varphi$ can be estimated, and the accurate calibration is realized.

3.2. Algorithm Flow. Assume that targets with different distances and speeds have been separated by applying coherent integration and eigenvalue decomposition in the signal processing process, thus, the echo $\mathbf{X}(\theta)$ only contains one target. In order to weaken the interference of noise, least mean square (LMS) is used to iteratively calculate the gain-phase error of array, and the target with high SNR is selected for estimating gain-phase errors during each iteration.

Figure 2 illustrates the processing scheme of LMS, where the $\mathbf{X}(n)$ represents the nth echo data. The targets with high SNR are selected, which can grant the ideal accuracy and efficiency of estimation, and these selected targets are put into the successive iteration for estimating the gain-phase errors. $\mathbf{Y}(n)$ represents the corrected results of output, and $\mathbf{R}(n)$ as the reference signal is the theoretical echo data corresponding to the estimated DOA by using the first two elements in $\mathbf{X}(n)$, $x_1(n)$ and $x_2(n)$. The estimated DOA $\widehat{\theta}$ can be defined as

$$\widehat{\theta} = \arcsin\left\{\operatorname{angle}\left[\frac{x_2(n)}{x_1(n)K(1,2)}\right]\right\}. \tag{9}$$

Hence, the reference signal is defined as

$$\mathbf{R}(n) = \begin{bmatrix} 1 & e^{jK(1,2)\sin\left(\widehat{\theta}\right)} & \cdots & e^{jK(M,N)\sin\left(\widehat{\theta}\right)} \end{bmatrix}. \tag{10}$$

The equation for the $\mathbf{Y}(n)$ and $\mathbf{E}(n)$ can be described as

$$\begin{aligned} \mathbf{Y}(n) &= \mathbf{X}(n)\mathbf{W}(n), \\ \mathbf{E}(n) &= \mathbf{R}(n) - \mathbf{Y}(n), \\ \mathbf{W}(n+1) &= \mathbf{W}(n) + \alpha\mathbf{E}(n)\mathbf{X}^*(n), \end{aligned} \tag{11}$$

where $\mathbf{W}(n)$ is the calibrated coefficient, α represents the learning factor, and $\mathbf{X}^*(n)$ is the conjugate for $\mathbf{X}(n)$. After completing the iteration, we obtain $\mathbf{W} \in \mathbb{C}^{MN\times 1}$ which is the calibration coefficient of the virtual array, and $\mathbf{W}$ could be reshaped into a matrix $\bar{\mathbf{W}} \in \mathbb{C}^{M\times N}$. The ratio of each column of $\bar{\mathbf{W}}$ to the other is the error between the two transmit elements; similarly, the ratio of each row of $\bar{\mathbf{W}}$ to the other is the error between the two receive elements. We can get the gain-phase errors of transmit array $\widehat{\mathbf{\Gamma}}_T$ and that of receive array $\widehat{\mathbf{\Gamma}}_R$ as follows.

$$\begin{aligned} \widehat{\mathbf{\Gamma}}_T &= \frac{\bar{\mathbf{W}}\bar{\mathbf{W}}_C^{\dagger}}{N}, \\ \widehat{\mathbf{\Gamma}}_R &= \frac{\left(\bar{\mathbf{W}}_R^{\dagger}\bar{\mathbf{W}}\right)^T}{M}, \end{aligned} \tag{12}$$

where $\bar{\mathbf{W}}_C \in \mathbb{C}^{1\times N}$ is the first column of $\bar{\mathbf{W}}$, $\bar{\mathbf{W}}_R \in \mathbb{C}^{M\times 1}$ is the first row of $\bar{\mathbf{W}}$, and $(\cdot)^{\dagger}$ is the pseudoinverse of a matrix.

Then, the DOA offset is estimated by using the statistical characteristics of the targets' DOA. In most cases, when deploying a new antenna array, all the antenna elements should be calibrated and tested. Consequently, there is a reasonable prospect that the intrinsic error of antenna array has been calibrated, and then, radar can normally operate over an ideal period. While a considerable amount of work has been done, the antenna array system absolutely be damaged due to the corrosion and wear of antennas, which causes the gain-phase errors of the antennas. We can use the detection data of the radar system recently deployed radar system to collect the characteristics of the DOA distribution of targets, and then, these characteristics will as reference data to correct the errors generated in the subsequent work.

For radars used to detect fixed areas or basically unchanged scenes, the statistical characteristics of the DOA of detected target are relatively stable in a long observation period. It is not surprised that the fluctuations of DOA characteristics in a short term also can be found.

Such as the road surveillance radar, it is used to monitor a confined area. For an urban highway, a large number of people leave from the residential area to the workplace in the morning, and the number of vehicles leaving the residential area will be significantly more than the vehicles entering the residential area, so that the average DOA of targets in a short period tends toward the side of the lane leaving the residential area. In contrast, when people return to the residential area in the evening, the average DOA of targets will tend toward the other side. In this paper, the DOA distribution characteristics of targets are estimated by using LSTM network. Together, the learning of DOA distribution characteristics in the initial stage helps to readily predict the distribution characteristics in the following stage, which ensures to timely calibrate the antennas array. There have been aroused interests in the performance capabilities of DOA estimation. Figure 3 shows the description above.

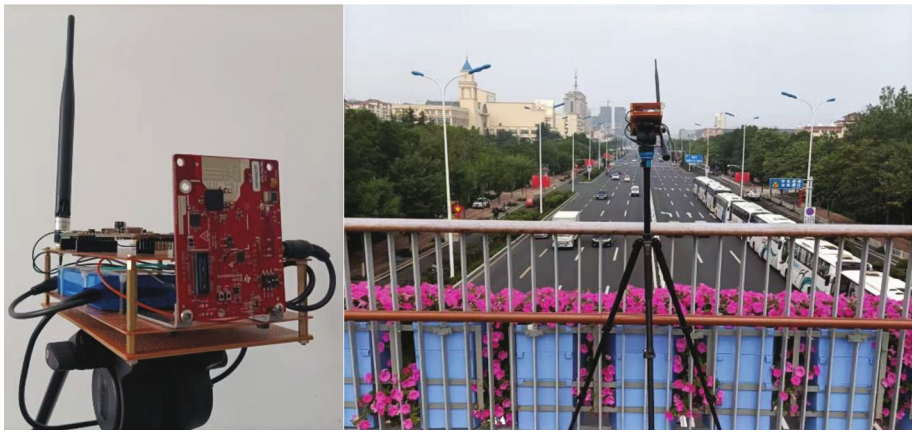

Figure 4: Images of millimeter-wave radar in the field experiment.

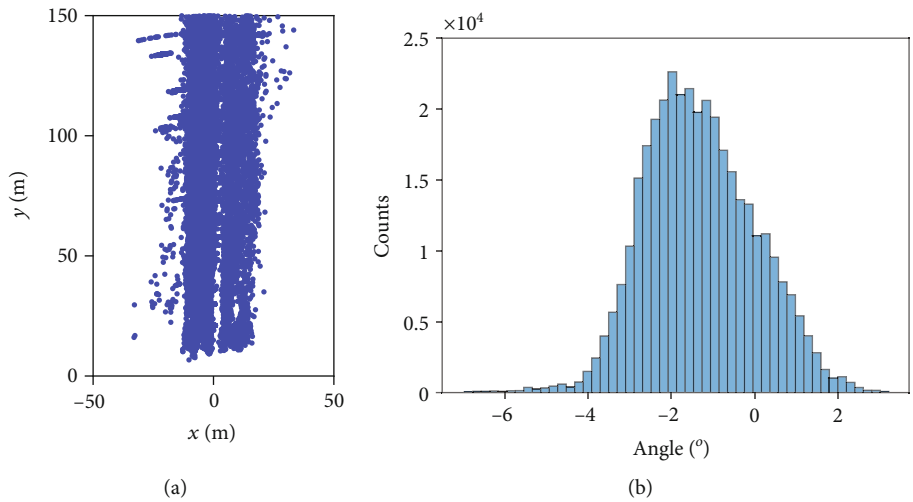

Figure 5: Targets detection results. (a) The location map of 354,000 targets. (b) The histogram of DOA distribution of 354,000 targets.

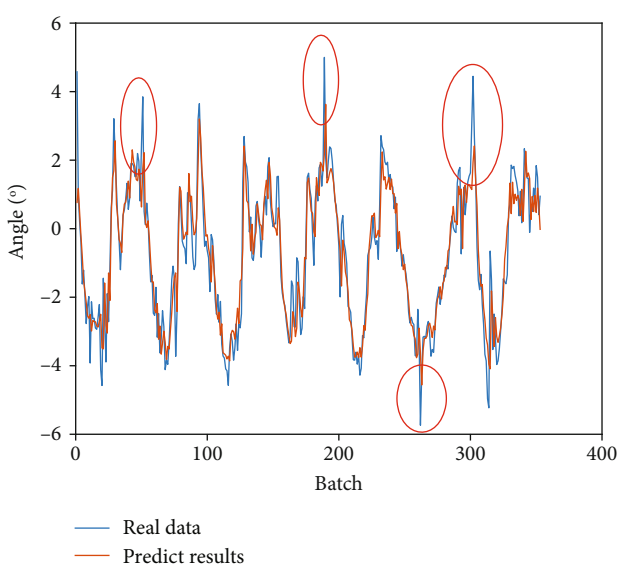

Figure 6: The prediction results of the DOA mean value of each group by using LSTM network.

4. Experiment Results and Discussion

We conducted an experiment with a millimeter-wave radar to monitor vehicles on the road. The radar is deployed on the pedestrian bridge where the main road connects the suburb and the urban area. A typical road monitoring installation along the middle of the road is shown in Figure 4.

We collected 14440 batches of data, containing a total of 354,000 targets. The distribution of the captured samples points is shown in Figure 5(a). And the histogram of DOA distribution is shown in Figure 5(b).

We first count the DOA of the targets in each frame of data, and all the average DOA of these targets was about -2 degrees. Then, we divide the 354,000 targets into 354 groups, and each group consists of 1000 detected targets. Next, the mean value of DOA of each group is calculated. Finally, the LSTM network is applied to estimate the mean value of the targets' DOA. The applied LSTM has 128 hidden units, the first 300 groups data are applied for training, and the rest of the groups are used for testing the prediction performance of LSTM. The prediction results are shown in Figure 6. As shown in Figure 6, the blue curve represents

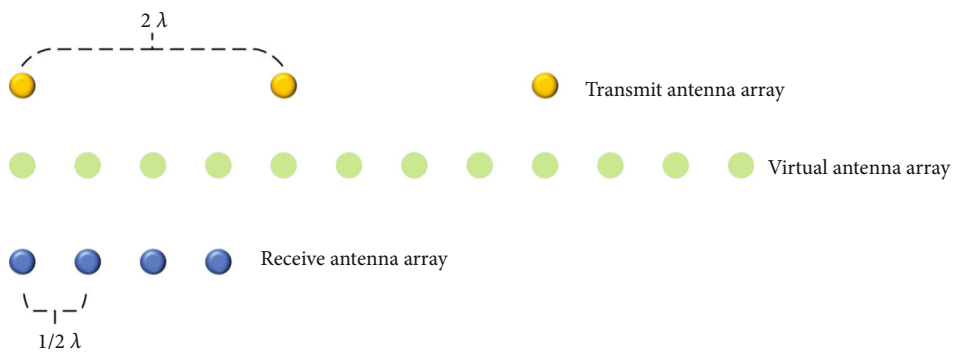

Figure 7: Schematic diagram of antenna array structure.

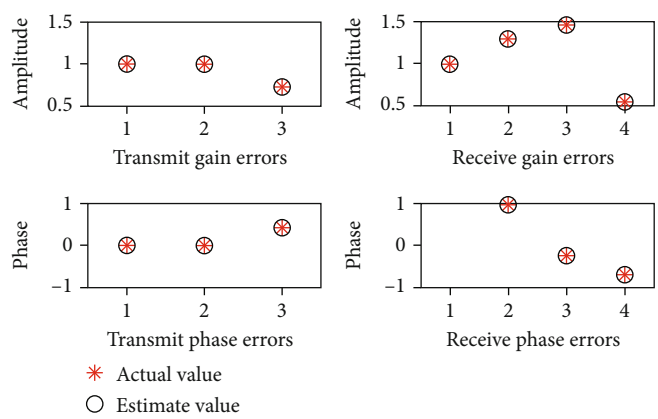

Figure 8: Gain-phase errors estimate results with SNR=30dB.

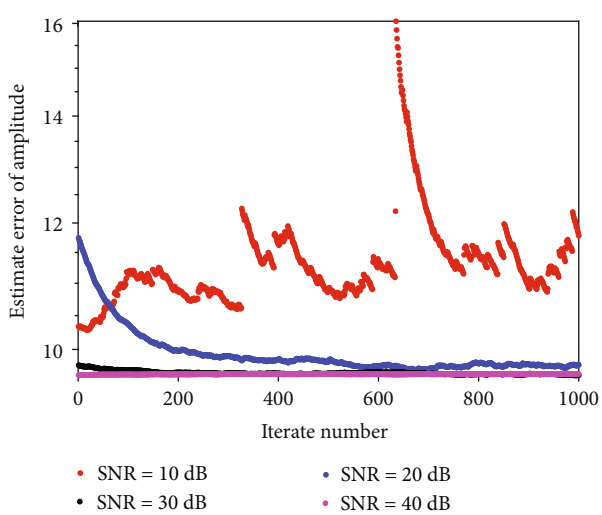

Figure 9: Estimate error of gain in different SNR.

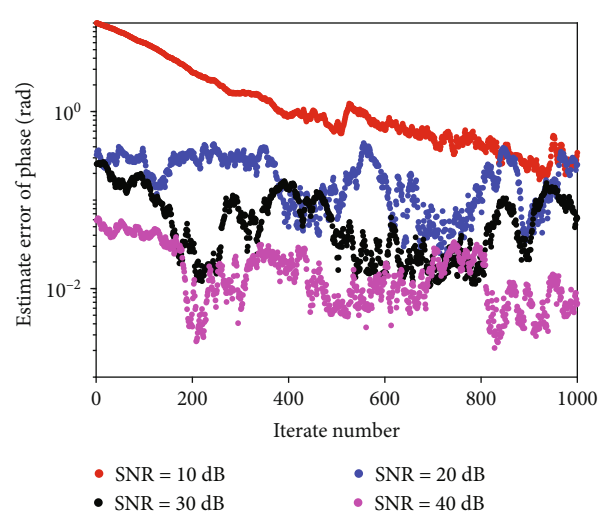

Figure 10: Estimate error of phase in different SNR.

the real DOA of 354 groups, and the red curve represents the predicted DOA by using LSTM network. Generally, the predicted results curve approaches to the real DOA. But we also find that some spikes and highlight them by using red circles. This phenomenon can be attributed that the amount of the data is not sufficient for training more ideal network structure, and we will also further improve the design of the LSTM network in the next work.

In order to verify the gain-phase error estimation ability of LMS algorithm, a set of original data are generated according to the detected target information. Specifically, suppose that a radar has three transmitting antennas and four receiving antennas, as depicted in Figure 7 where the

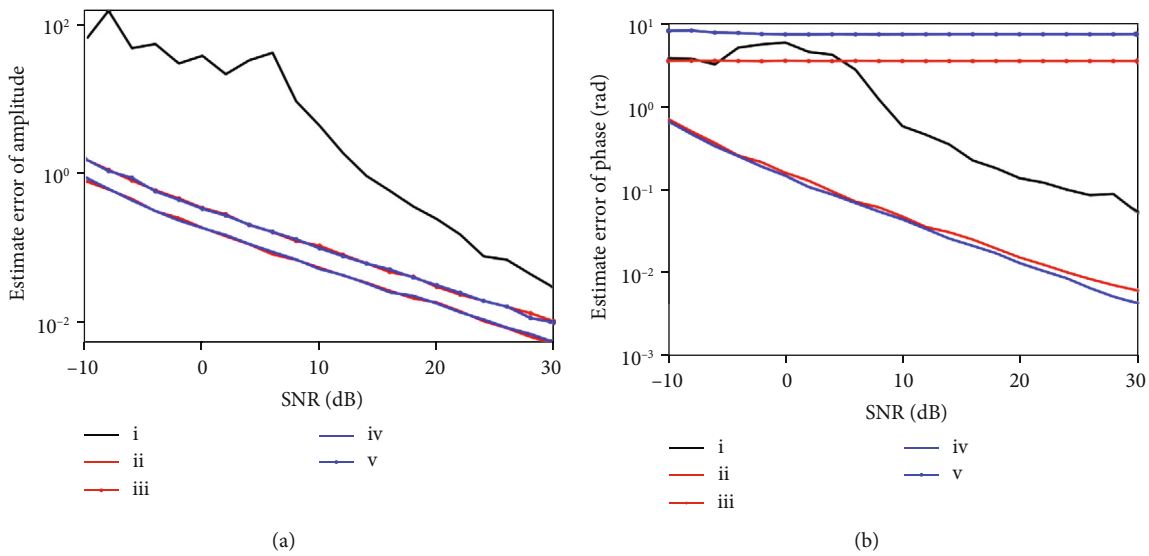

Figure 11: Estimate error compared with previous study. (a) The gain estimate error in different SNR. (b) The phase estimate error in different SNR. (i) are the results of LMS, (ii) are the results of MUSIC with 5 calibrated elements, (iii) are the results of MUSIC with 2 calibrated elements, (iv) are the results of ESPRIT with 5 calibrated elements, and (v) are the results of ESPRIT with 2 calibrated elements.

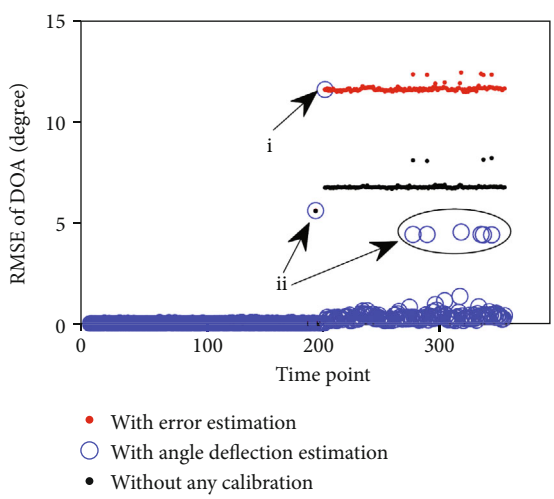

Figure 12: RMSE of DOA with a close to reality scenario, the gain-phase errors appear at (i), and (ii) is affected by SNR.

space between receiving antennas is half wavelength, the space between transmitting antennas is two times wavelength, and a 12-element virtual uniform linear array can be obtained. The simulated echo data is generated by associating with the information of detected real target, and the DOA of simulated data is the same as real data.

We used LMS algorithm to calibrate the gain-phase errors, and the estimated errors are shown in Figure 8. We assume that transmitting antenna 1, 2, and receiving antenna 1 have no errors, and other antennas have random gain-phase errors. The gain errors are uniformly distributed between 0.5 and 1.5, and the phase errors are uniformly distributed between $-\pi/2$ and $\pi/2$. The SNR of targets are 30 dB. The red stars represent the real gain or phase errors, and the black circle represents the estimated results. Clearly, the result comparison of estimated and real data implies that the proposed method successfully estimates the unknown targets.

Furthermore, for assessing the SNR effect for estimation accuracy, the simulations are run by performing different SNRs iterates from 0 to 1000. Figures 9 and 10 show the exemplary of the distinct relationship between the SNR and estimation accuracy, the SNR is higher, and the estimation accuracy is more ideal. This results also imply that the value of SNR has a considerable effect on estimation accuracy, so selecting the data with high SNR as input data can sufficiently facilitate the estimation performance of LMS.

Figure 11 shows the estimate error results of different algorithm. The simulation of LMS is conducted with 1000 iterates. A target with random angle is generated in each iterate. The simulation of MUSIC and ESPRIT is conducted with a target with 1000 snapshots. There are 2 experiments for MUSIC and ESPRIT, respectively. There are 2 elements that have been calibrated well in one experiment and 5 calibrated well elements in another. The results are the mean of 200 Monte Carlo trials for every experiments. Although the performance of LMS for gain error estimation is lower than others, but has a stable phase error estimation performance with only 2 elements.

At last, we simulate a real-world problematic situation, a MIMO radar system is deployed with well down calibration, and the stochastic gain-phase errors appear in every antenna element after a period of time. We simulated the process of such a scenario to verify the proposed method. The gain-phase errors appear in the 201th time point. Figure 12 shows the RMSE of DOA estimation of 1000 targets changed over time.

Figure 12 describes the RMSE of DOA, and we can observe that the value of RMSE is small in the absence of errors. At the i point, the estimation performance of DOA

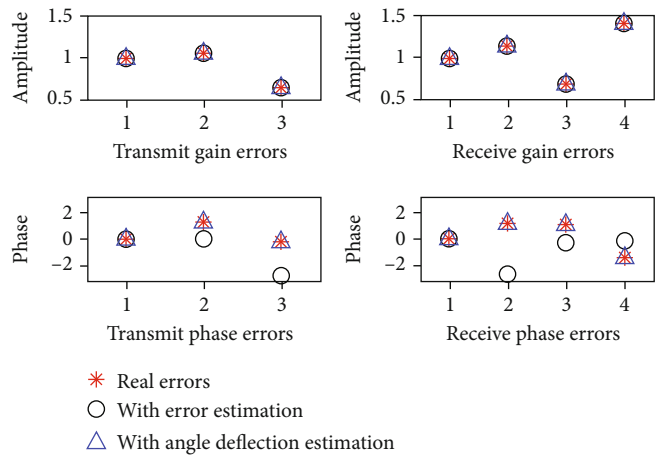

Figure 13: The phase error estimation results.

is suddenly degraded, which is depicted in black dots. After correcting the gain-phase error, the estimation performance of DOA is worse than before. However, after correcting DOA offset, the value of RMSE is obviously lower than before, which is shown in blue circle. At the ii point, some points appear in Figure 12, which can be attribute that the SNR of target is generated according to the SNR of real data, and the SNR at some moments is relatively small, causing a larger RMSE. But this phenomena does not affect the overall conclusion.

The results of phase error are shown in Figure 13. The amplitude errors can be estimated well with the error estimation by LMS, while the phase errors still have a deflection, which can be accurately estimated after angle deflection estimation using LSTM.

5. Conclusions

In this paper, an online calibration method of array gain-phase error has been proposed for a variety of radar array. This online error calibration method considering the characteristic of DOA distribution applies LSTM network to predict the subsequent DOA. The proposed method is feasible and simply operated because it does not require the external reference source or some calibrated antenna. Hence, the proposed method can be readily applied to long-term range surveillance of various targets due to the cost-effective advantage and feasible establishment. Numerical examples demonstrate improvements in high resolution multiple source locations, which has confirmed that taking the DOA distribution characteristic of targets as priori information and sufficiently learning this information can address problem concerning DOA estimation. Despite the promising results, this analysis opens new research directions, all aimed to improve the proposed algorithm system adaptability and confidence in enhancing estimation accuracy.

Data Availability

The data used to support the findings of this study are available from the corresponding author upon request.

Conflicts of Interest

The authors declare that there is no conflict of interest regarding the publication of this paper.

Acknowledgments

The research and publication of the article were funded by the National Natural Science Foundation of China (no. 62031015, no. 62171154, and no. 61971156), the Natural Science Foundation of Shandong Province (no. ZR2020MF007 and no. ZR2020MF013), and the Research Fund Program of Guangdong Key Laboratory of Aerospace Communication and Networking Technology (no. 2018B030322004).

References

[1] H. Krim and M. Viberg, "Two decades of array signal processing research: the parametric approach," *IEEE Signal Processing Magazine*, vol. 13, no. 4, pp. 67–94, 1996.

[2] H. L. Trees Van, "Appendix B: array processing literature," in *Detection, Estimation, and Modulation Theory, Optimum Array Processing*, pp. 1407–1413, John Wiley & Sons, 2002.

[3] A. B. Gershman and N. D. Sidiropoulos, "Space-time processing for MIMO communications," 2005, May 28, 2022, https://xueshu.baidu.com/usercenter/paper/show?paperid=d4cf071f317caaec1dffdf34fa6626ed&site=xueshu_se.

[4] E. G. Larsson, O. Edfors, F. Tufvesson, and T. L. Marzetta, "Massive MIMO for next generation wireless systems," *IEEE Communications Magazine*, vol. 52, no. 2, pp. 186–195, 2014.

[5] Y. Xu, B. Li, N. Zhao et al., "Coordinated direct and relay transmission with NOMA and network coding in Nakagami-*m* fading channels," *IEEE Transactions on Communications*, vol. 69, no. 1, pp. 207–222, 2021.

[6] E. Fishler, A. Haimovich, R. Blum, D. Chizhik, L. Cimini, and R. Valenzuela, "MIMO radar: an idea whose time has come," in *Proceedings of the 2004 IEEE Radar Conference (IEEE Cat. No.04CH37509)*, pp. 71–78, Philadelphia, PA, USA, 2004.

[7] E. Fishler, A. Haimovich, R. Blum, R. Cimini, D. Chizhik, and R. Valenzuela, "Performance of MIMO radar systems: advantages of angular diversity," in *Conference Record of the Thirty-*

Eighth Asilomar Conference on Signals, Systems and Computers, 2004, pp. 305–309, Pacific Grove, CA, USA, 2004.

[8] D. W. Bliss, K. W. Forsythe, S. K. Davis et al., "GMTI MIMO radar," in *2009 International Waveform Diversity and Design Conference*, pp. 118–122, Kissimmee, FL, USA, 2009.

[9] M. Liu, B. Li, Y. Chen et al., "Location parameter estimation of moving aerial target in space–air–ground-integrated networks-based IoV," *IEEE Internet of Things Journal*, vol. 9, no. 8, pp. 5696–5707, 2022.

[10] X. Zhang, L. Xu, L. Xu, and D. Xu, "Direction of departure (DOD) and direction of arrival (DOA) estimation in MIMO radar with reduced-dimension MUSIC," *IEEE Communications Letters*, vol. 14, no. 12, pp. 1161–1163, 2010.

[11] M. L. Bencheikh and Y. Wang, "Joint DOD-DOA estimation using combined ESPRIT-MUSIC approach in MIMO radar," *Electronics Letters*, vol. 46, no. 15, pp. 1081–1083, 2010.

[12] F. Wen, Z. Zhang, and G. Zhang, "Joint DOD and DOA estimation for bistatic MIMO radar: a covariance trilinear decomposition perspective," *IEEE Access*, vol. 7, pp. 53273–53283, 2019.

[13] A. M. Ahmed, U. S. K. P. M. Thanthrige, A. E. Gamal, and A. Sezgin, "Deep learning for DOA estimation in MIMO radar systems via emulation of large antenna arrays," *IEEE Communications Letters*, vol. 25, no. 5, pp. 1559–1563, 2021.

[14] X. Hua, Y. Ono, L. Peng, Y. Cheng, and H. Wang, "Target detection within nonhomogeneous clutter via total Bregman divergence-based matrix information geometry detectors," *IEEE Transactions on Signal Processing*, vol. 69, pp. 4326–4340, 2021.

[15] H. Srinath and V. U. Reddy, "Analysis of MUSIC algorithm with sensor gain and phase perturbations," *Signal Processing*, vol. 23, no. 3, pp. 245–256, 1991.

[16] H. Li, J. Geng, and J. Xie, "Robust adaptive beamforming based on covariance matrix reconstruction with RCB principle," *Digital Signal Processing*, vol. 127, article 103565, 2022.

[17] M. Liu, Z. Liu, W. Lu, Y. Chen, X. Gao, and N. Zhao, "Distributed few-shot learning for intelligent recognition of communication jamming," *IEEE Journal of Selected Topics in Signal Processing*, vol. 16, no. 3, pp. 395–405, 2022.

[18] Y. D. Guo, Y. S. Zhang, and N. N. Tong, "ESPRIT-like angle estimation for bistatic MIMO radar with gain and phase uncertainties," *Electronics Letters*, vol. 47, no. 17, pp. 996-997, 2011.

[19] L. Li, T. Fu, Y. Yang, M. Huang, Z. Han, and J. Li, "Joint angle estimation and array calibration using eigenspace in monostatic MIMO radar," *IEEE Access*, vol. 8, pp. 60645–60652, 2020.

[20] F. Wen, J. Shi, X. Wang, and L. Wang, "Angle estimation for MIMO radar in the presence of gain-phase errors with one instrumental Tx/Rx sensor: a theoretical and numerical study," *Remote Sensing*, vol. 13, no. 15, p. 2964, 2021.

[21] J. Li, L. He, Y. He, and X. Zhang, "Joint direction of arrival estimation and array calibration for coprime MIMO radar," *Digital Signal Processing*, vol. 94, pp. 67–74, 2019.

[22] J. Hu, E. Baidoo, L. Zhan, and Y. Tian, "Computationally efficient compressed sensing-based method via FG Nyström in bistatic MIMO radar with array gain-phase error effect," *International Journal of Antennas and Propagation*, vol. 2020, Article ID 1586353, 12 pages, 2020.

[23] W. Lu, P. Si, G. Huang et al., "SWIPT cooperative spectrum sharing for 6G-enabled cognitive IoT network," *IEEE Internet of Things Journal*, vol. 8, no. 20, pp. 15070–15080, 2021.

[24] Y. Xu, J. Tang, B. Li, N. Zhao, D. Niyato, and K.-K. Wong, "Adaptive aggregate transmission for device-to-multi-device aided cooperative NOMA networks," *IEEE Journal on Selected Areas in Communications*, vol. 40, no. 4, pp. 1355–1370, 2022.

[25] W. Lu, Y. Ding, Y. Gao et al., "Resource and trajectory optimization for secure communications in dual unmanned aerial vehicle mobile edge computing systems," *IEEE Transactions on Industrial Informatics*, vol. 18, no. 4, pp. 2704–2713, 2022.

[26] M. Liu, C. Liu, M. Li, Y. Chen, S. Zheng, and N. Zhao, "Intelligent passive detection of aerial target in space-air-ground integrated networks," *China Communications*, vol. 19, no. 1, pp. 52–63, 2022.

Hindawi
Wireless Communications and Mobile Computing
Volume 2022, Article ID 2906739, 10 pages
https://doi.org/10.1155/2022/2906739

Research Article

An Effective Scheme of Building Electromagnetic Map for Spectrum Sensing

Dongming Lin,[1] **Hongjun Wang**,[1] **Zhi Lin**,[1] **Kang An**,[2] **Zhexian Shen**,[1] **and Jiangzhou Wang**[3]

[1]*College of Electronic Engineering, National University of Defense Technology, Hefei 230037, China*
[2]*Sixty-Third Research Institute, National University of Defense Technology, Nanjing 210007, China*
[3]*School of Engineering, University of Kent, Canterbury CT2 7NZ, UK*

Correspondence should be addressed to Hongjun Wang; hongjun-wang@163.com

Received 27 May 2022; Accepted 28 June 2022; Published 25 July 2022

Academic Editor: Mingqian Liu

To address the severe spectrum scarcity problem and achieve efficient green communications, we propose a new and practical scheme to obtain electromagnetic data (ED) and a composite electromagnetic map reconstruction method (CEMRM). The scheme uses a small number of sensing nodes to obtain incomplete sampled ED, then uses CEMRM to reconstruct complete ED according to the incomplete ED and builds realistic electromagnetic maps (EMs) in various propagation scenarios. Specifically, we firstly adopt kriging (KG) method to obtain the geography-based ED (GED) according to geographical correlation of the locations of the sampled ED. Meanwhile, a novel algorithm, named filtered subdistrict sparsity adaptive matching pursuit (FSSAMP), is proposed to obtain the pure ED (PED) according to electromagnetic correlation of the sampled ED. Then, weight factors are mapped into the above two types of data and the fast gradient projection (FGP) method is employed to obtain the highly accurate combined ED (CED). Based on the CED, the accurate and practical EMs can be drawn. Simulation results demonstrate that the proposed scheme can provide more accurate ED and EMs than existing benchmark schemes in various propagation scenarios, and the built EMs can provide accurate information for the assessment of spectrum resources utilization to make spectrum resources efficiently used.

1. Introduction

The rapid development of wireless applications and blossoming growth of traffic demand lead to severe spectrum scarcity problem. To achieve efficient application of spectrum resources and green communications, it is necessary to obtain electromagnetic data (ED) first and then assess the spectrum resources utilization so as to adopt spectrum resources allocation method. In the existing methods to obtain ED, manual measurements cost highly especially in a large-scale area. Employing lots of human beings to obtain the ED is not realistic, and the obtained ED may be not accurate due to the human subjectivity. With the development of automation technology, sensing nodes replace human beings to obtain the ED [1]. However, the cost and effect are relative to the number of sensing nodes. If sensing nodes are deployed redundantly, the cost is high but accurate and complete ED can be obtained. If there are a small number of available sensing nodes deployed, the cost is greatly less than that when sensing nodes are deployed redundantly, and the obtained ED are accurate but incomplete [2]. However, the incomplete ED cannot provide sufficient information for assessing the usage of spectrum resources. The completeness degree of ED and cost are both proportional to the number of sensing nodes in a certain range. The mentioned three types of measurement methods cannot make a balance between the cost and effect. Therefore, it is necessary to study an effective and low-cost method to obtain ED.

An electromagnetic map (EM) [3] is a promising tool for assessing the usage of spectrum resources, which contains lots of information about electromagnetic spectrum resources. The EM can make spectrum resources efficiently

used, which can solve the spectrum scarcity problem and achieve efficient green communications. The existing works on EMs are mainly about the constructing methods of radio environment maps (REMs), whose methods can be classified into three categories, which are called indirect methods, direct methods, and hybrid methods. Indirect methods are mainly based on propagation models or radiation geographical positions, direct methods are mainly interpolation methods, and hybrid methods are the combination of indirect methods and direct methods.

In indirect methods, the authors of [4] proved that the propagation model can be used to construct the REM. ED of unsampled positions can be inferred from the known or estimated radiation source locations and the propagation model, and it is the main method used by the indirect methods to obtain the ED. However, the single electromagnetic propagation model cannot fit the dynamic electromagnetic environment, and the selection of relevant parameters is difficult without relevant information of electromagnetic environment, so the effect of the method based on the propagation model cannot be ensured in the dynamic and noncooperative electromagnetic environment [5, 6].

On the other hand, the direct methods need no information about electromagnetic environment especially propagation models, and they are used to reconstruct the ED according to the geographical correlation of the sampled positions. The kriging (KG) [7] is the mostly used algorithm, and its accuracy is satisfactory [8]. However, the accuracy of KG is influenced by the outliers [9], and the calculation complexity is high [10]. Different from KG, other interpolation methods are used to construct the REM, such as the local polynomial (LP) algorithm [11], nearest neighbour (NN) algorithm [12], and inverse distance weighting (IDW) algorithm [13]. However, LP is sensitive to neighbourhood distance, and a small searching neighbourhood distance will cause an empty hole in the data reconstruction. The data reconstruction result of NN is not continuous. IDW is sensitive to isolating outliers, and a lot of isolating outliers cause downfall in the accuracy when IDW is used in large-scale data reconstruction. Generally, the REM construction effect of existing interpolation methods is relatively lower when the number of sensing nodes is small [8].

In hybrid methods, the mostly used combination scheme is to combine the KG and propagation models [14, 15]. In fact, the combination of a single propagation model and KG is suitable for the special scenario, and the accuracy is much better than KG and the propagation model. However, the effect of the method is relatively lower in scenarios of other kinds of propagation models, and the methods also need information about propagation models in a certain content.

In the case of noncooperation, the information of the electromagnetic environment like propagation models cannot be obtained, even though some methods like maximum likelihood estimation [16] can be used to estimate the information, the error is not acceptable; moreover, the method based on a single propagation model cannot do well in scenarios of different propagation models. In the case that a small number of sensing nodes are available, the interpolation methods cannot obtain good results, and the accuracy needs improvement. As for the hybrid methods, these kinds of methods do badly in the case of noncooperation or the case that a small number of sensing nodes are available, and the method has high complexity. In order to achieve the reconstruction of EMs in the case of noncooperation and the case that a small number of sensing nodes are available, it is necessary to study an effective method.

To address the above challenges, this paper proposed a novel scheme to obtain accurate ED, reconstruct the practical electromagnetic signal map (which we refer to as an EM), and take the reference signal receiving power (RSRP) as the research object of EMs.

The contributions of the paper are summarized as follows:

(1) To achieve ED reconstruction, this paper proposes an improved sparsity adaptive matching pursuit (SAMP) algorithm, which reconstructs ED based on the electromagnetic correlation of the sampled ED. Besides, the processing time of the proposed improved SAMP is much less than that of the traditional SAMP algorithm

(2) To achieve the reconstruction of EMs in the noncooperation situation with a small number of sensing nodes, this paper proposes a composite EM reconstruction method (CEMRM) to obtain the complete and accurate ED and reconstruct realistic EMs. Simulation results show that the obtained EMs reconstructed by the CEMRM are more accurate than those reconstructed by existing methods

The organization of this paper is as follows. Section 2 describes the system model of the proposed scheme. Section 3 presents algorithm description about the proposed method. In Section 4, simulation results are presented. Finally, the paper draws the conclusions in Section 5.

2. System Model

Assuming that there are three base stations in the target area as shown in Figure 1, a small number of sensing nodes are deployed randomly in the target area, and the ratio of sensing nodes to the total number of ED is 2% (smaller than that in existing works [17]). First of all, the target area is divided into grids to ascertain the total number of ED and obtain the corresponding geographic positions. The values of ED are RSRP values. We just consider the electromagnetic datum in each grid center. When reconstructing a large-area EM, the total number of ED is huge. If we study the relation between the change in the specific quantities of sensing nodes and the accuracy of reconstructed EMs, the workload is huge and results are not accurate. However, if we study the relation between the change in the ratio of sensing nodes to the total number of ED and the accuracy of reconstructed EMs, the useless work can be decreased and the results are accurate. Therefore, this paper uses the ratio to describe the number of sensing nodes instead of the specific

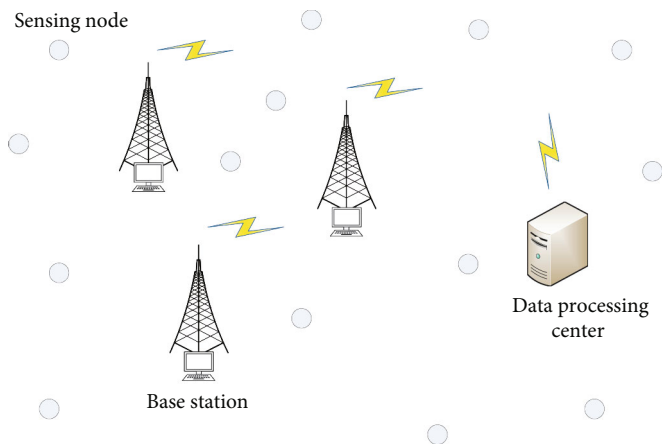

Figure 1: System model. The sketch of the proposed scheme to obtain the ED.

quantities. The sampled ED must be incomplete. After sampling the ED [18, 19], the incomplete data are sent to the data processing center, where CEMRM is adopted to reconstruct the precise EMs. The data processing center assesses the usage of spectrum resources according to the reconstructed EMs and then controls the working status of the base stations with the adopted spectrum resources allocation method. If the data processing center breaks down, the calculating task will be undertaken by the distributed calculating platform in the sensing nodes.

3. Algorithm Description

This section proposes the CEMRM to achieve ED reconstruction, which is shown in Figure 2.

Specifically, CEMRM consists of four parts. In the first part, KG is used to reconstruct the ED according to the incomplete data obtained by sensing nodes, and the obtained geography-based ED (GED) contain strong geographical correlation. At the same time, the filtered subdistric sparsity adaptive matching pursuit (FSSAMP) is used to reconstruct the ED according to the incomplete data obtained by sensing nodes, and the obtained pure ED (PED) contain strong electromagnetic correlation. The ED are affected by geography just in a certain extent, so the GED obtained by KG can be more accurate after being processed with the electromagnetic correlation. In order to make obtained ED containing both geographical and electromagnetic correlation, weight allocation is used to balance the two kinds of correlation.

$$\boldsymbol{G} = 0.8 \times \mathrm{GED} + 0.2 \times \mathrm{PED}. \tag{1}$$

After weight allocation, the primary ED, $\boldsymbol{G}$ is obtained. The fast gradient projection (FGP) is an algorithm to improve the data accuracy according to the correlation of data, so the FGP is promising to help improve the accuracy of the primary ED according to the weight allocation of the geographical and electromagnetic correlation. After $\boldsymbol{G}$ with strong correlation being processed by the FGP, more accurate combined ED (CED) can be obtained. Finally, the EM is drawn with isomagnetic lines according to the CED.

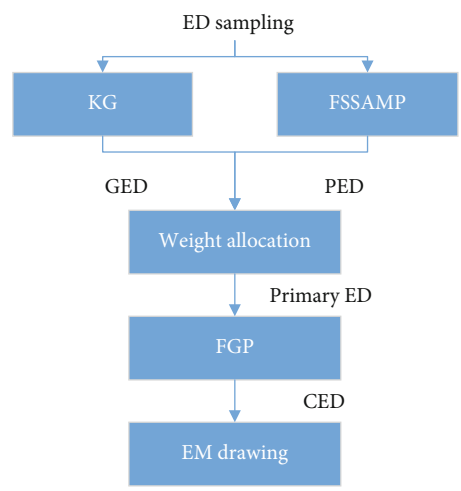

Figure 2: The structure of the proposed CEMRM. GED are the ED reconstructed by KG, PED are the ED reconstructed by FSSAMP.

The proposed CEMRM needs no electromagnetic information about the electromagnetic environment, and it just needs a small number of sensing nodes. With the help of electromagnetic correlation extracted by the FSSAMP, and accuracy improvement by the FGP, it can overcome the weakness that KG is sensitive to outliers and obtain realistic results.

3.1. Kriging. KG is an accurate interpolation algorithm and can reconstruct ED according to geographical correlation, and the obtained ED contain geographical correlation. The principal of KG to predict the RSRP is given by [7].

$$v_{\mathrm{out}}(\boldsymbol{h}) = \mathbf{w}^{\mathrm{T}}(\boldsymbol{h})\boldsymbol{\iota} + e(\boldsymbol{h}), \tag{2}$$

where $v_{\mathrm{out}}(\boldsymbol{h})$ is the value of the RSRP, and $\boldsymbol{h}$ is the location. $\mathbf{w}(\boldsymbol{h}) = [w_1(\boldsymbol{h}), w_2(\boldsymbol{h}), \cdots, w_N(\boldsymbol{h})]^{\mathrm{T}}$ is the vector containing N selected functions that consist of the regression model. $\boldsymbol{\iota} = [\iota_1, \iota_2, \cdots, \iota_N]^{\mathrm{T}}$ is the parameter vector of the model. $e(\boldsymbol{h})$

is a stochastic process satisfying the following conditions:

$$E[e(\boldsymbol{h})] = 0,$$
$$E\left[e(\boldsymbol{h}_i)e(\boldsymbol{h}_j)\right] = \tau^2 R(\boldsymbol{\kappa}, \boldsymbol{h}_i, \boldsymbol{h}_j), \tag{3}$$

where $E[\cdot]$ is an operation that calculates the expectation, $\boldsymbol{h}_i$, $\boldsymbol{h}_j$ are both input locations, $R(\boldsymbol{\kappa}, \boldsymbol{h}_i, \boldsymbol{h}_j)$ is the correlation model, τ^2 is the variance of $e(\boldsymbol{h})$, and $\boldsymbol{\kappa}$ is the parameter of the correlation model. The algorithm defines $[\boldsymbol{b}_1, \cdots, \boldsymbol{b}_q]$ as a set of sampling point locations whose value is $\mathbf{V} = [v_1, \cdots, v_q]^{\mathrm{T}}$. Then,

$$\widehat{\boldsymbol{\iota}} = \left(\mathbf{F}^{\mathrm{T}}\mathbf{R}^{-1}\mathbf{F}\right)^{-1}\mathbf{F}^{\mathrm{T}}\mathbf{R}^{-1}\mathbf{V},$$
$$\widehat{\tau}^2 = \frac{1}{q}(\mathbf{V} - \mathbf{F}\widehat{\boldsymbol{\iota}})^{\mathrm{T}}\mathbf{R}^{-1}(\mathbf{V} - \mathbf{F}\widehat{\boldsymbol{\iota}}), \tag{4}$$

where $\widehat{\boldsymbol{\iota}}$ and $\widehat{\tau}^2$ are the predicted values of the corresponding variables $\boldsymbol{\iota}$ and τ^2. $\mathbf{F}$ is a $q \times N$ matrix containing $\mathbf{w}(\boldsymbol{b}_i)$, for $i \in [1, q]$. $\mathbf{R}$ is a $q \times q$ correlation matrix of the sampling points containing $R_{ij} = R(\boldsymbol{\kappa}, \boldsymbol{b}_i, \boldsymbol{b}_j)$. The correlation function is defined as follows:

$$R(\boldsymbol{\kappa}, \boldsymbol{\mu}, \boldsymbol{h}) = \prod_{j=1}^{n} R_j\left(\boldsymbol{\kappa}, \mu_j - h_j\right), \tag{5}$$

where n is the dimension of sampling points. Note that the following condition should be ensured:

$$\min_{\boldsymbol{\kappa}}\left[\Lambda(\boldsymbol{\kappa}) = |\mathbf{R}|^{(1/q)}\tau^2\right], \tag{6}$$

where $|\cdot|$ calculates the determinant of a matrix. Here, the spherical model is adopted.

$$R_j(\boldsymbol{\kappa}, d_j) = 1 - 1.5\xi_j + 0.5\xi_j^3 \quad \xi_j = \min\left\{1, \kappa_j|d_j|\right\}, \tag{7}$$

where $d_j = \mu_j - h_j$. Then, the predicted RSRP v_{out} of the unsampled location $\boldsymbol{h}$ is shown as follows:

$$\widehat{v}_{\mathrm{out}}(\boldsymbol{h}) = \mathbf{w}^{\mathrm{T}}(\boldsymbol{h})\widehat{\boldsymbol{\iota}} + \mathbf{r}^{\mathrm{T}}(\boldsymbol{h})\mathbf{R}^{-1}(\mathbf{V} - \mathbf{F}\widehat{\boldsymbol{\iota}}),$$
$$\mathbf{r}(\boldsymbol{h}) = \left[R(\boldsymbol{\kappa}, \boldsymbol{h}, \boldsymbol{b}_1), \cdots, R\left(\boldsymbol{\kappa}, \boldsymbol{h}, \boldsymbol{b}_q\right)\right]^{\mathrm{T}}. \tag{8}$$

The complete ED obtained by the KG are $\mathrm{GED} = \widehat{\mathbf{v}}_{\mathrm{out}}$, where $\widehat{\mathbf{v}}_{\mathrm{out}}$ is the union of $\widehat{v}_{\mathrm{out}}(\mathbf{h})$.

3.2. Improved Sparsity Adaptive Matching Pursuit. The procedure of sampling ED with sensing nodes can be described as

$$\boldsymbol{y} = \boldsymbol{K}\boldsymbol{x}, \tag{9}$$

where $\boldsymbol{y} = [\cdots, 0, y_1, \cdots, 0, y_M, \cdots]^{\mathrm{T}}$ is the sampled ED containing M non-zero values, $\boldsymbol{x}$ is the real complete ED, $\boldsymbol{x} \in R^N$, and $M \ll N$ need to be met. Here, $\boldsymbol{K}$ is the observation matrix.

$$\boldsymbol{K} = \begin{bmatrix} \ddots & & & & \\ & 1 & & & \\ & & \ddots & & \\ & & & 0 & \\ & & & & \ddots \end{bmatrix}_{N\times N}, \tag{10}$$

where N is the total number of ED.

Since it is difficult to determine $\boldsymbol{x}$ directly, the problem is converted to

$$\min \|\boldsymbol{\theta}\|_{l_0},$$
$$\text{s.t.} \quad \boldsymbol{y} = \boldsymbol{A}\boldsymbol{\theta}, \tag{11}$$

where $\boldsymbol{A} = \boldsymbol{K}\boldsymbol{\Psi}$ is the sensing matrix, $\boldsymbol{\Psi}$ is the sparse base matrix, $\|\cdot\|_{l_0}$ is calculating the l_0-norm of a matrix, and $\boldsymbol{\theta}$ is the projection result of $\boldsymbol{x}$ in the sparse base matrix $\boldsymbol{\Psi}$, which is given by

$$\boldsymbol{\Psi} = \sqrt{N}\begin{bmatrix} 1 & 1 & \cdots & 1 \\ 1 & W_N^1 & \cdots & W_N^{N-1} \\ 1 & W_N^2 & \cdots & W_N^{2(N-1)} \\ \vdots & \vdots & & \vdots \\ 1 & W_N^{N-1} & \cdots & W_N^{(N-1)(N-1)} \end{bmatrix}_{N\times N}, \tag{12}$$

where $W_N = e^{((-j2\pi)/N)}$.

In order to solve Eq. (11), we improve the SAMP [20]. Firstly, the target area is divided into four parts, which are numbered as $\alpha \in [1, 2, 3, 4]$, and a certain number of sensing nodes are randomly deployed in four subareas, respectively. The number of sensing nodes in each subarea is same. Then, the algorithm reconstructs ED of each part parallelly or serially, and then they are integrated into a set of complete ED. Finally, the obtained complete ED are filtered by a median filter. The improved algorithm is summarized as follows.

Needed parameter: the sensing matrix $\boldsymbol{A}$, sampling ED $\boldsymbol{y}$ of the subarea, the step size $s = 4$, which is the number of subareas, and the observation matrix that being changed into the column vector format $\boldsymbol{K}$.

Step 1. Initialize parameters, the residual error $\boldsymbol{r_0} = \boldsymbol{y}$, index matrix $\boldsymbol{H_0} = \varnothing$, the element number $L = s$, $t = 1$, t is the iteration, $\boldsymbol{a}_j$ is the jth column of $\boldsymbol{A}$, stage index std = 1, $\widehat{\boldsymbol{\theta}} = 0_{N\times 1}$.

Step 2. $Y = \mathrm{abs}(\boldsymbol{A}^{\mathrm{T}}\boldsymbol{r_{t-1}})$ is calculated, and the algorithm chooses L maximum values, and obtains a union set ϱ_k containing the column codes of chosen values in $\boldsymbol{A}$.

Step 3. $C_k = \boldsymbol{H_{t-1}} \bigcup \varrho_k$, $\boldsymbol{A}_t = [\boldsymbol{a}_j], j \in C_k$.

Step 4. Least squares solution $\widehat{\boldsymbol{\theta}}_t = (\boldsymbol{A}_t^{\mathrm{T}}\boldsymbol{A}_t)^{-1}\boldsymbol{A}_t^{\mathrm{T}}\boldsymbol{y}$.

Step 5. The L elements with the biggest absolute values are chosen from $\widehat{\boldsymbol{\theta}}_t$, and the corresponding column vectors of the chosen values in $\boldsymbol{A}_t$ make up $\boldsymbol{A}_{t/L}$, the corresponding column codes of the chosen values are$\boldsymbol{H}_{t/L}$.

Step 6. The new residual error $\mathbf{r}_{tc}$ is updated. $\widehat{\boldsymbol{\theta}}_t = (\boldsymbol{A}_{t/L}^{\mathrm{T}}\boldsymbol{A}_{t/L})^{-1}\boldsymbol{A}_{t/L}^{\mathrm{T}}\boldsymbol{y}$, $\boldsymbol{r}_{tc} = \boldsymbol{y} - (\boldsymbol{A}_{t/L}\widehat{\boldsymbol{\theta}}_t)$.

Step 7. If $\|\boldsymbol{r}_{tc}\|_2 < 0.001$ which is $\|\boldsymbol{r}_{tc}\|_2 = 0$ in the original algorithm, $\boldsymbol{H}_t = \boldsymbol{H}_{t/L}$, and do Step 8 directly. If $\|\boldsymbol{r}_{tc}\|_2 \geq \|\boldsymbol{r}_{t-1}\|_2$, $\mathrm{std} = \mathrm{std} + 1$, $L = \mathrm{std} \times s$, $\boldsymbol{r}_t = \boldsymbol{r}_{t-1}, t = t + 1$, and return Step 2; at the same time, if the algorithm reaches the maximum iterations, $\boldsymbol{H}_t = \boldsymbol{H}_{t/L}$ and do Step 8. Or $\boldsymbol{H}_t = \boldsymbol{H}_{t/L}$, $\boldsymbol{r}_t = \boldsymbol{r}_{tc}$, $t = t + 1$ and return Step 2.

Step 8. Update $\widehat{\boldsymbol{\theta}}$, the values whose positions are $\boldsymbol{H}_t$ in $\widehat{\boldsymbol{\theta}}$ is $\widehat{\boldsymbol{\theta}}_t$.

Step 9. The corresponding ED of the sub area are $\boldsymbol{\Psi}\widehat{\boldsymbol{\theta}} \times (\boldsymbol{I} - \boldsymbol{K}) + \boldsymbol{y}$, $\boldsymbol{I}$ is the column vector made up of 1.

Step 10. A set of complete ED are obtained by data fusion, which are described as $\widehat{\boldsymbol{y}}_o = \mathrm{Union}(\boldsymbol{\Psi}_\alpha\widehat{\boldsymbol{\theta}}_\alpha \times (\boldsymbol{I} - \boldsymbol{K}_\alpha) + \boldsymbol{y}_\alpha)$, $\alpha \in [1, 2, 3, 4]$. The complete ED obtained by the FSSAMP are $\mathrm{PED} = \mathrm{Filter}(\widehat{\boldsymbol{y}}_o)$, where Union means the union of the data, $\boldsymbol{\Psi}_\alpha\widehat{\boldsymbol{\theta}}_\alpha \times (\boldsymbol{I} - \boldsymbol{K}_\alpha) + \boldsymbol{y}_\alpha$ is the ED of the corresponding subarea, $\|\cdot\|_2$ calculates the 2-norm of a matrix, and Filter is the median filter.

The median filtering is a kind of nonlinear filtering, and its principle is like

$$\begin{bmatrix} e_1 & e_2 & e_3 \\ e_4 & e_5 & e_6 \\ e_7 & e_8 & e_9 \end{bmatrix}_{3\times 3}, \tag{13}$$

where e_5 is set as the median value of e_1, e_2, e_3, e_4, e_5, e_6, e_7, e_8, and e_9; the values of $e_1 \sim e_9$ are known.

The median filtering can protect the edge information of ED and reduce the influence of isolating outliers, which can help to obtain more accurate results.

3.3. Fast Gradient Projection. The FGP is a good method using the data correlation to increase the precision of data. After the data obtained by Eq. (1) being processed by the FGP, more precise data can be obtained. The accuracy improvement of the FGP is described as a minimum optimization problem, which satisfies

$$\min_{\boldsymbol{E}} J(\boldsymbol{E}) = \frac{1}{2}\|\boldsymbol{E} - \boldsymbol{G}\|_2^2 + \varsigma \boldsymbol{TV}(\boldsymbol{E}), \tag{14}$$

$\|\cdot\|_2$ represents calculating the 2-norm of the matrix, $\boldsymbol{G}$ is the ED obtained by weight allocation, $\boldsymbol{E}$ is more precise ED which is the final result, and $\boldsymbol{TV}(\boldsymbol{E})$ is the total variation regularizer of $\boldsymbol{E}$, ς is the regularization parameter. The dimensions of $\boldsymbol{G}$ and $\boldsymbol{E}$ are both $ii \times jj$.

Table 1: The average running time results of the proposed improved SAMP (FSSAMP) and SAMP.

Type	FSSAMP	SAMP
Time/s	87.9546	1242.3315

In order to solve Eq. (14), we adopt the FGP, which is proposed in [21]. The procedure is given as follows.

First of all, parameters are initialized as $(\boldsymbol{D}_1, \boldsymbol{B}_1) = (\boldsymbol{c}_0, \boldsymbol{m}_0) = (\mathbf{0}_{(ii-1)\times jj}, \mathbf{0}_{ii\times(jj-1)})$, and $t_1 = 1$.

Then, it is an iterative procedure, in the step $p \in [1, N']$, the algorithm calculates

$$\begin{aligned} (\boldsymbol{c}_p, \boldsymbol{m}_p) &= U_{\ddot{\mathrm{y}}}\left\{(\boldsymbol{D}_p, \boldsymbol{B}_p) + \frac{1}{8\varsigma}\mathfrak{R}^T\left(U_O\left[G - \varsigma\mathfrak{R}(\boldsymbol{D}_p, \boldsymbol{B}_p)\right]\right)\right\}, \\ t_{p+1} &= \frac{1 + \sqrt{1 + 4t_p^2}}{2}, \\ (\boldsymbol{D}_{p+1}, \boldsymbol{B}_{p+1}) &= (\boldsymbol{c}_p, \boldsymbol{m}_p) + \left(\frac{t_p - 1}{t_{p+1}}\right)(\boldsymbol{c}_p - \boldsymbol{c}_{p-1}, \boldsymbol{m}_p - \boldsymbol{m}_{p-1}), \end{aligned} \tag{15}$$

where N' represents the total number of iterations; $\boldsymbol{c}_p$ represents the $\boldsymbol{c}$ in the pth iteration; $\boldsymbol{m}_p$ represents the $\boldsymbol{m}$ in the p th iteration; $\boldsymbol{D}_p$ represents the $\boldsymbol{D}$ in the pth iteration; and $\boldsymbol{B}_p$ represents the $\boldsymbol{B}$ in the pth iteration.

Finally, the more precise result $\boldsymbol{E}$ can be obtained.

$$\boldsymbol{E} = U_O[G - \varsigma\mathfrak{R}(\boldsymbol{c}_{N'}, \boldsymbol{m}_{N'})], \tag{16}$$

where $\boldsymbol{c}_{N'}$ and $\boldsymbol{m}_{N'}$ are obtained in the final iteration.

As a set of matrix pairs, $\ddot{\mathrm{y}}$ consists of $(\boldsymbol{c}, \boldsymbol{m})$. The dimension of $\boldsymbol{c}$ is $(ii - 1) \times jj$, $\boldsymbol{m}$ is $ii \times (jj - 1)$, and they satisfy

$$\begin{aligned} c_{l,n}^2 + m_{l,n}^2 \leq 1, &\quad l = 1, \cdots, ii - 1\,; n = 1, \cdots, jj - 1, \\ |c_{l,jj}| \leq 1, &\quad l = 1, \cdots, ii - 1, \\ |m_{ii,n}| \leq 1, &\quad n = 1, \cdots, jj - 1, \end{aligned} \tag{17}$$

where $\mathfrak{R}$ is an operation that satisfies $\mathfrak{R}(\boldsymbol{c}, \boldsymbol{m})_{l,n} = c_{l,n} + m_{l,n} - c_{l-1,n} - m_{l,n-1}, l = 1, \cdots, ii\,; n = 1, \cdots, jj$, and $c_{0,n} = m_{l,0} = c_{ii,n} = m_{l,jj} \equiv 0$. $\mathfrak{R}^{\mathrm{T}}$ is an operation that satisfies $\mathfrak{R}^{\mathrm{T}}(\boldsymbol{E}) = (\boldsymbol{c}, \boldsymbol{m})$, where $c_{l,n} = E_{l,n} - E_{l+1,n}, l = 1, \cdots, ii - 1, n = 1, \cdots, jj$, $m_{l,n} = E_{l,n} - E_{l,n+1}, l = 1, \cdots, ii, n = 1, \cdots, jj - 1$.

U_{y} means doing an orthogonal operation on the set y, and the meaning of U_O is similar to U_{y}. For example, if y $= Q_{n_1,n_2}$, the calculation is

$$U_{Q_{n_1,n_2}}(\boldsymbol{E})_{l,n} = \begin{cases} n_1 & E_{l,n} < n_1 \\ E_{l,n} & n_1 \leq E_{l,n} \leq n_2\,, \\ n_2 & E_{l,n} > n_2, \end{cases} \tag{18}$$

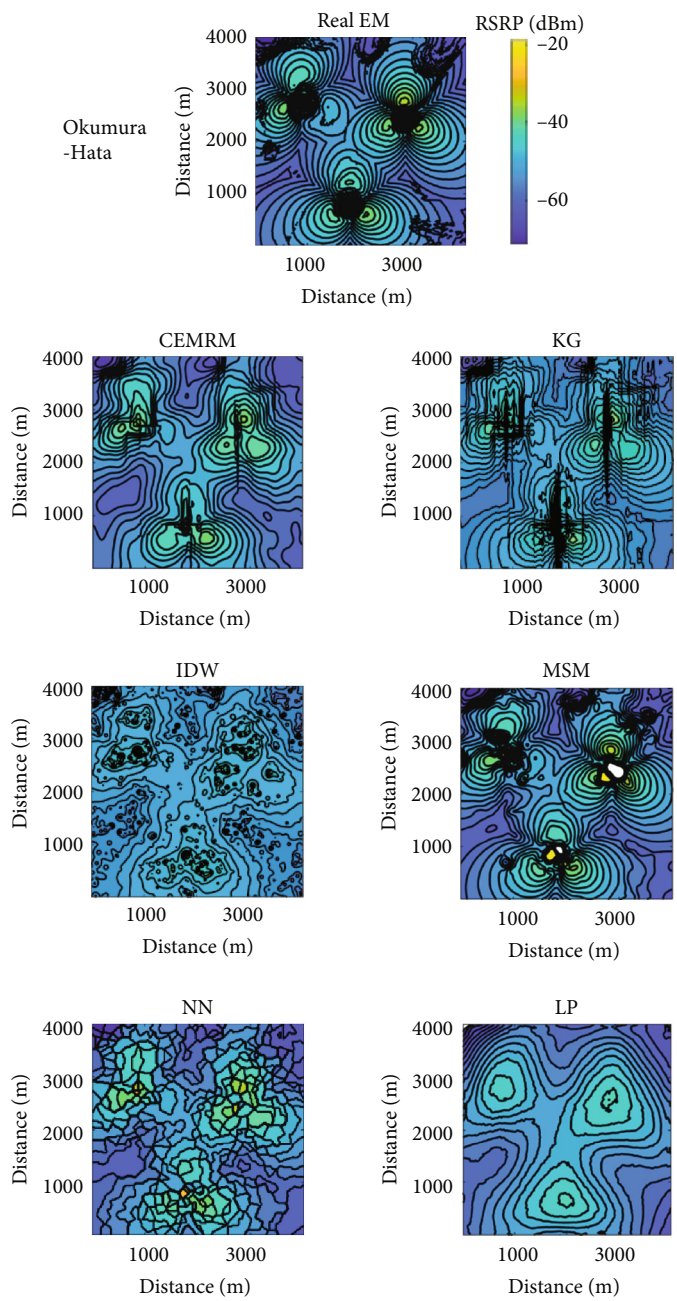

Figure 3: The reconstruction EM results of the proposed method and other five algorithms in the scenario of the Okumura-Hata model.

where Q_{n_1,n_2} is defined as

$$Q_{n_1,n_2}(\boldsymbol{E}) = [n_1 \leq E_{l,n} \leq n_2, \forall l, n]. \tag{19}$$

4. Simulation Results

4.1. Indicator Description. We use four indicators to demonstrate advantages of the proposed method, which are the root mean square error (RMSE), determination coefficient (R^2), robustness, and quality of the reconstructed EM (QoM).

RMSE represents the average error between the reconstructed ED and real ED. If the RMSE is small, the result is accurate. Equation (20) shows the calculating procedure of RMSE. R^2 represents the similarity of the data distribution between the reconstructed ED and real ED. If the value is high, the data distribution of the reconstructed ED is similar to that of the real ED. That is, the reconstructed EMs are realistic. Equation (21) shows the calculating procedure of R^2. What we study is the EM reconstruction with a small number of sensing nodes. Therefore, if the available sensing nodes decrease, the effect of the method should not decrease

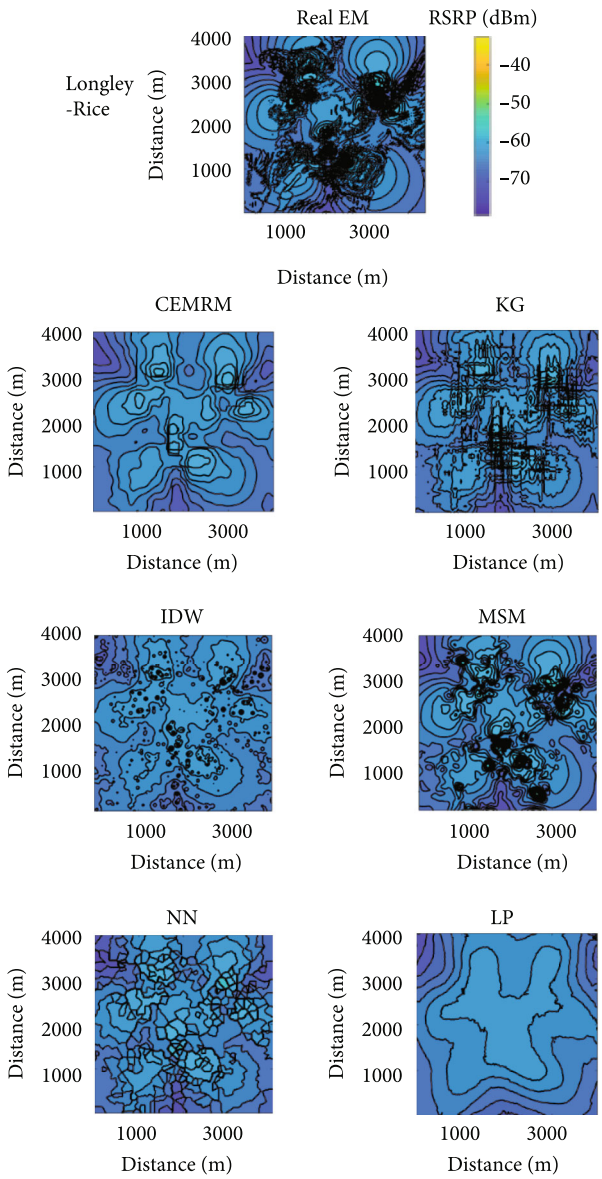

Figure 4: The reconstruction EM results of the proposed method and other five algorithms in the scenario of the Longley-Rice model.

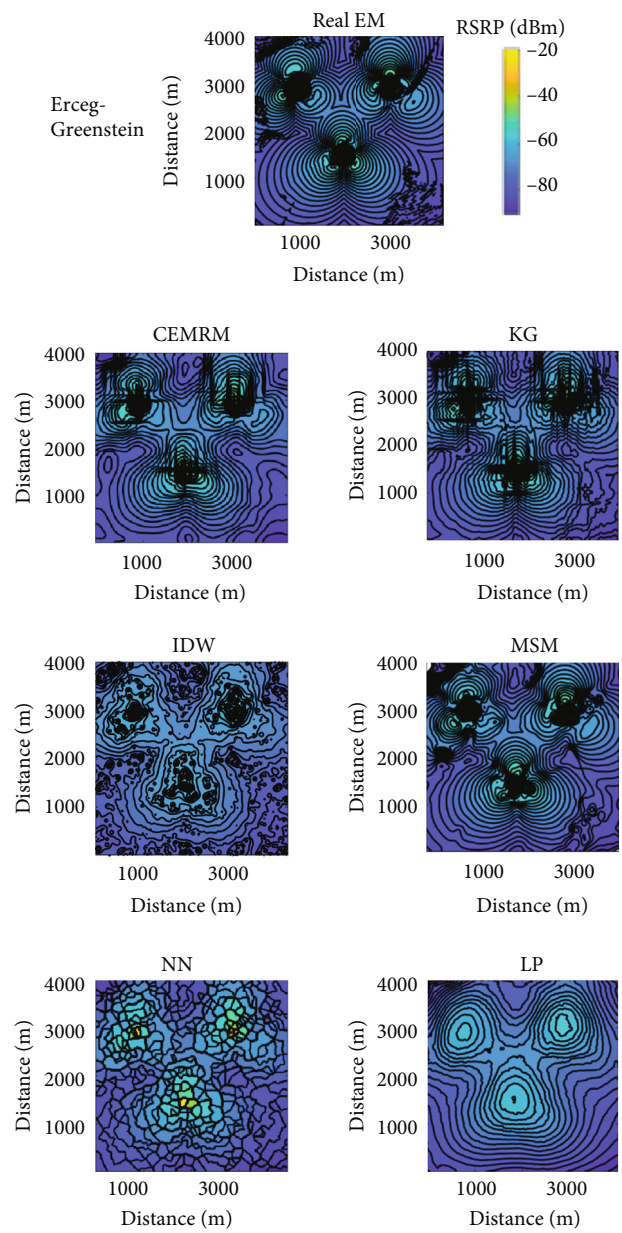

Figure 5: The reconstruction EM results of the proposed method and other five algorithms in the scenario of the Erceg-Greenstein model.

too much. That is, the method needs a good robustness. The robustness is defined as the changing range of the RMSE when the ratio of sensing nodes to the total number of ED decreases from 10% to 2%. QoM is mainly judged according to the bull's eye, the similarity of isomagnetic lines between the reconstructed result and the real EM. The RMSE and R^2 are given by

$$\mathrm{RMSE} = \frac{1}{ii \times jj} \sum_{l=1,n}^{ii} \sum_{l,n=1}^{jj} \left(\widehat{E_{l,n}} - E_{l,n} \right)^2, \tag{20}$$

$$\begin{aligned} \bar{E} &= \frac{1}{ii \times jj} \sum_{l=1,n}^{ii} \sum_{l,n=1}^{jj} E_{l,n}, \\ P_{\mathrm{tot}} &= \sum_{l=1,n}^{ii} \sum_{l,n=1}^{jj} \left(E_{l,n} - \bar{E} \right)^2, \\ P_{\mathrm{res}} &= \sum_{l=1,n}^{ii} \sum_{l,n=1}^{jj} \left(\widehat{E_{l,n}} - \bar{E} \right)^2, \\ R^2 &= 1 - \frac{P_{\mathrm{res}}}{P_{\mathrm{tot}}}, \end{aligned} \tag{21}$$

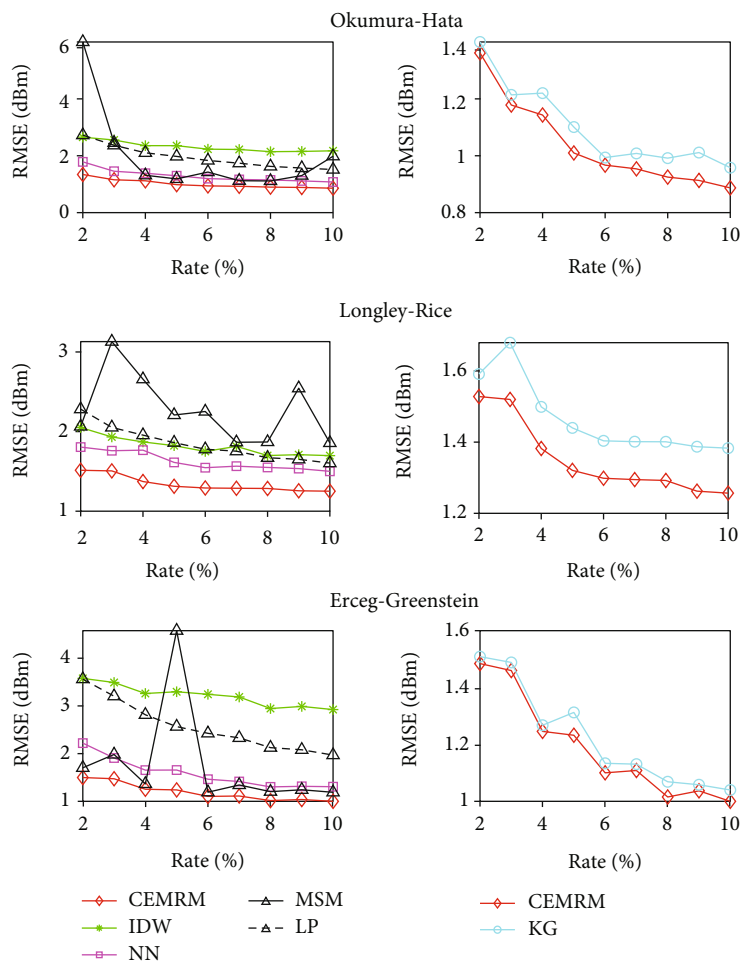

Figure 6: The RMSE results of the reconstructed EMs when the ratio of sensing nodes to the total number of ED decreases from 10% to 2%. IDW in [8], KG in [7], and MSM, NN, and LP in [22].

Table 2: R^2 of reconstruction EM results when the ratio of sensing nodes to the total number of ED is 2%.

Type	CEMRM	KG	IDW	MSM	LP	NN
Okumura-Hata	0.9539	0.9512	0.8198	0.0776	0.8097	0.9183
Longley-Rice	0.8398	0.8264	0.7040	0.7002	0.6330	0.7713
Erceg-Greenstein	0.9748	0.9739	0.8499	0.9671	0.8512	0.9433

where $\bar{E}$ is the average value of the real ED, $E_{l,n}$ is the (l, n)th real electromagnetic datum, $\widehat{E_{l,n}}$ is the corresponding reconstructed electromagnetic datum, P_{res} is the residual sum of squares, and P_{tot} is the total sum of squares.

4.2. Results and Analyses. Three base stations are arranged in an area of 4000 m × 4000 m, and the reference signal receiving power data of the long-term evolution (LTE) mobile communication network in this area are used as the experimental data. The data are generated by the currently highly recognized software Atoll, and the landform of Brussels are taken into account. The Okumura-Hata model, Longley-Rice model, and Erceg-Greenstein model are adopted as the propagation models. The frequency of electromagnetic signal is 2110 MHz, and the bandwidth is 10 MHz. The equivalent antenna height of base stations is set to 30 m, and that of detection equipments is 1.5 m. The extended matrix of the Longley-Rice model is set to 5500 m, and that of other models is set to 7000 m. All main matrices of three models are set to 4000 m. Other settings remain the original settings. The total number of the ED is 40000. The area is divided into four parts, and 200 low-cost sensing nodes are randomly deployed in each part, the ratio of sensing nodes to the total number of ED is 2%. The experimental platform is based on core i9, the software used is MATLAB R2020b, Atoll 2.8.0, Surfer 14.

If the terrain of the target area doesn't change drastically, the Okumura-Hata model is applicable. If the terrain of the target area changes drastically, the Longley-Rice model is applicable; the Erceg-Greenstein model is applicable for scenarios with shadowing. To obtain convincing results and decrease the redundant work, the abovementioned models are used.

Table 1 gives the average running time of the proposed FSSAMP and SAMP. It is seen that the average running time of FSSAMP is 7.08% accounting for that of SAMP, the proposed FSSAMP is faster than SAMP.

In order to prove the advantages of the proposed CEMRM, we adopt the modified shepard's method (MSM), KG, IDW, LP, and NN to reconstruct the EMs. What we study is the EM reconstruction in the noncooperation environment, the information of electromagnetic environment, especially the propagation models, cannot be obtained, so the indirect methods are not achievable.

Figures 3–5 show the reconstruction EM results in the different scenarios of three typical propagation models. From the three figures, it is seen that the results of IDW have lots of bull's eyes, the isomagnetic lines are greatly different from those of the real EMs; the results of MSM have fewer bull's eyes than those of IDW, there are two big white holes in the result; the results of NN have few bull's eyes, but the results are not continuous, which are different from the real EMs; the results of LP have few bull's eyes, but the results contain little changing information of electromagnetic wave, which are different from the real EMs; the results of KG have few bull's eyes, but the results cannot express the information at the locations close to base stations; the results of CEMRM have few bull's eyes, the results can express the information at the locations close to base stations, the results of CEMRM are more similar to real EMs than KG. To sum up, the QoM of CEMRM is better than that of any other algorithm mentioned above.

Figure 6 shows the changing situation in RMSE when the ratio of sensing nodes to the total number of ED decreases from 10% to 2%. It is obviously that the proposed CEMRM has the lowest RMSE in all situations. The average changing range in RMSE of the proposed CEMRM is 0.4264, the second smallest. The average changing range in RMSE of KG is 0.3887, which is the smallest. Compared with KG, the change of the proposed CEMRM in RMSE is more stable than that of KG. After comprehensive consideration, the proposed CEMRM has the better robustness than any other five algorithms.

Table 2 gives the result of R^2 between the reconstructed ED and real ED, and the ratio of sensing nodes to the total number of ED is 2%. From Table 2, it can be clearly seen that the R^2 of the results obtained by CEMRM is the largest, so the distribution of the reconstructed ED obtained by CEMRM is the most similar to the real ED.

From the comprehensive consideration of RMSE, R^2, robustness, QoM, it can be concluded that the effect of CEMRM is better than those of the existing KG, IDW, NN, LP, and MSM. The proposed CEMRM is promising to achieve the efficient application of spectrum resources and green communications in various fields [23, 24].

5. Conclusions

In order to obtain the complete and accurate ED with limited sensing nodes in the noncooperation situation, we proposed a new and practical scheme using EMs and a small number of sensing nodes, and an accurate EM reconstruction method, called CEMRM. After obtaining the incomplete sampled ED from sensing nodes, the proposed CEMRM can reconstruct the complete and accurate ED and build realistic EMs. The required minimum number of sensing nodes accounting for the total number of ED is just 2%. Compared to the existing methods of reconstructing the EMs, the proposed CEMRM remains better robustness against the decreasing of sensing nodes and obtains more accurate ED and EMs. The proposed scheme makes a good trade-off between the number of sensing nodes and accuracy of the obtained ED, and the obtained EMs can provide great support for assessing spectrum resources utilization. What we studied is helpful for green communications, high-efficiency spectrum resources utilization, and so on.

Data Availability

There are no available data.

Conflicts of Interest

The authors declare that they have no conflicts of interest.

Acknowledgments

This work was supported in part by the National Natural Science Foundation of China under grant 61971473.

References

[1] M. Liu, C. Liu, M. Li, Y. Chen, S. Zheng, and N. Zhao, "Intelligent passive detection of aerial target in space-air-ground integrated networks," *China Communications*, vol. 19, no. 1, pp. 52–63, 2022.

[2] M. Liu, B. Li, Y. Chen et al., "Location parameter estimation of moving aerial target in space-air-ground integrated networks-based IoV," *IEEE Internet of Things Journal*, vol. 9, no. 8, pp. 5696–5707, 2022.

[3] A. C. Suarez Rodriguez, N. Haider, Y. He, and E. Dutkiewicz, "Network optimisation in 5G networks: a radio environment map approach," *IEEE Transactions on Vehicular Technology*, vol. 69, no. 10, pp. 12043–12057, 2020.

[4] P. Gajewski, "Propagation models in radio environment map design," in *2018 Baltic URSI Symposium (URSI)*, pp. 234–237, Poznan, Poland, May 2018.

[5] M. Pesko, T. Javornik, A. Kosir, M. Stular, and M. Mohorcic, "Radio environment maps: the survey of construction methods," *KSII Transactions on Internet and Information Systems*, vol. 8, no. 11, pp. 3789–3809, 2014.

[6] H. B. Yilmaz and T. Tugcu, "Location estimation-based radio environment map construction in fading channels," *Wireless Communications and Mobile Computing*, vol. 15, no. 3, pp. 561–570, 2015.

[7] S. N. Lophaven, H. B. Nielsen, and J. Søndergaard, "DACE-A MATLAB kriging toolbox," IMM-TR-2002-12, Technical University of Denmark, 2002.

[8] M. Suchański, P. Kaniewski, J. Romanik, E. Golan, and K. Zubel, "Radio environment maps for military cognitive networks: density of small-scale sensor network vs. map quality," *EURASIP Journal on Wireless Communications and Networking*, vol. 2020, no. 1, 2020.

[9] X. Liu, F. Chen, and C. Lu, "Robust prediction and outlier detection for spatial datasets," in *12th IEEE International Conference on Data Mining*, pp. 469–478, Brussels Belgium, Dec. 2012.

[10] H. Xia, S. Zha, J. Huang, and J. Liu, "Radio environment map construction by adaptive ordinary kriging algorithm based on affinity propagation clustering," *International Journal of Distributed Sensor Networks*, vol. 16, no. 5, 2020.

[11] V. Fibriyani and N. Chamidah, "Prediction of inflation rate in Indonesia using local polynomial estimator for time series data," *Journal of Physics: Conference Series*, vol. 1776, no. 1, 2021.

[12] Y. Ruan, Y. Xiao, Z. Hao, and B. Liu, "A nearest-neighbor search model for distance metric learning," *Information Sciences*, vol. 552, pp. 261–277, 2021.

[13] J. Talvitie, M. Renfors, and E. S. Lohan, "Distance-based interpolation and extrapolation methods for RSS-based localization with indoor wireless signals," *IEEE Transactions on Vehicular Technology*, vol. 64, no. 4, pp. 1340–1353, 2015.

[14] K. Sato and T. Fujii, "Kriging-based interference power constraint: integrated design of the radio environment map and transmission power," *IEEE Transactions on Cognitive Communications and Networking*, vol. 3, no. 1, pp. 13–25, 2017.

[15] J. Li, Z. Gao, and Z. Pei, "The radio environment map parameter estimation using kriging method based on propagation model," *Journal of Computational Information Systems*, vol. 11, no. 20, pp. 7607–7616, 2015.

[16] K. Tsukamoto, M. Kitsunezuka, and K. Kunihiro, "Highly accurate radio environment mapping method based on transmitter localization and spatial interpolation in urban LoS/NLoS scenario," in *2018 IEEE Topical Conference on Wireless Sensors and Sensor Networks*, pp. 5–7, Anaheim, CA, USA, Jan. 2018.

[17] J. Lu, S. Zha, J. Huang, P. Liu, G. Chen, and S. Xu, "The iterative completion method of the spectrum map based on the difference of measurement values," in *2018 IEEE 3rd International Conference on Signal and Image Processing*, pp. 255–259, Shenzhen, China, Jul. 2018.

[18] Z. Lin, M. Lin, T. de Cola, J.-B. Wang, W.-P. Zhu, and J. Cheng, "Supporting IoT with rate-splitting multiple access in satellite and aerial-integrated networks," *IEEE Internet of Things Journal*, vol. 8, no. 14, pp. 11123–11134, 2021.

[19] J. Wang, R. Chen, J. Huang, F. Shu, Z. Chen, and G. Min, "Multiple-antenna spectrum sensing method with random arrivals of primary users," *IEEE Transactions on Vehicular Technology*, vol. 67, no. 9, pp. 8978–8983, 2018.

[20] T. T. Do, L. Gan, N. Nguyen, and T. D. Tran, "Sparsity adaptive matching pursuit algorithm for practical compressed sensing," in *Asilomar Conference on Signals, Systems and Computers*, pp. 581–587, Pacific Grove, CA, USA, Oct. 2008.

[21] A. Beck and M. Teboulle, "Fast gradient-based algorithms for constrained total variation image denoising and deblurring problems," *IEEE Transactions on Image Processing*, vol. 18, no. 11, pp. 2419–2434, 2009.

[22] "Surfer14," 2017, https://www.goldensoftware.com/products/surfer.

[23] Z. Lin, H. Niu, K. An et al., "Refracting RIS aided hybrid satellite-terrestrial relay networks: Joint beamforming design and optimization," *IEEE Transactions on Aerospace and Electronic Systems*, 2022.

[24] Z. Lin, M. Lin, J.-B. Wang, T. de Cola, and J. Wang, "Joint beamforming and power allocation for satellite-terrestrial integrated networks with non-orthogonal multiple access," *IEEE Journal of Selected Topics in Signal Processing*, vol. 13, no. 3, pp. 657–670, 2019.

Hindawi
Wireless Communications and Mobile Computing
Volume 2022, Article ID 8729079, 12 pages
https://doi.org/10.1155/2022/8729079

Research Article

Distributed Antenna-and-Relay Selection Schemes for MIMO Cooperative Relay Network

Yang Zhang, Wei Wang, Xiangmo Zhao, and Jun Hou

School of Information Engineering, Chang'an University, Xi'an 710064, China

Correspondence should be addressed to Jun Hou; jhou@chd.edu.cn

Received 24 May 2022; Accepted 21 June 2022; Published 13 July 2022

Academic Editor: Mingqian Liu

Relay selection, antenna selection, and link selection are three potent means to enrich network capacity in MIMO relaying networks. To reduce feedback overhead, in this paper, three distributed antenna-and-relay selection schemes are proposed for AF multiple-relay network, which is equipped with multiple antennas at nodes. Closed-form formulations of system outage probability are derived for these schemes, as well as the lower bounds and upper bounds. Furthermore, the approximate expressions of outage probability at high SNR regime are also derived, showing that the proposed optimal strategy can achieve full diversity order. In addition, link selection scheme can improve spectral efficiency since it saves one time slot when direct link is selected.

1. Introduction

The combined application of cooperative communications and multiple-input multiple-output (MIMO) techniques has attracted much attention in wireless networks [1–3]. It proves to be an effective means to increase system capacity and link reliability. However, these techniques increase the system size, complexity, and cost. Therefore, transmit antenna selection (TAS) methods are proposed at the transmitter side which also can achieve full cooperative diversity with lower complexity of implementation [4, 5]. At the receiver side, some diversity-combining techniques are used, such as maximal-ratio combining (MAC) and selection-combining (SC) [4].

In [6], the SER (symbol error rate) in a MIMO cooperative system which equipped an amplify-and-forward (AF) relay based on TAS/MAC was investigated. Furthermore, in [7], performance comparison between optimal TAS/MAC and TAS/SC strategies was performed in a multirelay MIMO system. Similar comparison was made in [8], which investigated a MIMO decode-and-forward (DF) relaying network. Moreover, authors analysed system outage of the optimal relay and antenna selection strategy in MIMO DF relaying system under Nakagami-m fading conditions in [9]. It is noteworthy that all the authors in [6–9] took no account of the direct link between source and destination. Various TAS strategies were proposed in [10–16] by considering direct path in the system. In [10], both optimal and suboptimal TAS/MAC strategies were proposed in cooperative system which can achieve full diversity. However, the implementation complexity was considerable. To overcome this, in [11], a suboptimal TAS/MAC scheme, namely, DAS was presented, which only needs a low delay/feedback overhead. In [12], two low-cost strategies (DAS/SC and DAS/LS) were proposed for relaying networks based on [11] which achieve full diversity order and nearly-full diversity order, respectively. In [13], similar schemes were proposed in a multiantenna relay system. Furthermore, in [14], one diversity-optimal and three suboptimal TAS/SC strategies were proposed in a multirelay network, which equipped with multiple antennas both at source and the destination and only one antenna at relay. The implementation complexity of three suboptimal schemes is simpler than the diversity-optimal scheme at the cost of reduced performance. In [15, 16], the performance of an optimal TAS/MAC strategy in MIMO AF relaying system is analysed, where the transmitting

antennas in source and relay are selected through the CSI estimates for all links to maximize the SNR received by the destination. Moreover, the distributed algorithms are potent methods in many communication scenarios [17, 18]. Most of the relay and antenna selection schemes in the literature need to estimate the CSI of all links, calculate the signal-to-noise ratio of each possible path at the destination, and require high complexity calculation at each node. In order to reduce implementation complexity, we proposed three distributed relay and antenna selection schemes in a MIMO AF relaying network. Exact formulations of the outage probability are derived as well as upper bounds and lower bounds for all three schemes. And asymptotic expressions at high SNR are also derived for the obtained bounds to evaluate the diversity orders of proposed schemes. Finally, comparisons of all proposed schemes are performed through simulations in terms of spectral efficiency and outage probability.

2. System Model

A MIMO AF relaying network is considered in this paper which compose by a source S with N_s antennas, a destination D with N_d antennas and M relays with N_r antennas, as shown in Figure 1. The direct link between S and D is available, and all nodes in this model are working in the half-duplex mode. The information received in D through the direct $(S_i \longrightarrow D_j)$ and relayed $(S_i \longrightarrow R_{q,l} \longrightarrow D_j)$ links are combined by means of SC, where $i \in \{1, 2, \cdots, N_s\}$, $p, q \in \{1, 2, \cdots, N_r\} p, q \in \{1, 2, \cdots, N_r\}$, $j, \in \{1, 2, \cdots, N_d\}$, and $l \in \{1, 2, \cdots, M\}$.

The transmit antenna and relay selection are executed at S and R before communication process, according to the procedure described in the next section. Then, the traditional two-phase amplify-and-forward cooperative transmission takes place as followed in [16]. Therefore, the end-to-end SNR is

$$\gamma^{i,l,q} = \max\left(\gamma_{S_iD_{j_1}}, \frac{\gamma_{S_iR_{p,l}}\gamma_{R_{q,l}D_{j2}}}{\gamma_{S_iR_{p,l}} + \gamma_{R_{q,l}D_{j2}} + 1}\right), \tag{1}$$

where $\gamma_{S_iD_{j_1}} \triangleq (P_S/N_0)|h_{S_i,D_{j1}}|^2$, $\gamma_{S_iR_{p,l}} \triangleq (P_S/N_0)|h_{S_i,R_{p,l}}|^2$, and $\gamma_{R_{q,l}D_{j2}} \triangleq (P_R/N_0)|h_{R_{q,l},D_{j2}}|^2$.

Herein, P_S and P_R are, respectively, transmit powers in source and relays. h_{S_i,D_j}, $h_{S_i,R_{p,l}}$, and $h_{R_{q,l},D_j}$ denote the channel coefficients between the ith antenna to the jth one in $S \longrightarrow D$ hop, between the ith antenna to the pth one in the $S \longrightarrow R_l$ hop, and the qth antenna to the jth antenna in the $R_l \longrightarrow D$ hop, respectively. N_0 is noise variance of additive white Gaussian noises (AWGNs). As in [19], the amplifying factor at R is $G \triangleq \sqrt{P_S/(P_S E[|h_{S_iR_{p,l}}|^2] + N_0)}$. We assume $\bar{\gamma}_{SD} \triangleq E[\gamma_{S_iD_{j_1}}]$, $\bar{\gamma}_{SR_l} \triangleq E[\gamma_{S_iR_{p,l}}]$, $\bar{\gamma}_{R_lD} \triangleq E[\gamma_{R_{q,l}D_{j2}}]$, $\forall i = 1, \cdots, N_s$, $\forall p = \forall q = 1, \cdots, N_r$, and $\forall j1 = \forall j2 = 1, \cdots, N_d$.

For convenience, some expressions used in this article are listed as

$$\begin{cases} \lambda_{SR_l} = \max_{1\le i\le N_s, 1\le p\le N_r}\left[\gamma_{S_iR_{p,l}}\right], \\ \lambda_{S_{i*}R_l} = \max_{1\le p\le N_r}\left[\gamma_{S_{i*}R_{p,l}}\right], \\ \lambda_{R_lD} = \max_{1\le q\le N_r, 1\le j\le N_d}\left[\gamma_{R_{q,l}D_j}\right], \\ \lambda_{SD} = \max_{1\le i\le N_s, 1\le j\le N_d}\left[\gamma_{S_iD_j}\right], \\ \lambda_l = \min\left(\lambda_{SR_l}, \lambda_{R_lD}\right). \end{cases} \tag{2}$$

The SNR in all links follow an exponential distribution, Therefore, the CDF of λ_{SR_l} is

$$\begin{aligned} F_{\lambda_{SR_l}}(t) &= \Pr\left\{\lambda_{SR_l} < t\right\} = \Pr\left\{\max_{1\le i\le N_s, 1\le p\le N_r}\left[\gamma_{S_iR_{p,l}}\right] < t\right\} \\ &= \left[1 - \exp\left(-\frac{t}{\bar{\gamma}_{SR_l}}\right)\right]^{N_sN_r}. \end{aligned} \tag{3}$$

Similarly [20], the CDF of $\lambda_{S_{i*}R_l}$, λ_{R_lD}, and λ_{SD} can be, respectively, obtained by $F_{\lambda_{S_{i*}R_l}}(t) = [1 - \exp(-t/\bar{\gamma}_{SR_l})]^{N_r}$, $F_{\lambda_{R_lD}}(t) = [1 - \exp(-t/\bar{\gamma}_{R_lD})]^{N_rN_d}$, and $F_{\lambda_{SD}}(t) = [1 - \exp(-t/\bar{\gamma}_{SD})]^{N_sN_d}$.

Therefore, the PDF of λ_{SR_l}, λ_{R_lD}, and λ_{SD} can be, respectively, expressed by

$$f_{\lambda_{SR_l}}(t) = \frac{dF_{\lambda_{SR_l}}(t)}{dt} = \frac{N_sN_r\exp\left(-t/\bar{\gamma}_{SR_l}\right)}{\bar{\gamma}_{SR_l}}\left[1 - \exp\left(-\frac{t}{\bar{\gamma}_{SR_l}}\right)\right]^{N_sN_r-1}, \tag{4}$$

$$f_{\lambda_{SD}}(t) = \frac{N_sN_d\exp(-t/\bar{\gamma}_{SD})}{\bar{\gamma}_{SD}}\left[1 - \exp\left(-\frac{t}{\bar{\gamma}_{SD}}\right)\right]^{N_sN_d-1}, \tag{5}$$

$$f_{\lambda_{R_lD}}(t) = \frac{N_rN_d\exp\left(-t/\bar{\gamma}_{R_lD}\right)}{\bar{\gamma}_{R_lD}}\left[1 - \exp\left(-\frac{t}{\bar{\gamma}_{R_lD}}\right)\right]^{N_rN_d-1}. \tag{6}$$

3. Antenna and Relay Selection Scheme

Optimal relay and transmitting antenna selection criterion [16] needs a large amount of feedback overhead and also considerable computation complexity in destination. Therefore, we propose three schemes to accomplish the relay and transmitting antenna selection by lower complexity and less feedback overhead. Moreover, the diversity-combining technique used in our work is SC which can also reduce the system complexity.

3.1. DAS/SC Optimal Scheme. The following is the steps involved in antenna and relay selection.

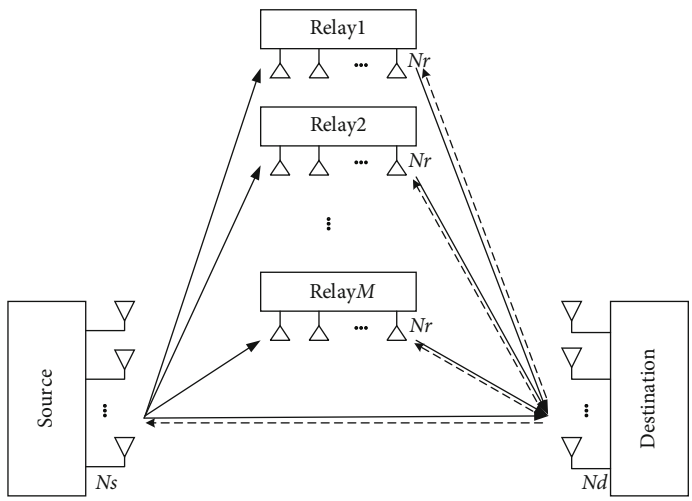

Figure 1: MIMO AF relaying network.

(i) *Step 1.* D from each antenna broadcasts 1-bit reverse pilot signal [13], thus, all relays and source can estimate instantaneous SNR value toward to D. Therefore, the best transmit antenna of l-th relay can be selected

$$\{q_l\} = \arg\ \max_{1\le q\le N_r, 1\le j\le N_d}\left[\gamma_{R_{q,l}D_j}\right]. \tag{7}$$

(ii) *Step 2.* The i -th source antenna broadcasts a pilot signal, and R and D receive this signal by means of SC

(iii) *Step 3.* Each relay amplifies and forwards the receive signal through the respective selected transmitting antenna in turn. D receives them by the means of SC and selects the best relay based on the following decision rule

$$\{l_i\} = \arg\ \max_{1\le l\le M, 1\le j\le N_d}\left[\frac{\gamma_{S_iR_{p_l,l}}\gamma_{R_{q_l,l}D_{j2}}}{\gamma_{S_iR_{p_l,l}}+\gamma_{R_{q_l,l}D_{j2}}+1}\right]. \tag{8}$$

Moreover, D combines signal from the best relay and the signal from Step 2 by the means of SC. Therefore, SNR of the system where signal delivered from the ith source antenna is

$$\gamma^{i,l_i,q_{l_i}} = \max\left\{\gamma_{S_iD_{j_1}}, \frac{\gamma_{S_iR_{p_l,l_i}}\gamma_{R_{q_l,l_i}D_{j2}}}{\gamma_{S_iR_{p_l,l_i}}+\gamma_{R_{q_l,l_i}D_{j2}}+1}\right\}. \tag{9}$$

(iv) *Step 4.* Let $i = i + 1$, make $i = N_s$ by repeating Steps 2 and 3. Then, the best transmit antenna of source in this system is

$$\{i*, j*, q*\} = \arg\ \max_i\left[\gamma^{i,l_i,q_{l_i}}\right], \tag{10}$$

where $i*$, $l*$, and $q*$ are the selected source transmitting antenna, the selected relay, and the relay transmitting antenna, respectively.

(v) *Step 5.* Source start communication process, where the $i*$ th source antenna deliver signals to destination with the aid of the $l*$ th relay. Here, D combines signal from S in first slot and signal from R in second slot using selective combining. End-to-end SNR of this system is

$$\gamma^{i*,l*,q*} = \max_i\left[\gamma^{i,l*,q*}\right]. \tag{11}$$

3.2. DAS/SC Suboptimal Scheme. The DAS/SC suboptimal strategy is presented to reduce signal overhead. The selection of source transmitting antenna relies solely on the direct link. The following is the steps involved in this scheme.

(i) *Step 1.* The same with Step 1 in DAS/SC optimal scheme. The best transmit antenna of source are selected based on the following decision rule

$$\{i*\} = \arg\ \max_{1\le i\le N_r, 1\le j\le N_d}\left[\gamma_{S_iD_j}\right]. \tag{12}$$

SNR from S to D is

$$\gamma_{S_{i*}D_{j1}} = \max_{1\le i\le N_r, 1\le j\le N_d}\left[\gamma_{S_iD_j}\right]. \tag{13}$$

(ii) *Step 2.* The $i*$ th source antenna broadcasts a pilot signal, and R receives this signal by means of SC. Then, each relay estimate SNR of the relayed $(S_i \longrightarrow R_{q,l} \longrightarrow D_j)$ link using

$$\gamma_{S_{i*}R_{p_l,l,q_l}D_j} = \frac{\gamma_{S_{i*}R_{p_l,l}}\gamma_{R_{q_l,l}D_j}}{\gamma_{S_{i*}R_{p_l,l}} + \gamma_{R_{q_l,l}D_j} + 1}. \tag{14}$$

Afterward, each relay node starts a timer according to its own estimate SNR. Similar to [21], the initial value T_l of this timer is inversely proportional to the relayed link SNR $\gamma_{S_{i*}R_{p_l,l,q_l}D_j}$, according to the following equation:

$$T_l = \left\lfloor \frac{\alpha}{\gamma_{S_{i*}R_{p_l,l,q_l}D_j}} \right\rfloor. \tag{15}$$

Here, α is a constant value.

(iii) *Step 3.* The "best" relay gets expired first. The relay selection can be expressed as (16). And it broadcasts feedback information. Other relays stop their timer as soon as receiving this information. Meanwhile, source starts its communication process, where the $i*$ th source antenna transmits signal to destination with the aid of the $l*$ th relay

$$\{l*\} = \arg\min\,[T_l]. \tag{16}$$

(iv) *Step 4.* Source start communication process. The end-to-end SNR in the network is

$$\gamma^{i*,l*,q*} = \max\left\{\gamma_{S_{i*}D_{j1}}, \gamma_{S_{i*}R_{p_{l*},l*,q_{l*}}D_{j2}}\right\}. \tag{17}$$

3.3. DAS/LS Scheme. The DAS/LS is proposed to improve the spectral efficiency. And the following are the steps contained in DAS/LS scheme for choosing relay and transmitting antenna.

(i) *Step 1.* The same with Step 1 in DAS/SC suboptimal scheme. The SNR from S to D is expressed in (13). If $\gamma_{S_{i*}D_{j1}} > 2^{R_0} - 1$, where R_0 is system transmission rate. S broadcasts feedback information to all R and D. And source starts communication process, where the $i*$ th source antenna delivers signal to destination only through the direct link

(ii) *Step 2.* If $\gamma_{S_{i*}D_{j1}} < 2^{R_0} - 1$, the $i*$ th source antenna broadcasts a pilot signal, and R receives this signal by means of SC. Then, each antenna estimates SNR of the relayed $(S_{i*} \longrightarrow R_l \longrightarrow D_j)$ link just like Step 2 and Step 3 in DAS/SC suboptimal scheme

(iii) *Step 3.* The transmitting antenna of source starts its communication process only through the relayed $(S_{i*} \longrightarrow R_{l*} \longrightarrow D_j)$ link

4. Performance Analysis

The outage probability of the proposed schemes is obtained in this chapter. And asymptotic analysis is executed, as well as the diversity order.

4.1. DAS/SC Optimal Scheme. Outage probability is mathematically formulated as

$$\begin{aligned}
P_{\text{out}}^{\text{opt-sc}} &= \Pr\left\{\frac{1}{2}\log\left(1+\gamma^{i*,l*,q*}\right) < R_0\right\} \\
&= \Pr\left\{\max\left[\gamma_{S_{i*}D_{j1}}, \underbrace{\frac{\gamma_{S_{i*}R_{p*,l*}}\gamma_{R_{q*,l*}D_{j2}}}{\gamma_{S_{i*}R_{p*,l*}} + \gamma_{R_{q*,l*}D_{j2}} + 1}}_{\gamma_{S_{i*}R_{p*},l*,q*}D_{j2}}\right] < 2^{2R_0} - 1\right\} \\
&= \Pr\left\{\max_{i,j}\gamma_{S_iD_j} < z\right\} \cdot \Pr\left\{\max_{i,p,l,q,j}\gamma_{S_iR_{p,l,q}D_j} < z\right\} \\
&= F_{\lambda_{SD}}(z) \cdot \prod_{l=1}^{M}\Pr\left\{\frac{\max_{i,p,l}\gamma_{S_iR_{p,l}} \cdot \max_{l,q,j}\gamma_{R_{l,q}D_j}}{\max_{i,p,l}\gamma_{S_iR_{p,l}} + \max_{l,q,j}\gamma_{R_{l,q}D_j} + 1} < z\right\} \\
&= F_{\lambda_{SD}}(z) \cdot \prod_{l=1}^{M}\underbrace{\Pr\left\{\frac{\lambda_{SR_l} \cdot \lambda_{R_lD}}{\lambda_{SR_l} + \lambda_{R_lD} + 1} < z\right\}}_{\psi},
\end{aligned} \tag{18}$$

where $z = 2^{2R_0} - 1$, and R_0 is the system transmission rate.

Theorem 1. *The exact outage expression of DAS/SC optimal strategy is given in (19).*

$$\begin{aligned}
P_{\text{out}}^{\text{opt-sc}} = \left[1 - \exp\left(-\frac{z}{\bar{\gamma}_{SD}}\right)\right]^{N_sN_d} \cdot \prod_{l=1}^{M}\Bigg\{\left[1 - \exp\left(-\frac{z}{\bar{\gamma}_{R_lD}}\right)\right]^{N_rN_d} + N_rN_d \cdot \Bigg\{\sum_{j=0}^{N_rN_d-1}\left[\binom{N_rN_d-1}{j} \cdot \frac{(-1)^j}{j+1}e^{-z\cdot(j+1)/\bar{\gamma}_{R_lD}}\right] \\
+ \sum_{i=1}^{N_sN_r}\sum_{j=0}^{N_rN_d-1}\binom{N_sN_r}{i}\binom{N_rN_d-1}{j}(-1)^{i+j}e^{-z\cdot i/\bar{\gamma}_{SR_l} - z\cdot(j+1)/\bar{\gamma}_{R_lD}} \cdot \sqrt{\frac{4i(z^2+z)}{\bar{\gamma}_{SR_l}\cdot\bar{\gamma}_{R_lD}(j+1)}}K_1\left(\sqrt{\frac{4i(j+1)(z^2+z)}{\bar{\gamma}_{SR_l}\cdot\bar{\gamma}_{R_lD}}}\right)\Bigg\}\Bigg\},
\end{aligned} \tag{19}$$

where $K_1(\bullet)$ denotes the modified Bessel function of the second kind.

Proof. See Appendix A. □

The expression is difficult to evaluate the diversity order. So, we analyse asymptotic outage expressions to get the diversity order. First, the analysis of lower bound is considered, which can be derives as

$$P_{\text{out-LB}}^{\text{opt-sc}} = F_{\lambda_{SD}}(z) \cdot \underbrace{\prod_{l=1}^{M}\left[F_{\lambda_{SR_l}}(z) + F_{\lambda_{R_lD}}(z) - F_{\lambda_{SR_l}}(z) \cdot F_{\lambda_{R_lD}}(z)\right]}_{\varphi}. \tag{20}$$

Proof. See Appendix B. □

Now, we concentrate on the behaviour of lower bound in high-SNR regime.

Corollary 2. *Asymptotic expression of φ in high-SNR regime is*

$$\varphi \simeq \sum_{i=0}^{M}\binom{M}{i}\left(\frac{z}{\bar{\gamma}_{SR}}\right)^{N_sN_r(M-i)}\left(\frac{z}{\bar{\gamma}_{RD}}\right)^{N_rN_di}. \tag{21}$$

Proof. See Appendix C. □

Then, an asymptotically expression for lower bound in high-SNR regime is

$$\begin{aligned} P_{\text{out-LB}}^{\text{opt-sc}} &\overset{\bar{\gamma}\longrightarrow\infty}{\simeq} \left[1-\exp\left(-\frac{z}{\bar{\gamma}_{SD}}\right)\right]^{N_sN_d} \cdot \sum_{l=0}^{M}\binom{M}{i}\left(\frac{z}{\bar{\gamma}_{SR}}\right)^{N_sN_r(M-i)}\left(\frac{z}{\bar{\gamma}_{RD}}\right)^{N_rN_di} \\ &\simeq \left(\frac{z}{\bar{\gamma}_{SD}}\right)^{N_sN_d} \cdot \sum_{l=0}^{M}\binom{M}{l}\left(\frac{z}{\bar{\gamma}_{SR}}\right)^{N_sN_r(M-i)}\left(\frac{z}{\bar{\gamma}_{RD}}\right)^{N_rN_di} \\ &= \sum_{l=0}^{M}\binom{M}{l}\frac{z^{N_sN_d+N_sN_r(M-l)+N_rN_dl}}{\bar{\gamma}_{SD}{}^{N_sN_d}\cdot\bar{\gamma}_{SR}{}^{N_sN_r(M-l)}\cdot\bar{\gamma}_{RD}{}^{N_rN_dl}}. \end{aligned} \tag{22}$$

For another, an upper bound for (18) is

$$\begin{aligned} P_{\text{out}}^{\text{opt-sc}} &= \Pr\left\{\max\left[\max_{i,j}\gamma_{S_iD_j}, \max_{i,p,l,q,j}\gamma_{S_iR_{p,l,q}D_j}\right] < 2^{2R_0}-1\right\} \simeq \Pr\left\{\max\left[\max_{i,j}\gamma_{S_iD_j}, \max_{i,p,l,q,j}\frac{\gamma_{S_iR_{p,l}}\gamma_{R_{q,l}D_j}}{\gamma_{S_iR_{p,l}}+\gamma_{R_{q,l}D_j}}\right] < 2^{2R_0}-1\right\} \\ &\underset{(e)}{\leq} \Pr\left\{\max_{i,j}\gamma_{S_iD_j} < z\right\} \cdot \Pr\left\{\max_{l}\left[\frac{1}{2}\min\left(\max\left(\gamma_{S_iR_{p,l}}\right), \max\left(\gamma_{R_{q,l}D_j}\right)\right)\right] < z\right\} = F_{\lambda_{SD}}(z) \cdot \underbrace{\prod_{l=1}^{M}\left[F_{\lambda_{SR_l}}(2z) + F_{\lambda_{R_lD}}(2z) - F_{\lambda_{SR_l}}(2z) \cdot F_{\lambda_{R_lD}}(2z)\right]}_{\phi} = P_{\text{out-UB}}^{\text{opt-sc}}, \end{aligned} \tag{23}$$

where (e) is obtained according to (B.2).

Similar to φ, ϕ in high-SNR regime is

$$\phi \simeq \sum_{i=0}^{M}\binom{M}{i}\left(\frac{2z}{\bar{\gamma}_{SR}}\right)^{N_sN_r(M-i)} \cdot \left(\frac{2z}{\bar{\gamma}_{RD}}\right)^{N_rN_di}. \tag{24}$$

Therefore, an asymptotically expression for upper bound in high-SNR regime is

$$P_{\text{out-UB}}^{\text{opt-sc}} \overset{\bar{\gamma}\longrightarrow\infty}{\simeq} \left[1-\exp\left(-\frac{z}{\bar{\gamma}_{SD}}\right)\right]^{N_sN_d} \cdot \sum_{i=0}^{M}\binom{M}{i}\left(\frac{2z}{\bar{\gamma}_{SR}}\right)^{N_sN_r(M-i)}\left(\frac{2z}{\bar{\gamma}_{RD}}\right)^{N_rN_di} \simeq \sum_{i=0}^{M}\binom{M}{i}\frac{z^{N_sN_d}(2z)^{N_sN_r(M-i)+N_rN_di}}{\bar{\gamma}_{SD}{}^{N_sN_d}\bar{\gamma}_{SR}{}^{N_sN_r(M-i)}\bar{\gamma}_{RD}{}^{N_rN_di}}. \tag{25}$$

Remark 3. As shown in (22) and (25), the diversity order of DAS/SC optimal strategy is equal to $N_sN_d + MN_r \min(N_s, N_d)$.

4.2. DAS/SC Suboptimal Scheme. Mathematica formulation for the outage probability of DAS/SC suboptimal strategy is

$$P_{\text{out}}^{\text{sub-sc}} = \Pr\left\{\frac{1}{2}\log\left(1+\gamma^{i*,l*,q*}\right) < R_0\right\} = \Pr\left\{\frac{1}{2}\log\left(1+\max_{i,j}\left[\gamma_{S_iD_j}, \gamma_{S_iR_{p,l,q}D_j}\right]\right) < R_0\right\}. \tag{26}$$

Similar to (19), the closed-form expression of outage probability is

$$\begin{aligned} P_{\text{out}}^{\text{opt-sc}} = {} & \left[1-\exp\left(-\frac{z}{\bar{\gamma}_{SD}}\right)\right]^{N_sN_d} \cdot \prod_{l=1}^{M}\left\{\left[1-\exp\left(-\frac{z}{\bar{\gamma}_{R_lD}}\right)\right]^{N_rN_d} + N_rN_d \cdot \left\{\sum_{j=0}^{N_rN_d-1}\left[\binom{N_rN_d-1}{j}\cdot\frac{(-1)^j}{j+1}e^{-z\cdot(j+1)/\bar{\gamma}_{R_lD}}\right]\right.\right. \\ & \left.\left. + \sum_{i=1}^{N_r}\sum_{j=0}^{N_rN_d-1}\binom{N_r}{i}\binom{N_rN_d-1}{j}(-1)^{i+j}e^{-z\cdot i/\bar{\gamma}_{SR_l}-z\cdot(j+1)/\bar{\gamma}_{R_lD}}\cdot\sqrt{\frac{4i(z^2+z)}{\bar{\gamma}_{SR_l}\cdot\bar{\gamma}_{R_lD}(j+1)}}K_1\left(\sqrt{\frac{4i(j+1)(z^2+z)}{\bar{\gamma}_{SR_l}\cdot\bar{\gamma}_{R_lD}}}\right)\right\}\right\}. \end{aligned} \tag{27}$$

It is not easy to get the exact solution to this probability. Alternatively, lower bound and upper bound for it are derived.

Similarly, lower bound and upper bounds of the DAS/SC suboptimal scheme are

$$P_{\text{out-LB}}^{\text{sub-sc}} = F_{\lambda_{SD}}(z)\cdot\prod_{l=1}^{M}\left[F_{\lambda_{S_{i*}R_l}}(z) + F_{\lambda_{R_lD}}(z) - F_{\lambda_{S_{i*}R_l}}(z)\cdot F_{\lambda_{R_lD}}(z)\right], \tag{28}$$

$$P_{\text{out-UB}}^{\text{sub-sc}} = F_{\lambda_{SD}}(z)\cdot\prod_{l=1}^{M}\left[F_{\lambda_{S_{i*}R_l}}(2z) + F_{\lambda_{R_lD}}(2z) - F_{\lambda_{S_{i*}R_l}}(2z)\cdot F_{\lambda_{R_lD}}(2z)\right]. \tag{29}$$

Asymptotically expressions for the lower and upper bounds in high-SNR regime are

$$P_{\text{out-LB}}^{\text{sub-sc}} \overset{\bar{\gamma}\longrightarrow\infty}{\simeq} \sum_{l=0}^{M}\binom{M}{l}\frac{z^{N_sN_d+N_r(M-l)+N_rN_dl}}{\bar{\gamma}_{SD}{}^{N_sN_d}\cdot\bar{\gamma}_{SR}{}^{N_r(M-l)}\cdot\bar{\gamma}_{RD}{}^{N_rN_dl}}, \tag{30}$$

$$P_{\text{out-UB}}^{\text{sub-sc}} \overset{\bar{\gamma}\longrightarrow\infty}{\simeq} \left[1-\exp\left(-\frac{t}{\bar{\gamma}_{SD}}\right)\right]^{N_sN_d}\cdot\sum_{i=0}^{M}\binom{M}{i}\left(\frac{2z}{\bar{\gamma}_{SR}}\right)^{N_r(M-i)}\left(\frac{2z}{\bar{\gamma}_{RD}}\right)^{N_rN_di} \simeq \sum_{i=0}^{M}\binom{M}{i}\frac{z^{N_sN_d}(2z)^{N_r(M-i)+N_rN_di}}{\bar{\gamma}_{SD}{}^{N_sN_d}\bar{\gamma}_{SR}{}^{N_r(M-i)}\bar{\gamma}_{RD}{}^{N_rN_di}}. \tag{31}$$

Remark 4. As shown in (30) and (31), the diversity order of DAS/SC suboptimal strategy is equal to $N_sN_d + MN_r \min(1, N_d)$.

4.3. DAS/LS Scheme. Outage probability of DAS/LS strategy is

$$P_{\text{out}}^{\text{DAS/LS}} = \Pr\left\{\max_{i,j}\gamma_{S_iD_j} < 2^{R_0}-1\right\}\bullet\Pr\left\{\frac{1}{2}\log\left(1+\max_{p,l,q,j}\gamma_{S_{i*}R_{p,l,q}D_j}\right) < R_0\right\}. \tag{32}$$

Again, closed-form expression can be obtained as

$$\begin{aligned} P_{\text{out}}^{\text{opt-sc}} = {} & \left[1-\exp\left(-\frac{2^{R_0}-1}{\bar{\gamma}_{SD}}\right)\right]^{N_sN_d} \cdot \prod_{l=1}^{M}\left\{\left[1-\exp\left(-\frac{z}{\bar{\gamma}_{R_lD}}\right)\right]^{N_rN_d} + N_rN_d \cdot \left\{\sum_{j=0}^{N_rN_d-1}\left[\binom{N_rN_d-1}{j}\cdot\frac{(-1)^j}{j+1}e^{-z\cdot(j+1)/\bar{\gamma}_{R_lD}}\right]\right.\right. \\ & \left.\left. + \sum_{i=1}^{N_r}\sum_{j=0}^{N_rN_d-1}\binom{N_r}{i}\binom{N_rN_d-1}{j}(-1)^{i+j}e^{-z\cdot i/\bar{\gamma}_{SR_l}-z\cdot(j+1)/\bar{\gamma}_{R_lD}}\cdot\sqrt{\frac{4i(z^2+z)}{\bar{\gamma}_{SR_l}\cdot\bar{\gamma}_{R_lD}(j+1)}}K_1\left(\sqrt{\frac{4i(j+1)(z^2+z)}{\bar{\gamma}_{SR_l}\cdot\bar{\gamma}_{R_lD}}}\right)\right\}\right\}. \end{aligned} \tag{33}$$

Again, we analyse its upper and lower bounds. The lower bound is given by

$$P_{\text{out}}^{\text{DAS/LS}} = \left[1 - \exp\left(-\frac{2^{R_0}-1}{\bar{\gamma}_{SD}}\right)\right]^{N_s N_d} \cdot \Pr\left\{\frac{1}{2}\log\left(1 + \max_{i,p,q,l,j}\left[\gamma_{S_i R_{p,l,q} D_j}\right]\right) < R_0\right\} \simeq F_{\lambda_{SD}}\left(2^{R_0}-1\right) \cdot \prod_{l=1}^{M}\left[F_{\lambda_{S*R_l}}(z) + F_{\lambda_{R_l D}}(z) - F_{\lambda_{S*R_l}}(z) \cdot F_{\lambda_{R_l D}}(z)\right] \triangleq P_{\text{out-LB}}^{\text{DAS/LS}}. \tag{34}$$

In high-SNR regime, (34) can be expressed as

$$P_{\text{out-LB}}^{\text{DAS/LS}} \overset{\gamma \longrightarrow \infty}{\simeq} \left(\frac{2^{R_0}-1}{\bar{\gamma}_{SD}}\right)^{N_s N_d} \cdot \sum_{i=0}^{M}\binom{M}{i}\left(\frac{z}{\bar{\gamma}_{SR}}\right)^{N_r(M-i)}\left(\frac{z}{\bar{\gamma}_{RD}}\right)^{N_r N_d i}. \tag{35}$$

On the other hand, the upper bound is

$$P_{\text{out-UB}}^{\text{DAS/LS}} = F_{\lambda_{SD}}\left(2^{R_0}-1\right) \cdot \prod_{l=1}^{M}\left[F_{\lambda_{SR_l}}(2z) + F_{\lambda_{R_l D}}(2z) - F_{\lambda_{SR_l}}(2z) \cdot F_{\lambda_{R_l D}}(2z)\right] \overset{\gamma \longrightarrow \infty}{\simeq} \left(\frac{2^{R_0}-1}{\bar{\gamma}_{SD}}\right)^{N_s N_d} \cdot \sum_{i=0}^{M}\binom{M}{i}\left(\frac{2z}{\bar{\gamma}_{SR}}\right)^{N_r(M-i)}\left(\frac{2z}{\bar{\gamma}_{RD}}\right)^{N_r N_d i}. \tag{36}$$

As shown in (35) and (36), the diversity order of DAS/LS scheme is equal to DAS/SC suboptimal one.

Now, we will analysis the mean spectral efficiency of S1 and S2. Assuming the spectral efficiency of the transmission only through direct link R_0. So in the DAS/SC optimal strategy and DAS/SC suboptimal strategy, the spectral efficiency is $R_0/2$ because it spends two slots in transmission. However, the transmission process in DAS/LS scheme is finished in one or two slots which depend on the direct link or relayed link choosing by the transmission. Therefore, in DAS/LS strategy, the spectral efficiency can be expressed as

$$\mathfrak{R} = R_0 \cdot \Pr\left\{\max_{i,j}\gamma_{S_i D_j} > 2^{R_0}-1\right\} + \frac{R_0}{2} \cdot \Pr\left\{\max_{i,j}\gamma_{S_i D_j} < 2^{R_0}-1\right\} = R_0 \cdot \left(1 - \left[1 - \exp\left(-\frac{2^{R_0}-1}{\bar{\gamma}_{SD}}\right)\right]^{N_s N_d}\right) + \frac{R_0}{2} \cdot \left[1 - \exp\left(-\frac{2^{R_0}-1}{\bar{\gamma}_{SD}}\right)\right]^{N_s N_d}. \tag{37}$$

5. Numerical Results and Discussions

The simulations are executed to verify analytical expressions in this section. Without loss of generality, as in [13], let distance between S and Dd_{SD} normalize to one, and d_{RD} and d_{SR} denote the distance of $R-D$ link and $S-R$ link, respectively. Let transmit power in S the same with which in R, i.e. $P = P_S = P_R$. Therefore, the SNR of these links can be expressed as $\bar{\gamma}_{SD} = Pd_{SD}^{-\beta}/N_0$, $\bar{\gamma}_{SR} = Pd_{SR}^{-\beta}/N_0$, and $\bar{\gamma}_{RD} \triangleq Pd_{RD}^{-\beta}/N_0$, where β denotes link loss exponent. Moreover, set $\beta = 2$ and the target spectral efficiency be $R_0 = 1$bps/Hz. For convenience, we use S1, S2, and S3 represent DAS/SC optimal scheme, DAS/SC suboptimal scheme, and DAS/LS scheme, respectively.

Figure 2 presents the normalized mean spectral efficiency versus $\bar{\gamma}_{SD}$. The number of antennas used at relay and destination is $N_R = N_D = 2$. The mean spectral efficiency of S3 increases with the increase of $\bar{\gamma}_{SD}$, while the spectral efficiency of S1 and S2 is always $R_0/2$. This is because with the increase of $\bar{\gamma}_{SD}$, the probability of $\max_{i,j}\gamma_{S_i D_j} > 2^{R_0}-1$ is increasing, and the direct link is more likely to be selected for transmission.

Figure 3 is outage performance versus d_{SR} for three proposed schemes with different number of antenna and relay. As we expected, $S1$ is better than $S2$. However, the performance of $S3$ is interesting. One may expect $S3$ is worse than $S2$, because $S3$ preselects the relaying or the direct path before transmission only relied on CSI of direct link, while $S2$ selects the link after transmission according to full CSI. For another, as mentioned in Figure 2, spectral efficiency of $S3$ is better than the other schemes. Furthermore, the SNR threshold of $S3$ decreases when direct link is chosen ($2^{R_0}-1$ for one slot and $2^{2R_0}-1$ for two slots). Therefore, $S3$ may outperform $S2$ or $S1$, according to antenna number and relay position in this system, as shown in Figure 3.

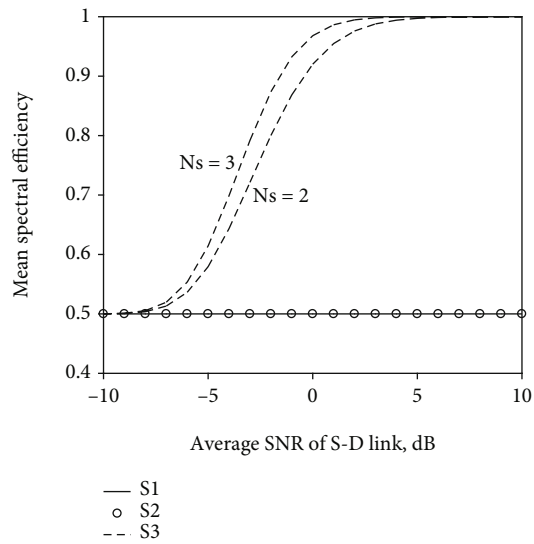

Figure 2: Comparison of proposed strategies in the aspect of spectral efficiency (dSR = 0.5).

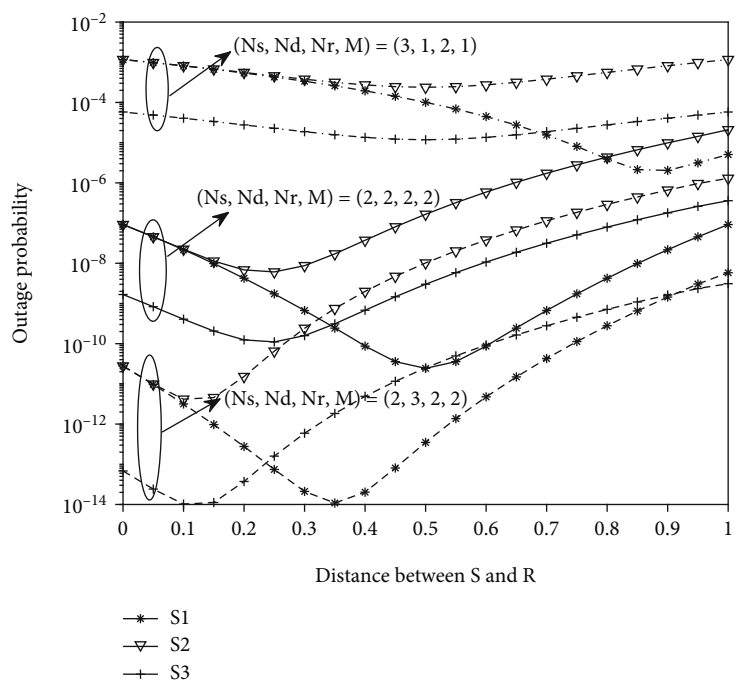

Figure 3: Comparison of proposed strategies in the aspect outage probability (PS/$N0$ = PR/$N0$ = 10 dB).

In Figure 3, for the set of $N_s = N_d$, outage probability of $S1$ reduces with the increase of d_{SR} when $0 < d_{SR} < 0.5$, while the outage probability increases with the increase of d_{SR} when $0.5 < d_{SR} < 1$. So the best performance of $S1$ is achieved when $d_{SR} = 0.5$. And it is figured that the best relay position of $S1$ is closer to the source when $N_s < N_d$, while it is closer to destination when $N_s > N_d$. This behaviour can be explained from (B.2), and the CSI of relaying link almost depends on the worse one between $S - R$ and $R - D$. When $N_s < N_d$, and $d_{SR} = 0.5$, the $S - R$ link is worse than $R - D$, so that the performance will be better when relay is closer to the source. Similar explanation can be used in the behaviour when $N_s > N_d$. In particular, best relay positions for $S1$ are around $d_{SR} \simeq 0.9$ for $N_s = 3$ and $N_d = 1$ and $d_{SR} \simeq 0.35$ for $N_s = 2$ and $N_d = 3$. However, the best relay position of $S2$ and $S3$ is not the same with $S1$, that is because the source transmitting antenna is chosen only by the direct link. And it is only one transmitting antenna for the relaying link. In

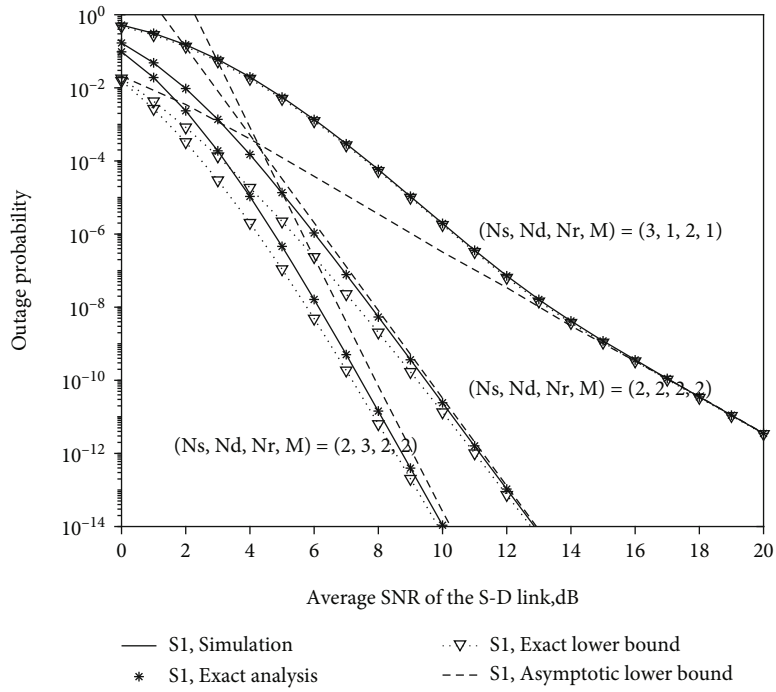

Figure 4: Outage probability versus SNR for $S1$.

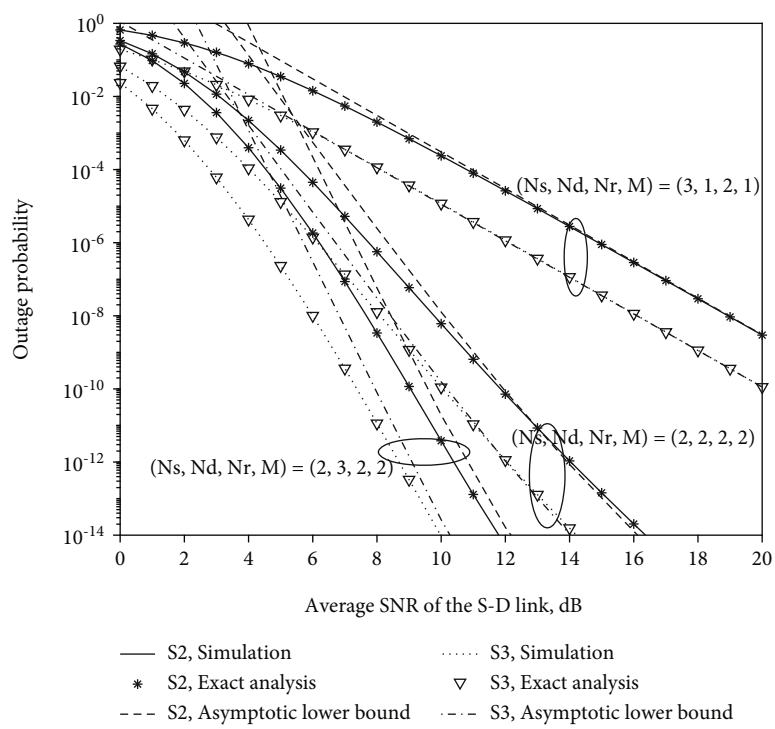

Figure 5: Outage probability versus SNR for $S2$ and $S3$.

particular, best relay positions for $S2$ and $S3$ are around $d_{SR} \simeq 0.5$ for $N_s = 1$ and $N_d = 3$, $d_{SR} \simeq 0.25$ for $N_s = 2$ and $N_d = 2$, and $d_{SR} \simeq 0.1$ for $N_s = 2$ and $N_d = 3$.

The system outage probability of S1 versus SNR with different sets (three scenarios with different antenna number) is conformed in Figure 4. In each scenario, relays have been placed in best relay position which is obtained in Figure 3. In order to verify the theoretical formula for $S1$, analytical results of lower bound and exact expressions are also presented. In this figure, we can see simulation results are close

to lower bounds, especially in high SNR range. The outage probability decreases with the increase of antenna number. Moreover, the simulation results are in accordance with asymptotic curves in high SNR regime, which confirm that $S1$ could achieve full diversity order.

Figure 5 is the average system outage probability of $S2$ and $S3$ versus the SNR with different sets (three scenarios with different antenna number). Again, relays have been placed in best relay position according to Figure 3. It can be observed that the system performance of $S3$ is always better than $S2$. Asymptotic curves confirmed that the diversity order of $S2$ and $S3$ is the same, which agree with our theoretical analysis. Furthermore, the more antennas at D, the better the system outage performance. In addition, the system performance improves with the increase of relay number.

6. Conclusions

A multiple-relay MIMO network with direct link has been studied using three amplify-and-forward relaying strategies with antenna and relay selection in this paper. The three strategies are proposed to reduce the implementation complexity and the amount of feedback overhead. Moreover, closed-form outage probability expressions are calculated, as well as the lower and upper asymptotic analytical expressions. The asymptotic results in high-SNR regime reveal the DAS/SC optimal scheme can achieve full diversity order of $N_sN_d + MN_r \min(N_s, N_d)$, while the DAS/SC suboptimal scheme and DAS/LS scheme achieve diversity order of $N_s N_d + MN_r$. Since the DAS/SC suboptimal scheme can select the best transmitting antenna without CSI of SR and RD links. The implementation complexity is less than the DAS/SC optimal scheme at the cost of performance degradation. In addition, mean spectral efficiency of DAS/LS scheme is analysed, which is higher than the other schemes.

Appendix

A. Proof of Theorem 1

ψ can be written as

$$\begin{aligned}
\psi &= \Pr\left\{\frac{\lambda_{SR_l}\cdot\lambda_{R_lD}}{\lambda_{SR_l}+\lambda_{R_lD}+1} < z\right\} = \Pr\left\{\lambda_{SR_l}\cdot\left(\lambda_{R_lD}-z\right) < \left(\lambda_{R_lD}+1\right)\cdot z\right\} = \Pr\left\{\lambda_{R_lD} < z\right\} + \Pr\left\{\lambda_{R_lD}\geq z, \lambda_{SR_l} < \frac{\left(\lambda_{R_lD}+1\right)\cdot z}{\lambda_{R_lD}-z}\right\} \\
&= F_{\lambda_{R_lD}}(z) + \int_z^{\infty} F_{\lambda_{SR_l}}\left(\frac{(t+1)\cdot z}{t-z}\right)\cdot f_{\lambda_{R_lD}}(t)dt \overset{(a)}{=} F_{\lambda_{R_lD}}(z) + \frac{N_rN_d}{\bar{\gamma}_{R_lD}}\int_z^{\infty}\sum_{i=0}^{N_sN_r}\sum_{j=0}^{N_rN_d-1}\binom{N_sN_r}{i}\binom{N_rN_d-1}{j}(-1)^{i+j}e^{-(t+1)\cdot z\cdot i/\bar{\gamma}_{SR_l}(t-z)-t\cdot j/\bar{\gamma}_{R_lD}-t/\bar{\gamma}_{R_lD}}dt \\
&= F_{\lambda_{R_lD}}(z) + \frac{N_rN_d}{\bar{\gamma}_{R_lD}}\cdot\sum_{i=0}^{N_sN_r}\sum_{j=0}^{N_rN_d-1}\binom{N_sN_r}{i}\binom{N_rN_d-1}{j}(-1)^{i+j}e^{-z\cdot i/\bar{\gamma}_{SR_l}-z\cdot(j+1)/\bar{\gamma}_{R_lD}}\int_0^{\infty}e^{-\left(z^2+z\right)\cdot i/\bar{\gamma}_{SR_l}\cdot x-x\cdot(j+1)/\bar{\gamma}_{R_lD}}dx \\
&\overset{(b)}{=} F_{\lambda_{R_lD}}(z) + N_rN_d\cdot\left\{\sum_{j=0}^{N_rN_d-1}\left[\binom{N_rN_d-1}{j}\cdot\frac{(-1)^{i+j}}{j+1}e^{-z\cdot(j+1)/\bar{\gamma}_{R_lD}}\right] + \sum_{i=1}^{N_sN_r}\sum_{j=0}^{N_rN_d-1}\binom{N_sN_r}{i}\binom{N_rN_d-1}{j}(-1)^{i+j}e^{-z\cdot i/\bar{\gamma}_{SR_l}-z\cdot(j+1)/\bar{\gamma}_{R_lD}}\cdot\sqrt{\frac{4i\left(z^2+z\right)}{\bar{\gamma}_{SR_l}\cdot\bar{\gamma}_{R_lD}(j+1)}}K_1\left(\sqrt{\frac{4i(j+1)\left(z^2+z\right)}{\bar{\gamma}_{SR_l}\cdot\bar{\gamma}_{R_lD}}}\right)\right\},
\end{aligned} \tag{A.1}$$

where (a) uses Binomial theorem, and (b) is calculated with the help of ([22], Eq. (3.324.1)). (20) can be obtained by plugging (A.1) into (18)

B. Lower-Bound Expression for DAS/SC Optimal Scheme

$$\begin{aligned}
P_{\text{out}}^{\text{opt-sc}} &= \Pr\left\{\max\left[\max_{i,j}\gamma_{S_iD_j}, \max_{i,p,l,q,j}\gamma_{S_iR_{p,l_q}D_j}\right] < 2^{2R_0}-1\right\} \simeq \Pr\left\{\max\left[\max_{i,j}\gamma_{S_iD_j}, \max_{i,p,l,q,j}\frac{\gamma_{S_iR_{p,l}}\gamma_{R_{q,l}D_j}}{\gamma_{S_iR_{p,l}}+\gamma_{R_{q,l}D_j}}\right] < 2^{2R_0}-1\right\} \\
&\underset{(c)}{\geq} \Pr\left\{\max\left[\max_{i,j}\gamma_{S_iD_j}, \max_{i,p,l,q,j}\left[\min\left(\gamma_{S_iR_{p,l}}, \gamma_{R_{q,l}D_j}\right)\right]\right] < z\right\} = \Pr\left\{\max\left[\lambda_{SD}, \max_{l}\left[\min\left(\lambda_{SR_l}, \lambda_{R_lD}\right)\right]\right] < z\right\} \\
&\triangleq P_{\text{out-LB}}^{\text{opt-sc}} = F_{\lambda_{SD}}(z)\cdot\prod_{l=1}^{M}F_{\lambda_l}(z) \underset{(d)}{=} F_{\lambda_{SD}}(z)\cdot\underbrace{\prod_{l=1}^{M}\left[F_{\lambda_{SR_l}}(z)+F_{\lambda_{R_lD}}(z)-F_{\lambda_{SR_l}}(z)\cdot F_{\lambda_{R_lD}}(z)\right]}_{\varphi},
\end{aligned} \tag{B.1}$$

where (c) is given as follow [11]:

$$\frac{1}{2}\min\left(\gamma_{S_iR_{p,l}},\gamma_{R_{q,l}D_j}\right)\le\frac{\gamma_{S_iR_{p,l}}\gamma_{R_{q,l}D_j}}{\gamma_{S_iR_{p,l}}+\gamma_{R_{q,l}D_j}}\le\min\left(\gamma_{S_iR_{p,l}},\gamma_{R_{q,l}D_j}\right). \tag{B.2}$$

And (d) is given as follows:

$$\begin{aligned}F_{\lambda_l}(t)&=\Pr(\lambda_l<t)=\Pr\left(\min\left(\lambda_{SR_l},\lambda_{R_lD}\right)<t\right)=1-\left[1-\Pr\left(\lambda_{SR_l}<t\right)\right]\\&\cdot\left[1-\Pr\left(\lambda_{R_lD}<t\right)\right]=F_{\lambda_{SR_l}}(t)+F_{\lambda_{R_lD}}(t)-F_{\lambda_{SR_l}}(t)\cdot F_{\lambda_{R_lD}}(t).\end{aligned} \tag{B.3}$$

C. Proof of Corollary 1

In the high-SNR regime, using the approximate formula $e^{-\alpha}\simeq^{\alpha\longrightarrow 0}1-\alpha$, and employing the lowest order terms corresponding to $1/\bar{\gamma}$, φ can be asymptotically expressed as

$$\begin{aligned}\varphi&\simeq\left[F_{\lambda_{SR_l}}(z)+F_{\lambda_{R_lD}}(z)\right]^M=\left[\left[1-\exp\left(-\frac{z}{\bar{\gamma}_{SR}}\right)\right]^{N_sN_r}+\left[1-\exp\left(-\frac{z}{\bar{\gamma}_{RD}}\right)\right]^{N_rN_d}\right]^M\\&\overset{\bar{\gamma}\longrightarrow\infty}{\simeq}\left[\left(\frac{z}{\bar{\gamma}_{SR}}\right)^{N_sN_r}+\left(\frac{z}{\bar{\gamma}_{RD}}\right)^{N_rN_d}\right]^M=\sum_{i=0}^{M}\binom{M}{i}\left(\frac{z}{\bar{\gamma}_{SR}}\right)^{N_sN_r(M-i)}\left(\frac{z}{\bar{\gamma}_{RD}}\right)^{N_rN_di}.\end{aligned} \tag{C.1}$$

Data Availability

The data used to support the findings of this study are available from the corresponding author upon request.

Conflicts of Interest

The authors declare that there is no conflict of interest regarding the publication of this paper.

Acknowledgments

This work was supported in part by the National Key Research and Development Program of China under Grant 2019YFB1600100, National Natural Science Foundation of China under Grant 61871059, and the Innovation Capability Support Program of Shaanxi under Grant 2021KJXX-102.

References

[1] V. S. Krishna and M. R. Bhatnagar, "A joint antenna and path selection technique in single-relay-based DF cooperative MIMO networks," *IEEE Transactions on Vehicular Technology*, vol. 65, no. 3, pp. 1340–1353, 2016.

[2] L. Du, Y. Tan, Y. Li, and Y. Chen, "On the energy efficiency of multicell massive MIMO with antenna selection and power allocation," *Wireless Communications and Mobile Computing*, Article ID 7224731, 11 pages, 2022.

[3] C. C. Hu and B. H. Chen, "Two-way MIMO relaying systems employing layered relay-and-antenna selection strategies," *IEEE Systems Journal*, vol. 12, no. 1, pp. 854–861, 2018.

[4] S. Sanayei and A. Nosratinia, "Antenna selection in MIMO systems," *IEEE Communications Magazine*, vol. 42, no. 10, pp. 68–73, 2004.

[5] J. Zhang, J. Ge, and Q. Ni, "Joint relay-and-antenna selection in relay-based MIMO-NOMA networks," in *2018 IEEE 87th Vehicular Technology Conference*, pp. 1–5, Porto, Portugal, 2018.

[6] P. L. Yeoh, M. Elkashlan, and I. B. Collings, "Exact and asymptotic SER of distributed TAS/MRC in MIMO relay networks," *IEEE Transactions Wireless Communications*, vol. 10, no. 3, pp. 751–756, 2011.

[7] P. L. Yeoh, M. Elkashlan, N. Yang, D. B. da Costa, and T. Q. Duong, "Unified analysis of transmit antenna selection in MIMO multirelay networks," *IEEE Transactions on Vehicular Technology*, vol. 62, no. 2, pp. 933–939, 2013.

[8] M. C. Ju, H. K. Song, and I. M. Kim, "Joint relay-and-antenna selection in multi-antenna relay networks," *IEEE Transactions on Communications*, vol. 58, no. 12, pp. 3417–3422, 2010.

[9] Y. Y. Zhang and J. H. Ge, "Joint antenna-and-relay selection in MIMO decode-and-forward relaying networks over Nakagami-m fading channels," *IEEE Signal Processing Letters*, vol. 24, no. 4, pp. 456–460, 2017.

[10] H. A. Suraweera, P. J. Smith, A. Nallanathan, and J. S. Thompson, "Amplify-and-forward relaying with optimal and suboptimal transmit antenna selection," *IEEE Transactions Wireless Communications*, vol. 10, no. 6, pp. 1874–1885, 2011.

[11] H. Ding, J. Ge, D. B. Costa, and T. Tsiftsis, "A novel distributed antenna selection scheme for fixed-gain amplify-and-forward relaying systems," *IEEE Transactions on Vehicular Technology*, vol. 61, no. 6, pp. 2836–2842, 2012.

[12] D. C. Gonzalez, D. B. da Costa, and J. C. S. S. Filho, "Distributed suboptimal schemes for TAS/SC and TAS/LS in fixed-gain AF relaying systems," *IEEE Transactions Wireless Communications*, vol. 13, no. 11, pp. 6041–6053, 2014.

[13] D. C. Gonzalez, D. B. da Costa, and J. C. S. S. Filho, "Distributed TAS/MRC and TAS/SC schemes for fixed-gain AF systems with multiantenna relay: outage performance," *IEEE Transactions Wireless Communications*, vol. 15, no. 6, pp. 4380–4392, 2016.

[14] R. Swaminathan, G. K. Karagiannidis, and R. Roy, "Joint antenna and relay selection strategies for decode-and-forward relay networks," *IEEE Transactions on Vehicular Technology*, vol. 65, no. 11, pp. 9041–9056, 2016.

[15] G. Amarasuriya, C. Tellambura, and M. Ardakani, "Performance analysis framework for transmit antenna selection strategies of cooperative MIMO AF relay networks," *IEEE Transactions on Vehicular Technology*, vol. 60, no. 7, pp. 3030–3044, 2011.

[16] L. Cao and X. Zhao, "Performance analysis of transmit antenna selection and relay selection in two-hop multiple MIMO relaying," in *7th International Conference on Communications and Networking in China*, pp. 667–672, Kunming, China, 2012.

[17] M. Liu, Z. Liu, W. Lu, Y. Chen, X. Gao, and N. Zhao, "Distributed few-shot learning for intelligent recognition of communication jamming," *IEEE Journal of Selected Topics in Signal Processing*, vol. 16, no. 3, pp. 395–405, 2022.

[18] M. Liu, C. Liu, M. Li, Y. Chen, S. Zheng, and N. Zhao, "Intelligent passive detection of aerial target in space-air-ground integrated networks," *China Communications*, vol. 19, no. 1, pp. 52–63, 2022.

[19] M. K. Simon and M. S. Alouini, *Digital Communication over Fading Channels*, Wiley, Hoboken, NJ, USA, 2nd edition, 2005.

[20] M. Liu, B. Li, Y. Chen et al., "Location parameter estimation of moving aerial target in space–air–ground-integrated networks-based IoV," *IEEE Internet of Things Journal*, vol. 9, no. 8, pp. 5696–5707, 2022.

[21] A. Bletsas, A. Khisti, D. P. Reed, and A. Lippman, "A simple cooperative diversity method based on network path selection," *IEEE Journal on Selected Areas in Communications*, vol. 24, no. 3, pp. 659–672, 2006.

[22] I. S. Gradshteyn and I. M. Ryzhik, *Table of Integrals, Series, and Products*, Academic, San Diego, CA, USA, 7th edition, 2007.

Hindawi
Wireless Communications and Mobile Computing
Volume 2022, Article ID 3667592, 10 pages
https://doi.org/10.1155/2022/3667592

Research Article

Waveform Reconstruction of DSSS Signal Based on VAE-GAN

Qi Feng,[1] **Junyi Zhang**,[1,2] **Li Chen**,[1] **and Fang Liu**[1,2]

[1]*Signal Intelligence and Electronic Warfare Department, The 54th Research Institute of China Electronics Technology Group Corporation, Shijiazhuang, 050011 Hebei, China*
[2]*Hebei Key Laboratory of Electromagnetic Spectrum Cognition and Control, China*

Correspondence should be addressed to Qi Feng; fq_learning@outlook.com

Received 20 April 2022; Accepted 6 June 2022; Published 4 July 2022

Academic Editor: Mingqian Liu

The complex electromagnetic environment will limit the efficacy of communication equipment. It is critical to construct a complex electromagnetic environment to test communication equipment in order to maximize its capability. One of the most important methods for constructing a complex electromagnetic environment is signal reconstruction. This paper proposes a VAE-GAN-based method for reconstructing direct sequence spread spectrum (DSSS) signals. In this method, the deep residual shrinkage network (DRSN) and self-attention mechanism are added to the encoder and discriminator of VAE-GAN. In feature learning, the DRSNs can reduce the redundant information caused by noise in the collected signal. The self-attention mechanism can establish the long-distance dependence between the input sequences, making it easier for the network to learn the samples' pseudonoise (PN) sequence features. In addition, feature loss is applied to the encoder and generator to improve network stability during training. The results of the experiments indicate that this method can reconstruct DSSS signals with the characteristics of the target signal.

1. Introduction

The electromagnetic environment of today is quite complex [1]. Communication signals are accompanied by more complicated signals such as jamming, inadvertent crosstalk, and natural thunderstorms [2–4], whether in the air, sea, or land. In order to adapt to the current development of the communication industry, in recent years, machine learning has been widely used to strengthen electromagnetic spectrum management and ensure the reliable transmission of wireless communication [5, 6]. The construction of a complex electromagnetic environment is important for improving the adaptability of its own communication system to a specific electromagnetic environment [7], and the reconstruction of noncooperating parties' communication signals is an important part of constructing a complex electromagnetic environment [8].

The traditional signal reconstruction approach necessitates complicated parameter measurement and analysis of the signal of the noncooperating party [9, 10], which increases the manual decision-making process and costs time. Furthermore, there are many complex signals with unique structures in today's electromagnetic environment. It is challenging to properly characterize the properties of a target signal using traditional methods, necessitating the development of a new signal reconstruction method. With the development of deep learning, generative adversarial networks [11] (GAN) provide the solution to this challenge. When the features of the target signal are unknown, GAN learns the distribution of samples in space through the competition of two neural networks and generates data that conforms to the target characteristics.

In terms of using GAN to reconstruct signals, predecessors have carried out much research. Qin [12] reconstructed AM and CPFSK signals by using improved CGAN, and the reconstructed signals accord with the characteristics of the sample; Yang et al. [13] used BEGAN to reconstruct BPSK and 8PSK signal waveforms with acceptable quality; Shi et al. [14] used GAN to reconstruct the signal transmitted by the defender, and the resulting QPSK wireless spoofing signal was used to deceive the defender, with a deception rate of 76.2%; Zhao and Jin [15] used a very basic GAN in

their research. The network generated communication interference waveforms such as BPSK, QPSK, 16QAM, and 2FSK, as well as verifying the network's generalization. However, for DSSS signals with more complex structures, general GAN tends to ignore the higher-dimensional features of the PN sequence during the learning process, so no solution has been proposed at present.

This paper presents a method of reconstructing DSSS signals based on VAE-GAN [16]. We add a DRSN [17, 18] and a self-attention mechanism [19] to the encoder and discriminator. The DRSN can denoise the sample signal, reduce the influence of noise on the original characteristics of the signal, and make the network focus on the DSSS signal characteristics during the learning process. In addition, the residual network part can make the model suitable for the training of a variety of DSSS samples with different PN sequence period lengths, which prevents network degradation. The self-attention mechanism can make the network pay attention to the correlation between data points at different positions in the whole input data, making it easier for the model to learn the PN sequence existing in the sample. We also replace the learned similarity part of the loss function of the generator and the encoder with a feature loss, which is more suitable for measuring signals containing PN sequences.

2. Signal Model and Basic Principles of VAE-GAN

2.1. DSSS Signal Model. DSSS technology employs PN sequences independent of information data as modulation waveforms to spread signal energy over a wide bandwidth much wider than the signal information bandwidth. It is widely used in military and commercial communication networks and systems due to its antijamming, security-enhancing, and multipath fading-adaptive properties. BPSK and QPSK are the most frequently used modulation methods in the DSSS system. This paper takes the QPSK modulation signal as the sample for the experiment. QPSK-DSSS modulates the signal's homophase and orthogonal components using PN sequences of the same length and period. Figure 1 shows the structure of the QPSK-DSSS modulation.

After passing through the serial-parallel converter (S/P), the binary information bitstream enters the in-phase and quadrature branches; the information sequences entering the two branches are spread spectrum modulated using different pseudocode sequences with the same period and code chip width; the spreading signal is then carrier modulated by mutually orthogonal carriers and sent to the bandpass filter (BPF); and finally, the spreading signal is superposed to form the QPSK-DSSS signal. The QPSK-DSSS signal $s(t)$ may be expressed as

$$s(t) = Ad_1(t)p_1(t)\cos 2\pi f_c t + Ad_2(t)p_2(t)\sin 2\pi f_c t, \quad (1)$$

where $d_1(t)$ and $d_2(t)$ represent two data signals in-phase and quadrature, respectively; $p_1(t)$ and $p_2(t)$ represent two DSSS waveforms, respectively; f_c is the carrier frequency; and A is the energy of each binary channel symbol components.

In general, we can use the receiver to collect the radio frequency signal of the communicating party. Finally, we can obtain the in-phase/quadrature-phase (I/Q) dual-channel sampling signal at a particular intermediate frequency. For various reasons, the spreading signal collected each time may have certain differences. In order to eliminate the influence of these differences on the generative model, before training the model, it is generally necessary to perform the necessary preprocessing on the sample signal in order to increase the stability and generality of the generative model.

When preparing the sample, the collected I/Q data is first converted to zero intermediate frequency, then the signal's frequency deviation and out-of-band noise are eliminated, and the signal is resampled. The captured signal's amplitude must be normalized to accelerate the algorithm's convergence and improve the model's accuracy. To ensure that the initial phase of the spreading code is controllable in the generated associated spread spectrum waveform, we estimate the spreading code period in the DSSS signal using cepstrum technology and then divide the continuous data according to the obtained spreading code period to ensure that the training samples' initial phases remain consistent. Assuming that the linear feedback shift register of the m sequence used to generate the DSSS signal is n stages, the period length of the PN sequence is $L = 2^n - 1$, the oversampling multiple is M, and the length of a single sample is P spreading code periods, and then, the length of a single sample is $L \times M \times P$.

2.2. Basic Principles of VAE-GAN. GAN has been one of the fastest-growing deep learning models in recent years. It consists of a generator and a discriminator, and it learns through the two game-playing neural networks. VAE-GAN is a combination of GAN and VAE. By comparing the difference between the generated and real data, VAE will calculate the mean value to determine the loss. However, the data generated in this way is unrealistic. After adding the discriminator to the VAE, it is necessary to make the loss between the generated data and the real data smaller and let the data generated by the generator fool the discriminator so that the discriminator will force the VAE's decoder to generate more realistic data. On the other hand, GAN's generator will follow the discriminator's guidance when generating data. However, it is challenging to balance the generator's and discriminator's capabilities, which can easily result in training instability. By combining VAE and GAN, the encoder can give the generator a loss function between real and generated data so that the network is more stable while it is being trained.

Figure 2 shows the VAE-GAN model. It is mainly composed of three networks. The encoder (E) is the first component. After the encoder processes the sample x, two vectors are generated, one representing the distribution's mean vector μ and the other representing the distribution's standard deviation vector σ. Then, sample $z = E(x)$ is sampled from the sample space defined in the two vectors as the input of

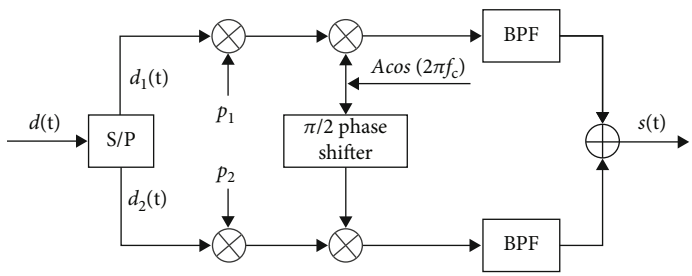

Figure 1: The transmitter structure of QPSK-DSSS.

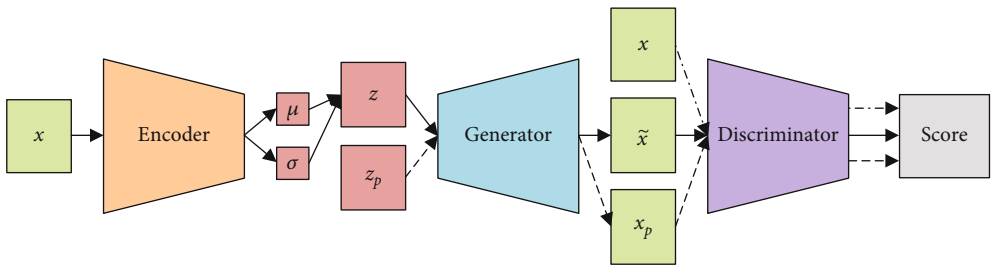

Figure 2: Framework of VAE-GAN.

the generator. However, the randomness of the sample will make it impossible to train these two values, so z is defined as $z = \mu + \sigma \cdot \xi$, where $\xi \sim N(0, 1)$. In this way, the randomness of the sample is transferred to ξ, so μ and σ can be trained at a certain time of training. The generator (G) is the second component. The generator will obtain the sampled data z from the sample space defined by the encoder and the sampled data z_p from the normal distribution during the training process. In the generation task after the training, the generator obtains the sampled data z_p from the normal distribution. The sample space defined by the encoder must be constrained to obey the normal distribution to ensure that the generator generates meaningful data. The generator receives the sampled data z and generates the data $\tilde{x} = G(z)$; similarly, the generator receives the sampled data z_p and generates the data $x_p = G(z_p)$. The discriminator (D) is the third component. The samples x and the generated data $\tilde{x}$ and x_p are, respectively, input into the discriminator. The discriminator will give the sample a higher score and the generated data a lower score.

We expect that the sample space defined by the encoder is as similar to the normal distribution as possible. The distribution between the two is measured using KL divergence L_{prior}.

$$L_{\text{prior}} = D_{\text{KL}}\left(Q(z|x) \| P(z_p)\right), \tag{2}$$

where $Q(z|x)$ represents the variational distribution encoded by the sample x and $P(z_p)$ represents the normal distribution.

In addition, it is hoped that the greater the probability of generating real data x through the latent variable z,

$$L_{\text{llike}}^{\text{Dis}_l} = -E_{Q(z|x)}[\log P(\text{D}(x)|z)], \tag{3}$$

where $L_{\text{llike}}^{\text{Dis}_l}$ is to reconstruct x by maximizing the natural logarithm $\log P(\text{D}(x)|z)$ by sampling from $Q(z|x)$. In specific engineering, this loss can be defined by calculating the distance between the generated data and the real data, that is, learned similarity $\|\tilde{x} - x\|$, so the loss function of the encoder is as follows:

$$L_{\text{E}} = L_{\text{llike}}^{\text{Dis}_l} + L_{\text{prior}}. \tag{4}$$

For the generator, we expect to minimize the distribution difference between the data generated by the generator using the latent variable z and the real data. Secondly, the generator also needs to receive the adversarial loss passed by the discriminator. It hopes that the data generated by the random noise and the data generated by the latent variable z can obtain higher scores in the discriminator. Therefore, the loss of the generator is as follows:

$$L_{\text{G}} = L_{\text{llike}}^{\text{Dis}_1} + \log\left(1 - \text{D}\left(x_p\right)\right) + \log\left(1 - \text{D}(\tilde{x})\right). \tag{5}$$

For the discriminator, the discriminator gives high scores to real samples and low scores to the data generated by the generator, so the loss of the discriminator is as follows:

$$L_{\text{D}} = -\log\left(\text{D}(x)\right) - \log\left(1\text{-D}(\tilde{x})\right) - \log\left(1\text{-D}\left(x_p\right)\right). \tag{6}$$

3. Methodology

3.1. Network Architecture. Figure 3 shows the encoder structure that we designed. Three different types of convolutional layers are used, as well as the DRSN with channel-wise thresholds (DRSN-CW) and self-attention mechanisms. In the figure, Conv1d (k, s, p) denotes a one-dimensional convolution layer in which k represents the size of the

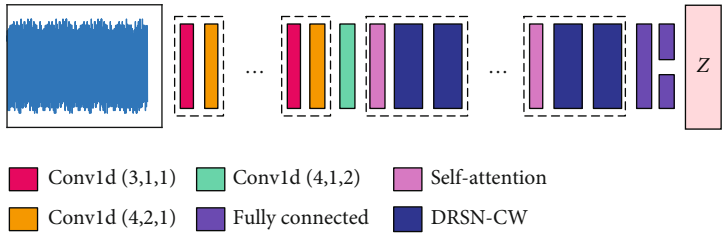

Figure 3: Encoder network structure.

convolution kernel, s represents the stride of the convolution, and p represents the padding added to both sides of the input. Divide the I/Q data of the sample into two channels and input them into the encoder. To begin, we use the Conv1d (3, 1, 1) and Conv1d (4, 2, 1) convolution layers to extract features in samples at varying scales. The output length remains unchanged after the data is input to the convolutional layer of Conv1d (3, 1, 1). The output length is halved after passing the data through the convolutional layer Conv1d (4, 2, 1). In Section 2.1, we mentioned that the length of a single data sample is $L \times M \times P$. The length of output data is reduced to L using a certain number of these two convolutional layers. The data is then supplied to the Conv1d (4, 1, 2) convolutional layer, where the length of the output data is now 2^n. After the data is output from the convolution layer, it will be batch normalized, and the Leaky ReLU activation function will be used as the activation function. After the above feature extraction, we use the self-attention mechanism to more effectively consider the dependencies between the input data samples and capture the spreading sequence features. The data output from the self-attention layer does not change the length and number of channels. Next, the DRSN-CW layer is utilized to denoise the features. The purpose is to eliminate the noise in the signal as much as feasible. Too much noise makes it difficult for the network to learn the features of the original signal, and it also causes the network to learn the features introduced by the noise. The residual part in DRSN-CW is also composed of two convolutional layers, Conv1d (3, 1, 1) and Conv1d (4, 2, 1), and Figure 4 shows the DRSN-CW module. After the data is input to the last DRSN-CW layer, the length of the output data is M, and then, the data is expanded on the full connection layer by affine transformation. The sample is converted into a 128-dimensional latent space through the reparameterization trick.

To make the trained generator generate signals faster in the actual generation task, we design the generator structure to be relatively simple and add the complexity required to complete the generation task to the encoder and discriminator. Figure 5 shows the structure of the generator. Upsample(2) indicates that upsampling multiplier is 2. The generator receives random noise as input and attempts to generate false signals with the target features. The dimension of random noise input to the generator is 128. The output length is $256 \times L$ after the fully connected layer. Then, the data undergoes an affine transformation, the number of channels becomes 256, and the length is changed to L. After

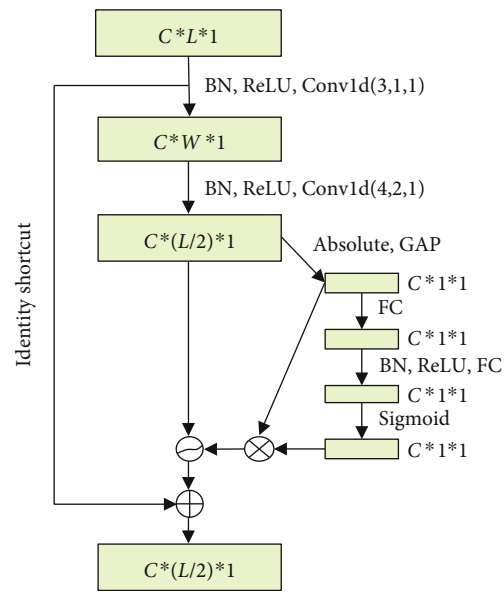

Figure 4: DRSN-CW module structure.

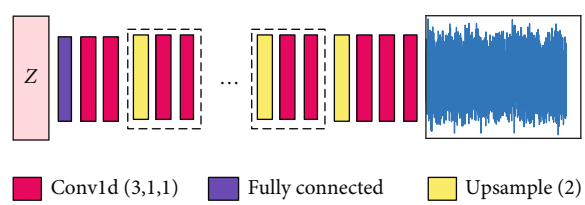

Figure 5: Generator network structure.

which the data passes through multiple Conv1d (3, 1, 2) layers and Upsample(2) layers, the final output channel number is 2, and the length of the generated signal is $L \times M \times P$.

The discriminator will distinguish whether the data is real or generated. The network structure of the discriminator we designed is similar to the encoder. Only the fully connected layer is different. Figure 6 shows the discriminator's structure. The data passes through the last DRSN-CW layer, then passes through three fully connected layers, and finally passes through the Sigmoid activation function to output the score given by the discriminator.

3.2. Improvement of Loss Function. Because the model's objective is to generate DSSS signals with the same characteristics as the sample, the generator should learn as much as possible about the target signal's features in order to fool

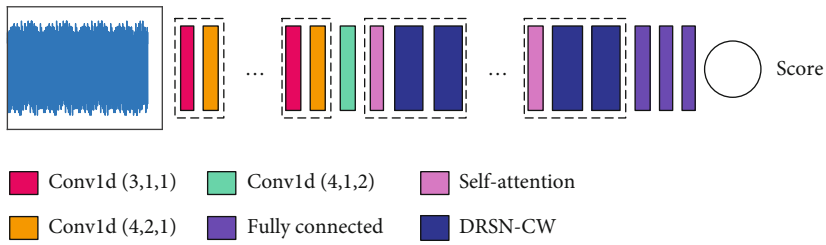

Figure 6: Discriminator network structure.

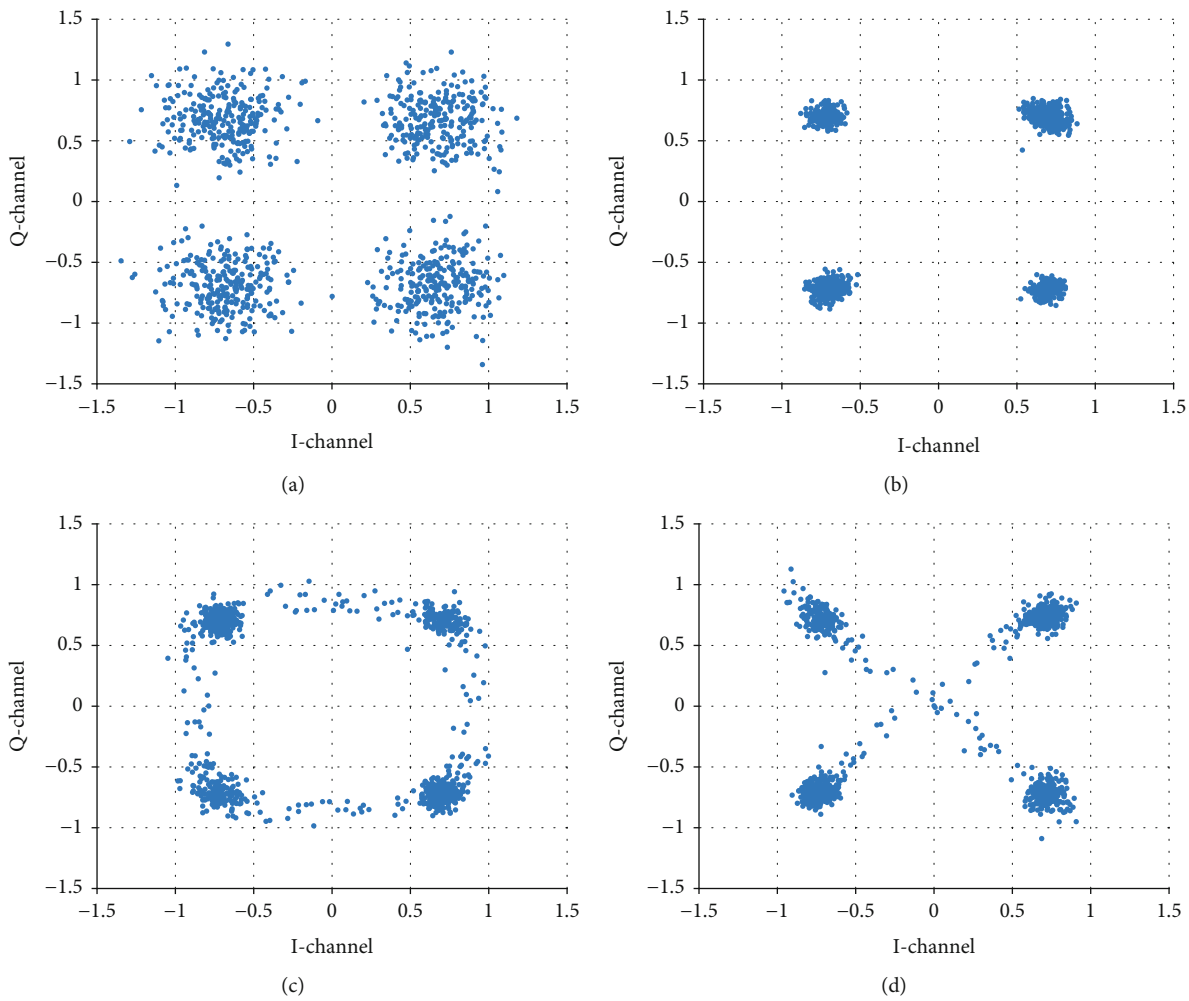

Figure 7: Sample and generated signal constellation.

the discriminator. However, during the early stages of GAN training, the generator's capability is often limited. The generator cannot generate signals with a similar distribution to the sample, but the discriminator can easily identify whether the signal is real or generated. This will cause $D(x) \longrightarrow 1$ in the loss function of the discriminator, while $D(x_p) \longrightarrow 0$ and $D(\tilde{x}) \longrightarrow 0$. When the generator is updated, the gradients of the generator are $\partial L_G / \partial D(x_p) \longrightarrow -\infty$ and $\partial L_G / \partial D(\tilde{x}) \longrightarrow -\infty$, resulting in unstable training of the generator. Additionally, the loss function of the learned similarity part in the encoder and generator cannot be used effectively, as two signals with the correct PN sequence period but opposing symbols will produce a large learned similarity loss value.

To overcome the aforementioned problems, we use the feature loss in the loss function of the generator and the encoder to replace the learned similarity loss. During

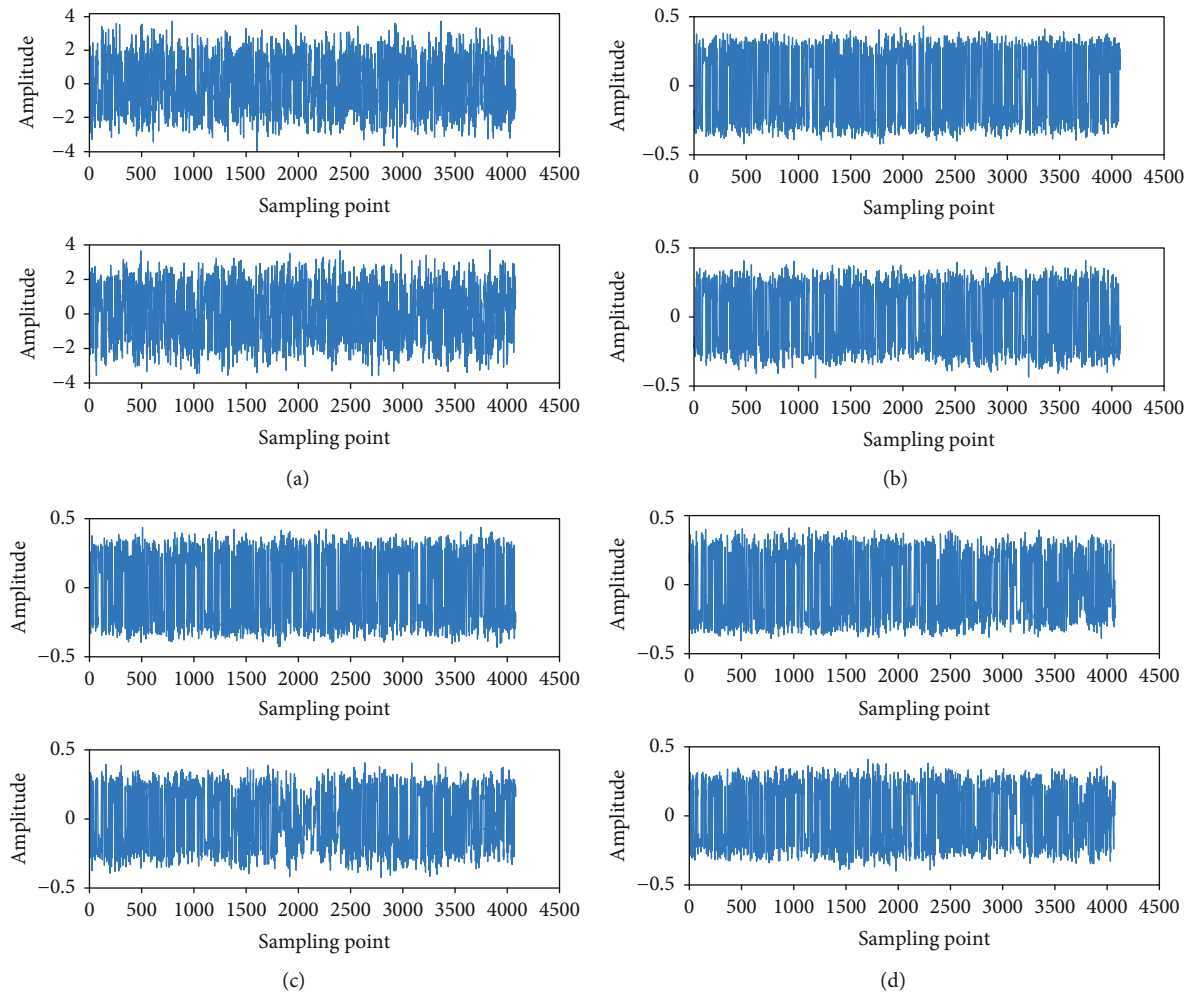

Figure 8: Sample and generated signal waveforms.

training, evaluate the reconstruction loss of samples and generated signals from the viewpoint of features in order to enhance the generator's and encoder's abilities. We select the output features of the fourth layer of the convolution network in the discriminator to construct the feature loss. If the fourth layer of the discriminator's feature output is $f_D(\cdot)$, the encoder's feature loss is

$$L_{\mathrm{E}_{\mathrm{feature}}} = \left\| \mathbb{E}_{x\sim p_{\mathrm{data}}} f_D(x) - \mathbb{E}_{\tilde{x}\sim G} f_D(\tilde{x}) \right\|_2^2., \tag{7}$$

The feature loss of the generator is

$$L_{\mathrm{G}_{\mathrm{feature}}} = \left\| \mathbb{E}_{x\sim p_{\mathrm{data}}} f_D(x) - \mathbb{E}_{x_p\sim G} f_D(x_p) \right\|_2^2., \tag{8}$$

So the loss function of the encoder is as follows:

$$L_{\mathrm{E}_{\mathrm{new}}} = L_{\mathrm{prior}} + L_{\mathrm{E}_{\mathrm{feature}}}.. \tag{9}$$

The loss function of the generator is as follows:

$$L_{\mathrm{G}_{\mathrm{new}}} = \log\left(1 - \mathrm{D}(x_p)\right) + \log\left(1 - \mathrm{D}(\tilde{x})\right) + L_{\mathrm{G}_{\mathrm{feature}}}. \tag{10}$$

We still use the discriminator loss from the original VAE-GAN.

4. Experimental Results and Analysis

4.1. Experimental Environment. The simulation experiments were performed on an Intel Core i9-10980XE desktop computer with a 3.00 GHz CPU and 256 GB of RAM, using two NVIDIA Quadro GV100 graphics cards. The Pythoh version is 3.8. The Pytorch version is 1.8.

4.2. Experimental Data Set. The experiment uses four types of samples with PN sequence period lengths of 31, 63, 127, and 255. The signal-to-noise ratio (SNR) is 5-15 dB, the noise is additive white Gaussian noise (AWGN), and the number of samples of each type is 5000. Each sample contains four symbol lengths, and the start position of the sample signal data is not the start position of the PN sequence period.

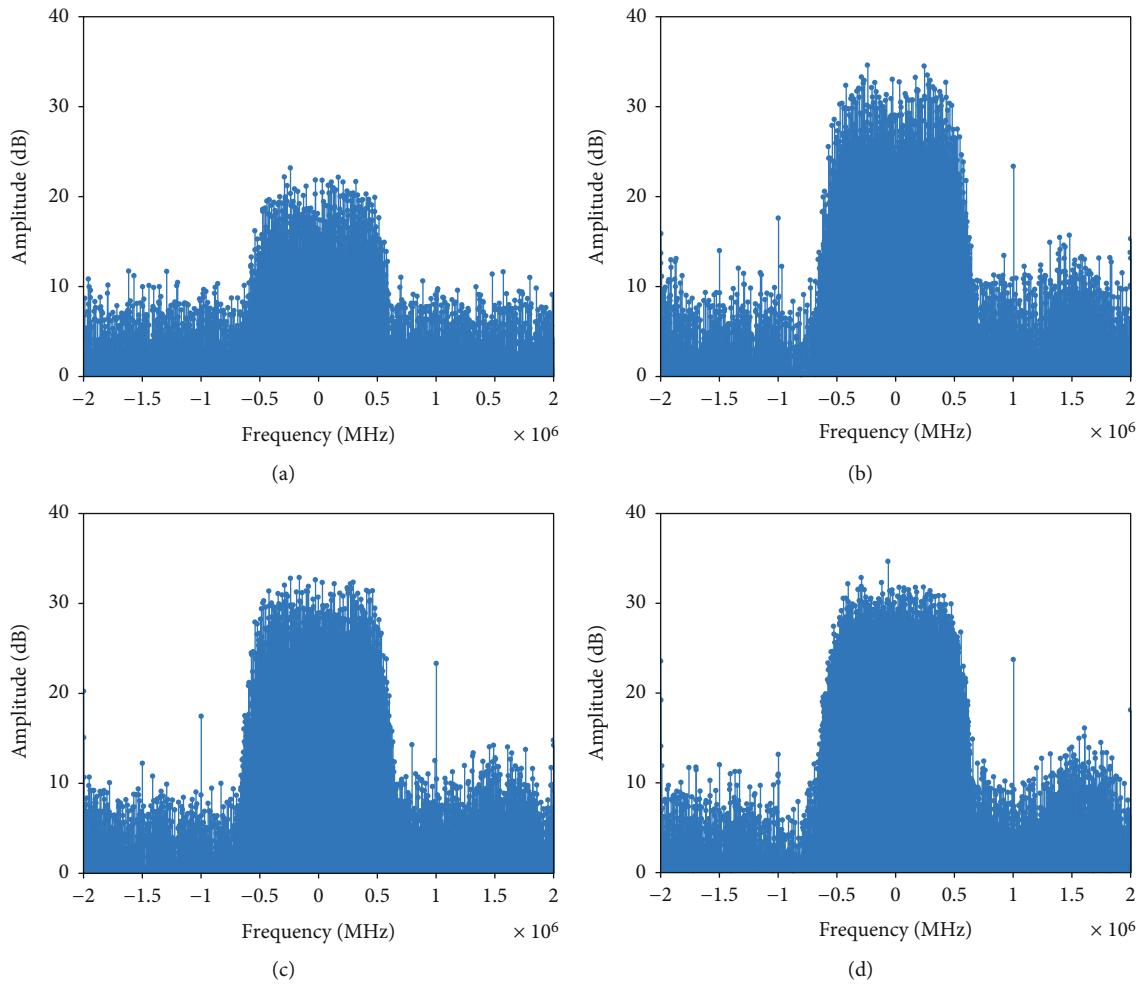

Figure 9: Sample and generated signal power spectral density.

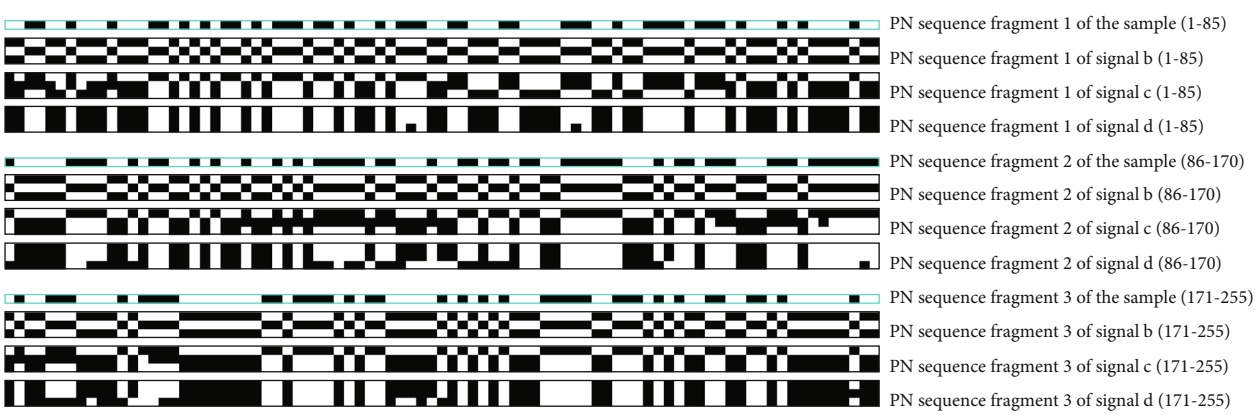

Figure 10: PN sequence of samples and generated signals.

We train the network for 300 epochs using Adam with a batch size of 16. The coefficients used for computing running averages of gradient and its square are 0.5 and 0.9, respectively. The learning rate of the encoder is set to 0.0001, the learning rate of the generator is set to 0.0003, and the learning rate of the discriminator is set to 0.0001.

4.3. Experimental Results and Analysis. Samples are fed into the network with experimental parameter set to train the model, using the VAE-GAN network architecture proposed in this paper. After the model training is completed, the samples are sampled from the random noise that obeys the normal distribution and input to the generator for signal

generation. Analyze the quality of the generated signal by comparing it with the sample.

Assuming that the length of the spreading code is 255, used by the sample, and the SNR is 10 dB, the generated results are displayed and analyzed. By inputting random noise into the generator to generate 1000 signals, the constellation diagrams of the generated signals can be divided into three categories, which are represented by the constellation diagrams shown in Figures 7(b)–7(d). The signals represented by these three constellation diagrams are hereinafter referred to as signals b, c, and d, respectively, where a is a sample constellation diagram. Figure 8 shows a time-domain waveform diagram corresponding to the constellation diagram in Figure 7. It can be seen that the constellation diagram of signal b conforms to QPSK modulation, and the constellation points are relatively dense. In the time-domain waveform, the amplitude of the waveform diagram of signal b is more regular than that of the sample signal. The constellation diagram of signal c appears as a ring. From the waveform diagram, it can be observed that the real part of the waveform of signal c is normal in the time domain, and the amplitude of the imaginary part waveform varies greatly at different sampling points, resulting in a ring on the constellation diagram. The constellation diagram of signal d depicts an "X" shape. From the waveform diagram, it can be seen that the amplitudes of the real part and imaginary part of the signal are lower at the sampling points at some corresponding positions. Without regard to the correctness of the spreading code in the signal, it can be considered that signal b is of high quality. In contrast, signals c and d reflect some distortion.

Estimate the power spectral density of the sample and the generated signal. The power spectral density of the sample is shown in Figure 9(a), and the power spectral density of the generated signal is shown in Figures 9(b)–9(d). It can be seen from Figure 9 that the spectrum of the generated data is located near the zero frequency, the generated signal is similar to the sample bandwidth, and the SNR of the generated signal is higher than that of the sample. Furthermore, we observed the difference in SNR between samples and generated signals at different SNRs and found no strict correspondence between them. In general, the SNR of the generated signal is 0-10 dB higher than the SNR of the samples.

Estimate the spreading code on each information bit of the generated signal. Count the number of chips that are consistent between the generated spreading code and the sample spreading code, and calculate the ratio of this value to the code length. Because the data generated by GAN is random, it is impossible to determine whether the spreading code of a certain information bit of the generated signal is the PN code of the sample or the inverse of the PN code, and then, there will be two different ratios. We take the higher ratio as the accuracy of the final generated spreading code and use its corresponding code to determine the data information bits. The closer the accuracy rate is to 50%, the worse the effect of the generated spreading code. We expect that the model can generate the spreading code with an accuracy rate of over 85%.

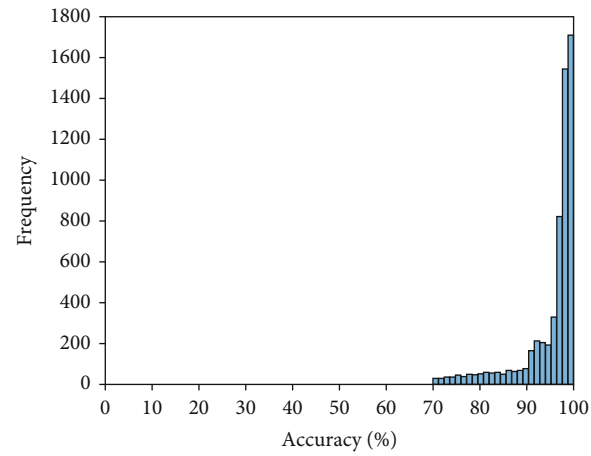

Figure 11: The histogram of the accuracy distribution of the PN sequence of the generated signal.

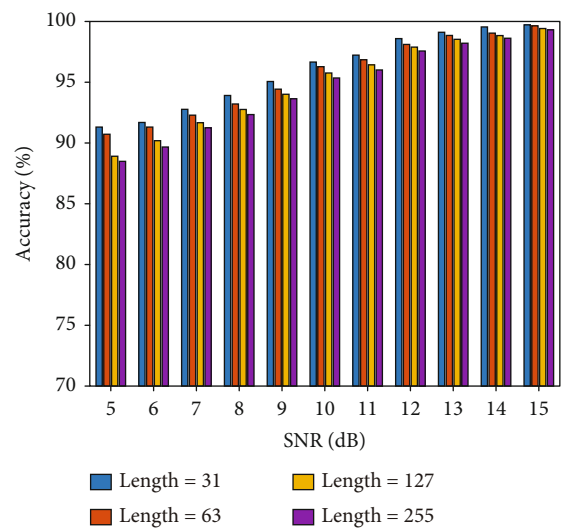

Figure 12: Average accuracy of PN sequence in generated signal.

The sample contains four spreading code period lengths. In this experiment, the starting position of the sample is different from the starting position of the spreading code. Experiments show that the generated signal and sample have consistent starting positions in the spreading code periods and that the generated signal's I/Q contains three complete spreading code periods. To show the spreading code generated by signals b, c, and d, we extract the spreading code generated by the sample's I channel, as illustrated in Figure 10. The white block represents chip "1," and the black block represents chip "0." Each complete sequence period is in a row, and each generated signal of the I channel has three rows. Due to space constraints, we have divided the entire period of the spreading code into three fragments for presentation. It can be concluded that the accuracy of the three spreading codes generated by signal b is 100%; the accuracy of the three spreading codes generated by signal c is 99.61%, 77.65%, and 100%, respectively; and the accuracy of the three spreading codes generated by signal d is 100%,

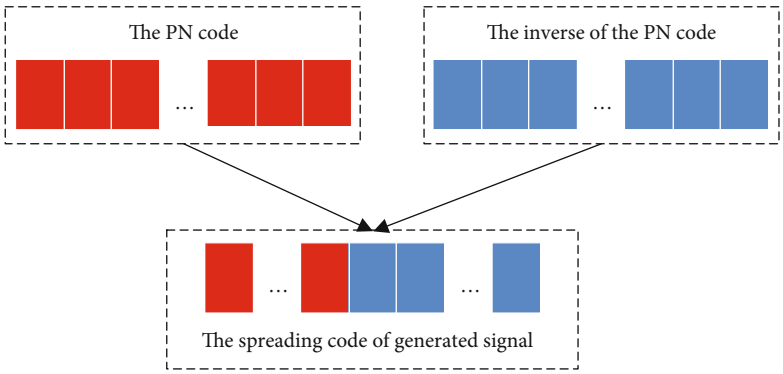

Figure 13: Partial spreading codes generated without self-attention mechanism.

99.61%, and 100%, respectively. Additionally, the three data signals generated contain different information.

Calculate the accuracy of the spreading code of 1000 generated signals. Each generated signal contains six complete spreading codes, resulting in a total of 6000 complete spreading codes. Calculate the accuracy of each spreading code separately. Figure 11 shows the spectrum histogram. When the spreading code length of the sample is 255, and the SNR is 10 dB, the accuracy rate of the PN sequence of the generated signal is greater than 70%, and the majority of them are between 90% and 100%. The average accuracy is 95.35%.

For the four types of samples with spreading code lengths of 31, 63, 127, and 255, we generate 1000 signals, respectively, when the SNR is 5-15 dB, and calculate the average accuracy rate of the spreading code of each generated signal. Figure 12 shows the results. At the same length of spreading code, with the improvement of the sample's SNR, the accuracy of the PN sequence of the generated signal is also gradually improved. The accuracy of the PN sequence of the generated signal is gradually reduced with an increase in the length of the spreading code of the sample.

We evaluated the model's performance without applying the self-attention mechanism. When the length of the spreading code used by the sample is 63 or less, there is little difference in the accuracy of the PN sequence of the generated signal whether the self-attention mechanism is used or not. When the length of the spreading code used by the sample is more than 63, the spreading code of some information bits of the signal generated by the network that does not use the self-attention mechanism will produce the phenomenon shown in Figure 13. In the figure, the red rectangle represents the PN sequence of the sample, and the blue rectangle represents its inverse PN sequence. The spreading code of a certain information bit in the generated signal will be spliced from the PN code and the inverse PN code. After testing 1000 generated signals, this situation usually occurs in one information bit of a generated signal, while the spreading code of other information bits is standard. This kind of signal accounts for about 18% of the total signal generated. However, if the self-attention mechanism is used, this situation will not occur.

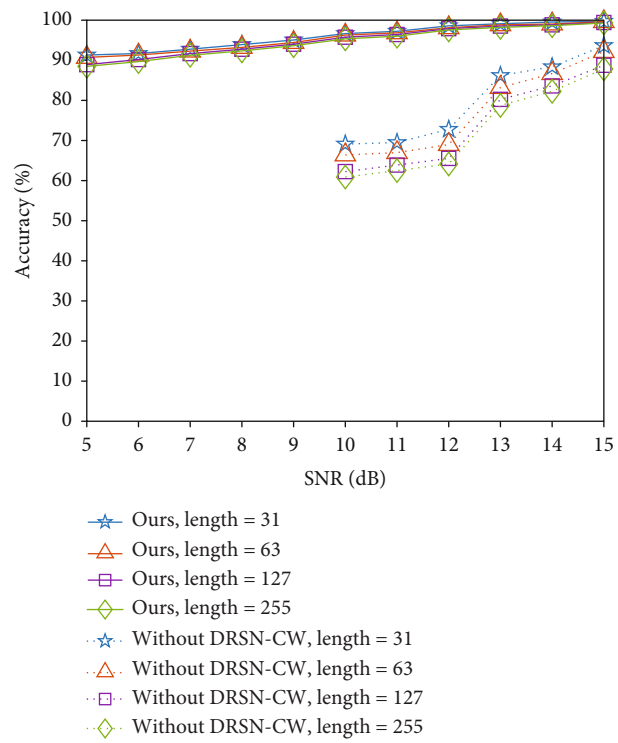

Figure 14: Comparison of average accuracy between the proposed model and the model without DRSN-CW.

We also tested the performance of the model without DRSN-CW. Figure 14 shows the performance comparison between the model and the model in this paper under different length spreading codes and different SNRs. Under the same code length and SNR, the average accuracy of the spreading codes generated by the model is far lower than the model in this paper, and they are sensitive to the changes in the SNR of samples. When the SNR is lower than 13 dB, the model's performance drops sharply. It can be seen that the spreading code of the generated signal at 10-12 dB is far below our tolerable error range, so we have not simulated the SNR below 10 dB. In this case, the network has been unable to effectively learn the PN sequence characteristics of the sample.

5. Conclusion

In this paper, we designed a GAN capable of reconstructing DSSS signals. This method avoids complex parametric analysis of the signal. The generation process is simple, and the model can be adapted to generate DSSS signals with varying PN sequence period lengths. This method is of great significance to the construction of a complex electromagnetic environment. In order to make the network learn the PN sequence characteristics of the DSSS signal, we introduced DRSNs and convolution modules based on the self-attention mechanism into the encoder and discriminator in VAE-GAN. The DRSN layer will denoise the sample. The self-attention network layer can capture the features of the PN sequence of the sample. Through the adversarial training in VAE-GAN, the generated signal with the characteristics of the target signal is finally obtained. The results show that the signal generated by the proposed network can learn the modulation pattern and spectral features of the sample, as well as the sample's PN code sequence. Although the network proposed in this paper is suitable for PN sequences with different code lengths, the effect in low SNR is unsatisfactory. The next step is to study the generation of DSSS signals in the lower SNR ratio. In addition, the I/Q in this paper uses the same PN sequence for modulation. Next, we will try to use different PN sequences.

Data Availability

The data that support the findings of this study are available from the corresponding author upon reasonable request.

Conflicts of Interest

The authors declared no potential conflicts of interest with respect to the research, authorship, and/or publication of this article.

References

[1] J. Y. Zhang and G. H. Wei, "New Development of Electromagnetic Compatibility in the Future: Cognitive Electromagnetic Environment Adaptation," in *2021 13th Global Symposium on Millimeter-Waves & Terahertz (GSMM)*pp. 1–3, China, May, Nanjing, China, 2021.

[2] V. G. Maksimenko, "Compensation for man-made interference during reception of an ultra-low-frequency electromagnetic field in the sea," *Journal of Communications Technology and Electronics*, vol. 65, no. 2, pp. 127–130, 2020.

[3] P. Händel and D. Rönnow, "MIMO and massive MIMO transmitter crosstalk," *IEEE Transactions on Wireless Communications*, vol. 19, no. 3, pp. 1882–1893, 2019.

[4] M. R. Ahmad, M. R. M. Esa, V. Cooray, and E. Dutkiewicz, "Interference from cloud-to-ground and cloud flashes in wireless communication system," *Electric Power Systems Research*, vol. 113, pp. 237–246, 2014.

[5] M. Q. Liu, Z. L. Liu, W. D. Lu, Y. Chen, X. Gao, and N. Zhao, "Distributed few-shot learning for intelligent recognition of communication jamming," *IEEE Journal of Selected Topics in Signal Processing*, vol. 16, no. 3, pp. 395–405, 2022.

[6] M. Q. Liu, J. K. Wang, N. Zhao, Y. Chen, H. Song, and R. Yu, "Radio frequency fingerprint collaborative intelligent identification using incremental learning," *IEEE Transactions on Network Science and Engineering*, p. 1, 2021.

[7] Y. G. Tang, T. T. Zhang, and X. J. Zhou, "Construction and Evaluation of Examination Conditions for Complex Electromagnetic Environment Based on Subject and Object," in *2019 IEEE 8th Joint International Information Technology and Artificial Intelligence Conference (ITAIC)*pp. 1174–1180, China, May, Chongqing, China, 2019.

[8] P. Zhou, "Overview on communication countermeasure jamming effect assessment method," *Communications Technology*, vol. 49, no. 8, pp. 1029–1033, 2016.

[9] X. W. Gu, Z. J. Zhao, and S. Lei, "Blind estimation of pseudo-random codes in periodic long code direct sequence spread spectrum signals," *IET Communications*, vol. 10, no. 11, pp. 1273–1281, 2016.

[10] J. B. Long, H. B. Wang, D. F. Zha, H. Fan, Z. Lao, and H. Wu, "Applications of an improved time-frequency filtering algorithm to signal reconstruction," *Mathematical Problems in Engineering*, vol. 2017, 14 pages, 2017.

[11] I. J. Goodfellow, J. Pouget-Abadie, M. Mirza et al., "Generativeadversarial networks," *Advances in Neural Information Processing Systems*, vol. 3, pp. 2672–2680, 2014.

[12] J. Qin, *Signal reconstruction based on generative adversarial networks*, Xidian University, 2018.

[13] H. J. Yang, L. Chen, and J. Y. Zhang, "Research on digital signal generation technology based on generative adversarial network," *Electronic Measurement Technology*, vol. 43, no. 20, pp. 127–132, 2020.

[14] Y. Shi, K. Davaslioglu, and Y. E. Sagduyu, "Generative adversarial network for wireless signal spoofing," in *Proceedings of the ACM Workshop on Wireless Security and Machine Learning - WiseML 2019*, pp. 55–60, Miami FL USA, 2019.

[15] F. Zhao and H. Jin, "Communication jamming waveform generation technology based on GAN," *Systems Engineering and Electronics*, vol. 43, no. 4, pp. 1080–1088, 2021.

[16] A. B. L. Larsen, S. K. Sønderby, H. Larochelle, and O. Winther, "Autoencoding beyond pixels using a learned similarity metric," in *International Conference on Machine Learning*, pp. 1558–1566, New York NY USA, 2016.

[17] M. H. Zhao, S. S. Zhong, X. Y. Fu, B. P. Tang, and M. Pecht, "Deep residual shrinkage networks for fault diagnosis," *IEEE Transactions on Industrial Informatics*, vol. 16, no. 7, pp. 4681–4690, 2019.

[18] W. B. Jiang and A. Liu, "Image motion deblurring based on deep residual shrinkage and generative adversarial networks," *Computational Intelligence and Neuroscience*, vol. 2022, Article ID 5605846, 15 pages, 2022.

[19] A. Vaswani, N. Shazeer, N. Parmar et al., "Attention is all you need," *Advances in Neural Information Processing Systems*, vol. 30, 2017.

Hindawi
Wireless Communications and Mobile Computing
Volume 2022, Article ID 2395996, 9 pages
https://doi.org/10.1155/2022/2395996

Research Article

Recognition of Electromagnetic Signals Based on the Spiking Convolutional Neural Network

Shifei Tao,[1,2] Shuai Xiao,[2] Shuaige Gong,[1] Huifu Wang,[2] Hao Ding,[3] and Hao Wang[2]

[1]*State Key Laboratory of Complex Electromagnetic Environment Effects on Electronics and Information System (CEMEE), Luoyang 471003, China*
[2]*School of Electrical and Optical Engineering, Nanjing University of Science and Technology, Nanjing 210094, China*
[3]*Engineering Training Center, Nanjing University of Science and Technology, Nanjing 210094, China*

Correspondence should be addressed to Shifei Tao; s.tao@njust.edu.cn

Received 20 May 2022; Accepted 10 June 2022; Published 24 June 2022

Academic Editor: Mingqian Liu

Feature extraction and recognition of signals are the bases of a cognitive radio. Traditional manual extraction for signals' features becomes difficult in the complex electromagnetic environment. Although convolutional neural networks (CNNs) can extract signal features automatically, they have low accuracy in recognizing electromagnetic signals at low signal-to-noise ratios (SNRs) due to the agility of signals. Considering the great potential of spiking neural networks (SNNs) in classification, a spiking convolution neural network (SCNN) for the recognition of electromagnetic signals is proposed in this paper. The SCNN effectively integrates the extraction ability of spatial features in CNNs and temporal features in SNNs. Since the SCNN is difficult to train, the strategy of surrogate gradient is proposed to train it. By taking the 2-dimensional time-frequency distribution of 6 signals as input, the SCNN can effectively identify different signals at low SNRs. The method proposed in this paper contributes to promote the research and application of SNNs in the recognition of electromagnetic signals.

1. Introduction

Modern electronic warfare is rapidly developing with the rise of electronic information technology. Electromagnetic signal identification becomes a critical part of a cognitive radio (CR) [1]. However, electromagnetic signal waveforms appear to be agile and heavily interfered in a diverse electromagnetic environment. The agility of signals reduces the performance of earlier recognition methods based on the interpulse feature [2]. Therefore, in-pulse features such as time-frequency features, wavelet packet features, wavelet ridge-frequency features, and higher-order spectrum are widely used for signal recognition by combining support vector machines (SVM) and deep learning (DL) [3]. As a type of DL, convolutional neural networks (CNNs) are widely used in target recognition and image classification. Due to their powerful capability for feature extraction and generalization, CNNs are quite effective in the recognition of radar signals [4, 5] and communication signals [6, 7].

In recent years, many studies have been done on electromagnetic signal recognition with CNNs. Some methods focus on preprocessing the input signals of CNNs to reduce noise interference [8–10]. Ye et al. use the time-frequency distribution preprocessed with binarization as the input of a 3-layer CNN for signal recognition. The recognition accuracy of signals at −6 dB is still above 90% [8]. Yao and Wang preprocess the time-frequency maps with more methods including symmetric mapping, primary energy ridge extraction, binarization, and image reset to reduce noise interference. Then, they use a pretrained CNN to identify the preprocessed time-frequency maps and obtain a higher accuracy than methods with manual feature extraction [9]. Denoising is also an optional method for preprocessing. When using a residual neural network (ResNet) to denoise time-frequency maps of radar signals, the Inception-V4 network which combines the inception structure and residual connections achieves a recognition accuracy of over 90% for signals at −10 dB [10]. Meanwhile, different features are constructed for signal recognition [11, 12]. Pu et al. use

orthogonal slices of Gaussian-smoothed fuzzy function as a feature extraction target. By learning the features of the orthogonal slices, the employed CNN achieves a recognition accuracy of 88.5% for signals at −6 dB [11]. Xie et al. firstly use chirp decomposition for preliminary classification of signals. Then, they take the Zernike matrix extracted from time-frequency maps as the input feature of a ResNet to complete further classification of the signals. Their method finally achieves good robust performance on signals' parameters [12]. Some other methods are committed to improving the structure of networks for improving the recognition accuracy [13–15]. Lin et al. propose a deep residual shrinkage attention network for signal recognition. They use the attention mechanism in ResNet to reduce the impact of redundant information. Finally, the deep residual shrinkage attention network achieves excellent recognition accuracy and good scalability at the same time [13]. In addition, better performance than either network alone can be achieved by combining the long- and short-term memory network (LSTM) and CNN. The combined network fuses time-domain features with time-frequency domain features, providing some improvement in the performance for signal recognition at low SNRs [14, 15].

Nonetheless, there are still some challenges to be considered and addressed. (1) Most of the CNN-based methods have low recognition accuracy for signals with low SNRs. (2) Recognizing electromagnetic signals with CNNs requires preprocessing methods or manually constructed features to reduce noise interference, increasing the complexity of signal processing. (3) Rare electromagnetic signal data, especially radar signal data, is difficult to meet the requirement for training deep CNNs. Furthermore, too large networks cannot easily be applied to mobile devices.

In contrast, spiking neural networks (SNNs) have great potential for development due to their biointerpretability and low power consumption. Li et al. use Gaussian-tuned coding to convert the time-frequency maps into pulses. Then, a single-layer SNN composed of tempotron neurons is used to process the pulses for signal recognition. Their simulations show that a single-layer SNN performs better than a 3-layer CNN [16]. Li et al.'s results suggest that a simple SNN may have better performance than a deeper CNN. Although deeper SNNs were less used due to difficulties in building and training in the beginning, some studies have shown that SNNs can be transformed from CNNs [17–19] or trained with a surrogate gradient [20, 21]. New methods for building and training SNNs enable SNNs to have good performance in classification. SNNs have achieved superior performance in efficiently processing complex and noisy spatial-temporal information [22]. SNNs show a higher potential for robustness in many ways compared to CNNs [23]. The information is less susceptible to random background noise in SNNs [24].

Thus, the purpose of this study is twofold. First, we propose a spiking convolution neural network (SCNN) for signal recognition in this paper. The SCNN combines the SNN with the CNN. It integrates the temporal and spatial information of the feature maps for better feature extraction. At the same time, the SCNN has a smaller model size compared to CNNs with the same accuracy. Second, the method of surrogate gradient for training the SCNN is given in this paper. In addition, two key parameters that affect the performance of the SCNN are analyzed and explained in detail. The remainder of this paper is summarized as follows. Section 2 describes the principles of time-frequency transform and SNNs besides the methods used in this paper. Section 3 determines the optimal values of two key parameters of the SCNN and compares the SCNN's performance with those of other networks. The noise generalization performance of the SCNN is analyzed at the end of this section. Finally, the conclusion is given in Section 4.

2. Theory and Methods

Figure 1 illustrates the process of identifying electromagnetic signals using the SCNN. The signals are first transformed into time-frequency maps. Then, the time-frequency maps are used as the input of the SCNN to complete the classification. Therefore, the first two layers of the SCNN are convolutional layers which are each followed by a layer composed of leaky integrate and fire (LIF) neurons. The feature maps after LIF neurons are then mapped to a pooling layer to reduce the dimension. And the two fully connected layers are each followed by a layer consisting of integrate and fire (IF) neurons. The number of LIF and IF neurons is the same as the size of the feature map of the previous layer. So, the LIF and IF layers do not change the size of the feature map.

2.1. Time-Frequency Distribution of Electromagnetic Signals. In order to avoid the features of one-dimensional signals being affected by noise, we use time-frequency distributions to get the features of signals. Different kernel functions correspond to different time-frequency distributions. A series of time-frequency distributions have been proposed, mainly including the Choi-Williams distribution (CWD), the smoothed pseudo-Wigner-Ville distribution (SPWVD), and the reduced interference distribution (RID) [25]. The CWD with minimal cross-terms among all unprocessed Cohen-like distributions is chosen in this paper. Its kernel function is shown in equation (1) as follows:

$$\phi(\theta, \tau) = e^{-\theta^2 \tau^2 / \sigma}. \tag{1}$$

The corresponding CWD is described in equation (2) as follows:

$$C(t, w) = \iiint \phi(\theta, \tau) s\left(u + \frac{\tau}{2}\right) s^*\left(u - \frac{\tau}{2}\right) e^{-j2\pi w\tau} e^{j2\pi(\theta u - \theta\tau)} du d\theta d\tau. \tag{2}$$

We use six signals commonly used in communication and radar, including the binary phase shift keying signal (2PSK), binary frequency shift keying signal (2FSK), quadratic frequency shift keying signal (4FSK), continuous wave signal (CW), linear frequency modulated signal (LFM), and nonlinear frequency modulated signal (NLFM). The Choi-Williams distributions of the 6 signals at 0 dB are given in Figure 2.

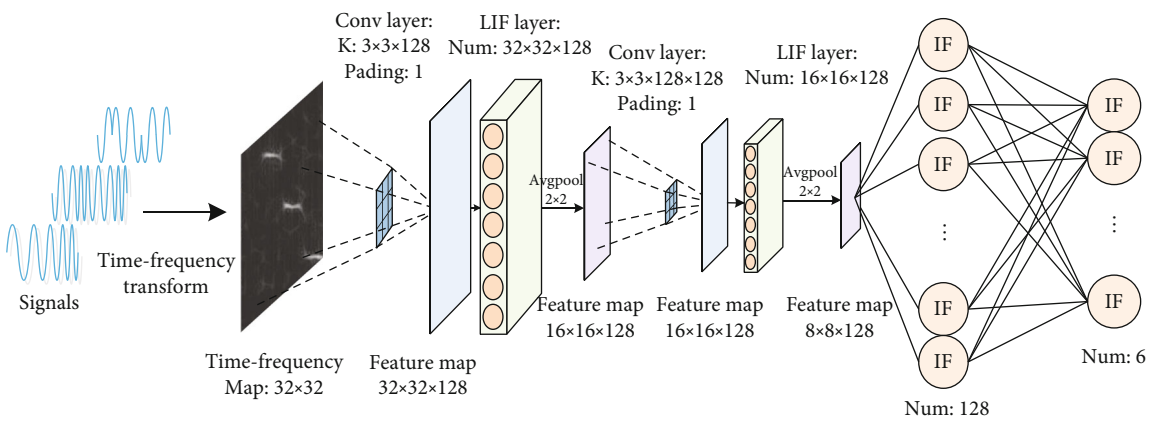

Figure 1: The process of identifying electromagnetic signals with the SCNN.

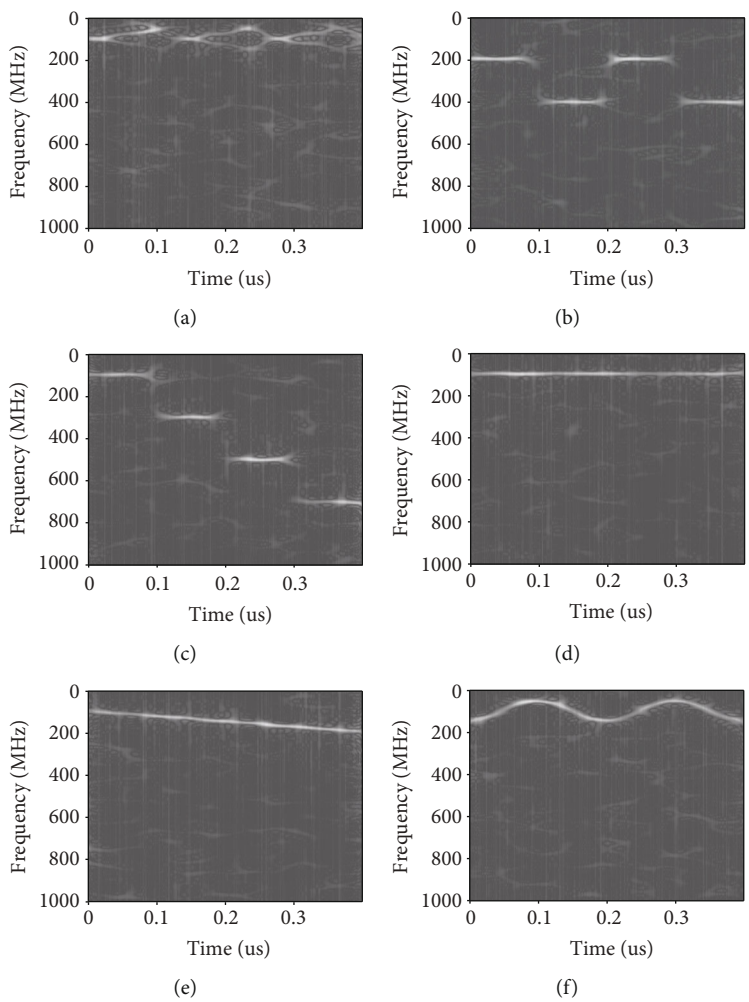

Figure 2: The Choi-Williams distributions of 6 electromagnetic signals at 0 dB. (a) 2PSK. (b) 2FSK. (c) 4FSK. (d) CW. (e) LFM. (f) NLFM.

2.2. Spiking Neural Network. Various spiking neuron models have emerged, including the Hodgkin-Huxley (HH) model, integrate-and-fire (IF) model, leaky-integrate-and-fire (LIF) model, and Izhikevich model [22]. Although its biological approximation is favourable, the HH model is computationally complex and inconvenient to use in practice. The simplified LIF and IF models have become common and widely used models, since they reduce the computational effort of the model while retaining the threshold-based membrane potential change rules of biological neurons. Both LIF and IF neurons are integral models. Their membrane potential is influenced not only by the input at the

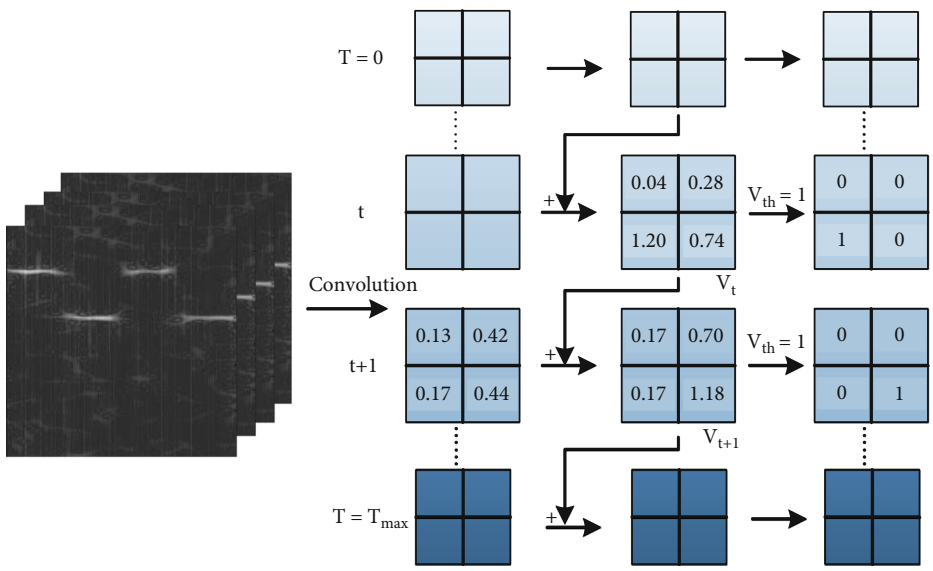

Figure 3: Activation of the SCNN based on threshold-based membrane potential change rules.

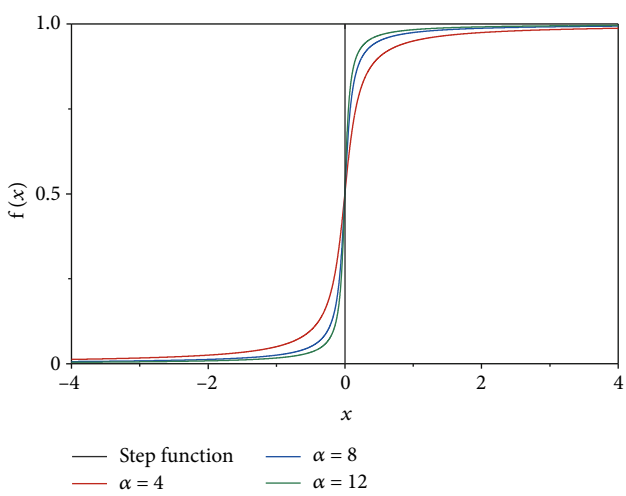

Figure 4: Approximation effect of the Atan function with different α. $f(x)$ is a step function or Atan function.

current moment but also by the membrane potential at the end of the previous moment. When the membrane potential does not exceed the threshold, the charging process of a continuous-time neuron can be expressed as equation (3) as follows:

$$\frac{dV(t)}{dt} = f(V(t), X(t)). \tag{3}$$

Equations (4) and (5) show the charging process of LIF and IF neurons, respectively.

$$\tau_n \frac{dV(t)}{dt} = -(V(t) - V_{\text{reset}}) + X(t), \tag{4}$$

$$\frac{dV(t)}{dt} = \frac{1}{C} X(t), \tag{5}$$

where τ_n is the time constant and V_{reset} is the reset voltage. An analytical solution to equation (4) cannot be obtained as the input $X(t)$ is a variable. The continuous differential equation is approximated by the discrete differential equation (6).

$$\begin{aligned} \tau_n(V[t] - V[t-1]) &= -(V[t-1] - V_{\text{reset}}) + X[t], \\ V[t] &= V[t-1] + X(t). \end{aligned} \tag{6}$$

For both discrete LIF and IF neurons, their forward propagation includes two processes, discharge and reset, in addition to the charging process. The discharge process can be expressed in equation (7).

$$S(t) = H\left(V_{\text{tmp}} - V_{\text{threshold}}\right), \tag{7}$$

where V_{tmp} is the voltage of the neuron before releasing the pulse after charging. $V_{\text{threshold}}$ is the threshold voltage at which the neuron is activated. $S(t)$ is the output pulse with a value of 1 for a released pulse and 0 for an unreleased pulse. $H(x)$ is the step function. For LIF and IF neurons, the difference lies in the charging process. The membrane potential of IF neurons remains unchanged in the absence of input, whereas the membrane potential of LIF neurons gradually falls below the resting potential in the absence of input due to leakage and then rises back to the resting potential.

2.3. Forward Propagation. As shown in Figure 1, the first convolutional layer is used directly for feature extraction and has no temporal state. It forms an autocoding layer with the LIF neurons in the second layer. Since the input of the first layer does not vary with time, additional computational effort can be reduced by placing this layer outside the process of time steps. In addition, batch normalization is

Table 1: Parameters of 6 signals.

Signals	Frequency (MHz)	Other parameters	Sampling rate (GHz)
2PSK	100	13-bit barker code encoding	2
2FSK	200/400	/	2
4FSK	100/300/500/700	/	2
CW	100	/	2
LFM	100	Time width: 0.4 μs, bandwidth 60 MHz	2
NLFM	100	Time width: 0.4 μs, bandwidth 60 MHz	2

Table 2: Simulation environment.

Environment	CPU	GPU	Coding language	Framework
Version	Intel i7-8700K@3.7 GHz	RTX2080	Python3.8.5	Pytorch1.8.1

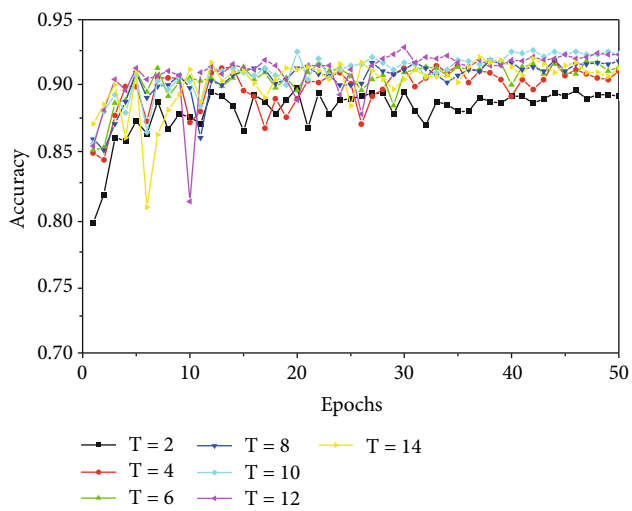

Figure 5: Impact of T on SCNN's performance when tested with signals at −12 dB.

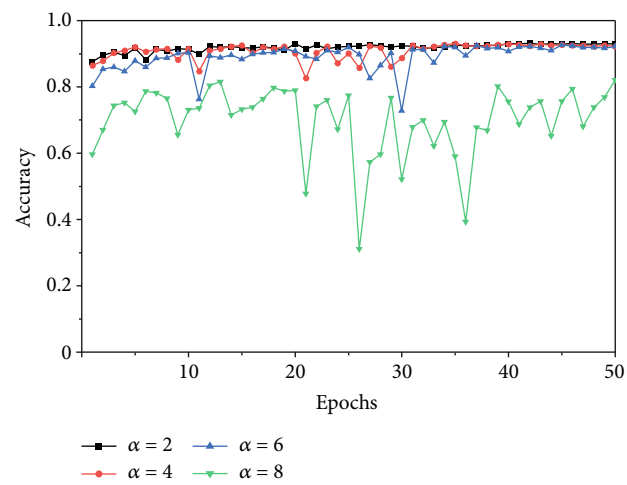

Figure 6: Impact of α on SCNN's performance when tested with signals at −12 dB.

performed after each convolution layer to accelerate the convergence of the SCNN.

Figure 3 shows the activation process of the SCNN in forward propagation. The eigenvalues of the time-frequency maps are assigned to the LIF neurons and then start to accumulate at the moment $T = 0$. When the activation threshold is reached, the LIF neuron releases a pulse and sets the membrane potential to $V_{\text{reset}} = 0$. If the neuron does not activate, the membrane potential is superimposed directly to the next moment $T = 1$. At the same time, if there is no input, the membrane potential will decay at a certain rate. This process is repeated until the end of the given time step. The size of the output feature map after the LIF neurons remains the same as the input size. This process completes the extraction of temporal features and achieves the fusion of spatial and temporal information.

Unlike the fully connected layers of CNNs which use probability for classification, the SCNN classifies signals by the frequency of pulses issued in time T. A higher frequency indicates a higher probability. The pulse frequency can be obtained as in equation (8), where j is the class of the signals and S^j_{sum} denotes the cumulative number of pulses issued by the j_{th} neuron in time T.

$$\text{Out}_j = \frac{S^j_{\text{sum}}}{T}. \tag{8}$$

Among all neurons in the last layer, the neuron with the highest pulse frequency corresponds to the predicted class of the input signal. Finally, the recognition accuracy of the SCNN can be determined by equation (9).

$$\text{Acc} = \frac{N_{\text{pre}}}{N_{\text{total}}}, \tag{9}$$

where N_{pre} is the number of signals correctly predicted and N_{total} is the total number of signals.

2.4. Backward Propagation. If the SCNN updates the weight w by backpropagating the error E_{total} with gradient descent, the chain rule in equation (10) gives its gradient transfer.

Table 3: Comparison of the composition of different networks.

Model	Layers	Model size (MB)
SNN1 [16]	1	0.376
CNN3 [8]	3	0.0094
LeNet5 [26]	5	0.239
Improved AlexNet8 [27]	8	99.4
VGG16 [28]	16	512
ResNet18 [29]	18	42.7
The proposed SCNN	8	4.58

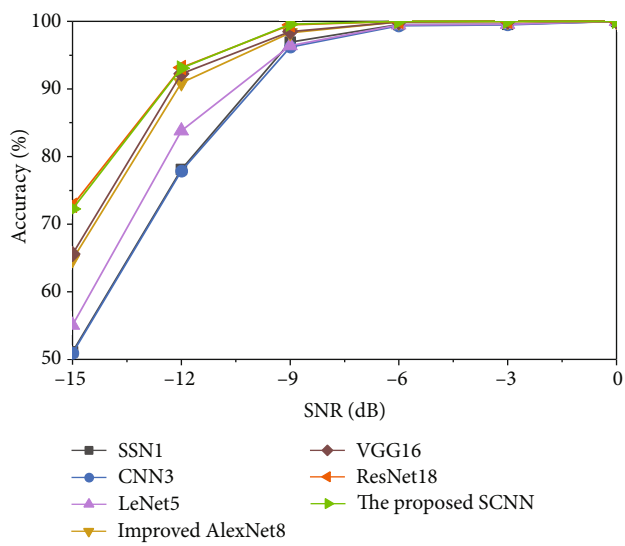

Figure 7: Comparison of the recognition accuracy of different networks for signals at different SNRs.

$$\frac{\partial E_{\text{total}}}{\partial w} = \frac{\partial E_{\text{total}}}{\partial S}\frac{\partial S}{\partial U}\frac{\partial U}{\partial w}, \tag{10}$$

where S denotes the output pulse and U denotes the membrane potential. As we know from equation (7), $\partial S/\partial U$ in equation (10) cannot be derived since $S(t)$ is a step function. The weights cannot be updated directly by gradient descent. Therefore, the method of surrogate gradient is proposed to train the SCNN. The commonly used surrogate functions are the sigmoid function and the Atan function. The approximation effects of the two functions are similar. The Atan function can be expressed as in equation (11).

$$f_A(x) = \frac{1}{\pi}\arctan\left(\frac{\pi}{2}\alpha x\right) + \frac{1}{2}. \tag{11}$$

The approximation effect of the Atan function on the step function under different α is shown in Figure 4. α can be regarded as the gradient factor. The larger its value, the larger the gradient is and the closer it is to the step function. However, too large α tends to gradient explosion at the threshold $x = 0$ and the gradient disappears far from the threshold, which finally leads to the weights not being updated in training. In this paper, the Atan function is used as the surrogate function. We analyze the effect of α to get its best value for optimal network performance.

3. Results and Discussion

In order to verify the advantages of the proposed SCNN in recognizing signals at low SNRs, 800 time-frequency maps of electromagnetic signals are generated for every 3 dB interval in the SNR range from 0 dB to −15 dB. 600 time-frequency maps are used for training, and 200 time-frequency maps are used for testing. To reduce computational effort, we used grayed-out time-frequency maps for training and testing. The time-frequency maps are scaled to a size of 32×32 using bicubic interpolation. Tables 1 and 2 show the signals' parameters and simulation environment, respectively. 64 time-frequency maps are taken as a batch. The learning rate is 0.1 at first and then changes by cosine annealing. Finally, the SCNN is optimized with the SGD optimizer.

3.1. Impact of the Time Step. As the SCNN accumulates pulses over time, its performance is affected by the length of the accumulation time. If the accumulation time is too short, the spiking neurons cannot be activated to fuse temporal and spatial information. If the accumulation time is too long, the network becomes very deep in time. The computational effort and inference delay of the SCNN are too much to meet the real-time requirement for signal recognition. In this paper, we should first determine an optimal time step T for accumulating pulses. Theoretically, T only affects the depth of the SCNN in time. And the gradient factor α only affects the backpropagation of inaccuracies. Actually, numerous experiments also show that T and α independently affect the performance of the SCNN. As a result, the optimal values of T and α can be obtained by controlling the variables T and α. First, α is kept unchanged. T is changed from 2 to 14. When recognizing 6 signals from 0 dB to −15 dB, the accuracy trends with iterations are consistent for the same T at different SNRs. Only the results of $\alpha = 2$ at −12 dB are shown in Figure 5 for limited pages. The accuracy of the SCNN can reach the maximum value and remains relatively stable after 40 iterations when $T = 10$ and $T = 12$. Since an increase in T will lead the increasing of delay, $T = 10$ is chosen as the optimal time step.

3.2. Impact of the Gradient Factor. Since T and α independently affect the performance of the SCNN, we can keep the time step $T = 10$ as we have gotten. The gradient factor α is changed from 2 to 8. When recognizing 6 signals from 0 dB to −15 dB, the trends of accuracy with iterations are consistent for the same α at different SNRs. Only the results at −12 dB are shown in Figure 6 for limited pages. As shown in Figure 6, the convergence of the SCNN worsens with increasing α. It can be seen that the recognition accuracy is the highest and most stable when $\alpha = 2$. And $\alpha = 2$ is finally adopted.

3.3. Result Comparison of Different Networks. Six electromagnetic signals at SNRs from 0 dB to −15 dB are identified with the SCNN when $T = 10$ and $\alpha = 2$. Other simulation

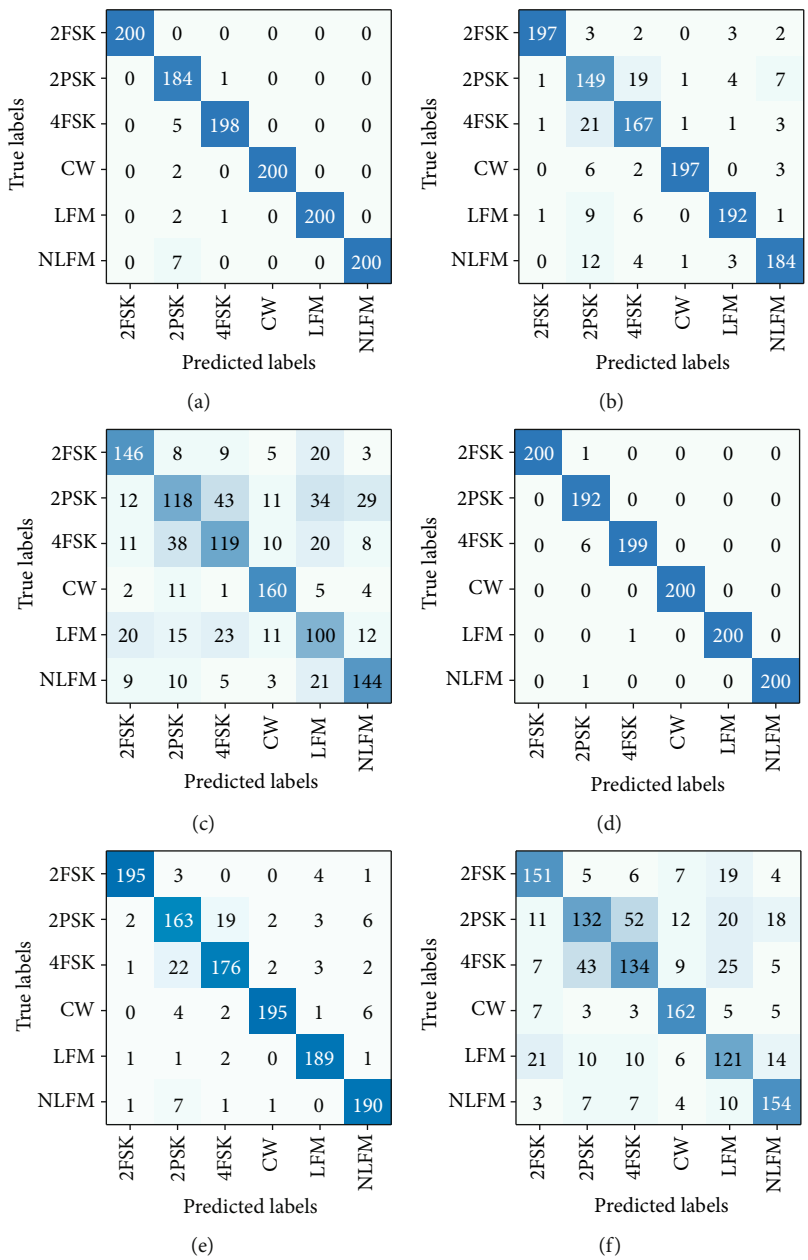

Figure 8: Confusion matrices of VGG16 and SCNN for 6 electromagnetic signals at −9 dB/−12 dB/−15 dB. (a) VGG16 tested at −9 dB. (b) VGG16 tested at −12 dB. (c) VGG16 tested at −15 dB. (d) SCNN tested at −9 dB. (e) SCNN tested at −12 dB. (f) SCNN tested at −15 dB.

settings are shown at the beginning of Section 3. Table 3 shows the composition and size of different networks. SNN1 is a single-layer SNN consisting of the temptron neurons [16]. CNN3 is a 3-layer CNN proposed by Ye et al. [8]. 5-layer LeNet5 is used by Guo et al. [26]. The improved AlexNet8 is proposed by Yang et al. [27]. VGG16 is used by Li and Zhu [28]. Furthermore, as the residual structure gives better performance of deep CNNs, we make a further comparison with an 18-layer ResNet18 with a residual structure [29].

As the recognition accuracy of different networks shown in Figure 7, it is found that the proposed SCNN and ResNet18 own better recognition accuracy among all the models at different SNRs. The reason that ResNet18 performs well is because of the inclusion of the residual structure [29]. Although the performance of ResNet18 is comparable to that of the SCNN, the ResNet18's model size is about 9 times of the proposed SCNN, which has been shown in Table 3. In Figure 7, we can also find out that the recognition accuracy of CNN3 is relatively low due to its simple structure. With the increasing of depth, the fit ability of CNN-based models is enhanced, resulting in the increasing of recognition accuracy for the six signals at different SNRs. Even so, the recognition accuracy of CNN-based models with a large number of layers, such as VGG16, is still lower than that of the proposed SCNN. The outstanding performance of the SCNN compared to CNNs is attributed to its accumulated information in time which

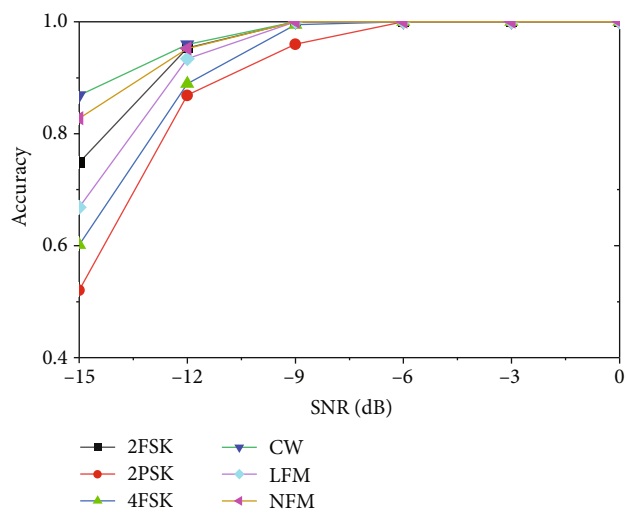

Figure 9: Recognition accuracy of the SCNN for each signal at different SNRs.

Table 4: Recognition accuracy of SCNN with different training and testing SNRs.

	Accuracy (%)			
SNR (dB)	0 (tested)	−3 (tested)	−6 (tested)	−9 (tested)
0 (trained)	100	100	91.25	50.66
−3 (trained)	100	100	98.08	60.08
−6 (trained)	100	100	99.83	90.58
−9 (trained)	100	100	99.91	99.16

compensates for its lack of spatial depth. The fusion of temporal and spatial information allows the SCNN to have good antinoise ability.

Based on the previous analysis, we know that VGG16 has the best performance for all CNNs without a residual structure. To further illustrate the advantages of the SCNN over ordinary CNNs without a residual structure, the confusion matrices of VGG16 and the SCNN are given in Figure 8. As the SNR decreases, the energy of noise covers the energy of signals. The energy distribution of different signals becomes blurred in the time-frequency maps, leading to a decrease in the recognition accuracy of both the VGG16 and SCNN for various signals. But in all, the overall recognition accuracy of the SCNN is still higher than that of the VGG16.

Figure 9 shows the recognition accuracy of the SCNN for each signal at different SNRs, in which we can see that the recognition of 2PSK is most susceptible to noise. This is because the energy of frequency components of 2PSK is relatively dispersed compared with other signals, which has been shown in Figure 2.

3.4. Analysis of Generalization Performance for Noise. In order to verify the generalization performance of the SCNN for noise, 6 electromagnetic signals at 0 dB, −3 dB, −6 dB, and −9 dB are used for training and testing. As shown in Table 4, the recognition accuracy is very high when the SNRs of trained signals are lower than or comparable with those of tested signals. Only when the SNRs of tested signals are much lower than those of trained signals will the recognition accuracy decline. So, it indicates that the SCNN has good generalization performance for noise in a certain SNR range.

4. Conclusions

The SCNN proposed in this paper utilizes the convolutional layer as visual perception. The LIF neurons and IF neurons are used to construct the convolutional layers and fully connected layers of the SCNN, respectively. The feature maps are converted into pulses to obtain temporal information, which enables the SCNN to perform well in the recognition of electromagnetic signals. And the outstanding recognition performance of the SCNN for electromagnetic signals at low SNRs is verified through the recognition of 6 signals at different SNRs. As a third-generation neural network, information transmission in the form of pulses in SNNs has stronger biological interpretability. The low power consumption of SNNs can get greater benefits in signal recognition.

Data Availability

The data used to support the findings of this study are available from the corresponding author upon request.

Conflicts of Interest

The authors declare that they have no conflicts of interest.

Acknowledgments

This work was supported by the State Key Laboratory of CEMEE (Grant no. CEMEE2022K0102A).

References

[1] J. S. Mu, Y. H. Tan, D. L. Xie, F. Zhang, and X. Jing, "CNN and DCGAN for spectrum sensors over rayleigh fading channel," *Wireless Communications and Mobile Computing*, vol. 2021, Article ID 9970600, 12 pages, 2021.

[2] G. M. Wang, S. W. Chen, J. Huang, X. Qin, and J. J. Yuan, "Radar emitter sorting and recognition based on multi-synchrosqueezing transform," *Modern Radar*, vol. 42, no. 3, pp. 49–56, 2020.

[3] X. F. Li, F. W. Dong, S. Zhang, and W. Guo, "A survey on deep learning techniques in wireless signal recognition," *Wireless Communications and Mobile Computing*, vol. 2019, Article ID 5629572, 12 pages, 2019.

[4] X. Qin, X. Zha, J. Huang, and L. Luo, "Radar waveform recognition based on deep residual network," in *The 8th IEEE Joint International Information Technology and Artificial Intelligence Conference*, pp. 892–896, Chongqing, China, 2019.

[5] T. Huynh-The, C. H. Hua, V. S. Doan, Q. V. Pham, and D. S. Kim, "Accurate deep CNN-based waveform recognition for intelligent radar systems," *IEEE Communications Letters*, vol. 25, no. 9, pp. 2938–2942, 2021.

[6] R. Ahmed, Y. Chen, and B. Hassan, "Deep learning-driven opportunistic spectrum access (OSA) framework for cognitive

5G and beyond 5G (B5G) networks," *Ad Hoc Networks*, vol. 123, pp. 102632–102645, 2021.

[7] M. Xu, J. Hou, P. Wu, Y. Liu, and Z. Lv, "Convolutional neural networks based on time frequency characteristics for modulation classification," *Journal of Computer Science and Technology*, vol. 47, no. 2, pp. 175–179, 2020.

[8] W. Q. Ye, Z. F. Yu, H. B. Wang, and K. Zhang, "Recognition algorithm of emitter signals based on CNN," *Computer Simulation*, vol. 36, no. 9, pp. 33–37, 2019.

[9] Y. Yao and Z. H. Wang, "Radar signal recognition based on time-frequency and CNN preprocessing," *Journal of Detection & Control*, vol. 40, no. 6, pp. 99–105, 2018.

[10] Y. H. Xiao, L. Wang, and Y. X. Guo, "Radar signal modulation type recognition based on denoising convolutional neural network," *Journal of Electronics & Information Technology*, vol. 43, no. 8, pp. 2300–2307, 2021.

[11] P. U. Yun-Wei, G. U. Jiang, L. I. Shou-Shou, and W. U. Hai-Xiao, "A recognition method for radar emitter signals based on convolutional neural network with multiple learning units," *Journal of Beijing University of Posts and Telecommunications*, vol. 44, no. 6, pp. 74–82, 2021.

[12] C. X. Xie, L. M. Zhang, and Z. G. Zhong, "Radar signal recognition based on time frequency feature extraction and residual neural network," *Systems Engineering and Electronics*, vol. 43, no. 4, pp. 917–926, 2021.

[13] P. Y. Cao, C. Z. Yang, C. Z. Chen, Z. S. Chen, L. Wang, and L. M. Shi, "Radar signal recognition method based on deep residual shrinkage attention network "In press"," *Systems Engineering and Electronics*, 2022.

[14] N. Wang, Y. Liu, L. Ma, Y. Yang, and H. Wang, "Multidimensional CNN-LSTM network for automatic modulation classification," *Electronics*, vol. 10, no. 14, p. 1649, 2021.

[15] L. M. Shi, C. Z. Yang, M. L. Wang, and B. Xu, "Recognition method of radar signal modulation method based on deep network," *Journal of Ordnance Equipment Engineering*, vol. 42, no. 6, 2021.

[16] W. Li, W. G. Zhu, and B. K. Zhu, "Modulation pattern recognition of radar emitter based on spiking neural network," *Telecommunication Engineering*, vol. 62, no. 1, pp. 11–16, 2022.

[17] X. Yang, Z. X. Zhang, W. P. Zhu, S. Yu, L. Liu, and N. Wu, "Deterministic conversion rule for CNNs to efficient spiking convolutional neural networks," *Science China (Information Sciences)*, vol. 63, no. 2, pp. 196–214, 2020.

[18] Y. Shang, Y. Li, F. You, and R. Zhao, "Conversion-based approach to obtain an SNN construction," *International Journal of Software Engineering and Knowledge Engineering*, vol. 30, no. 11, pp. 1801–1818, 2020.

[19] S. Takuya, R. Y. Zhang, and Y. Nakashima, "Training low-latency spiking neural network through knowledge distillation," in *IEEE Symposium on Low-Power and High-Speed Chips (IEEE COOL CHIPS)*, pp. 14–16, Tokyo, Japan, 2021.

[20] C. Zhang and F. Z. Tang, "Self-adaptive coding for spiking neural network," *Application Research of Computers*, vol. 39, no. 2, pp. 593–597, 2022.

[21] M. Y. Xu, "Spiking neural network training algorithm based on gradient descent," *Modern Computer*, vol. 27, no. 35, pp. 1–11, 2021.

[22] Y. F. Hu, G. Q. Li, Y. J. Wu, and L. Deng, "Spiking neural networks: a survey on recent advances and new directions," *Control and Decision*, vol. 36, no. 1, pp. 1–26, 2021.

[23] T. L. Zhang and B. Xu, "Research advances and perspectives on spiking neural networks," *Chinese Journal of Computers*, vol. 44, no. 9, pp. 1767–1785, 2021.

[24] X. Cheng, Y. Hao, J. Xu, and B. Xu, "LISNN: improving spiking neural networks with lateral interactions for robust object recognition," in *Proceedings of the International Joint Conference on Artificial Intelligence*, pp. 1519–1525, Yokohama, Japan, 2020.

[25] Y. P. Liu, C. Wang, and H. Y. Xia, "Application progress of time-frequency analysis for lidar," *Laser & Optoelectronics Progress*, vol. 55, no. 12, pp. 68–83, 2018.

[26] P. P. Guo and L. Y. Wu, "LPI radar signal recognition with convolution feature and discrimination dictionary learning," *Acta Armamentarii*, vol. 40, no. 9, pp. 1881–1889, 2019.

[27] J. Yang and H. Zhang, "LPI radar signal recognition based on improved Alex Net," *Modern Electronic Technology*, vol. 43, no. 5, pp. 57–60, 2020.

[28] K. Li and W. G. Zhu, "Radar emitter identification method based on deep learning," *Electronic Design Engineering*, vol. 28, no. 12, pp. 99–104, 2020.

[29] C. Dong, C. W. Zhuang, Y. Gao et al., "Mixed communication signal recognition based on residual neural network," *Radio Engineering*, vol. 50, no. 9, pp. 727–731, 2020.

Hindawi
Wireless Communications and Mobile Computing
Volume 2022, Article ID 6296954, 12 pages
https://doi.org/10.1155/2022/6296954

Research Article

Electromagnetic Signal Intelligent Identification Based on Radio Frequency Fingerprints

Jian Kang,[1] Hui Mu,[1] Hui Ren,[1] Jicheng Jia,[2] Lin Qi,[2] and Zherui Zhang[2]

[1]*Telecommunication Research from Beijing Institute of Astronautical System Engineering, Beijing 100076, China*
[2]*College of Information and Communication Engineering, Harbin Engineering University, Harbin 150001, China*

Correspondence should be addressed to Zherui Zhang; zhangzherui@hrbeu.edu.cn

Received 24 March 2022; Accepted 6 May 2022; Published 7 June 2022

Academic Editor: Mingqian Liu

Due to the open nature of WIFI connection, it is exposing its private information to the attackers. Traditional WIFI security methods are no longer able to meet the current security needs, and more and more wireless-side physical layer security solutions provide solutions, among which RF fingerprinting is an endogenous security technology with potential. Constructing an effective and accurate method to identify WIFI devices that steal information is a difficulty that today's society needs to face. The main problem is not only that the recognition accuracy is difficult to improve but also the problem of data shortage. In this paper, we first construct a large-scale WIFI real-world measurement dataset. Next, we use PSD and bispectrum features, as well as complex ResNet schemes for WIFI device identification experiments, and compare and analyze them from multiple perspectives. The experimental results show that the proposed algorithm can achieve up to 97% recognition accuracy among 100 devices. Moreover, when the SNR is 0 dB, the complex ResNet method can still achieve 78% recognition accuracy among 100 devices. Finally, this paper summarizes the experimental analysis of the measured dataset and discusses the open issues related to this area.

1. Introduction

According to IoT analytics, the Internet of Things (IoT) market is expanding at an accelerated rate and the number of connected IoT devices is increasing rapidly. In 2021, IoT analytics expects the number of connected IoT devices to grow by 9 percent to 12.3 billion active IoT devices worldwide. This number is expected to reach 30 billion by 2025. As shown in Figure 1, while IoT technology brings convenience to life, it also poses many security risks and its security is becoming increasingly prominent.

As a standard for high-throughput wireless connectivity, the IEEE 802.11 standard, or WIFI standard, is highly vulnerable to various attacks [1–3]. There are many methods for WIFI device identification. However, all these schemes have certain vulnerabilities and the standard IEEE 802.11 authentication method may encounter various attacks such as man-in-the-middle attacks, deauthentication flooding attacks, MAC address replication, and other attacks. Such security vulnerabilities can lead to serious system risks, so it becomes especially important to perform secure and accurate WIFI device identification.

In addition to the methods mentioned above, the identification and authentication of wireless devices can also be performed using Radio Frequency Fingerprinting (RFF) technology [4]. The concept of "RF fingerprinting" was first proposed in 2003, and this technology is a physical layer method to enhance the security of wireless networks by extracting the subtle features of radiation source devices to build device fingerprints similar to those in biology, thus completing device identification. The process of RF fingerprint extraction and identification is carried out in its physical layer, which can work alone as well as assist network-side security mechanisms to improve security for communication networks.

The basic characteristics of the physical layer of the device are only related to the hardware characteristics of the device itself, and the characteristics of the physical layer can accurately locate each machine in a large number of devices [5]. Although such hardware differences can be

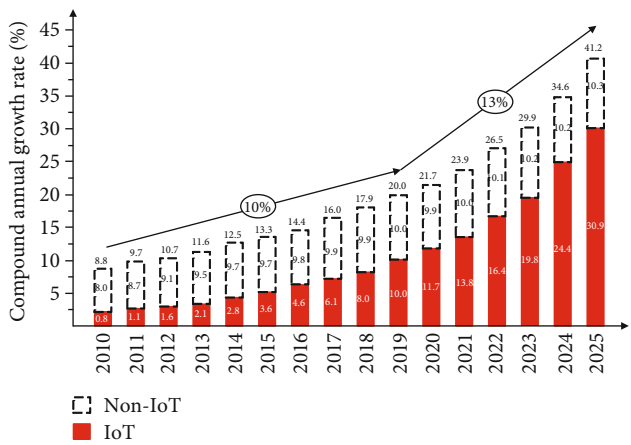

Figure 1: Trends in the number of IoT device connections.

reduced by more precise manufacturing and quality control means, they are usually not feasible in practical environments because they lead to significantly higher production costs. Physical layer-based security protection mechanisms have been extensively studied in recent years. They play an important role in network intrusion detection [6], fault diagnosis [7], target tracking [8, 9], radar detection [10, 11], etc.

RF fingerprinting technology has had important applications in radiation source identification systems, which can be used for secure identification and authentication of WIFI devices based on physical layer information. Fingerprint features are generated due to certain hardware "defects" introduced during the device manufacturing process, which are reflected in the communication signal and are similar to fingerprints in biology, which are also unique and difficult to be copied [5].

The individual identification of communication devices based on RF fingerprints is of great importance in many fields. In the military field, the use of RF fingerprint extraction and identification technology can identify important radar, communication, navigation, data chain and other radiation source individuals, grasp the identity and attributes of the user, and make strategic adjustments by tracking and monitoring enemy equipment, so as to grasp the initiative of military operations in the complex battlefield environment. In the civilian field, RF fingerprinting technology has important applications in wireless network security, equipment fault diagnosis, and quality management. Especially in the field of security of communication networks [12], the security problems brought by wireless communication networks due to their inherent openness need urgent attention [13], and most of the traditional methods for securing wireless networks are realized through authentication based on the physical layer above. Since RF fingerprinting is an inherent property of the physical layer of wireless devices, it is not easily tampered with and can effectively improve wireless network security, and RF fingerprinting technology can detect malicious network attacks, which is of great significance to enhance wireless network security.

In this paper, we address the problem of accurate identification of physical layer based on RF fingerprinting for a large number of WIFI devices working in real environment. It is planned to collect in batches for more than 100 WIFI devices in multiple channel environments to build the dataset. And multiple methods are used for identification testing. Therefore, the difficulty of this paper is that the number of devices to be identified is large and the recognition effect is difficult to improve due to the complex and diverse channel environment, but this paper is also more practical.

This paper will introduce three algorithms to solve the above problem. The main contributions of this paper are summarized as follows:

(1) We propose one of the largest WIFI real-world datasets available. This includes 100 WIFI devices of IEEE 802.11b standard, collected in various scenarios, including darkroom and laboratory, and various channel environments, including LoS and NLoS, using several spectrometer devices for real measurements. A total of 500 GB of WIFI signal dataset was constructed

(2) We designed two algorithms based on feature engineering, namely, power spectrum analysis and dual spectrum analysis, and conducted experiments on WIFI device identification. The results show that the two algorithms based on feature engineering can achieve more than 92% recognition accuracy on 100 devices. The performance, advantages, and shortcomings of the algorithms are compared from several perspectives. The experimental results are also fully analyzed

(3) We designed a deep learning-based algorithm for WIFI device recognition using a deep complex residual network. The results show that the algorithm can achieve more than 97% recognition accuracy on 100 devices. The experimental results are analyzed and compared with the two algorithms based on feature engineering

The rest of the paper is organized as follows. In Section 2, the work on RF fingerprinting is presented. In Section 3, the WIFI device recognition system of this paper is introduced and the acquisition process of the large-scale real-world dataset used in this paper is presented. The WIFI device recognition algorithm based on feature engineering and deep learning will be introduced in Section 4. And in Section 5, simulation experiments are conducted to compare and analyze the results from multiple perspectives. Finally, a summary of the full work is presented in Section 6, where the experimental results are summarized and analyzed.

2. Related Work

The RF fingerprint feature extraction and device identification system is shown in Figure 2.

Generally speaking, the radiation source identification system based on RF fingerprint technology is composed as follows: data acquisition part, preprocessing part, fingerprint feature calculation and extraction part, and classification and

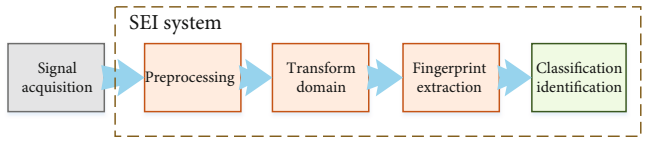

Figure 2: Block diagram of radiation source equipment classification and identification system.

identification part. Data acquisition part is the use of acquisition equipment for wireless or wired signal acquisition, usually using oscilloscopes, spectrometers, Universal Software Radio Peripheral (USRP), Software Defined Radio (SDR), and other equipment and platforms, etc. The performance and structure of the front-end equipment usually have an impact on the RF fingerprinting system, and the performance of the system and the performance, mobility, and portability of the acquisition equipment need to be considered. The preprocessing part is to perform data cleaning, interception, noise reduction, and other operations on the collected device signal data and to unify the multiple signals that may be collected by multiple devices, so that they can be applied to the calculation and extraction of fingerprint features. Fingerprint feature calculation and extraction is the most important part of the system, mainly through one or more signal processing algorithms to carry out transform domain analysis of the signal, so as to extract subtle features such as unintentional modulation that may otherwise be submerged in the modulated signal, find subtle differences in the signal that can be used to distinguish multiple devices, and output them as the device's RF fingerprint features. Finally, the classification and recognition part often uses generative or nongenerative classifiers, etc. The obtained fingerprint features are used to train the classifier, or they are fed to the already trained classifier to get the final recognition result, so that the RF fingerprint-based radiation source device recognition is achieved. Besides, there are data enhancement, data dimensionality reduction, and other components, which can be added or deleted as appropriate.

The transient and steady-state signal segments are considered separately for RF fingerprinting studies. Among them, the transient signal segment is a signal segment with a short duration of gradual power increase generated by the device at the moment of switching on and off. Since it is only related to the hardware circuit of the device and contains rich information about the subtle characteristics of the radiation source device, the transient signal is a suitable signal to be used for RF fingerprinting technology research [14, 15]. However, it is difficult to capture the signal segment quickly and accurately in a real system. The steady-state signal is the signal segment of the transmitter RF signal that operates stably at rated power, and the steady-state signal lasts longer and is easier to obtain than the transient signal [16]. The radiation source signal received by the receiver is shown in Figure 3, and it can be seen that the signal collected by the receiver is extremely rich, including the channel noise segment, transient signal segment, and steady-state signal segment.

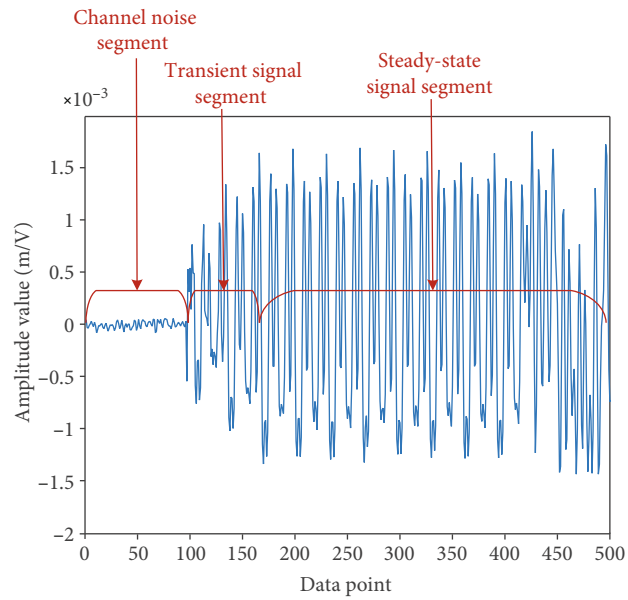

Figure 3: IEEE 802.11a wireless signal.

For the problem of individual identification of WIFI devices based on RF fingerprinting studied in this paper, the domestic and international research is summarized into the following five categories of methods.

2.1. RF Fingerprinting Based on Location Information. Location-based RF fingerprinting systems are built on features such as radio signal strength (RSS), channel state information (CSI), and channel frequency response (CFR), which are signal segments that contain location information about the target device. Therefore, these systems are designed to use the unique location information of the device for device identification.

Generally speaking, such systems mainly utilize the special structure of IEEE 802.11 standard frames of WIFI to extract the corresponding fingerprint features and perform device identification by processing data segments such as short training field (STF), long training field (LTF), and pilot frequencies.

In 2018, Li et al. used an FPGA- (Field Programmable Gate Array-) based platform to achieve 85% recognition rate in three devices using features, such as CSI, RSS, and received frequency bias extracted from the leading signal, and verified the algorithm and platform proposed in the paper in real-time communication with commercial WIFI devices in validity [17]. In 2019, the literature [18] proposed a RFF feature extraction method for the differential phase of the guide frequency (DPoP) and the amplitude of the quotient (AoQ) using the guide frequency, STF, and LTF of OFDM frames and used deep neural networks (DNN) to classify and identify a total of 55 WIFI devices for five devices, achieving 95% identification accuracy when the SNR was higher than 40 dB.

2.2. RF Fingerprinting Based on Transmission Signal. RF fingerprinting technology systems based on signal statistical

features are built on features extracted from transient and steady-state signals and presynchronization codes. These systems use the uniqueness of a fixed segment of all RF signal packets sent by the authenticated device for device identification. The feature extraction algorithms used are generally commonly used signal processing algorithms with advantages such as reproducibility and ease of implementation.

In 2019, Yang et al. collected the overall burst signal of a transmitter from power on to data communication to power off and proposed a classification scheme based on sparse representation (SRC), whose results indicated that the identification performance using multiple signal segments as RF fingerprints outperformed the results using only one signal segment [19]. In 2020, the literature [20] proposed the use of fractional order Fourier transform, power spectrum, and bispectral analysis of feature extraction method to achieve multiangle feature extraction, which can still achieve better recognition performance on 10 intercom devices even with low SNR.

2.3. RF Fingerprinting Based on RF Modulation Error. The RF fingerprinting system based on signal modulation errors is similar to the previous type of scheme, using transient and steady-state signal segments for feature extraction. The difference is that this part of the features has a strong physical meaning and is an unintentional modulation feature of the transmitter.

In 2020, it is also possible to use the constellation diagram feature of the signal for the extraction of fine features, the principle of which lies in the fact that communication standards specify that the signal modulation can have a certain range of errors, and this error is the feature space in the field of RF fingerprinting technology, thus enabling the RF fingerprinting of devices [21].

2.4. RF Fingerprinting Based on Physical Modeling. Mathematical modeling of key hardware components in wireless communication systems is also an extremely important task. The physical model obtained by modeling can also be used as a unique feature to distinguish different radiation source devices.

Such systems are mainly used to perform device identification by mathematical modeling of the overall system or a single device, and the obtained model will be used. The literature [22] allows the extraction of the nonlinear components of the radiation source device and the analysis of the signal in the frequency domain for the identification of the radiation source device. The literature [23], on the other hand, directly models the transmitter link as a whole and fits the model using a kernel regression model to obtain an RF fingerprint of the radiation source called FID, which can achieve 99% identification accuracy on 33 devices.

2.5. RF Fingerprinting Based on Deep Learning. Deep learning has achieved good results in a variety of classification domains, and the use of deep learning for transmitter identification is a feasible solution. Deep learning models directly use the RF signals sent by the device and can be trained by training a designed deep network model to classify the device [24–27].

In 2018, literature [28] used convolutional neural network (CNN) to classify wireless signals to identify IoT devices with 92.29% recognition accuracy on seven ZigBee devices and high channel robustness. In 2019, literature [29] proposed a neural network-based radiation source identification algorithm that can be executed on resource-constrained IoT devices and can achieve better good recognition performance, which provides a reference for the grounded application of the algorithm. In 2019, and for the small and zero-sample problem in deep learning, a ZSL framework for signal recognition and reconstructed convolutional neural network (SR2CNN) is proposed in the literature [30] to solve the relevant recognition problem in this case. Appropriate combinations of cross-entropy loss, central loss, and reconstruction loss as well as a suitable distance metric space are introduced to learn the representation of the signal semantic feature space so that the semantic features have a larger minimum interclass distance than the maximum intraclass distance. In 2021, the literature [31] used the actual collected ADS-B signals to construct a dataset that provides an in-depth study of the performance of the deep learning model and compares it with recognition benchmarks using machine learning and deep learning methods. An open-ended discussion is also provided.

To address the challenge that the existing models have large number of parameters and are difficult to deploy. Pruning methods have also been proposed in the literature that omit the less important convolutional filters and achieve equal or higher classification accuracies [32, 33]. In addition to this, there are distributed sensor systems that use incremental learning to solve the RF fingerprint identification problem [34].

The above analysis reveals that most of the existing algorithms can achieve better results in a certain scale of radiation source devices; however, they are more susceptible to noise, channel environment, etc. Some algorithms can achieve considerable results in a larger number of devices; however, their algorithms are more complex and more difficult to implement, which is not easy to carry out practical applications and deployments. Therefore, the current RF fingerprinting technology focuses on the need to solve the problem of achieving effective identification of large-scale radiation source devices easily and quickly in a variety of complex channel environments, which is the main research direction of this paper.

3. Dataset Construction

For the content to be studied in this paper, the dataset is constructed as follows. The data collection object is 100 IEEE 802.11b standard 2.4GHz WIFI network card modules. The selected 2.4GHz WIFI module model is ESP8266. The WIFI module is set to IEEE 802.11b WIFI standard communication mode through configuration, sending Beacon frame signal every 100 ms, and RF signal bandwidth 20 MHz. The module is a complete module, including WIFI chip, external circuit, and PCB antenna. In this paper, a spectrometer is

used for wireless acquisition of signal power triggers, and the FSW26 spectrometer from Rohde & Schwarz is selected. This spectrometer provides multiple sampling rates for the experiments.

Signal data acquisition and dataset construction are carried out using the abovementioned equipment. Wireless acquisition of LoS, multipath, and NLoS multipath channels in the laboratory and microwave darkroom is carried out using FSW26 spectrometers. Signal acquisition is mainly performed for 100 2.4 GHz WIFI modules, 100 5 GHz WIFI modules for management frame Beacon frames, and I/Q signal acquisition using 40 M, 80 M, and 160 M sampling rates in channel 1 and 6 transmission channels.

Data acquisition scenarios cover many scenarios, such as laboratory LoS, LoS multipath, NLoS multipath scenarios, and darkroom LoS scenarios, including the acquisition of WIFI signal data in scenarios with different receiving devices, different transmission channel numbers, and different channel environments.

The data acquisition platform is built using MATLAB and python-based platforms on the computer side, and the RF signal is automatically acquired from WIFI devices by using a network cable to connect the spectrum meter for control and setting the acquisition parameters, etc.

The data acquisition environment is set as follows. Among them, the laboratory LoS environment is the WIFI module, and the spectrum meter antenna is about 1 m apart; the laboratory NLoS environment is the WIFI module, and the spectrum meter antenna is about 2 meters apart, and there is a baffle in the direct path.

In several acquisition scenarios, the obtained WIFI signal data are stored in Excel xlsx file format using the data acquisition platform to record the I/Q two-way amplitude values of RF signals. The final dataset obtained is 500 GB in total.

4. System Implementation

This paper will study the performance of two commonly used signal processing algorithms, power spectral density analysis and bispectral analysis, in the field of RF fingerprinting technology, analyze their basic theory, and study their feasibility in the field of RF fingerprinting technology for WIFI devices. Besides, this paper will study the performance of the residual neural network model technique applied to WIFI device identification, analyze its basic theory, and introduce its complex processing form to study its feasibility in the field of WIFI device identification.

In this paper, we use the individual identification framework shown in Figure 1 to design the WIFI device identification system shown in Figure 4. The system includes a signal acquisition module, which uses a spectrum meter for power-triggered acquisition of WIFI signals. After that, the collected signals are intercepted as well as normalized. After that, the RFF calculation and extraction are performed, and this paper uses two methods of feature engineering and deep learning models for RFF extraction. Next, the system will build the RFF library for the training of the classifier. Finally, the output of the device recognition results is performed.

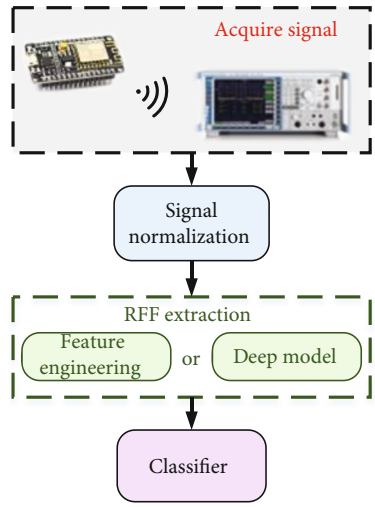

Figure 4: Block diagram of WIFI device identification process.

4.1. PSD-Based WIFI Device Recognition Algorithm. Power spectral density (PSD) analysis is a probabilistic statistical characterization of a random signal, which refers to the "power" (mean square value) per unit frequency band, also known as energy spectrum, power spectrum, spectral density, etc. Suppose there is a smooth random signal such as then the PSD is shown in

$$P(\omega) = |S(\omega)|^2, \tag{1}$$

where $S(\omega)$ is the Fourier transform of the smooth random signal $s(t)$, i.e.

$$S(\omega) = \int_{-\infty}^{+\infty} s(t) \cdot e^{-j\omega t} dt. \tag{2}$$

According to the Wiener-Khinchin theorem, the autocorrelation function of a smooth random signal and the power spectral density present a Fourier transform relationship. That is, the autocorrelation function of a signal can be used for its power spectral density estimation, which is also a classical method for power spectral density estimation.

Now, assume that the received signal is $s[n]\{n = 0, 1, 2, 3, \cdots, N-1\}$, where N is the number of received signal points, then the autocorrelation function $\widehat{R}_{ss}[\tau]$ of signal $s[n]$ can be expressed as

$$\widehat{R}_{ss}[\tau] = \frac{1}{N} \sum_{i=0}^{N-|\tau|-1} s[i]s^*[i+\tau]. \tag{3}$$

Since the received signal $s[n]$ is a smooth random process signal, its autocorrelation function is only related to the time interval τ, where $s^*[i]$ denotes the complex conjugate of signal $s[n]$.

After obtaining the autocorrelation function $\widehat{R}_{ss}[\tau]$, the power spectral density estimate $\widehat{P}(\omega)$ of signal $s[n]$ is shown in

$$\widehat{P}(\omega) = P_N(\omega) = \sum_{\tau=-(N-1)}^{N-1} \widehat{R}_{ss}[\tau] \cdot e^{-j\tau\omega T}. \tag{4}$$

It can be seen that the power spectral density estimate obtained indirectly using the autocorrelation function method is based on the average of the N-point signal $s[n]$, which is a limitation of using finite-length signals for power spectral density estimation. Therefore, in practical applications, the method of adding a window function is also used to make the power spectral density estimation more accurate, and the operation of adding a window is shown in

$$\widehat{P}(\omega) = \sum_{j=-\infty}^{\infty} W(j)\widehat{R}_{ss}[\tau]. \tag{5}$$

Among them, $W(j)$ is the window function, which can be selected as a series of window functions such as rectangular window and Hamming window.

Of course, different types of window functions can lead to different values of the final estimated power spectral density, which requires a comprehensive consideration of the estimated resolution, frequency band, and other parameters of interest, so as to select the appropriate window function.

Based on the above theoretical analysis and derivation, Algorithm 1 demonstrates the PSD-based RFF calculation and extraction designed in this paper.

After extracting the PSD RF fingerprint feature of the signal, it can be substituted into the framework of the RF fingerprint-based identification system shown in Figure 2 to realize the RF fingerprint-based WIFI device identification.

4.2. Bispectrum-Based WIFI Device Recognition Algorithm. High-order spectral analysis has good antinoise and time-varying properties because it can accurately extract phase and amplitude information, which can provide a better analysis basis in the complex and changing communication environment nowadays. High-order spectral analysis can perform multidimensional feature analysis of amplitude and phase information, while bispectral analysis can achieve the effect of suppressing Gaussian noise and is widely used in various signal processing analysis fields.

First of all, higher-order spectral analysis is a higher-order analytical extension of the power spectral density estimation of a signal, in other words, higher-order spectral analysis also satisfies the Wiener-Synchon theorem. Therefore, it is obtained that the order spectrum of a signal is related to its order cumulative quantity by the order Fourier transform. Then, the higher-order spectral analysis of a continuous random variable proceeds as follows.

(1) First determine the received signal $s[n]\{n = 0, 1, 2, 3, \cdots, N-1\}$, which has a sampling frequency of f_s and N_0 frequency sampling points in the bispectral domain with an interval of $\triangle_0 = f_s/N_0$

(2) Dividing the received signal $s[n]$ into K segments, each with M points, and centralizing each subsignal segment

(3) The DFT coefficients of each subsignal segment are calculated as shown in

$$S_i[m] = \frac{1}{M}\sum_{n=0}^{M-1} s_i[n]e^{-j2\pi nm/M} \tag{6}$$

where $m = 0, 1, \cdots, M/2$, $i = 0, 1, \cdots, K$, and $s_i[n]$ are the i th subsignal segment

(4) Next, the bispectral estimate of the ith subsignal segment $s_i[n]$ can be calculated

(5) Finally, the bispectral estimates of the K signal segment $s_i[n]$ are combined and averaged to obtain the bispectral estimate $B(\omega_1, \omega_2)$ of signal $s[n]$

$$\begin{aligned} B(\omega_1, \omega_2) &= \frac{1}{K}\sum_{K}^{i=1} B_i(\omega_1, \omega_2), \\ \omega_1 = \left(\frac{2\pi f_s}{N_0}\right)m_1, \omega_2 &= \left(\frac{2\pi f_s}{N_0}\right)m_2 \end{aligned} \tag{7}$$

After the above analysis, it has been possible to obtain the bispectrum analysis of the signal and realize the fast and simple bispectrum estimation by the simplification operation. However, the final obtained bispectrum is a two-dimensional complex image, and in the field of RF fingerprint technology, the processing of the image usually makes the efficiency of the operation reduced, and a dimensionality reduction method is needed to realize the conversion of the bispectrum analysis from a two-dimensional image to a one-dimensional vector. Here, we introduce the partial integration bispectrum analysis method, which integrates the two-dimensional bispectrum image to obtain the one-dimensional vector value through different integration paths to realize the information dimensionality reduction.

Radially Integrated Bispectra (RIB): The integration path is a straight line passing through the origin of coordinates, and the obtained integration value is RIB(α), as shown in

$$\mathrm{RIB}(\alpha) = \int_{0^+}^{1/(1+\alpha)} B(\omega_1, \alpha\omega_1)d\omega_1. \tag{8}$$

This RIB analysis is time-shift invariant as well as phase-invariant.

Axially Integrated Bispectra (AIB): The integration path is a straight line parallel to the coordinate axis, and the

Input: Signal, $s[n]$; signal points, N; FFT points, L; signal bandwidth, B_s; sampling frequency, f_s;
Output: PSD RF fingerprint features, RFF_{PSD};
1: The received signal $s[n]$ is normalized to obtain $s'[n]$.
2: The PSD of $s'[n]$ is obtained according to Equation (5).
$$\widehat{P}(\omega) = \sum_{j=-\infty}^{\infty} W(j)\widehat{R}_{ss}[\tau]$$
3: The $\widehat{P}(\omega)$ subsegment of the intercepted validity signal is used as the PSD RF fingerprint feature
$$RFF_{PSD} = P[L/2 - L \cdot B_s/2 \cdot f_s, (L/2) + (L \cdot B/2 \cdot f)]$$
4: **return** RFF_{PSD}.

Algorithm 1: RFF calculation and extraction based on PSD analysis.

obtained integration value is $\mathrm{AIB}(\omega)$, as shown in

$$\mathrm{AIB}(\omega) = \frac{1}{2\pi}\int_{-\infty}^{\infty} B(\omega_1, \omega_2)d\omega_2 = \frac{1}{2\pi}\int_{-\infty}^{\infty} B(\omega_1, \omega_2)d\omega_1. \tag{9}$$

The AIB analysis is time-shift invariant as well as scale-stretch invariant.

Circularly Integrated Bispectra (CIB): The integration path is a circle with the origin of coordinates as the center, and the obtained integration value is $\mathrm{CIB}(\alpha)$, as shown in

$$\mathrm{CIB}(\alpha) = \oint B(\alpha, \theta)d\theta. \tag{10}$$

CIB analysis is time-shift invariant as well as scale-stretch invariant.

Square Integrated Bispectra (SIB): The integration path is a rectangle centered at the origin of coordinates, and the obtained integration value is $\mathrm{SIB}(\omega)$, as shown in

$$\mathrm{SIB}(\omega) = \oint_{S_l} B(\omega_1, \omega_2)d\omega_1 d\omega_2. \tag{11}$$

The SIB analysis is time-shift invariant, phase-invariant, and scale-stretch invariant. Based on the above theoretical analysis and derivation, Algorithm 2 demonstrates the computation and extraction of bispectrum-based RFF designed in this paper.

The block diagram of the system based on the integral bispectrum method is the same as that of the power spectrum-based method and is not repeated here. In this paper, SIB is used as the feature extraction algorithm of choice.

4.3. Complex-ResNet-Based WIFI Device Recognition Algorithm. With the rise of data-driven algorithms, intelligent detection and recognition technologies have been greatly developed. Deep neural networks can learn different levels of features from data in an autonomous way, which has great advantages in the face of structured information and massive data. In this paper, we will study the performance of residual neural network model technology applied to WIFI device recognition, analyze its basic theory, and introduce its complex processing form to investigate its feasibility in the field of WIFI device recognition.

Wireless RF signals propagate in free space in the form of electromagnetic waves, and what is generally obtained at the receiving end is the complex form of the signal, with instantaneous amplitude and phase information. In signal processing, the real and imaginary parts of the complex RF signal are taken as the in-phase and quadrature signal taps, respectively. In the real number processing neural network model, the amplitude information of the signal is generally taken as the input data for processing. However, the phase information of the signal is also a very important RF signal feature, so it is not enough to use the real number neural network model for EM signal processing, but the model input and related processing of the neural network need to be modified to adapt to the wireless RF complex signal processing in the field of RF fingerprinting technology. Here, this subsection introduces the relevant processing of the complex neural network model and its difference from the real number model and constructs the complex ResNet model for WIFI device identification.

Complex convolution layer: The processing of the complex convolution layer is also performed by the convolution kernel, unlike the real convolution kernel, and the complex convolution kernel based on the complex convolution is used here.

Assuming that the input data is a complex signal vector $\vec{s} = \vec{x}_I + i \cdot \vec{x}_Q$, the convolution operation is performed through the complex weight matrix of the complex convolution kernel as shown in

$$\mathbf{W} \otimes \vec{s} = \left(\mathbf{A} \otimes \vec{x}_I - \mathbf{B} \otimes \vec{x}_Q\right) + i \cdot \left(\mathbf{B} \otimes \vec{x}_I + \mathbf{A} \otimes \vec{x}_Q\right), \tag{12}$$

where the complex weight matrix is $\mathbf{W} = \mathbf{A} + i \cdot \mathbf{B}$, and $\vec{x}_I$, $\vec{x}_Q$ is a vector of real numbers, and $\mathbf{A}$, $\mathbf{B}$ is a matrix of real numbers.

Complex fully-connected layer: The fully-connected layer of the traditional real neural network model is used to recognize the probabilistic output, and its input is the real feature map. In the complex neural network model, it is modified to a complex fully connected layer to maximize the use of the output features of the complex convolutional layer. The processing of the complex fully connected layer is based on the real fully connected layer, with the difference that four

Input: Signal, $s[n]$; signal points, N; FFT points, L;
Output: Bispectrum RF fingerprint features, RFF_{BS};
1: The received signal $s[n]$ is normalized to obtain $s'[n]$.
2: The bispectrum of $s'[n]$ is obtained according to Equation (7).

$$B(\omega_1, \omega_2) = 1/K \sum_{K}^{i=1} B_i(\omega_1, \omega_2)$$

3: Calculate the SIB of bispectrum estimation is used as the bispectrum RF fingerprint feature

$$RFF_{BS} = \oint_{S_l} B(\omega_1, \omega_2) d\omega_1 d\omega_2$$

4: **return** RFF_{BS}.

Algorithm 2: RFF calculation and extraction based on bispectrum analysis.

Table 1: Complex-ResNet and parameter setting.

Model structure	Active layer	Output size	Number of parameters
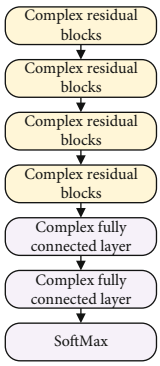	Complex residuals module	(None,512,32)	10432
	Complex residuals module	(None,256,32)	10912
	Complex residuals module	(None,128,32)	10912
	Complex residuals module	(None,64,32)	10912
	Complex fully connected layer	(None,256)	262400
	Complex fully connected layer	(None,256)	33024
	SoftMax layer	(None,200)	25800

Table 2: Complex residual model and parameter setting.

Complex residual block structure	Active layer	Kernel parameters	Output size	Number of parameters
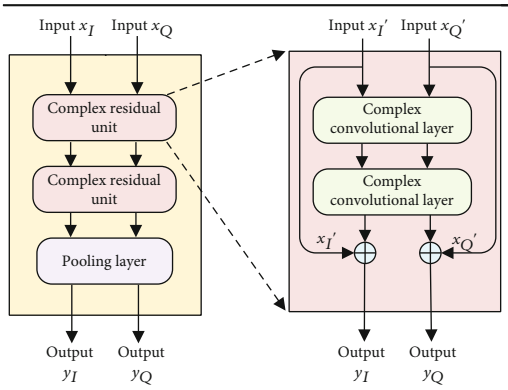	Complex convolutional layers	(16,1)	(None,1024,32)	64
	Complex convolutional layers	(16,5)	(None,1024,32)	2592
	Complex convolutional layers	(16,5)	(None,1024,32)	2592
	Complex convolutional layers	(16,5)	(None,1024,32)	2592
	Complex convolutional layers	(16,5)	(None,1024,32)	2592
	Pooling layer	2	(None,512,32)	0

product operations are required to achieve a more accurate probability estimation. The essence of the operation of the complex fully-connected layer is also the convolution operation of the tensor, so its calculation formula is the same as Equation (12) of the complex convolution layer, with the difference that its weights are two real values instead of a real matrix.

After the above complex adaptation of the convolutional and fully connected layers, the complex ResNet model can be built. The structure and parameters of the complex ResNet model constructed in this paper are shown in Table 1.

Among them, the relevant parameters of the complex residual module are shown in Table 2.

5. Results and Analysis

This section conducts relevant experiments using the dataset introduced in Section 3 to verify the performance of the RF fingerprinting system discussed in this paper. The relevant

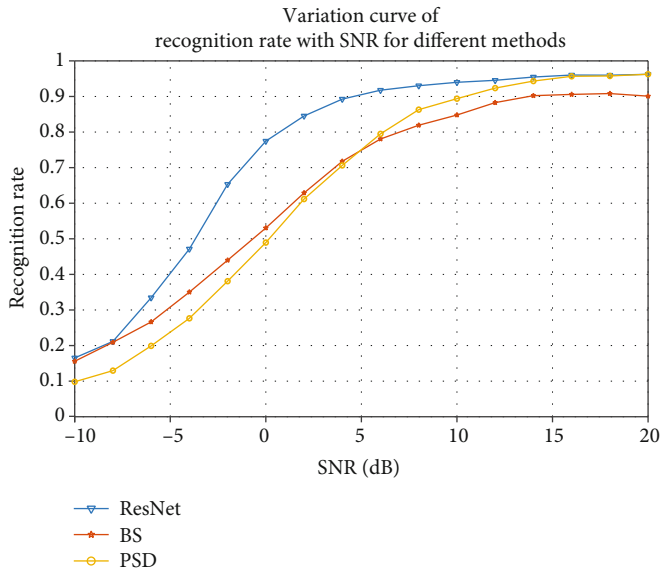

Figure 5: Recognition accuracy with SNR curve.

Table 3: Performance comparison of feature engineering methods in LoS and NLoS scenarios.

Method	Channel environment	Recognition accuracy	Signal length
PSD	LoS	96.4%	4096 points
BS	LoS	89.3%	4096 points
ResNet	LoS	96.7%	1024 points
PSD	NLoS	89.1%	4096 points
BS	NLoS	86.9%	4096 points
ResNet	NLoS	92.6%	1024 points

experimental analysis is performed specifically according to the data acquisition environment, including the analysis of the system's resistance performance to Gaussian white noise with different Signal-to-Noise Ratio (SNR) levels, the analysis of the adaptability to the channel environment, and the analysis of the user capacity of the features.

5.1. System Noise Immunity Analysis. The actual communication system is bound to be affected by various noises in the communication, and these noises will not only affect the communication quality but also cause the effects of feature diffusion and feature degradation in the field of RF fingerprint technology, which makes the performance of the identification system degrade. Therefore, in the test of the system, the noise immunity performance test is a very important test, and the experimental analysis of the noise immunity performance of the RF fingerprint features proposed in this paper is as follows.

In order to test the noise immunity performance of the RF fingerprint system, the dataset introduced in Section 3 is selected for the relevant experiments in this section, with a signal sampling rate of 40 M and a data acquisition environment of a laboratory LoS channel environment containing 100 classes of targets with 100 sample signal data for each class of targets. The ratio of training set to test set of KNN classifier is adjusted to 4 : 1, where the K value is set to 5. The noise interference environment is simulated by adding Gaussian white noise with different SNR levels to this dataset, and the testing of WIFI device recognition system is carried out, and its recognition accuracy under different SNR can reflect the noise immunity performance of the system.

The SNR variation of the signal after noise addition ranges from -10 dB: 2: 20 dB, with a total of 16 levels. The accuracy of the final system recognition with SNR variation curve is shown in Figure 5.

As can be seen from Figure 5, when the SNR is between -10 dB and 5 dB, the BS feature has a maximum improvement of about 8% compared with the PSD feature, and the recognition accuracy increases from 10% to 18.5% at -10 dB. When the SNR is higher than 5 dB, the PSD features have more performance, and the PSD features can reach 95% accuracy when the SNR is 20 dB.

In addition, the complex ResNet can obtain better performance compared to the feature engineering method. For example, when the SNR is 0 dB, the complex ResNet can achieve 78% recognition accuracy, while the feature engineering method can only achieve 50% recognition accuracy.

5.2. System Environmental Adaptability Analysis. In addition to noise, the complex and variable channel environment is also a major problem affecting the wireless signal quality. Also, the harsh channel environment can affect the stability of RF fingerprint features, and the drift of features can lead to poor recognition. In WIFI practical application scenarios, this paper considers laboratory indoor scenarios, which mainly include indoor LoS channels and NLoS channels. The experimental analysis of the environmental adaptation of the RF fingerprint features proposed in this paper is as follows.

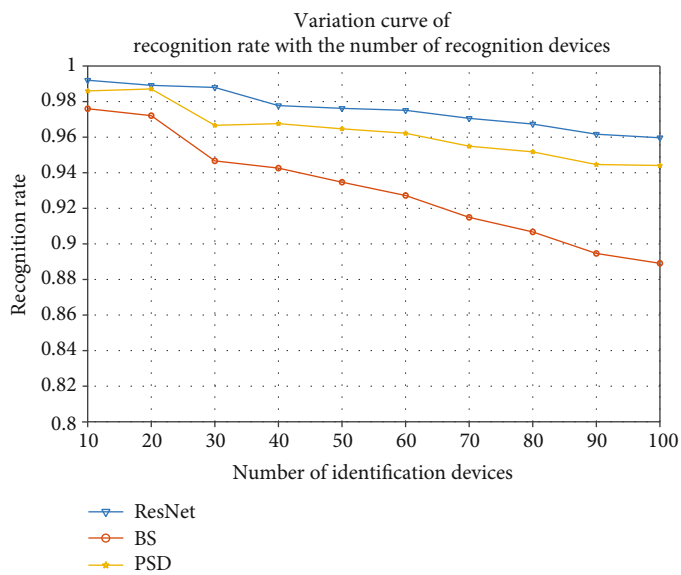

Figure 6: System recognition accuracy curve with the number of devices to be recognized.

In order to test the environmental adaptability of the RF fingerprint system, the dataset introduced in Section 3 is selected for relevant experiments in this section, both of which have a signal sampling rate of 40 M, and the data acquisition environments are laboratory LoS and laboratory NLoS channel environments, respectively, containing 100 classes of targets with 100 sample signal data for each class of targets. The ratio of training set and test set of KNN classifier is adjusted to 4 : 1, where the K value is set to 5. The experiment of WIFI device recognition based on RF fingerprint is conducted to test the recognition accuracy of the system under different channel environments.

The deep learning model constructed in this paper is used to conduct WIFI device recognition experiments in two channel environments using both PSD and BS features, and the results obtained are shown in Table 3.

The introduction of deep learning models such as ResNet will increase the environmental adaptability of the system. As can be seen from Table 3, deep learning methods have 1%-3% improvement in recognition accuracy over feature engineering methods under LoS and NLoS channel conditions. Complex-ResNet can achieve 92.6% recognition accuracy in NLoS scenarios, which has the best performance. And using 1024 points for recognition, it has higher efficiency in practical applications. This indicates that the deep learning method is more capable of automatically extracting signal features, and its recognition is better.

5.3. System User Capacity Analysis. After proposing an identification or device authentication system, its user capacity is also one of its important parameters. The user capacity can measure the maximum number of devices to be identified or authenticated that the system can accommodate to be online at the same time. When the number of online devices exceeds the system capacity, it will make the system unable to work properly and lead to system problems such as identification error and authentication failure. The experimental analysis of the user capacity of the RF fingerprint feature proposed in this paper is as follows.

In order to perform user capacity testing of the RF fingerprinting system, the dataset introduced in Section III is selected for relevant experiments in this section, with a signal sampling rate of 40 M and a data acquisition environment of a laboratory LoS channel environment containing 100 classes of targets with 100 sample signal data for each class of targets. WIFI device recognition experiments are conducted on this dataset to test the recognition accuracy of the system in a large number of device scenarios and to analyze the trends.

Feature engineering-based RF fingerprint feature extraction recognition tests are performed using four features. The final system recognition accuracy variation curve with the number of devices to be recognized is shown in Figure 6.

Analysis of Figure 6 shows that for a user capacity size with 96% recognition accuracy, the PSD feature can reach about 60 devices and the BS feature can reach about 25 devices. For a user capacity size with 90% recognition accuracy, the PSD feature can reach more than 100 devices and the BS feature can reach about 85 devices. And ResNet and other deep learning models can all reach more than 100 devices. This shows that deep learning methods have a greater potential. Compared with the article [35], the channel we use is more complex. Although the recognition accuracy decreases with the increase of the number of recognitions, it still remains at a high level, which shows the superiority of the method we use.

6. Conclusion

RF fingerprinting technology, as one of the important development directions to improve the security performance of wireless devices, has been widely studied in the past two decades. In this paper, we first construct a large-scale measured WIFI signal dataset with the characteristics of a large

number of devices, full channel scenarios, and a large data scale. And two methods based on feature engineering and deep learning are proposed for individual identification of WIFI devices. The comprehensive performance simulation results described in this paper can achieve better recognition accuracy both in the darkroom and in the laboratory, both in LoS environment and in NLoS environment, and after adding Gaussian white noise with a certain SNR.

Feature engineering-based RF fingerprint recognition methods are fast in model training, flexible and convenient, and easy to deploy. However, the traditional feature-based WIFI signal recognition methods are increasingly difficult to cope with the new characteristics of big data due to their need for a large amount of expert knowledge and limited data processing capacity. The deep learning-based methods show better performance in EM signal recognition due to their powerful nonlinear fitting ability and end-to-end learning mode.

However, through the research and analysis in this paper, it is found that there are still some problems in the field of RF fingerprint-based individual identification technology, such as the lack of a mathematical model for the forward derivation of the RF fingerprint generation process, i.e., the inability to quantify the differences in RF fingerprint features between devices; the poor adaptability and low extraction efficiency of RF fingerprints; and the privacy issues and possible attacks. We will conduct research and analysis in our future work.

Data Availability

The data that support the findings of this study are available from the corresponding author upon reasonable request.

Conflicts of Interest

The authors declared no potential conflicts of interest with respect to the research, authorship, and/or publication of this article.

Acknowledgments

This work is supported by the Fundamental Research Funds for the Central Universities (3072021CF0801).

References

[1] I. Ahmad, T. Kumar, M. Liyanage, J. Okwuibe, M. Ylianttila, and A. Gurtov, "Overview of 5G security challenges and solutions," *IEEE Communications Standards Magazine*, vol. 2, no. 1, pp. 36–43, 2018.

[2] X. S. Ji, K. Z. Huang, L. Jin et al., "Overview of 5G security technology," *Science China-Information Sciences*, vol. 61, no. 8, pp. 107–131, 2018.

[3] M. Wang, Y. Lin, Q. Tian, and G. Si, "Transfer learning promotes 6G wireless communications: recent advances and future challenges," *IEEE Transactions on Reliability*, vol. 70, no. 2, pp. 790–807, 2021.

[4] Z. Bao, Y. Lin, S. Zhang, Z. Li, and S. Mao, "Threat of Adversarial Attacks on DL-Based IoT Device Identification," *IEEE Internet of Things Journal*, vol. 9, no. 11, pp. 9012–9024, 2022.

[5] W. Wang, Z. Sun, S. Piao, B. Zhu, and K. Ren, "Wireless physical-layer identification: modeling and validation," *IEEE Transactions on Information Forensics and Security*, vol. 11, no. 9, pp. 2091–2106, 2016.

[6] T. D. Vo-Huu, T. D. Vo-Huu, and G. Noubir, "Fingerprinting Wi-Fi devices using software defined radios," in *9th ACM Conference on Security and Privacy in Wireless and Mobile Networks (WiSec)*, pp. 3–13, Darmstadt Germany, 2016.

[7] Q. Tian, J. C. Jia, and C. B. Hou, "Research on fingerprint identification of wireless devices based on information fusion," *Mobile Networks & Applications*, vol. 25, no. 6, pp. 2359–2366, 2020.

[8] R. Duan, Z. Li, and Y. Yin, "Improvement of LANDMARC indoor positioning algorithm," *International Journal of Performability Engineering*, vol. 16, no. 3, pp. 446–453, 2020.

[9] M. Liu, C. Liu, M. Li, Y. Chen, S. Zheng, and N. Zhao, "Intelligent passive detection of aerial target in space-air-ground integrated networks," *China Communications*, vol. 19, no. 1, pp. 52–63, 2022.

[10] X.-H. Ru, Z. Liu, W.-L. Jiang, and Z.-T. Huang, "Recognition performance analysis of instantaneous phase and its transformed features for radar emitter identification," *Iet Radar Sonar and Navigation*, vol. 10, no. 5, pp. 945–952, 2016.

[11] T. D. Ridder and R. M. Narayanan, "Radar detection performability under graceful degradation," *International Journal of Performability Engineering*, vol. 17, no. 8, pp. 666–675, 2021.

[12] A. C. Polak, S. Dolatshahi, and D. L. Goeckel, "Identifying wireless users via transmitter imperfections," *IEEE Journal on Selected Areas in Communications*, vol. 29, no. 7, pp. 1469–1479, 2011.

[13] J. W. Zhang, F. G. Wang, O. A. Dobre, and Z. D. Zhong, "Specific emitter identification via Hilbert-Huang transform in single-hop and relaying scenarios," *IEEE Transactions on Information Forensics and Security*, vol. 11, no. 6, pp. 1192–1205, 2016.

[14] J. Hall, M. Barbeau, and E. Kranakis, "Detection of transient in radio frequency fingerprinting using signal phase," *Wireless and Optical Communications*, pp. 13–18, 2003.

[15] B. Danev, D. Zanetti, and S. Capkun, "On physical-layer identification of wireless devices," *ACM Computing Surveys*, vol. 45, no. 1, pp. 1–29, 2012.

[16] N. Soltanieh, Y. Norouzi, Y. Yang, and N. C. Karmakar, "A review of radio frequency fingerprinting techniques," *IEEE Journal of Radio Frequency Identification*, vol. 4, no. 3, pp. 222–233, 2020.

[17] X. Li, J. Liu, B. Ding, Z. Li, H. Wu, and T. Wang, "TickSEC: a novel reconfigurable platform for WIFI physical layer security," in *2018 International Conference on Networking and Network Applications (NaNA)*, pp. 237–244, Xi'an, China, 2018.

[18] G. Li, J. Yu, Y. Xing, and A. Hu, "Location-invariant physical layer identification approach for WIFI devices," *IEEE Access*, vol. 7, pp. 106974–106986, 2019.

[19] K. Yang, J. Kang, J. Jang, and H. Lee, "Multimodal sparse representation-based classification scheme for RF fingerprinting," *IEEE Communications Letters*, vol. 23, no. 5, pp. 867–870, 2019.

[20] Y. Lin, J. Jia, S. Wang, B. Ge, and S. Mao, "Wireless device identification based on radio frequency fingerprint features,"

in *ICC 2020 - 2020 IEEE International Conference on Communications (ICC)*, pp. 1–6, Dublin, Ireland, 2020.

[21] L. Peng, J. Zhang, M. Liu, and A. Hu, "Deep learning based RF fingerprint identification using differential constellation trace figure," *IEEE Transactions on Vehicular Technology*, vol. 69, no. 1, pp. 1091–1095, 2020.

[22] A. C. Polak and D. L. Goeckel, "RF fingerprinting of users who actively mask their identities with artificial distortion," in *2011 Conference record of the forty fifth Asilomar conference on signals, Systems and Computers (ASILOMAR)*, pp. 270–274, Pacific Grove, CA, USA, 2011.

[23] T. Zheng, Z. Sun, and K. Ren, "FID: function modeling-based data-independent and channel-robust physical-layer identification," in *IEEE INFOCOM 2019 - IEEE Conference on Computer Communications*, pp. 199–207, Paris, France, 2019.

[24] Y. Lin, H. Zhao, X. Ma, Y. Tu, and M. Wang, "Adversarial attacks in modulation recognition with convolutional neural networks," *IEEE Transactions on Reliability*, vol. 70, no. 1, pp. 389–401, 2021.

[25] Y. Lin, Y. Tu, Z. Dou, L. Chen, and S. Mao, "Contour stella image and deep learning for signal recognition in the physical layer," *IEEE Transactions on Cognitive Communications and Networking*, vol. 7, no. 1, pp. 34–46, 2021.

[26] Y. Tu, Y. Lin, J. Wang, and J. U. Kim, "Semi-supervised learning with generative adversarial networks on digital signal modulation classification," *Cmc-Computers Materials & Continua*, vol. 55, no. 2, pp. 243–254, 2018.

[27] M. Liu, Z. Liu, W. Lu, Y. Chen, X. Gao, and N. Zhao, "Distributed few-shot learning for intelligent recognition of communication jamming," *IEEE Journal of Selected Topics in Signal Processing*, vol. 16, no. 3, pp. 395–405, 2022.

[28] K. Merchant, S. Revay, G. Stantchev, and B. Nousain, "Deep learning for RF device fingerprinting in cognitive communication networks," *IEEE Journal of Selected Topics in Signal Processing*, vol. 12, no. 1, pp. 160–167, 2018.

[29] J. M. McGinthy, L. J. Wong, and A. J. Michaels, "Groundwork for neural network-based specific emitter identification authentication for IoT," *IEEE Internet of Things Journal*, vol. 6, no. 4, pp. 6429–6440, 2019.

[30] Y. Dong, X. Jiang, H. Zhou, Y. Lin, and Q. Shi, "SR2CNN: zero-shot learning for signal recognition," *IEEE Transactions on Signal Processing*, vol. 69, pp. 2316–2329, 2021.

[31] Y. Tu, Y. Lin, H. Zha et al., "Large-scale real-world radio signal recognition with deep learning," *Chinese Journal of Aeronautics*, vol. 16, pp. 1–14, 2021.

[32] Y. Lin, Y. Tu, and Z. Dou, "An Improved Neural Network Pruning Technology for Automatic Modulation Classification in Edge Devices," *IEEE Transactions on Vehicular Technology*, vol. 69, no. 5, pp. 5703–5706, 2020.

[33] S. Zhang, L. Yun, T. Ya, and S. Mao, "Electromagnetic signal modulation recognition technology based on lightweight deep neural network," *Journal on Communications*, vol. 41, no. 11, pp. 12–21, 2020.

[34] M. Liu, J. Wang, N. Zhao, Y. Chen, H. Song, and R. Yu, "Radio frequency fingerprint collaborative intelligent identification using incremental learning," *IEEE Transactions on Network Science and Engineering*, pp. 1–11, 2021.

[35] Y. Peng, P. Liu, Y. Wang, G. Gui, B. Adebisi, and H. Gacanin, "Radio frequency fingerprint identification based on slice integration cooperation and heat constellation trace figure," *IEEE Wireless Communications Letters*, vol. 11, no. 3, pp. 543–547, 2022.

Hindawi
Wireless Communications and Mobile Computing
Volume 2022, Article ID 6327479, 8 pages
https://doi.org/10.1155/2022/6327479

Research Article

High-Efficiency Mitigation of Nonlinear Distortion in Microwave Photonics Link Assisted by Artificial Neural Network

Yihui Yin,[1] Wanli Yang,[2] Shifeng Xie,[2] and Binfeng Yun[1]

[1]*Advanced Photonics Center, Southeast University, Nanjing 210096, China*
[2]*The 34th Research Institute of China Electronics Technology Group Corporation, Guilin 541004, China*

Correspondence should be addressed to Binfeng Yun; ybf@seu.edu.cn

Received 11 April 2022; Accepted 9 May 2022; Published 1 June 2022

Academic Editor: Mingqian Liu

A microwave photonics radio over fiber link can deliver the radio frequency (RF) signal to realize the antenna remote. When the signal is a broadband and multicarrier RF signal, there are some linear distortions in the link, such as the crossmodulation distortion (XMD) and third-order intermodulation distortion (IMD_3). It will destroy the wide-bandwidth performance of the link. Traditional postdigital compensation methods for XMD and IMD_3 mitigation extract the baseband signal and reconstruct the compensation signal with calculated compensation factor. Here, a kind of artificial neural network genetic algorithm (ANN-GA) distortion compensation technique is proposed to seek the compensation factor instead of calculations. The neural network algorithm is used to fit the mapping function between the compensation factor and the distortion and give a set of predicted data as the original individual fitness value for the genetic algorithm. Based on the original value, the minimal distortion, the corresponding optimal compensation factors γ and α are found with optimization iterations. Taking advantage of the optimal compensation factors, based on the traditional postdigital compensation method, the distortion is mitigated with a suppression ratio of -84.4 dB. In our paper, the mitigation technology of the XMD and IMD_3 can be applied for any kinds of link instead of mathematically modelling the link and calculating the compensation factor. The technology can improve the intelligence and flexibility of microwave photonic link linearization design.

1. Introduction

With the development of the communication and radar applications, the demand for bandwidth is growing, which increases the complexity for the transmission, processing, and reception of the ultrabroadband, multicarrier RF signal based on the traditional electrical technology. However, the rapidly developing photonic technology will be a prospective analog signal processing platform. The microwave photonics technique combines the microwave and photonics and occupies both microwave advantage of precise spectrum processing and the photonics property of wideband, low loss, and strong immunity to electromagnetic interference [1]. The merits make the microwave photonics technology efficiently process the complex RF signals in microwave systems. In recent years, many kinds of multiple carrier radio over fiber (ROF) links are designed to realize the RF signal transmission and down-conversion. In radar and electronic countermeasure applications, the ROF link links the antenna and the data process center for getting the greater mobility and stronger resistance to damage. It is worth to note that the wideband, high sensitivity, and large dynamic range property of link are the key factors for improving the radar detection range and resolution [2]. However, there are some nonlinear distortion such as third-order inter modulation distortion (IMD_3) and crossmodulation distortion (XMD) deteriorating the dynamic range. Nonlinear distortion in ROF link is frequently introduced by the nonlinear response in laser, modulator, and detector. To solve the distortion problem in links, many kinds of linearization techniques are applied to the links. Some of the distortion mitigation methods are proposed by doing several designs in the modulation, such as constructing the cascaded or parallel electrooptic modulators [3–8]. In those designs, the two Mach-Zehnder modulators (MZMs) operate at

the opposite slope of the transfer functions to obtain the opposite phase of IMD_3 signal and cancel each other. In addition, electronic predistortion compensation [9, 10], feed-forward compensation [11, 12], and postdistortion compensation [13–17] are also important means. In digital compensation schemes, the digital processor circuit is designed to sample and extract the correction signal to suppress the distortion. For example, in postlinearization link, the correction signal is extracted by filters and processed in digital signal processor (DSP) to get the distortion compensation signal to suppress the link distortion. A typical postdistortion compensation link has demonstrated at least a 25 dB distortion suppression by a combination of electrooptics, microwave circuitry, and digital signal processing. In multiple-channel ROF links, the input signal is a broadband RF signal that consisted of multiple frequency components, so that the link linearity is deteriorated by not only IMD_3 but also by XMD. In [18], the XMD is suppressed by predistortion. In [19], the XMD is mitigated with postdistortion compensation. However, there are some weaknesses in the traditional digital distortion compensation. For example, the digital signal process is based on the precise mathematical model of the link. On the one hand, the present ROF link model is derived in small signal condition, which will be failed when the modulation depth is deeper. On the other hand, the mathematical model needs to be rederived according to variable link structures.

Artificial intelligence microwave photonics technique is an emerging direction in microwave photonics. The artificial neural network (ANN) has made tremendous progress contributing to the abilities of self-study, associate storage, high-speed search for the best solutions, and drawing arbitrarily complex nonlinear relationships. In recent years, the ANN is applied to the microwave photonics field to enhance the system performance [20–22]. Defining the input and output variables of a microwave photonics link, the link is mathematically viewed as a nonlinear function. Thus, by training the ANN with input and output data of the microwave photonics link, the ANN can fit the nonlinear mapping of the microwave photonics link. Then, the trained ANNS can predict the link function instead of deriving the mathematical model.

Combining the traditional digital distortion compensation method and the artificial neural network genetic algorithm (ANN-GA), a kind of ANN-GA-based distortion compensation technique is proposed for multicarrier downconversion microwave photonics link (MDC-MWPL) distortion mitigation. The traditional downconversion microwave link with the postdistortion compensation is composed of the laser, modulator and photodiode, analog digital converter (ADC), and a digital signal process (DSP). Based on the traditional link, the ANN-GA is added and realized by DSP. In the digital circuit, correction signal is extracted by the passband filter to reconstruct the compensation signal with the compensation factors γ and α, which are sought by the ANN-GA. The distortion XMD and IMD_3 will be eliminated with a suppression ratio great than -84.4 dB.

2. Principle of the Digital Distortion Compensation Process

2.1. Principle of the XMD Compensation. The schematic diagram of the proposed MDC-MWPL is shown in Figure 1. The light signal is generated by the laser and transmitted into modulator 1. The polarization controller between the laser and modulator 1 is used to adjust the light signal polarization state to be consistent with the modulator spindle. The RF signal is modulated to the light signal in modulator 1. Then, the output light signal from modulator 1 is delivered to modulator 2 and modulated by a local oscillator (LO) signal. The photodiode (PD) coverts the modulated light signal to electric signal and achieves downconverting the RF signal to the IF signal. The IF signal is sampled by the ADC module and converted to digital signal. Within the digital domain, by using the digital filters, the correction signals are extracted to reconstruct the compensation signal. In the DSP, the trained artificial neural network establishes the map relationship between the compensation factor and the distortion and gives the prediction values of the XMD, IMD_3, and the corresponding γ and α. With the normalization of the given compensation factor data and the reverse normalization of the prediction, the prediction values fill the role of the original fitness value in the genetic algorithm. Based on the original fitness value, the genetic algorithm will find the minimal fitness value (minimal distortion) and the corresponding compensation factors γ and α. Then, compensation signal with distortion mitigation is reconstructed using the compensation factors γ and α.

The sampled signal by the ADC module is extracted by narrow band-pass and low-pass digital filters and divided into two correction signals, denoted as signal 1 (S_1) and 2 (S_2), respectively. The two signals are used to construct a compensation signal to suppress the XMD and IMD_3. The signal processing for XMD mitigation is shown in Figure 2. To explain the signal processing mechanism, the process is expressed by the mathematically analytical method. Mathematically, the broadband multicarrier RF signal, denoted as $x(t)$, can be written as Equation (1), which is a sine function with a center frequency of ω_n, amplitude of $A_n(t)$, and the phase of $\phi_n(t)$.

$$x(t) = \sum_n A_n(t) \cos\left(\omega_n t + \phi_n(t)\right). \tag{1}$$

For an intensity modulation with direct detection link, the transfer function can be expanded in terms of the Tyler function as follows:

$$P(t) = a_0 + a_1 x(t) + a_2[x(t)]^2 + a_3[x(t)]^3 + . \cdots \tag{2}$$

Equation (2) contains the higher order distortion terms, such as $[x(t)]^2$ and $[x(t)]^3$. To extract the correction signal, the expression of the RF signal recovered from the PD is

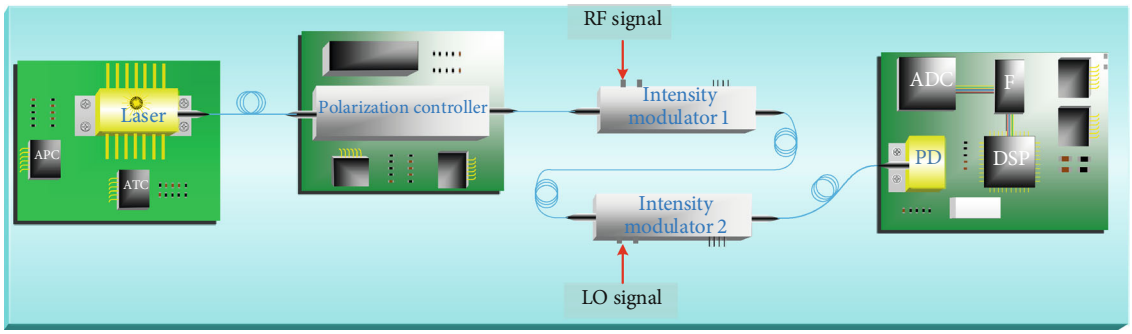

Figure 1: The multicarrier downconversion microwave photonics link with the DSP circuit for mitigating the nonlinear distortion.

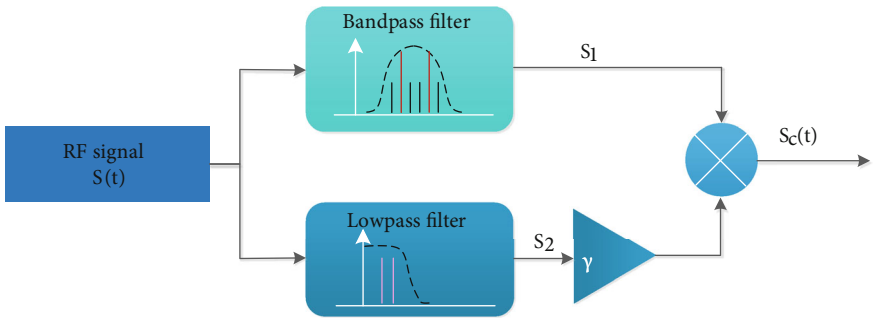

Figure 2: The diagram of the signal processing of reconstructing the compensation signal for XMD mitigation.

deduced by inserting Equation (1) into Equation (2).

$$S(t) = a_0 + a_1 \sum_n A_n \cos \omega_n t + a_2 \left(\sum_n A_n \cos \omega_n t \right)^2 + a_3 \left(\sum_n A_n \cos \omega_n t \right)^3 + \cdots \approx a_0 + a_2 \sum_n A_n^2 + \sum_n \left[a_1 + a_3 \left(A_n^2 + \sum_m A_m^2 \right) \right] A_n \cos \omega_n t, \quad (3)$$

where $\sum_m A_m^2(t)$ and $\sum_n A_n^2(t)$ are XMD and IMD term, respectively. We define the correction signal as the S_1 and S_2:

$$S_1 = \sum_n \left[a_1 + a_3 \left(A_n^2 + \sum_m A_m^2 \right) \right] A_n \cos \omega_n t, \quad (4)$$

$$S_2 = a_0 + a_2 \sum_n A_n^2, \quad (5)$$

where S_1 and S_2 contain the XMD and IMD_3, respectively. To extract the baseband signal S_1 and S_2 to construct the compensation signal, the digital filter is designed. S_1 and S_2 are filtered by the band-pass filter and low-pass filter, respectively. Then, the compensation signal for XMD mitigation is obtained as follows:

$$S_c(t) = S_1 * S_2^{\gamma}, \quad (6)$$

where γ is the XMD compensation factor. As shown in Figure 2, based on the digital signal process, the constructed compensation signal $S_c(t)$ is generated, and the XMD in $S_c(t)$ is mitigated. With traditional methods, the compensation factor γ is calculated by further solving the link mathematical small signal model, which is inapplicable to big signal drive link. To further optimize the distortion mitigation performance, a novel method to seek the compensation factor based on ANN-GA is proposed in Section 3.

2.2. Principle of the IMD_3 Compensation. In the compensation signal $S_c(t)$, the XMD is mitigated, while the IMD_3 still exists in signal $S_c(t)$. The IMD_3 is the largest odd distortion term in link, which is close to the main signal. To mitigate the IMD_3, the operation on signal S_1 is made to generate the signal $S_D(t)$ as follows:

$$S_D(t) = 1 + \alpha S_1^2, \quad (7)$$

where α is the IMD_3 compensation factor. Then, $S_D(t)$ is divided into $S_c(t)$ to construct a compensation signal $S_L(t)$ to suppress the IMD_3:

$$S_L(t) = \frac{S_D(t)}{S_c(t)} = \frac{1 + \alpha S_1^2}{S_c(t)}. \quad (8)$$

The whole flow chart is shown in Figure 3, in which the compensation flow consists of two main parts: XMD mitigation and IMD_3 mitigation. Both in the two parts, the

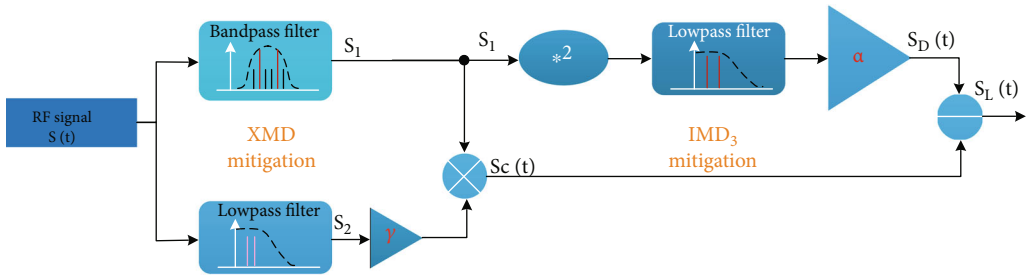

Figure 3: The diagram of the signal processing of reconstructing the compensation signal for IMD_3 mitigation.

compensation factors γ and α are key variables, which are sought by the ANN-GA introduced in Section 3.

3. Principle of the Distortion Mitigation Optimization Based on the ANN-GA

According to the principle of the XMD and IMD_3 compensation, the key factors which dominate the performance of distortion mitigation areγandα. In traditional methods, the γ and α are obtained by mathematical equation, which contains the variables such as modulator bias point and the output 3rd intermodulation point. Specifically, the accurate values of γ and α are calculated by solving the transfer function of link based on the small signal condition. However, in fact, different components, link structures, and operation conditions have variable link transfer functions. On the one hand, it needs to solve the link transfer function; on the other hand, the solved function cannot exactly fit the link in some situations, such as big signal drive. To intelligentize the compensation and improve the distortion mitigation ratio, the ANN-GA is proposed.

The process of seeking compensation factors γ and α based on the ANN-GA is divided into two main steps: Step 1: train backpropagation (BP) neural network, and predict the output of the link, and Step 2: seek the values of γ and α and the corresponding minimal values of XMD and IMD_3 by genetic algorithm. The detail flow is shown in Figure 4. The neural network prediction contains the network structure construction, data initialization, neural network training, test, and prediction. In the training process, the training times depend on the epochs and network targets, which is the termination condition (1). The genetic algorithm optimization contains the population initialization, individual fitness calculation, seeking optimal individual, selection operation, crossover operation, mutation operation, iteration, and updating optimal individual. The process from fitness calculation to mutation represents the evolution. Every time evolution will find the best fitness and replace the last fitness until the set generations are reached, which is the termination condition (2).

The BP neural network is one of the most widely used neural network models. It can learn and store a large number of input-output mapping without prior knowledge of the mathematical function equations. The BP network is composed of input layer, hidden layer, and output layer, in which each layer is composed of many parallel neurons. The neurons between

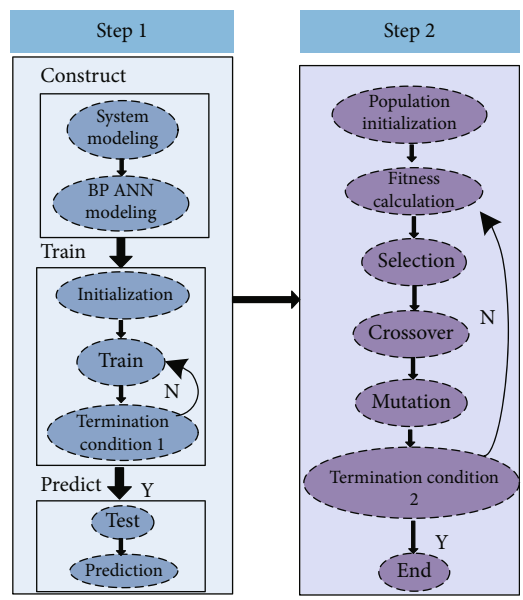

Figure 4: The flow chart of the ANN-GA.

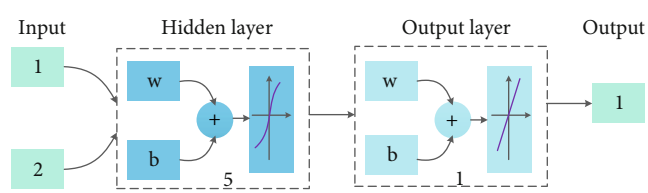

Figure 5: The structure of the neural network.

different layers are connected. But there is no mutual connection between the neurons of the same layer. Here, the compensation factors γ and α are identified as the inputs and the power level of XMD and IMD_3 as the outputs of the neural network. The prediction accuracy of the neural network is the key factor for the genetic algorithm to find the optimal compensation factors and the corresponding minimal XMD and IMD_3. The learning capability of the BP neural network is closely related to its structure, because the memory capacity of the network, the speed of training, and the amount of response depend on the structure, which corresponds to the number of hidden layers and nodes. According to the Kolmogorov theory, as long as there are enough hidden layer nodes, the neural network can approach a nonlinear function. A continuous function $F(x)$ in the closed intervals can be precisely implemented with a three-layer neural network, where the

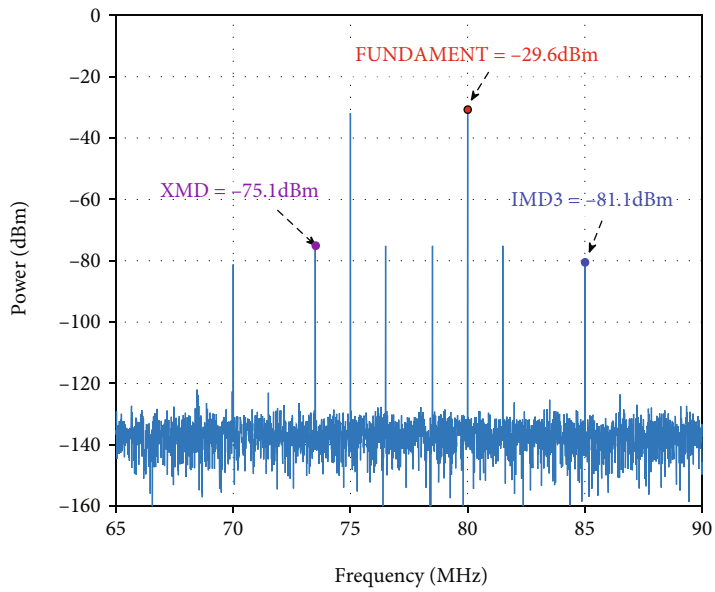

Figure 6: The output spectrum of the link without compensation.

number of nodes in the input layer is M, the number of nodes in the hidden layer is $K = 2M + 1$, and the number of nodes in the output layer is N. In fact, the number of nodes would be increased with the number of samples increasing. Here, we select the compensation factors γ and α as the inputs ($M = 2$, $K = 5$). And the output can be switched between XMD and IMD_3. So $N = 1$. The neural network structure is "2-5-1" type, as shown in Figure 5.

In the genetic algorithm, we need several iterations to find the optimal individual. For each iteration, the optimal individual is updated by conducting the selection, the crossover, and the mutation operations. Firstly, the original individual fitness value comes from the prediction of the BP neural network. The individual in the genetic algorithm is encoded as a real number, and the length of the individual depends on the number of the link output variables. If there are two variables, the length of the individual is 2. Then, the individuals that are more suited to the environment are selected to multiply the next generation from a group. The smaller the fitness value, the better the individual. Different from the selection, the two new individuals will be born after one crossover, which are used to seek the new point in group space. The mutation simulates the accidental process in natural genetic environment. If there are only selection and crossover, genetic algorithm cannot search the space beyond the initial gene combination, and the evolution process easily falls into the local solution. According to the optimization goal, the probability of crossover and mutation is set as needed.

4. Simulation Results and Analysis

To verify the theory, we design the simulation experiment. The link output spectrum without compensation is simulated in MATLAB, and the link structure is shown as Figure 1. In the simulation, the RF main signal is a dual-tone signal with the frequency interval of 5 MHz, at the frequency of 15 GHz and 15.005 GHz, respectively. The outband crosstalk signal is represented with a dual-tone signal with the frequency interval of 1.5 MHz, at the frequency of 3 GHz and 3.0015 GHz, respectively. The local oscillator signal is introduced to downconvert the RF signal to the IF signal at the frequency of 75 MHz and 80 MHz, respectively. The switching voltage of modulator, the effective responsivity of the PD, and the input optical power of the PD are set to 6 V, 0.9A/W, and 5 dBm, respectively. The output spectrum of the link without compensation is shown in Figure 6. As we can see, the IF signals are seriously interfered by XMD signals with the power of -75 dBm, at the frequency of 73.5 MHz, 76.5 MHz, 78.5 MHz, and 81.5 MHz, respectively. At the same time, the IF signals are interfered by IMD_3 signal with the power of -81.1 dBm, at the frequency of 70 MHz and 85 MHz, respectively.

To get the appropriate compensation factors γ and α, the BP neural network is trained using 5000 sets of data, in which each set of data consists of two inputs (γ and α) and two outputs (XMD and IMD_3). And 500 sets of data are used to test the fitting effect of the BP neural network. The deviation of the outputs predicted by BP neural network and the outputs expected is calculated:

$$\kappa = \mathrm{XMD}_{\mathrm{pre}} - \mathrm{XMD}_{\mathrm{exp}}, \tag{9}$$

where the $\mathrm{XMD}_{\mathrm{pre}}$ and $\mathrm{XMD}_{\mathrm{exp}}$ are prediction and expectation values of the XMD and IMD_3, respectively. According to Equation (9), the calculated results are shown in Figure 7. The XMD deviation ranges from -0.04 dB to 0.06 dB, which demonstrates a precise prediction of the BP neural network. The IMD_3 deviation mostly ranges from -2 dB to 2 dB. However, at some points, the deviation is up to 7 dB, which means that the BP neural network should

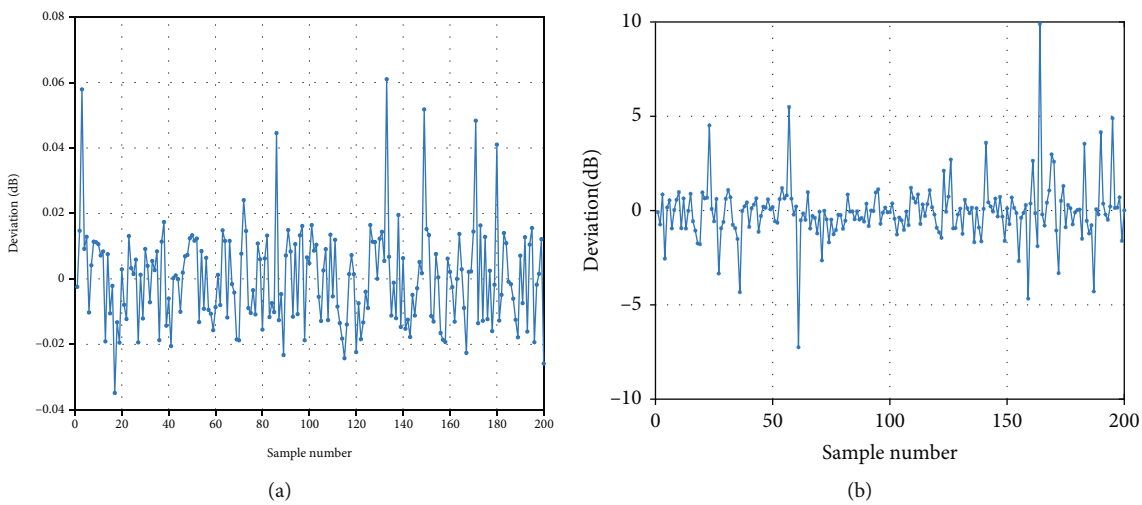

Figure 7: The prediction deviation of the trained ANN versus the number of samples: (a) for the XMD; (b) for the IMD_3.

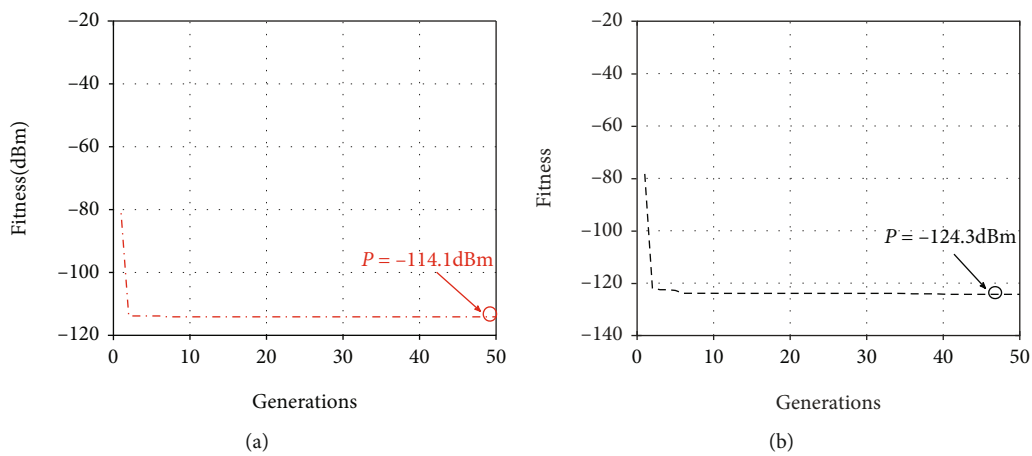

Figure 8: The fitness evolution curve versus the number of generations: (a) for XMD as the fitness; (b) for IMD_3 as the fitness.

ulteriorly improve the neural structure or enlarge the number of the sample.

From the calculated deviation results, in general, the ANN can accurately predict the output of the link. So, the predicted output can be approximately regarded as the actual output of the link.

After the BP neural work training, the genetic algorithm is used to seek the compensation factors γ and α and the corresponding optimal values of the XMD and IMD_3. The outputs of the BP neural work are used as the original individual fitness value of the genetic algorithm. The generation number, the population size, the crossover, and the mutation probability are set to 50, 20, 0.4, and 0.2, respectively. The evolution curve of the optimal individual fitness value in the optimization process is shown in Figure 8. From the evolution curve, the optimal individuals, XMD and IMD_3, are -114.1 dBm and -124.3 dBm, respectively, and the corresponding factor γ and α are -2.1 and 2980, respectively.

Then, the compensation process is added at the end of the link. To verify the compensation effect, the predicted

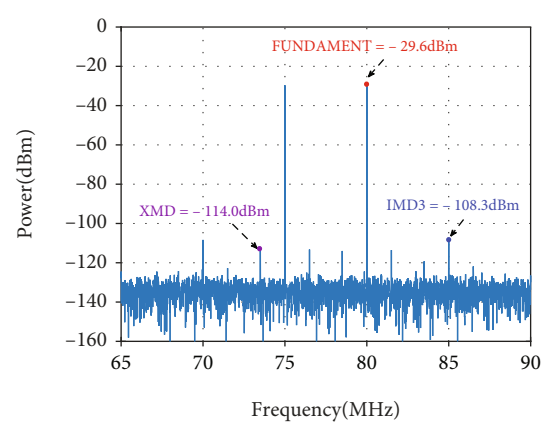

Figure 9: The spectrum of the link with the digital compensation applying the optimal compensation factor.

compensation factors are applied to the link to simulate the spectrum in MATALB. In the simulation experiment, the parameters are the same as the parameters in Figure 6 beside adding the compensation factors γ and α. The

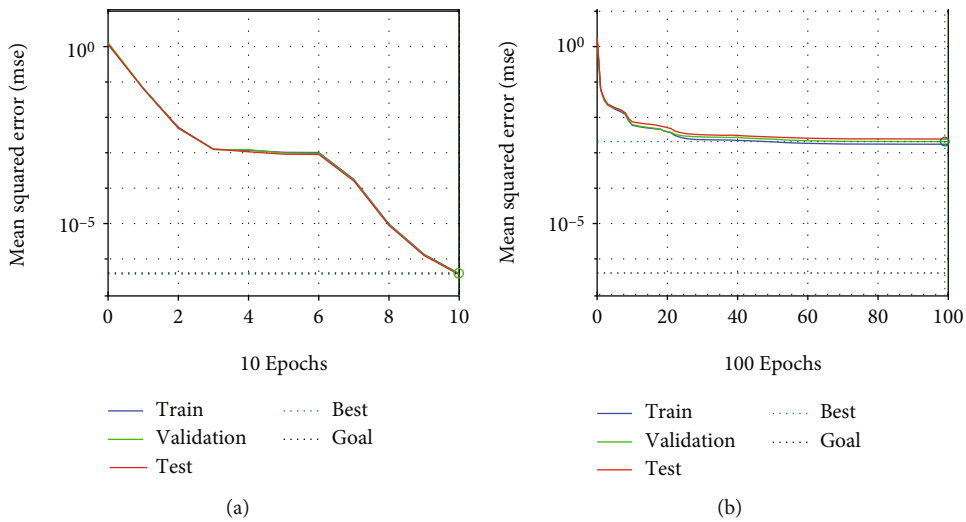

Figure 10: The mean square error in the BP algorithm versus the epochs for different nonlinear mapping: (a) for compensation factors as input and XMD as output: (b) for compensation factors as input and IMD_3 as output.

simulated spectrum with distortion mitigation based on the ANN-GA is shown in Figure 9. As we can see, the XMD and IMD_3 power level is about -114.0 dBm and -108.3 dBm, respectively. And the power level of XMD in Figure 9 is consistent with the predicted XMD in Figure 8(a). However, the IMD_3 in Figure 9 is 16 dB higher than the IMD_3 in Figure 8(b), which shows several differences between the prediction and simulation experiment.

Furthermore, to find the cause of the decline of prediction accuracy, the detailed discussion and analysis are conducted. The reason why prediction result of the IMD_3 shows the less precision may be that the prediction precision depends on the sample number and neural network structure. On the one hand, for the sample number, we add the sample number to 50000 and train the neural network. However, the prediction precision has no improvement. On the other hand, for the neural network, the BP neural network shows the limitation in fitting the complex nonlinear function. The BP neural network is based on the gradient descent algorithm, which means that the network relies on the instantaneous gradient value of the error curved surface. Due to the complex nonlinear mapping between the compensation factors γ and α and the IMD_3, there are some flat areas on error curved surface, where the error gradient changes slowly. To quantitatively analyze the changing process, the mean square error is expressed as follows:

$$\mathrm{MSE} = \frac{1}{n}\sum_{n}\left(D_{\mathrm{exp}} - D_{\mathrm{pre}}\right)^2, \tag{10}$$

where D_{exp} and D_{pre} are expectation and prediction value, respectively. As shown in Figure 10, the curves exhibit the mean square error changes versus the epochs. For the IMD_3 prediction, between the 20 and 100 epochs, the error falls slowly, shown in Figure 10(b), because there are many minimum points in the error curved surface for complex nonlinear function. And the minimum point will prevent BP neural network adjusting the weight to iterate effectively. The principle behind the weight adjustment is that the error gradient should be decreasing after adjusting the weight. However, the error gradient will be greater than zero once away from the minimum point. So it is the reason why the mean square error decreases slowly with the number of training sample increasing. In other words, the BP neural network gets into the local optimum. In the following research, we should change the BP algorithm. Conventional BP neural network only uses the gradient error to adjust the weight, that is, the information of the first derivative, while we can use the second derivative information to adjust the weight. The basic idea is that each iteration no longer follows a single negative gradient direction but follows the error to search along the direction of deterioration.

5. Conclusion

In this work, a microwave photonic link linearization technique is proposed by combining the traditional microwave photonic link digital distortion mitigation method and the artificial neural network. The recovered RF signal from the PD is digitized and filtered by band-pass and low-pass filters. The compensation signals are reconstructed by the signal process using the compensation factors and the filtered signal, where the compensation factors are obtained by the ANN-GA that consisted of BP neural network and genetic algorithm. The BP neural network learns the input-to-output mapping of the link and predicts the output value as the individual fitness value of the genetic algorithm. Based on the fitness value, the optimal compensation factors γ and α are found by the genetic algorithm. The simulation experiment shows that the power level of the mitigated XMD and IMD_3 is -114.0 dBm and -108.3 dBm, respectively. The combination of the artificial neural network and microwave photonics provides a new idea for the design of high-performance microwave photonics link. Different from the

traditional digital distortion compensation, the proposed technique can realize distortion compensation for any kinds of links and is independent of microwave photonics link structure and corresponding mathematical model. So it improves the intelligence and flexibility of microwave photonic link linearization design. However, it is worth to note that the BP neural network shows slightly insufficiently in fitting the complicated nonlinear link. So, developing more advanced and matched neural network may be the research hotspot for the intelligence microwave photonics.

Data Availability

All data included in this study are available upon request by contact with the corresponding author.

Disclosure

An earlier version of this work was presented as a conference paper at AICON 2021 [23].

Conflicts of Interest

The authors declare that they have no conflicts of interest.

Authors' Contributions

Yihui Yin and Wanli Yang are co-first author.

References

[1] J. Capmany and D. Novak, "Microwave photonics combines two worlds," *Nature Photonics*, vol. 1, pp. 319–330, 2007.

[2] R. W. Ridgway, C. L. Dohrman, and J. A. Conway, "Microwave photonics programs at DARPA," *Journal of Lightwave Technology*, vol. 32, no. 20, pp. 3428–3439, 2014.

[3] H. Skeie and R. V. Johnson, "Linearization of electro-optic modulators by a cascade coupling of phase modulating electrodes," *Proceedings of SPIE*, vol. 1583, pp. 153–164, 1991.

[4] J. L. Brooks, G. S. Maurer, and R. A. Becker, "Implementation and evaluation of a dual parallel linearization system for AM-SCM video transmission," *Journal of Lightwave Technology*, vol. 11, no. 1, pp. 34–41, 1993.

[5] M. Huang, J. Fu, and S. Pan, "Linearized analog photonic links based on a dual-parallel polarization modulator," *Optics Letters*, vol. 37, no. 11, pp. 1823–1825, 2012.

[6] Z. Zhu, S. Zhao, X. Li, K. Qu, T. Lin, and B. Lin, "Dynamic range improvement for an analog photonic link using an integrated electro-optic dual-polarization modulator," *IEEE Photonics Journal*, vol. 8, no. 2, pp. 1–10, 2016.

[7] D. Zhu, J. Chen, and S. Pan, "Multi-octave linearized analog photonic link based on a polarization-multiplexing dualparallel Mach-Zehnder modulator," *Optics Express*, vol. 24, no. 10, pp. 11009–11016, 2016.

[8] W. Jiang, Q. Tan, W. Qin et al., "A linearization analog photonic link with high third-order intermodulation distortion suppression based on dual-parallel Mach–Zehnder modulator," *IEEE Photonics Journal*, vol. 7, no. 3, pp. 1–8, 2015.

[9] V. Magoon and B. Jalali, "Electronic linearization and bias control for externally modulated fiber optic link," *International Topical Meeting on Microwave Photonics MWP 2000*, pp. 145–147, 2000.

[10] R. B. Childs and V. A. O'Byrne, "Multichannel AM video transmission using a high-power Nd: YAG laser and linearized external modulator," *IEEE Journal on Selected Areas in Communications*, vol. 8, no. 7, pp. 1369–1376, 1990.

[11] B. M. Haas and T. E. Murphy, "A simple, linearized, phase-modulated analog optical transmission system," *IEEE Photonics Technology Letters*, vol. 19, no. 10, pp. 729–731, 2007.

[12] B. Masella, B. Hraimel, and X. Zhang, "Enhanced spurious-free dynamic range using mixed polarization in optical single sideband Mach-Zehnder modulator," *Journal of Lightwave Technology*, vol. 27, no. 15, pp. 3034–3041, 2009.

[13] Q. Lv, K. Xu, Y. Dai, Y. Li, J. Wu, and J. Lin, "I/Q intensity-demodulation analog photonic link based on polarization modulator," *Optics Letters*, vol. 36, no. 23, pp. 4602–4604, 2011.

[14] T. R. Clark and M. L. Dennis, "Coherent optical phase-modulation link," *IEEE Photonics Technology Letters*, vol. 19, no. 16, pp. 1206–1208, 2007.

[15] X. Xie, Y. Dai, K. Xu et al., "Digital joint compensation of IMD_3 and XMD in broadband channelized RF photonic link," *Optics Express*, vol. 20, no. 23, pp. 25636–25643, 2012.

[16] Y. Cui, Y. Dai, F. Yin et al., "Enhanced spurious-free dynamic range in intensity-modulated analog photonic link using digital postprocessing," *IEEE Photonics Journal*, vol. 6, no. 2, pp. 1–8, 2014.

[17] Y. Dai, Y. Cui, X. Liang et al., "Performance improvement in analog photonics link incorporating digital post-compensation and low-noise electrical amplifier," *IEEE Photonics Journal*, vol. 6, no. 4, pp. 1–7, 2014.

[18] A. Agarwal, T. Banwell, P. Toliver, and T. K. Woodward, "Predistortion compensation of nonlinearities in channelized RF photonic links using a dual-port optical modulator," *IEEE Photonics Technology Letters*, vol. 23, no. 1, pp. 24–26, 2011.

[19] T. Banwell, A. Agarwal, P. Toliver, and T. K. Woodward, "Compensation of cross-gain modulation in filtered multichannel optical signal processing applications," in *2010 Conference on Optical Fiber Communication (OFC/NFOEC) collocated National Fiber Optic Engineers Conference*, pp. 1–3, San Diego, CA, USA, March 2010.

[20] X. Zou, S. Xu, S. Li, J. Chen, and W. Zou, "Optimization of the Brillouin instantaneous frequency measurement using convolutional neural networks," *Optics Letters*, vol. 44, no. 23, pp. 5723–5726, 2019.

[21] H. Ye, G. Y. Li, and B. H. Juang, "Power of deep learning for channel estimation and signal detection in OFDM systems," *IEEE Wireless Communications Letters*, vol. 7, no. 1, pp. 114–117, 2018.

[22] F. N. Khan, Q. Fan, C. Lu, and A. P. T. Lau, "An optical communication's perspective on machine learning and its applications," *Journal of Lightwave Technology*, vol. 37, no. 2, pp. 493–516, 2019.

[23] Y. Yin, W. Yang, X. Yang, Y. Qin, and H. Zhu, "Artificial neural network assisted mitigation of cross-modulation distortion in microwave photonics link," *International Conference on Artificial Intelligence for Communications and Networks*, vol. 396, pp. 493–503, 2021.

Hindawi
Wireless Communications and Mobile Computing
Volume 2022, Article ID 6595023, 6 pages
https://doi.org/10.1155/2022/6595023

Research Article

Performance Analysis of Product Channel for Relaying-Assisted Edge Computing in IoT Networks

Fusheng Zhu,[1] Liming Chen,[2] Wen Zhou,[3] Dan Deng,[4] Yanyi Rao,[5] Yajuan Tang,[6] Jun Liu,[7] Yuwei Zhang,[7] Jing Wang,[7] and Tao Cui[7]

[1]*Guangdong New Generation Communication and Network Innovative Institute (GDCNi), Guangzhou, China*
[2]*Electric Power Research Institute of CSG, Guangzhou, China*
[3]*Nanjing Forestry University, Nanjing, China*
[4]*University of Science and Technology of China, China*
[5]*Guangzhou University, Guangzhou, China*
[6]*Shantou University, Shantou, China*
[7]*Tsinghua University, Beijing, China*

Correspondence should be addressed to Jun Liu; junliu.thu@ieee.org

Received 4 May 2022; Revised 14 May 2022; Accepted 21 May 2022; Published 31 May 2022

Academic Editor: Mingqian Liu

In this paper, we analyze the typical product channel which is often encountered in wireless relaying channels, for relaying-assisted edge computing in Internet of Things (IoT) networks. Such analysis is of vital importance, as it is often encountered in wireless transmission. Specifically, we firstly derive a closed-form expression of the transmission outage probability in product channels, through solving involved complicated multivariate integral. We then simplify the expression through some approximation to the involved Bessel function, which can help obtain some meaningful findings to the system design. We finally provide some numerical results to verify that the presented analysis on the production channels is effective.

1. Introduction

Recently, Internet of Things (IoT) networks have been upgraded to a large extent [1, 2], thanks to the rapid progress in the wireless transmission and edge computing [3]. Moreover, the development of artificial intelligence also contributes to the upgraded IoT networks, such as the deep learning, transfer learning, and federated learning [4]. For these artificial intelligence algorithms, communication still plays an important role, since it can reduce the communication delay and power consumption, which can help speed up the intelligent algorithms and its convergence performance [5].

Moreover, an essential style in the MEC systems is the offloading strategy, which identifies the number of component of the jobs ought to be calculated by the CAPs. Essentially, offloading is actually to use the computational sources coming from the CAPs at the expense of communication [6, 7]. Many researches have been performed to accomplish a proper trade-off. Here, the authors in [8] examined the opportunistic CAP choice for the MEC connect with 2 CAPs and developed an optimal offloading strategy to enhance the outage efficiency in regard to latency as well as power usage. For multiuser multi-CAP MEC systems, the offloading might end up being rather complex [9, 10], as well as it is actually difficult to provide some logical services for the offloading. Within this particular situation, some smart formulas have actually been made a proposal to MEC systems, like deeper Q-network located formulas [11] as well as federated knowing located formulas [12, 13].

In further, the relaying technique has attracted a lot of attention from researchers including both the students and teachers. It has been widely applied in the IoT networks and edge computing. In particular, when the direct communication is poor due to the obstacles in the communication, the relaying can forward the signals and hence enhance the

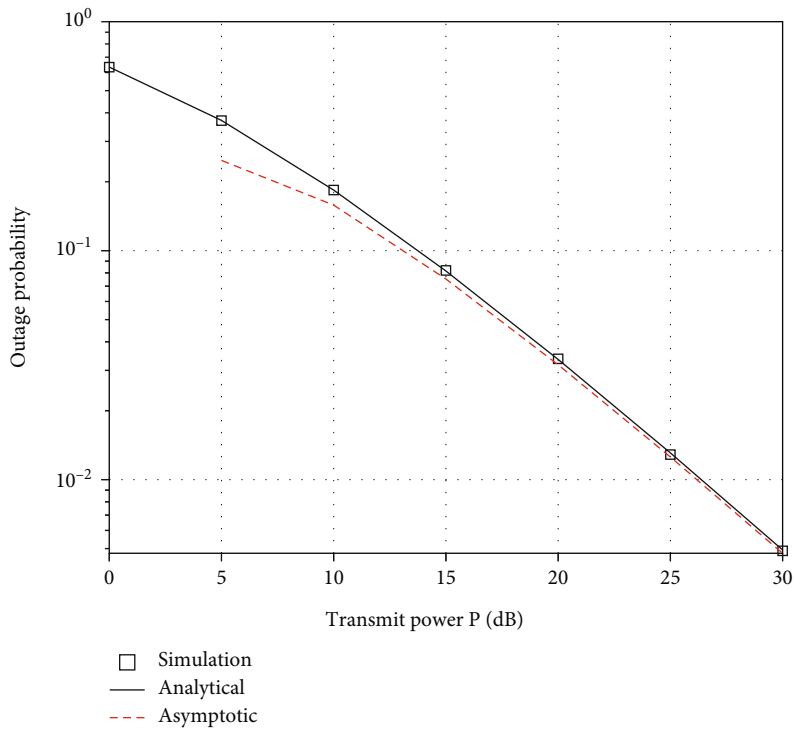

Figure 1: Comparison of three solutions versus the transmit power.

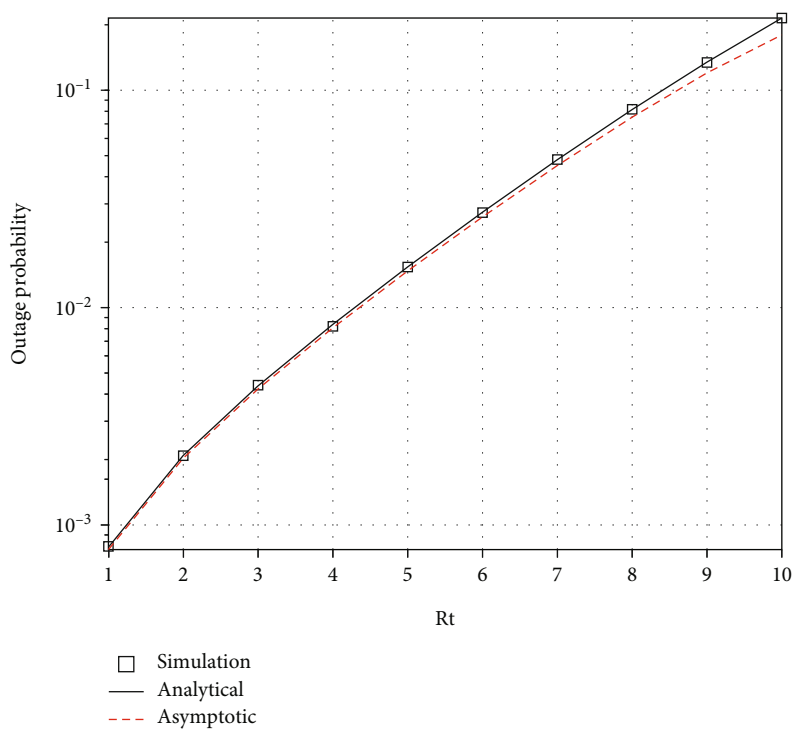

Figure 2: Comparison of three solutions versus R_t.

communication quality. Relaying technique has been also applied in the edge computing networks, whereas it can help assist the calculating tasks through relaying. However, the product channel is often encountered in the relaying transmission, which needs some further and deeper research to solve the hanged problems.

In this paper, we analyze the typical product channel which is often encountered in relaying channels, for

Table 1: Outage probability values of three solutions versus the transmit power.

Transmit power P (dB)	Simulation	Analytical	Asymptotic
0	6.3339×10^{-1}	6.3378×10^{-1}	0
5	3.7149×10^{-1}	3.7063×10^{-1}	2.4797×10^{-1}
10	1.8327×10^{-1}	1.8390×10^{-1}	1.5810×10^{-1}
15	8.1029×10^{-2}	8.1509×10^{-2}	7.5192×10^{-2}
20	3.3194×10^{-2}	3.3502×10^{-2}	3.1746×10^{-2}
25	1.305×10^{-2}	1.3084×10^{-2}	1.2559×10^{-2}
30	4.896×10^{-3}	4.9308×10^{-3}	4.7682×10^{-3}

Table 2: Outage probability values of three solutions versus R_t.

R_t	Simulation	Analytical	Asymptotic
1	8.15×10^{-4}	7.9041×10^{-4}	7.7047×10^{-4}
2	2.118×10^{-3}	2.0886×10^{-3}	2.0285×10^{-3}
3	4.374×10^{-3}	4.3651×10^{-3}	4.2241×10^{-3}
4	8.484×10^{-3}	8.3758×10^{-3}	8.0706×10^{-3}
5	1.5427×10^{-2}	1.5391×10^{-2}	1.4748×10^{-2}
6	2.739×10^{-2}	2.7487×10^{-2}	2.6137×10^{-2}
7	4.7893×10^{-2}	4.7924×10^{-2}	4.5047×10^{-2}
8	8.134×10^{-2}	8.151×10^{-2}	7.519×10^{-2}
9	1.3506×10^{-1}	1.347×10^{-1}	1.2019×10^{-1}
10	2.1435×10^{-1}	2.1486×10^{-1}	1.7968×10^{-1}

relaying-assisted edge computing in Internet of Things (IoT) networks. Such analysis is of vital importance, as it is often encountered in wireless channels. Specifically, we firstly give a closed-form expression of the transmission outage in product channels, through solving the involved multivariate integral. We then simplify the expression through some approximation to the involved Bessel function, which can help obtain some meaningful finding to the system design. We finally provide some numerical results to verify that the presented analysis on the production channels is effective.

2. System Model

According to the definition of signal-to-noise ratio (SNR), we can obtain the SNR of a specific channel by

$$\mathrm{SNR} = 10 \lg \left(\frac{Ph^2}{\sigma^2} \right), \tag{1}$$

where P is the transmit power, $h \sim \mathcal{CN}(0, \varepsilon)$ is the instantaneous channel parameter of the wireless link, and σ^2 is the variance of the additive white Gaussian noise (AWGN) at the receiver.

We write the probability that the SNR value of the channel composed of h_1 and h_2 that is less than R_t as follows:

$$P_{\mathrm{out}} = \Pr\left(\frac{P}{\sigma^2} (|h_1||h_2|)^2 < R_t \right). \tag{2}$$

Then, we obtain

$$P_{\mathrm{out}} = \Pr\left(|h_1||h_2|)^2 < \frac{\sigma^2 R_t}{P} \right). \tag{3}$$

For simplicity, we let $|h_1|^2 = x_1$ and $|h_2|^2 = x_2$, thus

$$P_{\mathrm{out}} = \Pr\left\{ x_1 x_2 < \frac{\sigma^2 R_t}{P} \right\} = \Pr\left\{ x_1 < \frac{\sigma^2 R_t}{P x_2} \right\}. \tag{4}$$

The probability density function of $f_{|h_k|^2}(x_k), k \in \{1, 2\}$ is

$$f_{|h_k|^2}(x_k) = \frac{1}{\beta_k} e^{-x_k/\beta_k}. \tag{5}$$

Let $H_1 = \sigma^2 R_t / P x_2$, thus we can have

$$\int_0^{H_1} \boxtimes f_{|h_1|^2}(x_1) dx_1 = \int_0^{H_1} \boxtimes \frac{1}{\beta_1} e^{-x_1/\beta_1} dx_1 = 1 - e^{-H_1/\beta_1}. \tag{6}$$

We can write P_{out} as follows:

$$\begin{aligned} P_{\mathrm{out}} &= \int_0^{+\infty} \left(1 - e^{-H_1/\beta_1} \right) f_{|h_2|^2}(x_2) dx_2 \\ &= \frac{1}{\beta_2} \int_0^{+\infty} \left(1 - e^{-\left(\sigma^2 R_t / P x_2\right)/\beta_1} \right) e^{-x_2/\beta_2} dx_2 \\ &= \frac{1}{\beta_2} \int_0^{+\infty} \left(1 - e^{-\sigma^2 R_t / P \beta_1 x_2} \right) e^{-x_2/\beta_2} dx_2. \end{aligned} \tag{7}$$

Let $A = \sigma^2 R_t / P$, we can obtain

$$P_{\mathrm{out}} = \frac{1}{\beta_2} \int_0^{+\infty} \boxtimes \left(1 - e^{-A/\beta_1 x_2} \right) e^{-x_2/\beta_2} dx_2. \tag{8}$$

By solving the integral formula, we can obtain

$$P_{\mathrm{out}} = 1 - \frac{1}{\beta_2} \sqrt{4A} K_1(x) \left(\sqrt{\frac{4A}{\beta_1 \beta_2}} \right), \tag{9}$$

where $K_1(x)$ is Bessel functions of the first order. In order to speed up the computation, we can approximate (9) as follows:

$$P_{\mathrm{out}} = \approx 1 - \frac{A}{\beta_1 \beta_2} \ln \left(\frac{4A}{e \beta_1 \beta_2} \right) + \beta_2. \tag{10}$$

3. Numerical and Simulation Results

In this part, we present some numerical and simulation results to verify the effect of outage probability analysis.

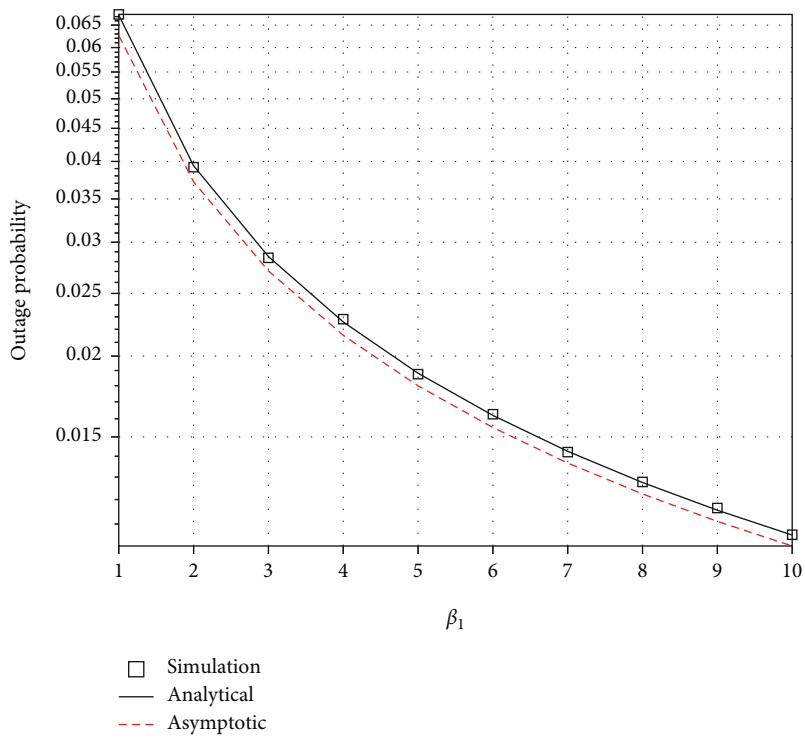

Figure 3: Comparison of three solutions versus β_1.

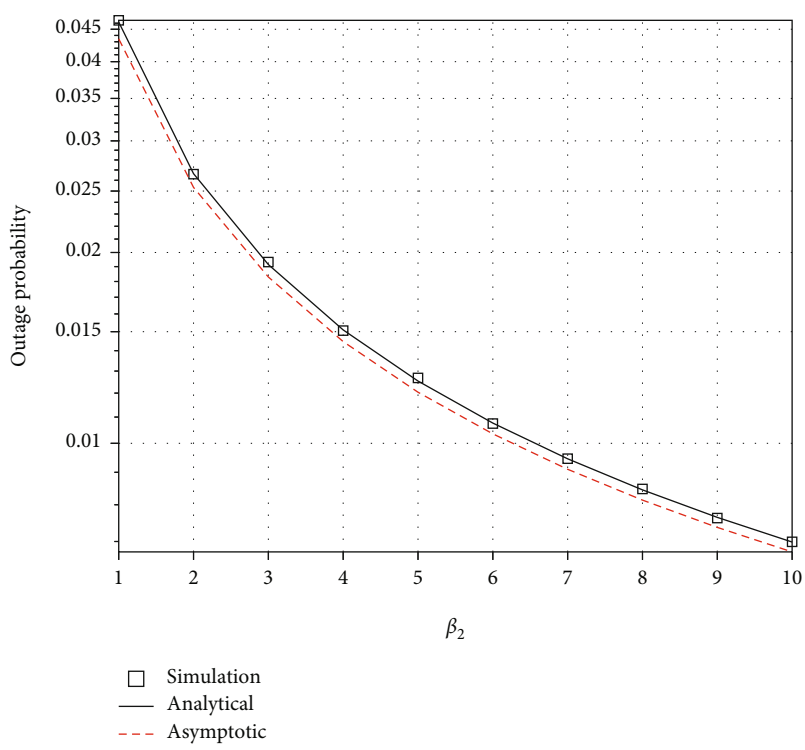

Figure 4: Comparison of three solutions versus β_2.

We compare the effects of simulation solutions, analytical solutions, and asymptotic solutions with different transmit powers and upper limit values of SNR in Figures 1 and 2 and Tables 1 and 2. Moreover, we analyze the impact of different β_1 and β_2 on outage probability in Figures 3 and 4 and Tables 3 and 4.

Figure 1 shows comparison of three solutions versus the transmit power, and the three solutions gradually decline as

Table 3: Outage probability values of three solutions versus β_1.

β_1	Simulation	Analytical	Asymptotic
1	6.7515×10^{-2}	6.7346×10^{-2}	6.2627×10^{-2}
2	3.919×10^{-2}	3.9384×10^{-2}	3.7196×10^{-2}
3	2.8379×10^{-2}	2.8507×10^{-2}	2.7091×10^{-2}
4	2.281×10^{-2}	2.2584×10^{-2}	2.1539×10^{-2}
5	1.8753×10^{-2}	1.8817×10^{-2}	1.7989×10^{-2}
6	1.626×10^{-2}	1.6191×10^{-2}	1.5507×10^{-2}
7	1.4209×10^{-2}	1.4249×10^{-2}	1.3665×10^{-2}
8	1.2776×10^{-2}	1.2749×10^{-2}	1.2240×10^{-2}
9	1.1643×10^{-2}	1.1553×10^{-2}	1.1102×10^{-2}
10	1.0587×10^{-2}	1.0576×10^{-2}	1.0171×10^{-2}

Table 4: Outage probability values of three solutions versus β_2.

β_2	Simulation	Analytical	Asymptotic
1	4.6547×10^{-2}	4.6193×10^{-2}	4.3462×10^{-2}
2	2.6644×10^{-2}	2.6630×10^{-2}	2.5335×10^{-2}
3	1.9154×10^{-2}	1.9141×10^{-2}	1.8295×10^{-2}
4	1.4985×10^{-2}	1.5097×10^{-2}	1.4469×10^{-2}
5	1.2491×10^{-2}	1.2538×10^{-2}	1.2039×10^{-2}
6	1.0802×10^{-2}	1.0762×10^{-2}	1.0349×10^{-2}
7	9.47×10^{-3}	9.4525×10^{-3}	9.0994×10^{-3}
8	8.286×10^{-3}	8.4437×10^{-3}	8.1356×10^{-3}
9	7.693×10^{-3}	7.6410×10^{-3}	7.3677×10^{-3}
10	6.964×10^{-3}	6.9860×10^{-3}	6.7405×10^{-3}

the transmit power gradually improves. The outage probability of the analytical solution reaches 4.9308×10^{-3} when the transmit power is 30 dB. Moreover, the simulation solutions almost coincide with the analytical solutions from transmit powers of 0 to 30 dB. The asymptotic solutions increasingly approximate the simulation solutions and the analytical solutions as the transmit power gradually improves. Specifically, when the transmit power is 30 dB, the outage probabilities of the analytical solution, the simulation solution, and the asymptotic solution are 4.9308×10^{-3}, 4.896×10^{-3}, and 4.7682×10^{-3}, respectively. The specific values of the three solutions are shown in Table 1.

In Figure 2, the outage probabilities of the analytical solutions, the simulation solutions, and the asymptotic solutions improve as the target R_t raises. The analytical solutions, the simulation solutions, and the asymptotic solutions almost coincide when R_t versus from 1 to 5, but the asymptotic solutions begin to markedly lower than the two other curves as R_t raises. For instance, the outage probabilities of the analytical solution, the simulation solution, and the asymptotic solution are 7.9041×10^{-4}, 8.15×10^{-4}, and 7.7047×10^{-4}, respectively, when R_t is 1, while the above three are 2.1486×10^{-1}, 2.1435×10^{-1}, and 1.7968×10^{-1}, respectively, when R_t is 10. The specific values of the three solutions are shown in Table 2.

Figures 3 and 4 demonstrate the effects of simulation solutions, analytical solutions, and asymptotic solutions with different β_1 and β_2. The outage probabilities of the analytical solutions, the simulation solutions, and the asymptotic solutions decline as the values of β_1 and β_2 increase, in both Figures 3 and 4. In addition, the analytical solutions and the simulation solutions basically coincide when β_1 and β_2 vary from 1 to 10. The outage probability values of the asymptotic solutions are all less than the analytical solutions and the simulation solutions in both Figures 3 and 4. For instance, the outage probabilities of the analytical solution, the simulation solution, and the asymptotic solution are 1.0576×10^{-2}, 1.0587×10^{-2}, and 1.0171×10^{-2}, respectively, when β_1 is 10, while the above three are 6.9860×10^{-3}, 6.964×10^{-3}, and 6.7405×10^{-3}, when β_2 is 10, respectively. We present the detailed values of the three solutions in Tables 3 and 4.

4. Conclusions

In this paper, we analyzed the typical product channel which was often encountered in relaying channels, for relaying-assisted edge computing in Internet of Things (IoT) networks. Such analysis was of vital importance, as it was often encountered in wireless channels. Specifically, we firstly gave a closed-form expression of the transmission outage in product channels, through solving the multivariate integral. We then simplified the expression through some approximation to the involved Bessel function, which could help obtain some meaningful finding to the system design. We finally presented some numerical results to verify that the presented analysis on the production channels was effective.

Data Availability

The data can be obtained through the email to the authors.

Conflicts of Interest

The authors declare that there is no conflict of interest regarding the publication of this work.

Acknowledgments

The work in this paper was supported by the Key-Area Research and Development Program of Guangdong Province (No. 2019B090904014) and the NSFC (No. 62871349).

References

[1] J. Zhao, X. Sun, Q. Li, and X. Ma, "Edge caching and computation management for real-time Internet of Vehicles: an online and distributed approach," *IEEE Transactions on Intelligent Transportation Systems*, vol. 22, no. 4, pp. 2183–2197, 2021.

[2] J. Xia, F. Zhou, X. Lai et al., "Cache aided decode-and-forward relaying networks: from the spatial view," *Wireless Communications and Mobile Computing*, vol. 2018, 9 pages, 2018.

[3] Z. Zhu, S. Wan, P. Fan, and K. B. Letaief, "Federated multiagent actor-critic learning for age sensitive mobile-edge computing," *IEEE Internet of Things Journal*, vol. 9, no. 2, pp. 1053–1067, 2022.

[4] S. Premkumar and A. N. Sigappi, "ASIS edge computing model to determine the communication protocols for IoT based irrigation," *Journal of Mobile Multimedia*, vol. 18, no. 3, 2022.

[5] F. Alqahtani, M. Al-Maitah, and O. A. Elshakankiry, "A proactive caching and offloading technique using machine learning for mobile edge computing users," *Computer Communications*, vol. 181, pp. 224–235, 2022.

[6] B. Wang, F. Gao, S. Jin, H. Lin, and G. Y. Li, "Spatial- and frequency-wideband effects in millimeter-wave massive MIMO systems," *IEEE Transactions on Signal Processing*, vol. 66, no. 13, pp. 3393–3406, 2018.

[7] X. Hu, C. Zhong, Y. Zhang, X. Chen, and Z. Zhang, "Location information aided multiple intelligent reflecting surface systems," *IEEE Transactions on Communications*, vol. 68, no. 12, pp. 7948–7962, 2020.

[8] H. Yan, L. Hu, X. Xiang, Z. Liu, and X. Yuan, "PPCL: privacy-preserving collaborative learning for mitigating indirect information leakage," *Information Sciences*, vol. 548, pp. 423–437, 2021.

[9] X. Lai, L. Fan, X. Lei, Y. Deng, G. K. Karagiannidis, and A. Nallanathan, "Secure mobile edge computing networks in the presence of multiple eavesdroppers," *IEEE Transactions on Communications*, vol. 70, no. 1, pp. 500–513, 2022.

[10] F. Zhou and R. Q. Hu, "Computation efficiency maximization in wireless-powered mobile edge computing networks," *IEEE Transactions on Wireless Communications*, vol. 19, no. 5, pp. 3170–3184, 2020.

[11] W. Zhou, D. Deng, J. Xia, and Z. Shao, "The precoder design with covariance feedback for simultaneous information and energy transmission systems," *Wireless Communications and Mobile Computing*, vol. 2018, Article ID 8472186, 17 pages, 2018.

[12] S. Arzykulov, A. Celik, G. Nauryzbayev, and A. M. Eltawil, "UAV-assisted cooperative & cognitive NOMA: deployment, clustering, and resource allocation," *IEEE Transactions on Cognitive Communications and Networking*, vol. 8, no. 1, pp. 263–281, 2022.

[13] R. Akbar, S. Prager, A. R. Silva, M. Moghaddam, and D. Entekhabi, "Wireless sensor network informed UAV path planning for soil moisture mapping," *IEEE Transactions on Geoscience and Remote Sensing*, vol. 60, pp. 1–13, 2022.

Hindawi
Wireless Communications and Mobile Computing
Volume 2022, Article ID 4055744, 7 pages
https://doi.org/10.1155/2022/4055744

Research Article

Design of the NCI Signal for BeiDou System Based on CCSK

Xinyue Li,[1] **Deyue Zou**,[1] **Yangzhen Zhao**,[1] **Xingzhong Liu**,[2] **and Qiang Chen**[2]

[1]*School of Information and Communication Engineering, Dalian University of Technology, Dalian 116081, China*
[2]*Guizhou Aerospace Linquan Motor co., Ltd, Guiyang 550081, China*

Correspondence should be addressed to Deyue Zou; zoudeyue@dlut.edu.cn

Received 12 February 2022; Revised 31 March 2022; Accepted 20 April 2022; Published 16 May 2022

Academic Editor: Mingqian Liu

Currently, BeiDou Navigation Satellite System (BDS) has been a mature satellite navigation system. However, the transmission rate of the navigation signal is low. A novel Navigation and Communication Integrated (NCI) signal had been proposed in our previous work, its transmission rate was improved compared with the traditional navigation signal. In addition, an optimization algorithm was proposed to avoid cross-correlation interference between the navigation signal and the communication signal. Based on the above theoretical system, this paper gives a specific design for the BDS. The communication signal used in BDS is selected basing on the optimization algorithm, and the original BDS signal is used as the navigation signal. In addition, the error correction coding and interleaving technique in BDS are applied to the NCI signal to further improve the compatibility between the signal and BDS. The simulation results verify the superiority of the optimization algorithm. It illustrates each communication signal selected is suitable for the navigation signal of each satellite in BDS.

1. Introduction

With the development of navigation positioning technology, the four major satellite navigation systems are becoming mature [1–3]. For example, satellites can be connected to the space-air-ground integrated networks [4] and play a key role in target recognition [5, 6]. Among them, BeiDou Navigation Satellite System (BDS) has the short message communication function. It is introduced that the D1 navigation message rate is 50 bps in Interface Control Document (ICD) of BDS [7]. And it is modulated with secondary coding at a rate of 1 kbps [8–11]. Several acquisition methods for the navigation signal with secondary coding are introduced in [8–11]. Even if the signal modulated with secondary coding was influenced by the symbol conversion, it still can be received correctly in normal condition. Although the signal of BDS is modulated with secondary coding with a rate of 1 kbps, its rate is still low. For how to improve the signal rate, the Cyclic Code Shift Keying (CCSK) [12–16] technology has been proposed, i.e., the spreading code of the communication signal is cyclically shifted. The CCSK technology is introduced in [12, 13]. The information is transmitted by the cyclic shift number of spreading code sequences, thereby the transmission rate of the CCSK signal is improved. The performance of the CCSK signal is analyzed theoretically in [14], and the upper limit of symbol error rate is given. The performance of the CCSK signal transmitted on different channels is analyzed in [15, 16]. It is verified that the CCSK signal still has good performance and its rate can be improved.

A novel Navigation and Communication Integrated (NCI) signal is proposed in [17]. The navigation signal refers to the D1 navigation message in BDS. The communication signal uses CCSK signal. Compared with the traditional navigation signal, the rate of the NCI signal is greatly improved. Therefore, the NCI signal can be applied to BDS to improve the signal rate and reduce the Time to First Fix (TTFF).

The NCI signal proposed in [17] is applied to BDS in this paper. The signal in BDS is used as the navigation signal. The communication signal which is most suitable for each navigation signal is selected basing on optimization algorithm. Compared with the traditional navigation signal in BDS, the NCI signal has a higher transmission rate. Section 2 introduces some related works. Section 3 describes the signal design for BDS. In section 4, simulation results and theoretical analysis are given. Finally, the thesis is summarized.

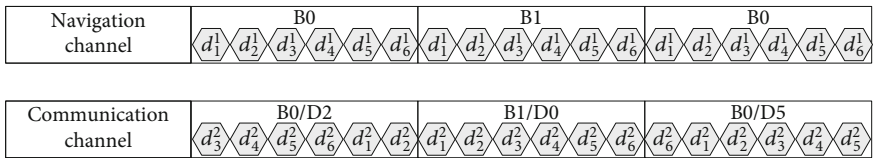

Figure 1: The NCI signal. B0 and B1 represent navigation data 0 and 1, respectively. D2, D0 and D5 denote cyclic shift number 2, 0 and 5. d denotes chip, where superscripts represent different ranging codes and subscripts represent different chips.

2. Related Work

2.1. Signal Structure. The NCI signal used in this paper can refer to [17]. The specific signal structure is shown in Figure 1. The navigation signal adopts the traditional BDS signal, it provides synchronization ability for the communication signal. The traditional receiver in service can be used without large-scale improvement, which saves the construction cost. As the communication signal, the CCSK signal improves the transmission rate and enhances the communication ability of the navigation system. They are transmitted synchronously at the same frequency and phase to achieve the effect of mutual enhancement.

2.2. BeiDou Signal. The ranging code used for the B1I signal in BDS is Gold sequence. The code length is 2046 and the code rate is 2.046 Mcps. In order to improve the reliability, the data code of the navigation message adopts the error correction coding and interleaving technique. The error-correcting code is BCH (15,11,1) code. Every two groups of BCH (15,11,1) code are converted in parallel-serial conversion and the interleaving is performed by bit interleaving. The specific process can refer to [7].

3. Signal Design

3.1. Optimal Cyclic Shift Set. An optimization algorithm is proposed in [17] to avoid the cross-correlation interference between the navigation signal and the communication signal. By optimizing the cyclic shift number of the communication signal, the value which is larger than the optimal threshold of the cross-correlation function overlies fitly on the self-correlation peak. Where the cross-correlation function is obtained by correlation between the NCI signal and the local signal. The optimal cyclic shift numbers constitute the Optimal Cyclic Shift Set (OCSS).

The parameter is represented by binary in BDS. While the communication signal transmits information through its cyclic shift number. The number of elements in the OCSS i.e., M is 2^n by designing the optimal threshold, where n is a positive integer. However, there are a large number of the same values in the cross-correlation function, it is impossible to make $M=2^n$ by adjusting an optimal threshold. So two optimal thresholds i.e., K_1 and K_2 need to be set to design two OCSSs i.e., $\mathbf{Q}_1$ and $\mathbf{Q}_2$. K_1 should meet the requirement that the number of elements in $\mathbf{Q}_1$ i.e., M_1 is less than 2^n and M_1 is the number closest to 2^n. K_2 should meet the requirement that the number of elements in $\mathbf{Q}_2$ i.e., M_2 is more than the 2^n and M_2 is the number closest to 2^n. M_2-2^n elements are deleted from $\mathbf{Q}_2$ because $\mathbf{Q}_1 \subseteq \mathbf{Q}_2$.

Table 1: Mapping relationship between optimal cyclic shift number and binary number.

Optimal cyclic shift number	Mapping number	7-bit data
41	0	0000000
47	1	0000001
52	2	0000010
65	3	0000011
90	4	0000100
...	...	...
2004	127	1111111

Above method can further achieve the compatibility between the NCI signal and BDS. Since the length of the ranging code is 2046, n cannot exceed 10. If n is too large, the superiority of the optimization algorithm is limited. If n is too small, the improvement of communication signal rate is not obvious. Therefore, the range of n can be appropriately set as $6 \sim 8$. n is selected as 7 in this paper. In this way, the cyclic shift number of the communication signal can be directly converted to binary number by mapping without additional coding. The specific mapping method is shown in Table 1.

3.2. Generation of Navigation Signal and Communication Signal. The navigation signal and the communication signal suitable for each satellite need to be generated before applying the NCI signal to BDS. The following describes this process.

Firstly, the spreading code used for the navigation signal i.e., the navigation code refers to the C_{B1I} code in BDS. The specific generation process can refer to [7]. The generation process of the spreading code used for the communication signal i.e., the communication code is similar to that of the navigation code. When the communication code is generated, the different taps of the shift register used for generating the G2 sequence perform modular sum to realize the different offsets of the G2 sequence phase. It uses one-tap, three-taps, four-taps etc. Two-taps is excluded because two-taps is already used when the navigation code is generated. We can get $\sum_{\substack{k=1 \\ k\neq 2}}^{11} C_{11}^k$ i.e., 1992 code sequences, where C_{11}^k denotes combination number formula. Besides, the code sequences need to meet the condition of balanced code. This selects out 495 suitable code sequences. Finally, 37 code sequences are selected from the 495 code sequences as communication codes of 37 satellites. The selection principle bases on the optimization algorithm to avoid better the

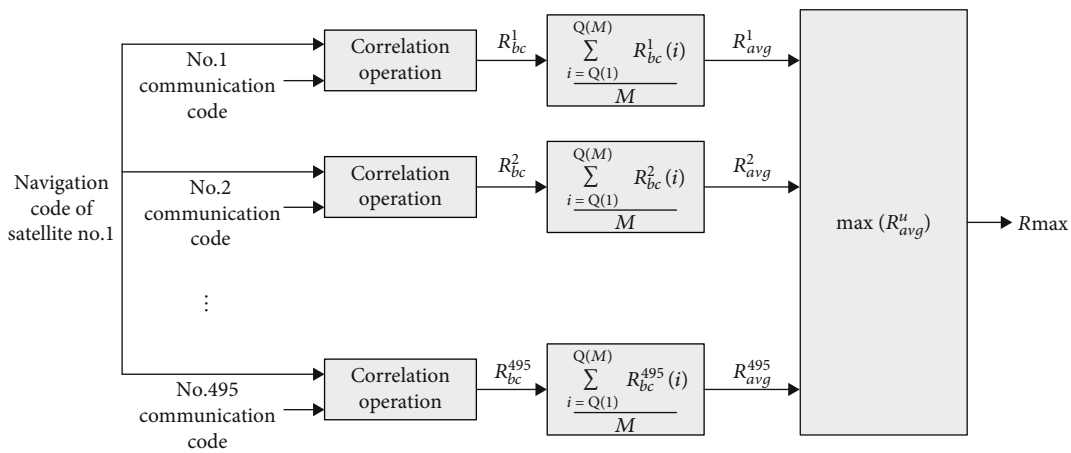

Figure 2: The flowchart of selecting communication code.

Table 2: The optimal cyclic shift for No.1 satellite.

Satellite's ID	OCSS
1	47, 52, 65, 90, 129, 159, 169, 178, 208, 218, 230, 250, 253, 261, 310, 368, 382, 404, 417, 427, 451, 462, 469, 517, 536, 543, 560, 568, 578, 599, 606, 661, 672, 709, 717, 738, 742, 749, 752, 813, 818, 843, 848, 866, 868, 880, 893, 902, 911, 929, 932, 945, 990, 998, 1020, 1069, 1074, 1076, 1153, 1156, 1193, 1203, 1218, 1219, 1244, 1252, 1254, 1275, 1280, 1294, 1301, 1312, 1325, 1335, 1341, 1344, 1355, 1381, 1382, 1389, 1391, 1393, 1399, 1419, 1428, 1448, 1454, 1460, 1468, 1492, 1499, 1500, 1508, 1520, 1533, 1570, 1600, 1612, 1617, 1625, 1637, 1644, 1649, 1661, 1668, 1687, 1702, 1712, 1724, 1735, 1737, 1748, 1801, 1823, 1851, 1856, 1864, 1868, 1874, 1875, 1880, 1915, 1952, 1961, 1972, 1986, 2004

cross-correlation interference between the navigation signal and the communication signal.

Taking the navigation code of satellite No.1 as an example, the most suitable communication code and the corresponding OCSS for this satellite need to be selected by this principle: to maximize the correlation peak between the NCI signal and the local signal by using the communication code, that is, the cross-correlation values that overlie on the self-correlation peaks are guaranteed to be statistical largest. Taking No.1 communication code as an example, the navigation code and the communication code perform the cross-correlation operation. We obtain the average value of M cross-correlation values that are all larger than the optimal threshold, i.e.,

$$R_{\text{avg}}^1 = \frac{\sum_{i=\mathbf{Q}(1)}^{\mathbf{Q}(M)} R_{bc}^1(i)}{M} \tag{1}$$

where $\mathbf{Q}$ denotes the OCSS, i is the optimal cyclic shift number, R_{bc}^1 is the cross-correlation function between the navigation code and the communication code. $R_{bc}^1(i)$ is larger than the optimal threshold. Other communication codes are similar with No.1 communication code, so 495 values are obtained. Finally, the maximum of 495 average values i.e.,

$$R_{\max} = \max\left(R_{\text{avg}}^u\right), u = 1, 2, \cdots, 495 \tag{2}$$

corresponding communication code is selected as the most suitable communication code for navigation code of satellite No.1. The specific selection process is shown in Figure 2.

According to this method, the most suitable communication codes for other navigation codes can be obtained. However, one communication code may be the most suitable one for different navigation satellites. Then, $R_{\max}$ which corresponds to the conflicting navigation codes need to be compared. The satellite with a larger $R_{\max}$, occupies this communication code. The most suitable communication codes for the conflicting satellites need to be re-selected. The second maximum of the average values i.e.,

$$\max_{R_{\text{avg}}^u \neq R_{\max}}\left(R_{\text{avg}}^u\right), u = 1, 2, \cdots, 495 \tag{3}$$

corresponding communication code is selected. Thus, the most suitable communication codes for the 37 navigation codes and their corresponding OCSSs can be obtained. Taking No.1 satellite as an example, its corresponding OCSS is shown in Table 2.

3.3. Structure Arrangement of the Navigation Message. As the data rate is greatly improved, the time for broadcasting the navigation message parameters is reduced. The navigation message parameters can be inserted into some time slots of the communication signal and broadcasted periodically. In order to further reduce the communication resources occupied by the navigation message parameters, some parameters unrelated to positioning can be deleted. Some parameters with less information can also be encapsulated together. Three types of frame are organized according to the different repetition periods of navigation message parameters, which are used to broadcast different types of

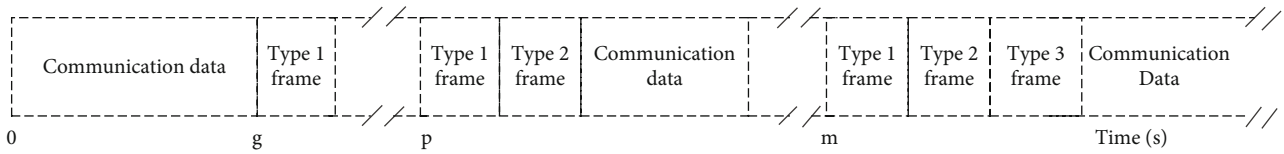

Figure 3: Frame structure format.

parameters. The repetition periods of three types of frame are set as g second, p second, and m second, respectively. Referring to the repetition periods of the navigation message parameters in ICD, g, p, and m can be set to 6, 30, and 720, respectively. If the repetition periods are too small, frequent broadcasting will take up more communication resources. If the repetition periods are too large and the broadcasting is not frequent, the TTFF will be extended. The positioning speed can be improved by inserting these frames into the head of the sub-frame. The specific frame structure is shown in Figure 3.

3.4. Encoding and Verification. In order to further improve the compatibility between the NCI signal and BDS, the error correction coding used in BDS is applied to the integration signal.

Firstly, the error correction coding and interleaving process are consistent with that in [7]. As shown in Figure 4, after the error correction coding and interleaving are applied to the navigation data, they are read out in every group of 7-bits. The 7-bits data are converted into decimal numbers and mapped to the optimal cyclic shift number in OCSS. The communication signal transmits information through the cyclic shift number. Thus, a period communication signal is modulated by CCSK technique with the corresponding optimal cyclic shift number. Every two groups of BCH code are encoded into 30-bit interleaved code in BDS. Thus, the remaining data are filled with zero if the data length cannot be divided by 7.

The receiver will calculate the cyclic shift number of the communication signal through the position of the correlation peak. And the cyclic shift number will be inversely mapped to a binary number of 7-bit, then the error correction decoding will be performed.

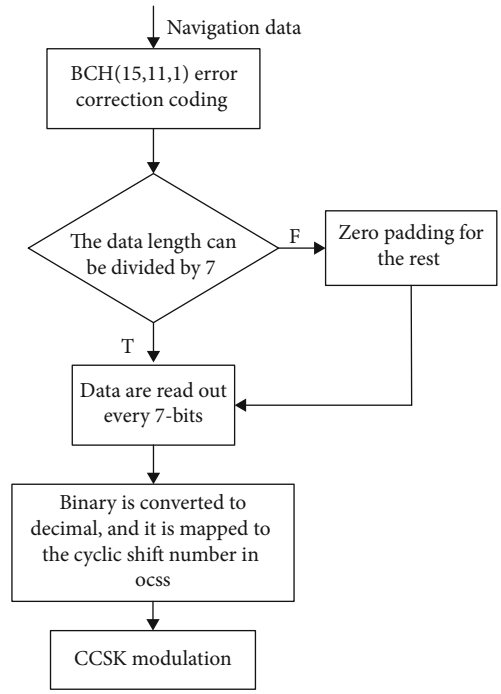

Figure 4: Schematic diagram of error correction coding of navigation message.

Table 3: Simulation parameters.

Specific parameters	Specific values
Carrier frequency	4.092 MHz
Sampling frequency	16.368 MHz
Spreading code length	2046
Code period	1 ms

4. Simulation and Analysis

The simulation results and performance analysis are given in this section. As shown in Table 3, the parameters used in the simulation refer to ICD.

In the simulation, the navigation code of satellite No.1 is used as the spreading code for the navigation signal, and the corresponding communication code is used as the spreading code for the communication signal.

4.1. Detection Performance Analysis. In order to verify the detection performance of the optimization algorithm, the detection probability (P_d) is simulated when the optimization algorithm is applied. Moreover, no communication signal and random cyclic shift of communication signal are included for compare. The P_d of the navigation signal is shown in Figure 5.

It can be known form Figure 5, the P_d increases with Signal-to-Noise Ratio (SNR), which is consistent with the theory. When OCSS is used, the P_d is significantly better than the other two cases. It is increased by about 9.3% when the BDS works at the minimum signal strength, i.e., the SNR is -27 dB. The side lobe of the correlation function is almost unchanged when the optimization algorithm is applied, but the correlation peak slightly increases. Thus, the signal's P_d is greatly improved.

The same simulation of communication signal is performed, as shown in Figure 6.

Similar to the P_d of the navigation signal, the P_d of the communication signal is obviously better than the other two cases when the optimization algorithm is used. The P_d

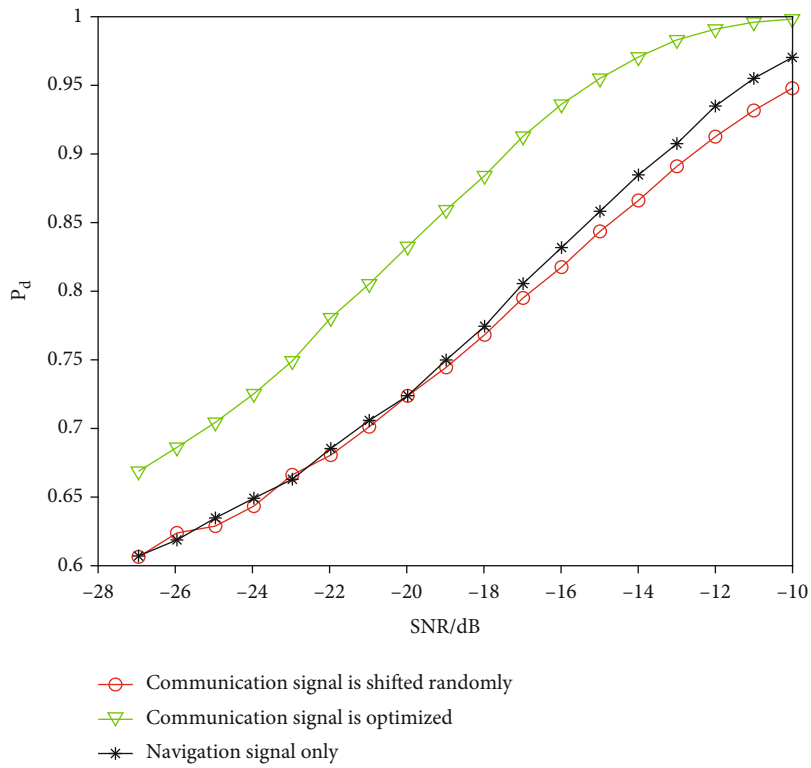

Figure 5: The P_d of the navigation signal.

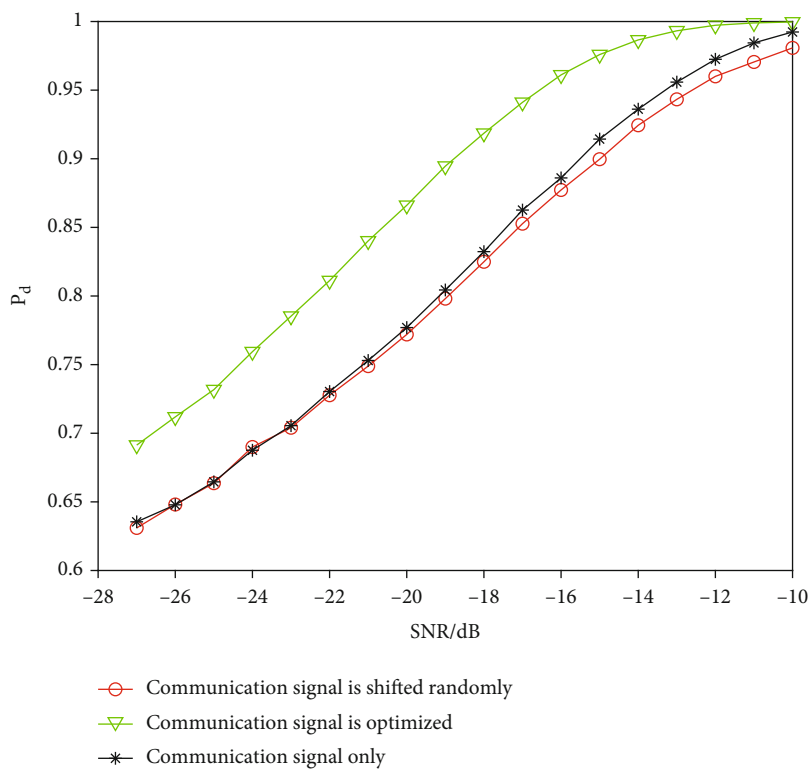

Figure 6: The P_d of the communication signal.

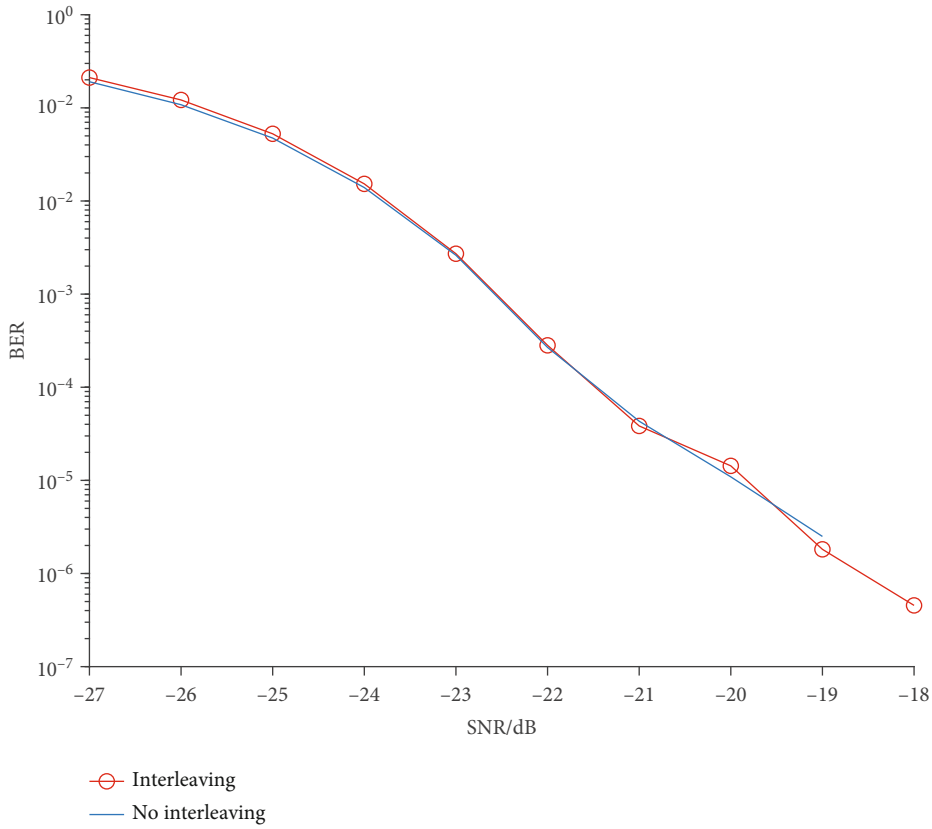

Figure 7: BER of the navigation signal.

of the communication signal is increased by about 8% when the SNR is -27 dB. Since the principle of the optimization algorithm is all the same. The only difference is that the local sequence is the navigation code or the communication code.

The above results show that the optimization algorithm can significantly improve the detection performance. It also verifies that the method proposed in Section 3.2 to select the most suitable communication code for each navigation code is effective.

4.2. Bit Error Performance Analysis. In order to verify the capability of the NCI signal to resist interference, the Bit Error Rate (BER) of the signal is simulated. There are two situations including BCH (15,11,1) coding and no error correction coding. The BER is shown in Figure 7.

It can be seen from Figure 7 that the BER of the signal is not improved although error correction coding and interleaving are applied to the integration signal. Because the cyclic shift number of the communication signal is inversely mapped to the 7-bits binary number. If a period signal is disturbed, the 7-bits binary number may have continuous errors. Therefore, the BER of the signal has not been further improved under the special interleaving mode in BDS.

4.3. Communication Rate Analysis. The information is carried by the cyclic shift number of the communication signal. Since the navigation signal is added for providing synchronization, it can be seen from Section 3.1 that a period communication signal can transmit 7 bits information. Thus, the signal rate is increased to 7 kbps. While the navigation message rate in BDS is 50 bps. It is 140 times higher than the original signal.

4.4. Positioning Speed Analysis. As the transmission rate of the signal is greatly improved, the navigation message parameters can be obtained faster. Therefore, the TTFF will reduce. Take the cold start mode of the receiver as an example, the valid satellite ephemeris and almanac is absent before positioning. The receiver need search all satellites one by one and demodulate the ephemeris parameters after capturing the signal. For the traditional navigation signal, a frame is divided into five sub-frames, each sub-frame lasts for 6 seconds, a total of 30 seconds. The ephemeris parameters of the first three sub-frames are required for positioning, so it takes at least 18 seconds to collect the ephemeris parameters. If other interference factors are considered, such as capture time and program loading time, the TTFF of cold start is generally about 60 seconds. It can be seen from section 4.3, after using the NCI signal to transmit information and adopting the optimization algorithm, the signal rate is increased to 7 kbps. So the time for broadcasting navigation message parameters is reduced. As shown in Figure 3, the ephemeris parameters required for positioning are inserted into the head of the sub-frame. It takes at least about 12 s to collect the ephemeris parameters, which is reduced by 6 seconds compared with the minimum TTFF of the traditional navigation signal. If other interference factors are considered, the TTFF is more than 12 seconds but less than 60 seconds.

4.5. Compatibility Analysis. The NCI signal have many similarities with the BDS signal, such as ranging code and carrier frequency. It preliminarily realizes the compatibility between the integration signal and BDS. The number of elements of the OCSS is 2^n. Thus, the cyclic shift number of the communication signal can be directly converted to binary by mapping. In this way, the compatibility between the integration signal and BDS is further realized. Therefore, some technologies including error correction coding and interleaving can be directly applied to the integration signal. It not only improves the reliability but also ensures the plug-and-play feature of this technology.

5. Conclusion

In this paper, a novel NCI signal is combined with BDS. And the navigation signal and communication signal suitable for BDS are generated basing on the optimization algorithm. The error correction coding and interleaving mode of BDS are also applied to the signal. The simulation results verify that the optimization algorithm can improve the detection performance. The detection probability of the navigation signal is increased by about 9.3% when the SNR is -27 dB. It further shows that method for selecting the communication signal basing on the optimization algorithm is effective. The addition of communication signal improves the transmission rate. It is increased by 140 times compared with that of the BDS signal, and the TTFF is also reduced. The deep integration of navigation positioning and communication is realized.

Data Availability

The data used to support this study are included within the paper or available from the corresponding author upon request.

Conflicts of Interest

The authors declare that there is no conflict of interest regarding the publication of this paper.

Acknowledgments

This work is supported by the National Natural Science Foundation of China (No.62171075) and IUI cooperation project (HX20200159, and HX20191149), and is a follow-up research of the National Natural Science Foundation of China (Youth) (No. 61701072).

References

[1] W. Huang and P. Defraigne, "BeiDou time transfer with the standard CGGTTS," *IEEE Transactions on Ultrasonics, Ferroelectrics, and Frequency Control*, vol. 63, no. 7, pp. 1005–1012, 2016.

[2] M. Z. H. Bhuiyan, S. Soderholm, S. Thombre, L. Ruotsalainen, M. Kirkko-Jaakkola, and H. Kuusniemi, "Performance Evaluation of Carrier-to-Noise Density Ratio Estimation Techniques for BeiDou Bl Signal," in *2014 Ubiquitous Positioning Indoor Navigation and Location Based Service (UPINLBS)*, pp. 19–25, Corpus Christi, TX, USA, 2014.

[3] M. S. Grewal, A. P. Andrews, and C. G. Bartone, "GNSS Signal Structure, Characteristics, and Information Utilization," in *Global Navigation Satellite Systems, Inertial Navigation, and Integration*, pp. 93–143, Wiley, 2020.

[4] M. Liu, C. Liu, M. Li, Y. Chen, S. Zheng, and N. Zhao, "Intelligent passive detection of aerial target in space-air-ground integrated networks," *China Communications*, vol. 19, no. 1, pp. 52–63, 2022.

[5] M. Liu, Z. Liu, W. Lu, Y. Chen, X. Gao, and N. Zhao, "Distributed few-shot learning for intelligent recognition of communication jamming," *IEEE Journal of Selected Topics in Signal Processing*, p. 1, 2021.

[6] M. Liu, J. Wang, N. Zhao, Y. Chen, H. Song, and R. Yu, "Radio frequency fingerprint collaborative intelligent identification using incremental learning," in *IEEE Transactions on Network Science and Engineering*, 2021.

[7] *BeiDou Navigation Satellite System Signal In Space Interface Control Document Open Service Signal (Version 2.0)*, 2013, http://www.beidou.gov.cn/zt/zcfg/201710/P020171202709829311027.pdf.

[8] X. X. Zhang, J. Yang, and Z. Zhao, "A B1I Signal Fast Acquisition Scheme of Beidou Soft Receiver," in *Proceedings of 2014 IEEE Chinese Guidance, Navigation and Control Conference*, pp. 1754–1759, Yantai, China, Aug. 2014.

[9] D. Borio, "M-Sequence and secondary code constraints for GNSS signal acquisition," *IEEE Transactions on Aerospace and Electronic Systems*, vol. 47, no. 2, pp. 928–945, 2011.

[10] A. M. Liu, L. Zhao, J. C. Ding, and J. Wang, "Grouping FFT based two-stage high sensitivity signal acquisition with sign transitions," *IEEE Access*, vol. 6, pp. 52479–52489, 2018.

[11] M. Z. H. Bhuiyan, S. Söderholm, S. Thombre, L. Ruotsalainen, and H. Kuusniemi, "Overcoming the challenges of BeiDou receiver implementation," *Sensors*, vol. 14, no. 11, pp. 22082–22098, 2014.

[12] L. Y. Wang and L. Zhou, "CSK-code Spectrum-spread technology and its application," *Information Security and Communications Privacy*, vol. 11, pp. 51–54, 2009.

[13] G. M. Dillard, M. Reuter, J. Zeiddler, and B. Zeidler, "Cyclic code shift keying: a low probability of intercept communication technique," *IEEE Transactions on Aerospace and Electronic Systems*, vol. 39, no. 3, pp. 786–798, 2003.

[14] C. Kao, C. Robertson, and K. Lin, "Performance Analysis and Simulation of Cyclic Code-Shift Keying," in *MILCOM 2008-2008 IEEE Military Communications Conference*, San Diego, CA, USA, 2008.

[15] C. Kao, F. Kragh, and C. Robertson, "Performance Analysis of a JTIDS/Link-16-Type Waveform Transmitted over Nakagami Fading Channels with Pulsed-Noise Interference," in *MILCOM 2008-2008 IEEE Military Communications Conference*, San Diego, CA, USA, 2008.

[16] I. Koromilas, C. Robertson, and F. Kragh, "Performance Analysis of the LINK-16/JTIDS Waveform with Concatenated Coding in Both AWGN and Pulsed-Noise Interference," in *MILCOM 2010-2010 Military Communications Conference*, pp. 2074–2081, San Jose, CA, USA, 2010.

[17] X. Y. Li, D. Y. Zou, X. Liu, and N. Zhao, "A method for improving navigation signal detection performance in integration of navigation and communication," in *Patent*, CN202010222941.5, China, 2021.

Hindawi
Wireless Communications and Mobile Computing
Volume 2022, Article ID 5428280, 12 pages
https://doi.org/10.1155/2022/5428280

Research Article

UAV Routing Protocol Based on Link Stability and Selectivity of Neighbor Nodes in ETX Metrics

Jinze Huang,[1] Fengbiao Zan,[2] Xin Liu,[2] and Da Chen[1]

[1]*School of Physics and Electronic Information Engineering, Qinghai Nationalities University, Xining 810007, China*
[2]*School of Computer Science, Qinghai Nationalities University, Xining 810007, China*

Correspondence should be addressed to Fengbiao Zan; zanfb@163.com

Received 9 February 2022; Accepted 28 March 2022; Published 14 May 2022

Academic Editor: Mingqian Liu

With the extensive application of UAVs in various fields, it becomes more important to design a routing protocol that ensures stable transmit between UAV groups. This is because UAV groups are densely packed, move fast, and communication links are fragile. Aiming at the intensive and highly maneuverable UAV group, the AODV-NLS-ETX—a routing protocol based on the link stability of neighbor nodes—is proposed on the basis of the ETX metric based AODV protocol. The protocol is simulated and compared with other protocols. The simulation results show that AODV-NLS-ETX is superior to other protocols in packet delivery rate and throughput under high shift speed, dense nodes, and high routing overhead. It can effectively reduce the high delay brought by the ETX mechanism. The delay is the most stable and is not easy to cause network congestion. It can be better applied to dense and highly mobile unmanned aerial vehicles.

1. Introduction

Nowadays, the advancement of science and technology has greatly promoted the wide use of UAVs. From the structural point of view, UAVs mainly include four types: fixed wing, rotating flapping wing, hybrid wing, and gas envelope [1], and it plays a huge role in high-altitude pesticide spraying, agricultural, forestry spectral monitoring, vertical take-off landing military monitoring, transportation of rescue materials, obstacle sensing, and satellite cooperative communication [2–7].

Generally, UAVs work collaboratively in the form of clusters, so relevant researches tend to replace UAVs with network nodes. The Manhattan model, random waypoint model, and random street model [8] are the major three simulation models that are suitable for UAVs, among which the random waypoint model is selected in this research. In the UAV ad hoc network, nodes move faster in a relatively limited area. When there is a long communication distance between the destination node and source node, the UAV ad hoc network, by virtue of its high dynamics, enables the two nodes to forward data packets at high-speed through relay nodes. In the real scenario, the internal data transmission between UAVs is completed via the dynamic variability of ad hoc network. Figure 1 shows the communication structure of UAV ad hoc network. The base station transmits the signal to UAV A, where the UAV A is equivalent to the source node in the network simulation scenario, while UAV B is the relay node, and UAV C is the destination node. When the communication distance between A and is C within the maximum communication range, then A will directly send data to C. Otherwise, A will firstly send data to B, and then B will forward to C so as to complete the communication.

Since UAV ad hoc network is featured by high intensity and dynamic, especially in the cluster operation, the problems of signal noise interference and communication system identification performance are particularly prominent [9, 10]. So it becomes a hotspot to improve the communication quality between UAVs, thereby making it significant to choose an appropriate ad hoc network routing protocol. Compared with other ad hoc network routing protocols,

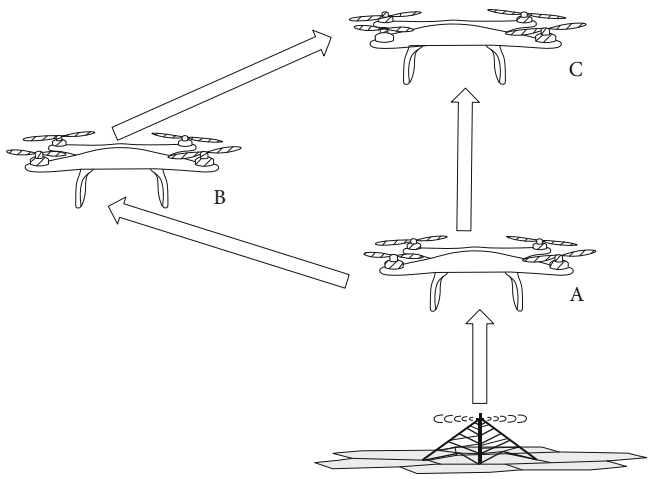

Figure 1: Communication structure of UAV ad hoc network.

AODV is widely used in UAV ad hoc network as it is convenient and efficient performance [11]. In contrast, the traditional AODV protocol is often faced with broken communication links and insufficient data information transmission in the UAV ad hoc network that is intensive, highly dynamic, and drastically changing. Designing a more efficient and stable routing protocol becomes quite important.

In response to such problems, many scholars proposed various stable and efficient protocols based on AODV. Bahloul et al. [12] designed a cluster-based UAV routing protocol (BR-AODV), which calculates in accordance with the on-demand routing mechanism of AODV and achieves routing maintenance as well as data transmission by introducing the base station discovery mechanism and Boids mechanism; Ramesh et al. [13] put forward a congestion adaptive routing protocol (CA-AODV) with a mechanism for monitoring node congestion, in which a warning will be issued between nodes once congestion occurs in the routing path so as to avoid node congestion; Wu et al. [14] mentioned an optimized protocol based on node residual energy and relative movement speed (EV-AODV), which considered the power of node receiving signal, the number of link hops and the node residual energy, normalized relative movement speed, as well as strengthened the node link mechanism; Tan et al. [15] presented an efficient digital signature algorithm based on elliptic curve cryptosystem and applied it to the AODV protocol; Chen et al. [16] proposed a greedy perimeter stateless routing protocol (TQNGPSR), which implemented flow balancing and evaluated the quality of wireless links by taking advantage of the neighboring congestion packets. In addition to above, there are still many other studies achieved good results in various indicators [17–22].

The ETX metric mechanism of AODV is suitable for slow-topologically stable networks. However, in the highly dynamic UAV ad hoc network, the ETX metric mechanism performs worse than the hop count metric mechanism of AODV. It is easy to cause network congestion and high delay, and the two mechanisms will generate much routing overhead in the large-scale mobility UAV ad hoc network, which affects the network performance. The current common research is how to reduce the routing overhead and improve its performance. For example, PAODV is mentioned in [23], which improves network performance by reducing routing overhead. Reference [24] proposed ND-AODV based on PAODV, further reducing the routing overhead and improving its performance. Reference [25] proposed three ETX mechanisms to reduce the routing overhead because of the high routing overhead of the ETX metric mechanism. But none of them consider enhancing their network performance in the case of high routing overhead.

Aiming at this problem, this paper proposes an ETX metric protocol AODV-NLS-ETX based on neighbor node link stability. This protocol reduces the retransmission information by using the neighbor node information and the HELLO packet setting information. Meanwhile, the node link stability is strengthened through taking ETX metric as the unit of AODV instead of hop count. In the case of high routing overhead, its network performance is further enhanced, making the ETX mechanism suitable for highly dynamic and dense UAV ad hoc networks.

To verify its performance, we compare and analyze the AODV-NLS-ETX protocol with the AODV protocol, the AODV-ETX protocol, the ND-AODV-ETX protocol and the ND-AODV protocol. The ND-AODV-ETX protocol is designed by combining the ND-AODV protocol with the ETX metric.

2. ND-AODV Protocol Principle

As a classic routing protocol, the AODV protocol will not be introduced here. The principle of ND-AODV protocol and ND-AODV-ETX is the same, except that the hop number mechanism is changed to the ETX mechanism, so we only introduce the ND-AODV protocol. The ND-AODV protocol is improved based on PAODV. PAODV sets two probability parameters $p1$ and $p2$ according to the node density. Choose $p1$ when the node density is small, and choose $p2$ when the node density is high. In order to judge whether the network density is sparse or dense, a threshold Avg is introduced, and its calculation formula is as follows:

$$Avg = \sum_{i=1}^{n} NBi/n. \tag{1}$$

The threshold can judge the density of the network. However, the probabilities $p1$ and $p2$ do not specify the optimal probability value in the reference [23], so the threshold is also difficult to calculate. In order to solve this problem, the reference [24] proposed the ND-AODV protocol.

The ND-AODV protocol introduces a new parameter pi; its calculation formula is as follows:

$$pi = \min\left(1, k/NBi\right). \tag{2}$$

According to the number of neighborhood node density, pi can be easily calculated, which solves the problem that $p1$

and $p2$ and the threshold in PAODV are difficult to calculate. However k as a constant value, it is necessary to judge its optimal value. In reference [24], $k = 11$ is optimal. k taking a high value will result in a high routing overhead. The range $10 \leq k \leq 15$ protocol has both high overhead and good performance. The range $k < 10$ reduce performance and low overhead. Since this paper studies how to improve the performance of the UAV ad hoc network under high routing overhead, but we also need a low-overhead comparison. Therefore, after careful consideration, the k value in ND-AODV and ND-AODV-ETX is chosen to be one without considering the optimal value.

3. Working Principle of Node Link

In this research, the proposed protocol includes two aspects: one is the selection of ETX node link and the other is the sending state and sending selection mechanism algorithm of HELLO packet in neighbor node. The protocol is designed to reduce retransmissions and strengthen link stability. Its working principle is introduced as follows.

3.1. Selection of ETX Node Link. As can be learned from the introduction in [26], the ETX metric mechanism monitors the expected number of transmissions on a link by installing a probe in each data packet. The traditional hop number mechanism in the AODV protocol will be replaced by the ETX metric in order to find out the propagation link with the smallest propagation value. If the node communication link is re-established, then the ETXr in a node link can be obtained by calculating the probability of successful forward transmission as well as reverse retransmission of the link. The ETXr is calculated as follows:

$$ETXr = \frac{1}{fr \times fd}. \tag{3}$$

f_r is the probability of successful link forward transmission, and f_d is the probability of successful link reverse transmission, indicating the ACK packet received from the destination node to the source node. Both of which can be calculated through data probe monitoring. The probability of successful link forward transmission cannot be directly calculated, but the f_r can be obtained according to the data probe detection in the period T during communication from the source node to the destination node. The reverse retransmission probability f_d is obtained by data probe packet transmission within w seconds, and the formula [26] is as follows:

$$fd = \frac{count(t - w, t)}{w/T}. \tag{4}$$

In Formula (4), the numerator represents the data probe packet actually received during the window w when the data packet is transmitted on the link, and the denominator represents the data probe packet that shall be received theoretically. Where we set the denominator to one and directly calculate the probability through the numerator.The ETX of the overall network link can be calculated by calculating the ETX through a single link.

$$ETX = \sum_{i=1}^{r} ETXr. \tag{5}$$

Assuming that there are r links in the network environment, then the overall ETX is the overall addition of a single link, as shown in Formula (5) [26]. In order to select a more stable ETX link, a threshold value of chain stability is set up. Since the probabilities of successful link forward transmission and reverse retransmission are fr and fd, respectively, then the probability of successful node link is f:

$$f = fr \times fd. \tag{6}$$

The probability of failed data transmission on a single node link can be calculated through f, which is the probability of node link breakage fl. In this research, fl is set as the threshold, and the probabilities of failed reverse retransmission are fld. When the threshold $fl<fld$ or $fl = fld$, the link will be discarded so as to select a more stable ETX link. In the transmission process of the ETX link, the probability of reverse retransmission is generally very small. However, the probability of retransmission will greatly increase in a highly dynamic UAV ad hoc network, which can be effectively reduced by setting the constraint condition of $fl<fld$. When in reverse transmission, set $fld = fl$, which indicates that the ETX transmission can be reduced when the probability of successful reverse transmission is almost equal to the successful transmission of the entire link $f \approx fd$, thereby selecting a more stable link. fl, fld, and the constraints are

$$fl = 1 - f, \tag{7}$$

$$fld = 1 - fd, \tag{8}$$

$$ETX = \begin{cases} \sum_{i=1}^{r} ETXr, fl < fld \| fl = fld \\ 0 \end{cases}. \tag{9}$$

ETX will be accumulated link by link within the constraints, while the unreliable links will be discarded outside the constraints; 0 in Formula (9) means that ETX is not calculated. In this case, the ETX metric becomes more stable, the retransmissions of data probe packets are reduced in the selected node link, and the reliability and stability of node link are improved, which contributes to a stable transmission of data probe packets and higher successful rate of data transmission.

3.2. Selection Sending Mechanism Algorithm of HELLO Packet in Neighbor Node. During the transmission, the ETX in the data probe packet of AODV protocol is constantly accumulated to select the routing path with the best quality. In the selection process, the sending of ETX is in line with the transmission mechanism of the HELLO packet, which will not affect the HELLO packet itself. At the same

time, HELLO packet is used to detect active routes, and the neighbor nodes determine the existence of active routes accordingly. However, in a highly dynamic UAV ad hoc network, the node link is so fragile that the HELLO packets are bound to be sent excessively in order to detect a new active route, which is likely to cause network congestion. In the case of network congestion, the ETX metric mechanism of AODV is useless as it may lead to higher delay. Therefore, in response to this situation, an algorithm for selecting the sending mechanism of HELLO packet between the neighbor nodes is proposed.

Figure 2 shows the process of selecting neighbor nodes in this algorithm. First, assume that node A is the source node and node D is the destination node, between which the established of communication link needs to be forwarded by a relay node. This algorithm restricts the node area within a circle. On this basis, when the distance d between two nodes is less than the radius R inside the circle, both nodes are defaulted as neighbor nodes, and then an effective link will be established between the nodes. Otherwise, no effective link will be established between the nodes. According to Figure 2, there are two approaches to establish a link between node A and node D: A-C-D and A-B-D. However, since the distance d between A and B is greater than the circle radius R, no effective path is established between nodes A and B. The dashed arrow in Figure 2 represents an invalid link while the solid arrow indicates a valid link. Similarly, for node B-D and node C-D, no effective link can be established because the distance d between node B and node D is greater than R. Thus, the final path is A-C-D, and stable link is established since neighbor nodes are selected.

After the node link is established, the node will provide connection information by broadcasting a HELLO packet so as to find the active path. At this moment, the data probe packet will be sent to establish a valid link. For the sake of preventing from sending too many HELLO packets, the link stability (LS) is set in this research.

$$LS = \frac{f}{\pi R^2 \times T}. \tag{10}$$

f is the probability of successfully sending data in node link, πR^2 is the area of the algorithm limited circle, and T is the sending period. In experimental simulation, the period T is set to 1 s to effectively reduce the synchronous sending effect caused by the data probe packet. By Formula (10), the probability of successfully sending data packets is dispersed to the link established by neighbor nodes inside the circle, the link stability threshold is established, and then the effective range of a link threshold is determined via algorithm simulation. On the condition of within this rang, the node will broadcast a HELLO packet to search for an active path, and the node will establish an ETX metric link. LS is set to unsigned 32 bits and the threshold range is set to $0x0000 < LS < 0x1111$, within which node congestion can be effectively controlled. The overall algorithm flow is shown in Figure 3.

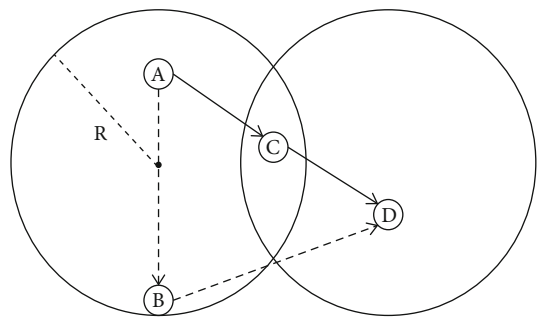

Figure 2: Neighbor node selection mechanism.

4. Working Mechanism of AODV-NLS-ETX

4.1. Route Request and Route Reply Process. The AODV-NLS-ETX protocol is improved based on AODV-ETX protocol [27]. The packet format of RREQ and RREP is the same as that of AODV-ETX, so its route request and route reply process are in accordance with ETX metric [26]. The packet format is as follows.

According to Table 1 and Table 2, the ETX metric mechanism is added to the packet formats of both RREQ and RRE P so that the corresponding routing table will be updated once a node sends such a packet. Figure 4 shows the process of AODV-NLS-ETX routing request and reply.

In Figure 4, node A is the source node, and node E is the destination node. Theoretically, there are three ways to establish a link from node A to node E: A-B-C-E, A-B-D-E, and A-B-C-D-E. First, node A sends an RREQ packet to node B. At this moment, the initial value of ETX is set to 0, and node D and node C separately receive the RREQ packet from node B so that the ETX value is calculated. In addition to receiving the RREQ packet from node B, node D also receives RREQ packet from node C. Different from the AODV protocol that discards the RREQ information from node D immediately, AODV-NLS-ETX protocol calculates the ETX value carried by node B and node D and discards the RREQ packet with larger ETX so as to select the link with the smallest ETX value. Similarly, the destination node E also selects the link with the smallest ETX value while receiving the RREQ packet from nodes D and C. As shown in Figure 4, the actual link finally selects A-B-C-E possibly because that the A-B-C-E link has the smallest ETX value and the lowest energy loss compared with the other two links. Then, the destination node E receives the RREQ packet, generates a RREP packet, replies to node A, and continuously updates the overall routing table.

4.2. Routing Maintenance Process. This protocol modifies the format of HELLO packet by adding the node link stability (LS). The modified format is shown in Table 3.

The modification of HELLO packet format not only enables protocol to reduce the number of RREQ packet requests in highly dynamic and intensive network topology, but also improves the reliability of data transmission and lowers the delay caused by link disconnection. The routing maintenance process of AODV-NLS-ETX is shown in Figure 5.

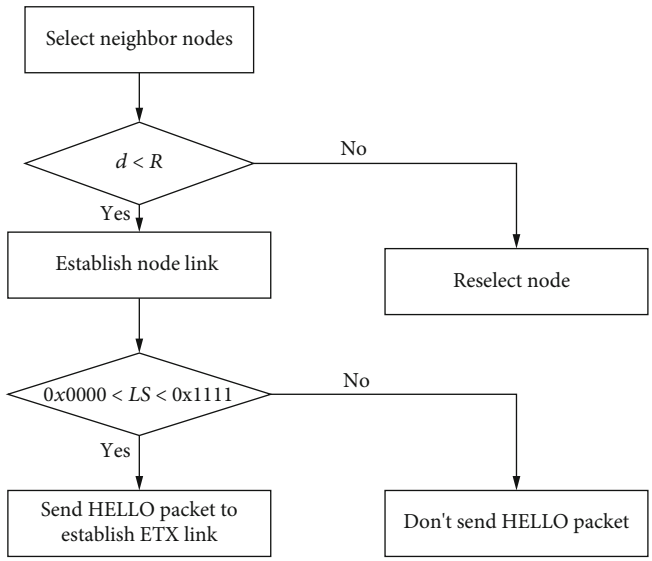

Figure 3: Algorithm flow of selecting and sending mechanism of the HELLO packet in neighbor node.

Table 1: RREQ packet format.

Type	J	R	G	D	U	Reserved	Hop count
RREQ ID							
Destination IP address							
Destination sequence number							
Originator IP address							
Originator sequence number							
ETX							

Table 2: RREP packet format.

Type	R	A	Reserved	Prefix Sz	Hop Count
Destination IP address					
Destination sequence number					
Originator IP address					
Life time					
ETX					

As indicated in Figure 5, it is assumed that there are two links between the source node A and the destination node E: A-B-C-E and A-B-D-E. When node B is ready to transmit HELLO packet to node C and node D during a certain period of time, first, node B and node C will check the link stability. When confirming within the specified range, node B will transmit HELLO packet to node C, or if the link has been disconnected, then node B will receive the RERR packet within specified time to repair the route or choose a new path. If the node link stability between node B and node D exceeds the threshold, then the HELLO packet will not be transmitted (the dotted line in the figure represents the unsuccessful transmission). As a result, the corresponding RREQ packet will not be sent, thereby reducing the number of requests and decreasing the sending of HELLO packet. Through this mechanism, the selected ETX metric link is more stable and firm so that the data transmission success rate is improved.

5. Analysis of Simulated Results

5.1. Performance Index. The indicator of routing overhead has been mentioned earlier in this article. Next, we will combine PDR, average end-to-end delay, and throughput to test the performance of five protocols in the UAV ad hoc network. The introduction of the four indicators is as follows.

PDR is the ratio of the data packet received by the destination node to that sent by the source node, which manifests the protocol reliability. The higher the ratio, the more reliable the protocol data transmission will be:

$$PDR = \frac{receivedpackets}{sentpackets}. \tag{11}$$

The average end-to-end delay is the ratio of the time the destination node receives the data packet minus the time the source node sends the data packet to the overall network receives the data packet. The smaller the delay, the better the network quality will be:

$$Delay = \frac{\sum_{i=1}^{packets}(endtime - starttime)}{packetsum}. \tag{12}$$

Throughput is the ratio of the total bytes received by the destination node to the network transmission time, which reflects the amount of network transmission information. The greater the ratio, the greater the amount of information, and the higher the protocol transmission efficiency will be:

$$Throughput = \frac{8 * ryBetes}{Tranmissiontime}. \tag{13}$$

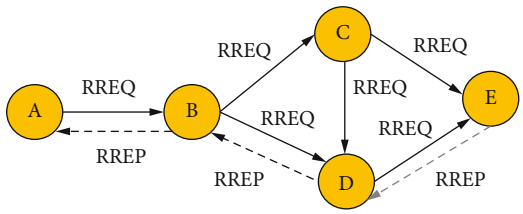

Figure 4: AODV-NLS-ETX routing request and reply process.

Table 3: HELLO packet format.

Type	Reserved
Destination IP address	
Destination sequence number	
Hop count	
Life time	
ETX	
Link stability	

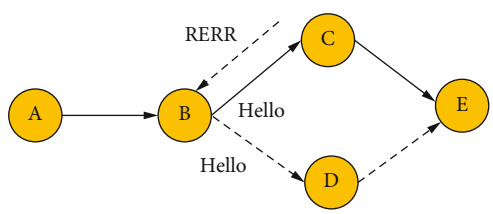

Figure 5: AODV-NLS-ETX routing maintenance process

Routing overhead is the ratio of the routing control packet sent by the network to the data packet received. The smaller the routing overhead, the fewer the additional control packets will be:

$$Overhead = \frac{\text{routing control packets}}{receivedpackets}. \quad (14)$$

5.2. Experimental Environment. In this research, the open source software NS3 is applied to simulate the UAV ad hoc network under the 4000 m × 4000 m rectangular ideal environment. For each simulation, the period is 300 s, the data packet size are 64 bytes, the transmission rate is 2048 bps, the MAC layer protocol is IEEE802.11b, and the maximum communication distance of the node is 1000 m. In the simulation environment, we selected two environments. One is to increase the moving speed to simulate a high mobility network, and the other is to increase the number of nodes to simulate a dense network. Change the random seed 10 times and take the average. Table 4 and Table 5 show the simulation scenarios.

5.3. Experimental Results. Figure 6 shows the change of PDR of five protocols with the number of nodes. As can be seen from the figure, the PDR of the AODV-NLS-ETX protocol is better than other protocols. The AODV-NLS-ETX protocol establishes links and sets constraints according to the neighbor node selection mechanism, enhancing the ETX link stability and improving the reliability of data transmission. The overall PDR of AODV-NLS-ETX is about 11% higher than that of AODV-ETX and about 11% higher than ND-AODV-ETX. Due to maintaining a fixed node moving speed, the transmission of the ETX measurement mechanism is better than the hop transmission mechanism. The PDR of AODV-ETX and ND-AODV-ETX is better than AODV and ND-AODV.

Table 4: Simulation scenario under different number of nodes.

Simulation parameter	Parameter setting
Simulation area	4000 m × 4000 m
Simulation model	Random waypoint
Communication link	10
Business source	CBR
MAC layer protocol	IEEE802.11b
Number of nodes	50, 55, 60, 65, and 70
Node movement speed	40 m/s
Max. Communication distance	1000 m

Table 5: Simulation scenario under different node movement speed.

Simulation parameter	Parameter setting
Simulation area	4000 m × 4000 m
Simulation model	Random waypoint
Communication link	10
Business source	CBR
MAC layer protocol	IEEE802.11b
Number of nodes	40
Node movement speed	20,25,30,35,and 40 (m/s)
Max. Communication distance	1000 m

Figure 7 shows how the throughput of the five protocols changes with the number of nodes. The throughput of the AODV-NLS-ETX protocol is also better than that of other protocols. In the early stage, with the node density increase, AODV-NLS-ETX needs to establish a stable ETX link through the probe packet, so the throughput decreases. With the establishment of the link, the data can be transmitted stably, so the throughput gradually increases. The throughput of the AODV-NLS-ETX protocol is about 12% higher than that of AODV-ETX and about 12% higher than that of the ND-AODV-ETX protocol.

Figure 8 shows the change in the delay of the five protocols with the number of nodes. Compared with AODV-ETX and ND-AODV-ETX protocols, the delay of the AODV-NLS-ETX protocol is significantly reduced, and the delay is not different from that of AODV and ND-AODV protocols, and it is very stable. This is because the AODV-NLS-ETX protocol reduces the detection of reverse data probe packets and retransmission to a certain extent. In addition, because a more stable link is selected, it is not easy to generate network

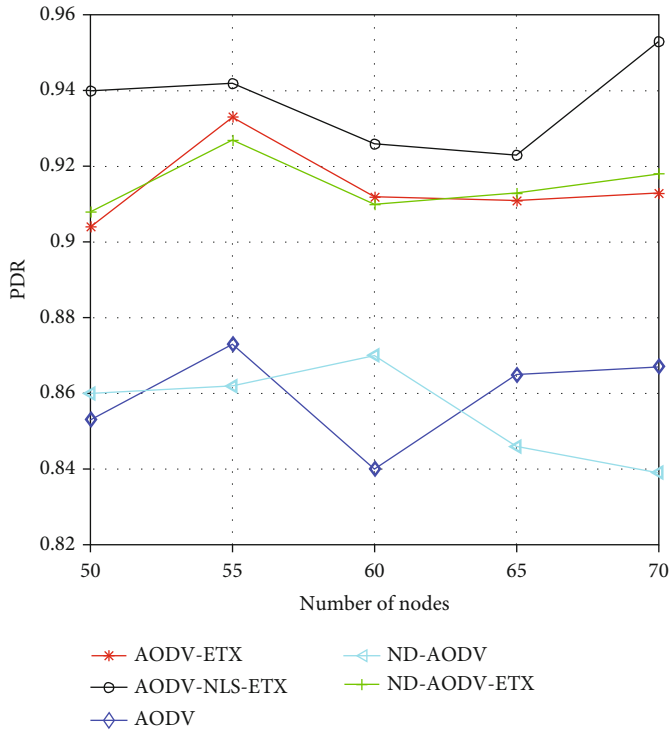

Figure 6: PDR under different number of nodes.

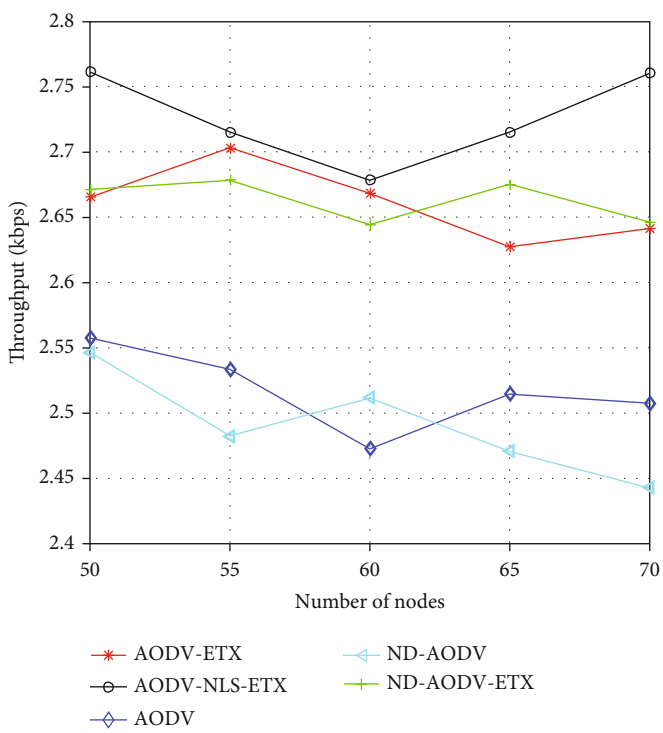

Figure 7: Throughput with different number of nodes.

congestion, so the delay is very stable. The reverse retransmission of AODV-ETX and ND-AODV-ETX will bring a high delay, and the performance is even inferior to the hop number mechanism of AODV and ND-AODV protocols.

Figure 9 shows the change in the overhead of the five protocols with the number of nodes. Compared with other protocols, the overhead of AODV-NLS-ETX is significantly higher than that of different protocols. This is because

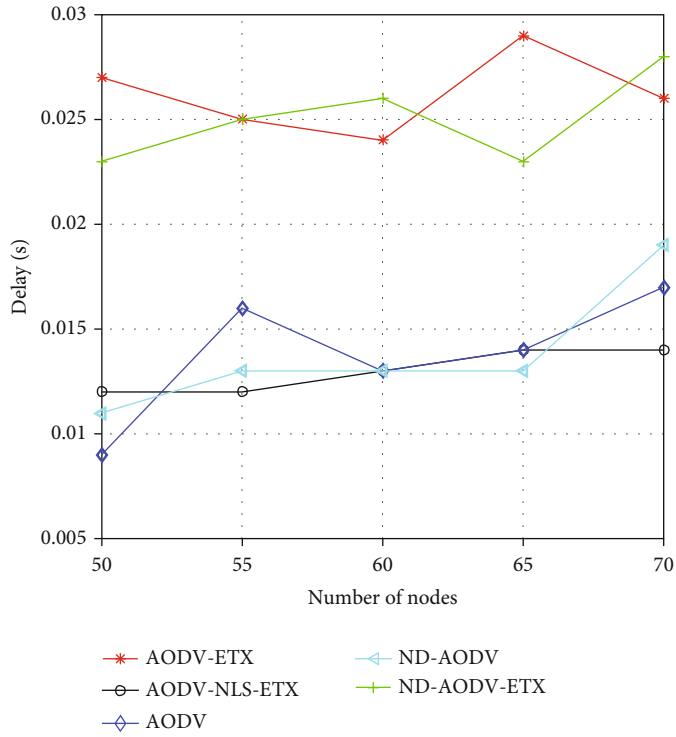

Figure 8: Delay with different number of nodes.

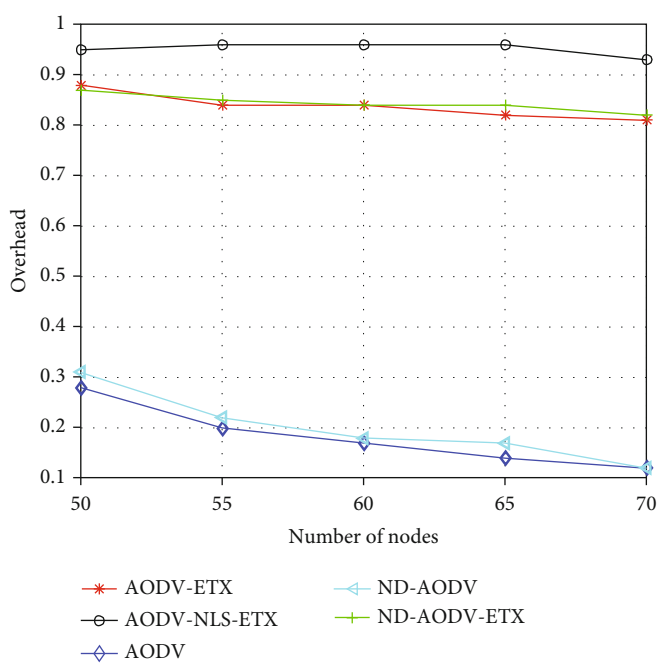

Figure 9: Overhead under different number of nodes.

AODV-NLS-ETX needs to broadcast more RREQ packets than AODV-ETX and ND-AODV-ETX to establish a stable link to generate a lot of overhead. The ETX mechanism itself occupies many bytes in the routing control packet, which will also produce a high routing overhead. Therefore, the overhead of the three protocols will be higher than that of AODV and ND-AODV.

Figure 10 describes the changes of PDR of the five protocols with the node speed. It can be seen that the PDR of ND-AODV-ETX and AODV-NLS-ETX shows a downward

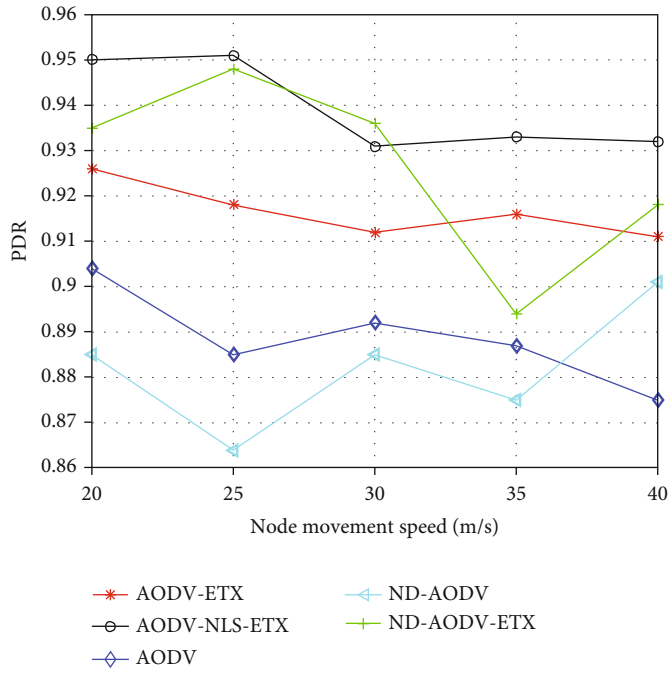

Figure 10: PDR at different node speeds.

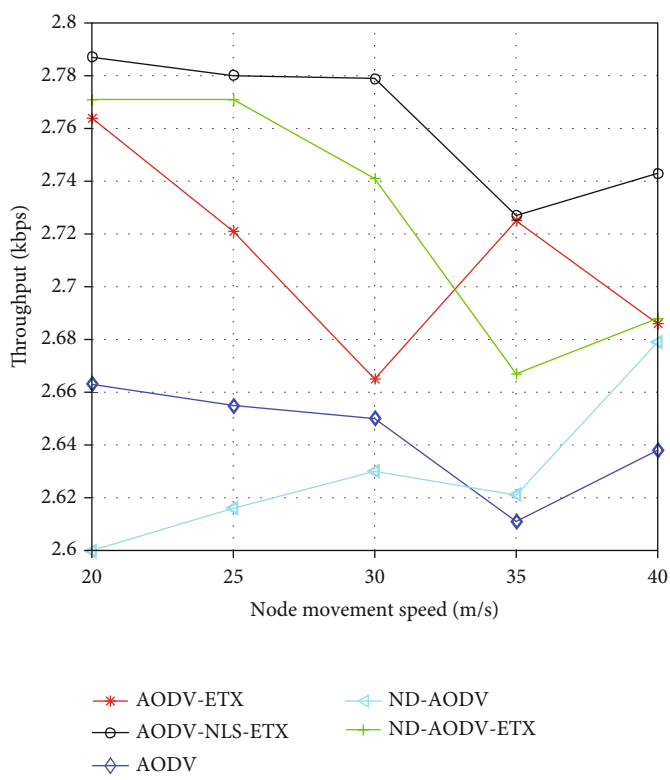

Figure 11: Throughput at different node speeds.

trend between 25 and 30 speeds. This is because the ETX link of the two protocols is broken in this speed range and the ETX link needs to be re-established to transmit data. However, because the link established by the ND-AODV-ETX protocol is not as stable as that of the AODV-NLS-ETX protocol, PDR shows a downward trend in an extended speed shift period overall performance is not superior to that of AODV-NLS-ETX. The PDR of AODV-NLS-ETX is about 11% higher than that of AODV-ETX and about 7% higher than that of ND-AODV-ETX.

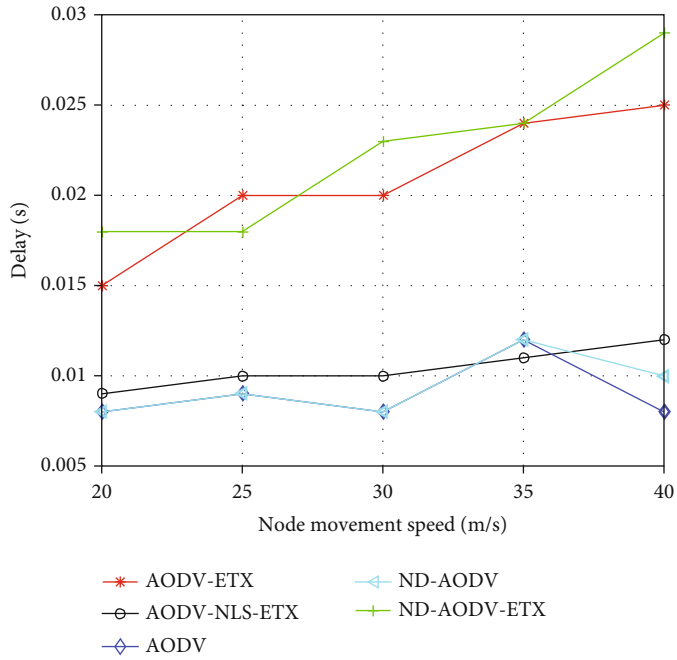

Figure 12: Delay at different node speeds.

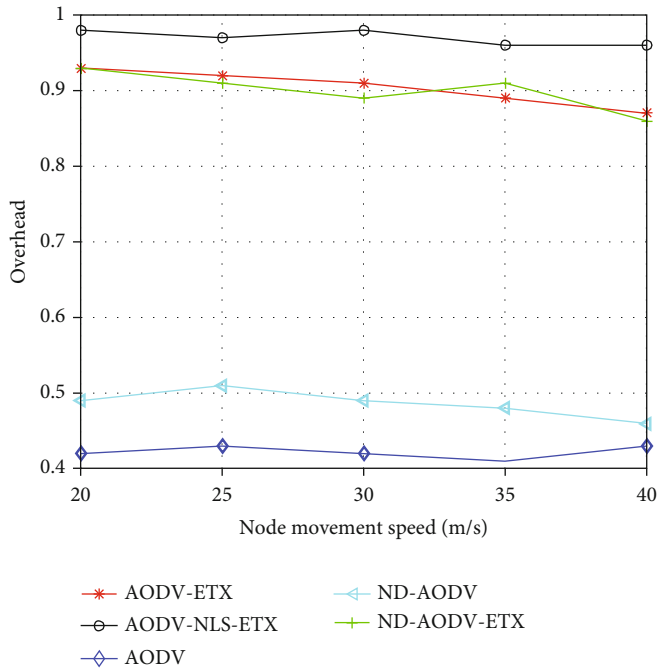

Figure 13: Overhead at different node speeds.

Figure 11 depicts the change of throughput with node moving speed. With the increase in node moving speed, the throughput of the AODV-NLS-ETX protocol is better than that of other protocols. Because the transmission link of the AODV-NLS-ETX protocol is relatively stable, the throughput will also show corresponding advantages. The throughput of the AODV-ETX protocol increases suddenly when the speed is shifted to 35 m/s. It may be that the throughput of AODV-ETX increases due to the relative rise of PDR and the increase of transmitted data. After that, the throughput decreases gradually and tends to be flat because the information remains effectively transmitted. The throughput of AODV-NLS-ETX is about 11% higher than that of AODV-ETX and about 5% higher than that of ND-AODV-ETX.

Figure 12 shows the change of average end-to-end delay with node moving speed. It can be seen that the delay of AODV-ETX and ND-AODV-ETX is always higher than

that of the AODV-NLS-ETX protocol. Because the ETX mechanism is easy to break the node-link in the high-speed scenario, and the reverse link data monitoring will also bring many retransmissions, the delay of these two protocols is very high. In the early speed change, the delay of ND-AODV and AODV is almost the same. This is because when the node density is relatively sparse, ND-AODV has little advantage over AODV, so the delay performance is the same. Due to network congestion, when the node speed is 35 m/s, the delay of both protocols suddenly increases. Although AODV-NLS-ETX has a slightly higher delay than the hop number mechanism protocols, its delay change is the most stable due to a stable link. It is not easy to cause network congestion, so it can be determined that AODV-NLS-ETX has more advantages in a high-speed environment.

Figure 13 shows how the routing overhead changes with the node speed. With the increase of the node speed, the routing overhead of each protocol is relatively high. Because AODV-NLS-ETX broadcasts more RREQ request packets and ETX itself adds larger routing control packets, the overhead is the highest. The routing overhead of the AODV-ETX protocol is almost the same as that of the ND-AODV-ETX protocol. The overhead of ND-AODV is significantly higher than that of AODV. This is because in the case of relatively sparse nodes, the increase of node moving speed causes an increase in routing request packets.

6. Conclusion

This paper proposes an ETX metric UAV routing protocol (AODV-NLS-ETX) based on the link stability of neighbor nodes. Compared with the other four protocols, the AODV-NLS-ETX protocol has higher overhead, but has good performance. It is superior to other protocols in packet delivery rate and throughput. In terms of delay, this protocol reduces the high delay brought by the ETX mechanism. Although the delay is slightly increased compared with AODV and ND-AODV, it is the most stable and is not easy to cause network congestion. Especially in the high-speed and intensive UAV ad hoc network scenario, this protocol has stronger stability and reliability, is suitable for high-speed large-scale drone scenarios, and can also meet more network requirements.

Data Availability

The data used to support the findings of this study are included within the article.

Conflicts of Interest

The authors declare that they have no conflict of interest.

Acknowledgments

This work was supported by the Tianjin University-Qinghai Nationalities University Independent Innovation Fund Project "Huangshui River Ecological Environment Monitoring and Governance," the Qinghai Provincial Network Comprehensive Key Laboratory Project, and the Qinghai Nationalities University Graduate Student Innovation Project (10M2021005). In addition, thanks are due to two scholars, Jevtic and Malnar, for their work on Github.

References

[1] C. Lee, S. Kim, and B. Chu, "A survey: flight mechanism and mechanical structure of the UAV," *International Journal of Precision Engineering and Manufacturing*, vol. 22, no. 4, pp. 719–743, 2021.

[2] M. F. F. Rahman, S. Fan, Y. Zhang, and L. Chen, "A comparative study on application of unmanned aerial vehicle systems in agriculture," *Agriculture*, vol. 11, no. 1, p. 22, 2021.

[3] T. Adão, J. Hruška, L. Pádua et al., "Hyperspectral imaging: a review on UAV-based sensors, data processing and applications for agriculture and forestry," *Remote Sensing*, vol. 9, no. 11, p. 1110, 2017.

[4] S. Yu, J. Heo, S. Jeong, and Y. Kwon, "Technical analysis of VTOL UAV," *Journal of Computer and Communications*, vol. 4, no. 15, pp. 92–97, 2016.

[5] D. Jo and Y. Kwon, "Development of rescue material transport UAV (unmanned aerial vehicle)," *World Journal of Engineering and Technology*, vol. 5, no. 4, pp. 720–729, 2017.

[6] N. Aswini, E. Krishna Kumar, and S. V. Uma, "UAV and obstacle sensing techniques – a perspective," *International Journal of Intelligent Unmanned Systems*, vol. 6, no. 1, pp. 32–46, 2018.

[7] M. Liu, Z. Liu, W. Lu, Y. Chen, X. Gao, and N. Zhao, "Distributed few-shot learning for intelligent recognition of communication jamming," *IEEE Journal of Selected Topics in Signal Processing*, 2021.

[8] L. Gupta, R. Jain, and G. Vaszkun, "Survey of important issues in UAV communication networks," *IEEE Communications Surveys & Tutorials*, vol. 18, no. 2, pp. 1123–1152, 2016.

[9] M. Liu, C. Liu, M. Li, Y. Chen, S. Zheng, and N. Zhao, "Intelligent passive detection of aerial target in space-air-ground integrated networks," *China Communications*, vol. 19, no. 1, p. 52, 2022.

[10] M. Liu, J. Wang, N. Zhao, Y. Chen, H. Song, and R. Yu, "Radio frequency fingerprint collaborative intelligent identification using incremental learning," *IEEE Transactions on Network Science and Engineering*, 2021.

[11] J. Maxa, G. Roudierem, and N. Larrieu, "Emulation-based performance evaluation of routing protocols for UAANETs," in *International Workshop on Communication Technologies for Vehicles: Nets4Cars/Nets4Trains/Nets4Aircraft 2015: Communication Technologies for Vehicles*, Lecture Notes in Computer Science, pp. 227–240, Springer, Cham, 2015.

[12] N. El Houda Bahloul, S. Boudjit, M. Abdennebi, and D. E. Boubiche, "A flocking-based on demand routing protocol for unmanned aerial vehicles," *Journal of Computer Science and Technology*, vol. 33, no. 2, pp. 263–276, 2018.

[13] B. Ramesh and D. Manjula, "CA-AODV: congestion adaptive AODV routing protocol for streaming video in Mobile ad hoc networks," *International Journal of Communications, Network and System Sciences*, vol. 1, no. 4, pp. 322–328, 2008.

[14] J. Wu, S. Shi, Z. Liu, and X. Gu, "Optimization of AODV routing protocol in UAV ad hoc network," in *Proceedings International Conference on ArtificialIntelligence for Communications*

and Networks (AICON), LNICST 286, pp. 472–478, Cham, 2019.

[15] X. Tan, Z. Zuo, S. Su, X. Guo, and X. Sun, "Research of security routing protocol for UAV communication network based on AODV," *Electronics*, vol. 9, no. 8, p. 1185, 2020.

[16] Y. Chen, N. Lyu, G. Song, B. W. Yang, and X. H. Jiang, "A traffic-aware Q-network enhanced routing protocol based on GPSR for unmanned aerial vehicle ad-hoc networks," *Frontiers of Information Technology & Electronic Engineering*, vol. 21, no. 9, pp. 1308–1320, 2020.

[17] M. F. Bedasa, A. S. Bedada, and W. B. Mulatu, "Adaptation of smart antenna with AODV routing protocol for ad hoc wireless networks," *Open Access Library Journal*, vol. 7, no. 7, pp. 1–21, 2020.

[18] A. Touzene and I. al-Yahyai, "Performance analysis of grid based AODV routing algorithm for AD hoc wireless networks," *International Journal of Communications, Network and System Sciences*, vol. 8, no. 13, pp. 523–532, 2015.

[19] D. K. Sharma, A. N. Patra, and C. Kumar, "P-AODV: a priority based route maintenance process in mobile ad hoc networks," *Wireless Personal Communications*, vol. 95, no. 4, pp. 4381–4402, 2017.

[20] O. Usman, O. Chughtai, N. Nawaz, Z. Kaleem, K. A. Khaliq, and L. D. Nguyen, "A reliable link-adaptive position-based routing protocol for flying ad hoc network," *Mobile Networks and Applications*, vol. 26, no. 4, p. 18201, 2021.

[21] S. Jobaer, Y. Zhang, M. A. Iqbal Hussain, and F. Ahmed, "UAV-assisted hybrid scheme for urban road safety based on VANETs," *Electronics*, vol. 9, no. 9, p. 1499, 2020.

[22] S. Priya and N. Kannan, "Refined trust energy-ad hoc on demand distance vector (ReTE-AODV) routing algorithm for secured routing in MANET," *Wireless Networks*, vol. 23, no. 7, pp. 2227–2237, 2017.

[23] N. Nabil, N. Najib, and J. Najib, "A review and a new approach to reduce routing overhead in MANETs," *Wireless Networks*, vol. 21, no. 4, pp. 1119–1139, 2014.

[24] M. Malnar and N. Jevtic, "An improvement of AODV protocol for the overhead reduction in scalable dynamic wireless ad hoc networks," *Wireless Networks*, vol. 28, no. 3, pp. 1039–1051, 2022.

[25] N. J. Jevtic and M. Z. Malnar, "Novel ETX-based metrics for overhead reduction in dynamic ad hoc networks," *IEEE Access*, vol. 7, pp. 116490–116504, 2019.

[26] N. J. Jevtic and M. Z. Malnar, "Implementation of ETX metric within the AODV protocol in the NS-3 simulator," *Telfor Journal*, vol. 10, no. 1, pp. 20–25, 2018.

[27] N. J. Jevtic and M. Z. Malnar, "The NS-3 simulatorimplementation of ETX metric within AODV protocol," in *2017 25th Telecommunication Forum (TELFOR)*, pp. 1–4, Belgrade, Serbia, 2017.

Hindawi
Wireless Communications and Mobile Computing
Volume 2022, Article ID 5326892, 16 pages
https://doi.org/10.1155/2022/5326892

Research Article

RF Fingerprint Extraction Method Based on CEEMDAN and Multidomain Joint Entropy

JianYu Wei, Lu Yu, Lei Zhu, and XingYu Zhou

Institute of Communication Engineering, Army Engineering University of PLA, Nanjing 210000, China

Correspondence should be addressed to Lu Yu; yulu_mail@263.net

Received 11 March 2022; Revised 10 April 2022; Accepted 13 April 2022; Published 10 May 2022

Academic Editor: Mingqian Liu

Specific emitter identification (SEI) can distinguish communication radio emitters with the fingerprint features carried by the received signal, and this technology has been widely used in military and civilian fields. However, in the real electromagnetic environment, the number of communication radio emitters is large and the signal-to-noise ratio (SNR) is low, which leads to poor nonlinear fingerprint analysis of SEI in a single domain. Therefore, combining the exploration of multiple domains of electromagnetic spatial information resources, this paper proposed a radio frequency (RF) fingerprint extraction method based on complementary ensemble empirical mode decomposition with adaptive noise (CEEMDAN) and multidomain joint entropy. The proposed method is an attempt and exploration further extraction of nonlinear fingerprint features in multiple domains. Firstly, considering the nonstationarity of the communication signal, this article adopts the CEEMDAN method to decompose the signal to multiple intrinsic mode functions (IMF). Then, the decomposed signal is represented in multiple spaces by a multidimensional phase space reconstruction technique. Nonlinear analysis of the original signal is performed in multiple spaces: multidimensional differential approximate entropy space, singular spectral entropy space, and power spectral entropy space. Finally, the support vector machine (SVM) is adopted in the classification stage. To demonstrate the robustness of the method, the method is verified on the universal software radio peripheral (USRP) dataset and the Northeastern University public dataset. In terms of the identification accuracy, the proposed method performs with 98.5% accuracy on the 5-class USRP dataset. It also performs with 94.7% accuracy on the 16-class public dataset. The experimental results show that the proposed method has a stable identification performance and has a more than 85% recognition rate in the SNR above 5dB.

1. Introduction

At present, electromagnetic spatial information resources have been elevated to national strategic resources and become one of the high points of the competitive game among contemporary great powers. Specific emitter identification (SEI) is a technique to identify individual radio emitters by extracting external features from a given signal [1], which has great significance in the field of electromagnetic space. The extraction of the fingerprint is the key step of the whole recognition process. The fingerprints of the radio emitter are due to the subtle differences in the production of each unit part of the transmitter such as semiconductors, resistors, and capacitors. Given that RF fingerprinting is unique for each emitter and difficult to fake, the SEI technique plays an important role in military and civil fields, such as battlefield spectrum management [2], and wireless network security [3].

As the fingerprint features of the emitter are affected by various parameter errors such as power amplifiers and frequency sources operating in the nonlinear region, there are many nonlinear components in the modulated signal such as harmonic distortion, transient intermodulation distortion, and cross modulation distortion. Therefore, the modulated signal of the radio emitter is nonlinear and nonstationary actually. We can regard the communication radio emitter as a nonlinear dynamic system, so the problem of fingerprint feature extraction of the radio emitter is

transformed into the problem of nonlinear parameter extraction in a nondynamic system. Carroll [4] creatively proposed that nonlinear dynamic parameters can be extracted from communication radio emitter as a fingerprint for SEI in 2007, and permutation entropy has been well used as an effective nonlinear feature extraction parameter. Normalized permutation entropy [5] extracted from the time-series signal completed the identification of four communication stations. Deng et al. [6] first proposed to use multidimensional entropy to extract an RF fingerprint that differentiates 3 wireless devices with an accuracy of over 93.7%. Xie et al. [7] improved the approximate entropy feature and proposed a differential approximate entropy feature extraction method, which has a good recognition effect on a 3-class task in the low signal-to-noise ratio (SNR). Sun et al. [8] performed nonlinear analysis on multiple wireless network card signals by extracting multidimensional approximate entropy and achieved a high recognition rate of 96.5% in 8 wireless network card signals of the same category. Li et al. [9] first proposed the reverse dispersion entropy (RDE), which not only could capture the subtle changes in the time and frequency domains of the signal but also have better noise robustness. This is beneficial to the mutation signal detection under different SNRs. It can be seen from the above that these methods have a good performance in analyzing the complexity of the waveform and angular structure of the signal in the time domain. Therefore, they obtain high identification accuracy in scenes with high SNR and a small number of individual radio emitters. However, these methods have a common disadvantage; that is, the nonlinear features in multiple domains of the signal are not considered. Due to the existence of multiple individual radio emitters, the difference between their nonlinear fingerprints in a single domain is getting smaller and smaller, and in the low SNR, subtle fingerprint features are easily drowned in noise. Therefore, we need more effective entropy features to represent the nonlinear fingerprint features of radio emitters.

With the development of electromagnetic spatial and temporal big data, information mining, and other technologies, people's understanding of electromagnetic waves gradually changed from the shallow domain (time domain, space domain) to the deep domain (energy domain, singular spectrum domain, and polarization domain). This allows more hidden features to be extracted through the technique of multi-information spatial fusion. In this paper, we propose a novel SEI method and study in the AWGN channel and Rayleigh fading channel. The main contributions are summarized as follows:

(1) We use the CEEMDAN method to extract the high-frequency components of the signal. This method not only helps to remove some environmental noise in the signal but also is beneficial to analyze the subtle features hidden in the signal

(2) Considering the fingerprint feature that exists in the time and frequency domains of the signal from Figure 1, we propose a multidomain joint entropy method to analyze the nonlinear feature in different domains. This method facilitates deep mining of signal fingerprints, which is more adaptable to the realistic complex electromagnetic space

(3) Considering that the nonlinearity of the transmitter and the phase angle structure of the signal are subtle and complex, we propose a multidimensional differential approximate entropy to improve the performance of entropy

(4) To evaluate the noise robustness and the superiority of the proposed method, we compare the performance of the proposed method with other entropy methods in the AWGN channel and Rayleigh fading channel

2. Proposed Feature Extraction Method and Classification

The workflow of this method is shown in Figure 2. First, the received signal is preprocessed, its steady-state part is extracted and segmented, and then, the CEEMDAN method is used to decompose it to obtain multiple intrinsic mode functions. Multidomain joint entropy is extracted from the part IMFs and composes feature vectors which are classified by the SVM in the end.

2.1. CEEMDAN Algorithm. The CEEMDAN algorithm is an improvement to the experience mode decomposition (EMD) algorithm, which is first proposed by [10]. It overcomes the modal aliasing problem in the EMD algorithm, avoids the decomposition error caused by white noise, and reduces the operation cost. It not only has the advantage of multiresolution of the wavelet transform but also overcomes the problem of wavelet base selection. Therefore, CEEMDAN has been widely used in signal processing, especially in dealing with nonlinear and nonstationary signals. The EMD [11] algorithm has serious modal aliasing [12] and end effect [13] phenomena. To suppress the modal aliasing phenomenon, the collective experience mode decomposition (EEMD) [14], the complete ensemble empirical mode decomposition (CEEMD) [14], and the complete ensemble empirical mode decomposition of adaptive noise (CEEMDAN) [15] are successively proposed. CEEMDAN replaces the random white noise with adaptive noise without a basis function [16]. The average residual signal is performed immediately to obtain the individual IMFs, which avoids passing errors to the next iteration. The specific process of the CEEMDAN algorithm is shown as follows:

(1) Defined $\mathrm{IMF}_j(t)(j = 1, 2, \cdots, J)$ is the jth mode obtained by CEEMDAN, and J is the number of the IMF in CEEMDAN. The operator $E_j(.)$ is the jth mode obtained by EMD, $\omega_i(t)\,(i = 1, 2, \cdots, I)$ is the ith added Gaussian white noise, and I is the number of times to add white noise. ε_j is the coefficient of the white noise added to the jth residual component. The ith white noise-added signal $u^i(t)$

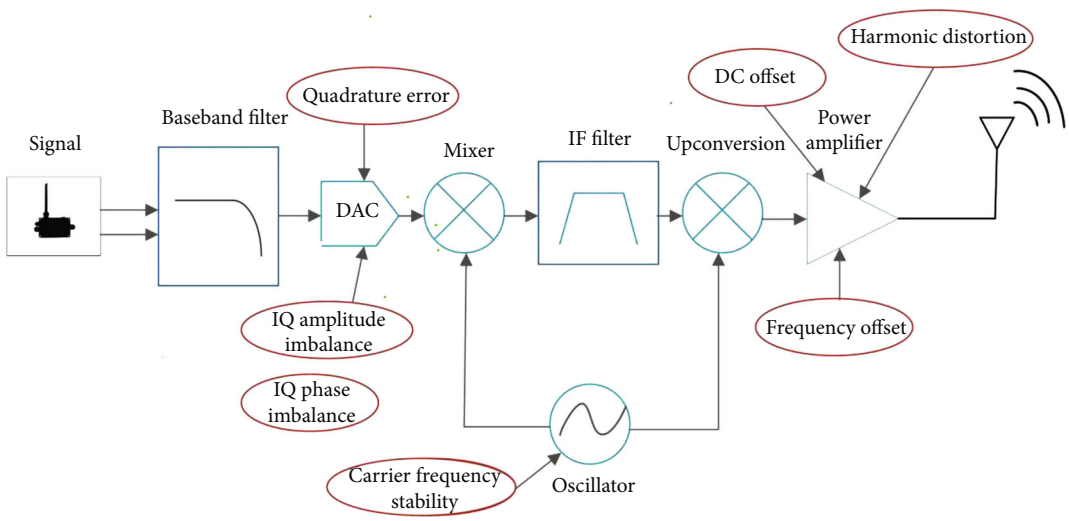

Figure 1: The mechanism of fingerprint generation of radio emitter transmitter.

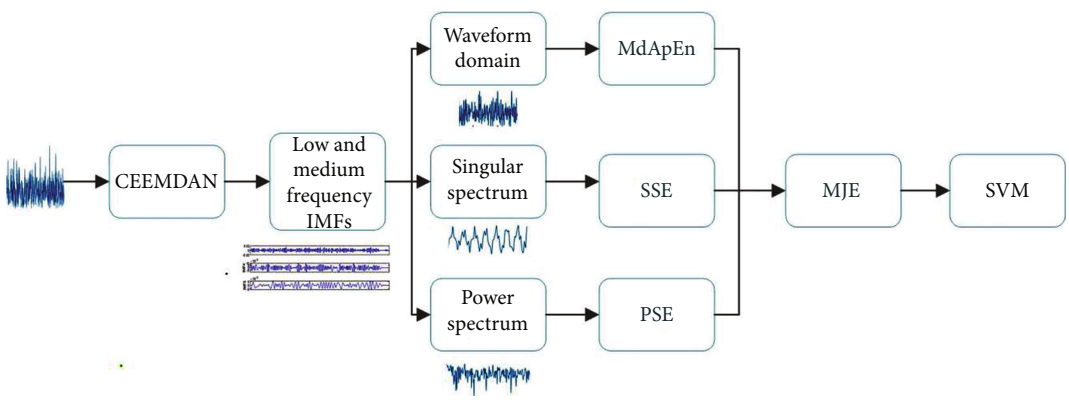

Figure 2: Flowchart of the CEEMDAN-MJE method.

$= u(t) + \varepsilon_0 \omega_i(t)$ $(i = 1, 2, \cdots, I)$. Then, the first mode calculated by averaging is

$$\mathrm{IMF}_1(t) = \frac{1}{I}\sum_{i=1}^{I} E_1\left(u^i(t)\right) \tag{1}$$

(2) Define the $r_k(t)$ which is the kth residual component. Calculating the first residual component is as follows:

$$r_1(t) = u(t) - \mathrm{IMF}_1(t) \tag{2}$$

(3) The signal $r_1(t) + \varepsilon_1 E_1(\omega_i(t))$ is decomposed by EMD. Then, the second mode calculated by averaging is

$$\mathrm{IMF}_2(t) = \frac{1}{I}\sum_{i=1}^{I} E_1\left(r_1(t) + \varepsilon_1 E_1(\omega_i(t))\right) \tag{3}$$

(4) Define the jth signal as

$$r_j(t) = r_{j-1}(t) - \mathrm{IMF}_j(t) \tag{4}$$

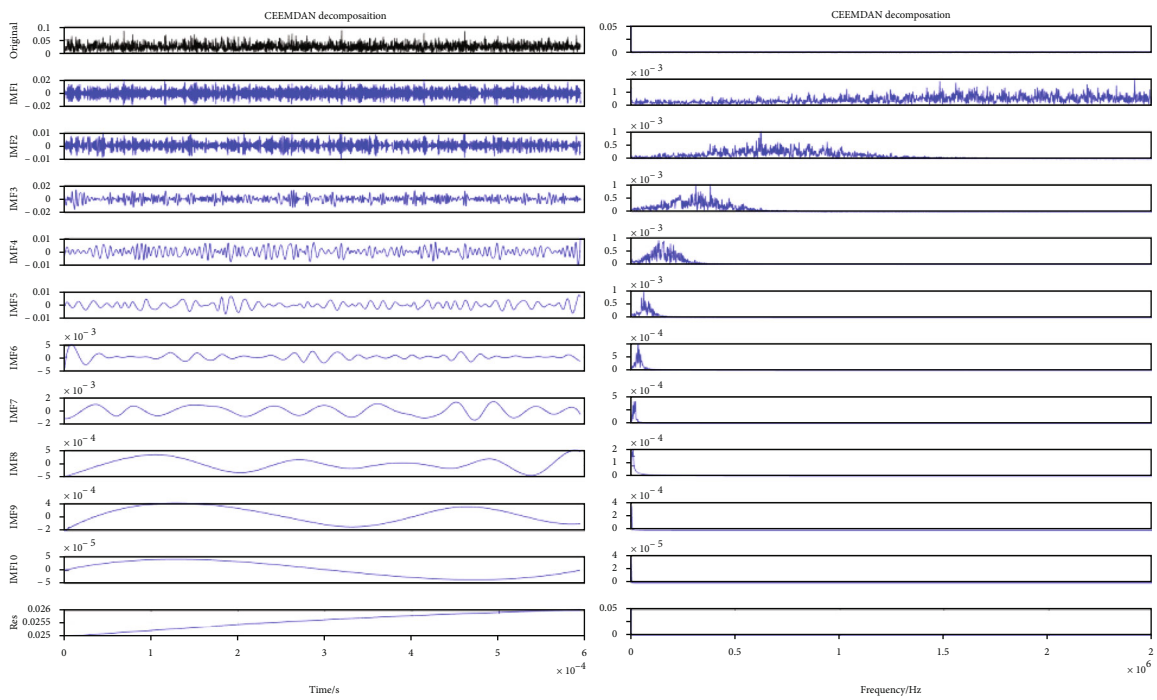

Figure 3: IMFs and spectrum after CEEMDAN decomposition of radio emitter 1.

(5) Decompose the jth signal $r_j(t) + \varepsilon_j E_j(\omega_i(t))$ $(i = 1, 2, \cdots, I)$ by EMD and obtain the jth component. Then, $(j+1)$th mode calculated by averaging is

$$\mathrm{IMF}_{j+1}(t) = \frac{1}{I}\sum_{i=1}^{I} E_1\left(r_j(t) + \varepsilon_j E_j(\omega_i(t))\right) \tag{5}$$

(6) The decomposition process continues until the number of extreme points does not exceed 2, and obtain the residual component $r(t)$. Finally, the signal $u(t)$ is expressed as

$$u(t) = \sum_{j=1}^{J} \mathrm{IMF}_j(t) + r(t) \tag{6}$$

The measured signal $x(t)$ is decomposed by the CEEMDAN algorithm to obtain a series of IMF components from high frequency to low frequency. The CEEMDAN algorithm can separate the different frequency components in the original signal, which is convenient for us to study the features of different frequency parts of the signal. Since the original signal is the sum of these IMF components and the residual, there is no loss of information during decomposition. It can be seen from Figures 3 and 4 that the radio emitter components of IMF2, IMF3, and IMF4 have great differences. Therefore, this paper conducts a nonlinear analysis in different domains for these three components.

2.2. Multidomain Joint Entropy Feature Analysis. In this paper, our innovation is that we propose to extract entropy features in different domains for the first time that represent nonlinear fingerprint features of the communication emitters. These entropy features have been used alone in signal recognition tasks, but this is the first time that they are used jointly. In fact, the nonlinear fingerprint of the signal is subtle and hidden in the waveform of the signal. What is more, according to [17], some fingerprint features have better performance in the frequency domain, such as frequency error, frequency offset, and carrier frequency instability. Therefore, we must use the MJE feature to improve the performance of SEI. In the time domain, we use the MdApEn and singular spectrum entropy (SSE). The MdApEn uses a multiple phase space reconstruction tool to extract features about the phase angle structure. It can represent the fingerprint feature about phase angle in the time domain, such as the IQ phase imbalance. But it pays more attention to the features related to the complexity of the phase angle structure in the time domain of the signal. So we use the singular spectral entropy to further extract nonlinear fingerprint features of the signal. From Figures 5 and 6, the signals of the different emitters have obvious differences in the same singular spectral entropy space. Therefore, the SSE could better reflect fingerprint differences between different emitters. In the frequency domain, the power spectrum analysis method is an effective means to analyze the feature of the signal. Therefore, we use the power spectrum entropy (PSE) to extract the nonlinear

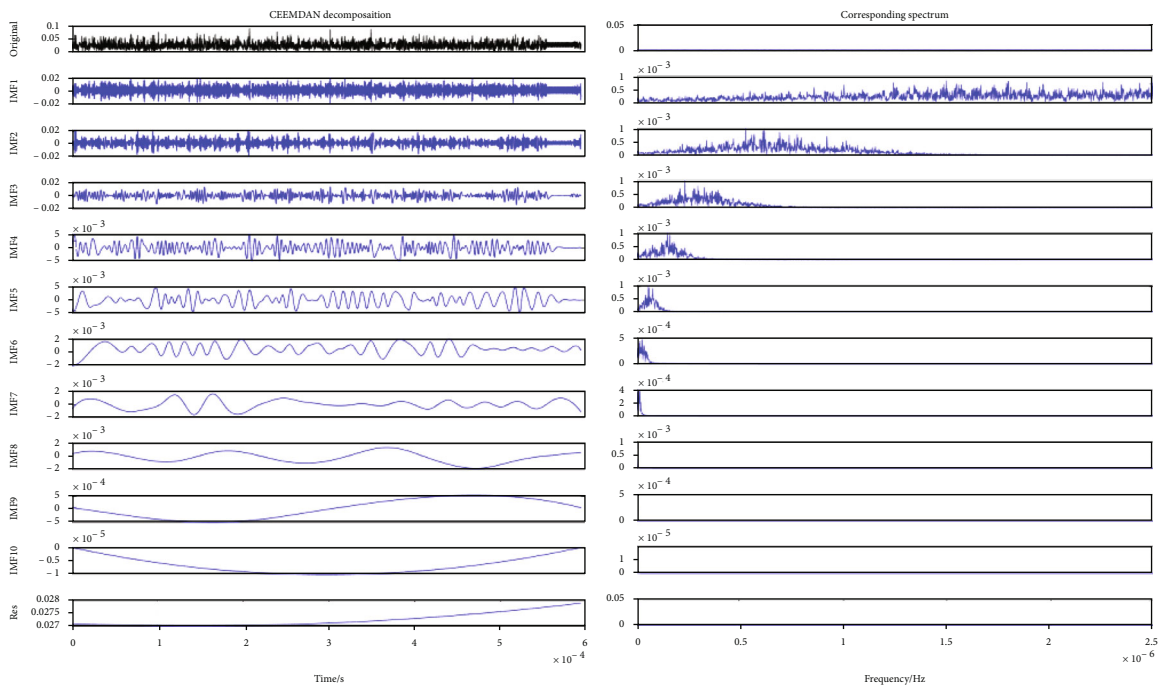

Figure 4: IMFs and spectrum after CEEMDAN decomposition of radio emitter 2.

fingerprint feature in the frequency domain, such as frequency offset and carrier frequency instability. What is more, as we experiment in the paper, the MJE has better performance in the accuracy rate in the lower SNR. Thus, it is important and feasible to use MJE as a feature in SEI.

2.2.1. Multidimensional Differential Approximate Entropy. In the 1990s, Pincus and Huang [18] proposed to use an approximate entropy to measure the complexity of the time series. Considering that the maximum distance method in approximate entropy cannot truly represent the similarity between different signals, Xie et al. [7] proposed the differential approximate entropy algorithm in 2018. They use the differential method to extract the phase angle factor for the discrete sequence of the signal, which can measure the phase similarity between signals. The generation mechanism of nonlinear fingerprint features of communication signals is more complicated, and it is difficult to achieve good results with any of the individual features. Therefore, this paper proposes a method of multidimensional phase space reconstruction to extract the differential approximate entropy of communication signals from different phase spaces. It can reflect the self-similarity of the original sequence more accurately, to calculate the phase angle complexity of the original signal.

Phase space reconstruction is an important tool for analyzing nonlinear signals. After the signal is reconstructed in phase space, more deep features can be extracted in different phase spaces. It is used to map the signal sequences $\{x(i), i = 1, 2, 3 \cdots N\}$ of the communication signal into a multidimensional phase space matrix through the embedded dimension and time delay τ, such as formula (7). Furthermore, the time delay τ is calculated according to the algorithm in [19].

$$X = \begin{bmatrix} x_1 \\ \vdots \\ x_i \\ x_M \end{bmatrix} = \begin{bmatrix} x(1) & x(1+\tau) & \cdots & x(1+(m-1)\tau) \\ \vdots & \vdots & & \cdots \\ x(i) & x(i+\tau) & \cdots & x(i+(m-1)\tau) \\ x(M) & x(M+\tau) & \cdots & x(N) \end{bmatrix}, \tag{7}$$

where $m(m \geq 2)$ is the dimension of the phase space embedding and $M = N - (m-1)\tau$ is the number of time series points in the phase space.

$$x_i = [x(i) \quad x(i+\tau) \quad \cdots \quad x(i+(m-1)\tau)]. \tag{8}$$

The specific steps of the MdApEn algorithm are as follows:

(1) The time series $\{x(i), i = 1, 2, 3 \cdots N\}$ of the signal are composed to form an m-dimensional vector x_i, $i = 1, 2, 3 \cdots M$

(2) Calculate the corresponding difference term in x_i, which is used to measure the angular structure of the signal sequence:

$$\begin{aligned} xd(i) &= [x(i+\tau) - x(i), \cdots, x(i+(m-1)\tau) - x(i+(m-2)\tau)] \\ &= [t(i), \cdots, t(i+m-2)] \end{aligned} \tag{9}$$

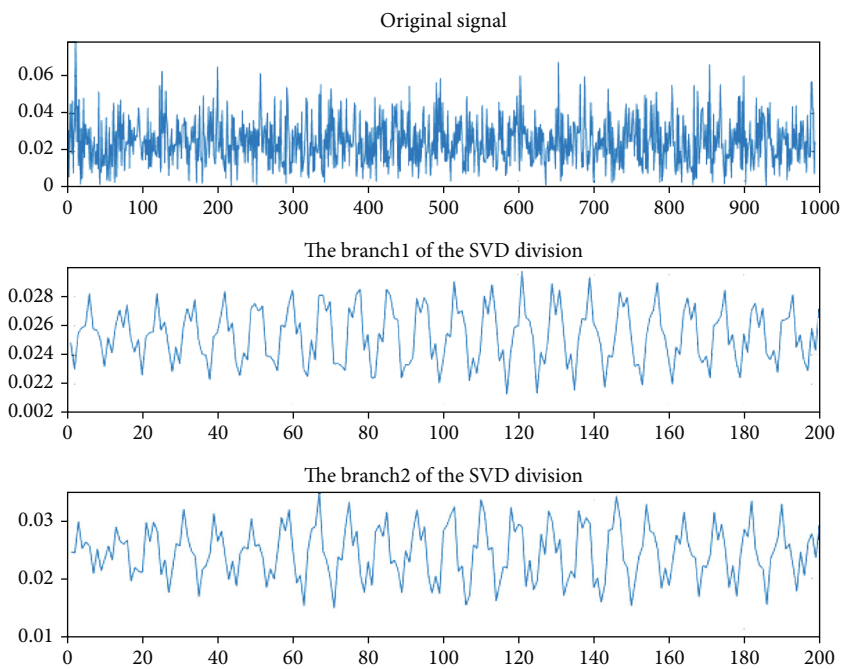

Figure 5: Singular spectral of radio emitter 1.

Define the distance between the different terms $xd(i)$ and $xd(j)$ as

$$d_{ij} = \frac{1}{m-1}\sum_{k=0}^{m-2}|t(i+k) - t(j+k)|. \tag{10}$$

(3) Given a threshold $r(r > 0)$. $\alpha(\alpha > 0)$ is a modified coefficient, and $E\{.\}$ is the mean of the signal $x(n)$:

$$r = \alpha\sqrt{E\{x(n)^2\} - [E\{x(n)\}]^2} \tag{11}$$

(4) Calculate the ratio of the difference item distance $d_{ij} < r$ to the total number of items for each item in $x(i)$, denoted as $C_i^m(r)$:

$$C_i^m(r) = \mathrm{num}\{d_{ij} < r\}/(N - (m-1)\tau) \tag{12}$$

(5) Take the logarithm of $C_i^m(r)$ to calculate the average value, and denote it as $\varphi^m(r)$:

$$\varphi^m(r) = \frac{\sum_{i=1}^{N-m+1}\ln C_i^m(r)}{N - (m-1)\tau} \tag{13}$$

(6) m++, repeat the process from 1 to 4 to get $\varphi^{m+1}(r)$

(7) Calculate differential approximate entropy:

$$H_d(m, r, N) = \varphi^m(r) - \varphi^{m+1}(r) \tag{14}$$

(8) Select the value of m to form a vector; m_i is the ith phase space dimension, which represents the ith embedded dimension of the differential signal:

$$\mathbf{m} = [m_1, m_2 \cdots m_i \cdots m_k] \tag{15}$$

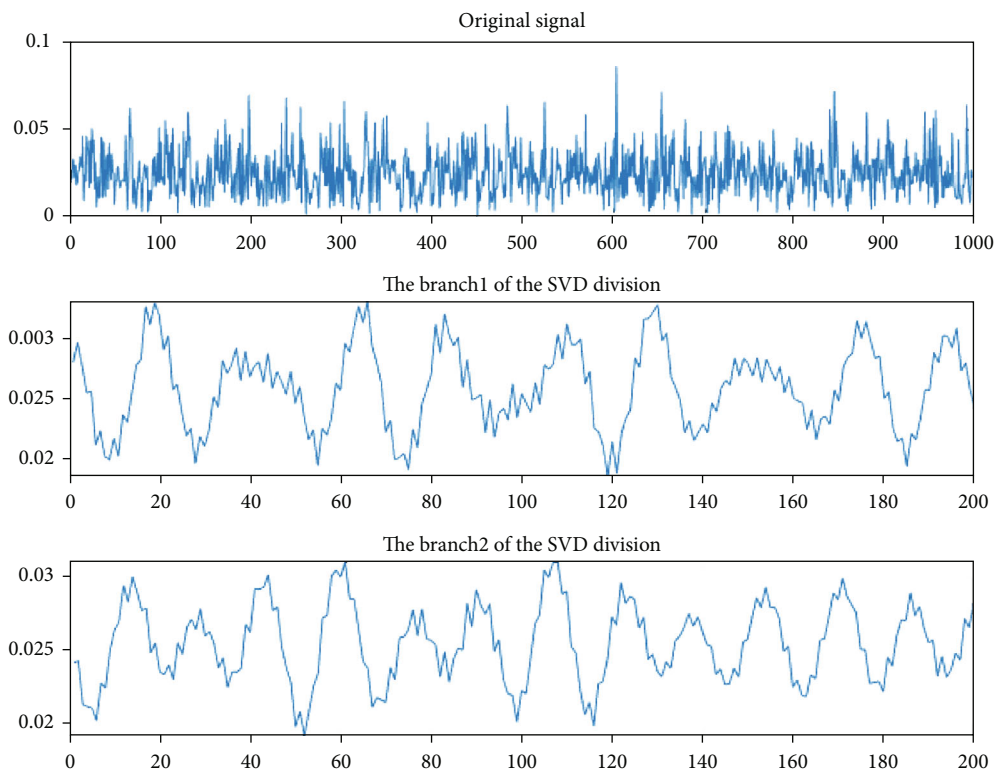

Figure 6: Singular spectral of radio emitter 2.

(9) Calculate the above formula for m_i to get $H_{di}(m_i, r, N)$, denoted as $H_d(m_i)$, which represents the differential approximate entropy of m_i, and normalize it to get

$$H_{di} = \frac{H_d(m_i)}{\ln(m_i!)}, \tag{16}$$

where ! is a symbol for the factorial operation

(10) Obtain the multidimensional differential approximate entropy:

$$H_M = [H_{C1} \cdots H_{Ci} \cdots H_{Ck}] \tag{17}$$

The MdApEn algorithm actually selects signal sequences of different phase spaces for differential processing, so that the corresponding differential terms could be obtained. They enable a more subtle analysis of the changes in the phase angle structure of the signal over a short period of time. The use of the multidimensional makes the analysis of the differential term of the signal more comprehensive. Therefore, it not only more accurately reflects the self-similarity of in the different phase angle structures of the signal segments but also facilitates the deep extraction of the nonlinear fingerprint features of the signal.

2.2.2. Singular Spectrum Entropy. Singular spectrum analysis is a common time-domain analysis method for signals. Its core idea is to reconstruct the time-domain signal and perform singular value decomposition to obtain its inherent complexity features. The singular spectrum entropy [20] essentially reflects the nonlinear features of the time-domain signal under the division of the singular spectrum. From the perspective of signal complexity analysis, it also reflects the energy distribution of the signal in the time domain. The internal inherent feature of the signal and the subtle state changes are also reflected in the time-domain energy distribution, which is closely related to the fingerprint features. As can be seen from Figures 6 and 7, there are subtle differences in the time-domain energy distribution of different communication radio emitters, so the complexity between them is different. Therefore, the singular spectrum entropy of different radio emitter signals has certain differences, and the singular spectrum entropy can reflect the fingerprint features of the signal's time-domain energy distribution to a certain extent.

The specific steps of the SSE algorithm are as follows:

(1) Mapping the discrete signals $\{x(i), i = 1, 2, 3 \cdots N\}$ at point N into the m-dimensional phase space matrix:

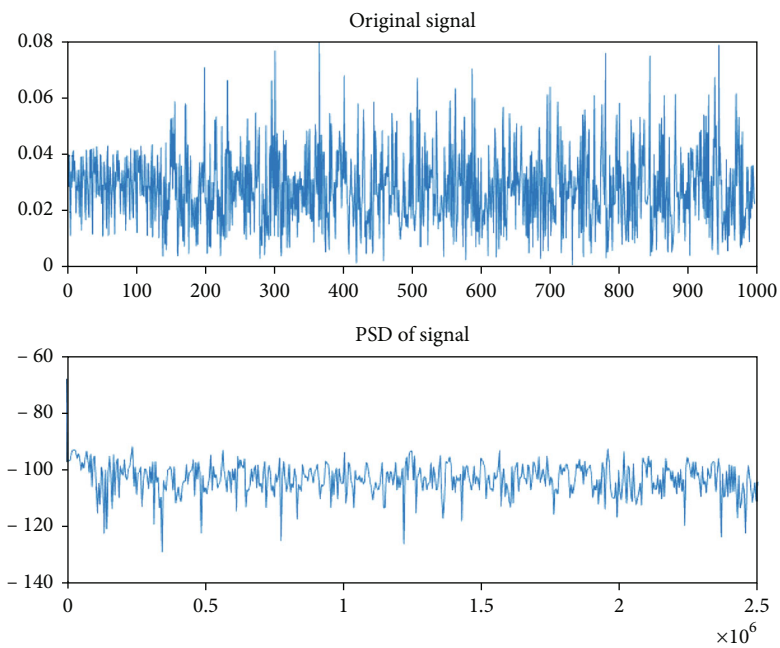

Figure 7: PSD of radio emitter 1.

$$X = \begin{bmatrix} x(1) & x(2) & & \cdots & x(M) \\ x(1+\tau) & x(2+\tau) & & \cdots & x(M+\tau) \\ \vdots & \vdots & \cdots & \vdots & \\ x(1+(\sigma-1)\tau) & x(2+(\sigma-1)\tau) & \cdots & x(M+(\sigma-1)\tau) & \end{bmatrix}, \tag{18}$$

where m is the dimension of the phase space embedding; M is generally no more than one-third of the signal length, i.e., $2 \le M \le (N/3)$; τ is the time delay (generally takes the value of 1); and $\sigma = \lceil (N - M + 1)/\tau \rceil$ is the number of time points in the phase space

(2) To decompose the phase space matrix into singular values, let the decomposition obtain m singular values, and arrange all the singular values in order of size to form a sequence $\{\lambda_i (i = 1, 2, \cdots, M)\}$, with $\lambda_1 \ge \lambda_2 \ge \cdots \ge \lambda_M$; then, $\{\lambda_i\}$ constitutes the singular spectrum of the original signal. If the number of nonzero singular values in λ_i is j, the value of j represents the total number of phase spaces contained in the phase space matrix X. And the value of each λ_i reflects the proportion of its corresponding subspace in all phase spaces

(3) From the correspondence between the singular values λ_i and the j subspaces in the phase space matrix X, it follows that the singular spectrum $\{\lambda_i\}$ analysis is a weighting division of the communication signal in the time domain, such that

$$p_i = \frac{\lambda_i}{\sum_{i=1}^{M} \lambda_i}. \tag{19}$$

Then, p_i is the share of the ith singular value in the whole singular spectrum. It also represents the share of the ith subspace in all phase spaces. The singular spectrum entropy of the signal in the time domain can be obtained according to the definition of Shannon entropy as

$$H_s = -\sum_{i=1}^{M} p_i \log p_i \tag{20}$$

(4) Information theory shows that when the entropy takes a great value, the system is in a steady state,

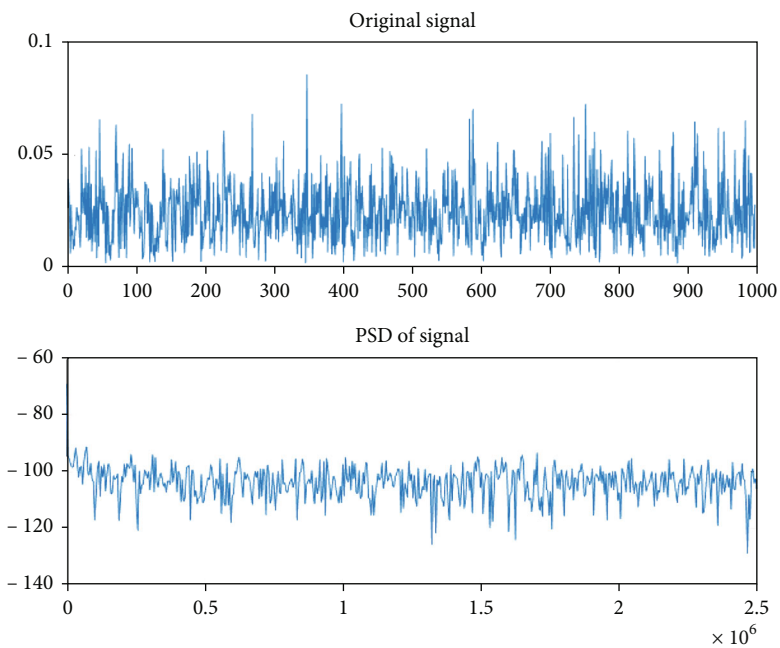

Figure 8: PSD of radio emitter 2.

and the energy distribution is more uniform at this time. And the white noise has the smallest difference in the singular spectrum energy distribution, so its singular spectrum entropy value is the largest, as can be seen from the above equation:

$$H_{S_{\max}} = -M \times \left(\frac{1}{M} \log \frac{1}{M}\right) = \log M. \tag{21}$$

The normalized singular spectral entropy facilitates a more intuitive comparison of signal complexities:

$$\overline{H_s} = \frac{-\sum_{i=1}^{M} p_i \log p_i}{logM} \tag{22}$$

From the perspective of the energy distribution of the signal, it is known that for different radio emitter signals, there is a subtle difference in the energy distribution obtained after its decomposition, and the difference can be effectively indicated through the extraction of a singular spectrum entropy features. From the perspective of signal nonlinear analysis, it can extract and amplify subtle changes in time series, which is closely related to the nonlinear fingerprint feature. Therefore, the singular spectrum entropy can extract the nonlinear fingerprint features of different subspaces under the phase space divided by the singular spectrum and weight by the value of the singular value, which can effectively reduce the influence of noise on the signal.

2.2.3. Power Spectrum Entropy. The fingerprint features and subtle state changes within the signal are often reflected in its frequency composition and changes in the energy distribution in the frequency domain, so spectral analysis of the signal is often more conducive to capturing subtle features that are not obvious in the time domain, and the nonlinear fingerprint features have different performances in the frequency domain. The power spectrum analysis method is an effective means to analyze the signal in the frequency domain.

The power spectrum is the abbreviation of power spectral density function, defined as the signal power per unit frequency band. It reflects the distribution of the signal power in the frequency domain; the uniformity of the power spectrum distribution can represent the complexity of the original signal. As can be seen from Figures 7 and 8, there are subtle differences in the uniformity of the power spectrum distribution of different communication radio emitters. What is more, the fingerprint features affect the uniform distribution of the power spectrum and are reflected in its subtle changes. Therefore, to a certain extent, the power spectrum entropy features can effectively extract the nonlinear fingerprint features of the radio emitter in the power spectrum domain.

The specific steps of the PSE algorithm are as follows:

(1) Discrete Fourier transform of the discrete signal $\{x(i), i = 1, 2, 3 \cdots N\}$ for N points:

$$X(k) = \sum_{n=0}^{N-1} x(n) e^{-j(2\pi/N)nk}, \tag{23}$$

where $k = 1, 2 \cdots N - 1$ is the frequency order

(2) Calculating the power spectrum density, according to the relationship between signal and energy, the

Table 1: Selection results of penalty coefficient c.

c	Ninefold cross-validation									Average
0.01	0.906	0.915	0.838	0.920	0.914	0.953	0.931	0.925	0.953	0.915
0.1	0.971	0.910	0.983	0.982	0.901	0.926	0.928	0.931	0.893	0.936
1	0.978	0.982	0.942	0.954	0.958	0.963	0.944	0.972	0.989	0.964
10	0.988	0.972	0.971	0.991	0.942	0.991	0.983	0.987	0.977	0.978
20	0.970	0.957	0.963	0.955	0.941	0.933	0.890	0.931	0.907	0.938

Table 2: Selection results of parameter gamma.

Gamma	Nine-fold cross-validation									Average
10	0.913	0.889	0.873	0.925	0.841	0.863	0.871	0.916	0.932	0.891
50	0.871	0.940	0.973	0.988	0.951	0.915	0.947	0.901	0.881	0.929
100	0.966	0.985	0.964	0.977	0.979	0.989	0.991	0.872	0.903	0.954
150	0.982	0.989	0.977	0.987	0.982	0.989	0.963	0.957	0.977	0.977
200	0.966	0.967	0.965	0.975	0.987	0.963	0.906	0.958	0.987	0.965

Input: Signal sequences $X(i.)$
Output: Multi-domain Joint Entropy
1. Initialization: M, $\boldsymbol{m}$, r, τ and σ;
2. Get the steady-state part of the signal and the corresponding IMF components are obtained by CEEMDAN decomposition of the signal;
3. From the relevant experience, the frequency distribution of the IMF is selected according to the high and medium frequency components for superposition noted as IMF
4. The multi-domain joint entropy feature is extracted for the IMF and is denoted as:
$\boldsymbol{H} = [H_M, \overline{H_s}, \overline{H_p}]$
5. Classification and recognition of $\boldsymbol{H}$ using SVM Classifier;

Algorithm 1: CEEMDAN-MJE method

power spectrum of each order frequency can be obtained:

$$S(k) = \frac{1}{N}|X(k)|^2 \tag{24}$$

(3) Calculating the power spectrum entropy, the power spectrum of each order frequency is essentially a division of the original signal in the frequency domain, and the total energy of the signal is $1/N$ times the sum of the energy $|X(k)|^2$ of each order frequency component, defining the weights of its power spectrum distribution as

$$q_k = \frac{S(k)}{\sum_{k=0}^{N-1} S(k)} \tag{25}$$

(4) Where q_k is the share of the kth order power spectral component in the whole power spectral components. From the definition of Shannon entropy, the power spectrum entropy is obtained as

$$H_p = -\sum_{i=1}^{N-1} q_k \log q_k \tag{26}$$

(5) When the entropy takes a great value, the system is in a stable state and the power spectrum is the most uniform. The white noise has the smallest difference in the power spectrum energy distribution, so its singular spectrum entropy value is the largest, as can be seen from the above equation:

$$H_{p_{\max}} = -N \times \left(\frac{1}{N} \log \frac{1}{N}\right) = \log N. \tag{27}$$

The normalized power spectrum entropy facilitates a more intuitive comparison of the signal complexity:

$$\overline{H_p} = \frac{-\sum_{i=1}^{N-1} q_k \log q_k}{logN} \tag{28}$$

From the perspective of signal complexity analysis, the power spectrum entropy can reflect the complexity of the signal energy under the power spectrum division. The simpler the signal is, the more concentrated the power spectrum energy distribution is, the smaller the power spectrum entropy is; the more complex the signal is, the more dispersed the power spectrum energy distribution is, the larger the power spectrum entropy is. For the special communication emitter signal, its fingerprint features affect the energy distribution of the power spectrum. Therefore, to a certain extent, we can use the power spectrum entropy to extract the nonlinear fingerprint features of the signal in the power spectrum domain.

2.3. Classifier Design. In machine learning methods, a large number of classifiers can be used for multiple classification tasks. The proposed algorithm in this paper uses the entropy feature vectors of the signal's different domains to analyze its nonlinear fingerprint features, which is originally a nonlinear classification problem. SVM is a classical machine intelligence algorithm based on the statistical learning theory, which is popular in multiple classification tasks. The classical model of SVM is a two-class classification model, which is defined as a linear classifier with a maximum interval on the feature space. It can also act as a nonlinear classifier when it encounters some linear inseparable problems. The core idea is using the suitable kernel function to map a linearly inseparable problem into a linearly separable problem in a high-dimensional space. In space, a separating hyperplane with the largest margin can be found using the structural risk minimization principle [21]. When the data are inseparable, the classification function is defined as

$$f(x) = \text{sign}\left[\left(\sum_{i=1}^{L} a_i y_i K(x_i, x_j)\right) + b\right], \tag{29}$$

where $K(x_i, x_j)$ is the kernel function, sign (.) is the symbolic function, a_i is the ith mode embedded dimension, and y_i is the ith label. Detailed information about SVM can be found in [21].

In this paper, we use Python3.8 as an interpreter in PyCharm 2021 for classification experiments. There are three classes for the classification problems in the SVM from sklearn, they are LinearSVC, NuSVC, and SVC. In this task, we select SVC as the SVM classifier which is suitable for the linear inseparable problem. In the SVC, we choose the default Gaussian kernel as the kernel function and select the appropriate penalty coefficient c and kernel function parameter gamma by taking cross-validation. As shown in Tables 1 and 2, we select the penalty coefficient c as 10 and the gamma as 150 for the experiment. The parameter "multiclass" includes one-versus-one and one-versus-all. Since the one-versus-one technique has better performance and is more suitable for practical use [22], we adopt it in this paper. The training set and test set are randomly divided in the ratio of 6 : 4. The experiments are repeated 50 times, and the average value of 50 experiments is taken as the final result.

Table 3: The computational complexity of the multidimensional entropy algorithms.

Algorithm	Computational complexity
MPE	$O(N-(m-1)\tau) + O(N * m \log m) + O(nk)$
MApEn	$O(N^2)$
MJE	$O(N^2 + 5N)$

Table 4: Under different signal lengths, the recognition rate of this method.

	$K = 3$	$K = 4$	$K = 5$
200	52.33%	49.87%	41.68%
400	70.23%	69.42%	60.72%
600	86.54%	85.48%	82.70%
800	95.65%	93.32%	91.17%
1000	97.56%	97.37%	97.01%
2000	98.73%	98.63%	98.54%

2.4. CEEMDAN-MJE Algorithm Summary. The nonlinear fingerprint of the radio emitter has different performances in different domains. In the time domain, the nonlinear features of the signal are hidden in the complex signal waveform, which affects the signal singular spectrum subspace distribution. In the frequency domain, the nonlinear features of the signal also affect the power spectrum energy distribution, so we first adopt the CEEMDAN method to decompose the signal into multiple IMF components in different frequency ranges, which reduces the complexity of the signal in each domain and also facilitates to analyze the properties of the signal in each frequency range. By analyzing the 3-dimensional differential approximate entropy, singular spectral entropy, and power spectral entropy extracted from some IMF components to form a 5-dimensional multidomain joint entropy feature, the nonlinear fingerprint of the radio emitter is extracted in multiple domains. The specific steps of the proposed method are as follows (Algorithm 1). The parameters involved in the algorithm and the specific process of signal preprocessing are discussed in the next section.

3. Experiment Results and Analysis

3.1. Data Acquisition and Setup. To verify the robustness of the proposed method, the experiment is carried out using the USRP dataset and the public dataset. The transmit signals of five N210 USRPs were collected in a laboratory confined space. The distance between the transmitter and the

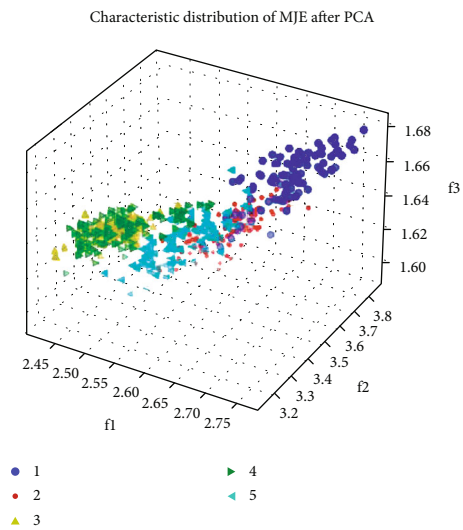

Figure 9: $L = 200$ distribution of MJE after PCA.

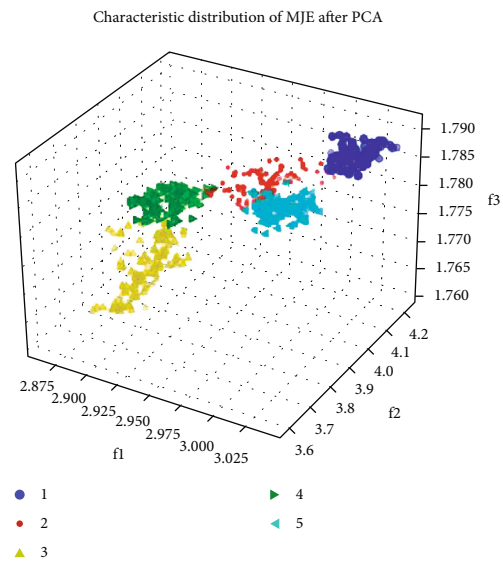

Figure 10: $L = 800$ distribution of MJE after PCA.

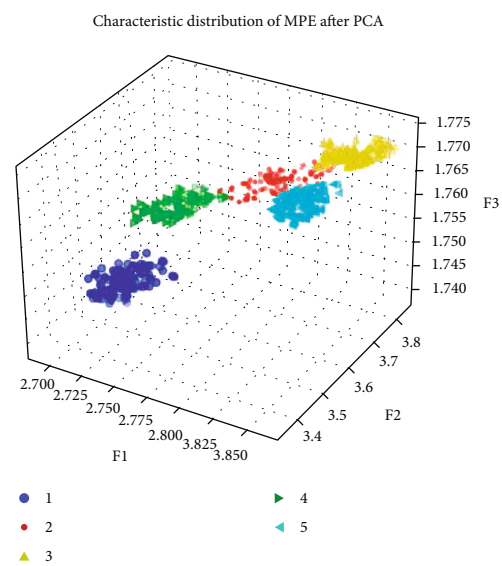

Figure 11: $L = 1000$ distribution of MJE after PCA.

receiver is 10 m, and there are obvious obstacles between them. The signal modulation method is unified by 8QAM. The sampling frequency is 5 MHz, and the carrier frequency is 1G Hz. The signal of each type of radio emitter is 10^7 magnitude IQ sample points, and the collected data frame is 5000 points/frame. In this paper, the 100000 IQ sample points are selected for each type of USRP, and the transient part in each frame is removed at first. Then, we extract the time envelope of the IQ signal, taking 1000 sample points as a sample and 100 samples for each type of USRP. From the experiment result, it is clear that the time-domain envelope of the signal is intricate and cannot be identified from the time domain only. Therefore, this paper uses the CEEMDAN-MJE method to extract features from the different domains of the signal. Finally, we use the Northeastern University public dataset to verify the classification effect of the proposed method in the 16-class dataset. Next, we discuss the four parts of the study, namely, experimental parameters, computational complexity analysis, sample length analysis, and the noise robustness of the proposed method.

3.2. Experimental Parameters. In the CEEMDAN-MJE method, the most important parameters are the choice of IMF and the multidomain joint entropy hyperparameters. After the envelope of the signal is passed through CEEMDAN, multiple IMF functions are generated. From Figures 4 and 5, it can be seen that IMF2, IMF3, and IMF4 are the high- and medium-frequency parts of the signal and have obvious differences from each other, so we select these three IMFs to extract the nonlinear features. In [8], it is known that the extracted nonlinear features are most obvious when the value of m is from 2 to 10 and $r = 3$. Since the IMF component of the signal is more complex, this paper uses the three-dimensional difference approximation entropy [7–9] for a nonlinear analysis of the IMF. In the singular spectrum entropy feature extraction, the time delay constant τ is usually taken as 1 and the phase space embedding dimension σ is taken as 200. Through the multidomain joint entropy feature extraction, we could extract the rich nonlinear components in the original signal. So it can contain a variety of nonlinear RF fingerprint information, and the feature vector composed is more conducive to the subsequent recognition task.

3.3. Computational Complexity Analysis. The computation of the method is mainly concentrated on the MJE. This section analyzes the computational complexity of the MJE and several common entropy features. In [8], the computational complexity of the MApEn is about $O(N^2k - \tau\sum_{i=1}^{k} m_i)$. In MdApEn, the complexity is about $O(N^2k - \tau\sum_{i=1}^{k} m_i) + O(k\sum_{i=1}^{k} m_i)$. Due to $N \gg \max\{\tau, k, m_i\}$, the complexity can be simplified to $O(N^2)$. In SSE, it could need $N - (\sigma - 1)\tau$ addition operations from (18), and according to (19)-(22), the calculation is about $O(M)$ $(M = N - (\sigma - 1)\tau)$. The computational

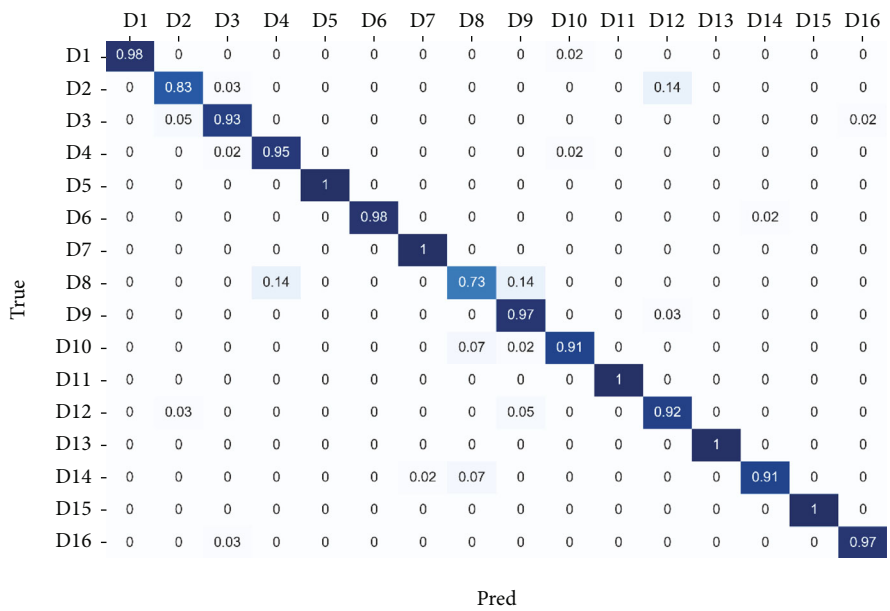

Figure 12: The confusion matrix of the 16-class radio emitter.

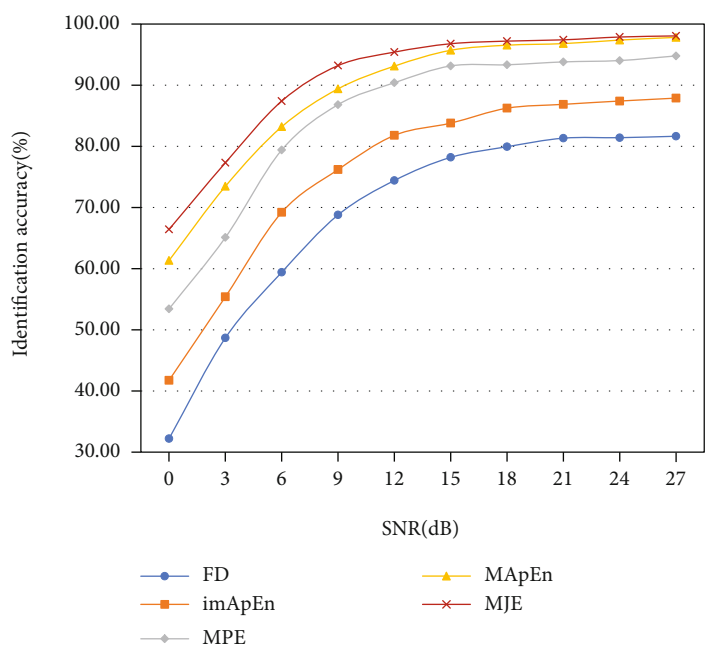

Figure 13: Identification performances under the AWGN channel.

complexity of SSE is about $O(2N)$. In PSE, it could need $2(N-1)$ addition operations from (23), and according to (25)-(26), the calculation is about $O(N-1)$. The computational complexity of PSE is about $O(3N)$. Therefore, the total computational complexity of the MJE is about $O(N^2+5N)$. In [6], the complexity of the multidimensional permutation entropy is about $O(N-(m-1)\tau)+O(N*m\log m)+O(nk)$, where n is dimensional of the permutation entropy and k is the number of the arrangement ways. In general, $N \gg \{m, k, n, \tau\}$. Therefore, the computational complexity of common algorithms is summarized in Table 3. The complexity of MJE is slightly higher than that of the MApEn, but it analyzes the nonlinear fingerprint of the signal from different domains. It is possible to extract more complete nonlinear features, which is beneficial to SEI technology. As shown in Table 3, the complexity of the MJE is mainly affected by the sample length, so we next analyze the choice of the sample length.

3.4. Sample Length Analysis. In the process of multidomain joint entropy extraction, the length of the signal sample

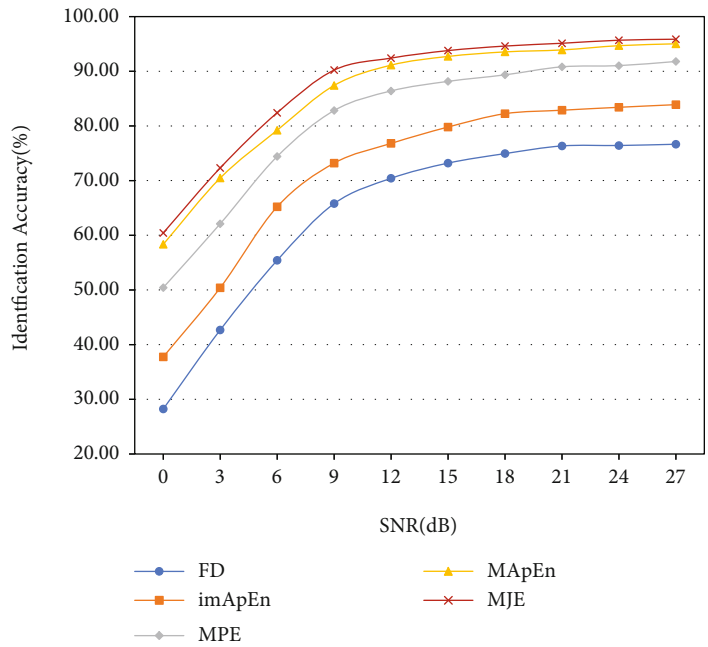

Figure 14: Identification performance under the Rayleigh fading channel.

has a great influence on the analysis of its entropy features. Theoretically, the longer the length of the signal, the more comprehensive the nonlinear features it contains. Therefore, within a certain range, increasing the length of the signal is beneficial to the study of signal identification. However, as the length of the sample signal increases, it not only increases the amount of experimental data but also increases the cost of computing. Therefore, this paper finds out the trend of the recognition rate with the length of the signal in the multiclassification problem through experimental comparison and provides a basis for the selection of the next sample length.

This time, the 5-class USRP dataset was selected, and the USRPs were named W1-W5. The IQ data of each USRP was taken out and divided according to 200, 400, 600, 800, 1000, and 2000 points per sample, and 100 samples were selected for each type of USRP. $K = 3$, 4 and 5 categories of the signal are selected for recognition experiments, and for $K = 3$, W1, W2, and W3 are selected; for $K = 4$, W1, W2, W3, and W4 are selected; and for $K = 5$, all categories are selected. In the signal recognition stage, the SVM classifier is selected. The training and test sets are randomly divided according to the ratio of 6 : 4. The experiments are repeated 50 times, and the average value of 50 experiments is taken as the final result. The recognition results obtained for different signal lengths are shown in Table 4.

As can be seen from Table 4, the length of the signal and the number of radio emitters have a great influence on the recognition rate of the experiment. As far as the length of the signal is concerned, the recognition rate increases more obviously when the number of sample points changes from 400 to 800, with an average increase of about 23%, while the recognition rate increases more slowly when it increases from 800 to 2000, with an average increase of only 3%. It can be seen that the longer the length of the signal, the more distinguishable the extracted fingerprint features are. To facilitate visualization, we reduce the 5-dimensional feature vector to 3-dimensional through principal component analysis (PCA). The PCA is a dimensionality reduction technique widely used in machine learning, which could extract the important components of the signal. Detailed information about PCA can be found in [23]. As shown in Figures 9–11, the distribution of different clusters represents the different radio emitter signals. Therefore, multidomain joint entropy needs samples of sufficient signal length. Too short samples are not enough to characterize the nonlinear features of its overall signal, and too long samples increase the computational cost. For the number of radio emitters, the recognition rate decreases with the same number of sample points when the number of radio emitters increases. This result is also consistent with the actual situation; when the number of radio emitters increases, the nonlinear features between each type of signal are less and less distinguishable in different domains. We need to increase the number of sample points, which enriches the nonlinear fingerprint features it contains. Therefore, the fingerprint features represented by MJE are more distinguishable.

Through the above analysis, on the 5-class USRP dataset, this paper uses 1000 data points per sample for the individual radio emitter identification task, and finally, only 100000 data points are used for each type of radio emitters, and the identification rate reaches more than 97%. If 2000 data points per sample are used for the experiment, the recognition rate is as high as 98.5%. To further verify the effectiveness of the method, this paper uses a Northeastern University public dataset of 16 classification problems, using

1000 sample points per sample and using 100,000 data points per type of radio emitter. The recognition rate reached 94.7%, and the confusion matrix results are shown in Figure 12. Let a_{ij} be the ith row and jth column of the confusion matrix, a_{ij} represents the probability that the emitter D_i is identified as the emitter D_j. Therefore, the confusion matrix further illustrates the effectiveness of the method for multiple types of radio emitter.

3.5. Noise Robustness of the Method. To evaluate the noise robustness of the proposed method, a series of controlled experiments are conducted in this paper using the USRP dataset. Four other different techniques based on steady-state entropy feature extraction were used in the experiments, and classification experiments were performed under the same conditions: (1) fractal dimension [24] (box dimension and information dimension); (2) multidimensional permutation entropy features [6], (3) improved approximate entropy features [7]; and (4) multidimensional approximate entropy features [8]. To ensure the fairness of the comparison, all features were preprocessed by the CEEMDAN algorithm before extraction, and the experiments were conducted under the same conditions. To further evaluate the noise robustness of the proposed method, we choose the Gaussian channel and Rayleigh fading channel to add different noises to the original signal and analyze the performance of different methods in the range of 0-25 dB SNR.

In the Gaussian channel, it can be seen from Figure 13 that using multidimensional entropy such as MPE, MApEn, and MJE to analyze the signal has a better recognition effect compared with one-dimensional entropy, which shows that the multidimensional entropy analysis method can extract more accurate nonlinear fingerprint information. The method in this paper further analyzes the entropy features in different domains of the signal that is different from the existing methods, and the experiments show that the multidomain joint entropy features have better recognition performance. Therefore, compared with the existing methods, the MJE method has greater advantages in extracting the nonlinear fingerprint features. To further evaluate the noise robustness of the method, the classification effect of the original signal under the influence of the Rayleigh fading channel is investigated in this paper. As can be seen from Figure 14, the recognition rate of the amplitude source signal in the Rayleigh fading channel environment is slightly lower than that in the Gaussian channel, because the fading coefficient α in the Rayleigh fading channel leads to greater randomness, blurs the fingerprint differences between radio emitters, and increases the difficulty of nonlinear feature extraction. But the nonlinear analysis of it from multiple domains can reduce the influence brought by its randomness and effectively extract the nonlinear fingerprint features of the signal. According to the above analysis, the method in this paper can achieve more than an 85% recognition rate in an environment above 5 dB SNR. It also has great noise robustness performance, which is better than other nonlinear feature extraction methods on the USRP dataset.

4. Conclusion

This paper is devoted to the study of individual identification of communication radio emitters by extracting the nonlinear fingerprint of communication signals. Since the nonlinear RF fingerprints have a complex generation procession, considering the large of nonlinear features in different domains, the signal is studied by nonlinear analysis in multiple domains. Considering more channel and environmental noise interference in the actual signal, which adds a lot of channel noise to the signal, the CEEMDAN algorithm is performed first, which reduces the influence of noise on the original signal. Then, the multidomain joint entropy features of the IMF of high-frequency components are extracted. Finally, a high recognition rate is achieved by the SVM classifier. Therefore, the multidomain joint entropy is beneficial to the analysis of its nonlinear fingerprint features. After the experimental research shows that the proposed method has good noise robustness performance and can achieve more than 85% recognition rate above 5 dB SNR. It also has good robustness in large numbers of radio emitters and can achieve a 94.7% recognition rate on the 16-class public dataset, so the CEEMDAN-MJE method is suitable for the individual identification of communication radio emitters in the case of multiple numbers and above 5 dB SNR. The Northeastern University public dataset download address is as follows: https://http://genesys-lab.org/oracle.

Data Availability

The Northeastern University public dataset (dataset#1) used to support the findings of this study is available from the corresponding address: https://genesys-lab.org/oracle. The 5-classified USRP dataset used to support the findings of this study has not been made available because there is some secret parameter information in the experimental data.

Conflicts of Interest

The authors declare that they have no known competing financial interests or personal relationships that could have appeared to influence the work reported in this paper.

References

[1] X. Dan, *Research on mechanism and methodology of Specific emitter identification [D]*, National University of Defense Technology, 2008, [Ph.D. dissertation].

[2] A. E. Spezio, "Electronic warfare systems," *IEEE Transactions on Microwave Theory and Techniques*, vol. 50, no. 3, pp. 633–644, 2002.

[3] O. Ureten and N. Serinken, "Wireless security through RF fingerprinting," *Canadian Journal of Electrical and Computer Engineering*, vol. 32, no. 1, pp. 27–33, 2007.

[4] T. L. Carroll, "A nonlinear dynamics method for signal identification," *Journal of Nonlinear Science*, vol. 17, no. 2, p. 023109, 2007.

[5] Y. Yuan, Z. Huang, F. Wang, and X. Wang, *Radio specific emitter identification based on nonlinear characteristics of signal*

[C], IEEE International Black Sea Conference on Communications and Networking. IEEE, 2015.

[6] S. Deng, Z. Huang, X. Wang, and G. Huang, "Radio frequency fingerprint extraction based on multidimension permutation entropy," *International Journal of Antennas and Propagation*, vol. 2017, 6 pages, 2017.

[7] Y. Xie and S. Wang, *Specific emitter identification based on nonlinear complexity of signal*, [C] IEEE International Conference on Signal Processing, Communications and Computing (ICSPCC), 2018.

[8] L. Sun, X. Wang, A. Yang, and Z. Huang, "Radio frequency fingerprint extraction based on multi-dimension approximate entropy," *IEEE Signal Processing Letters*, vol. 27, pp. 471–475, 2020.

[9] Y. Li, X. Gao, and L. Wang, "Reverse dispersion entropy: a new complexity measure for sensor signal," *Sensors*, vol. 19, no. 23, p. 5203, 2019.

[10] M. E. Torres, M. A. Colominas, G. Schlotthauer, and P. Flandrin, *A complete ensemble empirical mode decomposition with adaptive noise*, 2011 IEEE International Conference on Acoustics, Speech and Signal Processing (ICASSP), 2011.

[11] N. E. Huang, Z. Shen, S. R. Long et al., "The empirical mode decomposition and the Hilbert spectrum for nonlinear and non-stationary time series analysis [C]//The Royal Society A," *Mathematical Physical & Engineering Sciences*, vol. 454, no. 1971, pp. 903–995, 1998.

[12] "Xiao Hui Rong. Research on analytical methods of mutation components in time-varying signals [M]," *Harbin Institute of Technology*, 2020.

[13] X. Yang, G. Cheng, and H. Liu, "Improved empirical mode decomposition algorithm of processing complex signal for IoT application," *International Journal of Distributed Sensor Networks*, vol. 2015, 8 pages, 2015.

[14] W. Zhaohua and N. Huang, "Ensemble empirical mode decomposition: a noise-assisted data analysis method [J]," *Advances in Adaptive Data Analysis*, 2009.

[15] J. R. Yeh, J. S. Shieh, and N. E. Huang, "Complementary ensemble empirical mode decomposition: a novel noise enhanced data analysis method," *Advances in Adaptive Data Analysis*, vol. 2, no. 2, pp. 135–156, 2010.

[16] Y. Li, Y. Li, X. Chen, J. Yu, H. Yang, and L. Wang, "A new underwater acoustic signal denoising technique based on CEEMDAN, mutual information, permutation entropy, and wavelet threshold denoising," *Entropy*, vol. 20, no. 8, p. 563, 2018.

[17] N. Soltanieh, Y. Norouzi, Y. Yang, and N. C. Karmakar, "A review of radio frequency fingerprinting techniques," *IEEE Journal of Radio Frequency Identification*, vol. 4, no. 3, pp. 222–233, 2020.

[18] Steve Pincus and Wei Min Huang, "Approximate entropy: statistical properties and applications," *Statistics*, vol. 21, no. 11, pp. 3061–3077, 1992.

[19] H. S. Kim, R. Eykholt, and J. D. Salas, "Nonlinear dynamics, delay times, and embedding windows," *Physica D: Nonlinear Phenomena*, vol. 127, no. 1-2, pp. 48–60, 1999.

[20] J. Jiang, *Research on real-time signal measurement technology based on information entropy and its application [D]*, University of Electronic Science and Technology of China, 2017.

[21] J. C. B. Christopher, "A tutorial on support vector machines for pattern recognition," *Data Mining and Knowledge Discovery*, vol. 2, no. 2, pp. 121–167, 1998.

[22] K. R. Müller, S. Mika, G. Rätsch, K. Tsuda, and B. Schölkopf, "An introduction to kernel-based learning algorithms," *IEEE Transactions on Neural Networks*, vol. 12, no. 2, pp. 181–201, 2001, s.

[23] J. Shlens, *A tutorial on principal component analysis*, 2014.

[24] J. Dudczyk and A. Kawalec, "Fractal features of specific emitter identification," *Acta Physica Polonica A*, vol. 124, no. 3, pp. 406–409, 2013.

Hindawi
Wireless Communications and Mobile Computing
Volume 2022, Article ID 2857510, 17 pages
https://doi.org/10.1155/2022/2857510

Research Article

Blockchain-Empowered High-Frequency Spectrum Management IoT: A Multilayer PBFT Consensus Perspective

Xi Chen,[1] Jian Yang,[2] and Junfei Qiu[3]

[1]*School of Mechanical Engineering, Nanjing University of Science and Technology, Nanjing 210094, China*
[2]*Unit. 31107 of the Chinese People's Liberation Army, Nanjing 210014, China*
[3]*Beijing Research Institute of Information Technology, Beijing 10094, China*

Correspondence should be addressed to Jian Yang; yangjian_njust@foxmail.com

Received 27 February 2022; Revised 31 March 2022; Accepted 9 April 2022; Published 30 April 2022

Academic Editor: Mingqian Liu

High frequency (HF) is an important method for long-range communications and even the only mean when satellites are destroyed or interfered, which play an essential role in defense and economic construction. However, noncooperative frequency competition accompanied with power competition results in the continuously deterioration of HF electromagnetic environment. This article endeavors to resolve this issue through proposing blockchain-empowered HF spectrum management. Specifically, massive personal HF devices are organized around the preselected nodes to construct HF spectrum management IoT, further monitor, and share HF data through PBFT (Practical Byzantine Fault Tolerance) protocol. To address the scalability problem during the consensus, a multilayer PBFT consensus protocol is employed. Scalability evaluations show that increasing consensus layers of PBFT greatly reduces the communication complexity. Security assessments illustrate that the security performance will decline with the increase of layers. Tradeoff has been made between the communication complexity and security performance, indicating 2-4 layers PBFT is sufficient, which bring down the communication complexity and also achieve acceptable security performance.

1. Introduction

1.1. Background and Motivation. High frequency is an important method for long-range communication and even the only mean when the satellites are destroyed or interfered. Currently, wireless communication technologies, such as the 5th Generation Mobile Communication (5G) [1] and Internet of Things (IoTs) [2], are still in their booming era. Simultaneously, electromagnetic environment of high frequency (HF) band is persistently deteriorating, and HF background noise is increasing year by year, causing HF transmitters with hundreds or even thousands Watts hard to communicate well, which seriously threaten the survival and development of HF service.

So as to investigate the deteriorated degree of HF electromagnetic environment, we have monitored the evolution of HF electromagnetic environment for 5 years. The results are shown in Figures 1 and 2. From Figure 1, we can see that both the power and the number of HF signals are continuously increasing in the last 5 years. From Figure 2, we can see that in the past 5 years, the background noise of HF electromagnetic environment is increasing at a rate of 1 dB per year, which indicates that deteriorating trend of HF electromagnetic environment. How to reverse the deteriorating trend of HF electromagnetic environment? Our previous works indicate that *noncooperative frequency competition accompanied with power competition* is the key manual factor in the deterioration of HF electromagnetic environment [3]: The quality of HF communication largely depends on timely and accurately detecting of ionosphere evolution, which is hard to obtain, although hundreds of HF monitoring stations and ionosonde stations have been built. The reason is that HF transmitters neither know the ionosphere information in time nor guarantee the ionosphere of reflection point has HF monitoring stations or ionosonde stations. Then, people either blindly increase the transmission

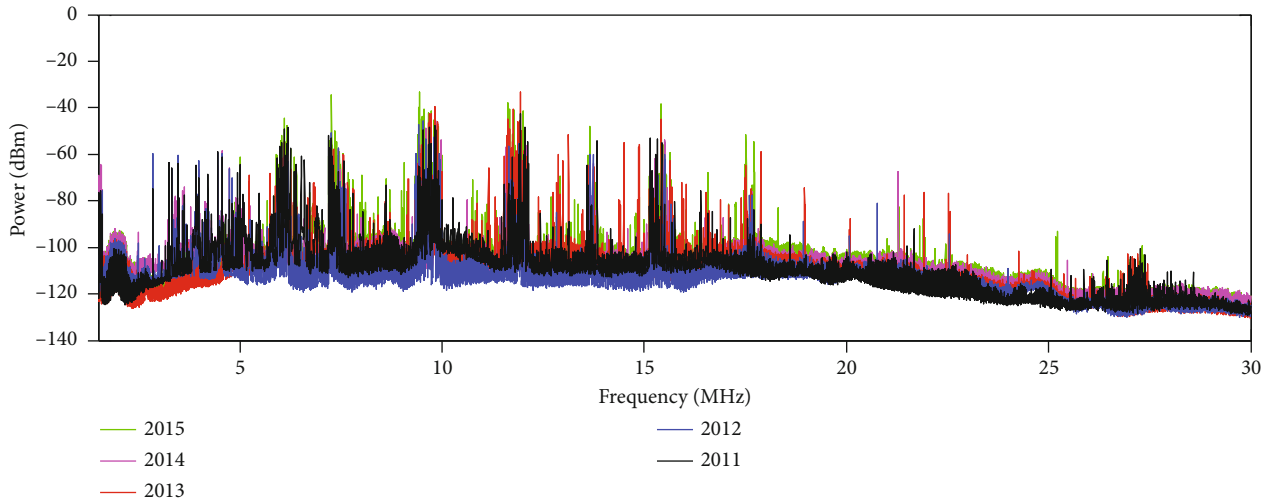

Figure 1: Five-year evolution of HF signals and HF electromagnetic environment.

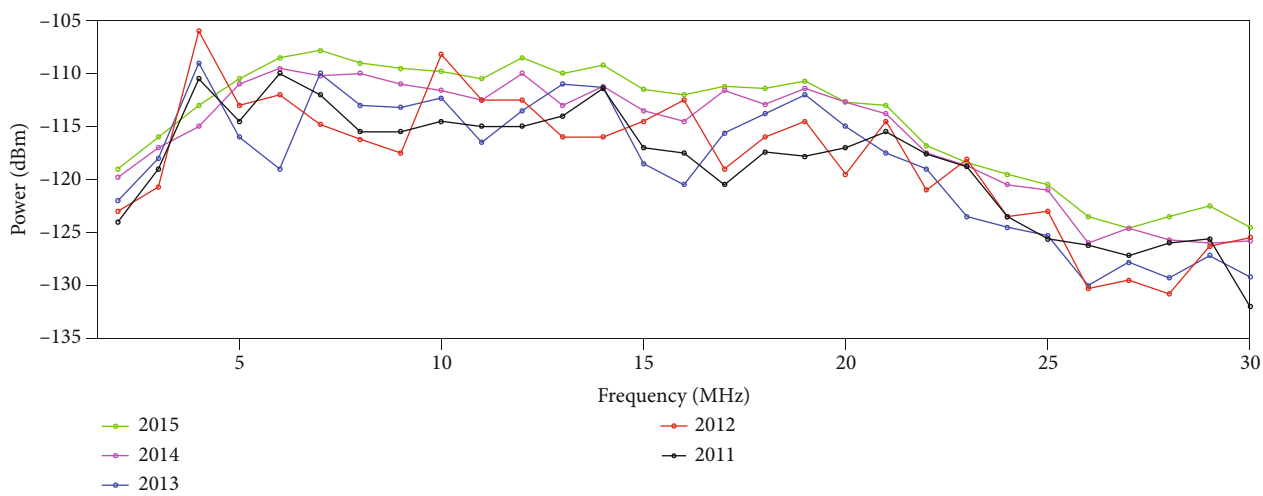

Figure 2: Five-year evolution of HF background noise.

power to improve communication quality or arbitrarily switch to idle (local) HF, i.e., the noncooperative frequency competition accompanied with power competition. It can be asserted that if we still insist utilizing HF resources in a *noncooperative* way, the earliest invented long-range communication method, HF will be probably destroyed by ourselves.

Firstly, how to change the noncooperative utilization mode of HF band? HF amateur service provides a solution. Amateur is a radiocommunication service used for self-training, intercommunication, and technical investigation [4]. HF amateurs are also called HAM and are distributed all over the world. If HF amateurs connect to each other and construct the HF spectrum management IoT, further monitor, and share the data of HF electromagnetic environment; HF transmitters no longer need to blindly increase the transmission power or arbitrarily switch to idle (local) HF; i.e. HF transmitters no longer need to adopt the noncooperative frequency utilization mode, finally promote the reduction of HF background noise, and improve the HF electromagnetic environment.

Secondly, how to motivate HF amateurs to construct the HF spectrum management IoT and monitor/share the data of HF electromagnetic environment? Emerging blockchain technology provides solution. Blockchain is a completely new distributed infrastructure and computing paradigm [5–7]. It applies a block-chain structure to store and authenticate data and distributed consensus algorithm to generate and update data, and asymmetric encryption to guarantee the security during data transmission, and smart contracts to operate and edit data. In a word, blockchain provides a safe and efficient solution for data transmission in distributed systems, which can be transplanted to HF band and construct the new framework of HF spectrum management IoT.

1.2. Related Works. Spectrum management was organized all along in a centralized manner, which was criticized for its inflexibility. The emergence of blockchain technology enables people to notice the natural connection between blockchain and spectrum management. In 2018 Mobile

World Congress, Rosenworcel, the speaker of FCC (Federal Communications Commission), said that blockchain can be recognized as lower-cost alternative of a centralized database to support shared access in specific spectrum bands [8]. Kotobi and Bilen in [9] attempted to apply blockchain to moving cognitive radio networks and proposed an Aloha medium-access protocol for dynamic spectrum access. Pei et al. in [10] combined cooperative spectrum sensing with mining in Bitcoin; each secondary user acts both a sensing node for cooperative sensing and a miner in blockchain network. After that, the applications of blockchain to spectrum management were investigated in [11, 12], including four typical scenarios, i.e., primary cooperative sharing, secondary cooperative sharing, primary noncooperative sharing, and secondary noncooperative sharing. The applications of blockchain in spectrum management are successively proceeded, some focus on UAV spectrum management [13, 14], some focus on the spectrum management in 5G/6G [15–17], and some focus on the spectrum management in Internet of Vehicles [18, 19].

In the rough, most blockchain can be divided into three categories, i.e., public blockchain, private blockchain, and consortium blockchain. Majority of early studies adopt public blockchain in the distributed spectrum management and apply proof-of-work (PoW) or proof-of-stake (PoS) as consensus protocol [9, 20, 21]. With the deepening of research, challenges gradually surfaced. Devices should be authenticated in spectrum management, no matter under a distributed or centralized manner. However, permissionless blockchain, i.e., public blockchain, is contrary to this requirement. Secondly, as time elapse, there will be increasing devices participating in the blockchain network, while private blockchain has fixed amount of nodes and cannot scale up later. A consortium blockchain is a special blockchain with multiple preselected nodes to establish the distributed shared database with moderate cost [14, 22]. For consortium blockchain, devices are allowed to join the blockchain only after authentication, which is in accordance with the concept of spectrum management IoT [23, 24].

Consensus protocol has always been seen as the core of the blockchain, which can be divided into two categories. One is represented by PoW or PoS; the other is represented by Practical Byzantine Fault Tolerance (PBFT) [20]. The following advantages indicate PBFT is more appropriate than PoW or PoS for spectrum management IoT. Firstly, compared with the throughput of PoW (7 Transactions Per Second (TPS)), the throughput of PBFT can achieve thousands of TPS [25, 26], which is essential for processing massive spectrum data. Secondly, the energy efficiency of PBFT is far superior to PoW. Considering that a large number of personal HF devices, i.e. HAMs, participate in the consensus, the simple consensus process of PBFT (consensus only performed among preselected nodes) represents higher energy efficiency compared with PoW or PoS (consensus is performed by all nodes). Thirdly, the confirmation delay of PoW sometimes can be up to hours, while that of PBFT is only milliseconds [27]. Last but not the least, the poor scalability of PBFT has always been criticized. In this article, multilayer PBFT is proposed to achieve a tradeoff between scalability and security for HF spectrum management IoT.

1.3. Contributions. Motivated by the aforementioned observations, in this article, we exploit the consortium blockchain to develop a HF spectrum management IoT and apply PBFT protocol to achieve consensus among edge computing nodes. A multilayer PBFT is proposed to solve the problem of scalability [28]. A tradeoff has been made between communication complexity and security, so as to derive the optimal structure of the blockchain-empowered HF spectrum management IoT. Specifically, the contributions of this article are summarized as follows:

(1) A blockchain-empowered HF spectrum management IoT is presented to motivate the personal HF devices to monitor and share the HF data for the first time. Massive personal HF devices are organized around the preselected nodes, i.e., 4G/5G base stations, to monitor and share the HF data, which bridges the gap between the collection of HF data and the inference of spectrum strategy

(2) A multilayer PBFT consensus protocol is employed to achieve the tradeoff between the scalability and security. The detailed operations of consensus process are illustrated to show how spectrum management agencies, 4G/5G base stations, and personal HF devices overcome the disadvantages of scalability while preserving the advantages of its throughput and energy efficiency

(3) Under the multilayer PBFT consensus, a tradeoff is formulated to obtain the optimal structure of HF spectrum management IoT, which jointly minimize the communication complexity and maintain an acceptable security performance

The rest of this article is organized as follows. Blockchain-empowered HF spectrum management framework and detailed operations are introduced in Section 2. In Section 3, a multilayer PBFT consensus is presented and the scalability of which is analyzed. In Section 4, the security of multilayer PBFT consensus is assessed to show the tradeoff between scalability and security. Scalability evaluation and security assessment are performed in Section 5, and conclusion has been made in Section 6.

2. Blockchain-Empowered Hf Spectrum Management

Blockchain is a decentralized database, a distributed infrastructure and computing paradigm, that uses block-chain structures to verify and store data and distributed consensus algorithms to generate and update data, asymmetric cryptography to ensure the security during the transmission and access, and smart contracts composed of automated script codes to program and manipulate data. In this section, a blockchain-empowered HF spectrum management IoT is

proposed to timely and accurately obtain the changes of HF electromagnetic environment.

2.1. Overview of the Blockchain-Empowered HF Spectrum Management. Consensus in blockchain can be divided into two categories. The first category is represented by PoW, which is a computational processing called "mining"; i.e., a set of participants called miners need to solve a complex computation problem, i.e., proof-of-work puzzle, to confirm and secure the integrity and validity of transactions before adding the records into the blockchain. The security and privacy of the blockchain depend on the distributed consensus mechanism managed by these miners. However, in traditional public/permissionless blockchain (such as Bitcoin or Ethereum), the consensus is performed by all nodes (miners), which results in high cost and low throughput. To relieve the computation-intensive challenge of constructing HF blockchain, unlike existing works, in this article, a consortium blockchain is explored to empower the operation of HF spectrum management. Consortium blockchain is permissioned blockchain in which the consensus process is executed by preselected nodes. The consensus process of consortium blockchain is Practical Byzantine Fault Tolerance (PBFT), i.e., the second consensus protocol, with the throughput up to thousands TPS, which is essential to the blockchain empowered HF spectrum management, considering the HF spectrum data can be seen as a kind of big data [29]. Furthermore, the framework of private blockchain is also inappropriate for HF spectrum management, as the user of HF spectrum management is still increasing, while the number of user in private blockchain is fixed. Consequently, consortium blockchain is more suitable for HF spectrum management IoT.

In the proposed HF spectrum management IoT, the limited computing resource and energy supply become one of major problems, especially for the communication and computing load in the consensus-reaching process. Instead, edge computing provides necessary computing and communication resources for the blockchain-empowered IoT [30]. For example, base stations equipped with small data center can accept offloaded computation-intensive jobs from adjacent IoT devices [31]. Then, we leverage edge computing as an enabler to offload the computation-intensive puzzles to proximate edge computing nodes. Compared with traditional cloud computing [32, 33], edge computing brings network resources (e.g., computation power and storage space) closer to the users, which can effectively shorten the transmission delay and reduce the energy consumption [34]. The consortium blockchain-empowered HF spectrum management IoT is illustrated in Figure 3, which consists of the following major entities.

(i) ITU HF Agency: ITU HF agency is a trusted authority and operated by International Telecommunication Union (ITU). In this framework, ITU HF agency is responsible for initializing the entire HF spectrum management IoT, including the preselected edge computing nodes. ITU HF agency authenticate personal HF devices, and generates the public/private keys for them. Note that the ITU HF agency is offline for most of the time. It does not serve as a central controller and is not conflict with the distributed characteristics.

(ii) Computing nodes: computing nodes include an ITU HF server (cloud computing node) and edge computing nodes. The ITU HF server is operated by ITU and deployed at the same location of ITU HF agency. ITU HF server provides huge storage space and powerful computing power for inferring HF spectrum strategy in a centralized manner. Unlike ITU HF agency, the ITU HF server is online most of the time. 4G/5G base stations serve as edge computing nodes and provide relatively high computing power and large storage space for inferring HF spectrum strategy in a distributed manner. The storage space of edge computing nodes is mainly used to store HF spectrum data.

(iii) Personal HF devices: personal HF devices, i.e., HF amateurs, also called HAM, are distrusted widely over the world. Generally, personal HF devices are responsible for monitoring HF electromagnetic environment and uploading HF data to the proximate edge computing nodes. In addition, HF spectrum data and transaction data are asymmetric encrypted before uploading or transmission.

Additionally, in the proposed framework, the HF blockchain composes of HF blocks, including HF spectrum data and transaction data. For each edge computing node, it packs the HF spectrum data and transaction data every period of time to generate a preadded HF block and broadcasts this preadded HF block to the surrounding edge computing nodes. The object is to reach consensus on the preadded HF block through PBFT protocol.

In the proposed framework, ITU HF agency is designed for authenticating personal HF devices and allocating public/private keys. The ITU HF server is deployed at the same place of ITU HF agency and provides large space and powerful computing power for storing HF spectrum data and inferring HF spectrum strategies. 4G/5G base stations are deployed in the edge, with the aim of providing relative large space and powerful computing power. Personal HF devices are located at the end of the network. Then, ITU HF agency, base stations, and personal HF equipment constitute an end-edge-cloud structure and apply edge computing to operate the blockchain-empowered HF spectrum management IoT.

2.2. Detailed Operations of the Blockchain-Empowered HF Spectrum Management IoT. In the operation of HF spectrum management IoT, the process can be divided into 3 steps, i.e., the collection of HF spectrum data, the generation of HF blocks, and the trading of HF spectrum data. We elaborate the details as follows.

(1) Collection of HF spectrum data: in the 5G era, base stations can be regarded as the nodes with powerful computing power and massive storage space, which

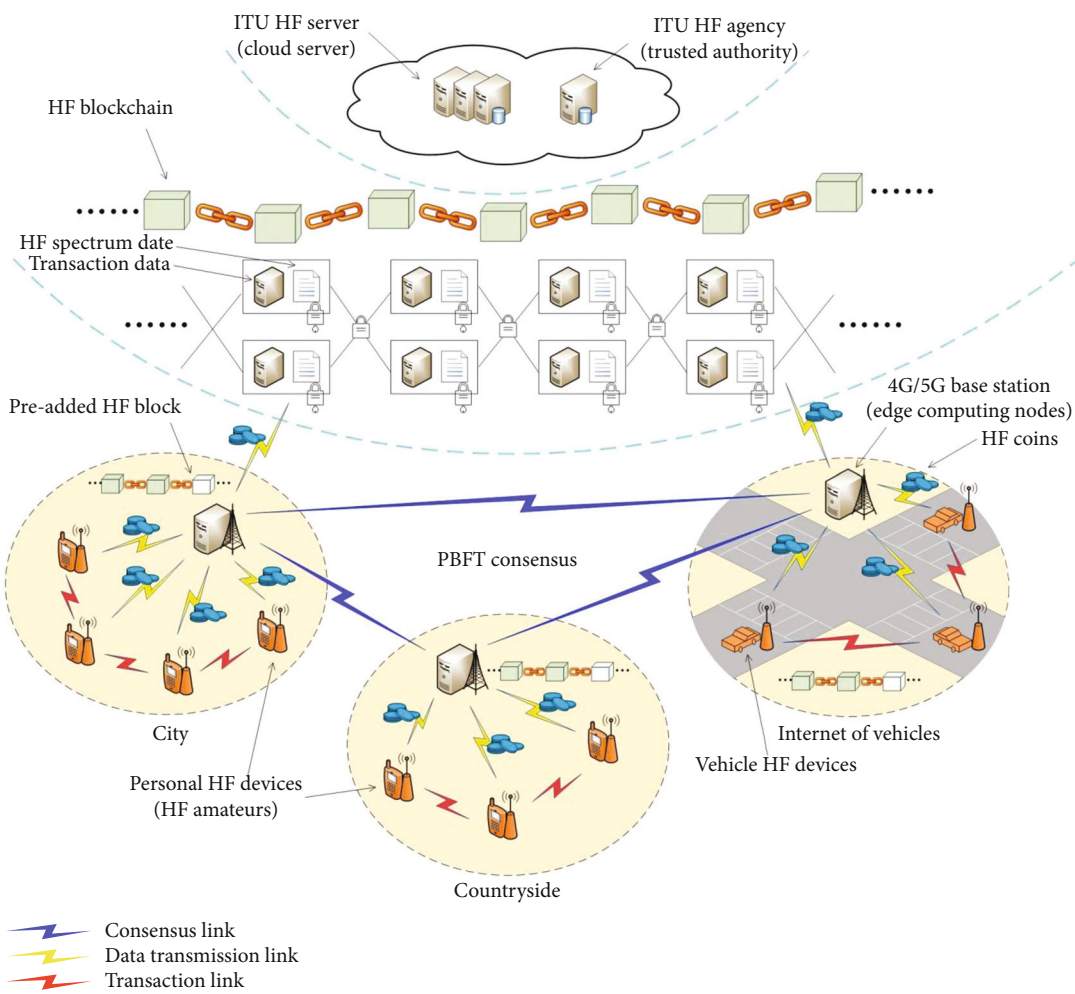

Figure 3: Consortium blockchain-empowered HF spectrum management IoT.

are deployed in a distributed manner. Here, each base station is assumed to manage surrounding HF electromagnetic environment. In ITU Spectrum Monitoring Handbook [35], 7 × 24-hour continuous spectrum monitoring is recognized sufficient to characterize the electromagnetic environment of a region. An HF electromagnetic environment is generally stable and partially dynamic. HF spectrum strategies of a certain region can be further inferred based on the collected HF spectrum data [36].

Personal HF devices can run an App that can be seen as smart contract, to automatically collect HF spectrum data. Personal HF devices upload the collected HF spectrum data to the proximate edge computing node for a period of time.

In the proposed framework, the automatically collected HF spectrum data has identical data structure that can be directly used by most personal HF devices. Intuitively, HF spectrum data is a kind of big data. If we use 1 byte to represent the HF spectrum data in a geospatial grid of 1000 m × 1000 m, and the frequency and time resolutions are assumed to 1 kHz and 100 ms, respectively. After one month, the total HF spectrum data size in the frequency band ranging from 2 to 30 MHz and a geospatial region of 100 km × 100 km can be as large as

$$\begin{aligned}&\frac{30\text{ days}}{\text{month}}\times\frac{24\text{ hours}}{\text{day}}\times\frac{3600\text{ seconds}}{\text{hour}}\times\frac{1\text{ hour}}{100\text{ ms}}\\&\quad\times\frac{28\text{ MHz}}{1\text{ kHz}}\times\frac{100\text{ km}\times100\text{ km}}{1\text{ km}\times1\text{ km}}\times1\text{ byte}\\&=7.257\times10^{15}\text{byte/month}\\&=7.257\times10^{3}\text{terabyte (TB)/month.}\end{aligned}\tag{1}$$

By comparison, Facebook, one of well-known big data examples, generates approximately 1.4×10^{4} TB per month. The size of HF spectrum data described above is approximately half of Facebook in the same duration. Moreover, the size of HF spectrum data will grow with the time duration and spatial scale, as well as the corresponding resolution in each dimension. It will cause heavy pressure to the ITU HF Server, needless to say under a centralized network framework.

Edge computing could efficiently processing HF spectrum data. Once the base station receives the HF spectrum

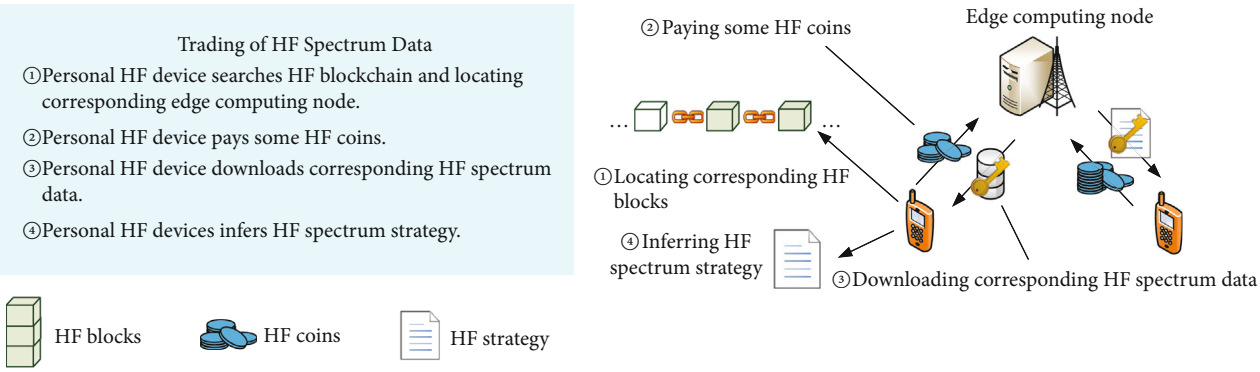

Figure 4: Trading of HF spectrum data.

data and transaction data that uploaded by personal HF devices, it extracts the key information from the HF spectrum data and generates a digest. The main body of HF spectrum data is locally stored in edge computing nodes.

(2) Trading of HF spectrum data: the uploaded HF spectrum data is divided into the digest and main body of HF spectrum data. Edge computing nodes cooperate through PBFT protocol to reach consensus on uploaded HF spectrum data to form the preadded HF blockchain. HF blockchain is stored online and saved as a copy in each edge computing node. It should not take a large space to store the HF blockchain and not take long to download the HF blockchain, since the HF blockchain only saves the digest of HF spectrum data, which indicates the main body of HF spectrum data is stored in which edge computing node. When personal HF devices need to download the main body of HF spectrum data for inferring HF spectrum strategy, it locates the exactly base station, i.e., the edge computing node, that the main body of HF spectrum data is stored and connects the base station to download through high speed 4G/5G channels.

If massive personal HF devices, i.e., HF amateurs, share HF spectrum data, HF strategy is expected to change from noncooperative frequency competition accompanied with power competition to cooperative competition and sharing. It will gradually reduce the HF background noise and improves HF electromagnetic environment. Consequently, personal HF devices need to make use of HF spectrum data to infer HF spectrum strategy. The above process can be concluded into four steps, as shown in Figure 4.

(i) Personal HF device searches HF blockchain and locates corresponding edge computing node through the digest that stored in HF block

(ii) Personal HF device pays some HF coins

(iii) Personal HF device downloads corresponding HF spectrum data

(iv) Personal HF device infers HF spectrum strategy according to the downloaded HF spectrum data

In the third step, when personal HF device needs to download corresponding HF spectrum data, there are two options:

(1) *Option 1: the main body of HF spectrum data is stored in* ***local*** *edge computing node.* Personal HF device pays some HF coins to local edge computing node and downloads corresponding HF spectrum data. Edge computing node receives minority HF coin and transfers majority HF coin to personal HF devices that provide HF spectrum data.

(2) *Option 2: the main body of HF spectrum data is stored in* ***foreign*** *edge computing node.* Personal HF device sends request to foreign edge computing node through local edge computing node and pay some HF coins beforehand. Foreign edge computing node transmits corresponding HF spectrum data through high-speed network, e.g., 4G/5G network, to the local edge computing node. Then, HF coins are transferred to personal HF devices that provide HF spectrum data.

In the fourth step, when personal HF device infers HF spectrum strategy according to the downloaded HF spectrum data, there are also two options.

(1) *Option 1: personal HF device infers HF spectrum strategy locally.* If personal HF device has enough computing power and storage space, it could infer HF spectrum strategy locally.

(2) *Option 2: local edge computing node assist personal HF device inferring HF spectrum strategy.* If personal HF devices do not have enough computing power, it could send the requirements to local edge computing node and pay some HF coins. With relative sufficient computing power and large storage space, local edge computing node could quickly infer the HF spectrum strategy and then transmit the results back to personal HF device.

Moreover, the security during the transmission is guaranteed by asymmetric encryption [37]. For instance, when personal HF device A transmits HF spectrum data Data_A to edge computing node B, device A downloads the public key of node B and encrypts Data_A:

$$\text{Record}_{\text{Data}} = \text{RSA}\left(\text{Data}_A, \text{key}_B^P\right). \tag{2}$$

$\text{Record}_{\text{Data}_A}$ is the encrypted HF spectrum data, RSA is the asymmetric encryption algorithm [38], and key_B^P is the public key of edge computing node B. When edge computing node B receives $\text{Record}_{\text{Data}_A}$, it decrypts with his private key key_B^P and obtains the HF spectrum data:

$$\text{Data}_\text{A} = \text{RSA}\left(\text{Record}_{\text{Data}_A}, \text{key}_B^S\right). \tag{3}$$

Secondly, personal HF devices can check whether HF spectrum data has been tampered. When personal HF device C uploads HF spectrum data Data_C to edge computing node, device C first generates the digest of Data_C through Hash algorithm [39]:

$$\text{Digest}_{\text{Data}_C} = \text{Hash}\left(\text{Data}_C, \text{key}_C^P\right). \tag{4}$$

Device C encrypts the digest $\text{Digest}_{\text{Data}_C}$ and generates digital signature:

$$\text{Sign}_{\text{Digest}} = \text{RSA}\left(\text{Digest}_{\text{Data}}, \text{key}_C^S\right). \tag{5}$$

Device C appends $\text{Sign}_{\text{Digest}}$ to the end of Data_C and uploads Data_C to edge computing node. Then, other personal HF devices can decrypt $\text{Sign}_{\text{Digest}}$ with the public key of device $C\text{key}_B^P$ and obtain $\text{Digest}_{\text{Data}_C}$:

$$\text{Digest}_{\text{Data}_C} = \text{RSA}\left(\text{Sign}_{\text{Digest}}, \text{key}_C^P\right). \tag{6}$$

Other personal HF devices apply Hash Algorithm to Data_C and obtain the digest $\text{Digest}'_{\text{Data}_C}$. Then, other personal HF devices compare $\text{Digest}'_{\text{Data}_C}$ with $\text{Digest}_{\text{Data}_C}$; if $\text{Digest}'_{\text{Data}_C} = \text{Digest}_{\text{Data}_C}$, it indicates that the HF spectrum data has not been tampered.

(3) Generation of HF Block: when the accumulated HF spectrum data of a certain region exceeds 7×24 hours, the base station iteratively discards redundant HF spectrum data to make it light-weighting. Once the accumulated HF spectrum data reach a certain amount, e.g., 24 hours, the edge computing node extracts the key information and generates a digest and packs with the transaction data to form the preadded HF block; then, broadcasts it to surrounding edge computing nodes and seeks for consensus. The preadded HF block contains a unique serial number, duration/spectrum range/monitoring location, time/frequency/spatial resolution, data size, and storage location (i.e., the location in the base station). The size of the preadded HF block is relatively small. Note that the preadded HF blocks are asymmetric encrypted (e.g., SHA-256 algorithm) by the private key of the edge computing node. When these edge computing nodes reach consensus about the preadded HF block, it will be appended at the end of the HF blockchain and becomes an official block. Note that other personal HF devices could decrypt HF block with the public key of edge computing node that uploaded online and easily obtain the location of demanding HF spectrum data through the digest of HF spectrum data. When the preadded HF block becomes an official one, the personal HF devices that provide the HF spectrum data will get some HF coins automatically as rewards. As stated above, the strategy that the HF spectrum data been divided into digest and main body and been stored in HF blockchain and edge computing node, respectively, not only greatly reduces the traffic load but also saves the computing power and energy consumed in the consensus process.

The structure of HF block is illustrated in Figure 5, including the digest of HF spectrum data, transaction data, timestamp, and the hash value of the previous block. HF blocks are linked end by end according to the timestamp, which record the time of consensus-reached. The subblocks are organized in the structure of Merkel Tree. Note that HF blocks only contain the digest of HF spectrum data, and the main body is stored at corresponding edge computing node. Similar to Bitcoin, the ITU HF server regularly releases HF coins for their contributions of collecting HF spectrum data. When surrounding edge computing nodes reach consensus on the preadded HF block, the HF block will be appended to the end of HF blockchain, personal HF devices that provide HF spectrum data and edge computing nodes participating in consensus both will be rewarded some HF coins. HF coins can be used to purchase additional HF bandwidth and additional HF spectrum usage rights.

3. Scalability of Multilayer PBFT Consensus

3.1. Multilayer PBFT Consensus. Before introducing the multilayer PBFT, we first review the single-layer PBFT protocol. Practical Byzantine Fault Tolerance was first presented to solve the malicious attacks in Byzantine General Problem [25, 26]. Figure 6 shows the flow chart of the single-layer PBFT; one primary node (replica 0) and three replicas work together to carry consensus process forward. The whole consensus process generally includes 5 steps, i.e., *request*, *preprepare*, *prepare*, *commit*, and *reply*. PBFT consensus is triggered by a client sending a *request* message to the primary node. Then, primary node broadcasts a *preprepare* message to other replicas. All replicas, including primary node, send messages to each other for checking the validity of the received

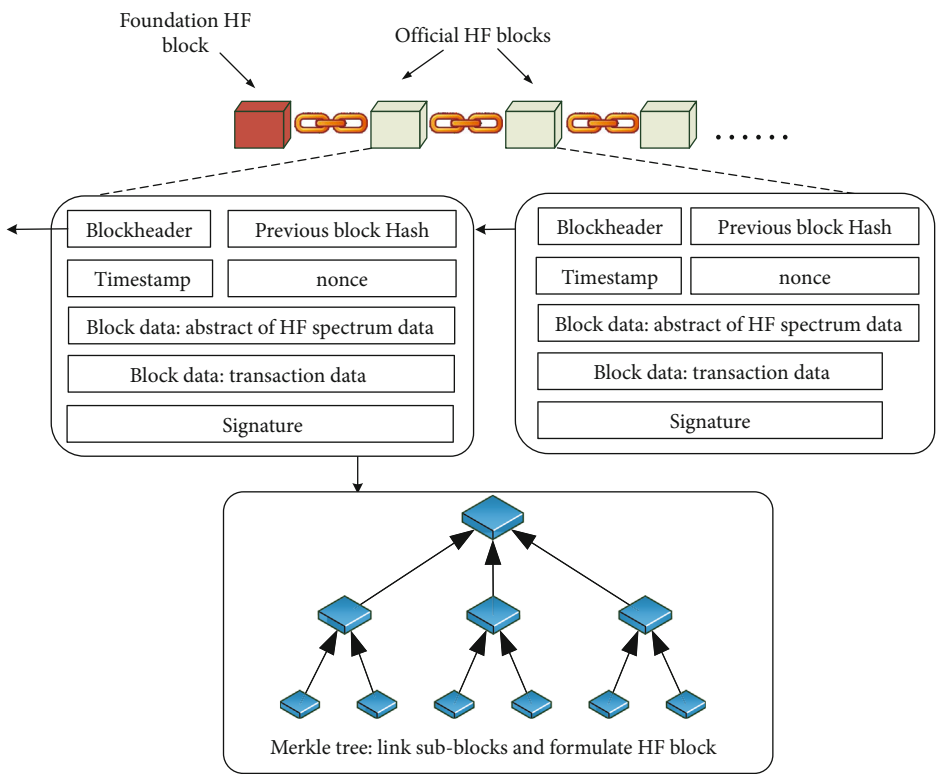

Figure 5: Structure of HF blocks.

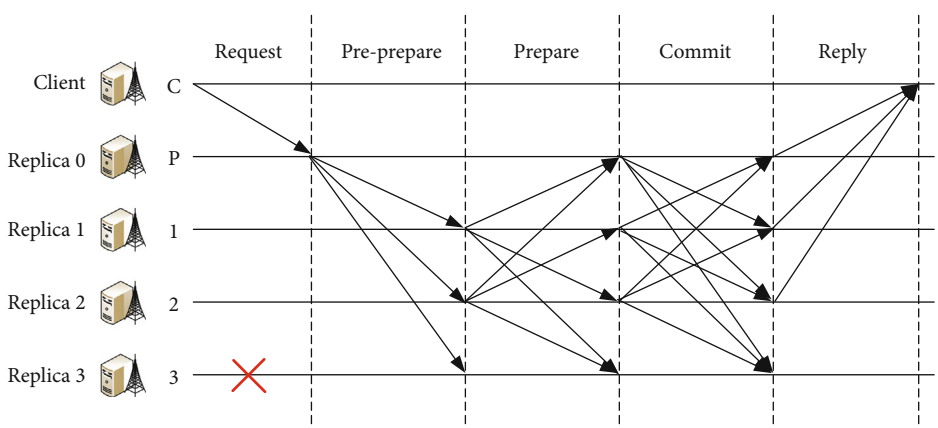

Figure 6: Single-layer PBFT consensus.

messages in *prepare* and *commit* steps. Finally, if an agreement is achieved in *reply* step, the preadded HF block will be added to end of HF blockchain.

PBFT consensus is designed to tolerate f faulty nodes with a total number of $3f + 1$ replicas [25, 26]. Therefore, the security threshold of the single-layer PBFT can be seen as f, given a total number of $3f + 1$ replicas participating the consensus process. From Figure 6, we can see that PBFT is a communication-intensive consensus process. Given the total number N, the single-layer PBFT requires $O(N^2)$ times internode communications to reach consensus. Obviously, the communication complexity will become increasingly unaffordable with the increasing of nodes. It is also the reason for the poor scalability of the PBFT consensus.

Next, a multilayer PFBT is applied to bring down the communication complexity to an acceptable level when the number of nodes sharply increases. Generally speaking, the core idea of the multilayer PBFT consensus is successively inserting a PBFT consensus between *commit* and *reply* steps to reduce the whole communication complexity [28]. The consensus process of the second layer is inserted after the *commit* step; after that, each node has generated his own judgment about whether the preadded HF block is valid. At this time, whether the PBFT consensus of the second layer is reached only affects the *reply* message of one replica in the first layer and will not affect the *reply* message of other replicas. As an example, Figure 7 illustrates the process of two-layer PBFT, Replica 3 is assumed to be a malicious

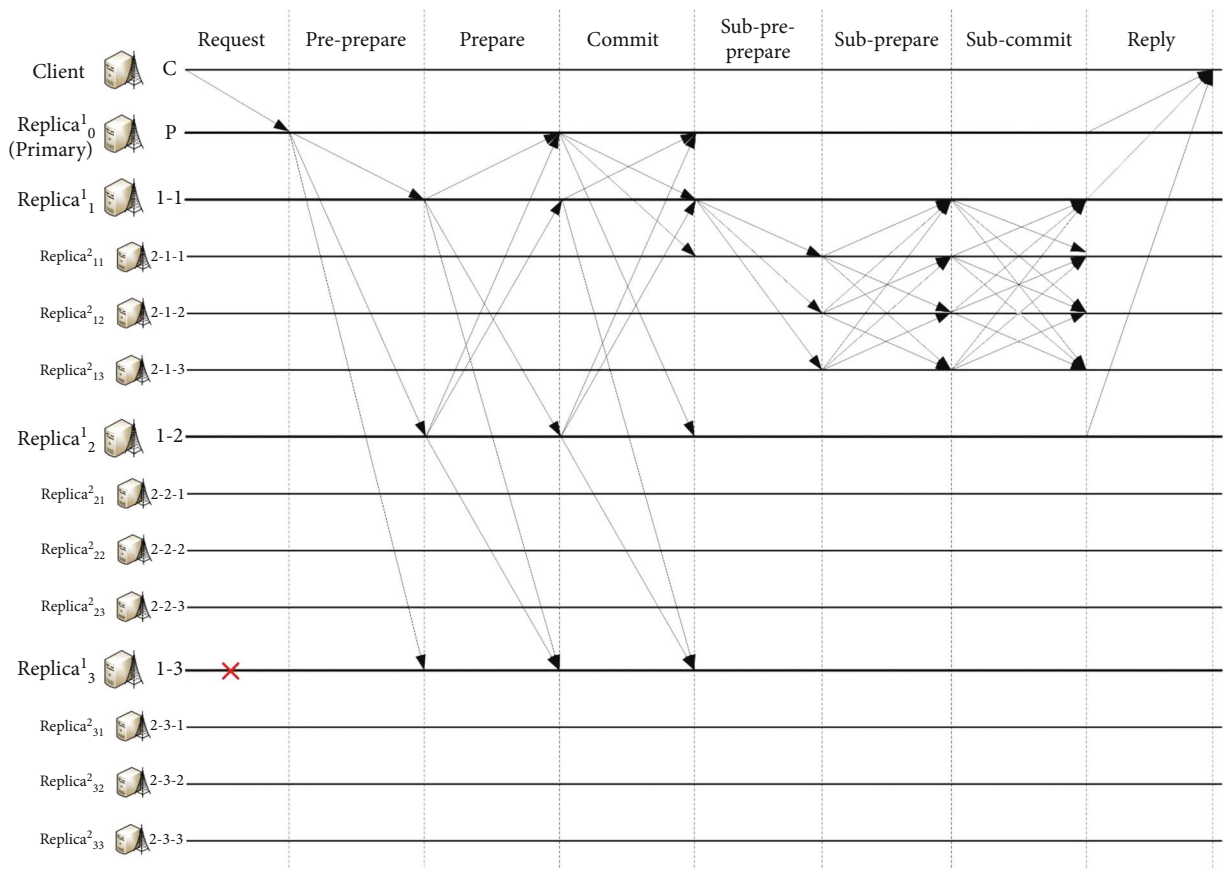

Figure 7: Multilayer PBFT consensus.

node, which is down during the whole consensus process, where the first layer contains $m_1 = 3$ replicas, and each serves as a primary node (Replica$^1_0$) with $m_2 = 3$ sublayer replicas in the second layer. Then, the total number of nodes in the double-layer PBFT consensus is $N = 1 + m_1 + m_1 m_2 = 13$. The pseudocodes of Primary, Replica^1_i, and Replica^2_i for two-layer PBFT consensus are described in Algorithms 1, 2, and 3, respectively. Note that we assume each group in the second layer contain the same number of nodes. A previous study has derived the communication complexity of a double-layer PBFT system [27].

3.2. Scalability of Multilayer PBFT Consensus. **Therem 1.** For a double-layer PBFT consensus process with m_1 replicas in the first layer and m_2 sublayer replicas in

$$C_2 = (m_1 + 1)^2 + m_1(m_2 + 1)^2. \tag{7}$$

Then, what is the optimal network structure that achieve the lowest communication complexity for the double-layer PBFT? The optimization problem can be formulated as

$$\begin{aligned} \text{Problem 1}: \quad & \min C = \min_{m,n} (m_1 + 1)^2 + m_1(m_2 + 1)^2 \\ & \text{s.t.} \quad m_1 \geq 4, m_2 \geq 3 \\ & \quad m_1, m_2 \in Z. \end{aligned} \tag{8}$$

As $N = 1 + m_1 + m_1 m_2$ is total number of nodes and the constrains are $m_1 \geq 4$, $m_2 \geq 3$, Problem 1 is a quadratic integer programming problem and is nonconvex. Substituting $m = N - 1/n + 1$ into Equation (8), we have

$$\begin{aligned} \text{Problem 2}: \quad & \min C = \min_{m,n} (m_1 + 1)^2 + m_1(m_2 + 1)^2 \\ & \text{s.t.} \quad m_1 \geq 4, m_2 \geq 3 \\ & \quad m_1, m_2 \in Z \\ & \quad N = 1 + m_1 + m_1 m_2. \end{aligned} \tag{9}$$

It is an integer programming problem and NP-hard problem. Considering that the feasible solution domain is not very large under the constraint $N = 1 + m_1 + m_1 m_2$, the optimal network structure can be solved by exhaustive searching.

Consider the case of multilayer PBFT, the communication complexity can be derived accordingly.

Therem 2. For a double-layer PBFT consensus process with m_1 replicas in the first layer and m_2 sublayer replicas in each subgroup, the communication complexity C_2 to reach consensus is

$$C_n = \sum_{i=1}^{n} m_{i-2} m_{i-1} (m_i + 1)^2. \tag{10}$$

```
while valid request^1 received=True do
  if client identity authenticated=True then
    m ← n
    multicasts pre−prepare^1 to Primary
  end if
end while
while valid prepare^1 received=True do
  if number of valid prepare^1 ≥ 2f then
    prepare^1=valid
    multicast commit^1 to Replica_i^1
  end if
end while
while valid commit^1 received=True do
  if number of valid commit^1 ≥ 2f then
    commit^1=valid
  end if
end while
while valid reply^1 received=True do
  if number of valid reply^1 ≥ 2f then
    reply client with reply^1
  end if
end while
```

Algorithm 1: Two-layer PBFT consensus: primary.

```
while valid pre-prepare^1 received=True do
  multicasts prepare^1 to Replica_i^1
end while
while valid prepare^1 received=True do
  if number of valid prepare^1 ≥ 2f then
    prepare^1=valid
    multicasts commit^1 to Replica_i^1
  end if
end while
while valid commit^1 received=True do
  if number of valid commit^1 ≥ 2f then
    commit^1=valid
    multicasts sub-pre-prepare^2 to Replica_i^2
  end if
end while
while valid sub-prepare^2 received=True do
  if number of valid sub-prepare^2 ≥ 2f then
    sub-prepare^2=valid
    reply primary with reply^1
  end if
end while
while valid sub-commit^2 received=True do
  if number of valid sub-commit^2 ≥ 2f then
    reply client with reply^1
  end if
end while
```

Algorithm 2: Two-layer PBFT consensus: Replica_i^1.

```
while valid sub-pre-prepare^2 received=True do
  multicasts sub-prepare^2 to Replica_i^2 in the same
  consensus group
end while
while valid sub-prepare^2 received=True do
  if number of valid sub-prepare^2 ≥ 2f then
    sub-prepare^2=valid
    multicasts sub-commit^2 to Replica_i^2 in the same
    consensus group
  end if
end while
while valid sub-commit^2 received=True do
  if number of valid sub-commit^2 ≥ 2f then
    sub-commit^2=valid
    send sub-reply^2 to group leader
  end if
end while
```

Algorithm 3: Two-layer PBFT consensus: Replica_i^2.

Based on the above analysis, we infer that, given the total number of edge computing nodes N, the minimum communication complexity can be achieved when PBFT consensus has the most layers. The PBFT consensus contains the most layers, meaning that each group only contains the least nodes, i.e., 3 nodes. At this time, PBFT consensus has the most layers $X_{\max}$:

$$X_{\max} = \lfloor \log_3(2N+1) \rfloor - 1. \tag{11}$$

Then, the total number of nodes in PBFT system N can be written as

$$N = 1 + 3 + 3^2 + \cdots + 3^{X_{\max}}. \tag{12}$$

Thus, the lowest communication complexity can be expressed as

$$C_{X_{\max}} = \sum_{i=1}^{X_{\max}} 3^{i-1}(3+1)^2 = 16 \times \frac{3^{X_{\max}} - 1}{3-1} = \frac{16N - 16}{3}. \tag{13}$$

It can be seen that the communication complexity C has a linear relationship with the number of edge computing nodes N. Intuitively, it is impossible to reduce the communication complexity without any cost. We can see in the following that the cost is the system security. Consequently, when we increase the layers of PBFT consensus to reduce the communication complexity, the security of PBFT consensus will be degraded at the same time. In order to maintain a basic security performance when we reduce the communication complexity, it is necessary to make a trade-off between communication complexity and system security. We discuss it in the following subsection.

4. Security Analysis of Multilayer PBFT Consensus

4.1. Security of Double-Layer PBFT Consensus. Security of double-layer PBFT is discussed firstly. Assume that the 1st

layer contain m_1 edge computing nodes, and each group in the 2nd layer contains m_2 nodes. The double-layer PBFT can reach consensus under following conditions: the summation of the number of malicious edge computing node i_1 (name as malicious nodes hereinafter) in the 1st layer and the number of groups j_2 of the 2nd layer that does not reach consensus (the head node is normal) should be less than or equal to $\lfloor m_1/3 \rfloor$, i.e., $0 \le i_1 + j_2 \le \lfloor m_1/3 \rfloor$. The 1st layer contains i_1 malicious nodes indicating that there are i groups that cannot reach consensus and there are j_2 groups failing to reach consensus in the 2nd layer meaning the head nodes of these groups are treated as malicious nodes.

If there are i_1 malicious nodes in the 1st layer, it means the number of groups that fails to reach consensus is no more than bm1 $\lfloor m_1/3 \rfloor - i_1$, i.e., $0 \le j_2 \le \lfloor m_1/3 \rfloor - i_1$. That is to say, two necessary conditions constitute the sufficient condition of consensus-reached. In the premise of the 1st layer contains no more of $\lfloor m_1/3 \rfloor$ malicious nodes, the 2nd layer contains no more than $\lfloor m_1/3 \rfloor - i_1$ groups that fail to reach consensus; then the system can reach consensus. We have the following definitions.

(i) Event A1: the 1st layer contains no more than $\lfloor m_1/3 \rfloor$ malicious nodes.

(ii) Event B2: the 2nd layer contains no more than $\lfloor m_1/3 \rfloor - i_1$ group that fails to reach consensus.

$P_{C_2} = P(A_1) \times P(B_2)$, P_{C_2} is the probability of consensus-reached for the double-layer PBFT. We have

$$\begin{aligned} P(A_1) &= \sum_{i_1=0}^{\lfloor m_1/3 \rfloor} C_{m_1}^{i_1} P_f^{i_1} \left(1 - P_f\right)^{(m_1 - i_1)}, \\ P(B_2) &= \sum_{j_2=0}^{\lfloor m_1/3 \rfloor - i_1} C_{m_1 - i_1}^{j_2} P_{g_2}^{j_2} \left(1 - P_{g_2}\right)^{(m_1 - i_1 - j_2)}, \end{aligned} \tag{14}$$

where P_f is the probability that the nodes of the 1st layer are malicious and P_{g_2} is the probability that the group of the 2nd layer fails to reach consensus, which is derived as follows.

If $\lfloor m_2/3 \rfloor + 1 \le i_2 \le m_2$ (the head node of the group in the 2nd layer is normal), the group fails to reach consensus. P_{g_2} can be written as

$$P_{g_2} = \sum_{i_2 = \lfloor m_2/3 \rfloor + 1}^{m_2} C_{m_2}^{i_2} P_f^{i_2} \left(1 - P_f\right)^{(m_2 - i_2)}. \tag{15}$$

The probability of consensus-reached for the double-layer PBFT is derived as

$$\begin{aligned} P_{C_2} = P(A_1) \times P(B_2) = &\sum_{i_1=0}^{\lfloor m_1/3 \rfloor} C_{m_1}^{i_1} P_f^{i_1} \left(1 - P_f\right)^{(m_1 - i_1)} \\ &\cdot \sum_{j_2=0}^{\lfloor m_1/3 \rfloor - i_1} C_{m_1 - i_1}^{j_2} P_{g_2}^{j_2} \left(1 - P_{g_2}\right)^{(m_1 - i_1 - j_2)}. \end{aligned} \tag{16}$$

4.2. Security of Multilayer PBFT Consensus. Next, we analyze the security performance of the three-layer PBFT and further derive the security performance of X-layer PBFT. Please note that the derivation of security performance of the three-layer PBFT has some differences with that of the double-layer PBFT. The number of nodes in the 1st layer is assumed to be m_1, and the numbers of nodes in the group of 2nd and 3rd layer are denoted as m_2 and m_3, respectively. The number of malicious nodes in the 1st layer is assumed to be i_1, and the numbers of malicious nodes in the group of 2nd and 3rd layer are denoted as i_2 and i_3, respectively.

The numbers of groups that do not reach consensus in the 2nd/3rd layer are assumed to be j_2 and j_3 (the head node is normal). We can infer that the consensus is reached or not is determined by the number of malicious node in the 1st layer i_1 and the number of groups that does not reach consensus in the 2nd layer j_2, i.e., $0 \le i_1 + j_2 \le \lfloor m_1/3 \rfloor$. Let $P(A_1)$ denote the probability that the number of malicious nodes in the 1st layer i_1 less than $\lfloor m_1/3 \rfloor$ and $P(B_2)$ represent the probability that the number of groups have not reached consensus in the 2nd layer j_2 less than $0 \le i_1 + j_2 \le \lfloor m_1/3 \rfloor - i_1$. Then, we have $P_{C_3} = P(A_1) \times P(B_2)$, where P_{C_3} is the probability of three-layer PBFT reaching consensus. We can derive

$$\begin{aligned} P(A_1) &= \sum_{i_1=0}^{\lfloor m_1/3 \rfloor} C_{m_1}^{i_1} P_f^{i_1} \left(1 - P_f\right)^{(m_1 - i_1)}, \\ P(B_2) &= \sum_{j_2=0}^{\lfloor m_1/3 \rfloor - i_1} C_{m_1 - i_1}^{j_2} P_{g_2}^{j_2} \left(1 - P_{g_2}\right)^{(m_1 - i_1 - j_2)}, \end{aligned} \tag{17}$$

where P_{g_2} is the probability that the group in the 2nd layer fails to reach consensus. Given the head node is normal, how does the group fail to reach consensus? Considering that there are m_2 nodes and i_2 malicious nodes in the 2nd layer and there are j_3 groups in the 3rd layer failing to reach consensus, when $\lfloor m_2/3 \rfloor + 1 \le i_2 + j_3 \le m_2$, the 2nd layer cannot reach consensus. We have

$$P_{g_2} = P(A_2) \times P\left(\overline{B_3}\right) + P\left(\overline{A_2}\right) = 1 - P(A_2)P(B_3). \tag{18}$$

Let $P(\overline{A_2})$ denote the probability that $i_2 \ge \lfloor m_2/3 \rfloor + 1$ and $P(\overline{B_3})$ denote the probability that $j_3 \ge \lfloor m_2/3 \rfloor + 1 - i_2$. Equation (18) indicates that, except for $i_2 \le \lfloor m_2/3 \rfloor$ and $j_3 \le \lfloor m_2/3 \rfloor - i_2$, the groups in the 2nd layer always cannot reach consensus. We have

$$\begin{aligned} P(A_2) &= \sum_{i_2=0}^{\lfloor m_2/3 \rfloor} C_{m_2}^{i_2} P_f^{i_2} \left(1 - P_f\right)^{(m_2 - i_2)}, \\ P(B_3) &= \sum_{j_3=0}^{\lfloor m_2/3 \rfloor - i_2} C_{m_2 - i_2}^{j_3} P_{g_3}^{j_3} \left(1 - P_{g_3}\right)^{(m_2 - i_2 - j_3)}, \end{aligned} \tag{19}$$

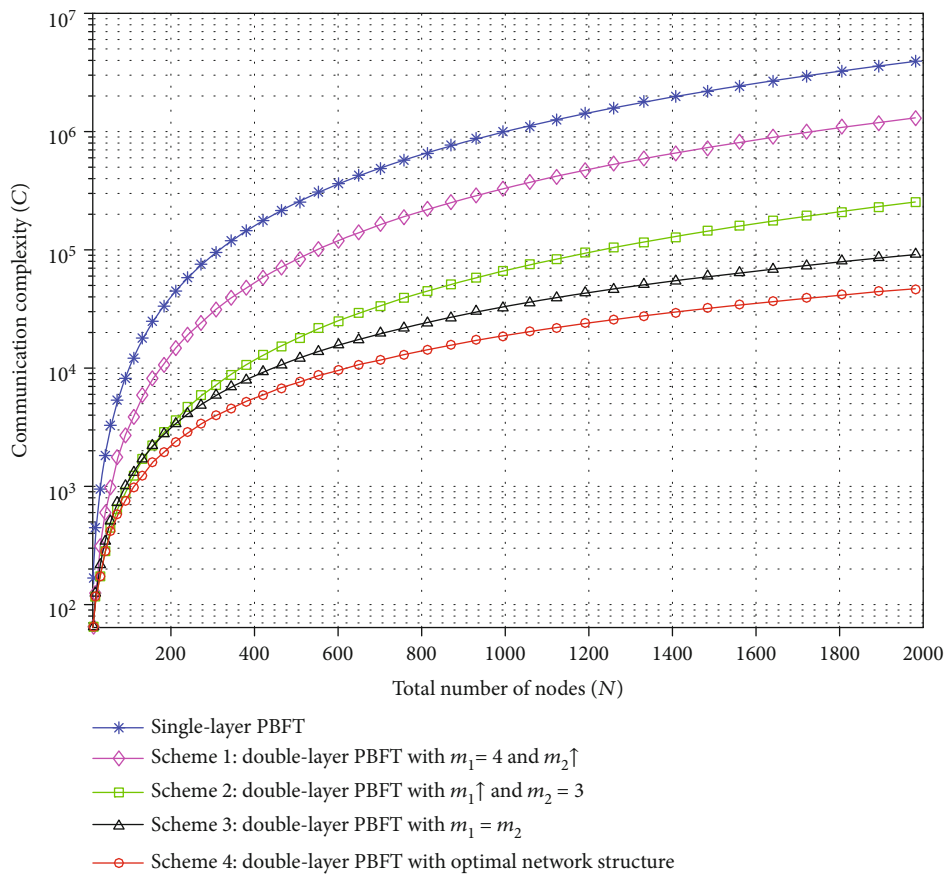

Figure 8: Communication complexity of single-layer and double-layer PBFT.

where P_{g_3} is the probability that the group in the 3rd layer fails to reach consensus. Similarly, we have

$$P_{g_3} = \sum_{i_3=\lfloor m_3/3 \rfloor+1}^{m_3} C_{m_3}^{i_3} P_f^{i_3} \left(1-P_f\right)^{(m_3-i_3)}, \tag{20}$$

indicating that the group in the 3rd layer cannot reach consensus when $\lfloor m_3/3 \rfloor + 1 \le i_3 \le m_3$.

Substituting (17)–(20) into $P_{C_3} = P(A_1) \times P(B_2)$, we can derive the probability of consensus-reached of three-layer PBFT. Then, the probability of consensus-reached of the X-layer PBFT can be derived as follows.

The numbers of nodes in the 1~X-th layer are assumed to be $m_1, \cdots, m_k, \cdots, m_X$. The numbers of malicious nodes in the 1~X-th layer are assumed to be $i_1, \cdots, i_k, \cdots, i_X$. The numbers of groups that do not reach consensus in the 2~X layer are denoted as $j_2, \cdots, j_k, \cdots, j_X$ (the head node is normal). The security of X-layer PBFT is

$$\begin{aligned} P_{C_X} = P(A_1) \times P(B_2) = &\sum_{i_1=0}^{\lfloor m_1/3 \rfloor} C_{m_1}^{i_1} P_f^{i_1} \left(1-P_f\right)^{(m_1-i_1)} \\ &\times \sum_{j_2=0}^{\lfloor m_1/3 \rfloor - i_1} C_{m_1-i_1}^{j_2} P_{g_k}^{j_2} \left(1-P_{g_k}\right)^{(m_1-i_1-j_2)}, , \end{aligned} \tag{21}$$

where P_{g_k} is given by

$$P_{g_k} = \begin{cases} \sum_{i_2=\lfloor m_2/3 \rfloor+1}^{m_2} C_{m_2}^{i_2} P_f^{i_2} \left(1-P_f\right)^{(m_2-i_2)}, & X=2, k=2, \\ \sum_{i_k=0}^{\lfloor m_k/3 \rfloor} C_{m_k}^{i_k} P_f^{i_k} \left(1-P_f\right)^{(m_k-i_k)} \times \sum_{j_{k+1}=\lfloor m_k/3 \rfloor+1-i_k}^{m_k} C_{m_k-i_k}^{j_{k+1}} P_{g_{k+1}}^{j_{k+1}} \left(1-P_{g_{k+1}}\right)^{(m_k-i_k-j_{k+1})} + \left(1-\sum_{i_k=0}^{\lfloor m_k/3 \rfloor} C_{m_k}^{i_k} P_f^{i_k} \left(1-P_f\right)^{(m_k-i_k)}\right), & X \ge 3, 2 \le k \le X-1, \\ \sum_{i_X=\lfloor m_X/3 \rfloor+1}^{m_X} C_{m_X}^{i_X} P_f^{i_X} \left(1-P_f\right)^{(m_X-i_X)}, & X \ge 3, k=X. \end{cases} \tag{22}$$

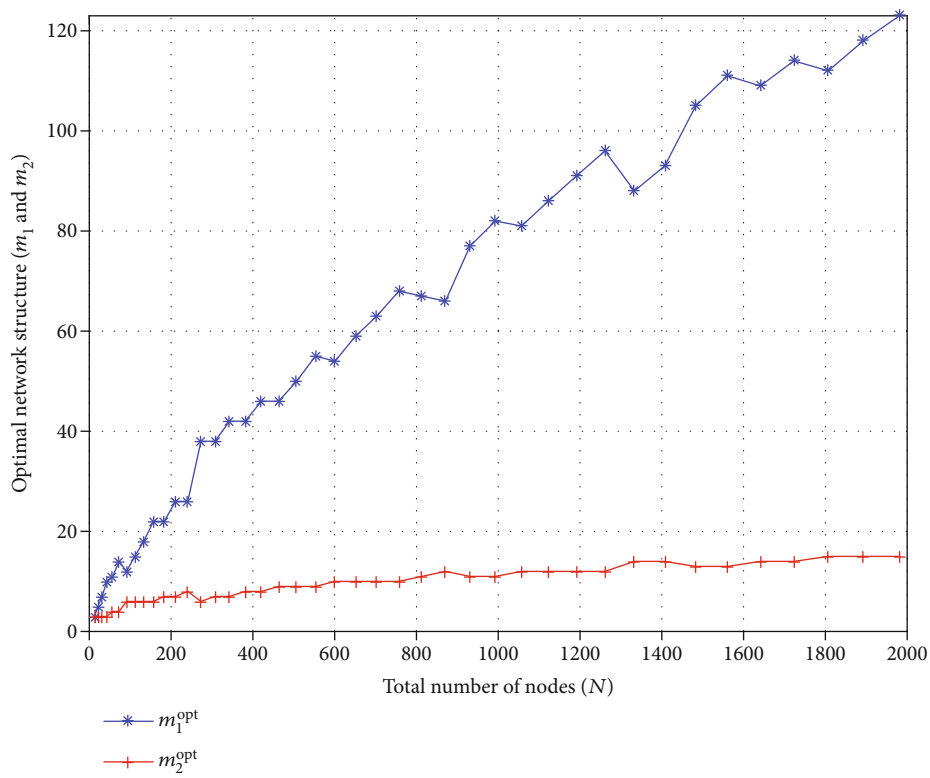

Figure 9: Optimal network structure of double-layer PBFT.

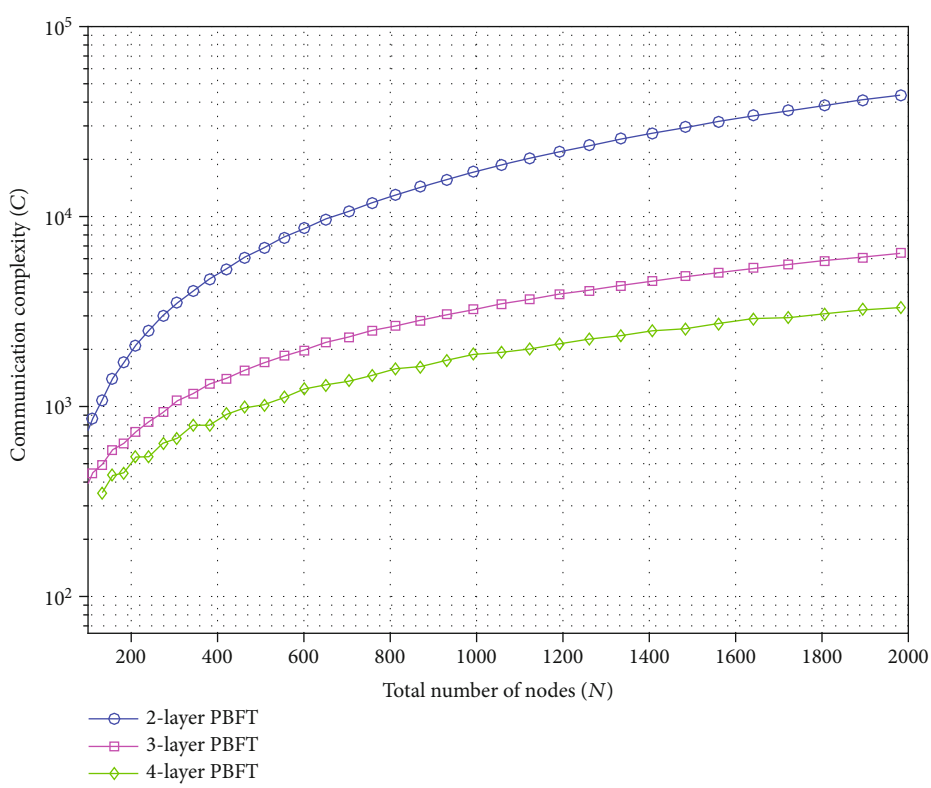

Figure 10: Communication complexity comparison of multi-layer PBFT under optimal network structure.

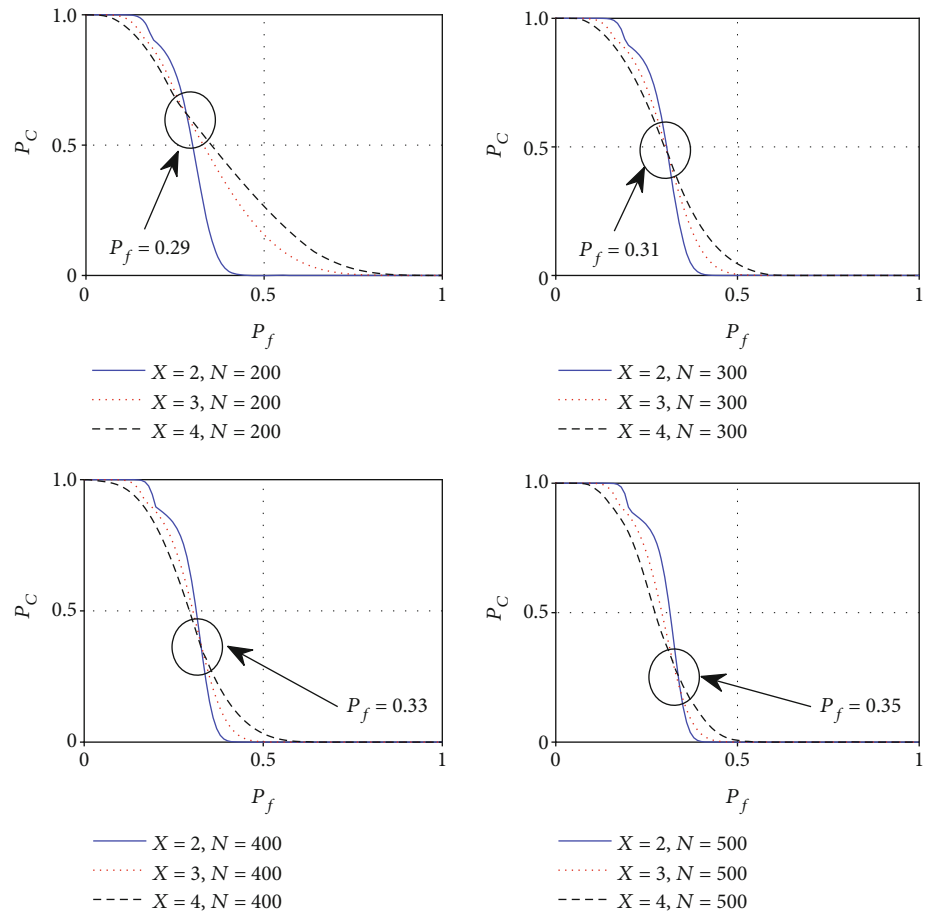

Figure 11: Security performance of multi-layer PBFT under given number of nodes.

5. Scalability Evaluations and Security Assessments

In this section, a scalability evaluation of the proposed multilayer PBFT consensus is firstly given. After that, some security assessments are provided to show that we should reasonably design the structure of multilayer PBFT consensus for the blockchain-empowered HF spectrum management, in order to tradeoff between scalability and security.

5.1. Scalability Evaluations of Multilayer PBFT Consensus. In this subsection, the scalability performance of multilayer PBFT consensus is demonstrated. Intuitively, the poor scalability of the PBFT consensus mainly comes from the sharply increasing of communication complexity as the number of nodes increases. Consequently, the scalability of the PBFT consensus will be greatly improved with the reduction of communication complexity.

In *Evaluation 1*, four schemes are demonstrated in Figure 8 to show the improvement in communication complexity of double-layer PBFT. In *Scheme 1*, double-layer PBFT, m_1 keeps the minimum ($m_1 = 4$, include one head node) and m_2 increases linearly. In *Scheme 2*, double-layer PBFT, m_1 increases linearly and m_2 keeps the minimum ($m_2 = 3$). In *Scheme 3*, double-layer PBFT with $m_1 = m_2$. In *Scheme 4*, double-layer PBFT with an optimal network structure achieves the lowest communication complexity. Evaluations are performed under the constraint of $N = 1 + m_1 + m_1 m_2$. Obviously, the communication complexity of double-layer PBFT is significantly reduced compared with that of single-layer PBFT. Secondly, the communication complexity of *Scheme 2* further reduced compared with that of *Scheme 1*, indicating that we should first increase the nodes in the 1st layer, i.e., m_1, rather than the nodes in each group of the 2nd layer, i.e., m_2. Thirdly, compared with the communication complexity of single-layer PBFT, the communication complexities of *Scheme 3* and *Scheme 4* reduce by at least 1 order of magnitude. Fourthly, the communication complexity of *Scheme 3* is relatively close to that of *Scheme 4*, indicating that $m_1 = m_2$ is a suboptimal solution when the optimal network structure cannot be obtained.

The optimal network structure of double-layer PBFT when the lowest communication complexity achieved is shown in Figure 9. It can be seen that as the total number of nodes increases, the number of nodes in the 1st layer, i.e., m_1^{opt}, increases almost linearly, while the number of nodes in each group of the 2nd layer, i.e., m_2^{opt}, hardly increases. From (6), we can see that the communication complexity of double-layer PBFT, i.e., C_2, has a linear relationship with m_1^2 and $m_1 m_2^2$. Therefore, for the double-layer PBFT, when

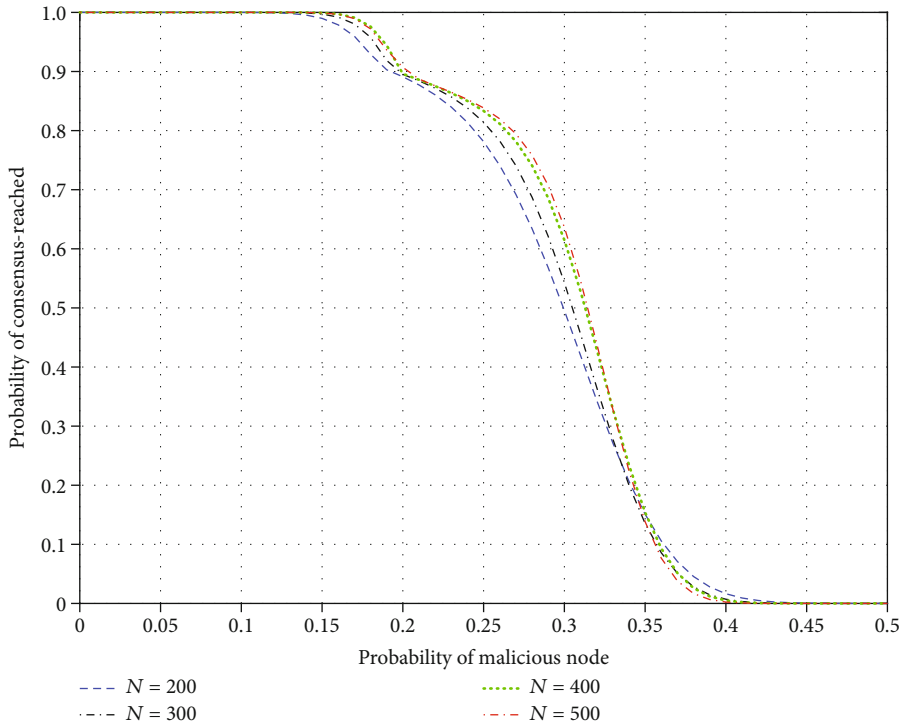

Figure 12: Security performance of double-layer PBFT under different N.

the total number of nodes increases, we should firstly increase the nodes in the 1st layer, i.e., m_1, rather than increase the nodes in the 2nd layer, i.e., m_2.

Figure 10 shows the lowest communication complexity under different layers PBFT with the variation of the number of nodes, which further confirms the conclusion that the more layers in PBFT are, the lower of communication complexity is.

5.2. Security Assessment of Multilayer PBFT Consensus. Given the total number of nodes $N = 100$, the security performance of X-layer PBFT ($X = 2$, $X = 3$, and $X = 4$) is illustrated in Figure 11. It can be seen that when P_f is relatively low, the probabilities of consensus-reached decrease with P_f. When P_f is relatively high, the probabilities of consensus-reached increase with P_f instead, which indicates that increasing PBFT layers does not always bring down the security performance. When P_f is relatively high, we have $P_{C_4} > P_{C_3} > P_{C_2}$. However, the security performance decreases sharply and becomes very poor at that time, and it is almost impossible to reach consensus for the multilayer PBFT. Secondly, with the increasing of N, the critical point, i.e., the intersection point of P_{C_2}, P_{C_3}, and P_{C_4}, gradually moves forward and indicates that the increasing of N will reduce the security performance.

The security performances of the double-layer PBFT under different number of nodes N are illustrated in Figure 12, given $N = 200/300/400/500$. It can be seen that when $P_f \leq 0.34$, increasing the number of nodes will improve the security performance (probability of consensus-reached). On the contrary, when $P_f > 0.34$, increasing the number of nodes will reduce the security performance (probability of consensus-reached).

Consequently, in order to greatly reduce the communication complexity and obtain an acceptable security performance, too many layers are unpractical. A 2- to 4-layer PBFT is sufficient to bring communication complexity down and also achieve an acceptable security performance.

6. Conclusion

In this article, a consortium blockchain-empowered HF spectrum management is exploited to improve the deteriorating HF electromagnetic environment; massive personal HF devices are organized around the preselected nodes to monitor and share HF data through PBFT protocol. To address the scalability problem, a multilayer PBFT consensus protocol is presented. Scalability evaluations shows that increasing the layers of PBFT greatly reduce the communication complexity. Security assessments illustrate that the security performance does not always decrease with the increasing of the layers of PBFT, but fewer layers indeed guarantee a better security performance. Tradeoff has been made between the communication complexity and security performance, a 2- to 4-layer PBFT is considered sufficient to bring the communication complexity down and also achieve an acceptable security performance. In a future work, it is interesting to extend the utilization of blockchain-empowered HF spectrum management for better improving HF electromagnetic environment, such as deployment optimization of edge computing nodes and spectrum strategy inference under energy constraint.

Data Availability

The supporting data are not yet open to public access.

Conflicts of Interest

The authors declare that they have no conflicts of interest.

References

[1] M. Shafi, A. F. Molisch, P. J. Smith et al., "5G: a tutorial overview of standards, trials, challenges, deployment, and practice," *IEEE Journal on Selected Areas in Communications*, vol. 35, no. 6, pp. 1201–1221, 2017.

[2] J. Gubbi, R. Buyya, S. Marusic, and M. Palaniswami, "Internet of things (IoT): a vision, architectural elements, and future directions," *Future Generation Computer System*, vol. 29, no. 7, pp. 1645–1660, 2013.

[3] ITU-R, "Technical and operational principles for HF sky-wave communication stations to improve the man-made noise HF environment," Question ITU-R 258/5, 2019.

[4] ITU-R, "Radio regulations," *Radio Regulations-Articles*, vol. 1, 2016.

[5] F. Tschorsch and B. Scheuermann, "Bitcoin and beyond: a technical survey on decentralized digital currencies," *IEEE Communications Surveys & Tutorials*, vol. 18, no. 3, pp. 2084–2123, 2016.

[6] A. Dorri, M. Steger, S. S. Kanhere, and R. Jurdak, "BlockChain: a distributed solution to automotive security and privacy," *IEEE Communications Magazine*, vol. 55, no. 12, pp. 119–125, 2017.

[7] T. Salman, M. Zolanvari, A. Erbad, R. Jain, and M. Samaka, "Security services using blockchains: a state of the art survey," *IEEE Communications Surveys & Tutorials*, vol. 21, no. 1, pp. 858–880, 2018.

[8] J. Rosenworcel, *Remarks of Commissioner Jessica Rosenworcel Mobile World Congress Americas*, Mobile World Congress Americas, Los Angeles, California, 2018.

[9] K. Kotobi and S. G. Bilen, "Secure blockchains for dynamic spectrum access: a decentralized database in moving cognitive radio networks enhances security and user access," *IEEE Vehicular Technology Magazine*, vol. 13, no. 1, pp. 32–39, 2018.

[10] Y. Pei, S. Hu, F. Zhong, D. Niyato, and Y. C. Liang, "Blockchain-enabled dynamic spectrum access: cooperative spectrum sensing, access and mining," in *2019 IEEE Global Communications Conference (GLOBECOM)*, pp. 1–6, Waikoloa, HI, USA, 2019.

[11] M. B. H. Weiss, K. Werbach, D. C. Sicker, and C. E. C. Bastidas, "On the application of blockchains to spectrum management," *IEEE Transactions on Cognitive Communications and Networking*, vol. 5, no. 2, pp. 193–205, 2019.

[12] M. Cao, L. Zhang, and B. Cao, "Toward on-device federated learning: a direct acyclic graph-based blockchain approach," *IEEE Transactions on Neural Networks and Learning Systems*, 2021.

[13] B. Shang, V. Marojevic, Y. Yi, A. S. Abdalla, and L. Liu, "Spectrum sharing for UAV communications: spatial spectrum sensing and open issues," *IEEE Vehicular Technology Magazine*, vol. 15, no. 2, pp. 104–112, 2020.

[14] J. Qiu, D. Grace, G. Ding, J. Yao, and Q. Wu, "Blockchain-based secure spectrum trading for unmanned-aerial-vehicle-assisted cellular networks: an operator's perspective," *IEEE Internet of Things Journal*, vol. 7, no. 1, pp. 451–466, 2020.

[15] T. Maksymyuk, J. Gazda, M. Volosin et al., "Blockchain-empowered framework for decentralized network management in 6G," *IEEE Communications Magazine*, vol. 58, no. 9, pp. 86–92, 2020.

[16] Z. Zhou, X. Chen, Y. Zhang, and S. Mumtaz, "Blockchain-empowered secure spectrum sharing for 5G heterogeneous networks," *IEEE Network*, vol. 34, no. 1, pp. 24–31, 2020.

[17] P. Gorla, V. Chamola, V. Hassija, and N. Ansari, "Blockchain based framework for modeling and evaluating 5G spectrum sharing," *IEEE Network*, vol. 35, no. 2, pp. 229–235, 2021.

[18] G. Rathee, F. Ahmad, F. Kurugollu, M. A. Azad, R. Iqbal, and M. Imran, "CRT-BIoV: a cognitive radio technique for blockchain-enabled internet of vehicles," *IEEE Transactions on Intelligent Transportation Systems*, vol. 22, no. 7, pp. 4005–4015, 2021.

[19] R. Zhu, H. Liu, X. Liu, S. Wan, and W. Hu, "Contract-theory-based secure spectrum sharing framework in internet of vehicles," *IEEE Consumer Electronics Magazine*, 2021.

[20] M. A. Ferrag, M. Derdour, M. Mukherjee, A. Derhab, L. Maglaras, and H. Janicke, "Blockchain technologies for the Internet of Things: research issues and challenges," *IEEE Internet of Things Journal*, vol. 6, no. 2, pp. 2188–2204, 2019.

[21] B. Cao, Z. Zhang, D. Feng et al., "Performance analysis and comparison of PoW, PoS and DAG based blockchains," *Digital Communications and Networks*, vol. 6, no. 4, pp. 480–485, 2020.

[22] D. Puthal, N. Malik, S. P. Mohanty, E. Kougianos, and G. Das, "Everything you wanted to know about the blockchain: its promise, components, processes, and problems," *IEEE Consumer Electronics Magazine*, vol. 7, no. 4, pp. 6–14, 2018.

[23] Y. Li, B. Cao, M. Peng, L. Zhang, D. Feng, and J. Yu, "Direct acyclic graph-based ledger for Internet of Things: performance and security analysis," *IEEE/ACM Transactions on Networking*, vol. 28, no. 4, pp. 1643–1656, 2020.

[24] Z. Li, J. Kang, R. Yu, D. Ye, Q. Deng, and Y. Zhang, "Consortium blockchain for secure energy trading in industrial Internet of Things," *IEEE Transactions on Industrial Informatics*, vol. 14, no. 8, pp. 3690–3700, 2018.

[25] M. Castro and B. Liskov, "Practical byzantine fault tolerance," in *Proc. of the 3rd Symp. Oper. Sys. Design Imple*, New Orleans, USA, 1999.

[26] M. Castro and B. Liskov, "Practical byzantine fault tolerance and proactive recovery," *ACM Transactions on Computer Systems (TOCS)*, vol. 20, no. 4, pp. 398–461, 2002.

[27] W. Li, C. Feng, L. Zhang, H. Xu, B. Cao, and M. A. Imran, "A scalable multi-layer PBFT consensus for blockchain," *IEEE Transactions on Parallel and Distributed Systems*, vol. 32, no. 5, pp. 1146–1160, 2021.

[28] W. Lv, X. Zhou, and Z. Yuan, "Design of tree topology based byzantine fault tolerance system," *The Journal of Communication*, vol. 38, no. Z2, pp. 143–150, 2017.

[29] Q. Wu, G. Ding, Z. Du, Y. Sun, M. Jo, and A. V. Vasilakos, "A cloud-based architecture for the internet of spectrum devices over future wireless networks," *IEEE Access*, vol. 4, pp. 2854–2862, 2016.

[30] Z. Xiong, Y. Zhang, D. Niyato, P. Wang, and Z. Han, "When mobile blockchain meets edge computing," *IEEE Communications Magazine*, vol. 56, no. 8, pp. 33–39, 2018.

[31] Y. Wu, J. Zheng, K. Guo, L. P. Qian, X. Shen, and Y. Cai, "Joint traffic scheduling and resource allocations for traffic offloading with secrecy-provisioning," *IEEE Transactions on Vehicular Technology*, vol. 66, no. 9, pp. 8315–8332, 2017.

[32] Y. Mao, C. You, J. Zhang, K. Huang, and K. B. Letaief, "A survey on mobile edge computing: the communication perspective," *IEEE Communications Surveys & Tutorials*, vol. 19, no. 4, pp. 2322–2358, 2017.

[33] N. Abbas, Y. Zhang, A. Taherkordi, and T. Skeie, "Mobile edge computing: a survey," *IEEE Internet of Things Journal*, vol. 5, no. 1, pp. 450–465, 2018.

[34] R. Yang, F. R. Yu, P. Si, Z. Yang, and Y. Zhang, "Integrated blockchain and edge computing systems: a survey, some research issues and challenges," *IEEE Communications Surveys & Tutorials*, vol. 21, no. 2, pp. 1508–1532, 2019.

[35] ITU-R SG01, *Handbook: Spectrum Monitoring*, ITU Publisher, Geneva, 2011.

[36] G. Ding, Y. Jiao, J. Wang et al., "Spectrum inference in cognitive radio networks: algorithms and applications," *IEEE Communications Surveys & Tutorials*, vol. 20, no. 1, pp. 150–182, 2017.

[37] N. Z. Aitzhan and D. Svetinovic, "Security and privacy in decentralized energy trading through multi-signatures, blockchain and anonymous messaging streams," *IEEE Transactions on Dependable and Secure Computing*, vol. 15, no. 5, pp. 840–852, 2018.

[38] M. B. Yassein, S. Aljawarneh, E. Qawasmeh, W. Mardini, and Y. Khamayseh, "Comprehensive study of symmetric key and asymmetric key encryption algorithms," in *2017 International Conference on Engineering and Technology (ICET)*, pp. 1–7, Antalya, Turkey, 2017.

[39] H. Gilbert and H. Handschuh, "Security analysis of SHA-256 and sisters," in *Selected Areas in Cryptography, SAC*, vol. 3006 of Lecture Notes in Computer Science, Springer, Berlin, Heidelberg, 2003.

Hindawi
Wireless Communications and Mobile Computing
Volume 2022, Article ID 9110292, 10 pages
https://doi.org/10.1155/2022/9110292

Research Article

Research on the Detection Technique of Situation Elements in Obscure Overlapping Scenes

Jinlong Liu and Kangda Cheng

Harbin Institute of Technology, Harbin 150000, China

Correspondence should be addressed to Jinlong Liu; yq20@hit.edu.cn

Received 17 February 2022; Accepted 14 March 2022; Published 11 April 2022

Academic Editor: Mingqian Liu

In recent years, some scholars have proposed to apply single-stage target detection algorithms such as YOLO (You Only Look Once) to situational element detection, but the traditional YOLO algorithm is to treat the target detection process as a regression problem, which cannot distinguish well between overlapping objects and has defects such as less accurate bounding boxes and hard to distinguish objects from the background, and it is difficult to cope with problems such as the higher overlap of targets to be detected and stronger target camouflage ability in obscured overlapping scenes. In this paper, we propose to add the attention module CBAM to the backbone network of the YOLOv3 model, to construct a SEDNet with high accuracy and good robustness for situational element detection, and to apply it to the situational element detection in occlusion overlapping scenes. We use SEDNet to classify and localize ten elemental targets, respectively. The analysis of experimental results shows that the SEDNet target detection model can complete element detection in complex environments with strong target camouflage, achieve end-to-end detection, and lay the technical foundation for the formation of complete situational awareness.

1. Introduction

Situational awareness was first used to study pilots' awareness and understanding of their flight environment and flight status and to help train pilots to develop the ability to judge and react correctly to current and future flight situations over time [1]. Later, it was widely used in decision-making, network information security, system supervision, etc. In 1995, Endsley defined situational awareness as the awareness of situational elements within a certain time and space environment and the understanding of the information obtained, which leads to the formation of a prediction of the state of these situational elements at the next moment [2]. This definition divides situational awareness into three phases, awareness, understanding, and prediction, which are shown schematically in Figure 1. Among them, situational element detection is the basis for forming situational awareness.

The traditional target detection network is difficult to accomplish the task of situational target detection in the context of high overlap of targets to be detected and strong target camouflage capability and is not applicable to the problem of situational awareness in obscured overlapping scenarios.

In 2019, Peng et al. [3] introduced the YOLO (You Only Look Once) algorithm to situational element identification and localization and achieved better results. However, because the YOLO algorithm treats the target detection process as a regression problem, it cannot distinguish overlapping objects well and suffers from deficiencies such as the lack of accurate bounding boxes and difficulty in distinguishing objects from the background, which makes it difficult to cope with the problems of high overlap of detected targets and strong camouflage of targets to be detected in obscured overlapping scenarios [4].

Attention mechanism may be the key to solving this problem. Woo et al. [5] showed that attention mechanisms could widely and effectively improve the performance of convolutional neural networks. Chengji et al. [6] introduced the attention mechanism into the YOLO model and

demonstrated that it could effectively improve the detection accuracy of the YOLO model. This paper conducts an exploratory study on this topic. This paper first describes the detection principle of YOLOv3 and its network structure, then describes the principle and structure of an attention module, then proposes a target detection network SEDNet based on the combination of YOLOv3 and CBAM attention module specifically for solving the situational element detection problem, and improves the loss function and training strategy. Finally, this paper constructs a SA situational element dataset and conducts training and validation experiments on the SA dataset. The experimental results show that SEDNet can complete the identification and localization of situational elements in real time effectively, which provides effective technical support to solve the situational element detection problem.

2. Related Works

2.1. The Network Structure of Baseline Model YOLOv3. YOLO [7] is a single-stage target detection model that treats the target detection problem as a regression problem with target region prediction and category prediction. YOLO enables real-time, high-precision detection that identifies the location of objects in an image and their categories at a glance. The method uses a single neural network to directly predict the bounding box and category probability of a target, which enables end-to-end target detection. At the same time, this method is much faster than other target detection methods (e.g., Fast R-CNN) and is more suitable for obscured overlapping scenarios.

Figure 2 gives a schematic diagram of the YOLO target detection model. As can be seen from the figure, when the YOLO model performs target detection, the original image is first divided into cells, and if the center point of the target to be detected is in a cell, then that cell is responsible for detecting this target. Each cell needs to detect a bounding box and a category probability. Each bounding box contains the information of x, y, w, and h and confidence, which are the center coordinates of the bounding box and are the length and width of the bounding box, respectively, and the confidence indicates the probability of predicting the target category and the accuracy of the target at that location. Based on the target categories in each cell and the corresponding bounding information, the location information, center coordinates, length, and width of the whole segmented area where each target is located can be calculated. The target windows with low probability are then removed according to the threshold value, and the redundant windows are removed by nonmaximal suppression, leaving the detection results.

The network structure of YOLOv3 [8] is mainly composed of two parts, Darknet-53 feature extraction network, and feature pyramid, with 75 convolutional layers and 3 detection layers, and its network structure is shown in Figure 3, where Inputs denotes input images, Conv2D denotes performing a 2D convolution operation, Residual Block denotes residual module Concat denotes concatenating the data, and UpSampling2D denotes performing an upsampling operation opposite to the pooling operation.

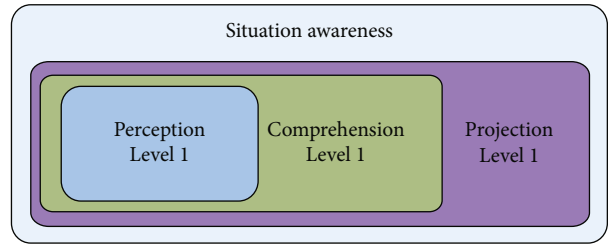

Figure 1: Schematic of the Endsley situational awareness model.

As shown in Figure 3, YOLOv3 uses Darknet53 as its backbone feature extraction network, whose main feature is the residual network, which is easy to optimize and can improve the accuracy by increasing the network depth, and its internal residual blocks use jump connections to alleviate the gradient disappearance problem caused by increasing the network depth in deep neural networks. Each convolution part of Darknet53 uses the unique DarknetConv2D structure and performs L2 regularization operation at each convolution and batch normalization and Leaky ReLU operation after completing the convolution. The mathematical expression of Leaky ReLU is shown.

$$y_i = \begin{cases} x_i, & \text{if } x_i \geq 0, \\ \dfrac{x_i}{\alpha_i}, & \text{if } x_i < 0. \end{cases} \tag{1}$$

In the YOLOv3 target detection model, the image input is first subjected to feature extraction through a five times downsampling process. YOLOv3 uses multiscale prediction to extract three feature layers for target detection, which are located in the middle layer, lower-middle layer, and bottom layer of the Darknet53. After completing the feature layer extraction, the three feature layers are processed by five convolutions, and the processed data are used to output the prediction results corresponding to this feature layer on the one hand and are used for upsampling after the deconvolution operation with UmSampling2d on the other hand, and the upsampled results are stacked with another feature layer to construct a feature pyramid, which can be used for multiscale feature extraction to obtain more effective features.

2.2. The Loss Function of Baseline Model YOLOv3. The loss function of YOLOv3 can be divided into three parts: coordinate error loss function, IoU error loss function, and classification error loss function.

$$L = L_1 + L_2 + L_3, \tag{2}$$

where L denotes the total loss function in the training process, L_1 denotes the coordinate error loss function, L_2 denotes the IoU error loss function, and L_3 denotes the

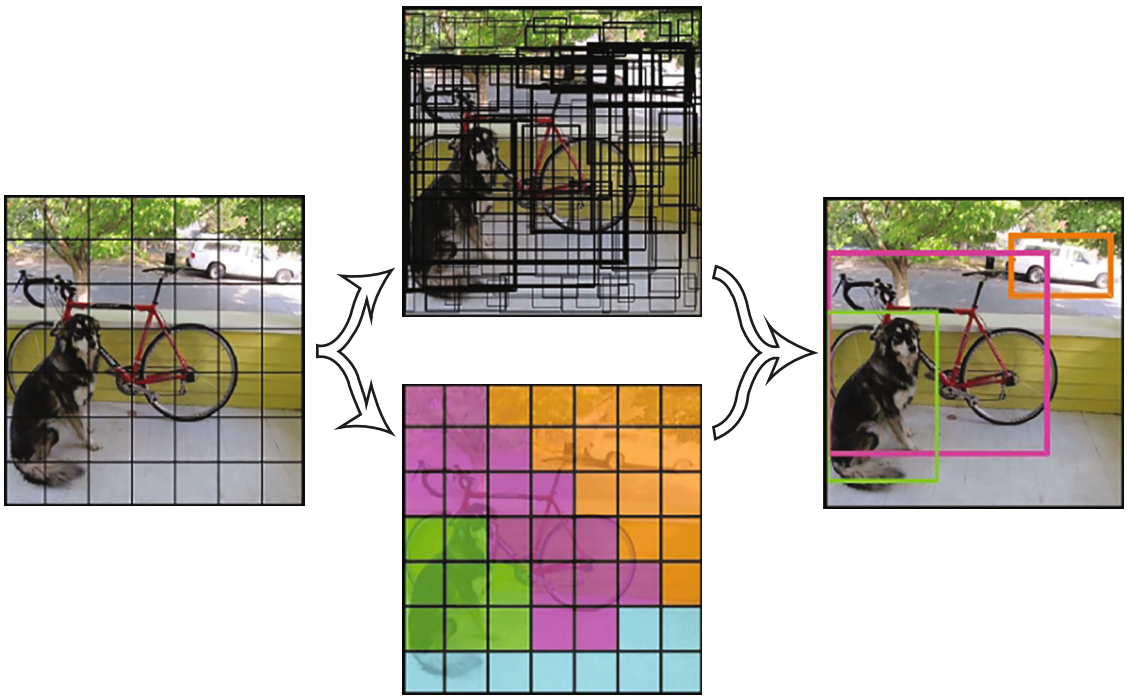

Figure 2: YOLO target detection model detection process schematic.

classification error loss function. L_1 can be calculated using

$$L_1 = \lambda_{\text{coord}} \sum_{i=0}^{s^2} \sum_{j=0}^{B} I_{ij}^{\text{obj}} \left[(x_i - x_i)^2 + (y_i - y_i)^2 \right] + \lambda_{\text{coord}} \sum_{i=0}^{S^2} \sum_{j=0}^{B} I_{ij}^{\text{obj}} \left[\left(\sqrt{w_i - \sqrt{w_i}} \right)^2 + \left(\sqrt{h_i - \sqrt{h_i}} \right)^2 \right], \tag{3}$$

where x_i, y_i, w_i, and h_i are the coordinate values and target proportions of the targets in the prediction frame, respectively, and $\hat{x}_i, \hat{y}_i$, $\hat{w}_i$, and $\hat{h}_i$ denote the coordinate values and target proportions of the targets in the actual frame, where $\lambda_{\text{coord}} = 0.5$; I_{ij}^{obj} indicates that the target has no target in the prediction frame of the ith raster. The square root of w and h is used to reduce the effect of w and h on the size targets.

IoU is the intersection-over-union of the prediction frame and the label frame, and the IoU error loss function L_2 can be calculated using

$$L_2 = \sum_{i=0}^{S^2} \sum_{j=0}^{B} I_{ij}^{\text{abj}} (C_i - C_i)^2 + \lambda_{\text{noobj}} \sum_{i=0}^{S^2} \sum_{j=0}^{B} I_{ij}^{\text{noobj}} (C_i - C_i)^2, \tag{4}$$

where C is the set of all categories, c is an element in C that denotes a specific category, and $Pi(C)$ denotes the confidence probability of the category on the ith cell. In addition, for the specificity of images, YOLOv3 adds two data scaling methods, scaling and rotation-based contrast enhancement and Gaussian white noise, which can mitigate the overfitting problem.

In the detection process, the image is passed through the YOLOv3 target detection model to obtain the feature map, and each position on the feature map is used to identify the attributes and positions of the targets through prediction frames with different aspect ratios and scales. The prediction frame is a clustering selection of regions with real labeled targets in the training set, and the dimension of the cluster center is selected as the dimension of the prediction frame.

YOLOv3 can perform target detection in real time, but the traditional YOLO model cannot well separate the foreground region from the background region and has difficulties in distinguishing overlapping objects. In situation element detection tasks, the target to be detected is often camouflaged according to the environment, causing the target to overlap with the environmental background or the target and the environmental background to be highly similar, so the classical YOLOv3 target detection model is difficult to be applied to the situation element detection problem.

Recent studies have shown that adding an attention mechanism to convolutional neural networks (CNNs) can exchange a very small increase in computational effort for a significant increase in accuracy. Therefore, to solve the above problem, this paper introduces the attention mechanism in the Darknet53 backbone network of YOLOv3 and constructs the Situation Element Detection Network (SED-Net) based on the attention mechanism.

2.3. Attention Mechanisms. The attention mechanism [9] is originally a mechanism unique to human vision, which is

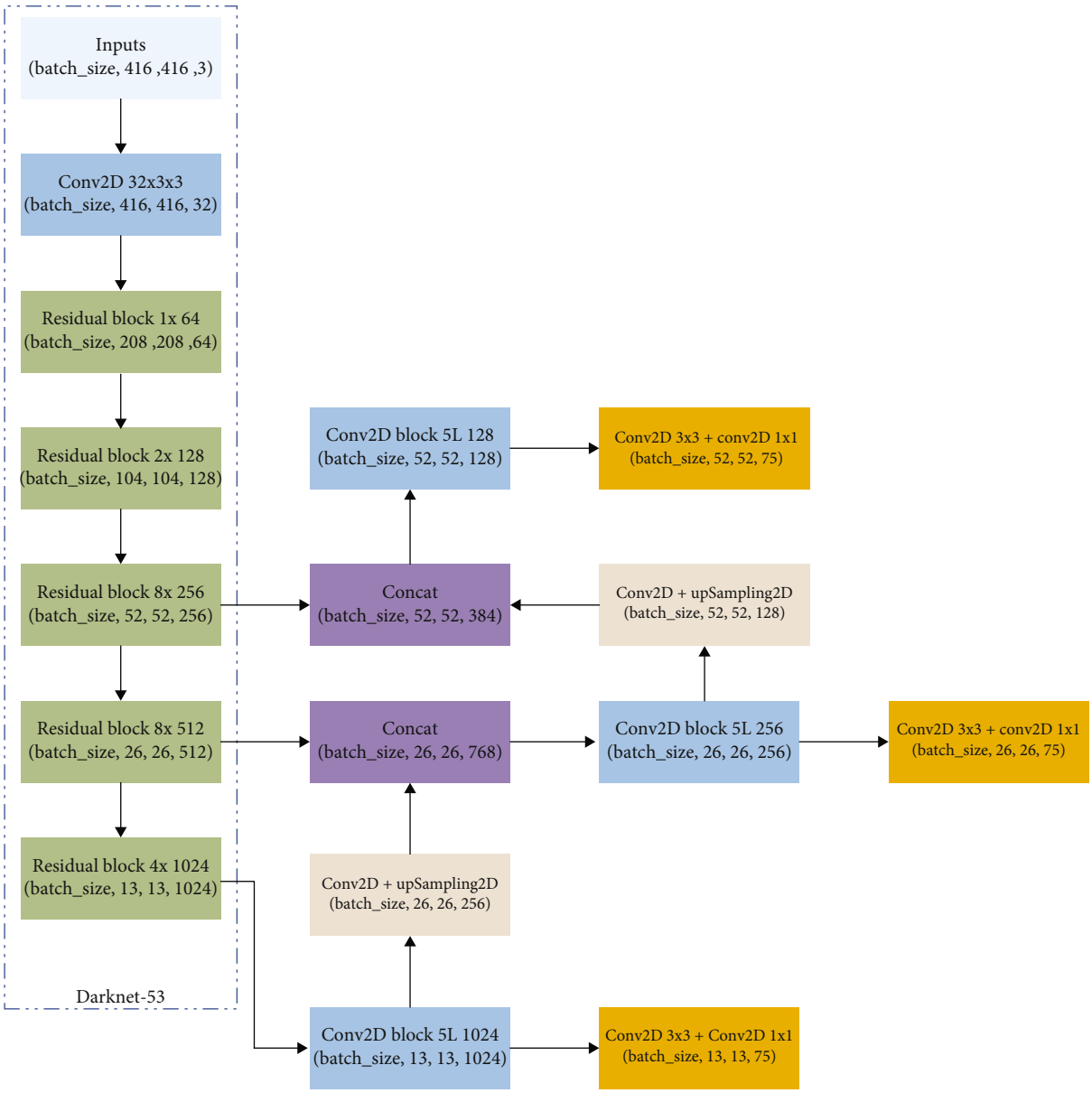

Figure 3: YOLO target detection model structure schematic.

the pointing and focusing of mental activity and consciousness on certain objects, and its basic function is to filter the information of important elements in the environmental elements. When humans observe a global image, they quickly identify the target area that needs attention and then devote more attention resources to this area and suppress information from other useless areas to obtain more detailed information about the target area that needs attention; this is the ability of humans to use limited attention resources to quickly filter out high-value information from a large amount of information. Attention mechanism greatly improves the accuracy and efficiency of human visual information processing, which is a unique advantage of humans.

The attention mechanism in the field of deep learning is borrowed from the attention mechanism of human vision by quickly scanning the global image, acquiring the target region that needs to be focused on, and then devoting more computational resources to that region to obtain more detailed information to be captured and suppressing the useless information in other regions.

Attention mechanisms can extract key local information from global information and can be easily embedded in existing network architectures to help extract key local features quickly. It can overcome the problems of difficult target localization, difficult target classification, and background interference caused by the detection of camouflaged targets in the situational awareness process, so it is important to conduct research on attention mechanisms in the field of situational awareness.

Recent studies have confirmed that attention mechanisms have great potential to improve the performance of deep convolutional neural networks (CNNs), and how to introduce attention modules into convolutional neural networks has attracted a lot of attention. There is no unique

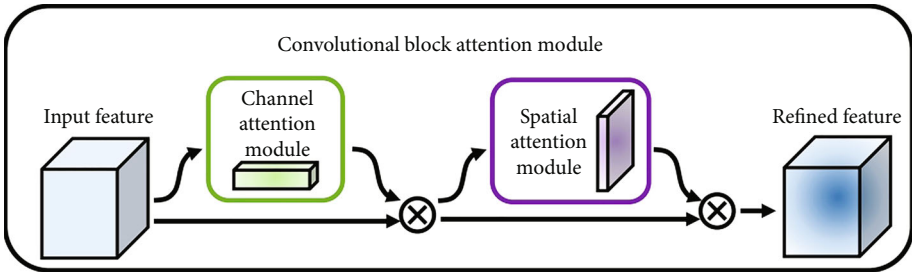

Figure 4: Convolutional block attention module structure schematic.

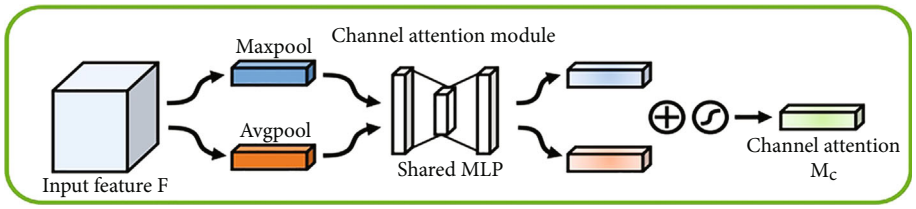

Figure 5: Schematic diagram of CBAM's channel attention module structure.

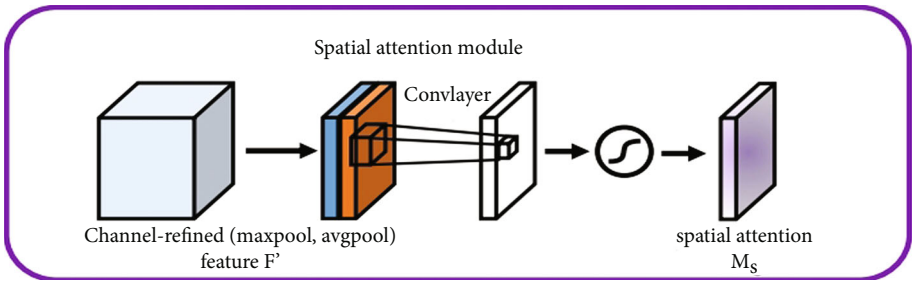

Figure 6: Schematic diagram of CBAM's spatial attention module structure.

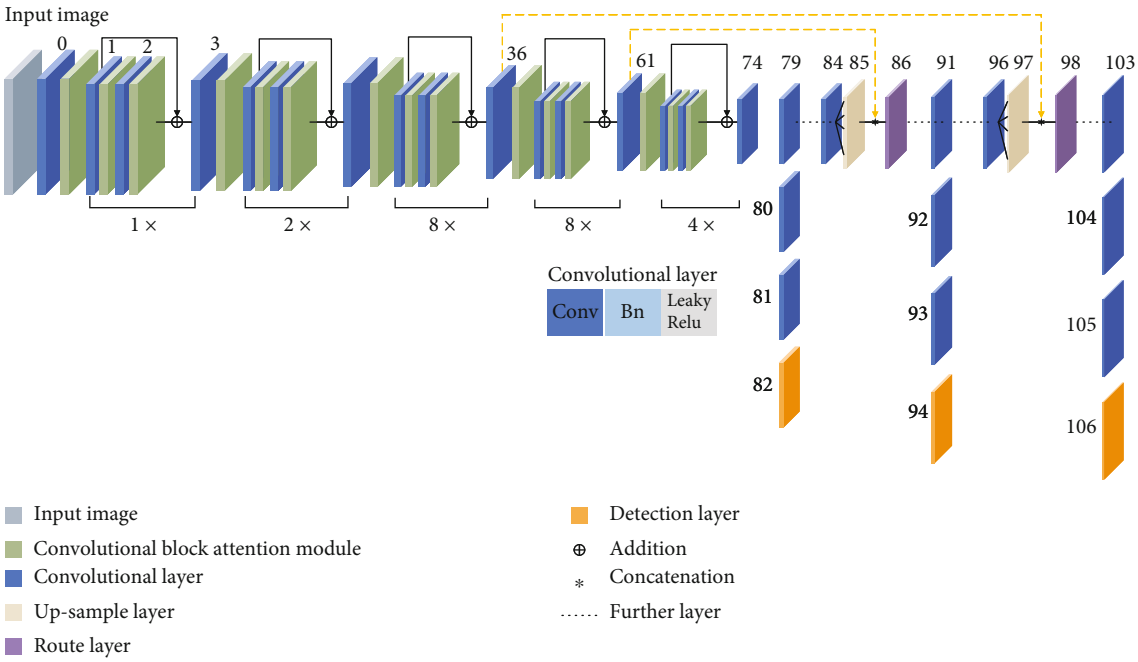

Figure 7: Schematic diagram of the overall network structure of the SEDNet model.

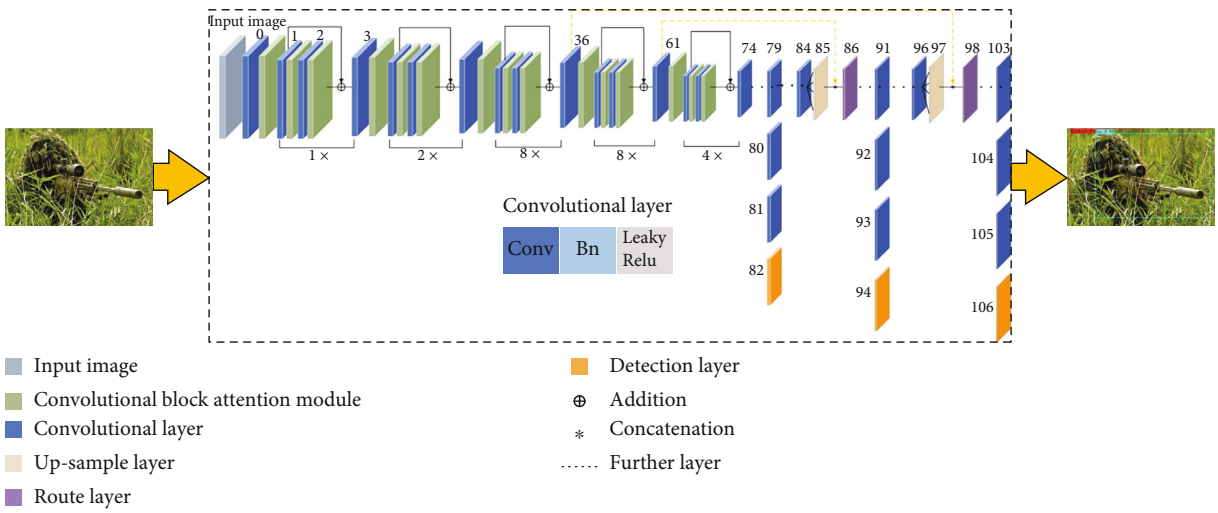

Figure 8: Situational element awareness model diagram.

Table 1: Comparison of the average accuracy rates of YOLOv3, SE-YOLO, and SEDNet.

	YOLOv3(%)	SE-YOLO(%)	SEDNet(%)
Submarine	89.09	94.10	99.12
UAV	77.20	80.00	92.93
Dog	90.03	90.86	90.65
Tank	65.71	79.87	89.20
Warship	72.96	83.10	87.92
Fighter	72.52	76.58	82.46
Soldier	61.34	73.63	80.38
Helicopter	55.98	75.33	78.49
Truck	48.87	67.41	72.55
Gun	38.53	48.90	64.64
mAP	67.22	76.98	83.83

way to introduce attention mechanisms into convolutional neural networks, either by adding attention mechanisms in the channel dimension or by adding attention mechanisms in the spatial dimension or by adding attention mechanisms in both the spatial and channel dimensions.

In 2018, Hu et al. [10] proposed the classical Squeeze-Excitation Network with feature compression and featured weight adjustment in the feature channel dimension. The results of applying it on the ResNet network showed that the technique not only significantly reduces the classification error rate but also effectively improves the mAP.

In 2019, Redmon et al. [7] introduced the attention mechanism into the YOLO algorithm, using weighted and filtered feature vectors to replace the original feature vectors for residual fusion and reducing the information loss in the fusion process by adding second-order terms. Experimental results on COCO and PASCAL VOC datasets show that the introduction of the attention mechanism in the YOLO model can effectively reduce the bounding box localization error and improve the detection accuracy.

Convolutional block attention module (CBAM) [7] is an attention mechanism that combines two dimensions of feature channels and feature spaces. Previous work has shown that CBAM can improve the performance of various deep CNN architectures, and it has shown good generalization ability in target detection and instance segmentation tasks. As shown in Figure 4, the CBAM module consists of a channel attention module and a spatial attention module.

CBAM uses not only average pooling to compress the feature map in the spatial dimension but also employs maximum pooling as a compliment. The structure diagram of the channel attention module of CBAM is shown in Figure 5, where MaxPool and AvgPool denote performing maximum pooling operation and average pooling operation, respectively, and MLP denotes multilayer perceptron.

The channel attention module of CBAM computes the feature mapping as shown in

$$M_c(F) = \sigma(\mathrm{MLP}(\mathrm{AvgPool}(F)) + \mathrm{MLP}(\mathrm{MaxPool}(F))), \quad (5)$$

$$M_c(F) = \sigma\left(W_1\left(W_0\left(F^c_{\mathrm{avg}}\right)\right) + W_1(W_0(F^c_{\mathrm{max}}))\right), \quad (6)$$

where F denotes the input feature maps and $F^c{}_{\mathrm{avg}}$ and $F^c{}_{\mathrm{max}}$ denote the feature maps that have been pooled on average and made large pooling, respectively. W_0 and W_1 denote the parameters of two of the layers in the multilayer perceptron, which use ReLU as the activation function for the neurons of the two-layer neural network. σ is the sigmoid function. At the time of calculation, $F^c{}_{\mathrm{avg}}$ and $F^c{}_{\mathrm{max}}$ share W_0 and W_1 in the multilayer perceptron.

Figure 6 shows the structure of the spatial attention module of CBAM. Unlike channel attention, spatial attention focuses on the location information of the target to be detected on the image. It first uses average pooling and maximum pooling in the channel dimension to obtain the information of the channel layer, then uses channel concatenation to concatenate the two-channel feature maps, and then uses a hidden layer containing a single convolution

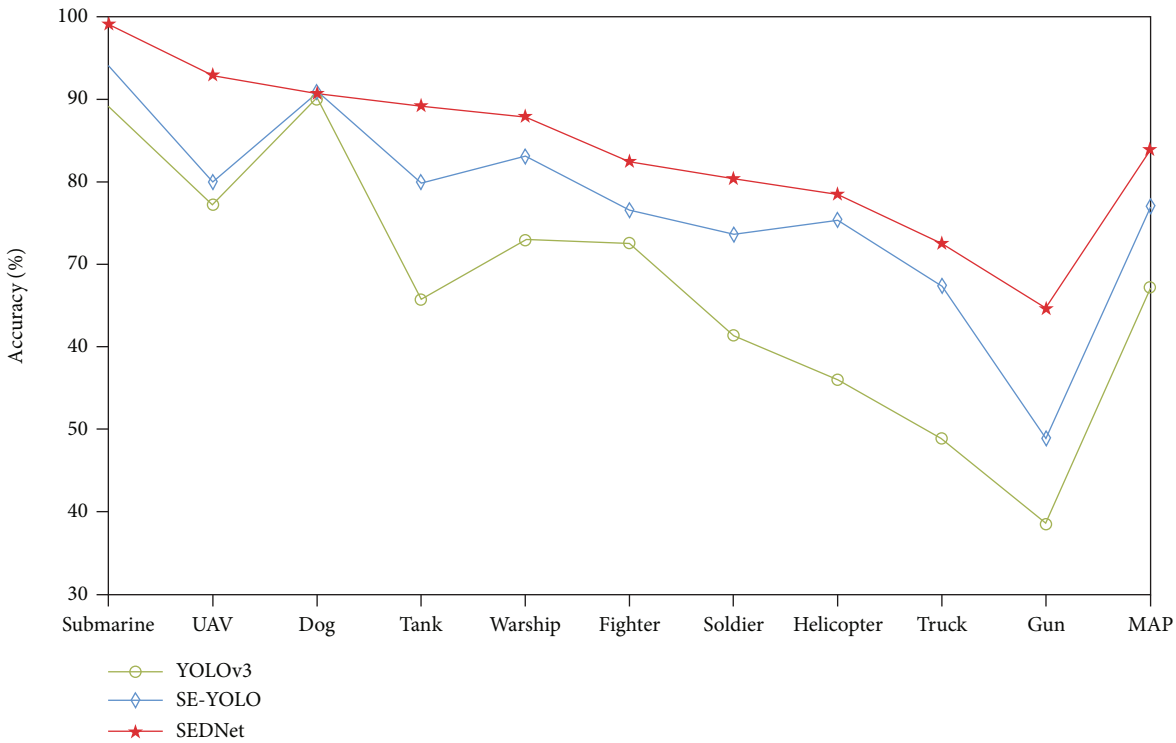

Figure 9: Comparison of the average accuracy rates of YOLOv3, SE-YOLO, and SEDNet.

kernel to convolve the feature maps after the above processing.

The spatial attention module of CBAM computes the feature mapping as shown in

$$M_s\left(F'\right) = \sigma\left(f^{7\times7}\left(\left[\text{AvgPool}\left(F'\right)\right]\right)\right), \tag{7}$$

$$M_s\left(F'\right) = \sigma\left(f^{7\times7}\left(\left[F'_{\text{avg}};{}'F_{\max}\right]\right)\right), \tag{8}$$

where F' denotes the feature map processed by the channel attention module, F'_{avg} and$'F_{\max}$ denote the feature map after average pooling and maximum pooling, respectively, $f^{7\times7}$ denotes the convolution operation with a convolution kernel size of 7×7, and σ is the sigmoid function.

CBAM is stable, effective, and versatile. Introducing it into the YOLOv3 backbone network can effectively improve the detection accuracy of the model at the cost of a small amount of calculation. Therefore, this paper chooses to embed CBAM in YOLOv3 to improve the target detection ability of the model in a complex environment with high target overlap and strong target camouflage ability.

3. Situational Element Awareness Model

3.1. Network Structure of Situational Element Awareness Model. In this paper, while keeping the structure of the YOLOv3 network basically unchanged, CBAM is embedded into the five downsampling processes of YOLOv3, and a CBAM is added to the convolutional layers of the Darknet53 backbone network and after the two convolutional layers of each residual module, to construct the situation elements detection network.

The introduction of CBAM can help the model extract key local information from global information and invest more computational resources in key areas to obtain more key detailed information and suppress useless information, to overcome the problems of difficult target localization, difficult classification, and background interference caused by the strong camouflage ability of detected targets in the process of situational element detection and improve the accuracy rate of the model in detecting situational elements. The network structure of the SEDNet model is shown in Figure 7.

3.2. The Loss Function of Situational Element Awareness Model. YOLOv3 uses the cross-entropy loss function to calculate the bounding box confidence error and introduces IoU indirectly as the optimized loss term in the calculation of the error term of the bounding box confidence, but directly using IoU as the loss function may have the following problems: if there is no overlap between the prediction box and the real box, IoU is 0 and the backpropagation gradient is 0, and further optimization of the loss function is not possible. And when the IoU is the same, there is also a difference in the way the prediction frame overlaps with the real frame. To solve the above problems, this paper uses the GIoU loss function. The GIoU loss function can be calculated by

$$\text{IoU} = \frac{A\cap B}{A\cup B}, \tag{9}$$

$$\mathrm{GIoU} = \mathrm{IoU} - \frac{C/(A \cup B)}{C}, \tag{10}$$

$$L_{\mathrm{GIoU}} = 1 - \mathrm{GIoU}, \tag{11}$$

where A denotes the prediction box and B denotes the real box. The GIoU has the same scale invariance as the IoU, and it solves the problem that the IoU cannot reflect the overlap mode and the loss function cannot be optimized when the IoU is zero. For obscured overlapping scenarios with strong target camouflage and high target overlap, using $(1 - \mathrm{GIoU})$ as the bounding box regression loss function can achieve better results.

To address the problem that difficult samples cannot be effectively learned due to the imbalance of positive and negative samples in single-stage target detection algorithms such as YOLOv3, the focal loss is used in this paper. Focal loss is calculated as shown in

$$\mathrm{FL} = -\alpha(1 - P_t)^{\gamma} 1g(P_t), \tag{12}$$

where FL denotes the focal loss function and P_t denotes the probability that the target is correctly classified. The focal loss adds a weight decay term to the traditional cross-entropy loss function, which makes the size of the weights decreases with the growth of P_t and increases with the decrease of P_t. The traditional cross-entropy loss function does not distinguish between easy and hard samples but adds up the same weights to obtain the total loss, which leads to the positive samples cannot being trained effectively. The focal loss effectively solves this problem.

In this paper, the loss function L' of the SEDNet model is constructed using the traditional cross-entropy loss function as the classification error loss function, the focal loss function as the bounding box object confidence loss function, and $(1 - \mathrm{GIoU})$ as the bounding box regression loss function [11], and L' can be calculated using

$$L' = L'_1 + L'_2 + L'_3, \tag{13}$$

$$L'_1 == \sum_{0}^{\mathrm{cellnumber}*B} I^{\mathrm{object}} \times \left(1 - \mathrm{GIoU}^{\mathrm{groundtruthpredict}}\right), \tag{14}$$

$$L'_2 = \sum_{0}^{\mathrm{cellnumber}*B} m \times \mathrm{focal\_loss}\left(\mathrm{CE}\left(p_{0,} q_0\right)\right), \tag{15}$$

$$L'_3 = \sum_{0}^{\mathrm{cellnumber}*B} I^{\mathrm{object}} \times \sum_{c=0}^{C} \mathrm{CE}(p(c), q(c)), \tag{16}$$

where L' is the loss function of SEDNet, $L_1{}'$ represents the bounding box loss function, $L_2{}'$ represents the bounding box object confidence loss function, and $L_3{}'$ is the bounding box regression loss function.

4. Experimental and Analysis

4.1. The Experimental Configuration. All experiments are based on a PC with an Intel(R) Core (TM) i7-8750H CPU @ 2.20 GHz, NVIDIA RTX 2070 GPU, the PyTorch framework.

We utilize Adam [12] to update the network weight. The initial learning rate of the network was set to 0.001, and the learning rate was reduced by 5% for each epoch experienced. Meanwhile, to further reduce the training time, the SEDNet network is trained to utilize migration learning in this paper. At the beginning of training, the parameters of some convolutional layers in the backbone network are initialized with the parameters in the pretraining weight file, and the parameters of some convolutional layers at the end are fine-tuned for training.

4.2. SA Dataset. In this paper, we used the labeling tool to manually label the collected target images to create a homemade SA dataset in VOC format for training. The situational element dataset, which is specially collected for this piece, contains ten types of targets, soldier, dog, gun, fighter, helicopter, UAV, tank, truck, warship, and submarine. In addition, to solve the overfitting problem, this paper performs data enhancement by scaling the collected images, mirror flipping, changing the brightness and contrast, and adding Gaussian noise [13], which enlarges the data volume by ten times and greatly improves the robustness and generalization ability of the network, allowing the limited data to produce more data value [14].

Figure 8 shows the schematic diagram of using SEDNet for the detection of situational elements in images with strong background interference and difficult situational target localization. From Figure 8, it can be seen that SEDNet can well overcome the problems of difficult target localization, difficult classification, and strong background interference in the process of posture element detection.

4.3. Comparison with Other Methods. To verify that the method proposed in this paper can accomplish situational element detection more effectively, experiments were conducted on the SA dataset with YOLOv3, YOLOv3 with the introduction of SENet (hereafter referred to as SE-YOLO), and the SEDNet model proposed in this paper, respectively. Randomly, 4680 images from 5850 images of the SA dataset were selected as the training set, and the remaining 1170 images were used as the test set for the experiments. Table 1 and Figure 9 show the comparison of the mean accuracy AP and the mean accuracy mAP for all classes of target detection by the conventional YOLOv3, SE-YOLOv3, and the method in this paper.

The experimental results on the SA dataset show that the mAP of SEDNet reaches a high level, improving 16.61% compared to the traditional YOLOv3 network and 6.85% compared to SE-YOLO, which proves that the SEDNet model proposed in this paper can significantly improve the performance of the deep learning network for situational element perception. In addition, both SEDNet and SE-YOLO have more significant improvements in the average accuracy rate compared with the traditional YOLOv3 network, which indicates that adding the attention module can effectively improve the model's ability to detect the situational elements.

The above results confirm the effectiveness and superiority of the work in this paper. Compared with the traditional YOLOv3 target detection algorithm, SEDNet achieves a large average accuracy improvement with only a small number of additional parameters and almost negligible computational effort and can detect targets more accurately in complex obscured overlapping scenarios with high target overlap and strong target camouflage capability and accurately obtain the location and class of most of the classes to be detected.

5. Conclusions

In order to explore a target detection algorithm suitable for situational element detection for the technical requirements of situational element detection, this paper proposes an efficient and accurate target detection network SEDNet based on the combination of YOLOv3 and CBAM. The main work of this paper has the following points.

(1) Introduces the research background and significance of this paper, analyzes the shortcomings of the current research work on situational element detection technology, and proposes solutions

(2) We propose a Situation Element Detection Network based on the combination of YOLOv3 and CBAM, which embeds CBAM into the downsampling process of YOLOv3, builds the network structure of SEDNet, and makes full use of the ability of CBAM to extract key local information from the global information. The network structure of SEDNet is built to take full advantage of CBAM's ability to extract key local information from global information, which overcomes the problems of difficult target localization, difficult classification, and strong background interference in the process of situational elements detection and improves the accuracy of the model in detecting situational elements

(3) We reconstructed the loss function based on traditional cross-entropy and focal loss and optimized the training strategy based on the K-means method, Adam algorithm, and migration learning method to improve the detection accuracy and training speed of the model

(4) We constructed the SA dataset and used data augmentation techniques to expand the training set data by a factor of 10 to avoid generating overfitting of the training results

(5) We performed the localization and classification of 10 common categories of situational elements, namely, soldiers, military dogs, guns, fighter jets, helicopter gunships, unmanned reconnaissance aircraft, tanks, military trucks, warships, and submarines, on the SA dataset. The experimental results show that SEDNet achieves an average accuracy of 83.83% on the SA dataset, and the mAP is improved by 16.61% compared with the traditional YOLOv3 target detection model, which verifies the effectiveness and superiority of the method in this paper

The SEDNet model can effectively solve the problems of multiple overlapping targets and strong target camouflage ability in complex environments that traditional target detection networks can hardly cope with and is applicable to the field of situational element perception. The research work in this paper lays the foundation for further research work on situational understanding, assisted decision-making, and assessment and provides important technical support.

Data Availability

The data used to support the findings of this study have been deposited in the GITHUB repository (https://github.com/chengkangda/1).

Conflicts of Interest

The authors declare that they have no competing interests.

References

[1] M. R. Endsley, "Situation awareness in aviation systems," *Handbook of Aviation Human Factors: Second Edition*, vol. 12, no. 1-12, p. 22, 1999.

[2] M. R. Endsley, "Toward a theory of situation awareness in dynamic systems," *Human Factors: The Journal of the Human Factors and Ergonomics Society*, vol. 37, no. 1, pp. 32–64, 1995.

[3] H. Peng, Y. Zhang, S. Yang, and B. Song, "Battlefield image situational awareness application based on deep learning," *IEEE Intelligent Systems*, vol. 35, no. 1, pp. 36–43, 2020.

[4] M. Liu, B. Li, Y. Chen et al., "Location parameter estimation of moving aerial target in space-air-ground integrated networks-based IoV," *IEEE Internet of Things Journal*, vol. 99, 2021.

[5] S. Woo, J. Park, J.-Y. Lee, and I. S. Kweon, "CBAM: convolutional block attention module," in *Computer Vision – ECCV 2018*, pp. 3–19, Springer, Cham, 2018.

[6] X. Chengji, X. Wang, and Y. Yang, "Attention-YOLO: YOLO detection algorithm with the introduction of attention mechanism," *Computer Engineering and Applications*, vol. 55, no. 6, pp. 13–125, 2019.

[7] J. Redmon, S. Divvala, R. Girshick, and A. Farhadi, "You only look once: unified, real-time object detection," in *Proceedings of the IEEE conference on computer vision and pattern recognition*, Las Vegas, NV, USA, 2015.

[8] J. Redmon and A. Farhadi, "YOLOv3: An Incremental Improvement," 2018, https://arxiv.org/1804.02767.

[9] B. Ali, "State-of-the-art in visual attention modeling," *IEEE Transactions on Pattern Analysis and Machine Intelligence*, vol. 35, no. 1, pp. 185–207, 2013.

[10] J. Hu, L. Shen, and G. Sun, "Squeeze-and-excitation networks," in *2018 IEEE/CVF Conference on Computer Vision and Pattern Recognition (CVPR)*, Salt Lake City, UT, USA, 2018.

[11] M. Liu, Z. Liu, W. Lu, Y. Chen, X. Gao, and N. Zhao, "Distributed few-shot learning for intelligent recognition of communication jamming," in *IEEE Journal of Selected Topics in Signal Processing*, 2021.

[12] D. Kingma and J. Ba, "A method for stochastic optimization," *Computer Science*, vol. 1412.6980, 2014.

[13] M. Liu, J. Wang, N. Zhao, Y. Chen, H. Song, and R. Yu, "Radio frequency fingerprint collaborative intelligent identification using incremental learning," *IEEE Transactions on Network Science and Engineering*, vol. 99, 2021.

[14] M. Liu, C. Liu, M. Li, Y. Chen, S. Zheng, and N. Zhao, "Intelligent passive detection of aerial target in space-air-ground integrated networks," *China Communications*, vol. 19, no. 1, pp. 52–63, 2022.

Hindawi
Wireless Communications and Mobile Computing
Volume 2022, Article ID 9041184, 12 pages
https://doi.org/10.1155/2022/9041184

Research Article

An Intelligent Hough Transform with Jaya of Multipopulation Cooperation for Diameter Estimation of Red-Hot Workpiece

Xinyu Zhang,[1,2] **Ke Chen**,[1,2] **Rong Mu**,[1,2] **Yanxi Yang**,[1,2] **and Jinghua Li**[1,2]

[1]*Shaanxi Key Laboratory of Complex System Control and Intelligent Information Processing, Xi'an University of Technology, Xi'an 710048, China*
[2]*Faculty of Automation and Information Engineering, Xi'an University of Technology, Xi'an 710048, China*

Correspondence should be addressed to Xinyu Zhang; xhyzzxy@126.com

Received 4 February 2022; Accepted 23 March 2022; Published 8 April 2022

Academic Editor: Mingqian Liu

Diameter is a critical metric during producing circular workpieces, but it is always challenging to measure accurately due to the existence of noise. The intelligent Hough transform with Jaya (IHTJ) is developed to solve this issue recently. However, it suffers from some disadvantages including unsatisfactory accuracy and convergence rate caused by the problem of trapping into local optimization in the case of inaccurate priori knowledge. In this paper, an IHTJ of multipopulation cooperation (IHTJMC) is proposed to overcome these disadvantages. Firstly, we analyse the problem of IHTJ in the diameter measurement. Secondly, a ring structure of the multipopulation cooperation is designed. In this structure, the whole population is divided into several subpopulations which evolve independently all the time. This can ensure a few best and worst solutions guide the evolution of the whole population at the same time. Then, we propose a migration strategy to finish the cooperation among the different subpopulations, which selects a few individuals from each subpopulation randomly, and exchange them with each other. This strategy can make the different subpopulations share the information among the entire population and improve the global search ability. Finally, three experiments are introduced to test the effectiveness of the IHTJMC. The experimental results demonstrate that the IHTJMC can restrain the problem of falling into local optimization significantly. Compared with the existing methods, it has superior accuracy and robustness for the diameter measurement of a circular workpiece which is heated to red state.

1. Introduction

Diameter is a critical parameter in many fields including monitoring the state of trains, inspecting the fuel injection, ceramic cylindrical workpiece manufacturing, polymeric fibre production, and monocrystal silicon growth [1–5]. In these fields, the diameter can be used to evaluate the quality of products or the operation state of equipment. If the diameter cannot be measured accurately, some unqualified products or faults cannot be found in time. This will lead to large economic losses or disasters. As a result, it is vital to measure the diameters precisely for some crucial workpiece production. However, it is very difficult to measure the diameter with the traditional contact measuring technologies in some high-temperature environments. For example, the traditional contact measuring technologies for the diameter have great limitations when the workpieces are burned red in the production of hot forgings. With the rapid development of charge coupled device (CCD) sensor and digital image processing technology, the diameter measurement based on the image processing technology has been developed [6–8]. Because this method is noncontact and has a high precision, it is used to measure the circular workpiece's diameter which is red-hot. The process of diameter measurement based on the image processing technology is as follows: firstly, capture the image of the circular workpiece by a CCD camera, and the workpiece is elliptical in the image because of the shooting angle; secondly, segment the image and extract the edge of the workpiece; finally, apply an ellipse fitting method to fit these extracted edge points, so as to obtain the diameter of the workpiece [9]. However, there are some heat radiation and dust in the production of hot forgings, which results

in massive noise in the previous image processing. This makes the edge points not be completely located on an ideal ellipse. As a result, it is really hard to get the precise parameters of the ellipse which consists of the edge points, and the diameter measurement cannot be obtained precisely. Consequently, it is so crucial to present a strong estimation method for elliptical parameters to measure diameter when the edge points of a red-hot circular workpiece include much noise.

Recently, lots of ellipse fitting methods have been proposed. They are mainly divided into three categories. The first category is the least square (LS) method. This kind of method searches the optimal ellipse parameters through making the distance between the ideal and real ellipse minimum. Its strengths are good realizability and instantaneity, but its robustness is unsatisfactory due to the effect of the noise, so its precision and robustness are poor [6, 10–12]. The second category is random sample consistency (RANSAC). In RANSAC, a subset is sampled from the edge points and then tested whether the points outside the subset meet the model. If so, the points are put into subsets. Repeat the above steps and get the subset including the most edge points so as to obtain the optimal ellipse which is corresponding to this subset. Compared with the LS method, RANSAC is more robust, but its detection accuracy is limited by the iterative times. When the iterative time is unreasonable, the errors of ellipse parameters are very large [13–15]. The last category is Hough transform (HT). This method maps the ellipse model into the parameter space and searches the optimal ellipse parameters by the enumeration in this space. Compared with the previous two categories, the HT method has stronger robustness and higher accuracy, so it is widely used in elliptic fitting [16–18]. However, the HT has some terrible disadvantages, such as the bad real-time performance and high memory footprint. As a result, it is very difficult to implement in the real application [19–21]. To overcome these, many scholars have developed the improved methods. Xu et al. propose the random HT (RHT) in [22], which greatly reduces memory consumption and computation by sampling pixels randomly. However, its performance is obviously impacted by noise in the image because of the introduction of solving equations. And then, a circle HT (CHT) architecture is proposed in [23], which can reduce the memory by 74% to 93%, with little reduction inaccuracy. It is utilized to find the inner and outer iris boundaries in eye images, but the accuracy and real-time performance of this method may decrease when there is additive Gaussian noise in the images. In [24], to solve the problem of low real-time performance in the track-before-detect algorithm based on HT (HT-TBD), an adaptive real-time recursive radial distance-time plane HT-TBD method was proposed. This method takes advantage of the adaptive approach to adjust the parameter space to realize the recursive detection. It can effectively raise the real-time performance of the method. With the development of artificial intelligence (AI) methods, some AI methods have been introduced in signal processing [25–27]. Recently, Zhang et al. propose an intelligent HT with Jaya (IHTJ) in [28], which transforms the ellipse fitting into an optimal problem, thus using Jaya to seek the optimum solution in the parameter space. The speed and accuracy of the HT are improved greatly. However, although Jaya has the good global search ability, it is unavoidable to trap into local optimization, and the convergence rate of the method gets slow when the range of the initial values is set unreasonable. This is because the prior knowledge cannot be obtained precisely in most practical applications, especially there are lots of noise in the edge points during the process of measuring the diameter of the red-hot circular workpiece. Therefore, it is really critical for the IHTJ to improve its global search ability so as to increase the accuracy and speed of measuring the diameter of the circular workpiece which is heated to red.

In this paper, an IHTJ of multipopulation cooperation (IHTJMC) is developed to overcome the issue in the diameter measurement of a circular workpiece which is heated to the red-hot state. The major work of this paper are as follows:

(1) We describe the problem of the diameter measurement in the production of a circular workpiece and analyse the reasons for the disadvantages of IHTJ

(2) An intelligent ring structure of multipopulation cooperation is proposed. It can improve the global search ability through dividing the population into several subpopulations which evolves independently with their own best and worst solutions

(3) We design the cooperative strategy based on the migration between the different subpopulations. This can enhance the global search ability and convergence rate further through exchanging the information among different subpopulations, so as to increase the accuracy and robustness of the diameter measurement

(4) The proposed method is tested by simulation and practical experiments, and the results are satisfactory

The remainder of this paper is summarized as follows: Section 2 introduces the problem of diameter measurement in the production of the red-hot circular workpiece and describes the disadvantages of the IHTJ. And the detail of the proposed method is introduced in Section 3. Section 4 makes the verification for the performance of the proposed method according to the simulation and practical experiments. Section 5 presents the conclusion.

2. Problem Description and IHTJ Review

2.1. Problem Description. In the process of producing a red-hot circular workpiece, it is really hard to measure its diameter directly due to the high-temperature environment. A noncontact measuring method is adopted to overcome this issue, which introduces the CCD and digital image processing technology. Figure 1 is the schematic of its principle. As shown in this figure, a CCD camera is installed above the workpiece to collect its image, and then, the edge point set

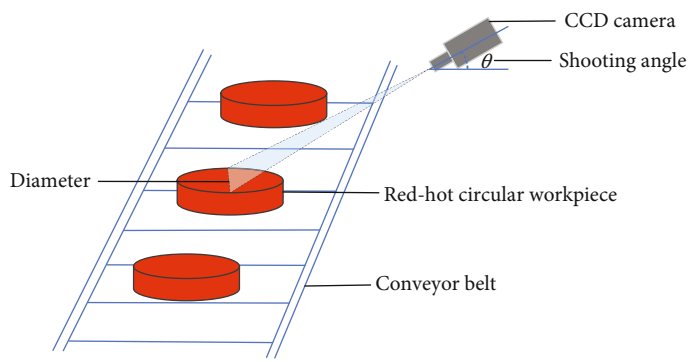

Figure 1: Principle of diameter measurement for red-hot workpieces with CCD camera.

of the workpiece contour can be obtained by image segmentation and edge extraction. Because there is an angle between the camera and the surface of the workpiece, the real diameter in the vertical direction shortens in the image and the contour of the circle workpiece is an ellipse in the image (the effect of errors and deviations is not considered here). Hence, the workpiece's diameter will be estimated by fitting these edge points.

Assume that the point set obtained through the edge extraction is $I = \{(x_1, y_1), (x_2, y_2), \cdots, (x_n, y_n)\}$, where n is the number of points in the set. Elliptic equation can be described as follows [9].

$$\frac{(x - x_c)^2}{a^2} + \frac{(y - y_c)^2}{b^2} = 1, \tag{1}$$

where a is the semimajor axis of the ellipse, b is the semiminor axis of the ellipse, and (x_c, y_c) is the centre coordinate of the ellipse.

Through fitting (1) with the set of edge points, the parameters of ellipse (a, b, x_c, y_c) can be obtained, and thus, the diameter of circular workpiece $2a$ can be obtained. Therefore, the diameter measurement is transformed into the ellipse fitting according to the point set. And the performance of diameter measurement depends on the ellipse fitting method [9].

2.2. IHTJ Review. HT is widely used to fit the ellipse because of its strong robustness, but it is not easy to realize in many practical problems. This is because it uses the exhaustive method, which leads to the bad real-time performance and high memory occupation. Especially, it gets worse in ellipse fitting because there are four parameters in an elliptic equation at least. To address this issue, the IHTJ is proposed in [28]. This method maps (1) into the parameter space and designs a fitness function firstly, and then, it transforms the ellipse fitting to seek the optimum value in the parametric space, which can get the peak value of the HT's accumulator. The fitness function is expressed by

$$F(a, b, x_c, y_c) = \sum_{i=1}^{n} f(a, b, x_c, y_c, x_i, y_i), \tag{2}$$

$$f(a, b, x_c, y_c, x_i, y_i) = \begin{cases} 0, & \psi(a, b, x_c, y_c, x_i, y_i) > T_f, \\ 1, & \psi(a, b, x_c, y_c, x_i, y_i) \le T_f, \end{cases} \tag{3}$$

$$\psi(a, b, x_c, y_c, x_i, y_i) = \left| \frac{(x_i - x_c)^2}{a^2} + \frac{(y_i - y_c)^2}{b^2} - 1 \right|, \tag{4}$$

where $F(a, b, x_c, y_c)$ is the accumulator of (a, b, x_c, y_c) in the HT method. Since it is impossible that all of the points are on the ellipse due to the existence of noise, a threshold T_f is considered in this equation, which can enhance the robustness of the method.

Then, an intelligent optimization method known as Jaya is introduced to overcome this problem and the IHTJ is developed. This method decreases the computational complexity and memory occupation of the HT greatly without any loss of robustness and accuracy. However, although Jaya has excellent global search ability, it still suffers from the problem of falling into local optimum. In some practical applications, it is very hard to obtain the prior information about the circular workpiece, so the scope of initial values cannot be set very accurate. This makes the problem of falling into local optimum worsen significantly, and it results in unsatisfactory convergence rate and diameter measurement of the red-hot workpiece. Therefore, it is really critical to improve the accuracy and convergence rate of IHTJ in the case of inaccurate scope of initial values during measuring the circular workpiece's diameter when it is heated red.

3. Proposed Method

To solve the problem that the IHTJ method falls into local optimal solution easily when the scope of initial values is inaccurate, this paper proposes an IHTJMC method that designs the structure of multipopulation cooperation and the collaborative strategy between different populations, so as to strengthen the information exchange and global search ability. Compared with the IHTJ method, this method can improve the convergence rate and the accuracy of diameter measurement due to the use of multipopulation cooperation. Meanwhile, it maintains the great robustness of the HT. In the following subsections, the details of IHTJMC and the full procedure are described.

3.1. Structure of Multipopulation Cooperation in IHTJMC. Due to the advantages of the small number of parameters and simple realization, Jaya is introduced into the IHTJ method to find the optimal solution in the parametric space for the diameter measurement of the red-hot circular workpiece. Unlike other swarm intelligence algorithms and evolutionary algorithms, Jaya considers the impacts of the optimal and the worst solution at the same time, so it has advanced optimization accuracy and search efficiency [29, 30]. And the IHTJ method has better efficiency and speed compared with the general HT. However, the similarity of the populations continues to increase with the increasing iterations, and the diversity of the whole population is low. As a result, the Jaya and IHTJ method are easy to trap in the local optimization, which misleads the results.

To improve the global search ability of the IHTJ, a collaborative structure of multipopulation is proposed in this paper. It is shown as Figure 2. In this structure, the whole population is divided into M subpopulations randomly after the initialization. The number of individuals in each subpopulation is N. At the beginning of every iteration, the cooperation is implemented between different subpopulations through the designed migration strategy. A few individuals are, respectively, chosen from subpopulation j and subpopulation $j+1$ randomly, where $j = 1, \cdots, M\text{-}1$, and then exchange them with each other. Next, do this operation in turn until $j = M - 1$. When $j = M$, sample the individuals from subpopulation M and subpopulation 1 randomly and replace them with each other. After that, all subpopulations form a ring structure, and the cooperation is finished in each subpopulation with the migration between the two different subpopulations. This structure introduces the idea of cooperation and improves the population diversities to improve the global search capability of Jaya by exchanging information between different subpopulations. Then, each subpopulation keeps independent all the time, and they finish the generation of new individuals through the mechanism of Jaya, in which the own best and worst individuals of each subpopulation are used to update the individuals. The details will be introduced in Section 3.2. At last, the global optimal solution is obtained from these M subpopulations.

Compared with the IHTJ, the proposed method introduces the multipopulation cooperation structure. It finishes the population evolution by dividing the whole population into M subpopulations rather than only one population. In this process, each subpopulation updates its individuals based on its own best and worst individual. This can enhance the diversity of population through implementing the population evolution based on more than one best and worst individual. Meanwhile, the cooperations between different subpopulations are achieved by the migration. It can improve the global search ability further by sharing the information between different subpopulations. Hence, it is helpful for the IHTJMC to raise the convergence rate of the method and the measuring accuracy of the red-hot workpiece's diameter, especially when the scope of initial values is inaccurate.

3.2. Optimization Strategy of IHTJMC. In the IHTJMC of this paper, the multipopulation migration is designed to realize the cooperation between different subpopulations. The purpose is to improve the population diversity through dispersing the entire population into a few subpopulations and sharing the information between different subpopulations. In this strategy, each subpopulation can search its own global optimal solution in its own subregion independently. Then, some individuals are sampled randomly from one subpopulation and are migrated into another. At the same time, the same number of individuals is also selected from the other subpopulation at random and migrated into this one. The historical and present information can be shared among different subpopulations effectively. Compared with the evolution including only one population, it is beneficial to improve the diversity of the entire population and the global search ability when some best and worst individuals guide the evolution of the population at the same time. As a result, IHTJMC can restrain the problem of local optimization while maintaining the superiority of IHTJ.

3.2.1. Fitness Function of IHTJMC. To maintain the superiority of the HT, the fitness function has been designed in the IHTJ method. This fitness function converts the ellipse fitting into the optimal problem of seeking the best elliptical parameters in the parametric space after the HT. It retains the robustness and precision of the HT as well as improving its real-time performance and memory occupancy through the introduction of the intelligent optimization algorithms. In order to guarantee that the algorithm has the great robustness, this fitness function is reserved in the IHTJMC. It is shown as (2)–(4) in Section 2.2.

3.2.2. Population Initialization. During the initialization, some parameters are set. They include the size of the population NP, the number of subpopulation M, the number of iterations G, and the initial population $\mathbf{x}_l = [x_1, x_2, x_3, x_4]$, where $l = 1, 2, \cdots, NP$. In $\mathbf{x}_l$, the four components are defined by the elliptical parameters. They are as follows: $x_1 = a$, $x_2 = b$, $x_3 = x_c$, and $x_4 = y_c$. In order to make the initial population cover the entire search space very well, the chaotic mapping is used to generate the initial individuals. It is calculated by

$$\mathbf{x}_l = \mathbf{x}^{\mathrm{L}} + \left(\mathbf{x}^{\mathrm{U}} - \mathbf{x}^{\mathrm{L}}\right) \times \tilde{\mathbf{x}}_l, \tag{5}$$

$$\tilde{\mathbf{x}}_l = \mu \cdot \tilde{\mathbf{x}}_{l-1}\left(1 - \tilde{\mathbf{x}}_{l-1}\right), \tag{6}$$

where $\mathbf{x}_l$ represents the $l_{\text{-th}}$ individual in the initial population, $\mathbf{x}^{\mathrm{U}}$ is the upper boundary, $\mathbf{x}^{\mathrm{L}}$ is the lower boundary, μ is the chaos factor and it is set to 4 in general, and $\tilde{\mathbf{x}}_l$ is the $l_{\text{-th}}$ individual after the chaotic mapping.

3.2.3. Subpopulation Division. To implement the multipopulation cooperation, NP individuals are divided into M subpopulations randomly after the population initialization, and the number of the individuals in each subpopulation N is NP/M. Throughout the process of iteration, these M subpopulations are always kept separated. Every

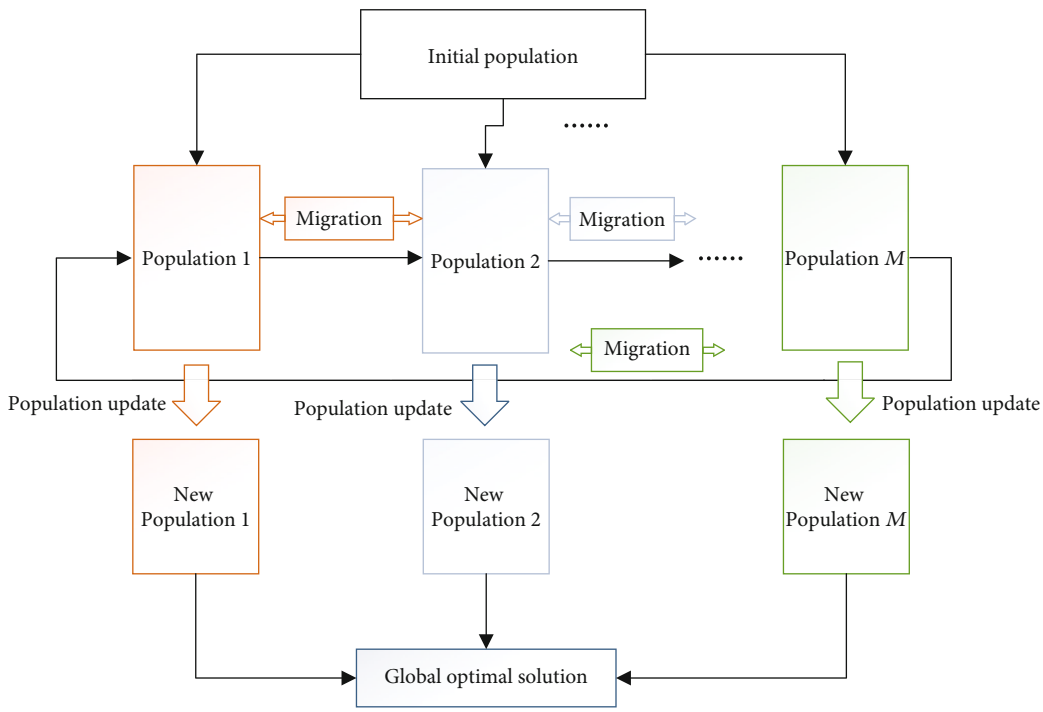

FIGURE 2: Collaborative structure of multipopulation.

subpopulation possesses its best and worst individual, and these best and worst individuals direct the evolution of its own subpopulation.

3.2.4. Subpopulation Migration. In the IHTJMC, migration is an important part which is used to achieve the cooperation between the different subpopulations. It can ensure that the information is shared among the different subpopulations. Based on the ring structure designed in Section 3.1, choose 20% of the individuals from the $j_{\text{-th}}$ and $(j+1)_{\text{-th}}$ subpopulation at random, respectively. Then, exchange these individuals between each other's subpopulations. Repeat this operation until $j = M - 1$. When $j = M$, do that between the $M_{\text{-th}}$ and first subpopulation. After that, all of subpopulations have finished the migration, and the cooperation of them has been achieved through the ring structure. As a result, the information from different subpopulations will enhance the search capacity of each subpopulation. It lays a good foundation for the generation of new individuals and the evolution of the whole population.

3.2.5. New Individual Generation. After the migration of subpopulations, these M subpopulations begin to iterate and evolve independently. Each subpopulation generates new individuals in its own search space. The new individual generation is expressed by

$$\mathbf{x}'^{k}_{l,j} = \mathbf{x}^{k}_{l,j} + \mathbf{r}_1\left(\mathbf{x}^{k}_{\text{best},j} - \left|\mathbf{x}^{k}_{l,j}\right|\right) - \mathbf{r}_2\left(\mathbf{x}^{k}_{\text{worst},j} - \left|\mathbf{x}^{k}_{l,j}\right|\right), \quad (7)$$

where $\mathbf{x}'^{k}_{l,j}$ represents the $l_{\text{-th}}$ new individual of the $j_{\text{-th}}$ population in the $k_{\text{-th}}$ iteration, $l = 1, \cdots, N$, $\mathbf{r}_1$, and $\mathbf{r}_2$ are the vectors sampled from [0,1] randomly, and $\mathbf{x}^{k}_{\text{best},j}$ and $\mathbf{x}^{k}_{\text{worst},j}$ represent the best and worst individual of the $j_{\text{-th}}$ population in the $k_{\text{-th}}$ iteration, respectively. The idea of "seeking advantages and avoiding disadvantages" is well reflected in (7). $\mathbf{r}_1(\mathbf{x}^{k}_{\text{best},j} - |\mathbf{x}^{k}_{l,j}|)$ corresponds to "advantages-seeking," which shows that the individuals of each subpopulation get close to the present optimal individual in the process of iteration constantly; $-\mathbf{r}_2(\mathbf{x}^{k}_{\text{worst},j} - |\mathbf{x}^{k}_{l,j}|)$ corresponds to "disadvantages-avoiding," which expresses that the individuals in each population keep moving away from the present worst individual in the iterative process.

3.2.6. Illegal Individuals Treatment. After generating new individuals, each subpopulation needs to detect whether the newly generated individuals are within the normal range. If not, these individuals are called illegal individuals and need to be repaired. They are repaired by

$$x'^{k}_{m,l,j} = \begin{cases} 2x^{\text{U}}_{m} - x'^{k}_{m,l,j}, & x'^{k}_{m,l,j} > x^{\text{U}}_{m}, \\ 2x^{\text{L}}_{m} - x'^{k}_{m,l,j}, & x'^{k}_{m,l,j} < x^{\text{L}}_{m}, \\ x'^{k}_{m,l,j}, & \text{otherwise}, \end{cases} \quad (8)$$

where $x'^{k}_{m,l,j}$ represents the $m_{\text{-th}}$ component of $\mathbf{x}'^{k}_{l,j}$, $m = 1, \cdots, 4$, and x^{U}_{m} and x^{L}_{m} are the upper and lower boundary of the $m_{\text{-th}}$ component, respectively.

3.2.7. Population Update. In this paper, the purpose is to search the maximum value of the fitness function in the parameter space after transforming the ellipse fitting into the optimization problem. As a result, it is necessary to

compare the fitness function value of the new individual $\mathbf{x}'^{k}_{l,j}$ with that of the previous individual $\mathbf{x}^{k}_{l,j}$ and determine which of them should be preserved into the $(k+1)_{\text{-th}}$ iteration. The individual update is calculated by

$$\mathbf{x}^{k+1}_{l,j} = \begin{cases} \mathbf{x}^{k}_{l,j} & F\left(\mathbf{x}'^{k}_{l,j}\right) \le F\left(\mathbf{x}^{k}_{l,j}\right), \\ \mathbf{x}'^{k}_{l,j} & F\left(\mathbf{x}'^{k}_{l,j}\right) > F\left(\mathbf{x}^{k}_{l,j}\right), \end{cases} \tag{9}$$

where $F(\cdot)$ represents the fitness function value which is determined by (2)-(4) in Section 2.2. As can be seen from (9), the new individual which owns lager fitness function value than the previous will be saved for the next iteration. Otherwise, it will be discarded and the previous one will be preserved into the next iteration. This can make the algorithm obtain the optimal solution in each subpopulation after a few iterations.

3.2.8. Best and Worst Individual Renewal. When all of the individuals in the M subpopulations are renewed, the best individual and the worst individual of every subpopulation in the $(k+1)_{\text{-th}}$ iteration are updated as follows:

$$\begin{cases} \mathbf{x}^{k+1}_{\text{best},j} = \arg\max\limits_{\mathbf{x}^{k+1}_{l,j}} F\left(\mathbf{x}^{k+1}_{l,j}\right), \\ \mathbf{x}^{k+1}_{\text{worst},j} = \arg\min\limits_{\mathbf{x}^{k+1}_{l,j}} F\left(\mathbf{x}^{k+1}_{l,j}\right). \end{cases} \tag{10}$$

At the same time, the best individual $\mathbf{x}^{k+1}_{\text{best}}$ and the worst individual $\mathbf{x}^{k+1}_{\text{worst}}$ of the whole population must be updated, too. They are obtained by

$$\begin{cases} \mathbf{x}^{k+1}_{\text{best}} = \arg\max\limits_{\mathbf{x}^{k+1}_{\text{best},j}} F\left(\mathbf{x}^{k+1}_{\text{best},j}\right), \\ \mathbf{x}^{k+1}_{\text{worst}} = \arg\min\limits_{\mathbf{x}^{k+1}_{\text{worst},j}} F\left(\mathbf{x}^{k+1}_{\text{worst},j}\right). \end{cases} \tag{11}$$

In the IHTJMC method, the processes of subpopulation migration, new individual generation, illegal individual treatment, population update, and best and worst individual renewal are implemented in turn repeatedly until it reaches the maximum number of iterations or stopping condition. Then, the optimal solution $\mathbf{x}_{\text{best}}$ is obtained in the last iteration, which makes the fitness function maximum. And the optimal parameters of the ellipse can be obtained, thereby obtaining the optimal measurement of the red-hot workpiece's diameter.

Compared with the HT, the IHTJMC can increase the running speed and decrease the memory occupation significantly because it uses the Jaya with multipopulation cooperation rather than traverses all of the solutions in the parametric space. Compared with the IHTJ, the IHTJMC increases the measuring accuracy and restrains the problem of trapping into the local optimization through introducing the optimization strategy based on the cooperation of the multipopulation.

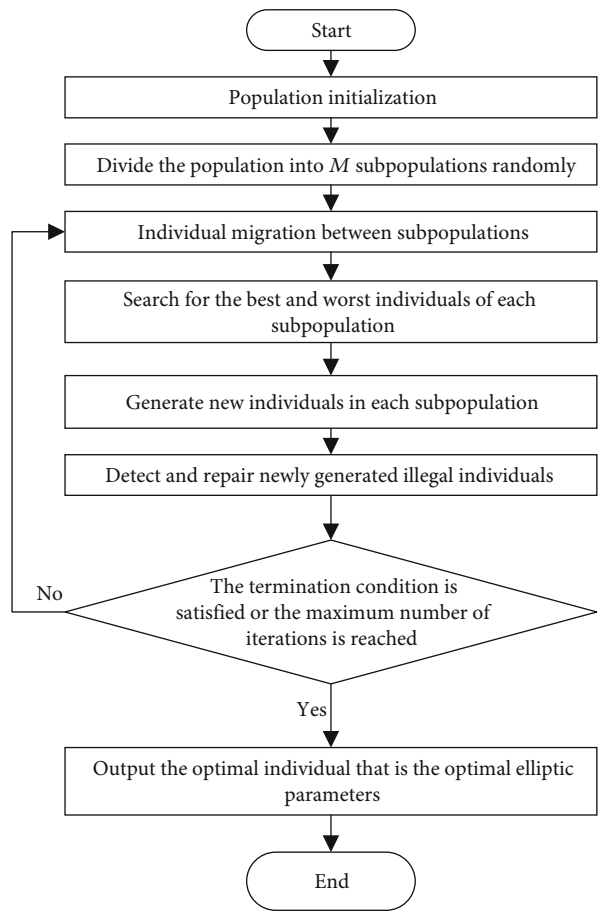

Figure 3: The flow chart of IHTJMC.

3.3. Implementation of IHTJMC. The implementation of IHTJMC is summarized as follows:

(1) Set the parameter initial values of the IHTJMC, such as the population size NP, the maximum number of iterations G, the number of the subpopulations M, and the stopping condition and T_f; then, generate the initial population through (5) and (6)

(2) Divide the whole population into M subpopulations according to Subpopulation Division

(3) Execute the migration between the different subpopulations according to Subpopulation Migration

(4) Calculate the best and worst individual of every subpopulation according to (10), and obtain the best and worst individual of the whole population through (11); then, generate new individual for each subpopulation by (7)

(5) Detect and treat illegal individuals according to (8) and update the population through (9)

Table 1: Test functions in experiment I.

Name	Expression formula	Dimension	Range
Sphere	$f_1(x) = \sum_{i=1}^{m} x_i^2$	5	[-100, 100]
Drop-wave	$f_2(x) = 1 + \cos\left(12\sqrt{x_1^2 + x_2^2}\right)/0.5\left(x_1^2 + x_2^2\right) + 2$	2	[-5.12, 5.12]
Girewank	$f_3(x) = 1/4000\sum_{i=1}^{m} x_i^2 + \prod_{i=1}^{m}\left(\cos x_i/\sqrt{i}\right)$	5	[-600, 600]
Rastrigin	$f_4(x) = \sum_{i=1}^{m} x_i^2 - 10\cos\left(2pi * x_i\right) + 10$	5	[-5.12, 5.12]
Rosenbrock	$f_5(x) = \sum_{i=1}^{m} 100\left(x_{i+1} - x_i^2\right)^2 + \left(x_i - 1\right)^2$	5	[-100, 100]
Schaffer	$f_6(x) = 0.5 + \left(\sin\sqrt{x_1^2 + x_2^2} - 0.5/\left[1 + 0.001\left(x_1^2 + x_2^2\right)\right]^2\right)$	2	[-100, 100]

(6) If the maximum number of iteration or stopping condition is reached, the optimal individual is output as the optimal solution; otherwise, return to step (3).

The flow chart of IHTJMC is shown in Figure 3 as follows.

4. Experiment and Result Analysis

In this section, three experiments are designed to test the superiority of the proposed method. The first experiment introduces six test functions to evaluate the performance of the proposed strategy based on the cooperation of multipopulation in the IHTJMC, which are widely used for the verification of the swarm intelligence optimization algorithms. The second is to test the performance of the IHTJMC through fitting a standard ellipse with some noise in simulation. The last one is to verify the performance of the IHTJMC for the diameter measurement with a red-hot gasket in a practical experiment.

4.1. Verification for Cooperation of Multiple Populations. In this experiment, six test functions including Sphere, Drop-wave, Girewank, Rastrigin, Rosenbrock, and Schaffer are introduced to test the effectiveness of the proposed strategy based on the cooperation of multiple populations in the IHTJMC. These functions are always utilized to verify the performance of the swarm intelligence optimization algorithms [31, 32]. They are shown in Table 1. At the same time, the unimproved Jaya which uses only one population is introduced into the comparison and the root mean square error (RMSE) is concerned as a performance index, and this experiment is implemented 30 times repeatedly and independently. The RMSE is calculated as follows:

$$\mathrm{RMSE} = \sqrt{\frac{1}{L}\frac{1}{K}\sum_{i=1}^{L}\sum_{j=1}^{K}\left(\widehat{x}_{i,j} - x_j\right)^2}, \tag{12}$$

where L is the number of independent experiments, $\widehat{x}_{i,j}$ is the $i_{\text{-th}}$ estimation of the $j_{\text{-th}}$ component, and x_j is the true value of the $j_{\text{-th}}$ component.

Table 2: RMSE of two methods in experiment I.

Function	Unimproved Jaya	Proposed
Sphere	2.3494e-19	7.8021e-20
Drop-wave	0.0019	0.0014
Girewank	6.8455	6.4910
Rastrigin	0.4698	0.3138
Rosenbrock	0.5389	0.1056
Schaffer	0.4058	0.0200

Table 2 shows the RMSE of the Jaya with only one population and the proposed strategy in 30 independent experiments, respectively. From Table 2, we can see that the RMSE of the Jaya with the proposed strategy for the six test functions is far superior to the unimproved Jaya. Compared with unimproved Jaya, the accuracy of the method with the proposed strategy is higher. This is because the cooperation of multipopulation can improve the diversity of the whole population, which possesses the strong ability of the information interaction between different subpopulations and the great evolutionary ability guided by multiple best and worst solutions.

Except for RMSE, the convergence curves of the methods are used to evaluate their convergence rates. The convergence curves of the Jaya with only one population and the proposed strategy for the six test functions are shown in Figures 4–9, respectively. These figures show that the Jaya with the proposed strategy has a higher convergence rate than the unimproved one. Especially in Figures 4–6, we can see that the unimproved Jaya traps into the local optimization and cannot jump out all the time. And the convergence curve of the Jaya with the proposed strategy is much better, because the global search capacity is enhanced due to the introduction of the cooperation of multiple populations. As a result, the search accuracy and convergence rate of the Jaya are significantly improved when the proposed strategy are added.

4.2. Ellipse Fitting Experiment. This experiment is used to verify the superiority of IHTJMC in the ellipse fitting. 100 data points are selected from an ellipse with Gaussian noise,

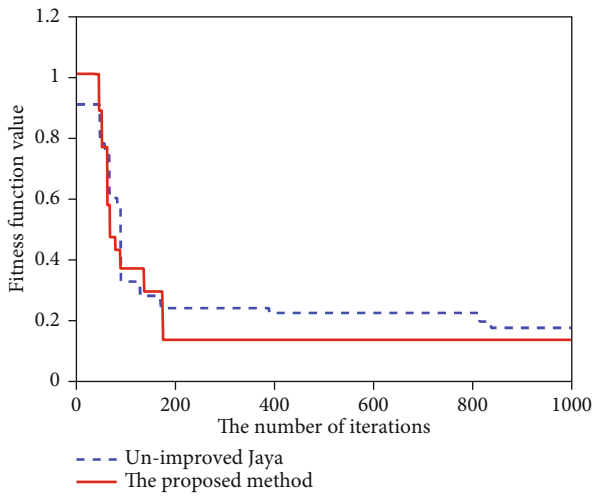

Figure 4: Convergence curves of Sphere with two methods.

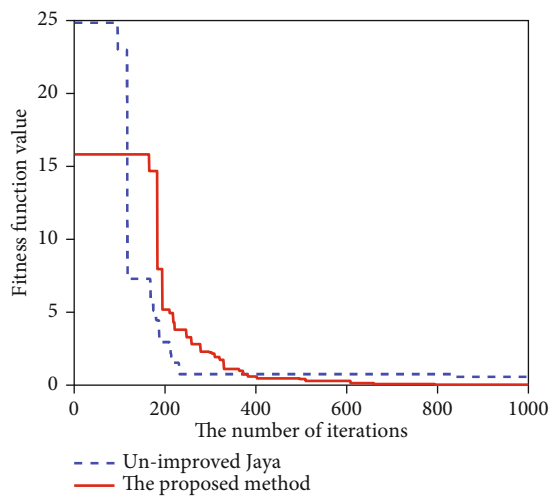

Figure 5: Convergence curves of Drop-wave with two methods.

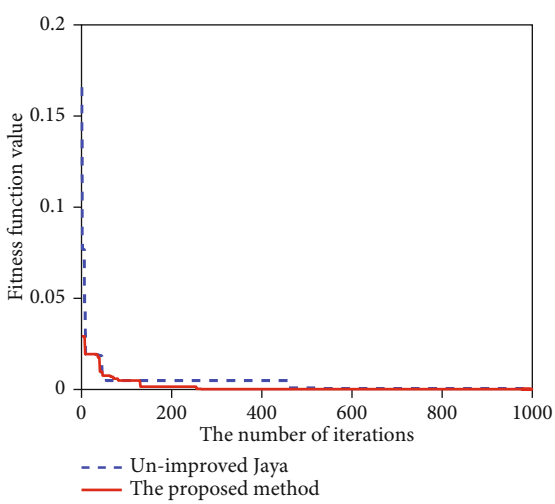

Figure 6: Convergence curves of Girewank with two methods.

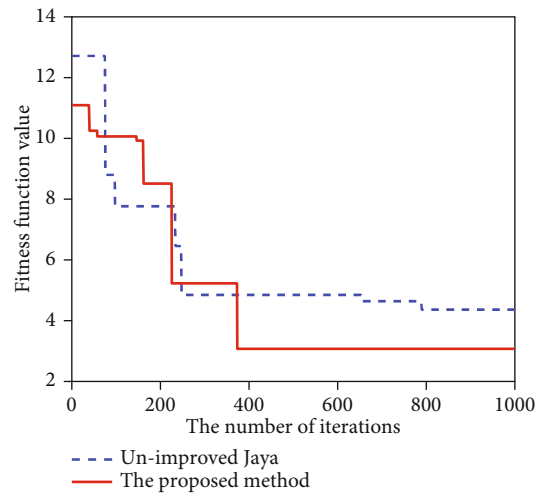

Figure 7: Convergence curves of Rastrigin with two methods.

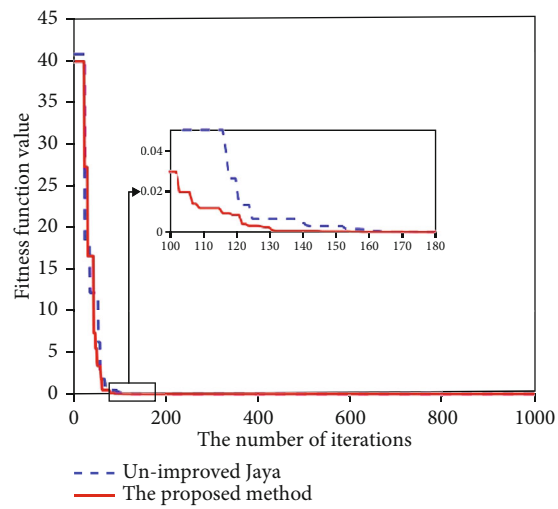

Figure 8: Convergence curves of Rosenbrock with two methods.

in which the parameters are set as $a = 7, b = 6, x_c = 9, y_c = 13$. The Gaussian noise variance is 0.01. These data points are shown in Figure 10. In order to test the superiority of IHTJMC better, a few existing methods including the IHTJ, direct least square (DLS), RHT, and RANSAC methods are introduced into the comparative evaluation. And RMSE is also considered as a performance index.

The parameter settings of these methods are as follows: the maximum number of iterations G is 1000, the number of the individuals NP is 90, T_f is 0.06, the termination condition is $Y_{gbest} > 94$, the number of subpopulations M is 3, the search scope is $[7 \pm 2, 6 \pm 2, 9 \pm 2, 13 \pm 2]$ (they are set double as large as those in [28]), and the experiment is also implemented 30 times repeatedly and independently.

Figure 11 provides the fitting results of these methods. We can see from this figure that the precision of the IHTJMC is better than those of other methods. Figure 12 presents the iteration curves of the fitness function with the IHTJ and IHTJMC, respectively. As shown in

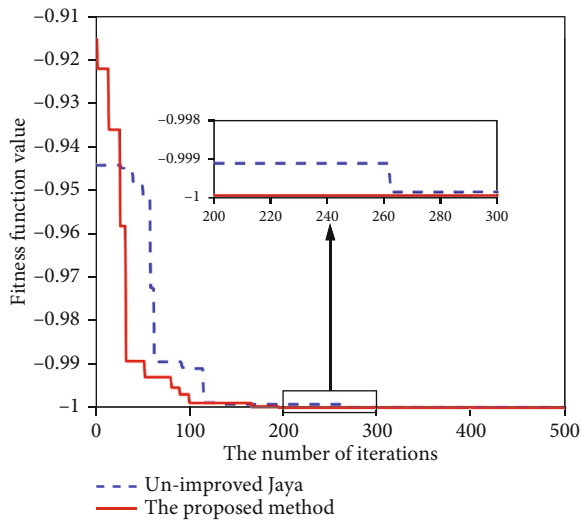

Figure 9: Convergence curves of Schaffer with two methods.

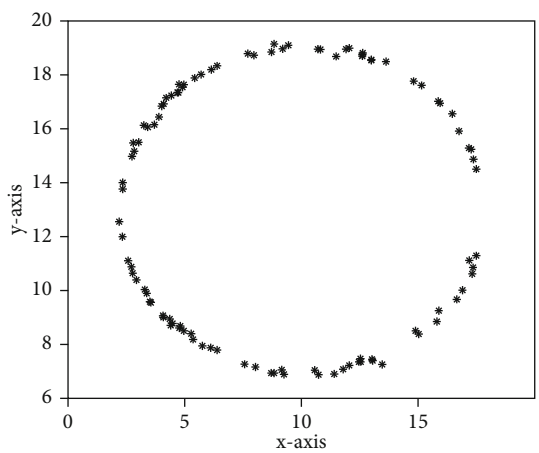

Figure 10: Ellipse data points containing Gaussian noise.

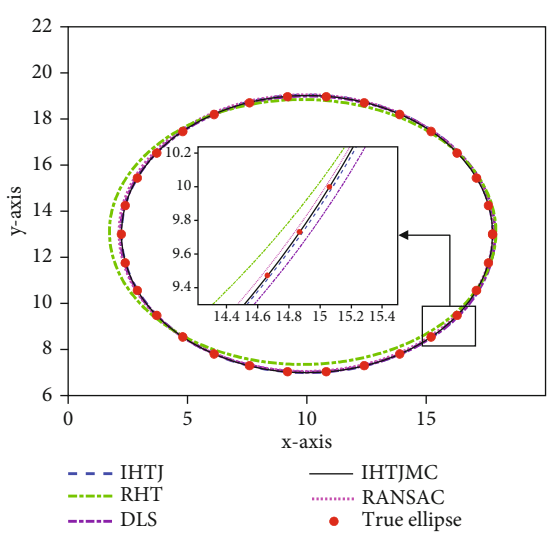

Figure 11: Comparative results of ellipse fitting in experiment II.

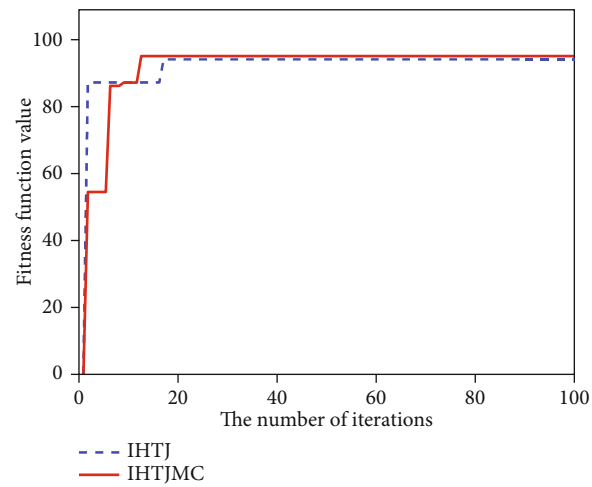

Figure 12: Iteration curves of fitness function with the IHTJ and IHTJMC in experiment II.

Table 3: RMSE of five methods in experiment II.

Method	a	b	x_c	y_c
IHTJMC	0.0115	0.0152	0.0081	0.0070
IHTJ	0.1248	0.0450	0.0704	0.0332
RHT	1.0612	0.7471	0.9324	0.6957
DLS	0.0621	0.0111	0.032	0.0078
RANSAC	0.2666	0.1154	0.2273	0.1556

Figure 12, the IHTJ converges at the $18_{\text{-th}}$ time, but the IHTJMC converges at the $13_{\text{-th}}$ time, so the convergence rate of the IHTJMC is superior to that of IHTJ. Moreover, the final value of fitness function of the IHTJ is less than that of the IHTJMC because the IHTJ has the problem of trapping into the local optimization, which is effectively suppressed in the IHTJMC through the introduction of the cooperation of multipopulation. Table 3 shows the RMSE of these methods in ellipse fitting, respectively. As shown in Table 3, the fitting accuracy of IHTJMC is much higher than those of other methods. As can be seen from these experimental results, the IHTJMC has better fitting accuracy than other methods. Compared with the IHTJ method, the IHTJMC has improved the fitting accuracy and convergence rate greatly when the search scope is doubled. This is because the cooperation strategy of multiple population strengthens the information exchange between the different subpopulations and can suppress the problem of the trapping local optimization effectively. As a result, it is very helpful to measure the workpiece's diameter accurately when the prior knowledge is inaccurate.

4.3. Diameter Measurement for Red-Hot Workpiece. To verify the IHTJMC for practical problems, it is used to measure the diameter of a gasket under high-temperature conditions. In this experiment, a CCD camera is used to capture image, and the edge point set which is used for ellipse fitting is obtained by image segmentation and edge extraction. Figure 13 is the image of the gasket under high temperature

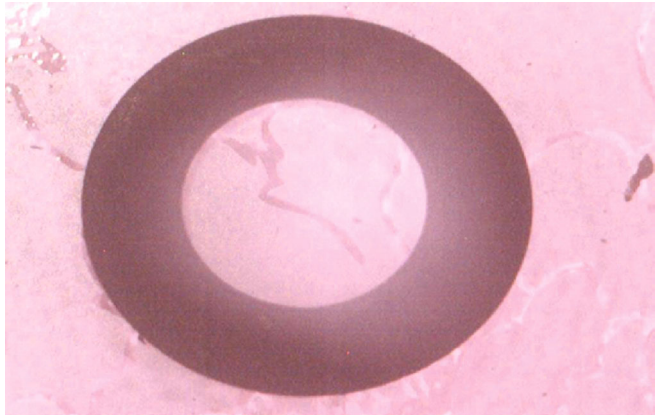

Figure 13: Image of red-hot gasket under high temperature.

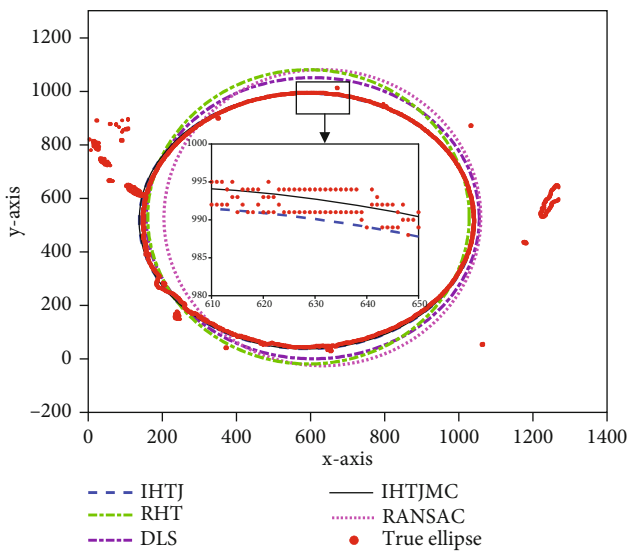

Figure 14: Ellipse fitting result of different methods in experiment III.

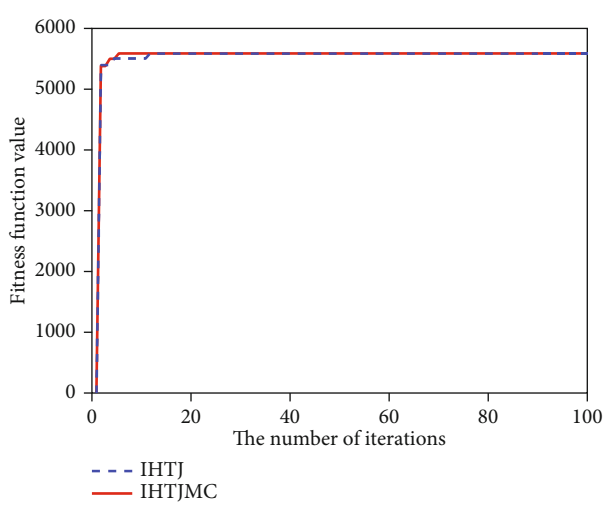

Figure 15: Iteration curves of fitness function with IHTJ and IHTJMC in experiment III.

Table 4: RMSE of diameter measurements with five methods in experiment III.

Method	RMSE
IHTJMC	0.0690
IHTJ	0.0959
RHT	4.3201
DLS	1.1412
RANSAC	1.9916

after the adjustment of CCD camera is finished. Because there is a shooting angle that is shown in Figure 1, the image of the gasket actually includes two ellipses: an inner ellipse and an outer ellipse. In this experiment, the diameter of the inner ellipse is used to calibrate, and the diameter of the outer ellipse is used to verify.

The parameters are set as follows: maximum number G of iterations is 1000, the number of the individuals NP is 90, the termination condition is $Y_{\text{gbest}} > 5600$, the number of subpopulations M is 3, the search scope is set twice as big as that in [28], and the experiment is run 30 times independently, too.

The results of ellipse fitting are shown in Figure 14. We can see from this figure that the result of the IHTJMC is closer to the true value compared with other methods, and the accuracy of the IHTJMC is highest. Figure 15 presents the iteration curves of fitness function in the IHTJ and IHTJMC, respectively. As shown in the figure, the IHTJ converges at the $12_{\text{-th}}$ time, and the IHTJMC converges at the 5_{th} time. This proves that the convergence rate of the IHTJMC is superior to that of the IHTJ. Table 4 shows the comparison of RMSE of these methods. From the table, we can see that the accuracy of the IHTJMC for diameter measurement is much higher than those of other methods.

As can be seen from these experimental results, the measuring accuracy and converge rate are greatly raised after the improvement for the IHTJ with the cooperation strategy of multiple populations. It not only inherits the strengths of superior robustness and accuracy in HT but also overcomes the weakness of trapping into local optimization in the IHTJ and improves the accuracy and robustness of the IHTJ.

Therefore, the IHTJMC provides a more effective method for the diameter measurement in many complex industrial applications, especially the prior knowledge is inaccurate.

5. Conclusion

In this paper, IHTJMC is developed to address the disadvantage of the IHTJ in diameter measurement of a red-hot workpiece. In this method, a collaborative structure of multi-population is proposed, and the migration strategy is designed to finish the cooperation between different subpopulations. The problem of trapping into local optimization is restrained and the global search ability is improved greatly. Three experiments are designed to test the effectiveness of the IHTJMC. Compared with the existing methods, the IHTJMC has better accuracy and robustness. It preserves the advantages of the IHTJ including high accuracy and strong robustness and improves the global search capacity of the IHTJ. It is beneficial to solve the problem of diameter measurement when the priori knowledge is not accurate. In future, how to restrain the effect of the error and the aberration during the measurement is an important subject in this field. At the same time, the better migration strategy will be further researched in the IHTJMC and the superior experimental scheme will be designed in the future.

Data Availability

In experiment I, six test functions including Sphere, Dropwave, Girewank, Rastrigin, Rosenbrock, and Schaffer are used to test the effectiveness of the proposed strategy based on the cooperation of multiple populations in the IHTJMC. These functions are always used to verify the performance of the swarm intelligence optimization algorithms. They are shown in Table 1 of the manuscript. In experiment II, 100 data points are selected from an ellipse with Gaussian noise, in which the parameters are set in the manuscript. The Gaussian noise variance is 0.01. These data points are shown in Figure 9 of the manuscript. The image of the last experiment can be obtained through sending an e-mail to the corresponding author.

Conflicts of Interest

The authors declare that there is no conflict of interest regarding the publication of this paper.

Acknowledgments

This work was supported by the National Natural Science Foundation (NNSF) of China [grant numbers 62003261, 61702410, 62073258, and 61871318] and Natural Science Basic Research Plan in Shaanxi Province of China [grant numbers 2020JQ-645 and 2020JQ-650].

References

[1] X. Pan, Z. Liu, and G. Zhang, "On-site reliable wheel size measurement based on multisensor data fusion," *IEEE Transactions on Instrumentation and Measurement*, vol. 68, no. 11, pp. 4575–4589, 2019.

[2] Y.-C. Zhang, C. Luo, X.-B. Fu, and Y. M. Chen, "Automatic measurement method for the size of large forgings based on scattering on rough surface," *IET Science, Measurement & Technology*, vol. 11, no. 1, pp. 118–124, 2017.

[3] S. Zhu, R. Huang, J. R. Avila et al., "Simultaneous measurements of wire diameter and conductivity using a combined inductive and capacitive sensor," *IEEE Sensors Journal*, vol. 20, no. 19, pp. 11617–11624, 2020.

[4] S. Babashakoori and M. Ezoji, "Average fiber diameter measurement in scanning electron microscopy images based on Gabor filtering and Hough transform," *Measurement*, vol. 141, pp. 364–370, 2019.

[5] M. Torabi, S. M. Mousavi, and D. Younesian, "A high accuracy imaging and measurement system for wheel diameter inspection of railroad vehicles," *IEEE Transactions on Industrial Electronics*, vol. 65, no. 10, pp. 8239–8249, 2018.

[6] X. Zhang, D. Liu, X. Wang, and X. Zhang, "Advanced ellipse fitting algorithm based on ADMM and hybrid BFGS method," *IEEE Transactions on Instrumentation and Measurement*, vol. 70, article 3515111, 2021.

[7] Y. Kang, J. Gong, Y. Xu et al., "Ultrahigh-precision diameter control of nanofiber using direct mode cutoff feedback," *IEEE Photonics Technology Letters*, vol. 32, no. 5, pp. 219–222, 2020.

[8] J. Jamaludin and R. A. Rahim, "Online optical tomography system for detecting and measuring the diameters of solid and transparent objects," *IEEE Sensors Journal*, vol. 16, no. 16, pp. 6175–6183, 2016.

[9] D. Liu and J. Liang, "A Bayesian approach to diameter estimation in the diameter control system of silicon single crystal growth," *IEEE Transactions on Instrumentation and Measurement*, vol. 60, no. 4, pp. 1307–1315, 2011.

[10] J. Liang, P. Li, D. Zhou et al., "Robust ellipse fitting via alternating direction method of multipliers," *Signal Processing*, vol. 164, pp. 30–40, 2019.

[11] M. Kesäniemi and K. Virtanen, "Direct least square fitting of hyperellipsoids," *IEEE Transactions on Pattern Analysis and Machine Intelligence*, vol. 40, no. 1, pp. 63–76, 2018.

[12] J. Liang, Y. Wang, and X. Zeng, "Robust ellipse fitting via half-quadratic and semidefinite relaxation optimization," *IEEE Transactions on Image Processing*, vol. 24, no. 11, pp. 4276–4286, 2015.

[13] P. C. Niedfeldt and R. W. Beard, "Convergence and complexity analysis of recursive-RANSAC: a new multiple target tracking algorithm," *IEEE Transactions on Automatic Control*, vol. 61, no. 2, pp. 456–461, 2016.

[14] T. Thomas, A. George, and K. I. Devi, "Effective iris recognition system," *Procedia Technology*, vol. 25, pp. 464–472, 2016.

[15] M. Kumar and N. B. Puhan, "RANSAC lens boundary feature based kernel SVM for transparent contact lens detection," *IET Biometrics*, vol. 8, no. 3, pp. 177–184, 2019.

[16] S. Huang, W. Jin, M. Ye et al., "A vision based method for automated measurement of circular fiber cross-sections," *Measurement*, vol. 162, article 107913, 2020.

[17] Y. Liu, J. Liu, and Y. Ke, "A detection and recognition system of pointer meters in substations based on computer vision," *Measurement*, vol. 152, article 107333, 2020.

[18] C. Lu, S. Xia, M. Shao, and Y. Fu, "Arc-support line segments revisited: an efficient high-quality ellipse detection," *IEEE Transactions on Image Processing*, vol. 29, pp. 768–781, 2020.

[19] R. O. Duda and P. E. Hart, "Use of the Hough transformation to detect lines and curves in pictures," *Communications of the ACM*, vol. 15, no. 1, pp. 11–15, 1972.

[20] N. Kiryati, Y. Eldar, and A. M. Bruckstein, "A probabilistic Hough transform," *Pattern Recognition*, vol. 24, no. 4, pp. 303–316, 1991.

[21] H. Yuen, J. Illingworth, and J. Kittler, "Detecting partially occluded ellipses using the Hough transform," *Image and Vision Computing*, vol. 7, no. 1, pp. 31–37, 1989.

[22] L. Xu, E. Oja, and P. Kultanen, "A new curve detection method: randomized Hough transform (RHT)," *Pattern Recognition Letters*, vol. 11, no. 5, pp. 331–338, 1990.

[23] V. Kumar, A. Asati, and A. Gupta, "Memory-efficient architecture of circle hough transform and its FPGA implementation for iris localisation," *IET Image Processing*, vol. 12, no. 10, pp. 1753–1761, 2018.

[24] L. Li, G. Wang, X. Zhang, and H. Yu, "Adaptive real-time recursive radial distance-time plane Hough transform track-before-detect algorithm for hypersonic target," *IET Radar, Sonar & Navigation*, vol. 14, no. 1, pp. 138–146, 2020.

[25] M. Liu, Z. Liu, W. Lu, Y. Chen, X. Gao, and N. Zhao, "Distributed few-shot learning for intelligent recognition of communication jamming," *IEEE Journal of Selected Topics in Signal Processing*, p. 1, 2021.

[26] M. Liu, J. Wang, N. Zhao, Y. Chen, H. Song, and R. Yu, "Radio frequency fingerprint collaborative intelligent identification using incremental learning," *IEEE Transactions on Network Science and Engineering*, 2021.

[27] M. Liu, C. Liu, M. Li, Y. Chen, S. Zheng, and N. Zhao, "Intelligent passive detection of aerial target in space-air-ground integrated networks," *China Communications*, vol. 19, no. 1, pp. 52–63, 2022.

[28] X. Zhang, R. Mu, K. Chen, Y. Yang, and Y. Chen, "Intelligent Hough transform with Jaya to detect the diameter of red-hot circular workpiece," *IEEE Sensors Journal*, vol. 21, no. 1, pp. 560–567, 2021.

[29] R. Rao, "Jaya: a simple and new optimization algorithm for solving constrained and unconstrained optimization problems," *International Journal of Industrial Engineering Computations*, vol. 7, no. 1, pp. 19–34, 2016.

[30] K. Gao, F. Yang, M. Zhou, Q. Pan, and P. N. Suganthan, "Flexible job-shop rescheduling for new job insertion by using discrete Jaya algorithm," *IEEE Transactions on Cybernetics*, vol. 49, no. 5, pp. 1944–1955, 2019.

[31] S. Zhang, J. Xu, L. H. Lee, E. P. Chew, W. P. Wong, and C. H. Chen, "Optimal computing budget allocation for particle swarm optimization in stochastic optimization," *IEEE Transactions on Evolutionary Computation*, vol. 21, no. 2, pp. 206–219, 2017.

[32] J. Tian, Y. Tan, J. Zeng, C. Sun, and Y. Jin, "Multiobjective infill criterion driven Gaussian process-assisted particle swarm optimization of high-dimensional expensive problems," *IEEE Transactions on Evolutionary Computation*, vol. 23, no. 3, pp. 459–472, 2019.

Hindawi
Wireless Communications and Mobile Computing
Volume 2022, Article ID 7941367, 14 pages
https://doi.org/10.1155/2022/7941367

Research Article

A Novel Approach of Protocol Behavior Identification for TDMA-Based Frequency Hopping Communication

Junyi Zhang,[1] **Mengtian Tan**,[2] **Fei Shi**,[1] **Yong Yang**,[1] **and Zhutian Yang**[3]

[1]*The 54th Research Institute of CETC, Shijiazhuang 050081, China*
[2]*School of Electronics and Information Engineering, Harbin Institute of Technology, Shenzhen 518055, China*
[3]*School of Electronics and Information Engineering, Harbin Institute of Technology, Harbin 150001, China*

Correspondence should be addressed to Yong Yang; yangyong5454@126.com

Received 14 February 2022; Revised 10 March 2022; Accepted 12 March 2022; Published 30 March 2022

Academic Editor: Mingqian Liu

Frequency hopping (FH) communication technology is adopted widely in military and civil fields, due to its excellent communication characteristics such as antisearch and anti-interference. Efficient reconnaissance methods of FH communication are becoming a research hotspot. In this paper, a novel reconnaissance approach for FH communication emitters is proposed, by using the TMDA protocol behavior identification. Based on the signalling used in the TDMA protocol, the protocol behavior for FH communication can be specified. These behaviors are usually used for the process controlling of FH communication and network maintenance. Therefore, recognition of FH communication protocol behaviors can be used for emitter intention reasoning indirectly. Simulation results show that the proposed approach is effective and potential for application.

1. Introduction

Frequency hopping (FH) communication is an important application of spread spectrum communication, which was widely used in both military and civil affairs [1–5]. Due to its excellent anti-interference ability, as well as its capability to increase the security of wireless services, FH has been implemented diffusely, e.g., in Bluetooth [6], advanced extremely high-frequency (AEHF) communication satellites [7], Military Strategic and Tactical Relay (MILSTAR) communication satellites [8], and emerging dynamic communication systems [9]. FH communication proves practical in various radiofrequency systems, and it is developing toward faster hopping speed and higher hopping-frequency bandwidth, which will strengthen the original advantages of FH communication in both military and civil applications.

Meanwhile, due to a wide application in military fields, the activities of FH communication emitters gradually become an important source of information in electronic reconnaissance. However, advanced FH technology has brought great challenges to electronic countermeasures. Wider bandwidths, more complex frequency variations, along with many other factors further complicate the electromagnetic spectrum, increasing the difficulty of extracting effective information. Therefore, many researchers have devoted efforts to spectrum cognition in complex electromagnetic environments [10–14]. The cognition process, which is an integral section for the awareness of complex situations, connects the perception of signals with decision making process [15–19].

Electromagnetic countermeasures in a complex electromagnetic environment necessitate not only the analysis of the signal but also the cognition of communication emitter behaviors, such as broadcast, relay, and link establishment. Specifically, various parameters of FH signals and control signalling used in protocols manifest the behavior of communication emitters. Therefore, the identification of protocol behaviors can be a novel approach information retrieval for electronic countermeasures. If the mapping relation between signals and the behavior of the FH communication emitter can be successfully established, it would provide a tremendous positive impact on future communication countermeasures. However, to our best knowledge, the research on frequency

hopping communication signals mainly lies in the reconnaissance of frequency hopping communication signals, including signal detection, interception, sorting, and parameter estimation [20–23], few on the cognition of radiation source target.

Against this background, this paper proposes a new scheme for electromagnetic countermeasures based on FH communication signals, that is, through signal processing technology, according to the electromagnetic signal law formed by the radiation source target performing specific functions, the behavior and related task information of the radiation source target can be recognized. The proposed method solves two main problems, i.e., the positioning of the signalling signal and the identification of the signalling signal, by using noncooperative signal blind demodulation and machine learning.

The rest of this paper is organized as follows. Section 2 presents the system model. Section 3 introduces the positioning of the signalling signal. Section 4 presents the recognition of the radiation source target behavior, followed by performance evaluation in Section 5. Finally, Section 6 concludes this paper.

2. System Model

In this research, we propose a new scheme for communication emitter reconnaissance. We consider a frequency hopping communication system in the VHF band. There are two important models to be built in the system. One is the time frame sequence model of FH communication. The other is the radiation source target model of FH communication.

The time frame sequence model of FH communication is built based on the TDMA communication protocol, which is complete, representative, and widely used in many kinds of frequency hopping communication equipment, such as frequency hopping radio. Besides, the method proposed in this paper is generalizable to recognition under other protocols. Therefore, it is assumed that a TDMA protocol is adopted in the FH communication system, where there exist N nodes in the network. In a super time frame (STF), each node has a time frame (TF) for transmitting, and each time frame contains 14 time slots (TS). In this protocol, the frequency hopping rate of the radio communication is 64000/105 hops/sec, namely, 64000 frequency hops within 105 seconds. The time for 40 frequency hops is defined as a time slot, and 140 bytes are transmitted within the duration of a time slot.

A time slot is divided into three parts: synchronization sequence, data, and control sequence. From the 0th to 7th hops, the Walsh synchronization sequence is transmitted, which is used for time slot synchronization. From the 8th to 37th hops, the information data sequence is transmitted for radio communication, which includes signalling sequence and voice data sequence. Within the last 2 hops, the control sequence is transmitted, which is used for transmit-receive switching, information proofreading and protection.

The time slot types in a time frame are generally divided into three types: fixed time slot type (fixed slot (FS)), static time slot type (static slot (SS)), and dynamic time slot type (dynamic slot (DS)). The fixed time slot type refers to the time slot that is permanently occupied by a certain node. Generally, the first time slot of a frame is the fixed time slot fixedly occupied by the central node. The static time slots refer to the time slots that are fixedly allocated to certain nodes in a time frame. The allocation of the static time slots in different time frames is different. The dynamic time slots refer to the time slots that can be reserved and occupied by any node, that is, the occupancy of time slots is dynamically allocated. The allocation formula for static and dynamic time slots in each time frame is as follows:

Static time slots (SS):

$$P_{\mathrm{id}} = (5F_{\mathrm{id}} + \mathrm{SS}_{\mathrm{id}})\%N. \tag{1}$$

Dynamic time slots (DS):

$$P_{\mathrm{id}} = \left[N\frac{(7-5D_{\mathrm{id}})\%8}{8} + F_{\mathrm{id}}\right]\%N, \tag{2}$$

where P_{id} denotes the time slot number; F_{id} denotes the time frame number in a superframe, and the value is $0, 1, 2..N-1$; SS_{id} denotes the static time slot number in a time frame, and the value is $0, 1\ldots4$; N denotes the number of nodes in the network; and D_{id} denotes the dynamic time slot number in a time frame, and the value is $0, 1\ldots7$.

We assume that the protocol in this research is conflict free, where only the node with the time slot occupancy can send data in the time slot, while other nodes cannot send and can only be in the receiving state.

In order to match the encoding rate of the voice encoder in the frequency hopping radio communication system, one-way unidirectional voice data transmission needs to occupy two time slots in a time frame. Two time slots form a group, and 8 dynamic time slots are divided into 4 groups. The 4 groups are called reserved time slots, which are used to transmit voice data.

Signalling is used in the communication protocol to establish and remove communication links and transmit voice data. According to the different functions, signalling can be divided into three types: time slots reservation control signalling (AC), reservation links control signalling (RC), and voice data transmission signalling (RD). The three types of signalling include 11 specific signalling types, and each signalling has a length of 19 bits, including 8-bit long feature codes and 11-bit long signalling content. The voice transmission types in the protocol are generally divided into three types: unicast direct voice transmission, relay voice transmission, and broadcast voice transmission. Among them, unicast direct voice transmission can be divided into unicast one-way voice transmission and unicast bilateral voice transmission; relay voice transmission can be divided into relay one-way voice transmission and relay bilateral voice transmission. Each transmission type corresponds to a different signalling transfer process, which is also the theoretical basis for us to realize the target behavior recognition of the radiation source based on the signalling signal.

So far, we can achieve time-frame sequence modeling, the schematic diagram of the time-frame sequence model is shown in Figure 1.

The target modeling of the frequency hopping communication radiation source is realized based on the composition and working principle of the frequency hopping communication system. The composition and working principle of the frequency hopping communication system are shown in Figures 2 and 3.

In the transmitter, the baseband signal is digitally modulated to generate the corresponding modulation signal $m(t)$, and the frequency synthesizer is controlled by the FH sequence generator to synthesize the local oscillator signal of the corresponding frequency. The local oscillator signal $p(t)$ can be expressed as

$$p(t) = \cos\left[(\omega_0 + n\omega_\Delta)t + \varphi_n\right], \tag{3}$$

where ω_0 denotes the center frequency of transmitter and ω_Δ denotes the FH interval of the frequency synthesizer.

The modulated signal $m(t)$ is then mixed with the local oscillator signal $p(t)$ to obtain the transmitted signal $S_t(t)$ whose frequency hops with time:

$$s_t(t) = m(t)\cos\left[(\omega_0 + n\omega_\Delta)t + \varphi_n\right]. \tag{4}$$

During transmission, there are other frequency interferences $J(t)$ and noise $n(t)$ in the channel at this time, and the FH signals transmitted by other network stations in the FH communication system $s_j(t)$. Therefore, the mixed signal $s_r(t)$ that reaches the receiver part is

$$s_r(t) = s_t(t) + \sum_{j=1}^{k} s_j(t) + n(t) + J(t). \tag{5}$$

In the case of FH synchronization at the receiver part, the local oscillator frequency synthesized by the frequency synthesizer has the same hopping rule as the transmitter part and there is always an intermediate frequency difference ω_I between the local oscillator frequency at the transmitter part and the receiver part. The local oscillator frequency synchronously generated by the frequency synthesizer at the receiver part is $\omega_r + n(t)\omega_\Delta$, where ω_r is the center frequency, $\omega_I = \omega_r - \omega_0$, $n(t)$ is an integer that changes over time, and ω_Δ is the FH interval of the frequency synthesizer.

Mixing the received signal $s_r(t)$ with the local oscillator signal of the receiver $p_r(t)$ can get

$$s_p(t) = s_r(t)p_r(t) = \left[s_t(t) + \sum_{j=1}^{k} s_j(t) + n(t) + J(t)\right] \cdot \cos\left[(\omega_r(t) + n\omega_\Delta)t + \varphi_r\right]. \tag{6}$$

If the transmitting and receiving parts maintain a high degree of synchronization, the transmitted signal $s_t(t)$ is substituted into the above formula to obtain

$$s_p(t) = \frac{1}{2}m(t)\left\{\cos(\omega_I t + \varphi_I) + \cos\left[(\omega_r + \omega_0 + 2n\omega_\Delta)t + \varphi_r + \varphi_n\right]\right\} + \left[\sum_{j=1}^{k} s_j(t) + n(t) + J(t)\right]\cos\left[(\omega_r(t) + n\omega_\Delta)t + \varphi_r\right]. \tag{7}$$

In order to extract the intermediate frequency signal $m(t)\cos(\omega_I t + \varphi_I)$ carrying the relevant information of the modulation signal $m(t)$ in the above formula, we can use the intermediate frequency filtering method to extract the intermediate frequency signal and filter out other interference signals. Therefore, the useful signal component $s_d(t)$ obtained by intermediate frequency filtering is

$$s_d(t) = m(t)\cos(\omega_I t + \varphi_I). \tag{8}$$

Then, the intermediate frequency signal $s_d(t)$ is sent to the intermediate frequency mixer to obtain the information modulated signal $m(t)$. The modulated signal is demodulated and decoded to obtain the source information it carries.

3. Signalling Signal Location

In order to identify the behavior of the FH communication emitter, the signalling information should be extracted. Because signalling is usually used for link control, such as establishment, supervision, and teardown, the technical route of the entire implementation method is shown in Figure 4.

According to the TDMA communication protocol mentioned, the signallings are at the beginning of the time slot sequence. Therefore, in order to recognize the kind of signalling through signalling signal accurately, signalling signal location is necessary. Otherwise, the length of signal input to CNN is too long, and the recognition accuracy cannot be guaranteed. Therefore, to extract the signalling information, the signalling should be located first. Signalling location can be realized in two steps: frame length estimation and frame structure analysis. The frame structure analysis is to determine the location of signalling according to the frame length estimation result. After the location of signalling is determined, the signalling signal location is realized combining the relevant parameters of the intermediate frequency signal.

3.1. Frame Length Estimation. Frame structure analysis refers to the following: For noncooperative communication systems, through intercepted communication signals, to obtain the greatest understanding of the time frame encapsulation structure used by the communication system to transmit information. To achieve frame structure analysis of noncooperative signals, the first thing to achieve is to accurately estimate the length of the time frame.

Since most of the frame header sequences in communication systems are sequences with good autocorrelation or cross-correlation characteristics, the sequence length between two frame headers can be regarded as the length of a frame. Thereby, the autocorrelation search algorithm can be used to find the frame header sequence, and then, the length of frame can be estimated.

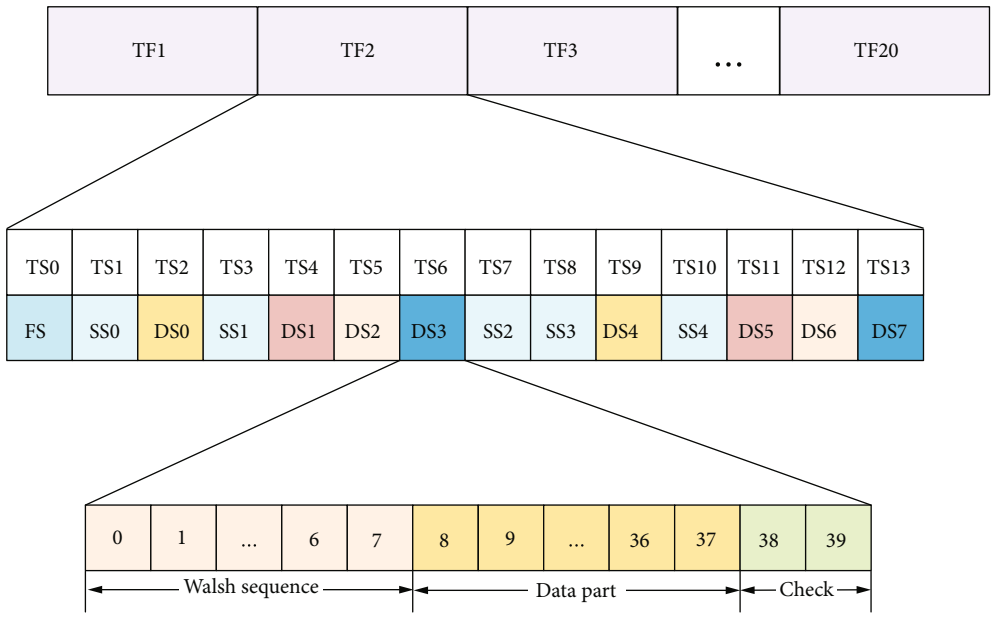

Figure 1: Schematic diagram of time frame sequence modeling.

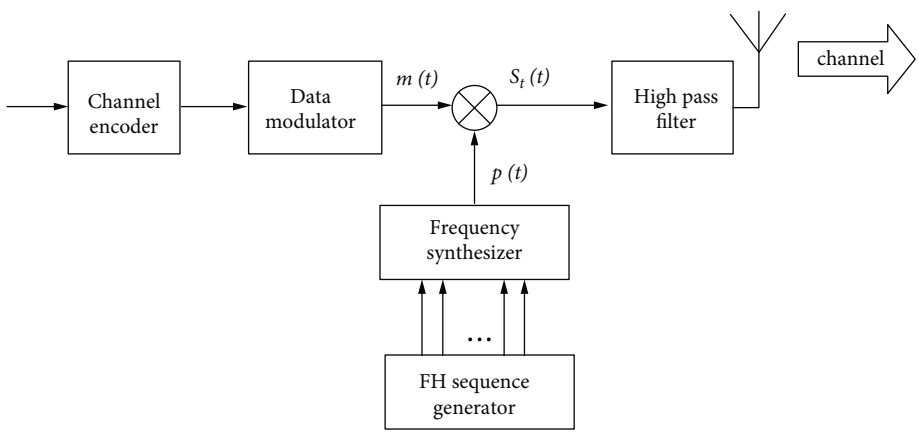

Figure 2: Transmitter part of frequency hopping communication system.

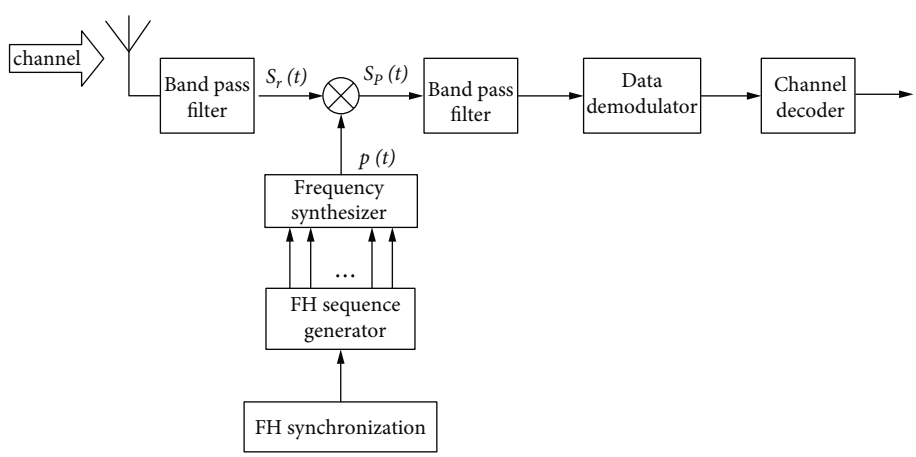

Figure 3: Receiver part of frequency hopping communication system.

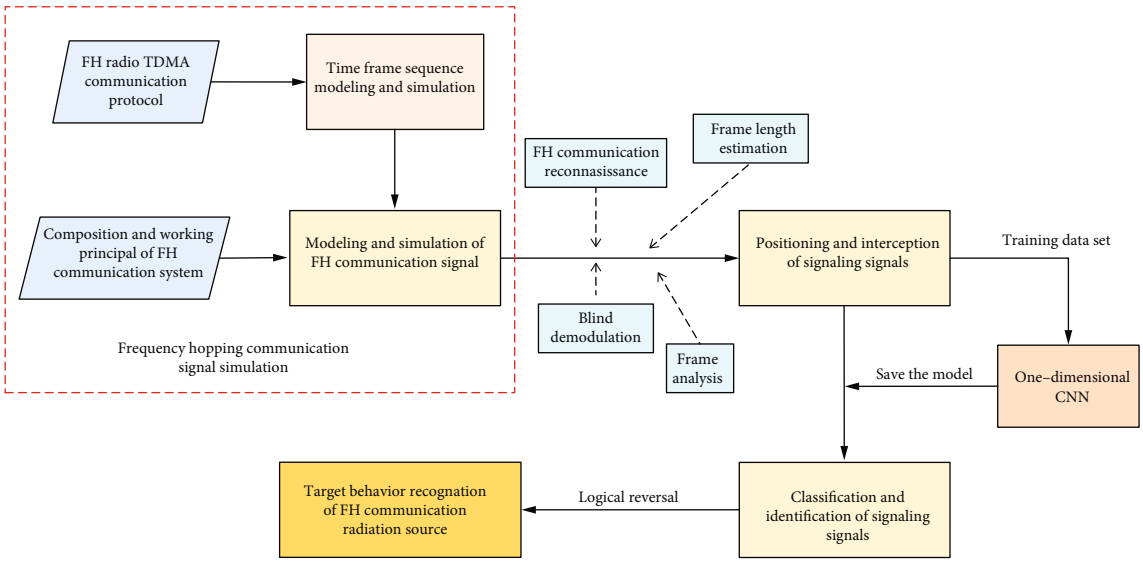

Figure 4: The technical route of the entire implementation method.

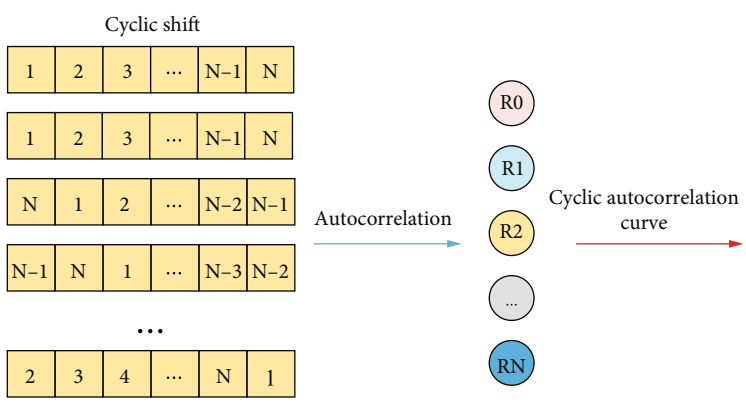

Figure 5: Schematic diagram of the frame length estimation algorithm.

In this paper, a simple and convenient estimation approach is adopted for frame length based on cyclic autocorrelation. The algorithm realization schematic diagram is shown as in Figure 5.

The input of this algorithm is the 0-1 bit stream data obtained after the noncooperative signal is demodulated, and the output is the curve corresponding to the cyclic autocorrelation result. Cyclic autocorrelation is to perform autocorrelation processing after the sequence is cyclically shifted. Because the beginning of the time frame is generally a synchronous sequence, which has good autocorrelation and cross-correlation characteristics. So, periodic spikes will appear in the cyclic autocorrelation results. The peak appearance period corresponds to the length of the time frame. So the average correlation peak distance can be calculated according to the position of correlation peak, and then, the estimation of the frame length can be realized. The corresponding formula of the frame length estimation algorithm for cyclic autocorrelation is

$$R_m(k) = x(k) \cdot x_m(k), \tag{9}$$

where $x(k)$ is the sequence of the frame length to be estimated, $x_m(k)$ is the result of m point cyclic shift of $x(k)$, $R_m(k)$ is the autocorrelation result of the sequence $x(k)$ and $x_m(k)$, and the values of m and k are $m = 0, 1, \cdots N-1$; $k = 0, 1, \cdots N-1$, where N is the length of the sequence.

3.2. Frame Structure Analysis. After the frame length estimation is realized, the next step is to analyze the frame structure according to the frame length estimation result. The algorithm used is a frame structure analysis algorithm based on cumulative filtering. The basic principle of this algorithm is based on the similarity of the frame structure in each frame and the similar content of the frame header. The symbol stream data recovered by demodulation is accumulated in the unit of frame length, so as to realize the analysis of the frame structure. The schematic diagram of the algorithm principle is shown in Figure 6.

Based on the above processing steps, the length of a time frame, the number of time slots in a time frame, the length of a time slot, the position of the time slot in a time frame, and the beginning sequence length of the time slot are determined through the above processing. Based on this information

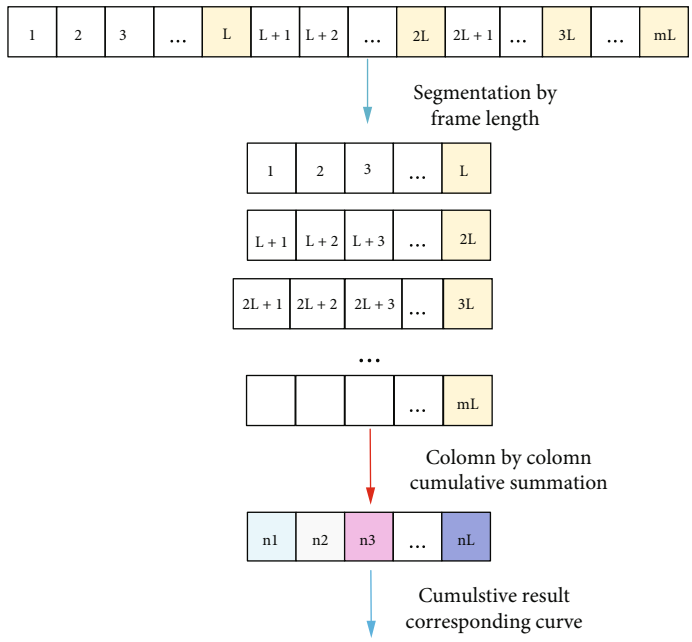

Figure 6: Schematic diagram of the frame structure analysis algorithm principle.

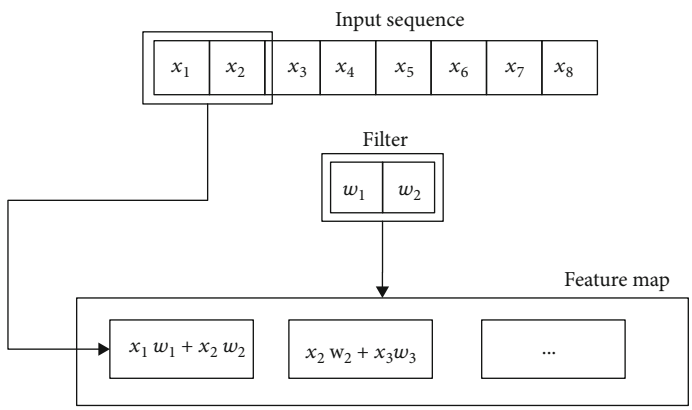

Figure 7: Basic principle of one-dimensional convolution.

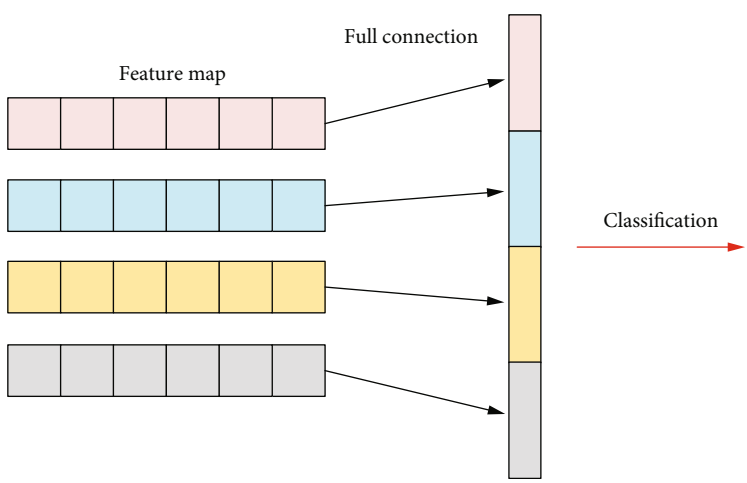

Figure 8: Principle of the flatten method.

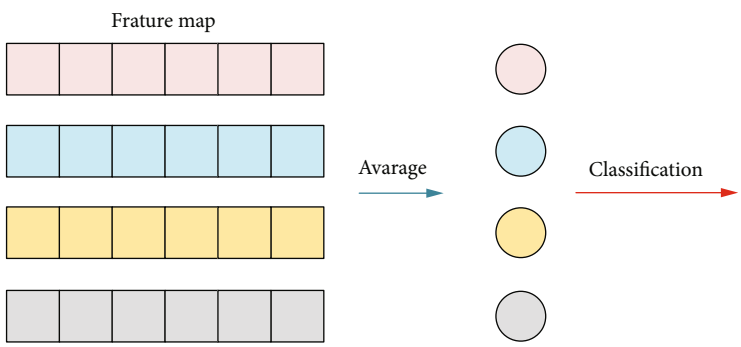

Figure 9: Principle of the global average pooling method.

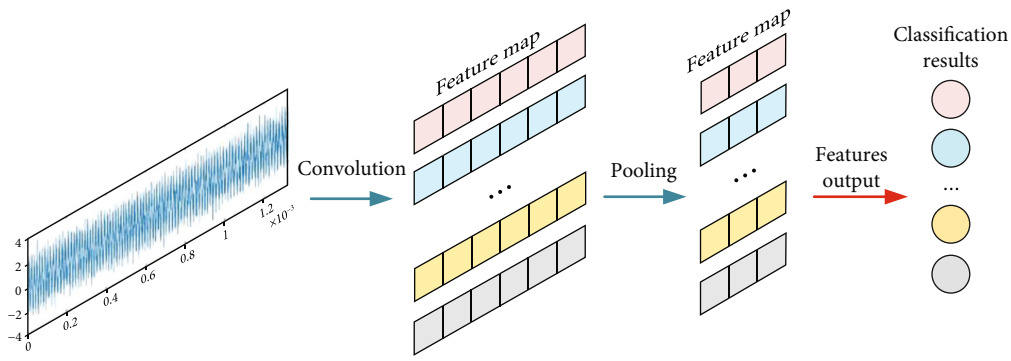

Figure 10: Schematic diagram of the one-dimensional CNN network structure.

Table 1: Structural parameters of network.

Layer	Type	Parameter	Output
1	Conv1D	(80, 10, 3)	(334, 80)
2	MaxPooling1D	(2, 2)	(167, 80)
3	Conv1D	(40, 6, 2)	(84, 40)
4	MaxPooling1D	(2, 2)	(42, 40)
5	Conv1D	(40, 3, 3)	(14, 40)
6	MaxPooling1D	(2, 2)	(7, 40)
7	Conv1D	(60, 2, 1)	(7, 60)
8	MaxPooling1D	(2, 2)	(3, 60)
9	GlobalAveragerPooling1D	—	(1, 60)
10	Dense	60	3660
11	Dense	30	1830
12	Dense	12	372

obtained, the possible position of the signalling sequence is determined, and the carrier frequency, symbol rate, and other parameters related to the signal are combined to realize the location and interception of the signalling signal in the dehopping signal.

4. Signalling Recognition

Machine learning has a good performance in many types of recognition, because it can extract features from the input training data and reduce the incompleteness caused by artificial settings. The convolutional neural network (CNN) is a widely used machine learning structure. CNN is a feed-forward neural network whose artificial neurons can respond to surrounding units within a certain coverage area. In this paper, our network input is signalling signals, which are fixed-length time series. Since one-dimensional CNN has higher recognition accuracy when processing signals in large length, it is chosen for the recognition of signalling signals in this paper. Using the three characteristics of CNN (local perception, weight sharing, and maximum pooling), we can realize the type recognition of signalling signals. Figure 7 shows the basic principle of one-dimensional convolution.

After the feature map is obtained, in order to further refine the features, pooling technology is also used. Similar to the two-dimensional convolution technology, methods such as maximum pooling and average pooling are also used in one-dimensional convolution. Besides, before using the pooling technique, an activation function is also needed to increase the nonlinear factor.

After the refined features are obtained, the flatten method or the global average pooling method is also used to turn many feature maps into a feature vector so that the classification function can be used to classify the samples. The flatten method is to connect all the elements of each feature map to a single neuron. The principle is shown in Figure 8.

Although the flatten method looks simple, it has a big problem, namely, the amount of calculation. When the number and scale of feature maps are very large, adding a fully connected layer will increase the number of model

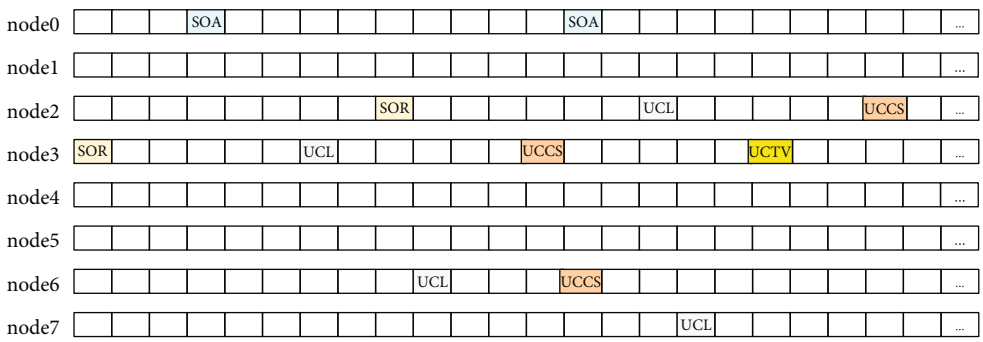

Figure 11: Schematic diagram of time slot signalling transfer between nodes.

$k = \{0, 1, \cdots N-1\} \longrightarrow N$ nodes of the network
$L^j \rightarrow$number of time slot signalling of the jth node
$S_{\text{SOR}} \rightarrow$SOR signalling search results
$S_{\text{UCL}} \rightarrow$UCL signalling search results
for $k = 1 : N$ do
  for $n = 1 : L^k$ do
    $i = 0$, search the SOR signalling
    $m = 0$, search the UCL signalling
    if *find the SOR signalling* then
      $S_{\text{SOR}}(i+1) = (k, n)$
    end
    if *find the UCL signalling* then
      $S_{\text{UCL}}(m+1) = (k, n)$
    end
  end
end
determine the central node and the calling node of voice transmission based on S_{SOR}
determine the called node of voice transmission based on S_{UCL}
divide the three nodes(the calling node, the called node, and the central node)
for $k = C \rightarrow$the calling node number do
  for $n = 1 : L$ do
    $p = 0$, search the SOF signalling
      if *find the SOF signalling* then
      $S_{\text{SOF}}(p+1) = (C, n)$
      end
    end
end
based on S_{SOR}, S_{SOF}
intercept all the middle time slot signallings of the three nodes

Algorithm 1: Division and interception of time slot signallings

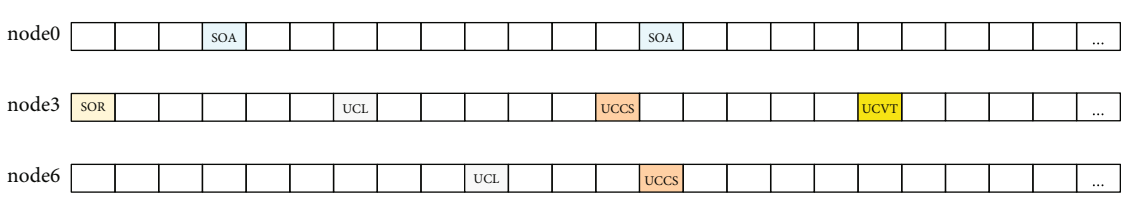

Figure 12: Time slot signalling division result 1.

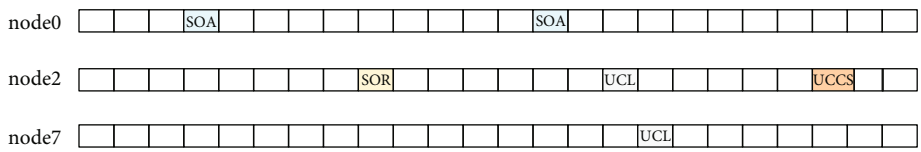

Figure 13: Time slot signalling division result 2.

Table 2: Parameters of simulation configuration.

Parameter	Value
Bit rate (R_b)	51200/3 bits/s
Bit interval (T_b)	3/51200 s
Frequency hopping rate (hopRate)	64000/105 s^{-1}
Number of bits per hop (bitsPerHop)	28
Number of samples per bit (sampNum)	354
Frequency hopping bandwidth (BW)	6 MHz
Frequency hopping frequency points (freqNum)	100
Frequency hopping interval (freqInterval)	60 KHz
Frequency hopping center frequency (f_c)	6 MHz
Number of signalling bits	19

parameters dramatically. In order to solve this problem, the global average pooling method can be used.

The global average pooling method is to form a feature vector by the average value of the elements in each feature map and then send the obtained feature vector to the classification function to obtain the classification result of the sample. Because the global average pooling method obtains the average value of each feature map without using a fully connected layer, it saves a lot of computing resources. The principle diagram of the global average pooling method is shown in Figure 9.

Before the data is input to the neural network, the data needs to be preprocessed. The main purpose of preprocessing is to reduce the dimensionality of the input signal data, making it easier to be processed by the neural network, while maintaining the information in the original signal, and improving the accuracy of network classification and recognition. Our convolutional network processes fixed-length signal sequences, so we need to perform fixed-length interception when intercepting signalling signals to make them have a uniform length. At the same time, the intercepted signals can be sampled at intervals to reduce the data dimension. If not preprocessed, the dimensionality of the input signal data will be quite large, which may contribute to long training time and low accuracy of network recognition. Therefore, the input of network is preprocessed IF signal which is converted from frequency hopping signal after dehopping and have a uniform length, while the output of network is the signalling type of the communication protocol. The one-dimensional CNN network structure is shown in Figure 10. And the structural parameters of the network are shown in Table 1.

5. Protocol Behavior Identification

During the positioning and recognition of signallings, types and time of arrival of signallings can be obtained. Next step is to identify the behavior of the emitter based on the signalling used. A schematic diagram of time slot signalling transmission of each node in the voice transmission process is shown in Figure 11.

The time slots allocation of each node is different, and the occupancy of the node time slots in voice transmission is also different. At the same time, because the communication protocol supports two unidirectional voice transmissions at the same time, the time slot signallings between nodes are interleaved and mixed together. Therefore, it is more difficult to recognize the behavior of the emitter directly based on the time slot signalling types of all nodes in the entire network. It is necessary to further divide and intercept the time slot signallings based on the nodes participating in the communication. The specific division and interception steps are as Algorithm 1:

The results obtained by dividing the time slot signalling are shown in Figures 12 and 13.

Based on the characteristic signalling in the time slot signallings, the type of the emitter voice transmission is temporarily determined and then calculated the chronological matching degree between the intercepted time slot signallings and the theoretical signalling combination and use it as the correct identification rate of the emitter behavior. The calculation formula of the chronological matching degree is as follows:

$$P_{\text{match}} = \frac{\sum_{i=1}^{N} s_i}{N}. \tag{10}$$

In the above formula, s_i is the consistency between the time slot signalling type and the theoretical signalling type in the voice transmission process; if they are consistent, s_i is 1; otherwise, it is 0; and N is the total number of theoretical signallings from the beginning to the end of a voice transmission process.

The calculation of matching degree can guarantee high accuracy in protocol behavior recognition despite multiple signalling recognition results being incorrect. Even though multiple signalling recognition results are incorrect, we can still calculate the chronological matching degree, which is used as the correct identification rate of the protocol behavior. And by comparing the correct identification rate of different protocol behaviors, we can choose the maximum of them to ensure high accuracy in protocol behavior recognition.

6. Experiment and Analysis

In this section, we achieve frame length estimation and frame structure analysis using related algorithms, then achieve signalling signal positioning and interception based on the analysis results, and finally achieve the emitter behavior identification based on the signalling signal identification results.

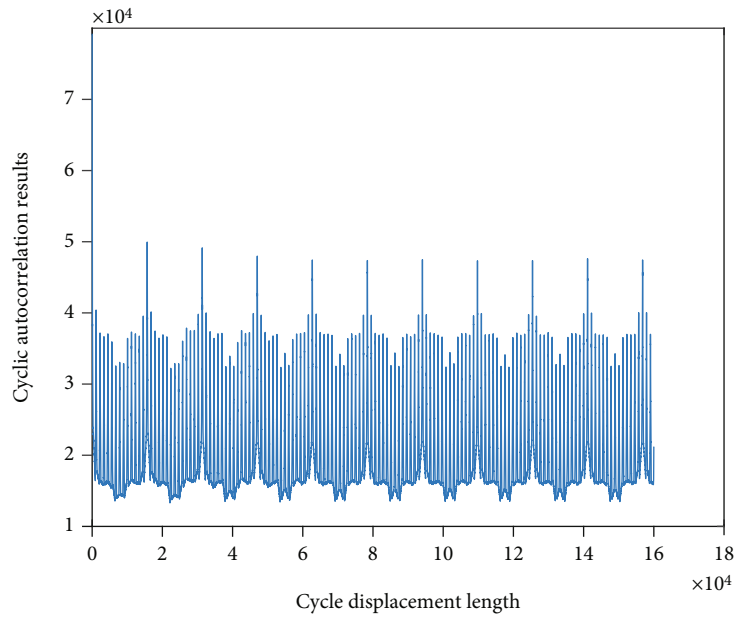

Figure 14: Partial cyclic autocorrelation curve.

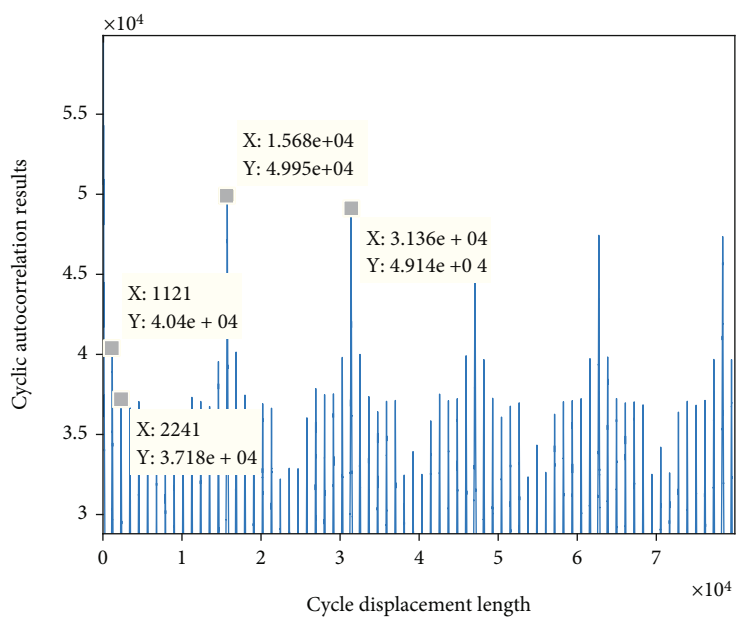

Figure 15: Partial enlargement of the cyclic autocorrelation curve.

Firstly, we consider a FH communication network with 8 nodes, including 1 master node and 7 ordinary nodes. It is assumed that the transmission of information between nodes follows the aforementioned FH radio TDMA networking protocol, and the digital modulation mode of baseband signal is MSK (minimum shift keying), which is a modulation method having good performance and widely used in communication systems. The relevant parameter settings for signalling signal simulation are shown in Table 2.

Next, we estimate the length of the time frame using cyclic autocorrelation, and the simulation results of the algorithm are shown in Figure 14. Periodic spikes appear in the cyclic autocorrelation results, with the continuous increase of the cyclic shift length. There are multiple secondary peaks between the highest spikes.

The results of the algorithm in Figure 14 are partially enlarged, and the distance between the highest peaks and the second peaks can be measured more accurately, as

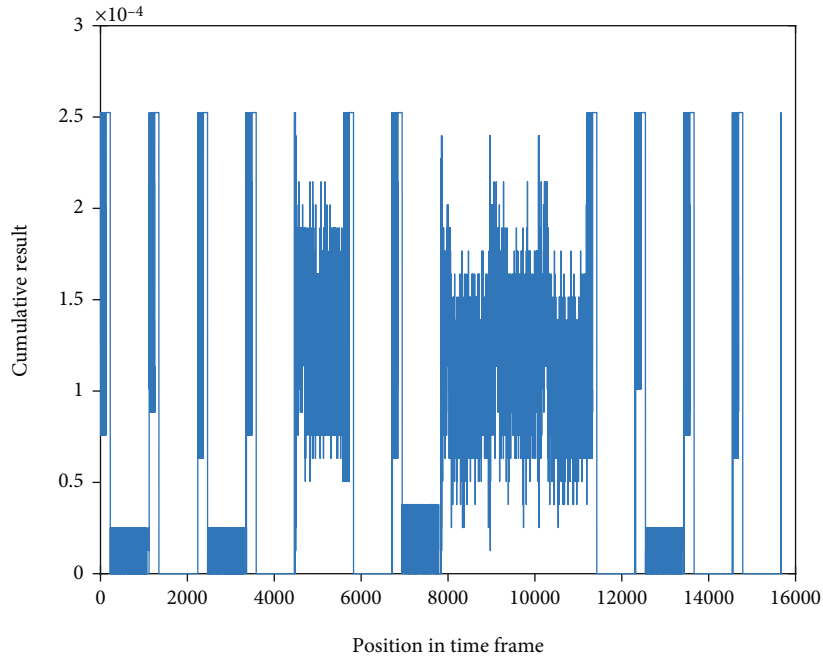

Figure 16: Simulation results of the frame structure analysis algorithm.

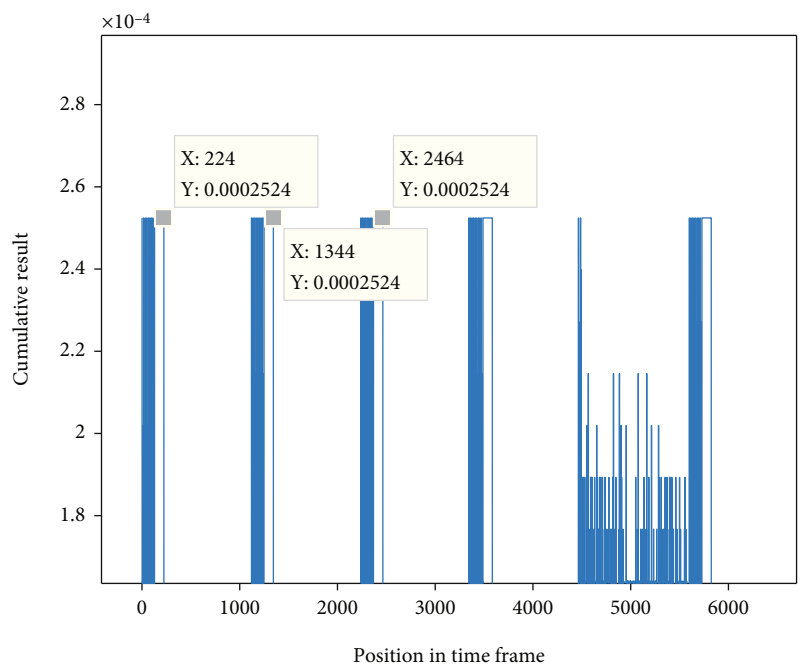

Figure 17: Partially enlarged results of algorithm simulation.

shown in Figure 15. Taking the average of multiple measurements of the peak distance in the amplified cyclic autocorrelation results, the distance between the highest peaks is about 15680, and the distance between the second peaks is about 1120, which is exactly consistent with the hypothetical communication protocol, indicating that the simulation results of the algorithm are completely correct.

Then, based on the estimation result of the time frame length, we achieve the analysis of the frame structure using the cumulative filtering algorithm, and the simulation result of the algorithm is shown in Figure 16. It can be found that there is a periodic structure inside the time frame. The number of the periodic structure in a time frame is about 14, which is in full compliance with the hypothetical communication protocol.

Similarly, the analysis result of the frame structure is further partially enlarged to more accurately determine the length of the periodic structure and the length of the initial

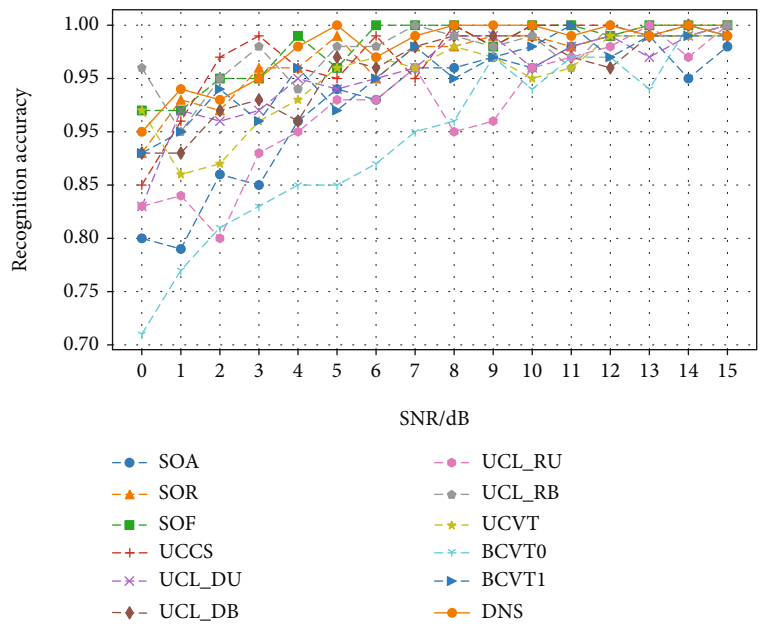

Figure 18: The recognition accuracy rate of 12 kinds of signalling under different signal-to-noise ratio conditions.

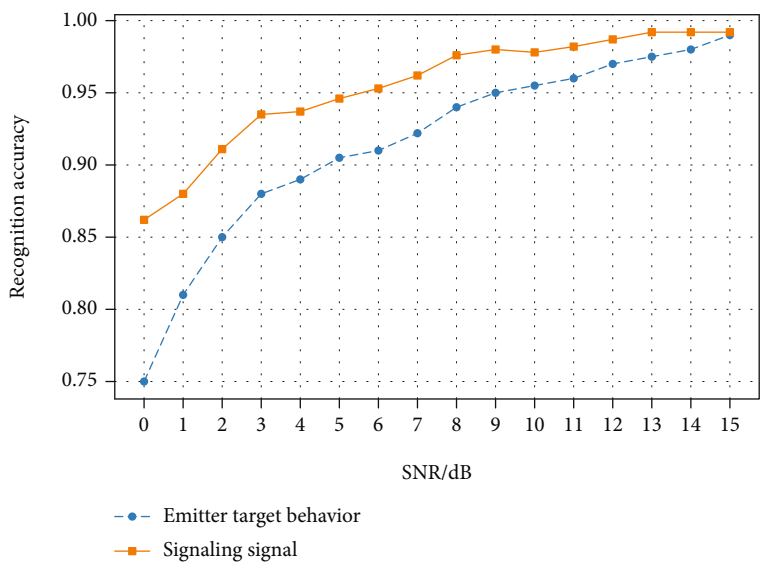

Figure 19: The average recognition accuracy of signalling signals and the target behavior recognition accuracy of the radiation source under different signal-to-noise ratio conditions.

sequence. The analysis result of the partially enlarged frame structure is shown in Figure 17. In the time frame analysis result, the length of the periodic structure is about 1240, and the length of the beginning sequence is about 224. Based on this, the position of the signalling sequence in the time frame is determined, and the positioning and interception of the signalling signal is realized combining the signal-related parameters.

After that, we identify the intercepted signalling signals using the convolutional neural network to obtain the signalling type of each signalling signal. The variation of the recognition accuracy of the 12 signalling signals with the signal-to-noise ratio is shown in Figure 18. The average recognition accuracy of 12 types of signalling is calculated to be 95.2% according to the single signalling recognition accuracy under the condition of single signal-to-noise ratio. In addition, we made statistics on the misidentification of each signalling signal under the condition of single signal-to-noise ratio. It is found that identification confusion among several types of signalling signal is prone to occur, and error detection and correction of signalling signal recognition can be realized based on this.

At the same time, the stability and robustness of the neural network have been verified. We have generated signals in different lengths by other digital modulation methods to verify the stability and robustness of the neural network. The digital modulation methods include BPSK, FSK, ASK, and MSK. The accuracies of signal recognition for the four modulation methods are all above 90% on average, and longer signal data can also be well recognized by the neural network, which indicate the stability and robustness of the neural networks we used in this paper.

At last, we realize the behavior recognition of the emitter by logical inversion according to the protocol, based on the recognition result of the signalling signal. Figure 19 shows the average recognition accuracy of the signalling signal and the emitter behavior under the condition of 0-15 dB signal-to-noise ratio. It can be seen from the figure that when the signal-to-noise ratio is 3 dB, the average behavior recognition accuracy has reached over 85%.

7. Conclusions

Based on the existing related technologies and theories of frequency hopping communication, this paper focuses on solving the two major technical problems of signalling signal positioning and signalling signal recognition. Finally, by identifying the type of the time slot signalling signal, the FH communication emitter behavior recognition is realized. This paper is oriented to the intelligent reconnaissance needs of FH communication stations and explores the cognitive mechanism and methods of the FH communication emitter behavior. According to the electromagnetic signal law formed by the FH communication emitter performing specific functions, the method of identifying the behavior of the emitter based on the signalling signal identification is studied. This paper focuses on the realization of key technologies such as signalling signal positioning and interception and signalling type recognition, lays a foundation for the emitter cognition of related information such as the behavior and tasks in complex electromagnetic environments, and is of great significance to improve the intelligent countermeasures in the electromagnetic spectrum domain.

Data Availability

The data used in this study is generated by simulation according to frequency hopping communication TDMA protocol. The [MAT] data used to support the findings of this study are included within the manuscript.

Conflicts of Interest

The authors declare that they have no conflicts of interest

References

[1] Q. Liu and M. P. Fok, "Ultrafast and wideband microwave photonic frequency-hopping systems: a review," *Applied Sciences*, vol. 10, no. 2, p. 521, 2020.

[2] W. Lu, Y. Ding, Y. Gao et al., "Resource and trajectory optimization for secure communications in dual unmanned aerial vehicle mobile edge computing systems," *IEEE Transactions on Industrial Informatics*, vol. 18, no. 4, pp. 2704–2713, 2022.

[3] R. Zhi, L. Zhang, and Z. Zhou, "Cognitive frequency hopping," in *2008 3rd International Conference on Cognitive Radio Oriented Wireless Networks and Communications (CrownCom 2008)*, pp. 1–4, Singapore, 2008.

[4] W. Hu, D. Willkomm, M. Abusubaih et al., "Cognitive radios for dynamic spectrum access - dynamic frequency hopping communities for efficient IEEE 802.22 operation," *IEEE Communications Magazine*, vol. 45, no. 5, pp. 80–87, 2007.

[5] M. Liu, Z. Liu, L. Weidang, Y. Chen, X. Gao, and N. Zhao, "Distributed few-shot learning for intelligent recognition of communication jamming," *IEEE Journal of Selected Topics in Signal Processing*, p. 1, 2021.

[6] B. R. Mahafza, *Introduction to Radar Analysis*, Chapman and Hall/CRC, Second Edition edition, 2017.

[7] N. J. Muller, *Bluetooth Demystified*, McGraw Hill, 2001.

[8] M. Liu, J. Wang, N. Zhao, Y. Chen, H. Song, and Y. Richard, "Radio frequency fingerprint collaborative intelligent identification using incremental learning," *IEEE Transactions on Network Science and Engineering*, 2021.

[9] M. Liu, C. Liu, M. Li, Y. Chen, S. Zheng, and N. Zhao, "Intelligent passive detection of aerial target in space-air-ground integrated networks," *China Communications*, vol. 19, no. 1, pp. 52–63, 2022.

[10] D. A. Fritz, D. W. Moy, and R. A. Nichols, "Modeling and simulation of advanced EHF efficiency enhancements," in *MILCOM 1999. IEEE Military Communications. Conference Proceedings*, Atlantic City, NJ, USA, 2002.

[11] J. P. Montgomery, D. L. Runyon, and J. A. Fuller, "Large multibeam lens antennas for EHF SATCOM," in *MILCOM 88, 21st Century Military Communications - What's Possible?'. Conference record. Military Communications Conference*, San Diego, CA, USA, 1988.

[12] M. Simon, J. Omura, R. Scholtz, and B. Levitt, *Spread Spectrum Communications Handbook*, The McGraw-Hill Companies, Inc., 1994.

[13] V. Bezruk, "Methods of random signals recognition," in *2006 International Conference - Modern Problems of Radio Engineering, Telecommunications, and Computer Science*, Lviv, UKraine, 2007.

[14] Q. Wen, "An overview of the study of the complexity of the complex electromagnetic environments," in *2015 8th International Symposium on Computational Intelligence and Design (ISCID)*, Hangzhou, China, 2015.

[15] Q. Liu, X. Zhai, Z. Bao, Y. Liu, and Y. Wang, "Electromagnetic compatibility design of a certain information system command vehicle in complex electromagnetic environment," *Engineering*, vol. 576, pp. 707–713, 2020.

[16] F. Yang, Z. Dong, and X. Duan, "Research on computation and simulation technology of battlefield complex electromagnetic environment," *IOP Conference Series Materials Science and Engineering*, vol. 635, no. 1, article 012018, 2019.

[17] X. Li, Z. Nan, S. Yi, and F. R. Yu, "Interference alignment based on antenna selection with imperfect channel state information in cognitive radio networks," *IEEE Transactions on Vehicular Technology*, vol. 65, no. 7, pp. 5497–5511, 2016.

[18] B. Zhao, L. Xin, J. Liu, and Q. Ding, "Research on narrowband interference suppression and diversity characteristics in fast frequency-hopping communication systems," *International*

Journal of Future Generation Communication and Networking, vol. 9, no. 4, pp. 315–322, 2016.

[19] S. Dean, A. A. Khuder, and M. N. Abdullah, "Comparison and investigation of hopping rate estimation processes," in *International Conference on Information and Communication Technologies: from Theory to Applications*, Damascus, Syria, 2008.

[20] D. Peng, T. Peng, X. Tang, and X. Niu, "A class of optimal frequency hopping sequences based upon the theory of power residues," in *Sequences and Their Applications - SETA 2008, 5th International Conference*, Lexington, KY, USA, September 2008.

[21] X. U. Shanding, X. W. Cao, and X. U. Guangkui, "A Class of Frequency-Hopping Sequences Set with a Multiple of Prime Number Length," *Acta Electronica Sinica*, no. 10, pp. 1930–1935, 2015.

[22] J. Wang, X. Yang, and X. Peng, "A linear method for TDOA estimation of frequency-hopping signal," in *Wireless Communications, Networking and Mobile Computing (WiCOM), 2012 8th International Conference*, Shanghai, China, 2012.

[23] J. T. Guo, "Time-frequency analysis of frequency hopping signals based on particle swarm optimization," *Applied Mechanics and Materials*, vol. 195, pp. 265–269, 2012.